CODEN: JASMAN

The Journal of the Acoustical Society of America

ISSN: 0001-4966

Vol. 117, No. 2 February 2005

(Continued)

THE JOURNAL OF THE ACOUSTICAL SOCIETY OF AMERICA VOL. 117, NO. 2, FEBRUARY 2005

CONTENTS—*Continued from preceding page*

(Continued)

THE JOURNAL OF THE ACOUSTICAL SOCIETY OF AMERICA VOL. 117, NO. 2, FEBRUARY 2005

CONTENTS—*Continued from preceding page*

(Continued)

THE JOURNAL OF THE ACOUSTICAL SOCIETY OF AMERICA VOL. 117, NO. 2, FEBRUARY 2005

CONTENTS—*Continued from preceding page*

ACOUSTICAL NEWS—USA

Elaine Moran
Acoustical Society of America, Suite 1NO1, 2 Huntington Quadrangle, Melville, NY 11747-4502

Editor's Note: *Readers of this Journal are encouraged to submit news items on awards, appointments, and other activities about themselves or their colleagues. Deadline dates for news items and notices are 2 months prior to publication.*

Marion S. Dohen selected recipient of the 2004 Stetson Award

Marion S. Dohen

ASA member Marion S. Dohen was selected the recipient of the 2004–05 Raymond H. Stetson Scholarship in Phonetics and Speech Production. Ms. Dohen is a graduate student in the Institute of Spoken Communication at the Institut National Polytechnique de Grenoble. Ms. Dohen received an Undergraduate engineering degree and a M.S. degree from the Institut National Polytechnique due Grenoble. Her current work includes kinematics of speech prosody and audiovisual perception of prosody.

The Stetson Scholarship, which was established in 1998, honors the memory of Professor Raymond H. Stetson, a pioneer investigator in phonetics and speech science. Its purpose is to facilitate the research efforts of promising graduate students and postgraduates. The Scholarship includes a $3000 stipend for one academic year. Past recipients have been Roger Steeve (1999), Elizabeth K. Johnson (2000), Jeffery Jones (2001), Meena Agarwal (2002), and Cynthia Clopper (2003).

Applications for the award are due in March each year. For further information about the award, please contact the Acoustical Society of America, Suite 1 NO 1, 2 Huntington Quadrangle, Melville, NY 11747-4502, Tel: 516-576-2360; Fax: 516-576-2377; e-mail: asa@aip.org; Web: http://asa.aip.org. Application information can also be found on the ASA Home Page at ⟨http://asa.aip.org/fellowships.html⟩.

USA Meetings Calendar

Listed below is a summary of meetings related to acoustics to be held in the U.S. in the near future. The month/year notation refers to the issue in which a complete meeting announcement appeared.

2005

16–20 May	149th Meeting joint with the Canadian Acoustical Association, Vancouver, Canada [Acoustical Society of America, Suite 1 NO 1, 2 Huntington Quadrangle, Melville, NY 11747-4502; Tel.: 516-576-2360; Fax: 516-576-2377; E-mail: asa@aip.org; WWW: http://asa.aip.org].
16–19 May	Society of Automotive Engineering Noise & Vibration Conference, Traverse City, MI [Patti Kreh, SAE International, 755 W. Big Beaver Rd., Ste. 1600, Troy, MI 48084; Tel.: 248-273-2474; E-mail: pkreh@sae.org].
18–22 July	17th International Symposium on Nonlinear Acoustics, State College, PA [Anthony Atchley, The Pennsylvania State University, 217 Applied Research Lab Building, University Park, PA 16802; Tel.: 814-865-6364; E-mail: ISNA17@outreach.psu.edu; WWW: http://www.outreach.psu.edu/c&i/isna17/].
17–21 October	150th Meeting joint with Noise-Con, Minneapolis, Minnesota [Acoustical Society of America, Suite 1NO1, 2 Huntington Quadrangle, Melville, NY 11747-4502; Tel.: 516-576-2360; Fax: 516-576-2377; E-mail: asa@aip.org; WWW: http://asa.aip.org].

Cumulative Indexes to the Journal of the Acoustical Society of America

Ordering information: Orders must be paid by check or money order in U.S. funds drawn on a U.S. bank or by Mastercard, Visa, or American Express credit cards. Send orders to Circulation and Fulfillment Division, American Institute of Physics, Suite 1 NO 1, 2 Huntington Quadrangle, Melville, NY 11747-4502; Tel.: 516-576-2270. Non-U.S. orders add $11 per index.

Some indexes are out of print as noted below.

Volumes 1–10, 1929–1938: JASA, and Contemporary Literature, 1937–1939. Classified by subject and indexed by author. Pp. 131. Price: $5 to members; $ to nonmembers.

Volumes 11–20, 1939–1948: JASA, Contemporary Literature and Patents. Classified by subject and indexed by author and inventor. Pp. 395. Out of print.

Volumes 21–30, 1949–1958: JASA, Contemporary Literature and Patents. Classified by subject and indexed by author and inventor. Pp. 952. Price: $20 to members; $75 to nonmembers.

Volumes 31–35, 1959–1963: JASA, Contemporary Literature and Patents. Classified by subject and indexed by author and inventor. Pp. 1140. Price: $20 to members; $90 to nonmembers.

Volumes 36–44, 1964–1968: JASA and Patents. Classified by subject and indexed by author and inventor. Pp. 485. Out of print.

Volumes 36–44, 1964–1968: Contemporary Literature. Classified by subject and indexed by author. Pp. 1060. Out of print.

Volumes 45–54, 1969–1973: JASA and Patents. Classified by subject and indexed by author and inventor. Pp. 540. Price: $20 (paperbound); $25 to members $25 (clothbound); $60 to nonmembers (clothbound).

Volumes 55–64, 1974–1978: JASA and Patents. Classified by subject and indexed by author and inventor. Pp. 816. Price: $20 (paperbound); $25 to members (clothbound); $60 to nonmembers (clothbound).

Volumes 65–74, 1979–1983: JASA and Patents. Classified by subject and indexed by author and inventor. Pp. 624. Price: $25 to members (paperbound); $75 to nonmembers (clothbound).

Volumes 75–84, 1984–1988: JASA and Patents. Classified by subject and indexed by author and inventor. Pp. 625. Price: $30 to members (paperbound); $80 to nonmembers (clothbound).

Volumes 85–94, 1989–1993: JASA and Patents. Classified by subject and indexed by author and inventor. Pp. 736. Price: $30 to members (paperbound); $80 to nonmembers.

Volumes 95–104, 1994–1998: JASA and Patents. Classified by subject and indexed by author and inventor. Pp. 632, Price: $40 to members (paperbound); $90 to nonmembers (clothbound).

Volumes 105–114, 1999–2003: JASA and Patents. Classified by subject and indexed by author and inventor. Pp. 616, Price: $50 to members; $90 to nonmembers (paperbound).

ACOUSTICAL NEWS—INTERNATIONAL

Walter G. Mayer
Physics Department, Georgetown University, Washington, DC 20057

Honors for Juan A. Gallego-Juárez

Professor Juan A. Gallego-Juárez of the Instituto de Acústica, CSIC Madrid, a Fellow of the Society, was awarded the degree of *Doctor Honoris Causa* by the University of Santiago de Chile. He also received the University's Gold Medal for his many accomplishments referred to in the citation. He was honored because of his internationally recognized research in power ultrasonics and his efforts to find applications of the work to human endeavors. The citation also mentions his efforts toward a better world through science and collaboration. He was also cited for his constant contributions to the University of Santiago de Chile through his selection of young researchers as well as to the formation of new ultrasound laboratories. The ceremony of Investiture took place 31 August 2004.

International Meetings Calendar

Below are announcements of meetings and conferences to be held abroad. Entries preceded by an * are new or updated listings.

March 2005

14–17 **31st Annual Meeting of the German Acoustical Society (DAGA'05)**, Munich, Germany. (Web: daga2005.de)

14–17 **Spring Meeting of the Acoustical Society of Japan**, Koganei, Japan (Acoustical Society of Japan, Nakaura 5th-Bldg., 2-18-20 Sotokanda, Chiyoda-ku, Tokyo 101-0021, Japan; Fax: +81 3 5256 1022; Web: www.asj.gr.jp/index-en.html)

21–22 **Sonar Transducers and Numerical Modelling in Underwater Acoustics**, Teddington, UK (Fax: +44 1727 850553; Web: www.npl.co.uk/acoustics/events/ioaconference2005)

April 2005

18–21 **International Conference on Emerging Technologies of Noise and Vibration Analysis and Control**, Saint Raphaël, France (Fax: +33 4 72 43 87 12; e-mail: goran.pavic@insa-lyon.fr)

May 2005

16–20 **149th Meeting of the Acoustical Society of America**, Vancouver, British Columbia, Canada (ASA, Suite 1NO1, 2 Huntington Quadrangle, Melville, NY 11747-4502 USA; Fax: +1 516 576 2377; Web: asa.aip.org)

June 2005

1–3 ***1st International Symposium on Advanced Technology of Vibration and Sound**, Hiroshima, Japan (Web: dezima.ike.tottori-u.ac.jp/vstech2005)

20–23 **IEEE Oceans05 Europe**, Brest, France (ENST Bretagne—Technopôle Brest Iroise, 29238 Brest Cedex, France; Fax: +33 229 00 1098; Web: www.oceans05europe.org)

23–24 **2nd Congress of the Alps-Adria Acoustical Association (AAAA2005)**, Opatija, Croatia (Web: had.zea.fer.hr)

28–1 **International Conference on Underwater Acoustic Measurements: Technologies and Results**, Heraklion, Crete, Greece (Web: UAmeasurements2005.iacm.forth.gr)

July 2005

4–8 **Turkish International Conference on Acoustics 2005: New Concepts for Harbor Protection, Littoral Security, and Underwater Acoustic Communications**, Istanbul, Turkey (Web: www.tica05.org/tica05)

11–14 ***12th International Congress on Sound and Vibration**, Lisbon, Portugal (Web: www.icsv12.ist.utl.pt)

August 2005

6–10 **Inter-Noise**, Rio de Janeiro, Brazil (Web: www.internoise2005.ufsc.br)

28–2 **EAA Forum Acusticum Budapest 2005**, Budapest, Hungary (I. Bába, OPAKFI, Fö u. 68, Budapest 1027, Hungary; Fax: +36 1 202 0452; Web: www.fa2005.org)

28–1 ***World Congress on Ultrasonics Merged with Ultrasonic International (WCU/UI'05)**, Beijing, China (Secretariat of WCU 2005, Institute of Acoustics, Chinese Academy of Sciences, P.O. Box 2712 Beijing, 100080 China; Fax: +86 10 62553898; Web: www.ioa.ac.cn/wcu-ui-05)

September 2005

4–8 **9th Eurospeech Conference (EUROSPEECH'2005)**, Lisbon, Portugal (Fax: +351 213145843; Web: www.interspeech2005.org)

5–9 **Boundary Influences in High Frequency, Shallow Water Acoustics**, Bath, UK (Web: acoustics2005.ac.uk)

18–21 ***IEEE International Ultrasonics Symposium**, Rotterdam, The Netherlands (Web: www.ieee-uffc.org)

20–22 ***International Symposium on Environmental Vibrations**, Okayama, Japan (Web: isev2005.civil.okayama-u.ac.jp)

27–29 **Autumn Meeting of the Acoustical Society of Japan**, Sendai, Japan (Acoustical Society of Japan, Nakaura 5th-Bldg., 2-18-20 Sotokanda, Chiyoda-ku, Tokyo 101-0021, Japan; Fax: +81 3 5256 1022; Web: www.asj.gr.jp/index-en.html)

October 2005

12–14 ***Acoustics Week in Canada**, London, Ontario, Canada (Web: caa-aca.ca)

19–21 **36th Spanish Congress on Acoustics Joint with 2005 Iberian Meeting on Acoustics**, Terrassa, Barcelona, Spain (Sociedad Española de Acústica, Serrano 114, 28006 Madrid, Spain; Fax: +34 914 117 651; Web: www.ia.csic.es/sea/index.html)

25–26 ***Autumn Conference 2005 of the UK Institute of Acoustics**, Oxford, UK (Web: www.ioa.org.uk)

November 2005

4–5 ***Reproduced Sound 21**, Oxford, UK (Web: www.ioa.org.uk)

June 2006

05–06 **6th European Conference on Noise Control (EURONOISE2006)**, Tampere, Finland (Fax: +358 9 7206 4711; Web: www.acoustics.hut.fi/asf)

26–28 **9th Western Pacific Acoustics Conference (WESPAC 9)**, Seoul, Korea (Web: www.wespac9.org)

 0001-4966/2005/117(2)/467/2/$20.00

July 2006
3–7 *__13th International Congress on Sound and Vibration (ICSV13)__, Vienna, Austria (Web: info.tuwienac.at/icsv13)

September 2006
13–15 *__Autumn Meeting of the Acoustical Society of Japan__, Kanazawa, Japan (Acoustical Society of Japan, Nakaura 5th-Bldg., 2-18-20 Sotokanda, Chiyoda-ku, Tokyo 101-0021, Japan; Fax: +81 3 5256 1022; Web: www.asj.gr.jp/index-en.html)

July 2007
9–12 **14th International Congress on Sound and Vibration (ICSV14)**, Cairns, Australia (e-mail: n.kessissoglou@unsw.edu.au)

August 2007
27–31 *__Interspeech 2007__ Antwerp, Belgium (e-mail: conf@isca-speech.org)

September 2007
2–7 **19th International Congress on Acoustics (ICA2007)**, Madrid, Spain (SEA, Serrano 144, 28006 Madrid, Spain; Web: www.ica2007madrid.org)
9–12 **ICA Satellite Symposium on Musical Acoustics (ISMA2007)**, Barcelona, Spain (SEA, Serano 144, 28006 Madrid, Spain; Web: www.ica2007madrid.org)

June 2008
23–27 **Joint Meeting of European Acoustical Association (EAA), Acoustical Society of America (ASA), and Acoustical Society of France (SFA)**, Paris, France (e-mail: phillipe.blanc-benon@ec-lyon.fr)

July 2008
28–1 *__9th International Congress on Noise as a Public Health Problem__, Mashantucket, Pequot Tribal Nation (ICBEN 9, P.O. Box 1609, Groton CT 06340-1609, USA: Web: www.icben.org)

Preliminary Announcements

May 2006
15–19 *__IEEE International Conference on Acoustics, Speech, and Signal Processing__, Toulouse, France.

August 2010
TBA *__20th International Congress on Acoustics (ICA2010)__, Sydney, Australia (Web: www.acoustics.asn.au)

REVIEWS OF ACOUSTICAL PATENTS

Lloyd Rice
11222 Flatiron Drive, Lafayette, Colorado 80026

The purpose of these acoustical patent reviews is to provide enough information for a Journal reader to decide whether to seek more information from the patent itself. Any opinions expressed here are those of reviewers as individuals and are not legal opinions. Printed copies of United States Patents may be ordered at $3.00 each from the Commissioner of Patents and Trademarks, Washington, DC 20231. Patents are available via the Internet at http://www.uspto.gov.

Reviewers for this issue:

GEORGE L. AUGSPURGER, *Perception, Incorporated, Box 39536, Los Angeles, California 90039*
JOHN M. EARGLE, *JME Consulting Corporation, 7034 Macapa Drive, Los Angeles, California 90068*
DAVID PREVES, *Starkey Laboratories, 6600 Washington Ave. S., Eden Prairie, Minnesota 55344*
DANIEL R. RAICHEL, *2727 Moore Lane, Fort Collins, Colorado 80526*
CARL J. ROSENBERG, *Acentech, Incorporated, 33 Moulton Street, Cambridge, Massachusetts 02138*
NEIL A. SHAW, *Menlo Scientific Acoustics, Inc., Post Office Box 1610, Topanga, California 90290*
WILLIAM THOMPSON, JR., *Pennsylvania State University, University Park, Pennsylvania 16802*
ROBERT C. WAAG, *University of Rochester, Department of Electrical and Computer Engineering, Rochester, New York 14627*

6,795,557

43.20.Ks SOUND REPRODUCTION EQUIPMENT AND METHOD FOR REDUCING THE LEVEL OF ACOUSTICAL REFLECTIONS IN A ROOM

Aki Mäkivirta and Ari Varla, assignors to Genelec Oy
21 September 2004 (Class 381/66); filed in Finland 17 June 1998

Standing waves are a problem in small rooms. In small listening rooms, such as recording studios, standing waves are usually caused by the introduction of low-frequency sound energy by one or more loudspeakers. In this patent, standing waves are described as low-frequency acoustic reflections. The invention proposes a solution that uses one or more loudspeakers in room **102** to provide for the desired cancellation of, or at least a reduction in, standing waves due to the sound emitted in the longitudinal direction (for this figure) from loudspeaker **2**. The signal used to drive loudspeaker **3** is the same as presented to loudspeaker **2**, but it is low-pass filtered, delayed, scaled, and inverted. The signal chain for loudspeaker **3**

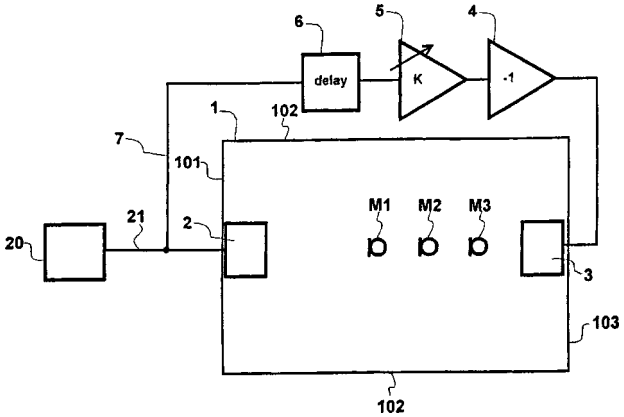

can be initially tuned by using microphones **M1**, **M2**, and **M3**. The patent states that, if the program and cancellation loudspeakers are the same, the tuning is simpler and easier to accomplish. By using loudspeakers on the side wall, and presumably the ceiling, other ''low-frequency acoustic reflections'' in these axes can be similarly attenuated. And, if you are a loudspeaker manufacturer, you get to sell not only the program loudspeakers but also the cancellation loudspeakers and the cancellation signal processing unit. A description of the prior art is presented that provides the reader with a brief introduction to some of the ways of using electroacoustic means to reduce standing-wave effects in a room.—NAS

6,782,732

43.20.Ye METHOD FOR NON-DESTRUCTIVE STRESS WAVE TESTING OF WOOD

Yan-San Huang and Shin-Shin Chen, assignors to Taiwan Forestry Research Institute
31 August 2004 (Class 73/12.07); filed 10 February 2003

When dealing with natural materials, the physical characteristics of the material can vary from lot to lot and even from sample to sample. The natural material under investigation here is wood. In order to evaluate the characteristics of a sample **S**, the specimen under test is placed on sensor **1**, which is an accelerometer with up to three orthogonal sensing components. By striking the specimen with a striking device **2**, which can be a hammer, a compression pulse wave develops in the sample. These waves are sensed

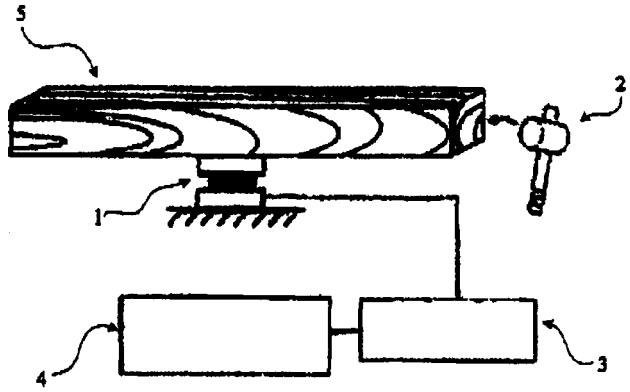

by the transducer **1**, the output of which is processed by device **3**, which may be a charge amplifier, whose output is then analyzed by device **4**, which may be a FFT analyzer. One supposes that many samples are tested to build up the large library of transforms for reference to determine the fundamental frequency, which one assumes is also initially found using other methods. The patent states that, from the fundamental frequency, one can deduce the speed of sound and dynamic modulus of elasticity for the sample under test. One also assumes that the hammer blow is made in a way that is fairly repeatable, of known force and duration. The prior art referenced appears to have used a microphone for the sensing transducer.—NAS

6,782,970

43.20.Ye ACOUSTIC SOURCE USING A SHAFTLESS ELECTRICAL HAMMER

Chung Chang, assignor to Schlumberger Technology Corporation
31 August 2004 (Class 181/101); filed 25 April 2002

Many acoustic measurements rely on a hammer, sometimes with suitable accelerometer attached, to excite a substrate while simultaneously measuring the vibration of the substrate using other accelerometers. This patent replaces the hammer with a magnetic metal mass that is accelerated within a solenoid to strike and excite by impact formations around a borehole. The patent describes how Hertzian contact theory can be used to characterize the impact. A shaftless acoustic source contains bullet **4** which is accelerated by

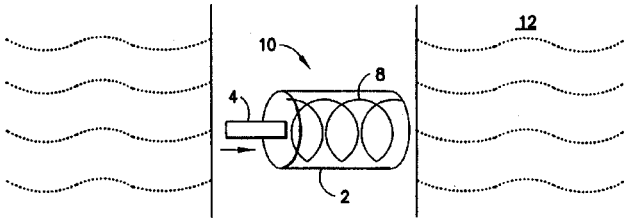

coil **8** in solenoid **2** when a current pulse is applied to the coil. The pulse is such that it stops when the bullet reaches the middle of the coil as the magnetic field is uniform and changes sign at the middle of the coil. A means of retracting the bullet is also described to prevent potential loss of the bullet. The patent maintains that forces between 3000 and 5000 pounds with contact times between 100 and 300 μs can be achieved. The patent as issued contains errors in the text and confusion over what may or not be prior art in a figure.—NAS

6,788,796

43.38.Ar DIFFERENTIAL MICROPHONE

Ronald Miles *et al.*, assignors to The Research Foundation of the State University of New York
7 September 2004 (Class 381/357); filed 1 August 2001

A silicon-based, micro-fabricated microphone moving assembly is described that has overall dimensions of about 1 by 2 mm and is about 1 micron thick. Operating in both torsional and transverse modes, it provides both pressure and gradient components, and the output is that of a first-order directional microphone. The inclusion of mass elements on the minuscule structure provides the necessary equalization for flat electrical output. The patent is supported both by detailed drawings and a thorough mathematical exposition.—JME

6,792,123

43.38.Ar ELECTROACOUSTIC TRANSDUCER

Gino Pavlovic, assignor to AKG Acoustics GmbH
14 September 2004 (Class 381/174); filed in Austria 14 February 2001

Small electret microphone elements used in close-talking communications applications are subject to high moisture levels. Normally, the robust design of these elements is sufficient to keep them working, but in extreme cases the accumulation of moisture may cause malfunction. This patent suggests a small resistive heating element, located on the rear of the perforated backplate, as a means of keeping the assembly dry at all times.—JME

6,791,902

43.30.Sf PORTABLE FISH FINDER

Mark Steiner *et al.*, assignors to Techsonic Industries, Incorporated
14 September 2004 (Class 367/99); filed 30 May 2002

This patent describes a portable fish-finding sonar device wherein the visual display unit, the associated electronics, the battery, the cable, and the transducer conveniently store in, or are an integral part of, a compact hand-carryable housing unit.—WT

6,790,180

43.35.Yb APPARATUS, SYSTEMS, AND METHODS FOR MEASURING POWER OUTPUT OF AN ULTRASOUND TRANSDUCER

Shuki Vitek, assignor to Insightec-TxSonics Limited
14 September 2004 (Class 600/438); filed 3 December 2001

This apparatus for measuring the acoustic energy emitted by an ultrasound transducer consists of a container filled with a liquid and a buoyant body floating at a specific level in the liquid. When the ultrasound transducer sends acoustic energy to the buoyant body, the body floats at a different level in the liquid, with the displaced volume directly related to the power of the ultrasound acoustic energy. The float level signal may be directed to a controller for adjusting the power output of the ultrasound transducer.—DRR

6,795,561

43.38.Ar PANEL DRIVE

Graham Bank, assignor to New Transducers Limited
21 September 2004 (Class 381/152); filed in the United Kingdom 8 July 1999

The assignee for this patent holds a large portfolio of patents relating to what are (colloquially) known as distributed mode loudspeakers (DML), although in this patent they are described as bending-wave loudspeakers. Many of these patents describe DMLs (or BWLs) that use discrete transducers (described in the patent as exciters) to excite the flat panel. What if you want to have a DML/BWL and the preferred location for the exciters can't be used since another piece of equipment is in the way or if the panel is in fact transparent? Thus, the present patent. (The patent admits that it is difficult to make conventional exciters transparent.) The patent states that by

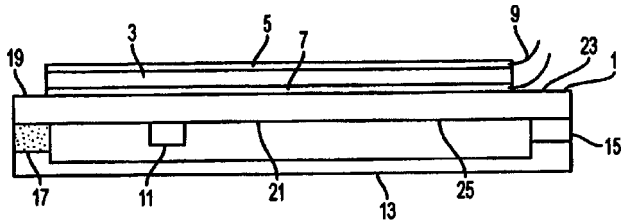

using a thin film that can change shape when an electric signal is applied, and by laminating or gluing the film to both sides of a flat panel substrate, the flat panel can be excited. An important aspect of the invention is how a reaction mass is implemented, which can be a mass **11** attached to the panel **1** or simply by clamping the edge(s) of the panel. An example of a 150 $\times$135-mm-sized unit is described where each part used in the embodiment is listed by manufacturer and model number. A sample frequency plot is provided for another embodiment. The sensitivity, efficiency, and other performance parameters, including what happens with larger panels, are not discussed.—NAS

6,795,719

43.38.Ar MICROPHONE ASSEMBLY FOR A PORTABLE TELEPHONE WITH A FOLDABLE FLAP ELEMENT

Seiji Miyashita *et al.*, assignors to Matsushita Electric Industrial Company, Limited
21 September 2004 (Class 455/575.3); filed in Japan 8 July 1997

This is a continuation of United States Patent Application Serial Number 09/110514, filed 6 July 1998. It essentially describes a variation in the standard jacket or sheath in which virtually all cellphones are carried. The abstract says it all: ''A built-in microphone is provided in a flap hinged to a body in a closable manner. Sound-collection holes are formed in interior and exterior flaps of the flap for collecting sound into the microphone. Even when the flap is in either a closed state or an open state, communication becomes feasible.''—JME

6,788,791

43.38.Hz DELAY NETWORK MICROPHONES WITH HARMONIC NESTING

Steven S. Smith *et al.*, assignors to Shure Incorporated
7 September 2004 (Class 381/92); filed 20 December 2002

The patent describes a composite microphone made up of a number of octave-wide sections. Each section contains a pressure element which is fed through a number of small tubes whose open ends are appropriately arrayed in the intended pickup location. There are as many of these assemblies as there are octaves in the transmission path, and the physical spacing of the array tube openings is scaled appropriately for each octave. The individual

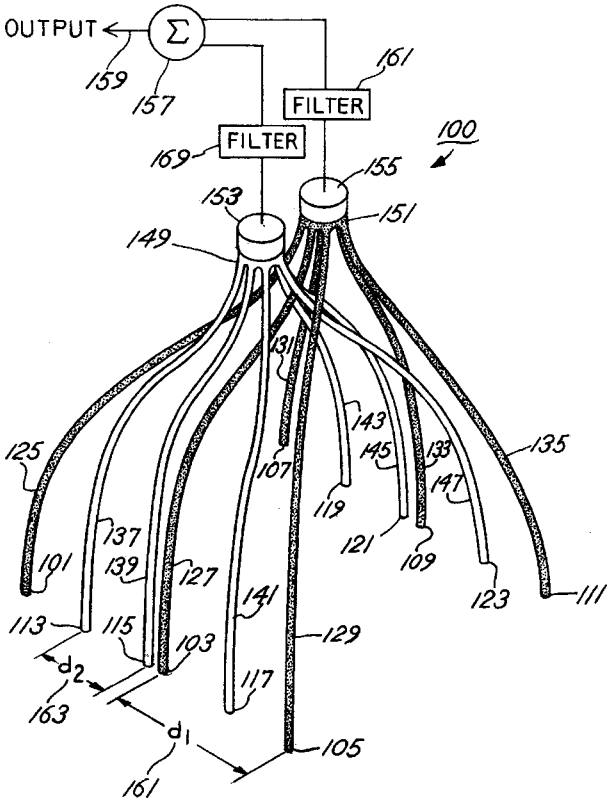

pickup elements are bandpass filtered and summed to produce an overall wideband pickup pattern that is fairly uniform over the operating frequency range. One application of the system is in an automobile, where the array tube openings are placed around the periphery of a rear-view mirror, creating a net pickup pattern that is clearly in line with the driver and useful for hands-free communication.—JME

6,795,558

43.38.Hz MICROPHONE ARRAY APPARATUS

Naoshi Matsuo, assignor to Fujitsu Limited
21 September 2004 (Class 381/92); filed in Japan 26 June 1997

This is yet another entry in the area of complex systems that, among other features, combines video and audio pickup, both coordinated as an aid to hands-free operation of conferencing systems. The patent has 22 figures, is just over 30 pages, and reads like a thesis. Its single claim takes up only 2 inches of the final column of text. It seems to this reviewer that, more than anything else, the intent of the patent is to stake out new territory in filter application than to describe an actual working system.—JME

6,778,675

43.38.Ja SPEAKER DEVICE

Yoshito Maruo, Sakado-ski, Saitama, Japan
17 August 2004 (Class 381/335); filed in Japan 22 January 2001

A favorite approach to high-end loudspeaker design is a group of bandlimited transducers pointing in various directions. With enough tweak-

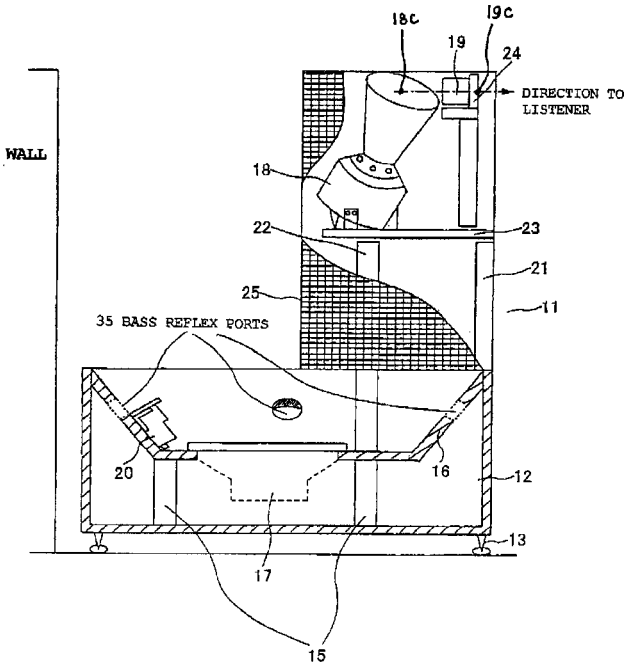

ing, good sound quality can be achieved. This Japanese inventor envisions a bowl-shaped woofer cabinet **12** sitting on spikes **13**. High-frequency transducers **18** and **19** are located above in a fin-shaped spire.—GLA

6,769,509

43.38.Ja POLE SPEAKER

Ronald Paul Harwood, Farmington Hills, Michigan
3 August 2004 (Class 181/199); filed 19 December 2002

Audio inventors seem to be fascinated with the idea of combining loudspeakers with lighting instruments. In this case, the mounting flange **24** of a street light pole is spaced above concrete base **28** to provide a slot for sound to emerge through grillwork **36**. A mounting plate **14** supports loudspeaker **16** and resonating chamber **18**, including tubular port **20** and sound

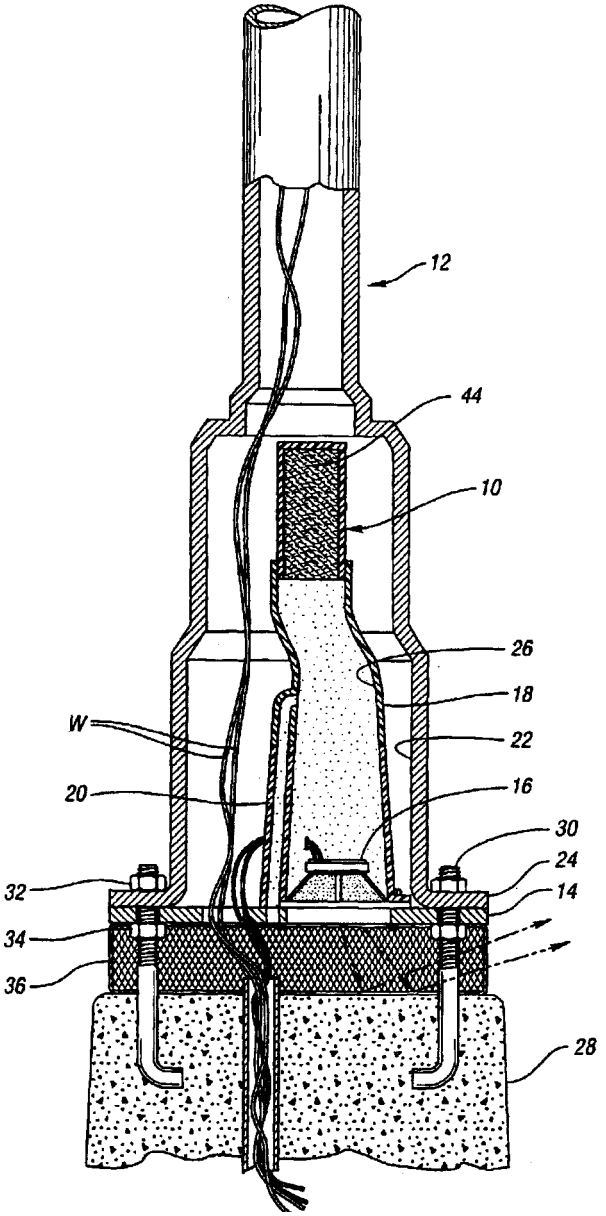

damping material **44**. The speaker module is composed of several parts that can be inserted through an existing light pole's access opening and assembled inside. The arrangement seems better suited to decorative area lights than commercial street lights, but seems awkward even in this application.—GLA

6,779,627

43.38.Ja FLAT PANEL SOUND RADIATOR WITH FIRE PROTECTIVE BACK BOX

William E. Beakes *et al.*, assignors to AWI Licensing Company
24 August 2004 (Class 181/150); filed 11 September 2002

A flat panel loudspeaker can be disguised as a lay-in ceiling tile. In this application, its rear surface is exposed to the plenum space and may not meet fire code requirements. A conventional back box large enough to maintain good low-frequency response would be unwieldy and expensive. Instead, the inventors suggest that large cutouts **33** in a shallow back box **28**

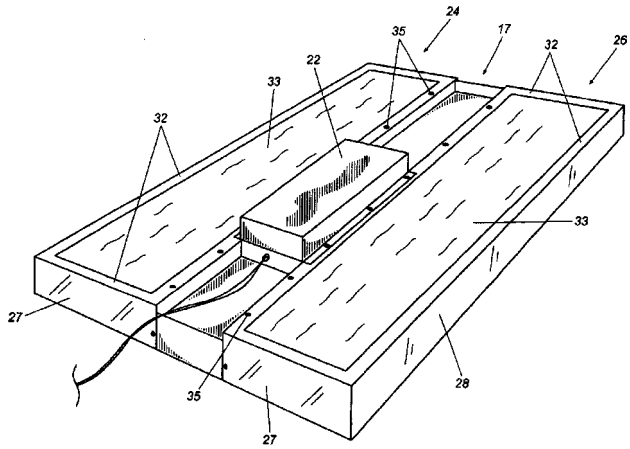

be fitted with compressed fiberglass board. The acoustic effects of cavity size vs damping were tested subjectively to demonstrate that flame spread requirements can be met without compromising performance. It might be even easier to use fiberglass board for the entire back box, but that is known prior art.—GLA

6,778,676

43.38.Kb ACOUSTIC TRANSMISSION CONNECTION, HEADSET WITH ACOUSTIC TRANSMISSION CONNECTION, AND USES OF THE ACOUSTIC TRANSMISSION CONNECTION

Torben Groth and Peter Møller, assignors to GN Netcom A/S
17 August 2004 (Class 381/382); filed in Denmark 25 May 2000

Although the patent title refers to a headset, the invention could be used with any kind of sound pickup probe in which a tube conveys energy from an acoustic source to a microphone. The novel feature is a conical ''acoustic impedance matching'' device that couples the microphone to the tube, thus smoothing response by damping standing waves. The patent also describes a unidirectional two-tube variant.—GLA

6,774,769

43.38.Si VIBRATING ALERT DEVICE

Kazunari Okada, assignor to Sanyo Seimitsu Corporation; Sanyo Electric Company, Limited
10 August 2004 (Class 340/407.1); filed in Japan 23 May 2001

Imagine that you get behind the wheel of your automobile while carrying your cellular phone in its vibrating mode. You are momentarily startled by an incoming call, causing you to nudge a pedestrian who

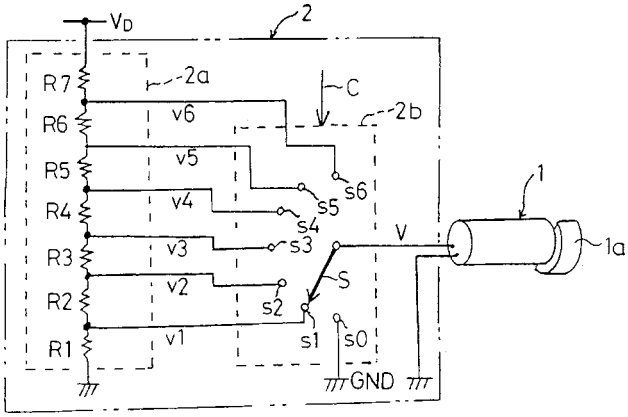

promptly sues you. You, in turn, sue the phone manufacturer. To avoid this scenario, Sanyo proposes to gradually increase the voltage to the vibration

motor in a series of discrete steps, thus avoiding both wasted electrical power and possible legal liability.—GLA

6,775,390

43.38.Si HEADSET WITH MOVABLE EARPHONES

Peter Schmidt *et al.*, assignors to Hello Direct, Incorporated
10 August 2004 (Class 381/371); filed 24 December 2001

The title of this patent does not suggest anything out of the ordinary, which may be why more than 100 prior patents are cited as references. The exploded view shows a conventional speaker element **40** which is fitted to

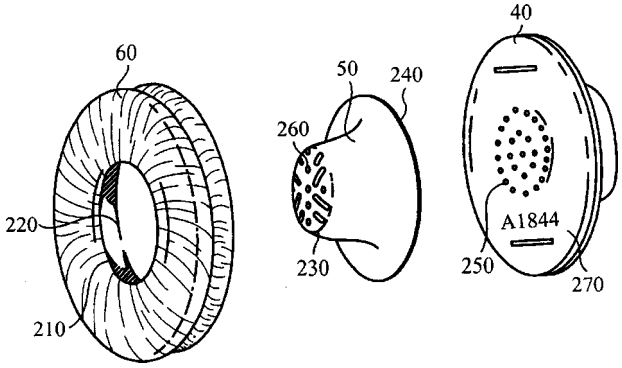

"sound funneling device" **50**. The shape of this device supports cushion **60** while conducting sound to the entrance of the ear canal. The goal is to provide a comfortable, tight seal as near the ear canal as possible.—GLA

6,791,519

43.38.Si SOUND AND VISION SYSTEM

Ronaldus Maria Aarts and Mark Thomas Johnson, assignors to Koninklijke Philips Electronics N.V.
14 September 2004 (Class 345/87); filed in the European Patent Office 4 April 2001

As cell phones and other personal electronic devices get smaller and smaller, and the need to squeeze even more costs from the bill of materials becomes more and more important, manufacturers of these devices are hard at work to have one device do the work of several. This patent describes how the visual display device on a cell phone and similar equipment can also be fabricated to act as the audio transducer. The patent for this sound and vision system states that the frequencies of interest for the visual display are in the 50–60-Hz range for the refresh rate and 100 kHz and above for the data rate, both of which fall outside the range of interest for the audio signal. The patent says that for speech the frequency range of interest is about 300 to 3400 Hz (this device appears to be headed for telephones). Embodiments that use plasma and LCD technologies are described in what is another tube of paint in the assignee's paintbox of patents for devices of this sort.—NAS

6,772,024

43.38.Vk METHOD, APPARATUS AND STORAGE MEDIUM FOR ADJUSTING THE PHASE OF SOUND FROM MULTIPLE SPEAKER UNITS

Kazuo Fujii, assignor to International Business Machines Corporation
3 August 2004 (Class 700/94); filed in Japan 6 January 2000

Computer games can make good use of multichannel surround sound. But, suppose that your computer was purchased with only two front speakers and you later purchase a pair of rear speakers. How do you insure that all four units operate with the same polarity? To a computer programmer the answer is obvious: plug in a test microphone and run a simple little program to sequentially sample the wavefronts produced by a 1-kHz signal source and then calculate the resulting phase differences in degrees. Assuming that all of the speakers are equidistant from the microphone, the method shown can actually work, but it is a little like estimating the size of a cattle herd by counting the legs and dividing by four.—GLA

6,786,707

43.40.Tm STRUCTURE FOR REDUCING NOISE AND VIBRATION OF SCROLL COMPRESSOR

Young Gi Kim, assignor to LG Electronics Incorporated
7 September 2004 (Class 417/363); filed in the Republic of Korea 27 July 2001

Scroll compressors can be loud and may also transmit vibrations to the supporting structure. In many cases, the noise and vibration can be reduced by enclosing the compressor, and even the device to which it is attached, in a separate enclosure, and by using vibration mounts. The patent does this for you by surrounding the compressor unit with structure **11**, using spring

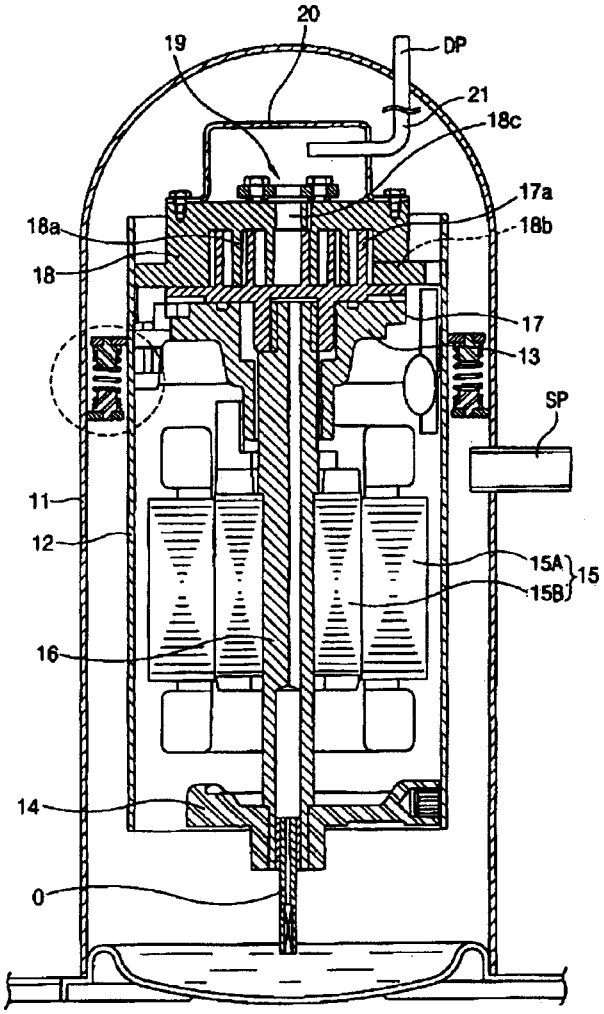

vibration isolator supports (identified by the dotted circle) between inner compressor support **12** and the external shell **11**, using a discharge pipe **21** that has a resilient spiral construction, and providing what appears to be a labyrinth path from the supply pipe **SP**. No data are provided regarding the reduction in noise and vibration, but some mitigation should be provided nonetheless.—NAS

6,786,172

43.40.Tm SHOCK ABSORBING BOAT

Leonard Loffler, Miami, Florida
7 September 2004 (Class 114/363); filed 8 September 2003

This patent describes a small boat designed to reduce the shock and vibration associated with high-speed travel that might be transmitted to those seated within the boat. This isolation is accomplished by pivotally mounting the seating platform at the transom, which is usually subjected to the least amount of up and down motion, and then further supporting this platform with springs and shock absorbers attached between the platform and the hull.—WT

6,792,324

43.50.Ed DEVICE FOR DETERMINING AND CHARACTERIZING NOISES GENERATED BY MASTICATION OF FOOD

Marian Trinkel, Kreuzau, Germany
14 September 2004 (Class 700/94); filed in Germany 13 December 1999

This is a rather amusing device for simulating, measuring, and characterizing noises generated by chewing food. The device features a mastication device and microphones deployed in an enclosure, optimally a dummy head for audio recording. A second set of microphones for sound conducted by solid material, simulating bone conduction, may be provided

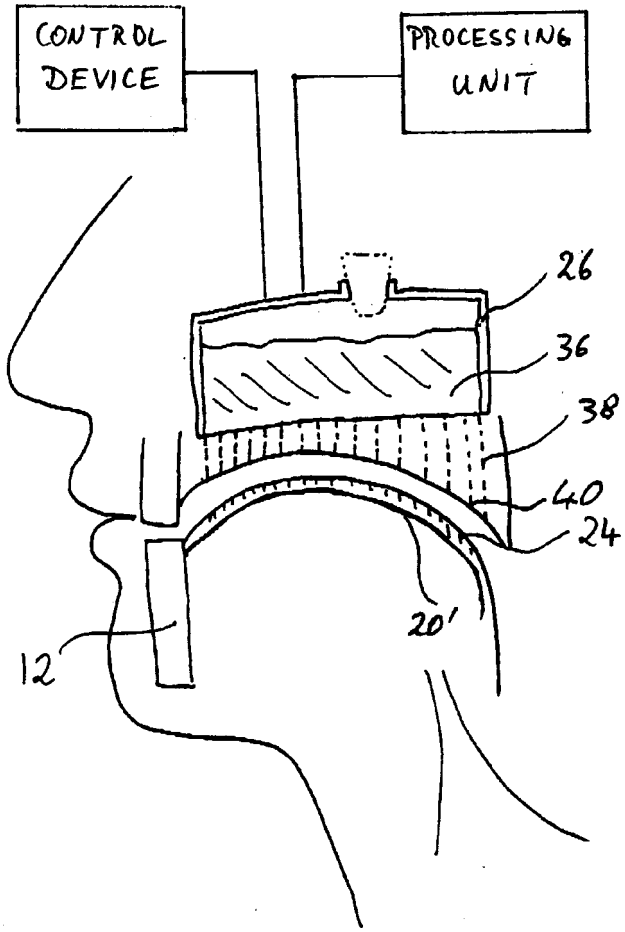

in order to capture a sound as near natural as possible. Since the tongue is active during the chewing process, it is presumably advantageous to simulate the tongue action during the chewing process. The device can be a membrane that is actuated electrically, mechanically, pneumatically, or actuated by a liquid. Salivation also plays a part in affecting the acoustics, so a moistening device is provided for moistening the food.—DRR

6,782,971

43.55.Ev SERVICEABLE ACOUSTIC INTERIORS

Steven Dutton and John Phillips, assignors to ETS-Lindgren, L.P.
31 August 2004 (Class 181/284); filed 23 August 2002

This mechanical holding system enables installation and removal of sound-absorbing panels to a wall by a simple and quick process. The panels can be slipped upward into an engaging upper channel, then shifted downward into a receiving lower channel.—CJR

6,793,037

43.55.Pe STRUCTURED MOLDED PARTS FOR SOUND ABSORPTION

Gerhard Babuke *et al.*, assignors to Fraunhofer-Gesellschaft zur Foerderung der angewandten Forschung e.V.
21 September 2004 (Class 181/293); filed in Germany 17 December 1998

The patent describes preformed, open-cell foam sound-absorptive elements that provide a broad band of sound absorption with significantly less overall depth than other such elements (wedge absorbers). These preformed

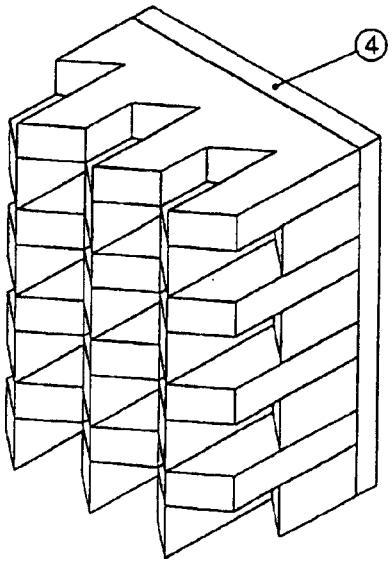

bodies ostensibly accomplish this goal by having a plane base layer of a defined thickness as well as a columnar structure in front of the base layer, and there is a one-sided bevel cut on top of this column.—CJR

6,790,520

43.55.Wk VIBRATION DAMPENING LAMINATE

John Todd *et al.*, assignors to Collins & Aikman Products Company
14 September 2004 (Class 428/318.4); filed 20 July 2000

Here is another variation on a lightweight vibration damping laminate for an automobile interior. The laminate comprises a constraining layer, a viscoelastic adhesive layer, a foam spacing layer, and a pressure-sensitive adhesive layer that is contoured to fit the profile of the panel that is to be soundproofed and vibration damped.—CJR

6,786,860

43.66.Ts HEARING AID DESIGN

Albert A. Maltan *et al.*, assignors to Advanced Bionics Corporation
7 September 2004 (Class 600/25); filed 3 October 2002

A hearing aid module is inserted into a tube located in a tunnel formed in the soft tissue connecting the space behind the pinna of the ear with the ear canal. A remote control allows the wearer to make simple adjustments of volume and frequency response, and the telemetry circuitry facilitates wireless programming from an external programmer.—DAP

6,792,114

43.66.Ts INTEGRATED HEARING AID PERFORMANCE MEASUREMENT AND INITIALIZATION SYSTEM

James Mitchell Kates *et al.*, assignors to GN ReSound A/S
14 September 2004 (Class 381/60); filed 6 October 1999

Hearing aid self-test capability is facilitated by including a test signal generator and a test program in a digital hearing aid. Determining the transfer function of the acoustic feedback path is done by putting the hearing aid

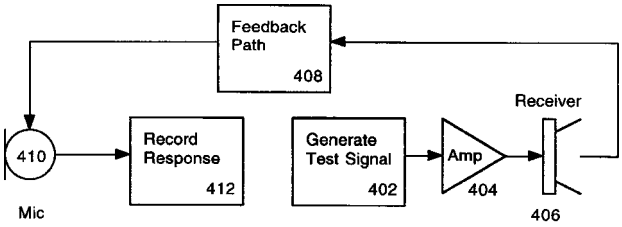

400

into open-loop mode while the hearing aid is being worn, and the microphone transfer function is determined using the DSP as a computer. Parameters in the hearing aid are initialized in accordance with the results of the self-test performance measurements.—DAP

6,794,989

43.66.Ts SPORTS SIGNALLING DEVICE FOR HEARING IMPAIRED PERSONS

Kara Jean Naegely *et al.*, all of Pittsburgh, Pennsylvania
21 September 2004 (Class 340/573.1); filed 19 June 2002

This wireless device is designed to enable a deaf person participating in a field sport to receive instructions. The device includes a transmitter unit which responds to a physical impulse produced by an instructor and transmits an instruction as a wireless output signal. A portable unit adapted to be carried by the hearing-impaired person converts the wireless signal into an instruction in the form of an LED display and/or vibrator action. The receiving unit presumably should be made rugged enough to withstand the rigors of rough play.—DRR

6,795,562

43.66.Ts EAR WAX GUARD FOR AN IN-THE-EAR HEARING AID AND A MEANS FOR USE AT INSERTION AND REMOVAL HEREOF

Finn Gunnersen and Jan Tøpholm, assignors to Widex A/S
21 September 2004 (Class 381/325); filed in Denmark 10 July 1998

A removable wax guard system is described for protecting in-the-ear

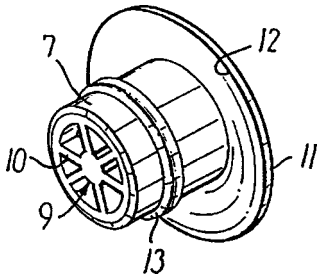

hearing aids. An insertion/extraction tool positions the wax guard in the end of the tube forming the hearing aid sound outlet.—DAP

6,786,873

43.66.Yw PORTABLE HANDHELD HEARING SCREENING DEVICE AND METHOD WITH INTERNET ACCESS AND LINK TO HEARING SCREENING DATABASE

Peter Zoth, Gilching, Germany *et al.*
7 September 2004 (Class 600/559); filed 25 September 2002

A method and device are described for audiological screening of infants and newborns by generating one or more stimuli with an audiological screening device. Acoustic transmitters in each ear canal generate otoacoustic emissions, collect and transmit the otoacoustic emissions and brain-stem response signals, analyze the response signals, and transmit the data to a remote central computer server for further analysis and storage. The server connection is via a built-in or attached modem or global information network.—DRR

6,746,131

43.72.Ar SOUND ACTIVATED LIQUID DISPLAY DEVICE

Steven G. Goldstein and Mark R. Barton, assignors to Steven G. Goldstein
8 June 2004 (Class 362/96); filed 11 February 2002

This is basically a voice-controlled lava lamp. The fluids are described as ''two immiscible liquids of different densities, colors, and viscosities.'' A microphone and audio processor arrangement produce state changes in a

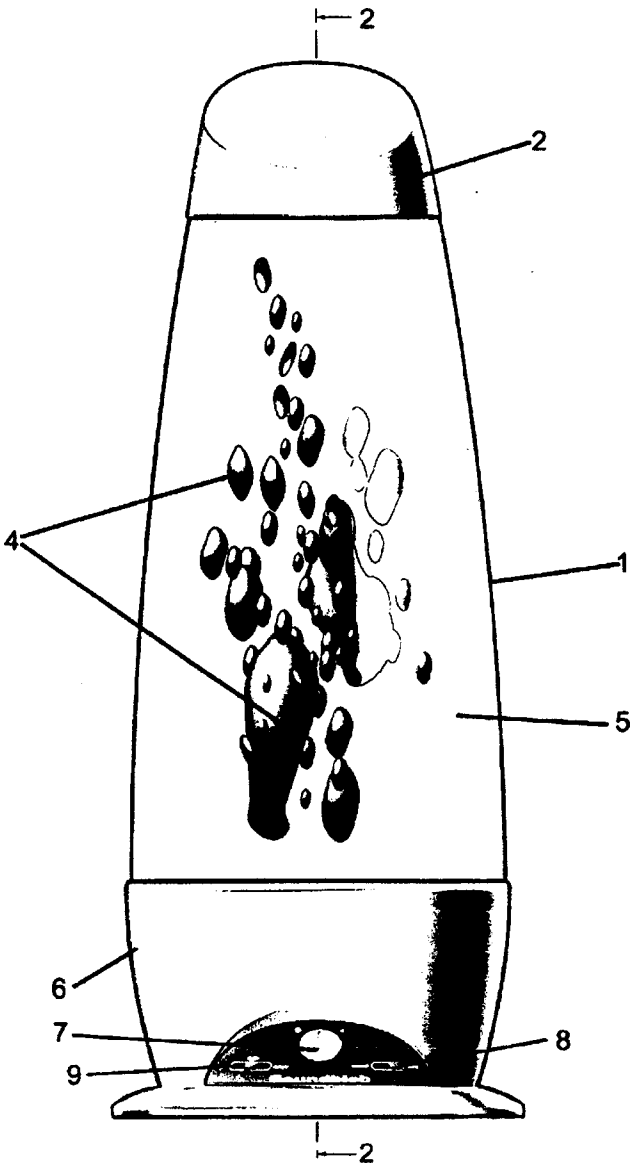

pump controller based on sound level, speech pitch, or other audio patterns. A random number generator adds some of the traditional lava lamp excitement.—DLR

6,748,358

43.72.Ja ELECTRONIC SPEAKING DOCUMENT VIEWER, AUTHORING SYSTEM FOR CREATING AND EDITING ELECTRONIC CONTENTS TO BE REPRODUCED BY THE ELECTRONIC SPEAKING DOCUMENT VIEWER, SEMICONDUCTOR STORAGE CARD AND INFORMATION PROVIDER SERVER

Hiroshi Iwasaki *et al.*, assignors to Kabushiki Kaisha Toshiba
8 June 2004 (Class 704/258); filed in Japan 5 October 1999

This electronic document viewer provides speech output of the content to accompany the visual images. A central feature of the system is that the speech is represented in the form of an intermediate ''phonogramic'' language, which contains speech pitch, accent, and timing information, as well as the katakana glyph graphic information. The intermediate representation may also include sync codes, said to provide an easier mechanism to index the text by content.—DLR

6,748,361

43.72.Ja PERSONAL SPEECH ASSISTANT SUPPORTING A DIALOG MANAGER

Liam David Comerford *et al.*, assignors to International Business Machines Corporation
8 June 2004 (Class 704/275); filed 14 December 1999

Here is another little box to carry around or, as suggested by one of the patent's figures, a box to hold your other little boxes. The idea is more profound. This box would serve as a knowledgeable voice interface to all of your other little boxes, including the VCR, or other household gadgets. It would know how to run all of the other gadgets and would have a sophisticated dialog management system for a more useable voice interaction. But, perhaps most importantly, it would learn your ways and preferences and would quickly adapt to your styles of work and speech. Clearly, in the greater scheme of things, this box has to shrink to become all of the other little boxes.—DLR

6,751,592

43.72.Ja SPEECH SYNTHESIZING APPARATUS, AND RECORDING MEDIUM THAT STORES TEXT-TO-SPEECH CONVERSION PROGRAM AND CAN BE READ MECHANICALLY

Yoshinori Shiga, assignor to Kabushiki Kaisha Toshiba
15 June 2004 (Class 704/258); filed in Japan 12 January 1999

This speech synthesis system, based on, and described with examples from, the Japanese language, appears to be a fairly humdrum text-to-speech system. A notable feature is a system for speaking a particular word or phrase with contrastive emphasis. The phonetic dictionary is provided in three forms, described as ''intelligibility ranks.'' These phonetic dictionaries are constructed following the analysis of human speech produced under varying ''intelligibility'' conditions, such as rate of speaking, etc.—DLR

6,747,566

43.72.Ne VOICE-ACTIVATED REMOTE CONTROL UNIT FOR MULTIPLE ELECTRICAL APPARATUSES

Shaw-Yuan Hou, Taipei, Taiwan, Province of China
8 June 2004 (Class 340/825.69); filed 12 March 2001

This is a voice-controlled universal remote control for use in a home video/audio entertainment center. The extremely short patent says little more than that. There is a brief mention of a way to operate multiple devices simultaneously, and the single claim does cover a sort of angular pattern arrangement of multiple infrared beams.—DLR

6,748,353

43.72.Ne AUTHORING LANGUAGE TRANSLATOR

Edwin C. Iliff, assignor to First Opinion Corporation
8 June 2004 (Class 704/9); filed 8 March 1999

This fairly elaborate system would provide automated access by telephone for medical history, diagnosis, and information requests. Once a caller has been identified, particularly in the case of a diagnostic situation, an immediate appraisal is made of the severity of the problem and the urgency required for further interactions. The argument is made that 90% of patient complaints are limited to the most common 100 conditions and that these conditions can be adequately diagnosed with information obtained solely by access to a thorough medical history. Given these assumptions, extra attention is paid to the acquisition of accurate and current medical histories, which are then updated continuously. Specific commercial voice recognition hardware and software items are cited in the patent.—DLR

6,751,593

43.72.Ne DATA PROCESSING SYSTEM WITH BLOCK ATTRIBUTE-BASED VOCALIZATION MECHANISM

Hideo Tetsumoto, assignor to Fujitsu Limited
15 June 2004 (Class 704/270.1); filed in Japan 30 June 2000

This is a speech recognizer/synthesizer attached to an Internet interface. The recognizer is equipped to convert Internet site descriptions into page access (URL) strings and to download the addressed page. The control software has routines to extract text and certain formatting information from pages of HTML files received from the network. In addition to speaking the displayable content, the synthesizer can also voice certain page layout details, such as font size or text placement on the page.—DLR

6,789,061

43.72.Ne METHOD AND SYSTEM FOR GENERATING SQUEEZED ACOUSTIC MODELS FOR SPECIALIZED SPEECH RECOGNIZER

Volker Fischer *et al.*, assignors to International Business Machines Corporation
7 September 2004 (Class 704/240); filed in the European Patent Office 25 August 1999

A second speech recognizer, tailored to a specific application, is generated automatically from a first speech recognizer. The first recognizer's set of states and probability density functions are utilized to distinguish the application.—DAP

6,792,083

43.72.Ne METHOD AND DEVICE FOR ACTIVATING A VOICE-CONTROLLED FUNCTION IN A MULTI-STATION NETWORK THROUGH USING BOTH SPEAKER-DEPENDENT AND SPEAKER-INDEPENDENT SPEECH RECOGNITION

Franciscus J. L. Dams *et al.*, assignors to Koninklijke Philips Electronics N.V.
14 September 2004 (Class 379/88.01); filed in the European Patent Office 7 October 1997

Speaker-independent speech recognition is first performed on incoming calls to a voice-controlled network. If that speech recognition determination was successful, a template is then assigned to the speech origin and stored so that speaker-dependent recognition can be used in future calls from that source.—DAP

6,795,533

43.72.Ne INTERMEDIATE VOICE AND DTMF DETECTOR DEVICE FOR IMPROVED SPEECH RECOGNITION UTILIZATION AND PENETRATION

Paul Andrew Erb and Dieter Schulz, assignors to Mitel Knowledge Corporation
21 September 2004 (Class 379/88.01); filed 20 August 2002

In order to utilize a speech recognition engine only when it is needed, e.g., for speaking the name of the destination rather than having to dial a phone number, a voice and DTMF detector monitors calls prior to allocating the speech recognition resource. The result is more immediate servicing for required voice-decoding applications without increasing the number of speech recognition engines.—DAP

6,795,534

43.72.Ne DATA RECORDING SYSTEM FOR IP TELEPHONE COMMUNICATION

Tadanori Noguchi, assignor to NEC Corporation
21 September 2004 (Class 379/88.17); filed in Japan 4 September 2000

A data recording system is provided for IP telephony that eliminates

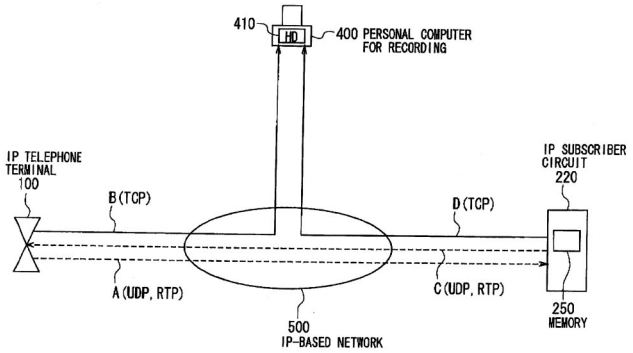

the need to retransmit audio IP packets that are lost during high-traffic periods on the IP-based network.—DAP

6,747,685

43.72.Pf CONFERENCE CALLING

Ronnie Bernard Francis Taib *et al.*, assignors to Motorola, Incorporated
8 June 2004 (Class 348/14.01); filed in the European Patent Office 13 September 2001

This patent presents a scheme for identifying each speaker during a teleconference hookup. As each user joins the conference, a talker identification function analyzes a ''standard portion of speech'' and accepts a ''screen name'' or other ID for the new user. As each person speaks, the speaker's ID appears on other users' displays. None of the technology to do any of this is discussed at all.—DLR

6,783,493

43.80.Qf ULTRASOUND PROBE WITH INTEGRATED ELECTRONICS

Alice M. Chiang *et al.*, assignors to TeraTech Corporation
31 August 2004 (Class 600/437); filed 22 February 2001

This hand-held ultrasound system includes integrated electronics inside an ergonomic housing. The electronic circuitry performs control, beamforming, and transducer drive functions. The circuitry communicates with a host computer via an industry-standard, high-speed serial bus. The ultra-

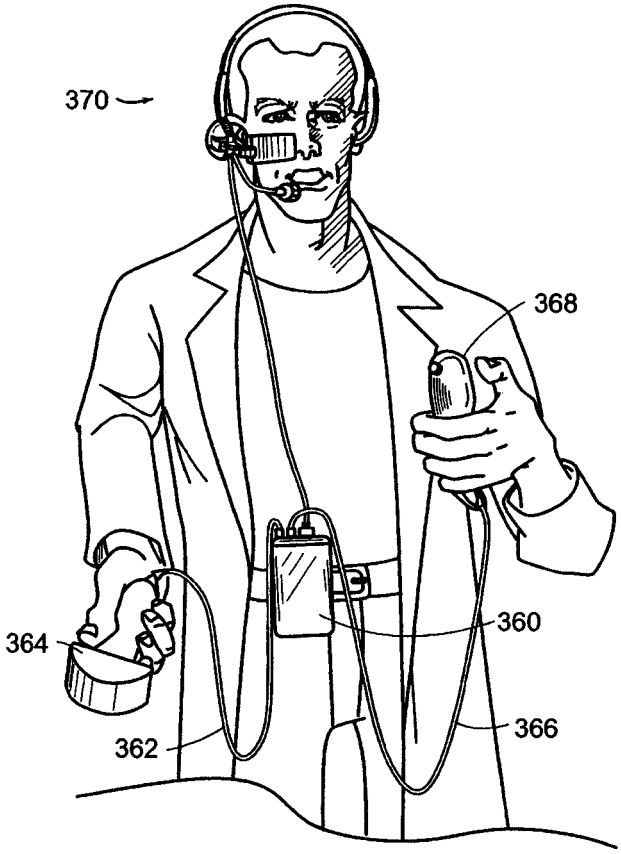

sonic imaging system works on a commercially available computer without specific hardware modifications and is adapted to interface with an external application without modification to the ultrasonic imaging system. Thus, a user can gather ultrasonic data on a fairly standard PC and employ the gathered data without specialized, exotic hardware modifications.—DRR

6,786,868

43.80.Qf ULTRASONIC TOMOGRAPH

Rainer Stotzka *et al.*, assignors to Forschungszentrum Karlsruhe GmbH
7 September 2004 (Class 600/437); filed in Germany 11 October 2000

The high-resolution ultrasonic tomograph described in this patent depends on transmission, scattering, and impulse-echo methods for examination of tissue of the extremities, particularly the female breast and the male reproductive organs. The device consists of a container with an open top and contains ultrasonic transducers arranged along the wall of the container, a coupling medium disposed in the container, and a computer-based control and evaluation unit with a functioning memory. The control and evaluation unit is connected to the ultrasonic transducers in such a manner that the ultrasound signals emitted from at least one transducer form an ultrasonic impulse that is received by all the other transducers in parallel, and is amplified, filtered, and digitized to yield electric signals which are stored in the functioning memory as a data set.—DRR

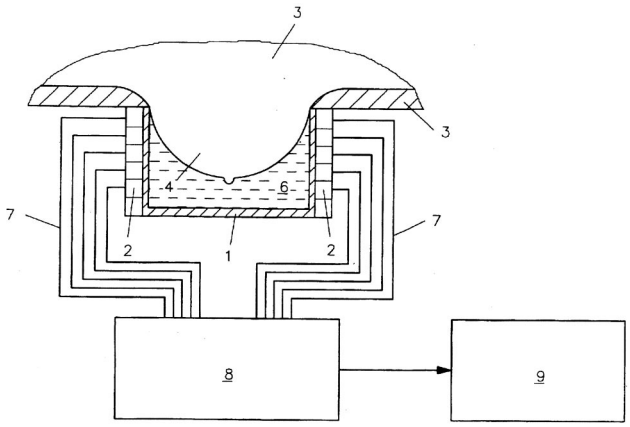

6,790,183

43.80.Qf METHOD AND APPARATUS FOR DISPLAYING BODY SOUNDS AND PERFORMING DIAGNOSIS BASED ON BODY SOUND ANALYSIS

Raymond L. H. Murphy, Wellesley, Massachusetts
14 September 2004 (Class 600/532); filed 21 February 2002

The purpose of this device is to facilitate medical diagnosis on the basis of the recording, reviewing, and analysis of body sounds. It is also intended to generate graphical displays of detected abnormal body sounds, as well as to provide diagnoses based on an analysis of recorded body sounds. The system consists of several transducers placed at various sites around the patient's chest. The microphones are coupled to A/D converters and signal-processing circuitry. A data collection program organizes and formats the data for display or printing. The combinatorial display contains

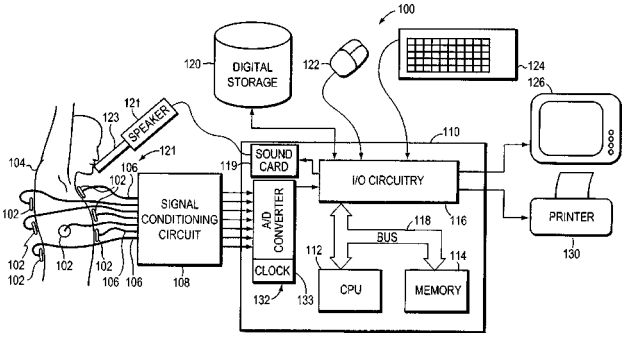

at least two elements. In one element, the data are shown for both inspiration and expiration combined on a time scale. In the other display element, the data for inspiration and expiration are shown individually on another time scale that is time-expanded relative to the first time scale. The system may also include application programs for detecting and classifying abnormal sounds, which may be displayed in a variety of formats to facilitate diagnosis. The system may include an analysis program for comparing the selected criteria corresponding to the detected abnormal sounds with predefined thresholds in order to provide a most probable diagnosis.—DRR

6,790,184

43.80.Qf DEVICE FOR MEDICAL PERCUSSION

Jonathan S. Thierman, assignor to Sure-Shot Medical Device, Incorporated
14 September 2004 (Class 600/553); filed 5 September 2002

This device clips onto the end of a stethoscope to provide additional information during the percussion portion of a physical examination of the

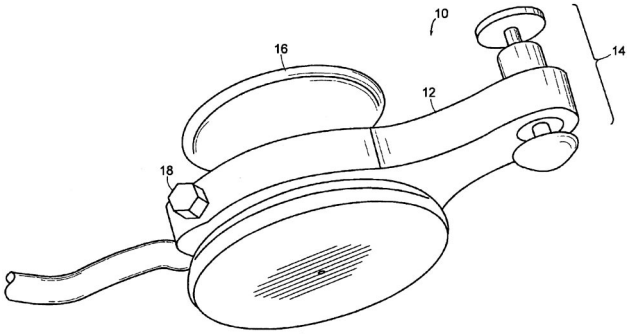

thorax or abdomen. It is essentially a small mechanical ''tapper'' operated by pressing a small plunger with the index finger of the hand holding the stethoscope against the patient's body.—DRR

6,790,187

43.80.Sh SYSTEMS AND METHODS FOR APPLYING ULTRASONIC ENERGY

Todd A. Thompson *et al.*, assignors to TIMI 3 Systems, Incorporated
14 September 2004 (Class 601/2); filed 23 August 2001

This patent covers systems and methods for increasing blood perfusion, e.g., in the treatment of myocardial infarction, strokes, and vascular diseases. The applicator consists of an ultrasound transducer and a chamber containing a pressure-sensitive acoustic coupling medium in acoustic communication with the ultrasound radiation. Operation of the ultrasound transducer yields acoustic energy at a selected intensity level. The system senses

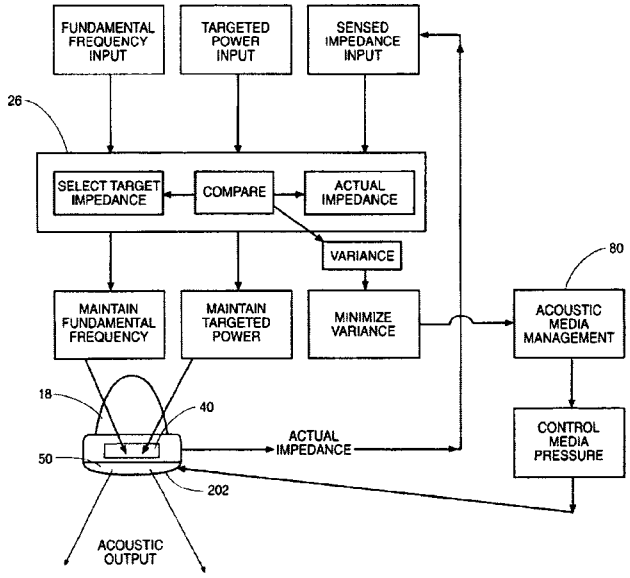

a system parameter and compares it with a preset desired level. Based on the comparison, the pressure within the chamber is varied. In one embodiment, the system parameter is that of impedance. In another embodiment, chamber pressure is varied to sustain an essentially constant output. Yet another embodiment allows the acoustic coupling medium to conduct heat from the ultrasound transducer.—DRR

6,793,635

43.80.Sh DEVICES HAVING DEPLOYABLE ULTRASOUND TRANSDUCERS AND METHOD OF USE OF SAME

Thomas P. Ryan and Alexander J. Sinton, assignors to Ethicon, Incorporated
21 September 2004 (Class 601/2); filed 28 June 2002

This medical device for thermal ablation therapy contains a means for emitting ultrasound energy that heats tissue. Provision is also included for inserting the device and moving the ultrasound emitter. Piezoelectric transducers are securely mounted on carriers which move the emitters. The method for thermal ablation therapy using ultrasound entails positioning an

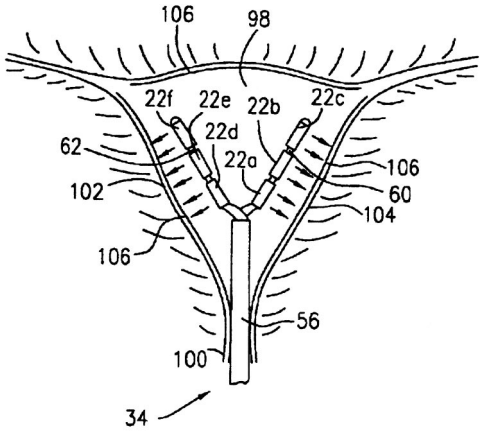

ultrasound device into a deployed position and activating the transducers to emit ultrasound energy for a predetermined period of time. In this configuration, the device can be used to treat menorrhagia, a condition that is characterized by extended or irregular menstrual cycles or excessive amounts of bleeding during these cycles.—DRR

6,783,496

43.80.Vj METHOD AND APPARATUS FOR IMPROVING CONTRAST-TO-TISSUE RATIO IN ULTRASOUND CONTRAST IMAGING WITH SUBHARMONIC IMAGING

Xiaohui Hao and Richard Yun Chiao, assignors to GE Medical Systems Global Technology Company, LLC
31 August 2004 (Class 600/458); filed 1 November 2002

Two pulses are transmitted. The first pulse is centered around a fundamental frequency while the second pulse has a subharmonic frequency based on the fundamental. The two pulses are phase inverted with respect to each other. Echoes received from the first and second pulses are filtered at subharmonic or higher harmonic frequencies to remove tissue response and pass contrast-agent response.—RCW

6,793,626

43.80.Vj ULTRASONIC SCATTERER, ULTRASONIC IMAGING METHOD AND ULTRASONIC IMAGING APPARATUS

Hirohiko Tsuzuki, assignor to Fuji Photo Film Company, Limited
21 September 2004 (Class 600/458); filed in Japan 17 January 2001

Gas-containing particles are employed as scatterers. Imaging is accomplished by first using a transmit waveform of ten or more cycles. After a fixed time, a waveform consisting of less than ten cycles is transmitted. Subharmonic echoes are processed to produce an image.—RCW

6,783,497

43.80.Vj TWO-DIMENSIONAL ULTRASONIC ARRAY WITH ASYMMETRIC APERTURES

Stephen Michael Grenon and Ronald E. Hileman, assignors to Volumetrics Medical Imaging, Incorporated
31 August 2004 (Class 600/459); filed 23 May 2002

This is a sparsely populated array with separate zones for transmitting and receiving. In one form, an inner array with a small effective aperture is

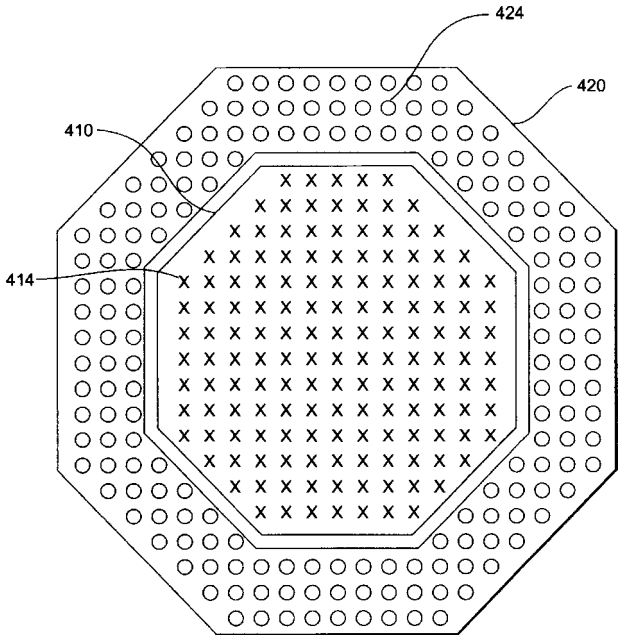

used for transmission, and an outer array with a large effective aperture is used for reception. The combination of asymmetric apertures facilitates use of parallel processing.—RCW

6,790,181

43.80.Vj OVERLAPPED SCANNING FOR MULTI-DIRECTIONAL COMPOUNDING OF ULTRASOUND IMAGES

Anming He Cai and Rickard C. Loftman, assignors to Acuson Corporation

14 September 2004 (Class 600/443); filed 13 September 2002

A compound image is formed from frames of ultrasound echo data acquired with different steering angles. A majority of scan lines for each frame is pointed in the same relative direction and a minority of the scan

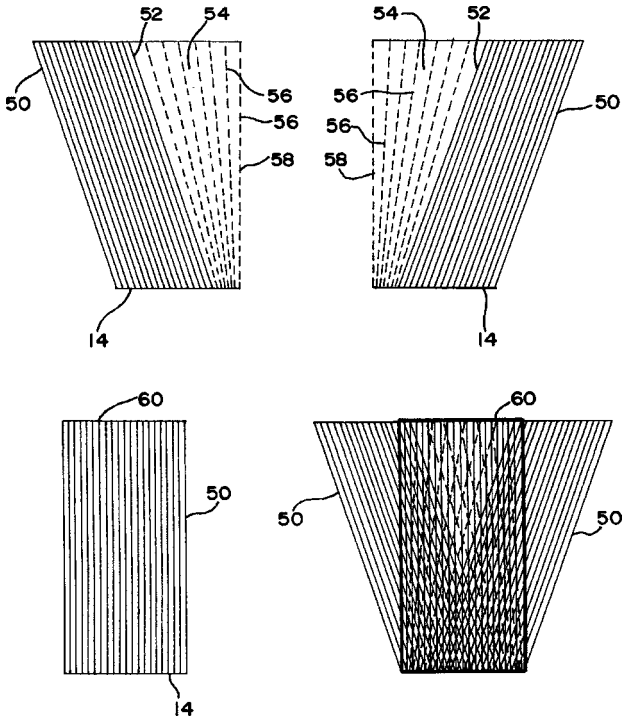

lines is steered at different angles. This realizes benefits of spatial compounding without the need to filter for reduction of scan-line artifacts.—RCW

LETTERS TO THE EDITOR

This Letters section is for publishing (a) brief acoustical research or applied acoustical reports, (b) comments on articles or letters previously published in this Journal, and (c) a reply by the article author to criticism by the Letter author in (b). Extensive reports should be submitted as articles, not in a letter series. Letters are peer-reviewed on the same basis as articles, but usually require less review time before acceptance. Letters cannot exceed four printed pages (approximately 3000–4000 words) including figures, tables, references, and a required abstract of about 100 words.

Help! There are 60 screaming kids in my lab!—Outreach activities for 5th graders (L)

Corinne M. Darvennes[a)]
Department of Mechanical Engineering, Tennessee Technological University, Box 5014, Cookeville, Tennessee 38505-5014

(Received 29 March 2004; revised 14 October 2004; accepted 24 November 2004)

In this letter a day of hands-on activities for 60 5th graders is described in the Acoustics and Vibrations Laboratory at TTU. This includes the logistics of having 60 kids in the lab and keeping their attention, a description of each activity, and the equipment used. The purpose of this publication is to encourage my colleagues to reach out to the next generation of scientists and engineers, by showing them that a few well-targeted activities do not take a gargantuan effort but have a big impact. © *2005 Acoustical Society of America.* [DOI: 10.1121/1.1850072]

PACS numbers: 43.10.Sv [TDR] Pages: 483–485

I. INTRODUCTION

In this letter a day of hands-on activities is described for 60 5th graders in the Acoustics and Vibrations Laboratory at Tennessee Technological University. Tennessee ranks 42 out of 50 states in terms of education.[1] Most students' exposure to science has been in the classroom, by teachers who are typically intimidated by the subject. Fifth and sixth grades are good ages to target outreach activities because the children are independent enough not to require constant monitoring and policing but are not overly affected by confidence issues yet. The goal for this day was to make the children realize that science and engineering can be fun and within their reach.

II. LOGISTICS

Having 60 5th graders in the lab at once entails a little bit of preparation. First, most kids that age have a short attention span, about 10–15 min, before they start getting restless. Therefore, the activities should last at most 15 min each. Another consideration is that they should all have a chance to play with the equipment and fully participate in the activities. Given the time allotted, that meant a total of ten activities. Consequently, the teachers divided the students into ten groups of six prior to arriving at the lab. They chose to separate the boys from the girls.

College students, both graduate and undergraduate, make great helpers. They are good role models and show the kids that a college education is not reserved to a small elite. Typically, at least one helper is needed per activity and one chaperone per group (parents and teachers work well for that). The ten activities are described in the following sections. In addition, a mid-morning snack was an enjoyable break and a good opportunity to experience the ''cocktail party effect.''

III. ACTIVITIES

A. Hearing and hearing loss

The purpose of this activity was to teach how the ear works, and the danger of noise-induced hearing loss. The tools used included ''Mediacoustic: Teaching acoustics by computer,''[2] a model of an ear (thanks to a local pediatrician), and pictures from the JASA calendar. Mediacoustic is a teaching software package for acoustics that uses multimedia techniques combining sound, text, pictures, and animations to illustrate many acoustic principles, both theoretical and practical. The module on hearing includes an animation of the ear when sound impinges on it. It is an effective tool to explain how the ear works. The animation is complemented by the model that can be taken apart to show the various parts of the ear; this is especially useful for haptic learners.

The module titled ''Noise, hearing damage'' in Mediacoustic is very powerful to show the negative effect of noise on hearing. It includes audioclips of music as heard via normal hearing and the same clips filtered to simulate what is heard by a carpenter who has been exposed to noise for 17 years and by a miner who has been exposed for 35 years. The pictures of bird hair cells in the JASA calendar help visualize the hearing loss mechanism. This is a good starting

a)Electronic mail: CDarvennes@tntech.edu

point for discussion about what constitutes noise that is likely to cause hearing damage. Examples such as loud music and hunting or target practice at the shooting range were brought up by the children as potentially too loud.

B. Hearing protection devices and reverberation

Popping balloons, listening to the time it takes for sound to decay, and comparing the decay seemed a fun way to experience two reverberation rooms with very different acoustic characteristics. To emphasize the lesson learned in the previous activity, each child was fitted with foam earplugs before going into the reverberation chambers.

C. Sound measurement

The children were put in pairs for this activity and each pair was given a sound level meter (Larson Davis SLM/dosimeter model 712). First, they measured the level of their voices, then several sound sources were turned on to evaluate different effects. The measurements took place in a small machine shop and several electric tools were used as noise sources. A shop vac was a good source to look at the effect of distance on sound and also to demonstrate how loud 85 dB is and to relate sound level to hearing safety. In the next step, two identical sanders were turned on individually and then together, to demonstrate dB additions (75 dB+75 dB=78 dB was a surprise but, for this age group, we did not discuss log functions to explain this phenomenon). The activity ended with one tool on and sound levels measured next to a wall, next to a wall/floor corner and, finally, next to a corner between three surfaces. The measurements showed the expected 3 dB increase with each additional surface. The children also put their ears close to the wall to experience the increase for themselves.

D. Sound visualization

The purpose of this activity was to visualize sound and differentiate between time and frequency data. A variety of sources were used: tuning forks, the voice (although no fifth grader was willing to sing), a kazoo, a bell, and a few noise making toys. The system consisted of Vernier LabPro® interface and microphone, and Logger Pro® software.[3] LabPro interface is a small hand-held data acquisition unit that can interface with computers, calculators, or PDAs and provides affordable, clean data. It can interface with up to four analog and two digital sensors at a time. The software identifies the type of sensor used and sets up the display automatically. In the case of a microphone, the time signal is displayed but a window can easily be added to display a FFT. First, using a tuning fork, the time axis is adjusted so that the children can count the number of peaks in 1/10 or 1/100 of a second and relate that number to the frequency on the FFT display. Different tuning forks show the same type of pattern and the children can relate the change in frequency to the change in fork dimensions. You can also discuss what occurs when using tuning forks of the same frequency made of different materials. After understanding the relationship between time and frequency, it is time to play with other noise sources.

E. Screaming contest

A screaming contest was organized in the anechoic chamber. A teacher was recruited to measure the sound levels because she knew all the students' names and could log them quickly. The sound level meter was a CEL model 275 set on slow and A weighting. The children were sent in the room one at a time, fitted with headphones, and allowed to scream to their heart's content. Prizes were awarded at the end of the day for the three loudest levels. Levels over 100 dBA were not uncommon and the loudest levels were around 106 dBA.

This was a fun way for the kids to release energy halfway through the day and was by far the most popular activity. The teachers loved the opportunity to scream at least as much as did the kids. This type of activity, however, does not always work well with pre-teens and teens who tend to be more self-conscious.

F. Visualizing frequency

A couple of strobe lights were available as another means of visualizing frequency. Moving targets included tuning forks, a motor, a fan, and toys. The strobe light was set to match the frequencies of the objects, then the motions were slowed down and ''reversed'' by slightly increasing and decreasing the strobe frequency. Checking all the frequencies ahead of time is highly recommended, since the students did not have too much patience hunting for them. Slowing down the motion of the tuning forks and seeing how much motion is actually involved is still impressive to that age group.

G. Vibrations

An air track was used to show vibrations of a one degree-of-freedom system. Various masses and springs were available to look at their effect on the natural frequency. The springs were passed around to experience different stiffnesses. Finally, a spring was attached to a variable speed motor to illustrate resonance and beating. Resonance was an exciting phenomenon to see but that age group had no interest in discussing how this relates to car vibrations and out of balance tires; that seems to change when they approach driving age, though.

H. Ultrasound

The Vernier data acquisition systems[3] were used with ultrasonic motion detectors to display position, velocity, and acceleration. This illustrated the fact that sound is reflected from objects. Knowing the speed of sound and measuring the time it takes for the sound to come back, the distance to the object can be measured. The targets included balls, to illustrate free falls; cars on a ramp, for a rolling motion; and a cup hanging from the ceiling with rubber bands to be used either as a long pendulum or as a one degree-of-freedom vibrating system. Letting the children run in front of the motion detector would have been a better activity for fifth graders.

I. Standing waves

One-dimensional standing waves were demonstrated with a water tube and two different tuning forks. The amplification of the tones can clearly be heard when an open tube is moved in and out of the water to a height that matches the wavelength of the tuning fork. This is a good demonstration to show the concept of wavelength and its relationship to frequency. Circular Chladni plates were used to show two-dimensional waves. The plates were driven by a violin bow. The children enjoyed touching the edge of the plate with a finger and watching the nodal lines move with it.

J. Slinky races

This activity, like the screaming contest, was provided to have a fun break. It took place in a large hallway. Each pair of children chose a slinky (choices included plastic or metal) and hung on to one end each. They sat across from each other at each end of the room with their slinkies stretched on the floor between them. They were shown how to send longitudinal and transverse waves, and the effect of tension. There was a little bit of time for practice, followed by the races. Prizes were given in each group for the fastest slinky wave sent across the room.

IV. CONCLUSIONS

The overall format worked well. Groups of six were often divided in subgroups of two or three, allowing each child access to all the equipment and full hands-on participation in all activities. Short activities were a whirlwind for the activity leaders but the students never had time to get bored or fidgety. The teachers reported a lot of positive feedback. They received appreciative calls from many parents, which was apparently unusual but very rewarding. Also, several students decided they wanted to become engineers or scientists. This is probably a short-lived interest and more regular interactions would be needed to sustain it.

ACKNOWLEDGMENTS

I would like to thank all the organizers and participants to the take-5 sessions at the ASA meetings, they planted the seeds that inspired me to play with the kids. I would also like to acknowledge all the helpers who made that day possible: Glenn Focht, Jiyao Li, Suman Nalla, Nagesh Panduga, Tina Rice, Brahmaji Vasantharao, and Yongxin Wang.

[1] *Education State Rankings 2003–2004*, 2nd ed. (Morgan Quitno Press, Lawrence, KS, 2003).

[2] ''Mediacoustic: Teaching Acoustics by Computers,'' CD-ROM available from 01db Inc., http://www.01dbinc.com/01db_shop/index.cfm, 1997.

[3] http://www.vernier.com/physics/index.html, last accessed 9 March, 2004.

Some comments on Sabine absorption coefficient (L)

K. S. Sum[a)]
School of Mechanical Engineering, The University of Western Australia, 35 Stirling Highway, Crawley, Western Australia 6009

(Received 10 June 2004; revised 1 September 2004; accepted 8 September 2004)

The case of a nonzero reverberation time when all absorptive surfaces in a room have values of Sabine absorption coefficient of one, the existence of values of the coefficient that are larger than one, and the difference of the coefficient from the statistical absorption coefficient, are well known. So far, the reasons for these phenomena are still unclear. This letter provides a new perspective to the classical problem of sound absorption where physical interpretations of the Sabine absorption coefficient are given for different types of absorptive surface and conditions of the sound field in rooms. © *2005 Acoustical Society of America.* [DOI: 10.1121/1.1810237]

PACS numbers: 43.55.Br, 43.55.Dt, 43.55.Ev [NX] Pages: 486–489

I. INTRODUCTION

The concept of sound absorption coefficient has been used in various reverberation formulas. The coefficient was defined as the ratio of sound energy absorbed by the surface to the sound energy incident on the surface regardless of the formulas used. However, experimental data from the early work by Morris *et al.*[1] showed that not only different formulas give different values of the absorption coefficient of the same surface in a room, but individual formulas also produce a considerable variation in the coefficient of the same surface when measured in different rooms. The same observations would also be obtained from those different reverberation times in rooms that were calculated by various formulas for the same value of absorption coefficient as presented by Neubauer.[2]

Sixty-five years ago, Hunt[3] has pointed out that under the present definition of the term ''sound absorption coefficient,'' there is little justification for considering it as a unique or fully measurable/resolvable property of absorptive surfaces in nonanechoic rooms. The reason is because individual surfaces in the rooms are not acoustically isolated. Therefore, he suggested that the coefficient should be assigned an explicit meaning when its value is calculated by inserting into a specific formula, values of certain parameters that are obtained under specified conditions. He also recommended the use of the term ''chamber coefficient'' because the absorption coefficient is a function of the room in which the measurement is made. The explicit meaning would deny the presumption that the same formula and the same value of the coefficient will always predict accurately the reverberation time in different rooms.

The Sabine equation has been accepted in various standards for the measurements of reverberation time and absorption coefficient. But, comparisons have always been made between the reverberation times in a room predicted by this equation and by other means using values of absorption coefficient that were obtained/calibrated in other rooms. When there were discrepancies in the results, the conclusion drawn was almost always adverse on the Sabine equation. Thus, if the sound absorption coefficient is not a fully resolvable/quantifiable property under its present definition as stated by Hunt,[3] and the Sabine coefficient exists in the Sabine equation only as a parameter of inverse proportionality to the reverberation time, then the use of this equation depends on how the Sabine coefficient is defined and determined. In other words, the Sabine absorption coefficient is a major source of uncertainty in the application of the Sabine equation, and its definition must first be resolved. Hence, it is necessary to understand the physical representation of the values of this coefficient for different sound-field conditions.

In this letter, an analytical and a numerical comparison are made between the statistical absorption coefficient (also known as random-incidence absorption coefficient) and the Sabine absorption coefficient. In the latter comparison, values of both absorption coefficients are obtained for different reverberation times and background absorption in rooms. The background absorption is defined as the sound dissipation in the rooms when the absorptive surface of interest is not present. The statistical absorption coefficient is calculated by the Eyring equation and defined as the ratio of absorbed to incident sound energy of a diffuse sound field. Based on the similarity and the difference between both absorption coefficients, and a review of some previously derived expressions in the form of the Sabine equation, physical interpretations of the Sabine absorption coefficient are provided for locally and modally reactive absorptive surfaces and for both diffuse and nondiffuse sound fields.

II. STATISTICAL ABSORPTION COEFFICIENT AND SABINE ABSORPTION COEFFICIENT

Consider the mean energy of the sound field in a room at time t, $E(t)$, which is space-averaged over excitation and measurement locations in the room. Correspondingly, let $\bar{\alpha}$ denotes the mean absorption coefficient, which describes the ratio of the average absorbed to the average incident energy in a given decay range of the sound field. So, $\bar{\alpha}$ represents the average or global dissipativity in the entire sound field that corresponds to all combinations of excitation and measurement positions rather than a local dissipativity that corresponds to an individual combination. If E_0 is the initial sound energy at the start of the decay range at $t=t_0$, and there are an average of N reflections from all absorptive sur-

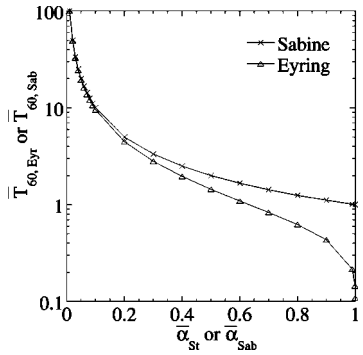

FIG. 1. Variation of the normalized reverberation times with the mean statistical and Sabine absorption coefficients.

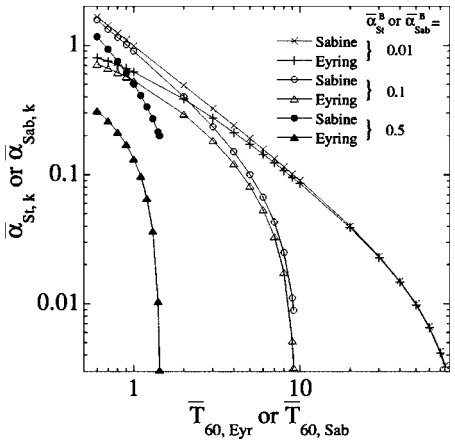

FIG. 2. Variation of the statistical and Sabine absorption coefficients of the kth surface with the normalized reverberation times for three different background absorptions.

faces in the room after $t-t_0$ seconds, then $E(t)=E_0(1-\overline{\alpha})^N$ for $t\geqslant t_0$, where $N=(t-t_0)n$ and n is the average number of reflections per second. In the special case when the sound field is diffuse, the latter is denoted as n_{dif} and given by[4] $n_{\mathrm{dif}}=c_0A_T/4V_0$ (i.e., the mean free path is $4V_0/A_T$). c_0 is the speed of sound in air, A_T is the total area of the absorptive surfaces, and V_0 is the volume of the room. A diffuse sound field means that the sound intensity at each observation point is equal in all directions after each reflection, where sound waves travel with an equal probability in every direction. Since this condition is a subset of an ergodic sound field, the term ''diffuse'' is more specific and widely used than ''ergodic'' [ergodicity has been well explained in the literatures (e.g., Ref. 5)]. Under the diffuse condition, the mean statistical absorption coefficient, $\overline{\alpha}_{\mathrm{St}}$, is defined and the energy is given by $E_{\mathrm{dif}}(t)=E_0(1-\overline{\alpha}_{\mathrm{St}})^{(t-t_0)n_{\mathrm{dif}}}=E_0e^{(t-t_0)n_{\mathrm{dif}}\ln(1-\overline{\alpha}_{\mathrm{St}})}$. By taking logarithmic and multiplying by a factor of 10, $10\log E_{\mathrm{dif}}(t)=10(t-t_0)n_{\mathrm{dif}}\ln(1-\overline{\alpha}_{\mathrm{St}})\log e+10\log E_0$, where $-10n_{\mathrm{dif}}\ln(1-\overline{\alpha}_{\mathrm{St}})\log e$ (dB/s) is the energy decay rate. This rate can be written as $-1.086c_0A_T\ln(1-\overline{\alpha}_{\mathrm{St}})/V_0$ after the substitution of n_{dif} by its expression. When the decay is extrapolated to 60 dB, the time taken for a 60-dB decay is thus given by

$$T_{60,\mathrm{Eyr}}=-55.3V_0/c_0A_T\ln(1-\overline{\alpha}_{\mathrm{St}}). \tag{1}$$

Equation (1) is the Eyring equation. From a series expansion, $-\ln(1-\overline{\alpha}_{\mathrm{St}})=\overline{\alpha}_{\mathrm{St}}+\overline{\alpha}^2_{\mathrm{St}}/2+\overline{\alpha}^3_{\mathrm{St}}/3+\overline{\alpha}^4_{\mathrm{St}}/4+\cdots$, and if only the first term of the series is considered,[6] then a different 60-dB decay time would be obtained by Eq. (1). By denoting this decay time as $T_{60,\mathrm{Sab}}$ and replacing $\overline{\alpha}_{\mathrm{St}}$ by $\overline{\alpha}_{\mathrm{Sab}}$, Eq. (1) becomes

$$T_{60,\mathrm{Sab}}=55.3V_0/c_0A_T\overline{\alpha}_{\mathrm{Sab}}, \tag{2}$$

which is the Sabine equation. $\overline{\alpha}_{\mathrm{Sab}}$ is called the mean Sabine absorption coefficient.

Figure 1 shows the variation of $\overline{T}_{60,\mathrm{Eyr}}$ and $\overline{T}_{60,\mathrm{Sab}}$, respectively, with $\overline{\alpha}_{\mathrm{St}}$ and $\overline{\alpha}_{\mathrm{Sab}}$. $T_{60,\mathrm{Eyr}}(=c_0A_TT_{60,\mathrm{Eyr}}/55.3V_0)$ is a nondimensional $T_{60,\mathrm{Eyr}}$ and $T_{60,\mathrm{Sab}}(=c_0A_TT_{60,\mathrm{Sab}}/55.3V_0)$ is a nondimensional $T_{60,\mathrm{Sab}}$. It can be seen that $T_{60,\mathrm{Sab}}$ is nonzero when $\overline{\alpha}_{\mathrm{Sab}}=1$. Also, $T_{60,\mathrm{Eyr}}$ and $T_{60,\mathrm{Sab}}$ agree well only when the values of the absorption coefficients are small. This observation can be explained by the series expansion of $\ln(1-\overline{\alpha}_{\mathrm{St}})$ that for small values of $\overline{\alpha}_{\mathrm{St}}$, all higher-order terms in the series are negligible and thus, $-\ln(1-\overline{\alpha}_{\mathrm{St}})\approx\overline{\alpha}_{\mathrm{St}}$. So, $T_{60,\mathrm{Eyr}}\approx T_{60,\mathrm{Sab}}$ when the value of $\overline{\alpha}_{\mathrm{Sab}}$ is also small. The result agrees with the remark of Joyce[6] that the Sabine equation yields an exact reverberation time in an ergodic sound field when the surface absorptivity is weak. It is also consistent with those of Hodgson[7] which showed the values of sound absorption coefficient of an absorptive surface in a diffuse sound field obtained by the Eyring and the Sabine equations are close to each other when the surface absorption is low.

Consider a room with M different absorptive surfaces. The statistical absorption coefficient of the kth surface, $\alpha_{\mathrm{St},k}$, can be written in such a way that[4]

$$\overline{\alpha}_{\mathrm{St}}=\left(A_k\alpha_{\mathrm{St},k}+\sum_{i=1}^{M-1}A_i\alpha_{\mathrm{St},i}\right)\Big/A_T+\alpha_{\mathrm{air}}=\overline{\alpha}_{\mathrm{St},k}+\overline{\alpha}^B_{\mathrm{St}}. \tag{3}$$

$\overline{\alpha}^B_{\mathrm{St}}$ describes the background absorption of sound in the room and includes the air absorption, α_{air}. A_k and $\overline{\alpha}_{\mathrm{St},k}$ are the area and area-weighted statistical absorption coefficient of the kth surface. By using Eq. (1) to substitute for $\overline{\alpha}_{\mathrm{St}}$,

$$\overline{\alpha}_{\mathrm{St,k}}=1-e^{-1/\overline{T}_{60,\mathrm{Eyr}}}-\overline{\alpha}^B_{\mathrm{St}}. \tag{4}$$

By expanding the exponential term in a series, Eq. (4) can be reexpressed as

$$\overline{\alpha}_{\mathrm{St},k}=1/\overline{T}_{60,\mathrm{Eyr}}-1/2\overline{T}^2_{60,\mathrm{Eyr}}+1/6\overline{T}^3_{60,\mathrm{Eyr}}-1/24\overline{T}^4_{60,\mathrm{Eyr}}+\cdots-\overline{\alpha}^B_{\mathrm{St}}. \tag{5}$$

Similarly, the Sabine absorption coefficient of the kth surface, $\alpha_{\mathrm{Sab},k}$, can be written in such a way that

$$\overline{\alpha}_{\mathrm{Sab}}=\left(A_k\alpha_{\mathrm{Sab},k}+\sum_{\mathrm{i}=1}^{M-1}A_i\alpha_{\mathrm{Sab},i}\right)\Big/A_T+\alpha_{\mathrm{air}}=\overline{\alpha}_{\mathrm{Sab},k}+\overline{\alpha}^B_{\mathrm{Sab}}, \tag{6}$$

where $\overline{\alpha}_{\mathrm{Sab},k}$ is the area-weighted Sabine absorption coefficient of the surface and $\overline{\alpha}^B_{\mathrm{Sab}}$ describes the background absorption. By using Eq. (2) to substitute for $\overline{\alpha}_{\mathrm{Sab}}$,

$$\overline{\alpha}_{\mathrm{Sab},k}=1/\overline{T}_{60,\mathrm{Sab}}-\overline{\alpha}^B_{\mathrm{Sab}}. \tag{7}$$

Equations (4) and (7) indicate that $\overline{\alpha}_{\mathrm{St},k}$ and $\overline{\alpha}_{\mathrm{Sab},k}$ do not only depend on the nondimensional reverberation time of the room, but also the background absorption. Thus, if two different rooms have different background absorption, the absorption coefficients would have different values even the reverberation times of the rooms are equal when the same surface is tested. Figure 2 shows the variation of both ab-

sorption coefficients with the reverberation time for three different values of background absorption. It is obvious that $\bar{\alpha}_{\mathrm{Sab},k}$ agrees well with $\bar{\alpha}_{\mathrm{St},k}$ only if the reverberation time is long and the background absorption is low. This observation can be explained as follows. For a given background absorption that is low, the higher-order terms of $T_{60,\mathrm{Eyr}}$ in Eq. (5) are negligible when the reverberation time is long. So, $\bar{\alpha}_{\mathrm{St},k} \approx 1/T_{60,\mathrm{Eyr}} - \bar{\alpha}^B_{\mathrm{St}}$. Since this approximation is in the same form as Eq. (7), the values of $\bar{\alpha}_{\mathrm{St},k}$ and $\bar{\alpha}_{\mathrm{Sab},k}$ are close to each other for the same reverberation time and background absorption. However, if a given background absorption is not low, the value of $1/T_{60,\mathrm{Eyr}} - \bar{\alpha}^B_{\mathrm{St}}$ in Eq. (5) is comparable or much smaller than the total of the higher-order terms for both small and large values of $T_{60,\mathrm{Eyr}}$. Therefore, as can be seen in Fig. 2, the discrepancy between $\bar{\alpha}_{\mathrm{St},k}$ and $\bar{\alpha}_{\mathrm{Sab},k}$ increases with the background absorption, and is consistently large for a high background absorption. Also, some combinations of low values of $T_{60,\mathrm{Sab}}$ and $\bar{\alpha}_{\mathrm{Sab}}$ give large values of $\bar{\alpha}_{\mathrm{Sab},k}$ where $\alpha_{\mathrm{Sab},k}$ can exceed one.

Based on the above comparison with the results of Eyring equation, the present definition of sound absorption coefficient (but under the condition of a diffuse sound field) can be used for the Sabine absorption coefficient of an absorptive surface in a room, α_{Sab}, only if both the surface and background absorptions are low such that the reverberation time of the room is long. When the surface and/or background absorption is not low such that the reverberation time is short, this interpretation for α_{Sab} is no longer valid. Hodgson[7] has concluded that the Eyring equation is more consistent than the Sabine equation in the prediction of a diffuse-field sound absorption coefficient. In fact, it can be seen from Eq. (1) that the Eyring equation constrains the value of $\bar{\alpha}_{\mathrm{St}}$ to between 0 and 1 which complies with the definition of sound absorption coefficient. On the contrary, this definition has been violated when higher-order terms are not included in the derivation of the Sabine equation as mentioned above. So, the value of $\bar{\alpha}_{\mathrm{Sab}}$ becomes unconstrained [see Eq. (2)]. From Eq. (2), it is obvious that $\bar{\alpha}_{\mathrm{Sab}}=1$ does not give a zero reverberation time and the equation allows the value of $\bar{\alpha}_{\mathrm{Sab}}$ to be greater than 1. The latter was frequently encountered in both numerical and experimental studies. Hence, $\alpha_{\mathrm{Sab}}=1$ does not imply a fully absorbent surface. The foregoing explanation can be further justified using the energy decay rate, $d[N\bar{\alpha}E(t)]/dt$. This rate can be written as $\bar{\alpha}E(t)dN/dt$ only if $\bar{\alpha}E(t)$ varies slowly with time where $\bar{\alpha}$ has to be small. By replacing $\bar{\alpha}$ with $\bar{\alpha}_{\mathrm{Sab}}$ and dN/dt with $n_{\mathrm{dif}}=c_0A_T/4V_0$, $\bar{\alpha}E(t)dN/dt$ was often used in previous works to derive the decay rate for the Sabine equation as $c_0A_T\bar{\alpha}_{\mathrm{Sab}}/4V_0$. Since one has already made an implicit assumption of a small $\bar{\alpha}_{\mathrm{Sab}}$ when $\bar{\alpha}_{\mathrm{Sab}}E(t)dN/dt$ is used, $\bar{\alpha}_{\mathrm{Sab}}$ will violate the definition of sound absorption coefficient if this assumption is neglected during the derivation of the Sabine equation. Thus, the Sabine absorption coefficient has different physical meanings when the surface and/or background absorption is not low such that the reverberation time is short and the sound field is not diffuse.

For a general sound field in a room, the 60-dB decay time of the sound field in a band of center frequency ω_0 is given by $T_{60}=4.4\pi/\eta_{\mathrm{ac}}\omega_0=4.4\pi/\Delta\omega_{3\ \mathrm{dB}}$. η_{ac} is the average loss factor of acoustic modes in the band and $\Delta\omega_{3\ \mathrm{dB}}$ is the average half-power bandwidth of the modes. By equating this expression to Eq. (2), Lyon[8] provided a way to describe $\bar{\alpha}_{\mathrm{Sab}}$ in terms of $\Delta\omega_{3\ \mathrm{dB}}$ or the modal-overlap factor of the sound field, M_a, where

$$\bar{\alpha}_{\mathrm{Sab}}=4V_0\Delta\omega_{3\ \mathrm{dB}}/c_0A_T=4V_0M_a/c_0A_Tn_a(\omega). \tag{8a}$$

$n_a(\omega)$ is the modal density of the sound field. From Eq. (8a), $\bar{\alpha}_{\mathrm{Sab}}$ can be interpreted as a nondimensional average half-power bandwidth of the acoustic modes or a normalized modal-overlap factor of the sound field. If $\Delta\omega^B_{3\ \mathrm{dB}}$ and M^B_a denote the half-power bandwidth and modal-overlap factor that correspond to the background absorption, it can be shown from Eqs. (6) and (8a) that

$$\begin{aligned}\bar{\alpha}_{\mathrm{Sab},k}&=4V_0[\Delta\omega_{3\ \mathrm{dB}}/A_T-\Delta\omega^B_{3\ \mathrm{dB}}/(A_T-A_k)]/c_0\\&=4V_0[M_a/A_T-M^B_a/(A_T-A_k)]/c_0n_a(\omega),\end{aligned} \tag{8b}$$

where $\bar{\alpha}_{\mathrm{Sab},k}$ can be interpreted as the change in the half-power bandwidth or modal-overlap factor of the sound field due to the absorption by the surface. The description of α_{Sab} of an absorptive surface in terms of its acoustical properties depends on whether the surface is locally reactive or modally reactive.

III. α_{Sab} OF LOCALLY REACTIVE AND MODALLY REACTIVE SURFACES

By using the eigenfunction of acoustic modes in enclosed spaces, Morse[9] derived expressions for the 60-dB decay time of individual modes of a rectangular room and a cylindrical room in the form of the Sabine equation. Locally reactive absorptive surfaces in the rooms were considered where the absorption of each surface is described by its specific acoustical impedance, ζ. As illustrative examples, cases of $|\zeta|\gg 1$ are presented here. For the rectangular room, the decay time of the ith mode with indices of (u,v,w) in the x, y, and z directions is[9]

$$T_{ai}=55.3V_0/c_0(\varepsilon_ua_x+\varepsilon_va_y+\varepsilon_wa_z), \tag{9a}$$

$$a_m=\sum_{k\in m\ \mathrm{wall}} 8A_k\mathrm{Real}[1/\zeta_k]. \tag{9b}$$

In Eq. (9a), ε_u, ε_v, $\varepsilon_w=\frac{1}{2}$ if u, v, $w=0$ and ε_u, ε_v, $\varepsilon_w=1$ if u, v, $w>0$. ζ_k is the specific acoustical impedance of the kth surface on the m-wall where $m=x$, $m=y$, and $m=z$, respectively, denote the walls that are perpendicular to the x, y, and z axis. For the cylindrical room,

$$T_{ai}=55.3V_0/c_0\{\varepsilon_wa_z+a_r/[1-(u/\pi\beta_{uv})^2]\}, \tag{10}$$

where $m=r$ denotes the cylindrical wall and $m=z$ denotes the walls at both ends of the room. β_{uv} describes the eigenvalue of the ith mode with indices of (u,v), and its values for various combinations of u and v are well documented in the literatures (e.g., Ref. 9).

When the sound field is dominated by a single acoustic mode, comparisons of Eqs. (2) and (6) with Eqs. (9a) and (10) yield $\alpha_{\mathrm{Sab},k}=8\varepsilon_q\mathrm{Real}[1/\zeta_k]$ ($q=u$, v or w) if the kth surface is on any of the walls in the rectangular room or the

ends of the cylindrical room. If the surface is on the cylindrical wall, then $\alpha_{\mathrm{Sab},k}=8\,\mathrm{Real}[1/\zeta_k]/[1-(u/\pi\beta_{uv})^2]$. These expressions show that $\alpha_{\mathrm{Sab},k}$ depends on both the mode type and the impedance of the surface. As a result, $\alpha_{\mathrm{Sab},k}$ varies with the reverberation time, the background absorption, and the location of the surface in the room. The reverberation time and background absorption are also implicit in the impedance. It can be shown that these three dependences of $\alpha_{\mathrm{Sab},k}$ persist even when the sound field is controlled by a few acoustic modes. In this case, $\alpha_{\mathrm{Sab},k}$ represents the average dissipation of energy in the modes by the surface. At low or medium frequencies, the mode types for the rectangular room are mainly axial, tangential, and oblique in combinations, and a mixture of low- and high-order modes for the cylindrical room. These mode types have large differences in the values of ε_q and $1-(u/\pi\beta_{uv})^2$. At high frequencies, most of the modes in the rectangular room are oblique, while in the cylindrical room, high-order modes are dominant. In this case, $\varepsilon_q=1$ and $1-(u/\pi\beta_{uv})^2\approx 1$ for most of the modes. Thus, $\alpha_{\mathrm{Sab},k}$ is independent of the mode type (i.e., a feature of a diffuse sound field) and only dependent on ζ_k. From the preceding discussion, α_{Sab} of a locally reactive surface can be interpreted in terms of mode type and the specific acoustical impedance of the surface.

As far as a modally reactive surface is concerned, Pan and Bies[10] have used the concept of loss factor to obtain a physical interpretation for α_{Sab} of the surface. By solving the quasi-transient energy-balance equations of a vibrating structure and the sound field in a room, the decay rate of the sound field can be expressed in the form of the Sabine equation where α_{Sab} of the structure was derived as[10]

$$\alpha_{\mathrm{Sab}}\approx 2V_0\omega_0[\,\eta_a+\eta_s+\eta_{as}+\eta_{sa}-\sqrt{(\eta_a+\eta_{as}-\eta_s-\eta_{sa})^2+4\eta_{as}\eta_{sa}}-2\eta_a]/c_0A_s. \tag{11}$$

In Eq. (11), A_s is the surface area of the structure, η_a is the internal loss factor of the sound field that describes the background absorption, and η_s is the internal loss factor of the structure that describes the energy dissipativity in the structure without the influence of the sound field. η_{as} is the coupling loss factor from the sound field to the structure that describes the sound absorptivity by the structure, and η_{sa} is the coupling loss factor from the structure to the sound field that describes the sound radiativity from the structure. η_{sa} is directly proportional to the radiation efficiency of the structure, σ_{rad}.[10] It is obvious that α_{Sab} does not only account for the sound absorption by the structure, but it also includes the sound radiation when the structure is vibrating. In other words, α_{Sab} of a modally reactive surface can be interpreted in terms of acoustical properties of the sound field and the surface described by η_a and η_s, as well as the sound absorption and radiation of the surface described by η_{as} and η_{sa}.

IV. CONCLUSIONS

Physical meanings of the Sabine absorption coefficient, α_{Sab}, have been explained for different types of absorptive surface and conditions of the sound field in a room. In all cases, α_{Sab} represents the mean/global dissipativity of sound energy that is space-averaged over excitation and measurement locations in the room for a given decay range. It can be interpreted as the ratio of absorbed to incident sound energy of a diffuse sound field only if the surface and background absorptions in the room are small such that the reverberation time of the sound field is long. The reason is because the present definition of sound absorption coefficient has been violated in the derivation of the Sabine equation. However, the Sabine absorption coefficient can still be used as a dissipation factor in a general sound field. The mean Sabine absorption coefficient, $\overline{\alpha}_{\mathrm{Sab}}$, associated with all dissipations of sound in a room, can be interpreted as a nondimensional average half-power bandwidth of acoustic modes in the band of interest or a normalized modal-overlap factor of the sound field. The area-weighted Sabine absorption coefficient of the kth surface, $\overline{\alpha}_{\mathrm{Sab},k}$, can be interpreted as the change in the half-power bandwidth or modal-overlap factor due to the absorption by the surface. For a locally reactive surface, its α_{Sab} can be interpreted in terms of its acoustical impedance and the type of acoustic modes that dominate the sound-field decay. On the other hand, α_{Sab} of a modally reactive surface can be interpreted in terms of the internal and coupling loss factors of the sound field and the surface. Since α_{Sab} has different physical meanings and depends on acoustical properties of both the surface and the room as well as the location of the surface, it is definable only within the Sabine equation. These also suggest that a different name for α_{Sab} should be employed (e.g., Sabine absorption factor) to avoid the use of the words ''absorption coefficient,'' which can lead to the presumption that α_{Sab} has the definition of sound absorption coefficient. This presumption can cause the use of the Sabine equation to be problematic.

[a]Electronic mail: ksum@mech.uwa.edu.au

[1] R. M. Morris, G. M. Nixon, and J. S. Parkinson, ''Variations in sound absorption coefficients as obtained by the reverberation chamber method,'' J. Acoust. Soc. Am. **9**, 234–243 (1938).
[2] R. O. Neubauer, ''Existing reverberation time formulae—a comparison with computer simulated reverberation times,'' in Proceedings of the 8th International Congress on Sound and Vibration, Hong Kong (2001), pp. 805–812.
[3] F. V. Hunt, ''The sound absorption coefficient problem,'' J. Acoust. Soc. Am. **11**, 38–40 (1939).
[4] H. Kuttruff, ''Reverberation and steady state energy density in diffuse sound fields,'' in *Room Acoustics* (Applied Science, London, 1979), 2nd ed., Chap. 5.
[5] W. B. Joyce, ''Sabine's reverberation time and ergodic auditoriums,'' J. Acoust. Soc. Am. **58**, 643–655 (1975).
[6] W. B. Joyce, ''Power series for the reverberation time,'' J. Acoust. Soc. Am. **67**, 564–571 (1980).
[7] M. Hodgson, ''Experimental evaluation of the accuracy of the Sabine and Eyring theories in the case of non-low surface absorption,'' J. Acoust. Soc. Am. **94**, 835–840 (1993).
[8] R. H. Lyon, ''Statistical analysis of power injection and response in structures and rooms,'' J. Acoust. Soc. Am. **45**, 545–565 (1969).
[9] P. M. Morse, ''Standing waves of sound,'' in *Vibration and Sound* (American Institute of Physics, New York, 1976), Chap. 8.
[10] J. Pan and D. A. Bies, ''The effect of fluid-structural coupling on acoustical decays in a reverberation room in the high frequency range,'' J. Acoust. Soc. Am. **87**, 718–727 (1990).

A note on pure-tone masking by broadband noise under free-field and insert-phone conditions (L)

Adrianus J. M. Houtsma
U.S. Army Aeromedical Research Laboratory, Fort Rucker, Alabama 36362-0577[a)]

(Received 31 August 2004; revised 18 October 2004; accepted 3 November 2004)

Free-field experiments on masking of low-frequency tones by broadband noise, as reported by Fidell, *et al.* [J. Acoust. Soc. Am. **73**, 628–638 (1983)] should, in principle, yield the same results as the recently reported insert-phone experiment by Houtsma [J. Acoust. Soc. Am. **115**, 967–970 (2004)]. Indeed, if Fidell *et al.*'s data are converted to critical ratios and compared with the recent insert-earphone results, both turn out to be quite similar and significantly different from Hawkins and Stevens' classical critical ratio results. [DOI: 10.1121/1.1841611]

PACS numbers: 43.66.Dc [NFV] Pages: 490–491

Recently, Houtsma (2004) reported new critical ratio measurements, performed with insert earphones, which yielded low-frequency results that were substantially different from the classical results of Hawkins and Stevens (1950). Since then, Fidell and Horonjeff have pointed out in private communication that a study by their team (Fidell *et al.*, 1983), which had similar general aims and was referenced in Houtsma (2004), was performed under free-field listening conditions. Because free-field presentation is another way to circumvent acoustic coupling losses at low frequencies, it seems logical for them to have found a critical ratio (CR) function similar to ours, and substantially different from the CR function of Hawkins and Stevens. Indeed, the minimum of CR estimates measured with supra-aural phones, shown in Fig. 1 of Fidell *et al.* (1983), appears to occur at a higher frequency (about 300 Hz) than the minimum of their free-field CR estimate shown in Fig. 4 (about 200 Hz). Thus, the CR results reported by Houtsma and by Fidell *et al.* appear similar, at least qualitatively.

A more precise and quantitative comparison is shown in Fig. 1, which is for the most part identical to Fig. 2 of Houtsma (2004). It shows the insert phone obtained CR estimates (filled circles) obtained by Houtsma (2004), a linear fit to these data between 90 and 1000 Hz (solid line), and the classical CR function of Hawkins and Stevens (dashed line). In addition, six of the seven data points of Fidell *et al.*'s (1983) study 1, displayed in their Table II and Fig. 4, are shown as crosses (a seventh data point, also measured at 125 Hz, was omitted). To convert Fidell *et al.*'s masked thresholds to CRs, a constant k value of 0.5 was assumed in order to obtain an approximate best fit, using Eq. (1) from Houtsma (2004).

Fidell *et al.*'s (1983) data, replotted in Fig. 1, appear to be quite consistent with Houtsma's (2004) results for frequencies above 90 Hz. Both data sets are clearly different from the classical CR estimates of Hawkins and Stevens (1950) and later replications (Fletcher, 1953; Green, McKey, and Licklider, 1959), all performed with supra-aural headphones. Thus, Fidell and his team deserve recognition for having done the CR masking experiment in a physically more controlled manner than most or all of their predecessors. The fact, however, that they did not explicitly point at the difference that such stimulus control makes, is the main reason for the present letter.

The results of the studies by Fidell *et al.* (1983) and Houtsma (2004) differ in at least two respects. One difference is that, at frequencies below 100 Hz, the apparent ''upturn'' of Fidell *et al.*'s (1983) CR estimates appears to progress at a somewhat gentler rate. This may be the result of the higher level of the low-pass masking noise used for the 40- and 63-Hz signals. This upturn below 100 Hz could reflect a systematic change in detection efficiency, as quantified by the k value in Houtsma (2004), Eq. (1), or it could reflect a gradual breakdown of the simple power spectrum model of Eq. (1) when, at very low frequencies, the signal detection process may become dominated by factors other than the noise power in a certain cochlear passband. The upturn should not be interpreted as evidence for a widening of the critical band at low frequencies, since estimation of auditory bandwidth from broadband masking data assumes that the power spectrum filter model is valid and that it is the sole cause of signal audibility. In fact, modern notched-noise masking techniques, that allow separate and independent estimates of a filter's width and detection efficiency, have provided evidence for a continuously decreasing auditory filter bandwidth down to 100 Hz (Glasberg and Moore, 1990; Moore and Sek, 1995).

Another difference with the Fidell *et al.* (1983) study is that the k function used by Houtsma (2004) to reconcile CR and ERB (equivalent rectangular bandwidth) measures is not U-, but rather L-shaped. Its flat slope (i.e., constant k) at high frequencies appears consistent with two classical notions that (a) the human auditory filter bank approaches an approximate constant-Q system for frequencies above 1000 Hz (Zwicker and Feldtkeller, 1967; Glasberg and Moore, 1990), and that (b) thresholds for pure tones masked by broadband noise tend to increase by 3 dB per octave at high frequencies (Hawkins and Stevens, 1950). Results from recent simultaneous and forward masking experiments with notched-noise maskers, in which masking and suppression effects can be

[a)]The opinions, interpretations, and conclusions contained in this letter are those of the author and are not necessarily endorsed by the U.S. Army and/or Department of Defense.

 0001-4966/2005/117(2)/490/2/$22.50

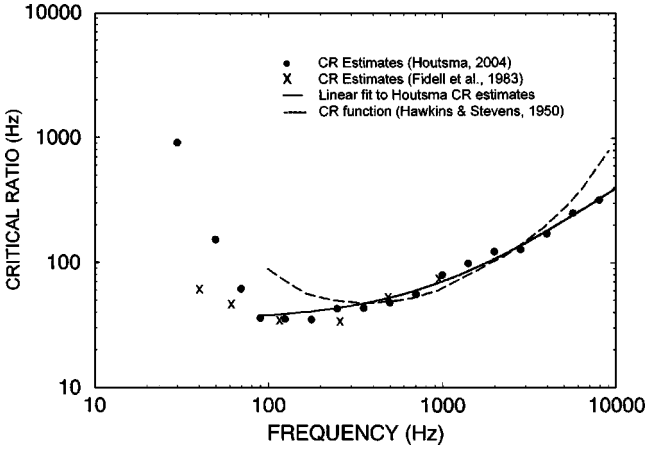

FIG. 1. Critical ratio values obtained from broadband noise masking data by Houtsma (2004, solid dots), Fidell *et al.* (1983, crosses), and Hawkins and Stevens (1950, dashed line). The solid line represents a best linear fit (CR $=0.0367f+34$) to the Houtsma (2004) CR estimates, computed from masked thresholds with the simple formula $S=N_0$ (CR), where S is the threshold signal power and N_0 the spectral density of the broadband masker.

separated, seem to suggest that cochlear bandwidth increases more slowly than proportionally with increasing frequency between 1000 and 8000 Hz (Oxenham and Shera, 2003). In that case, a 3-dB per octave increase in broadband masked thresholds can only be explained by a decreasing detection efficiency between 1 and 8 kHz, leading to a U-shaped k function. This would be consistent with Fidell *et al.*'s (1983) findings, and also with a recent analysis of Baker, Rosen, and Darling's (1998) data provided by Glasberg and Moore (2000).

Finally, it should be clear that simultaneous broadband masking data are insufficient for teasing apart the separate effects of auditory filter bandwidth and detection efficiency, both as a function of frequency. Their effects are always intertwined, and estimates of one can only be made if certain assumptions are made about the other. Nevertheless, with the emergence of new experimental techniques that are capable of yielding independent estimates of aural resolution and detection efficiency (e.g., Glasberg and Moore, 1990; van de Par and Kohlrausch, 1999; Oxenham and Shera, 2003), the combination of new results should always remain consistent with results from simultaneous broadband masking experiments, provided that these are sufficiently free of measurement artifacts.

ACKNOWLEDGMENTS

The author is indebted to Brian C.J. Moore and to an anonymous reviewer for helpful comments on an earlier version of the manuscript.

Baker, R.J., Rosen, S., and Darling, A.M. (**1998**). ''An efficient characterization of human auditory filtering across level and frequency that is also physiologically reasonable,'' in *Psychophysical and Physiological Advances in Hearing*, edited by A.R. Palmer, A. Rees, A.Q. Summerfield, and R. Meddis (Whurr, London).

Fidell, S., Horonjeff, R., Teffeteller, S., and Green, D.M. (**1983**). ''Effective masking bandwidth at low frequencies,'' J. Acoust. Soc. Am. **73**, 628–638.

Fletcher, H. (**1953**). *Speech and Hearing in Communication* (Van Nostrand, New York).

Glasberg, B.R., and Moore, B.C.J. (**1990**). ''Derivation of auditory filter shapes from notched-noise data,'' Hear. Res. **47**, 103–138.

Glasberg, B.R., and Moore, B.C.J. (**2000**). ''Frequency selectivity as a function of level and frequency measured with uniformly exciting notched noise,'' J. Acoust. Soc. Am. **108**, 2318–2328.

Green, D.M., McKey, M., and Licklider, J. (**1959**). ''Detection of a pulsed sinusoid in noise as a function of frequency,'' J. Acoust. Soc. Am. **31**, 1446–1452.

Hawkins, J.E., and Stevens, S.S. (**1950**). ''The masking of pure tones and speech by white noise,'' J. Acoust. Soc. Am. **22**, 6–13.

Houtsma, A.J.M. (**2004**). ''Hawkins and Stevens revisited with insert earphones,'' J. Acoust. Soc. Am. **115**, 967–970.

Moore, B.C.J., and Sek, A. (**1995**). ''Auditory filtering and the critical bandwidth at low frequencies,'' in *Advances in Hearing Research*, edited by G.A. Manley, G.M. Klump, C. Köppl, H. Fastl, and H. Oeckinghaus (World Scientific, Singapore).

Oxenham, A.J., and Shera, C.A. (**2003**). ''Estimates of human cochlear tuning at low levels using forward and simultaneous masking,'' J. Assoc. Res. Otolaryngol. **4**, 541–554.

van de Par, S., and Kohlrausch, A. (**1999**). ''Dependence of binaural masking level difference on center frequency, masker bandwidth, and interaural parameters,'' J. Acoust. Soc. Am. **106**, 1940–1947.

Zwicker, E., and Feldtkeller, R. (**1967**). *Das Ohr als Nachrichtenempfänger* (Hirzel, Stuttgart).

Acoustical wave propagator for time-domain dynamic stress concentration in a plate with a sharp change of section

S. Z. Peng and J. Pan[a)]
Centre for Acoustics, Dynamics and Vibration, School of Mechanical Engineering, The University of Western Australia, Crawley, WA 6009, Australia

(Received 23 March 2004; revised 6 September 2004; accepted 1 October 2004)

The acoustical wave propagator technique is applied to study the time-domain dynamic stress concentration in a two-dimensional flexible plate with a sharp change of section. As a wave packet approaches the plate discontinuity where the sharp change of thickness is introduced, the spatial interference patterns in the displacement of the plate and internal stresses vary with time. The constructive interference of stresses is referred to as time-domain stress concentration. The superposition of wave fronts of incident and reflected wave packets is used to explain the spatial distribution of the interference patterns. The increase of dynamic stress near the vicinity of the discontinuity boundary of the plate is studied as a function of time and the thickness ratio of the plates. © *2004 Acoustical Society of America.* [DOI: 10.1121/1.1823231]

PACS numbers: 43.20.Bi, 43.20.Fn, 43.20.Gp, 43.40.Dx [ANN] Pages: 492–502

I. INTRODUCTION

The development of damage identification techniques for vibrating structures such as ships and aircraft structures has become a focus of substantially growing research efforts. The prediction of dynamic stress in these structures may help to understand mechanisms associated with the damage, and to develop tools for detecting them. Of these structures, the study of dynamic stress concentration at the sharp change of sections of a plate has generated some interesting results. Ungar[1] utilized statistical energy analysis (SEA) to estimate the average mean square stress in mechanical systems subjected to a broad frequency band excitation. He demonstrated that dynamic stress concentration was an increase in dynamic stress at a boundary or a discontinuity due to evanescent wave effects. Stearn[2,3] studied the concentration of dynamic stress in an infinite flat plate at a change of section. Depending on its angle of incidence with respect to the change, a bending wave in such plates may be subjected to partial or total reflection, the resulting interference leading to the stress concentration. Pan *et al.*[4] studied the spatial variation in dynamic stress in finite beams subjected to different boundary conditions and broadband excitation at a point. It was shown that the stress spatial distribution depended on the driving force location, frequency characteristics, and boundary conditions. Cortinez and Laura[5] examined vibrating rectangular plates with discontinuously varying thickness by means of the Kantorovich extended method. Lee and Bergman[6] introduced an elemental dynamic flexibility method to formulate and solve the free and forced vibration problems of stepped Euler–Bernoulli beams and stepped rectangular thin plates. Shankar[7] utilized SEA and finite element analysis models to study the dynamic stress concentration factors of a flat plate. However, all these studies focused on the stress distributions in the vicinity of discontinuities in the frequency domain. There is still the need for effective and accurate methods to investigate the time-domain wave scattering and dynamic stress concentration, as many practical stress problems are essentially transient. Some work has been done for transient wave propagation in a plate with irregularities. Liu and his colleagues[8,9] introduced a strip element method for the transient analysis of symmetric laminated plates. They also presented a local point interpolation method for stress analysis of two-dimensional solids. Hayashi[10] with co-workers[11] used the semianalytical finite element method to investigate wave propagation in laminated plates with delamination. Galan and Abascal[12] introduced a hybrid boundary element–finite element technique in Lamb wave scattering by defects in homogeneous isotropic plates. Song *et al.*[13] investigated transmission and reflection of guided waves in an overlap plate. Pan and Wang[14] extended the work by Tal-Ezer and Kosloff[15] and developed the method of acoustical wave propagator (AWP) for investigating the propagation and scattering of a one-dimensional acoustic wave packet. The AWP method combines the Chebyshev polynomial expansion and fast Fourier transformation, and allows effective and accurate prediction of wave packet evolution with large time steps.

Most recently, Peng *et al.*[16] investigated wave propagation, coefficients of reflection and transmission in a one-dimensional stepped beam by using the AWP technique. They derived the exact analytical solution of a stepped beam under a Gaussian impulse excitation, and compared the predicted results obtained by the AWP technique with these exact solutions. The time-domain analysis shows a general understanding of wave propagation and scattering in a simple one-dimensional structure with a discontinuity. The motivation of this paper mainly focuses on the AWP method to flexible wave motion in two-dimensional (2D) plates and applying this method to study the time-domain dynamic stress concentration in a plate with a sharp change of section. The superposition of wave fronts of incident and reflected wave packets is used to explain the spatial location of the interference patterns. The effects of the thickness ratio of the

a)Electronic mail: pan@mech.uwa.edu.au

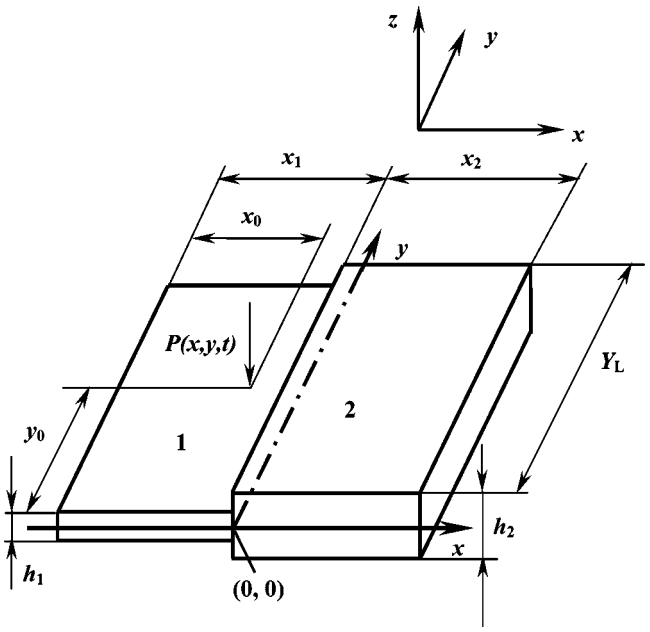

FIG. 1. Illustration of a stepped plate model.

plates on dynamic stress distribution near the vicinity of the discontinuity boundary of the plate are studied in detail.

II. STEP PLATE MODEL AND ACOUSTICAL WAVE PROPAGATOR

A portion of a stepped plate model is illustrated in Fig. 1. This model consists of two thin and homogeneous, elastic, and isotropic subplates of the same material and semi-infinite size, with uniform thicknesses of h_1 and h_2, respectively. The middle plane of this structure is chosen to be the xy plane. The boundary conditions then become $\sigma_z=0$, $\tau_{xz}=0$, and $\tau_{zy}=0$ at the $z=\pm h_1/2$ and $z=\pm h_2/2$ planes, where σ_z, τ_{xz}, and τ_{zy} are the normal and shear stresses, respectively. Only bending waves in the plate are considered and they are treated as two-dimensional waves. As illustrated in Fig. 1, a plate may be subjected to a distributed and time-dependent external pressure load $P(x,y,t)$ or an initial disturbance as initial conditions. The moments and shear forces due to internal stress resultants in the plate are then generated as responses to the external force and/or initial disturbance. Two kinds of moments, bending moments M_x and M_y, and twisting moments M_{xy} and M_{yx}, are involved.

Based on the hypotheses concerning the kinematics of deformation by the classical Kirchhoff's thin plate theory, let R_x, R_y, and R_{xy} be the radius of curvature of the displaced plate element in the planes parallel to the xz, yz, and xy planes, respectively. If small deflections and slopes are assumed, the corresponding curvatures can be approximated by $-\partial^2 W/\partial x^2$, $-\partial^2 W/\partial y^2$, and $-\partial^2 W/\partial x\partial y$, where $W(x,y,t)$ is the displacement of the plate in the z direction. The strain at distance R_x, from the neutral plane will be proportional to z, as described in the classical Kirchhoff's thin plate theory. The strain components are then given by[17]

$$\varepsilon_x=-z\frac{\partial^2 W}{\partial x^2},\quad \varepsilon_y=-z\frac{\partial^2 W}{\partial y^2},\quad \varepsilon_{xy}=-z\frac{\partial^2 W}{\partial x\partial y}, \tag{1}$$

where z is as a function of

$$h(x,y)=\begin{cases} h_1 & -x_1\leqslant x\leqslant 0 \\ h_2 & 0<x\leqslant x_2 \end{cases},$$

h_1 and h_2 denote the thickness of subplate 1 and subplate 2, respectively.

Thus, the stresses are determined by

$$\sigma_x=-\frac{Ez}{1-\upsilon^2}\left(\frac{\partial^2 W}{\partial x^2}+\upsilon\frac{\partial^2 W}{\partial y^2}\right),$$

$$\sigma_y=-\frac{Ez}{1-\upsilon^2}\left(\frac{\partial^2 W}{\partial y^2}+\upsilon\frac{\partial^2 W}{\partial x^2}\right),\quad \sigma_{xy}=-\frac{Ez}{1+\upsilon}\left(\frac{\partial^2 W}{\partial x\partial y}\right), \tag{2}$$

where E and υ are, respectively, the Young's modulus and Poisson's ratio of the plate.

The principal stress σ_P as a function of z and the displacement $W(x,y,t)$, is calculated by[18]

$$\sigma_P=\frac{\sigma_x+\sigma_y}{2}+\frac{\sqrt{(\sigma_x-\sigma_y)^2+4(\sigma_{xy})^2}}{2}. \tag{3}$$

The bending and twisting moments are given by

$$M_x=-D(x,y)\left(\frac{\partial^2 W}{\partial x^2}+\upsilon\frac{\partial^2 W}{\partial y^2}\right),$$

$$M_y=-D(x,y)\left(\frac{\partial^2 W}{\partial y^2}+\upsilon\frac{\partial^2 W}{\partial x^2}\right), \tag{4}$$

$$M_{xy}=-D(x,y)(1-\upsilon)\frac{\partial^2 W}{\partial x\partial y},$$

where

$$D(x,y)=\frac{Eh^3(x,y)}{12(1-\upsilon^2)}$$

is the flexural rigidity of the plate.

A state vector ϕ consisting of the velocity $V(x,y,t)$, the bending moments $M_x(x,y,t)$, $M_y(x,y,t)$, and one of the twisting moments $M_{xy}(x,y,t)$ of the plate element is selected to derive the acoustic wave propagator for flexural waves in a thin plate with a sharp change of section. Based on the moments and displacement relationship in the z direction and the flexural wave equation in a two-dimensional plate, we obtain the system state equation:

$$\frac{\partial}{\partial t}\begin{bmatrix} V(x,y,t) \\ M_x(x,y,t) \\ M_y(x,y,t) \\ M_{xy}(x,y,t) \end{bmatrix}=-\hat{\mathbf{H}}\begin{bmatrix} V(x,y,t) \\ M_x(x,y,t) \\ M_y(x,y,t) \\ M_{xy}(x,y,t) \end{bmatrix}, \tag{5}$$

where

$$\hat{\mathbf{H}}=\begin{bmatrix} 0 & -\frac{1}{\rho h(x,y)}\frac{\partial^2}{\partial x^2} & -\frac{1}{\rho h(x,y)}\frac{\partial^2}{\partial y^2} & -\frac{2}{\rho h(x,y)}\frac{\partial^2}{\partial x\partial y} \\ D(x,y)\left(\frac{\partial^2}{\partial x^2}+\upsilon\frac{\partial^2}{\partial y^2}\right) & 0 & 0 & 0 \\ D(x,y)\left(\frac{\partial^2}{\partial y^2}+\upsilon\frac{\partial^2}{\partial x^2}\right) & 0 & 0 & 0 \\ D(x,y)(1-\upsilon)\frac{\partial^2}{\partial x\partial y} & 0 & 0 & 0 \end{bmatrix}, \tag{6}$$

where ρ is the density of the plate.

Equation (5) with respect to time can be written in the form

$$\phi(x,y,t)=e^{-(t-t_0)\hat{\mathbf{H}}}\phi(x,y,t_0), \tag{7}$$

where $e^{-(t-t_0)\hat{\mathbf{H}}}$ is defined as the acoustical wave propagator.

The state vector $\phi(x,y,t)$ at instant t can be evaluated by the operation of the acoustical wave propagator acting upon the initial state vector $\phi(x,y,t_0)$. The boundary and spatial variation of the acoustical media are readily included in the system operator $\hat{\mathbf{H}}$ by defining the parameters in $\hat{\mathbf{H}}(D(x,y),E,\upsilon,\rho,h(x,y))$ as functions of position.

III. IMPLEMENTATION OF THE AWP

The implementation of the AWP has been discussed in detail in Refs. 14 and 19. From Eqs. (1), (2), (4), and (7), we are able to obtain complete information about the whole system [$W(x,y,t)$, $V(x,y,t)$, M_x, M_y, M_{xy}, ε_x, ε_y, ε_{xy}, σ_x, σ_y, and σ_{xy}] in the time domain by propagating the exponential propagator over the initial state for a length of time. Furthermore, we can obtain the principal stress distribution, particularly near the vicinity of discontinuities. To implement the AWP, the system operator $\hat{\mathbf{H}}$ needs to be normalized to ensure a convergent Chebyshev polynomial expansion,

$$\hat{\mathbf{H}}'=\frac{\hat{\mathbf{H}}}{\lambda_{\max}}, \tag{8}$$

where $\lambda_{\max}$ denotes the maximum eigenvalue of the system operator. Then the acoustical wave propagator is expanded in Chebyshev polynomials of the first kind. Equation (7) can be approximated by a sum of $N+1$ polynomials,

$$\begin{aligned}\phi(x,y,t)&=e^{-(t-t_0)\hat{\mathbf{H}}}\phi(x,y,t_0)\\ &\approx\sum_{n=0}^{N}a_n(R)T_n(\hat{\mathbf{H}}')\phi(x,y,t_0),\end{aligned} \tag{9}$$

where $R=(t-t_0)\lambda_{\max}$; T_n denotes the Chebyshev polynomial of degree n. The expansion coefficients a_n are obtained by utilizing the modified Bessel function of the first kind. $a_n(R)=2I_n(R)$ except $a_0(R)=I_0(R)$ and $I_n(R)$ is the nth-order modified Bessel function of the first kind.

Thus the AWP operation becomes the application of the normalized system operator $\hat{\mathbf{H}}'$ on the initial state vector, which mainly involves the evaluation of spatial derivatives. A fast Fourier transformation scheme is adopted to evaluate the spatial derivatives. Therefore, the calculation of the spatial derivatives of function $\phi(x,y,t)$ is obtained by the following inverse Fourier transformations:

$$\begin{aligned}\frac{\partial^2}{\partial x^2}\phi(x,y,t)&=F^{-1}\{(jk_x)^2F[\phi(x,y,t)]\},\\ \frac{\partial^2}{\partial y^2}\phi(x,y,t)&=F^{-1}\{(jk_y)^2F[\phi(x,y,t)]\},\\ \frac{\partial^2}{\partial x\partial y}\phi(x,y,t)&=F^{-1}\{(jk_x)(jk_y)F[\phi(x,y,t)]\},\end{aligned} \tag{10}$$

where $F^{-1}\{\ \}$ and $F[\ ]$ represent the inverse Fourier transformation and Fourier transformation, respectively; k_x and k_y are the wave numbers as in e^{jk_xx} and e^{jk_yy}, respectively.

The sampling interval is chosen to represent the highest frequency component of interest in the medium. When the spatial sampling intervals of Δx and Δy are given, the maximum bending wave number $k_{B_{\max}}$ can be calculated by

$$\sqrt{\left(\frac{\pi}{\Delta x}\right)^2+\left(\frac{\pi}{\Delta y}\right)^2}.$$

Accuracy and computational efficiency of this Chebyshev-Fourier scheme have been examined by the comparison of the predicted results obtained by the AWP technique with the exact analytical solutions and other numerical methods. More details are described in Refs. 14 and 19. In this paper, we focus on the features of time-domain stress concentration and the effect of the thickness ratio of the plates on the concentration.

IV. RESULTS AND DISCUSSION

The following initial state vector was selected:

$$\phi(x,y,0)=\begin{bmatrix}0\\ M_x(x,y,0)\\ M_y(x,y,0)\\ M_{xy}(x,y,0)\end{bmatrix}, \tag{11}$$

where $M_x(x,y,0)$, $M_y(x,y,0)$ and $M_{xy}(x,y,0)$ are related to the initial displacement,

$$W(x,y,0)=W_0\exp\left(-\frac{[(x-x_0)^2+(y-y_0)^2]}{4\sigma_0^2}\right);$$

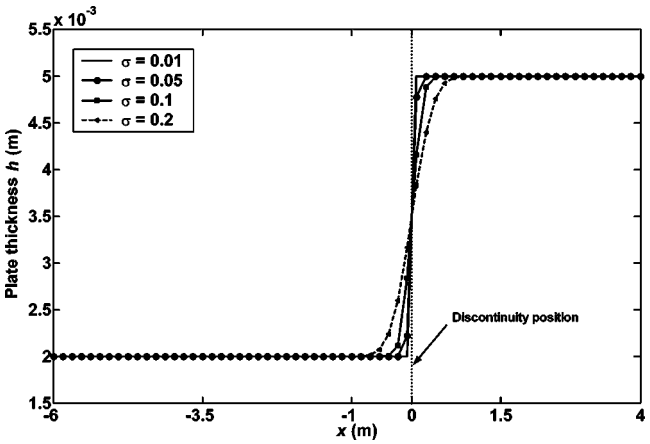

FIG. 2. The smoothing effect of different Gaussian factors σ at the thickness discontinuity when the number of grid points $N=64$.

W_0 and σ_0 represent the magnitude of the initial displacement and a Gaussian factor, respectively.

In using the acoustical wave propagator technique, the boundary of waves is described in terms of wave propagation properties of the media as function of position. For example, since $h(x,y)$ does not vary in the y direction, it can be expressed as

$$h(x,y)=\begin{cases} h_1 & -x_1 \leqslant x \leqslant 0 \\ h_2 & 0 < x \leqslant x_2 \end{cases},$$

where $x=0$ is the location of the discontinuity between two subplates. A discontinuity in the plate thickness is need to describe the nature of the step plate. To overcome the numerical difficulty posed by this thickness discontinuity, a boundary-smoothing technique introduced by using the following convolution with a Gaussian function $G(x)$ is required:

$$\overline{h}(x)=\frac{1}{2\pi}\int h(\tau)G(\tau)e^{-jx\tau}d\tau$$
$$=F^{-1}\{F[h(x)]F[e^{-(\xi-x)^2/\sigma^2}]\}, \quad (12)$$

where σ denotes the Gaussian factor, which determines the spatial spread of the smoothing region. It is noted that σ is related to the number of grid points over which the step change in thickness, N_d, is near discontinuity. Figure 2 shows the ''smoothed'' thickness discontinuity as a function of σ when $N=64$. As σ increases, the slope of the curve around the discontinuity becomes smooth. Table I describes the relationship among N, σ, and N_d. For example, when N is constant, N_d increases with σ. Similarly, when σ is constant, N_d increases with N. Theoretically speaking, smaller σ is preferred to choose to eliminate an error caused by this boundary-smoothing technique. However, for a sharp discontinuity, larger σ is necessary. In addition, a sufficient number of grid points over which the step changes in thickness are required to represent the correct derivatives. It is critical to choose a suitable N and σ to meet the demands of numerical convergence and computational efficiency. Figure 3 shows the effect of N and σ on the predicted results of the principal stress σ_P. When the smoothing Gaussian factor $\sigma=0.005$,

TABLE I. Relationship among N, Gaussian factor σ, and N_d.

N	Gaussian factor σ	N_d
64	0.01	1
	0.05	3
	0.1	7
	0.2	12
100	0.01	1
	0.05	5
	0.1	10
	0.2	19
128	0.01	2–3
	0.05	7
	0.1	13
	0.2	25
200	0.01	3–4
	0.05	9
	0.1	21
	0.2	40

the error between the predicted results obtained by the AWP technique and the exact analytical solutions are zero, as shown in Fig. 3(a)(1). As σ increases, the error caused by the smoothing technique increases exponentially, as shown in Figs. 3(a)(2)–3(a)(8). When $\sigma=0.1$, the introduced error by the smoothing technique can match the predicted results. In this case, $\sigma=0.01$ was used providing that the convergence is satisfied. To investigate the effect of this smoothing technique on the predicted results, when $N<128$, due to less points involved in the calculation, the curves of the principal stress σ_P, as shown in Figs. 3(b)(1) and 3(b)(2), are wave lines. The accumulation of numerical error gives inaccurate predictions. In some cases, as time increases, this accumulation will become worse and worse. Finally the dispersion of the calculation will happen. Further increase in N will slowly improve the accuracy of the predicted results of the principal stress σ_P, as shown in Figs. 3(b)(4) and 3(b)(5). Therefore, a minimum number of grid points, $N=128$, is required for accurate calculation.

Figure 4 shows the time evolution of the displacement in a stepped plate at four successive instants. The distribution of an initial Gaussian displacement is illustrated in Fig. 4(a). When $t=0.01275$ s, Fig. 4(b) shows slight wave interference around the discontinuity. The most interesting feature in Figs. 4(c) and 4(d) is the spatial wave interference patterns in the time-domain displacement. It is known that at a discontinuity, the incident bending waves are partly reflected, and the interference between the incident and reflected waves causes constructive and destructive displacement zones, as shown in Figs. 4(c) and 4(d). The principle can be quantitatively explained by the interference of sound pressure in front of a wall, as illustrated in Fig. 5, where the solid curves represent the incident spherical pressure wave packets, and the dotted curves represent the reflected packets by the wall. The magnitude of the combined pressure field depends on how the incident and reflected waves are superimposed at the instant of observation. For example, when the positive peak of the incident wave at a location meets the positive peak of the reflected wave, the sound pressure at this location in-

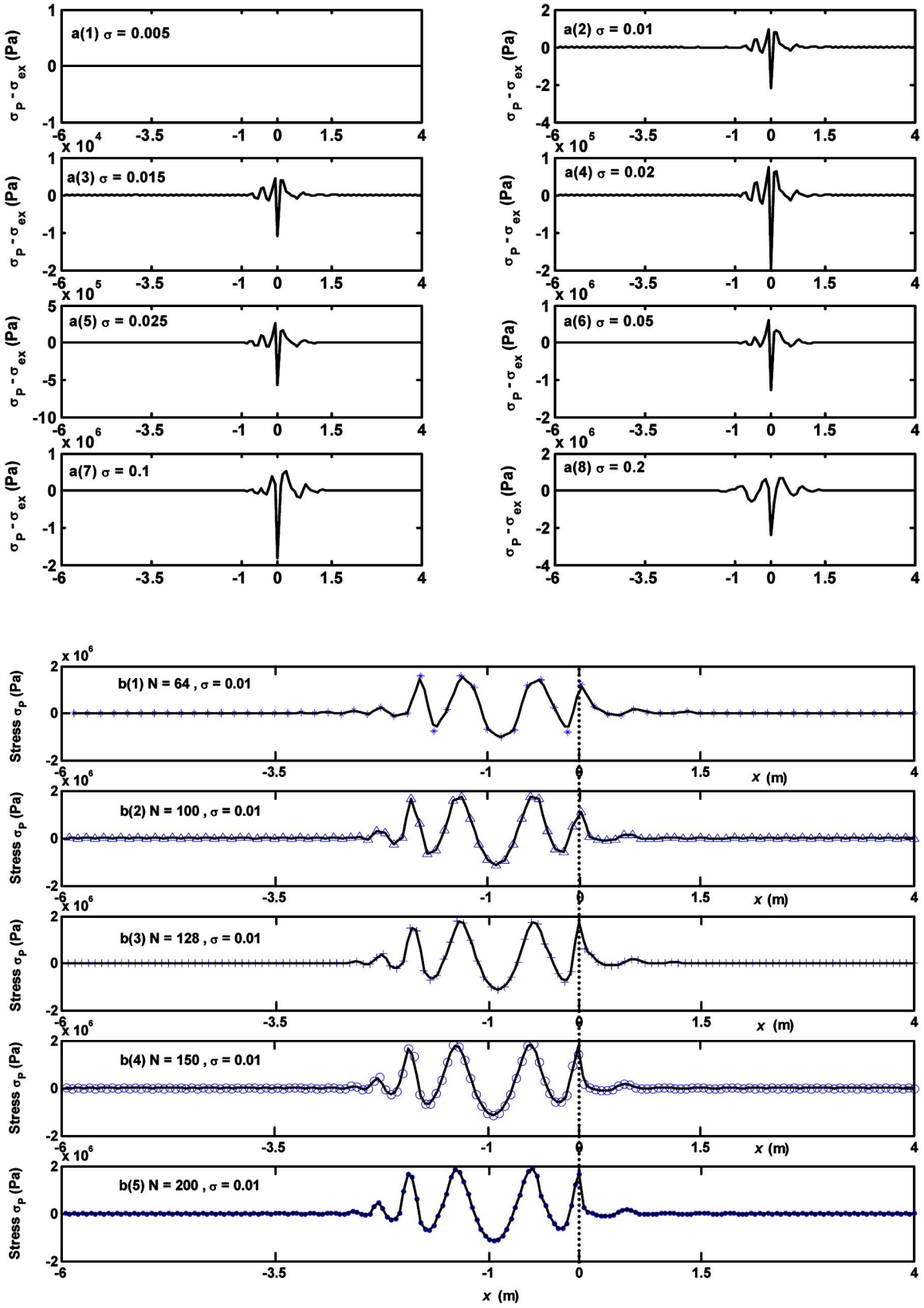

FIG. 3. Effect of the Gaussian factor σ and number of grid points N on the principal stress σ_P when $t=0.01$ s.

creases. The slashed solid lines show the maximum sound pressure locations.

To explain the patterns in Fig. 4, the reflected wave packet is analyzed, and the distribution of its displacement in subplate 1 is illustrated in Fig. 6. The total wave field in the subplate is a combination of the incident waves and the reflected waves. They are described by $\phi(x,y,t)^{(t)} = \phi(x,y,t)^{(i)} + \phi(x,y,t)^{(r)}$, where superscripts i, r, and t represent the incident, reflected, and total waves, respectively. It is noted that the incident waves are the same as

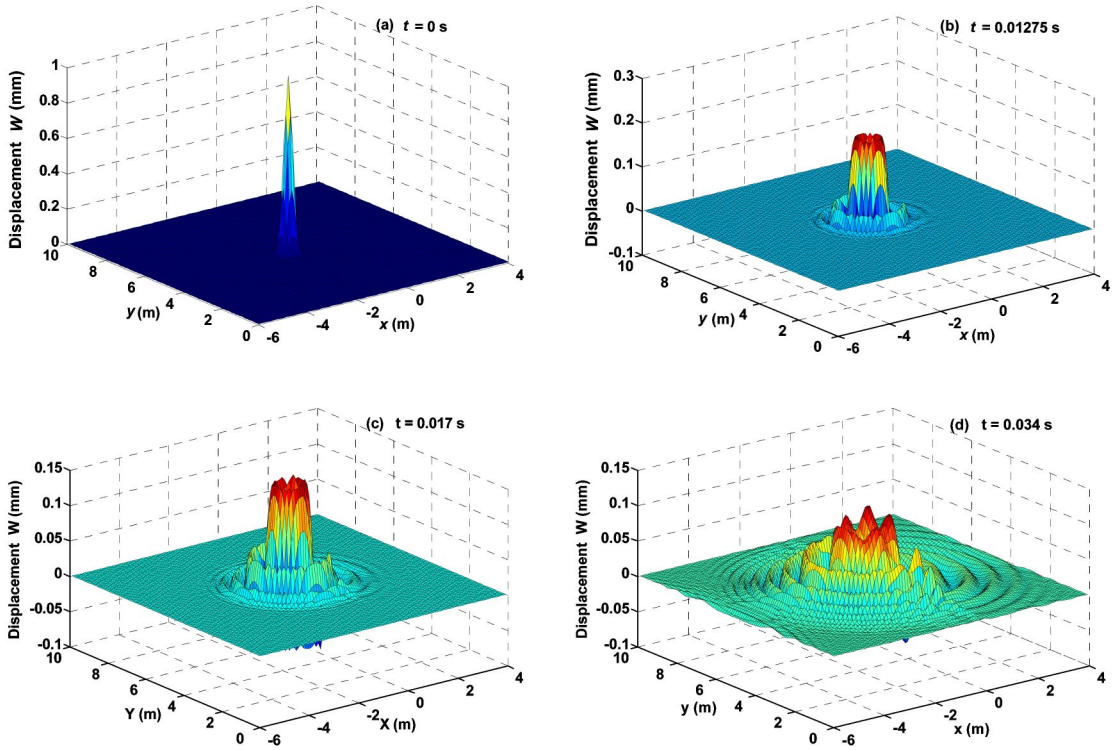

FIG. 4. Distributed flexural wave displacement W (mm) in a stepped plate at different time instants.

those without the discontinuity, which were investigated by Peng and Pan.[19] In this paper, we concentrate on the reflected waves. When $t=0.017$ s, one observation from Fig. 6(a) is that not only the reflected waves but also the incident waves have larger magnitudes at the first and second principal crests than the others. The results in Fig. 4(c) agree well with the above-mentioned analysis: the combined waves should have large increases in amplitude at the first and second principal crests. In addition, the combined waves as shown in Figs. 4(c) and 4(d) near the discontinuity have similar distributions to the reflected waves illustrated in Figs. 6(a) and 6(b). At $t=0.034$ s, another observation from Fig. 6(b) is that more reflected waves spread out and focus on two arcs near the discontinuity.

In contrast to an incident spherical wave, the magnitude of each component in the Gaussian wave packet varies with

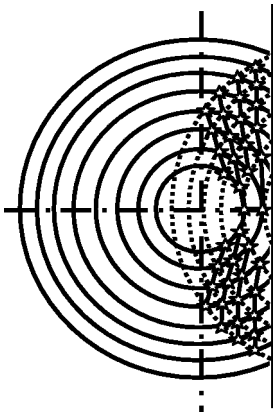

FIG. 5. Interference between the incident spherical waves and their reflected waves from a rigid wall.

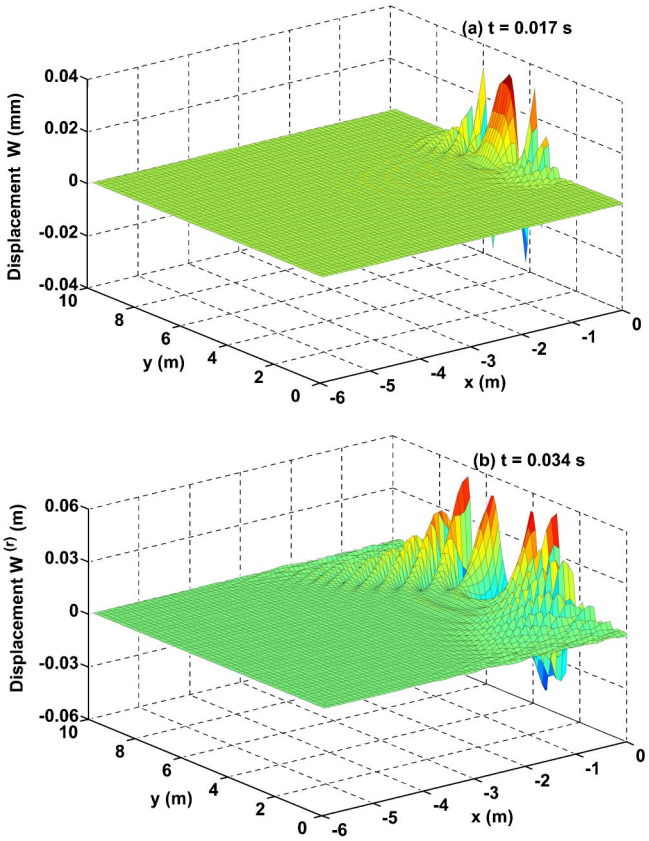

FIG. 6. Displacement of reflected waves $W^{(r)}$ in subplate 1 at different time instants.

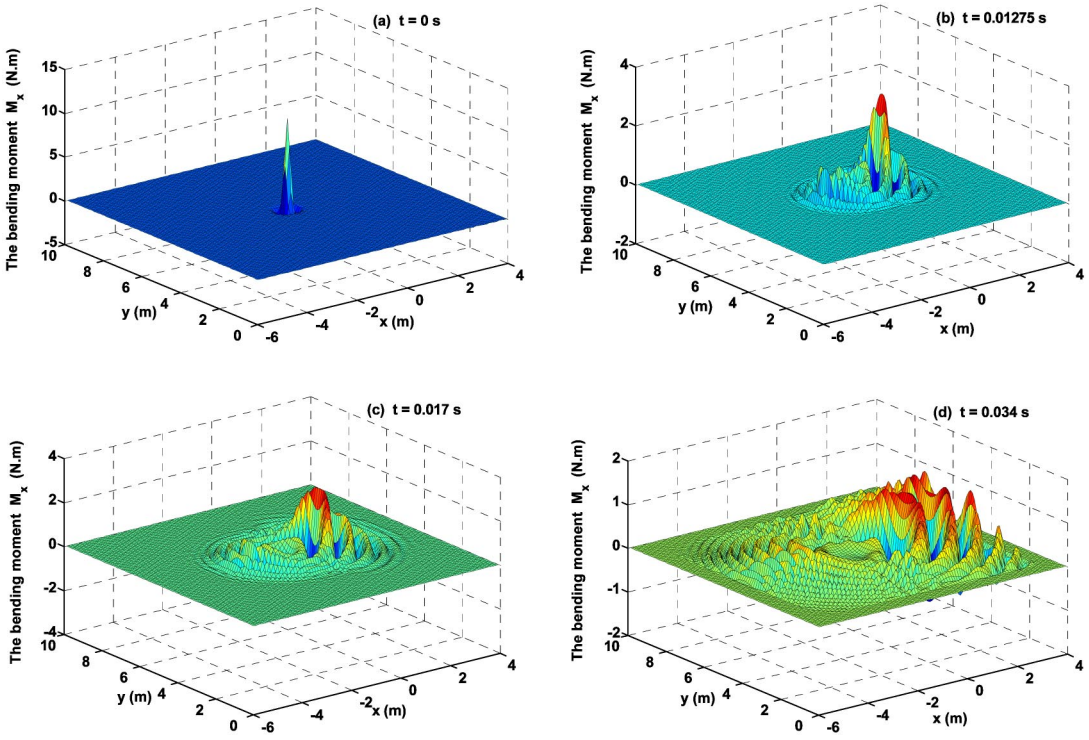

FIG. 7. Distribution of the bending moment M_x in a stepped plate at different time instants.

time. As mentioned earlier, the reflected waves vary with the incident waves, discontinuity conditions, and material properties. With an increase in time, the magnitude and distribution of the combined waves will change with the incident waves and reflected waves. Figure 6 gives a reasonable explanation of the distribution of displacement of flexural waves in a stepped plate as shown in Figs. 4(c) and 4(d).

Figure 7 shows the time evolution of the bending moment M_x in a stepped plate by the CPE/FFT scheme. The distribution of an initial moment is illustrated in Fig. 7(a) and it includes negative components. It is noted that, at $t=0.01275$ s, the moments in subplate 2 are much higher than those in subplate 1. In particular, the magnitudes of the second and third principal crests near the discontinuity are much larger than of the others. One reason is that the second and third principal crests of the incident waves have bigger magnitudes than the others described by Peng *et al.*[19,20] Another reason is that M_x given in Eq. (4) is a cubic function of the plate thickness. Due to the effect of the Poisson's ratio, the distribution of M_x is much different in magnitude and shape from that of displacement as shown in Fig. 4. For example, the maximum amplitude of M_x decreases quickly from 10.286 N m at $t=0$ s to 3.348 N m at $t=0.012\,75$ s. However, when time increases to 0.024 s, its amplitude only decreases slowly to 2.693 N m. At $t=0.034$ s, subplate 2 experiences more attenuation than subplate 1. It is noted that the magnitude of M_x for each total wave component in subplate 2 is still much larger than that in subplate 1. Similarly, this phenomenon is also observed from Fig. 7(d). Figure 8 shows the distribution of the bending moment of the reflected waves $M_x^{(r)}$ in subplate 1 at $t=0.017$ s and $t=0.034$ s. One can observe from Figs. 8(a) and 8(b) that the distributions of $M_x^{(r)}$ are similar to those in Figs. 6(a) and

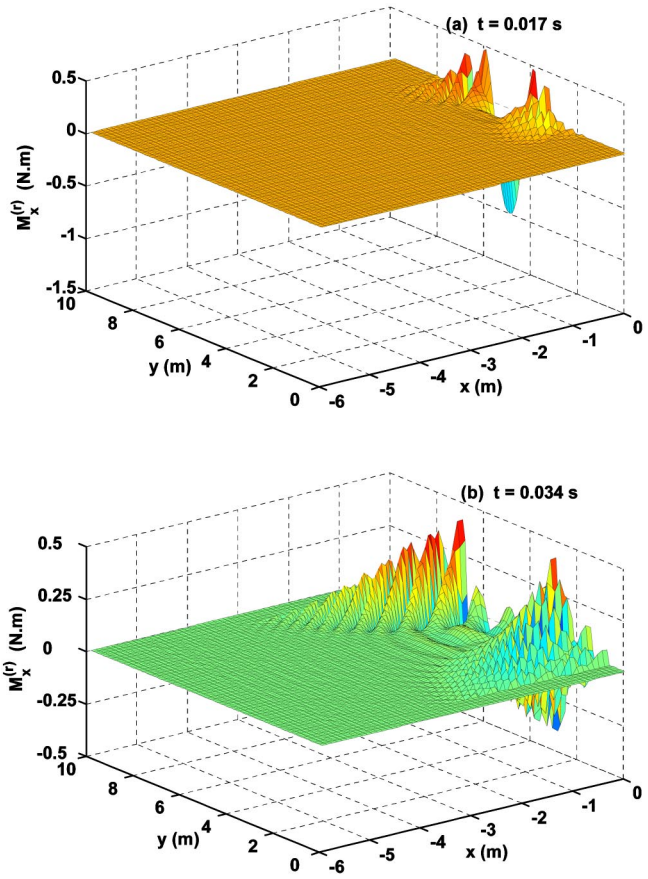

FIG. 8. Bending moment of reflected waves $M_x^{(r)}$ in subplate 1 at different time instants.

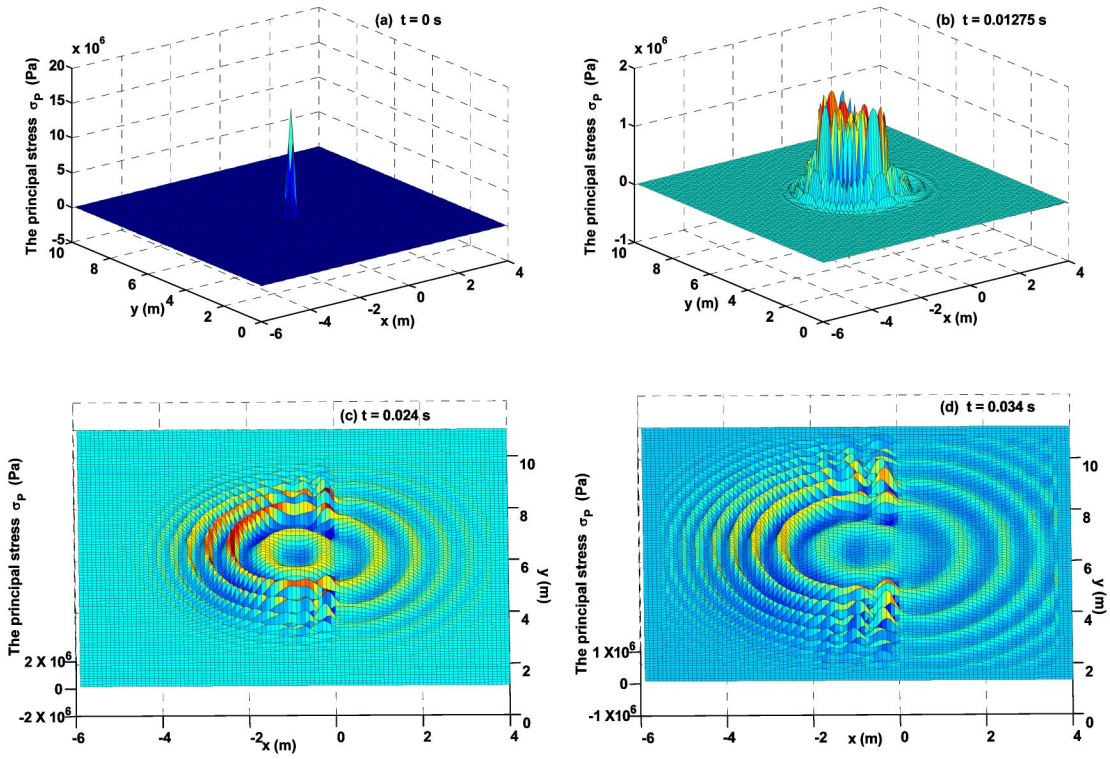

FIG. 9. Distribution of the principal stress σ_P in a stepped plate at different time instants.

6(b), respectively, except in magnitude. The closer the combined waves are to the discontinuity, the larger their magnitudes. These results have good agreement with those illustrated in Figs. 7(c) and 7(d).

Fatigue failures happen frequently in regions with a high stress concentration. Therefore, an understanding of the distribution of dynamic stress concentration is important in engineering design. Figure 9 shows the distribution of the principal dynamic stress σ_P in a stepped plate at different time instants. At $t=0$ s, an initial stress is concentrated on a small central area. As time increases, the principal stress concentration begins to spread out with decreased magnitude. At $t=0.017$ s, the magnitude of the principal stress in subplate 1 is much larger than that in subplate 2. In particular, at the discontinuity, two sharp peaks exist in the second and third principal crests. At $t=0.034$ s, two curve stress concentrations are distributed around this discontinuity. The degree of curve depends mainly on the plate thickness ratio, the material properties of the subplates, and the distance between the distributed location and discontinuity. With the exception of the magnitude, the principal stress distribution of the reflected waves as shown in Fig. 10 has a similar distribution to both the displacement of the reflected waves $W^{(r)}$ in Fig. 6 and the bending moment of the reflected waves $M_x^{(r)}$ in Fig. 8. The above-noted analysis of reflected waves supports the simulation results of the displacement, bending moment, and principal stress as shown in Figs. 4, 7, and 9, respectively.

It is necessary to investigate in detail the effect of the plate thickness ratio of the subplates on the displacement, moment and principal stress. The distribution of displacement is plotted in Fig. 11 for different thickness ratios along $y=5$ m at $t=0.017$ s and $t=0.034$ s. At $t=0.017$ s, the dis-

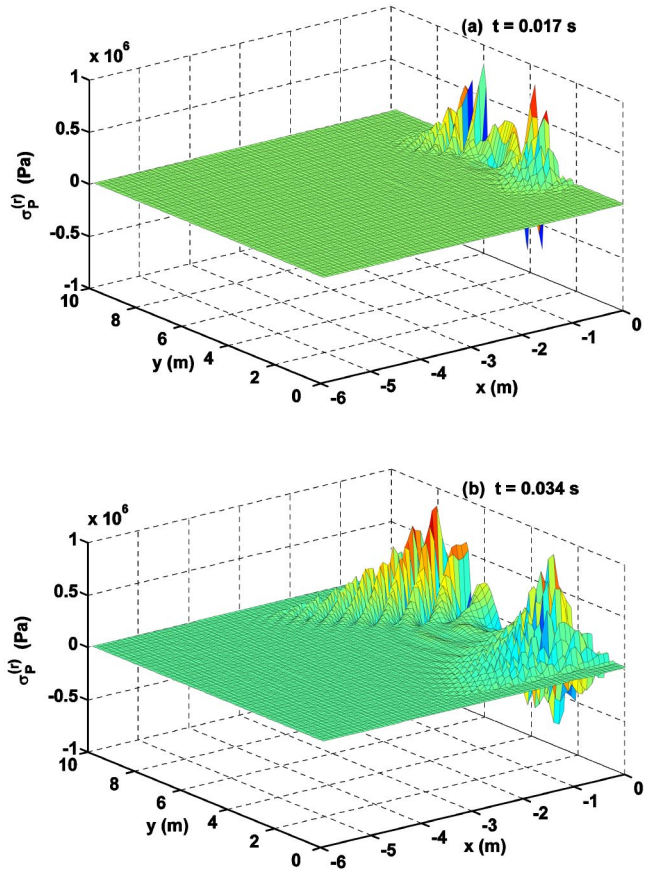

FIG. 10. Principal stress of reflected waves $\sigma_P^{(r)}$ in subplate 1 at different time instants.

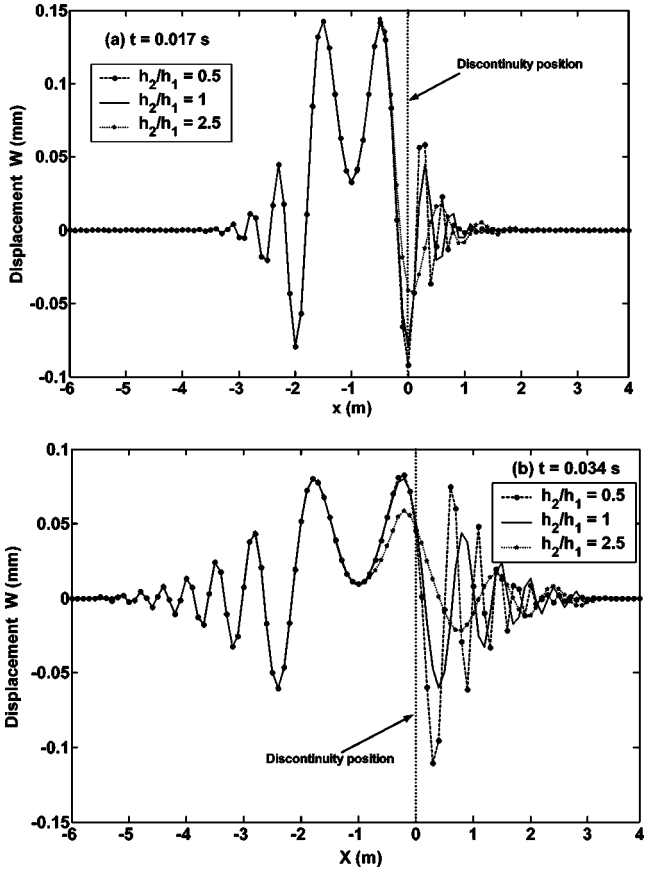

FIG. 11. Effect of the thickness ratio of the subplates on the displacement W (mm) along $y=5$ m at different time instants.

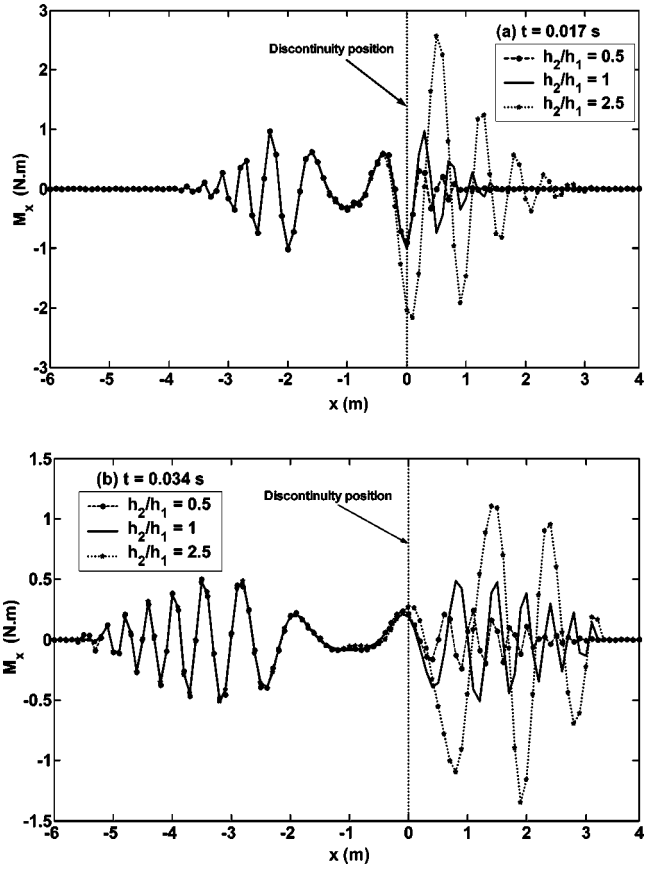

FIG. 12. Effect of the thickness ratio of the subplates on the bending moment M_x along $y=5$ m at different time instants.

placement varies in subplate 2 due to the effect of the reflected waves. As mentioned earlier, when the thickness ratio $\gamma>1$, only the transmitted waves exist in subplate 2 and the reflected waves in subplate 1. When the thickness ratio $\gamma<1$, more waves are transmitted to subplate 2 and there are fewer reflected waves with smaller magnitudes left in subplate 1. Therefore, the possibility of constructive interference gives rise to high stress in subplate 2. At $t=0.034$ s, the reflected waves largely occur between $x=-1.2$ m and $x=-0.2$ m in subplate 1 for $\gamma>1$ [see Fig. 11(b)]. For $\gamma<1$, Fig. 11(b) shows that a very different distribution of displacement occurred from $x=0.2$ m to $x=1.4$ m in subplate 2.

The bending moment increases with the plate thickness in subplate 2. At $t=0.017$ s, Figure 12(a) shows that for $\gamma>1$, the transmitted waves propagate with larger bending moments and wider interval distances between peaks in subplate 2; whereas for $\gamma<1$, the transmitted waves propagate with smaller bending moments and narrower interval distances between peaks in subplate 2, as illustrated in Fig. 12(a). As time increases, the reflected waves are distributed from $x=-1$ m to $x=0$ m as shown in Fig. 12(b). The magnitude and position of each principal crest in sub plate 2 vary with time. However, very different from the displacement distribution in Fig. 11(b), Fig. 12(b) shows that the reflected waves are distributed more widely, from $x=-2.8$ m to $x=0$ m.

The effect of the thickness ratio of the subplates γ on the principal stress distribution along $y=5$ m at different time instants was also studied in a similar way. As shown in Fig. 13, when $\gamma>1$, the principal stress concentration is located near the discontinuity in subplate 1. When $\gamma<1$, the principal stress concentration is located near the discontinuity in subplate 2. The distribution of the principal stress depends on γ. The closer γ is to 1, the closer is the principal stress to the discontinuity. As time increases, for $\gamma>1$, the reflected waves propagate in the opposite direction to the incident waves and combine with the incident waves, therefore cause an increase in stress as shown in Fig. 13(b). If the incident waves arrive at the discontinuity, they decompose into two parts, which are defined by $\phi(x,y,t)^{(i)}=\phi(x,y,t)^{(\mathrm{re})}+\phi(x,y,t)^{(\mathrm{tr})}$, where superscripts re and tr represent the reflected waves and transmitted waves, respectively. It is reasonable to assume that there are no other kinds of waves. It is noted that the principal stress of the transmitted waves decreases with the thickness of the subplates. As shown in Fig. 13(b) for $\gamma>1$, the reflected waves will dominate in subplate 1; whereas for $\gamma<1$, Fig. 13(b) shows that the transmitted waves dominate in subplate 2 and have larger values than the incident waves. A special case is when $\gamma=1$, where the entire plate becomes a single thin plate with a uniform thickness. In this case, there are no reflected waves and the transmitted waves equal the incident waves. As time increases, the principal stress will be distributed in each principal crest with a circular shape with the same magnitude and spread out with decreased magnitude.[19]

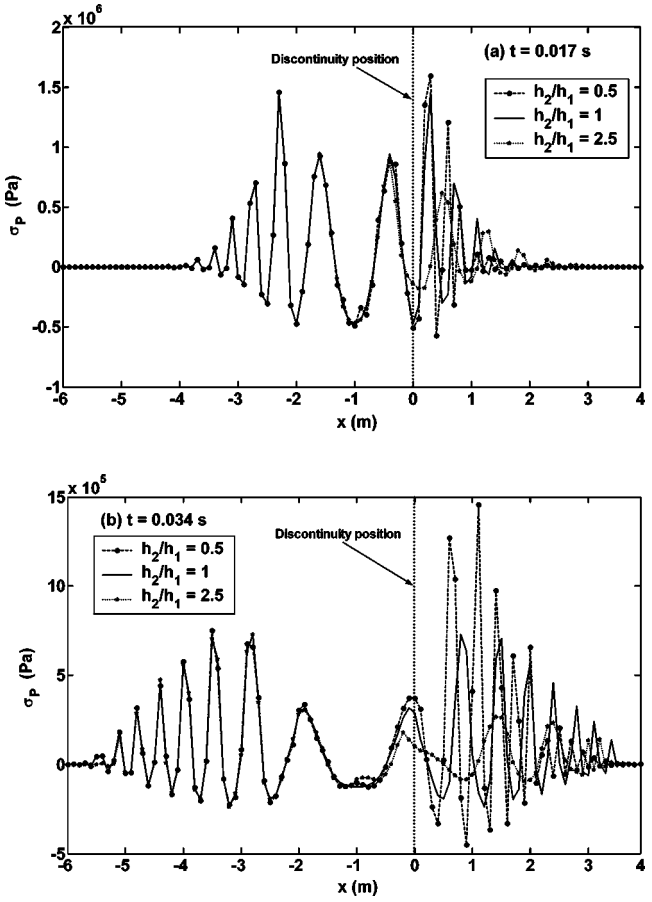

FIG. 13. Effect of the thickness ratio of the subplates on the principal stress σ_P along $y=5$ m at different time instants.

A further investigation was made into the dynamic stress concentration factor at a given location on the plate to show the effects of the step on dynamic stress concentration. It is defined as the ratio of the maximum value of the stress in the presence of the discontinuity (as the wave packet passes the discontinuity) to the maximum value without the discontinuity at the same location in the frequency domain.[1] In this paper, the dynamic stress concentration factor is evaluated in the time domain. Similarly, it is defined as the ratio of the maximum value of the stress with the discontinuity to the maximum value without the discontinuity at the same location. It is noted that such a factor is dependent upon the incident wave packets and reflected waves. Locations near the discontinuity are chosen to observe the principal stress distribution in the time domain. The predicted dynamic stress concentration factors at these locations at any instant can be obtained. These factors will change with time. However, the distribution of the dynamic stress concentration due to the effect of the reflection by the step is mainly focused on two curve areas around the discontinuity. The maximum value of the factors reaches 3 and it agrees with the value predicted in the frequency domain by Stearn.[2] Thus this proves that with the AWP technique, the principal dynamic stress and its concentration factor at any point and at any time can be easily predicted.

V. CONCLUSIONS

In this paper, the acoustical wave propagator technique is extended to describe the time-domain wave scattering and dynamic stress concentration in a two-dimensional thin plate with a sharp change of section. A Chebyshev polynomial expansion scheme combined with fast Fourier transformation is implemented to operate the acoustical wave propagator. This scheme can be used to predict the time-domain distributions of wave propagation and dynamic stress concentration at any point of interest and at any time. The distributions of displacement, bending moment, and dynamic stress are discussed in detail. The analysis of the reflected waves gives good support to these distributions. In addition, the effects of the thickness ratio of subplates γ on the wave propagation and principal dynamic stress distribution are investigated.

The model presented in this paper does not take into account three-dimensional (3D) stress, which may relate to the stress right at structure discontinuity. However, this does not invalidate the approach and the results, because the paper still contributes to our understanding of the phenomena outside the immediate vicinity of the step. For further study of detection of premature fatigue failure in complex structures, especially for thick plate structures, a detailed 3D stress analysis of the near field of longitudinal waves (Rayleith, Lamb waves) and high-order modes might give some new information that the existing 2D model cannot provide.

ACKNOWLEDGMENTS

The authors are grateful for Dr. J.B. Wang's and Dr. K.S. Sum's help in the numerical analysis. S.Z. Peng would like to thank the University of Western Australia for the financial support from the Dr. Julian Hunka Scholarship and an Australian Postgraduate Research Scholarship. The second author wish to thank the Chinese National Science Foundation (Project No. 60340420325).

[1] E.E. Ungar, "Transmission of plate flexural waves through reinforcing beams; dynamic stress concentration," J. Acoust. Soc. Am. **33**, 633–639 (1961).
[2] S.M. Stearn, "The concentration of dynamic stress in a plate at a sharp change of section," J. Sound Vib. **15**, 353–365 (1971).
[3] S.M. Stearn, "Spatial vibration of stress, strain and acceleration in structures subject to broad frequency band excitation," J. Sound Vib. **12**, 85–97 (1970).
[4] J. Pan, M.P. Norton and D. Karczub, "Broad band dynamic stress concentration in finite structures," Costs of Noise-Processings: Internoise-91, Vol. **1–2**, pp. 679–682.
[5] V.H. Cortinez and P.A.A. Laura, "Analysis of vibrating rectangular plates of discontinuously varying thickness by means of the Kantorovich extended method," J. Sound Vib. **137**, 457–461 (1990).
[6] J. Lee and L.A. Bergman, "The vibration of stepped beams and rectangular plates by an elemental dynamic flexibility method," J. Sound Vib. **171**, 617–640 (1994).
[7] K. Shankar, "A study of the dynamic stress concentration factors of a flat plate for SEA applications," J. Sound Vib. **217**, 97–111 (1998).
[8] G.R. Liu and Y.T. Gu, "A local point interpolation method for stress analysis of two-dimensional solids," Struct. Eng. Mech. **11**, 221–236 (2001).
[9] Y.Y. Wang, K.Y. Lam, and G.R. Liu, "A strip element method for the transient analysis of symmetric laminated plates," Int. J. Solids Struct. **38**, 241–259 (2001).
[10] T. Hayashi, "Multiple reflections of lamb waves at a delamination," Ultrasonics **40**, 193–197 (2002).
[11] T. Hayashi, K. Kawashima, Z.Q. Sun, and J.L. Rose, "Semi analytical

finite element analysis of ultrasonic focusing in a pipe,'' AIP Conference Proceedings, Washington, DC, 2002, pp. 250–255.
[12] J.M. Galan and R. Abascal, ''Lamb wave scattering by defects: A hybrid boundary element-finite element formulation,'' AIP Conference Proceedings, Marne, USA, 2001, pp. 211–218.
[13] W.J. Song, J.L. Rose, J.M. Galan and R. Abascal, ''Transmission and reflection of guided waves in a plate overlap,'' AIP Conference Proceedings, Washington, DC, 2002, pp. 1088–1094.
[14] J. Pan and J.B. Wang, ''Acoustical wave propagator,'' J. Acoust. Soc. Am. **108**, 481–487 (2000).
[15] H. Tal-Ezer and R. Kosloff, ''An accurate and efficient scheme for propagating the time-dependent Schrödinger equation,'' J. Chem. Phys. **81**, 3967–3971 (1984).
[16] S.Z. Peng, J. Pan, and K.S. Sum, ''Vibration analysis of one-dimensional structures with discontinuities using the acoustical wave propagator method,'' Proceedings of ICA2004, the 18th International Congress on Acoustics, Kyoto, Japan, 2004, pp. 2931–2934.
[17] Y.Y. Yu, *Vibration of Elastic Plates* (Springer, New York, 1996).
[18] W.F. Riley, L.D. Sturges, and D.H. Morris, *Mechanics of Materials* (Wiley, New York, 1999).
[19] S.Z. Peng and J. Pan, ''Acoustical wave propagator for time-domain flexural waves in thin plates,'' J. Acoust. Soc. Am. **115**, 467–474 (2004).
[20] S.Z. Peng, J. Pan, and K.S. Sum, ''Acoustical wave propagator technique for time-domain analysis of flexural wave scattering and dynamic stress concentration in a heterogeneous plate with multiple cylindrical patches,'' Proceedings of the Tenth International Congress on Sound and Vibration, Stockholm, Sweden, 2003, pp. 5021–5028.

Equations for finite-difference, time-domain simulation of sound propagation in moving inhomogeneous media and numerical implementation[a)]

Vladimir E. Ostashev
NOAA/Environmental Technology Laboratory, Boulder, Colorado 80305, and Department of Physics, New Mexico State University, Las Cruces, New Mexico 88003

D. Keith Wilson and Lanbo Liu
U.S. Army Engineer Research and Development Center, Hanover, New Hampshire 03755

David F. Aldridge and Neill P. Symons
Department of Geophysical Technology, Sandia National Labs., Albuquerque, New Mexico 87185

David Marlin
U.S. Army Research Laboratory, White Sands Missile Range, New Mexico 88002

(Received 24 February 2004; revision received 14 October 2004; accepted 5 November 2004)

Finite-difference, time-domain (FDTD) calculations are typically performed with partial differential equations that are first order in time. Equation sets appropriate for FDTD calculations in a moving inhomogeneous medium (with an emphasis on the atmosphere) are derived and discussed in this paper. Two candidate equation sets, both derived from linearized equations of fluid dynamics, are proposed. The first, which contains three coupled equations for the sound pressure, vector acoustic velocity, and acoustic density, is obtained without any approximations. The second, which contains two coupled equations for the sound pressure and vector acoustic velocity, is derived by ignoring terms proportional to the divergence of the medium velocity and the gradient of the ambient pressure. It is shown that the second set has the same or a wider range of applicability than equations for the sound pressure that have been previously used for analytical and numerical studies of sound propagation in a moving atmosphere. Practical FDTD implementation of the second set of equations is discussed. Results show good agreement with theoretical predictions of the sound pressure due to a point monochromatic source in a uniform, high Mach number flow and with Fast Field Program calculations of sound propagation in a stratified moving atmosphere. © *2005 Acoustical Society of America.* [DOI: 10.1121/1.1841531]

PACS numbers: 43.20.Bi, 43.28.Js [MO] Pages: 503–517

I. INTRODUCTION

Finite-difference, time-domain (FDTD) techniques have drawn substantial interest recently due to their ability to readily handle complicated phenomena in outdoor sound propagation such as scattering from buildings and trees, dynamic turbulence fields, complex moving source distributions, and propagation of transient signals.[1–8] These phenomena are difficult to handle with frequency–domain techniques that are currently widely used, such as parabolic equation approximations and the Fast Field Program (FFP). FDTD techniques typically solve coupled sets of partial differential equations that are first order in time. In this regard, they are a departure from methodologies such as the parabolic approximation, which solve a single equation for the sound pressure that is second order in time. Many such single equations for the sound pressure in a moving inhomogeneous medium are known in the literature (see Refs. 9–14 and references therein). Although these equations were obtained with different assumptions and/or approximations, all contain second- or higher-order derivatives of the sound pressure with respect to time, and are therefore not amenable to first-order FDTD techniques. Our main goal in the present paper is to derive equation sets that are appropriate as starting equations in FDTD simulations of sound propagation in a moving inhomogeneous atmosphere and to study the range of applicability of these sets.

The most general possible approach to sound propagation in a moving inhomogeneous medium would be based on a direct solution of the complete set of linearized equations of fluid dynamics,[9–11,15] which are first-order partial differential equations. Although this set could be used as starting equations for FDTD codes, even with modern computers it is too involved to be practical. Furthermore, this set contains the ambient pressure and entropy, which are not usually considered in studies of sound propagation in the atmosphere. Therefore, it is worthwhile to find simplified equation sets for use in FDTD calculations.

In the present paper, the complete set of linearized equations of fluid dynamics in a moving inhomogeneous medium is reduced to two simpler sets that are first order in time and

[a)]Portions of this work were presented in V. E. Ostashev, L. Liu, D. K. Wilson, M. L. Moran, D. F. Aldridge, and D. Marlin, "Starting equations for direct numerical simulation of sound propagation in the atmosphere," *Proceedings of the 10th International Symposium on Long Range Sound Propagation*, Grenoble, France, Sept. 2002, pp. 73–81.

amenable to FDTD implementation. The first set contains three coupled equations involving the sound pressure, vector acoustic (particle) velocity, and acoustic density. No approximations are made in deriving this set. The second set contains two coupled equations for the sound pressure and vector acoustic velocity. Although the second set describes sound propagation only approximately, the assumptions involved in deriving the second set are quite reasonable in atmospheric acoustics: Terms proportional to the divergence of the medium velocity and the gradient of the ambient atmospheric pressure are ignored. To better understand the range of applicability of the second set, we compare the set with equations for the sound pressure that have been previously used in analytical and numerical studies of sound propagation in a moving atmosphere. It is shown that the second set has the same or a wider range of applicability than these equations for the sound pressure.

Furthermore in the present paper, a basic numerical algorithm for solving the second set of equations in two-dimensional (2-D) moving inhomogeneous media is developed. Issues related to the finite-difference approximation of the spatial and temporal derivatives are discussed. FDTD solutions are obtained for a homogenous uniformly moving medium and for a stratified moving atmosphere. The first of these solutions is compared with an analytical formula for the sound pressure due to a point monochromatic source in a uniformly moving medium. The second solution is compared with predictions from before FFP.

Although the explicit emphasis of the discussion in this paper is on sound propagation in a moving inhomogeneous atmosphere, most of the derived equations are also valid for a general case of sound propagation in a moving inhomogeneous medium with an arbitrary equation of state, e.g., in the ocean with currents. Equations presented in the paper are also compared with those known in aeroacoustics.

The paper is organized as follows. In Sec. II, we consider the complete set of equations of fluid dynamics and their linearization. In Sec. III, the linearized equations are reduced to the set of three coupled equations for the sound pressure, acoustic velocity, and acoustic density. In Sec. IV, we consider the set of two coupled equations for the acoustic pressure and acoustic velocity. Numerical implementation of this set is considered in Sec. V.

II. EQUATIONS OF FLUID DYNAMICS AND THEIR LINEARIZATION

Let $\tilde{P}(\mathbf{R},t)$ be the pressure, $\tilde{\varrho}(\mathbf{R},t)$ the density, $\tilde{\mathbf{v}}(\mathbf{R},t)$ the velocity vector, and $\tilde{S}(\mathbf{R},t)$ the entropy in a medium. Here, $\mathbf{R}=(x,y,z)$ are the Cartesian coordinates, and t is time. These functions satisfy a complete set of fluid dynamic equations (e.g. Ref. 16):

$$\left(\frac{\partial}{\partial t}+\tilde{\mathbf{v}}\cdot\boldsymbol{\nabla}\right)\tilde{\mathbf{v}}+\frac{\boldsymbol{\nabla}\tilde{P}}{\tilde{\varrho}}-\mathbf{g}=\mathbf{F}/\tilde{\varrho}, \tag{1}$$

$$\left(\frac{\partial}{\partial t}+\tilde{\mathbf{v}}\cdot\boldsymbol{\nabla}\right)\tilde{\varrho}+\tilde{\varrho}\boldsymbol{\nabla}\cdot\tilde{\mathbf{v}}=\tilde{\varrho}Q, \tag{2}$$

$$\left(\frac{\partial}{\partial t}+\tilde{\mathbf{v}}\cdot\boldsymbol{\nabla}\right)\tilde{S}=0, \tag{3}$$

$$\tilde{P}=\tilde{P}(\tilde{\varrho},\tilde{S}). \tag{4}$$

In Eqs. (1)–(4), $\boldsymbol{\nabla}=(\partial/\partial x,\partial/\partial y,\partial/\partial z)$, $\mathbf{g}=(0,0,g)$ is the acceleration due to gravity, and $\mathbf{F}$ and Q characterize a force acting on the medium and a mass source, respectively. For simplicity, we do not consider the case when a passive component is dissolved in a medium (e.g., water vapor in the dry air, or salt in water). This case is considered in detail elsewhere.[9,17]

If a sound wave propagates in a medium, in Eqs. (1)–(4) $\tilde{P}$, $\tilde{\varrho}$, $\tilde{\mathbf{v}}$, and $\tilde{S}$ can be expressed in the following form: $\tilde{P}=P+p$, $\tilde{\varrho}=\varrho+\eta$, $\tilde{\mathbf{v}}=\mathbf{v}+\mathbf{w}$, and $\tilde{S}=S+s$. Here, P, ϱ, $\mathbf{v}$, and S are the ambient values (i.e., the values in the absence of a sound wave) of the pressure, density, medium velocity, and entropy in a medium, and p, η, $\mathbf{w}$, and s are their fluctuations due to a propagating sound wave. In order to obtain equations for a sound wave, Eqs. (1)–(4) are linearized with respect to p, η, $\mathbf{w}$, and s. Assuming that a sound wave is generated by the mass source Q and/or the force $\mathbf{F}$ and introducing the full derivative with respect to time $d/dt=\partial/\partial t+\mathbf{v}\cdot\boldsymbol{\nabla}$, we have

$$\frac{d\mathbf{w}}{dt}+(\mathbf{w}\cdot\boldsymbol{\nabla})\mathbf{v}+\frac{\boldsymbol{\nabla}p}{\varrho}-\frac{\eta\boldsymbol{\nabla}P}{\varrho^2}=\mathbf{F}/\varrho, \tag{5}$$

$$\frac{d\eta}{dt}+(\mathbf{w}\cdot\boldsymbol{\nabla})\varrho+\varrho\boldsymbol{\nabla}\cdot\mathbf{w}+\eta\boldsymbol{\nabla}\cdot\mathbf{v}=\varrho Q, \tag{6}$$

$$\frac{ds}{dt}+(\mathbf{w}\cdot\boldsymbol{\nabla})S=0, \tag{7}$$

$$p=\eta c^2+hs. \tag{8}$$

Here, $c=\sqrt{\partial P(\varrho,S)/\partial\varrho}$ is the adiabatic sound speed, and the parameter h is given by $h=\partial P(\varrho,S)/\partial S$. The set of Eqs. (5)–(8) provides a most general description of sound propagation in a moving inhomogeneous medium with only one component. In order to calculate p, η, $\mathbf{w}$, and s, one needs to know the ambient quantities c, ϱ, $\mathbf{v}$, P, S, and h. Note that Eqs. (5)–(8) describe the propagation of both acoustic and internal gravity waves, as well as vorticity and entropy waves (e.g., Ref. 18).

Equations (5)–(8) were derived for the first time by Blokhintzev in 1946.[17] Since then, these equations have been widely used in studies of sound propagation (e.g., Refs. 9–11). In the general case of a moving inhomogeneous medium, Eqs. (5)–(8) cannot be exactly reduced to a single equation for the sound pressure p. In the literature, Eqs. (5)–(8) have been reduced to equations for p, making use of different approximations or assumptions about the ambient medium. These equations for p were subsequently used for analytical and numerical studies of sound propagation. They are discussed in Sec. IV. Note that the equations for p known in the literature contain the following ambient quantities: c, ϱ, and $\mathbf{v}$. On the other hand, the linearized equations of fluid dynamics, Eqs. (5)–(8), contain not only c, ϱ, and $\mathbf{v}$, but

also P, S, and h. This fact indicates that the effect of P, S, and h on sound propagation is probably small for most of problems considered so far in the literature.

The effect of medium motion on sound propagation is also studied in aeroacoustics, e.g., see Refs. 12, 19–24 and references therein. In aeroacoustics, the starting equations coincide with Eqs. (1)–(4) but might also include terms describing viscosity and thermal conductivity in a medium. Using these equations of fluid dynamics, equations for sound waves are derived which have some similarities with Eqs. (5)–(8). For example, Eqs. (5)–(8) are equivalent to Eqs. (1.11) from Ref. 12, and Eq. (6) can be found in Refs. 19, 22, 23. The main difference between Eqs. (5)–(8) and those in aeroacoustics are sound sources. In atmospheric acoustics, in Eqs. (5)–(8) the sources $\mathbf{F}$ and Q are assumed to be known and are loudspeakers, car engines, etc. In aeroacoustics, these sources have to be calculated and are those due to ambient flow. Furthermore in some formulations in aeroacoustics, the left-hand side of Eq. (5) contains nonlinear terms.[21–23] Note that FDTD calculations are nowadays widely used in aeroacoustics, e.g., Refs. 19, 20, 24.

Also note that in aeroacoustics it is sometimes assumed that the ambient medium is incompressible and/or isentropic, i.e., $S=\text{const}$. Generally, these assumptions are inappropriate for atmospheric acoustics. Indeed, sound waves can be significantly scattered by density fluctuations, e.g., see Sec. 6.1.4 from Ref. 9. Furthermore, in a stratified atmosphere S depends on the height above the ground. The range of applicability of the assumption $S=\text{const}$ (which is equivalent to $s=0$ or $p=c^2\eta$) is studied in Sec. 2.2.4 from Ref. 9. For a stratified medium, this assumption is not applicable if the scale of the ambient density variations is smaller than the sound wave length or if the ambient density noticeably changes with height.

III. SET OF THREE COUPLED EQUATIONS

A. Moving medium with an arbitrary equation of state

Applying the operator $(\partial/\partial t+\tilde{\mathbf{v}}\cdot\boldsymbol{\nabla})$ to both sides of Eq. (4) and using Eq. (3), we have

$$\left(\frac{\partial}{\partial t}+\tilde{\mathbf{v}}\cdot\boldsymbol{\nabla}\right)\tilde{P}=\tilde{c}^2\left(\frac{\partial}{\partial t}+\tilde{\mathbf{v}}\cdot\boldsymbol{\nabla}\right)\tilde{\varrho}, \tag{9}$$

where $\tilde{c}^2=\partial\tilde{P}(\tilde{\varrho},\tilde{S})/\partial\tilde{\varrho}$ differs from the square of the adiabatic sound speed $c^2=\partial P(\varrho,S)/\partial\varrho$. Using Eq. (2), Eq. (9) can be written as

$$\left(\frac{\partial}{\partial t}+\tilde{\mathbf{v}}\cdot\boldsymbol{\nabla}\right)\tilde{P}+\tilde{c}^2\tilde{\varrho}\boldsymbol{\nabla}\cdot\tilde{\mathbf{v}}=\tilde{c}^2\tilde{\varrho}Q. \tag{10}$$

The next step is to linearize Eq. (10) to obtain an equation for acoustic quantities. To do so we need to calculate the value of $\tilde{c}^2=\partial\tilde{P}(\tilde{\varrho},\tilde{S})/\partial\tilde{\varrho}$ to the first order in acoustic perturbations. In this formula, we express $\tilde{\varrho}$ and $\tilde{S}$ as the sums $\tilde{\varrho}=\varrho+\eta$ and $\tilde{S}=S+s$, decompose the function P into Taylor series, and keep the terms of the first order in η and s:

$$\begin{aligned}\tilde{c}^2&=\frac{\partial\tilde{P}(\tilde{\varrho},\tilde{S})}{\partial\tilde{\varrho}}=\frac{\partial}{\partial\varrho}P(\varrho+\eta,S+s)\\&=\frac{\partial}{\partial\varrho}\left[P(\varrho,S)+\frac{\partial P(\varrho,S)}{\partial\varrho}\eta+\frac{\partial P(\varrho,S)}{\partial S}s\right]\\&=\frac{\partial P(\varrho,S)}{\partial\varrho}+\frac{\partial^2P(\varrho,S)}{\partial\varrho^2}\eta+\frac{\partial^2P(\varrho,S)}{\partial\varrho\,\partial S}s.\end{aligned} \tag{11}$$

The first term in the last line of this equation is equal to c^2. Denoting $\beta=\partial^2P(\varrho,S)/\partial\varrho^2$ and $\alpha=\partial^2P(\varrho,S)/\partial\varrho\,\partial S$, we have $\tilde{c}^2=c^2+\beta\eta+\alpha s=c^2+(c^2)'$. Here, $(c^2)'=\beta\eta+\alpha s$ are fluctuations in the squared sound speed due to a propagating sound wave. In this formula, s can be replaced by its value from Eq. (8): $s=(p-c^2\eta)/h$. As a result, we obtain the desired formula for fluctuations in the squared sound speed: $(c^2)'=(\beta-\alpha c^2/h)\eta+\alpha p/h$.

Now we can linearize Eq. (10). In this equation, we express $\tilde{P}$, $\tilde{\varrho}$, $\tilde{\mathbf{v}}$, and $\tilde{c}^2$ as the sums: $\tilde{P}=P+p$, $\tilde{\varrho}=\varrho+\eta$, $\tilde{\mathbf{v}}=\mathbf{v}+\mathbf{w}$, and $\tilde{c}^2=c^2+(c^2)'$. Linearizing the resulting equation with respect to acoustic quantities, we have

$$\frac{dp}{dt}+\varrho c^2\boldsymbol{\nabla}\cdot\mathbf{w}+\mathbf{w}\cdot\boldsymbol{\nabla}P+(c^2\eta+\varrho(c^2)')\boldsymbol{\nabla}\cdot\mathbf{v}=\varrho c^2Q. \tag{12}$$

In this equation, $(c^2)'$ is replaced by its value obtained above. As a result, we arrive at the following equation for dp/dt:

$$\begin{aligned}\frac{dp}{dt}+\varrho c^2\boldsymbol{\nabla}\cdot\mathbf{w}+\mathbf{w}\cdot\boldsymbol{\nabla}P+\{[\varrho\beta+c^2(1-\alpha\varrho/h)]\eta\\+(\alpha\varrho/h)p\}\boldsymbol{\nabla}\cdot\mathbf{v}=\varrho c^2Q.\end{aligned} \tag{13}$$

Equations (5), (6), and (13) comprise a desired set of three coupled equations for p, $\mathbf{w}$, and η. This set was obtained from linearized equations of fluid dynamics, Eqs. (5)–(8), without any approximations. The set can be used as starting equations for FDTD simulations. In this set, one needs to know the following ambient quantities: c, ϱ, $\mathbf{v}$, P, α, β, and h.

B. Set of three equations for an ideal gas

In most applications, the atmosphere can be considered as an ideal gas. In this case, the equation of state reads (e.g., Refs. 9, 17) as

$$P=P_0(\varrho/\varrho_0)^\gamma\exp[(\gamma-1)(S-S_0)/R_a], \tag{14}$$

where $\gamma=1.4$ is the ratio of specific heats at constant pressure and constant volume, R_a is the gas constant for the air, and the subscript 0 indicates reference values of P, ϱ, and S. Using Eq. (14), the sound speed c and the coefficients α, β, and h appearing in Eq. (13) can be calculated: $c^2=\gamma P/\varrho$, $\alpha=\gamma(\gamma-1)P/(\varrho R_a)$, $\beta=\gamma(\gamma-1)P/\varrho^2$, and $h=(\gamma-1)P/R_a$. Substituting these values into Eq. (13), we have

$$\frac{dp}{dt}+\varrho c^2\boldsymbol{\nabla}\cdot\mathbf{w}+\mathbf{w}\cdot\boldsymbol{\nabla}P+\gamma p\boldsymbol{\nabla}\cdot\mathbf{v}=\varrho c^2Q. \tag{15}$$

A set of Eqs. (5), (6), and (15) is a closed set of three coupled equations for p, $\mathbf{w}$, and η for the case of an ideal

gas. To solve these equations, one needs to know the following ambient quantities: c, ϱ, $\mathbf{v}$, and P.

Let us compare Eqs. (5), (6), and (15) with a closed set of equations for p and $\mathbf{w}$ from Ref. 1; see Eqs. (12) and (13) from that reference. The latter set was used in Refs. 1, 2 as starting equations for FDTD simulations of outdoor sound propagation. If $Q=0$, Eq. (15) in the present paper is essentially the same as Eq. (13) from Ref. 1. [Note that Eq. (15) is also used in aeroacoustics, e.g., Ref. 19.] Furthermore for the case of a nonabsorbing medium, Eq. (12) from Ref. 1 is given by

$$\frac{d\mathbf{w}}{dt}+(\mathbf{w}\cdot\nabla)\mathbf{v}+\frac{\nabla p}{\varrho}-\frac{p\nabla P}{\gamma P\varrho}=0. \tag{16}$$

Let us show that this equation is an approximate version of Eq. (5) in the present paper. Indeed, in Eq. (5) we replace η by its value from Eq. (8): $\eta=(p-hs)/c^2$, and assume that $s=0$. If $\mathbf{F}=0$, the resulting equation coincides with Eq. (16). Thus, for an ideal gas and $\mathbf{F}=0$ and $Q=0$, Eqs. (12) and (13) from Ref. 1 are equivalent to Eqs. (5) and (15) in the present paper if s can be set to 0. The range of applicability of the approximation $s=0$ is considered above.

IV. SET OF TWO COUPLED EQUATIONS

A. Set of equations for *p* and w

In atmospheric acoustics, Eqs. (5) and (13) can be simplified since v is always much less than c. First, using Ref. 16, it can be shown that $\nabla\cdot\mathbf{v}\sim v^3/(c^2L)$, where L is the length scale of variations in the density ϱ. Therefore, in Eq. (13) the term proportional to $\nabla\cdot\mathbf{v}$ can be ignored to order v^2/c^2. Second, in Eqs. (5) and (13) the terms proportional to ∇P can also be ignored. Indeed, in a moving inhomogeneous atmosphere ∇P is of the order v^2/c^2 so that these terms can be ignored to order v/c. Furthermore, in a stratified atmosphere, $\nabla P=-g\varrho$, where g is the acceleration due to gravity. It is known that, in linearized equations of fluid dynamics, terms proportional to g are important for internal gravity waves and can be omitted for acoustic waves.

With these approximations, Eqs. (13) and (5) become

$$\left(\frac{\partial}{\partial t}+\mathbf{v}\cdot\nabla\right)p+\varrho c^2\nabla\cdot\mathbf{w}=\varrho c^2Q, \tag{17}$$

$$\left(\frac{\partial}{\partial t}+\mathbf{v}\cdot\nabla\right)\mathbf{w}+(\mathbf{w}\cdot\nabla)\mathbf{v}+\frac{\nabla p}{\varrho}=\mathbf{F}/\varrho. \tag{18}$$

Equations (17) and (18) comprise the desired closed set of two coupled equations for p and $\mathbf{w}$. This set can also be used in FDTD simulations of sound propagation in the atmosphere. In order to solve this set, one needs to know the following ambient quantities: c, ϱ, and $\mathbf{v}$. These ambient quantities appear in equations for the sound pressure p that have been most often used for analytical and numerical studies of sound propagation in moving media. The set of Eqs. (17) and (18) is simpler than the set of three coupled equations, Eqs. (5), (6), and (13), and does not contain the ambient quantities P, α, β, and h. It can be shown that Eqs. (17) and (18) describe the propagation of acoustic and vorticity waves but do not describe entropy or internal gravity waves.

Equations (17) and (18) were derived in Ref. 25 [see also Eqs. (2.68) and (2.69) from Ref. 9] using a different approach. In these references, Eqs. (17) and (18) were derived for the case of a moving inhomogeneous medium with more than one component (e.g., humid air or salt water). Equations (17) and (18) are somewhat similar to the starting equations in FDTD simulations used in Ref. 3; see Eqs. (10) and (12) from that reference. The last of these equations coincides with Eq. (17) while the first is given by

$$\frac{\partial\mathbf{w}}{\partial t}-\mathbf{w}\times(\nabla\times\mathbf{v})+\frac{\nabla p}{\varrho_0}+\nabla[\mathbf{w}\cdot\mathbf{v}]=0. \tag{19}$$

Using vector algebra, the left-hand side of this equation can be written as a left-hand side of Eq. (18) plus an extra term $\mathbf{v}\times(\nabla\times\mathbf{w})$. Equations (10) and (12) from Ref. 3 were obtained using several assumptions that were not employed in the present paper when deriving Eqs. (17) and (18): $\partial\mathbf{v}/\partial t=\partial\varrho/\partial t=\nabla\varrho=0$, c is constant, and $\partial\mathbf{w}/\partial t\gg\mathbf{v}\times(\nabla\times\mathbf{w})$. It follows from the last inequality that the ''extra'' term $\mathbf{v}\times(\nabla\times\mathbf{w})$ in Eq. (19) can actually be omitted. Note that in Ref. 4 different starting equations were used in simulations of sound propagation in a muffler with a low Mach number flow. The use of Eq. (19) resulted in increase of stability in such simulations.

Also note that equations for p and $\mathbf{w}$ similar to Eqs. (17) and (18) are used in aeroacoustics, e.g. Refs. 20, 24. The left-hand sides of Eqs. (7) in Ref. 20 contain several extra terms in comparison with the left-hand sides of Eqs. (17) and (18) which, however, vanish if $\nabla P=0$ and $\nabla\cdot\mathbf{v}=0$. The left-hand sides of Eqs. (75) and (76) in Ref. 24 also contain extra terms in comparison with the left-hand sides of Eqs. (17) and (18), e.g., terms proportional to the gradients of c and ϱ. The right-hand sides of the equations in Refs. 20, 24 describe aeroacoustic sources and differ from those in Eqs. (17) and (18).

At the beginning of this section, we provided sufficient conditions for the applicability of Eqs. (17) and (18). Actually, the range of applicability of these equations can be much wider. Note that it is quite difficult to estimate with what accuracy one can ignore certain terms in differential equations. We will study the range of applicability of Eqs. (17) and (18) by comparing them with equations for the sound pressure p presented in Secs. IV B–IV F, which have been most often used for analytical and numerical studies of sound propagation in moving media and whose ranges of applicability are well known. This will allow us to show that Eqs. (17) and (18) have the same of a wider range of applicability than these equations for p and, in many cases, describe sound propagation to any order in v/c. For simplicity, in the rest of this section, we assume that $\mathbf{F}=0$, $Q=0$, and the medium velocity is subsonic.

B. Nonmoving medium

Consider the case of a nonmoving medium when $\mathbf{v}=0$. In this case, the set of linearized equations of fluid dynamics, Eqs. (5)–(8), can be exactly (without any approximations) reduced to a single equation for sound pressure p (e.g., see Eq. (1.11) from Ref. 11):

$$\frac{\partial}{\partial t}\left(\frac{1}{\varrho c^2}\frac{\partial p}{\partial t}\right)-\boldsymbol{\nabla}\cdot\left(\frac{\boldsymbol{\nabla} p}{\varrho}\right)=0. \tag{20}$$

For the considered case of a nonmoving medium, Eqs. (17) and (18) can also be reduced to a single equation for p. This equation coincides with Eq. (20). Therefore, Eqs. (17) and (18) describe sound propagation exactly if $\mathbf{v}=0$.

C. Homogeneous uniformly moving medium

A medium is homogeneous and uniformly moving if the ambient quantities c, $\mathbf{v}$, etc. do not depend on $\mathbf{R}$ and t. For such a medium, the linearized equations of fluid dynamics, Eqs. (5)–(8) can also be exactly reduced to a single equation for p (see Sec. 2.3.6 from Ref. 9 and references therein):

$$\left(\frac{\partial}{\partial t}+\mathbf{v}\cdot\boldsymbol{\nabla}\right)^2 p-c^2\nabla^2 p=0. \tag{21}$$

For the case of a homogeneous uniformly moving medium, Eqs. (17) and (18) can be reduced to the equation for p that coincides with Eq. (21). Therefore, Eqs. (17) and (18) describe sound propagation exactly in a homogeneous uniformly moving medium. In particular, they correctly account for terms of any order in v/c.

D. Stratified moving medium

Now let us consider the case of a stratified medium when the ambient quantities c, ϱ, $\mathbf{v}$, etc. depend only on the vertical coordinate z. We will assume that the vertical component of $\mathbf{v}$ is zero: $\mathbf{v}=(\mathbf{v}_\perp,0)$, where $\mathbf{v}_\perp$ is a horizontal component of the medium velocity vector. In this subsection, we reduce Eqs. (17) and (18) to a single equation for the spectral density of the sound pressure and show that this equation coincides with the equation for the spectral density that can be derived from Eqs. (5)–(8).

For a stratified moving medium, Eq. (17) can be written as

$$\left(\frac{\partial}{\partial t}+\mathbf{v}_\perp\cdot\boldsymbol{\nabla}_\perp\right)p+\varrho c^2\left(\boldsymbol{\nabla}_\perp\cdot\mathbf{w}_\perp+\frac{\partial w_z}{\partial z}\right)=0. \tag{22}$$

Here, $\boldsymbol{\nabla}_\perp=(\partial/\partial x,\partial/\partial y)$, and $\mathbf{w}_\perp$ and w_z are the horizontal and vertical components of the vector $\mathbf{w}=(\mathbf{w}_\perp,w_z)$. Equation (18) can be written as two equations:

$$\left(\frac{\partial}{\partial t}+\mathbf{v}_\perp\cdot\boldsymbol{\nabla}_\perp\right)w_z+\frac{1}{\varrho}\frac{\partial p}{\partial z}=0, \tag{23}$$

$$\left(\frac{\partial}{\partial t}+\mathbf{v}_\perp\cdot\boldsymbol{\nabla}_\perp\right)\mathbf{w}_\perp+w_z\mathbf{v}_\perp'+\frac{\boldsymbol{\nabla}_\perp p}{\varrho}=0. \tag{24}$$

Here, $\mathbf{v}_\perp'=d\mathbf{v}_\perp/dz$. Let p, $\mathbf{w}_\perp$, and w_z be expressed as Fourier integrals:

$$p(\mathbf{r},z,t)=\int\int d\mathbf{a}\int d\omega\,\exp(i\mathbf{a}\cdot\mathbf{r}-i\omega t)\hat{p}(\mathbf{a},z,\omega), \tag{25}$$

$$w_z(\mathbf{r},z,t)=\int\int d\mathbf{a}\int d\omega\,\exp(i\mathbf{a}\cdot\mathbf{r}-i\omega t)\hat{w}_z(\mathbf{a},z,\omega), \tag{26}$$

$$\mathbf{w}_\perp(\mathbf{r},z,t)=\int\int d\mathbf{a}\int d\omega\,\exp(i\mathbf{a}\cdot\mathbf{r}-i\omega t)\hat{\mathbf{w}}_\perp(\mathbf{a},z,\omega). \tag{27}$$

Here, $\mathbf{r}=(x,y)$ are the horizontal coordinates, $\mathbf{a}$ is the horizontal component of the wave vector, ω is the frequency of a sound wave, and $\hat{p}$, $\hat{w}_z$, and $\hat{\mathbf{w}}_\perp$ are the spectral densities of p, w_z, and $\mathbf{w}_\perp$. We substitute Eqs. (25)–(27) into Eqs. (22)–(24). As a result, we obtain a set of equations for $\hat{p}$, $\hat{w}_z$, and $\hat{\mathbf{w}}_\perp$:

$$-i(\omega-\mathbf{a}\cdot\mathbf{v}_\perp)\hat{p}+i\varrho c^2\mathbf{a}\cdot\hat{\mathbf{w}}_\perp+\varrho c^2\frac{\partial\hat{w}_z}{\partial z}=0, \tag{28}$$

$$-i(\omega-\mathbf{a}\cdot\mathbf{v}_\perp)\hat{w}_z+\frac{1}{\varrho}\frac{\partial\hat{p}}{\partial z}=0, \tag{29}$$

$$-i(\omega-\mathbf{a}\cdot\mathbf{v}_\perp)\hat{\mathbf{w}}_\perp+\mathbf{v}_\perp'\hat{w}_z+\frac{i\mathbf{a}\hat{p}}{\varrho}=0. \tag{30}$$

After some algebra, this set of equations can be reduced to a single equation for $\hat{p}$:

$$\frac{\partial^2\hat{p}}{\partial z^2}+\left(\frac{2\mathbf{a}\cdot\mathbf{v}_\perp'}{\omega-\mathbf{a}\cdot\mathbf{v}_\perp}-\frac{\varrho'}{\varrho}\right)\frac{\partial\hat{p}}{\partial z}+\left(\frac{(\omega-\mathbf{a}\cdot\mathbf{v}_\perp)^2}{c^2}-a^2\right)\hat{p}=0, \tag{31}$$

where $\varrho'=d\varrho/dz$.

For the considered case of a stratified moving medium, a single equation for $\hat{p}$ can also be derived from Eqs. (5)–(8) without any approximations. This equation for p is given by Eq. (2.61) from Ref. 9. Setting $g=0$ in this equation (i.e. ignoring internal gravity waves) one obtains Eq. (31). Therefore, Eqs. (17) and (18) describe sound propagation exactly in a stratified moving medium, and, hence, correctly account for terms of any order in v/c.

E. Turbulent medium

Probably the most general of the equations describing the propagation of a monochromatic sound wave in turbulent media with temperature and velocity fluctuations is given by Eq. (6.1) from Ref. 9:

$$\left[\Delta+k_0^2(1+\varepsilon)-\left(\boldsymbol{\nabla}\ln\frac{\varrho}{\varrho_0}\right)\cdot\boldsymbol{\nabla}-\frac{2i}{\omega}\frac{\partial v_i}{\partial x_j}\frac{\partial^2}{\partial x_i\partial x_j}+\frac{2ik_0}{c_0}\mathbf{v}\cdot\boldsymbol{\nabla}\right]p(\mathbf{R})=0. \tag{32}$$

Here, $\Delta=\partial^2/\partial x^2+\partial^2/\partial y^2+\partial^2/\partial z^2$; $\varepsilon=c_0^2/c^2-1$; k_0, c_0, and ϱ_0 are the reference values of the wave number, adiabatic sound speed, and density; x_1, x_2, x_3 stand for x, y, z; $v_1=v_x$, $v_2=v_y$, $v_3=v_z$ are the components of the medium velocity vector $\mathbf{v}$; and repeated subscripts are summed from 1 to 3. Furthermore, the dependence of the sound pressure on the time factor $\exp(-i\omega t)$ is omitted.

The range of applicability of Eq. (32) is considered in detail in Sec. 2.3 from Ref. 9. This equation was used for calculations of the sound scattering cross section per unit volume of a sound wave propagating in a turbulent medium with temperature and velocity fluctuations. Also it was employed as a starting equation for developing a theory of mul-

tiple scattering of a sound wave propagating in such a turbulent medium; see Ref. 9 and references therein. Furthermore, starting from Eq. (32), parabolic and wide-angle parabolic equations were derived and used in analytical and numerical studies of sound propagation in a turbulent medium, e.g., Ref. 26. For example, a parabolic equation deduced from Eq. (32) reads as

$$2ik_0\frac{\partial p}{\partial x}+\Delta_\perp p+2k_0^2\left(1+\frac{\varepsilon_{\mathrm{mov}}}{2}\right)p=0. \tag{33}$$

Here, the predominant direction of sound propagation coincides with the x-axis, $\Delta_\perp=(\partial^2/\partial y^2,\partial^2/\partial z^2)$, and $\varepsilon_{\mathrm{mov}}=\varepsilon-2v_x/c_0$.

In Ref. 9, Eq. (32) was derived starting from the set of Eqs. (17) and (18) and using some approximations. Therefore, this set has the same or a wider range of applicability than equations for p that have been used in the literature for analytical and numerical studies of sound propagation in a turbulent medium with temperature and velocity fluctuations.

F. Geometrical acoustics

Sound propagation in a moving inhomogeneous medium is often described in geometrical acoustics approximation which is applicable if the sound wavelength is much smaller than the scale of medium inhomogeneities. In geometrical acoustics, the phase of a sound wave can be obtained as a solution of the eikonal equation, and its amplitude from the transport equation. In this subsection, starting from Eqs. (17) and (18), we derive eikonal and transport equations and show that they are in agreement with those deduced from Eqs. (5)–(8).

Let us express p and $\mathbf{w}$ in the following form:

$$p(\mathbf{R},t)=\exp(ik_0\Theta(\mathbf{R},t))p_A(\mathbf{R},t), \tag{34}$$

$$\mathbf{w}(\mathbf{R},t)=\exp(ik_0\Theta(\mathbf{R},t))\mathbf{w}_A(\mathbf{R},t). \tag{35}$$

Here, $\Theta(\mathbf{R},t)$ is the phase function, and p_A and $\mathbf{w}_A$ are the amplitudes of p and $\mathbf{w}$. Substituting Eqs. (34) and (35) into Eqs. (17) and (18), we have

$$ik_0\left(\varrho c^2\mathbf{w}_A\cdot\boldsymbol{\nabla}\Theta+p_A\frac{d\Theta}{dt}\right)=-\frac{dp_A}{dt}-\varrho c^2\boldsymbol{\nabla}\cdot\mathbf{w}_A, \tag{36}$$

$$ik_0\left(\mathbf{w}_A\frac{d\Theta}{dt}+\frac{p_A\boldsymbol{\nabla}\Theta}{\varrho}\right)=-\frac{d\mathbf{w}_A}{dt}-(\mathbf{w}_A\cdot\boldsymbol{\nabla})\mathbf{v}-\frac{\boldsymbol{\nabla}p_A}{\varrho}. \tag{37}$$

In geometrical acoustics, p_A and $\mathbf{w}_A$ are expressed as a series in a small parameter proportional to $1/k_0$:

$$p_A=p_1+\frac{p_2}{ik_0}+\frac{p_3}{(ik_0)^2}+\ldots, \tag{38}$$

$$\mathbf{w}_A=\mathbf{w}_1+\frac{\mathbf{w}_2}{ik_0}+\frac{\mathbf{w}_3}{(ik_0)^2}+\ldots. \tag{39}$$

Substituting Eqs. (38) and (39) into Eqs. (36) and (37) and equating terms proportional to k_0, we arrive at a set of equations:

$$\varrho c^2\mathbf{w}_1\cdot\boldsymbol{\nabla}\Theta+p_1\frac{d\Theta}{dt}=0, \tag{40}$$

$$\mathbf{w}_1\frac{d\Theta}{dt}+p_1\frac{\boldsymbol{\nabla}\Theta}{\varrho}=0. \tag{41}$$

Equating terms proportional to k_0^0, we obtain another set:

$$\varrho c^2\mathbf{w}_2\cdot\boldsymbol{\nabla}\Theta+p_2\frac{d\Theta}{dt}=-\frac{dp_1}{dt}-\varrho c^2\boldsymbol{\nabla}\cdot\mathbf{w}_1, \tag{42}$$

$$\mathbf{w}_2\frac{d\Theta}{dt}+\frac{p_2\boldsymbol{\nabla}\Theta}{\varrho}=-\frac{d\mathbf{w}_1}{dt}-(\mathbf{w}_1\cdot\boldsymbol{\nabla})\mathbf{v}-\frac{\boldsymbol{\nabla}p_1}{\varrho}. \tag{43}$$

From Eq. (41), we have

$$\mathbf{w}_1=-\frac{p_1}{\varrho}\frac{\boldsymbol{\nabla}\Theta}{d\Theta/dt}. \tag{44}$$

Substituting this value of $\mathbf{w}_1$ into Eq. (40), we obtain

$$\left[\left(\frac{d\Theta}{dt}\right)^2-c^2(\boldsymbol{\nabla}\Theta)^2\right]p_1=0. \tag{45}$$

From this equation, we obtain an eikonal equation for the phase function:

$$\frac{d\Theta}{dt}=-c|\boldsymbol{\nabla}\Theta|. \tag{46}$$

Here, a sign in front of $|\boldsymbol{\nabla}\Theta|$ is chosen in accordance with the time convention $\exp(-i\omega t)$. Equation (46) coincides exactly with the eikonal equation for sound waves in a moving inhomogeneous medium (e.g., see Eq. (3.15) from Ref. 9) which can be derived from Eqs. (5)–(8) in a geometrical acoustics approximation. Thus, in this approximation, Eqs. (17) and (18) exactly describe the phase of a sound wave and, hence, account for terms of any order in v/c.

Substituting the value of $d\Theta/dt$ from Eq. (46) into Eq. (44), we have

$$\mathbf{w}_1=\frac{p_1}{\varrho}\frac{\boldsymbol{\nabla}\Theta}{c|\boldsymbol{\nabla}\Theta|}=\frac{p_1\mathbf{n}}{\varrho c}, \tag{47}$$

where $\mathbf{n}=\boldsymbol{\nabla}\Theta/|\boldsymbol{\nabla}\Theta|$ is the unit vector normal to the phase front. Now we multiply Eq. (42) by $d\Theta/dt$ and multiply Eq. (43) by $c^2\varrho\boldsymbol{\nabla}\Theta$. Then, we subtract the latter equation from the former. After some algebra and using Eq. (46), it can be shown that the sum of all terms proportional to p_2 and $\mathbf{w}_2$ is zero. The resulting equation reads as

$$\frac{dp_1}{dt}+c\mathbf{n}\cdot\boldsymbol{\nabla}p_1+\varrho c\mathbf{n}\cdot\frac{d\mathbf{w}_1}{dt}+\varrho c\mathbf{n}\cdot(\mathbf{w}_1\cdot\boldsymbol{\nabla})\mathbf{v}+\varrho c^2\boldsymbol{\nabla}\cdot\mathbf{w}_1=0. \tag{48}$$

In this equation, $\mathbf{w}_1$ is replaced by its value given by Eq. (47). As a result, we obtain

$$\frac{\varrho\mathbf{n}}{c}\cdot\frac{d}{dt}\left(\frac{\mathbf{n}p_1}{\varrho c}\right)+\frac{1}{c^2}\frac{dp_1}{dt}+\frac{\mathbf{n}\cdot\boldsymbol{\nabla}p_1}{c}+\varrho\boldsymbol{\nabla}\cdot\left(\frac{\mathbf{n}p_1}{\varrho c}\right)+\frac{p_1\mathbf{n}\cdot(\mathbf{n}\cdot\boldsymbol{\nabla})\mathbf{v}}{c^2}=0. \tag{49}$$

In geometrical acoustics, the amplitude p_A of the sound pressure is approximated by p_1. Equation (49) is a closed equation for p_1; i.e., it is a transport equation.

The second term on the left-hand side of Eq. (49) can be written as

$$\frac{1}{c^2}\frac{dp_1}{dt}=\frac{d}{dt}\left(\frac{p_1}{c^2}\right)+\frac{p_1}{c^4}\frac{dc^2}{dt}=\frac{d}{dt}\left(\frac{p_1}{c^2}\right)+\frac{p_1}{c^4}\frac{\beta d\varrho}{dt}. \quad (50)$$

Here, we used the formula $dc^2/dt=\beta d\varrho/dt$; see Eq. (2.63) from Ref. 9. According to Eq. (2), $d\varrho/dt$ in Eq. (50) can be replaced with $-\varrho\nabla\cdot\mathbf{v}$. When deriving Eqs. (17) and (18), terms proportional to $\nabla\cdot\mathbf{v}$ were ignored. Therefore, the last term on the right-hand side of Eq. (50) should also be ignored. In this case, Eq. (49) can be written as

$$\frac{\varrho\mathbf{n}}{c}\cdot\frac{d}{dt}\left(\frac{\mathbf{n}p_1}{\varrho c}\right)+\frac{d}{dt}\left(\frac{p_1}{c^2}\right)+\frac{\mathbf{n}\cdot\nabla p_1}{c}+\varrho\nabla\cdot\left(\frac{\mathbf{n}p_1}{\varrho c}\right)+\frac{p_1\mathbf{n}\cdot(\mathbf{n}\cdot\nabla)\mathbf{v}}{c^2}=0. \quad (51)$$

This equation coincides with Eq. (3.18) from Ref. 9 if in the latter equation terms proportional to $\nabla\cdot\mathbf{v}$ are ignored. Equation (3.18) is an exact transport equation for p_1 in the geometrical acoustics derived from Eqs. (5)–(8). Thus, if the terms proportional to $\nabla\cdot\mathbf{v}$ are ignored, Eqs. (17) and (18) exactly describe the amplitude of a sound wave in a geometrical acoustics approximation, and correctly account for terms of any order in v/c. Note that in Ref. 9 starting from the transport equation, Eq. (3.18), a law of acoustic energy conservation in geometrical acoustics of moving media is derived; see Eq. (3.21) from that reference. Since Eq. (51) coincides with Eq. (3.18), the same law [i.e., Eq. (3.21) from Ref. 9] can be derived from Eq. (51) provided that the terms proportional to $\nabla\cdot\mathbf{v}$ are ignored.

G. Discussion

Thus, by comparing a set of Eqs. (17) and (18) with the equations for p which are widely used in atmospheric acoustics, we determined that this set has the same or a wider range of applicability than these equations for p. Note that there are other equations for p known in the literature (see Refs. 9, 11, 17 and references therein): Monin's equation, Pierce's equations, equation for the velocity quasi-potential, the Andreev–Rusakov–Blokhintzev equation, etc. Most of these equations have narrower ranges of applicability than the equations presented above and have been seldom used for calculations of p.

V. NUMERICAL IMPLEMENTATION

In this section, we describe simple algorithms for FDTD solutions of Eqs. (17) and (18) in the two spatial dimensions x and y. Isolating the partial derivatives with respect to time on the left side of these equations, we have

$$\frac{\partial p}{\partial t}=-\left(v_x\frac{\partial}{\partial x}+v_y\frac{\partial}{\partial y}\right)p-\kappa\left(\frac{\partial w_x}{\partial x}+\frac{\partial w_y}{\partial y}\right)+\kappa Q, \quad (52)$$

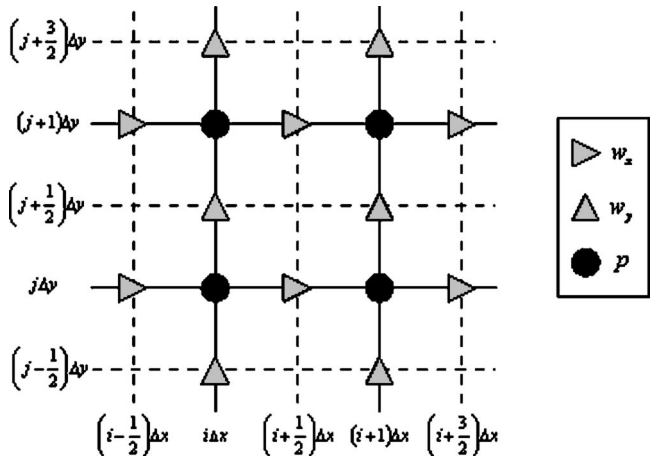

FIG. 1. Spatially staggered finite-difference grid used for the calculations in this article.

$$\frac{\partial w_x}{\partial t}=-\left(w_x\frac{\partial}{\partial x}+w_y\frac{\partial}{\partial y}\right)v_x-\left(v_x\frac{\partial}{\partial x}+v_y\frac{\partial}{\partial y}\right)w_x-b\frac{\partial p}{\partial x}+bF_x, \quad (53)$$

$$\frac{\partial w_y}{\partial t}=-\left(w_x\frac{\partial}{\partial x}+w_y\frac{\partial}{\partial y}\right)v_y-\left(v_x\frac{\partial}{\partial x}+v_y\frac{\partial}{\partial y}\right)w_y-b\frac{\partial p}{\partial y}+bF_y, \quad (54)$$

where $b=1/\rho$ is the mass buoyancy and $\kappa=\rho c^2$ is the adiabatic bulk modulus. In Eqs. (52)–(54), the subscripts x and y indicate components along the corresponding coordinate axes.

The primary numerical issues pertinent to solving these equations in a moving inhomogeneous medium are summarized and addressed in Secs. V A–V C. Example calculations are provided in Secs. V D and V E.

A. Spatial finite-difference approximations

The spatial finite-difference (FD) network considered here stores the pressure and particle velocities on a grid that is staggered in space, as shown in Fig. 1. The pressure is stored at integer node positions, namely $x=i\,\Delta x$ and $y=j\,\Delta y$, where i and j are integers and Δx and Δy are the grid intervals in the x- and y-directions. The x-components of the acoustic velocity, w_x, are staggered (offset) by $\Delta x/2$ in the x-direction. The y-components of the acoustic velocity, w_y, are staggered by $\Delta y/2$ in the y-direction. This staggered grid design is widely used for wave propagation calculations in nonmoving media.[27–30] Here we furthermore store v_x and F_x at the w_x nodes, and v_y and F_y at the w_y nodes. The quantities b, κ, and Q are stored at the pressure nodes.

For simplicity, we consider in this article only a second-order accurate, spatially centered FD scheme. A centered solution of Eqs. (52)–(54) requires an evaluation of each of the terms of the right-hand sides of these equations at the grid nodes where the field variable on the left-hand side is stored. One of the main motivations for using the spatially staggered

grid is that it conveniently provides compact, centered spatial differences for many of the derivatives in Eqs. (52)–(54). For example, $\partial w_x/\partial x$ in Eq. (52) is

$$\partial w_x(i\,\Delta x, j\,\Delta y, t)/\partial x \simeq \{w_x[(i+1/2)\Delta x, j\,\Delta y, t] - w_x[(i-1/2)\Delta x, j\,\Delta y, t]\}/\Delta x \quad (55)$$

and $\partial p/\partial y$ in Eq. (54) is

$$\partial p[i\,\Delta x,(j+1/2)\Delta y,t]/\partial y \simeq \{p[i\,\Delta x,(j+1)\Delta y,t] - p[i\,\Delta x, j\,\Delta y, t]\}/\Delta y. \quad (56)$$

The derivatives $\partial p/\partial x$ and $\partial w_y/\partial y$ follow similarly. The body source terms can all be evaluated directly, since they are already stored at the grid nodes where the FD approximations are centered. The same is true of κ, which is stored at the pressure grid nodes and needed in Eq. (52). Regarding Eqs. (53) and (54), the values for b can be determined at the needed locations by averaging neighboring grid points.

The implementation of the remaining terms, particular to the moving medium, is somewhat more complicated. For example, the derivatives of the pressure field in Eq. (52), $\partial p/\partial x$ and $\partial p/\partial y$, cannot be centered at $x = i\,\Delta x$ and $y = j\,\Delta y$ from approximations across a single grid interval. Centered approximations can be formed across two grid intervals, however, as suggested in Ref. 2. For example,

$$\partial p(i\,\Delta x, j\,\Delta y, t)/\partial x \simeq \{p[(i+1)\Delta x, j\,\Delta y, t] - p[(i-1)\Delta x, j\,\Delta y, t]\}/2\Delta x. \quad (57)$$

Neighboring grid points can be averaged to find the wind velocity components v_x and v_y at $x = i\,\Delta x$ and $y = j\,\Delta y$, which multiply the derivatives $\partial p/\partial x$ and $\partial p/\partial y$, respectively, in Eq. (52). Similarly, the spatial derivatives of the particle velocities in Eqs. (53) and (54) can be approximated over two grid intervals. In Eq. (53), the quantities w_y and v_y (multiplying the derivatives $\partial v_x/\partial y$ and $\partial w_x/\partial y$, respectively) are needed at the grid point $x = (i+1/2)\Delta x$ and $y = j\,\Delta y$. Referring to Fig. 1, a reasonable way to obtain these quantities would be to average the four closest grid nodes:

$$w_y[(i+1/2)\Delta x, j\,\Delta y, t] \simeq \frac{1}{4}\{w_y[(i+1)\Delta x,(j+1/2)\Delta y,t] + w_y[i\,\Delta x,(j+1/2)\Delta y,t] + w_y[(i+1)\Delta x,(j-1/2)\Delta y,t] + w_y[i\,\Delta x,(j-1/2)\Delta y,t]\}, \quad (58)$$

and likewise for v_y. The quantities w_x and v_x, multiplying the derivatives $\partial v_y/\partial x$ and $\partial w_y/\partial x$ in Eq. (54), can be obtained similarly.

B. Advancing the solution in time

Let us define the functions f_p, f_x, and f_y as the right-hand sides of Eqs. (52), (53), and (54), respectively. For example, we write

$$\frac{\partial p(i\,\Delta x, j\,\Delta y, t)}{\partial t} = f_p[i\,\Delta x, j\,\Delta y, \mathbf{p}(t), \mathbf{w}_x(t), \mathbf{w}_y(t), \mathbf{s}(t)], \quad (59)$$

where $\mathbf{p}(t)$, $\mathbf{w}_x(t)$, and $\mathbf{w}_y(t)$ are matrices containing the pressures and acoustic velocities at all available grid nodes. For convenience, $\mathbf{s}(t)$ is used here as short hand for the combined source and medium properties (b, κ, v_x, v_y, Q, F_x, and F_y) at all available grid nodes. (Note that $f_p[i\,\Delta x, j\,\Delta y, \mathbf{p}(t), \mathbf{w}_x(t), \mathbf{w}_y(t), \mathbf{s}(t)]$ in actuality depends only on the fields at a small number of neighboring grid points of $(i\,\Delta x, j\,\Delta y)$ when second-order spatial differencing is used. The notation here is general enough, though, to accommodate spatial differencing of an arbitrarily high order.)

For a nonmoving medium, the solution is typically advanced in time using a staggered temporal grid, in which the pressures are stored at the integer time steps $t = l\,\Delta t$ and the particle velocities at the half-integer time steps $t = (l+1/2)\Delta t$.[27–30] The acoustic velocities and pressures are updated in an alternating "leap-frog" fashion, with the fields from the previous time step being overwritten in place. Considering the moving media equations, approximation of the time derivative in Eq. (59) with a finite difference centered on $t = (l+1/2)\Delta t$ (that is, $\partial p[i\,\Delta x, j\,\Delta y, (l+1/2)\Delta t]/\partial t \simeq \{p[i\,\Delta x, j\,\Delta y, (l+1)\Delta t] - p[i\,\Delta x, j\,\Delta y, l\,\Delta t]\}/\Delta t$) results in the following equation for updating the pressure field:

$$p[i\,\Delta x, j\,\Delta y, (l+1)\Delta t] = p[i\,\Delta x, j\,\Delta y, l\,\Delta t] + \Delta t\, f_p[i\,\Delta x, j\,\Delta y, \mathbf{p}[(l+1/2)\Delta t], \mathbf{w}_x[(l+1/2)\Delta t], \mathbf{w}_y[(l+1/2)\Delta t], \mathbf{s}[(l+1/2)\Delta t]]. \quad (60)$$

Note that this equation requires the pressure field at the half-integer time steps, i.e., $t = (l+1/2)\Delta t$. In the staggered leap-frog scheme, however, the pressure is unavailable at the half-integer time steps. A similar centered approximation for the acoustic velocities indicates that they are needed on the integer time steps in order to advance the solution, which is again problematic. If one attempts to address this problem by linearly interpolating between adjacent time steps (i.e., by setting $\mathbf{p}[(l+1/2)\Delta t] \simeq \{\mathbf{p}[l\,\Delta t] + \mathbf{p}[(l+1)\Delta t]\}/2$ in Eq. (60)), explicit updating equations (a solution of Eq. (60) for $p[i\,\Delta x, j\,\Delta y, (l+1)\Delta t]$ that does not require the pressure field at nearby grid points at the time step $t = (l+1)\Delta t$) cannot be obtained. Hence the customary staggered leap-frog approach does not lead to an explicit updating scheme for the acoustic fields in a moving medium. The staggered leap-frog scheme can be rigorously implemented only when the terms particular to the moving medium (those involving v_x and v_y) are removed from Eqs. (52)–(54).

A possible work-around would be to use the pressure field $\mathbf{p}(l\,\Delta t)$ in place of $\mathbf{p}[(l+1/2)\Delta t]$ when evaluating f_p, and $\mathbf{w}_x[(l-1/2)\Delta t]$ and $\mathbf{w}_y[(l-1/2)\Delta t]$ in place of $\mathbf{w}_x(l\,\Delta t)$ and $\mathbf{w}_y(l\,\Delta t)$ when evaluating f_x and f_y. This nonrigorous procedure uses the Euler (forward difference) method to evaluate the moving-media terms while maintaining the leap-frog approach for the remaining terms. From a programming standpoint, the algorithm proceeds in essen-

tially the same manner as the staggered leap-frog method for a nonmoving medium. The calculations in Ref. 2 appear to use such a procedure. But the stability and accuracy of this algorithm are unclear. An alternative is provided in Ref. 4, which uses a perturbative solution based on the assumption that the flow velocity is small.

Here we would like to develop a general technique that is applicable to high Mach numbers. The simplest way to accomplish this is to abandon the staggered temporal grid and form centered finite differences over *two* time steps. The pressure updating equation, based on the approximation $\partial p(i\,\Delta x,\ j\,\Delta y,\ l\,\Delta t)/\partial t \simeq \{p[i\,\Delta x,\ j\,\Delta y,(l+1)\Delta t] - p[i\ \Delta x,\ j\Delta y,(l-1)\Delta t]\}/2\,\Delta t$, is

$$\begin{aligned} p[i\,\Delta x,j\,\Delta y,(l+1)\Delta t] &= p[i\,\Delta x,j\,\Delta y,(l-1)\Delta t] \\ &\quad + 2\,\Delta t\, f_p[i\,\Delta x,j\,\Delta y,\mathbf{p}(l\,\Delta t),\mathbf{w}_x(l\,\Delta t), \\ &\qquad \mathbf{w}_y(l\,\Delta t),\mathbf{s}(l\,\Delta t)]. \end{aligned} \tag{61}$$

Similarly, we derive

$$\begin{aligned} w_x[(i+1/2)\Delta x,j\,\Delta y,(l+1)\Delta t] &= w_x[(i+1/2)\Delta x,j\,\Delta y,(l-1)\Delta t] + 2\,\Delta t\, f_x[(i \\ &\quad + 1/2)\Delta x,j\,\Delta y,\mathbf{p}(l\,\Delta t),\mathbf{w}_x(l\,\Delta t),\mathbf{w}_y(l\,\Delta t),\mathbf{s}(l\,\Delta t)], \end{aligned} \tag{62}$$

$$\begin{aligned} w_y[i\,\Delta x,(j+1/2)\Delta y,(l+1)\Delta t] &= w_y[i\,\Delta x,(j+1/2)\Delta y,(l-1)\Delta t] \\ &\quad + 2\,\Delta t\, f_y[i\,\Delta x,(j+1/2)\Delta y,\mathbf{p}(l\,\Delta t),\mathbf{w}_x \\ &\qquad (l\,\Delta t),\mathbf{w}_y(l\,\Delta t),\mathbf{s}(l\,\Delta t)]. \end{aligned} \tag{63}$$

Somewhat confusingly, this general temporal updating scheme has also been called the ''leap-frog'' scheme in the literature,[31] since it involves alternately overwriting the wavefield variables at even and odd integer time steps based on calculations with the fields at the intervening time step. We call this scheme here the *nonstaggered leap-frog*. The primary disadvantage, in comparison to the staggered leap-frog scheme, is that the fields must be stored over two time steps, rather than just one. Additionally, the numerical dispersion and instability characteristics are inferior to those of the conventional staggered scheme due to the advancement of the wavefield variables over two time steps instead of one. On the other hand, the nonstaggered leap-frog does provide a simple and rigorous centered finite-difference scheme that is not specialized to low Mach number flows. Other common numerical integration methods, such as the Runge–Kutta family, can also be readily applied to the nonstaggered-in-time grid. Some of the calculations following later in this section use a fourth-order Runge–Kutta method, which is described in Ref. 32 and many other texts. We have also developed a staggered-in-time method that is valid for high Mach numbers but requires the fields to be stored over two time levels. This method was briefly discussed in Ref. 6.

Note that our present numerical modeling efforts are directed toward demonstrating the applicability and feasibility of FDTD techniques for simulating sound propagation in a moving atmosphere. We have not undertaken a comprehensive comparative analysis of the many alternative numerical strategies available for the solution of Eqs. (17) and (18). However, several of these approaches (including the pseudospectral method, higher-order spatial and/or temporal finite-difference operators, and the dispersion relation preserving (DRP) technique) yield accurate simulations of sound propagation with fewer grid intervals per wavelength compared with our numerical examples. In particular, the DRP method, involving optimized numerical values of the finite-difference operator coefficients (e.g., Ref. 18), can be readily introduced into our FDTD algorithmic framework.

C. Dependence of grid increments on Mach number

For numerical stability of the 2-D FDTD calculation, the time step Δt and grid spacing Δr must be chosen to satisfy the Courant condition, $C<1/\sqrt{2}$ (e.g., see Ref. 33), where the Courant number is defined as

$$C=\frac{u\,\Delta t}{\Delta r}. \tag{64}$$

Here, u is the speed at which the sound energy propagates. [For a nonuniform grid, $\Delta r=1/\sqrt{(\Delta x)^{-2}+(\Delta y)^{-2}}$.] Since the grid spacing must generally be a small fraction of a wavelength for good numerical accuracy, the Courant condition in practice imposes a limitation on the maximum time step possible for stable calculations. An even smaller time step may be necessary for good accuracy, however.

Let us consider the implications of the Courant condition for propagation in a uniform flow. In this case, u is determined by a combination of the sound speed and wind velocity. In the downwind direction, we have $u=u_+=c+v$. In the upwind direction, $u=u_-=c-v$. The wavelengths in these two directions are $\lambda_+=(c+v)/f$ and $\lambda_-=(c-v)/f$, respectively, where f is the frequency. Since the wavelength is shortest in the *upwind* direction, the value of λ_- dictates the grid spacing. We set

$$\Delta r=\frac{\lambda_-}{N}=\frac{\lambda}{N}(1-M), \tag{65}$$

where N is the number of grid points per wavelength in the upwind direction, $M=v/c$ is the Mach number, and $\lambda=c/f$ is the wavelength for the medium at rest. If N is to be fixed at a constant value, a finer grid is required as M increases. Regarding the time step, the Courant condition implies

$$\Delta t<\frac{\lambda_-}{\mathrm{Nu}}. \tag{66}$$

This condition is most difficult to meet when u is largest, which is the case in the *downwind* direction. Therefore we must use u_+ in the preceding inequality if we are to have accurate results throughout the domain; specifically, we must set

$$\Delta t<\frac{\lambda_-}{\mathrm{Nu}_+}=\frac{1}{Nf}\,\frac{1-M}{1+M}. \tag{67}$$

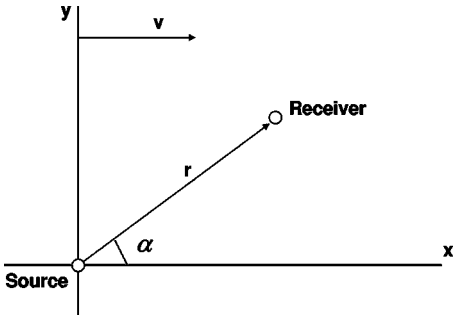

FIG. 2. The geometry of the problem.

Therefore the time step must also be shortened as M increases. For example, the time step at $M=1/3$ must be 1/2 the value necessary at $M=0$. At $M=2/3$, the time step must be 1/5 the value at $M=0$. The reduction of the required time step and grid spacing combine to make calculations at large Mach numbers computationally expensive.

D. Example calculations

In this subsection, we use the developed algorithm for FDTD solutions of Eqs. (52)–(54) to compute the sound field p in a 2-D homogeneous uniformly moving medium. The geometry of the problem is shown in Fig. 2. A point monochromatic source is located at the origin of the Cartesian coordinate system x,y. The medium velocity $\mathbf{v}$ is parallel to the x-axis. We will first obtain an analytical formula for p for this geometry.

In a homogeneous uniformly moving medium, c, ϱ, and $\mathbf{v}$ are constant so that $\boldsymbol{\nabla}\cdot\mathbf{v}=0$ and $\boldsymbol{\nabla}P=0$. Therefore, Eqs. (17) and (18) describe sound propagation exactly for this case and are valid for an arbitrary value of the Mach number M. They can be written as

$$\left(\frac{\partial}{\partial t}+\mathbf{v}\cdot\boldsymbol{\nabla}\right)p+\varrho c^2\boldsymbol{\nabla}\cdot\mathbf{w}=\varrho c^2 Q, \tag{68}$$

$$\left(\frac{\partial}{\partial t}+\mathbf{v}\cdot\boldsymbol{\nabla}\right)\mathbf{w}+\frac{\boldsymbol{\nabla}p}{\varrho}=0. \tag{69}$$

Here, p and $\mathbf{w}$ are functions of the coordinates x, y and time t, $\boldsymbol{\nabla}=(\partial/\partial x,\partial/\partial y)$, and the function Q is given by

$$Q=\frac{2iA}{\varrho\omega}e^{-i\omega t}\delta(x)\,\delta(y), \tag{70}$$

where δ is the delta function and the factor A characterizes the source amplitude. In Eqs. (68) and (69), for simplicity, it is assumed that $\mathbf{F}=0$.

Assuming that $v<c$, the following solution of Eqs. (68) and (69) is obtained in the Appendix:

$$p(r,\alpha,M)=\frac{iA}{2(1-M^2)^{3/2}}\left(H_0^{(1)}(\xi)-\frac{iM\cos\alpha}{\sqrt{1-M^2\sin^2\alpha}}H_1^{(1)}(\xi)\right)\times\exp\left[-\frac{ikMr\cos\alpha}{1-M^2}\right]. \tag{71}$$

Here, $k=\omega/c$, $H_0^{(1)}$, and $H_1^{(1)}$ are the Hankel functions, $\xi=kr\sqrt{1-M^2\sin^2\alpha}/(1-M^2)$, and r and α are the polar coordinates shown in Fig. 2. For $kr\gg1$, the Hankel functions can be approximated by their asymptotics. This results in the desired formula for the sound pressure:

$$p(r,\alpha,M)=\frac{A(\sqrt{1-M^2\sin^2\alpha}-M\cos\alpha)}{\sqrt{2\pi kr}(1-M^2)(1-M^2\sin^2\alpha)^{3/4}}\times\exp\left[\frac{i(\sqrt{1-M^2\sin^2\alpha}-M\cos\alpha)kr}{1-M^2}+\frac{i\pi}{4}\right]. \tag{72}$$

Note that a sound field due to a point monochromatic source in a 2-D homogeneous uniformly moving medium was also studied in Ref. 18 by a different approach. The phase factor obtained in that reference is essentially the same as that in Eq. (72). Only a general expression for the amplitude factor was presented in Ref. 18 which does not allow a detailed comparison with the amplitude factor in Eq. (72).

Let us now consider the FDTD calculations of the sound field for the geometry in Fig. 2. In these calculations, the source consists of a finite-duration harmonic signal with a cosine taper function applied at the beginning and the end. The tapering alleviates numerical dispersion of high frequencies, which becomes evident when there is an abrupt change in the source emission. The tapered source equation is

$$\tilde{Q}(t)=\begin{cases}(1/2)[1-\cos(\pi t/T_1)]\cos(2\pi f+\phi), & 0\leqslant t<T_1,\\ \cos(2\pi f+\phi), & T_1\leqslant t\leqslant T-T_2,\\ (1/2)[1+\cos(\pi(t-T)/T_2)]\cos(2\pi f+\phi), & T-T_2<t\leqslant T,\\ 0, \quad \text{otherwise.}\end{cases} \tag{73}$$

Here, ϕ is the source phase, T_1 is the duration of the initiation taper, and T_2 is the duration of the termination taper. All calculations in this paper use tapering over an interval of 3 periods in the harmonic wave ($T_1=T_2=3/f$) and a total signal duration of 10 periods ($T=10/f$).

Figure 3 shows the pressure field for a 100 Hz source in a uniform Mach 0.3 flow. The field is shown at 0.11 s, or 0.01 s after the source has been turned off. The distance between wave fronts is smaller upwind than downwind. The calculations use the fourth-order Runge–Kutta method with a staggered spatial grid and a nonstaggered temporal grid. The spatial domain is 100 m by 100 m, with 800 grid points in each direction. This results in approximately 19 grid points per wavelength in the upwind direction. The time step was set to 0.145 ms, which implies a Courant number of 0.40 in a nonmoving medium but 0.52 in the downwind direction of the $M=0.3$ flow. Using the run shown in Fig. 3, the azimuthal dependence of the normalized sound pressure magnitude $|p(r,\alpha,M)/p(r,0,0)|$ for values of kr ranging from 1 to 100 was compared to the theoretical far-field result calculated from Eq. (72). Excellent agreement was found between theoretical predictions and FDTD simulations for $kr\gtrsim10$.

The azimuthal dependence of $|p(r,\alpha,M)/p(r,0,0)|$ at $kr=20$ is compared for several numerical methods in Fig. 4.

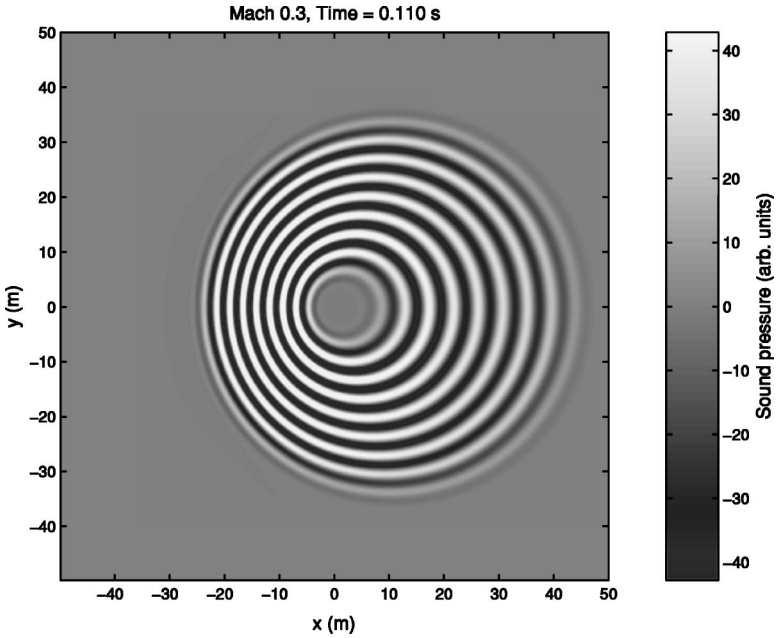

FIG. 3. Wavefronts of the sound pressure due to a point source located at the point $x=0$ and $y=0$ for $M=0.3$. The medium velocity is in the direction of the x-axis.

The methods include the staggered (with forward-differencing of the moving medium terms mentioned in Sec. V B) and nonstaggered leap-frog approaches and the fourth-order Runge–Kutta. The time step for the leap-frog methods was 0.036 ms (1/4 that used for the Runge–Kutta), so that the computational times of all calculations are roughly equal. The Runge–Kutta and nonstaggered leap-frog provide graphically indistinguishable results. The staggered leap-frog, however, systematically underpredicts the amplitude in the downwind direction and overpredicts in the upwind direction. The actual sound pressure signals at $t=0.11$ s, calculated from the staggered and nonstaggered leap-frog approaches, are overlaid in Fig. 5. In the downwind direction, the staggered leap-frog method provides a smooth prediction at distances greater than about 22 m. The noisy appearance at shorter distances is due to numerical instability, which was clear from the rapid temporal growth of these features we observed as the calculation progressed. We conclude that the staggered leap-frog approach, when applied to a moving medium, is less accurate and more prone to numerical instability. This is likely due to the nonsymmetric temporal finite difference approximations for the moving medium terms.

Figure 6 shows the azimuthal dependence of $|p(r,\alpha,M)/p(r,0,0)|$ for $M=0$, 0.3, and 0.6. All FDTD calculations for this figure use the fourth-order Runge–Kutta method. Two calculated curves are shown: one for a low-resolution run with 800×800 grid points and a time step of 0.145 ms, and the other for a high-resolution run with 1600×1600 grid points and a time step of 0.0362 ms. For $M=0.3$, both grid resolutions yield nearly exact agreement with Eq. (72). At $M=0.6$, the low-resolution run has 11 spatial grid nodes per wavelength in the upwind direction and a downwind Courant number of 0.64. The high-resolution grid has 22 spatial grid nodes per wavelength in

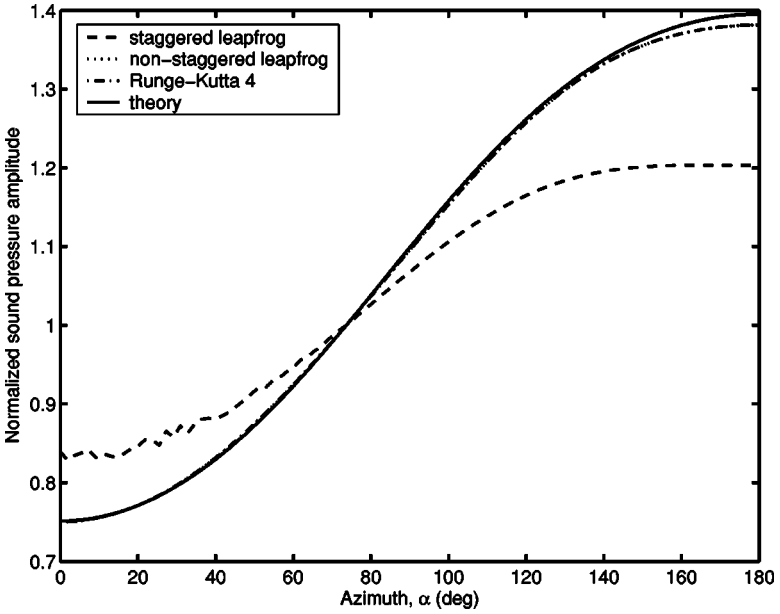

FIG. 4. Normalized sound pressure amplitude $|p(r,\alpha,M)/p(r,0,0)|$ versus the azimuthal angle α for $M=0.3$ and $kr=20$. The staggered and nonstaggered leap-frog methods and the fourth-order Runge–Kutta are compared to the theoretical solution. The nonstaggered leap-frog and Runge–Kutta methods are graphically indistinguishable.

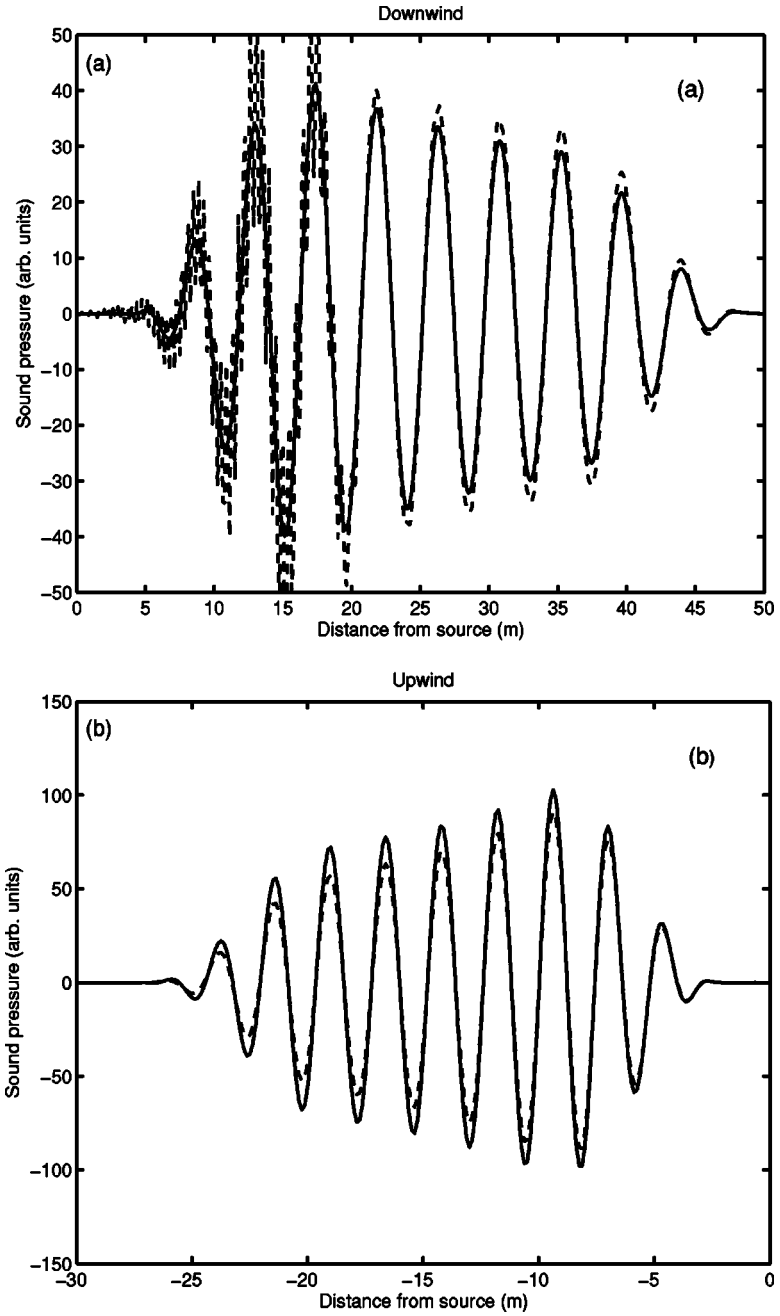

FIG. 5. Sound pressure traces for (a) downwind and (b) upwind propagation. Calculations from the staggered and nonstaggered leap-frog methods are shown (dashed and solid lines, respectively).

the upwind direction and a downwind Courant number of 0.32. Agreement with theory at $M=0.6$ is very good for the high-resolution run. The low-resolution run substantially underpredicts the upwind amplitude.

Finally note that it follows from Figs. 4 and 6 that the sound pressure is largest for $\alpha=180°$, i.e., in the upwind direction. This dependence is also evident upon close examination in Fig. 3.

E. Comparison of FDTD and FFP calculations

The computational examples so far in this paper have been for uniform flows. However, the numerical methods and equations upon which they are based apply to nonuniform flows as well. In this section, we consider an example calculation for a flow with constant shear. The point source and receiver are both located at a height of 20 m and the frequency is 100 Hz. The computational domain is 200 m by 100 m and has 600 by 300 grid points. The time step is 7.73×10^{-4} s and the fourth-order Runge–Kutta method is used. A rigid boundary condition is applied at the ground surface ($y=0$ m). An absorbing layer in the upper one-fifth of the simulation domain removes unwanted numerical reflections. (The implementation of the rigid ground boundary condition and the absorbing layer is described in Ref. 34. Realistic ground boundary conditions in a FDTD simulation of sound propagation in the atmosphere are considered in Ref. 35.)

Calculated transmission loss (sound level relative to free space at 1 m from the source) results are shown in Figs. 7(a) and 7(b). The first of these figures is for a zero-wind condition and the second is for a horizontal (x-direction) wind speed of $v(y)=\mu y$, where the gradient μ is 1 s^{-1}. For Fig.

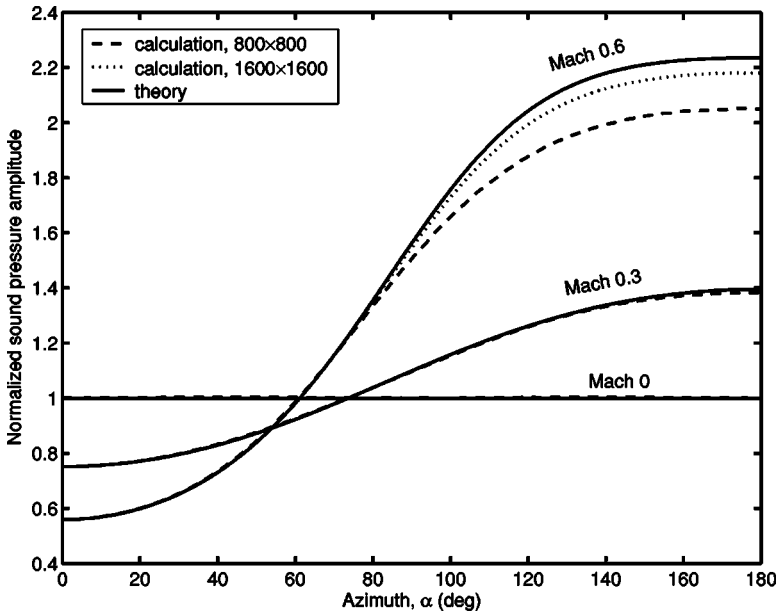

FIG. 6. Normalized sound pressure amplitude $|p(r,\alpha,M)/p(r,0,0)|$ versus the azimuthal angle α for $M=0$, 0.3, and 0.6. The fourth-order Runge–Kutta method was used. The calculation with 800×800 grid points had a spatial resolution of 0.125 m and time step 0.145 ms, whereas the 1600×1600 calculation had a spatial resolution of 0.0625 m and time step 0.0362 ms.

7(a), the FDTD results are compared with both the exact solution for a point source above the rigid boundary and calculations from the FFP developed in Ref. 36. The FDTD results are nearly indistinguishable from the exact solution. The FFP is also in good agreement, although there is some systematic underprediction of the interference minima, particularly so near the source. This is likely due to the far-field approximation inherent to the FFP. For the case with constant shear, Fig. 7(b), the interference pattern is shifted. The FDTD and FFP continue to show very similar small discrepancies near the source. On the basis of the results shown in Fig. 7(a), it is highly likely that the FDTD is more accurate. The FDTD calculations required about 100 times as long to complete as the FFP on a single-processor computer. As would be expected, the FFP is more efficient for calculations at a limited number of frequencies in a horizontally stratified medium.

VI. CONCLUSIONS

In the present paper, we have considered starting equations for FDTD simulations of sound propagation in a moving inhomogeneous atmosphere. FDTD techniques can provide a very accurate description of sound propagation in complex environments.

A most general description of sound propagation in a moving inhomogeneous medium is based on the complete set of linearized equations of fluid dynamics, Eqs. (5)–(8). However, this set is too involved to be effectively employed in FDTD simulations of outdoor sound propagation. In this paper, the linearized equations of fluid dynamics were reduced to two simpler sets of equations which can be used as starting equations for FDTD simulations.

The first set of equations contains three coupled equations, Eqs. (5), (6), and (13), for the sound pressure p, acoustic velocity $\mathbf{w}$, and acoustic density η. This set is an exact consequence of the linearized equations of fluid dynamics, Eqs. (5)–(8). To solve the first set of equations, one needs to know the following ambient quantities: the adiabatic sound speed c, density ϱ, medium velocity $\mathbf{v}$, pressure P, and the parameters α, β, and h. The atmosphere can be modeled as an ideal gas to a very good accuracy. In this case, the first set of equations simplifies and is given by Eqs. (5), (6), and (15). Now it contains the following ambient quantities: c, ϱ, $\mathbf{v}$, and P.

The second set of starting equations for FDTD simulations contains two coupled equations for the sound pressure p and acoustic velocity $\mathbf{w}$, Eqs. (17) and (18). In order to solve this set one needs to know a fewer number of the ambient quantities: c, ϱ, and $\mathbf{v}$. Note that namely these ambient quantities appeared in most of equations for the sound pressure p which have been previously used for analytical and numerical studies of outdoor sound propagation. The second set was derived from Eqs. (5)–(8) assuming that terms proportional to the divergence of the medium velocity and the gradient of the ambient pressure can be ignored. Both these assumptions are reasonable in atmospheric acoustics. To better understand the range of applicability of the second set, it was compared with equations for the sound pressure p which have been most often used for analytical and numerical studies of sound propagation in a moving inhomogeneous medium. It was shown that the second set has the same or wider range of applicability than these equations for p. Thus, a relatively simple set of Eqs. (17) and (18), which is however rather general, seems very attractive as starting equations for FDTD simulations.

The numerical algorithms for FDTD solutions of the second set of equations were developed for the case of a 2-D inhomogeneous moving medium. It was shown that the staggered-in-time grid approach commonly applied to nonmoving media cannot be applied directly for the moving case. However, fairly simple alternatives based on nonstaggered-in-time grids are available. We used the resulting algorithms to calculate the sound pressure due to a point source in a homogeneous uniformly moving medium. The results obtained were found in excellent agreement with analytical predictions even for a Mach number as high as 0.6.

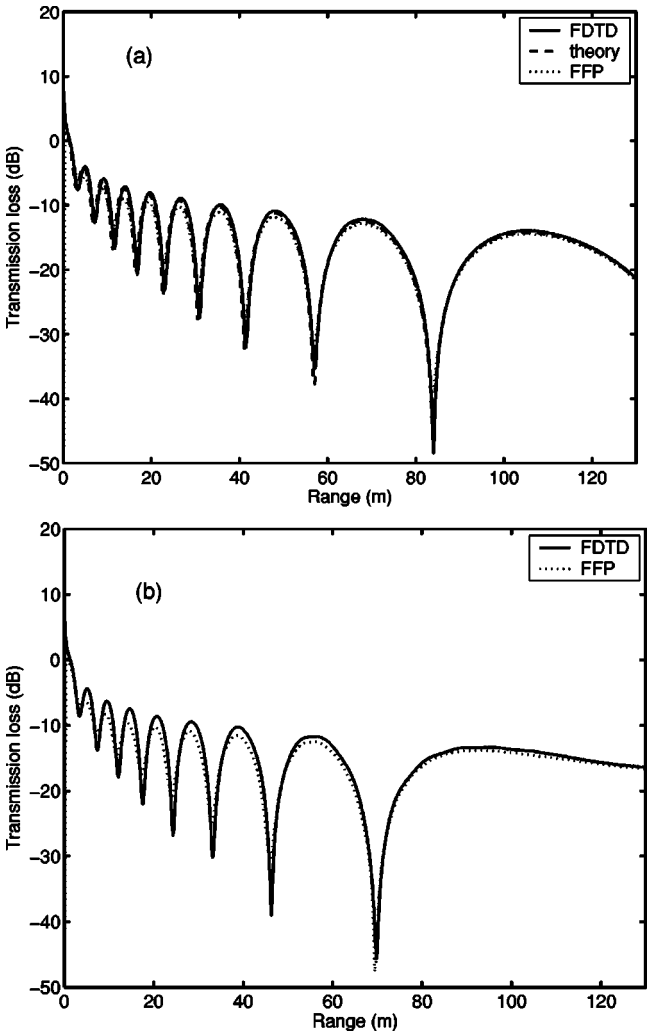

FIG. 7. Comparisons between the transmission loss calculated with different methods. (a) Homogeneous atmosphere without wind. (b) Atmosphere with linearly increasing wind velocity.

Furthermore, using the algorithm developed, we calculated the sound field due to a point source in a stratified moving atmosphere. The results obtained are in a good agreement with the FFP solution.

Finally note that Eqs. (17) and (18) have already been used as starting equations in FDTD simulations of sound propagation in 3-D moving media with realistic velocity fields. The results obtained were published in proceedings of conferences.[5–8] These realistic velocity fields include the following: kinematic turbulence generated by quasi-wavelets,[5,6] 3-D stratified moving atmosphere,[6] and atmospheric turbulence generated by large-eddy simulation.[7] In Ref. 8, FDTD simulations were used to numerically study infrasound propagation in a moving atmosphere over distances of several hundred km. The largest run to date incorporated over 1.5 billion nodes and took about 100 hours on 500 Compaq EV6 parallel processors.[8]

ACKNOWLEDGMENTS

This article is partly based upon work supported by the DoD High-Performance Computing Modernization Office project ''High-Resolution Modeling of Acoustic Wave Propagation in Atmospheric Environments'' and the U.S. Army Research Office Grant No. DAAG19-01-1-0640.

APPENDIX: SOUND FIELD DUE TO A POINT MONOCHROMATIC SOURCE IN A HOMOGENEOUS UNIFORMLY MOVING MEDIUM

In this appendix, we derive a formula for the sound pressure due to a point monochromatic source located in a 2-D homogeneous uniformly moving medium (see Fig. 2).

For this geometry, Eqs. (68) and (69) can be reduced to a single equation for the sound pressure:

$$\left(\frac{\partial}{\partial t}+\mathbf{v}\cdot\boldsymbol{\nabla}\right)^2 p-c^2\nabla^2 p=\varrho c^2\left(\frac{\partial}{\partial t}+\mathbf{v}\cdot\boldsymbol{\nabla}\right)Q. \tag{A1}$$

Here, the source function Q is given by Eq. (70) and contains the time factor $\exp(-i\omega t)$. In what follows, this time factor is omitted. Furthermore, taking into account that the medium velocity is parallel to the x-axis, Eq. (A1) can be written as

$$\left(\frac{\partial^2}{\partial x^2}+\frac{\partial^2}{\partial y^2}+k^2+2ikM\frac{\partial}{\partial x}-M^2\frac{\partial^2}{\partial x^2}\right)p(x,y)$$

$$=\frac{2iA}{\omega}\left(i\omega-v\frac{\partial}{\partial x}\right)\delta(x)\,\delta(y). \tag{A2}$$

Let

$$p(x,y)=\frac{2iA}{\omega}\left(i\omega-v\frac{\partial}{\partial x}\right)\Phi(x,y). \tag{A3}$$

Substituting this formula into Eq. (A2), we obtain the following equation for the function $\Phi(x,y)$:

$$\left[\frac{\partial^2}{\partial x^2}+\frac{\partial^2}{\partial y^2}-\left(-ik+M\frac{\partial}{\partial x}\right)^2\right]\Phi(x,y)=\delta(x)\,\delta(y). \tag{A4}$$

In this equation, let us make the following transformations:

$$x=\sqrt{1-M^2}X,\quad k=\sqrt{1-M^2}K,$$

$$\Phi(x,y)=\exp(-iKMX)\Psi(X,y). \tag{A5}$$

As a result, we obtain the following equation for the fuinction $\Psi(X,y)$:

$$\left[\frac{\partial^2}{\partial X^2}+\frac{\partial^2}{\partial y^2}+K^2\right]\Psi(X,y)=\frac{1}{\sqrt{1-M^2}}\,\delta(X)\,\delta(y). \tag{A6}$$

A solution of this equation is well known:

$$\Psi(X,y)=-\frac{i}{4\sqrt{1-M^2}}H_0^{(1)}(K\sqrt{X^2+y^2}). \tag{A7}$$

Using this expression for Ψ and Eqs. (A3) and (A5), we obtain a desired formula for the sound pressure of a point monochromatic source in a 2-D homogeneous uniformly moving medium:

$$p(x,y)=\frac{iA}{2(1-M^2)^{3/2}}\left[H_0^{(1)}(\xi)-\frac{iMkx}{\xi(1-M^2)}H_1^{(1)}(\xi)\right]$$

$$\times\exp\left(-\frac{ixkM}{1-M^2}\right). \tag{A8}$$

Here, $\xi = (k/\sqrt{1-M^2})\sqrt{x^2/(1-M^2)+y^2}$. In polar coordinates, Eq. (A8) becomes Eq. (71).

[1] R. Blumrich and D. Heinmann, "A linearized Eulerian sound propagation model for studies of complex meteorological effects," J. Acoust. Soc. Am. **112**, 446–455 (2002).

[2] E. M. Salomons, R. Blumrich, and D. Heinmann, "Eulerian time-domain model for sound propagation over a finite-impedance ground surface. Comparison with frequency-domain models," Acust. Acta Acust. **88**, 483–492 (2002).

[3] T. Van Renterghem and D. Botteldoren, "Numerical simulation of the effect of trees on downwind noise barrier performance," Acust. Acta Acust. **89**, 764–778 (2003).

[4] T. Van Renterghem, "The finite-difference time-domain method for simulation of sound propagation in a moving medium," Doctoral thesis, Universiteit Gent, 2003.

[5] D. K. Wilson, M. L. Moran, L. Liu, V. E. Ostashev, D. F. Aldridge, N. P. Symons, and D. H. Marlin, "Development of a high-fidelity simulation capability for battlefield acoustics," in *Proceedings of SPIE AeroSense 2003*, Orlando, FL, 2003.

[6] D. H. Marlin, D. F. Aldridge, N. P. Symons, D. K. Wilson, and V. E. Ostashev, "Finite-difference time-domain acoustic wave propagation in complex atmospheric environments: Second year results," in *Proceedings of the Military Sensing Symposia (MSS) Specialty Group on Battlefield Acoustic and Seismic Sensing, Magnetic and Electric Field Sensors*, Laurel, MD, 2003.

[7] D. K. Wilson, N. P. Symons, E. G. Patton, P. P. Sullivan, D. H. Marlin, D. F. Aldridge, V. E. Ostashev, S. A. Ketcham, E. L. Andreas, and S. L. Collier, "Simulation of sound propagation through high-resolution atmospheric boundary layer turbulence fields," in *Proceedings of the 16th American Meteorological Society Symposium on Boundary Layers and Turbulence*, Portland, ME, 2004.

[8] N. P. Symons, D. F. Aldridge, D. H. Marlin, D. K. Wilson, E. G. Patton, P. P. Sullivan, S. L. Collier, V. E. Ostashev and D. P. Drob, "3D staggered-grid finite-difference simulation of sound refraction and scattering in moving media," in *Proceedings of the 11th International Symposium on Long Range Sound Propagation*, Fairlee, VT, 2004.

[9] V. E. Ostashev, *Acoustics in Moving Inhomogeneous Media* (E&FN SPON, London, 1997).

[10] A. D. Pierce, *Acoustics—An Introduction to its Physical Principles and Applications* (McGraw-Hill, New York, 1989).

[11] L. M. Brekhovskikh and O. A. Godin, *Acoustics of Layered Media* (Springer-Verlag, Berlin, 1992).

[12] M. E. Goldstein, *Aeroacoustics* (McGraw-Hill, New York, 1976).

[13] V. I. Tatarskii, *The Effects of the Turbulent Atmosphere on Wave Propagation* (Israel Program for Scientific Translation, Jerusalem, 1971).

[14] A. D. Pierce, "Wave equation for sound in fluids with unsteady inhomogeneous flow," J. Acoust. Soc. Am. **87**, 2292–2299 (1990).

[15] D. F. Aldridge, "Acoustic wave equations for a linear viscous fluid and an ideal fluid," SAND Report SAND2002-2060, Sandia National Laboratories, Albuquerque, NM, 2002. (Available from the U.S. Dept. of Commerce National Technical Information Service, http://www.ntis.gov/ordering.htm.)

[16] L. D. Landau and E. M. Lifshitz, *Fluid Mechanics* (Pergamon, New York, 1987).

[17] D. I. Blokhintzev, *Acoustics of an Inhomogeneous Moving Medium* (Nauka, Moscow, 1946) (in Russian); (English translation, Department of Physics, Brown Univ., Providence, RI, 1956).

[18] C. K. W. Tam and Y. C. Webb, "Dispersion-relation-preserving finite difference schemes for computational acoustics," J. Comput. Phys. **107**, 262–281 (1993).

[19] C. Bogey, C. Bailly, and D. Juvé, "Computation of flow noise using source terms in linearized Euler's equations," AIAA J. **40**, 235–243 (2002).

[20] C. Bailly, P. Lafon, and S. Candel, "A stochastic approach to compute noise generation and radiation of free turbulent flows," AIAA Paper No. 95-092, 1995.

[21] J. C. Hardin and D. S. Pope, "An acoustic/viscous splitting technique for computational aeroacoustics," Theor. Comput. Fluid Dyn. **6**, 323–340 (1994).

[22] W. Z. Shen and J. N. Sorensen, "Aeroacoustic modeling of low-speed flows," Theor. Comput. Fluid Dyn. **13**, 271–289 (1999).

[23] W. Z. Shen and J. N. Sorensen, "Aeroacoustic modeling of turbulent airfoil flows," AIAA J. **39**, 1057–1064 (2001).

[24] R. Ewert and W. Schroder, "Acoustic perturbation equations based on flow decomposition via source filtering," J. Comput. Phys. **188**, 365–398 (2003).

[25] V. E. Ostashev, "On sound wave propagation in a three-dimensional inhomogeneous moving medium," in *Diffraction and Wave Propagation in Inhomogeneous Media* (MPTI Press, Moscow, 1987), pp. 42–49.

[26] Ph. Blanc-Benon, L. Dallois, and D. Juvé, "Long range sound propagation in a turbulent atmosphere within the parabolic approximation," Acust. Acta Acust. **87**, 659–669 (2001).

[27] K. S. Yee, "Numerical solution of initial boundary value problems involving Maxwell's equations in isotropic media," IEEE Trans. Antennas Propag. **14**, 302–307 (1966).

[28] D. Botteldooren, "Acoustical finite-difference time-domain simulation in a quasi-Cartesian grid," J. Acoust. Soc. Am. **95**, 2313–2319 (1994).

[29] R. W. Graves, "Simulating seismic wave propagation in 3D elastic media using staggered-grid finite differences," Bull. Seismol. Soc. Am. **86**, 1091–1106 (1996).

[30] J. O. A. Robertsson, J. O. Blanch, and W. W. Symnes, "Viscoelastic finite-difference modeling," Geophysics **59**, 1444–1456 (1994).

[31] A. Kasahara, "Computational aspects of numerical models for weather prediction and climate simulation," in *Methods in Computational Physics*, edited by J. Chang (Academic, New York, 1977), pp. 1–66.

[32] E. Kreyszig, *Advanced Engineering Mathematics*, 6th ed. (Wiley, New York, 1988).

[33] L. R. Lines, R. Slawinski, and R. P. Bording, "A recipe for stability of finite-difference wave-equation computations," Geophysics **64**, 967–969 (1999).

[34] D. K. Wilson and L. Liu, "Finite-difference, time-domain simulation of sound propagation in a dynamic atmosphere," Cold Regions Research and Engineering Laboratory Technical Report ERDC-CRREL TR-04-12, Hanover, NH, 2004, p. 63, available from the National Technical Information Center, http://www.ntis.gov/, Technical Report, ADA423222.

[35] S. L. Collier, V. E. Ostashev, D. K. Wilson, and D. H. Marlin, "Implementation of ground boundary conditions in a finite-difference time-domain model of acoustic wave propagation," in *Proceedings of the Military Sensing Symposia (MSS) Specialty Group on Battlefield Acoustic and Seismic Sensing, Magnetic and Electric Field Sensors*, Laurel, MD, 2003.

[36] D. K. Wilson, "Sound field computations in a stratified, moving medium," J. Acoust. Soc. Am. **94**, 400–407 (1993).

Approximate high-order dynamic theory of a fluid layer in between two thick solids

Dmitry D. Zakharov[a)]
FESBE, London South Bank University, 103 Borough Road, London SE1 0AA, United Kingdom

(Received 6 July 2004; revised 29 November 2004; accepted 1 December 2004)

A thin layer of heavy fluid with bound faces is considered first. For the sake of simplicity, the effects of vortex and viscosity are neglected. Two cases of compressible and incompressible fluids are treated, assuming that a thickness-over-wavelength ratio is a small parameter. For the internal state of medium the relations between the quantities on the layer surfaces are deduced. In contrast to the standard approach, which expands the propagator matrix into power series of a small wave number, the asymptotic integration of 3D equations and boundary conditions of fluid dynamics is performed. Respective relations are represented in a recurrent form and permit one to obtain the high-order components of the displacements and pressure rather simply. When considering two thick solids with a fluid in between, this result is used to derive the so-called ''impedance boundary conditions'' (IBC) with a relative asymptotic error up to tenth order. Tests show their validity until the first quasiresonance frequency of a layer, so, the analysis is not just long wave but essentially low frequency. Thus, these IBC are applicable to reduce the dimension in the analysis of challenged multicomponent system of fluid-coupled solids in a reasonable frequency range. © *2005 Acoustical Society of America.* [DOI: 10.1121/1.1850406]

PACS numbers: 43.20.El, 43.20.Px, 43.20.Tb, 43.35.Bf [LLT] Pages: 518–527

I. INTRODUCTION

The term ''impedance boundary conditions'' (IBC) has been introduced by Leontovich[1] while studying conducting surface, and his approximation involved electromagnetic field and its normal derivatives. Since such approximate boundary conditions are widely used in electrodynamics,[2,3] they remain a simple but powerful instrument to describe the surface phenomena.[4] Similar results have been obtained also in the modeling of thin layers in elasticity.[5,6] Physically, they are based on the fact that for a layer with fixed faces (or immersed in a very stiff medium) the first dispersion curve begins with a certain nonzero cutoff frequency $\Omega \neq 0$. For this reason, the leading approximation of the internal state of a layer at low frequency can be described without differential equations, but algebraically. Thus, IBC are necessarily long wave and their leading terms are ''quasistatic.'' The IBC for elastic layer and for viscoelastic adhesive bond have been derived using direct analysis of propagator matrix.[7] On introducing the small dimensionless wave number kh the propagator matrix is expanded into a power series, which is truncated with the relative asymptotic error $O(kh)$ or $O(kh)^2$, respectively.[7–9] In what follows, we use the propagator matrix only for testing and deduce IBC from the asymptotic analysis of the 3D boundary value problem to the dynamic equations of fluid. For the sake of simplicity, the effects of vortex and viscosity are neglected. Our small parameter ϵ—a fraction of the layer half-thickness over the characteristic wavelength—is used to scale variables and to derive recurrent relations between the components of asymptotic power series for all quantities. The very efficient method of asymptotic integration[5,10] permits us to deduce IBC of high order, up to the asymptotic error $O(\epsilon^{10})$ in this publication. In fact, these IBC may play the same role as the approximation of the transmission function, which is essentially low frequency but possibly not just long wave.

Thus, the obtained IBC can be used to reduce the problem dimension in the analysis of challenged multicomponent system of fluid-coupled solids in a reasonable frequency range. Let us mention just two such: study of the spectral properties of a *set of fluid-coupled thick solids* (e.g., plates or laminates) and calculation of the *near field*, radiated by *a fluid-coupled ultrasonic transducer* into structural member. The couplants are often used when facing the imperfect (not polished) surface. Naturally, the result depends on the fluid properties and thickness, and their influence to the field should be taken into account.[11] Since the area of the contact spot underneath the transducer (or of its perplex wedge) is of finite size, some boundary effect caused by the ends can be expected. However, we may say *a priori* that the effect is smooth due to the longitudinal motions in the fluid layer, which is wider than this area, caused by the ends. So, the neglecting of these ends for thin couplant seems reasonable because the longitudinal motion in the fluid does not affect the pressure and the transverse displacement too much. The total problem is subdivided into two others: a *local* problem to seek the pressure on the interface of the infinite couplant and inspected solid; and a problem to calculate the solid response to this pressure, but distributed on a finite area of contact spot. Our IBC may help only in solving the local problem. Of course, further development needs to take into account the possible fluid viscosity.

The paper is organized as follows: In Sec. II the problem is formulated for a fluid layer with given displacements on

[a)]Present address: FESBE, London South Bank University, 103 Borough Road, London SE1 0AA, United Kingdom. Electronic mail: dd_zakh@mail.ru

its surfaces. The asymptotic series for main physical quantities are presented. In Sec. III the recurrent relations between the displacements and pressure on the surfaces are derived. The dimensional form of IBC of tenth order is obtained and the limit cases are studied in Sec. IV. Section V describes the IBC of high order for two fluid-coupled solids, and Sec. VI presents a few numerical tests for two fluid-coupled elastic half-spaces with incident wave falling to the interface from the top solid. Finally, we discuss the validity of the asymptotic model in Sec. VII and sum up with a conclusion.

II. SCALING IN FLUID AND ASYMPTOTIC SERIES

Let a fluid layer occupy a region $-\infty<X_1,\ X_2<\infty$, $|X_3|\leqslant h\ (H=2h)$, where $\mathbf{X}\equiv X_\alpha \mathbf{i}_\alpha$ $(\alpha=1,2)$, $Z\equiv X_3$ are Cartesian coordinates. The fluid is assumed to be linear, nonviscous, and Newtonian, with mass density ρ and sound velocity c. To begin with, consider the boundary conditions on the lower and upper fluid surfaces $Z=\mp h$ in the form of given normal displacements $U_3=U^{\mp}(\mathbf{X},T)$ (T is time).

Introduce the potential Ψ of the fluid displacements and assume the characteristic longitudinal scale L of dynamic process to be much larger than the half thickness h, i.e., $\epsilon=h/L\ll 1$. The main equations and constitutive relations are written as follows:

$$(B-\partial_Z^2)\Psi=0,\quad B\equiv c^{-2}\partial_T^2-\Delta,\quad \Delta\equiv\partial_{X_1}^2+\partial_{X_2}^2 \tag{1}$$

$$U_\alpha=\partial_{X_\alpha}\Psi,\quad U_3=\partial_Z\Psi, \tag{2}$$

$$P=-\rho\partial_T^2\Psi, \tag{3}$$

where U_3, U_α are components of the displacement vector and P is the acoustic pressure.

Denote $\zeta^{\mp}\equiv U_Z|_{Z=\mp h}$ and set the direction of the Z axis against the gravity. Then, the total pressure $P_*^{\mp}$ on the lower/upper surface includes gravitational terms and acquires the form

$$P_*^{\mp}=-\rho\partial_T^2\Psi|_{Z=\mp h}-\rho g'\zeta^{\mp}=P^{\mp}-\rho g'\zeta^{\mp}\quad (g'\approx 9.8\ \text{m/s}^2), \tag{4}$$

$$\zeta^{\mp}\equiv U^{\mp}. \tag{5}$$

Now, proceed to the dimensionless quantities. Normalize the coordinates and time as follows:

$$Z=zh,\quad \mathbf{X}=\mathbf{x}L,\qquad T=tT_0,\quad (T_0=\epsilon^a L/c), \tag{6}$$

where the degree a is to be determined further. For the time-harmonic waves $e^{-i\omega T}$ the respective time scale has, of course, the order ω^{-1}, and it is possible to speak about the order $\omega\sim\epsilon^{-a}$ of this single frequency. But, we prefer to introduce the parameter a to be able to describe a more complicated case, e.g., the transition wave in the form of integral to the frequency interval.

The differential operator and derivatives are

$$\partial_X=L^{-1}\partial_x,\quad \partial_Z=h^{-1}\partial_z,$$

$$\partial_T^2=T_0^{-2}\partial_t^2=(c/L)^2\epsilon^{-2a}\partial_t^2,$$

$$B-\partial_Z^2\equiv L^{-2}\{\epsilon^{-2a}\partial_t^2-\epsilon^{-2}\partial_z^2-\nabla^2\},\quad (\nabla^2\equiv\partial_1^2+\partial_2^2).$$

Similarly to the classical shallow-water approach,[10] the potential, displacements, and pressure are sought in the form of asymptotic power series with respect to ϵ

$$\begin{aligned}&\Psi=h^2\epsilon^{\lambda}(\psi^0+\epsilon\psi^1+\cdots),\\ &U_\alpha=h\epsilon^{\lambda+1}(u_\alpha^0+\epsilon u_\alpha^1+\cdots)\quad(\alpha=1,2),\\ &U_Z=h\epsilon^{\lambda}(u_z^0+\epsilon u_z^1+\cdots),\\ &P=\rho c^2\epsilon^{\lambda+2-2a}(p^0+\epsilon p^1+\cdots),\end{aligned} \tag{7}$$

where the degree λ has to be determined as well and $h\epsilon^{\lambda}=L\epsilon^{\lambda+1}$.

Remark 1. In this scaling the compressible fluid is considered. If it is not compressible the operator $B\equiv c^{-2}\partial_T^2-(\partial_Z^2+\Delta)$ should be replaced by $B\equiv-\partial_Z^2-\Delta$ and in the formula (6) the sound speed c is replaced by the speed $c=\sqrt{g'H}$ of the gravitational wave. Other steps remain unchanged.

III. RELATIONS FOR THE QUANTITIES ON THE UPPER AND LOWER SURFACES

Upon the choice $a=0$ the substitution of the asymptotic series (7) into Eq. (1) and relations (2), (3) yields a set of recurrent formulas

$$\partial_z^2\psi^l=A\psi^{l-2},\quad (A\equiv\partial_t^2-\nabla^2), \tag{8}$$

$$u_z^l=\partial_z\psi^l,\quad u_\alpha^l=\partial_\alpha\psi^l, \tag{9}$$

$$p^l=-\rho\partial_t^2\psi^l,\quad (l=0,1,2,...). \tag{10}$$

The nonzero values in (8)–(10) correspond to the nonnegative indices only. So, $\partial_z^2\psi^l=0$ as $l<2$.

Remark 2. Let us briefly explain the choice $a=0$. If not, Eq. (8) acquires the form

$$\partial_z^2\psi^l=\partial_t^2\psi^{l+2a-2}-\nabla^2\psi^{l-2}.$$

For the integer nonpositive values a the equation above is recurrent, but the dynamic process is essentially long wave. The case $a=0$ covers this very long-wave description as well with an explicit physical meaning—time scaling by the sound velocity in fluid layer. At $a\geqslant 1$ the above relation is physically inconsistent, which is easy to show for $l=0$, 1. In terms of frequency ranges the scale with $a=0$ corresponds to $\omega\leqslant O(1)$ as $\epsilon\to+0$.

Introduce the additional notations for the half-sum and half-difference of the displacements on the fluid surfaces

$$\xi=\frac{\zeta^+ +\zeta^-}{2},\quad \eta=\frac{\zeta^+ -\zeta^-}{2},$$

which are independent of z and can be expanded into asymptotic series similarly to (7)

$$\xi=h\epsilon^{\lambda}(\xi^0+\epsilon\xi^1+\cdots),\quad (\xi\leftrightarrow\eta).$$

Hence, setting $l=0$, 1 and $n\geqslant 0$, we obtain from (8) and (9) the recurrent chain

$$\psi^{l+2n}=\sum_{k=0}^{2n+1}\frac{z^k}{k!}\psi_k^{l+2n}(\mathbf{x},t),$$

$$\psi_k^{l+2n}=\frac{1}{k(k-1)}A\psi_{k-2}^{l+2n-2}\quad(k\geqslant 2),$$

$$\psi_1^{l+2n}=\xi^{l+2n}-\sum_{m=1}^{2m+1\leqslant 2n+1}\frac{1}{(2m)!}\psi_{2m+1}^{l+2n},$$

$$\psi_2^{l+2n}=\eta^{l+2n}-\sum_{m=1}^{2m\leqslant 2n+1}\frac{1}{(2m-1)!}\psi_{2m}^{l+2n}=A\psi_0^{l+2n-2} \tag{11}$$

$$u_z^{l+2n}=\sum_{k=1}^{2n+1}\frac{z^{k-1}}{(k-1)!}\psi_k^{l+2n}(\mathbf{x},t).$$

As one can see, the basic step in this recurrent chain equals 2.

Remark 3. In the above formulas the upper indices correspond to the degree of ϵ in the respective asymptotic series (7). For chosen values of n and l, all the terms with negative upper index in the right-hand side equal zero.

For $n=0$ we have $\partial_z^2\psi^l=0$ with the respective components of the field given by

$$\psi^l=\psi_0^l(\mathbf{x},t)+z\psi_1^l(\mathbf{x},t),\quad u_z^l=\psi_1^l(\mathbf{x},t),$$

$$u_\alpha^l=\partial_\alpha\psi^l(\mathbf{x},t),\quad p^l=-\partial_t^2\psi_0^l.$$

At $z=\mp 1$ the displacement field should possess enough freedom to satisfy the boundary conditions (5), but as seen u_z^l is constant across the thickness. Hence, we should set $\psi_1^l(\mathbf{x},t)=0$ and

$$\psi^l=\psi_0^l(\mathbf{x},t),\quad u_z^l=0,\quad u_\alpha^l=\partial_\alpha\psi_0^l(\mathbf{x},t)\neq 0,$$

$$p^l=-\partial_t^2\psi_0^l=p^{\pm,l}\neq 0.$$

For $n=1$ the expressions for the potentials, normal displacement, and pressure (10) become more interesting. From Eq. (8) we obtain a set of formulas

$$\partial_z^2\psi^{l+2}=A\psi^l=A\psi_0^l\Rightarrow\psi^{l+2}=\psi_0^{l+2}+z\psi_1^{l+2}+\frac{z^2}{2!}A\psi_0^l,$$

$$u_z^{l+2}=\psi_1^{l+2}+zA\psi_0^l=\xi^{l+2}+z\eta^{l+2},$$

$$Ap^{\pm,l}=-\partial_t^2A\psi_0^l=-\partial_t^2\eta^{l+2},$$

$$\psi^{l+2}=\psi_0^{l+2}+z\xi^{l+2}+\frac{z^2}{2!}\eta^{l+2},$$

$$p^{l+2}=-\partial_t^2\psi^{l+2}=-\partial_t^2\left(\psi_0^{l+2}+z\xi^{l+2}+\frac{z^2}{2!}\eta^{l+2}\right).$$

This is also an illustration of the origin of the general recurrent relations. After these two steps one can easily predict the formulas (11).

In general, the equation $\eta^{l+2}=A\psi_0^l$ gives some information about the potential $\psi_0^l(\mathbf{x},t)$, but since the fluid layer has no ends in the horizontal directions the displacements $u_\alpha^l=\partial_\alpha\psi_0^l(\mathbf{x},t)$ and potential itself remain undetermined.

Besides the formulas (2)–(5), we may relate the pressure on the surfaces from previous step and the half-difference of the displacements. Note that for the half-sum and half-difference of pressures on the upper/lower surfaces

$$p^{\mp,l}\equiv-\partial_t^2\psi^l|_{z=\mp 1},$$

one can easily obtain

$$\frac{p^{+,l}-p^{-,l}}{2}=0,$$

$$A\left(\frac{p^{+,l}+p^{-,l}}{2}\right)=-\partial_t^2\left(\frac{\zeta^+-\zeta^-}{2}\right)^{l+2}.$$

In a similar way the relations can be obtained for any $l+2n$.

Omitting the cumbersome formulas for $n=2, 3, 4$ let us represent the final results for the last step $n=5$ considered in this section

$$\psi^{l+10}=\sum_{k=0}^{10}\frac{z^k}{k!}\psi_k^{l+10},\quad u_z^{l+10}=\sum_{k=1}^{10}\frac{z^{k-1}}{(k-1)!}\psi_k^{l+10},$$

$$\begin{aligned}Ap^{\mp,l+8}=-\partial_t^2\Bigg\{&\eta^{l+10}\mp A\xi^{l+8}+\left(\frac{1}{2!}-\frac{1}{3!}\right)A\eta^{l+8}\mp\left(\frac{1}{3!}-\frac{1}{2!}\right)A^2\xi^{l+6}+\left(\frac{1}{4!}-\frac{1}{2!3!}+\frac{1}{3!^2}-\frac{1}{5!}\right)A^2\eta^{l+6}\\&\mp\left(\frac{1}{5!}-\frac{1}{2!3!}+\frac{1}{2!^2}-\frac{1}{4!}\right)A^3\xi^{l+4}+\left(\frac{1}{6!}-\frac{1}{4!3!}+\frac{1}{2!3!^2}-\frac{1}{2!5!}-\frac{1}{3!^3}+\frac{2}{3!5!}-\frac{1}{7!}\right)A^3\eta^{l+4}\\&\mp\left(\frac{1}{7!}-\frac{1}{2!5!}-\frac{1}{3!4!}-\frac{1}{2!^3}+\frac{1}{2!^23!}+\frac{2}{2!4!}-\frac{1}{6!}\right)A^4\xi^{l+2}+\left(\frac{1}{7!9!}-\frac{1}{6!9!}-\frac{1}{2!3!^3}+\frac{2}{2!3!5!}+\frac{1}{3!^4}-\frac{3}{3!^25!}+\frac{1}{3!7!}+\frac{1}{3!^24!}-\frac{1}{4!5!}\right.\\&\left.+\frac{1}{5!^2}+\frac{1}{6!8!}-\frac{1}{7!8!}\right)A^4\eta^{l+2}\Bigg\}.\end{aligned}$$

Then, the pressure and displacements on the surfaces are related by formulas

$$\frac{p^{+,l+8}-p^{-,l+8}}{2}=-\partial_t^2\Big\{0+\xi^{l+8}-\frac{1}{3}A\xi^{l+6}+\frac{2}{15}A^2\xi^{l+4}-\frac{17}{315}A^3\xi^{l+2}\Big\},$$
$$A\left(\frac{p^{+,l+8}+p^{-,l+8}}{2}\right)=-\partial_t^2\Big\{\eta^{l+10}+\frac{1}{3}A\eta^{l+8}-\frac{1}{45}A^2\eta^{l+6}+\frac{2}{945}A^3\eta^{l+4}-\frac{1\,343}{38\,102\,400}A^4\eta^{l+2}\Big\}. \tag{12}$$

The results at smaller n can be found from (12) subtracting 2 consequently from the upper indices and by truncating the terms with negative upper indices in the right-hand side.

IV. DIMENSIONAL FORM

On the basis of relations (12) let us now proceed to the dimensional boundary relations. To this end rewrite first the relations (12) in the dimensional form. Multiplying both sides in (12) by respective ϵ powers at $n=0-4$ and collecting terms $\epsilon^k p^k$, $\epsilon^k\xi^k$, and $\epsilon^k\eta^k$ in both sides, we proceed to the dimensional variables, displacements, pressure, and operators and obtain

$$P^+-P^-=-h\rho\partial_T^2\{0+1-\tfrac{1}{3}h^2B+\tfrac{2}{15}h^4B^2-\tfrac{17}{315}h^6B^3\}\times(U_Z^++U_Z^-),$$
$$hB(P^++P^-)=-\partial_T^2\Big\{1+\tfrac{1}{3}h^2B-\tfrac{1}{45}h^4B^2+\tfrac{2}{945}h^6B^3-\frac{1\,343}{38\,102\,400}h^8B^4\Big\}(U_Z^+-U_Z^-). \tag{13}$$

Remark 4. The degree λ is undetermined yet. Its value depends on the problem considered. When using the conditions (5) on the fluid surfaces and assuming $\zeta^{\mp}=O(1)$ as $\epsilon\to+0$, we should complete the recurrent formulas (8)–(11) by an additional requirement

$$u_z^{l+2n}\big|_{z=\mp1}=L^{-1}\zeta^{\mp}(\mathbf{x},t)\,\delta^0_{\lambda+1+l+2n},$$

where $\delta^0_{\lambda+l+2n+1}$ is a Kronecker delta. Since the first nonzero component in both sides appears at $l+2n=2$, the first respective value to check is $\lambda=-3$. By analyzing the recurrent chain (8)–(11) for different upper indices it is easy to show that this value is consistent. Then, the asymptotic series for the normal displacement can be rewritten in the form

$$U_z=h\epsilon^{-3}(0+\epsilon0+\epsilon^2u_z^2+\epsilon^3u_z^3+\cdots)=L(u_z^2+\epsilon^1u_z^3+\cdots).$$

However, relations (13) themselves do not specify the value λ in the explicit form.

V. HIGH-ORDER IMPEDANCE BOUNDARY CONDITIONS

Now, investigate the differences from above, caused by the hydroelastic contact. Suppose that the fluid layer is placed in between two elastic anisotropic thick solids, marked by the sign − and +, respectively. Each of them is described by the dynamic equation of anisotropic elasticity, complemented by the boundary conditions of the hydroelastic contact at $Z=\mp h$, which involve the normal stresses $\sigma_{ZZ}^{\mp}$ and tangent stresses $\sigma_{\alpha Z}^{\mp}$

$$P^{\mp}=-\sigma_{ZZ}^{\mp}+(\rho_{\mp}+\rho)g'U_Z^{\mp},\quad \sigma_{\alpha Z}^{\mp}=0\quad(\alpha=1,2),\quad \zeta^{\mp}\equiv U_Z^{\mp}. \tag{14}$$

The scaling procedure in each solid differs from that in the fluid layer only for coordinate Z, namely

$$Z=zL,\quad \mathbf{X}=\mathbf{x}L,\quad T=tT_0,\quad T_0=L/c. \tag{15}$$

Remark 5. Let us make an additional comment to the choice of a time scale. As seen in (15), the time scale is the same as in the fluid, i.e., we do not consider a contrast situation when the ratio of speeds in different media is comparable with ϵ power. If doing so, the case of the low-speed fluid is nevertheless covered by the same description and the respective terms of inertia in the thick solids will be small; but, when the speed in the fluid is much greater than those in the thick solids some additional difficulty may appear. In this case the choice $a=0$ is no longer universal. Another example concerns the stratified heavy fluid with slightly different mass densities, where, besides the acoustical waves, the internal gravitational wave on the fluid interface may exist. The appropriate speed is proportional to $\sqrt{g'H}$ and, to describe this low process only the required time scale is $L/\sqrt{g'H}\sim\epsilon^{-1/2}$. The respective process in solid may be quasistatic.

Applying (15) to the dynamic equations of anisotropic elasticity and to the Hooke law, we observe no small parameters appearing in these relations, which look absolutely similar both in the dimensional and the dimensionless forms. As a result, each of the dimensionless displacements or stresses in solids is sought in the form of asymptotic series, caused by the hydroelastic contact only. For the dimensionless quantities this contact at $z=\mp1$ is described by the following boundary conditions:

$$p^{\mp,l-2-\lambda}=-\sigma_z^{\mp,l}+(1+\rho_{\mp}/\rho)g\zeta^{\mp,l-1-\lambda}\quad(g=g'L/c^2),\quad \sigma_{\alpha z}^{\mp,l}=0,\quad \zeta^{\mp,l-1-\lambda}=u_z^{\mp,l}. \tag{16}$$

The displacements are normalized by the wavelength L and the stresses—by ρc^2, which is assumed to be of the *same order* as *the elastic moduli*. In the fluid layer the above asymptotic integration can be repeated by taking account of (14) instead of (5).

Note that we do not need to specify the value λ now, and, in general, may deal with a formal series, e.g., such as

$$U_Z = h(\cdots + \epsilon^{-1}u_z^{-1} + u_z^0 + \epsilon u_z^1 + \cdots)$$
$$= L\epsilon(\cdots + \epsilon^{-1}u_z^{-1} + u_z^0 + \epsilon u_z^1 + \cdots),$$

and with respective series for other quantities. The first left term in brackets follows from boundary value problem of the fluid–solid interaction and depends on the input, i.e., the perturbation in solids. The relations obtained in previous sections hold since they are independent of λ.

A comparison of formulas (14), (16), and (13) results in six dimensional *impedance boundary conditions* for two fluid-coupled elastic solids

$$-\sigma_{ZZ}^+ + (\rho_+ + \rho)g' U_Z^+ + \sigma_{ZZ}^- - (\rho_- + \rho)g' U_Z^-$$
$$= -h\rho\partial_T^2\{0 + 1 - \tfrac{1}{3}h^2B + \tfrac{2}{15}h^4B^2 - \tfrac{17}{315}h^6B^3\}(U_Z^+ + U_Z^-),$$
$$\sigma_{\alpha Z}^{\pm} = 0 \quad (\alpha = 1,2), \tag{17}$$
$$hB\{-\sigma_{ZZ}^+ + (\rho_+ + \rho)g' U_Z^+ - \sigma_{ZZ}^- + (\rho_- + \rho)g' U_Z^-\}$$
$$= -\partial_T^2\left\{1 + \tfrac{1}{3}h^2B - \tfrac{1}{45}h^4B^2 + \tfrac{2}{945}h^6B^3 - \frac{1\,343}{38\,102\,400}h^8B^4\right\}(U_Z^+ - U_Z^-).$$

Again for the compressible fluid we set the differential operator $B \equiv c^{-2}\partial_T^2 - \Delta$ and for the incompressible one ($c \to +\infty$) $B \equiv -\Delta$. In the latter, formally, we use a larger time scale $T_0 \sim \epsilon^{-1/2}$ (see Remark 1).

In the limit case $h \to +0$ the IBC (17) yield

$$-\sigma_{ZZ}^+ + (\rho_+ + \rho)g' U_Z^+ + \sigma_{ZZ}^- - (\rho_- + \rho)g' U_Z^- = 0,$$
$$\sigma_{\alpha Z}^{\pm} = 0,$$
$$\partial_T^2(U_Z^+ - U_Z^-) = 0,$$

and we have zero tangent stresses, coincidence of the normal displacements and, within the gravitational terms, coincidence of normal stresses at the interface. Hence, neglecting the gravitational term, we arrive at the *limit case* of a pure *slip contact*.

VI. NUMERICAL VALIDATION

Let us now validate the obtained IBC using partial time-harmonic wave $e^{-i\omega T}$, which seems to be a reasonable test. To this end we obtain an exact solution with the use of propagator matrix (see the Appendix). Consider a contact between two elastic half-spaces, made of polystyrene (Po) and/or aluminum (Al), and coupled by water (Wa). The latter is considered as a compressible inviscid Newtonian fluid, or as an incompressible fluid whose sound speed $c \to +\infty$.

The mass densities and sound speeds of media are presented in Table I. In what follows the incident *P*– or *S*–harmonic wave falls from the upper half-space +, is reflected by the interface, and transmitted by the fluid layer into the lower half-space –. Thus, for each type of incident wave the response by the half-spaces consists of four waves with complex magnitudes *M*, marked by +, − and *P*, *S*, respectively, and normalized by the magnitude of the incident wave M^{in}. A comparison of these dimensionless magnitudes, obtained using IBC (17), against direct evaluation using a propagator matrix is carried out. The propagator matrix and necessary data are reproduced in the Appendix.

TABLE I. Parameters of media.

	Al	Po	Wa
Mass density ρ, kg/m^3	2700	1060	1000
Wave speed c, m/s	$c_P = 6320$ $c_S = 3080$	$c_P = 2350$ $c_S = 1150$	($c = 1400$) for compressible fluid

As a criterion of comparison, introduce the relative mean-square error *e* as follows:

$$e = \left\{\frac{1}{4}\sum_{[+,-;P,S]}\left|\frac{M^{\text{as}} - M^{\text{ex}}}{M^{\text{ex}}}\right|^2\right\}^{1/2} \times 100\%,$$

where M^{as} corresponds to the asymptotic solution and M^{ex} to the exact one. Let us show a few illustrations, which look typical when applying IBC (17) to different media.

In Figs. 1(a)–(d), the absolute values of magnitudes and the relative error *e* are presented for the contact Po–Wa–Al (water is compressible). The incident *P* wave or *S* wave falls with the angle 80 deg to the interface. The curves with indices $n = 1,2,...,5$ correspond to the asymptotic order $O(\epsilon^{2n})$ of IBC (17); symbols *P*r, *Pt*, and *S*r, *St* denote the reflected (half-space +) and transition (half-space –) *P* and *S* waves. In Fig. 1 the graphs are plotted against H/L, where *L* is the wavelength in the fluid $L = cT_0$, $T_0 = 2\pi/\omega$ (ω is the frequency).

Figures 2(a)–(d) represent the results for the "symmetrical" contact Al–Wa–Al with the incident wave falling at the interface with the angle 60 deg.

As one can see, the significant improvement begins with the second iteration of the accuracy $O(\epsilon^4)$ and continues till $n = 5$. The physical limit of this model is the first quasiresonance frequency of the fluid layer, which is near one-half (the deviation from one-half is caused by the fluid–solid interaction). For the highest iteration the numerical error of 1% is achieved at $H/L \approx 0.33$, and it is about 5% at $H/L \approx 0.4$. Of course, in practice the error of 20% is rather large already, but the graphs are plotted up to 100% to compare the behavior of the low- and high-order models. The first quasiresonance looks similar to the vertical asymptote and one may guess its approximate value using the models derived.

The presence of a thin fluid layer in between solids does not change the Snell's law in principle. But, the magnitudes of the reflected and transmitted waves may vary. At the critical angle the derived model also approximates the physics well. The illustration is presented in Figs. 3(a) and (b), where the incident *S* wave falls from the top half-space to the interface of Al–Wa–Al. For the critical angle the error *e* [Fig. 3(b)] remains in the same frame as previously. The super-

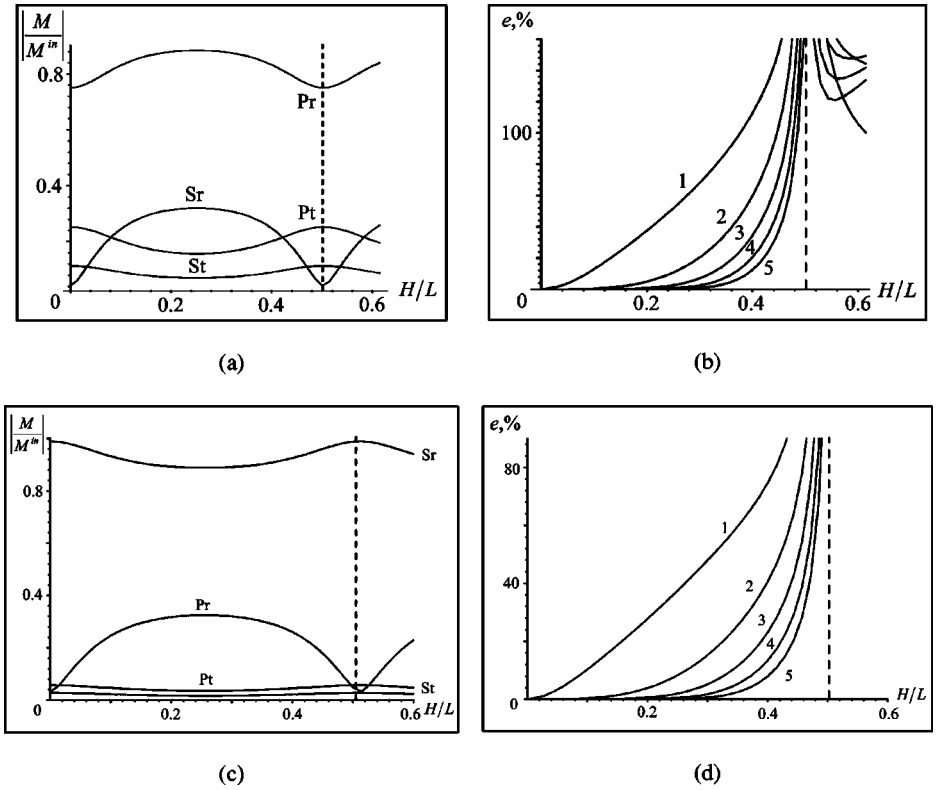

FIG. 1. Media contact Po–Wa (compressible)-Al at incident P wave (a), (b) and S wave (c), (d) falling at 80 deg to the interface: (a), (c) exact solution; (b), (d) relative error of asymptotics.

critical angles checked cause nothing new in context of the model validation. To be brief, we omit these pictures here.

For the incompressible fluid the interval of the IBC validity can be extended. Considering the same combinations of media Po, Wa, Al, but setting $c=+\infty$ in fluid, we arrive at the small numerical error even when the parameter H/L or $kh=\pi H/L$ is no longer small.

In Figs. 4(a)–(d) for the contact problem Al–Wa–Al, the relative error under incident angle 45 deg of P and S waves is about 5% at $H/L\approx 1$ and $n=5$. In this figure the

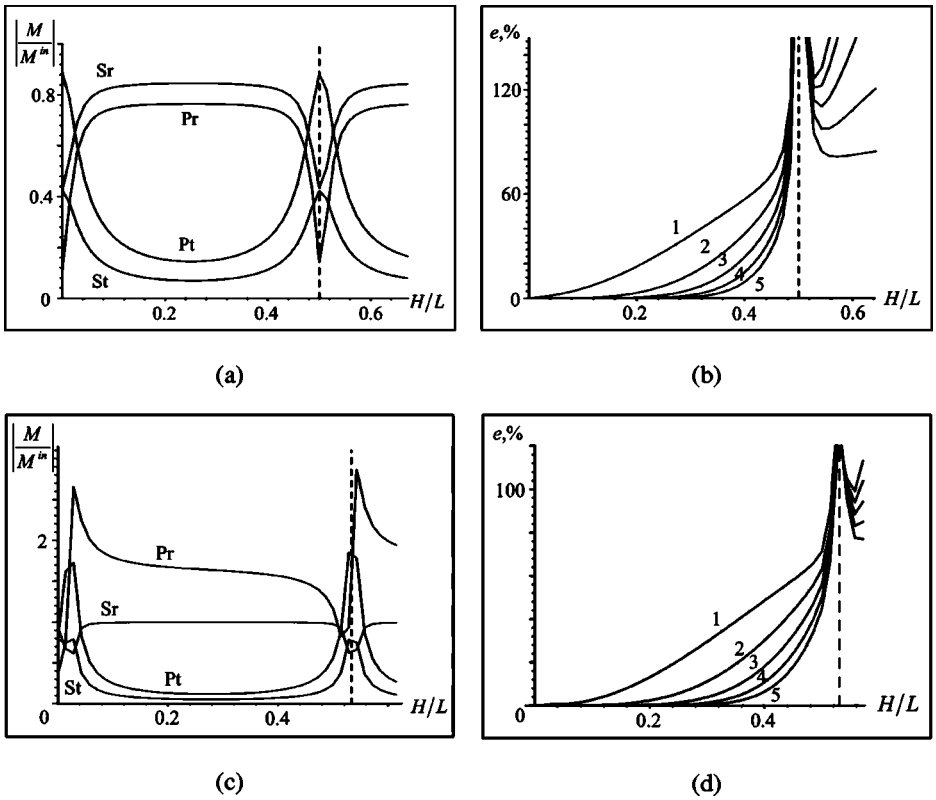

FIG. 2. Media contact Al–Wa(compressible)-Al at incident P wave (a), (b) and S wave (c), (d) falling at 60 deg to the interface: (a), (c) exact solution; (b), (d) relative error of asymptotics.

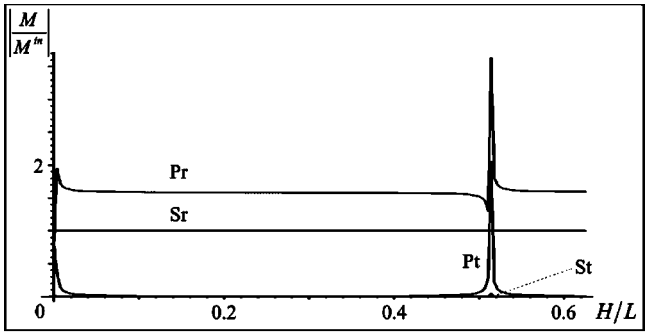

(a)

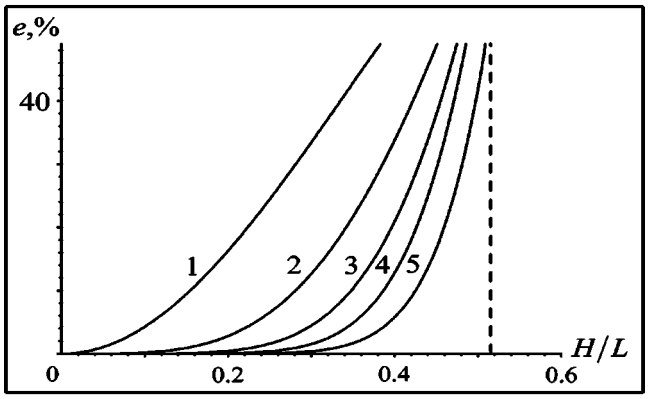

(b)

FIG. 3. Media contact Al–Wa(compressible)-Al at incident *S* wave falling at the critical angle to the interface: (a) exact solution; (b) relative error of asymptotics.

longitudinal scale L is set as $L=L_+=c_S^+T_0$, which is *much shorter* than the wavelength of the characteristic gravitational wave in fluid (see Remark 1).

The high numerical accuracy also occurs for Po–Wa–Al media [see Figs. 5(a)–(d)], where the incident angle of *P* and *S* waves is 10 deg.

Thus, the impedance boundary conditions (17) are rather efficient and may cover the frequency interval practically until the first quasiresonance of the fluid layer.

VII. DISCUSSION

The deduced IBC seem to be much more efficient than the approximate low-order boundary conditions obtained from the asymptotic analysis of the propagator matrix.[7–9] Indeed, the procedure of asymptotic integration applied in this paper is direct, based on 3D dynamic equations and boundary conditions of hydroelasticity, and permits one to derive the model of any order using recurrent relations. The relative accuracy of each recurrent step is $O(\epsilon^2)$ and, as one can see, even the second step leads to the essential improvement of the model. It can be explained by the appearance of the iterated B operator in the right-hand side of (17). Each iteration moves the right bound of the validity interval closer and closer to the first quasiresonance frequency of the fluid layer. The possibility to replace the fluid by relations on the interfaces reflects the fundamental property of propagation modes. Thus, the time-harmonic modes in the layer with fixed surface and bottom, described by

$$(\omega^2 c^{-2}+\partial_{X_1}^2+\partial_{X_2}^2+\partial_Z^2)\Psi=0,$$

$$U_3\equiv\partial_Z\Psi|_{Z=\mp h}=0,$$

result in

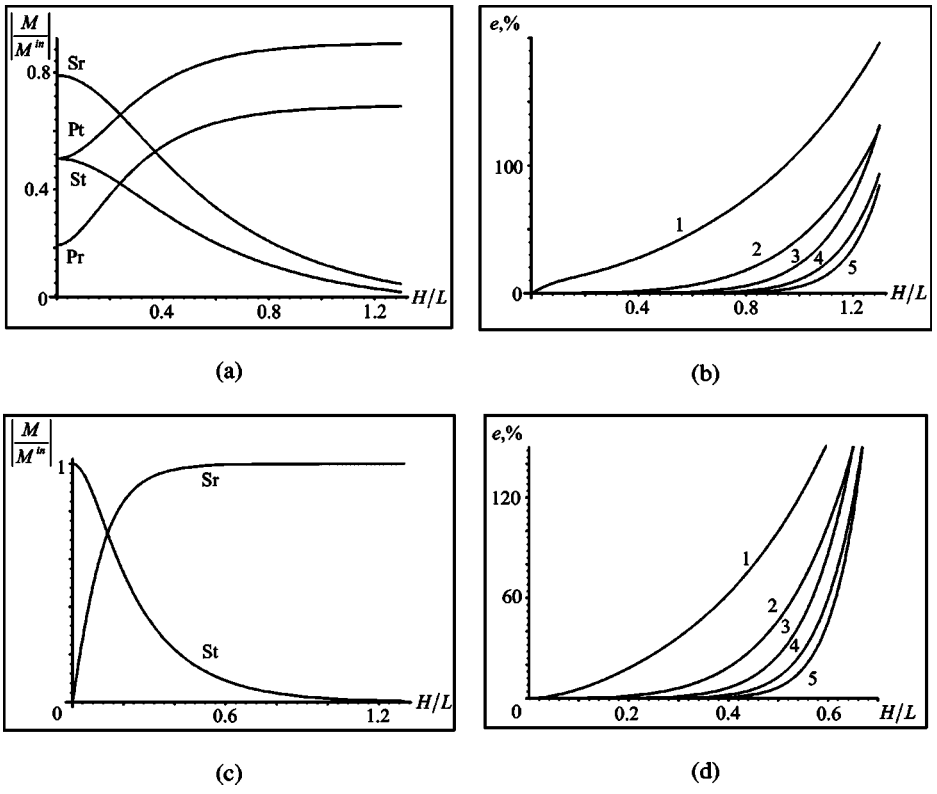

(a) (b)

(c) (d)

FIG. 4. Media contact Al–Wa(incompressible)-Al at incident *P* wave (a), (b) and *S* wave (c), (d) falling at 45 deg to the interface: (a), (c) exact solution; (b), (d) relative error of asymptotics.

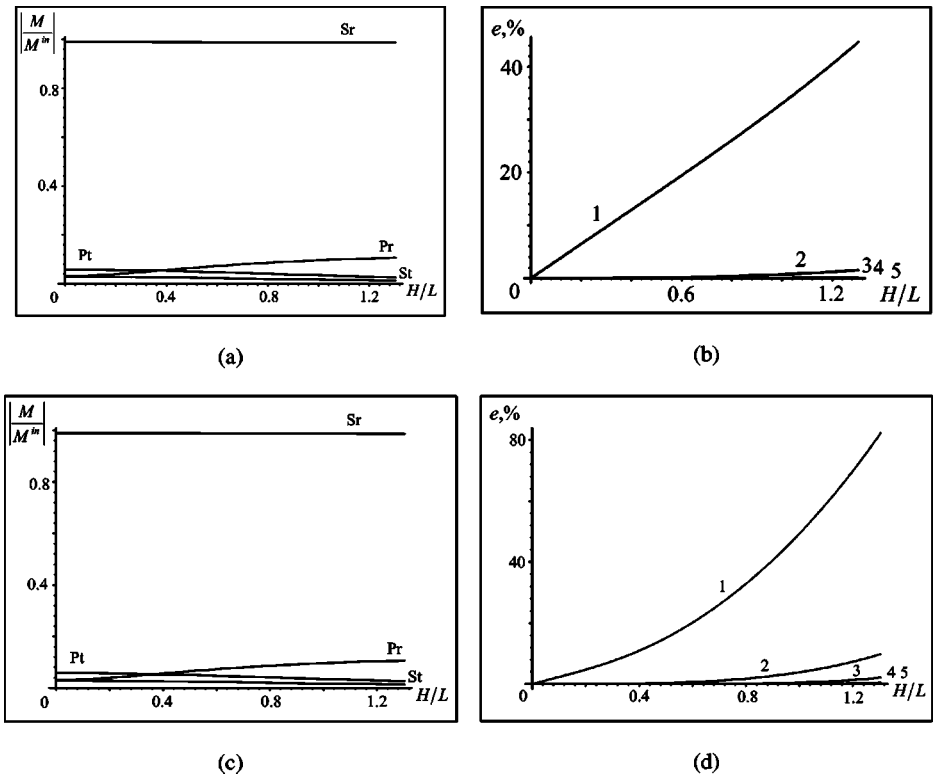

FIG. 5. Media contact Po–Wa(incompressible)-Al at incident *P* wave (a), (b) and *S* wave (c), (d) falling at 80 deg to the interface: (a), (c) exact solution; (b), (d) relative error of asymptotics.

$$\Psi_n=(a_n\sin p_nZ+b_n\cos p_nZ)e^{i(\mathbf{kX}-\omega T)},\quad n=1,2,...,$$

$$(a_n,b_n)=\begin{cases}(1,0), & n \text{ is odd}\\ (0,1), & n \text{ is even}\end{cases},\quad p_n=\frac{\pi n}{2h},$$

$$\omega^2c^{-2}-|\mathbf{k}|^2=p_n^2.$$

Since the dimensionless resonance frequencies $\Omega_n\equiv\omega h/c=\pi n/2>0$, there is no mode propagating in fluid at low frequency, and relations (17) approximate the internal state of layer up to $H/L=1/2$. The hydroelastic contact does not perturb this situation too much.

Remark 6. By the way, in the vicinity of the resonance frequency Ω_n the wave number $|\mathbf{k}|h\ll 1$ and the respective time scale for the high-frequency but long-wave propagating mode is rather small as $n=O(1)$, $\epsilon\to+0$

$$T_0=\frac{2\pi}{\omega}=\frac{2\pi}{c\sqrt{p_n^2+|\mathbf{k}|^2}}=\frac{2\pi L\epsilon}{c\sqrt{(\pi n/2)^2+|\mathbf{k}h|^2}}=O(\epsilon).$$

Hence, for this case in the scaling formula (6) the dynamicity index $a=1$. One possible further development of the model is the asymptotic analysis of this situation.

In practice, due to the high difference of scales in media, this low-frequency model of the fluid may help in modeling the short-wave phenomena in solids. It can be implemented to the time-consuming NDE problems involving multicomponent systems of fluid-coupled solids. In addition, the model takes into account the multiple refractions inside the layer. To give an example, consider an angled beam transducer with the pulse frequency band $\omega=0$–5 MHz placed on the polystyrene wedge and coupled to aluminum by water with a thickness $H=0.5$ mm. The ratio $0<H/L<1/3$. In the modeling of radiated near field the dimension of the problem can be reduced using relations (17). Since the perspective wedge is usually surrounded by acoustically damping material, the total problem is naturally separated into two parts: to determine the stress σ_{ZZ}^- from the *local* problem for two fluid coupled half-spaces, and to seek the wave field in the lower half-space using σ_{ZZ}^- as the input signal on the contact spot. The magnitude of σ_{ZZ}^- has been measured in Ref. 11.

When the fluid layer is not compressible, there is no longer the physical bound 1/2 in the frequency domain and the longitudinal scale can be even shorter—of the order of the elastic wavelength instead of the fluid gravitational wavelength. This is a remarkable fact because formally we began the procedure with a larger time scale, $T_0\sim\epsilon^{-1/2}$. Note, also, that in the numerical tests presented the influence of gravity can be neglected. However, we prefer to include these terms in view of the limit case, when the immersed fluid is rather heavier than two surrounding solids.

VIII. CONCLUSION

The efficient direct asymptotic integration approach, applied to the 3D dynamic equations and boundary conditions of hydroelasticity, results in the so-called *impedance boundary conditions* (17). So, the action of the fluid layer immersed in between two thick solids can be replaced by these conditions. Due to the recurrent nature of asymptotic procedures, the IBC of any order can be found rather easier than by analyzing the asymptotic expansion of the propagator matrix. In this paper we restrict ourselves to the asymptotic accuracy $O(\epsilon^{10})$. The numerical tests demonstrate that the frequency loop up to the first quasiresonance of the fluid layer can be described in this way. For the incompressible fluid the interval of validity can reach the value 1. So, the obtained results are valid at low frequency but possibly not long-wave process.

ACKNOWLEDGMENTS

This work has been carried out in the framework of the EPRRC Grant GR/M31552/01, which is gratefully acknowledged. The author is also thankful to the unknown reviewers who helped to greatly improve the text of this paper.

APPENDIX: PROPAGATOR MATRIX

Consider the time-harmonic field of the fluid layer and of the isotropic elastic half-spaces in the plane (X,Z) geometry. To be brief, the factor $e^{-i\omega T}$ is omitted. Then, in the compressible fluid layer the normal displacements and pressure are as follows:

$$U_Z=\chi(M_1e^{\chi Z}-M_2e^{-\chi Z})e^{i\gamma X},\quad P=\rho\omega^2(M_1e^{\chi Z}+M_2e^{-\chi Z})e^{i\gamma X},$$

where

$$\chi=\sqrt{\gamma^2-k^2},\quad k=\omega/c,\quad \gamma=k^+_{P,S}\sin\theta^{\rm in}_{P,S},\quad k^\pm_{P,S}\equiv\omega/c^\pm_{P,S},$$

and $\theta^{\rm in}_{P,S}$ is the angle of incidence for P or S wave, falling from the top, with respect to the normal to the interface. Note that for the incompressible fluid $c=\infty$ and $k=0$, $\chi=\gamma$.

In the elastic isotropic half-spaces $\pm$ the normal displacement and stresses for the reflected and transmitted P and S waves acquire the form

$$\begin{bmatrix}U_Z\\ \sigma_{XZ}\\ \sigma_{ZZ}\end{bmatrix}^\pm=M^\pm_P\begin{bmatrix}\pm\cos\theta^\pm_P\\ \pm ik^\pm_P\mu^\pm\sin 2\theta^\pm_P\\ ik^\pm_P\mu^\pm F^\pm_P\end{bmatrix}e^{i\mathbf{k}^\pm_P\mathbf{r}}+M^\pm_S\begin{bmatrix}\sin\theta^\pm_S\\ -ik^\pm_S\mu^\pm\cos 2\theta^\pm_S\\ \pm ik^\pm_S\mu^\pm\sin 2\theta^\pm_S\end{bmatrix}e^{i\mathbf{k}^\pm_S\mathbf{r}},$$

$$\mathbf{k}^\pm_{P,S}=k^\pm_{P,S}(\sin\theta^\pm_{P,S},\pm\cos\theta^\pm_{P,S}),\quad \mathbf{r}=(X,Z),$$

$$F^\pm_P=\frac{\cos^2\theta^\pm_P-\nu^\pm\cos 2\theta^\pm_P}{1/2-\nu^\pm},$$

where $\mu^\pm$ and $\nu^\pm$ are shear moduli and Poisson's ratios of media, respectively. The angles of reflection $\theta^+_{P,S}$ and transmission $\theta^-_{P,S}$ satisfy Snell's law

$$\frac{\sin\theta^\pm_{P,S}}{c^\pm_{P,S}}=\frac{\sin\theta^{\rm in}_{P,S}}{c^+_{P,S}},\quad \left(\theta^{\rm critical}_\pm=\arcsin\frac{c^\pm_S}{c^\pm_P}\right).$$

Thus, when an incident wave is given in the form

$$\begin{bmatrix}U_Z\\ \sigma_{XZ}\\ \sigma_{ZZ}\end{bmatrix}^{\rm in}=M^{\rm in}_P\begin{bmatrix}-\cos\theta^{\rm in}_P\\ -ik^+_P\mu^+\sin 2\theta^{\rm in}_P\\ ik^+_P\mu^+\dfrac{\cos^2\theta^{\rm in}_P-\nu^+\cos 2\theta^{\rm in}_P}{1/2-\nu^+}\end{bmatrix}e^{i\mathbf{k}^{\rm in}_P\mathbf{r}}+M^{\rm in}_S\begin{bmatrix}\sin\theta^{\rm in}_S\\ -ik^+_S\mu^+\cos 2\theta^{\rm in}_S\\ -ik^+_S\mu^+\sin 2\theta^{\rm in}_S\end{bmatrix}e^{i\mathbf{k}^{\rm in}_S\mathbf{r}},$$

$$\mathbf{k}^{\rm in}_{P,S}=k^+_{P,S}(\sin\theta^{\rm in}_{P,S},-\cos\theta^{\rm in}_{P,S}).$$

The exact solution is determined by a set of six complex magnitudes $\mathbf{M}=[M^+_P\,M^+_S\,M_1\,M_2\,M^-_P\,M^-_S]^T$, which is sought from six boundary conditions at the interfaces

$$Z=h:\quad U^+_Z+U^{\rm in}_Z=U_Z,$$

$$P^+=-\sigma^+_{ZZ}-\sigma^{\rm in}_{ZZ}+(\rho_++\rho)g'U_Z,\quad \sigma^+_{XZ}+\sigma^{\rm in}_{XZ}=0;$$

$$Z=-h:\quad U^-_Z=U_Z,$$

$$P^-=-\sigma^-_{ZZ}+(\rho_-+\rho)g'U^-_Z,\quad \sigma^-_{XZ}=0.$$

The latter result in the matrix equation

$$\mathbf{P}\times\mathbf{M}=-\mathbf{P}^{\rm in}\times\mathbf{M}^{\rm in},$$

$$\mathbf{M}^{\rm in}=[M^{\rm in}_P\;\;M^{\rm in}_S\;\;0\;\;0\;\;0\;\;0]^T,$$

with propagator matrix

$$\mathbf{P}=\begin{bmatrix}-E^+_P\cos\theta^+_P & -E^+_S\sin\theta^+_S & \chi E^+ & -\chi E^- & 0 & 0\\ -ik^+_PE^+_P\sin 2\theta^+_P & ik^+_SE^+_S\cos 2\theta^+_S & 0 & 0 & 0 & 0\\ -ik^+_PE^+_PF^+_P & -ik^+_SE^+_S\sin 2\theta^+_S & G^+_1E^+ & -G^+_2E^- & 0 & 0\\ 0 & 0 & \chi E^- & -\chi E^+ & E^-_P\cos\theta^-_P & -E^-_S\sin\theta^-_S\\ 0 & 0 & 0 & 0 & ik^-_PE^-_P\sin 2\theta^-_P & ik^-_SE^-_S\cos 2\theta^-_S\\ 0 & 0 & G^-_1E^- & -G^-_2E^+ & -ik^-_PE^-_PF^-_P & ik^-_SE^-_S\sin 2\theta^-_S\end{bmatrix},$$

where

$$E^\pm_{P,S}=e^{ik^\pm_{P,S}h\cos\theta^\pm_{P,S}},\quad E^\pm=e^{\pm\chi h},\quad G^\pm_1=\frac{[(\rho_\pm+\rho)g'\chi-\rho\omega^2]}{\mu^\pm},\quad G^\pm_2=\frac{[(\rho_\pm+\rho)g'\chi+\rho\omega^2]}{\mu^\pm},$$

and

$$\mathbf{P}^{\mathrm{in}}=\begin{bmatrix} -E_P^{\mathrm{in}}\cos\theta_P^{\mathrm{in}} & E_S^{\mathrm{in}}\sin\theta_S^{\mathrm{in}} & 0 & 0 & 0 & 0 \\ -ik_P^+E_P^{\mathrm{in}}\sin 2\theta_P^{\mathrm{in}} & -ik_S^+E_S^{\mathrm{in}}\cos 2\theta_S^{\mathrm{in}} & 0 & 0 & 0 & 0 \\ ik_P^+E_P^{\mathrm{in}}F_P^{\mathrm{in}}+\dfrac{\rho_+ g' E_P^{\mathrm{in}}}{\mu^+}\cos\theta_P^{\mathrm{in}} & -ik_S^+E_S^{\mathrm{in}}\sin 2\theta_S^{\mathrm{in}}-\dfrac{\rho_+ g' E_S^{\mathrm{in}}}{\mu^+}\sin\theta_S^{\mathrm{in}} & 0 & 0 & 0 & 0 \\ 0 & 0 & 0 & 0 & 0 & 0 \\ 0 & 0 & 0 & 0 & 0 & 0 \\ 0 & 0 & 0 & 0 & 0 & 0 \end{bmatrix},$$

$$E_{P,S}^{\mathrm{in}}=e^{-ik_{P,S}^+h\cos\theta_{P,S}^{\mathrm{in}}},\quad F_P^{\mathrm{in}}=\frac{\cos^2\theta_P^{\mathrm{in}}-\nu^+\cos 2\theta_P^{\mathrm{in}}}{1/2-\nu^+}.$$

The respective results of the magnitude evaluation are presented in Figs. 1, 2(a), (c), and 3(a) for the compressible fluid, and in Figs. 4, 5(a), (c) for the incompressible one.

[1] M. A. Leontovich, "On approximate boundary conditions for electromagnetic field on a surface of well conducing bodies," Investigations of Radio-Wave Propagation, part 2, 5–12, USSR Acad. Sci. (1948) (in Russian).

[2] T. B. A. Senior and J. L. Volakis, *Approximate Boundary Conditions in electromagnetics*, IEEE Electromagnetic Wave Series, **41** (Institute of Electrical Engineers, London, 1995).

[3] H. Ammary and J. D. Nedelec, "Generalized impedance boundary conditions for the Maxwell equations and singular perturbation problems," Commun. Partial Differ. Equ. **24**, 821–849 (1999).

[4] I. M. Kagalova, "The impedance boundary conditions and effective surface impedance of inhomogeneous metals," Physica B **338**, 38–43 (2003).

[5] A. L. Goldenweiser, "The general theory of elastic bodies (shells, coatings, and linings)," Mech. Solids **3**, 3–17 (1992) (in Russian).

[6] L. A. Agalovyan and R. C. Gevorkyan, "On the asymptotic solution of mixed 3D problem for double layer anisotropic plate," J. Appl. Math. Mech. **50**, 202–208 (1986).

[7] S. I. Rokhlin and D. Marom, "Study of adhesive bonds using low-frequency obliquely ultrasonic waves," J. Acoust. Soc. Am. **80**, 585–590 (1986).

[8] S. I. Rokhlin and W. Huang, "Ultrasonic wave interaction with a thin anisotropic layer between two anisotropic solids. II. Second order asymptotic boundary conditions," J. Acoust. Soc. Am. **94**, 3405–3420 (1993).

[9] A. J. Niklasson, S. K. Datta, and M. L. Dunn, "On ultrasonic guided waves in a thin anisotropic layer lying between two isotropic layers," J. Acoust. Soc. Am. **108**, 2005–2011 (2000).

[10] J. V. Wehausen and E. V. Laitone, "Surface Waves," in *Handbuch der Physik*, edited by S. Flugge (Springer, Berlin, 1960), Vol. 9, pp. 446–778.

[11] M. C. M. Bakker and M. D. Verwij, "Experimental validation of two elastodynamic models for the wave field generated by ultrasonic transducers," J. Acoust. Soc. Am. **113**, 1850–1862 (2003).

The attenuation of the higher-order cross-section modes in a duct with a thin porous layer

Yean Yin and Kirill V. Horoshenkov[a)]
School of Engineering, Design and Technology, University of Bradford, West Yorks, BD7 1DP United Kingdom

(Received 24 December 2003; revised 20 September 2004; accepted 30 September 2004)

A numerical method for sound propagation of higher-order cross-sectional modes in a duct of arbitrary cross-section and boundary conditions with nonzero, complex acoustic admittance has been considered. This method assumes that the cross-section of the duct is uniform and that the duct is of a considerable length so that the longitudinal modes can be neglected. The problem is reduced to a two-dimensional (2D) finite element (FE) solution, from which a set of cross-sectional eigen-values and eigen-functions are determined. This result is used to obtain the modal frequencies, velocities and the attenuation coefficients. The 2D FE solution is then extended to three-dimensional via the normal mode decomposition technique. The numerical solution is validated against experimental data for sound propagation in a pipe with inner walls partially covered by coarse sand or granulated rubber. The values of the eigen-frequencies calculated from the proposed numerical model are validated against those predicted by the standard analytical solution for both a circular and rectangular pipe with rigid walls. It is shown that the considered numerical method is useful for predicting the sound pressure distribution, attenuation, and eigen-frequencies in a duct with acoustically nonrigid boundary conditions. The purpose of this work is to pave the way for the development of an efficient inverse problem solution for the remote characterization of the acoustic boundary conditions in natural and artificial waveguides.
[DOI: 10.1121/1.1823211]

PACS numbers: 43.20.Hq, 43.20.Mv [MO] Pages: 528–535

I. INTRODUCTION

The accurate prediction and modeling of individual acoustic modes in ducts is important for many applications such as noise propagation, underwater acoustics, and condition monitoring. Unfortunately, except for a few simple cases such as rectangular and circular ducts with rigid or pressure release boundaries, there are no analytical solutions to this problem. Even for rectangular and circular ducts with nonrigid boundary conditions the analytical solutions become impractical. The finite element method (FEM) and boundary element method (BEM) are alternative techniques for solving such problems. However, practical implementation of FEM and BEM in three dimensions above the frequency of the ring mode is computationally demanding and mathematically complicated because of the overwhelming amount of data related to the required degrees of freedom and the boundary condition. The purpose of this work is to validate a combined two-dimensional (2D)-to-three-dimensional (3D) solution in which a simply implemented 2D finite element acoustic model is linked to a 3D normal mode decomposition technique.

The idea of using the FEM to predict sound propagation is not new. Gladwell introduced FEM for acoustics as early as 1965.[1,2] In the 70's Graggs and Kagawa *et al.* applied a 2D FEM to model damped axis-symmetric problems and showed in that a good agreement between numerical and experimental results could be obtained.[3,4] Successful applications of FEM to the modeling of duct noise propagation in the presence and absence of flow have been reported by Astley, Eversman, and Cummings.[5–8]

Although these and other more recent works (e.g., Kirby)[9] demonstrated that the method can successfully predict the sound field in a duct with an arbitrary cross-section and boundary conditions, the application of this method has been largely limited to evanescent and low-order modes. The purpose of this work is to investigate the attenuation of the higher-order modes and the accuracy of the method with a view that this information can be used for the remote characterization of the boundary conditions of a duct.

This paper presents a combined solution similar to that proposed recently by Kirby[9] which is used to predict the eigen-functions and attenuation of higher-order modes in a duct lined with loose porous sediment. The amplitude of the cross-sectional modes in the duct is modeled by FEM and the numerical result is then used in the normal model decomposition method to extend the solution into the 3D space. In addition to more complex methods proposed by Astley and Cummings[7] and Kirby[9] we show that the boundary conditions in the duct can be predicted by a simple impedance model if the porous layer is relatively thin. In this way the FEM formulation does not require the discretization of the sediment domain, which improves considerably the efficiency of the method. We argue that in the case of higher-order modes the accurate determination of the modal wavenumbers in the porous layer is a rather difficult task and that the result can be extremely sensitive to the parameters of the

[a)]Author to whom correspondence should be addressed; electronic address: k.horoshenkov@bradford.ac.uk

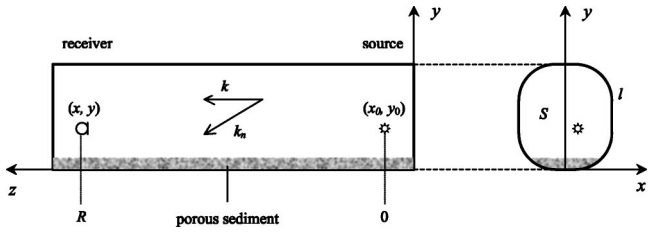

FIG. 1. Geometry of the problem of sound propagation in a duct.

layer and its geometry. A simple and practical FEM solution is essential for the development of efficient inverse problem solvers which enable to predict the properties of the porous lining from the acoustic attenuation data. This is the topic of the follow-up publication by the authors.

The work also presents a comparison of modal frequencies predicted by the FEM and by theory. It is shown that the assumption for the locally reacting admittance is valid for the considered types of the porous sediment. The predicted values of the attenuation coefficients are compared favorably with experimental data. An efficient method for measuring the attenuation in the duct is proposed and discussed.

II. BASIC THEORY OF SOUND PROPAGATION IN DUCT

The duct considered here has arbitrary shape and uniform cross-section along it length as shown in Fig. 1. It is sufficiently long so that the longitudinal modes can be neglected. The thickness of the duct wall is assumed to be sufficiently thick so that the energy transmitted through the wall can be neglected. A section of the inner wall of the duct is coated with acoustically absorbing material of which the surface acoustic admittance is defined as β. According to classical modal analysis, the total sound pressure, P, in the duct is a superposition of an infinite number of individual modes[10]

$$P(x,y,z,t)=\sum_n A_n p_n(x,y)e^{ik_n z-i\omega t}, \tag{1}$$

where $A_n=p_n(x_0,y_0)$ is the modal excitation coefficient, $p_n(x,y)$ is the acoustic pressure, and k_n are the modal wavenumber for the n-th mode propagating in the direction z (see Fig. 1), ω is angular frequency, and t is the time. The axis z runs parallel to the axis of symmetry of the duct (see Fig. 1). The acoustic pressure in every mode, p_n, satisfies the Helmholtz wave equation

$$\nabla^2 p_n(\mathbf{r})+\chi_n^2 p_n(\mathbf{r})=0, \quad \mathbf{r}\in S, \tag{2}$$

where $\mathbf{r}=(x,y)$, S is a 2D region denoting the cross-sectional area of the duct. The relation between the modal wavenumbers in Eqs. (1) and (2) are defined as follows:

$$k_n=\sqrt{k^2-\chi_n^2}, \tag{3}$$

where χ_n is the eigen-value of n-th mode, defined in x-y plane and $k=\omega/c$ is the wavenumber in air.

Along with Eq. (2) we demand that the boundary conditions for the acoustic pressure in the duct, $p(\mathbf{r_s})$, should be satisfied everywhere on the wall,[10] i.e.:

$$\frac{\partial p(\mathbf{r_s})}{\partial \mathbf{n}}=jk\beta(\mathbf{r_s})p(\mathbf{r_s}), \quad \mathbf{r_s}\in l, \tag{4}$$

where l is the line defining the cross-section S, $l\in S$ and $\beta(\mathbf{r_s})$ is the coordinate-dependent admittance on the inner surface of the duct, and the normal $\mathbf{n}$ is directed into the wall of the duct.

III. FINITE ELEMENT ANALYSIS

We apply a finite element formulation to obtain the numerical solution of Eq. (2) in the cross-sectional area of the duct, S. In this case, Eq. (2) becomes

$$\nabla^2 p(x,y)+k^2 p(x,y)=0 \tag{5}$$

with boundary conditions defined by Eq. (4).

In the finite element formulation, the cross-sectional area of the duct, S, is divided into M small elements and there are V nodes in the discretised domain. Therefore, the solution for the sound pressure in S can be approximated by[11]

$$p\approx\tilde{p}=\sum_{i=1}^{V} N_i p_i, \tag{6}$$

where N_i is the interpolated shape function and p_i is the acoustic pressure at i-th node. We denote the weight-function as W_j, $(j=1,2,...V)$ and apply it to Eq. (5) so that it can be expressed in following integral form:[11]

$$\int\int_S W_j(\nabla^2\tilde{p}+k^2\tilde{p})ds=0. \tag{7}$$

Expanding the equation earlier yields

$$\int\int_S W_j\nabla^2\tilde{p}ds+\int\int_S W_j k^2\tilde{p}ds=0. \tag{8}$$

Using the integration by parts rule, the first part of Eq. (8) can be expressed as

$$\int\int_S W_j\nabla^2\tilde{p}ds=\int\int_S W_j\nabla\cdot(\nabla\tilde{p})ds = \oint_l W_j\nabla\tilde{p}dl-\int\int_S \nabla\tilde{p}\nabla W_j ds, \tag{9}$$

where $\cdot$ denotes the vector product.

It is common to assume that

$$\nabla\tilde{p}=\frac{\partial\tilde{p}}{\partial\mathbf{n}}\approx\frac{\partial p}{\partial\mathbf{n}} \tag{10}$$

so the final form of the Eq. (8) is given by

$$\int\int_S \nabla W_j \cdot (\nabla \tilde{p}) ds + \oint_l W_j \nabla \tilde{p} dl + \int\int_S k^2 W_j \tilde{p} ds$$
$$= -\int\int_S \nabla W_j \cdot (\nabla \tilde{p}) dx dy + \oint_l W_j \left(\frac{\partial \tilde{p}}{\partial \mathbf{n}} \right) dl$$
$$+ \int\int_S k^2 W_j \tilde{p} dx dy. \quad (11)$$

Substituting boundary condition (4) into Eq. (11) yields

$$-\int\int_S \nabla W_j \cdot (\nabla \tilde{p}) dx dy + \oint_l W_j jk\beta \tilde{p} dl$$
$$+ \int\int_S k^2 W_j \tilde{p} dx dy = 0. \quad (12)$$

By using the Galerkin method,[11] where it is proposed that $W_j = N_j$ $(j = 1,2...V)$ Eq. (12) can be expanded in its discrete form to

$$\sum_{i=1}^{V} \left(-\int\int_S \nabla N_j \cdot (\nabla N_i) dx dy p_i + \oint_l N_i jk\beta_{ij} N_j dl p_i \right.$$
$$\left. + \int\int_S k^2 N_i N_j dx dy p_i \right) = 0. \quad (13)$$

Finally, in the matrix form, this can be written as

$$[K]p + jk[D]p + k^2[M]p = 0, \quad (14)$$

where

$$[K] = -\int\int_S \nabla N_i \cdot \nabla N_j dx dy, \quad [D] = \oint_l N_i N_j \beta_{ij} dl,$$
$$[M] = \int\int_S N_i N_j dx dy \quad (i,j = 1,2,....V).$$

Matrices K, D, and M are usually called stiffness, damping, and mass matrices, respectively. By considering the relation between p, χ_n, and k,[11] Eq. (14) can also be written in its differential form

$$[K]p + [D]\dot{p} + [M]\ddot{p} = 0, \quad (15)$$

where $\dot{p}$ and $\ddot{p}$ represent first and second order spatial derivatives of p, respectively.

The form of Eq. (14) is a typical quadratic eigen-equation. There are numerous papers presenting the solutions for it (e.g., see a rigorous summary of these methods in Ref. 12). The simplest way is to transform Eq. (14) into a linear eigen-value equation as following. Let $jk = \chi$, then Eq. (14) can be rewritten as the following:

$$[K]p + \chi[D]p - \chi^2[M]p = 0 \quad (16)$$

The earlier equation can be transformed if multiplied by the inversion matrix $[M]^{-1}$, i.e.:

$$\{-\chi^2 I + [K][M]^{-1} + \chi[D][M]^{-1}\}p = 0, \quad (17)$$

which also can be expressed further in the form of

$$\begin{bmatrix} \chi p \\ \chi^2 p \end{bmatrix} = \begin{bmatrix} 0 & I \\ [K][M]^{-1} & [D][M]^{-1} \end{bmatrix} \begin{bmatrix} p \\ \chi p \end{bmatrix}. \quad (18)$$

Rearranging the terms in Eq. (18) yields

$$\begin{bmatrix} 0 & I \\ [K][M]^{-1} & [D][M]^{-1} \end{bmatrix} \begin{bmatrix} p \\ \chi p \end{bmatrix} - \chi \begin{bmatrix} p \\ \chi p \end{bmatrix} = 0, \quad (19)$$

which can be presented in a more convenient form

$$\left\{ \begin{bmatrix} 0 & I \\ [K][M]^{-1} & [D][M]^{-1} \end{bmatrix} - \chi I \right\} \begin{bmatrix} p \\ \chi p \end{bmatrix} = 0, \quad (20)$$

where I is the unit matrix.

Equation (20) is a standard eigen-value problem, which can be solved by standard methods such as QZ algorithm (see page 267 in Ref. 12). The solution of Eq. (20) consists of two parts. The first part is the eigen-vectors $p_i (i = 1,2,...V)$ which determine the pressure distributions of individual modes (eigen-functions $p_n(x,y)$) and the other part is the eigen-values χ_i which are linked to the modal wavenumbers χ_n used in Eq. (3). Based on the eigen-values χ_i, the modal frequencies, phase velocities, and attenuation coefficients can be obtained.

The authors propose to use a linear form of the interpolation function, N_i, in Exp. (6) and three-node triangular elements in the FE mesh. In order to control the accuracy of calculations the often used $<\lambda/10$ element size for the maximum length of a side of the triangular elements is adopted to generate the FE mesh.

IV. COMPARISONS OF THE MODAL FREQUENCIES CALCULATED BY ANALYTICAL RESULTS AND BY FEM

An analytical solution for sound propagation in a duct can be obtained only in the case of a regular duct with rectangular or circular cross-section and first- or second-order boundary conditions (rigid or pressure release). Here, we provide a comparison between the values of the eigen-frequencies obtained from the analytical solution[10] and from the proposed FEM method described in Sec. III.

A. Rectangular duct

First, we consider a regular rectangular duct with rigid wall and a cross-section 1.0 m wide and 0.6 m high. The analytical expression for the modal wavenumbers of the rectangular duct is given by[10]

$$k_{n_x,n_y} = \pi \sqrt{\left(\frac{n_x}{L_x}\right)^2 + \left(\frac{n_y}{L_y}\right)^2} \quad n_x, n_y = 0,1,2,..., \quad (21)$$

where L_x is the width of the duct and L_y is its height.

The numerical solution obtained from the FEM formulation Eq. (20) has been compared with the analytical result from Eq. (21). The FEM mesh which was used had 480 nodes and 874 elements to ensure sufficient spatial resolution

TABLE I. Eigen-frequencies corresponding to the first four cross-sectional modes for sound propagation in a rectangular duct.

n_x	n_y	Analytical solution (Hz)	Numerical solution by FEM (Hz)	Relative error (%)
1	0	171.50	171.63	0.076
0	1	285.83	286.16	0.113
1	1	333.34	334.26	0.277
2	0	343.00	344.07	0.310

throughout the considered frequency range. The interpolated function was chosen to be linear for ease of handling.

The results of the comparison are summarized in Table I which lists the values of the eigen-frequencies, predicted by the analytical and numerical solutions. The results agree well with a maximum error of 0.31% on the case of the (2,0) mode.

B. Circular duct

We consider a circular duct with internal diameter of 75 mm. The first four higher-order-modes which propagate in the duct are: (1,0), (2,0), (0,1), and (1,1). The frequencies of these modes are obtained from the following analytical expression:

$$f_{n_1,n_2} = \frac{\alpha_{n_1,n_2} c}{d}, \tag{22}$$

where $\alpha_{n_1 n_2}$ are the analytically predicted eigen-numbers, which are tabulated on page 511 of Ref. 10, c is the sound speed and d is the inner diameter of the pipe.

The results of the comparison between the eigen-frequencies predicted by the FEM and those predicted from the analytical solution are listed in Table II. The FEM mesh has a total of 320 nodes and 630 triangular elements and the FEM algorithm employs a linear interpolated function. The results suggest that the accuracy of the numerically predicted eigen-frequencies is better then 2% for the four, lowest eigen-modes considered in the analysis.

Obviously, triangular elements in the FEM mesh cannot perfectly reproduce a boundary with finite curvature, e.g., circular boundary shape. However, if the number of the triangular elements, M, is large, then the discretization error is likely to be small. The number of elements which the authors adopted for their work guarantees that the relative discretization error is less then 5×10^{-4}.

TABLE II. Eigen-frequencies corresponding to the first four cross-sectional modes for sound propagation in a circular duct.

(n_1-n_2)th mode	Frequency (Hz) (theory)	Frequency (Hz) (FEM)	Relative error (%)
(1,0)	$2.655e+3$	$2.669e+3$	0.53
(2,0)	$4.401e+3$	$4.458e+3$	1.3
(0,1)	$5.527e+3$	$5.584e+3$	1.03
(1,1)	$6.061e+3$	$6.176e+3$	1.9

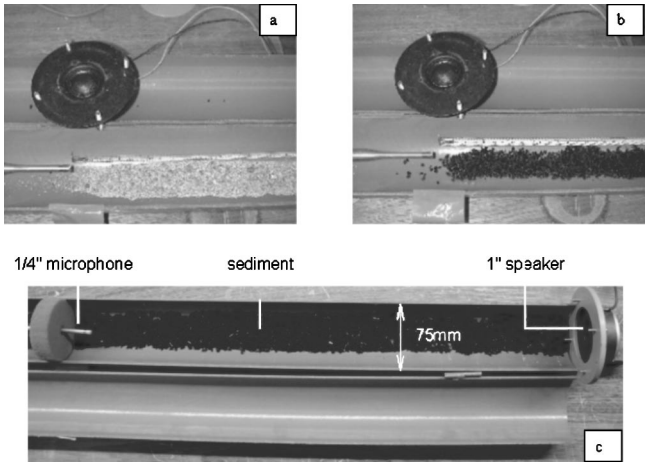

FIG. 2. The method of deposition of (a) angular sand and (b) granulated rubber, in a 75 mm pipe. The relative positions of a 1 in. loudspeaker and 1/4 in. microphone are also shown in part (c) of this figure.

V. EXPERIMENTAL METHOD AND DATA PROCESSING

A 1.5 m section of a uPVC pipe with the internal diameter of 75 mm and external diameter of 81 mm was selected for the experiment (see Fig. 2). It was assumed that the thickness of the pipe was sufficiently large and the density of plastic sufficiently high to neglect acoustic coupling between the airborne sound in the pipe and the mechanical vibration in the walls in the considered frequency range of 1000–40 000 Hz. The pipe was bisected to allow easy deposition of a controlled amount of sediment. The two halves of the pipe were then held together with adhesive tape.

One end of the pipe was terminated with a 25 mm dome tweeter which was installed in a 100 mm acoustically rigid baffle (see Fig. 2(c)). The surface area ratio of the soft tweeter dome to rigid baffle was 11%. A 1/4 in. B&K microphone was installed at the other end of the pipe in a ring of stiff, high-porosity foam (see Fig. 2(c)). In this configuration and with the pipe empty the short sound pulses emitted by the speaker propagated with a relatively low acoustic attenuation which was close to that predicted by the ISO 9613-1.

Both the source and the receiver were aligned in the middle of the pipe section. The distance between the source and receiver was 1.5 m, which was sufficient to observe the geometrical dispersion of several individual modes. A maximum-length sequence data acquisition and signal processing system (MLSSA) was used in the experiments.[13]

Two different porous materials are considered: granulated rubber and angular sand. These materials were spread continuously between the source and the receiver as shown in Fig. 2. The width of the layer was between 40 and 50 mm.

The admittances of two materials have been measured in experiments using the Bruel and Kjaer two microphone impedance measurement tube (type 4206) and dual channel signal analyzer (type 2032). Figure 3 shows the measured and predicted values of the admittance for (a) a 5 mm hard-backed layer of sand and (b) a 4 mm hard-backed layer of granulated rubber. These results were used in the FEM computation. As the frequency range for the measured admittance is 10 Hz–6.3 kHz, it is not possible to use the mea-

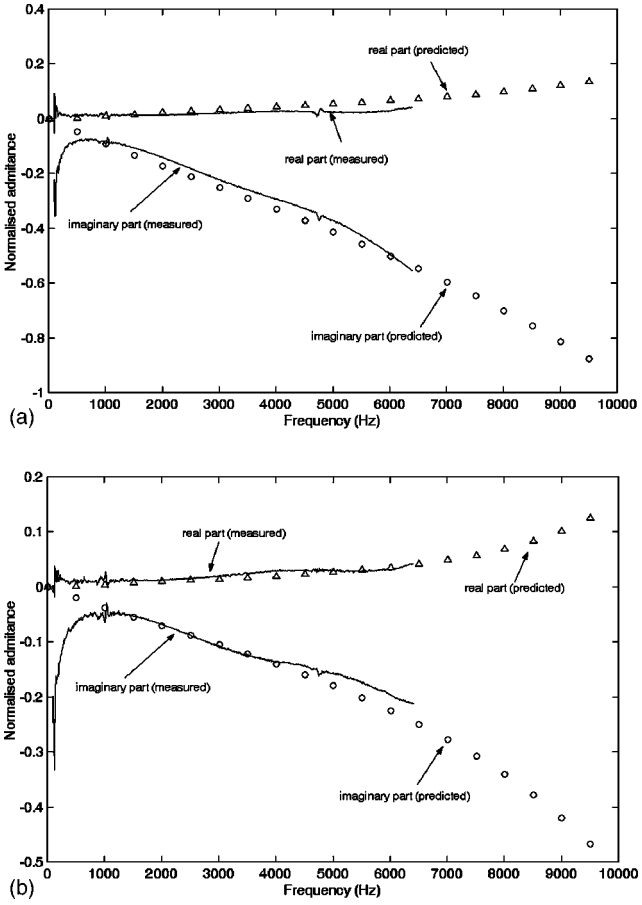

FIG. 3. The measured and predicted values of surface admittance for (a) granulated rubber and (b) angular sand.

sured data beyond the 6.3 kHz range. An alternative method was used to determine the admittance in the high frequency region, based on the model proposed by Horoshenkov *et al.*[14] Table III shows the physical parameters deduced from the measured data, which enable the high frequency admittance to be extrapolated.

The relative sound pressure level (SPL) was measured as a function of the time. These data were filtered using a sixth order Butterworth passband filter. A fast Fourier transform was then applied to obtain the refined structure of the sound pressure spectrum around the selected mode and to determine the modal attenuation.

As the microphone is situated at the center of the cross-section of the duct, only the $(0,j)$th ($j=1,2,3...$) modes have strong sound pressure levels while the amplitude of the other modes is close to zero.[10] Figures 4(a)–(c) show the SPL spectra for the empty pipe and for the pipe with layers of granulated rubber and coarse sand, respectively. The brighter areas on the graphs correspond to the greater sound pressure levels. The horizontal axis corresponds to the propagation distance, $D=ct$, and the vertical axis corresponds to the frequency of the sound.

TABLE III. Nonacoustical parameters of the two porous materials used in the experiment.

Material	Flow resistivity (R) kPa s m^{-2}	Porosity (Ω)	Tortuosity (q)	Standard deviation (σ)	Thickness (d) mm
Sand	43.0	0.35	1.2	0.1	5.0
Granulated rubber	9.8	0.40	1.2	0.1	4.0

The data indicate that there are several clearly visible propagating modes in the acoustic spectrum for which the attenuation is relatively low. The frequencies of these components can be predicted from the boundary conditions and geometry of the pipe (e.g., Ref. 10). The predicted frequencies for the two obvious modes, (0,1) and (0,2), closely agree with those determined from the experiment (see Table II). The reflections from the ends of the pipe are clearly visible in the form of vertical periodical lines (see Fig. 4(a)). Similar reflections will occur if there are lateral connections in the pipe or if the cross-section of the pipe varies suddenly along its length.

Figure 4(b) shows the spectral variation of the acoustic response of the pipe with a layer of rubber. The effect of the rubber layer is clearly observed throughout the considered frequency range. There is a noticeable decrease in the energy of the (0,1) mode and a very pronounced reduction in the case of the (0,2) mode as well as the other higher-order modes, which results from the acoustic absorption in the porous layer and its surface roughness. At shorter distances there is a considerable reduction in the sound pressure level at certain frequencies (e.g., 13.3, 14.4, 15.0, 16.0, and 17.4 kHz in Fig. 4(b)) at early times of arrival. These frequencies where the pressure minima tend to occur are different from the case of the empty pipe and their values are determined by the geometry of the pipe and the admittance of the porous layer. Similar effects can be observed in Fig. 4(c) which shows the spectral variation of the sound pressure level for propagation in the pipe with a layer of coarse sand. These effects are distinguishable from those for rubber, particularly in the case of the (0,2) mode.

VI. COMPARISONS OF RESULTS FOR ATTENUATION COEFICIENTS

When the boundary is rigid, the eigen-values which correspond to the propagating modes are real which means that there is no absorption by the wall of the duct. If the boundary is not rigid, then the eigen-values become complex, and their imaginary part accounts for sound attenuation in the duct due to the finite wall impedance. The relation between the 2D and 3D wavenumbers is defined[10]

$$k_n \equiv \mathrm{Re}[\lambda_n] + i\,\mathrm{Im}[\lambda_n] = \sqrt{\left(\frac{\omega}{c}\right)^2 - \chi_n^2}, \tag{23}$$

where k_n has the same meanings as shown in Eqs. (1) and (3), $2\pi/\lambda_n$ is the complex modal wavelength and $\mathrm{Im}[\lambda_n]$ is the attenuation coefficient for the specified n-th mode, which means that the pressure amplitude attenuates by a factor of e^{-1} in a distance $1/\mathrm{Im}[\lambda_n]$.

The most useful result of the numerical modeling is the attenuation coefficient, from which it is possible to determine the rate of the sound energy dissipation in the pipe. The attenuation coefficient for every individual mode is a constant provided that the admittance is independent of the co-

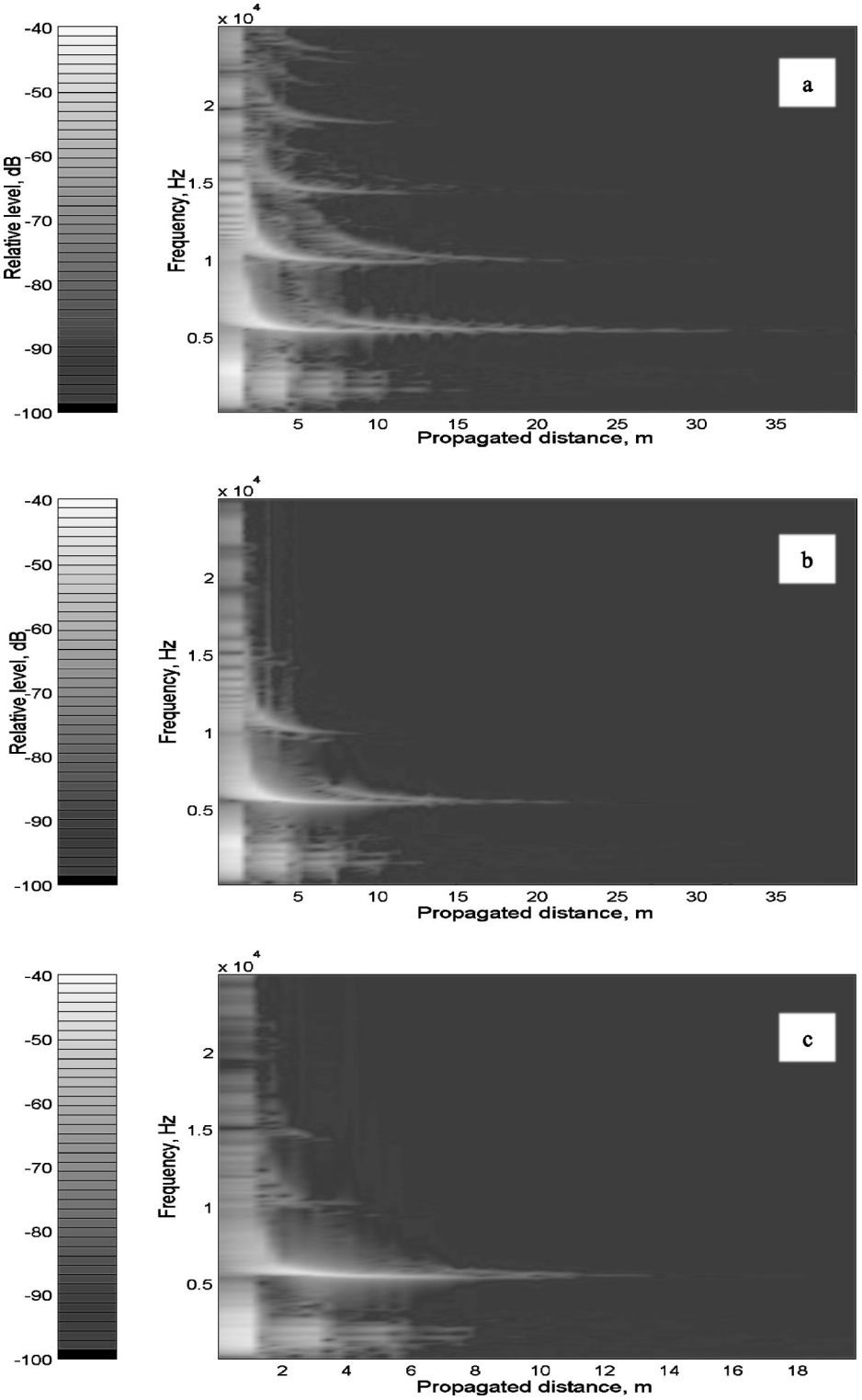

FIG. 4. The spectrograms for the relative sound pressure level for (a) the empty duct and for the duct filled with (b) a layer of granulated rubber and (c) a layer of angular sand.

coordinate z. In this case, the pressure amplitude attenuates exponentially as the normal mode wave propagates along the duct. If the decibel scale is adopted, then the dependence of the relative sound pressure as a function of distance will become linear.

Figures 5(a) and 5(b) show the relative SPL for two selected modes (0,1) and (0,2), respectively. The levels are plotted as a function of the propagation distance for the empty pipe and for the pipe with layers of sand and rubber. These results were obtained by filtering the measured time response of the pipe within a spectral window which included the fundamental frequency of the mode. The width of the spectral window was set to 5.0–6.0 kHz for mode (0,1) and 9.5–10.5 kHz for mode (0,2). The relative sound pressure level was calculated using an averaging time of 4.5 ms. This value corresponds to a spatial interval of 1.5 m, which is close to the length of the pipe. The measured value of the attenuation was deduced from the filtered data using the standard regression analysis. The modal attenuation coefficients deduced for the empty pipe account for the energy dissipa-

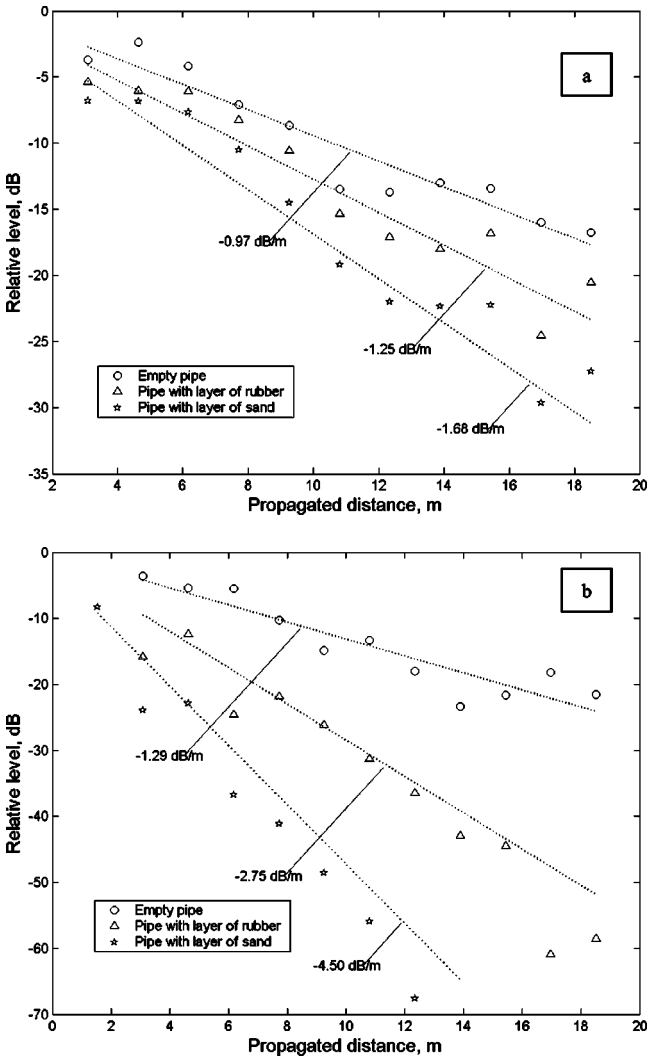

FIG. 5. The relative sound pressure level measured and predicted by FEM, (a) for the (0,1) mode and (b) for the (0,2) mode.

tion at the ends of the pipe and for the finite values of the pipe wall impedance. These values were used to calibrate the finite element model so that the above effects could be accounted for heuristically.

Figure 5(a) show the relative sound pressure levels and the predicted values of the acoustic attenuation for the (0,1) mode in the case of the empty pipe and the pipe with layers of granulated rubber and coarse sand. The straight solid lines are the numerical results calculated by the FEM and the measured data are illustrated by the points. The values of the nonacoustic parameters used for the prediction are listed in Table III. The predicted and measured values of the attenuation coefficients are summarized in Table IV. Similarly, the measured sound pressure levels and predicted attenuation data for mode (0,2) are presented in Fig. 5(b).

The results suggest that the attenuation of individual cross-sectional modes is affected by the presence of even a tiny amount of porous sediment. In the cases reported here the amount of porous sediment introduced did not exceed 1.5% of the cross-sectional area of the pipe. In the case of the (0,1) mode the increase in attenuation due to the presence of a 4.0 mm layer of granulated rubber is 0.25 dB/m. In the case of coarse sand the attenuation of this mode increases further to 0.61 dB/m (see Table IV and Fig. 5(a)). These variations are easily detectable using modern methods of data acquisition and signal processing, e.g., the proposed MLS method.

TABLE IV. The predicted and deduced values of the attenuation coefficient (dB/m).

		Experiment		Numerical result	
Mode	Empty	Rubber	Sand	Rubber	Sand
(0−1)	−0.97	−1.23	−1.58	−1.25	−1.68
(0−2)	−1.29	−3.06	−5.19	−2.75	−4.50

The change in the attenuation of the (0,2) mode due to the presence of the porous layer is more pronounced. In the case of a 4.0 mm layer of rubber the increase in the attenuation coefficient is 1.77 dB/m. The deposition of a 5.0 mm layer of sand results in a 3.90 dB/m increase in the attenuation coefficient in comparison with that for an empty pipe.

The values of the attenuation coefficient predicted by the FEM agree closely with those deduced from the measured data. In the case of the (0,1) mode the maximum discrepancy is approximately 6%. In the case of the (0,2) mode this discrepancy is within 15%.

VII. PRESSURE DISTRIBUTION PATTERNS OF INDIVIDUAL MODES

The wave associated with each mode is characterized by its cross-sectional pressure distribution as it travels along the duct. The cross-sectional pressure distribution, $p_{n_1 n_2}(x,y)$ is predicted by the eigen-vectors which are the solutions of Eq. (20). The information about the modal energy distribution provides the basis for the selection of optimal receiver and source positions which can be used to improve the temporal and spatial resolution of individual modes in the pipe.

Figures 6(a) and 6(b) present the sound pressure contours for the first four cross-sectional modes in the case of the empty pipe and in the case of the pipe with a 3.0 mm layer of granulated rubber. In the top row, the contours for the (1,0) and (2,0) modes are presented. In the bottom row, the modes are (0,1) and (0,3). If the boundary is rigid, then the modal shapes are axi-symmetric. The porous layer (shown by black solid lines in the graphs) in the pipe results in the redistribution of the acoustic energy so that the symmetry may no longer be valid (see Fig. 6(b)). There appear to be distinctive changes in the modal patterns, which are particularly pronounced in the case of (2,0) mode (near the bottom of the pipe) and the (0,1) mode around 2/3 of the pipe radius (see Fig. 6(b)). If the porous layer is uniformly laid on the bottom of the pipe, then the resultant modal pattern changes from axisymmetric to being symmetrical about a vertical axis. This result can be exploited if an array of receivers is used in the experiment or if the position of the receiver is carefully adjusted to maximise the sensitivity of the acoustic system. The optimal position for the sound and receivers is determined by the maximum value of the modal pressure.

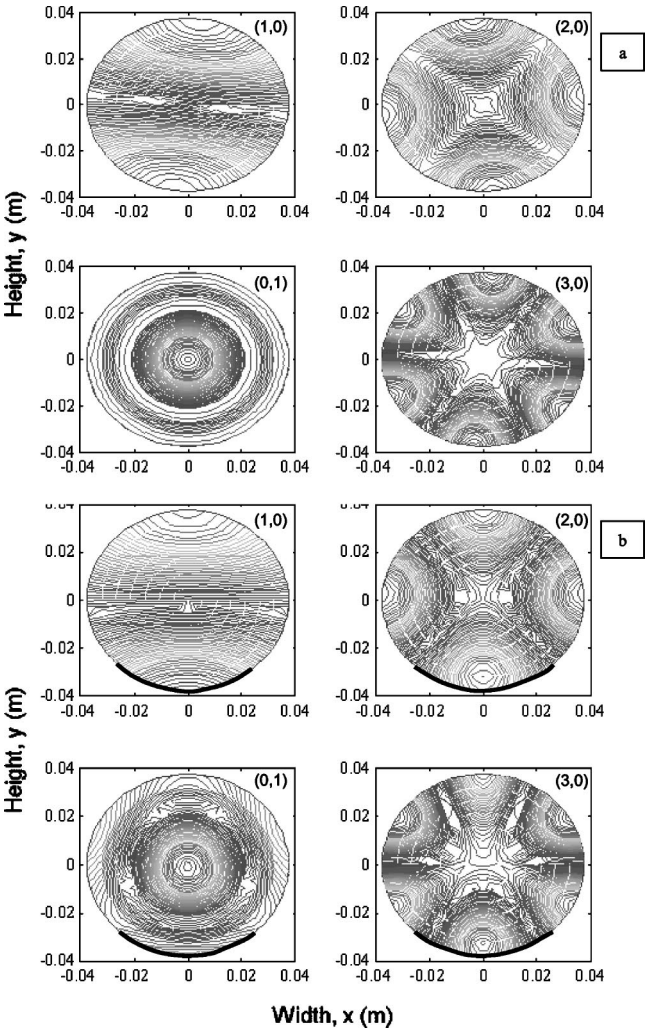

FIG. 6. The acoustic modal pressure patterns predicted by FEM, (a) for the duct with rigid walls and (b) for the duct with a layer of granulated rubber. The numbers in the graphs indicate the indices of the corresponding mode and the thick line shows the extent of the sediment.

VIII. CONCLUSIONS

An efficient numerical model for sound propagation in an arbitrary shaped duct with variable admittance on its inner surface has been validated against experimental data obtained for a 75 mm uPVC circular pipe lined with a small amount of porous sediment. The solution combines a 2D finite element solution and the normal mode decomposition technique. The values of the modal frequencies predicted by the model also agree closely with those predicted by the standard theory for sound propagation in circular ducts. An efficient method of measurement of the modal attenuation in the pipe has also been proposed. The experimental method accounts for the effects of the reflections from the ends of the empty pipe and the finite values of the pipe wall impedance and does not require multiple measurements of sound pressure along the length of the pipe.

The results demonstrate that the modal attenuation in the pipe can be accurately predicted provided the values of the microscopic parameters of porous sediment are known. The increase in the modal attenuation due to the presence of even a small amount of sediment in the pipe is pronounced and measurable. The value of the modal attenuation increases for higher-order modes, which is attributed to the improved coupling between the airborne modes and the porous layer.

The finite element solution is used to illustrate that the modal pressure distribution (i.e., modal excitation coefficient) is noticeably affected by presence of the porous layer. It is suggested that this solution can be a useful tool for the optimization of the sensitivity of the acoustic instrumentation used for the remote characterization of the boundary conditions in ducts and pipes.

ACKNOWLEDGMENTS

The authors would like to acknowledge the financial support of this work provided by the UK's Engineering and Physical Sciences Research Council (EPRSC Grant No. GR/R34752/01). The authors are grateful to Professor David Hothersall for his useful comments.

[1] G. M. L. Gladwell, "A finite element method for acoustics," 1965, *Proc. 5th Int. Cong. Acoust., paper* L.33, 1965.
[2] G. M. L. Gladwell, "A variational formulation of damped acousto-structural vibration problems," J. Sound Vib. **4**, 172–186 (1966).
[3] A. Graggs, "A finite element method for damped acoustic systems: An application to evaluate the performance of reactive mufflers," J. Sound Vib. **48**, 377–392 (1976).
[4] Y. Kagawa, T. Yamabuchi, and A. Mori, "Finite element simulation of an axisymmetric acoustic transmission system with a sound absorbing wall," J. Sound Vib. **53**, 357–374 (1977).
[5] R. J. Astley and W. Eversman, "A finite element method for transmission in non-uniform ducts without flow: Comparison with the method of weighted residuals," J. Sound Vib. **57**, 367–388 (1978).
[6] R. J. Astley and W. Eversman, "A finite element formulation of the eigenvalue problem in lined ducts with flow," J. Sound Vib. **65**, 61–74 (1979).
[7] R. J. Astley and A. Cummings, "A finite element scheme for attenuation in ducts lined with porous material: Comparison with experiment," J. Sound Vib. **116**, 239–263 (1987).
[8] R. J. Astley, A. Cummings, and N. Sormaz, "A finite element scheme for acoustic propagation in flexible-walled ducts with bulk-reacting liners, and comparison with experiment," J. Sound Vib. **150**, 119–138 (1991).
[9] R. Kirby, "Transmission loss prediction for dissipative silences of arbitrary cross-section in the presence of mean flow," J. Acoust. Soc. Am. **114**, 200–209 (2003).
[10] P. M. Morse and K. U. Ingard, *Theoretical Acoustics* (Princeton University Press, Princeton, 1986).
[11] R. D. Cook, D. S. Malkus, and M. E. Plesha, *Concept and Applications of Finite Element Analysis*, 3rd ed. (Wiley, New York, 1989).
[12] F. Tisseur and K. Meerbergen, "The quadratic eigenvalue problem," SIAM Rev. **43**, 235–286 (2001).
[13] D. Rife and J. Vanderkooy, "Transfer-function measurement with maximum-length sequences," J. Audio Eng. Soc. **37**, 419–443 (1989).
[14] K. V. Horoshenkov, K. Attenborough, and S. N. Chandler-Wilde, "Pade approximants for the acoustical properties of rigid frame porous media with pore size distribution," J. Acoust. Soc. Am. **104**, 1198–1209 (1998).

Measurements and empirical model of the acoustic properties of reticulated vitreous carbon

Ralph T. Muehleisen[a)]
Civil and Architectural Engineering, Illinois Institute of Technology, Chicago, Illinois 60616

C. Walter Beamer IV
Civil, Environmental, and Architectural Engineering, University of Colorado, Boulder, Colorado 80309

Brandon D. Tinianov
Quiet Solution, Sunnyvale, California 94085

(Received 7 June 2004; revised 27 November 2004; accepted 30 November 2004)

Reticulated vitreous carbon (RVC) is a highly porous, rigid, open cell carbon foam structure with a high melting point, good chemical inertness, and low bulk thermal conductivity. For the proper design of acoustic devices such as acoustic absorbers and thermoacoustic stacks and regenerators utilizing RVC, the acoustic properties of RVC must be known. From knowledge of the complex characteristic impedance and wave number most other acoustic properties can be computed. In this investigation, the four-microphone transfer matrix measurement method is used to measure the complex characteristic impedance and wave number for 60 to 300 pore-per-inch RVC foams with flow resistivities from 1759 to 10 782 Pa s m^{-2} in the frequency range of 330 Hz–2 kHz. The data are found to be poorly predicted by the fibrous material empirical model developed by Delany and Bazley, the open cell plastic foam empirical model developed by Qunli, or the Johnson–Allard microstructural model. A new empirical power law model is developed and is shown to provide good predictions of the acoustic properties over the frequency range of measurement. Uncertainty estimates for the constants of the model are also computed. © *2005 Acoustical Society of America.*
[DOI: 10.1121/1.1850343]

PACS numbers: 43.20.Hq, 43.55.Ev, 43.20.Ye, 43.58.Bh [RR] Pages: 536–544

I. INTRODUCTION

Porous materials are used in a variety of acoustic applications including sound absorbers for noise and reverberation control and as stacks and regenerators in mechanical and thermoacoustic heat engines and refrigerators. Fibrous porous materials such as fiberglass and mineral wools lack the structural rigidity for many applications. Many open cell plastic foams have limited structural strength and cannot be used in high temperature or harsh chemical environments. Many open cell metal and ceramic foams have good structural strength and rigidity and can be used in harsh environments but lack the very high porosities and low thermal conductivity of fibrous materials and open cell plastic foams. There is a great need for a high porosity material with high strength and rigidity and low thermal conductivity for use as a sound absorber in harsh environments and for use as a regenerator or stack material for high temperature mechanical and thermoacoustic heat engines. One such material is reticulated vitreous carbon[1] (RVC).

RVC is a highly porous, rigid, open-cell foam structure composed of vitreous (amorphous) carbon with properties of high porosity, high strength and rigidity, low bulk thermal conductivity, good electrical conductivity, a high melting point, chemical inertness, and ease of construction. Because it has only recently been considered for acoustical applications, not much is known about acoustical properties of RVC. Wilen[2] and Petculescu[3] measured the viscous and thermal dissipation functions for RVC, and Adeff *et al.*[4] measured the performance of RVC used as a stack in thermoacoustic prime-movers. Muehleisen and Beamer presented additional measurements of the viscous and thermal dissipation functions for RVC.[5] However, to date, no measurements or theoretical models of flow resistivity, characteristic impedance, or wave number of RVC appear to have been published.

In this paper, new experimental measurements of the complex characteristic impedance, $\hat{Z}_c$, and wave number, $\hat{k}_c$, of 60 to 300 pore per inch (PPI) RVC with flow resistivities from 1759 to 10 782 Pa s m^{-2} over a range of frequencies from 330 Hz to 2 kHz are presented. From the measurements, an empirical power law model is developed to characterize $\hat{Z}_c$ and $\hat{k}_c$ as a function of the nondimensional frequency $\rho_0 f/\sigma$, where ρ_0 is the ambient air density and σ is the flow resistivity of the RVC. The data and new model are compared to the empirical model of Delany and Bazley[6] that was developed from measurements of fibrous absorbers, to the empirical model of Qunli[7] that was developed from measurements of open cell plastic foams, and to a popular microstructural model developed by Allard.[8]

II. BACKGROUND

Theoretical prediction of the acoustic properties of porous materials is a difficult task because of the complicated structure of the materials. Zwikker and Kosten[9] and Biot[10,11]

a)Electronic mail: muehleisen@iit.edu

developed the first popular porous media models. A thorough review of these models and further developments through the early 1980s was performed by Attenborough.[12] Subsequently, Attenborough[13] and Champoux and Stinson[14,15] developed modified microstructural models. Lambert[16] developed a model for elastic frame open cell foams by combining aspects of both the Zwikker and the Biot models. Allard[8,17] developed a five parameter model for rigid frame porous media, based on the work of Johnson,[18,19] that works well at low and high frequencies. Wilson[20,21] developed a relaxational model which can be considered a simplification of the microstructural models. Most recently, Horoshenkov[22] and Umnova[23] developed variations of the Allard model that are applicable to granular materials. All of the models require knowledge of the flow resistivity of the material, but the different models require additional knowledge about the microscopic structure of the material or other physical characteristics of the material. Since measurement of characteristics other than flow resistivity can be difficult, the need for additional information makes use of these models difficult to apply for reticulated open cell foams or fibrous materials with a random fiber orientation where that information may not be available or cannot be estimated.

Instead of working out a theory of acoustic propagation in porous media from a study of the microstructural details, one could instead measure the properties and develop empirical models for prediction of similar materials. Delany and Bazley[6] measured the properties of a wide range of fibrous materials and developed an empirical power law model to predict the characteristic impedance and wave number from only a knowledge of flow resistivity. Allard and Champoux[24] developed an empirical model for the dynamic density and bulk modulus (from which the characteristic impedance and wave number can be obtained) in fibrous materials which can be used at lower frequencies than the Delany equations. Qunli[7] and Cummings[25] both measured the properties of open cell plastic foam and developed power laws of the same form as Delany.

In the acoustic characterization of porous media, measurements of the complex characteristic impedance, $\hat{Z}_c$, and wave number, $\hat{k}_c$, are extremely useful because they are necessary quantities for computing propagation through a porous media and can also be used to obtain many other acoustic parameters. Several methods for measuring these acoustic properties have been developed. The one- and two-microphone standing wave tube methods of measuring acoustic properties are well researched and standards for their use have been developed.[26,27] Both methods require either multiple samples of varying thickness or multiple termination impedances of the measurement system to be able to measure both $\hat{Z}_c$ and $\hat{k}_c$. The three-microphone method[28,29] and four-microphone method[30] can determine both $\hat{Z}_c$ and $\hat{k}_c$ from a single sample. In a previous paper,[31] the current authors showed that for a high porosity, low flow resistivity material like RVC, the four-microphone method produces the most accurate measure of the acoustic properties of a single sample.

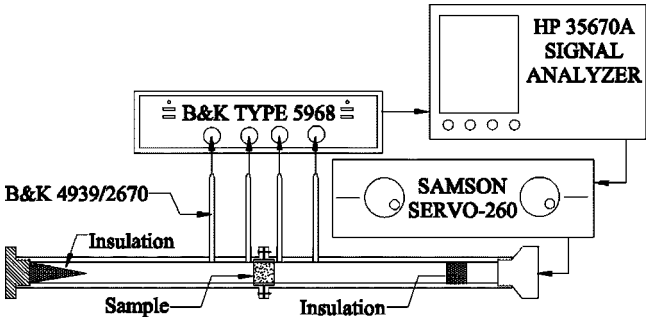

FIG. 1. Schematic diagram of the measurement system for the four-microphone transfer matrix method.

III. EXPERIMENTAL PROCEDURE

A. Instrumentation and setup

The measurements are taken using a four-microphone transfer matrix measurement system as shown in Fig. 1. The wave tube is made up of two sections of aluminum pipe with a 1 in. (25.4 mm) inner diameter and a 1.5 in. (38.1 mm) outer diameter. The two sections are held together with two four-hole collars. The measurement samples are mounted between the collars. The other ends of the tubes have a threaded opening to accept either a rigid termination plug or a standard 1 $\frac{1}{8}$ in. (28.6 mm) compression driver. Two microphone sampling holes are drilled near the locations of the measurement samples. To reduce standing waves, which can lead to increased error in measuring the phase shift between the microphones,[31] an 8 in. (203 mm) long tapered piece of insulation is inserted between the rigid termination and the fourth microphone and a $\frac{1}{2}$ in. (12.7 mm) long piece of insulation is added between the driver and the first microphone.

The local ambient temperature is measured with a type T thermocouple and a HH506R Omega Thermocouple reader. The local ambient pressure at the time of the measurement is obtained from a nearby NOAA weather station.

The tube is excited by a University Sound 1828R Compression Driver driven by a 130 W Samson Servo 260 power amplifier. A Hewlett Packard (HP) 35670A Dynamic Signal Analyzer is used as the signal source and to record the measured data. The four acoustic pressures are measured with four Bruel and Kjaer (B&K) 4939 1/4 in. (6.4 mm) microphones, fitted to B&K 2670 pre-amps powered by a B&K 5968 Acoustic Front End. The microphone signals are sent from the B&K 5968 to the HP 35670A for analysis without further signal conditioning. The HP 35670A computes and records the transfer function between the microphones.

B. Sample preparation

The RVC was supplied by the manufacturer in 6×6×1 in. (152×152×25.4 mm) rectangular sheets. The sheets were identified by the number of pores-per-inch (PPI) with sheets having a PPI of 60, 80, 100, 200, and 300. According to the manufacturer,[1] RVC from 25 to 100 PPI are manufactured individually and all have a porosity of about 97%. The 200 and 300 PPI RVC are manufactured by compressing nominal 100 PPI RVC and have reduced porosities of 94% and 91%, respectively.

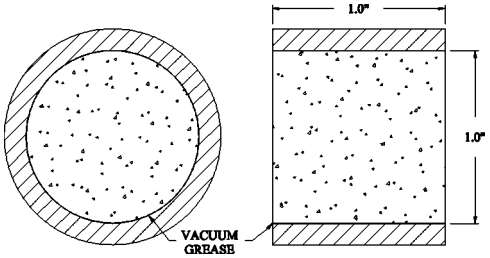

FIG. 2. Plan and section views of the sample.

Two measurement samples of each type are punched out of a 1 in. (25.4 mm) thick sheet of the RVC by a 1-in.-diam punch. The resulting cylinders are then placed in a plastic sleeve for protection as shown in Fig. 2. Before the sample is placed in the sleeve, a thin layer of vacuum grease is applied to the outer edge of the sample. The vacuum grease holds the sample tightly in the sleeve and helps prevent acoustic waves from traveling through the gap between the sample and sleeve, forcing the waves instead to go through the sample. The wave tube has a cylindrical void that will accept a 1 in. (25.4 mm) diameter sample in the plastic sleeve. The remaining RVC was used for flow resistivity measurements and other acoustic experiments.

C. Measurement procedure

To measure the microphone transfer functions, the signal analyzer is used in swept-sine mode and swept from 50 Hz to 2 kHz with 401 points per sweep, a 50 cycle settling time, and a 100 cycle averaging time per frequency. For the tests, the analyzer is set for automatic adjustment of the source level and input range using grounded, ac coupled inputs. During the experiment, the pressure at each microphone location is recorded by the signal analyzer and the transfer functions between them are computed and stored. After one sweep, microphones one and two are exchanged and another measurement is taken. This process is repeated two more times, exchanging microphone one with microphones three and four. Table I shows the microphone positions for each of the four runs. These extra data are used to calibrate the transfer functions using an extension of the microphone switching method described by Chung and Blaser.[32] This measurement procedure was completed on each of the two samples.

The measured transfer function between channels i and j as measured by the HP 35670A, which we will call M_{ij}, consists of the ratio of the pressure measurements, P_i and P_j, multiplied by C_i and C_j, calibration factors related to the microphone, microphone preamplifier, the acoustic front end, and the measurement channel of the analyzer. The relation between M_{ij}, P_i, and C_i for all the measurement runs is shown in Table II. The calibration factors can be eliminated to obtain the desired pressure transfer functions H_{21}, H_{31}, and H_{41}, by combining the measured transfer functions as follows:

$$H_{21}=\frac{P_2}{P_1}=\sqrt[4]{\frac{M_{21a}}{M_{21b}}\times\frac{M_{31a}}{M_{31b}}\times\frac{M_{41a}}{M_{41b}}}, \tag{1}$$

$$H_{31}=\frac{P_3}{P_1}=\sqrt[4]{\frac{M_{31a}}{M_{31c}}\times\frac{M_{21a}}{M_{21c}}\times\frac{M_{41a}}{M_{41c}}}, \tag{2}$$

$$H_{41}=\frac{P_4}{P_1}=\sqrt[4]{\frac{M_{41a}}{M_{41d}}\times\frac{M_{21a}}{M_{21d}}\times\frac{M_{31a}}{M_{31d}}}. \tag{3}$$

The transfer function H_{21} could have been estimated using only the measurements M_{21a} and M_{21b}, however it was found that including the additional measurements in the calibration produced a more repeatable result.

Ambient pressure and temperature are recorded for the measurements of each sample. Because the ambient temperature and pressure are not necessarily identical for the measurements of the two samples, neither the measured transfer functions nor the computed $\hat{Z}_c$ and $\hat{k}_c$ from the two samples can be averaged. Instead, values of $\hat{Z}_c$ normalized by $\rho_0 c_0$ and the values of $\hat{k}_c$ normalized by ω/c_0 computed for each of the two samples are averaged to provide the measured values used in the empirical modeling.

TABLE I. Microphone locations for four measurement runs.

Run	Position 1	Position 2	Position 3	Position 4
A	Mic 1	Mic 2	Mic 3	Mic 4
B	Mic 2	Mic 1	Mic 3	Mic 4
C	Mic 3	Mic 2	Mic 1	Mic 4
D	Mic 4	Mic 2	Mic 3	Mic 1

TABLE II. Output from HP analyzer.

	Analyzer output			
Run	M_{11}	M_{21}	M_{31}	M_{41}
A	$\frac{P_1C_1}{P_1C_1}$	$\frac{P_2C_2}{P_1C_1}$	$\frac{P_3C_3}{P_1C_1}$	$\frac{P_4C_4}{P_1C_1}$
B	$\frac{P_2C_1}{P_2C_1}$	$\frac{P_1C_2}{P_2C_1}$	$\frac{P_3C_3}{P_2C_1}$	$\frac{P_4C_4}{P_2C_1}$
C	$\frac{P_3C_1}{P_3C_1}$	$\frac{P_2C_2}{P_3C_1}$	$\frac{P_1C_3}{P_3C_1}$	$\frac{P_4C_4}{P_3C_1}$
D	$\frac{P_4C_1}{P_4C_1}$	$\frac{P_2C_2}{P_4C_1}$	$\frac{P_3C_3}{P_4C_1}$	$\frac{P_1C_4}{P_4C_1}$

D. Flow resistivity

The flow resistivity, σ, was measured at the Acoustic Labs of the Johns Manville Corporation using the method of ASTM Standard C522-87[33] which has an interlaboratory reproducibility of 3.3%. The measured σ values range from 1759 to 10 782 Pa s m^{-2} as shown in Table IV. Also shown in Table IV is the porosity, ϕ, which is the expected value stated by the manufacturer for each of the sample porosities.

E. Important dimensions and measurement uncertainties

In order to determine uncertainties for the measurement results, the uncertainties in the instruments and the input parameters must be known. Knowledge of the measurement uncertainties will allow an estimation of the uncertainties of

TABLE III. Important dimensions and uncertainties.

Name	Dimension (mm)	Error
Mic spacing 1–2	52.3	±0.5 mm
Mic spacing 2–3	37.6	±0.5 mm
Mic spacing 3–4	52.7	±0.5 mm
Tube radius	12.7	±0.5 mm
Ambient temperature		±0.8 °C
Ambient pressure		±0.1 kPa
Transfer function magnitude		±0.5%
Transfer function phase		±0.5°
Flow resistivity		±3.3%

the constants of the empirical models and are required for accurate curve fitting and testing the goodness-of-fit of the empirical model to the data.

Table III details the important dimensions and uncertainties of the system components and uncertainties of the measurement equipment itself. The uncertainty in the temperature, pressure, and transfer function measurements are obtained from published specifications of the measurement systems. Systematic magnitude and phase errors from the microphone and preamplifiers are removed using the microphone switching calibration discussed earlier and the random uncertainties produced by that instrumentation (i.e., microphone and preamplifier noise) are negligible compared to the random uncertainties of the transfer function measurement and are not included in the analysis.

IV. THEORY

A. Measurement theory

The four-microphone transfer function method can be considered an extension of the two-microphone method, and so the frequency limitations of the two-microphone method[34] are applicable and frequency limitations for measurement based on microphone spacing should be considered. In particular, a measurement system will have significantly increased errors for frequencies outside of the range of $0.1<ks/\pi<0.8$ where $k=\omega/c_0$ is the acoustic wave number and s is the microphone separation. For our experimental setup the useful lower frequency limit is about 330 Hz and hence only our data measured at frequencies above 330 Hz are included in this analysis.

The basic measurement setup for the four-microphone method is shown in Fig. 3. A sample of thickness d is mounted in a tube of diameter a between two pairs of microphones and ensonified. Microphones 1 and 2 are separated by a distance S_{12} and microphone 2 is at a distance l_2 from the front of the sample. Microphones 3 and 4 are separated by a distance S_{34} with microphone 3 at a distance l_3 from the far end of the sample.

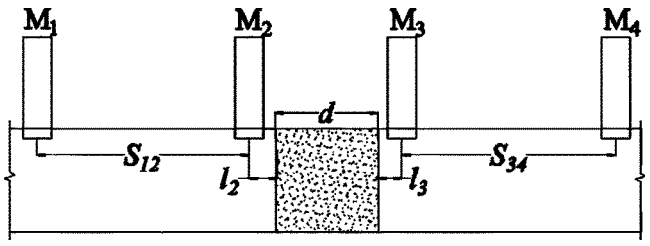

FIG. 3. Four-microphone system diagram.

Using the measured pressure transfer functions $\hat{H}_{12}$, $\hat{H}_{13}$, and $\hat{H}_{14}$ and the acoustic pressure of microphone 1, $\hat{p}_1$, the acoustic pressures at the front and back of the sample, $\hat{p}_0$ and $\hat{p}_d$, and the acoustic velocity at the front and back of the sample, $\hat{u}_0$ and $\hat{u}_d$, are found to be

$$\hat{p}_0=\hat{p}_1\frac{\hat{H}_{21}\sin(\hat{k}_t(S_{12}+l_2))-\sin(\hat{k}_t l_2)}{\sin(\hat{k}_t S_{12})}, \tag{4}$$

$$\hat{p}_d=\hat{p}_1\frac{\hat{H}_{31}\sin(\hat{k}_t(S_{34}+l_3))-\hat{H}_{41}\sin(\hat{k}_t l_3)}{\sin(\hat{k}_t S_{34})}, \tag{5}$$

$$\hat{u}_0=j\hat{p}_1\frac{\hat{H}_{21}\cos(\hat{k}_t(S_{12}+l_2))-\cos(\hat{k}_t l_2)}{\hat{Z}_t\sin(\hat{k}_t S_{12})}, \tag{6}$$

$$\hat{u}_d=j\hat{p}_1\frac{\hat{H}_{41}\cos(\hat{k}_t l_3)-\hat{H}_{31}\cos(\hat{k}_t(S_{34}+l_3))}{\hat{Z}_t\sin(\hat{k}_t S_{34})}, \tag{7}$$

where $\hat{Z}_t$ and $\hat{k}_t$ are the characteristic impedance and wave number of the air in the wave tube including the effects of tube damping and $j=\sqrt{-1}$.

From the acoustic pressure and velocity on the sample faces, the transfer matrix elements, $\hat{T}_{11}$, $\hat{T}_{12}$, and $\hat{T}_{21}$ are computed as[30]

$$\hat{T}_{11}=\frac{\hat{p}_d\hat{u}_d+\hat{p}_0\hat{u}_0}{\hat{p}_d\hat{u}_0+\hat{p}_0\hat{u}_d}, \tag{8}$$

$$\hat{T}_{12}=\frac{\hat{p}_0^2-\hat{p}_d^2}{\hat{p}_d\hat{u}_0+\hat{p}_0\hat{u}_d}, \tag{9}$$

$$\hat{T}_{21}=\frac{\hat{u}_0^2-\hat{u}_d^2}{\hat{p}_d\hat{u}_0+\hat{p}_0\hat{u}_d}. \tag{10}$$

Finally, the complex characteristic impedance $\hat{Z}_c$ and the wave number $\hat{k}_c$ are obtained from the transfer matrix elements using

$$\hat{Z}_c=R_c+jX_c=\sqrt{\frac{\hat{T}_{12}}{\hat{T}_{21}}}, \tag{11}$$

$$\hat{k}_c=\beta_c+j\alpha_c=\frac{1}{d}\cos^{-1}(\hat{T}_{11})=\frac{1}{d}\sin^{-1}(\sqrt{-\hat{T}_{12}\hat{T}_{21}}). \tag{12}$$

B. Uncertainty analysis and data regression

The uncertainty in the computed characteristic impedance and wave number are determined using the following Monte Carlo method. The inputs to the analysis equations are perturbed by a Gaussian distributed random variable with a standard deviation equal to the uncertainty bounds of the given input and the resulting impedance and wave number are computed. This procedure is repeated many times until the mean values and the standard deviations of the computed quantities converged toward a final value. For the measurements described in this paper, the mean and standard deviation converged at about 10 000 iterations. To ensure an accu-

TABLE IV. Static flow resistivity, σ, and porosity, ϕ, of samples.

Sample PPI	σ (Pa s m^{-2})	ϕ (%)
60	1 759± 53	97
80	3 742±111	97
100	3 348±101	97
200	5 964±179	94
300	10 782±323	91

rate result, the analysis was run for 100 000 iterations. While there are a large number of inputs to the computation, the uncertainties in the transfer function measurements are extremely dominant[31] so the required number of iterations for convergence were limited.

The measured characteristic impedances, $\hat{Z}_c$, are normalized by the characteristic impedance of air, $\rho_0 c_0$, and the measured wave numbers, $\hat{k}_c$, are normalized by the wave number of air, ω/c_0. Plotting the normalized data on a log–log graph as a function of normalized frequency, $C=\rho_0 f/\sigma$, shows that the data can be adequately represented by a power law of the same form as developed by Delany and Qunli:

$$\hat{Z}_n=\frac{\hat{Z}_c}{\rho_0 c_0}=R_n+jX_n=1+a_z C^{b_z}+jc_z C^{d_z}, \tag{13}$$

$$\hat{k}_n=\frac{\hat{k}_c c_0}{\omega}=\beta_n+j\alpha_n=1+a_k C^{b_k}+jc_k C^{d_k}. \tag{14}$$

Equations (13) and (14) can be linearized by breaking them into their real and imaginary parts and then taking the natural log of each side of the equation. This linearization is applied, and a weighted linear regression is performed on the following:

$$\ln(R_n-1)=\ln(a_z)+\ln(C)b_z, \tag{15}$$

$$\ln(-X_n)=\ln(c_z)+\ln(C)d_z, \tag{16}$$

$$\ln(\beta_n-1)=\ln(a_k)+\ln(C)b_k, \tag{17}$$

$$\ln(-\alpha_n)=\ln(c_k)+\ln(C)d_k. \tag{18}$$

The basis of the regression procedure is a weighted least-squares fit[35] which involves minimization of the quantity

$$\chi^2=\sum_{i=1}^{N}\frac{(y_{mi}-y_{pi})^2}{\epsilon_i^2}, \tag{19}$$

where y_{mi} are the measured data we are trying to fit, y_{pi} are the predicted data from the model, and ϵ_i are the uncertainties in each of the measured data points, y_{mi}. Since we are fitting quantities that are functions of $\hat{Z}_n$ and $\hat{k}_n$ and not $\hat{Z}_n$ and $\hat{k}_n$ themselves, we must compute the uncertainties in the data we are actually trying to fit. For example, since we do not actually fit data to R_n but instead fit $\ln(R_n-1)$ the uncertainty in the data to be fit is

$$\epsilon_i=\frac{\partial \ln(R_n-1)}{\partial R_{ni}}\delta R_{ni}=\frac{\delta R_{ni}}{R_{ni}-1}, \tag{20}$$

TABLE V. Empirical power law constants.

Quantity	Delany	Qunli	Present work
a_z	0.0571	0.212	0.2283±0.0026
b_z	−0.754	−0.607	−0.4884±0.0059
c_z	0.087	0.105	0.1038±0.0007
d_z	−0.732	−0.607	−0.8155±0.0034
a_k	0.0978	0.163	0.0898±0.0007
b_k	−0.0700	−0.592	−0.8453±0.0037
c_k	0.189	0.188	0.2049±0.0004
d_k	−0.595	−0.544	−0.7215±0.0012

where δR_{ni} are the individual uncertainties in the data R_{ni}. The weights of the regression are the square of the inverse of the uncertainties in the data to be fit. The uncertainty in the fitted constants was determined using standard weighted regression procedures.

To evaluate the goodness-of-fit of our new model and compare other models to the data, we determine the value of the reduced chi-squared, $\chi_\nu^2=\chi^2/(N-2)$, where χ^2 is defined earlier and N is the number of data points. If our model is a good fit to the data, the measurement errors follow a Gaussian distribution about the true value, and our uncertainty estimates are accurate, χ_ν^2 should be a value close to unity. A χ_ν^2 much less than unity does not indicate a better fit to the data, but instead indicates that the measurement errors do not fit a Gaussian distribution about the true value, or our uncertainty estimates were exaggerated, or both. A χ_ν^2 with a value much larger than unity can indicate a poor fit, but could also indicate an underestimation of the uncertainty or again, that the measurement errors do not fit a Gaussian distribution, or both. A visual inspection of the fit can be used to help determine the cause of a large value for χ_ν^2.

C. Microstructural theory

For a more complete analysis, the data should be compared to a microstructural theory. The Johnson–Allard model[17] is a general model that in the low and high frequency limit should fit all rigid frame porous media. In his theory, Allard developed the following expressions for the complex effective density, $\hat{\rho}_e$, and the complex bulk modulus, $\hat{K}$:

$$\hat{\rho}_e=\rho_0\left(\alpha_\infty+\frac{\sigma\phi}{j\omega\rho_0}\sqrt{1+\frac{4j\alpha_\infty^2\eta\rho_0\omega}{\sigma^2\Lambda^2\phi^2}}\right) \tag{21}$$

and

$$\hat{K}=P_0\left[1-\left(1-\frac{1}{\gamma}\right)\left(1+\frac{8\eta}{j\Lambda'^2\omega\rho_0\,\mathrm{Pr}}\hat{A}(\omega)\right)^{-1}\right]^{-1}, \tag{22}$$

where

TABLE VI. Goodness-of-fit, χ_ν^2, for the regression analysis.

Model	$\ln(R_n-1)$	$\ln(-X_n)$	$\ln(\beta_n)$	$\ln(-\alpha_n)$
New power law	0.19	0.43	1.02	0.89
Delany and Bazley	24.0	17.6	6.43	98.0
Qunli	0.70	25.3	5.31	168.3

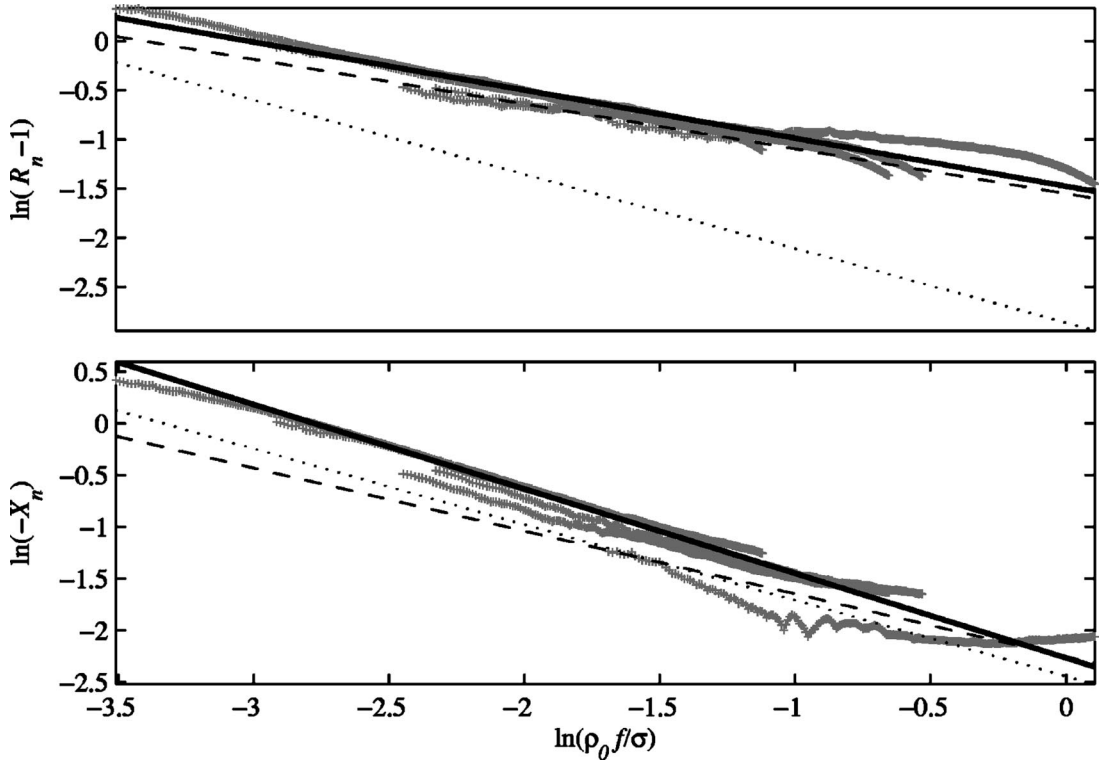

FIG. 4. Comparison of $\ln(R_n-1)$ and $\ln(-X_n)$ as a function of $\ln(\rho_0 f/\sigma)$ for all the sample data and the empirical models. Plotted are measured data (+), new empirical model (—), and the empirical models of Delany and Bazley (···) and Qunli (---).

$$\hat{A}(\omega)=\sqrt{1+\frac{j\rho_0\omega\,\mathrm{Pr}\,\Lambda'^2}{16\eta}}. \tag{23}$$

In the above expressions the fluid in the porous material is described by the ratio of specific heats, γ, the Prandtl number, Pr, and the viscosity, η. The porous material is described by the flow resistivity, σ, the porosity, ϕ, the tortuosity, α_∞, the characteristic viscous length, Λ, and the characteristic thermal length, Λ'. The characteristic impedance and wave number are then given by

$$\hat{Z}_c=\sqrt{\hat{\rho}_e\hat{K}} \tag{24}$$

and

$$\hat{k}_c=\omega\sqrt{\hat{\rho}_e/\hat{K}}. \tag{25}$$

In order to compare our data to the Johnson–Allard model we must determine the material parameters, σ, ϕ, α_∞, Λ, Λ'. The flow resistivity, σ, is measured for each sample as described in Sec. III D. The RVC manufacturer has stated values of the porosity, ϕ, and has a chart that gives estimated values of surface area to volume ratio for the various pore sizes from which the characteristic thermal length, Λ', can be estimated. Since our laboratory lacked the equipment to directly measure the tortuosity, α_∞, or the characteristic viscous length, Λ, we instead tried to fit the model to our measured impedance and wave number data with α_∞ and Λ as free parameters. Unfortunately, the resulting fit yielded unrealistic values for α_∞. Because of the very thin and reticulated nature of the RVC cell frame, tortuosity should be a value close to unity, so a fit can be done with $\alpha_\infty=1$ to determine the values of Λ to minimize the error of the fit to the measured data. This is done separately for each sample.

V. RESULTS AND DISCUSSION

The measured flow resistivity of the samples is shown in Table IV. It is quite interesting to note that the 80 PPI sample has a higher flow resistivity than the 100 PPI. This is consistent with the measurement results that show a slightly larger impedance and wave number for the 80 PPI sample. The 80 PPI sample does visually appear to have a larger pore size than the 100 PPI material. What this may mean is that PPI is not a useful measurement property of RVC for acoustic purposes. Several more samples of RVC of different porosities should be obtained to determine if the 80 PPI sample that was measured was abnormal or if PPI is indeed poorly related to the flow resistivity of the material. The resulting empirical equations from the regression analysis are

$$\hat{Z}_c=\rho_0 c_0(1+0.2283C^{-0.4884}-j0.1038C^{-0.8155}) \tag{26}$$

and

$$\hat{k}_c=\frac{\omega}{c_0}(1+0.0898C^{-0.8453}-j0.2049C^{-0.7215}), \tag{27}$$

where $C=\rho_0 f/\sigma$. The constant values for the new empirical model for the real and imaginary parts of the normalized characteristic impedance and wave number along with their uncertainties for the values are shown in Table V. The table also presents the values obtained in the fits by Delany and Bazley and by Qunli for comparison. The values of the goodness-of-fit parameter, χ^2_ν, for the new empirical law and

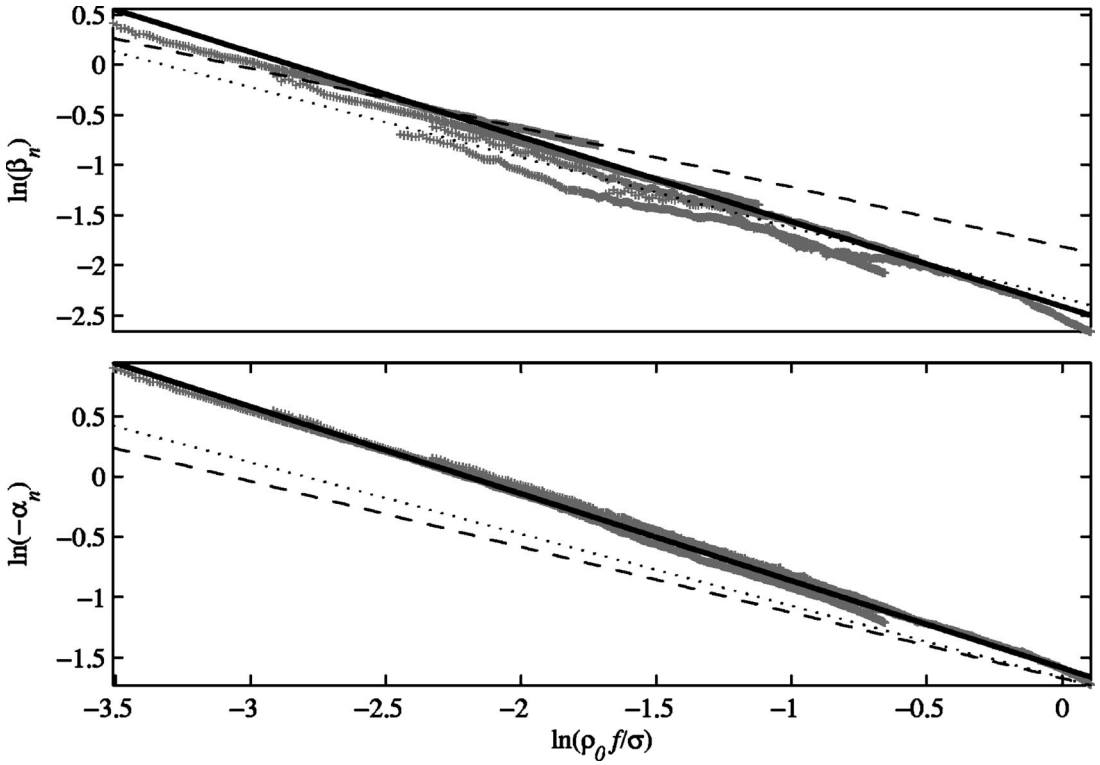

FIG. 5. Comparison of $\ln(\beta_n)$ and $\ln(-\alpha_n)$ as a function of $\ln(\rho_0 f/\sigma)$ for all the sample data and the empirical models. Plotted are measured data (+), new empirical model (—), and the empirical models of Delany and Bazley (···) and Qunli (---).

for the models of the Delany and Bazley and Qunli are shown in Table VI. Plots of the linearized data, the new empirical model, and the models of Delany and Bazley and Qunli are shown in Figs. 4 and 5. The results of χ_ν^2 computation show that the new empirical model is an acceptable predictor of both the real and imaginary parts of the normalized characteristic impedance and wave number, R_n, X_n, α_n, and β_n. The χ_ν^2 for the new model fit of $\ln(R_n-1)$ is a little low, indicating that the uncertainties in the measurement of R_n may have been overestimated. The Qunli model was found to be an acceptable predictor of only R_n while the Delany and Bazley model is not an acceptable predictor of any of the quantities.

Table VII shows the values of the characteristic viscous and thermal lengths, Λ and Λ', resulting from the fit of the data to the Johnson–Allard microstructural model and estimated from the surface area to volume ratio chart of the manufacturer. Because the model was fit individually for each sample PPI, the overall χ_ν^2 for the model was not computed.

An inspection of Figs. 4 and 5 confirms what the χ_ν^2 calculations suggest, that the new empirical model is, in general, a much better fit than either the Qunli or Delany and Bazley model. For the R_n regression results shown in Fig. 4, it appears the Qunli model fits the R_n data much better than the Delany model, but not quite as well as the new model. Figure 5 shows that both the Delany and Qunli models seem to fit the β_n data fairly well, but not as well as the new empirical model.

Figures 6–10 show comparisons of the measured R_n, X_n, β_n and α_n to the predictions of the empirical models and the Johnson–Allard microstructural model fit for each of the PPI. Error bars on the measurement are included. To make it easier to read the graphs, every tenth measured data point is plotted on the curves. An inspection of all the figures shows

TABLE VII. Characteristic viscous and thermal lengths of RVC samples.

Sample PPI	Λ (m)	Λ' (m)
60	2.2e−4	5.9e−3
80	1.0e−4	4.0e−3
100	1.0e−4	4.3e−3
200	5.7e−5	3.2e−3
300	3.8e−5	2.5e−3

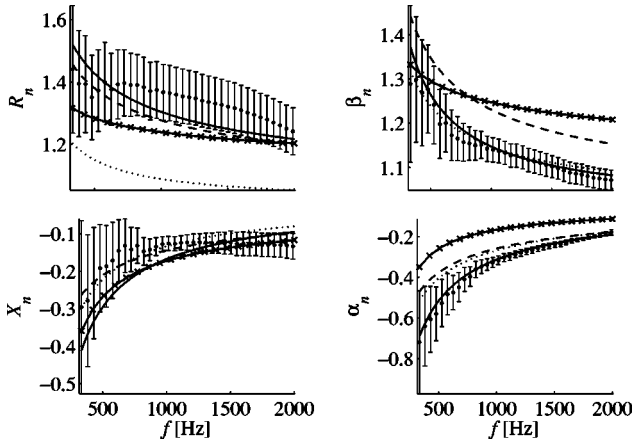

FIG. 6. Comparison of measured R_n, X_n, β_n, and α_n and empirical predictions as a function of $\rho_0 f/\sigma$ for the 60 PPI RVC samples with σ=1749 Pa s m^{-2}. Plotted are the measured data (·), the new empirical model (—), the empirical models of Delany (···) and Qunli (---), and the Johnson–Allard microstructural model (×).

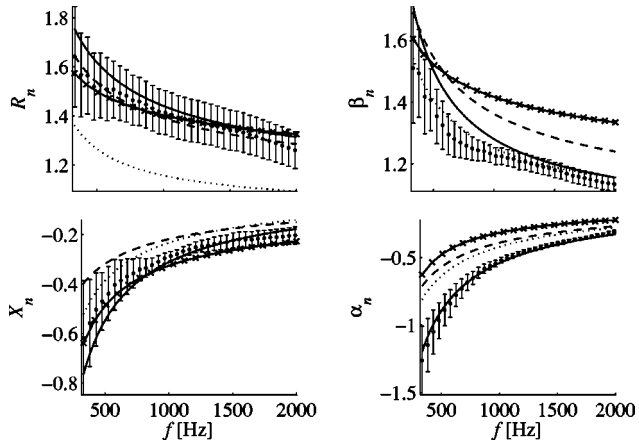

FIG. 7. Comparison of measured R_n, X_n, β_n, and α_n and empirical predictions as a function of $\rho_0 f/\sigma$ for the 80 PPI RVC samples with $\sigma=3742$ Pa s m^{-2}. Plotted are the measured data ($\cdot$), the new empirical model (—), the empirical models of Delany ($\cdots$) and Qunli (---), and the Johnson–Allard microstructural model ($\times$).

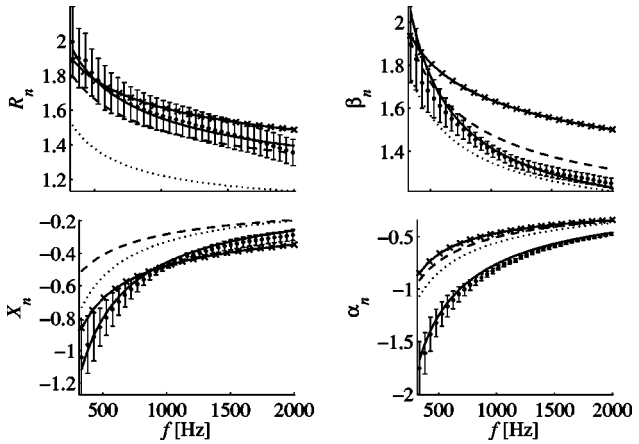

FIG. 9. Comparison of measured R_n, X_n, β_n, and α_n and empirical predictions as a function of $\rho_0 f/\sigma$ for the 200 PPI RVC samples with $\sigma=5974$ Pa s m^{-2}. Plotted are the measured data ($\cdot$), the new empirical model (—), the empirical models of Delany ($\cdots$) and Qunli (---), and the Johnson–Allard microstructural model ($\times$).

that except for the low frequency predictions of β_n for the 80 and 300 PPI samples, the predictions of the new empirical model are within the error bars of nearly all the measured data of all the samples.

The Delany and Bazley model prediction is within the error bars of nearly all the measured data for only X_n of the 60 PPI sample as shown in Fig. 6 and for β_n of the 60 and 80 PPI samples as shown in Figs. 6 and 7. The Qunli model fairs a bit better. The Qunli model predictions fall within the error bars over most of the measurements of R_n for all the samples—consistent with the low value of χ^2_ν for the model of R_n. It also is a good predictor of X_n for the 60 PPI sample.

The microstructural model was mostly within the error bars of X_n and β_n for the 60 PPI sample and for R_n and X_n of the 80, 100, 200, and 300 PPI samples. Overall the microstructural model fits better than the Delany and Bazley empirical model but not as well as the Qunli empirical model. A close inspection will show that the high frequency slope of the Johnson–Allard model is very close to that of the measured data as expected by the model. A fit of the data to the Johnson–Allard model at only high frequencies would have produced a better match at high frequencies, but a far worse match at low frequencies and a much higher overall error. It is clear that advances in the microstructural modeling are required for accurate modeling of RVC in the lower and mid-frequency ranges.

VI. CONCLUSIONS

The four-microphone transfer matrix method was used to measure the complex characteristic impedance, $\hat{Z}_c$, and wave number, $\hat{k}_c$, for 60–300 PPI reticulated vitreous carbon in the frequency range of 330–2000 Hz. Uncertainty estimates of the measured $\hat{Z}_c$ and $\hat{k}_c$ were determined by Monte Carlo methods. Inspection of the data suggested that they would be well modeled by an empirical power law of

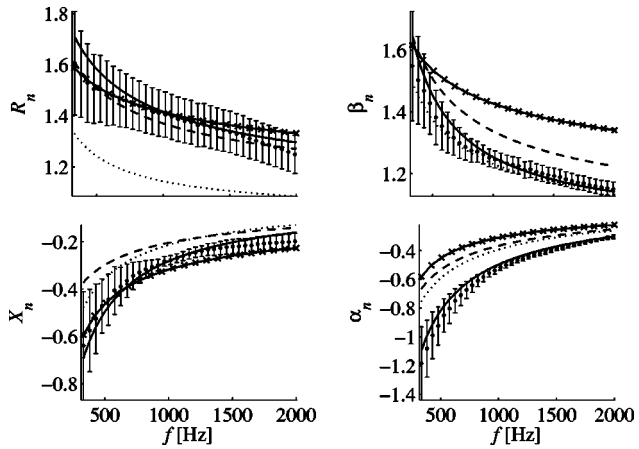

FIG. 8. Comparison of measured R_n, X_n, β_n, and α_n and empirical predictions as a function of $\rho_0 f/\sigma$ for the 100 PPI RVC samples with $\sigma=3348$ Pa s m^{-2}. Plotted are the measured data ($\cdot$), the new empirical model (—), the empirical models of Delany ($\cdots$) and Qunli (---), and the Johnson–Allard microstructural model ($\times$).

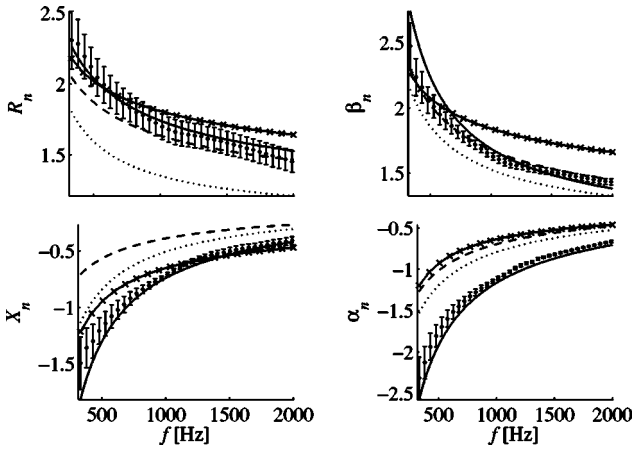

FIG. 10. Comparison of measured R_n, X_n, β_n, and α_n and empirical predictions as a function of $\rho_0 f/\sigma$ for the 300 PPI RVC samples with $\sigma=10782$ Pa s m^{-2}. Plotted are the measured data ($\cdot$), the new empirical model (—), the empirical models of Delany ($\cdots$) and Qunli (---), and the Johnson–Allard microstructural model ($\times$).

the same form as the empirical models developed by Delany for fibrous absorbers and by Qunli for open cell foam absorbers.

The measured data were fit to a power law and uncertainty bounds on the constants were determined by a weighted least-squares analysis. The measured data were also compared to the empirical models of Delany and Bazley, Qunli, and the Johnson–Allard microstructural model. The χ^2_ν goodness-of-fit measure indicated that the new empirical model was a good predictor of the acoustic properties of RVC while the other empirical models were not.

Plots of the measured data against the new empirical model, against the empirical models of Delany and Bazley and Qunli, and against the Johnson–Allard microstructural model confirm the goodness-of-fit measures and show that the microstructural model fits the measured data better than the Delany and Bazley model but worse than the Qunli model and far worse new empirical model. A new microstructural model needs to be developed for accurate prediction of the acoustic properties of RVC over the frequency ranges used in this study.

ACKNOWLEDGMENT

This work was supported by the Office of Naval Research.

[1] ERG Aerospace, Reticulated Vitreous Carbon (RVC) is manufactured by ERG Materials & Aerospace Corporation, 900 Standford Avenue, Oakland, CA 94608.
[2] L. A. Wilen, ''Dynamic measurements of the thermal dissapation function of reticulated vitreous carbon,'' J. Acoust. Soc. Am. **109**, 179–184 (2001).
[3] A. Petculescu and L. A. Wilen, ''Lumped-element technique for the measurement of complex density,'' J. Acoust. Soc. Am. **110**, 1950–1957 (2001).
[4] J. A. Adeff, T. J. Hofler, A. A. Atchley, and W. C. Moss, ''Measurements with reticulated vitreous carbon stacks thermoacoustic prime movers and refrigerators,'' J. Acoust. Soc. Am. **104**, 32–38 (1998).
[5] R. T. Muehleisen and C. W. Beamer IV, ''Thermoviscous functions of wire mesh and rvc stacks,'' J. Acoust. Soc. Am. **109**, 2404 (2001).
[6] M. E. Delany and E. N. Bazley, ''Acoustic properties of fibrous absorbent materials,'' Appl. Acoust. **3**, 105–116 (1970).
[7] W. Qunli, ''Empirical relations between acoustical properties and flow resistivity of porous plastic open-cell foam,'' Appl. Acoust. **25**, 141–148 (1988).
[8] J.-F. Allard, P. Herzog, and D. Lafarge, ''Recent topics concerning the acoustics of fibrous and porous materials,'' Appl. Acoust. **39**, 3–21 (1993).
[9] C. Zwikker and C. W. Kosten, *Sound Absorbing Materials* (Elsevier, Amsterdam, 1949).
[10] M. A. Biot, ''Theory of propagation of elastic waves in a fluid-saturated porous solid. I. Low frequency range,'' J. Acoust. Soc. Am. **28**, 168–178 (1956).
[11] M. A. Biot, ''Theory of propagation of elastic waves in a fluid-saturated porous solid. II. Higher frequency range,'' J. Acoust. Soc. Am. **28**, 179–191 (1956).
[12] K. Attenborough, ''Acoustical characteristics of porous materials,'' Phys. Rep. **82**, 179–227 (1982).
[13] K. Attenborough, ''Acoustical characteristics of rigid fibrous absorbents and granular materials,'' J. Acoust. Soc. Am. **73**, 785–799 (1983).
[14] Y. Champoux and M. R. Stinson, ''On acoustical models for sound propagation in rigid frame porous materials and the influence of shape factors,'' J. Acoust. Soc. Am. **92**, 1120–1131 (1992).
[15] M. R. Stinson and Y. Champoux, ''Propagation of sound and the assignment of shape factors in model porous materials having simple pore geometries,'' J. Acoust. Soc. Am. **91**, 685–695 (1992).
[16] R. F. Lambert, ''Propagation of sound in highly porous open-cell elastic foams,'' J. Acoust. Soc. Am. **73**, 1131–1138 (1983).
[17] J. F. Allard, *Propagation of Sound in Porous Media* (Elsevier Science, Essex, UK, 1993).
[18] D. L. Johnson, J. Koplik, and L. M. Schwartz, ''New pore-size parameter characterizing transport in porous media,'' Phys. Rev. Lett. **57**, 2564–2567 (1986).
[19] D. L. Johnson, J. Koplik, and R. Dashen, ''Theory of dynamic permeability and tortuosity in fluid-saturated porous media,'' J. Fluid Mech. **176**, 379–402 (1987).
[20] D. K. Wilson, ''Relaxation-matched modeling of propagation through porous media, including fractal pore structure,'' J. Acoust. Soc. Am. **94**, 1136–1145 (1993).
[21] D. K. Wilson, ''Simple, relaxational models for the acoustical properties of porous media,'' Appl. Acoust. **50**, 171–188 (1997).
[22] K. V. Horoshenkov and M. J. Swift, ''The acoustic properties of granular materials with pore size distribution close to log-normal,'' J. Acoust. Soc. Am. **110**, 2371–2378 (2001).
[23] O. Umnova, K. Attenborough, and K. M. Li, ''A cell model for the acoustical properties of packings of spheres,'' Acta Acust. (Beijing) **87**, 226–235 (2001).
[24] J.-F. Allard and Y. Champoux, ''New empirical equations for sound propagation in rigid frame fibrous materials,'' J. Acoust. Soc. Am. **91**, 3346–3353 (1992).
[25] A. Cummings and S. P. Beadle, ''Acoustic properties of reticulated plastic foams,'' J. Sound Vib. **1975**, 115–133 (1993).
[26] ASTM C 384, Standard Test Method for Impedance and Absorption of Acoustical Materials by the Impedance Tube Method, 2003.
[27] ASTM E 1050, Standard Test Method for Impedance and Absorption of Acoustical Materials Using a Tube, Two Microphones and a Digital Frequency Analysis System, 1998.
[28] Y. Champoux and M. R. Stinson, ''Measurement of the characteristic impedance and propagation constant of materials having high flow resistivity,'' J. Acoust. Soc. Am. **90**, 2182–2191 (1991).
[29] J. E. McIntosh, M. T. Zuroski, and R. F. Lambert, ''Standing wave appa ratus for measuring fundamental properties of acoustic materials in air,'' J. Acoust. Soc. Am. **88**, 1929–1938 (1990).
[30] B. H. Song and J. S. Bolton, ''A transfer-matrix approach for estimating the characteristic impedance and wave numbers of limp and rigid porous materials,'' J. Acoust. Soc. Am. **107**, 1131–1152 (2000).
[31] R. T. Muehleisen and C. W. Beamer IV, ''Comparison of errors in the three- and four-microphone methods used in the measurement of the acoustic properties of porous materials,'' Acoust. Res. Lett. Online **3**, 112–117 (2002).
[32] J. Y. Chung and D. A. Blaser, ''Transfer function method of measuring in-duct acoustic properties. I. theory,'' J. Acoust. Soc. Am. **68**, 907–913 (1980).
[33] ASTM C 522, Standard Test Method for Air Flow Restance of Acoustical Materials, 2003.
[34] M. Abom and H. Boden, ''Error analysis of two-microphone measurements in ducts with flow,'' J. Acoust. Soc. Am. **83**, 2429–2438 (1988).
[35] P. R. Bevington and D. K. Robinson, *Data Reduction and Error Analysis for The Physical Sciences*, 2 ed. (McGraw–Hill, New York, 1991).

Investigation of the phase velocities of guided acoustic waves in soft porous layers

L. Boeckx, P. Leclaire, P. Khurana, C. Glorieux,[a] and W. Lauriks[b]
Laboratorium voor Akoestiek en Thermische Fysica, Katholieke Universiteit Leuven, Celestijnenlaan 200D, B-3001 Heverlee, Belgium

J. F. Allard
Laboratoire d'Acoustique de l'Université du Maine, UMR CNRS 6613, Avenue Olivier Messiaen, 72085 Le Mans Cédex, France

(Received 30 August 2004; revised 21 October 2004; accepted 16 November 2004)

A new experimental method for measuring the phase velocities of guided acoustic waves in soft poroelastic or poroviscoelastic plates is proposed. The method is based on the generation of standing waves in the material and on the spatial Fourier transform of the displacement profile of the upper surface. The plate is glued on a rigid substrate so that it has a free upper surface and a nonmoving lower surface. The displacement is measured with a laser Doppler vibrometer along a line corresponding to the direction of propagation of plane surface waves. A continuous sine with varying frequencies was chosen as excitation signal to maximize the precision of the measurements. The spatial Fourier transform provides the wave numbers, and the phase velocities are obtained from the relationship between wave number and frequency. The phase velocities of several guided modes could be measured in a highly porous foam saturated by air. The modes were also studied theoretically and, from the theoretical results, the experimental results, and a fitting procedure, it was possible to determine the frequency behavior of the complex shear modulus and of the complex Poisson ratio from 200 Hz to 1.4 kHz, in a frequency range higher than the traditional methods. © *2005 Acoustical Society of America.* [DOI: 10.1121/1.1847848]

PACS numbers: 43.20.Jr, 43.20.Ks, 43.20.Mv [RLW] Pages: 545–554

I. INTRODUCTION

The acoustical properties of porous materials can generally be well described in a wide frequency range with Biot's theory,[1] which involves the determination of a number of physical parameters. In many cases for air-saturated materials, the porous frame can be considered to be much more rigid and heavier than air, and a simplified model can be used in the rigid frame approximation. Many studies have been successfully carried out in this approximation and are reported in Ref. 2. There is also a growing interest in applications where the frequency dependence of the mechanical rigidity of the material should be taken into account in the full Biot theory for poroelastic and poroviscoelastic media.[3,4,2] However, the main limitation of the full model is the lack of data on the dynamic rigidities of the porous frame. Classical methods for determining these parameters involve the application of vibrations to samples[5–10] (e.g., rods, cubes, or small plates) of finite sizes with respect to the wavelengths involved. The properties (resonance frequencies, damping, dynamic behavior) of the transfer function between the response and the excitation yield the mechanical properties of the excited structure. However, the frequency range described in these methods is limited to the lower part of the audible frequency range (typically below 400 Hz). A new method for measuring the shear modulus of air-filled porous materials based on the propagation of Rayleigh waves in thick layers was recently proposed by Allard *et al.*[11] and provided useful information above 3 kHz. More recently, Allard *et al.*[12] have proposed a new method of measurement in thinner samples in which Biot's shear wave is excited. This method is based on the effect of the resonance of the porous frame around the quarter shear wavelength on the pole of the reflection coefficient.

Surface waves at the interface between a fluid and a porous solid have been studied theoretically by many authors and in particular by Deresiewicz,[13] and Feng and Johnson[14] for liquid saturated media. The surface wave in the air above a porous absorbing material and rough surfaces was studied theoretically and experimentally by Attenborough,[15,16] Attenborough and Chen,[17] Lauriks *et al.*,[18] Kelders *et al.*,[19] and Allard *et al.*[20]

In this article, we investigate the propagation of guided waves in a layer of porous material in a wide frequency range, from the typical frequencies of the classical vibrational methods to the high-frequency limit of the Rayleigh wave. First results of this work were presented in Kyoto.[21] Together with a complete model for guided waves in a soft porous material on a rigid substrate, a new experimental method is proposed in this article for the determination of the modes of propagation in a plate of finite sizes. This method, characterized by an increased signal-to-noise ratio and measurement accuracy, is based on the generation of standing waves in the layer of porous material. Lamb waves in plates with free surfaces, and other surface waves in layers or at interfaces have been extensively studied and led to many

[a]Also: postdoctoral researcher FWO-Vlaanderen, Belgium.
[b]Author to whom correspondence should be addressed. Electronic mail: walter.lauriks@fys.kuleuven.ac.be

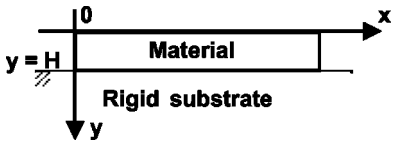

FIG. 1. Layer of material on a rigid substrate and system of coordinates.

applications from material characterization at ultrasonic frequencies[22] to the oil industry. Theoretical references in this area are provided by the books by Royer and Dieulesaint,[23] Viktorov,[24] and Ewing, Jardetsky, and Press.[25] The theoretical results of our study are presented in the next section. The experimental principle of the new method for measuring the phase velocities of the different modes in of porous layers is presented in Sec. III and applied in Sec. IV to a melamine foam. The phase velocities of two modes were measured and used as reference velocities for the fitting of the dispersion curves leading to the determination of the frequency variations of the complex shear modulus and Poisson ratio.

II. GUIDED WAVES IN A LAYER OF POROUS MATERIAL

Results for a nonporous solid of thickness H lying on a rigid substrate are presented first. This simple case will be very useful to the study of the porous case in providing the general shape of the curves, the cutoff frequencies, and the limit velocities that should be expected. Many porous materials in practical applications have a high porosity, a low flow resistivity, and a tortuosity close to 1. For these materials the couplings are relatively low, and the model for nonporous material will reasonably approximate the porous case. The full model for porous layers on a rigid substrate is presented in Sec. II B, which better describes materials for which the couplings are higher.

A. Guided waves in a layer of soft elastic material on a rigid substrate

Ewing, Jardetsky, and Press[25] (p. 189) have studied surface waves in a solid layer over a semi-infinite solid. The frequency spectrum at ultrasonic frequencies of the surface acoustic wave in a solid film over a solid substrate was also studied analytically by Gusev and Hess.[26] The configuration for a soft, solid layer lying on a rigid substrate is shown in Fig. 1. Following the standard derivation, by choosing the potentials to be linear combinations of sines and cosines and from the application of the appropriate boundary conditions on stresses and displacements at the interfaces, the following dispersion equation is obtained:

$$-4k^2(k^2-q^2)-\sin pH \sin qH\left[\frac{k^2}{pq}(k^2-q^2)^2+4k^2pq\right] + \cos pH \cos qH[4k^4+(k^2-q^2)^2]=0, \quad (1)$$

where k, p, and q are the wave numbers defined in the classical Lamb theory. Figure 2(a) shows an example of dispersion curves obtained from a numerical search of the roots of Eq. (1). The usual Lamb dispersion curves are shown in Fig. 2(b) for the same material but for a plate of thickness

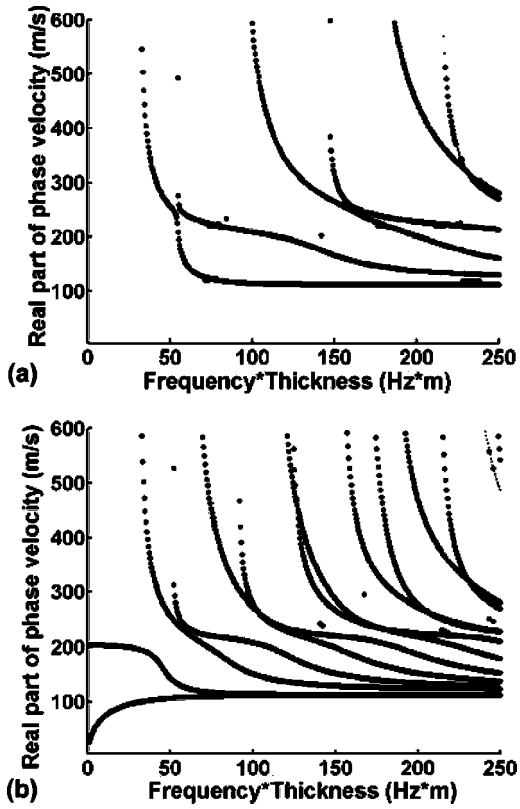

FIG. 2. Phase velocities vs frequency×thickness for (a) a plate of thickness H of an elastic material on a rigid substrate; (b) a Lamb plate of thickness $2H$. In both cases the material density is 14 kg/m^3, $V_L=222$ m/s, and $V_T=122$ m/s.

$2H$. The main difference with the Lamb plate is the absence of modes without cutoff frequency and a greater spacing between the modes associated with the change in thickness. Since the thickness always appears in a product with the wave number or with the frequency in the dispersion equation, doubling (halving) the thickness is equivalent to compressing (expanding) the frequency scale. The cutoff frequencies are given by

$$\omega_c=(2m+1)\frac{\pi V_T}{2H} \quad \text{and} \quad \omega_c=(2m+1)\frac{\pi V_L}{2H}, \quad m=0,1,2,..., \quad (2)$$

where V_L and V_T are, respectively, the velocities of the bulk compressional and shear waves in the material. The study of the high-frequency behavior shows that the first mode tends to the Rayleigh mode and that the velocities of higher order modes tend to the bulk shear velocity.

The results presented above do not account for the presence of a fluid surrounding the layer. The effect of the fluid can be included by replacing the zero in the right-hand side of the equation of dispersion by a fluid term (see Viktorov,[24] p. 117 for the Lamb case). The main influence of the presence of a loading fluid is the possible existence of a fluid wave that is damped along the y axis, hence localized above the surface (Scholte wave) and/or the possibility for the modes in the layer to ''leak out'' (radiate) energy in the fluid (leaky Rayleigh wave or leaky Lamb modes). A large body of literature is dedicated to the study of ultrasonic surface

waves in fluid-loaded media. The reader is referred to the thesis by Van de Rostyne[27] for an extensive and recent review. The fluid is air in our study and its influence has been neglected in the case of guided waves in nonporous layers on a rigid substrate. However, air is accounted for in the following section where a porous material is studied.

B. Guided waves in a porous layer on a rigid substrate and saturated by air

The configuration examined in the previous section involves boundary conditions that are of great interest for the study of highly porous sound-absorbing materials. These very soft materials have a Young's modulus between 10^4 and to 10^6 Pa, typically. For these materials the rigid substrate or the Lamb boundary conditions are fairly easy to set up experimentally and to control.

1. Biot's equations of poroelasticity

In Biot's linear equations of poroelasticity[28] (Biot's second formulation is used here), the total stress tensor τ_{ij} and the fluid pressure P_f in the pores are given by

$$\tau_{ij}=2\mu\varepsilon_{ij}+\delta_{ij}(\lambda_c\varepsilon-\alpha M\zeta), \tag{3a}$$

$$P_f=-\alpha M\varepsilon+M\zeta, \tag{3b}$$

with

$$\lambda_c=\lambda+\alpha^2 M, \tag{4}$$

$$\varepsilon_{ij}=\tfrac{1}{2}(u_{i,j}+u_{j,i}), \tag{5}$$

$$\varepsilon=\varepsilon_{11}+\varepsilon_{22}+\varepsilon_{33}=\operatorname{div}\boldsymbol{u}, \tag{6}$$

$$\zeta=-\operatorname{div} w, \tag{7}$$

$$\boldsymbol{w}=\phi(\boldsymbol{U}-\boldsymbol{u}). \tag{8}$$

In these equations, λ and μ are the Lamé constants of the porous frame, α and M are, respectively, an elastic coupling factor and a rigidity associated with the fluid. They were both defined by Biot and Willis.[29] ε_{ij} is the strain tensor of the solid and depends on the solid displacement $\boldsymbol{u}$. ε is the solid dilatation, ϕ the porosity, ζ the fluid content, and $\boldsymbol{w}$ corresponds to the displacement of the fluid $\boldsymbol{U}$ relative to the solid.

2. Boundary conditions

The porous plate is set in the same configuration as the elastic plate of Sec. II A and the system of coordinates is unchanged. In this configuration, the boundary conditions are expressed as follows:

At $y=0$:

$\tau_{12}=0$,

$\tau_{22}=-p$ where p is the pressure of the fluid surrounding the layer,

$P_f=p$,

$u_y+w_y=U_f$ where U_f is the displacement of matter in the surrounding fluid.

At $y=H$:

$u_y=0$,

$u_x=0$,

$w_x=0$.

3. Choice of a functional form for the displacement potentials

Two compressional waves and one shear wave can propagate in fluid-saturated porous material, and the displacements of matter are written in terms of two scalar potentials φ_1 and φ_2 and one vector potential ψ

$$\boldsymbol{u}=\nabla\varphi_1+\nabla\varphi_2+\nabla\times\psi, \tag{9}$$

$$\boldsymbol{w}=\phi(\boldsymbol{U}-\boldsymbol{u})=\phi\nabla\varphi_1(\mu_1-1)+\phi\nabla\varphi_2(\mu_2-1)+\phi\nabla\times\psi(\mu_3-1), \tag{10}$$

where the coefficients μ_1, μ_2, and μ_3 correspond to the amplitude ratios of the waves in the porous material[3,11]

$$\mu_i=\frac{Pk_i-\omega^2\rho_{11}}{\omega^2\rho_{12}-Qk_i},\quad i=1,2 \tag{11a}$$

$$\mu_3=\frac{\rho_{12}}{\rho_{22}}. \tag{11b}$$

In these expressions k_i $(i=1,2)$ are the wave numbers of the Biot compressional waves. The elastic coefficients P and Q were defined by Biot and Willis.[29] These can be related to λ, μ, to the rigidity of the fluid K_f and of the solid K_s and to the porosity ϕ. The following approximation can be used for highly porous materials saturated by air:[3]

$$P\approx\frac{2}{3}\mu+\lambda+\frac{(1-\phi)}{\phi}K_f, \tag{12a}$$

$$Q\approx K_f(1-\phi). \tag{12b}$$

The following relations are also needed:[29]

$$\alpha=\left(1-\frac{Q}{R}\right)\phi \tag{13a}$$

$$\text{and}\quad M=\frac{R}{Q^2}, \tag{13b}$$

with $R\approx\phi K_f$ in the approximation of an air saturated highly porous material.[3] ρ_{11}, ρ_{12}, ρ_{22} are the coefficients of a density matrix and are functions of the tortuosity α_∞

$$\rho_{11}=(1-\phi)\rho_s+(\alpha_\infty-1)\phi\rho_f, \tag{14}$$

$$\rho_{12}=-(\alpha_\infty-1)\phi\rho_f, \tag{15}$$

$$\rho_{22}=\alpha_\infty\phi\rho_f. \tag{16}$$

The velocities of the two compressional and of the shear waves were given by Biot.[1,28] They are obtained from

$$\frac{1}{V_{Li}^2}=\frac{1}{2}\frac{P\rho_{22}+R\rho_{11}-2Q\rho_{12}}{PR-Q^2}\left[1\pm\left(1-4\frac{(PR-Q^2)(\rho_{11}\rho_{22}-\rho_{12}^2)}{(P\rho_{22}+R\rho_{11}-2Q\rho_{12})^2}\right)^{1/2}\right],\qquad i=1,2 \tag{17}$$

$$V_T=\sqrt{\frac{\mu}{(1-\phi)\rho_s+\left(1-\frac{1}{\alpha_\infty}\right)\phi\rho_f}}. \tag{18}$$

The wave attenuation by viscous frictions and thermal exchanges between the solid and the fluid can be formulated through the use of a complex dynamic tortuosity $\alpha(\omega)$ to replace α_∞ and of a complex air compressibility (see Ref. 2). These involve the flow resistivity σ of the porous material and the viscous and thermal lengths Λ and Λ'. For the first three potentials, a linear combination of sines and cosines is chosen

$$\varphi_1=(A_1\cos p_1y+A_2\sin p_1y)e^{i(\omega t-kx)}, \tag{19}$$

$$\varphi_2=(B_1\cos p_2y+B_2\sin p_2y)e^{i(\omega t-kx)}, \tag{20}$$

$$\psi=(C_1\cos qy+C_2\sin qy)e^{i(\omega t-kx)}, \tag{21}$$

$$\varphi_f=De^{\gamma y}e^{i(\omega t-kx)}\quad\text{for}\quad y\leqslant 0, \tag{22}$$

where A_1, A_2, B_1, B_2, C_1, C_2, and D are constants. ω is the angular frequency and t is the time. The potentials depend on x and y and satisfy the following equations of propagation:

$$\nabla^2\varphi_1-\frac{1}{V_{L1}^2}\frac{\partial^2\varphi_1}{\partial t^2}=0, \tag{23a}$$

$$\nabla^2\varphi_2-\frac{1}{V_{L2}^2}\frac{\partial^2\varphi_2}{\partial t^2}=0 \tag{23b}$$

$$\text{and}\quad \nabla^2\psi-\frac{1}{V_T^2}\frac{\partial^2\psi}{\partial t^2}=0. \tag{23c}$$

Harmonic solutions in ω and k yield for a propagation along x

$$\frac{\partial^2\varphi_1}{\partial y^2}+p_1^2\varphi_1=0, \tag{24a}$$

$$\frac{\partial^2\varphi_2}{\partial y^2}+p_2^2\varphi_2=0, \tag{24b}$$

$$\text{and}\quad \frac{\partial^2\psi}{\partial y^2}+q^2\psi=0, \tag{24c}$$

where the coefficients p_1, p_2, and q are wave numbers associated with the propagation of the fast, slow, and shear waves, respectively

$$p_1^2=\frac{\omega^2}{V_{L1}^2}-k^2, \tag{25a}$$

$$p_2^2=\frac{\omega^2}{V_{L2}^2}-k^2, \tag{25b}$$

$$\text{and}\quad q^2=\frac{\omega^2}{V_T^2}-k^2. \tag{25c}$$

The fluid surrounding the layer is included in the model, and a potential φ_f, associated with the wave in the fluid must also be defined. This potential satisfies

$$\nabla^2\varphi_f-\frac{1}{V_f^2}\frac{\partial^2\varphi_f}{\partial t^2}, \tag{26a}$$

$$\frac{\partial^2\varphi_f}{\partial y^2}-\gamma^2\varphi_f=0. \tag{26b}$$

The dependence on y of φ_f is such that the y component of the propagation constant γ is given by

$$\gamma^2=k^2-\frac{\omega^2}{V_f^2}, \tag{27}$$

where V_f is the free velocity in the fluid. Referring to discussion of Sec. II A and to the form chosen for the potential in Eq. (22), the main features of the components of the wave numbers of the wave in the surrounding fluid are the following:

(i) $\mathrm{Im}(k)\geqslant 0$. This condition should always be fulfilled and will insure that the amplitude of the wave decreases as x increases (or is constant in the undamped case). The definition used for k is $k=\mathrm{Re}(k)+i\,\mathrm{Im}(k)$.

(ii) $\mathrm{Re}(\gamma)>0$. This corresponds to a fluid wave localized above the interface, i.e., a Scholte wave (semi-infinite solid) or an A wave (plate). If $\mathrm{Im}(k)=0$ in condition (i) the modes are undamped along x.

(iii) $\mathrm{Re}(\gamma)=0$ and $\mathrm{Im}(\gamma)>0$. This situation is one where the wave can propagate in the entire fluid half-space and is not localized near the interface. This is made possible if both the radiation condition $\mathrm{Re}(\gamma)=0$ and the causality requirement $\mathrm{Im}(\gamma)>0$ for a wave to travel from the interface and not toward it are fulfilled. In this case the guided modes in the layer will radiate or leak out energy in the fluid. Since $\gamma=\omega\sqrt{1/V^2-1/V_f^2}$, the consequences of these conditions on the velocities are that the phase velocity of the guided wave must be greater than the free velocity of the fluid for the condition to be fulfilled. The wave will be radiative for supersonic guided modes. The nature of the fluid mode (localized or radiative) can also change with frequency as the phase velocity varies and can cross the value V_f.

4. Determinant of the boundary conditions—Dispersion equation

The displacements u_x and u_y are obtained from writing the spatial derivatives of the potentials in Eq. (9)

$$u_x = \frac{\partial \varphi_1}{\partial x} + \frac{\partial \varphi_2}{\partial x} + \frac{\partial \psi}{\partial y}, \tag{28a}$$

$$\text{and } u_y = \frac{\partial \varphi_1}{\partial y} + \frac{\partial \varphi_2}{\partial y} - \frac{\partial \psi}{\partial y}. \tag{28b}$$

Similarly, the components of the relative displacement $\boldsymbol{w}$ are obtained from Eq. (10). The other parameters and the useful elements of the stress and strain tensors are calculated from Eqs. (3) to (8). After expressing the boundary conditions given in Sec. II B 2, a 7×7 determinant is found

$$\begin{vmatrix} 0 & D_{12} & 0 & D_{14} & D_{15} & 0 & 0 \\ D_{21} & 0 & D_{23} & 0 & 0 & D_{26} & D_{27} \\ D_{31} & 0 & D_{33} & 0 & 0 & 0 & D_{37} \\ 0 & D_{42} & 0 & D_{44} & D_{45} & 0 & D_{47} \\ D_{51} & D_{52} & D_{53} & D_{54} & D_{55} & D_{56} & 0 \\ D_{61} & D_{62} & D_{63} & D_{64} & D_{65} & D_{66} & 0 \\ D_{71} & D_{72} & D_{73} & D_{74} & D_{75} & D_{76} & 0 \end{vmatrix} = 0. \tag{29}$$

The coefficients of the matrix are given in the Appendix. Finding the zeros of this determinant, i.e., solving the equation

$$\text{Det}(\omega, k, H, \ldots) = 0, \tag{30}$$

provides a relationship between ω and k, the equation of dispersion. This relationship is not explicit and must be determined numerically. In general, this determinant has complex values and Eq. (30) should also be solved in the complex plane to account for attenuation mechanisms. This means that the initial values of k must be complex in the numerical algorithm to solve Eq. (30). The theoretical calculation of the dispersion curves for a highly porous melamine foam and an application to the evaluation of the dynamic complex elastic moduli are proposed in Sec. IV.

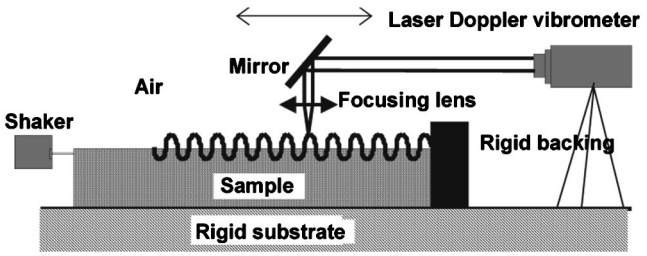

FIG. 3. Experimental setup for the generation and detection of standing waves in a layer of material on a rigid substrate.

III. EXPERIMENTAL PRINCIPLE FOR MEASURING THE PHASE VELOCITIES OF GUIDED ACOUSTIC MODES IN POROUS MEDIA

A. Experimental setup

The experimental principle is described in Fig. 3, where a layer of porous material is glued on a plane rigid substrate so that the displacement of the porous frame is zero at the interface between the material and the substrate. Double-faced tape and a mounting spray were used, in order to obtain uniform boundary conditions over the whole interface. An optical table with a rigidity and a density much greater than that of the porous layer was used as a semi-infinite rigid substrate. The porous layer was excited at one end with a thin aluminum strip used as a line source attached to a shaker at one end and to the sample at the other end with the help of double-faced tape. The shaker was fed with a continuous sinusoidal signal provided by the function generator unit of an SRS SR780 2-channel signal analyzer, and the frequency could be varied. The signal analyzer incorporates a lock-in amplifier. The other end of the layer was glued on a rigid end so that incident waves could be reflected. The difference in impedance is large and it can be assumed that the reflection coefficient at the interface between the rigid end and the

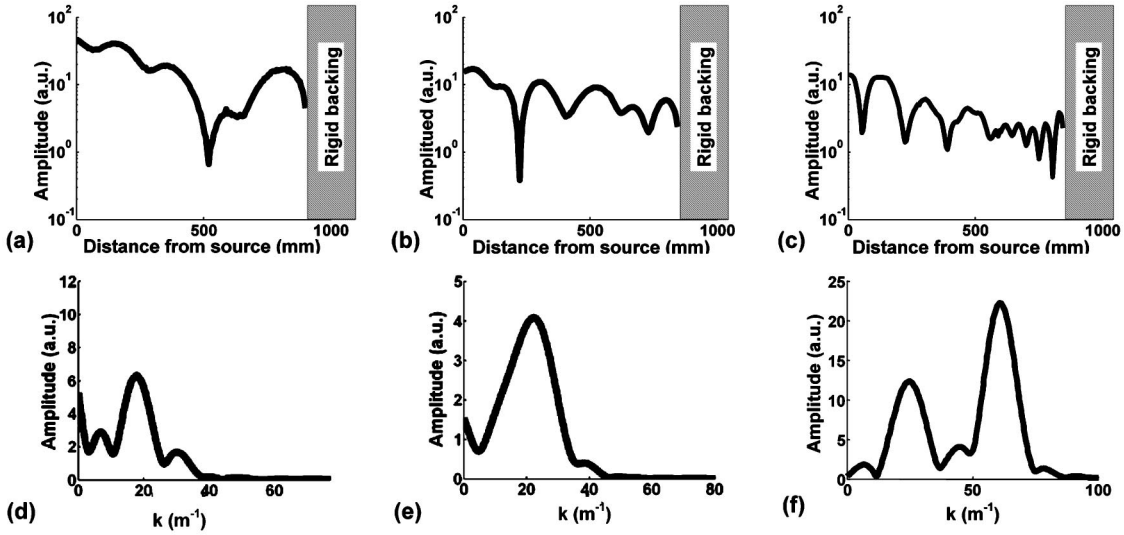

FIG. 4. (a), (b), and (c): Experimental standing wave patterns. (d), (e), and (f): Spatial Fourier transforms of the measured standing wave patterns. (a) and (d) 256 Hz; (b) and (e) 424 Hz; (c) and (f) 1041 Hz.

TABLE I. Phase velocities of the surface modes in a layer of material on a rigid substrate at different frequencies.

Freq (Hz)	Phase velocities of modes (m/s)				
1041	933	266	146	108	84
424	120	69			
256	253	91	50		

TABLE II. Material parameters for the melamine foam.

Tortuosity α_∞	Flow resistivity Ns/m^4 σ	Viscous dimension μm Λ	Thermal dimension μm Λ'	Frame density kg/m^3 ρ	Porosity ϕ
1.01	12 000	100	150	13.96	0.98

plate is 1. The displacement of the surface of the layer was measured with the help of a laser vibrometer. The measurement point on the surface was allowed to move along a line parallel to the x axis. The laser beam at the output of the laser was collimated and a mirror/lens arrangement insured that the beam was always focused on the surface of the material at any position of the beam. Reflection of the laser beam on the material was achieved with the help of a strip of reflective tape in the path of the scanning beam. The entire setup was automated and placed in a semianechoic chamber. For each frequency, the path was scanned with a typical step of 1 to 5 mm and the amplitude and phase of the signal were recorded at each position. Once the data were recorded, the spatial Fourier transform of the displacement profile in the vicinity of the rigid end was calculated.

B. Standing wave pattern, spatial Fourier transform and phase velocities

Figure 4 shows the standing wave patterns measured at 256, 424, and 1041 Hz, and the amplitude of their respective Fourier transforms plotted in arbitrary units. The experimental data processing scheme is the following: the spatial Fourier transform $A(k, f_j)$ of the standing wave pattern at each frequency f_j gives a continuous spectrum with maxima indicating the wave numbers $k_{i,j}^{\max}$ of the modes present in the material. The phase velocities are then simply obtained by $v = \omega / k_{i,j}^{\max}$. The phase velocities of the maxima that have been identified are indicated in Table I. The highest velocities in Table I correspond to the peaks with smaller values of wave number, but these modes can be accounted for only when their wavelengths are sufficiently smaller than the size of the sample. The differences in peak amplitudes are due to differences in the mode amplitudes and to the fact that the detection takes place in the normal direction. The modes with the highest amplitudes are those with main displacements along the y axis. The source configuration plays a role in the excitation efficiency of the modes. The source/material impedance matching is also of great importance in the uniformity of the source amplitude with frequency. The key advantages of this method are that more energy can be delivered at a given frequency and that the signals are continuous, not localized in time. Since the excitation is a continuous sine, the rigid backing of the sample is used in order to create a spatial profile of the sample surface near the reflector that does not depend on time.

However, as can be seen in Fig. 4(c), the standing wave pattern is most clearly observed near the rigid end of the sample and for higher frequencies. This can be explained by the reduced influence of the source in this area and at these frequencies. The waves are mainly propagative near the source and standing near the rigid end. In this article, the attention is focused on the detection of the spatial periodicities that appear in the standing wave field created by the reflection. At low frequencies, the waves traveling toward and reflected from the rigid end have a fairly low attenuation, and the influence of the source can extend over long distances. At higher frequencies, the attenuation is greater and higher excitation amplitudes are necessary. In practice, overheating of the source and nonlinear effects in the material near the source are limitations to the maximum amplitude applicable.

To isolate the ''standing'' part of the wave pattern near the rigid end, and to reduce the source effect, a spatial window can be used when calculating the spatial Fourier transform. This window is designed to reduce the amplitudes of the displacement profile near the source. The source effect manifests itself by the presence of dominant peaks of amplitude at low wave numbers in the spatial spectrum. The length of the spatial window should also vary when the frequency varies, as the spatial extent of the source effect changes with frequency. Because it is quite difficult yet to find a reliable guideline for applying a window at varying frequencies, the data were processed twice, with and without window; only the most certain points were retained. Thus, the dominant source effect can be filtered out to obtain the modes propagating with a small wavelength. As can be seen in Fig. 4(d), small ripples are present in the spectrum. These are a consequence of the finite sample dimensions and of the discontinuities introduced in the periodization in the numerical implementation of the Fourier transform. A second function of spatially windowing the standing wave pattern is to reduce the amplitude of these ripples.

IV. APPLICATION TO A HIGHLY POROUS MATERIAL AND FITTING OF THE COMPLEX SHEAR MODULUS AND POISSON RATIO

A. Theoretical dispersion curves

A highly porous melamine foam with a thickness of 10 cm (the material parameters are given in Table II) was studied theoretically and experimentally using the technique described in the previous section. Calculated dispersion curves for this material are presented in Fig. 5. The real parts of the phase velocities of the modes are given in Fig. 5(a) and the imaginary parts in Fig. 5(b). A shear modulus μ of 110 000 Pa, obtained from the high-frequency limit of the experimental results, and a Poisson ratio ν of 0.25 were used in the simulation. Imaginary parts of 10% of their respective real parts were added to these coefficients to simulate structural damping. The simulation includes both the Biot attenuation

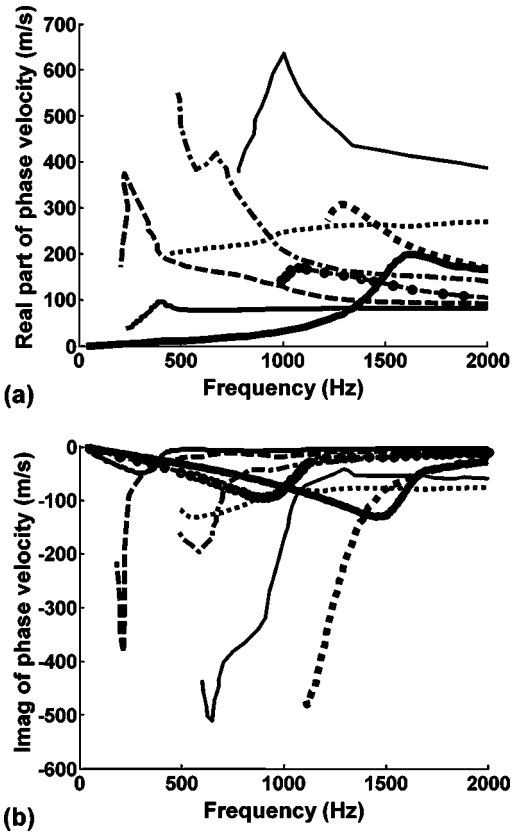

FIG. 5. Dispersion curves calculated by solving Eq. (30) numerically for a melamine foam of 0.1-m thickness. (a) Real part and (b) imaginary part of the phase velocities. The anomalous behavior of the dashed-curve mode around 250 Hz is due to numerical error.

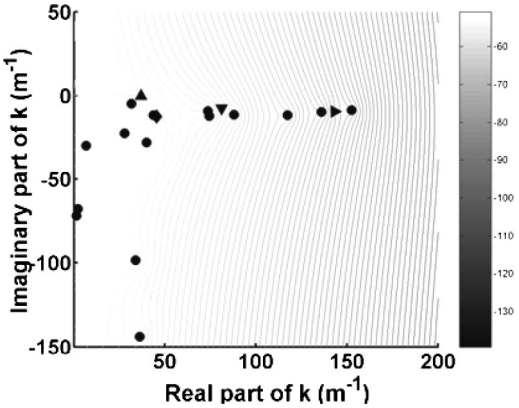

FIG. 6. Root search of Eq. (30) in the complex k plane at 2000 Hz. The spots correspond to the roots found numerically. The downward triangle, the diamond, the right and the upward triangle correspond, respectively, to the first, to the second longitudinal Biot wave number, to the transverse Biot wave numbers, and to the fluid wave number.

mechanism in a porous medium and the structural damping associated with complex Young and shear moduli. The damped modes were calculated by searching the zeros of the determinant (29) in the complex plane (no attenuation mechanism was considered in Sec. II A and undamped modes were obtained from a root search on the real axis). A simple numerical algorithm was developed that seems to give good results. The idea is to locate the maxima of the $|\mathrm{Det}(\omega,k,H,\ldots)|^{-1}$ surface in the complex k plane, which is equivalent to solving (30) but with the advantage that this function is real-valued and easier to handle. Numerically, this function can be represented by a large matrix, any value of which has a row and a column index that correspond to the discretized real and imaginary parts of k. The root search was done in a MATLAB routine where a smaller square matrix was used to ''scan'' the large matrix of data to find the local maxima. The size of this ''scanning'' matrix can be chosen so that there is only one maximum in it. The condition that the maximum found in the scanning matrix must not be on its edges must be fulfilled because it does not necessarily correspond to a local maximum of the large matrix. Several simple methods can be used to implement this condition numerically. This zero search algorithm is simple and fast enough for our study. Figure 6 shows an example of contour plot of the function $|\mathrm{Det}(\omega,k,H,\ldots)|^{-1}$ at 2000 Hz for a melamine foam as an example of root search in the complex k plane. The sign convention used for k in the numerical algorithm was $k=\mathrm{Re}(k)-i\,\mathrm{Im}(k)$, and the lower-right quadrant of the k space was used. The dots correspond to the maxima found, i.e., the roots of Eq. (30). The downward triangle, the diamond, the right- and the upward triangles are trivial solutions of Eq. (30). They correspond, respectively, to Biot's first and second compressional wave numbers, to Biot's shear wave number, and to the fluid wave number (these modes are not shown in Fig. 5). In addition, each mode was calculated separately by using a branch-following algorithm in which a root is being traced from high to low frequencies.

B. Interpretation of the theoretical results

When comparing the results with those obtained from the results of Sec. II A, in which the porous solid is considered as an effective nonporous solid, it is found that more modes exist in the porous case. This result can be associated with the existence of the fluid and solid phases. The interpretation can be made easier by considering, in a first approach, the purely theoretical case of a porous layer with a rigorously zero coupling between the two Biot waves. In such a case, one may consider two decoupled sets of guided waves in the porous layer: the structure-borne guided waves and the fluid-borne guided waves. If Biot's structure-borne bulk waves (compressional and shear) were nondispersive at all, the structure-borne set of guided modes in the layer would correspond exactly to the modes obtained from the effective solid model of Sec. II A. The new result is the possible existence of a second set of guided modes associated with Biot's fluid-borne wave. This result is a direct consequence of the addition of the term containing the scalar potential φ_2 associated with Biot's wave of the second kind in Eq. (9). Including this potential results in increasing the number of solutions for the dispersion equation and therefore the number of modes in the porous system. The porous material studied in this article is such that the coupling between the two compressional waves is weak, and so it is thought that the interpretation given above should hold for this material. However, the coupling, even though very small, always exists in real experimental conditions and it is thought that the main effect of the coupling will be the possibility for the

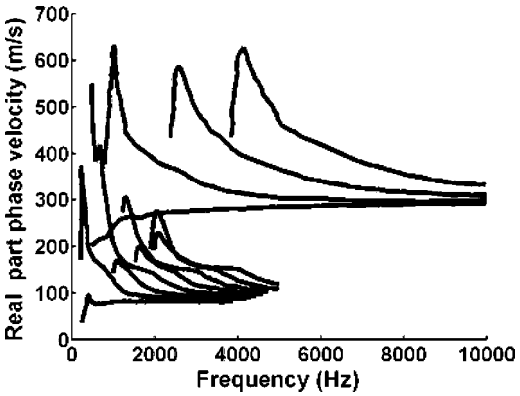

FIG. 7. Real part of the dispersion curves calculated as a function of frequency for a melamine foam of 0.1 m thickness up to 10 kHz.

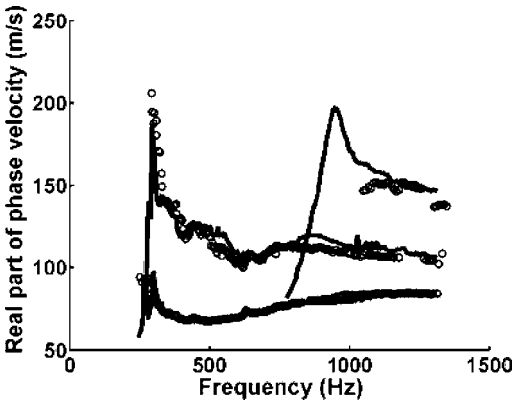

FIG. 8. Measured phase velocities (circles) and fitted modes (solid lines) for a melamine foam.

structure- and fluid-borne guided waves to exchange energy. It is difficult to envisage the detection of any of the fluid-borne modes at the moment with the current experimental setup designed to measure the displacement of the solid structure only.

Another consequence of the porous nature of the layer is the possible loss of energy by viscous and thermal interactions in the pores resulting in a higher attenuation for the guided modes in the porous material than for an equivalent elastic solid in which only structural damping is accounted for. On average and for all the modes, about 15% extra damping should be attributed to Biot's attenuation in the dispersion curves of Fig. 5. While this result holds only for the porous material studied in this article, Biot's attenuation should in general affect both the damping and the dispersion of the modes. In addition to the existence of the fluid-borne dispersion curves, the existence of a second compressional wave in a porous medium has a very interesting consequence. As frequency increases, it can be seen in Fig. 5(a) that the thin dotted line and the thin solid line tend to the velocity of the Biot wave of the second kind. In the material studied, the Biot wave of the second kind is faster than the Biot wave of the first kind at high frequencies, and is slower than the free velocity in the surrounding fluid. The curves are plotted in a wider frequency range in Fig. 7, clearly showing the two sets of dispersion curves. The shear velocity acts as asymptotic values toward which the structure-borne modes tend. While this behavior can be expected in a nonporous solid, the existence of a second velocity limit in porous media corresponding to the velocity of the Biot wave of the second kind is new. This behavior can be related to the fact that the fluid-borne modes propagate in an equivalent ''fluid plate.'' In such a plate, the shear velocity is zero and the modes tend to the bulk compressional velocity in the high-frequency limit.[30] The existence of a compressional and a shear limit velocity can also be observed in materials for which the coupling between the compressional and shear waves is small, such as in highly attenuative plastic plates.[31] The attenuation mechanisms and the presence of a loading fluid are responsible for the existence of the maxima observed in the dispersion curves of Figs. 5 and 7.

C. Fitting of the dispersion curves

The new experimental method was used to determine the phase velocities in a layer of melamine foam. The sample was set up as shown in Fig. 3 and a continuous sine excitation with frequencies varying from 150 to 1500 Hz was applied. The measurements were performed at a temperature of 21 °C and variations remained within 5% of this value. Two clear maxima could be traced throughout the measured frequency domain. These provided the velocities of the first two modes of the dispersion curves. The results are shown in Fig. 8. Several data points seem to provide evidence for the existence of a third mode. It was found that a variation in frequency of the elastic coefficients and the use of the complete porous model was needed to fit the variations of the first two modes. The solid lines indicate a fit where the shear modulus and its imaginary part were allowed to vary. The parameters for the fit are the real and imaginary parts of the shear modulus and the Poisson ratio. All other physical parameters: porosity, permeability, tortuosity, thermal and viscous characteristic lengths, were measured. Standard methods exist for the first two parameters. The last three parameters were determined using ultrasonic transmission methods (see Ref. 32 and references therein). In the fitting process, the experimental results were assumed to correspond to the first two modes (indicated by the medium thick solid line and the dashed line) of Fig. 5(a). This indirectly provided a guess for the initial value of the shear modulus as the first mode tends asymptotically to the Rayleigh velocity, which depends on the shear modulus. A separate measurement of the Rayleigh velocity at high frequency was performed on a smaller sample of the same material and was consistent with the high-frequency asymptotic limit. An initial value of 0.25 was used for the Poisson coefficient. The imaginary part of the Poisson coefficient was allowed to vary within 20% of the real part. The values obtained for the shear modulus, the Poisson coefficients, and their imaginary parts are given in Fig. 9. A variation of the shear modulus between 0.05 and 0.12 GPa was obtained in the frequency range investigated. Although the measurement error is difficult to estimate precisely, the discrepancy between the fit and the measured phase velocities gives an indication. It was noticed that the fit is less sensitive to the Poisson ratio than to the

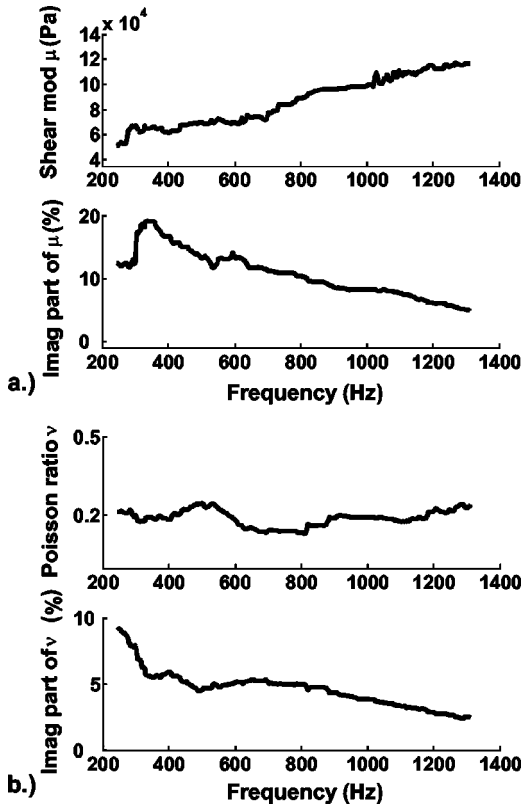

FIG. 9. Fitted real and imaginary parts of the shear modulus and Poisson ratio against frequency. The imaginary parts are plotted in percentage of the real parts.

shear modulus. As a consequence, one may consider the result to be reliable for the shear modulus while only giving an order of magnitude for the variations of the Poisson ratio.

Although precise literature values on the variation of the shear modulus for this type of highly porous foams are scarce, the values measured in this study can be compared to other measurements.[9,10] In Ref. 10, vibration measurements on this type of foam (melamine) gave a range of variation for the Young's modulus between 1.5×10^5 Pa and 2.3×10^5 Pa between 200 and 1000 Hz. Considering a real part of Poisson ratio around 0.2 [obtained from the fit in Fig. 9(b)], the corresponding range for the shear modulus is between 6.2×10^4 Pa and 9.6×10^4 Pa. In the same frequency range, the results we obtained vary between 7×10^4 Pa and 10×10^4 Pa [real part of the shear modulus in Fig. 9(a)], showing a good consistency with the results of Ref. 10 and a difference between 4% and 11%. The error on the Poisson ratio should also be added when carrying out the comparison. This type of material exhibits a non-negligible anisotropy, and the way the material is cut can explain the differences observed. However, the range of values obtained is confirmed by static tests, by the traditional lower frequency measurement methods, and by the Rayleigh wave measurement method[11] that was also performed on this material in the high-frequency limit.

V. CONCLUSION

A new experimental technique for measuring the dynamic complex shear modulus and Poisson ratio of porous materials was proposed and applied to a highly porous melamine foam. This method is based on the generation of standing waves in the layer and accounts for the dispersion of guided acoustic waves in the layer of material lying on a rigid substrate. The dispersion of the modes was also studied theoretically and new, interesting results were found on the consequences of the existence of two compressional waves in a porous material. The coupling between the two Biot compressional waves is fairly low in the material studied, and structure-borne and fluid-borne guided waves were predicted. It was also found that the velocity of the Biot compressional wave of the second kind acts as a limit velocity for the fluid-borne dispersion curves, and that a significant additional damping was induced by the inclusion of Biot's parameters in the model.

The experimental results are consistent with other measurements on this material and with the results obtained from static tests and traditional methods. Although this method allows description of a higher frequency range than the traditional methods, it is still limited by the lack of a reliable line source that can be used to excite high-frequency vibrations with sufficient amplitude. Other materials, experimental configurations, theoretical development, as well as new excitation techniques are currently being investigated. In particular, a porous layer with its two surfaces free (Lamb conditions) is being studied experimentally and theoretically. This work should allow the study of more rigid materials and the exploration of a higher frequency range.

APPENDIX:

The elements of the determinant in Eq. (29) are given by

$$
\begin{aligned}
&D_{12}=-2ikp_1,\\
&D_{14}=-2ikp_2,\\
&D_{15}=k^2-q^2,\\
&D_{21}=-2\mu p_1^2-(k^2+p_1^2)(\lambda_c+\alpha M\phi(\mu_1-1)),\\
&D_{23}=-2\mu p_2^2-(k^2+p_2^2)(\lambda_c+\alpha M\phi(\mu_2-1)),\\
&D_{26}=2ikq\mu,\\
&D_{27}=-K_f(-k^2+\gamma^2),\\
&D_{31}=(k^2+p_1^2)M(\alpha+\phi(\mu_1-1)),\\
&D_{33}=(k^2+p_2^2)M(\alpha+\phi(\mu_2-1)),\\
&D_{37}=K_f(-k^2+\gamma^2),\\
&D_{42}=p_1(1+\phi(\mu_1-1)),\\
&D_{44}=p_2(1+\phi(\mu_2-1)),\\
&D_{45}=ik(1+\phi(\mu_3-1)),\\
&D_{47}=-\gamma,\\
&D_{51}=-p_1\sin p_1H,\\
&D_{52}=p_1\cos p_1H,\\
&D_{53}=-p_2\sin p_2H,\\
&D_{54}=p_2\cos p_2H,\\
&D_{55}=ik\cos qH,\\
&D_{56}=ik\sin qH,\\
&D_{61}=-ik\cos p_1H,\\
&D_{62}=-ik\sin p_1H,\\
&D_{63}=-ik\cos p_2H,\\
&D_{64}=-ik\sin p_2H,\\
&D_{65}=-q\sin qH,\\
&D_{66}=q\cos qH,\\
&D_{71}=-\phi(\mu_1-1)p_1\sin p_1H,
\end{aligned}
$$

$$D_{72} = \phi(\mu_1 - 1)p_1 \cos p_1 H,$$
$$D_{73} = -\phi(\mu_2 - 1)p_2 \sin p_2 H,$$
$$D_{74} = \phi(\mu_2 - 1)p_2 \cos p_2 H,$$
$$D_{75} = i\phi(\mu_3 - 1)k \cos qH,$$
$$D_{76} = i\phi(\mu_3 - 1)k \sin qH.$$

[1] M. A. Biot, ''Theory of propagation of elastic waves in a fluid-saturated porous solid,'' J. Acoust. Soc. Am. **28**, 168–191 (1956).
[2] J. F. Allard, *Propagation of Sound in Porous Media: Modeling Sound Absorbing Materials* (Chapman & Hall, London, 1993).
[3] A. Bardot, B. Brouard, and J. F. Allard, ''Frame decoupling at low frequency in thin porous layers saturated by air,'' J. Appl. Phys. **79**, 8223–8229 (1996).
[4] J. F. Allard, C. Depollier, Ph. Guignouard, and P. Rebillard, ''Effect of resonance on the surface impedance of glass wool of high density and thickness,'' J. Acoust. Soc. Am. **89**, 999–1001 (1991).
[5] T. Pritz, ''Transfer function method for investigating the complex modulus of acoustic materials: Rod-like specimen,'' J. Sound Vib. **81**, 359–376 (1982).
[6] T. Pritz, ''Frequency dependence of frame dynamic characteristics of mineral and glass wool materials,'' J. Sound Vib. **106**, 161–169 (1986).
[7] T. Pritz, ''Dynamic Young's modulus, and loss factor of plastic foams for impact sound isolation,'' J. Sound Vib. **178**, 315–322 (1994).
[8] T. Pritz, ''Measurement methods of complex Poisson's ratio of viscoelastic materials,'' Appl. Acoust. **60**, 279–292 (2000).
[9] A. Sfaoui, ''On the viscoelasticity of the polyurethane foam,'' J. Acoust. Soc. Am. **97**, 1046–1052 (1995).
[10] L. Jaouen, ''Contribution à la caractérisation mécanique de matériaux poro-viscoélastiques en vibro-acoustique,'' (Contribution to the mechanical characterization of poroviscoelastic materials in vibroacoustics), Ph.D. thesis, Université de Sherbrooke, Canada, 2003.
[11] J. F. Allard, G. Jansens, G. Vermeir, and W. Lauriks, ''Frame-borne surface waves in air-saturated porous media,'' J. Acoust. Soc. Am. **111**, 690–696 (2002).
[12] J. F. Allard, M. Henry, L. Boeckx, P. Leclaire, and W. Lauriks, ''Acoustical measurement of the shear modulus for thin porous layers,'' J. Acoust. Soc. Am. (submitted).
[13] H. Deresiewicz, ''The effect of boundaries on wave propagation in a liquid-filled porous solid. IV. Surface waves in a half space,'' Bull. Seismol. Soc. Am. **52**, 627–638 (1962).
[14] S. Feng and D. L. Johnson, ''High-Frequency acoustic properties of a fluid/porous solid interface. I. New surface mode,'' J. Acoust. Soc. Am. **74**, 906–914 (1983).
[15] K. Attenborough, ''Review of ground effects on outdoor sound propagation from continuous broadband sources,'' Appl. Acoust. **24**, 289–319 (1988).
[16] K. Attenborough, ''Solid particle motion induced by a point source above a poroelastic half-space,'' J. Acoust. Soc. Am. **86**, 1085–1092 (1989).
[17] K. Attenborough and Y. Chen, ''Surface waves at an interface between air and an air-filled poroelastic ground,'' J. Acoust. Soc. Am. **87**, 1010–1016 (1990).
[18] W. Lauriks, L. Kelders, and J. F. Allard, ''Surface waves and leaky waves above a porous layer,'' Wave Motion **28**, 57–67 (1998).
[19] L. Kelders, W. Lauriks, and J. F. Allard, ''Surface waves above thin porous layers saturated by air at ultrasonic frequencies,'' J. Acoust. Soc. Am. **104**, 882–889 (1998).
[20] J. F. Allard, M. Henry, C. Glorieux, S. Petillion, and W. Lauriks, ''Laser-induced surface modes at an air-porous medium interface,'' J. Appl. Phys. **93**, 1298–1304 (2003).
[21] L. Boeckx, P. Leclaire, C. Glorieux, W. Lauriks, and J. F. Allard, ''Measuring the dynamic shear modulus of poroelastic foams in the audible frequency range,'' in Proceedings International Congress in Acoustics, Kyoto, 4–9 April 2004.
[22] D. E. Chimenti, ''Guided waves in plates and their use in materials characterization,'' Appl. Mech. Rev. **50**, 247–284 (1997).
[23] D. Royer, and E. Dieulesaint, *Elastic Waves in Solids: Free and Guided Propagation* (Springer, Berlin, 1999), Vol. 1.
[24] I. A. Viktorov, *Rayleigh and Lamb Waves* (Plenum, New York, 1967).
[25] W. M. Ewing, W. S. Jardetsky, and F. Press, *Elastic Waves in Layered Media* (McGraw-Hill, New York, 1957).
[26] V. Gusev and P. Hess, ''Theory of photothermal depth profiling via Rayleigh-type surface-acoustic-wave detection,'' Appl. Phys. A: Mater. Sci. Process. **61**, 299–310 (1995).
[27] K. Van de Rostyne, ''Laser ultrasonic study of wave propagation at fluid–solid interfaces,'' Ph.D. thesis, Katholieke Universiteit Leuven, Belgium, 2001.
[28] M. A. Biot, ''Mechanics of deformation and acoustic propagation in porous media,'' J. Appl. Phys. **33**, 1482–1498 (1962).
[29] M. A. Biot and D. G. Willis, ''The elastic coefficients of the theory of consolidation,'' J. Appl. Mech. **24**, 594–601 (1957).
[30] H. Überall, B. Hosten, M. Deschamps, and A. Gérard, ''Repulsion of phase-velocity dispersion curves and the nature of plate vibrations,'' J. Acoust. Soc. Am. **96**, 908–917 (1994).
[31] C. W. Chan and P. Cawley, ''Lamb waves in highly attenuative plastic plates,'' J. Acoust. Soc. Am. **104**, 874–881 (1998).
[32] P. Leclaire, L. Kelders, W. Lauriks, M. Melon, N. Brown, and B. Castagnède, ''Determination of the viscous and thermal characteristic lengths of plastic foams by ultrasonic measurements in helium and air,'' J. Appl. Phys. **80**, 2009–2012 (1996).

Reconstruction of vibroacoustic fields in half-space by using hybrid near-field acoustical holography

Xiang Zhao and Sean F. Wu
Department of Mechanical Engineering, Wayne State University, Detroit, Michigan 48202

(Received 31 October 2003; revised 5 October 2004; accepted 23 November 2004)

In this paper we examine the accuracy and efficiency of reconstructing the vibroacoustic quantities generated by a vibrating structure in half-space by using hybrid near-field acoustic holography (NAH) and modified Helmholtz equation least squares (HELS) formulations. In hybrid NAH, we combine modified HELS with an inverse boundary element method (IBEM) to reconstruct a vibroacoustic field. The main advantage of this approach is that the majority of the input data can be regenerated but not measured, thus the efficiency is greatly enhanced. In modified HELS, we expand the field acoustic pressure in terms of outgoing and incoming spherical waves and specify the corresponding expansion coefficients by solving a system of equations obtained by matching the assumed-form solution to the measured acoustic pressure. Here the system of equations is ill conditioned and Tikhonov regularization is implemented through singular value decomposition (SVD) and the generalized cross-validation (GCV) method. Numerical examples of a dilating and oscillating spheres and finite cylinder are demonstrated. Test results show that hybrid NAH can yield a more accurate reconstruction than does a modified HELS, but a modified HELS is more efficient than is hybrid NAH [Work supported by NSF].
[DOI: 10.1121/1.1847994]

PACS numbers: 43.20.Rz, 43.35.Sx, 43.50.Yw [EGW] Pages: 555–565

I. INTRODUCTION

Near-field acoustic holography (NAH) has made significant progress over the past two decades in reconstructing the vibroacoustic quantities generated by an arbitrary structure in a free field. Currently, there are three basic approaches in NAH: (1) Fourier acoustics,[1–3] which is suitable for separable geometry such as an infinite plane and cylinder, and a sphere; (2) the inverse boundary element method (IBEM) that can handle arbitrary geometry and has no restriction on measurement locations;[4–12] and (3) the Helmholtz equation least squares (HELS) method[13–18] that can handle arbitrary geometry and requires fewer input data than does IBEM. However, HELS is not ideal for a highly irregular surface due to a slow convergence of an expansion solution. To improve the accuracy and efficiency of reconstruction, a combined Helmholtz equation-least squares (CHELS)[19] is developed that combines the advantages of HELS and IBEM. However, in CHELS measurements must be taken on a hypothetical spherical surface. Thus, for arbitrary source geometry the accuracy of measurement may be inconsistent and the reconstruction may not be satisfactory.

Recently, hybrid NAH[20] is developed for reconstructing the vibroacoustic quantities generated by an arbitrary object. This hybrid NAH is based on a modified HELS formulation that expands the acoustic pressure in terms of both outgoing and incoming spherical waves. Since hybrid NAH allows for the measurement and regeneration of the acoustic pressure over a conformal surface at close range to an arbitrary source surface, the evanescent waves can be captured and the reconstruction accuracy and efficiency be enhanced.

All NAH approaches developed thus far has focused on an unbounded exterior region or an enclosed interior region. In practice, most vibrating structures are mounted on a solid foundation or close to reflecting surfaces with finite surface acoustic impedance. For NAH to become an effective and robust diagnostic tool, the effect of acoustic pressure reflection from nearby surfaces must be considered.

As a starting point, we consider the reconstruction of the vibroacoustic field generated by a finite object above an infinite, rigid baffle so that the benchmark data can be generated numerically without too much difficulty. In particular, we want to examine the efficiency and accuracy of reconstruction given by hybrid NAH and modified HELS formulations. In Secs. II–V we provide overviews of helmholtz integral formulations for half-space, modified HELS, hybrid NAH, and the regularization and parameter choice method. In Sec. VI we depict a test setup and examples and discuss the test results. Conclusions are drawn in Sec. VII.

II. BOUNDARY INTEGRAL FORMULATION FOR HALF-SPACE

Consider acoustic radiation with time dependence $e^{-i\omega t}$ from a vibrating object in the domain Ω bounded by an infinite baffle S_0 at a constant frequency. The effect of this baffle is accounted for by using the image source theory, and the acoustic pressure anywhere in Ω is expressed as the sum of contributions from the source and its image, which is conveniently expressed by using the half-space Green's function,[21]

$$G_H(\mathbf{x}|\mathbf{x}_S;\omega)=\frac{e^{ikR}}{R}+\beta\frac{e^{ikR'}}{R'}, \tag{1}$$

where $R=|\mathbf{x}-\mathbf{x}_S|$ is the distance between a field point $\mathbf{x}\in\Omega$ and a surface point $\mathbf{x}_S\in S$, $R'=|\mathbf{x}-\mathbf{x}_S'|$ the distance between $\mathbf{x}$ and its mirror image $\mathbf{x}_S'$ of $\mathbf{x}_S$ (see Fig. 1), $k=\omega/c$ is the

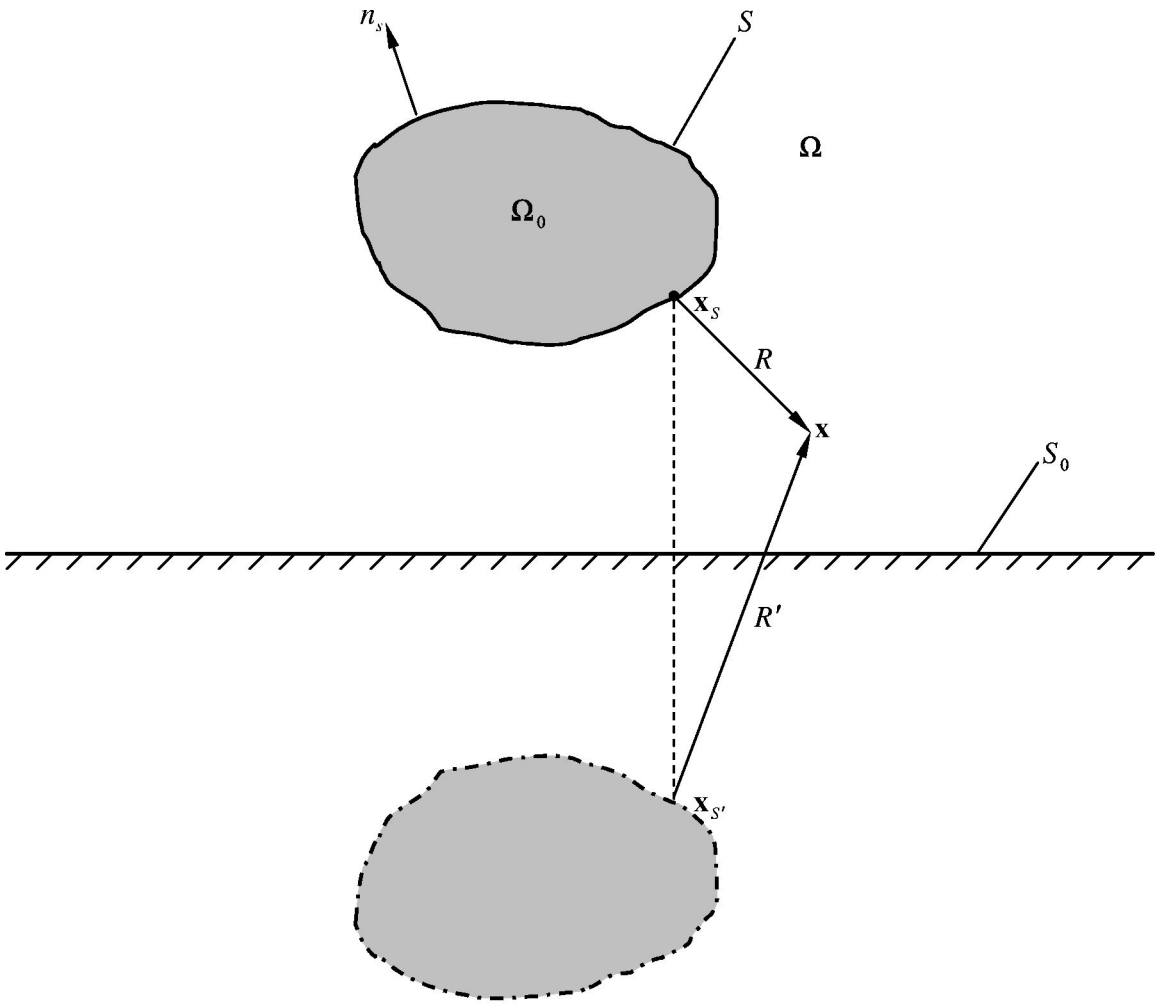

FIG. 1. Image method for acoustic radiation from a vibrating body in half-space.

acoustic wave number with c being the speed of sound of the fluid medium and ω being the angular frequency. The acoustic pressure reflection coefficient β is equal to 1 if a baffle is a rigid surface and -1 if it is a pressure-release surface. For a baffle with finite acoustic impedance, there is no closed-form solution for the half-space Green's function and Eq. (1) is a good approximation only when $\mathbf{x}$ is at least one-half wavelength away from the baffle.[21]

Substituting the half-space Green's function (1) in the Helmholtz integral formulation yields an integral formulation for the field acoustic pressure,[22]

$$C_0(\mathbf{x})p(\mathbf{x};\omega)=\frac{1}{4\pi}\int\int_S\left[p(\mathbf{x}_S;\omega)\frac{\partial G_H(\mathbf{x}|\mathbf{x}_S;\omega)}{\partial n_S}-i\omega\rho_0 v(\mathbf{x}_S;\omega)G_H(\mathbf{x}|\mathbf{x}_S;\omega)\right]dS, \quad (2)$$

where n_S is the unit normal pointing into Ω, $C_0(\mathbf{x})$ is unit for $\mathbf{x}\in\Omega$, zero for $\mathbf{x}\in\Omega_0$, and one-half for $\mathbf{x}_S\in S$, provided there is a unique tangent to S at $\mathbf{x}_S$. A general formulation for $C_0(\mathbf{x})$, including the case in which $\mathbf{x}_S$ may be located at an edge or corner of S, is[23]

$$C_0(\mathbf{x})=1+\frac{1}{4\pi}\int\int_S\frac{\partial}{\partial n_S}\left(\frac{1}{R}\right)dS. \quad (3)$$

Note that the singularity of the integrand in Eq. (3) can be circumvented by using the Cauchy principal value, and the evaluation of the integrals in Eq. (2) is no more complex than it is for a free-space case. Although there is a slight increase in the computer time needed to evaluate integrals in Eq. (2), this increase is more than offset by the computer time saved in not requiring evaluations of the integrals over the entire baffle surface.

III. MODIFIED HELS

The HELS formulation[14] can be modified to include contributions from the incoming waves. This is especially important in describing the acoustic pressure field radiated from a finite object in a region bounded by some reflecting surfaces:

$$p(\mathbf{x};\omega)=\sum_{j=1}^{J}\left[C_j(\omega)\Psi_j^{(1)}(\mathbf{x};\omega)+D_j(\omega)\Psi_j^{(2)}(\mathbf{x};\omega)\right], \quad (4)$$

where $\Psi_j^{(1)}(\mathbf{x};\omega)$ and $\Psi_j^{(2)}(\mathbf{x};\omega)$ are the particular solutions to the Helmholtz equation and can be written under the spherical coordinates as

$$\Psi_j^{(1)}(\mathbf{x};\omega)\equiv\Psi_{nl}^{(1)}(r,\theta,\phi;\omega)=h_n^{(1)}(kr)Y_n^l(\theta,\phi), \quad (5a)$$

$$\Psi_j^{(2)}(\mathbf{x};\omega)\equiv\Psi_{nl}^{(2)}(r,\theta,\phi;\omega)=h_n^{(2)}(kr)Y_n^l(\theta,\phi), \quad (5b)$$

where $h_n^{(1)}(kr)$ and $h_n^{(2)}(kr)$ represent the spherical Hankel functions of order n of the first and second kinds, respectively, and $Y_n^l(\theta,\phi)$ are the spherical harmonics. The indices j, n, and l in Eq. (5) are related through $j=n^2+n+l+1$ with n starting from 0 to N and l varying from $-n$ to $+n$. Thus, for each n and l we have $j=1$ to J, where J implies the maximum number of expansion terms $J=(N+1)^2$.

Physically, the terms on the right side of Eq. (4) represent the outgoing and incoming spherical waves, respectively. The expansion solution given by (4) is complete and uniformly convergent when $j\to\infty$.[24] However, such a series expansion cannot be realized in practice. So we utilize a finite expansion (4) to approximate the acoustic pressure in Ω, including the source surface S and reflecting boundary surface S_0. For convenience sake, let us rewrite Eq. (4) in a matrix form to describe the acoustic pressure on a source surface,

$$\mathbf{p}(\mathbf{x}_S;\omega)=\boldsymbol{\Psi}(\mathbf{x}_S;\omega)\hat{\mathbf{C}}(\omega), \quad (6)$$

where $\mathbf{p}(\mathbf{x}_S;\omega)$ represents a column vector containing acoustic pressure on a source surface, $\boldsymbol{\Psi}(\mathbf{x}_S;\omega)$ and $\hat{\mathbf{C}}(\omega)$ imply the matrix and column vector, respectively, that are defined by

$$\boldsymbol{\Psi}(\mathbf{x}_S;\omega)=\begin{bmatrix} \Psi_1^{(1)}(\mathbf{x}_1;\omega) & \Psi_1^{(2)}(\mathbf{x}_1;\omega) & \Psi_2^{(1)}(\mathbf{x}_1;\omega) & \Psi_2^{(2)}(\mathbf{x}_1;\omega) & \cdots & \Psi_J^{(1)}(\mathbf{x}_1;\omega) & \Psi_J^{(2)}(\mathbf{x}_1;\omega) \\ \Psi_1^{(1)}(\mathbf{x}_2;\omega) & \Psi_1^{(2)}(\mathbf{x}_2;\omega) & \Psi_2^{(1)}(\mathbf{x}_2;\omega) & \Psi_2^{(2)}(\mathbf{x}_2;\omega) & \cdots & \Psi_J^{(1)}(\mathbf{x}_2;\omega) & \Psi_J^{(2)}(\mathbf{x}_2;\omega) \\ \vdots & \vdots & \vdots & \vdots & \ddots & \vdots & \vdots \\ \Psi_1^{(1)}(\mathbf{x}_\zeta;\omega) & \Psi_1^{(2)}(\mathbf{x}_\zeta;\omega) & \Psi_2^{(1)}(\mathbf{x}_\zeta;\omega) & \Psi_2^{(2)}(\mathbf{x}_\zeta;\omega) & \cdots & \Psi_J^{(1)}(\mathbf{x}_\zeta;\omega) & \Psi_J^{(2)}(\mathbf{x}_\zeta;\omega) \end{bmatrix} \quad (7a)$$

$$\hat{\mathbf{C}}(\omega)=\{C_1,D_1,C_2,D_2,\ldots,C_J,D_J\}^T, \quad (7b)$$

where a subscript ζ implies the total number of reconstruction points and a superscript T represents a transposition.

Next, we match the assumed-form solution (4) to the acoustic pressure measured on a hypothetical conformal surface Γ that encloses the source at close range,

$$\boldsymbol{\Psi}(\mathbf{x}^\Gamma;\omega)\hat{\mathbf{C}}(\omega)=\mathbf{p}(\mathbf{x}^\Gamma;\omega), \quad (8)$$

where $\mathbf{x}^\Gamma=\{x_m^\Gamma\}^T\in\Gamma$, $m=1$ to M_0. Note that, in general, $M_0>2J$; thus Eq. (8) becomes an overdetermined system of equations.

To derive a general formulation for projecting acoustic pressure back toward a source surface S, we first solve Eq. (6) for the expansion coefficients $\hat{\mathbf{C}}(\omega)$

$$\hat{\mathbf{C}}(\omega)=\boldsymbol{\Psi}(\mathbf{x}_S;\omega)^\dagger\mathbf{p}(\mathbf{x}_S;\omega), \quad (9)$$

where $\boldsymbol{\Psi}(\mathbf{x}_S;\omega)^\dagger=(\boldsymbol{\Psi}(\mathbf{x}_S;\omega)^H\boldsymbol{\Psi}(\mathbf{x}_S;\omega))^{-1}\boldsymbol{\Psi}(\mathbf{x}_S;\omega)^H$ is a pseudo-inversion of $\boldsymbol{\Psi}(\mathbf{x}_S;\omega)$; here a superscript H indicates a conjugate transpose. Substituting Eq. (9) into (8) then yields

$$\mathbf{G}_p(\mathbf{x}^\Gamma|\mathbf{x}_S;\omega)\mathbf{p}(\mathbf{x}_S;\omega)=\mathbf{p}(\mathbf{x}^\Gamma;\omega), \quad (10)$$

where $\mathbf{G}_p(\mathbf{x}^\Gamma|\mathbf{x}_S;\omega)=\boldsymbol{\Psi}(\mathbf{x}^\Gamma;\omega)\boldsymbol{\Psi}(\mathbf{x}_S;\omega)^\dagger$ is the transfer matrix that correlates $\mathbf{p}(\mathbf{x}^\Gamma;\omega)$ on Γ to $\mathbf{p}(\mathbf{x}_S;\omega)$ on S. The solution to Eq. (10) can be written as

$$\mathbf{p}(\mathbf{x}_S;\omega)=\mathbf{G}_p(\mathbf{x}^\Gamma|\mathbf{x}_S;\omega)^\dagger\mathbf{p}(\mathbf{x}^\Gamma;\omega). \quad (11)$$

Similarly, we derive a formulation correlating the normal surface velocity $\nu(\mathbf{x}_S;\omega)$ to the measured acoustic pressure on Γ. To this end, we apply the Euler's equation to Eq. (6) on a source surface S,

$$\mathbf{v}(\mathbf{x}_S;\omega)=\boldsymbol{\Phi}(\mathbf{x}_S;\omega)\hat{\mathbf{C}}(\omega), \quad (12)$$

where $\boldsymbol{\Phi}(\mathbf{x}_S;\omega)=(1/i\omega\rho_0)\partial\boldsymbol{\Psi}(\mathbf{x}_S;\omega)/\partial n_S$. Taking a pseudo-inversion in (12), we obtain

$$\hat{\mathbf{C}}(\omega)=\boldsymbol{\Phi}(\mathbf{x}_S;\omega)^\dagger\mathbf{v}(\mathbf{x}_S;\omega), \quad (13)$$

where $\boldsymbol{\Phi}(\mathbf{x}_S;\omega)^\dagger=(\boldsymbol{\Phi}(\mathbf{x}_S;\omega)^H\boldsymbol{\Phi}(\mathbf{x}_S;\omega))^{-1}\boldsymbol{\Phi}(\mathbf{x}_S;\omega)^H$. Substituting Eq. (13) into (8) leads to

$$\mathbf{G}_\nu(\mathbf{x}^\Gamma|\mathbf{x}_S;\omega)\mathbf{v}(\mathbf{x}_S;\omega)=\mathbf{p}(\mathbf{x}^\Gamma;\omega), \quad (14)$$

where $\mathbf{G}_\nu(\mathbf{x}^\Gamma|\mathbf{x}_S;\omega)=\boldsymbol{\Psi}(\mathbf{x}^\Gamma;\omega)\boldsymbol{\Phi}(\mathbf{x}_S;\omega)^\dagger$ is the transfer matrix for reconstructing the normal surface velocity based on the acoustic pressure measured on Γ. The solution for the normal surface velocity $\mathbf{v}(\mathbf{x}_S;\omega)$ can then be written as

$$\mathbf{v}(\mathbf{x}_S;\omega)=\mathbf{G}_\nu(\mathbf{x}^\Gamma|\mathbf{x}_S;\omega)^\dagger\mathbf{p}(\mathbf{x}^\Gamma;\omega). \quad (15)$$

IV. HYBRID NAH

The Helmholtz integral formulations are suitable for reconstructing acoustic radiation from an arbitrary structure. Since these integral formulations are implemented via BEM, this approach is known as inverse BEM or IBEM. One major disadvantage of IBEM is that the number of discrete nodes required for describing the vibroacoustic quantities on an arbitrary source surface may be large, which necessitates taking a large number of acoustic pressure measurements and making a reconstruction process time consuming and costly. On the other hand, the modified HELS formulations can handle arbitrary geometry with relatively fewer measurements than does IBEM, but the reconstruction accuracy may be low, owing to a slow convergence of an expansion solution.

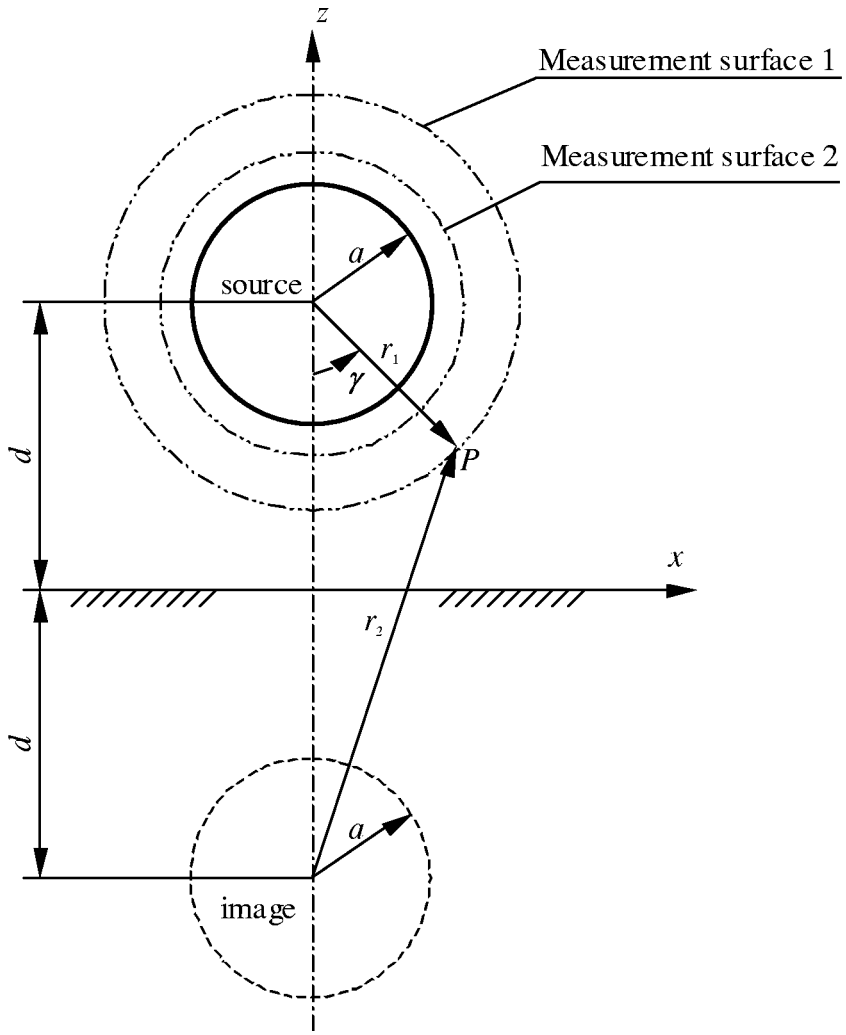

FIG. 2. Schematic of acoustic pressure measurements over a vibrating sphere in half-space.

Hybrid NAH combines the advantages of IBEM and modified HELS by replacing the majority of the input data required by IBEM with those regenerated by modified HELS, thus greatly reducing the reconstruction time yet without sacrificing too much its accuracy. This feature of hybrid NAH is illustrated in Ref. 20 for reconstructing vibroacoustic quantities in a free field. Here we extend hybrid NAH to the reconstruction of vibroacoustic quantities in half-space. The procedures of hybrid NAH are as follows. First, we take measurements of acoustic pressure $p(\mathbf{x}^{\Gamma};\omega)$ on a conformal surface around a source and use half of the measured data to solve Eq. (8) for the coefficients $\hat{C}_j(\omega)$, $j=1$ to $2J$ $(2J<M_0=M/2)$. Next, we optimize the number of expansion terms by minimizing the residue of reconstructed acoustic pressures with respect to the measured data. This process can be expressed mathematically as

$$\min_{\hat{C}_1,\hat{C}_2,\ldots,\hat{C}_J} \|p_J(\mathbf{x}^{\Gamma};\omega)-p(\mathbf{x}^{\Gamma};\omega)\|_2, \quad \mathbf{x}^{\Gamma}=\{x_m^{\Gamma}\}^T\in\Gamma,$$

$$x_m^{\Gamma}\in\Gamma, \quad m=1 \text{ to } M/2, \tag{16a}$$

$$\min_J \|p_J(\mathbf{x}^{\Gamma};\omega)-p(\mathbf{x}^{\Gamma};\omega)\|_2, \quad \mathbf{x}^{\Gamma}=\{x_m^{\Gamma}\}^T\in\Gamma,$$

$$x_m^{\Gamma}\in\Gamma, \quad m=1 \text{ to } M. \tag{16b}$$

Note that if measurements are taken over two conformal surfaces separated by a small distance, one can use Eq. (16a) to solve the expansion coefficients with respect to the outer layer and Eq. (16b) to determine the value of J_{op} with respect to all the measured data. The value of J_{op} is optimized with respect to a particular set of measurements and may change with the frequency. Once the optimal expansion functions are specified, we can regenerate as much acoustic pressure on Γ as necessary. The errors in the regenerated data are of the same order as those of measured ones since the acoustic pressure is regenerated on a measurement surface and the residue is minimized by Eq. (16). Consequently, there is no need to take more measurements than necessary.

Suppose that we employ BEM to implement the Helmholtz integral formulation (2) and discretize the surface of a vibrating object into elements with a total of N_0 nodes. Then we can correlate the surface acoustic pressure and normal surface velocity on these N_0 nodes to the measured acoustic pressure through the following matrix equations:[20]

$$\mathbf{T}_p(\mathbf{x}_i^{\Gamma}|\mathbf{x}_S;\omega)\mathbf{p}(\mathbf{x}_S;\omega)=\mathbf{p}(\mathbf{x}_i^{\Gamma};\omega), \tag{17a}$$

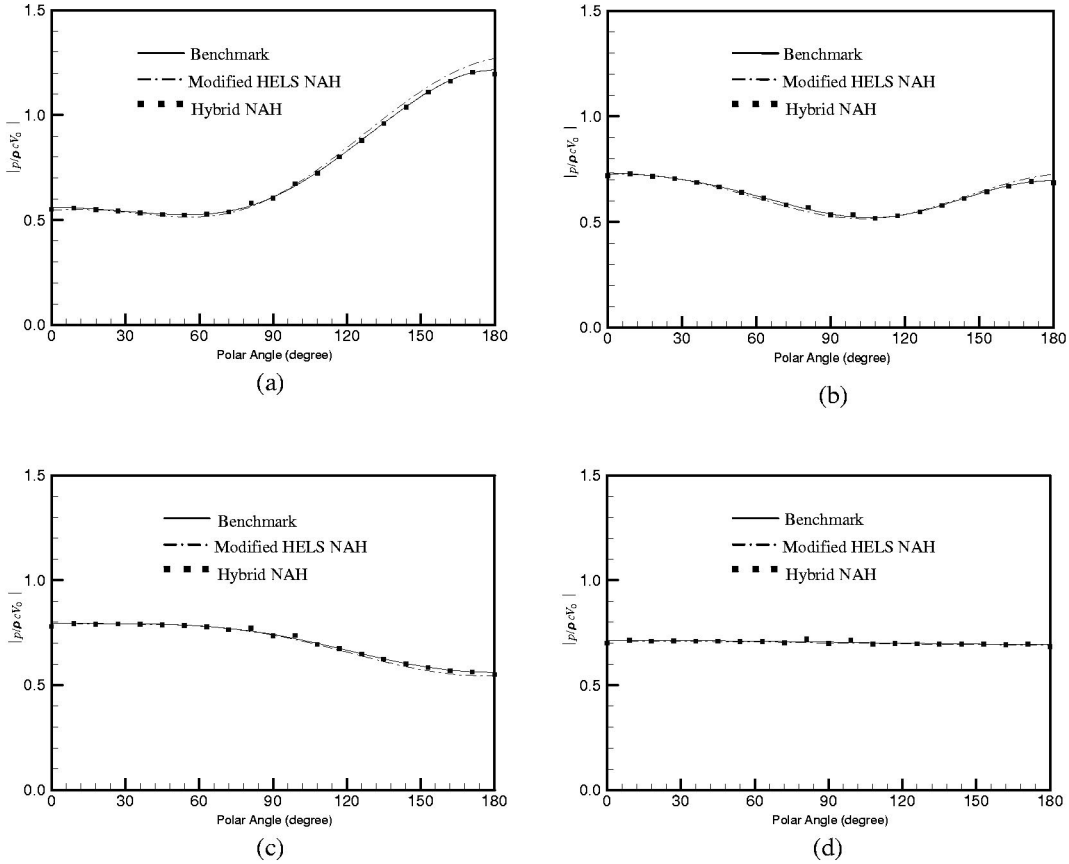

FIG. 3. A comparison of the reconstructed acoustic pressure distributions on the surface of a dilating sphere at $ka=1$. (a) $d=1.5a$; (b) $d=2a$; (c) $d=3a$; (d) $d=50a$.

$$\mathbf{T}_v(\mathbf{x}_i^\Gamma|\mathbf{x}_S;\omega)\mathbf{v}(\mathbf{x}_S;\omega)=\mathbf{p}(\mathbf{x}_i^\Gamma;\omega), \tag{17b}$$

where $\mathbf{x}_i^\Gamma=\{x_i^\Gamma\}\in\Gamma$, $i=1$ to N_0, $\mathbf{T}_p(\mathbf{x}_i^\Gamma|\mathbf{x}_S;\omega)$ and $\mathbf{T}_v(\mathbf{x}_i^\Gamma|\mathbf{x}_S;\omega)$ are given, respectively, by

$$\begin{aligned}\mathbf{T}_p(\mathbf{x}_i^\Gamma|\mathbf{x}_S;\omega)=(4\pi)^{-1}\{&\mathbf{D}(\mathbf{x}_i^\Gamma|\mathbf{x}_S;\omega)\\&+\mathbf{M}(\mathbf{x}_i^\Gamma|\mathbf{x}_S;\omega)\mathbf{M}(\mathbf{x}_{S'}|\mathbf{x}_S;\omega)^{-1}[2\pi\mathbf{I}\\&-\mathbf{D}(\mathbf{x}_{S'}|\mathbf{x}_S;\omega)]\},\end{aligned} \tag{18a}$$

$$\begin{aligned}\mathbf{T}_v(\mathbf{x}_i^\Gamma|\mathbf{x}_S;\omega)=-(4\pi)^{-1}\{&\mathbf{D}(\mathbf{x}_i^\Gamma|\mathbf{x}_S;\omega)[2\pi\mathbf{I}\\&-\mathbf{D}(\mathbf{x}_{S'}|\mathbf{x}_S;\omega)]^{-1}\mathbf{M}(\mathbf{x}_{S'}|\mathbf{x}_S;\omega)\\&+\mathbf{M}(\mathbf{x}_i^\Gamma|\mathbf{x}_S;\omega)\},\end{aligned} \tag{18b}$$

where $\mathbf{M}(\mathbf{x}_i^\Gamma|\mathbf{x}_S;\omega)$ and $\mathbf{D}(\mathbf{x}_i^\Gamma|\mathbf{x}_S;\omega)$ indicate the effects of monopoles and dipoles on a field point, respectively; whereas $\mathbf{M}(\mathbf{x}_{S'}|\mathbf{x}_S;\omega)$ and $\mathbf{D}(\mathbf{x}_{S'}|\mathbf{x}_S;\omega)$ implies the effects of monopoles and dipoles on a surface point, respectively.

In general, the number of discrete nodes N_0 needed to describe the vibroacoustic quantities on an arbitrarily shaped source surface can be very large. Accordingly, the amount of measurements required may be large, which makes the reconstruction process very time consuming and complex. The advantage of hybrid NAH is that we only need to take a finite number of measurements, say, M ($M\ll N_0$), and then use Eq. (16) to determine an optimal set of the expansion functions and to regenerate all N_0 input data. Reference 20 demonstrates an example in which the acoustic pressures reconstructed on an arbitrarily shaped engine by using IBEM are compared with those reconstructed by using hybrid NAH. Results illustrate that both methods produced the same level of accuracy in reconstruction, but hybrid NAH needed half as much as the input data required by IBEM. When the same (reduced) input data were used in IBEM, the reconstructed acoustic pressures became greatly distorted.

Using hybrid NAH with a finite number of measurements of acoustic pressures on the surface Γ, we can then regenerate as much acoustic pressures as necessary:

$$\mathbf{p}(\mathbf{x}_i^\Gamma;\omega)=\boldsymbol{\Psi}(\mathbf{x}_i^\Gamma;\omega)\boldsymbol{\Psi}(\mathbf{x}^\Gamma;\omega)^\dagger\mathbf{p}(\mathbf{x}^\Gamma;\omega), \tag{19}$$

where $\boldsymbol{\Psi}(\mathbf{x}^\Gamma;\omega)^\dagger=(\boldsymbol{\Psi}(\mathbf{x}^\Gamma;\omega)^H\boldsymbol{\Psi}(\mathbf{x}^\Gamma;\omega))^{-1}\boldsymbol{\Psi}(\mathbf{x}^\Gamma;\omega)^H$, $\mathbf{x}^\Gamma=\{x_m^\Gamma\}^T\in\Gamma$, $m=1$ to $M/2$, and $\mathbf{x}_i^\Gamma=\{x_i^\Gamma\}\in\Gamma$, $i=1$ to N_0. Since $M\ll N_0$, the measurement complexities are significantly reduced and the reconstruction efficiency is greatly enhanced.

V. REGULARIZATION

Equation (17) is the discretized Fredholm integral equation of the first kind, which is mathematically ill posed when source terms under the integral sign are sought, based on the input given on the right side.[25,26] Similarly, the matrix equations (10) and (14) derived in the modified HELS for reconstructing the vibroacoustic quantities on an arbitrary source surface are ill conditioned. Therefore it is very difficult, if possible at all, to solve these equations by taking a pseudo-

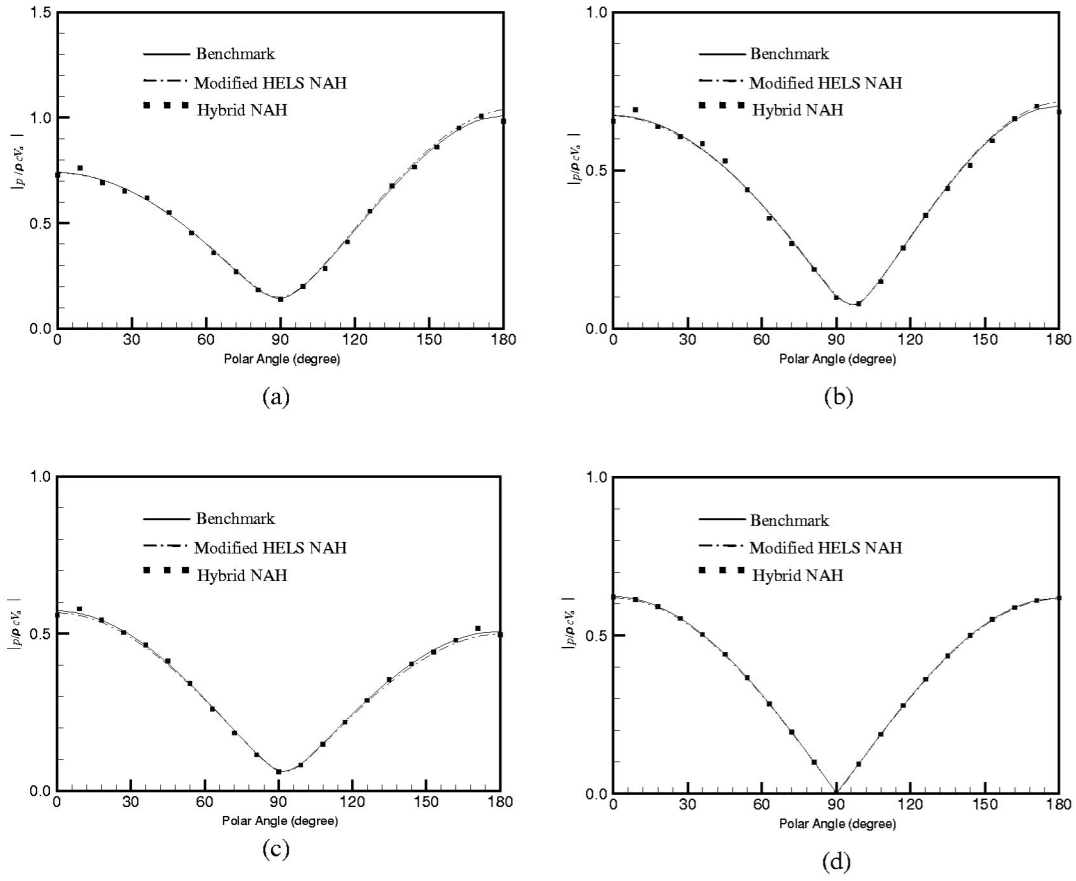

FIG. 4. A comparison of the reconstructed acoustic pressure distributions on the surface of an oscillating sphere at $ka=1$. (a) $d=1.5a$; (b) $d=2a$; (c) $d=3a$; (d) $d=50a$.

inversion to get a satisfactory reconstruction. To overcome this difficulty, we must regularize the transfer matrices $\mathbf{G}_p$, $\mathbf{G}_v$, $\mathbf{T}_p$, and $\mathbf{T}_v$. In this study we choose to use a modified Tikhonov regularization (TR)[27,28] implemented by SVD together with a parameter choice method of GCV.[29]

$$J_\alpha(\mathbf{q})=\|\mathbf{Hq}-\mathbf{p}\|_2^2+\alpha\|\mathbf{Lq}\|_2^2, \tag{20}$$

where $\mathbf{q}$ is the vector that stands for the source field to be reconstructed, for example, surface acoustic pressure or normal surface velocity, which depends on the regularization parameter α, $\mathbf{p}$ is the vector representing the measured acoustic pressures, $\mathbf{H}$ is a (Hermitian) transfer matrix relating $\mathbf{p}$ to $\mathbf{q}$, and $\mathbf{L}$ is the weighting function matrix used to suppress evanescent waves in reconstruction. If $\mathbf{L}$ is an identify matrix, all singular values will be weighted equally. In most cases, however, only small singular values that represent evanescent waves will cause distortion in reconstruction. So the matrix $\mathbf{L}$ needs to be selected properly to achieve an optimal result.[30] Accordingly, we can write $\mathbf{q}$,

$$\mathbf{q}=\mathbf{V}\mathbf{F}^\alpha\mathbf{\Sigma}^{-1}\mathbf{U}^H\mathbf{p}, \tag{21}$$

where $\mathbf{U}$ and $\mathbf{V}$ are the unitary matrices that contain the left and right singular vectors of the transfer matrix $\mathbf{H}$, respectively, $\mathbf{\Sigma}$ is the diagonal matrix that contains the singular values of $\mathbf{H}$, and $\mathbf{F}^\alpha$ is the diagonal matrix that acts as the low-pass filter in the modified TR devised to eliminate the high wave numbers:

$$\mathbf{F}^\alpha=\mathrm{diag}\left(\ldots,\frac{\sigma_j^2(\alpha+\sigma_j^2)^2}{\alpha^3+\sigma_j^2(\alpha+\sigma_j^2)^2},\ldots\right), \tag{22}$$

where σ_j is the jth singular value of transfer matrix $\mathbf{H}$, and the regularization parameter α is determined by GCV through a minimization process,

$$\min_\alpha\left(\frac{\|\mathbf{F}_h^\alpha\mathbf{U}^H\mathbf{p}\|_2^2}{[\mathrm{Tr}(\mathbf{F}_h^\alpha)]^2}\right), \tag{23}$$

where $\mathbf{F}_h^\alpha$ implies a high-pass filter for the modified TR, given by

$$\mathbf{F}_h^\alpha\equiv\mathbf{I}-\mathbf{F}^\alpha=\mathrm{diag}\left(\ldots,\frac{\alpha^3}{\alpha^3+\sigma_j^2(\alpha+\sigma_j^2)^2},\ldots\right), \tag{24}$$

where $\mathbf{I}$ represents an identify matrix.

There are two points that need to be cleared in carrying out regularization. The first is that in modified HELS formulations (10) and (14), the number of measurements M is not always equal to that of reconstruction points ζ. In many cases, it is a good idea to take more measurements than reconstruction points, i.e., $M>\zeta$. This is true especially when we want to focus on some "hot spots" to acquire a detailed visualization of the vibroacoustic field on a source surface, which is a unique feature of HELS. Under this condition, one can simply fill the null space of the high-pass filter by unity,

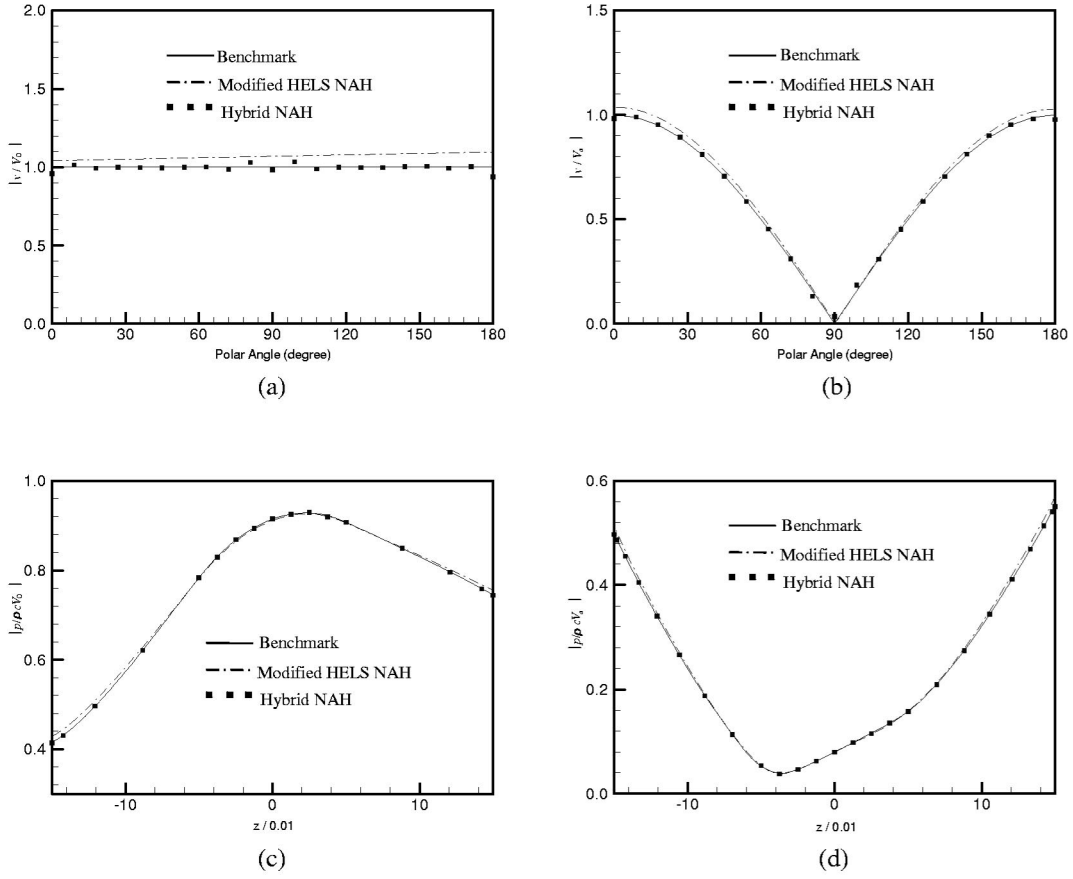

FIG. 5. A comparison of the reconstructed acoustic quantities on the surface of a sphere and a cylinder with $b/a=0.5$ at $ka=1$ and $d=3a$. (a) Normal surface velocity of a dilating sphere; (b) normal surface velocity of an oscillating sphere; (c) surface acoustic pressure of a dilating cylinder; (d) surface acoustic pressure of an oscillating cylinder.

$$\mathbf{F}_h^{\alpha}=\mathrm{diag}(\mathbf{F}_h^{\alpha},\mathbf{I})_{M\times\zeta}, \tag{25}$$

where the dimensions of matrices $\mathbf{F}_h^{\alpha}$ and $\mathbf{I}$ are $\zeta\times\zeta$ and $(M-\zeta)\times(M-\zeta)$, respectively.

Second, the transfer matrices $\mathbf{G}_p$ and $\mathbf{G}_v$ in (10) and (14) depend on the number of expansion terms J, thus the regularization process is J dependent. Our test results show that a cost-effective way of regularization is to first employ Eq. (16) to find the value J_{op} and use this value throughout the entire regularization process (21) to (25).

It is emphasized that one may use other regularization to solve an inverse acoustic radiation problem. The present choice is by no means the best for reconstructing the vibroacoustic field generated by a complex vibrating structure. From a theoretical standpoint, it is better to try different regularization schemes simultaneously and pick the best one that gives minimum L-2 norm errors in reconstruction for each frequency. However, this may prolong reconstruction. Thus a compromise must be made in applications.

VI. NUMERICAL EXAMPLES

In this section we use modified HELS and hybrid NAH to reconstruct vibroacoustic quantities on the surfaces of vibrating objects in half-space. In all cases, the normal surface velocity is preselected and the surface and field acoustic pressures are calculated numerically by using BEM codes. In particular, in modified HELS we take the field acoustic pressure as input data directly to Eqs. (10) and (14) to reconstruct the surface acoustic quantities. While in hybrid NAH we take field acoustic pressure as the input to the modified HELS formulation (16) to determine an optimal set of expansion functions, and use (19) to regenerate as much acoustic pressure as necessary on the same measurement surface Γ. The regenerated acoustic pressure is subsequently taken as the input data to IBEM formulation (17) to reconstruct the surface acoustic quantities. Note that here no symmetry properties are utilized in numerical computation and the fluid density and speed of sound are set at $\rho=1.21$ kg/m^3 and $c=344$ m/s, respectively.

The first case is a sphere of radius a in half-space bounded by an infinite and rigid baffle at the $z=0$ plane. The distance from the center of the sphere to the baffle is d and the polar angle of an observer at $\mathbf{x}$ with respect to the $-z$-axis direction is γ (see Fig. 2). The benchmark surface acoustic pressure, normal surface velocity, and the field acoustic pressure on the measurement surfaces are generated by the half-space integral formulation,[21] with the source surface being discretized into 1200 linear triangular elements and 602 nodes.

The second case is concerned with a finite circular cylinder with two spherical endcaps of radius a and half-length b in half space. The distance from the center of the cylinder to the baffle is d. Once again, the benchmark values of acoustic pressure and normal velocity on the cylindrical sur-

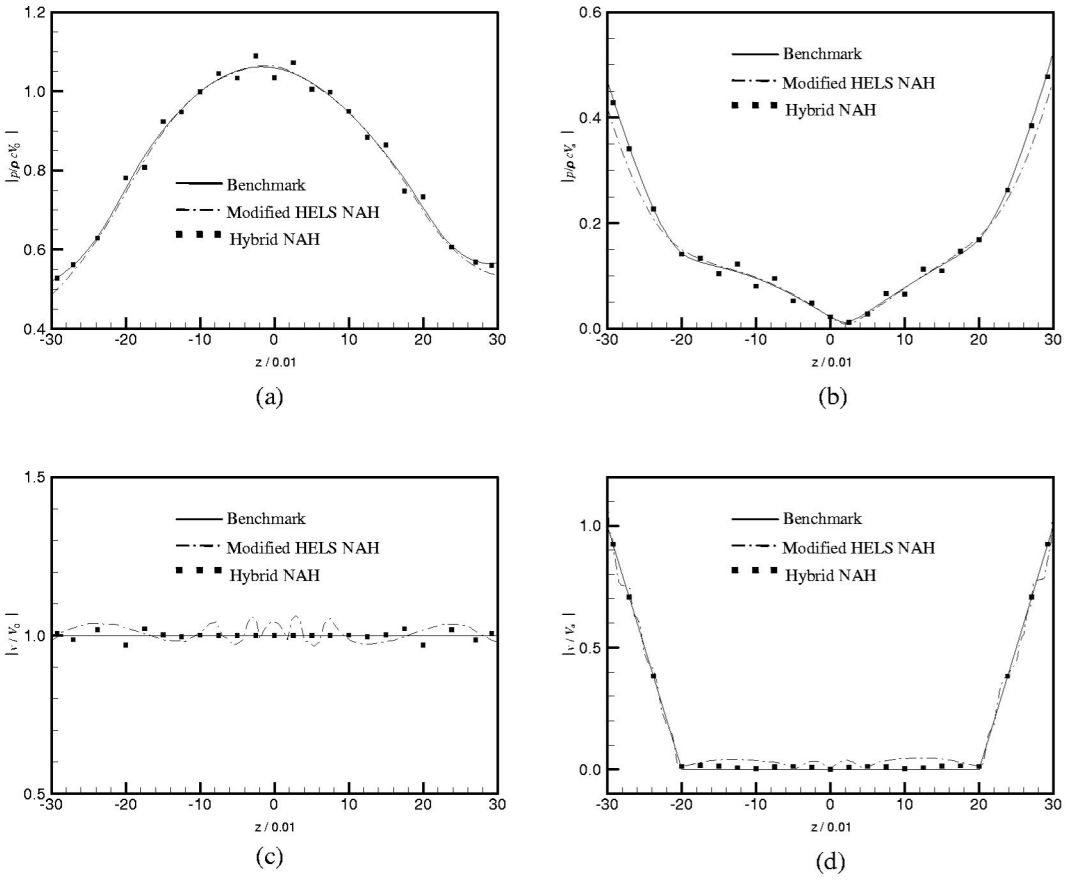

FIG. 6. Comparisons of dimensionless acoustic quantities on the surface of a cylinder with $b/a=2$ at $ka=1$ and $d=5a$. (a) Surface acoustic pressure for a dilating cylinder; (b) surface acoustic pressure for an oscillating cylinder; (c) normal surface velocity for a dilating cylinder; (d) normal surface velocity for an oscillating cylinder.

face and the field acoustic pressure are generated by BEM codes, with the cylindrical surface being discretized into 960 triangular elements with 482 nodes for a half-length to radius ratio $b/a=0.5$, and 1536 triangular elements with 770 nodes for $b/a=2$.

A. Vibrating spheres in half-space

In validating modified HELS for reconstructing acoustic radiation in half-space, we take acoustic pressure measurements over two conformal surfaces that are separated from the source surface at distances of 2 and 5 mm, respectively. Note that it is not necessary to always use two layers of measurements since the modified HELS formulation has accounted for the effects of outgoing and incoming spherical waves. However, our numerical tests show that by taking acoustic pressure measurements on two conformal surfaces around a source in the presence of a reflecting surface, we can get more satisfactory results than relying on one conformal surface in the modified HELS. On the other hand, we only take acoustic pressure measurements on a single conformal surface with 5 mm clearance from the source surface in using hybrid NAH in half-space. In all cases, we use half the measured data to determine the expansion coefficients and the rest to specify an optimal number of expansion functions. For brevity, however, we only display reconstruction results at $ka=1$ in each case.

The first example is the reconstruction of acoustic radiation from a dilating sphere of radius $a=0.1$ m with the amplitude of normal surface velocity $V_0=0.01$ m/s. In using modified HELS, we take 31 measurements each along the generator of two conformal surfaces, so total measurements are $M=62$. (Note that the discrete nodes on the source surface are $N_0=602$.) These input data are used to reconstruct acoustic pressure and normal velocity on the source surface. This process is repeated for the source at different vertical distances d. Results show that the optimal numbers of the expansion functions determined by Eq. (16a) are $J_{\mathrm{op}}=7$ for reconstructing the surface acoustic pressure and normal surface velocity at $d=1.5a$, $d=2a$, and $d=3a$; and $J_{\mathrm{op}}=2$ for $d=50a$. Note that J_{op} implies the number of pairs of the outgoing and incoming waves in the expansion functions.

On the other hand, in using a hybrid NAH method we take $M=151$ measurements and use Eq. (19) to regenerate 602 input data on the same measurement surface, which are taken as the input to Eq. (21) to reconstruct the acoustic pressure and normal velocity on the source surface. Again, this process is repeated for the source at different vertical distances d. The optimal pairs of expansion functions provided by Eq. (16) are $J_{\mathrm{op}}=37$ for $d=1.5a$ and $d=2a$; and $J_{\mathrm{op}}=26$ for $d=3a$ and $d=50a$.

Next, we consider a sphere oscillating in the z-axis direction with a velocity amplitude $V_a=0.01$ m/s. We take the same numbers of measurements and follow the same proce-

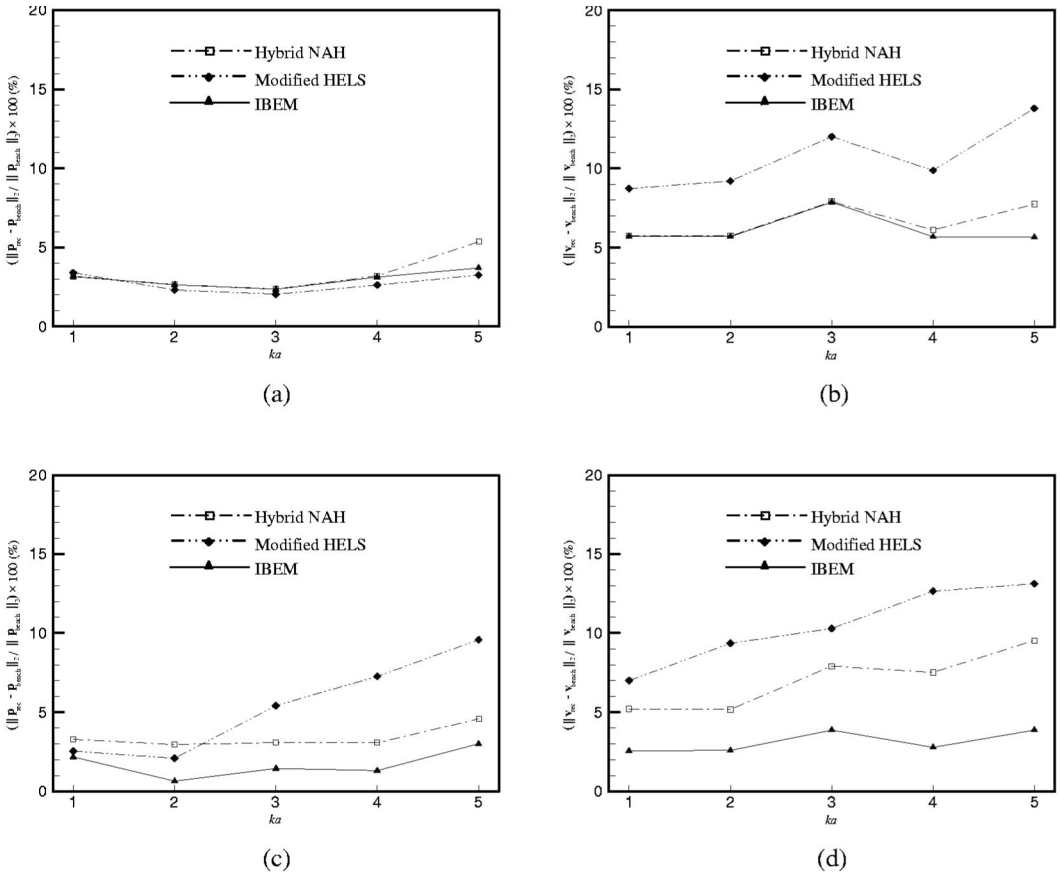

FIG. 7. Comparisons of relative error norms of surface acoustic quantities versus ka. (a) Surface acoustic pressure for a dilating sphere at $d=3a$; (b) normal surface velocity for a dilating sphere at $d=3a$; (c) surface acoustic pressure for a dilating cylinder with $b/a=2$ and $d=5a$; (d) normal surface velocity of a dilating cylinder with $b/a=2$ and $d=5a$.

dures as those described for a dilating sphere to reconstruct the acoustic pressure and normal velocity on the source surface using modified HELS and hybrid NAH, respectively. Results show that the optimal pairs of expansion functions in modified HELS are $J_{\text{op}}=7$ for reconstructing the surface acoustic pressure and normal velocity at $d=1.5a$, $d=2a$, and $d=3a$; $J_{\text{op}}=4$ for reconstructing surface acoustic pressure and $J_{\text{op}}=2$ for reconstructing surface normal velocity at $d=50a$. In hybrid NAH, the optimal expansion functions are $J_{\text{op}}=37$ for $d=1.5a$; $J_{\text{op}}=26$ for $d=2a$; and $J_{\text{op}}=27$ for $d=3a$ and $d=50a$.

Figures 3 and 4 summarize comparisons of normalized reconstructed surface acoustic pressures versus benchmark values for a dilating sphere and an oscillating sphere, respectively, at different vertical distances d. In all cases satisfactory agreements are obtained via modified HELS and hybrid NAH formulations. Note that because of the presence of an infinite rigid baffle, the acoustic pressure distributions on the surfaces of dilating and oscillating spheres are different from those of the same spheres in a free field [see Figs. 3(a), 3(b), and 3(c) and Figs. 4(a), 4(b), and 4(c)]. For example, the radiation pattern for a dilating sphere is no longer omnidirectional as it is in a free field. This difference is caused by interference between the direct wave and the waves reflected from the baffle. However, this interference diminishes as the sphere moves away from the baffle [see Figs. 3(d) and 4(d)], and the radiation patterns return to those of a sphere in a free field.

Figures 5(a) and 5(b) illustrate the comparisons of the normalized reconstructed surface normal velocity versus the benchmark values for a dilating and an oscillating sphere, respectively. Again, satisfactory reconstruction is obtained in all cases at different distances d. For brevity, we only present the results of $d=3a$ for both dilating and oscillating spheres in this paper.

B. Vibrating cylinders in half-space

Here we consider cylinders with different half-length to radius ratios that are either dilating with amplitude of the normal surface velocity $V_0=0.01$ m/s or oscillating along the z-axis direction with amplitude of velocity $V_a=0.01$ m/s.

First, we consider cylinders with an aspect ratio $b/a=0.5$ with $a=0.1$ m and $d=3a$. In using modified HELS, we take $M=94$ measurements to reconstruct the acoustic pressure and normal velocity on the source surface. The total discrete nodes on the cylindrical surface are 482. Test results show that the optimal pairs of expansion functions for reconstructing the acoustic pressure and normal velocity on the surface of a dilating cylinder are $J_{\text{op}}=15$ and 14, respectively; and those for reconstructing surface acoustic pressure

and normal velocity on the surface of an oscillating cylinder are $J_{op}=19$ and 25, respectively.

Next, we take $M=121$ measurements and use hybrid NAH to reconstruct the surface acoustic quantities. The corresponding optimal pairs of expansion functions are $J_{op}=18$ for the dilating cylinder and $J_{op}=27$ for the oscillating cylinder.

Finally, we consider cylinders with an aspect ratio $b/a=2$ with $a=0.1$ m and $d=5a$, and follow the same procedures as those described above. We take $M=121$ measurements for modified HELS and $M=193$ for hybrid NAH to reconstruct the acoustic quantities at all 770 discrete nodes on the surface. The optimal pairs of expansion functions are $J_{op}=9$ and 11 for the dilating cylinder; and $J_{op}=10$ and 17 for the oscillating cylinder in reconstructing surface acoustic pressure and normal velocity in modified HELS. In hybrid NAH, we found $J_{op}=17$ and 26 for the dilating and oscillating cylinders, respectively.

Figures 5(c) and 5(d) summarize comparisons of the normalized reconstructed surface acoustic pressures versus benchmark values for dilating and oscillating cylinders with an aspect ratio $b/a=0.5$, respectively. Similar comparisons of the normalized reconstructed surface acoustic pressures with benchmark data for dilating and oscillating cylinders with an aspect ratio $b/a=2$ are shown in Figs. 6(a) and 6(b), respectively. Our study shows that the normal surface velocity is satisfactorily reconstructed for both dilating and oscillating cylinders with different aspect ratios b/a. For brevity, only comparisons of the normalized reconstructed surface normal velocity versus the benchmark value for dilating and oscillating cylinders with an aspect ratio $b/a=2$ are plotted [see Figs. 6(c) and 6(d)].

To examine the performance of using modified HELS and hybrid NAH to reconstruct acoustic quantities in half-space, we calculate the relative errors $\|\mathbf{p}_{rec}-\mathbf{p}_{bench}\|_2/\|\mathbf{p}_{bench}\|_2$ and $\|\mathbf{v}_{rec}-\mathbf{v}_{bench}\|_2/\|\mathbf{v}_{bench}\|_2$ from $ka=1$ to 5 with sources located at different vertical distances, where $\mathbf{p}_{rec}$ and $\mathbf{p}_{bench}$ indicate the reconstructed and benchmark surface acoustic pressures, respectively, and $\mathbf{v}_{rec}$ and $\mathbf{v}_{bench}$ represent the reconstructed and benchmark normal surface velocities, respectively. Figure 7 summarizes the relative errors in reconstruction obtained via modified HELS and hybrid NAH for a dilating sphere at $d=3a$ and those for a dilating cylinder with an aspect ratio $b/a=2$ at $d=5a$ from the baffle, respectively. It is seen that both modified HELS and hybrid NAH can yield satisfactory reconstruction. However, the errors in reconstructing the surface acoustic pressure are smaller than those in reconstructing the normal surface velocity in general. In particular, hybrid NAH can produce more accurate reconstruction than does modified HELS, but modified HELS requires fewer measurements than does hybrid NAH.

VII. CONCLUSIONS

Both modified HELS and hybrid NAH can be used to reconstruct acoustic quantities on the surface of a vibrating object in half-space. In general, hybrid NAH can produce a more accurate reconstruction than does modified HELS. However, modified HELS requires fewer measurements than does hybrid NAH. Hence, in practice, if a large amount of measurements are needed to reconstruct vibroacoustic quantities, modified HELS may be selected in order to make the reconstruction process cost effective. On the other hand, if the measurements are not excessive, hybrid NAH should be used in order to produce an accurate reconstruction.

ACKNOWLEDGMENT

This work was supported by National Science Foundation, Grant No. CMS-9802847.

[1] E. G. Williams and J. D. Maynard, "Holographic imaging without the wavelength resolution limit," Phys. Rev. Lett. **45**, 554–557 (1980).
[2] E. G. Williams, J. D. Maynard, and E. Skudrzky, "Sound source reconstructions using a microphone array," J. Acoust. Soc. Am. **68**, 340–344 (1980).
[3] E. G. Williams, H. D. Dardy, and R. G. Fink, "Neafield acoustical holography using an underwater automated scanner," J. Acoust. Soc. Am. **78**, 789–798 (1985).
[4] E. G. Williams, *Fourier Acoustics: Sound Radiation and Nearfield Acoustical Holography* (Academic, San Diego, CA, 1999), pp. 184–186.
[5] B. K. Gardner and R. J. Bernhard, "A noise source identification technique using an inverse Helmholtz integral equation method," ASME J. Vib., Acoust., Stress, Reliab. Des. **110**, 84–90 (1988).
[6] W. A. Veronesi and J. D. Maynard, "Digital holographic reconstruction of sources with arbitrarily shaped surfaces," J. Acoust. Soc. Am. **85**, 588–598 (1989).
[7] G. V. Borgiotti, A. Sarkissian, E. G. Williams, and L. Schuetz, "Conformal generalized near-field acoustic holography for axisymmetric geometries," J. Acoust. Soc. Am. **88**, 199–209 (1990).
[8] G. T. Kim and B. H. Lee, "3-D sound source reconstruction and field reprediction using the Helmholtz integral equation," J. Sound Vib. **136**, 245–261 (1990).
[9] M. R. Bai, "Application of BEM (boundary element method)-based acoustic holography to radiation analysis of sound sources with arbitrarily shaped geometries," J. Acoust. Soc. Am. **92**, 533–549 (1992).
[10] B. K. Kim and J. G. Ih, "On the reconstruction of the vibro-acoustic field over the surface enclosing an interior space using the boundary element method," J. Acoust. Soc. Am. **100**, 3003–3016 (1996).
[11] E. G. Williams, B. H. Houston, P. C. Herdic, S. T. Raveendra, and B. Gardner, "Interior near-field acoustical holography in flight," J. Acoust. Soc. Am. **108**, 1451–1463 (2000).
[12] Z. Zhang, N. Vlahopoulos, S. T. Raveendra, T. Allen, and K. Y. Zhang, "A computational acoustic field reconstruction process based on an indirect boundary element formulation," J. Acoust. Soc. Am. **108**, 2167–2178 (2000).
[13] Z. Wang and S. F. Wu, "Helmholtz equation—least-squares method for reconstructing the acoustic pressure field," J. Acoust. Soc. Am. **102**, 2020–2032 (1997).
[14] S. F. Wu, "On reconstruction of acoustic pressure fields using the Helmholtz equation least squares method," J. Acoust. Soc. Am. **107**, 2511–2522 (2000).
[15] N. Rayess and S. F. Wu, "Experimental validations of the HELS method for reconstructing acoustic radiation from a complex vibrating structure," J. Acoust. Soc. Am. **107**, 2955–2964 (2000).
[16] S. F. Wu, N. Rayess, and X. Zhao, "Visualization of acoustic radiation from a vibrating bowling ball," J. Acoust. Soc. Am. **109**, 2771–2779 (2001).
[17] S. F. Wu and J. Yu, "Reconstructing interior acoustic pressure fields via Helmholtz equation least-squares method," J. Acoust. Soc. Am. **104**, 2054–2060 (1998).
[18] V. Isokov and S. F. Wu, "On theory and application of the Helmholtz equation least squares method in inverse acoustics," Inverse Probl. **18**, 1147–1159 (2002).
[19] S. F. Wu and X. Zhao, "Combined Helmholtz equation-least squares method for reconstructing acoustic radiation from arbitrarily shaped object," J. Acoust. Soc. Am. **112**, 179–188 (2002).
[20] S. F. Wu, "Hybrid nearfield acoustical holography," J. Acoust. Soc. Am. **115**, 207–217 (2004).

[21] P. M. Morse and K. U. Ingard, *Theoretical Acoustics* (Princeton University Press, Princeton, NJ, 1986), pp. 367–372.
[22] A. F. Seybert and B. Soenarko, ''Radiation and scattering of acoustic waves from bodies of arbitrary shape in a three-dimensional half space,'' ASME J. Vib., Acoust., Stress, Reliab. Des. **110**, 112–117 (1988).
[23] *Boundary Element Acoustics: Fundamental and Computer Codes*, edited by T. W. Wu (WIT Press, Southampton and Boston, 2000).
[24] I. N. Vekua, ''On completeness of a system of metaharmonic functions,'' Dokl. Akad. Nauk SSSR **90**, 715–718 (1953) (in Russian).
[25] S. Twomey, ''On the numerical solution of Fredholm integral equations of the first kind by the inversion of the linear system produced by quadrature,'' J. Assoc. Comput. Mach. **10**, 97–101 (1962).
[26] P. C. Hansen, *Rank-Deficient and Discrete Ill-Posed Problems* (SIAM, Philadelphia, PA, 1998).
[27] A. N. Tikhonov, ''On stability of inverse problems,'' Dokl. Akad. Nauk SSSR **39**, 176–179 (1943).
[28] N. Tikhonov and V. Y. Arsenin, *Solutions of Ill-Posed Problems* (Wiley, New York, 1977); see Chap. 2, pp. 71–73.
[29] G. H. Golub, M. Heath, and G. Wahba, ''Generalized cross-validation as a method for choosing a good ridge parameter,'' Technometrics **21**, 215–223 (1979).
[30] E. G. Williams, ''Regularization methods for near-field acoustical holography,'' J. Acoust. Soc. Am. **110**, 1976–1988 (2001).

Nonlinear focusing of acoustic shock waves at a caustic cusp

Régis Marchiano[a] and François Coulouvrat
Laboratoire de Modélisation en Mécanique, Université Pierre et Marie Curie and CNRS (UMR 7607), 4 place Jussieu, 75252 Paris Cedex 05, France

Jean-Louis Thomas
Laboratoire des Milieux Désordonnés et Hétérogènes, Université Pierre et Marie Curie and CNRS (UMR 7603), 4 place Jussieu, 75252 Paris Cedex 05, France

(Received 4 May 2004; revised 27 October 2004; accepted 7 November 2004)

The present study investigates the focusing of acoustical weak shock waves incoming on a cusped caustic. The theoretical model is based on the Khokhlov–Zabolotskaya equation and its specific boundary conditions. Based on the so-called Guiraud's similitude law for a step shock, a new explanation about the wavefront unfolding due to nonlinear self-refraction is proposed. This effect is shown to be associated not only to nonlinearities, as expected by previous authors, but also to the nonlocal geometry of the wavefront. Numerical simulations confirm the sensitivity of the process to wavefront geometry. Theoretical modeling and numerical simulations are substantiated by an original experiment. This one is carried out in two steps. First, the canonical Pearcey function is synthesized in linear regime by the inverse filter technique. In the second step, the same wavefront is emitted but with a high amplitude to generate shock waves during the propagation. The experimental results are compared with remarkable agreement to the numerical ones. Finally, applications to sonic boom are briefly discussed.
[DOI: 10.1121/1.1841551]

PACS numbers: 43.25.Cb, 43.25.Jh, 43.28.Mw [MFH] Pages: 566–577

I. INTRODUCTION

The focusing of finite amplitude waves on a cusped caustic is a physical phenomenon which may occur in different circumstances: sonic boom focusing produced either by the aircraft's manoeuvres or by the atmospheric turbulence or wavefront distortion encountered in medical imaging or nondestructive evaluation through heterogeneous medium. For all cases, it is important to better understand and control this phenomenon in order to either avoid it (sonic boom) or take benefits from it (imaging or nondestructive evaluation).

A caustic is an envelope of rays. It corresponds to a surface of amplification of the wavefield. There exist different kinds of caustics: fold, cusp, swallow-tail, and so on. All of these are described and classified by the theory of catastrophes (Thom, 1972). An important result of this theory is that for a wavefield, caustics can be interpreted as structurally stable focuses (Berry, 1976). In this framework, the perfect point focus is unstable and is likely to degenerate into a stable caustic such as a cusped caustic. Moreover, the theory of catastrophes also provides the generic form for the high frequency limit of the pressure field around the caustics in the linear regime, where diffraction cannot be neglected and is the main physical mechanism. This is the reason why this theory is also called the diffraction theory of catastrophes (Berry, 1976). For a cusped caustic this analytical solution is the Pearcey function (Pearcey, 1946). The reader is referred to Marston (1992) for a review of acoustical caustics in linear regime (with smooth waves).

If the incoming waves are shock waves, the Pearcey function is not valid because it predicts peaks of infinite amplitude on the cusped caustic (Coulouvrat, 2000). Note that this problem presents many analogies with the problem of the fold caustic for which the analytical solution—the Airy function—also leads to an infinite amplitude if the incoming waves present shocks (Guiraud, 1965). This is obviously physically meaningless, and experimental investigations performed during flight tests (Wanner *et al.*, 1972; Downing *et al.*, 1998) or laboratory experiments (Davy and Blackstock, 1971; Sanai *et al.*, 1976; Sturtevant and Kulkarny, 1976), despite an important amplification of amplitude and a change in the temporal waveform associated to diffraction, clearly show a limitation of the amplitude. Guiraud (1965) was the first to propose nonlinearities as the additional limiting mechanism for the case of fold caustics. He derived the so-called nonlinear Tricomi equation satisfied by the pressure field around the caustic. An approximate numerical solution was designed by Gill and Seebass (1973) based on the hodograph transform, and recently a fully numerical solution has been developed (Marchiano *et al.*, 2003a). Estimations by Plotkin and Cantril (1976) and later by Downing *et al.* (1998) showed the Gill and Seebass solution matched reasonably well with flight tests, while Marchiano *et al.* (2003b) demonstrated nice agreement with numerical solutions of Guiraud's model by means of a carefully scaled experiment in water tank.

For cusped caustics, in order to estimate the amplitude of the pressure at the tip of a cusped caustic, Pierce (1971) derived a similarity rule stipulating that the amplitude varies as the power $\frac{2}{3}$ of the incoming shock wave. But that result is valid for an incoming step function only. Using the asymptotic method of matched expansions, Cramer and See-

[a]Electronic mail: marchi@lmm.jussieu.fr

bass (1978) showed that around the cusped caustic, the pressure is governed by the Khokhlov–Zabolotskaya equation (Zabolotskaya and Khokhlov, 1969). That first model, valid for a 2D homogeneous medium, has been extended to the 3D case (Cramer, 1981a) and to the case of an axisymetric arête (Cramer, 1981b). In accordance with Guiraud's assumptions on the fold caustic (Guiraud, 1965) and with the theory of catastrophes, Coulouvrat (2000) showed that it is possible to derive the KZ equation considering a boundary layer around the cusp where the main physical mechanisms are diffraction and local nonlinear effects. Moreover, he derived the full associated boundary conditions which make it possible to solve the problem numerically for any incoming waveform.

In this paper, after a brief recall of the modeling associated with a cusped caustic (Sec. II), a detailed discussion about the Guiraud similitude laws for a cusped caustic, derived by Coulouvrat (2000), is presented (Sec. III). In particular, the wavefront unfolding observed by Piacsek (2002) is examined with both theoretical and numerical approaches, and a new mechanism for explaining it is proposed. However, numerical tests are not sufficient by themselves to conclude about the validity of the assumptions of the theoretical modeling, and an experimental confirmation is required, as presented in Sec. IV using ultrasonic shock waves in a water tank (Sec. IV). To our knowledge, this is the first time that theory and experiments have been compared quantitatively. This approach allows us to confirm definitively the assumptions of the theory and to validate the computer code.

II. THEORETICAL BACKGROUND: THE KZ EQUATION

In a two-dimensional, homogeneous and inviscid fluid of sound speed c_0, we consider the propagation of a concave wavefront having at point O (chosen as the origin) a minimum of radius of curvature, noted R_0. In the present section, it is assumed the wavefront is part of a continuous wave with angular frequency ω and wave number $k_0=\omega/c_0$. The case of a shock front will be discussed in next section. The x axis is chosen tangent to, and the z axis normal to, the wavefront at the origin (Fig. 1). During the propagation, that wavefront generates a cusped caustic at the distance R_0 from the origin. The wavefront having a minimum of the radius of curvature, the tip of the caustic is oriented towards the origin. The cusped caustic splits the space into two distinct zones (Fig. 1): one, labeled zone I, where only one ray passes through each point (area located outside the branches of the caustic), and one, labeled zone II, where three rays pass through each point (area located within the branches of the caustic).

Introducing the geometrical parameter $a=\frac{9}{8}R_0^2R_0^{\parallel}$, where $R_0^{\parallel}$ is the second derivative with respect to x at the origin O, Coulouvrat (2000) defines the characteristic diffraction length-scale in the z direction:

$$L_z=\left(\frac{4a}{27k_0}\right)^{1/2}, \tag{1}$$

and the characteristic diffraction length-scale in the x direction:

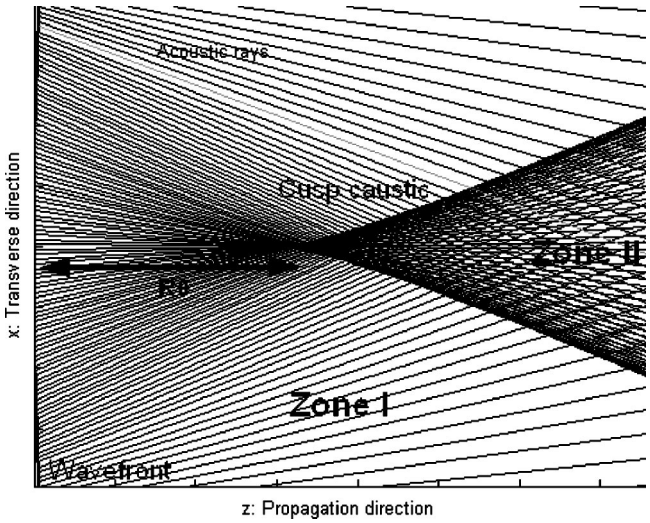

FIG. 1. Geometry of the caustic. Note that, in order to emphasize the caustic geometry, the scales of the transverse and propagation directions are not the same.

$$L_x=\left(\frac{a}{27k_0^3}\right)^{1/4}. \tag{2}$$

The diffraction length-scales are used to define the spatial dimensionless variables characterizing the problem in the longitudinal direction,

$$\overline{z}=(z-R_0)/L_z, \tag{3}$$

and in the transverse direction,

$$\overline{x}=x/L_x. \tag{4}$$

The dimensionless retarded time is also introduced to describe propagation in the main direction, t being the physical time:

$$\overline{t}=\omega(t-z/c_0). \tag{5}$$

Lastly, the dimensionless pressure is introduced:

$$\overline{p}=\frac{p}{p_0}, \tag{6}$$

where p is the acoustical pressure and p_0 is chosen as the amplitude of the incoming pressure field before focus at one characteristic distance L_z (the amplitude at $\overline{z}=-1$).

Cramer and Seebass (1978) and Coulouvrat (2000) show that, in the neighborhood of the cusp, the pressure is solution of the Khokhlov–Zabolotskaya equation (KZ equation):

$$\frac{\partial^2\overline{p}}{\partial\overline{z}\partial\overline{t}}=\frac{\partial^2\overline{p}}{\partial\overline{x}^2}+\mu\frac{\partial^2\overline{p}^2}{\partial\overline{t}^2}, \tag{7}$$

where μ is a parameter measuring the amplitude of the nonlinear effects in comparison with diffraction ones:

$$\mu=\beta M\left(\frac{k_0a}{27}\right)^{1/2}=\beta\frac{p_0}{\rho_0c_0^2}\left(\frac{k_0a}{27}\right)^{1/2}, \tag{8}$$

with $\beta=1+B/2A$ (where $B/2A$ is the nonlinearity parameter of the medium) and $M=p_0/\rho_0c_0^2$ the acoustical Mach number (where ρ_0 is the density of the medium at rest).

The boundary conditions associated with the problem are determined by an asymptotic matching with the geometrical acoustics away from the cusp (Coulouvrat, 2000):

$$\overline{p}(\overline{x},\overline{z},\overline{t}) \xrightarrow[\sqrt{\overline{x}^2+\overline{z}^2}\to\infty]{} \frac{1}{\sqrt{|6\overline{\alpha}^2-\overline{z}|}} F(\overline{t}+\overline{\alpha x}+\overline{\alpha}^2\overline{z}-\overline{\alpha}^4), \quad (9)$$

where $\overline{\alpha}(\overline{x},\overline{z})$ is the only real root of $\overline{x}+2\overline{\alpha z}-4\overline{\alpha}^3=0$ and F is the dimensionless incoming signal waveform. The phase function $\overline{t}+\overline{\alpha x}+\overline{\alpha}^2\overline{z}-\overline{\alpha}^4$ describes the curvature of the wavefront as it approaches the caustic, while the coefficient $1/\sqrt{|6\overline{\alpha}^2-\overline{z}|}$ measures the subsequent geometrical amplification. This expression is valid only in zone I (Fig. 1), where only one ray [one root $\overline{\alpha}(\overline{x},\overline{z})$] passes through each point, and sufficiently far from the caustics so that local diffraction effects can be neglected (geometrical approximation).

The boundary condition Eq. (9) completes the formulation of the problem and makes it numerically tractable. For the linear case ($\mu=0$), Coulouvrat (2000) shows that the solution of Eqs. (7) and (9) can be expressed in terms of the Pearcey function (1946), in agreement with the diffraction catastrophe theory (Berry, 1976; Marston, 1992). For the nonlinear case, a new algorithm solving the KZ equation is presented in Appendix A.

III. GUIRAUD'S SIMILITUDE FOR A STEP SHOCK

We briefly recall here the similitude law obtained by Cramer and Seebass (1978) and Coulouvrat (2000) generalizing to a cusped caustic the Guiraud's similitude (1965) for a fold caustic. Introducing the new scaling $\overline{p}=\mu^{-1/3}\tilde{p}$, $\overline{t}=\mu^{4/3}\tilde{t}$, $\overline{x}=\mu\tilde{x}$, $\overline{z}=\mu^{2/3}\tilde{z}$ and $\overline{\alpha}=\mu^{1/3}\tilde{\alpha}$, the KZ equation becomes

$$\frac{\partial^2\tilde{p}}{\partial\tilde{z}\partial\tilde{t}}=\frac{\partial^2\tilde{p}}{\partial\tilde{x}^2}+\frac{\partial^2}{\partial\tilde{t}^2}(\tilde{p}^2), \quad (10)$$

and the associated boundary condition

$$\tilde{p}(\tilde{x},\tilde{z},\tilde{t})\approx\frac{1}{\sqrt{|\tilde{z}-6\tilde{\alpha}^2|}}F[\mu(\tilde{t}+\tilde{\alpha}\tilde{x}+\tilde{\alpha}^2\tilde{z}-\tilde{\alpha}^4)] \quad (11)$$

with $\tilde{\alpha}$ the only real root of the polynomial $\tilde{x}+2\tilde{\alpha}\tilde{z}-4\tilde{\alpha}^3=0$.

With the new scaling, the KZ equation [Eq. (10)] no longer involves the nonlinear parameter μ which now appears in the boundary conditions [Eq. (11)]. Thus, for an incoming step shock which is invariant by temporal dilatation [$F(\overline{t})=0$ if $\overline{t}<0$ and $F(\overline{t})=1$ if $\overline{t}>0$], the whole problem [Eqs. (10) and (11)] is independent of the nonlinear parameter: this is a self-similar solution (with respect to the nonlinear parameter), known as Guiraud's similitude. Expressing the similitude variables "$\sim$" in physical terms, one finds

$$\tilde{p}=p\left[\frac{\beta}{\rho_0 c_0^2 p_0^2}\left(\frac{k_0 a}{27}\right)^{1/2}\right]^{1/3}.$$

However, the amplitude p_0 is defined as the incoming pressure amplitude at one boundary layer thickness away from the cusp. But for a step shock, there is no main frequency, therefore the choice of this thickness is arbitrary. Taking into account the convergence of the pressure field according to the boundary condition Eq. (9), it is therefore suitable to write $p_0=P_{ref}(a/L_z)^{1/2}$, where P_{ref} is a reference pressure level now independent of the frequency (a being now the only physical length of the problem). This finally yields

$$\tilde{p}=p\left[\frac{2\beta}{27\rho_0 c_0^2 P_{ref}^2}\right]^{1/3} \quad (12)$$

and results for other variables can be deduced similarly:

$$\begin{aligned}
&\tilde{t}=\frac{6}{2^{1/3}}\left(\frac{\rho_0 c_0^2}{\beta P_{ref}}\right)^{3/4}\frac{c_0}{a}(t-z/c_0),\\
&\tilde{x}=54^{1/2}\left(\frac{\rho_0 c_0^2}{\beta P_{ref}}\right)\frac{x}{a},\quad \tilde{z}=\frac{9}{4^{1/3}}\left(\frac{\rho_0 c_0^2}{\beta P_{ref}}\right)^{2/3}\frac{z}{a},\\
&\tilde{\alpha}=2^{1/6}\sqrt{3}\left(\frac{\rho_0 c_0^2}{\beta P_{ref}}\right)^{1/3}\frac{\alpha}{R_0}.
\end{aligned} \quad (13)$$

Relations (12) and (13) are all independent of frequency, indicating that Guiraud's scaling is the correct one for an incoming signal with no characteristic frequency. As a counterpart, the scaling is nonlinear. Especially, Eq. (12) shows that the focused pressure varies as power $\frac{2}{3}$ of the incoming amplitude, in agreement with Pierce's (1971) dimensional analysis later confirmed by Cramer and Seebass (1978). The characteristic space variables increase as power $\frac{2}{3}$ of the amplitude along the axis, and power 1 transversely, while characteristic time increases as power $\frac{3}{4}$.

Guiraud's similitude is the key point in solving the issue of weak shocks focusing. Whitham (1956) conjectured that the nonlinear self-refraction prevents wavefront folding as the central part of the shock front tends to become plane. That is the mechanism of "wavefront unfolding." This view point, also supported by Marston (1988), has been numerically investigated by Prasad and Sangeeta (1999) using a weak nonlinear ray theory but for Mach numbers (from 1.05 to 1.2) significantly larger than acoustical ones. This seems contradictory to Guiraud's similitude, which *demonstrates* (provided the basic assumptions sustaining the KZ equation are valid, as will be demonstrated in Sec. IV) that the solution is independent of the amplitude after correct rescaling, at least in the weak shock approximation of the KZ equation. Experiments by Sturtevant and Kulkarny (1976, Figure 17) confirm that for weak shock waves (Mach 1.005 and 1.03), the geometrical shape of the wavefront remains such that there is no self-refraction, though for stronger shocks beyond the acoustical limit (Mach 1.1 and 1.5) this is no longer valid. On the contrary, using numerical simulations of the NPE equation, Piacsek (2002) observes wavefront unfolding even in the acoustical limit. But for the "ideal" wavefront Eq. (9) leading to a "perfect" cusped caustic, Guiraud's similitude demonstrates that this should not happen.

To elucidate this issue, we have performed numerical simulations of the two cases: first for the "ideal" wavefront Eq. (9) exactly associated to Pearcey solution in the linear regime, and for the wavefront proposed by Piacsek [his equation (5)]. This last wavefront involves two parameters. These ones have been chosen so that both wavefronts have the

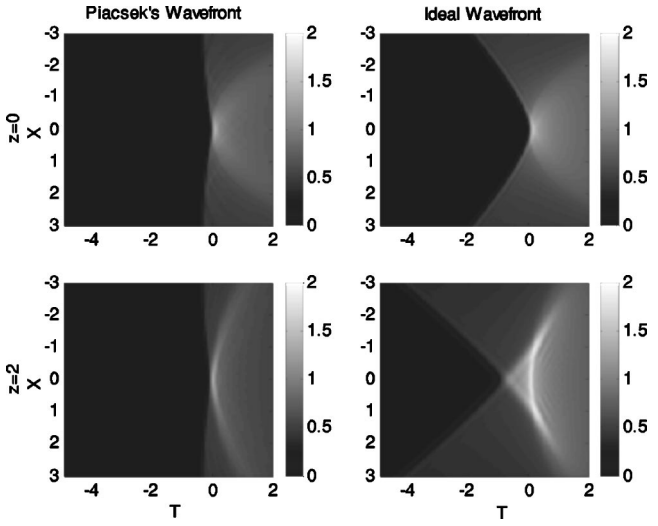

FIG. 2. Numerically simulated dimensionless pressure fields $\overline{p}$ at $\overline{z}=0$ and $\overline{z}=2$ in linear regime ($\mu=0$) as a function of time (horizontal) and transverse space variable $\overline{x}$ (vertical) for a step shock. Vertical bar indicates correspondance between gray and dimensionless pressure levels. Comparison between Piacsek's ''real'' wavefront (left column) and ''ideal'' wavefront Eq. (9) (right column).

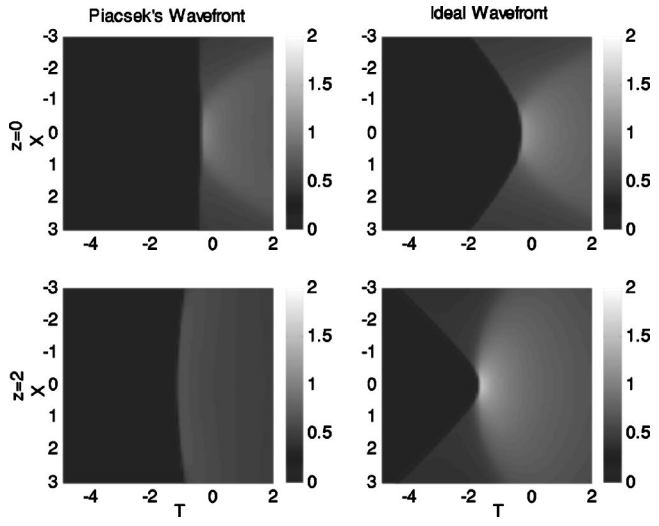

FIG. 3. Numerically simulated dimensionless pressure fields $\overline{p}$ at $\overline{z}=0$ and $\overline{z}=2$ in nonlinear regime ($\mu=1$) as a function of time (horizontal) and transverse space variable $\overline{x}$ (vertical) for a step shock. Vertical bar indicates correspondance between gray and dimensionless pressure levels. Comparison between Piacsek's ''real'' wavefront (left column) and ''ideal'' wavefront Eq. (9) (right column).

same values R_0 and $R_0^{\parallel}$ at their center. So, locally, the two wavefronts have the same geometry. Therefore, according to catastrophe theory, in the high frequency limit and in the linear regime, the two are locally equivalent around the cusp of the caustic. However, far from the center, the ''ideal'' one, Eq. (9), is still converging with a shape perfectly suited to a cusped caustic, while Piacesk'one gets flat, and is therefore not focusing any more.

The numerical simulations are performed for a step shock using a new code solving the KZ equation in the temporal domain (see the Appendix for further technical details and code validation). Piacsek' wavefront is used in the initial plane $z=0$. Laterally, the solution is matched to an analytical solution of the inviscid Burgers' equation (nonlinear plane wave). Results of the simulations are shown in linear regime ($\mu=0$ in the KZ equation) on Fig. 2. The two wavefronts clearly focus at $\overline{z}=0$ with the same amplitude. Beyond this point, they exhibit the characteristic swallow tail form at $\overline{z}=2$. Note, however, that the focusing effects are much more localized for Piascek's wavefront, as far from the axis it is not focusing any more. In nonlinear regime ($\mu=1$, Fig. 3), the results are quite different. The ''ideal'' wavefront Eq. (9) always leads to form a cusped caustic but now the focus is strongly shifted, around point $\overline{z}=2$ (very similar to the curve for $\overline{z}=0$ in linear regime). On the contrary, the Piascek's wavefront is flattened, an effect already described by Piacsek (2002). Note that nonlinear effects are visible for both cases: the time when the step shock (in $\overline{x}=0$) occurs is no longer zero but shifted to an earlier time for higher amplitude.

As soon as the wavefront deviates from the ''ideal'' wavefront Eq. (9), there is some critical amplitude beyond which the current shape of the wavefront (which has all chances to deviate at some distance from the ideal one) plays a role. Indeed, as the pressure amplitude increases, Guiraud's self-similar solution requires rays from a larger region of the wavefront [Eq. (13) for α, increasing as power $\frac{1}{3}$ of the amplitude]. So, if the transverse size of the wavefront where it is close to the ideal one is not large enough, the cusped caustic cannot be actually synthesized in nonlinear regime. This is equivalent to the linear catastrophe theory (leading to the Pearcey function), which is a local, high frequency approximation. When wavelength increases, this approximation degrades or conversely the size of the wavefront should be increased. Here, the phenomenon is analogous, but the wavelength increase is associated with the nonlinear increase of the characteristic length scales of Guiraud's similitude with the amplitude. Consequently, beyond some amplitude, any real wavefront will deviate from the Guiraud's similitude, which will appear as a wave front unfolding. So the conclusion is that there is indeed wave front unfolding, but it is not intrinsically a nonlinear phenomenon (at least for acoustic shock waves). It is a more complex process, where the self-similar solution of Guiraud becomes invalid with increasing amplitudes because the characteristic lengths increase with amplitude, so that the actual shape of the wavefront (and not only its local asymptotic shape) gets more and more important.

IV. EXPERIMENTAL SYNTHESIS OF A CUSPED CAUSTIC

In order to verify the assumptions of the theory, an experimental study has been performed. The experiments are made in a water tank with ultrasonic waves (central frequency: 1 MHz) emitted by an array of 256 rectangular piezoelectric transducers (Imasonic, France). The transducers are displayed on a rectangular aperture (32 rows, 8 lines). Each of them is driven individually by programmable broadband linear amplifiers (Lecoeur Electronique, France). Those amplifiers allow us to specify the shape, phase and amplitude of the signal emitted by a transducer. Each transducer can emit a plane wave up to 5×10^5 Pa amplitude. A broadband calibrated membrane hydrophone (1 to 40 MHz) associated

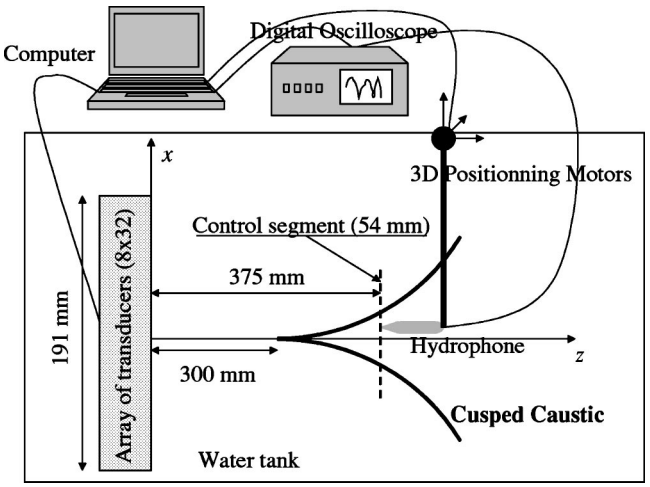

FIG. 4. Experimental setup.

with a digital oscilloscope measures the acoustic field. The small active diameter of the hydrophone (0.2 mm), ensures a good resolution to scan the acoustic field. The hydrophone can be moved along the three directions of space inside the water tank by programmable step-by-step motors (Fig. 4). The whole experimental setup is automated.

The experimental synthesis of a cusped caustic in linear and nonlinear regimes presented here is achieved in two stages. First of all, the signals to be emitted by the array in order to synthesize a cusped caustic in linear regime are determined. That stage is achieved by the inverse filter technique (Tanter *et al.*, 2000). Once the signals producing the cusped caustic are known, the second stage consists in emitting them with a high amplitude to produce nonlinearity. This methodology has been employed successfully to synthesize fold caustics in the nonlinear regime (Marchiano *et al.*, 2003b).

The geometrical parameters of the cusp are chosen as follows: $R_0=300$ mm and $R_0^{\|}=63/R_0$. With the choice of the propagation medium (water, $c_0\approx 1500$ m/s) and the frequency of the waves ($f_0=1$ MHz), the choice of the values of R_0 and $R_0^{\|}$ fixes the geometry of the problem, and in particular the diffraction length-scales: $L_z=27.4$ mm in the propagation direction and $L_x=1.8$ mm in the transverse direction. This choice results from the compromise between the size of the focal length and the distance between the array of transducers and the tip of the caustic. The latter distance must be large enough to ensure the presence of shock waves. The shock formation distance for a plane wave emitted by the array of transducers is about 300 mm. Nevertheless, this distance is shorter in the case of a focused wave such as the emitted wave. So, the chosen distance (300 mm) is sufficiently far from the array to ensure the presence of shock wave. Figure 5 shows the acoustical rays launched by an unlimited [Fig. 5(a)] and a limited [Fig. 5(b)] wavefront producing the cusped caustic with the geometrical parameters R_0 and $R_0^{\|}$ defined above. The size of the limited wavefront corresponds to the aperture of the array of transducers used for the experiments (191 mm). On both figures, the cusped caustic appears clearly, especially the tip of the cusp located 300 mm away from the wavefront (the array). As

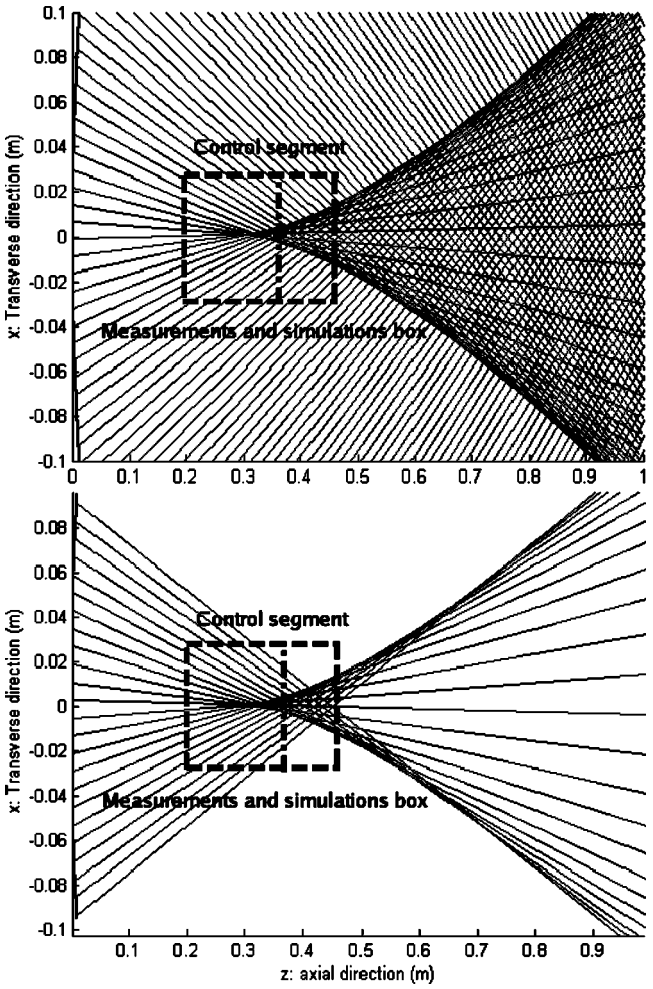

FIG. 5. Acoustical rays launched by (a) an unlimited and (b) a limited aperture. Note that the scales of the transverse and propagation directions are not the same. The dotted box indicates the domain where measurements and simulations are performed. The dotted line represents the position of the control segment.

mentioned in Sec. I, for an unlimited wavefront, the cusped caustic splits the plane Oxz into two zones: a zone with one ray and a zone with three rays. For a limited aperture, the situation is different. Three zones can be distinguished: a zone with no ray, a zone with one ray, and a zone with three rays. Nevertheless, near the tip of the cusp, the field is identical to the modeled phenomenon. That zone corresponds to the area where the theory described in Sec. 1 is valid and where we can make comparison between theory and experiment.

To synthesize the cusped caustic in linear regime, the inverse filter technique is used. The first stage of this technique consists in measuring the propagation operator between the array of transducers and a set of control points, where the target field must be synthesized. The linear solution to the problem is the Pearcey function. So the target field is defined from that function, which depends on the two spatial variables x and z and is computed from the code presented in Sec. II with $\mu=0$. Because of technical considerations (size of the memory, duration of the experiment), we choose to impose the Pearcey function not on a plane (natural choice for a function of two variables) but along a seg-

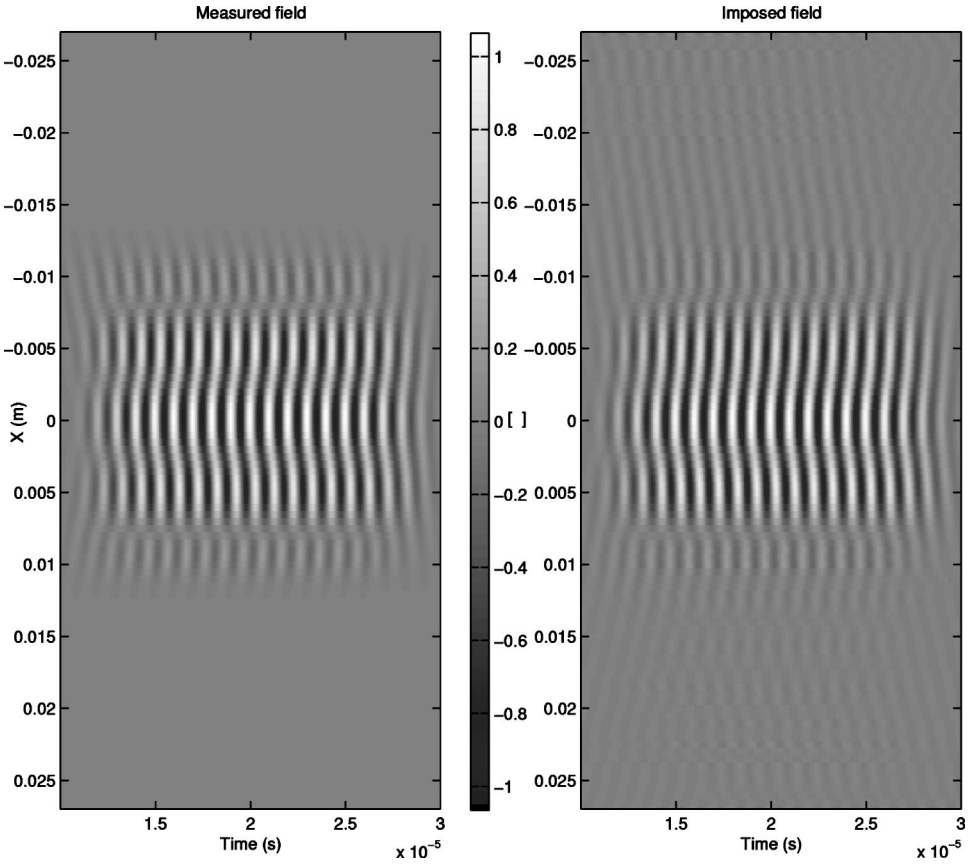

FIG. 6. Spatio temporal pressure field (a) imposed and (b) measured along the control segment (horizontal: time variable; vertical: transverse space variable; gray levels: pressure levels).

ment only. We define this control segment located 382 mm away from the array. Its length is 54 mm and it is discretized by 108 points equally spaced every 0.5 mm. The size and the location of the control segment have been chosen in order that the segment is behind the tip of the cusp and crosses the caustic so that it is located partially in zone I and partially in zone II. So, imposing the acoustic field on that segment makes the acoustic field strongly stressed. The propagation operator is measured between that control segment and the array of transducers. Then, the propagation operator is regularized and inversed by a singular value decomposition.

The incoming function used to compute the pattern (the Pearcey function) is a sinusoidal function with a dozen cycles. Nevertheless, such a computed field does not take into account the finite size of the array of transducers and corresponds to the ideal situation depicted on Fig. 5(a). To impose a realistic pattern on the control segment, a function is applied on the field previously computed. The windowing keeps the central part of the field and eliminates the lateral parts as illustrated on Fig. 6(a). This new pattern is used to calculate the signals to emit by the transducers. Then, those signals are emitted at low amplitude to ensure a linear propagation and the pressure is measured on the control points. Figure 6(b) shows the field measured along the control segment compared to the pattern imposed [Fig. 6(a)]. The agreement between the two fields is very good; the main characteristics of the target field are well recovered: the structure with three lobes and the shape of the wavefronts. This comparison proves that the field corresponding to a cusped caustic can be synthesized along a segment.

In order to confirm that the cusped caustic is synthesized in the whole space (and not only on the control segment) a scan on a bigger grid is achieved. The grid is 240 mm long in the z direction (100 mm before the tip and 140 mm after the tip, the step is 2 mm) and 54 mm large in the x direction (27 mm on each side of Oz axis, the step is 0.5 mm). So, there are 12 360 points on the new measurement grid (the limits of the grid are the dashed lines on Fig. 5). The pressure is measured with a temporal sampling of 50 MHz.

To compare the experimental measurements to the numerical simulations discussed in Sec. II, only the incoming waveform is necessary as an input argument. This data is extracted directly from the experimental measurements 100 mm away from the tip of the cusp on the propagation axis Oz. In order to perform comparisons with the experimental results, the pressure field is computed on a grid corresponding to the experimental one. Figure 7 presents the experimental field (left column) and the numerical simulations (right column) in the transverse direction x as a function of the time at five different distances z from the tip of the cusp (-100, -50, 0, 50, and 100 mm). The agreement between the two series of fields is very good, in particular near the symmetry axis. The main differences between the experimental and the simulated fields are located off axis. Far away from the tip of the cusp (100 mm before), the wavefront is converging and its amplitude in the transverse direction is quite homogeneous. The closer to the tip the wavefront is, the stronger at the center of the beam the amplitude is. This is due to the focusing effects. At the tip and slightly after it, the beam is narrow and 100 mm after the tip it is clearly diverging.

Figure 8 displays the amplitude at 1 MHz measured on

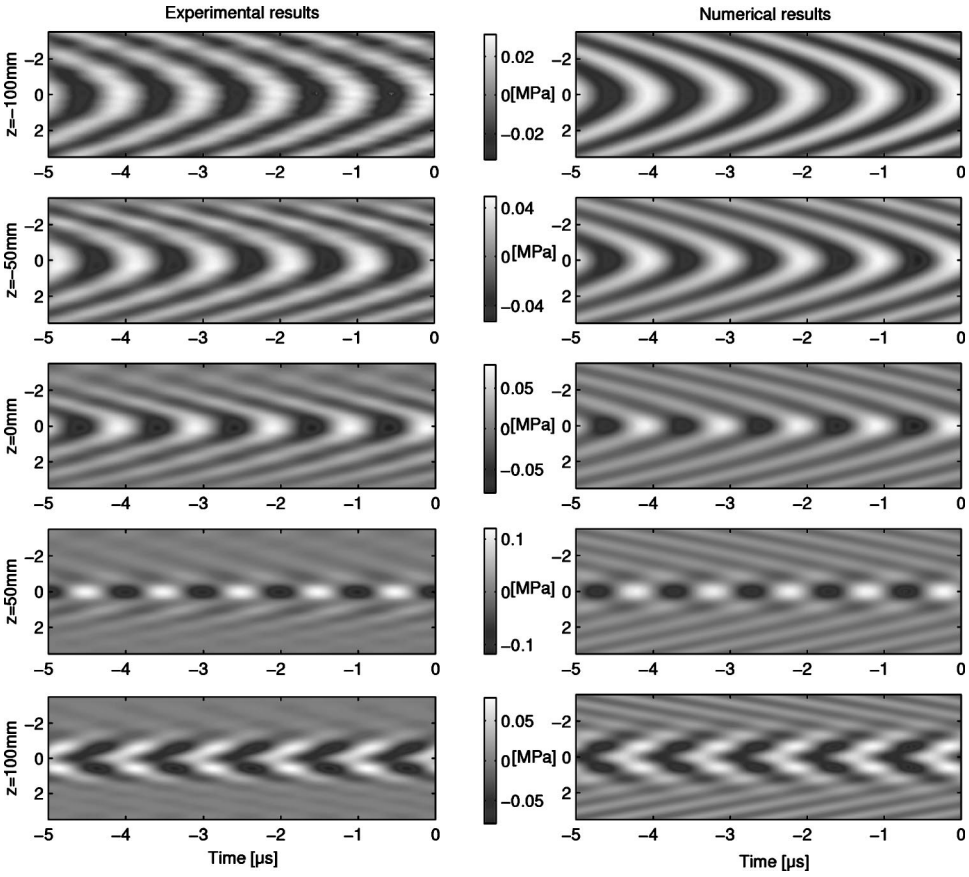

FIG. 7. Comparison between measured (left column) and numerically simulated (right column) pressure field in linear regime as a function of time (horizontal variable) and transverse variable x (vertical variable) at five different distances $z=-100$, -50, 0, 50, and 100 mm (gray levels: pressure levels).

each point of the scan grid in grayscale (black corresponds to zero and white corresponds to high intensity), compared to the contours of the Pearcey function (dashed white lines, with the same color levels). The agreement is still very good, especially near the Oz axis. The position and the amplitude of the main lobe are well recovered. The positions of the

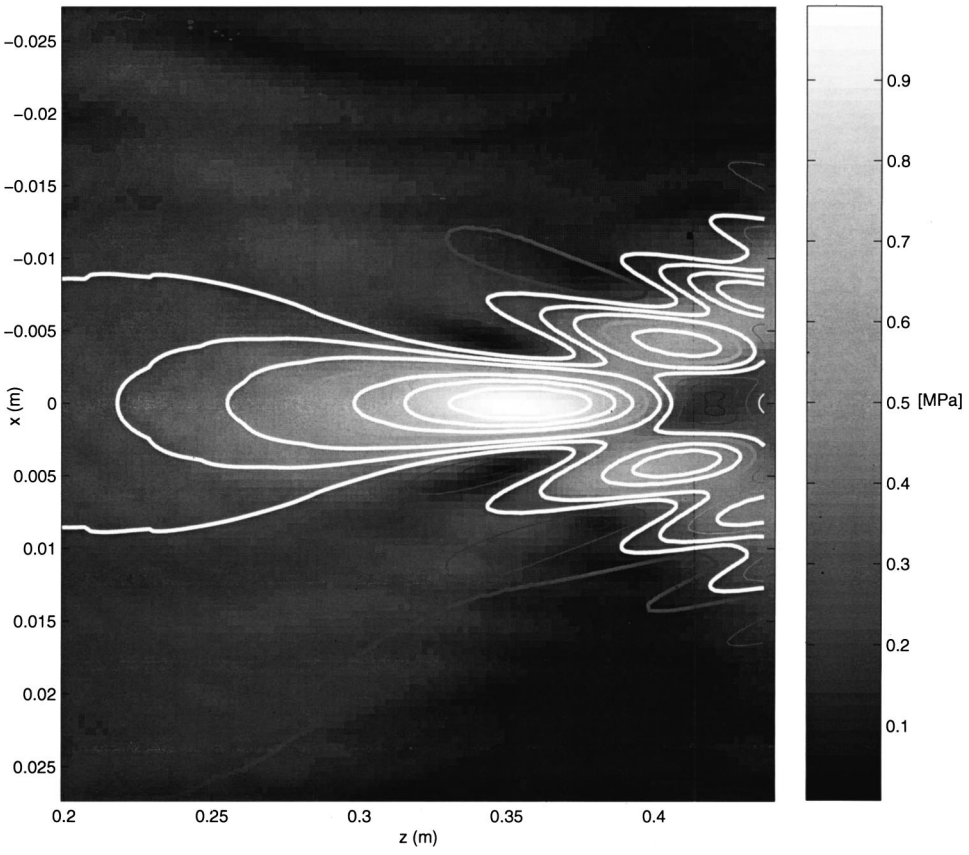

FIG. 8. Comparison between measured pressure field and the theoretical Pearcey function (white contour lines) in linear regime (gray levels: pressure levels).

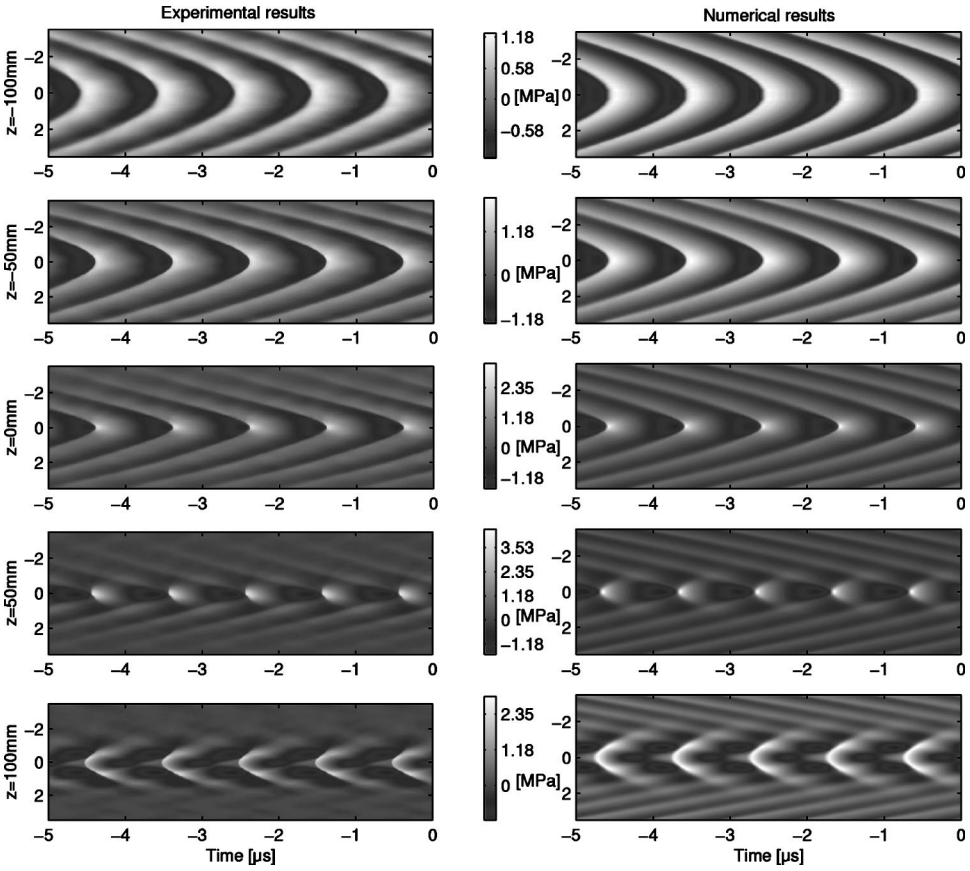

FIG. 9. Comparison between measured (left column) and numerically simulated (right column) pressure field in nonlinear regime as a function of time (horizontal variable) and transverse variable x (vertical variable) at five different distances $z=-100$, -50, 0, 50, and 100 mm (gray levels: pressure levels).

secondary lobes are matching relatively well but the amplitudes of the experimental measurements are lower than the simulated ones. These results confirm that the experimental setup is only usable near the Oz axis because of the finite size of the emitting array. Nevertheless, these results show that the experimental setup associated with the inverse filter technique permits the synthesis of a cusped caustic in the linear regime of 2-D space.

To study the focusing of weak shock waves at a cusped caustic, the previous computed signals by inverse filter technique are now emitted with high amplitude. Because of the high amplitude, nonlinear effects take place during the propagation between the array of transducers and the caustic cusp. The nonlinear effects induce a steepening of the temporal profile of the waves in accordance with the laws of nonlinear acoustics. The shock formation distance being shorter than the distance between the array of transducers and the cusped caustic, the incoming signal has shocks before tangenting the caustic. Once the high amplitude signals are emitted, the pressure is measured on the same grid as in linear regime but with a temporal sampling of 250 MHz. The results are given in Fig. 9 (left column), which shows the pressure fields in the transverse direction x as function of the time at five different locations z from the tip of the caustic (-100, -50, 0, 50, and 100 mm). The five images are different from those of the linear case (Fig. 7). Far before the caustic (-100 mm), the amplitude distribution is homogeneous and the shocks appear to be formed as indicated by the sharp transitions between black and white. As for the linear case, -50 mm away from the tip, the focusing effects increase the amplitude of the center of the beam. At the tip of the cusp the transverse size of the beam is narrower than in the linear case. Moreover, the compression phases (white areas) are shorter in time than the expansion ones (black areas), and the positive peaks are higher than the negative ones. This asymmetric waveform distorsion is well-known to result from a combination of diffraction and nonlinearity effects (see, for instance, Hamilton, 1998, p. 258).

The maximal overpressure is 66.82×10^5 Pa peak/peak (48.94×10^5 Pa for the positive part and 17.87×10^5 Pa for the negative one). It is detected on the Oz axis, 35 mm after the tip of the cusp. For a plane wave, the maximum overpressure at this distance is 10×10^5 Pa peak/peak. The amplification coefficient defined as the ratio between the overpressure in the focused case and the overpressure for a plane wave is consequently of 6.68. If only the positive part is taken into account, the amplification coefficient becomes 9.78. This coefficient is greater than for a fold caustic for which the corresponding values are respectively about 1.9 (peak to peak) and 3.8 (amplification of the positive part only). Moreover, note that this value of the amplification coefficient for a cusped caustic is in agreement with the value of about 9 found by Wanner *et al.* (1972) for sonic boom.

The numerical simulations in nonlinear regime require two input arguments which are extracted from the experimental results: the waveform of the incoming function and the nonlinear coefficient μ. The waveform of the incoming function is directly extracted from the experimental data on the Oz axis 100 mm before the tip of the cusp (sufficiently far before the cusp). The temporal profile for one period is given in Fig. 10 (dash line). The signal carries a shock which

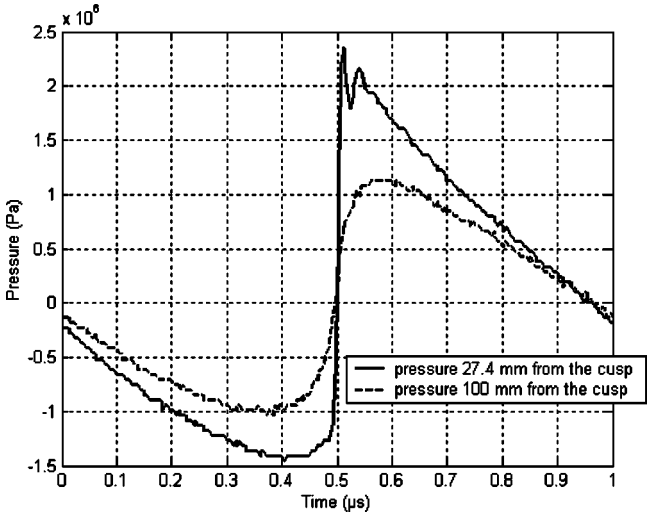

FIG. 10. Incoming signal (one period) measured at one boundary layer (-27.4 mm, solid line) and at -100 mm (dash line) from the tip of the cusped caustic in nonlinear regime.

is practically formed (the rise time is about 80 ns). The nonlinear coefficient $\mu=\beta(p_0/\rho_0 c_0^2)(k_0 a/27)^{1/2}$ [Eq. (8)] is calculated from the value of the pressure measured 27.4 mm before the tip of the caustic (distance equal to one diffraction length L_z), in agreement with theory. Note that the two inputs for the numerical code are extracted at two different ranges. At that distance, the pressure is 39.5×10^5 Pa and the shock is saturated with a measured rise time of 15 ns [Fig. 10 (solid line)]. Consequently, the value of the nonlinear coefficient is $\mu=0.35$. The numerical simulations are made with those two input arguments for a numerical grid corresponding to the experimental one. The results are given in Fig. 9 (right column). The agreement with the experimental results is excellent, especially around the Oz axis as in the previous comparisons. These results prove that the numerical solver simulates the physical reality with a good precision. Figure 11 shows the pressure (in Pa) as a function of the time (in μs) on the Oz axis at four different distances from the tip of the caustic (-100, -28, 0, and 100 mm); the solid lines are the experimental results while the dashed lines are the simulated ones. The numerical simulations fit the experimental results with a very good precision since the amplification level and the shock positions are recovered. Nevertheless, there is a little disagreement for the rise time, which is longer in the simulations than in the experiments. This may be due to numerical dissipation occurring during the resolution of the diffraction part. Indeed, while the numerical solver for Burgers' equation is a shock fitting algorithm, the method used to solve the linear KZ equation is a shock capturing algorithm. Shocks are not treated explicitly as such in the linear, diffraction part of the split-step algorithm. The finite differences automatically stabilize the algorithm by introducing numerical viscosity, which artificially increases the rise time.

CONCLUSION AND OUTLOOKS

A new explanation about the wavefront unfolding effect sometimes associated with acoustical shock waves incoming

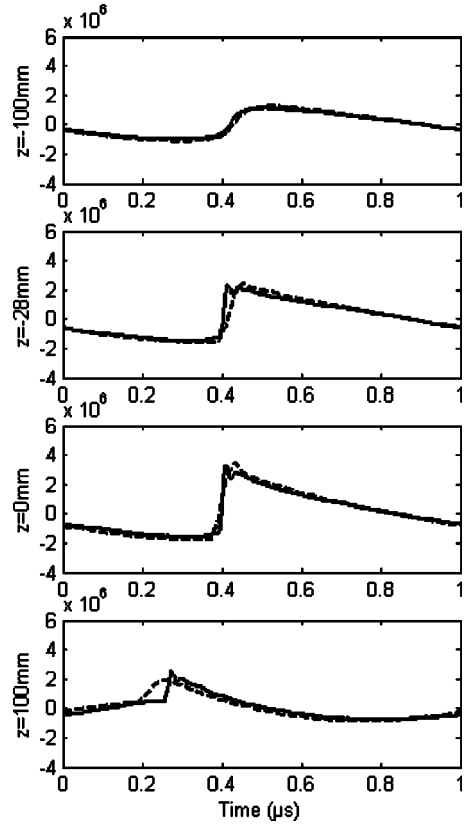

FIG. 11. Comparisons between measured (solid lines) and simulated (dash lines) pressure waveforms (in Pa) in nonlinear regime on the axis $x=0$ at four different distances from the tip of the cusped caustic ($z=-100$, -28, 0, and 100 mm).

on a cusped caustic has been proposed through original theoretical and numerical studies. This effect does not seem to be intrinsically nonlinear as expected by previous authors but associated both with nonlinearities and the geometry of the wavefront. Quantitative comparisons between numerical simulations and experimental results have demonstrated the validity of the theoretical modeling and the accuracy of the numerical code. Besides, as the numerical code is validated both experimentally and numerically, it is now possible to use it to simulate other configurations than those used in the experiments. In particular, it is interesting to apply this code to the prediction of sonic boom focusing in the case of complex aircraft maneuvers, that is to say, the focusing of an "N" wave at a cusped caustic. Figure 12 presents the time dependence of the pressure at three different locations near the cusp ($\bar{z}=0$, $\bar{x}=0$ for case a, $\bar{z}=1$, $\bar{x}=0.45$ for case b and $\bar{z}=2$, $\bar{x}=0.8$ for case c) for a nonlinearity parameter $\mu=0.1$ and an incoming "N" wave [$F(\tau)=-\tau$ if $|\tau|<1$,0 else]. On the tip of the caustic [Fig. 12(a)], the signal has no precursor and it begins with a steep shock. The second signal [Fig. 12(b)] displays a structure with two shocks visible at the beginning of the signal (noted 1 and 2 on the figure). The amplitude is weaker than on the Oz axis since the focusing effects are less important off axis. The structure of the signal [Fig. 12(c)] is made of three shocks associated with the interaction of three different signals in accordance with the theory which stipulates that in zone II three rays (and consequently three signals) pass through each point. Therefore, it

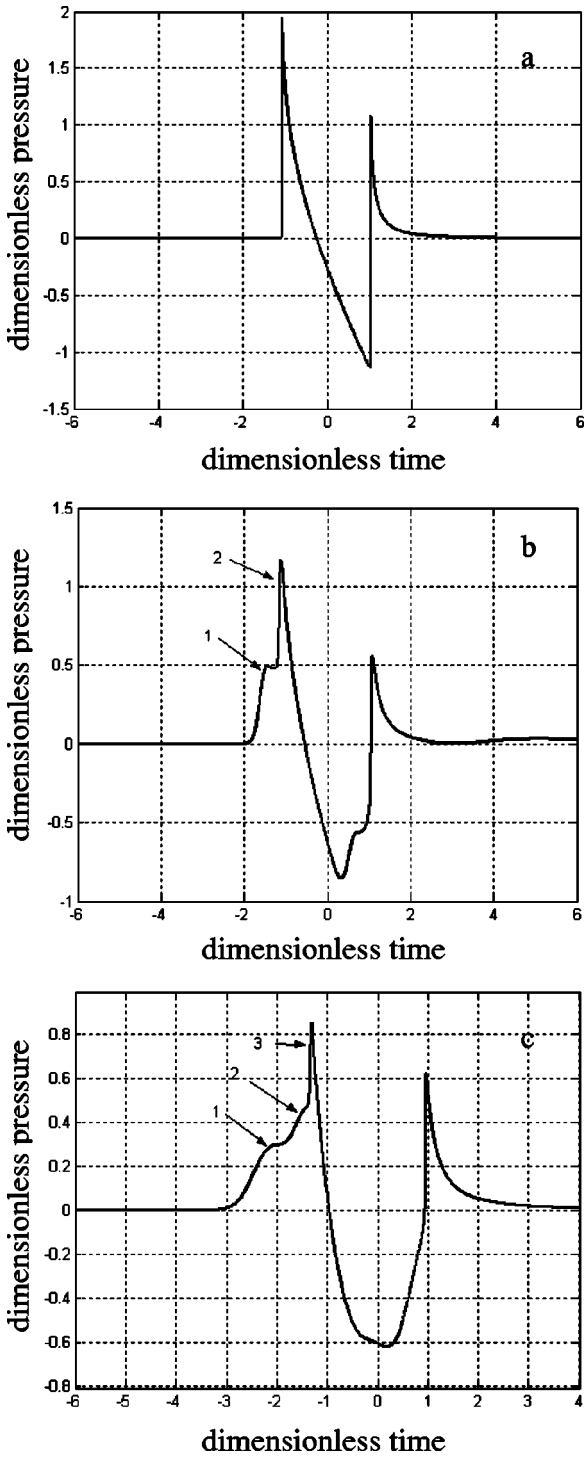

FIG. 12. Numerical simulations of the pressure time waveforms at three points near the cusped caustic cusp [(a) $\bar{z}=0$, $\bar{x}=0$; (b) $\bar{z}=1$, $\bar{x}=0.45$; and (c) $\bar{z}=2$, $\bar{x}=0.8$] for an "N" wave in nonlinear regime ($\mu=0.1$).

is possible to compare the numerical results with existing experimental measurements of sonic boom focusing. In particular, we can notice that the waveform obtained numerically in cases *a* and *b* corresponds to the waveforms already observed by Wanner *et al.* (1972, Fig. 15, microphones 17, 18 and 19 and Fig. 16 microphone 13) in the case of a supersonic aircraft entering into turn. Those results are another qualitative validation of the numerical code. Note that no signal with the characteristic of Fig. 12(c) has been recorded by Wanner *et al.* (1972), since no measurement has been performed inside the branch of the cusped caustic where the corresponding point lies. Also noticeable is the magnitude order of amplification in the experimental setup: around 3 for a fold caustic and 9 for a cusp caustic, the same magnitude orders as measured for sonic boom. Finally, complex waveforms as illustrated by Fig. 12 indicate caustics of higher order than the fold caustics may play an important role for explaining messy waveforms observed for sonic boom in the turbulent atmospheric boundary layer.

Considering the importance of the geometry effect on the focusing process as demonstrated in Sec. III, it would be desirable to improve the links between the aircraft maneuvers and the geometry of the cusped caustic. For real atmospheres, this would imply in particular to generalize the theoretical model to a 3D heterogeneous and moving medium, a task far from easy.

ACKNOWLEDGMENTS

This investigation have been carried out under a contract awarded by the European Commission, Contract No. G4RD-CT-2000-00398.

APPENDIX: THE NUMERICAL CODE

1. Presentation of the numerical method

To our knowledge, only one previous study is dedicated to the numerical simulation of the focusing of shock waves at a cusped caustic (Piacsek, 1995), based on the NPE equation [nonlinear paraxial equation (McDonald and Kuperman, 1987)]. This numerical study has been applied to investigate distortion of a sonic boom rippled wavefront (Piacsek, 2002), in order to validate the Pierce and Maglieri (1972) model of sonic boom wavefront folding in a turbulent atmosphere. However, no quantitative validation was presented. Here, relying on catastrophe theory and Guiraud scaling law, we are able to validate quantitatively the numerical resolution, before comparing it with experiments.

The theoretical model being based on the KZ equation, we have modified an algorithm solving the KZ equation previously used to study the nonlinear Fresnel diffraction of shock waves (Coulouvrat and Marchiano, 2003). That new algorithm solves the KZ equation [Eq. (7)] associated with the boundary conditions [Eq. (9)] in the temporal domain. The problem is formulated with the potential variable instead of the pressure. The potential is more suited to take into account shock waves. Indeed, a discontinuity for the pressure corresponds to an angular point for the potential. This approach has already been fruitful to solve the nonlinear Tricomi equation in the case of the focusing of weak shock waves at a fold caustic (Marchiano *et al.*, 2003a). The dimensionless potential is calculated from the dimensionless pressure:

$$\overline{p}=\frac{\partial\overline{\phi}}{\partial\overline{t}}. \tag{A1}$$

The KZ equation for the potential is

$$\frac{\partial^2\overline{\phi}}{\partial\overline{z}\partial\overline{t}}=\frac{\partial^2\overline{\phi}}{\partial\overline{x}^2}+\mu\frac{\partial}{\partial\overline{t}}\left(\frac{\partial\overline{\phi}}{\partial\overline{t}}\right)^2, \tag{A2}$$

Apart from the nonlinear term, this equation is identical to the equation for pressure [Eq. (7)]. The associated boundary conditions, valid only in zone I (Fig. 1), are

$$\overline{\phi}(\overline{x},\overline{z},\overline{t}) \xrightarrow[\sqrt{\overline{x}^2+\overline{z}^2}\to\infty]{} \frac{1}{\sqrt{|6\overline{\alpha}^2-\overline{z}|}} \times\int_{-\infty}^{\overline{t}} F(\overline{t}'+\overline{\alpha}\overline{x}+\overline{\alpha}^2\overline{z}-\overline{\alpha}^4)d\overline{t}'. \tag{A3}$$

The problem is symmetrical about the propagation axis Oz. Therefore it is possible to solve the problem for only one-half of the plane Oxz, in order to reduce the size of the computational domain. So the following symmetry condition is added to the boundary conditions [Eq. (16)]:

$$\frac{\partial}{\partial\overline{x}}\overline{\phi}(\overline{x}=0,\overline{z},\overline{t})=0. \tag{A4}$$

Note that these boundary conditions correspond to the cusped caustic and can be changed. To treat the real wavefront in Sec. III, a wavefront similar to the one used by Piacsek (2002) has been computed in the initial plane and nonlinear plane waves are used for the other boundary conditions.

In order to calculate the numerical solutions of the problem, the space variables are discretized on a regular grid. The points are equally spaced in the $\overline{z}$ direction starting from plane $\overline{Z}^-$ to plane $\overline{Z}^+$ with a step $\Delta\overline{z}$. They are also equally spaced in the $\overline{x}$ direction from 0 to $\overline{X}^+$ with a step $\Delta\overline{x}$. The time is discretized with a step $\Delta\overline{t}$.

The KZ equation [Eq. (15)] is solved plane after plane following the $\overline{z}$ direction. For each $\Delta\overline{z}$, the numerical solutions of the KZ equation are computed using the split-step method (Ames, 1977). This scheme has been widely used to solve the KZK [acronym of Khokhlov–Zabolotskaya–Kuznetsov, see Kuznetsov (1970)] equation which is a KZ equation taking into account the attenuation [see Hamilton (1998) for a review]. The split-step scheme consists in splitting the KZ equation into two simpler equations. The first one takes into account the diffraction. It is the linear KZ equation:

$$\frac{\partial^2\overline{\phi}}{\partial\overline{z}\partial\overline{t}}=\frac{\partial^2\overline{\phi}}{\partial\overline{x}^2}. \tag{A5}$$

The second one deals with the nonlinear effects. It is the Burgers equation for the potential:

$$\frac{\partial^2\overline{\phi}}{\partial\overline{z}\partial\overline{t}}=\mu\frac{\partial}{\partial\overline{t}}\left(\frac{\partial\overline{\phi}}{\partial\overline{t}}\right)^2. \tag{A6}$$

At each plane, first the linear KZ equation is solved numerically by an implicit finite differences scheme in the time domain based on the Lee and Hamilton scheme (1995). This scheme has originally been developed to solve the KZ equation for pressure in the framework of the beam propagation. It can easily be adapted to solve the KZ equation for potential since these two equations have the same form. Only the boundary conditions are different. Once the solution of the linear KZ is computed, it is used to initialize the calculation of the solution of the Burgers equation for potential on an elementary step $\Delta\overline{z}$. That solution is calculated semi-analytically with the Hayes graphical method (1969), which was recently adapted for the numerical procedure by Coulouvrat and Marchiano (2003) and Marchiano *et al.* (2003a). Finally, on a $\Delta\overline{z}$ step, the solution takes into account the diffraction and the nonlinear effects. The coupling between diffraction and nonlinearity is assured by the repetition of the procedure plane after plane. Note that, as the solution of the linear KZ equation, the solution of the Burgers equation is obtained in the temporal domain so that the whole resolution is achieved in the time domain. Moreover, there is no stability condition necessary to solve the Burgers equation (the solution is semi-analytical) or the linear KZ equation (the scheme is fully implicit). Finally, the pressure is calculated from Eq. (14) by a second-order finite differences scheme applied to the potential solution and a symmetry about the axis of propagation Oz permits to recover the pressure on the whole domain.

2. Validation of the algorithm

According to Guiraud's scaling for the cusped caustic [see Sec. III and Coulouvrat (2000)], if the incoming function is a step shock, the following quantities are constant for the point where the pressure is maximal: $\overline{p}_{\max}/\mu^{-1/3}=C_p$, $\overline{t}_{\max}/\mu^{4/3}=C_t$, $\overline{x}_{\max}/\mu=C_x$ and $\overline{z}_{\max}/\mu^{2/3}=C_z$, where $\overline{p}_{\max}$ represents the value of the maximal pressure, $\overline{t}_{\max}$ is the time for which the pressure is maximal, $\overline{x}_{\max}$, $\overline{z}_{\max}$ is the position where the pressure is maximal, and C_p, C_t, C_x and C_t are constants. These similitude laws are a good way to check the numerical code quantitatively, as they imply a strong coupling between nonlinearity and diffraction. Figure 13 shows that the numerical results are in very good agreement with the theoretical predictions. Indeed, the four ratios are practically constant for the values of μ greater than 0.02. This agreement shows that the amplitude of the peaks is limited and follows the similitude law $\tilde{p}_{\max}\mu^{-1/3}$. For the values of the nonlinear parameter under the threshold $\mu=0.02$, the results are not so good because the nonlinear effects are too small and the numerical resolution would require a more refined mesh grid than the one used. This result provides a quantitative validation of the numerical procedure. This kind of validation has already been used to validate a numerical code solving the nonlinear Tricomi equation with the Guiraud similitude law (Auger and Coulouvrat, 2002; Marchiano *et al.*, 2003a). Nevertheless, the results of those works were not in a such good agreement as the present ones, especially concerning the similitude law following the temporal variable. The very good agreement obtained in the

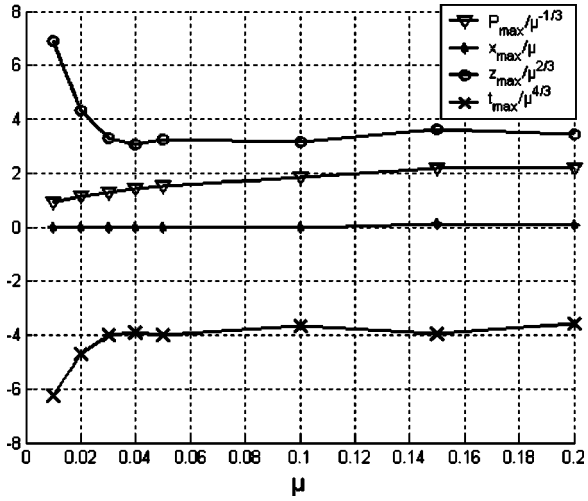

FIG. 13. Numerical check of theoretical Guiraud's similitude law.

present work is due to the fact that the numerical solver is now entirely in the time domain, contrarily to the case of the resolution of the nonlinear Tricomi equation for which the diffraction equation is solved in the frequency domain. This difference is important because for an algorithm in the time domain, it is possible to impose in the boundary condition an incoming step function to check the similitude law, whereas it is impossible for the nonlinear Tricomi solver, for which only artificially periodic incoming signals are available. The use of an algorithm in the frequency domain for the nonlinear Tricomi equation was required by the mixed elliptic/hyperbolic type of the equation, while the KZ equation is fully hyperbolic.

Finally, we indicate that a modified version of the present code has already been used to confirm theoretical predictions in a study about the nonlinear Fresnel diffraction of weak shock waves (Coulouvrat and Marchiano, 2003). In that previous study, the numerical code was similar to the code presented here except for the boundary conditions. The agreement between theoretical predictions and numerical results on self-similar solutions of the nonlinear KZ equation also permitted us to validate quantitatively the numerical method.

Ames, W. F. (**1977**). *Numerical Methods for Partial Differential Equations* (Academic, New York), pp. 315–467.

Auger, T., and Coulouvrat, F. (**2002**). ''Numerical simulation of sonic boom focusing,'' AIAA J. **40**, 1726–1734.

Berry, M. V. (**1976**). ''Waves and Thom's theorem,'' Adv. Phys. **25**, 1–26.

Coulouvrat, F. (**2000**). ''Focusing of weak acoustic shock waves at a caustic cusp,'' Wave Motion **32**, 233–245.

Coulouvrat, F., and Marchiano, R. (**2003**). ''Nonlinear Fresnel diffraction of weak shock waves,'' J. Acoust. Soc. Am. **114**, 1749–1757.

Cramer, M. S. (**1981a**). ''Focusing of weak three-dimensional shock waves,'' AIAA J. **19**, 1363–1365.

Cramer, M. S. (**1981b**). ''Focusing of weak shock waves at an axisymmetric arête,'' J. Fluid Mech. **110**, 249–253.

Cramer, M. S., and Seebass, A. R. (**1978**). ''Focusing of weak shock waves at an arête,'' J. Fluid Mech. **88**, 209–222.

Davy, B. A., and Blackstock, D. T. (**1971**). ''Measurements of the refraction and diffraction of a short *N* wave by a gas-filled soap bubble,'' J. Acoust. Soc. Am. **49**, 732–737.

Downing, M., Zamot, N., Moss, C., Morin, D., Wolski, E., Chung, S., Plotkin, K., and Maglieri, D. (**1998**). ''Controlled focused sonic booms from maneuvering aircraft,'' J. Acoust. Soc. Am. **104**, 112–121.

Gill, P. M., and Seebass, A. R. (**1973**). ''Nonlinear acoustic behavior at a caustic: an approximate analytical solution,'' AIAA Aeroacoustics Conference, Seattle (MIT, Cambridge), AIAA Paper 73-1037, pp. 353–386.

Guiraud, J.-P. (**1965**). ''Acoustique géométrique, bruit balistique des avions supersoniques et focalisation (Geometrical acoustics, balistic noise of supersonic aircraft and focusing),'' J. Mec. **4**, 215–267 (in French).

Hamilton, M. F. (**1998**). ''Sound beams,'' in *Nonlinear Acoustics*, edited by M. F. Hamilton and D. T. Blackstock (Academic, San Diego), pp. 233–261.

Hayes, W. D., Haefeli, R. C., Kulsrud, H. E. (**1969**). ''Sonic boom propagation in a stratified atmosphere with computer program,'' NASA CR-1299.

Kuznetsov, V. P. (**1970**). ''Equations of nonlinear acoustics,'' Sov. Phys. Acoust. **16**, 467–470.

Lee, Y.-S., and Hamilton, M. F. (**1995**). ''Time-domain modeling of pulsed finite-amplitude sound beams,'' J. Acoust. Soc. Am. **97**, 906–917.

Marchiano, R., Coulouvrat, F., and Grenon,, R. (**2003a**). ''Numerical simulation of shock wave focusing at fold caustics, with application to sonic boom,'' J. Acoust. Soc. Am. **114**, 1758–1771.

Marchiano, R., Thomas, J.-L., and Coulouvrat, F. (**2003b**). ''Experimental simulation of supersonic superboom in a water tank: nonlinear focusing of weak shock waves at a fold caustic,'' Phys. Rev. Lett. **91**(18), 184301(1-4).

Marston, P. L. (**1988**). ''Wavefront geometries giving transverse cusp and hyperbolic umbilic foci in acoustic shocks,'' in *Shock Waves in Condensed Matter 1987*, edited by S. C. Schmidt and N. C. Holmes (Elsevier, Amsterdam).

Marston, P. L. (**1992**). ''Geometrical and catastrophe optics methods in scattering,'' in *High Frequency and Pulse Scattering, Physical Acoustics*, edited by A. D. Pierce and R. N. Thurston (Academic, San Diego), Vol. XXI, pp. 1–234.

McDonald, B. E., and Kuperman, W. A. (**1987**). ''Time domain formulation for pulse propagation including nonlinear behavior at a caustic,'' J. Acoust. Soc. Am. **81**, 1406–1417.

Pearcey, T. (**1946**). ''The structure of an electromagnetic field in the neighbourhood of a cusp of a caustic,'' Philos. Mag. **37**, 311–317.

Piacsek, A. A. (**1995**). ''A numerical study of a weak step shocks that focus in two dimensions,'' Ph.D. thesis, Pennsylvania State University.

Piacsek, A. A. (**2002**). ''Atmospheric turbulence conditions leading to focused and folded sonic boom wave fronts,'' J. Acoust. Soc. Am. **111**, 520–529.

Pierce, A. D. (**1971**). ''Maximum overpressures of sonic boom near the cusp of caustics,'' in *Noise and Vibration Control Engineering*, edited by M. J. Crocker (Purdue U. P., West Lafayette), pp. 478–487.

Pierce, A. D., and Maglieri, D. J. (**1972**). ''Effects of atmospheric irregularities on sonic boom propagation,'' J. Acoust. Soc. Am. **51**, 702–721.

Plotkin, K. J., and Cantril, J. M. (**1976**). ''Prediction of sonic boom at focus,'' AIAA Paper 76-2, AIAA 14th Aerospace Sciences Meeting, Washington.

Prasad, P., and Sangeeta, K. (**1999**). ''Numerical simulation of converging nonlinear wavefronts,'' J. Fluid Mech. **385**, 1–20.

Sanaï, M., Toong, T. Y., and Pierce, A. D. (**1976**). ''Ballistic range experiments on superboom generated at increasing flight Mach numbers,'' J. Acoust. Soc. Am. **59**, 520–524.

Sturtevant, B., and Kulkarny, V. A. (**1976**). ''The focusing of weak shock waves,'' J. Fluid Mech. **73**, 651–671.

Tanter, M., Thomas, J.-L., and Fink, M. (**2000**). ''Time reversal and inverse filter,'' J. Acoust. Soc. Am. **108**, 223–234.

Thom, R. (**1972**). *Stabilité structurelle et morphogenèse* (Benjamin, Reading), pp. 72–107 (in French); English translation: *Structural stability and morphogenesis* (Benjamin, Reading, 1975).

Wanner, J.-C., Vallée, J., Vivier, C., and Théry, C. (**1972**). ''Theoretical and experimental studies of the focus of sonic booms,'' J. Acoust. Soc. Am. **52**, 13–32.

Whitham, G. B. (**1956**). ''On the propagation of weak shock waves,'' J. Fluid Mech. **1**, 290–318.

Zabolotskaya, E. A., and Khokhlov, R. V. (**1969**). ''Quasi-plane waves in the nonlinear acoustics of confined beams,'' Sov. Phys. Acoust. **15**, 35–40.

High-intensity rocket noise: Nonlinear propagation, atmospheric absorption, and characterization

Sally Anne McInerny[a] and Semih M. Ölçmen
Department of Aerospace Engineering and Mechanics, The University of Alabama, P.O. Box 870280, Tuscaloosa, Alabama 35487-0280

(Received 24 August 2004; revised 1 November 2004; accepted 6 November 2004)

Analyses of rocket noise data measured at far-field locations during the launch of a large rocket and a smaller rocket are presented. Weak shocks are present in all of the data sets. In order to characterize these shocks, those segments of the waveforms where the acoustic pressure is increasing are isolated and the rate of increase in pressure plotted versus magnitude of pressure rise. The plots follow a trend consistent with random noise at low values of pressure rise, then transition to the pressure-squared dependence expected for weak shocks at higher pressure rise values. Power spectral densities of the noise during the period of maximum overall sound-pressure levels display high- and low-frequency spectral slopes that are close to those predicted for shock-dominated noise. It is concluded that shocks must be included in propagation models if high frequency levels are to be estimated as a function of distance from the source. Initial shock thicknesses will have to be characterized experimentally and will require instrumentation with a bandwidth well in excess of 20 kHz. Reflection-free data are essential if meaningful assessments of the statistical properties of the noise are to be made. © *2005 Acoustical Society of America.* [DOI: 10.1121/1.1841711]

PACS numbers: 43.25.Cb, 43.28.Mw, 43.28.Bj [MFH] Pages: 578–591

I. INTRODUCTION

Time-domain data recordings of far-field sound pressures were obtained during a series of rocket launches in the late 1980s and early 1990s.[1–3] The data were rich in shock content, where the term ''shock'' is used to describe a pressure rise from a minimum to a maximum over a time that is less than 1/10 of the average period of the overall sound-pressure waveform. Data showed that in the far field, high-frequency sound-pressure levels decreased with distance less than expected on the basis of linear absorption,[1] consistent with previous observations of high-intensity jet and rocket noise.[4–6]

Currently, there is renewed interest in modeling the propagation of high-intensity jet noise. Better estimates of high-frequency attenuation are needed if community noise levels are to be accurately assessed for the latest generation of military jets.[7] In this paper, the rocket noise data that were analyzed in Refs. 1–3 are revisited in the context of nonlinear acoustics and weak shock theory. Data analysis and visualization methods are applied to characterize the transfer of energy from the peak frequency in the spectrum, and the extent to which shocks control the high-frequency spectral levels and their attenuation.

II. FIELD MEASUREMENTS

The launch vehicle noise data examined here were recorded in the late 1980s and early 1990s as part of an effort to monitor the effects of rocket noise on the demographics of endangered species that breed and nest in the vicinity of launch sites.[1–3] The goal of the measurements was to obtain data representative of sound levels experienced by wildlife during a launch. Sound-level meters were placed upright on the ground with their microphones about 37 cm above the ground. Consequently, the data contained ground reflections. Temperature and humidity measurements, as would be needed for propagation studies, were not required. Information on the vehicles and measurement sites for the data sets examined here is given in Tables I and II.

A. Instrumentation

Bruel & Kjaer model 2230 sound-level meters (SLMs) with model 4155 microphones were used to record all of the rocket noise data sets. The ac output of the SLMs was recorded on TEAC digital audio tape (DAT recorders) at a sample rate of 48 000 sps. The frequency response of each SLM was measured *exclusive of the microphone*. Typically, the SLM response was 1.0 dB down at frequencies from 3.5 to 7 Hz and down 3.0 dB at frequencies from 2 to 3.5 Hz.[1] Calibration curves provided with the model 4155 microphones only extend down to 20 Hz, but product information sheets for Bruel & Kjaer condenser microphone cartridges 4133 to 4181 indicate the 3.0-dB down point between 1 and 3 Hz. The influence of low-frequency instrumentation roll-off on rocket noise metrics was examined in Ref. 3.

The high-frequency roll-off of the 4155 microphone varies with angle of incidence, and the angle of incidence varies with time during the launch. The type 2230 SLM is ''equipped with a $\frac{1}{2}$ inch prepolarized condenser microphone Type 4155. It has a linear 0° free field frequency response which is well suited for measurements in free field conditions....'' [9] The typical 0° free field response for the 2230 fitted with a 4155 microphone (see Fig. 3, p. 375 of Ref. 2) begins to roll off rapidly above 17 kHz, but each

[a]Electronic mail: smcinerny@coe.eng.ua.edu

TABLE I. Engine mechanical power, sound-power level, and peak frequencies of the rocket noise data sets examined. Sound power levels given in dB re: 10^{-12} W were calculated using acoustic efficiencies[8] of 0.004 and 0.0053 for the Scout and Titan IV, respectively. Peak frequencies correspond to the peak in the constant bandwidth power spectral density calculated over the 3-dB down period.

	W_m	L_W	F_{peak}
Scout	6.4×10^{8} W	184 dB	60 Hz
Titan IV	1.5×10^{10} W	199 dB	16 Hz

TABLE II. Overall sound-pressure levels in dB re: $20E-6$ Pa over the 3.0-dB down period, distance of the measurement sites from the launch pad, d, and from the source, R. The distance from the exhaust to the measurement location during the period of maximum overall sound pressure levels, R, was estimated based on a peak angle of directivity of 60°, so that $R = d/\sin(60)$.

	d (km)	R (km)	L_{eq} (dB)
Scout—Site A	0.36	0.42	126.4
Scout—Site B	0.64	0.74	119.9
Scout—Site C	0.94	1.09	116.0
Scout—Site D	1.22	1.41	113.1
Titan IV—Site A	0.82	0.95	139.9
Titan IV—Site B	2.00	2.3	129.7
Titan IV—Site C	3.41	3.94	127.0
Titan IV—Site D	5.79	6.69	120.1
Titan IV—Site E	13.15	15.2	110.6

system can be expected to vary somewhat from this nominal response. Peak frequencies in the constant bandwidth power spectral densities (PSDs) of the measured rocket noise data are well below 200 Hz and PSD levels at 10 kHz are down more than 60 dB from the peak. For these reasons, an upper frequency limitation of 15 kHz was considered more than adequate.

B. The 3-dB down time period

Figure 1 is the plot of a typical pressure versus time recording, Fig. 1(a), along with the corresponding 1-s averaged overall SPL (calculated using 99% overlap), Fig. 1(b). The initial pressure pulse seen in Fig. 1(a) is the overpressure pulse generated when the solid rocket engine is ignited. This pulse propagates outward over the ground and is rapidly attenuated, so that it is not seen in recordings made at distant sites. After the overpressure pulse, noise levels are initially low, corresponding to radiation angles (measured from the exhaust axis) close to 90°. For some sites, there were line-of-sight issues during this initial time period. As the vehicle rises, however, there is a direct line-of-sight from the exhaust plume(s) to all of the measurement sites and no ground-effect issues. Sound levels increase, reach a maximum, and then slowly decrease corresponding to the passage of the radiation angle from 90° through the peak directivity angle and then to smaller angles—measured relative to the exhaust axis.[1,10] The data analyzed for this paper correspond to the time period in which the OASPLs were within 3 dB of their maximum (as determined using a 1.0-s average with 99% overlap). See Fig. 1(b). This provides a reasonable balance between the desire for statistically stationary data sets and longer record lengths to reduce random error.

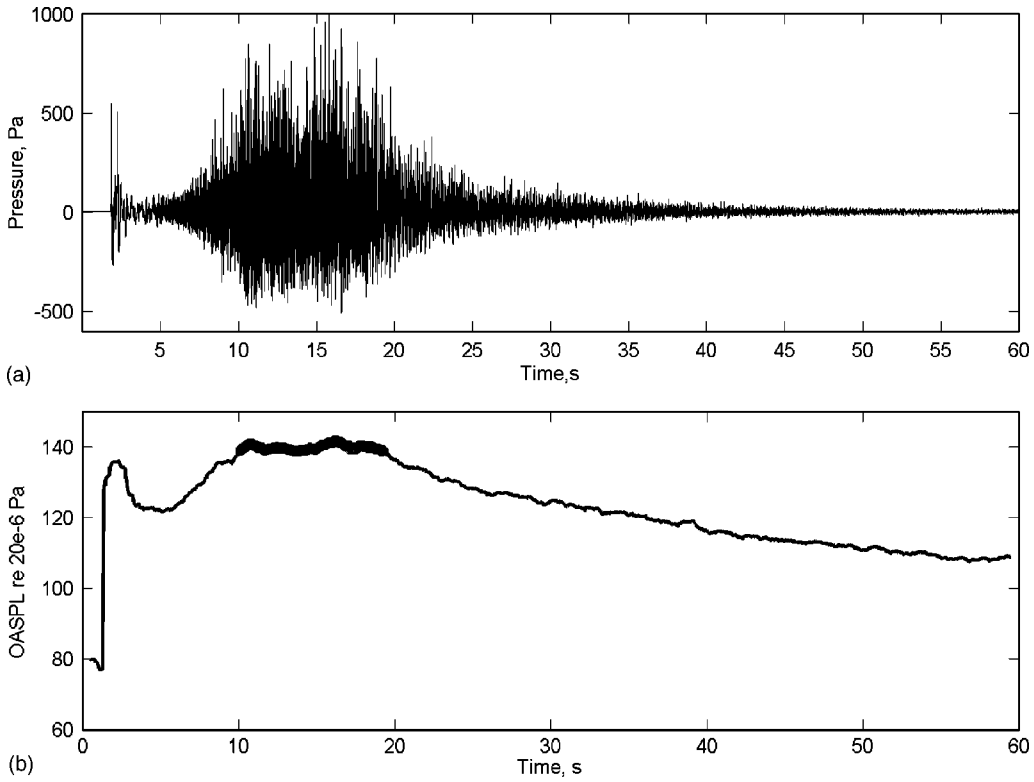

FIG. 1. Sound-pressure level versus time at Titan IV site A: (a) instantaneous; and (b) 1-s averaged. The 3-db down period is indicated by the dark circles in (b).

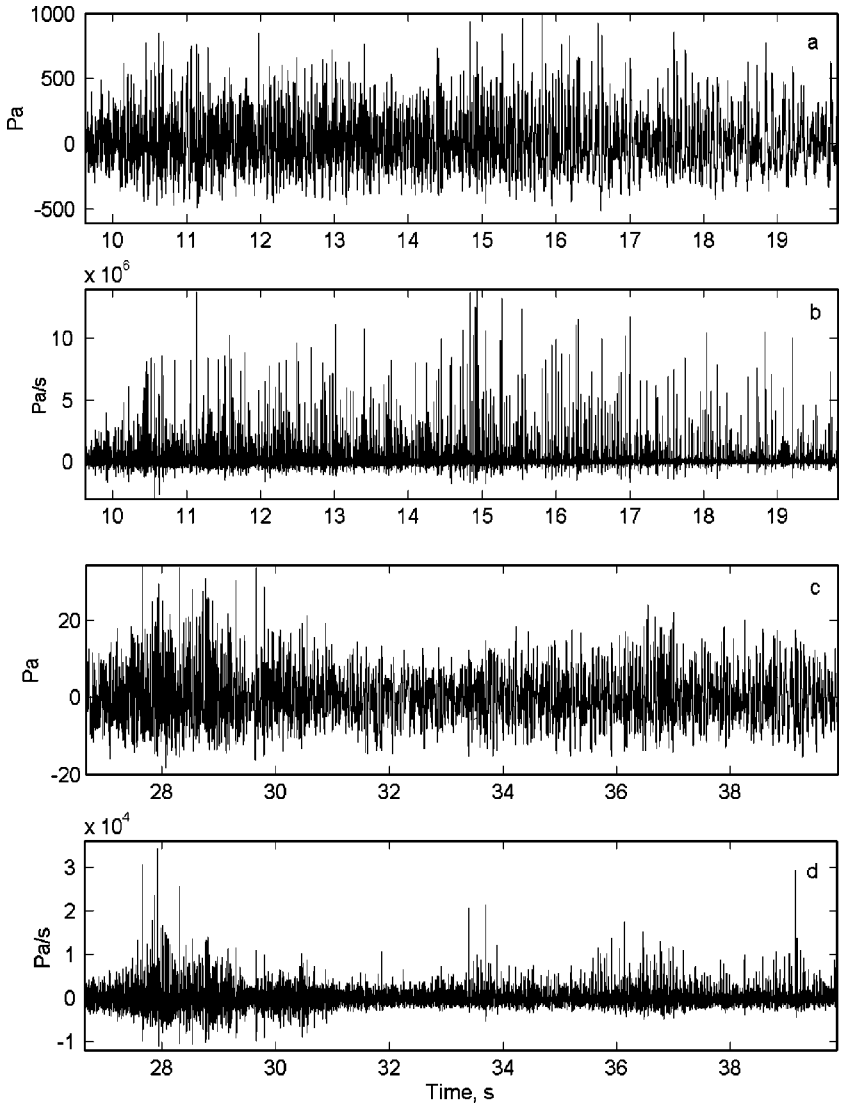

FIG. 2. Titan IV pressure and time rate of change of the pressure versus time over the 3-dB down period: (a) site A, pressure versus time; (b) site A, pressure time rate of change versus time; (c) site E, pressure versus time; and (d) site E, pressure time rate of change versus time. Note that the recording times are not coordinated to a common start time.

C. Random noise sequences

As a point of reference, results obtained for two of the data sets, Titan IV sites A and E, are compared to those that would be obtained for random noise distributions of the same power spectral densities. The two random noise sequences were generated as follows. A normally distributed random noise sequence was generated and taken to have the same sample rate as the data. The Fourier transform of the noise was weighted so as to have the same spectral amplitudes (without the reflective interference dip) as the measured data at that site. A reflection with a delay of 1.5 ms (a typical reflection delay at the time of peak acoustics) was added to the shaped random noise in the time domain; and, finally, the result was scaled so that the rms amplitude was equal to that of the measured data.

III. ANALYSES AND RESULTS

The data are analyzed to compare the characteristics of noise measured at different sites during the same launch. The data sets compared do not represent the same noise measured at different propagation distances; they are noise radiated from the plume, in the peak directivity direction, at different times during the ascent. Comparison of the data sets, then, rests on the assumption that the source and the propagation paths are statistically similar. Trajectory effects, turbulence, wind, and temperature gradients are likely to have been present, but are not accounted for. Changes in source characteristics with flight speed are also neglected. Given that the engine exhaust velocity relative to the nozzle exit plane, U_e, exceeded 2400 m/s ($U_e/c_o \sim 7$, where c_o is the speed of sound in air at 20 °C) and for the radiation times in question, except perhaps those of the most distant Titan IV site, the vehicle speed was less than Mach one (i.e., $V_{\text{veh}}/c_o = 1$), this assumption is reasonable.

A. Shock waveforms

Plots of sound pressure versus time and the time rate of change of the pressure versus time at the Titan IV measurement sites closest to and most distant from the launch pad are shown in Fig. 2. The presence of shocks is readily revealed by the rate of change plots, Figs. 2(b) and (d). The time rate of change of the pressure was approximated using a forward difference routine. Central differencing was not used in order to preserve the true difference values at the beginning and end of a shock waveform. Difference operations are prob-

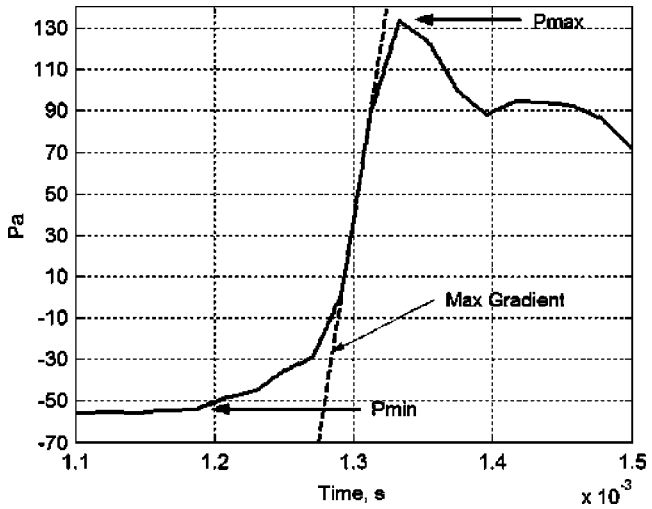

FIG. 3. Determination of P_{max}, P_{min}, and maximum rate of increase. This example is the shock with the highest rate of increase in the Titan IV site C data set.

lematic if the data contain high levels of spurious noise, but it is clear from the results obtained that the results here are dominated by the high rise rates of the shock waveforms. The maximum values of the pressure time rate of change in Fig. 2(b) are understated as a consequence of high-frequency instrumentation limits. Plots of the rate of increase in the pressure versus the magnitude of the pressure rise presented later in the paper will make this clear.

The pressure data are skewed, but much less skewed than the time rate of change of the pressure. Despite the relatively low sound levels at the most distant site, site E, Figs. 2(c) and (d), a positive skewness and large positive pressure time derivatives, reflecting steep pressure rises, are evident. Representative skewness values for these and other data sets were reported in Refs. 1 and 10. The skewness of the pressure—but not the time rate of change of the pressure—in the Titan data, where the peak frequency in the 3-dB down PSD is around 16 Hz, may have been affected by low-frequency instrumentation roll-off.[3]

Individual shock waveforms were identified in the data sets as follows. The change in sign of the time rate of change of the pressure was used to determine indices corresponding to pressure minima and pressure maxima. See Fig. 3. Between subsequent minima and maxima (i.e., during periods when the pressure was rising), the maximum instantaneous rate of increase in the pressure was determined. The difference between the maximum and minimum pressure was taken as the pressure rise; the time midway between the minimum and subsequent maximum was taken as the time of the shock.

Efforts to remove reflected shocks from the analysis sets proved unsuccessful. All of the methods attempted had the effect of eliminating some strong initial shocks, as well as some of the reflections. This means that two ''shocks'' may then be identified with different portions of the same waveform, i.e., with the initial and reflected shocks.

The shock waveforms measured at the nearest and furthest Titan IV measurement sites that had the largest time

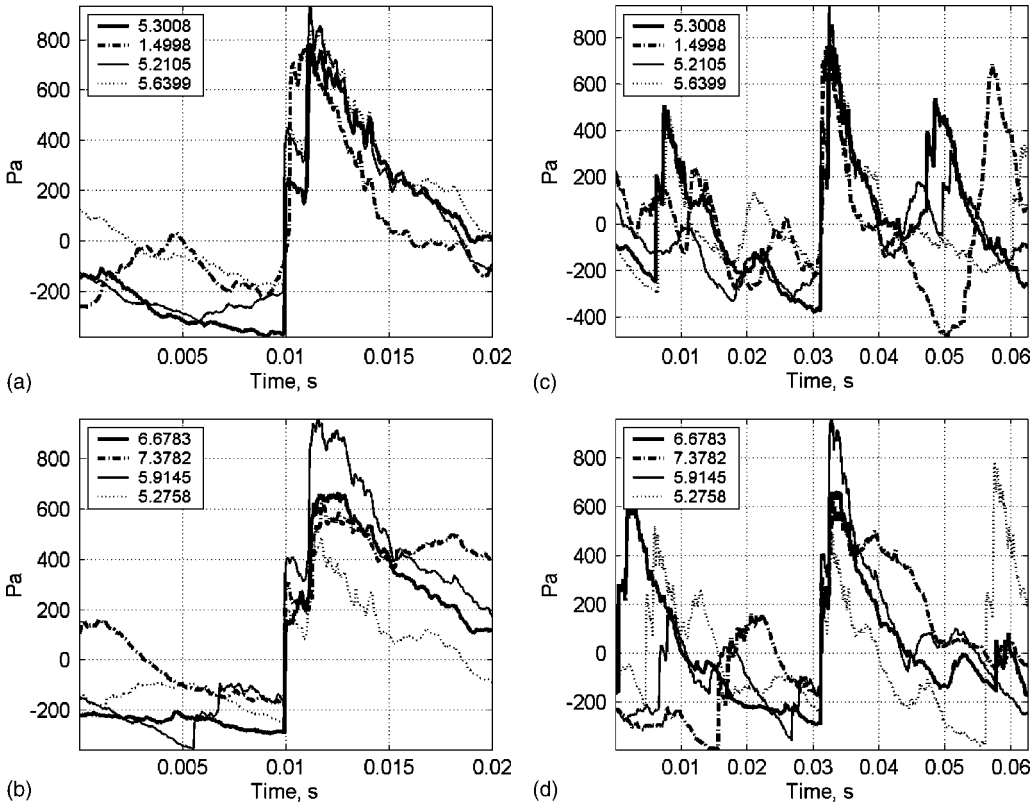

FIG. 4. Titan IV site A shocks: (a) the four shocks with the largest and (b) the next largest instantaneous rates of pressure increase, plotted over a 20-ms time span; (c) and (d) the same shocks plotted over a 62-ms time span. The time of each shock (midpoint) relative to the start of the 3-dB down time period is indicated in the legend.

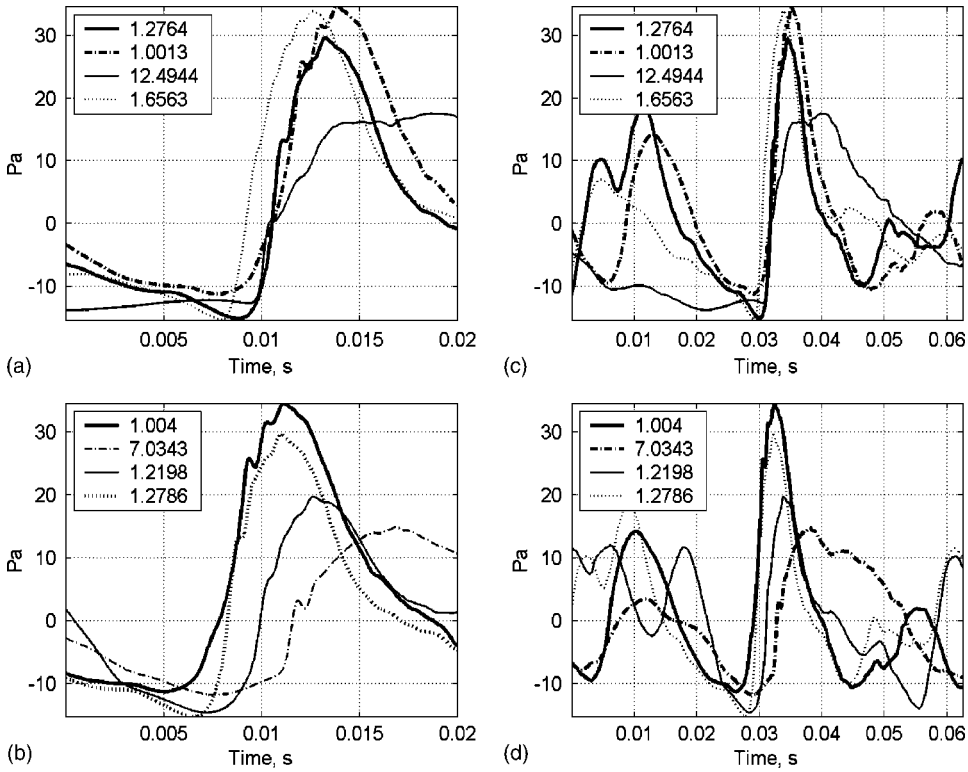

FIG. 5. Titan IV site E shocks: (a) the four shocks with the largest and (b) the next largest instantaneous rates of pressure increase, plotted over a 20-ms time span; (c) and (d) the same shocks plotted over a 62-ms time span. The time of each shock (midpoint) relative to the start of the 3-dB down time period is indicated in the legend.

rates of increase are shown in Figs. 4 and 5, respectively. These are the same data sets for which the sound pressure and time rate of change of the pressure, over the entire 3-dB down period, are plotted in Fig. 2. The times of the shocks, relative to the start of the 3-dB down time period, are indicated in the legends of Figs. 4 and 5. Figures 4(a), 4(b), 5(a), and 5(b) are expanded plots of the shocks over a 20-ms duration; the plots in Figs. 4(c), 4(d), 5(c), and 5(d) are the same shocks, respectively, plotted over a longer time period (approximately $1/f_{\text{peak}}$). The shocks are plotted so that the median time between the pressure minima and maxima are aligned in the center of the plot. (Additional plots of shock waveforms can be found in Figs. 3 to 6 of Ref. 1.)

Reflected shocks can be clearly seen in the 20-ms plots of Figs. 4(a) and (b). In Figs. 4 and 5, earlier times (see the legends) correspond to larger angles of incidence (relative to the vertical) and, therefore, shorter time delays between the initial and reflected shock waves. This is most easily seen in Fig. 4(a). Note, also, that two different pressure minimum/maximum pairs on the same waveform are identified as different shocks by the dot-dash line in Fig. 5(a) and the heavy solid line in Fig. 5(b).

Note the sharp transitions at the beginnings and ends of the shocks in Fig. 4. This can be contrasted with the smooth transitions seen in the site E ($\sim$15 km from the source) waveforms of Fig. 5, where the shortest rise time is on the order of 2–3 ms. A relationship between the shock rise time and the frequency at which the power spectral density transitions to a more rapid rate of decrease with increasing frequency is expected, as discussed in a later section.

Figure 6 is an expanded plot of the shocks in Fig. 4(a). It can be seen that the shocks with the largest rate of increase recorded at Titan IV site A (a distance of approximately 950 m from the source) have a rise time of around 1/20 of a millisecond. This corresponds to a frequency, $1/t_{\text{rise}}$, of 20 kHz, a limit forced by the high-frequency instrumentation response.

B. Time rate of increase versus pressure rise magnitude

To gain insight into the relationship between shock thickness, L_{sh}, and losses in a fluid medium, Pierce examined an idealized model of a stationary weak shock (i.e., one that propagates without a change in shape).[11,12] Pierce showed that this length is linearly proportional to the diffusivity, δ, of the medium

$$L_{sh}=\frac{4\rho_o c_o \delta}{\beta P_{sh}}, \tag{1}$$

where P_{sh} is the pressure rise across the shock and ρ_o is the ambient air density. For an ideal gas, $\beta=(1+\gamma)/2$, where γ is the ratio of specific heats. In air, $\beta=1.2$.

Taking $L_{sh}=t_{\text{rise}}c_o$, the shock rise time is

$$t_{\text{rise}}=\frac{4\rho_o \delta}{\beta P_{sh}}. \tag{2}$$

The diffusivity, δ, is related to the absorption coefficient, α, as

$$\alpha \approx \frac{\delta\omega^2}{2c_o^3}, \quad \text{when} \quad \alpha \ll \omega/c_o. \tag{3}$$

The condition $\alpha \ll \omega/c_o$ means that the rate of change in the pressure due to absorption is much less than the rate of change due to the oscillations at frequency ω.

Sonic boom rise times as a function of pressure rise, assuming steady shocks, were calculated by Kang and compared to measured sonic boom data in Ref. 13. The compari-

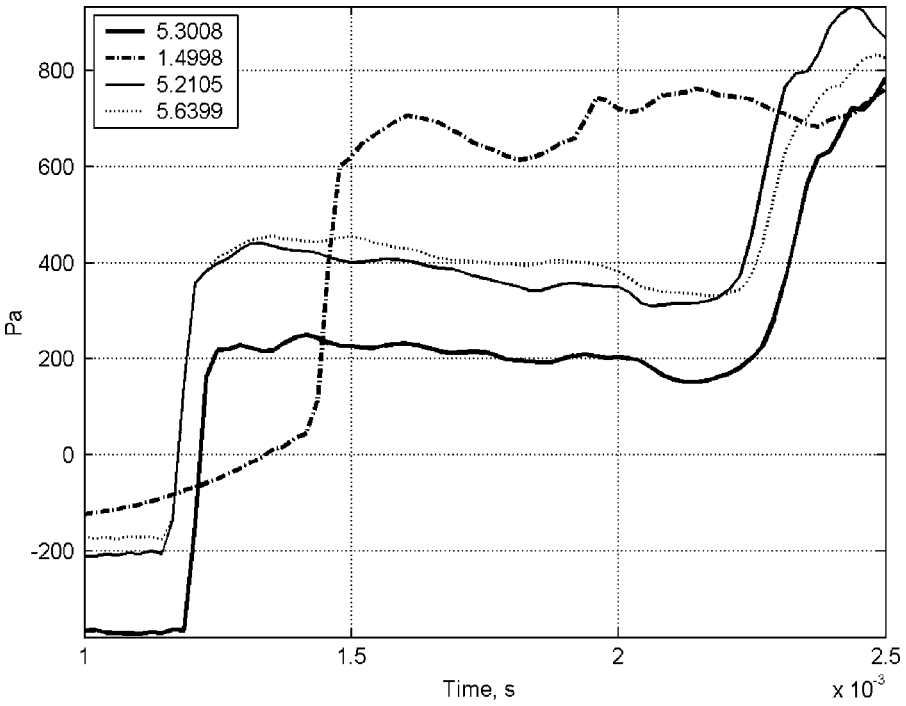

FIG. 6. Expanded view of the four shocks with the largest instantaneous rates of pressure increase in Fig. 4. Note that the time axis gridlines are spaced at 0.5 ms.

son, reproduced in Refs. 14 and 15, is quite favorable; measured data follow the predicted trend, although average rise times tend to be higher than predicted. References 14–17 examined the effect of turbulence on sonic boom rise times. On average, turbulence decreases the pressure rise and increases the rise time. The average increase in rise time is more dramatic than the decrease in pressure.[14] Reference 17 also concluded that nonlinear distortion is weakened in the presence of turbulence.

In air, diffusivity (and, therefore, attenuation) is due to relaxation processes as well as thermo-viscous losses. Equation (3) can still be used for α provided that the speed of sound and diffusivity are replaced with effective values c_* and δ_*.[12] In air at standard conditions, the diffusivity is given by

$$\delta_* = 1.9\times 10^{-6} + \frac{6.4}{f_{O_2}} + \frac{1.2}{f_{N_2}} \ \text{m}^2/\text{s} \quad \text{for } f < f_{N_2} \ (t_{\text{rise}} > 1/f_{N_2}), \tag{4a}$$

$$\delta_* = 1.9\times 10^{-6} + \frac{6.4}{f_{O_2}} \ \text{m}^2/\text{s} \quad \text{for } f_{N_2} < f < f_{O_2} \ (1/f_{N_2} > t_{\text{rise}} > 1/f_{O_2}), \tag{4b}$$

$$\delta_* = 1.9\times 10^{-6} \ \text{m}^2/\text{s} \quad \text{for } f > f_{O_2} \ (t_{\text{rise}} < 1/f_{O_2}), \tag{4c}$$

where f_{O_2} and f_{N_2} are the oxygen and nitrogen relaxation frequencies, respectively.[12] (Atmospheric absorption is generally given in dB/m or dB per 1000 m. Values for α can be calculated from these using the relationship $10\log_{10} p^2 = 10\log_{10} e^{-2\alpha r} p_o^2 r_o^2/r^2$, so that the attenuation in dB/m is $10\log_{10} e^{-2\alpha}$.)

At low frequencies (long shock rise times), the diffusivity/attenuation is due to thermo-viscous-as well as both nitrogen and oxygen relaxation effects—Eq. (4a). Above the nitrogen relaxation frequency, attenuation due to nitrogen relaxation drops out, leaving only thermo-viscous- and oxygen relaxation effects—Eq. (4b). Above the oxygen relaxation frequency, the diffusivity/attenuation is due only to thermo-viscous effects—Eq. (4c). Oxygen and nitrogen relaxation frequencies depend on temperature and humidity;[18,19] hence, so does the structure of a shock.[20,21]

In Ref. 16, the authors calculate shock thickness versus pressure rise for explosive waves. The calculated results clearly show the effect of the change in diffusivity with pressure rise. At low pressures, where $t_{\text{rise}} > 1/f_{N_2}$, a log–log plot of the results follows a straight line determined by Eq. (2) with δ_* given by Eq. (4a). Then, as the pressure increases and the rise time decreases to the point where $1/f_{N_2} > t_{\text{rise}} > 1/f_{O_2}$, there is a transition to a line dictated by Eq. (4b). It is interesting to note that, in the calculations of Ref. 16, dispersion effects associated with molecular relaxation were accounted for, but were found to affect these results only in the transition region between the two diffusivity dependences.

In this paper, the time rate of increase of the pressure is plotted as a function of the pressure rise, Δp. Using $P_{sh} = \Delta p$ and $dp/dt \sim \Delta p/t_{\text{rise}}$, one obtains from Eq. (2)

$$\frac{dp}{dt} \sim \frac{\beta}{4\rho_o \delta} \Delta p^2. \tag{5}$$

In logarithmic terms, this is

$$\log_{10}\frac{dp}{dt} \sim \log_{10}\frac{\beta}{4\rho_o\delta} + \log_{10}\Delta p^2. \tag{6}$$

When plotted logarithmically, then, the time rate of increase in the pressure for a weak shock should fall on a straight line $\log_{10}\Delta p^2$ that is offset by $\log_{10}\beta/(4\rho_o\delta)$. This offset will increase when the pressure rise increases to the point where the rise time is less than $1/f_{N_2}$, so that δ_* decreases from that

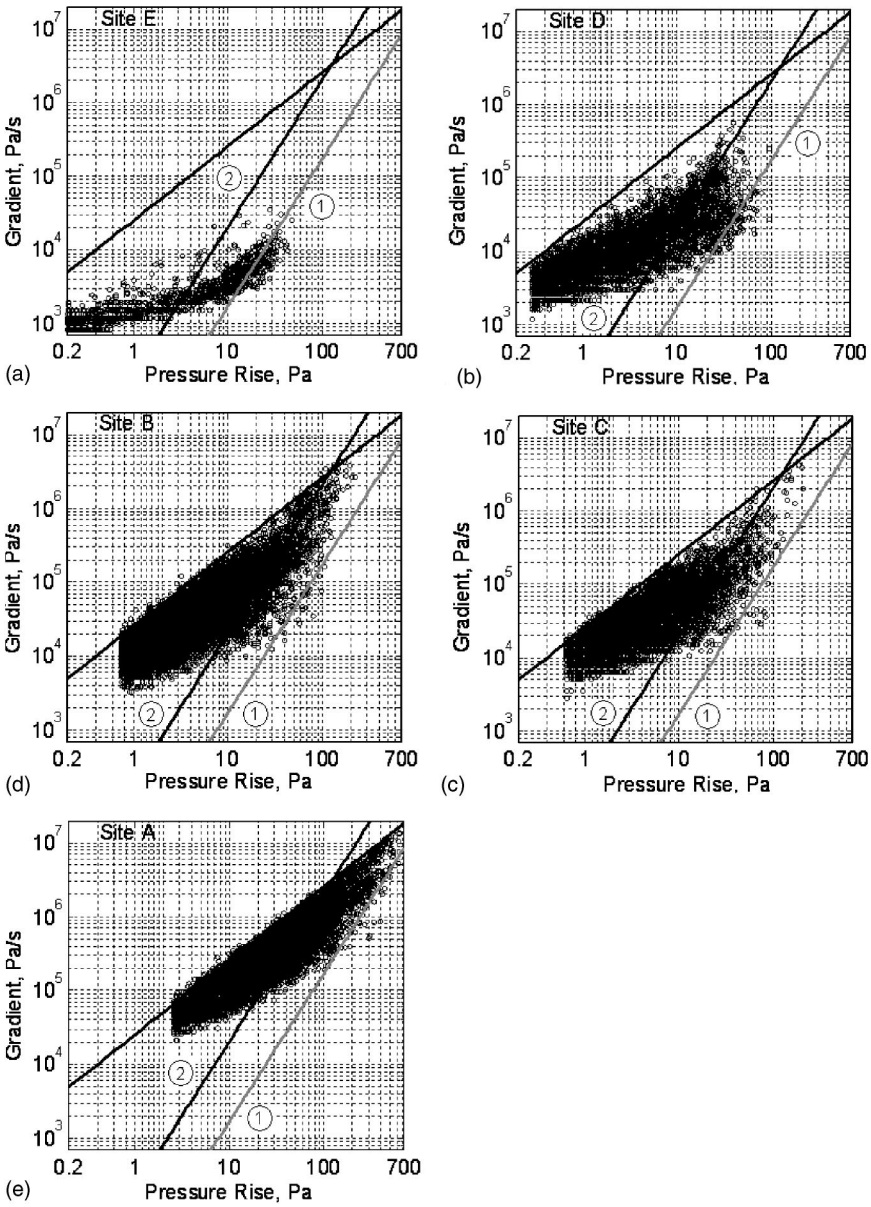

FIG. 7. Time rate of increase versus magnitude of pressure rise for the Titan IV sites, ordered from farthest to closest to the source. Starting clockwise from top left: (a) site E ~15.2 km from the source; (b) site D ~6.69 km; (c) site C~3.94 km; (d) site B~2.3 km; and (e) site A (left) ~950 m from source. See the text.

given by Eq. (4a) to that given by Eq. (4b). A transition to yet another, higher, offset would be expected if the magnitude of the pressure rise were to increase to the point where t_{rise} was shorter than $1/f_{O_2}$.

To clarify the calculation of pressure rise/time rate of increase pairs, consider the pressure minimum $P_{\min}=p(i)$ and the subsequent pressure maximum at $P_{\max}=p(j)$ in Fig. 3. The pressure rise/time rate of increase pairs were calculated as

$$\begin{aligned}\Delta p &= p_{\max}-p_{\min}=p(j)-p(i),\\ dp/dt &= \max[(p(k+1)-p(k))/\Delta t] \qquad (7)\\ &= \max[(p(k+1)-p(k))f_{\text{sample}}] \quad \text{for } k=i,j-1.\end{aligned}$$

The shock pressure rise is, then, the overall pressure rise, whereas the time rate of increase is the maximum instantaneous value regardless of where it occurs within the period of pressure rise. The pressure difference in the time rate of increase calculation in Eq. (7) is limited by the quantization steps in the data at low pressures, the effect of which is seen in some of the results. The pressure rise/time rate of increase pairs presented are limited to those for which the pressure rise was at least 0.3% or more of the maximum pressure rise measured at that site.

Figures 7–9 contain plots of the time rate of increase versus pressure rise. In these figures, the solid black line with the lesser slope is $dp/dt=25000\Delta p$. This line provides an indication of the limit imposed on the results by both the high-frequency instrumentation response and the data sample rate; see Eq. (7). The two steeper parallel lines, labeled 1 and 2, follow a pressure-squared dependence. The difference between these pressure-squared lines is that line 2 reflects a lower diffusivity corresponding to the shorter rise times of stronger shocks where $1/t_{\text{rise}}>f_{N_2}$. These two lines will be referred to as "the longer rise time shock fit," line 1, and "the shorter rise time shock fit," line 2.

The Titan IV data sets in Fig. 7 span the greatest variation in distance from the source of any of the time-domain data sets available. The results in this figure are ordered from the furthest to the closest site to the source, starting clock-

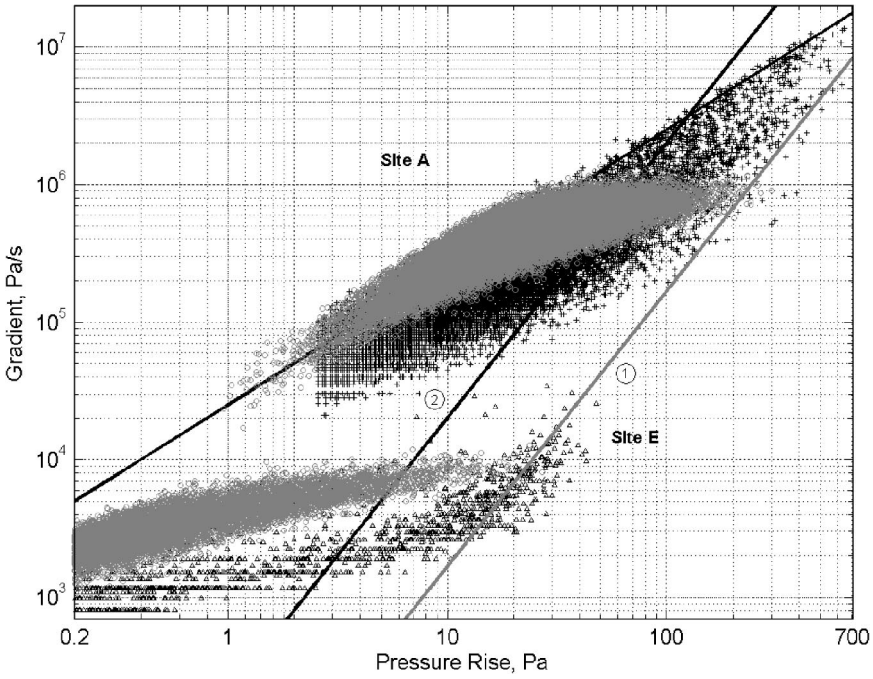

FIG. 8. Time rate of increase versus magnitude of pressure rise for Titan IV sites A and E compared to those for random noise with a 1.5-ms delayed reflection and the same spectral distributions: black crosses—Titan IV site A; black triangles—Titan IV site E; gray circles—corresponding normal random noise sets. See the text.

wise from the top left, so that plots for the next-nearest sites are directly adjacent and visual comparisons are more easily made. The longer rise-time shock fit, line 1 in the Fig. 7 plots, was chosen so as to provide a visual best fit through the portion of the site E data [Fig. 7(a)] following a pressure-squared dependence. The shorter rise-time shock fit, line 2, was chosen to do the same for the site C data [Fig. 7(c). There is an offset corresponding to a factor of 12 between these two lines.

Beginning with Fig. 7(a), it can be seen that for the larger pressure rises the data begin to follow the longer rise-time shock fit (line 1). Then, moving closer to the source in Figs. 7(b) and then (c), it can be seen that the larger pressure risedata begins a transition from the longer rise-time shock fit to the shorter rise-time shock fit (line 2). By site B in Fig. 7(d), however, the high-frequency instrumentation limit is affecting the results; at the closest Titan IV measurement, site A in Fig. 7(e), the results are severely affected by the limited instrumentation bandwidth.

In Fig. 8, the time rate of increase versus pressure rise

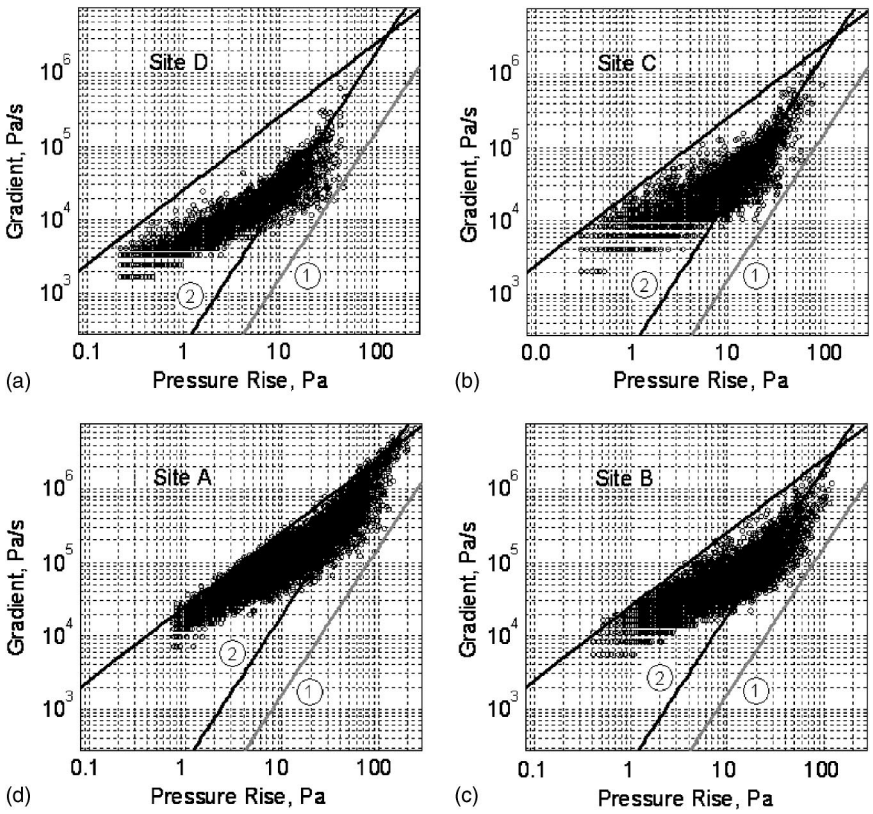

FIG. 9. Time rate of increase versus magnitude of pressure rise for the Scout sites, ordered from farthest to closest to the source. Clockwise from top left: (a) site D~1.41 km from source; (b) site C~1.09 km; (c) site B~740 m; and (d) site A~400 m from source. See the text.

TABLE III. Relaxation frequencies and diffusivities (for $1/t_{\text{rise}} < f_{O_2}$) over a range of temperatures and relative humidities.

T	RH	f_{N_2} Hz	f_{O_2} Hz	δ in m^2/s $1/t_{\text{rise}} > f_{N_2}$	δ in m^2/s $1/t_{\text{rise}} < f_{N_2}$	Ratio of δ values
21 °C	30%	90	4 618	1.388*E* − 03	1.475*E* − 02	11
	50%	222	17 710	3.633*E* − 04	5.766*E* − 03	16
	70%	438	42 696	1.518*E* − 04	2.891*E* − 03	19
15.6 °C	50%	151	10 656	6.025*E* − 04	8.555*E* − 03	14
	70%	299	27 303	2.363*E* − 04	4.253*E* − 03	18

for Titan IV sites E and A (the most distant and closest sites) are compared to the same for the random noise sets. It can be seen from Fig. 8 that the random noise data do not follow the pressure-squared dependence regardless of the pressure rise magnitude. In contrast, the actual data follow a random data trend up until a transition pressure, where they then begin to display the shock behavior predicted by Eq. (6). This is very evident in the site E data in Fig. 8, but it is obscured by high-frequency instrumentation limits at site A.

In the Scout results plotted in Fig. 9, the shorter rise-time shock fit was placed so as to provide a visual best fit through the Scout site B data in Fig. 9(c). The factor of 12 offset between the shorter and longer rise-time shock fits found for the Titan IV data (Fig. 7) was used in the Scout plots to place the longer rise-time shock fit relative to the shorter rise time fit in Fig. 9; there were no data sets sufficiently far away from the source to establish the longer rise-time shock fit based on a visual best fit through the data. Note that the offset between the pressure-squared dependence expected when $1/t_{\text{rise}} < f_{N_2}$ and that when $1/t_{\text{rise}} > f_{N_2}$ will depend on the temperature and relative humidity, which in all likelihood actually did differ between the Scout and the Titan IV measurements. The effect of the instrumentation bandwidth limit begins to be seen in the site A results [Fig. 9(d)].

Values of δ corresponding to the longer and shorter rise-time shock fits (lines 1 and 2, respectively) in the Titan IV data, Fig. 7, and to the shorter rise-time shock fit in the Scout data, Fig. 9, were estimated using Eq. (6). The diffusivity values corresponding to the shorter (line 2) and longer (line 1) rise-time shock fits in the Titan IV plots, Fig. 7, are $\delta \sim 1.24\times10^{-3}$ m^2/s and $\delta \sim 1.49\times10^{-2}$ m^2/s, respectively. The diffusivity value determined for the shorter (line 2) rise-time shock fit in the Scout data, Fig. 9, is $\delta \sim 1.33x10^{-3}$ m^2/s. Because the temperature and humidity were not recorded, one can only bound reasonably expected values of δ. Values for a range of temperatures and relative humidities that might reasonably be expected at the measurement sites are given in Table III.

These results indicate that rocket noise can be viewed as a distribution of weak shocks plus small-scale (relatively small pressure rise) random noise. As the propagation distance increases, the importance of the shocks decreases and the noise becomes more nearly a random noise distribution subject to linear absorption laws. Even 15 km from the source, however, the Titan IV sound-pressure data retained vestiges of weak shock behavior. See Figs. 5 and 7(a).

C. Power spectral densities

Gurbatov *et al.*[11] found that for initially Gaussian random noise in a lossless medium, the spectrum beyond the shock formation distance approaches one with a spectrum that increases as f^2 at low frequencies and decreases as $1/f^2$ at high frequencies. The $1/f^2$ drop-off in the power spectrum is expected for a sawtooth or *N* wave,[11] and indicates that the high-frequency end of the spectrum is controlled by the shocks. In a lossy fluid, the spectrum will drop off more rapidly due to absorption at very high frequencies. Kang and Pierce found that it was the rise portion of a steady-state shock that controls the rate at which the energy spectrum decreases at very high frequencies.[22] They found that the $1/f^2$ (6-dB per octave) slope expected for a sawtooth- or *N* wave held up to $f = 1/t_{\text{rise}}$. Beyond this frequency, the spectrum dropped off at 12 dB per octave. (In Chap. 12 of Ref. 11, Gurbatov states that ''if shock fronts are considered to be perfect discontinuities of zero duration, the spectrum falls off according to the power law ω^{-2}. In a dissipative medium at sufficiently high frequencies, this law is replaced with the exponential dependence of $e^{-\omega t_r}$, where t_r characterizes the shock rise time. In a medium with weak attenuation and dispersion...the high-frequency spectrum falls off'' as ω^{-4}. This is a drop off rate of 12 dB per octave.)

Sound-pressure PSDs are calculated using a Hanning window and 50% overlap processing. The PSDs are derived from FFTs with a spectral resolution of 2.93 Hz below 400 Hz and 11.82 Hz above 400 Hz. In the PSD plots, straight (dotted black) lines are used to indicate the f^2 and $1/f^2$ dependences at low and high frequencies, respectively.

The PSDs for the Titan IV and Scout data sets are plotted in Fig. 10. Figures 10(a) and (c) are the PSDs for the Titan IV and Scout data sets, respectively, without any corrections. In Figs. 10(b) and (d), the levels at the more distant sites have been corrected for spherical spreading, only, to the equivalent levels at site A. High-frequency noise-floor effects can be seen in the Scout site D and Titan IV sites D and E spectra. [Dimensionless forms of Figs. 10(b) and (d) were provided in Ref. 2.]

The spectra at the closest measurement sites display spectral slopes at high and low frequencies that are very close to those expected for sawtooth waves and to those measured for *N* waves,[15] as indicated by the straight dashed lines at the top of each plot. The slightly steeper slope at high frequencies in the Titan IV site A PSD may be due to instrumentation roll-off. Within the uncertainty of the data and the measurement systems, no further waveform steepening

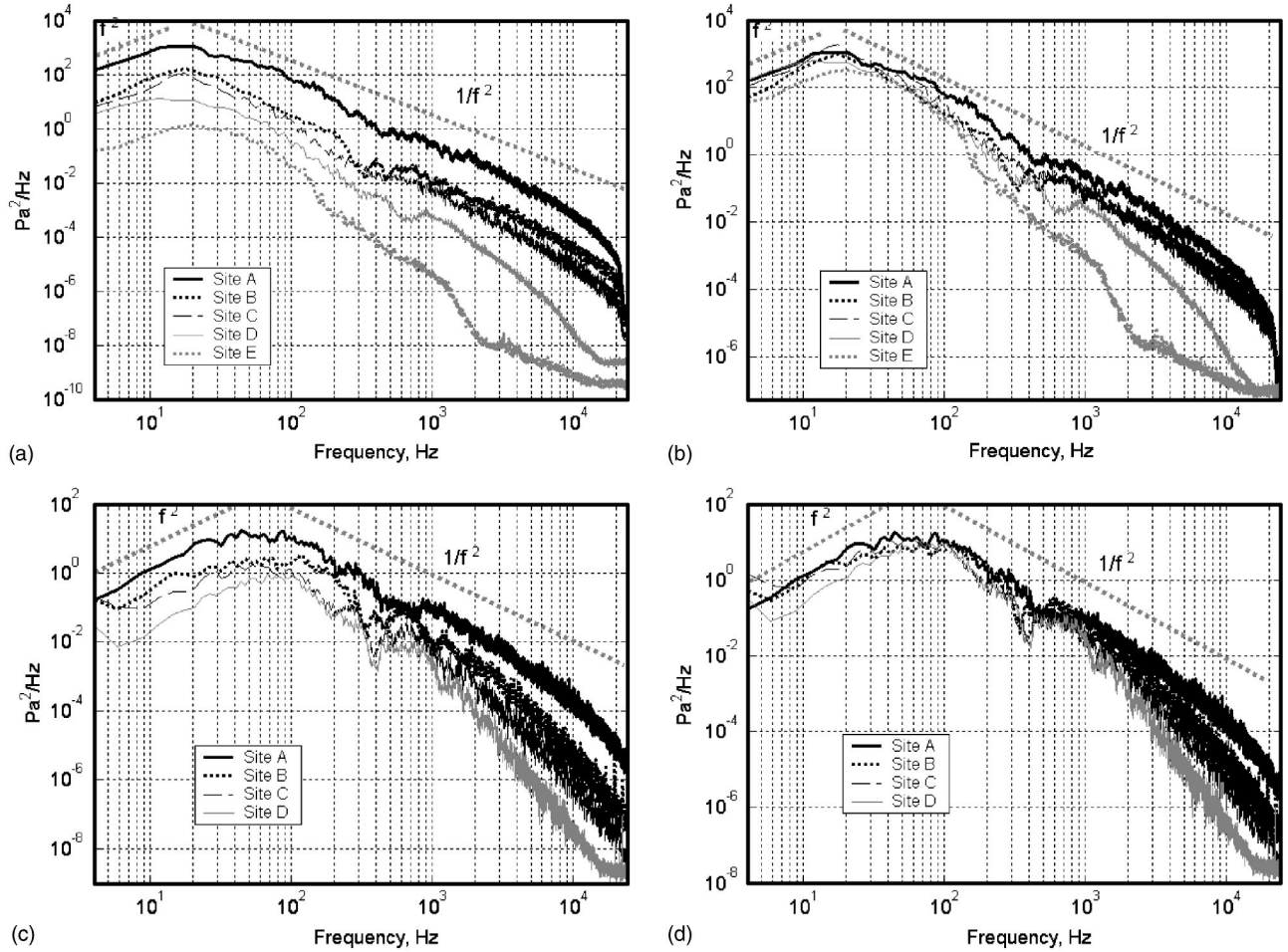

FIG. 10. Sound-pressure power spectral densities: (a) Titan IV PSDs; (b) Titan IV PSDs corrected—for spherical spreading only—to equivalent levels at Titan IV site A; (c) Scout PSDs; and (d) Scout PSDs corrected—for spherical spreading only—to equivalent levels at Scout site A. Results represent 57 or more spectral averages.

(which would be reflected in the high-frequency end of the spectrum) is evident beyond the nearest measurement site.

Although not apparent in Fig. 10(a), there must have been absorptive losses between Titan IV sites A, B, and C. That these losses are not reflected in 0–20-kHz spectra of Figs. 10(a) and (b) once again indicates that the instrumentation bandwidth was not sufficient. It is interesting to note the appearance of a second steeper slope in the most distant Titan IV site E spectrum between ~1000 and 2000 Hz. The rise time of the shock with the highest time rate of increase at this site was estimated, from Fig. 5, to be 2–3 ms, which corresponds to $f=333-500$ Hz. The change in slope of the site E spectrum occurs, however, above 1000 Hz. The relationship between the knee in the site E spectrum, the slope in the spectrum above this frequency, and the distribution of shock rise times bears further investigation.

Again, these results indicate that rocket noise can be viewed as a distribution of weak shocks plus small-scale (relatively small pressure rise) random noise. Over a considerable distance, absorption is concentrated at the shock fronts and the spectrum maintains a high-frequency slope close to that expected for a sawtooth wave—up to a frequency on the order of 1 over the shock rise time.

D. Howell and Morfey's Q/S plots

Howell and Morfey[4–6] examined the influence of nonlinear effects on the power spectral density, $S(\omega)$, starting from the generalized Burger's equation with frequency-dependent absorption. For spherical spreading, one of their results can be written

$$\frac{1}{2}\frac{\partial}{\partial r}S(r,\omega)=-\left(\frac{1}{r}+\frac{\delta\omega^2}{c_o^3}\right)S(r,\omega)-\frac{\beta}{2\rho_o c_o^3}Q(r,\omega), \tag{8}$$

where $Q(r,\omega)=\text{imag}[FT(p^2)\cdot(FT(p))^*]$, i.e., the imaginary part of the cross spectrum of the pressure squared and the pressure. The ratio of the second to the first term on the right-hand side provides an indication of the relative importance of nonlinear effects as a function of frequency

$$\frac{r}{(1+r\,\delta\omega^2/c_o^3)}\,\frac{\beta}{2\rho_o c_o^3}\,\frac{Q(r,\omega)}{S(r,\omega)}. \tag{9}$$

Defining normalized quantities Q_N and S_N as

$$Q(r,\omega)\equiv p_{\text{rms}}^3 Q_N(r,\omega) \quad \text{and} \quad S(r,\omega)\equiv p_{\text{rms}}^2 S_N(r,\omega),$$

and using $p_{\text{rms}}\approx p_o r_o/r$, Eq. (9) becomes

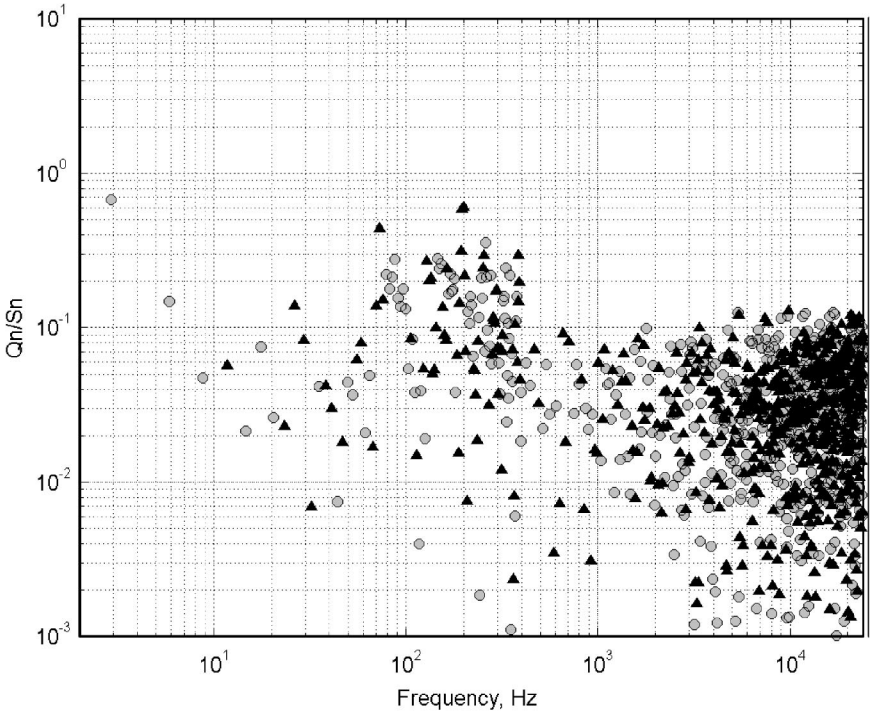

FIG. 11. $Q_N(r,\omega)/S_N(r,\omega)$ for shaped random noise with 1.5-ms delayed reflection and same PSD as Titan IV site A. Gray filled circles indicate values where $Q(r,\omega)$ was positive, corresponding to energy transfer out of the spectrum at that frequency; black triangles indicate energy transfer in.

$$\frac{p_o r_o}{(1+2\alpha r)}\frac{\beta}{2\rho_o c_o^3}\left[\frac{Q_N(r,\omega)}{S_N(r,\omega)}\right]. \tag{10}$$

The substitution of $p \approx p_o r_o / r$ assumes that absorption has a negligible effect on the overall rms pressure. This is a good assumption for the rocket data examined here, because the peak frequencies in the sound power spectral densities are below 100 Hz. At distances and frequencies where $r \ll 1/2\alpha$, the quantity in Eq. (10) is independent of r. The term in square brackets in Eq. (10) will be examined as a measure of the influence of nonlinear energy transfer on the noise spectra. In the $Q_N(r,\omega)/S_N(r,\omega)$ plots, a 4-Hz resolution is used up to 400 Hz and a 40-Hz resolution used above 400 Hz. Gray filled circles are used to indicate values where $Q(r,\omega)$ was positive, corresponding to energy transfer out of the spectrum at that frequency; black triangles indicate energy transfer into a frequency.

In Fig. 11, the results obtained for the shaped random noise of the same spectral distribution as the closest Titan IV site and with a 1.5-ms delayed reflection are shown. The reflection (see the spectral dip in the PSDs of Fig. 10) results in an increase in values of $Q_N(r,\omega)/S_N(r,\omega)$, although it is clear that there is no real net positive or negative energy transfer across any frequency range. These results can be contrasted with those obtained for the Titan IV data sets in Fig. 12. In Fig. 12, there is a clearly defined low-frequency region associated with energy transfer out of the spectrum (gray filled circles). The peak occurs at a frequency a little above the peak frequency in the PSDs of Fig. 10. Reflective interference effects are also evident between 100 and 600 Hz.

Consider the plots for sites A through C in Figs. 12(e), (d), and (c), respectively. The plots in Fig. 12 indicate that at each of these sites energy is being transferred to frequencies above 1000 Hz and that this energy transfer is increasingly significant (relative to the PSD levels) as the frequency increases. After accounting for spherical spreading, the 0–20 kHz PSDs at these sites (Fig. 10) were practically the same. It is believed that the final ramp-up in the $Q_N(r,\omega)/S_N(r,\omega)$ results above 15 kHz in Fig. 12 is a consequence of instrumentation limits.

The results for site D, Fig. 12(b), do not rise consistently above 10 kHz, but begin to drop off above ~11 kHz. It can be seen from Fig. 10 that high-frequency absorption effects were first apparent in the spectrum at this site. Above about 18 kHz, the values of $Q_N(r,\omega)/S_N(r,\omega)$ at site D are randomly positive and negative, suggesting that the results are in the noise floor. This can also be seen in the values of $Q_N(r,\omega)/S_N(r,\omega)$ at site E, Fig. 12(a), above ~1400 Hz.

Plots of $Q_N(r,\omega)/S_N(r,\omega)$ are given for the Scout sites in Fig. 13. The peak frequency in the Scout PSDs is around 60 Hz. Based on the Titan IV results just presented, energy transfer out of the spectrum may be expected to peak at a frequency somewhat above this. The lack of a smooth rise and fall in the values around this peak, as was seen in the Titan IV results, may be attributable to reflective interference effects. At frequencies above 2 kHz, the results for sites A through C indicate increasingly significant energy transfer into the spectrum with increasing frequency. The effect of absorption on the Scout PSDs (Fig. 10) was not seen in the 0–20-kHz spectra until site D. In Fig. 13(a), it can be seen that at this site there is a rapid decrease in energy transferred into the spectrum above 14 kHz.

A question that one might hope to answer based on these and the spectral results is, ''Beyond what distance and above what frequency can linear absorption be assumed?'' However, correct interpretation of the results in Figs. 12 and 13 is not entirely clear. Further study of the meaning of specific features and the magnitudes in the $Q_N(r,\omega)/S_N(r,\omega)$ plots

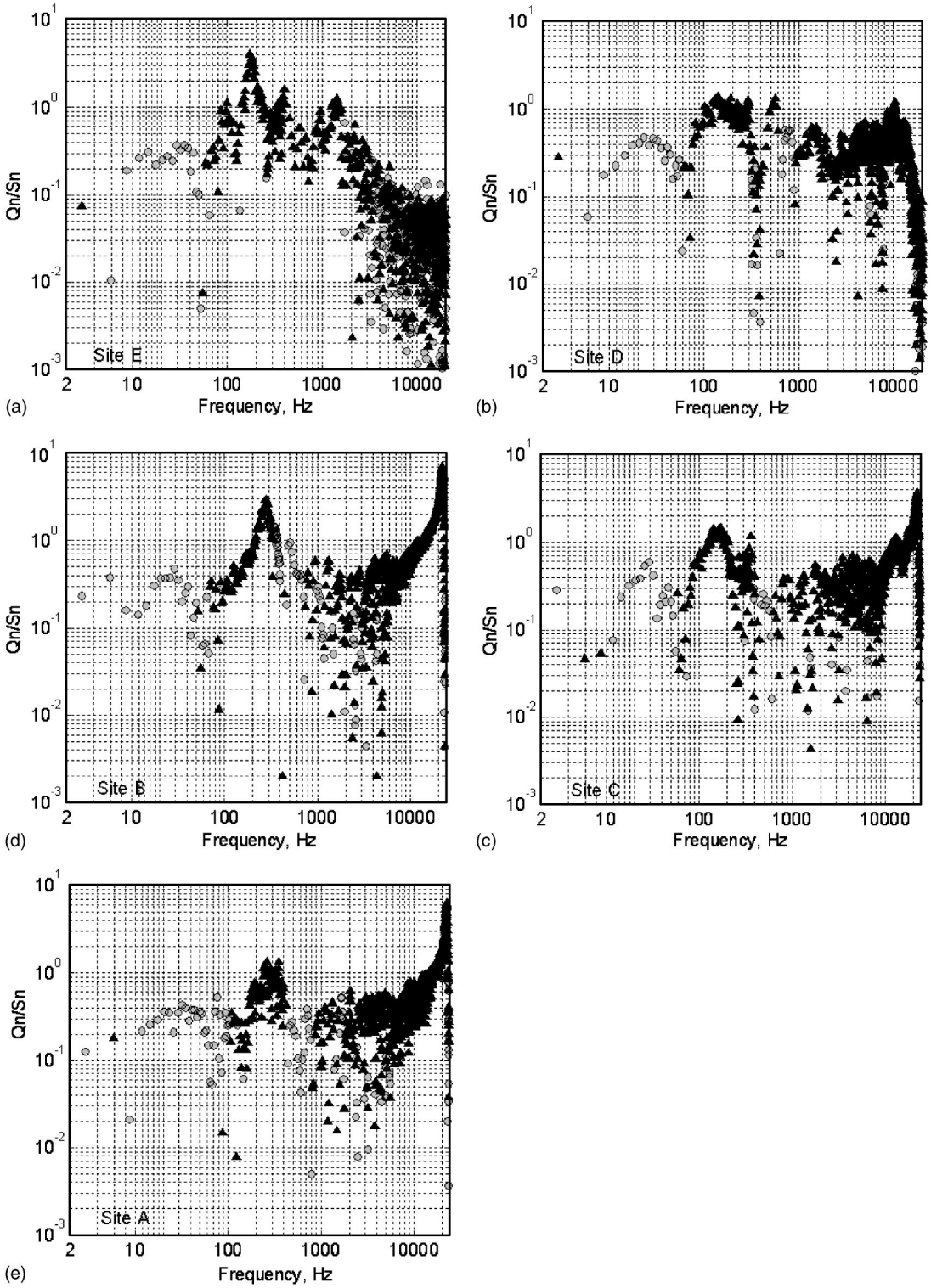

FIG. 12. $Q_N(r,\omega)/S_N(r,\omega)$ for Titan IV sites, ordered from farthest to closest to the source. Starting clockwise from top left: (a) site E~15.2 km from the source; (b) site D~6.69 km; (c) site C~3.94 km; (d) site B~2.3 km; and (e) site A (left)~950 m from source. Gray filled circles indicate values where $Q(r,\omega)$ was positive, corresponding to energy transfer out of the spectrum at that frequency; black triangles indicate energy transfer in.

for these and other types of sound-pressure distributions is needed.

IV. CONCLUSION

Rocket noise data measured at far-field locations during the launch of a large rocket (Titan IV) and a smaller rocket (Scout) were examined. Shocks were present in the data measured at all of the measurement sites. Plots of the maximum time rate of increase versus pressure rise followed a trend consistent with random noise at low pressures and, then, transitioned to the pressure-squared dependence expected for shocks at higher pressures. The bandwidth of the instrumentation used to measure the data (~5–20 kHz) was clearly not sufficient to accurately measure the rise phase of

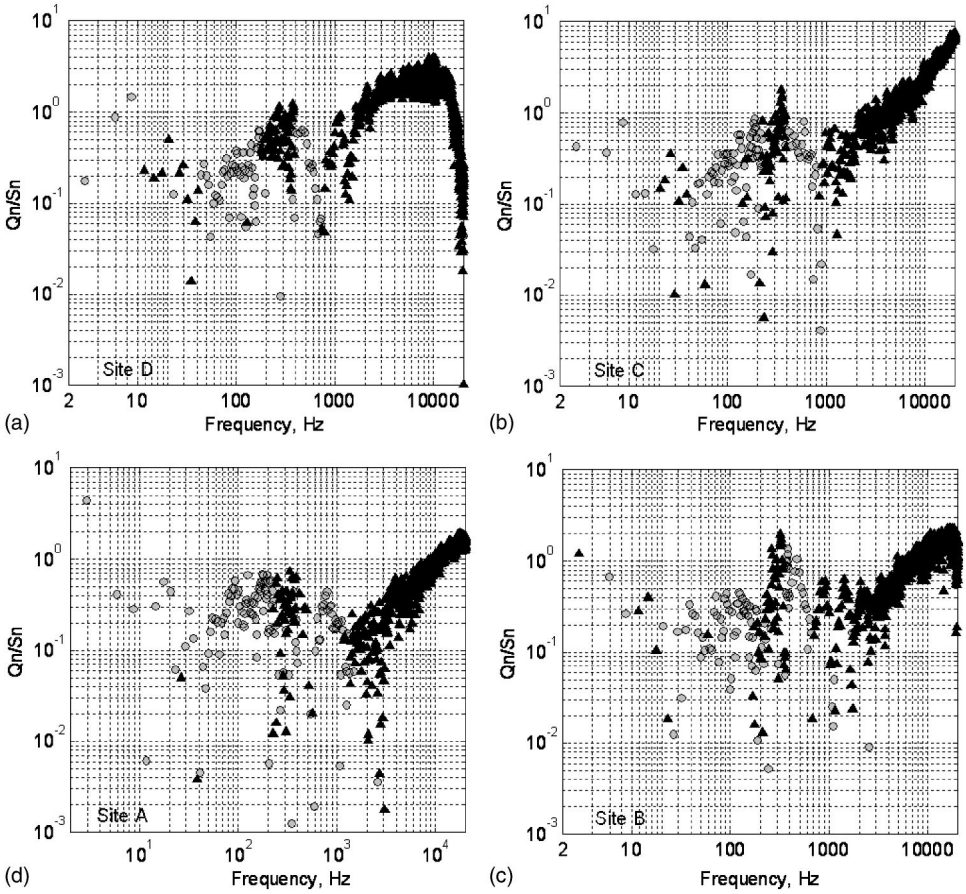

FIG. 13. $Q_N(r,\omega)/S_N(r,\omega)$ for Scout sites, ordered from farthest to closest to the source. Clockwise from top left: (a) site D$\sim$1.41 km from source; (b) site C$\sim$1.09 km; (c) site B$\sim$740 m; and (d) site A$\sim$400 m from source. Gray filled circles indicate values where $Q(r,\omega)$ was positive, corresponding to energy transfer out of the spectrum at that frequency; black triangles indicate energy transfer in.

the shocks at the three closest measurement sites for both the small and large rocket; also, the data sets contained ground reflections that influenced the results.

Power spectral densities of the noise measured during the period of maximum acoustics displayed high- and low-frequency spectral slopes very close to those expected for noise dominated by fully developed shocks. The PSDs at the two or three closest measurement sites retained a nearly self-similar shape over the 0–20-kHz frequency range, appearing to reflect an absence of atmospheric absorption. It is believed that an increase in shock thicknesses with increasing distance (due to absorption) would have been reflected in the spectrum at frequencies above 20 kHz.

A metric developed by Morfey[4] to assess the relative importance of nonlinear effects indicated a consistent but relatively small energy transfer out of the spectrum at low frequencies near the peak in the sound-pressure PSD. Mid-frequency results were rendered useless by reflective interference effects. Energy transfer was into the spectrum at high frequencies, up until a frequency and distance at which absorption effects dominated.

In summary, the far-field noise radiated by rockets (and, perhaps, high-power afterburning turbojets engines) is characterized by shocks. The propagation of these shocks must be included in propagation models if high-frequency levels, as needed for environmental impact assessments, are to be estimated as a function of distance from the source. Initial shock thicknesses will have to be characterized experimentally and will require instrumentation with a bandwidth well in excess of 20 kHz. Reflection-free data are essential if meaningful assessments of the statistical properties of the noise are to be made.

ACKNOWLEDGMENTS

The work presented here was supported by Wyle Laboratories as part of a larger SERDP project, and by The National Center for Physical Acoustics. It was completed while the author was on sabbatical leave at the Institute for Sound and Vibration Research in Southampton, England. Technical guidance provided by Professor Chris L. Morfey (ISVR) is gratefully acknowledged, as is the encouragement and input from Professor Victor Sparrow (Pennsylvania State University).

[1] S. A. McInerny, "Launch vehicle acoustics. II. Statistics of the time domain data," J. Aircr. **33**, 511–517 (1996).
[2] S. A. McInerny, "Launch vehicles acoustics. I. Overall levels and spectral characteristics," J. Aircr. **33**, 518–523 (1996).
[3] S. A. McInerny, J. K. Francine, B. S. Stewart, and P. H. Thorsen, "The influence of low frequency instrumentation response on metrics used to characterize rocket noise," J. Acoust. Soc. Am. **102**, 2780–2785 (1997).
[4] C. L. Morfey, "Nonlinear Propagation of Jet Noise in the Atmosphere," Technical Report TR 80004, Royal Aircraft Establishment, January, 1980.
[5] C. L. Morfey and G. P. Howell, "Nonlinear propagation of aircraft noise in the atmosphere," AIAA J. **19**, 986–992 (1981).
[6] C. L. Morfey, "Aperiodic signal propagation at finite amplitudes: Some practical applications," in *Proceedings of the 10th International Symposium on Nonlinear Acoustics*, edited by A. Nakmura (Teikohsha, Kadoma, Japan, 1984), 199–206.
[7] V. W. Sparrow, K. L. Gee, K. J. Plotkin, and J. M. Downing, "Military aircraft noise and nonlinear acoustics," Paper 1pNS13, First Pan-American/Iberian Meeting on Acoustics, 144th ASA/3rd Iberoamerican CA/9th Mexican CA, 2 December 2002.

[8] S. H. Guest, ''Acoustic Efficiency Trends for High Thrust Boosters,'' NASA TN D-1999, Marshall Space Flight Center (1964).
[9] *Electronic Instruments*, 1986 Bruel & Kjaer Master Catalogue (Bruel & Kjaer, Denmark, 1986).
[10] S. A. McInerny, J. K. Wickiser, and R. H. Mellen, ''Rocket noise propagation,'' American Society of Mechanical Engineers, Noise Control and Acoustics Division (Publication) NCA, Vol. 24, ASME Noise Control and Acoustics Division, 37–50 (1997).
[11] *Nonlinear Acoustics*, edited by M. F. Hamilton and D. T. Blackstock (Academic, San Diego, 1998).
[12] A. D. Pierce, *Acoustics: An Introduction to Its Physical Principles and Applications* (McGraw-Hill, New York, 1981).
[13] J. Kang, ''Nonlinear acoustic propagation of shock waves through the atmosphere with molecular relaxation,'' Ph.D. thesis, Department of Mechanical Engineering, Pennsylvania State University (1991), as cited in Ref. 14, below.
[14] B. Lipkens and D. T. Blackstock, ''Model experiment to study sonic boom propagation through turbulence. I. Model experiment and general results,'' J. Acoust. Soc. Am. **103**, 148–158 (1998).
[15] B. Lipkens, ''Model experiment to study sonic boom propagation through turbulence. III. Validation of sonic boom propagation models,'' J. Acoust. Soc. Am. **111**, 509–519 (2002).
[16] H. E. Bass, R. Raspet, J. P. Chambers, and M. Kelly, ''Modification of sonic boom wave forms during propagation from the source to the ground,'' J. Acoust. Soc. Am. **111**, 481–486 (2002).
[17] P. Blanc-Benon, B. Lipkens, L. Dallois, M. F. Hamilton, and D. T. Blackstock, ''Propagation of finite amplitude sound through turbulence: Modeling with geometrical acoustics and the parabolic approximation,'' J. Acoust. Soc. Am. **111**, 487–498 (2002).
[18] ANSI S1.26-1995 (R1999), ''Method for the Calculation of Absorption of Sound by the Atmosphere'' (American National Standards Institute, New York, 1999).
[19] L. E. Kinsler, A. R. Frey, A. B. Coppens, and J. V. Sanders, *Fundamentals of Acoustics*, 3rd ed. (Wiley, New York, 1982).
[20] J. P. Hodgson and N. H. Johannesen, ''Real gas effects in very weak shock waves in the atmosphere and the structure of sonic bangs,'' J. Fluid Mech. **50**, 17–20 (1971).
[21] J. P. Hodgson, ''Vibrational relaxation effects in weak shock waves in air and the structure of sonic bangs,'' J. Fluid Mech. **58**, 187–196 (1973).
[22] J. Kang and A. D. Pierce, ''Profiles of Fourier transforms of weak shocks propagating through a relaxing atmosphere,'' in *Proceedings of 3rd IMACS Symposium Computational Acoustics, Cambridge* (Elsevier Science, North-Holland, Amsterdam, 1992), Vol. 2, pp. 195–207.

Nonlinear acoustic scattering by a partially closed surface-breaking crack

Claudio Pecorari and Milan Poznić
Marcus Wallenberg Laboratory, Royal Institute of Technology, 100 44 Stockholm, Sweden

(Received 23 April 2004; revised 22 November 2004; accepted 25 November 2004)

A theoretical model describing the nonlinear scattering of acoustic waves by surface-breaking cracks with faces in partial contact is presented. The nonlinear properties of the crack are accounted for by suitable boundary conditions that are derived from micromechanical models of the dynamics of elastic rough surfaces in contact. Both linear and nonlinear responses of the crack are shown to be largest for a shear vertical wave incident on the surface containing the crack at an angle just above the critical angle for longitudinal waves. These findings question the fitness for the purpose of a conventional inspection method, which utilizes shear vertical waves at 45° of incidence to search for surface-breaking cracks in many engineering components. For angles of incidence proximal to the critical angle of longitudinal waves, the efficiency of the second harmonic's generation appears to be the highest. Thanks to the increased sensitivity to surface-breaking cracks, this configuration seems to offer a solution to the localization problem, a task that has eluded nonlinear techniques operating under other circumstances. Finally, this model suggests a simple interpretation of the highly localized nonlinear response of delaminations in composite materials.
 [DOI: 10.1121/1.1850052]

PACS numbers: 43.25.Dc, 43.25.Jh, 43.25.Ts, 43.35.Zc [MFH] Pages: 592–600

I. INTRODUCTION

Material components containing cracks respond to an external dynamic perturbation in a nonlinear manner.[1,2] For instance, when insonified by a harmonic wave, the spectrum of the acoustic response of a cracked sample has been shown to display higher-order harmonic components, which are not found in samples without cracks. Similarly, if a component containing a partially closed crack is tested simultaneously by two harmonic waves of frequencies f_1 and f_2, with $f_1 \gg f_2$, signals are generated within the sample, which contain sideband components at frequencies $f_1 \pm f_2$. These, again, are not found in the acoustic fields generated by scattering events in material components without cracks.

An even richer phenomenology[3] can be observed when the amplitude of the excitation is increased beyond the threshold value at which clapping between the crack's faces is activated. For example, the generation of subharmonic components, which is the first step toward a chaotic regime of vibration, can be observed by progressively increasing the excitation amplitude. Nonlinear effects caused by the dissipation of the acoustic energy have also been reported in experiments conducted on cracked glass samples.[4,5]

The experiments mentioned above are often performed with continuous waves at frequencies that are well below the MHz range, so that the wavelength of the waves propagating within the inspected component is of the order of several centimeters. As the whole volume of the material is insonified, and the acoustic response is commonly detected by using a stationary sensor, the localization of the defect under such experimental conditions is a very difficult task.

An important variation of this approach is that developed by Krohn *et al.*[6] in which the local response of a composite plate to a low-frequency, large-amplitude acoustic wave source is detected by a scanning laser interferometer. In these experiments, the plate's thickness is much smaller than the wavelength of the probing acoustic wave. The large values of the wave amplitude utilized in these experiments suggest that the mechanism responsible for the nonlinear response of the plate is clapping between the faces of the delamination. This hypothesis is further supported by the presence of harmonics of very high order in the scattered acoustic field. Images of the plate formed by displaying the amplitude variation of higher-order harmonics, or other nonlinear components, show a feature of great importance for practical applications: the highly localized nonlinear response of the defect, which decays by as many as 20 dB as the observation point moves away from the defect. A convincing explanation of such an interesting phenomenon has yet to be provided.

A few authors have developed models that predict the nonlinear response of cracks with faces interacting with each other. Achenbach and Norris[7] have analyzed the effect of clapping on the linear response of a crack insonified by an incident wave. Boundary conditions along the crack's faces, which require the continuity of the total displacement when the crack is closed, and set the total applied stress to zero when the crack is open, have been used. Hirose and Achenbach[8] have developed a sophisticated mathematical approach to modeling nonlinear scattering by a circular crack with clapping faces. The time evolution of the clapping faces is followed by numerically solving an appropriate integral equation, the solution of which is used to evaluate the scattered field in the space–time domain. The harmonic content of the scattered field is recovered via a Fourier analysis of the latter. A similar approach has also been adopted by Hirose,[9] who employs more realistic boundary conditions at the crack's face. In fact, Hirose considers the interaction between the crack's faces to occur only at discrete locations

and at instants that are determined by the time evolution of the applied load, by the crack's initial conditions, and by the topography of the two surfaces. Donskoy, Sutin, and Ekimov[10] have proposed a simplified mathematical scheme to account for the effect of the nonlinearity introduced by Hertzian contacts between the crack surfaces that are assumed to be rough and nonconforming. To this end, they have used the spring model[11] for imperfect interfaces to formulate the nonlinear boundary conditions at the surface of the crack. Thus, the dynamics of a collection of contacts is simulated by that of two distributions of nonlinear springs having normal and tangential stiffness constants, K_N and K_T, respectively. Donskoy *et al.*, however, have considered only the effect of the normal mode of vibration on the nonlinear scattering process.

While all the theoretical work cited above concerns itself with cracks that are imbedded into the bulk of the hosting material component, in this investigation the focus is on the acoustic response of surface-breaking cracks, of which stress-corrosion cracks are typical and extremely important examples. The mathematical description of the problem at hand is provided by an extension of a previous model[12] dealing with the linear wave scattering by surface-breaking cracks with faces in partial contact to include the generation of the second harmonic component. As in the work of Donskoy *et al.*, the spring model for imperfect interfaces is employed to incorporate the nonlinear properties of the crack into the boundary conditions enforced on the total scattering field along the crack faces. In this investigation, however, the nonlinear dynamics of rough surfaces in contact is described in terms of a more recent approach.[13] The latter yields the nonlinear dependence of both spring constants, K_N and K_T, on the local relative approach between the crack's faces. A closer examination shows that both the force law governing the interaction between asperities in contact and the surface topography play a key role in determining such dependence. The nonlinear scattering problem is solved by using a standard perturbation technique, the small perturbation parameter naturally arising from the normalization of the boundary conditions as a measure of the system's nonlinearity. The dependence of the scattered second harmonic on the type of incident wave, on the interface spring constants, on the crack depth, and on the spatial coordinates of the observation point is investigated. The spatial evolution of the linear and nonlinear components of the scattered field is also evaluated up to distances of the order of ten wavelengths of the incident wave from the crack. A discussion of the relevance of these results on the nondestructive inspection of components containing surface-breaking cracks concludes this work.

As a final remark, it is stressed that the purpose of the model developed in this work is limited to the following: (i) providing general guidance to optimize the configuration of the inspection system to detect shallow surface-breaking cracks; and (ii) aiding physical intuition in the interpretation of experimental results with respect to the role played by the relevant physical and geometrical parameters of the system. No claim is made as to the potential use of this model to accurately predict the acoustic response of real cracks in hosting materials with a complex microstructure. The number of parameters determining the acoustic response of a real crack under such circumstances is too large, and our knowledge of their values is so poor that the goal of providing accurate theoretical predictions of acoustic scattering experiments carried out in real life situations is simply unattainable at the present time and, perhaps, will remain so for some time.

II. THEORY

A complete set of boundary conditions to be enforced on the total acoustic field at an interface between two rough surfaces in contact has been derived by Pecorari[13] under the assumption that the interaction between the asperities is purely elastic. If the interface is assumed to coincide with the plane of equation $x_1=0$, the boundary conditions are

$$\frac{1}{2}(\sigma_{31}^{+}+\sigma_{31}^{-})=K_{T,0}\,\Delta\nu-K_{T,N}\,\Delta u\,\Delta\nu-\frac{1}{2}K_{T,1}\Bigg[(\Delta\nu^2-\Delta\nu_{\max}^2)\operatorname{sgn}\left(\frac{\partial\Delta\nu}{\partial t}\right)+\Delta\nu\,\Delta\nu_{\max}\Bigg], \quad (1a)$$

$$\frac{1}{2}(\sigma_{11}^{+}+\sigma_{11}^{-})=K_{N,0}\,\Delta u-K_{N,1}\,\Delta u^2, \quad (1b)$$

$$\sigma_{31}^{+}=\sigma_{31}^{-}, \quad (1c)$$

$$\sigma_{11}^{+}=\sigma_{11}^{-}. \quad (1d)$$

In Eqs. (1a)–(1d), u and ν are the components of the total displacement in the x_1 and x_3 directions, respectively, $\Delta u=(u^{+}-u^{-})$ and $\Delta\nu=(\nu^{+}-\nu^{-})$ are the corresponding interface opening displacements, and $\sigma_{ij}^{+,-}$, with $i, j=1, 3$, is the ijth stress component of the stress field acting on the interface. The superscript $+(-)$ refers to the half-spaces for which x_1 is positive (negative). All the field quantities are to be understood to be functions of time, t. The coefficients K's are derived from suitable micromechanics models, which assume the elastic normal and tangential interaction between asperities to be described by the Hertz[14] and Mindlin and Deresiewicz[15] models, respectively, of two elastic spheres in contact. In particular, $K_{N,0}$ and $K_{T,0}$ can be found to be[13]

$$K_{N,0}=n\left\langle\frac{E}{1-\nu^2}\right\rangle\langle\beta^{1/2}\rangle\int_0^{\delta_0}(\delta_0-z)^{1/2}\varphi(z)dz, \quad (2)$$

and

$$K_{T,0}=2n\left\langle\frac{E}{(1+\nu)(2-\nu)}\right\rangle\langle\beta^{1/2}\rangle\int_0^{\delta_0}(\delta_0-z)^{1/2}\varphi(z)dz. \quad (3)$$

In Eqs. (2) and (3), n is the number of contacts per unit area, E and ν are the Young modulus and the Poisson ratio of the material, respectively, β is the radius of curvature of the asperities, and φ is the height distribution of the asperities of the composite surface. The latter is defined by a linear combination of the profiles of the two surfaces, which maps the actual contacts of the interface onto the asperities of the composite surface.[13] The quantity δ_0 defines the approach between the mean planes of the two rough surfaces caused by the external load, and it is null when no external pressure is

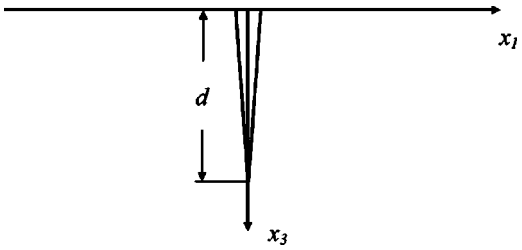

FIG. 1. Schematic representation of the surface-breaking crack and of the coordinate systems used in the model.

acting on the interface. The symbol $\langle \cdots \rangle$ indicates a statistical average. Thus, $K_{N,0}$ and $K_{T,0}$ can be evaluated numerically in terms of the mechanical and topographic properties of the two rough surfaces in contact. The magnitude of K_N and K_T varies with the load applied to the interface, and so does the ratio K_T/K_N, which, however, remains of the order of 0.5. Similar expressions can be found for $K_{N,1}$, $K_{T,1}$, and $K_{N,T}$. The reader who is interested in further details is referred to the original paper.[13]

To the first order of approximation, the nonlinear effect due to the hysteretic component of the tangential stiffness is shown to be responsible for the generation of higher harmonics of odd order, the magnitude of which is considerably smaller than that of the second harmonic generated by the nonlinearity due to K_N. For this reason, in Eq. (1a) those terms that are linked to the latter mechanism can be neglected to obtain the following simplified version of nonlinear boundary conditions:

$$\frac{1}{2}(\sigma_{31}^{+}+\sigma_{31}^{-}) = K_{T,0}\,\Delta\nu - K_{T,N}\,\Delta u\,\Delta\nu, \tag{4a}$$

$$\frac{1}{2}(\sigma_{11}^{+}+\sigma_{11}^{-}) = K_{N,0}\,\Delta u - K_{N,1}\,\Delta u^2, \tag{4b}$$

$$\sigma_{31}^{+} = \sigma_{31}^{-}, \tag{4c}$$

$$\sigma_{11}^{+} = \sigma_{11}^{-}. \tag{4d}$$

Equations (4a) and (4b) describe an imperfect interface, the stiffness constants of which increase when the surfaces in partial contact approach each other. Furthermore, since the spring model for an imperfect interface is an effective approach to describing the interface properties, and the latter are assumed constant along the interface, the term ''partial contact'' is to be understood as referring to the discontinuity of the contact that occurs at a microscopic level.

The mathematical formulation of the problem in which an incident wave is scattered by a surface-breaking crack with nonlinear boundary conditions is presented next. The crack is assumed to be positioned on the positive semiplane of equation $x_1=0$, with its mouth placed at the origin of the coordinate system, while its tip reaches a depth d below the surface of the medium. The latter occupies the half-space defined by $x_3 \geqslant 0$ (see Fig. 1).

Following the approach by Achenbach *et al.*[16] and Mendelsohn *et al.*,[17] the original problem is decomposed into a symmetric and an antisymmetric part, which are solved in the quarter-space $x_1 \geqslant 0$, $x_3 \geqslant 0$. The boundary conditions associated with these problems are as follows: *symmetric problem*,

$$\sigma_{13}^{+}=0, \quad x_1=0, \quad 0 \leqslant x_3 < \infty, \tag{5a}$$

$$\sigma_{11}^{+} = K_{N,0}\,\Delta u - K_{N,1}\,\Delta u^2, \quad 0 \leqslant x_3 < d, \tag{5b}$$

$$u=0, \quad d \leqslant x_3 < \infty; \tag{5c}$$

antisymmetric problem,

$$\sigma_{11}^{+}=0, \quad x_1=0, \quad 0 \leqslant x_3 < \infty, \tag{6a}$$

$$\sigma_{13}^{+} = K_{T,0}\,\Delta\nu - K_{T,N}\,\Delta u\,\Delta\nu, \quad 0 \leqslant x_3 < d, \tag{6b}$$

$$\nu=0, \quad d \leqslant x_3 < \infty. \tag{6c}$$

In Eq. (5b) and Eq. (6b), σ_{ij}^{+} are the components of the total stress field on the side of the crack facing the quarter-space for which $x_1>0$. They include the contribution of the incident wave. In both problems, the components σ_{33} and σ_{31} of the total stress field must be null at the surface $x_3=0$. Note that, in view of the continuity of σ_{11} and σ_{31} across the contacting surfaces of the crack as given by Eqs. (4c) and (4d), Eq. (5b) and Eq. (6b) can be formulated only in terms of the total stress components on the positive face of the crack.

Since the material half-space supporting the propagation of the acoustic waves is linear, the same equations of motion used by Achenbach *et al.*[16] and Mendelsohn *et al.*[17] apply,

$$c_L^2\frac{\partial^2 u}{\partial x_1^2} + c_T^2\frac{\partial^2 u}{\partial x_3^2} + (c_L^2-c_T^2)\frac{\partial^2 \nu}{\partial x_1\,\partial x_3} = \frac{\partial^2 u}{\partial t^2}, \tag{7}$$

$$c_L^2\frac{\partial^2 \nu}{\partial x_1^2} + c_T^2\frac{\partial^2 \nu}{\partial x_3^2} + (c_L^2-c_T^2)\frac{\partial^2 u}{\partial x_1\,\partial x_3} = \frac{\partial^2 \nu}{\partial t^2}. \tag{8}$$

In Eq. (7) and Eq. (8), c_L and c_T are the phase velocities of longitudinal and shear waves, respectively.

It is convenient to formulate the problem in nondimensional form. To this end, the displacement components are normalized with respect to the amplitude of the incident wave, A_{in}: $U=u/A_{\text{in}}$, $V=\nu/A_{\text{in}}$; the coordinates are rescaled with respect to the wave number of the longitudinal wave, k_L: $x_i=X_i/k_L$, and time is normalized by ω: $t=\tau/\omega$. Then, Eq. (7) and Eq. (8) become

$$\frac{\partial^2 U}{\partial X_1^2} + \frac{1}{\kappa^2}\frac{\partial^2 U}{\partial X_3^2} + \left(1-\frac{1}{\kappa^2}\right)\frac{\partial^2 V}{\partial X_1\,\partial X_3} = \frac{\partial^2 U}{\partial \tau^2}, \tag{9}$$

$$\frac{\partial^2 V}{\partial X_1^2} + \frac{1}{\kappa^2}\frac{\partial^2 V}{\partial X_3^2} + \left(1-\frac{1}{\kappa^2}\right)\frac{\partial^2 U}{\partial X_1\,\partial X_3} = \frac{\partial^2 V}{\partial \tau^2}, \tag{10}$$

in which $\kappa=c_L/c_T$.

The boundary conditions are also similarly transformed, and, in particular, Eq. (5b) and Eq. (6b) become

$$\kappa^2\frac{\partial U^{+}}{\partial X_1} + (\kappa^2-2)\frac{\partial V^{+}}{\partial X_3} = \overline{K}_N(1-\epsilon\,\Delta U)\Delta U, \quad 0 \leqslant X_3 < D, \tag{11}$$

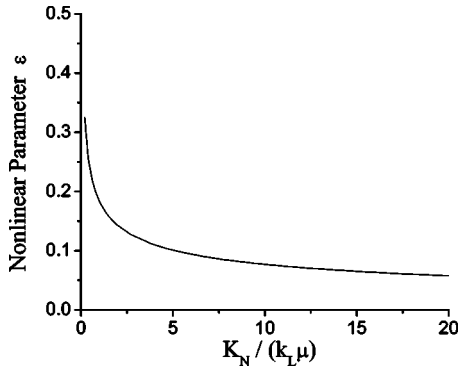

FIG. 2. Nonlinear parameter versus normalized interfacial normal stiffness. The interface is formed by two rough surfaces in contact. The rms roughness of the two surfaces is equal to 0.23 μm, and the material is steel. Further details are to be found in Ref. 13.

$$\frac{\partial U^+}{\partial X_3}+\frac{\partial V^+}{\partial X_1}=\overline{K}_T(1-\epsilon\,\Delta U)\Delta V, \quad 0\leqslant X_3<D, \tag{12}$$

respectively, where $D=k_L d$. In the latter equations, U^+ and V^+ are the normalized total displacement components on the positive side of the crack, while $\overline{K}_N=K_{N,0}/(k_L\mu)$ and $\overline{K}_T=K_{T,0}/(k_L\mu)$ are the normalized normal and tangential interfacial stiffness, where μ is the shear modulus of the material. Finally, $\epsilon=(K_{N,1}/K_{N,0})A_{\rm in}=(K_{T,N}/K_{T,0})A_{\rm in}$ measures the relative variation of the normal and of the tangential interfacial stiffness due to a change of the normal interface opening displacement equal to the amplitude of the incident wave.[13] Note that the proportionality between ϵ and $A_{\rm in}$ implies the quadratic dependence of the amplitude of the actual scattered second harmonic on $A_{\rm in}$. The magnitude of ϵ can be shown to be a monotonically decreasing function of the normalized interfacial stiffness, always being much smaller than one, except for interfaces that are nearly open, for which it tends to diverge. In this work, the dependence of ϵ on the normalized interface stiffness $\overline{K}_N$ is that found by Pecorari[13] for a steel–steel interface between two rough surfaces with rms roughness $\sigma=0.23$ μm (Fig. 2) each, and an incident longitudinal wave with an amplitude $A_{\rm in}=3$ nm. Thanks to this behavior of the nonlinear parameter ϵ, perturbation theory can be used to search for an approximate solution of the problem for nearly all the physically attainable interface conditions. Thus, solutions of the normalized equations of motion are sought in terms of power series of the small parameter ϵ,

$$U(\vec{X},\tau)=U_0(\vec{X},\tau)+\epsilon U_1(\vec{X},\tau)+\cdots, \tag{13}$$

$$V(\vec{X},\tau)=V_0(\vec{X},\tau)+\epsilon V_1(\vec{X},\tau)+\cdots, \tag{14}$$

where the terms proportional to ϵ or its powers play the role of small corrections to U_0 and V_0. By introducing the power series for U and V in the boundary conditions associated to the problem, and regrouping the terms that contain the same power of ϵ, a hierarchy of sets of boundary conditions for U_m and V_m, $m=0,1,...$, is obtained. In particular, the boundary conditions derived from Eqs. (5a)–(5c) for the solutions of the symmetric zeroth-order problem are found to be

$$\frac{\partial U_0^+}{\partial X_3}+\frac{\partial V_0^+}{\partial X_1}=0, \quad X_1=0, \quad 0\leqslant X_3<\infty, \tag{15a}$$

$$\kappa^2\frac{\partial U_0^+}{\partial X_1}+(\kappa^2-2)\frac{\partial V_0^+}{\partial X_3}=\overline{K}_N\,\Delta U_0, \quad 0\leqslant X_3<D, \tag{15b}$$

$$U_0=0, \quad D\leqslant X_3<\infty, \tag{15c}$$

while those for the antisymmetric one are

$$\kappa^2\frac{\partial U_0^+}{\partial X_1}+(\kappa^2-2)\frac{\partial V_0^+}{\partial X_3}=0, \quad X_1=0, \quad 0\leqslant X_3<\infty, \tag{16a}$$

$$\frac{\partial U_0^+}{\partial X_3}+\frac{\partial V_0^+}{\partial X_1}=\overline{K}_T\,\Delta V_0, \quad 0\leqslant X_3<D, \tag{16b}$$

$$V_0=0, \quad D\leqslant X_3<\infty. \tag{16c}$$

Similarly, those for the symmetric first-order problem are

$$\frac{\partial U_1^+}{\partial X_3}+\frac{\partial V_1^+}{\partial X_1}=0, \quad X_1=0, \quad 0\leqslant X_3<\infty, \tag{17a}$$

$$\kappa^2\frac{\partial U_1^+}{\partial X_1}+(\kappa^2-2)\frac{\partial V_1^+}{\partial X_3}=\overline{K}_N\,\Delta U_1-\overline{K}_N\,\Delta U_0^2, \quad 0\leqslant X_3<D, \tag{17b}$$

$$U_1=0, \quad D\leqslant X_3<\infty, \tag{17c}$$

while the boundary conditions for the antisymmetric problem are

$$\kappa^2\frac{\partial U_1^+}{\partial X_1}+(\kappa^2-2)\frac{\partial V_1^+}{\partial X_3}=0, \quad X_1=0, \quad 0\leqslant X_3<\infty, \tag{18a}$$

$$\frac{\partial U_1^+}{\partial X_3}+\frac{\partial V_1^+}{\partial X_1}=\overline{K}_T\,\Delta V_1-\overline{K}_T\,\Delta V_0\,\Delta U_0, \quad 0\leqslant X_3<D, \tag{18b}$$

$$V_1=0, \quad D\leqslant X_3<\infty. \tag{18c}$$

Note the terms $\overline{K}_N\,\Delta U_0^2$ in Eq. (17b) and $\overline{K}_T\,\Delta V_0\,\Delta U_0$ in Eq. (18b) play the role the incident field has in the zeroth-order problem. Being products of solutions of the latter problem, in addition to a time-independent term that is of no importance in the present investigation, these terms contain contributions having a frequency that is twice that of the incident wave. Indeed, the solutions of the equations of motion, Eq. (9) and Eq. (10), having the same period of normalized incident wave, $T=2\pi$, can be expressed as a Fourier series over all the higher harmonics of the fundamental,

$$U(\vec{X},\tau)=\sum_{m=-\infty}^{+\infty}U(\vec{X}|m)\exp(-jm\tau), \tag{19}$$

$$V(\vec{X},\tau)=\sum_{m=-\infty}^{+\infty}V(\vec{X}|m)\exp(-jm\tau), \tag{20}$$

where $m\neq 0$, $\vec{X}=(X_1,X_3)$, and $U(\vec{X}|m)$ and $V(\vec{X}|m)$ are the solutions of the coupled linear differential equations,

$$\frac{\partial^2 U}{\partial X_1^2}+\frac{1}{\kappa^2}\frac{\partial^2 U}{\partial X_3^2}+\left(1-\frac{1}{\kappa^2}\right)\frac{\partial^2 V}{\partial X_1\,\partial X_3}=-m^2U, \tag{21}$$

$$\frac{\partial^2 V}{\partial X_1^2}+\frac{1}{\kappa^2}\frac{\partial^2 V}{\partial X_3^2}+\left(1-\frac{1}{\kappa^2}\right)\frac{\partial^2 U}{\partial X_1\,\partial X_3}=-m^2V. \tag{22}$$

Therefore, the solutions of the mth-order boundary conditions contain harmonic components of order $(m+1)$ at most. The solutions of Eq. (21) and Eq. (22) for the symmetric problem can be expressed as follows:

$$\begin{aligned}U^s(\vec{X}|m)=&\frac{2}{\pi}\int_0^\infty(\zeta A_m^s e^{-m\alpha_L X_3}\\&-2\kappa^{-2}\alpha_T C_m^s e^{-m\alpha_T X_3})\sin(m\zeta X_1)\,d\zeta\\&+\frac{2}{\pi}\int_0^\infty(\alpha_L B_m^s e^{-m\alpha_L X_1}\\&+2\kappa^{-2}\zeta D_m^s e^{-m\alpha_T X_1})\cos(m\zeta X_3)\,d\zeta,\end{aligned} \tag{23}$$

$$\begin{aligned}V^s(\vec{X}|m)=&\frac{2}{\pi}\int_0^\infty(\alpha_L A_m^s e^{-m\alpha_L X_3}\\&-2\kappa^{-2}\zeta C_m^s e^{-m\alpha_T X_3})\cos(m\zeta X_1)\,d\zeta\\&+\frac{2}{\pi}\int_0^\infty(\zeta B_m^s e^{-m\alpha_L X_1}\\&+2\kappa^{-2}\alpha_T D_m^s e^{-m\alpha_T X_1})\sin(m\zeta X_3)\,d\zeta,\end{aligned} \tag{24}$$

while those of the antisymmetric problem are

$$\begin{aligned}U^a(\vec{X}|m)=&\frac{2}{\pi}\int_0^\infty(\zeta A_m^a e^{-m\alpha_L X_3}\\&-2\kappa^{-2}\alpha_T C_m^a e^{-m\alpha_T X_3})\cos(m\zeta X_1)\,d\zeta\\&+\frac{2}{\pi}\int_0^\infty(\alpha_L B_m^a e^{-m\alpha_L X_1}\\&+2\kappa^{-2}\zeta D_m^a e^{-m\alpha_T X_1})\sin(m\zeta X_3)\,d\zeta,\end{aligned} \tag{25}$$

$$\begin{aligned}V^a(\vec{X}|m)=&\frac{2}{\pi}\int_0^\infty(-\alpha_L A_m^a e^{-m\alpha_L X_3}\\&+2\kappa^{-2}\zeta C_m^a e^{-m\alpha_T X_3})\sin(m\zeta X_1)\,d\zeta\\&-\frac{2}{\pi}\int_0^\infty(\zeta B_m^a e^{-m\alpha_L X_1}\\&+2\kappa^{-2}\alpha_T D_m^a e^{-m\alpha_T X_1})\cos(m\zeta X_3)\,d\zeta.\end{aligned} \tag{26}$$

In Eq. (23) to Eq. (26), $A_m^{s,a}$, $B_m^{s,a}$, $C_m^{s,a}$, $D_m^{s,a}$ are unknown functions of ζ to be determined by enforcing the appropriate boundary conditions, and α_L and α_T are defined on the real axis so that

$$\alpha_L=\begin{cases}\sqrt{\zeta^2-1}, & \text{if } \zeta\geqslant 1,\\ -j\sqrt{1-\zeta^2}, & \text{if } \zeta<1,\end{cases}$$

and

$$\alpha_T=\begin{cases}\sqrt{\zeta^2-\kappa^2}, & \text{if } \zeta\geqslant \kappa^2,\\ -j\sqrt{\kappa^2-\zeta^2}, & \text{if } \zeta<\kappa^2.\end{cases}$$

The total components of the normalized displacement fields are recovered from the solution of the symmetric and antisymmetric problems according to the following rules:

$$U(X_1,X_3)=U^s(X_1,X_3)+U^a(X_1,X_3),\quad \text{for } X_1>0,$$

$$U(|X_1|,X_3)=-U^s(|X_1|,X_3)+U^a(|X_1|,X_3),\quad \text{for } X_1<0,$$

$$V(X_1,X_3)=V^s(X_1,X_3)+V^a(X_1,X_3),\quad \text{for } X_1>0,$$

$$V(|X_1|,X_3)=V^s(|X_1|,X_3)-V^a(|X_1|,X_3),\quad \text{for } X_1<0.$$

The details of the mathematical procedure to solve these problems were reported in the work of Achenbach *et al.*[16] and Mendelsohn *et al.*,[17] and will not be repeated here. The only relevant addition to that treatment is the explicit and repeated use of the harmonic balance method to match the time dependence of the scattered field with that of the driving terms given either by the incident field in the boundary conditions for the zeroth-order problems, or by the products of the zeroth-order components in Eq. (17b) and Eq. (18b). The solutions of the zeroth-order problem, thus, can be shown to contain only contributions with the same frequency as the incident field, while those of the first-order system, disregarding a constant term of no interest for the present investigation, describe scattered fields with frequency twice that of the incident wave.

III. NUMERICAL RESULTS

The number of parameters that determine the dynamics of an interface between two rough surfaces in contact is considerable, and that of those that are required to describe the nonlinear scattering of an acoustic wave from a surface-breaking crack with faces in partial contact even more so. As an exhaustive parametric study would go beyond the scope of the present work, the focus here is only on those parameters that most notably affect the detection and localization of the nonlinear defect of interest here. Both shear vertical (SV) and Rayleigh wave incidence are considered next. The frequency of the incident wave is set to be $f=5$ MHz, and the material hosting the crack is steel throughout this work.

A. Shear vertical incidence

SV waves are commonly used for the nondestructive inspection of components in nuclear power plants and in the railway industry when searching for cracks breaking the surface opposite that on which the transmitter in placed. Such waves are often sent into the component along a direction of propagation that forms an angle of 45° with the normal to the surface.

Given the importance of SV waves as a probing tool for surface-breaking cracks, this investigation starts by considering the effect of the angle of incidence, θ_{in}, of such a mode on the acoustic response of a partially closed, surface-breaking crack. The angle of incidence is measured from the x_3 axis, that is to say, from the plane containing the crack. The incident wave is assumed to propagate from infinity toward the stress-free surface with a propagation vector $\vec{k}_T$. In

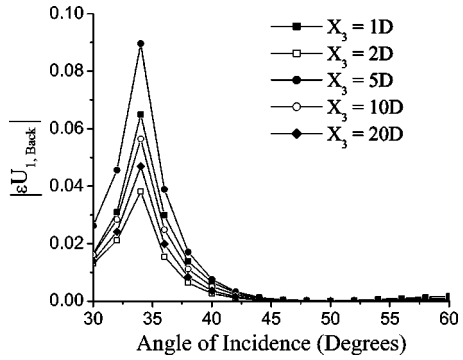

FIG. 3. Normalized backscattered horizontal displacement of the nonlinear field versus the angle of incidence for increasing values of the normalized depth of the observation point. The latter is measured in terms of the normalized crack's depth, D. The normalized crack's depth is $D=0.5$, while $\bar{K}_N=1.95$ and $\epsilon=0.144$.

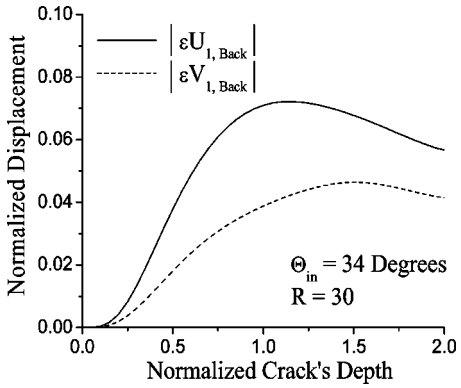

FIG. 4. Normalized backscattered components of the nonlinear displacement as a function of the normalized crack's depth. The angle on incidence is equal to 34°, and the observation point is at a normalized distance, R, equal to 30 from the crack's mouth along the propagation direction of the incident wave. Also, $\bar{K}_N=1.95$ and $\epsilon=0.144$.

all the following simulations, the dependence of the nonlinear parameter ϵ on the interface stiffness is that shown in Fig. 2, and the amplitude of the incident wave, A_{in}, is equal to 3 nm.

Figure 3 shows the dependence on the angle of incidence, θ_{in}, of the horizontal components of the nonlinear backscattered total field at increasing depth within the bulk of the material. A similar behavior is displayed by the vertical components. The angle of incidence is varied by moving the observation point along a surface parallel to the stress-free surface of the half-space. This is done to simulate the common experimental conditions in which the inspecting transducer is moved along a surface that is parallel to that containing the crack. Note that in this and all the subsequent figures the following notation convention has been used: $U(\vec{X}|m)=U_m(\vec{X})$, and $V(\vec{X}|m)=V_m(\vec{X})$. The most relevant feature of Fig. 3 is the marked peak around the critical angle of the longitudinal wave, θ_L, which is equal to 34° in steel. Needless to say, the validity of the considerations that follow does not depend on the specific value of the critical angle, θ_L, which may vary with the material. The enhanced response at θ_L can be easily explained by considering that, at θ_L and in a small neighborhood of it, the amplitude of the reflected longitudinal wave can be considerably larger (in fact, in steel it is 4.3 times larger) than the amplitude of the incident wave. Furthermore, in the neighborhood of θ_L the dominant component of the total incident field is σ_{11}, which, more efficiently than any other, excites the normal vibration mode of the crack. Of relevance because contrary to the assumptions underlying the method most commonly employed to search for surface-breaking cracks is also the considerably smaller response around 45° angle of incidence. Not surprisingly, similar considerations and results are found to hold also for the scattered waves with frequency equal to that of the incident field. Finally, as similarly displayed also in Fig. 5 later, the amplitude of the scattered signal is shown to vary in a nonmonotonic way as the coordinate of the observation point varies.

The effect of the crack's depth on the modulus of the normalized horizontal and vertical displacement components of the second harmonic component is illustrated in Fig. 4. The angle of incidence of the incident SV wave is equal to 34°, while the normalized interface stiffness and the nonlinear parameter are $\bar{K}_N=1.95$ and $\epsilon=0.144$, respectively. The observation point is placed along the direction of propagation of the incident wave at a normalized distance $R=k_L r=30$ from the crack's mouth, where r indicates the actual distance. Results concerning the magnitude of the linear components show the latter to increase up to a value of D of the order of 1.5, after which they remain at the same level for values of D up to 2. This value of D corresponds to an actual crack depth of about $2\lambda_T/3$, where λ_T is the wavelength of the incident wave. The nonlinear components (see Fig. 4), on the other hand, reach their maximum values around $D=1$, after which they tend to decrease, and, similarly to the components of the first harmonics,[17] further oscillate with amplitudes that decrease with increasing crack depth. Deeper cracks are expected to produce nonlinear components having a modulus within the ranges shown in Fig. 4.

The magnitude of the nonlinear response predicted by the model and presented in these examples is large enough that some doubt may be cast on the accuracy of a first-order approximation. A closer examination of the results, however, shows that for smaller values of ϵ corresponding to closer cracks, and at angles of incidence not too close to the critical angle of the longitudinal waves, the magnitude of the second harmonic field generated upon scattering is well within the range of values where the perturbation approach provides accurate results. Indeed, the case of a SV wave incident at 34° is, to some extent, special. To examine this point, the dependence of the ratio between the absolute values of the horizontal displacement of the scattered second and first harmonic components on the normalized crack dimension, D, has been examined for two values of θ_{in}, 45° and 60°, which are commonly used in ultrasonic inspections, as well as for 34°. The results indicate that the response at 45° is always more than 10 dB below that at 34° incidence for all values of the normalized crack, D, less than 2. Similarly, the response at 60° remains considerably below that at 34° incidence for values of $D<1$, and asymptotically approaches the latter for $D>1$. The conclusion to draw from this is that, not only the absolute levels of the linear and nonlinear backscattered fields are higher at the critical angle for longitudinal waves

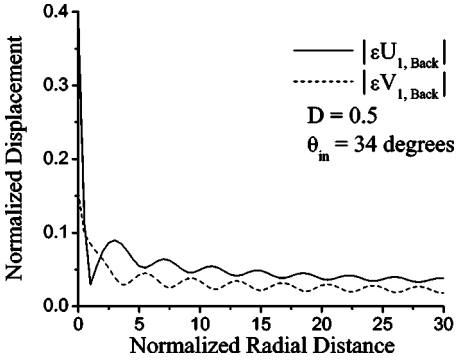

FIG. 5. Normalized backscattered components of the nonlinear field versus distance from the crack's mouth. The observation point is placed along the propagation direction of the incident wave, i.e., $\theta_{\text{in}}=34°$. The normalized crack's depth is $D=0.5$, $K_N=1.95$, and $\epsilon=0.144$.

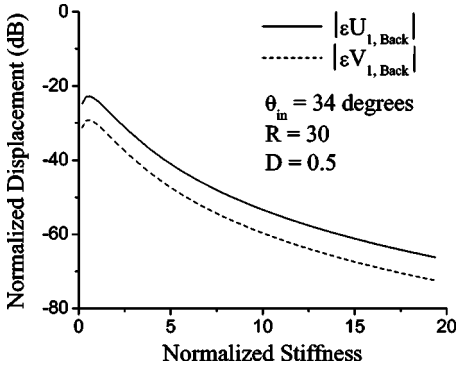

FIG. 6. Normalized backscattered horizontal component of the nonlinear displacement field versus the normalized interfacial stiffness. The normalized distance of the observation point is $R=30$. The remaining system parameters are those of the preceding figure.

than at any other angle of incidence, but also the efficiency of the second harmonic generation is the highest for angles of incidence just above θ_L, especially for cracks with depth $D<1$. In addition, if accurate numerical evaluations of the scattered wave field under these conditions are sought, terms containing higher powers of ϵ should be retained in the perturbation series of Eqs. (13) and (14).

Next, the variation of the modulus of the Cartesian components of the backscattered displacement field with the distance from the crack is considered for a shear wave incident at 34°. The observation point moves along the direction of propagation of the incident wave. The normalized depth of the crack is $D=0.5$, which is approximately equal to $0.15\lambda_T$, while the normalized interface stiffness $K_N=1.95$ and the nonlinear parameter $\epsilon=0.144$. Figure 5 illustrates the dependence of the scattered second harmonic on the distance of the observation point from the crack's mouth, R. The latter moves along the direction of propagation of the incident wave, which is defined by the angle of incidence $\theta_L=34°$. The horizontal component shows a rapid decay to occur within a normalized distance equal to 2 from the crack's mouth, while the vertical component tends to decay more slowly. This behavior may be understood in terms of the increasing constraining effect of the surrounding material on the motion of the particles as the observation point moves away from the surfaces of both the crack and half-space.

Figure 6 shows the variation of the modulus of ϵU_1 and ϵV_1 with the interface closure, i.e., for increasing values of the normalized interface stiffness K_N. The observation point is placed along the backscattering direction at a normalized distance $R=30$ from the crack's mouth. The normalized crack depth is $D=0.5$. After an initial dramatic increase from $-\infty$ corresponding to the formation of first contacts, the modulus of the Cartesian nonlinear components decay in a monotonic fashion that strongly resembles that predicted for the nonlinear response on an infinite interface.

In the introduction, results obtained by Krohn *et al.*[6] were reported for their relevance to the issue of defect location by means of nonlinear ultrasonic techniques. In particular, it was mentioned that using laser interferometric detection, a highly localized nonlinear response of delaminations could be detected within thin composite plates. It was also reported that, so far, no convincing explanation for such a strong localization has been found, although some form of trapping mechanism of the energy carried by the higher harmonic wave has been hypothesized.[18] Although apparently simplistic, two remarks are in order. The first concerns the detection technique employed in that work, which is sensitive to the displacement component normal to the inspected surface. The second remark regards the fact that the delamination is likely to be roughly parallel to the surface on which the measurements are carried out. Therefore, considering that in the experiments mentioned above the wavelength of the acoustic excitation is much larger than the plate's thickness, it is reasonable to conceive that the behavior of the normal component of the displacement of the higher harmonic wave detected at the stress-free surface closely resembles the normal crack opening displacement. Calculations have been carried out with this model and presented in Fig. 7, which illustrates the dependence of ϵU_1, that is to say, the nonlinear displacement component normal to the crack surface, on the coordinate X_3 at $X_1=0^-$. The crack's normalized depth is $D=0.5$, the normalized interface stiffness and nonlinear parameter are $K_N=1.95$ and $\epsilon=0.144$, respectively. A sudden drop of the modulus of ϵU_1 is observed at the crack tip, which exceeds 30 dB. This prediction of the model suggests that the highly localized nonlinear response detected by the interferometric technique follows the spatial dependence of

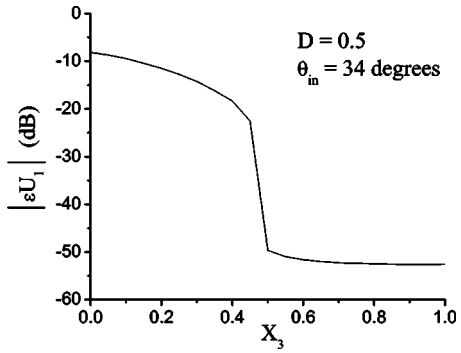

FIG. 7. The dependence of the normalized nonlinear component of the displacement normal to the crack on X_3 for $X_1=0$. The system parameters are those of Fig. 5.

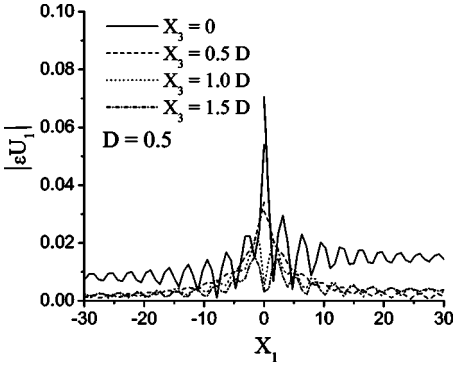

FIG. 8. Normalized backscattered horizontal displacement of the nonlinear field versus X_1 at four different values of X_3. The latter is measured in terms of normalized crack's depth, D. The normalized crack's depth is $D=0.5$, while $\overline{K}_N=1.95$ and $\epsilon=0.144$.

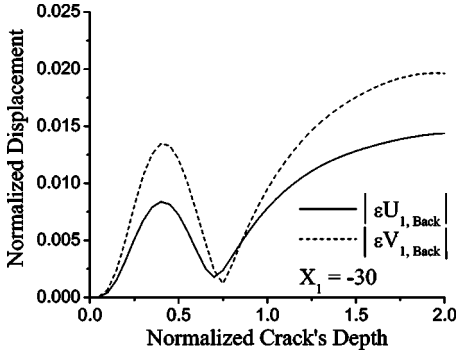

FIG. 9. Normalized backscattered components of the nonlinear field versus the normalized crack's depth. The observation point is placed on the surface of the half-space at a normalized distance $X_1=-30$. The normalized crack's depth is $D=0.5$, $\overline{K}_N=1.95$, and $\epsilon=0.144$.

the normal component of the opening displacement of the delamination.

Finally, it should be remarked that, for all the cases considered so far, very similar theoretical results have been obtained for the same field variables in the forward scattering direction, and, for this reason, they have not been presented here.

B. Rayleigh wave incidence

The case of a Rayleigh wave insonifying a partially closed surface-breaking crack is considered next. The amplitude of the horizontal displacement component of the incident wave at the stress-free surface is chosen to be equal to 3 nm: $u_{\text{in}}(x_1,x_3=0)=3$ nm.

Figure 8 illustrates the behavior of the modulus of the second harmonic component of the horizontal displacement at four values of the depth, X_3, as a function of the variable X_1. The dependence of the first harmonic component displays features similar to those of the second harmonic, and, therefore, is not shown here. The normalized crack's depth is $D=0.5$, and the interfacial stiffness and the nonlinear parameter are again $\overline{K}_N=1.95$ and $\epsilon=0.144$. As in the case of SV incidence, in the plane $X_1=0$ the displacement component normal to the crack's plane undergoes a dramatic and sudden drop at the tip of the crack. The forward scattered second harmonic wave is also shown to approach an average value slightly higher than that of the backward scattered component as the value of X_1 increases in both directions.

The effect of the interface closure on the modulus of both vertical and horizontal second harmonic components of the displacement field is also investigated. The behavior of these components is found to closely resemble that already seen in Fig. 6.

Finally, Fig. 9 and Fig. 10 show the backward and forward normalized Cartesian components of the nonlinear scattered field, respectively, at a distance $|X_1|=30$ on the surface of the half-space as functions of the normalized crack's depth, D. The values of the interfacial stiffness and of the nonlinear parameter are those already used in Fig. 8. A remarkable difference of behavior between the forward and the backward components can be easily noticed, as the former increases nearly monotonically with the crack's depth up to $D\approx 1$ to remain roughly at the same level afterward, while the latter displays pronounced interference features for values of $D<1$. Worth noting is also the considerably higher values of the forward scattered field compared to that scattered in the opposite direction.

IV. SUMMARY AND CONCLUDING REMARKS

A theoretical model that predicts the generation of the second harmonic component upon scattering of an incident harmonic wave by a surface-breaking crack with faces in partial contact has been presented. The cases of shear vertical and Rayleigh wave incidence have been considered, and for each, the effect of parameters such as the angle of incidence, the crack's depth, and the crack's closure on the nonlinear response of the crack have been examined. The nonlinearity of the scattering defect has been introduced into the mathematical formulation of the problem by extending the boundary conditions at the crack's contacting faces to account for the nonlinear effect of the two-dimensional distribution of elastic contacts. It has been shown that when cracks with depth not larger than λ_T are insonified by a shear vertical wave, the highest linear and nonlinear responses of such defects occur when the latter are insonified at an angle slightly higher than the critical angle of the longitudinal wave, θ_L. Further, the generation of the second harmonic has been found to be the most efficient in such a configuration. The

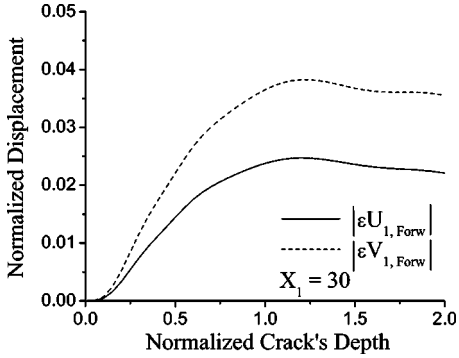

FIG. 10. Normalized forward scattered components of the nonlinear field versus the normalized crack's depth. The observation point is placed on the surface of the half-space at a normalized distance $X_1=30$. The normalized crack's depth is $D=0.5$, $\overline{K}_N=1.95$, and $\epsilon=0.144$.

relevance of this finding stems in part from the fact that they force us to reconsider the suitability of the inspection methods currently used to search for surface-breaking cracks utilizing SV waves at 45° incidence, regardless of the depth of the crack sought and the hosting material. As demonstrated in this work, the sensitivity of a SV wave inspecting such defects at 45° incidence is much lower than that at and just above θ_L. This problem is further investigated elsewhere.[19]

An additional important advantage offered by the use of SV waves at or just above θ_L concerns the localization of a defect. In fact, the exploitation of the efficient mode conversion of the incident SV wave into an evanescent longitudinal wave propagating along the surface renders this configuration considerably more sensitive to crack-like defects located at the surface of the sample than to any other defect placed along the direction of propagation of the incident field. Therefore, in search of surface-breaking cracks that are located on the surface opposite that which is scanned by an ultrasonic probe by means of both linear and nonlinear scattering techniques employing beams of finite lateral dimensions, the setup providing the highest sensitivity offers also a solution to the localization problem.

Of further concern to the localization problem, the model presented here suggests a simple and plausible interpretation of recent experimental results by Krohn *et al.*[6] showing a highly localized nonlinear response of delaminations in composite materials. In fact, the model indicates that the experimental observations capture the very rapid decay of the nonlinear opening displacement normal to the delamination occurring beyond the borders of the latter. The model predicts a magnitude of such a drop to be of the order of 30 dB, which exceeds the experimentally observed behavior by at least 10 dB. A possible reason for such an overestimation may be the asymmetric position of the actual delamination within the plate's cross section. In fact, if located outside the midplane of the plate, the crack is expected to generate a scattered field that cannot be decomposed into symmetric and antisymmetric parts, the former yielding a nearly null contribution to the component of the displacement field normal to the plane containing the crack [Eq. (17c)].

Finally, for both SV and Rayleigh wave incidence, the magnitude of the nonlinear response displays a similar behavior with respect to variations of the interfacial stiffness. After reaching an absolute maximum for values of the normalized stiffness proximal to 1, they monotonically decay for increasing values of K_N, as has already been noticed in the case of an infinite interface formed by rough surfaces in contact.

ACKNOWLEDGMENTS

This work was supported by the Swedish Inspectorate for Nuclear Power (SKI), under Contract No. 14.43-010902,01156, and by the Swedish Center for Nuclear Technology under the contract entitled ''Detection of stress-corrosion cracks by means of nonlinear scattering of ultrasonic waves.''

[1] I. Y. Solodov, ''Ultrasonics of non-linear contacts: propagation, reflection and NDE applications,'' Ultrasonics **36**, 383–390 (1998).
[2] I. Y. Solodov, N. Krohn, and G. Busse, ''CAN: an example of nonclassical acoustic nonlinearity in solids,'' Ultrasonics **40**, 621–625 (2002).
[3] I. Y. Solodov and B. A. Korshak, ''Instability, chaos, and 'memory' in acoustic wave–crack interaction,'' Phys. Rev. Lett. **88**, 014303 (2002).
[4] V. Y. Zaistev, V. Gusev, and B. Castagnede, ''Observation of the 'Luxenburg–Gorky' effect for elastic waves,'' Ultrasonics **40**, 627–631 (2002).
[5] V. Y. Zaistev, V. Gusev, and B. Castagnede, ''Luxenburg–Gorky effect retooled for elastic waves: a mechanism and experimental evidence,'' Phys. Rev. Lett. **89**, 105502 (2002).
[6] N. Krohn, R. Stoessel, and G. Busse, ''Acoustic non-linearity for defect selective imaging,'' Ultrasonics **40**, 633–637 (2002).
[7] J. D. Achenbach and A. N. Norris, ''Loss of specular reflection due to nonlinear crack–face interaction,'' J. Nondestruct. Eval. **3**, 229–239 (1982).
[8] S. Hirose and J. D. Achenbach, ''Higher harmonics in the far field due to the dynamic crack–face contacting,'' J. Acoust. Soc. Am. **93**, 142–147 (1993).
[9] S. Hirose, ''2-D scattering by a crack with contact boundary conditions,'' Wave Motion **19**, 37–49 (1994).
[10] D. Donskoy, A. Sutin, and A. Ekimov, ''Nonlinear acoustic interaction on contact interfaces and its use for nondestructive testing,'' NDT & E Int. **34**, 231–238 (2001).
[11] J. M. Baik and R. B. Thompson, ''Ultrasonic scattering from imperfect interfaces: a quasi-static model,'' J. Nondestruct. Eval. **4**, 177–196 (1984).
[12] C. Pecorari, ''Scattering of a Rayleigh wave by a surface-breaking crack with faces in partial contact,'' Wave Motion **33**, 259–270 (2001).
[13] C. Pecorari, ''Nonlinear interaction of plane ultrasonic waves with an interface between rough surfaces in contact,'' J. Acoust. Soc. Am. **113**, 3065–3072 (2003).
[14] K. L. Johnson, *Contact Mechanics* (Cambridge University Press, New York, 1985).
[15] R. D. Mindlin and H. Deresiewicz, ''Elastic spheres in contact under varying oblique forces,'' J. Appl. Mech. **20**, 327–344 (1953).
[16] J. D. Achenbach, L. M. Keer, and D. A. Mendelsohn, ''Elastodynamic analysis of an edge crack,'' J. Appl. Mech. **47**, 551–556 (1980).
[17] D. A. Mendelsohn, J. D. Achenbach, and L. M. Keer, ''Scattering of elastic waves by a surface-breaking crack,'' Wave Motion **2**, 277–292 (1980).
[18] I. Y. Solodov, ''Ultrasonics of nonlinear interfaces in solids: new physical aspects and NDE applications,'' *Proceedings of the 5th Ultrasonics World Conference*, 2003, pp. 555–564.
[19] C. Pecorari, ''A note on the sensitivity of SV wave scattering to surface-breaking crack,'' to appear in Ultrasonics.

Resonant properties of a nonlinear dissipative layer excited by a vibrating boundary: Q-factor and frequency response

B. O. Enflo[a)]
Department of Mechanics, Kungl. Tekniska Högskolan, S-10044 Stockholm, Sweden

C. M. Hedberg[b)] and O. V. Rudenko[c)]
Blekinge Institute of Technology, S-371 79 Karlskrona, Sweden

(Received 29 March 2004; revised 19 May 2004; accepted 10 October 2004)

Simplified nonlinear evolution equations describing non-steady-state forced vibrations in an acoustic resonator having one closed end and the other end periodically oscillating are derived. An approach based on a nonlinear functional equation is used. The nonlinear Q-factor and the nonlinear frequency response of the resonator are calculated for steady-state oscillations of both inviscid and dissipative media. The general expression for the mean intensity of the acoustic wave in terms of the characteristic value of a Mathieu function is derived. The process of development of a standing wave is described analytically on the base of exact nonlinear solutions for different laws of periodic motion of the wall. For harmonic excitation the wave profiles are described by Mathieu functions, and their mean energy characteristics by the corresponding eigenvalues. The sawtooth-shaped motion of the boundary leads to a similar process of evolution of the profile, but the solution has a very simple form. Some possibilities to enhance the Q-factor of a nonlinear system by suppression of nonlinear energy losses are discussed. © *2005 Acoustical Society of America.*
[DOI: 10.1121/1.1828548]

PACS numbers: 43.25.Gf [MFH] Pages: 601–612

I. INTRODUCTION

The resonance is known as one of the most interesting phenomena in the physics of vibrations and waves. It manifests itself markedly, if the dependence of the amplitude of a forced oscillation on frequency (i.e., the frequency response) has a sharp maximum. In this case, the ratio of the central frequency ω_0 of the spectral line imaging the response to the characteristic width of this line is large in magnitude. This ratio, known as the Q-factor, can be used as a measure of the ''quality'' of a resonant system. At large values of Q the system can contain high density of vibratonal energy, because the ratio of the steady-state forced oscillation and the external driving force is equal to Q.

For $Q \gg 1$ the approach to the equilibrium state goes on very slowly, because the characteristic relaxation time is about Q/ω_0. The duration of the increase of the vibration amplitude (or decrease, if the source is shut off) contains a great number of periods which is of the order of Q.

The excitation of strong vibrations in a high-Q system can lead to the appearance of nonlinear effects, the best known example of which is the destruction of the system. On the other hand, high-Q devices are used for the most precise measurements in different branches and applications.

This work is devoted to the analysis of the frequency response and Q-factor of a nonlinear acoustic resonator.

Standing waves are of great interest for nonlinear wave theory and technologies.[1–3] Using high-Q resonators, it is possible to accumulate a considerable amount of acoustic energy and provide, in consequence, conditions for clear manifestaition of nonlinear phenomena[4] even in case of a weak power source. Extremely high Q-factor magnitudes, $Q \sim 10^8 - 10^9$, were reached in mechanical resonators designed for the detection of bursts of gravitational waves.[5] Very strong vibrations were excited in gas-filled resonators of complicated shape, in particular conical or bulb-shaped ones.[6]

At small amplitudes of vibration, the Q-factor is limited by linear absorption caused by dissipative properties of both the medium inside the cavity of the resonator and its boundaries, as well as by radiation losses essential for open resonators. All these types of absorption do not depend on the amplitude. Therefore, for a resonator of given design, the Q-factor is the constant suitable for estimation of its ''quality.''

As the amplitude increases, nonlinear phenomena become important. The progressive distortion of the wave profile often leads to formation of shocks which are responsible for additional nonlinear losses. This nonlinear absorption depends on the ''strength'' of the wave (namely, on its amplitude, peak pressure, intensity, etc.) and can be several orders higher than the usual linear one.[3] Consequently, the Q-factor is now determined not only by the design of the nonlinear resonator, but by the strength of the internal acoustic field as well.

The nonlinear Q-factor was earlier evaluated by the rate of dying-down of free standing waves between two rigid walls.[7] It was also calculated for the forced steady-state vibration in this resonator excited by an external force with the same spatial distribution as the fundamental mode.[8] However, only wave profiles and spectra were studied in detail for

[a)]Electronic mail: benflo@mech.kth.se
[b)]Author to whom correspondence should be addressed. Electronic mail: claes.hedberg@bth.se
[c)]Also at Department of Acoustics, Faculty of Physics, Moscow State University, 119899 Moscow, Russia.

the most typical statement of the problem, in which one rigid wall of the resonator is immovable, and the other wall oscillates periodically (see, for example, Refs. 2, 9–11). Such principal characteristics of this nonlinear resonator as Q-factor and frequency response have not been adequately explored. Some new findings related to the Q-factor are published in Ref. 12. More comprehensive results are given below.

II. SIMPLIFIED APPROACH AND BASIC NONLINEAR EQUATIONS

Evidently, in a linear one-dimensional system the standing wave can be composed of two plane waves propagating in opposite directions:

$$\Phi(x,t)=\varphi_1\left(t-\frac{x}{c}\right)+\varphi_2\left(t+\frac{x}{c}\right); \tag{1}$$

here Φ is potential of particle velocity $\vec{u}=-\nabla\Phi$, and c is sound velocity. It seems that Chester[9] was first to use the representation (1) to describe approximately the nonlinear field in the cavity of a resonator. This idea was explained and applied to nonlinear standing waves between rigid immovable walls,[7,8] where the field is described as the sum (1) of two Riemann or Burgers traveling waves. Each of these waves can be distorted significantly by nonlinear self-action, resulting into the formation of a sawtooth-shaped profile from the initial harmonic one with no contribution from the cross-interaction of two counterpropagating waves. In other words, each wave is distorted by itself during the propagation, but there is no energy exchange between them. The idea of ''nonlinear superposition'' can be used for any wave field described by different mathematical models (see, for example, Ref. 13). Similar approaches have been used later in many works (see, for example, Refs. 11 and 14). Waveguide modes can also be described by a modification of this approach;[15] the nonlinear Brillouin modes were formed[15] by two strongly distorted waves intersecting at equal angles to the axes of a waveguide.

The idea of ''nonlinear superposition'' was clearly explained in Ref. 12. In short, the successive approximation solution to any nonlinear model governing the field of cross-secting waves contains both resonant and nonresonant parts. After several periods of vibration the nonresonant waves become much weaker than the resonant ones, and cannot paticipate significantly in nonlinear energy exchange. Each of two cross-secting (in particular, counterpropagating) waves generates its higher harmonics, but the cross-interaction process can be neglected if the waves are periodic in time. This conclusion is easily seen to be as valid for periodic waves intersecting at any sufficiently large angles,[15] not necessarily equal to 180°, as for counterpropagating waves in 1D geometry.

After these comments, the approximate solution can be written as the sum of two traveling Riemann waves (for an inviscid fluid):

$$\begin{aligned} u&=u_1+u_2\\ &=F_1\left(\omega t-\kappa x+\frac{\epsilon}{c^2}\omega x F_1\right)+F_2\left(\omega t+\kappa x+\frac{\epsilon}{c^2}\omega x F_2\right), \end{aligned} \tag{2}$$

where $F_{1,2}$ are auxiliary functions describing wave profiles, and ϵ is a nonlinearity parameter.

The solution (2) must satisfy the boundary condition on the immovable wall,

$$u(x=0,t)=0, \tag{3}$$

and the boundary condition on the vibrating boundary,

$$u(x=L,t)=A\sin\omega t. \tag{4}$$

From (2) and (3) follows $F_1=-F_2=F$. The unknown function F must be determined from the second boundary condition (4). This determination reduces (2) to the functional equation

$$F\left(\omega t-\kappa L+\frac{\epsilon}{c}\kappa LF\right)-F\left(\omega t+\kappa L-\frac{\epsilon}{c}\kappa LF\right)=A\sin\omega t. \tag{5}$$

The equation (5) is very complicated and cannot be solved exactly analytically. Nevertheless, it can be simplified for most interesting cases, if the following three conditions are satisfied.

First, the length of the resonator must be small in comparison with the shock formation length:[3,4]

$$L\ll\frac{c^2}{\epsilon\omega|F|_{\max}}, \tag{6}$$

where $|F|_{\max}$ is the maximum amplitude of the function F.

Second, the frequency ω of vibration of the right-hand boundary must differ slightly from a resonant frequency $n\omega_0$:

$$\kappa L=\pi n+\Delta,\quad \Delta=\pi\frac{\omega-n\omega_0}{\omega_0}\ll 1, \tag{7}$$

where Δ is the discrepancy and $\omega_0=\pi c/L$ is the frequency of the fundamental eigenmode $n=1$.

Third, the energy influx during one period $2\pi/\omega$ from the vibrating boundary to the resonator must be small in comparison with the accumulated energy; in other words,

$$Q\gg 1. \tag{8}$$

The case of vicinity of the fundamental mode ($n=1$) is now considered. Using the weak nonlinearity condition (6) and formulas (7) with the smallness condition for Δ we replace the left-hand side of Eq. (5) by two terms of its series expansion:

$$\begin{aligned} &F\left(\omega t-\kappa L+\frac{\epsilon}{c}\kappa LF\right)-F\left(\omega t+\kappa L-\frac{\epsilon}{c}\kappa LF\right)\\ &\quad=F\left(\omega t-\pi-\Delta+\frac{\epsilon(\pi+\Delta)F}{c}\right)\\ &\qquad-F\left(\omega t+\pi+\Delta-\frac{\epsilon(\pi+\Delta)F}{c}\right)\\ &\quad\approx[F(\omega t-\pi)-F(\omega t+\pi)]\\ &\qquad-\left(\Delta-\frac{\pi\epsilon F}{c}\right)[F'(\omega t-\pi)+F'(\omega t+\pi)]. \end{aligned} \tag{9}$$

Because the right-hand side of Eq. (5) is a periodic function, and the Q-factor is presumed to be large (8), the unknown function F must be quasiperiodic. Therefore, its variation during one period can be replaced in Eq. (9) by the derivative

$$F(\omega t-\pi)-F(\omega t+\pi)\approx -2\pi\mu\frac{\partial F(\omega t+\pi)}{\partial(\mu\omega t)}. \tag{10}$$

Here $\mu\ll 1$ is a small parameter, the physical meaning of which will be clear later. Using (9) and (10) the equation (5) takes the form

$$\mu\frac{\partial F}{\partial(\mu\omega t/\pi)}+\left(\Delta-\frac{\pi\epsilon F}{c}\right)\frac{\partial F(\omega t+\pi)}{\partial(\omega t)}=-\frac{A}{2}\sin\omega t. \tag{11}$$

Introducing new dimensionless variables and constants

$$U=\frac{F}{c},\quad M=\frac{A}{c},\quad \xi=\omega t+\pi,\quad T=\frac{\omega t}{\pi}, \tag{12}$$

one can rewrite the simplified evolution equation (11) as

$$\frac{\partial U}{\partial T}+\Delta\frac{\partial U}{\partial\xi}-\pi\epsilon U\frac{\partial U}{\partial\xi}=\frac{M}{2}\sin\xi. \tag{13}$$

The equation (13) was derived earlier[17] to describe the sound excitation by a moving laser beam (see also Refs. 18 and 19); it was named ''inhomogeneous Riemann equation with discrepancy.'' It should be emphasized that the temporal variables ξ and T are ''fast'' and ''slow'' time, respectively. From Eq. (13) it follows that the small parameter μ at the derivative on slow time T can play the role of any small number: Δ, M or $U\sim M$.

The evolution equation (13) can be generalized. The boundary $x=L$ can execute not only harmonic vibration but any periodic one. In this case, the boundary condition (4) must be replaced by

$$u(x=L,t)=Af(\omega t), \tag{14}$$

where f is an arbitrary function with the period 2π. The boundary condition (14) leads to a simplified evolution equation, which differs from (13) in its right-hand side, now equaling

$$-\frac{M}{2}f(\xi-\pi). \tag{15}$$

Next generalization of (13) takes into consideration the effective viscosity, $b\neq 0$. In Ref. 20 an equation similar to (13) and (15) was derived with account for dissipation and finite displacement of the vibrating boundary:

$$\frac{\partial U}{\partial T}+\Delta\frac{\partial U}{\partial\xi}-M\phi(\xi)-D\frac{\partial^2 U}{\partial\xi^2}=\frac{M}{2}\phi'(\xi), \tag{16}$$

where $\phi'(\xi)$ is a periodic function and the dimensionless number D, determining the weak absorption of a wave passing through the length L of a resonator, is defined as

$$D=\frac{b\omega^2 L}{2c^3\rho}\ll 1. \tag{17}$$

However, the volume nonlinearity ($\epsilon\neq 0$) was not considered in Ref. 20.

The objective of the present work is the simultaneous consideration of effects of dissipation and nonlinearity. Because all the phenomena leading to the progressive distortion of the wave are supposed to be weak, the corresponding terms in the evolution equation must be additive.[3,16]. So, combining Eqs. (13), (15) and (16) we derive

$$\frac{\partial U}{\partial T}+\Delta\frac{\partial U}{\partial\xi}-\pi\epsilon U\frac{\partial U}{\partial\xi}-D\frac{\partial^2 U}{\partial\xi^2}=-\frac{M}{2}f(\xi-\pi). \tag{18}$$

The equation (18) was named ''inhomogeneous Burgers equation.'' [21] Its main properties were studied in Refs. 21 and 22 in the context of stimulated Brillouin scattering of light by nonlinear hypersonic waves.

III. STEADY-STATE VIBRATIONS

The establishment of a steady-state field in a resonator is a result of competition between energy inflow from a vibrating source and its losses caused by linear dissipation and nonlinear absorption. The equilibrium state reached at $T\to\infty$ can be described by the ordinary differential equation, obtained by integration of Eq. (18) at $\partial U/\partial T=0$. The simplest case of periodic sawtooth-shaped motion of boundary is considered first. It corresponds to the right-hand side of (18) being equal to $-(M/2)\xi/\pi$ inside the interval $\pi\leqslant\xi\leqslant\pi$ and periodically continued outside. For this case the steady-state equation is

$$D\frac{dU}{d\xi}+\frac{\pi\epsilon}{2}(U^2-C^2)-\Delta U=\frac{\pi M}{4}\left(\frac{\xi^2}{\pi^2}-\frac{1}{3}\right). \tag{19}$$

The constant C in (19) is an arbitrary constant, which has an important physical meaning. From (19) follows

$$\overline{U^2}=\frac{1}{2\pi}\int_{-\pi}^{\pi}U^2\,d\xi=C^2. \tag{20}$$

Thus the constant C^2 is the normalized intensity of one of two counterpropagating waves. The mean value of U is assumed to be zero:

$$\overline{U}=\frac{1}{2\pi}\int_{-\pi}^{\pi}U\,d\xi=0. \tag{21}$$

For negligible weak linear absorption, $D\to 0$, the solution of the quadratic equation corresponding to Eq. (19) is

$$U=\frac{\Delta}{\pi\epsilon}\pm\sqrt{\left(\frac{\Delta}{\pi\epsilon}\right)^2+C^2+\frac{M}{2\epsilon}\left(\frac{\xi^2}{\pi^2}-\frac{1}{3}\right)}. \tag{22}$$

For small Mach numbers, $M\ll 3\Delta^2/\pi^2\epsilon$, the linear solution can be derived from one of the branches of the solution (22), namely from the ''$-$'' branch for $\Delta>0$ and from the ''$+$'' branch for $\Delta<0$:

$$U=-\frac{\pi M}{4|\Delta|}\operatorname{sgn}\Delta\left(\frac{\xi^2}{\pi^2}-\frac{1}{3}\right),\quad C^2=\overline{U^2}=\frac{\pi^2M^2}{180\Delta^2}\ll\frac{M}{3\epsilon}. \tag{23}$$

The inequality in the last member of (23) justifies the neglect of C^2 in the derivation from (22) of the expression for U in the first equation of (23).

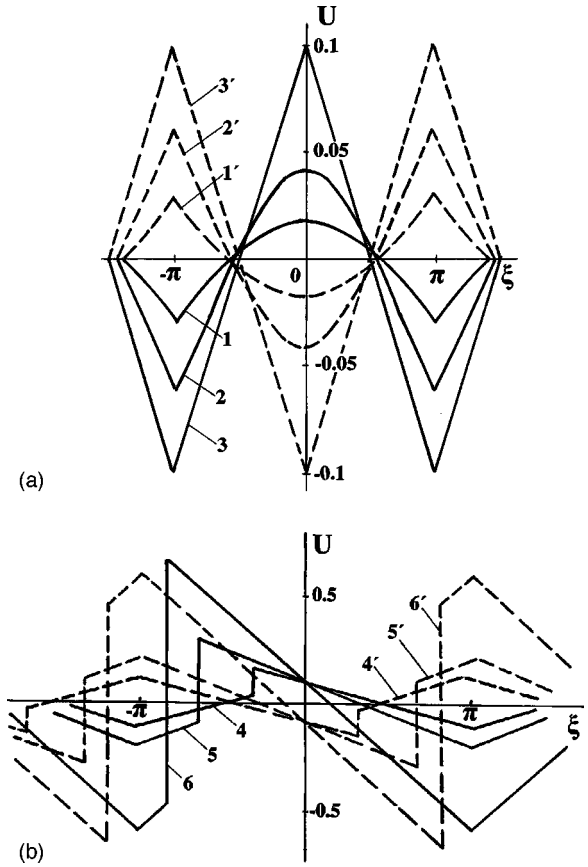

FIG. 1. (a) Temporal profile U of one of two counter-propagating waves forming the steady-state vibration in a nondissipative layer. The dimensionless amplitude $M=A/c$ of the sawtooth-shaped vibration of the boundary is small enough and U does not contain shocks. $(M/2\epsilon)\cdot 10^2$ equals 1, 2.25 and 4 for the curves 1, 2 and 3 correspondingly. (b) The same profiles as in (a) are constructed for greater magnitudes of M. The profiles 4, 5 and 6 corresponding to $(M/2\epsilon)\cdot 10^2=4$, 9 and 49 contain shocks.

With increasing M, up to a certain limiting value M_*, which will be determined later, the waveform undergoes progressive nonlinear distortion [Fig. 1(a)], but is still described by one of the branches of the solution (22).

The solid curves 1, 2 and 3 in Fig. 1(a) are constructed for positive discrepancy $\Delta=0.1\pi\epsilon$, and the dashed curves for the same negative discrepancy. Increase in the number of the curve corresponds to increase in the amplitude of boundary vibration: $10^2(M/2\epsilon)=1$, 2.25 and 4.

In order to construct curves in Fig. 1(a), the constant C^2 has been determined as a solution of an algebraic eigenvalue problem. The condition (21) applied to (22) leads to the following equation for C^2:

$$\frac{2\Delta}{\pi\epsilon}=\sqrt{\left(\frac{\Delta}{\pi\epsilon}\right)^2+C^2+\frac{M}{3\epsilon}}+\frac{(\Delta/\pi\epsilon)^2+C^2-M/6\epsilon}{\sqrt{M/2\epsilon}}\times\operatorname{arsinh}\frac{\sqrt{M/2\epsilon}}{\sqrt{(\Delta/\pi\epsilon)^2+C^2-M/6\epsilon}}. \tag{24}$$

Maximum value $M=M_*$ at which Eq. (24) has a real solution $C=\Delta/(\sqrt{3}\pi\epsilon)$ is determined by the condition

$$\sqrt{\frac{M}{2\epsilon}}=\frac{2|\Delta|}{\pi\epsilon},\quad M=\frac{8}{\pi^2\epsilon}\Delta^2\equiv M_*. \tag{25}$$

At $M=M_*$ the bifurcation happens, and the steady-state waveform becomes discontinuous. The shock front appears at each period of the wave, connecting the two branches of solution (22).

Let the solution U at the moment ξ_0 lie on the "minus" branch of (22). With increasing time $\xi>\xi_0$ the solution must jump to the "plus" branch; otherwise the condition $\overline{U}=0$ cannot be satisfied. The moment $\xi=\xi_{SH}$ of the jump corresponds to the position of a shock of compression. However, the shock of rarefaction is prohibited in usual media with quadratic nonlinearity, where the velocity of propagation increases with increasing magnitude of the disturbance.[24] Therefore, both branches of the solution (22) must have one common point in each period. If and only if the common point exists, the transition can go on in the opposite direction, from the "+" to the "−" branch, without jump.

The common point exists if the expression under the square root in (22) is equal to zero, or

$$C^2=\frac{M}{6\epsilon}-\left(\frac{\Delta}{\pi\epsilon}\right)^2. \tag{26}$$

For given eigenvalue (26) the solution (22) reduces to

$$U=\frac{\Delta}{\pi\epsilon}\pm\sqrt{\frac{M}{2\epsilon}}\left|\frac{\xi}{\pi}\right|. \tag{27}$$

In order to determine the position of the shock in the wave profile it is necessary to apply the condition $\overline{U}=0$ to the solution (27):

$$\int_{-\pi}^{\xi_{SH}}\left(\frac{\Delta}{\pi\epsilon}+\sqrt{\frac{M}{2\epsilon}}\frac{\xi}{\pi}\right)d\xi+\int_{\xi_{SH}}^{\pi}\left(\frac{\Delta}{\pi\epsilon}-\sqrt{\frac{M}{2\epsilon}}\frac{\xi}{\pi}\right)d\xi=0. \tag{28}$$

From the condition (28) follows

$$\xi_{SH}=-\pi\sqrt{1-\frac{2\Delta}{\pi}\sqrt{\frac{2}{\epsilon M}}}. \tag{29}$$

The equation (29) is valid for the condition $M\geqslant M_*$ [cf. (25)].

The solution (27), with account for Eq. (29) defining the position of the shock, is shown in Fig. 1(b), which is a continuation of Fig. 1(a) for greater Mach numbers. With increasing $M>M_*$, the shock appearing initially at $\xi=0$ moves to the position $\xi=-\pi$ (for $\Delta>0$), which can be reached only at $M\to\infty$ [cf. (29)]. The solid curves 4, 5 and 6 in Fig. 1(b) are constructed for $10^2(M/2\epsilon)=4$, 9 and 49 correspondingly.

The dashed curves in Fig. 1(b) demonstrate a similar behavior of the wave profile at equal negative discrepancy $\Delta=-0.1\pi\epsilon$. In this case the shock appears at $M=M_*$ in the point $\xi=0$ and moves to the point $\xi=\pi$ for $M\to\infty$.

In Fig. 2 the nonlinear frequency response is given. The curves 1–3 are constructed for different Mach numbers $(M/2\epsilon)=0.25$, 1 and 2.25 and demonstrate the dependence of $C=\sqrt{\overline{U^2}}$ on the discrepancy (7) from the resonant frequency ω_0. Straight lines

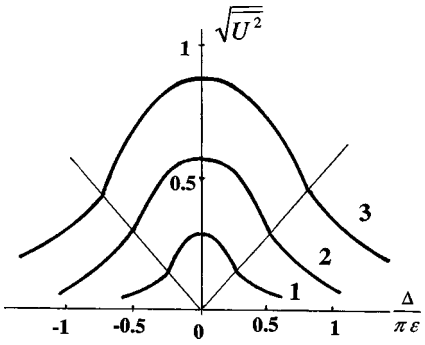

FIG. 2. Nonlinear frequency response defined as rms normalized particle velocity. Curves 1–3 are constructed for different amplitudes of boundary vibration ($M/2\epsilon = 0.25$, 1 and 2.25).

$$\sqrt{\overline{U^2}} = \frac{1}{\sqrt{3}} \frac{\Delta}{\pi\epsilon} \tag{30}$$

are separatrixes. Below these lines the curves in Fig. 2 are constructed by the solution (22) and (24) for wave profiles which do not contain the shocks. Exactly on the lines (30) the Mach number M is equal to M_* and the transition to the discontinuous solution takes place. So, above the lines (30) another solution [Eq. (27)] was used for calculation of the frequency response.

The frequency response is analyzed not for the dependence of the amplitude on frequency, as is customary for linear vibration, but for the root-mean-square (rms) particle velocity $\sqrt{\overline{U^2}}$. Because of the fact that the acoustic field U contains a great number of harmonics, the usual definition of frequency response is meaningless.

However, by analogy with the use of frequency response in the evaluation of the Q-factor of a linear resonator, it is possible to evaluate the Q-factor of a nonlinear resonator. As for the linear oscillator, the Q-factor can be defined in two ways: (1) as the ratio between amplitudes of internal and external (driving) vibrations at resonance ($\Delta = 0$) and (2) as a ratio between the resonant frequency and the spectral width of the frequency response. The first way leads to the calculation, using (12) and (26),

$$Q_{NL} = \frac{c(\sqrt{\overline{U^2}})_{\Delta=0}}{A} = \frac{c}{A}\sqrt{\frac{M}{6\epsilon}} = \frac{1}{\sqrt{6\epsilon M}}. \tag{31}$$

The second way uses the definition of Δ in (7) and the result (25):

$$Q_{NL} = \frac{1}{\Delta} = \frac{2\sqrt{2}}{\pi}\frac{1}{\sqrt{\epsilon M}}, \tag{32}$$

which differs slightly from (31). The nonlinear Q-factor Q_{NL} thus is proportional to $(\epsilon M)^{-1/2}$ with a coefficient $O(1)$ depending on the definition.

For the amplitude of the vibration of the boundary $A = 10$ cm/s the nonlinear evaluation (31) gives for gaseous media $Q \approx 20$. This value is much lower than the value of the linear Q-factor, which is in this case

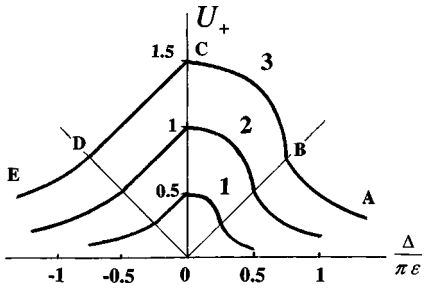

FIG. 3. Nonlinear frequency response defined as positive peak particle velocity on the wave profiles shown in Fig. 1. The boundary vibration amplitude $M/2\epsilon$ equals to 0.25, 1 and 2.25 for curves 1, 2 and 3 respectively.

$$Q = \frac{1}{2\sqrt{2}D} = \frac{c^3\rho}{\sqrt{2}b\omega_0 L} = \frac{c^2\rho}{\sqrt{2}\pi b\omega_0}, \tag{33}$$

depending on the effective viscosity b and the resonance frequency $\omega_0 = \pi c/L$. For air-filled resonators at typical frequencies about several kHz the linear evaluation (33) gives $Q \approx 10^3 - 10^4$.

The dependence of the rms velocity $\sqrt{\overline{U^2}}$ on the discrepancy Δ shown in Fig. 2 is not the only possible definition of nonlinear frequency response. For example, the dependence $U_+(\Delta)$, where U_+ is the positive peak value of U, is also important. This response is shown in Fig. 3 by solid curves for the three values of $M/2\epsilon$ equal to 0.25, 1 and 2.25. The analytical expressions of the sections AB, BC, CD and DE of each curve are different. Namely, U_+ equals to

$$\begin{aligned}
&\frac{\Delta}{\pi\epsilon} - \sqrt{\left(\frac{\Delta}{\pi\epsilon}\right)^2 + C^2 - \frac{M}{6\epsilon}} \quad \text{(AB)},\\
&\frac{\Delta}{\pi\epsilon} + \sqrt{\frac{M}{2\epsilon} - 2\frac{\Delta}{\pi\epsilon}\sqrt{\frac{M}{2\epsilon}}} \quad \text{(BC)},\\
&-\frac{|\Delta|}{\pi\epsilon} + \sqrt{\frac{M}{2\epsilon}} \quad \text{(CD)},\\
&-\frac{|\Delta|}{\pi\epsilon} + \sqrt{\left(\frac{\Delta}{\pi\epsilon}\right)^2 + C^2 + \frac{M}{3\epsilon}} \quad \text{(DE)}.
\end{aligned} \tag{34}$$

Here the eigenvalue C^2 is determined by Eq. (24)

The straight lines 1 and 2 are the same separatrices as in Fig. 2. Note that U_+ is placed on the top of the shock front only for the section BC; for the other three sections U_+ belongs to smooth portions of the wave profile.

The next important case corresponds to the ordinary differential equation like (19), and with $f = \sin\xi$, i.e., harmonic vibration of the boundary:

$$D\frac{dU}{d\xi} + \frac{\pi\epsilon}{2}(U^2 - C^2) - \Delta U = \frac{M}{2}\cos\xi. \tag{35}$$

Wave profiles for this case were constructed in Ref. 12, but frequency response was not considered there. To understand the behavior at curves in Figs. 5 and 6, it is necessary to give auxiliary formulas using the notations of the present article.

For negligible weak linear absorption, $D \to 0$, the solution of the quadratic equation corresponding to Eq. (35) is

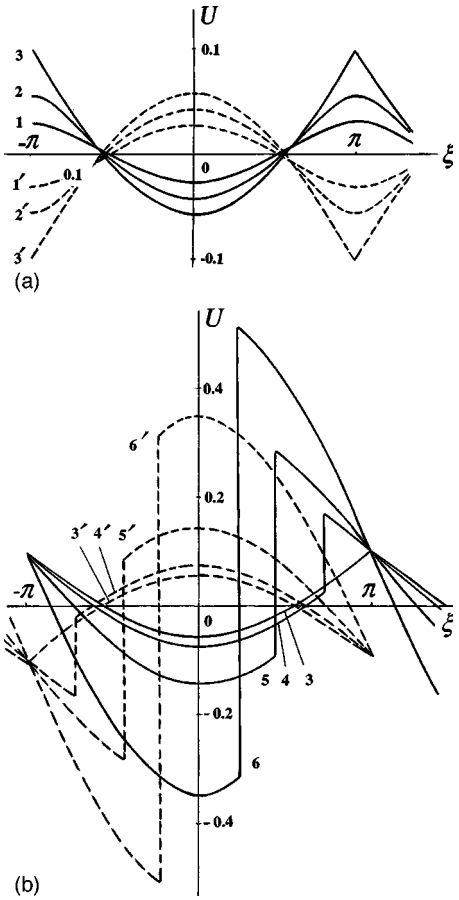

FIG. 4. (a) Temporal profile U of one of two counter-propagating waves forming the steady-state vibration in a nondissipative layer. The dimensionless amplitude $M=A/c$ of the harmonic vibration of the boundary is small enough and U does not contain shocks. $(M/\pi\epsilon)\cdot 10^3$ equals 5.6, 9.1 and 12.3 for the curves 1, 2 and 3 correspondingly. (b) The same profiles as in (a) are constructed for greater magnitudes of M. The profiles 4, 5 and 6 corresponding to $(M/\pi\epsilon)\cdot 10^2=1.5$, 3 and 10 contain shocks.

$$U=\frac{\Delta}{\pi\epsilon}\pm\sqrt{\left(\frac{\Delta}{\pi\epsilon}\right)^2+C^2+\frac{M}{\pi\epsilon}\cos\xi}. \tag{36}$$

For small Mach numbers, $M\ll\Delta^2/\pi\epsilon$, the linear solution is

$$U=-\frac{M}{2|\Delta|}\operatorname{sgn}\Delta\cos\xi,\quad C^2=\overline{U^2}=\frac{M^2}{8\Delta^2}\ll\frac{M}{\pi\epsilon}. \tag{37}$$

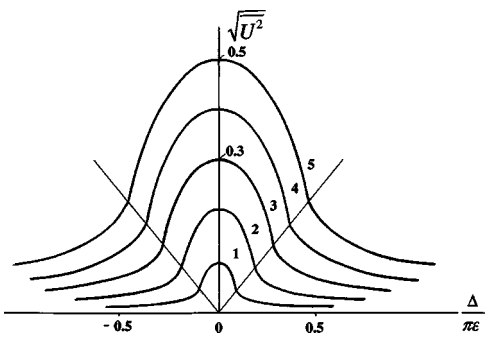

FIG. 5. Nonlinear frequency response defined as rms normalized particle velocity. Curves 1–5 are constructed for different amplitudes of boundary vibration $[(M/\pi\epsilon)\cdot 10^2=1,\ 4,\ 9,\ 16$ and $25]$.

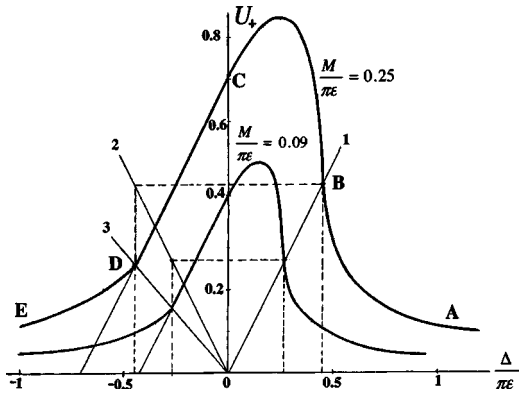

FIG. 6. Nonlinear frequency response defined as positive peak particle velocity on the wave profiles shown in Fig. 4. The boundary vibration amplitude $M/\pi\epsilon$ equals 0.09 and 0.25.

With increasing M the waveform undergoes progressive nonlinear distortion [Fig. 4(a)], but is still described by one of the branches of the solution (36).

The solid curves 1, 2 and 3 in Fig. 4(a) are constructed for positive discrepancy $\Delta=0.1\pi\epsilon$, and the dashed curves for the same negative discrepancy. Increase in the number of the curve corresponds to increase in the amplitude of boundary vibration: $10^3(M/\pi\epsilon)=5.6$, 9.1 and 12.3.

In order to construct curves in Fig. 4(a), the constant C^2 has been determined as a solution of an algebraic eigenvalue problem. The condition (21) applied to (36) leads to the following equation for C^2:

$$\frac{\Delta}{\pi\epsilon}=\frac{2}{\pi}\sqrt{\left(\frac{\Delta}{\pi\epsilon}\right)^2+C^2+\frac{M}{\pi\epsilon}}\times E\left(\frac{2M/\pi\epsilon}{\sqrt{(\Delta/\pi\epsilon)^2+C^2+M/\pi\epsilon}}\right). \tag{38}$$

Here $E()$ is the complete elliptic integral of the second kind.[23]

The solution of Eq. (38) can be written in parametric form:

$$C^2=\frac{M}{\pi\epsilon}\left[\frac{2}{m}-1-\frac{8}{\pi^2}\frac{E^2(m)}{m}\right],$$

$$\frac{\Delta}{\pi\epsilon}=\pm\frac{2\sqrt{2}}{\pi}\sqrt{\frac{M}{\pi\epsilon}}\frac{E(m)}{\sqrt{m}}, \tag{39}$$

where m is a parameter. The argument m of the function $E(m)$ is defined in the region $0\leqslant m\leqslant 1$.[23] From (38) follows that the corresponding region for the discrepancy Δ is given by

$$\frac{2\sqrt{2}}{\pi}\sqrt{\frac{M}{\pi\epsilon}}\leqslant\frac{|\Delta|}{\pi\epsilon}<\infty\Rightarrow M\leqslant\frac{\pi}{8\epsilon}\Delta^2\equiv M_*. \tag{40}$$

At $M=M_*$ the bifurcation happens, and the steady-state waveform becomes discontinuous. The shock front appears at each period of the wave, connecting the two branches of solution (36).

For a discontinuous wave

$$C^2=\frac{M}{\pi\epsilon}-\left(\frac{\Delta}{\pi\epsilon}\right)^2. \tag{41}$$

For a given eigenvalue (41) the solution (36) reduces to

$$U=\frac{\Delta}{\pi\epsilon}\pm\sqrt{\frac{2M}{\pi\epsilon}}\left|\cos\frac{\xi}{2}\right|. \tag{42}$$

The shock front position ξ_{SH}, determined by the condition $\overline{U}=0$, satisfies the equation

$$\sin\left(\frac{\xi_{SH}}{2}\right)=\frac{\Delta}{2}\sqrt{\frac{\pi}{2\epsilon M}}. \tag{43}$$

From (43) we find that the condition $|\sin(\xi_{SH}/2)|\leqslant 1$ is equivalent with the condition $M\geqslant M_*$ [cf. (40)].

The solution (42), with account for Eq. (43) defining the position of the shock, is shown in Fig. 4(b), which is a continuation of Fig. 4(a) for greater Mach numbers. The curve 3 in Fig. 4(b), corresponding to $M=M_*$, is the same as the curve 3 in Fig. 4(a). With increasing $M>M_*$, the shock appearing initially at $\xi=\pi$ (for $\Delta>0$) moves to the position $\xi=0$, which can be reached only at $M\to\infty$ [cf. (43)]. The solid curves 4, 5 and 6 in Fig. 4(b) are constructed for $10^2(M/\pi\epsilon)=1.5$, 3 and 10 correspondingly.

The dashed curves in Fig. 4(b) demonstrate similar behavior of the wave profile at equal negative discrepancy $\Delta=-0.1\pi\epsilon$. In this case the shock appears at $M=M_*$ in the point $\xi=-\pi$ and moves to the point $\xi=0$ for $M\to\infty$.

In Fig. 5 the nonlinear frequency response is given. The curves 1–5 are constructed for different Mach numbers $10^2(M/\pi\epsilon)=1$, 4, 9, 16 and 25, and demonstrate the dependence of $C=\sqrt{\overline{U^2}}$ on the discrepancy (7) from the resonant frequency ω_0. Straight lines

$$\sqrt{\overline{U^2}}=\pm\sqrt{\frac{\pi^2}{8}-1}\left(\frac{\Delta}{\pi\epsilon}\right) \tag{44}$$

are separatrixes. Below these lines the curves in Fig. 5 are constructed by the solution (37) for wave profiles which do not contain the shocks. Exactly on the lines (44) the Mach number M is equal to M_* and the transition to the discontinuous solution takes place. So, above the lines (44) another solution [Eq. (42)] was used for calculation of the frequency response.

As earlier, the Q-factor can be defined in two ways [see (31) and (32)]. The first definition leads to a formula analogous to (31):

$$Q_{NL}=\frac{c(\sqrt{\overline{U^2}})_{\Delta=0}}{A}=\frac{c}{A}\sqrt{\frac{M}{\pi\epsilon}}=\frac{1}{\sqrt{M\pi\epsilon}}. \tag{45}$$

The second way gives the result

$$Q_{NL}=\frac{1}{\Delta}=\frac{\pi}{2\sqrt{2}}\frac{1}{\sqrt{M\pi\epsilon}}, \tag{46}$$

which differs slightly from (45).

The dependence $U_+(\Delta)$, where U_+ is the positive peak value of U, is shown in Fig. 6 by solid curves for the two values of $M/\pi\epsilon$ equal to 0.25 and 0.09. The analytical expressions of the sections AB, BC, CD and DE of each curve are different. Namely, U_+ equals to

$$\begin{aligned}
&\frac{\Delta}{\pi\epsilon}-\sqrt{\left(\frac{\Delta}{\pi\epsilon}\right)^2+C^2-\frac{M}{\pi\epsilon}} \quad \text{(AB)},\\
&\frac{\Delta}{\pi\epsilon}+\sqrt{2}\sqrt{\frac{M}{\pi\epsilon}-\frac{\pi^2}{8}\left(\frac{\Delta}{\pi\epsilon}\right)^2} \quad \text{(BC)},\\
&-\frac{|\Delta|}{\pi\epsilon}+\sqrt{2}\sqrt{\frac{M}{\pi\epsilon}} \quad \text{(CD)},\\
&-\frac{|\Delta|}{\pi\epsilon}+\sqrt{\left(\frac{\Delta}{\pi\epsilon}\right)^2+C^2+\frac{M}{\pi\epsilon}} \quad \text{(DE)}.
\end{aligned} \tag{47}$$

Here the eigenvalue C^2 is determined by Eq. (39). The straight lines 1 and 2 are the same separatrixes as in Fig. 5. The line 3 separating sections CD and DE is described by

$$U_+=\left(\frac{\pi}{2}-1\right)\frac{\Delta}{\pi\epsilon}. \tag{48}$$

Note that U_+ is placed on the top of the shock front only for the section BC; for the other three sections U_+ belongs to smooth portions of the wave profile.

The maximum value of U_+ is located not at $\Delta=0$, as a maximum in Fig. 5, but at some positive discrepancy:

$$\begin{aligned}
&(U_+)_{\max}=\sqrt{2}\left(1+\frac{4}{\pi^2}\right)\sqrt{\frac{M}{\pi\epsilon}},\\
&\left(\frac{\Delta}{\pi\epsilon}\right)_{\max}=\frac{2\sqrt{2}}{\pi\sqrt{1+\pi^2/4}}\sqrt{\frac{M}{\pi\epsilon}}.
\end{aligned} \tag{49}$$

IV. STEADY-STATE VIBRATION IN A DISSIPATIVE MEDIUM AT HARMONIC EXCITATION

The problem considered in the preceding section is generalized here to a standing wave in a resonator filled with an absorbing medium. Such a problem setting is more complicated because derivatives of higher order appears in the wave equation due to nonzero dissipation $D\neq 0$. The analytical solution can be written in terms of known special functions only for harmonic motion of boundary. Fortunately, this case is most interesting for applications. The mathematical approach used here is similar to that developed by O. Rudenko[21] to describe high-power hypersonic wave generated at Brillouin scattering. It was shown that the high-frequency acoustic wave excited by interacting laser beams is described by the Mathieu function

$$c\mathrm{e}_0(z,q) \tag{50}$$

and its intensity is equal accurately to the characteristic value a_0 of the Mathieu function (50). This basic result was derived for a physical problem quite different from the concerned one. Moreover, it was published 30 years ago as a brief letter to the editor. That is why it is necessary to describe here some peculiarities of calculation and physical matter.

The standing waves in an absorbing layer ($D \neq 0$) must be studied on the base of differential equation (35). Using the transformation

$$U = \frac{2D}{\pi\epsilon}\frac{d}{d\xi}\ln W, \tag{51}$$

the nonlinear equation (35) of the first order is reduced to the linear equation of the second order:

$$\frac{d^2W}{d\xi^2} - \frac{\Delta}{D}\frac{dW}{d\xi} = \left(\frac{\pi\epsilon}{2D}\right)^2\left[C^2 + \frac{M}{\pi\epsilon}\cos\xi\right]W. \tag{52}$$

In particular, for zero discrepancy ($\Delta = 0$), the equation (52) can be transformed into the canonical form of the Mathieu equation:[9]

$$\frac{d^2W}{dz^2} + \left[-\left(\frac{\pi\epsilon}{D}\right)^2 C^2 - \frac{\pi\epsilon M}{D^2}\cos 2z\right]W = 0, \quad z = \frac{\xi}{2}. \tag{53}$$

It is seen from Eq. (51) that the condition $\overline{U} = 0$ calls for the periodicity of the function W. Consequently, W can be written in terms of Mathieu functions.[23] The solution satisfying the transition to the linear limit ($M \to 0$) is

$$W = ce_0\left(z, q = \frac{\pi\epsilon M}{2D^2}\right). \tag{54}$$

The intensity C^2 of the wave is determined by the characteristic value $a_0(q)$ of the Mathieu function ce_0 (50):

$$\overline{U^2} = C^2 = -\left(\frac{D}{\pi\epsilon}\right)^2 a_0(q). \tag{55}$$

For weak excitation, using the two first terms of a series expansion[23] of a_0 for $q \ll 1$,

$$a_0 \approx -\frac{q^2}{2} + \frac{7q^4}{128}, \tag{56}$$

one can calculate $\overline{U^2}$:

$$\overline{U^2} = \frac{M^2}{8D^2} - \frac{7}{2048}\frac{(\pi\epsilon)^2 M^4}{D^6}. \tag{57}$$

The first term in (57) corresponds to the well-known linear result.

Using another asymptotic expansion for the characteristic value a_0 at $q \gg 1$,[23]

$$a_0 \approx -2q + 2\sqrt{q} - \frac{1}{4} - \frac{1}{32\sqrt{q}}, \tag{58}$$

one can calculate the intensity for strong vibration of the boundary by means of (55):

$$\overline{U^2} \approx \frac{M}{\pi\epsilon} - \sqrt{2}\frac{D}{\pi\epsilon}\sqrt{\frac{M}{\pi\epsilon}} + \frac{1}{4}\left(\frac{D}{\pi\epsilon}\right)^2 + \frac{1}{16}\left(\frac{D}{\pi\epsilon}\right)^4\frac{\pi\epsilon}{M}. \tag{59}$$

An important characteristic of a resonator, its Q-factor, depends now on the absorption D:

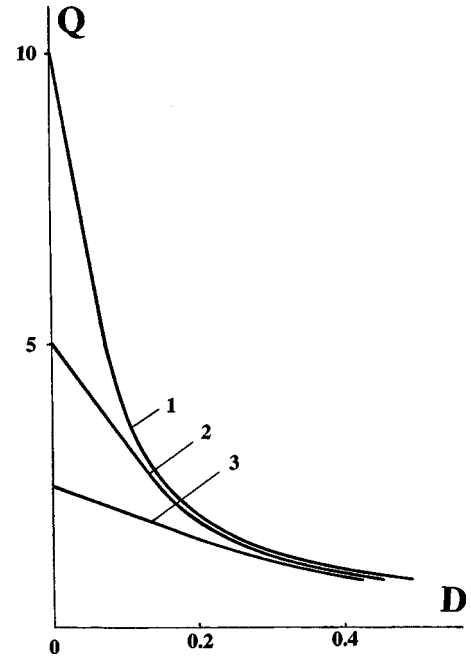

FIG. 7. Dependence of the Q-factor on the dimensionless dissipation D for three values of $\pi\epsilon M$ equal to 0.01, 0.04 and 0.16.

$$Q = \frac{1}{M}\sqrt{\overline{U^2}} \approx \frac{1}{\sqrt{\pi\epsilon M}}\left(1 - \frac{\sqrt{2}}{2}d - \frac{1}{8}d^2 + \frac{\sqrt{2}}{16}d^3 + \frac{3}{128}d^4\right),$$

$$d \equiv \frac{D}{\sqrt{\pi\epsilon M}}. \tag{60}$$

For $D = 0$ the result (60) rearranges into the (45) for a non-dissipative medium.

For weak nonlinear distortion the quasi-linear Q-factor can be calculated on the base of Eq. (57):

$$Q = \frac{1}{2\sqrt{2}D}\left(1 - \frac{7}{512}\frac{1}{d^4}\right). \tag{61}$$

For $M \to 0$ or for $d \to \infty$ the equation (61) rearranges to the equation (33), valid in linear theory.

For arbitrary values of dissipation D the Q-factor equals to

$$Q = Q_{NL}\Psi(d = DQ_{NL}), \tag{62}$$

where the nonlinear Q-factor Q_{NL} is determined by Eq. (45) and $\Psi(d)$ is given by

$$\Psi(d) = \sqrt{-d^2 a_0\left(q = \frac{1}{2d^2}\right)}. \tag{63}$$

The dependence of Q on D is shown in Fig. 7. The curves 1–3 are constructed by use of Eqs. (62) and (63) for three values of $\pi\epsilon M$ equal to 0.01, 0.04 and 0.16, correspondingly. Increase in the dimensionless dissipation number D, defined in Eq. (17), leads to decrease in the Q-factor. For small D-values the nonlinear absorption begins to play an important role for the decreasing of Q.

The analysis of the nonlinear frequency response calls for the solution to Eq. (52) at nonzero discrepancy, $\Delta \neq 0$. In

this general case the nonlinear equation (35) can also be reduced to a Mathieu equation. Instead of (51) we put

$$U=\frac{2D}{\pi\epsilon}\frac{d}{d\xi}\ln\left(w\exp\left(\frac{\Delta}{2D}\xi\right)\right). \tag{64}$$

Inserting (64) into (35) we obtain

$$\frac{d^2w}{d\xi^2}=\left(\frac{\pi\epsilon}{2D}\right)^2\left[C^2+\left(\frac{\Delta}{\pi\epsilon}\right)^2+\frac{M}{\pi\epsilon}\cos\xi\right]w. \tag{65}$$

It is still required that the mean value of U is zero. By use of (64) follows

$$\overline{U}=\frac{\Delta}{\pi\epsilon}+\frac{2D}{\pi\epsilon}[\ln w(\pi)-\ln w(-\pi)]=0. \tag{66}$$

Consequently, w is not a periodic function and cannot be expressed through Mathieu functions.[23] Since the needed results cannot be found in Ref. 23 as well as in analogous tables, it is necessary to seek for an approximate solution to Eq. (35) or its linearized version (65).

For small Mach numbers M the mean intensity equals to

$$\overline{U^2}=\frac{M^2}{8(\Delta^2+D^2)}-\frac{(\pi\epsilon)^2M^4}{512}\frac{7D^2-5\Delta^2}{(\Delta^2+D^2)^3(\Delta^2+4D^2)}. \tag{67}$$

In order to derive the result (67), the first four approximations were calculated in the solution of Eq. (35) by the method of successive approximations. This solution is described by very complicated formulas and is therefore not presented here.

For zero discrepancy $(\Delta=0)$ the result (67) rearranges to form the result (57), obtained from the theory of Mathieu functions.

In the opposite limiting case, i.e., $q\gg1$, the mean intensity depending on M, Δ and D for waves containing shocks can be calculated by another approach. The wave profile governed by Eq. (35) is found by the method of matched asymptotic expansions.[25,26] This profile is presented as a sum of an ''outer'' solution, describing the smooth section of the profile, and an ''inner'' solution, describing the structure of a shock front of finite width. Thereafter, the averaging over the period of the square of this sum solution gives the intensity

$$\overline{U^2}=\left[\frac{M}{\pi\epsilon}-\left(\frac{\Delta}{\pi\epsilon}\right)^2\right]-\sqrt{2}\frac{D}{\pi\epsilon}\sqrt{\frac{M}{\pi\epsilon}-\frac{\pi^2}{8}\left(\frac{\Delta}{\pi\epsilon}\right)^2}. \tag{68}$$

At resonance, $\Delta\to0$, the equation (68) reduces to the result (59) of the theory of Mathieu functions.

The calculation of the asymptotic $(q\gg1)$ solution described above is rather complicated. It contains features important for nonlinear perturbation theory and will be the subject of another work.

It follows from Eq. (68) that the nonlinear frequency response (solid curve 1 in Fig. 8) decreases with account for weak dissipation (dashed curve 2). Analogously, the linear frequency response (67), shown by the solid curve 3 in Fig. 8, decreases in its main part, with account for weak nonlinearity.

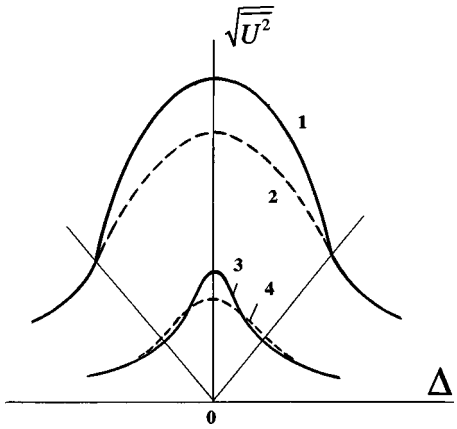

FIG. 8. Decrease in the nonlinear frequency response (curve 1) caused by weak dissipation (curve 2), and decrease in the linear frequency response (curve 3) with account for weak nonlinearity (curve 4)

V. DEVELOPMENT OF STANDING WAVES

Non-steady-state nonlinear vibrations in resonators have been studied much less than the stationary ones.[11,12] The evolution equation (18) offers the possibility to study the transient process for any periodic motion of the boundary.

For the saw-tooth-like right-hand side of Eq. (18) considered in the beginning of Sec. III the non-steady-state solution at $(\Delta=0)$ has a very simple form:[12]

$$U=-\sqrt{\frac{M}{2\epsilon}}\tanh\left(T\sqrt{\frac{\epsilon M}{2}}\right)\frac{\xi}{\pi},\quad -\pi\leqslant\xi\leqslant\pi. \tag{69}$$

The ratio of the root mean square particle velocity of the standing wave to the ''amplitude'' of the harmonic boundary vibration M tends, at $t\to\infty$, to the value Q_{NL} (31) calculated for steady-state vibration.

For a harmonic vibration of the boundary $x=L$ the right-hand side of Eq. (18) takes the form $(M/2)\sin\xi$. For this case the substitution (51) transforms (18) into the linear partial differential equation

$$\frac{\partial W}{\partial T}+\Delta\frac{\partial W}{\partial\xi}-D\frac{\partial^2W}{\partial\xi^2}=-\frac{1}{2}qD\cos\xi W. \tag{70}$$

By the substitution

$$W=\exp\left(-\frac{1}{4}aDT\right)y(z),\quad z=\frac{\xi}{2}, \tag{71}$$

where a is a constant, the ordinary differential equation for the function $y(z)$ can be derived from (70):

$$\frac{d^2y}{dz^2}-2\frac{\Delta}{D}\frac{dy}{dz}+(a-2q\cos2z)y=0. \tag{72}$$

At zero discrepancy, $\Delta=0$, the equation (72) transforms into the canonical form of the differential equation for Mathieu functions. This is the resonant case, which can be studied in detail. The corresponding mathematical results were derived in Ref. 22 for another physical problem, but these results can be adopted for non-steady-state vibrations of resonators.

For zero initial condition $U(T=0,\xi)$ the solution of Eq. (70) can be written as a series of even Mathieu functions:

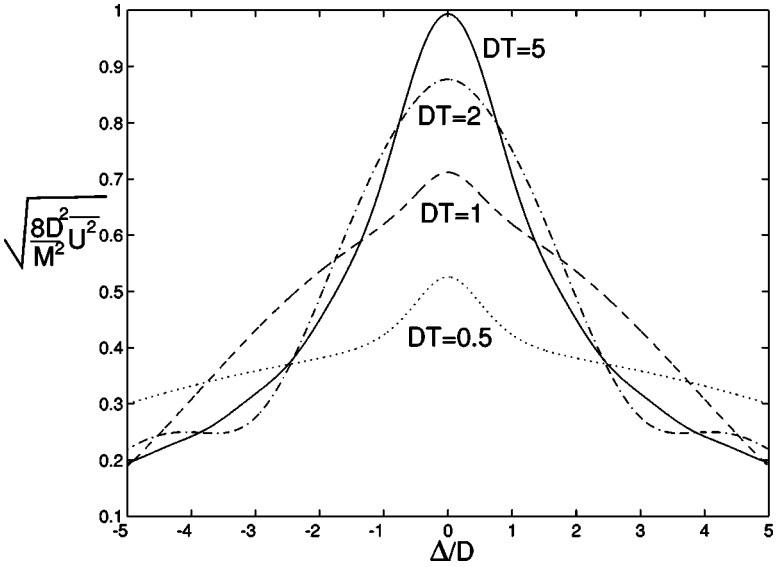

FIG. 9. Non-steady-state frequency response from Eq. (79) with $(\pi\epsilon M/2D^2)=3$. Both nonlinearity and dissipation are taken into account.

$$W=\sum_{n=0}^{\infty} a_{2n}\exp\left[-\frac{1}{4}a_{2n}(q)DT\right]ce_{2n}\left(\frac{\xi}{2},q\right), \tag{73}$$

where a_{2n} is given as

$$a_{2n}=\frac{\int_0^{2\pi} ce_0(\xi/2,q)\,d\xi}{\int_0^{2\pi} ce_{2n}^2(\xi/2,q)\,d\xi}. \tag{74}$$

The steady-state solution resulting from (73) and (51) at $T\to\infty$,

$$U=\frac{2D}{\pi\epsilon}\frac{d}{d\xi}\ln ce_0\left(\frac{\xi}{2},\frac{\pi\epsilon M}{2D^2}\right), \tag{75}$$

coincides with the results (54) and (51) of Sec. V. For $q\gg 1$ the solution (75) takes the form

$$U=\sqrt{\frac{2M}{\pi\epsilon}}\left\{\cos\frac{\xi}{2}-\frac{2\exp(-2\sqrt{q}\xi)}{1+\exp(-2\sqrt{q}\xi)}\right\},\quad 0\leqslant\xi\leqslant\pi, \tag{76}$$

and for $q\to\infty$ it does not depend on the linear absorption (i.e., on q) at all:

$$U=\sqrt{\frac{2M}{\pi\epsilon}}\cos\frac{\xi}{2}\,\mathrm{sgn}\,\xi,\quad -\pi\leqslant\xi\leqslant\pi. \tag{77}$$

The solution (77) coincides with (27) for $\Delta=0$.

The increase in energy of resonator in the resonator can be studied on the base of solution (73) for zero discrepancy and by numerical methods only. Instead, it is possible to develop the theory for analytical description of the process of accumulation of acoustic energy. The approximate solution to inhomogeneous Burgers Eq. (18) is used here with account for all principal parameters: nonlinearity, absorption and discrepancy. This solution,

$$\begin{aligned}U=&\frac{M}{2\sqrt{D^2+\Delta^2}}\sin\left(\xi-\arctan\frac{\Delta}{D}\right)\\&-\frac{M\exp(-DT)}{2\sqrt{D^2+\Delta^2}}\sin\left[\xi-\Delta T-\arctan\frac{\Delta}{D}+\pi\epsilon TM\right.\\&\left.-\frac{\pi\epsilon TU}{2\sqrt{D^2+\Delta^2}}\sin\left(\xi-\arctan\frac{\Delta}{D}\right)\right],\end{aligned} \tag{78}$$

is derived by the method of transition to implicit variable used many times earlier (see, for example, Refs. 13, 27, and 28). Calculations are rather complicated and therefore they are omitted here. As is shown in Ref. 27, solutions of the type (78) are of good accuracy in two limiting cases: at highly expressed nonlinear distortion of the wave profile, but in the region where a shock is yet not formed, or at weak nonlinearity, but at any T.

Using the solution (78), U^2 may be averaged over one period. The solution to this intricate problem is

$$\begin{aligned}\overline{U^2}=&\frac{M^2}{8(D^2+\Delta^2)}\left[1-2\mathrm{e}^{-DT}\right.\\&\left.\times\frac{2J_1(\pi\epsilon TM/[2\sqrt{D^2+\Delta^2}\mathrm{e}^{-DT}])}{(\pi\epsilon TM/[2\sqrt{D^2+\Delta^2}\mathrm{e}^{-DT}])}\cos(\Delta T)+\mathrm{e}^{-2DT}\right].\end{aligned} \tag{79}$$

One can easily check the validity of this result at small values of M as the equation (79) for the acoustic energy in the cavity of the resonator turns into the corresponding linear solution.

In conclusion, the non-steady-state solutions to Eq. (18) are given here for weakly expressed nonlinear effects. Expand the periodic right-hand side of Eq. (18) in a Fourier series:

$$-\frac{M}{2}f(\xi-\pi)=\frac{M}{2}\sum_{n=1}^{\infty}(\alpha_n\cos n\xi+\beta_n\sin n\xi). \tag{80}$$

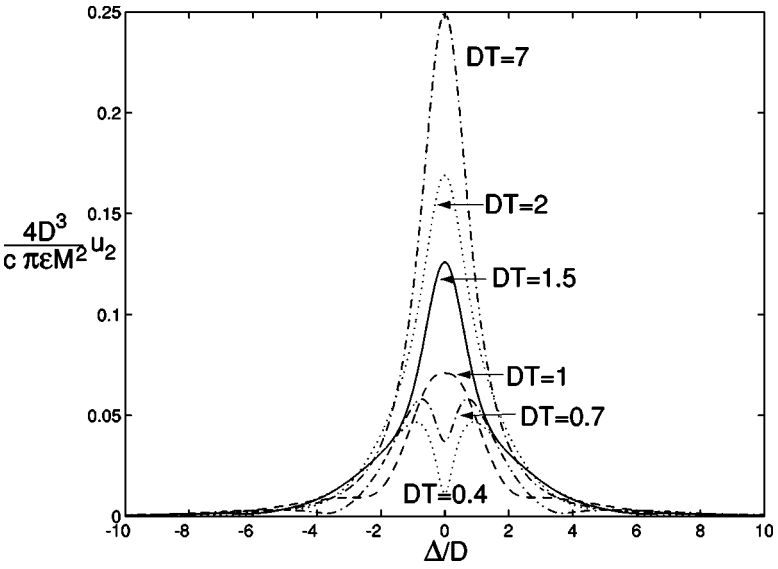

FIG. 10. Temporal evolution of the spectral line of the second harmonic [normalized amplitude versus discrepancy calculated from solution (84) and (85) with account for dissipative properties of the nonlinear medium].

The corresponding solution to Eq. (18) with the nonlinear term neglected equals

$$U=\frac{M}{2}\sum_{n=1}^{\infty} C_n[\sin(n\xi-\phi_n) - \exp(-n^2 DT)\sin(n\xi-n\Delta T-\phi_n)], \tag{81}$$

where

$$C_n=\frac{1}{n}\sqrt{\frac{\alpha_n^2+\beta_n^2}{\Delta^2+n^2D^2}}, \qquad \phi_n=\arctan\frac{\Delta\beta_n-nD\alpha_n}{\Delta\alpha_n+nD\beta_n}. \tag{82}$$

For example, at harmonic excitation ($\alpha_n=0$, $\beta_1=1$ and $\beta_n=0$ for $n\neq 1$), the standing wave has the same shape as the fundamental mode of (80):

$$\frac{u^{(1)}(x,t)}{c}=-\frac{M}{\sqrt{D^2+\Delta^2}}\sin kx[\cos(\omega t-\phi_1) - \exp(-DT)\cos(\omega t-\phi_1-\Delta T)]. \tag{83}$$

Using the linear solution (83), the nonlinear correction term is calculated by the successive approximation method:

$$\frac{u^{(2)}(x,t)}{c}=\frac{\pi\epsilon}{4}\frac{M^2}{D^2+\Delta^2}\sin 2kx\sum_{m=1}^{3}\Phi_m(t). \tag{84}$$

Here

$$\Phi_1=[(4D)^2+(2\Delta)^2]^{-1/2}[\sin(2\eta-\phi_{1/2}) - \exp(-4DT)\sin(2\eta-2\Delta T-\phi_{1/2}),$$

$$\Phi_2=-2[(3D)^2+(3\Delta)^2]^{-1/2}[\exp(-DT)\sin(2\eta+\Delta T - \phi_1)-\exp(-4DT)\sin(2\eta-2\Delta T-\phi_1)],$$

$$\Phi_3=[(2D)^2+(4\Delta)^2]^{-1/2}[\exp(-2DT)\sin(2\eta+2\Delta T-\phi_2) - \exp(-4DT)\sin(2\eta-2\Delta T-\phi_2)], \tag{85}$$

where $\eta=\omega t-\phi_1$. Evidently, the second approximation (84) corresponds to the second mode excited by nonlinear transfer from the fundamental mode.

The simple analytical expressions (83) and (84) offer a clear view of how the process of establishment of modes goes on at any dissipation D and discrepancy Δ. The increase in amplitudes, as well as the evolution of spectral lines (or ''instantaneous'' frequency response), can be analyzed for the first and second harmonics at small $M/\sqrt{D^2+\Delta^2}$. A plot of the nonlinear correction term time evolution based on Eq. (85) is seen in Fig. 10.

VI. CONCLUSIONS

In order to increase the intensity of a standing wave, one has to enhance the Q-factor of the nonlinear resonator. As was shown above [cf. (31) and (32)], the limiting magnitude of Q is determined by nonlinear absorption caused by the formation of steep shock fronts.

Different methods have been suggested to suppress the proccess of shock formation. Zarembo *et al.*[29] suggest a resonator, of which one boundary has a frequency-dependent impedance; each reflection from this boundary introduces phase shifts between different harmonics distroying the front. Lawrenson *et al.*,[6] Ladbury,[30] and Ilinskii *et al.*[31] have realized the idea of controlling the waveform and phase shifts between harmonics using resonators of complex shape. Rudenko[32] suggested the method of controlling nonlinear energy flows between harmonics by introducing selective absorbers, which can be used, in particular, to enhance the Q-factor by suppressing the ''key'' frequencies.[33] This method was realized experimentally,[34] but its possibilities are being studied up to now.[35,36]

Quite another approach to enhance Q with no changes in the design of the resonator was suggested in Ref. 37. It was shown that the unfavorable effects of nonlinearity due to the movable boundary can be suppressed if the boundary executes a vibration of special form. More specifically, in order to provide harmonic vibration in the cavity, the resonator

must be excited by a periodic sequence of short ''jerks'' of its boundary.

If the usual linear Q-factor of a resonator is high enough, the significant acoustic energy can be accumulated in the cavity even if the source of the external pump of energy is weak. High-intensity vibration can easily be generated and nonlinear phenomena come into play. In particular, Q falls down, and, therefore, even strong increase in pump (energy inflow) leads to weak amplification of the standing wave. Definitions of frequency response by the relative rms of the acoustic field or by the maximum magnitude are given, suitable for different applications. Resonant curves illustrating nonlinear frequency response are constructed. The dependence of Q on the intensity of excitation and on linear properties are studied. Both wave profiles and energy characteristics for steady-state vibration and its development are analyzed. Different possibilities to enhance Q and the energy of acoustic vibration are discussed.

To analyze these phenomena, the analytic approach to high-intensity standing waves is used, based on nonlinear functional equations. The problem is radically simplified by separation of resonant and nonresonant nonlinear interactions, by introduction of small parameters and different temporal scales, and by reducing functional equations to differential ones.

[1] A. B. Coppens and A. A. Atchley, ''Nonlinear standing waves in cavities,'' in *Encyclopedia of Acoustics* (Wiley, New York, 1997), pp. 237–246.

[2] M. A. Ilhamov, R. G. Zaripov, R. G. Galiullin, and V. B. Repin, ''Nonlinear oscillations of a gas in a tube,'' Appl. Mech. Rev. **49**, 137–154 (1996).

[3] O. V. Rudenko and S. I. Soluyan, *Theoretical Foundations of Nonlinear Acoustics* (Plenum, Consultants Bureau, New York, 1977).

[4] M. F. Hamilton and D. T. Blackstock (eds.), *Nonlinear Acoustics* (Academic, San Diego, 1997).

[5] V. B. Braginsky, V. P. Mitrofanov, and V. I. Panov, *Systems with Small Dissipation* (Chicago U.P., Chicago, 1985).

[6] C. C. Lawrenson, B. Lipkens, T. S. Lucas, D. K. Perkins, and T. W. van Doren, ''Measurement of macroscopic standing waves in oscillating closed cavities,'' J. Acoust. Soc. Am. **104**, 623–636 (1998).

[7] V. V. Kaner, O. V. Rudenko, and R. V. Khokhlov, ''Theory of nonlinear oscillations in acoustic resonators,'' Sov. Phys. Acoust. **23**, 432–437 (1977).

[8] V. V. Kaner, A. A. Karabutov, and O. V. Rudenko, ''Nonlinear effects in acoustical resonators,'' in *Nonlinear Acoustics* (Institute of Applied Physics Edition, Gorki, 1980) (in Russian), pp. 135–140.

[9] W. Chester, ''Resonant oscillations in closed tubes,'' J. Fluid Mech. **18**, 44–66 (1964).

[10] S. Temkin, ''Propagating and standing sawtooth waves,'' J. Acoust. Soc. Am. **45**, 224–227 (1969).

[11] V. E. Gusev, ''Buildup of forced oscillations in acoustic resonator,'' Sov. Phys. Acoust. **30**, 121–125 (1984).

[12] O. V. Rudenko, C. M. Hedberg, and B. O. Enflo, ''Nonlinear standing waves in a layer excited by periodic motion of its boundary,'' Acoust. Phys. **47**, 452–460 (2001).

[13] V. P. Kuznetsov, ''Equations of nonlinear acoustics,'' Sov. Phys. Acoust. **16**, 467–470 (1971).

[14] C. Nyberg, ''Spectral analysis of a two frequency driven resonance in a closed tube,'' Acoust. Phys. **45**, 86–93 (1999).

[15] V. V. Kaner and O. V. Rudenko, ''Propagation of waves of finite amplitude in acoustic waveguides,'' Moscow Univ. Phys. Bull. **33**(4), ■–■ (1978).

[16] M. B. Vinogradova, O. V. Rudenko, and A. P. Sukhorukov, *Theory of Waves, 2nd edition* (Nauka, Moscow, 1990) (in Russian).

[17] A. A. Karabutov and O. V. Rudenko, ''Nonlinear plane waves excited by volume sources in a medium moving with transonic velocity,'' Sov. Phys. Acoust. **25**, 306–309 (1980).

[18] B. K. Novikov, O. V. Rudenko, and V. I. Timoshenko, *Nonlinear Underwater Acoustics* (American Institute of Physics, New York, 1987).

[19] V. E. Gusev and A. A. Karabutov, *Laser Optoacoustics* (American Institute of Physics, New York, 1993).

[20] O. V. Rudenko and A. V. Shanin, ''Nonlinear phenomena accompanying the development of oscillations excited in a layer of a linear dissipative medium by finite displacements of its boundary,'' Acoust. Phys. **46**, 334–341 (2000).

[21] O. V. Rudenko, ''Feasibility of generation of high-power hypersound with the aid of laser radiation,'' JETP Lett. **20**, 203–204 (1974).

[22] A. A. Karabutov, E. A. Lapshin, and O. V. Rudenko, ''Interaction between light waves and sound under acoustic nonlinearity conditions,'' Sov. Phys. JETP **44**, 58–63 (1976).

[23] M. Abramovitz and I. A. Stegun, *Handbook of Mathematical Functions* (Dover, New York, 1970).

[24] L. D. Landau and E. M. Lifshitz, *Fluid Mechanics* (Pergamon, London, 1959).

[25] B. O. Enflo, ''Saturation of nonlinear spherical and cylindrical sound waves,'' J. Acoust. Soc. Am. **99**, 1960–1964 (1996).

[26] M. Van Dyke, *Perturbation Methods in Fluid Mechanics* (Parabolic, Stanford, CA, 1975).

[27] Yu. R. Lapidus and O. V. Rudenko, ''New approximations and results of the theory of nonlinear acoustic beams'' Sov. Phys. Acoust. **30**, 473–476 (1984).

[28] O. V. Rudenko, ''Interactions of intense noise waves,'' Sov. Phys. Usp. **29**(7), 620–641 (1986).

[29] L. K. Zarembo, O. Yu. Serdobol'skaya, and I. P. Chernobai, ''Effect of phase shifts accompanying the boundary reflection on the nonlinear interaction of longitudinal waves in solids,'' Sov. Phys. Acoust. **18**, 333–338 (1972).

[30] R. Ladbury, ''Ultrahigh-energy promise new technologies,'' Phys. Today **51**, 23–24 (1998).

[31] Y. A. Ilinskii, B. Lipkens, T. S. Lucas, T. W. Van Doren, and E. A. Zabolotskaya, ''A theoretical model of nonlinear standing waves in an oscillatory closed cavity,'' J. Acoust. Soc. Am. **104**, 623–636 (1998).

[32] O. V. Rudenko, ''On the problem of artificial nonlinear media with resonance absorbers,'' Sov. Phys. Acoust. **29**, 234–237 (1983).

[33] O. V. Rudenko, ''Nonlinear acoustics: progress, prospects and problems,'' Priroda (Nature) **7**, 16–26 (1986).

[34] V. G. Andreev, V. E. Gusev, A. A. Karabutov, O. V. Rudenko, and O. A. Sapoznikov, ''Enhancement of Q-factor of a nonlinear acoustic resonator by a selectively absorbing mirror,'' Sov. Phys. Acoust. **31**, 162–163 (1985).

[35] V. A. Khokhlova, S. S. Kashcheeva, M. A. Averkiou, and L. A. Crum, ''Effect of selective absorption on nonlinear interactions in high intesity acoustic beams,'' in *Nonlinear Acoustics at the Turn of the Millennium, Proceedings of ISNA 15*, edited by W. Lauterborn and T. Kurz, AIP Conf. Proc. **524**, 151–154 (2000).

[36] O. V. Rudenko, A. L. Sobisevich, L. E. Sobisevich, and C. M. Hedberg, ''Enhancement of energy and Q-factor of a nonlinear resonator with an increase in its losses,'' Dokl. Phys. **47**, 330–333 (2002).

[37] O. V. Rudenko, ''Nonlinear oscillations of linearly deformed medium in a closed resonator excited by finite displacements of its boundary,'' Acoust. Phys. **45**, 351–356 (1999).

Measurement and modeling of three-dimensional sound intensity variations due to shallow-water internal waves

Mohsen Badiey[a)]
College of Marine Studies, University of Delaware, Newark, Delaware 19716

Boris G. Katsnelson
Voronezh State University, Universitetskaya Sq. 1, Voronezh 394006, Russia

James F. Lynch
Woods Hole Oceanographic Institution, Woods Hole, Massachusetts 02543

Serguey Pereselkov
Voronezh State University, Universitetskaya Sq. 1, Voronezh 394006, Russia

William L. Siegmann
Rensselaer Polytechnic Institute, Troy, New York 12180

(Received April 21, 2004; revised October 14, 2004; accepted October 15, 2004)

Broadband acoustic data (30–160 Hz) from the SWARM'95 experiment are analyzed to investigate acoustic signal variability in the presence of ocean internal waves. Temporal variations in the intensity of the received signals were observed over periods of 10 to 15 min. These fluctuations are synchronous in depth and are dependent upon the water column variability. They can be explained by significant horizontal refraction taking place when the orientation of the acoustic track is nearly parallel to the fronts of the internal waves. Analyses based on the equations of vertical modes and horizontal rays and on a parabolic equation in the horizontal plane are carried out and show interesting frequency-dependent behavior of the intensity. Good agreement is obtained between theoretical calculations and experimental data. © *2005 Acoustical Society of America.* [DOI: 10.1121/1.1828571]

PACS numbers: 43.30.Bp, 43.30.Dr, 43.30.Es, 43.30.Zk [AIT] Pages: 613–625

I. INTRODUCTION

The generation of nonlinear internal solitary waves (ISWs) in density-stratified shallow-water regions is typically due to tidal interaction with topographical features. When the bathymetry shoals at the continental shelf, the change in water depth can cause a hydraulic jump condition from which ISW packets can arise and propagate shoreward. Linear internal tides impinging upon the shelf at the so-called ''critical angle'' can also steepen into nonlinear waves[1] because of the shoaling bottom. These nonlinear ISWs create a strongly anisotropic (directionally dependent) medium affecting acoustic waves that propagate through them. Sound-speed anisotropy in general can be structural (for example, from sediment layering, where layer formation processes are directional) or dynamical (for example, from a field of internal waves propagating along the continental shelf), but the implication here is that one or more organized processes generate the directionality. Whether the environment is deterministic or random, the anisotropy has the potential of generating directional dependence in acoustic propagation. When broadband acoustic waves are transmitted through an anisotropic medium such as the ISW packets, amplitude and phase fluctuations arise that are strongly related to the characteristics of individual solitons. Quantifying the interaction between these two types of waves is of interest for both underwater acoustics and shallow-water oceanography.

Sound-field fluctuations due to internal waves in shallow-water regions have been studied in several experiments where low-frequency sound propagates in the presence of internal soliton trains. The first paper in this area[2] examined the frequency spectra variability in the Yellow Sea and recorded significant (up to 20 dB) intensity decreases for specific frequencies. This was referred to as an ''anomalous attenuation'' and was reported as the result of resonant interactions between acoustic waves and the quasiperiodic spatial structure created by an ISW train propagating nearly parallel to the acoustic propagation direction. At nearly the same time another study showed the acoustic field variability in the presence of ISWs.[3] The acoustic propagation direction was oriented about 10 deg to the ISW fronts, and an adiabatic description of the sound propagation was appropriate for the reported conditions. The intensity showed temporal fluctuations well correlated with water column oscillations from the ISWs, and the amplitude of these fluctuations was about 1–2 dB. In 1995 the multi-institutional SWARM'95 experiment was conducted on the New Jersey continental shelf and showed strong variability, of up to 7 dB, for broadband signal propagation through ISWs.[4–7] Experimental results presented in 1999 for the Gulf of Mexico[8] showed relatively small intensity fluctuations that were also correlated with ISWs. In that experiment the angle between the acoustic

[a)]Electronic mail: badiey@udel.edu

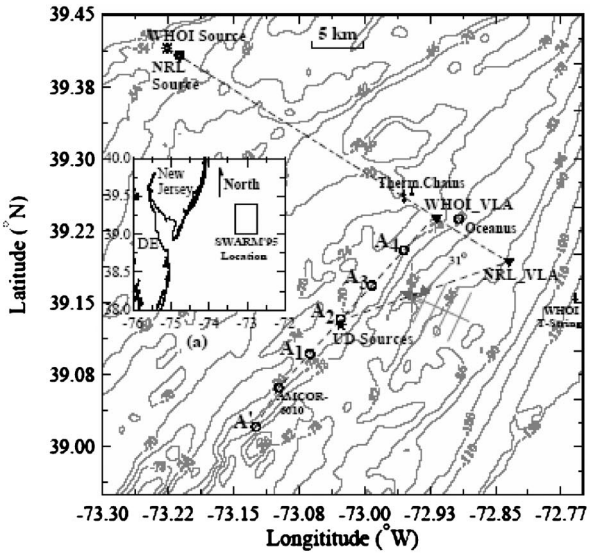

(a)

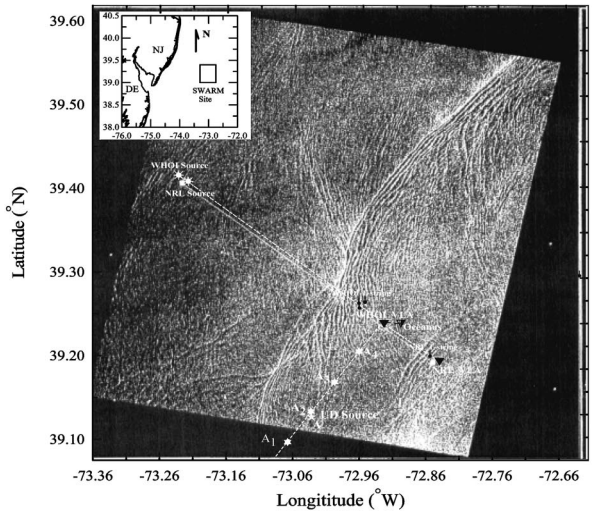

(b)

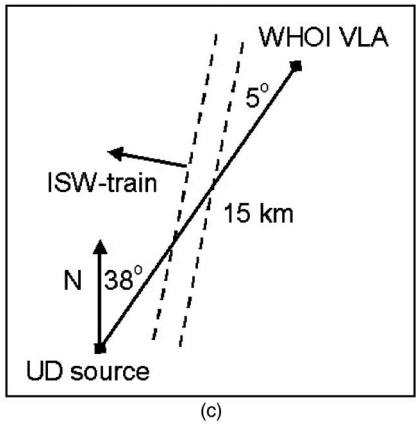

(c)

FIG. 1. (a) Location of SWARM'95 experiment. (b) Satellite picture for 31 August 1995, showing internal wave activity at the experimental site. (c) Schematic diagram of acoustic source and receiver positions relative to the internal solitary wave fronts (dashed lines).

track and ISW fronts was $\beta \sim 30$ deg, and mode coupling was reported as the reason for the fluctuations. All of the aforementioned work demonstrates two important points: a correlation between behavior of the acoustic signals and the ISWs, and the significance of the angle between the propagation directions of the acoustic waves and the ISWs. The main feature of these cases that differs from the present work is the orientation of the acoustic track relative to the ISW, which leads to different properties of the acoustic signals.

Along with papers on experiments, a number of theoretical studies appeared over the past few years. Two mechanisms that can cause significant fluctuations of the sound intensity in the presence of ISWs are mode coupling due to ISWs,[9,10] and ''resonant absorption'' that can take place if the horizontal spectrum of the ISW train is sufficiently narrow.[11,12] Another mechanism is horizontal refraction causing focusing and defocusing of intensity in horizontal plane.[13,14] Modeling of sound fluctuations due to horizontal refraction for conditions of the Sea of Japan showed significant synchronicity of intensity fluctuations in depth for a vertical line array.[15] Fluctuations of up to 10 dB in the frequency domain were demonstrated in Ref. 16 to arise from horizontal refraction, depending on the angle β. Modeling of sound propagation in shallow water in the presence of internal wave fields, both background waves and solitons, was conducted using a fully three-dimensional (3D) PE technique,[17,18] and significant variations and coherence degradation were observed.

All the above studies have contributed toward the understanding of the complex problem of acoustic signal interactions with ISWs. In this paper we review the experimental observations of intensity fluctuations and provide a theoretical foundation to explain 3D effects on the acoustic field due to the anisotropic nature of the water column resulting from ISWs. The evident cause of the intensity variations is horizontal refraction, a conclusion supported from a different viewpoint by computational results in Ref. 19.

The paper is organized as follows. In Sec. II the 1995 SWARM experiment is described in detail. Then, a model is presented for a shallow-water channel containing internal waves and with characteristics that generally correspond to the SWARM region. Next, we discuss 3D sound propagation through internal waves, in particular the approach using horizontal rays and vertical modes, the frequency-dependent effects predicted by this approach, and the replacement of the horizontal rays by a parabolic equation. A discussion of results comes next, followed by detailed conclusions and recommendations for future work.

II. SWARM'95 EXPERIMENT

The goal of the SWARM'95 experiment was to quantify effects of water column and ocean bottom sound-speed inhomogeneities on acoustic transmissions in shallow regions.[1,7] The experiment was conducted in the Mid-Atlantic Bight on the continental shelf region directly off Atlantic City, NJ [see Fig. 1(a)], where internal wave activity had been observed via satellite [Fig. 1(b)]. Several research vessels participated in the experiment, including R/V OCEANUS, R/V CAPE HATTERAS, and R/V ENDEAVOR. Principal investigators in the project included researchers from the Naval Research Laboratory (NRL), Woods Hole Oceanographic Institution (WHOI), the University of Delaware (UD), and the Naval Postgraduate School. Many oceanographic measuring sys-

tems, as well as two vertical line arrays, were deployed to collect simultaneously both acoustic and detailed environmental data.

In this paper we focus on one part of the experiment, dealing with broadband acoustic signals generated by the UD source and received at the WHOI vertical line array (WVLA) [see Fig. 1(c)]. This array was positioned at 39°14.25′ N and 72°54.55′ W. It consisted of 16 elements, each with a sampling rate of 1395 Hz, that spanned the water column from 14.9 to 67.4 m with a spacing of 3.5 m. Five temperature sensors were attached to the WVLA at 12.5, 22.5, 30.5, 50.5, and 60.5 m. This propagation track was designed as UD to WHOI and had the capability to emphasize the azimuthal dependence of the acoustic field from the horizontally anisotropic propagation environment. In particular, the acoustic propagation path ran nearly parallel to the internal wavefronts, in contrast to other paths where different fixed sources were placed so that acoustic tracks ran nearly perpendicular to the internal wavefronts.[7] Since bathymetry can significantly affect acoustic transmissions, the experimental configuration was chosen to have an essentially flat sea bottom for the entire UD to WHOI track.

During the experiment, numerous sensors were deployed in support of the acoustic measurements. The R/V ENDEAVOR performed high-resolution oceanographic surveys using conductivity–temperature–depth (CTD) casts and tows. High-frequency (200 and 300 kHz) imaging sonars were used to record internal waves. These measurements were necessary to characterize the generation, propagation, dispersion, and decay of the internal waves and the background field. The environmental data were supplemented by CTD data acquired by the R/V OCEANUS and R/V CAPE HATTERAS and by internally recording oceanographic instrumentation moorings. The latter included two moored ADCP units, six thermistor arrays, and internally recording temperature sensors distributed over the two acoustic receiving arrays. During the experiment, both direct observations and satellite images indicated strong internal wave activity occurring over a large portion of the experiment site. Unfortunately, no satellite images of the internal waves are available during the reported 2-h experimental period.

A 2-h segment of temperature data from 4 August 1995 is shown in Fig. 2. These temperature time series are from thermistor sensors located on the WVLA (12.5 to 60.5 m from the sea surface). During this period the mixed layer depth is about 15 m, and a negative temperature gradient extends from 15 to 30 m. Figure 3 displays multiple CTD casts that show the envelope of vertical thermocline fluctuations for this day. The sound speed changes from about 1535 m/s above the thermocline to 1480 m/s below. Both the depth and thickness of the surface and bottom mixed layers change with time. The temperatures in the surface and bottom mixed layers show much less variation than in the thermocline region. The periodicity of the temperature fluctuations shown in the Fig. 2 segment is about 10 to 15 min and is typical of the entire experimental period. These fluctuations are referred to as short-term, in comparison with the longer-period (about 12 h) fluctuations associated with tidal forcing. Although not shown here, similar features are also found in

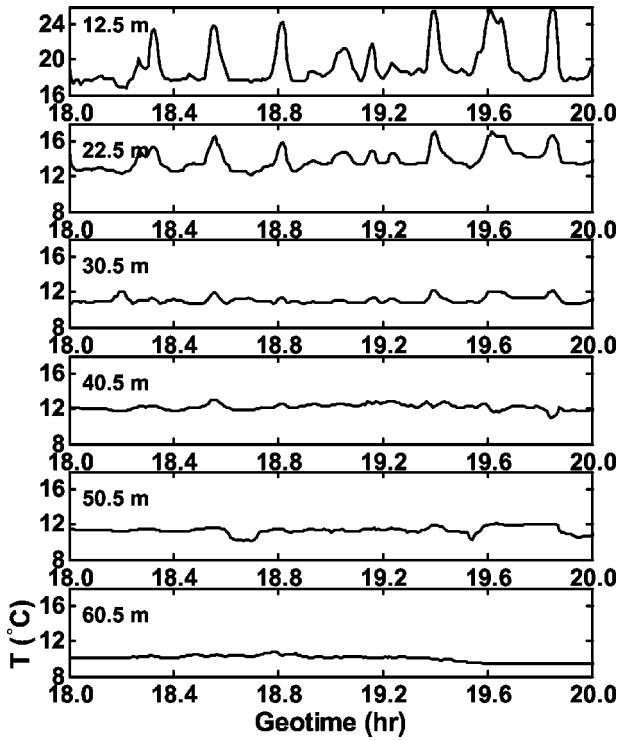

FIG. 2. Measured temperature profiles at six depths on the WHOI VLA versus geotime for 18:00–20:00 GMT on 4 August 1995.

data collected from other temperature sensors at different sites, including the source location.

Throughout the experiment, two different acoustic signals were transmitted from the R/V CAPE HATTERAS every minute. One was from an airgun source (pulse duration 0.1 s) and the other was a linear-frequency-modulated (LFM) sweep (pulse duration 30 s) transmitted by a J-15 transducer. The source signatures were highly repeatable, as verified by a large number of time series obtained from a monitor hydrophone near the sources.[7] Although both types of acoustic signals are available for analysis, we focus on the airgun data

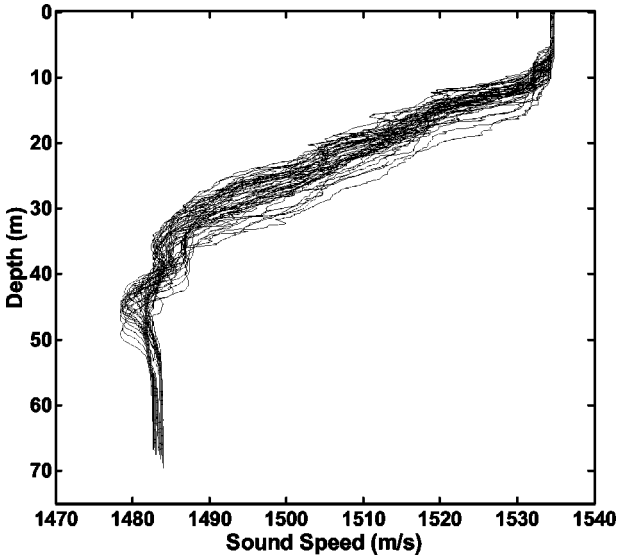

FIG. 3. Sound-speed profiles measured on WVLA showing thermocline fluctuations during the passage of ISWs for 18:00–20:00 GMT on 4 August 1995.

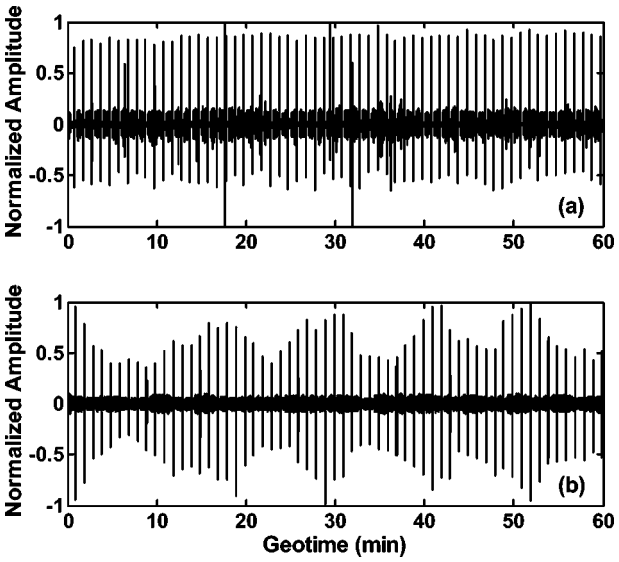

FIG. 4. Normalized pressure amplitude versus geotime from 19:00 to 20:00 GMT on 4 August 1995, measured: (a) at 2 m from the source, and (b) on the WHOI VLA 14.98 km from the source at a hydrophone 45 m from the sea surface. Note that amplitude variations at the source are negligible compared to those at the receiver.

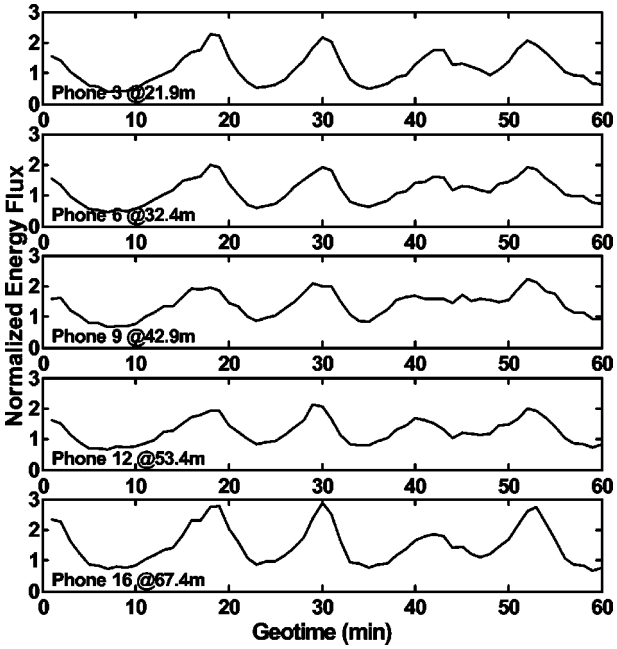

FIG. 5. Total time-integrated intensity $I(z,T)$ versus geotime for signals at five receiver depths.

here. The frequency spectrum of the monitor phone, also shown in Ref. 7, is dominated by peak at 32 Hz (with half-power width about 5 Hz), plus much smaller peaks at harmonics of this fundamental.

While the source ship stayed at a fixed location for several hours, the airgun source transmitted acoustic signals approximately every minute. During the interval 18:00 to 20:00 GMT on 4 August 1995, the source was placed at 12 m below the sea surface (just above the thermocline) at position A2 in Fig. 1(a), about 15 km from the WVLA. A segment of acoustic data from geotime 19:00 to 20:00 GMT is shown in Fig. 4. The reference hydrophone collected the data at the source location, and the received signals are from the WVLA. Signals were transmitted every 60.038 s. The near-source airgun signatures [Fig. 4(a)] show nearly constant amplitude over time, whereas the corresponding WVLA signals show considerable fluctuations over the hour [Fig. 4(b)]. The approximately periodic fluctuations of amplitude observed in the arrivals (the spikes) are due to internal waves that were present between the source and receiver during this period, as will be demonstrated in subsequent sections.

The WVLA received signals show strong fluctuations in amplitude versus geotime, indicating acoustic scattering by a fully developed ISW packet along the source–receiver path. Comparison of Figs. 2 and 4 shows correlation between the patterns of the internal waves and the acoustic signals. In particular, the acoustic and oceanographic fluctuations have essentially the same periodicity.

The source spectrum $S(\omega)$ of the radiated signal $f(t)$ is

$$S(\omega)=\frac{1}{2\pi}\int_{-\infty}^{\infty} f(t)e^{i\omega t}dt, \tag{1}$$

where $f(t)$ represents the pressure signature of the source. The total radiated pulse energy is

$$E_0=\frac{1}{4\pi\rho c}\int_{-\infty}^{\infty} f^2(t)dt=\frac{1}{\rho c}\int_0^{\infty}|S(\omega)|^2 d\omega. \tag{2}$$

Using the estimated airgun source power with a pulse duration of ~0.1 s, combined with the amplitude of the sound field at a distance of 2 m (~15 kPa), the source level at 1 m is calculated to be 210 dB re: 1 μPa. In this paper we use the spectrum of the source monitor[7] for $S(\omega)$ and calculate all frequency integrals over 30 to 160 Hz. Because of our objectives here, it is not necessary to account for differences between the measured spectra of the monitor and the actual spectra of the source.[12]

For subsequent derivations we denote the sound pressure of the received signal by $p(z_j,t,T_i)$, where T_i is the geotime (in 1-min intervals, denoted by the subscript) from 19:00 to 20:00 GMT and z_j is the jth hydrophone on the WVLA. The indices i and j are omitted where no confusion occurs.

The total time-integrated intensity (i.e., Energy Flux) of a received acoustic pulse at depth z on the WVLA is represented by

$$I(z,T)=\int_T^{T+\Delta t}\frac{p^2}{\rho c}dt, \tag{3}$$

where Δt is the duration of received pulse (~1 s). Equation (3) was calculated for each of the 60 pulse signals received during that hour, and the results are shown for five representative WVLA elements in Fig. 5.

Several features of the fluctuations in Fig. 5 deserve detailed discussion. First, significant amplitude fluctuations occur, of up to 7 dB. This value cannot be explained simply by local displacements of the thermocline level. Estimates of the intensity fluctuations due to changes of the sound-speed profile via thermocline displacements along a 2D slice (the usual acoustic path) produce only up to 15% variation in the received intensity. Thus, some explanation beyond a 2D physi-

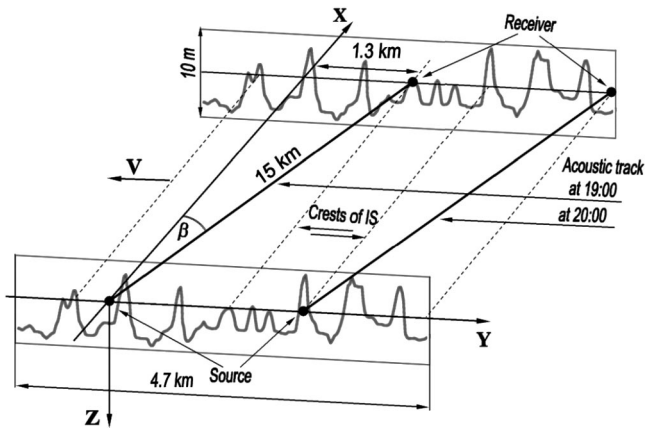

FIG. 6. Schematic diagram of the source–receiver track useful for modeling. The region between the two solid parallel lines corresponds to the geotime period between 19:00 and 20:00 on 4 August 1995.

cal mechanism is needed. Second, amplitude fluctuations at different depths show only weak dependence on depth. Moreover, they are effectively synchronous, meaning that at any geotime a simultaneous increase or decrease takes place for practically all depths, and show small increases near the bottom. Thus, they cannot result from changes in modal interference patterns, which generally stem from thermocline oscillations near the receiver. Third, the received acoustic signals correlate closely with ISW oscillations. The number and period of the oscillations in the thermocline variability from 19:00 to 20:00 GMT (Fig. 2) correspond to the same quantities observed in the fluctuations of energy flux (Fig. 5).

The first two observations above cannot be explained by interference between waveguide modes. However, they can quite naturally be interpreted as manifestations of 3D horizontal refraction.

III. SHALLOW-WATER CHANNEL MODEL WITH INTERNAL WAVES

To model the shallow-water waveguide in the experiment, a Cartesian coordinate system is chosen with x and y in the horizontal plane and z axis directed downwards, as shown in Fig. 6. The air–sea interface corresponds to $z=0$ and the flat bottom is $z=H=70$ m. The sound source is at the point $\mathbf{r}_S=0$, z_S, and the receiving array is at $r_R=(x_R,y_R)$ with a source–receiver separation $L\sim 15$ km. Along the track the sound-speed profile is $c(\mathbf{r},z,T)=c_0(z)+\delta c(\mathbf{r},z,T)$, where $c_0(z)$ is the mean sound-speed profile in the absence of ISWs and $\delta c(\mathbf{r},z,T)$ is the perturbation due to internal waves. The vector $\mathbf{r}=(x,y)$ denotes a point in the horizontal plane. The mean profile, obtained from the experimental data[7] in Fig. 3, consists of a thermocline layer extending about 25 m between two near-isospeed layers. The sound-speed variation between the isospeed layers is over 50 m/s, which gives a large value ($\sim 2\ \mathrm{s}^{-1}$) for the vertical gradient of the thermocline. The geoacoustic parameters in the bottom are selected as sound speed $c_1=1750$ m/s, $\rho_1=1.8\ \mathrm{kg/m}^3$, and attenuation coefficient $\alpha_f=0.25$ dB/(km·Hz), based on previous work at the SWARM site.[1]

Next, a time-varying model is needed for sound-speed fluctuations in the water column for any geotime T and location. For this purpose isopycnal (that is, isodensity) surfaces $\zeta(\mathbf{r},z,T)$ are constructed from the experimental data. This approach is used, rather than an analytical model, in order to preserve more of the detail in the measured sound-channel fluctuations. The ISW packet is assumed to have a plane wavefront parallel to the x axis and to move at speed V in the negative-y direction

$$\zeta(\mathbf{r},z,T)=\zeta\left(\mathbf{r}_R,z,T+\frac{y-y_R}{V}\right). \tag{4}$$

The parameter V was not measured directly from the ISW wavefronts but rather is estimated from KdV soliton theory. The Appendix provides an approximate value for $V\sim 0.65$ m/s at the SWARM site, which is in reasonable agreement with other estimates of this parameter made there. Note that the acoustic track has an angle of $\beta\sim 5$ deg with the x axis, so the source and receiver are on different ISW fronts for a given geotime (see Fig. 6). The spatial shift along the y axis between the source and receiver is $y_R\sim 1300$ m.

Equation (4) leads to a perturbation of the sound-speed profile due to the ISW

$$\delta c(\mathbf{r},z,T)=Qc_0(z)N^2(z)\zeta(\mathbf{r},z,T), \tag{5}$$

where $N(z)=(gd\rho/\rho dz)^{1/2}$ is the Brunt–Vaisala frequency and $Q\sim 2.4\ \mathrm{s}^2/\mathrm{m}$.[20] To obtain ζ isothermal, rather than isopycnal, displacements in the data are tracked, since vertical profiles of both salinity and temperature are required for isopycnals. This approximation introduces only a small error. In shallow water the main part of the energy of an ISW is in its first mode $\Phi(z)$, so that the displacement in Eq. (5) is written as $\zeta(\mathbf{r},z,T)=\Phi(z)\zeta_s[\mathbf{r}_R,T+(y-y_R)/V]$. The modal normalization condition is $\max(\Phi)=1$, so ζ_s is the modeled displacement of the isopycnal at the depth where $\Phi(z)=1$.

IV. 3D SOUND PROPAGATION THROUGH INTERNAL WAVES

The complex amplitude of the sound field due to a broadband source is expressed by the spectral Fourier integral

$$P(\mathbf{r},z,t)=2\int_0^\infty S(\omega)\Psi(\mathbf{r},z,\omega)e^{-i\omega t}d\omega, \tag{6}$$

where $S(\omega)$ is the spectrum of the radiated signal and $\Psi(\mathbf{r},z;\omega)$ is a spectral component of the sound-pressure field at any point $(\mathbf{r},z)$. For brevity the geotime parameter T and source coordinates $(\mathbf{r}_s,z_s)$ are omitted from the arguments of Ψ (and elsewhere where no confusion arises). The pressure component satisfies the inhomogeneous Helmholtz equation with a point source of unit amplitude on its right side. A series expansion of this Green's function Ψ in modal eigenfunctions yields

$$\Psi(\mathbf{r},z,\omega)=\sum_l \psi_l(\mathbf{r},z,T)P_l(\mathbf{r}), \tag{7}$$

where the $\psi_l(\mathbf{r},z,T)$ are the adiabatic (local) vertical modes and the P_l are the modal amplitudes. The complex eigenval-

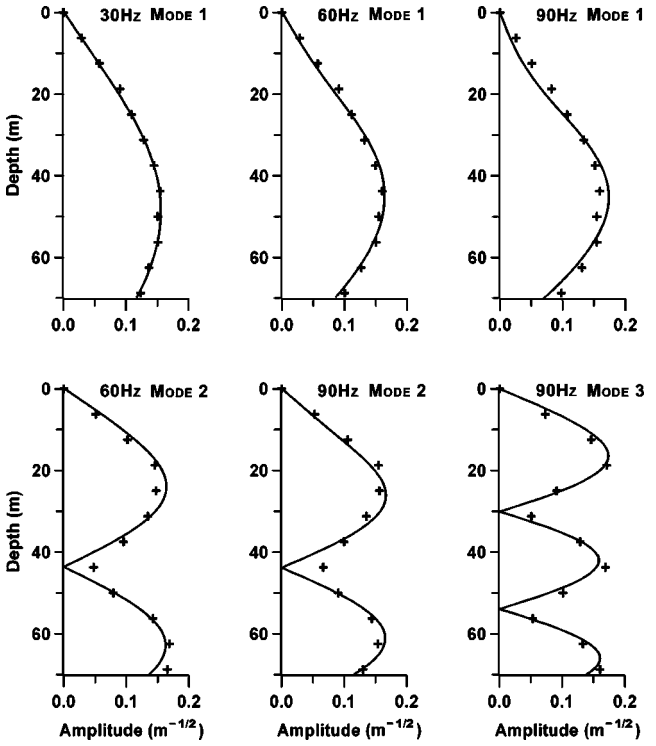

FIG. 7. Normalized vertical mode functions (modes 1 and either 2 or 3) for frequencies 30, 60, and 90 Hz. Solid curves show theoretical results based on Eq. (9); crosses show modal decomposition results from data.

ues are expressed as $\xi_l = q_l + \gamma_l/2$, and can be obtained from the boundary value problem

$$\frac{d^2\psi_l(\mathbf{r},z,T)}{dz^2} + \left\{ \frac{\omega^2}{[c_0(z)+\delta c(\mathbf{r},z,T)]^2} - \xi_l^2(\mathbf{r},T) \right\} \times \psi_l(\mathbf{r},z,T) = 0, \tag{8}$$

subject to the usual surface and bottom boundary conditions and interface conditions. Normalized vertical modes calculated from Eq. (8) for different frequencies at the receiver $\mathbf{r} = \mathbf{r}_R$ and geotime 19:00 are shown in Fig. 7, along with modes extracted from the SWARM data. Excellent agreement between the calculated and the experimental modes indicates that the parameters selected for the sound-speed formulas adequately represent the experimental waveguide.

Next, Eq. (8) is substituted into Eq. (7) and mode coupling terms are neglected, which is consistent with the adiabatic mode assumption.[21] The latter is a reasonable approximation for along-crest propagation in the modeled waveguide. Therefore, the modal amplitudes $P_l(\mathbf{r})$ satisfy the equation

$$\left[\frac{\partial^2}{\partial x^2} + \frac{\partial^2}{\partial y^2} + \xi_l^2(\mathbf{r}) \right] P_l(\mathbf{r}) = 0. \tag{9}$$

Equation (9) is a 2D Helmholtz equation in which the squared adiabatic eigenvalues play the role of the squared wave vector (which itself is proportional to the refraction index). In the present case ξ_l is complex and its imaginary part incorporates modal attenuation.

The total time-integrated intensity of a broadband signal at any point is expressed from Eqs. (3), (6), and (7) by

$$I(\mathbf{r},z) = \frac{4\pi}{\rho c} \int_0^\infty d\omega |S(\omega)|^2 \sum_l |P_l(\mathbf{r})|^2 \psi_l^2(\mathbf{r},z). \tag{10}$$

As usual in such calculations, the cross terms that appear in Eq. (10) (those with $l \neq m$, where m is the other summation index) are neglected. The justification relies on the spatial scale of the cross terms being determined by Λ_{lm}, which is the interference wavelength that is inversely proportional to the difference of horizontal wave numbers l and m. Specifically, integration over frequency from Eq. (6) corresponds to a summation of terms from Eq. (7) with different frequency-dependent scales Λ_{lm} of interference beating. If the signal frequency bandwidth $\delta\omega \geqslant \omega\Lambda_{lm}/L$, then the cross terms are negligible. For our situation $\delta\omega \sim 130$ Hz, $\Lambda_{lm} \leqslant 1$ km, the center frequency ω is no larger than 150 Hz, and $L \sim 15$ km, so the condition for elimination of the cross terms is easily satisfied. The main quantity to be calculated is $P_l(\mathbf{r})$ from Eq. (9).

A. Horizontal rays and vertical modes

A 2D ray solution for Eq. (9) has been published by Weinberg and Burridge using their theory of "horizontal rays (HRs) and vertical modes".[22] The function $P_l(\mathbf{r})$ is assumed in the form

$$P_l(\mathbf{r}) = \sum_m A_{ml}(\mathbf{r}) \exp[i\theta_{ml}(\mathbf{r})], \tag{11}$$

where $A_{ml}(x,y)$ is the amplitude and $\theta_{ml}(x,y)$ is the eikonal for the mth HR component of the lth vertical mode $\psi_l(\mathbf{r},z)$. In general, multiple HRs for a given vertical mode can reach the point of observation. These rays have separate trajectories and different amplitudes and eikonals. Thus, a summation over all horizontal eigenrays (i.e., with the index m) is required. The amplitude and the eikonal satisfy traditional 2D equations of ray acoustics[21,23]

$$(\nabla_r \theta_{ml})^2 = q_l^2(\mathbf{r}), \tag{12}$$

$$2\nabla_r A_{ml} \nabla_r \theta_{ml} + A_{ml} \nabla_r^2 \theta_{ml} + q_l \gamma_l A_{ml} = 0, \tag{13}$$

where $\nabla_r = (\partial/\partial x, \partial/\partial y)$.

Ray trajectories in the horizontal plane are found from the ordinary differential equations

$$\frac{d\mathbf{r}_{ml}}{dt} = U_l \boldsymbol{\tau}_{ml}, \tag{14}$$

$$\frac{d\mathbf{q}_{ml}}{dt} = U_l \nabla q_l, \tag{15}$$

where $dt = U_l^{-1}\sqrt{(dx)^2+(dy)^2}$ is a measure of arrival time for mode l, $\boldsymbol{\tau}_{ml}(\mathbf{r}) = \nabla_\mathbf{r}\theta_{ml}(\mathbf{r})/|\theta_{ml}(\mathbf{r})|$ is a unit tangent vector to the horizontal ray, $\nabla_\perp = \nabla_\mathbf{r} - \boldsymbol{\tau}(\boldsymbol{\tau}\nabla_\mathbf{r})$ is the transverse gradient, $U_l = (dq_l/d\omega)^{-1}$ is the group velocity of the lth vertical mode, and $\mathbf{q}_{nl} = q_l \boldsymbol{\tau}_{nl}$ is the wave vector (tangent to ray n for vertical mode l). Equations (14) and (15) describe space-time HRs,[23] because arrival time is the ray parameter. Using these equations one can find both the trajectories of the HRs and arrival times of the corresponding modal pulses. These equations must be accompanied by conditions at the source $\mathbf{r}_s$ such that $\mathbf{r}_l(t;\mathbf{r}_S,\boldsymbol{\tau}_S)|_{t=0} = \mathbf{r}_S$ and

$\mathbf{q}_l(\mathbf{r}_l,t;\mathbf{r}_s,\boldsymbol{\tau}_s)|_{\mathbf{r}_l=\mathbf{r}_s,t=0}=q_l(x_s,y_s)\boldsymbol{\tau}_s$. If one defines $\boldsymbol{\tau}_S=(\cos\chi_S,\sin\chi_S)$, where χ_S is the HR angle at the source, then χ_S and t can be considered as ray coordinates. Also, if χ_S is fixed, a separate HR can be obtained, and for fixed t, a wavefront exists in the horizontal plane. The HRs allow construction of the eikonal function along a ray path

$$\theta_l(\mathbf{r},t)=\theta_l(\mathbf{r}_s,0)+\int_0^t U_l q_l[\mathbf{r}(t')]dt'. \tag{16}$$

Because the spatial scale of q_l in the horizontal plane is $|q_l/\nabla_r q_l|$, this value must be much greater than a wavelength for applicability of HR theory. The amplitude of the HRs can be written as

$$A_l(t)=A_l(0)/\sqrt{J}\exp\left\{ i\,\theta_l(\mathbf{r},t)-\int_0^t \gamma_l[\mathbf{r}(t')]/2dt'\right\}, \tag{17}$$

where $J(t)$ describes the divergence of HRs; $J(t)=d\Omega_t/d\Omega_0$ is the ratio of the lengths of corresponding pieces of wavefronts along a ray tube.

An effective squared wave vector in the horizontal plane is on the right side of Eq. (12). Equivalently, an effective mode-dependent refraction index can be introduced, $n_l(\mathbf{r})=q_l(\mathbf{r})/q_l^0$, where q_l^0 is an eigenvalue for the waveguide without ISWs. Because of the small perturbation $|\delta c|\ll c_0$, which correspondingly implies $|q_l-q_l^0|\ll q_l^0$, the refraction index for HRs is a sum of the unperturbed value 1 and a small perturbation μ_l due to ISWs, which depends upon horizontal coordinates and T

$$n_l^2(\mathbf{r},T)=1+\mu_l(\mathbf{r},T). \tag{18}$$

The quantity μ_l has appeared in various publications (for example, see Ref. 15)

$$\mu_l(\mathbf{r},T)=-\frac{2Qk^2}{(q_l^0)^2}\int_0^H[\psi_l^0(z)]^2N^2(z)\Phi(z)\zeta(\mathbf{r},z,T)dz$$

$$=-\nu_l\zeta_s\left(\mathbf{r}_R,T+\frac{y-y_R}{V}\right). \tag{19}$$

The second equality in Eq. (19) uses the two factors ν_l and $\zeta_s(\mathbf{r},T)$, where ζ_s was explained in Sec. III and is determined by the shape of the ISW train. The other factor

$$\nu_l=\frac{2Qk^2}{(q_l^0)^2}\int_0^H[\psi_l^0(z)]^2N^2(z)\Phi(z)dz, \tag{20}$$

depends on the waveguide parameters.

The refractive index in the horizontal plane depends on frequency through its dependence on the eigenfunction, because of the overlap of the eigenfunction with the thermocline layer.[16] Generally the eigenfunctions are not strongly frequency dependent. However, the portion of the eigenfunction overlapping the thermocline can be sensitive to frequency (see, for example, Fig. 7). Values of $|\overline{\mu_l}|=\nu_l\zeta_s$ are shown in Fig. 8 as a function of frequency and characterize the refractive index when the ISW amplitude ζ_s is at its maximum ($\sim$10 m).

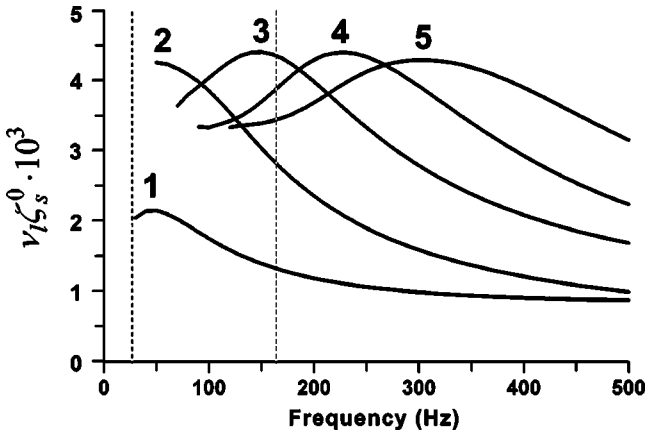

FIG. 8. Frequency-dependent index of refraction for horizontal rays at the maximum ISW amplitude (10 m), calculated for the five lowest vertical modes. Dashed lines indicate the approximate frequency band of interest in the airgun data (30–160 Hz).

An example is provided here of a simple estimate of the refraction index for an HR (as shown in Ref. 14), using numbers that are typical of SWARM. If $h_t/H\sim 0.2$, where h_t is thickness of the thermocline, then the average Brunt–Vaisala frequency in that layer is $N_0\sim 12$ cph or $\sim$0.02 rad/s. Consequently from Eq. (20), $\nu_l\sim 4\times 10^{-4}\,\mathrm{m}^{-1}$, so the correction to the squared refraction index in the horizontal plane is $|\overline{\mu_l}|\sim 4\times 10^{-4}\zeta_s$. This value corresponds to the detailed calculations from Eq. (20) in Fig. 8.

The negative sign in Eq. (19) means that if a minimum displacement ($\zeta=0$) falls on the source, then the refraction index has a local maximum at this point as a function of y. In this case HRs emitted from the source deviate toward the x axis, denoted as ''defocusing'' [Fig. 9(a)]. If a maximum displacement (soliton peak) falls on the source, then ''focusing'' [Fig. 9(b)] occurs. Using the reciprocity principle, this argument also applies from the viewpoint of incoming rays. In the SWARM experiment, the available record of ISWs was obtained at the receiving array, so it is appropriate to apply these ideas for incoming rays.

To estimate how the space-time distribution of the sound field is affected by a passing ISW train using the HRs, consider an angular sector in the xy plane where the emitted HRs (at angle χ_0, as shown in Fig. 10) have turning points in the region between two peaks of the ISW train. This situation reflects the focusing, or increasing intensity within this region. Using the waveguide parameters appropriate for SWARM gives a critical angle estimate $\chi_0\sim 2\sqrt{|\nu_l\zeta_s|}\sim 8$ deg for this example. The maximum longitudinal scale X_0 for focusing is half a ray cycle distance in the horizontal plane for rays with deviation of order $\Lambda/2$, where Λ is the distance between adjacent peaks in the ISW train in the y direction, as shown in Fig. 10. This can be estimated as

$$X_0=\int_0^{\overline{y}}\frac{dy}{tg\chi(y)}=\int_0^{\Lambda/2}\frac{dy}{\sqrt{\nu_l\zeta_s(y)}}\sim\frac{2\Lambda}{\chi_0}. \tag{21}$$

For example, if $\Lambda\sim$400 m and $\zeta_0\sim$10 m, then $X_0\sim$6 km. This means that the ''critical region'' where the horizontal refraction can be manifested is within the sector with central angle χ_0 and distances greater than X_0 from the source (see

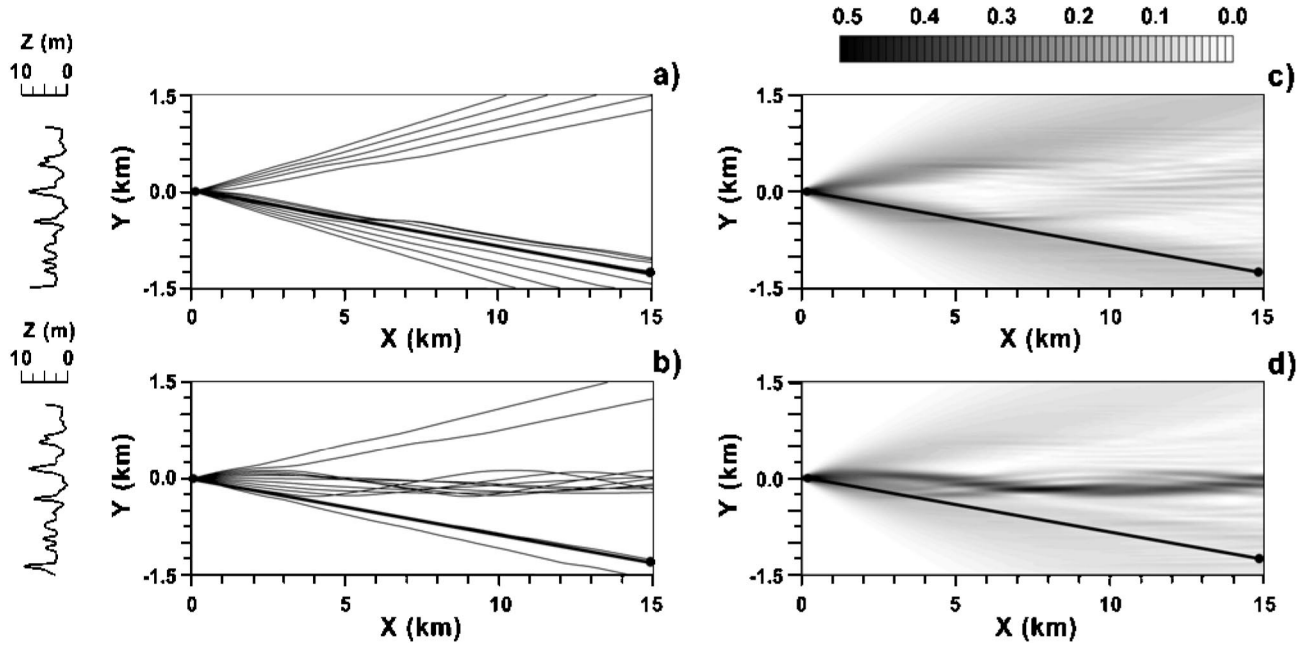

FIG. 9. (a) Ray theory calculation of the acoustic field in the horizontal plane corresponding to geotime 19:16 GMT, showing defocusing by horizontal refraction and an energy maximum; (b) same as (a), but corresponding to geotime 19:22 GMT, showing focusing and an energy minimum; (c) and (d), same as (a) and (b) but using the PE method. Corresponding ISW positions are shown to the left of each plot, and bold straight lines denote the source–receiver track.

Fig. 10). This explains why, in the SWARM experiment, the source–receiver separation and ISW parameters and positions (see Fig. 1) permit the influence of horizontal refraction on the sound field to be observed. In Fig. 9, HRs are presented for two geotimes (19:16 and 19:22 GMT) that correspond to a maximum and minimum in the time dependence of time-integrated intensity, as shown in Fig. 5. The intensity maximum corresponds to the case of defocusing, whereas the minimum (19:22 GMT) corresponds to focusing.

Using HRs one can roughly estimate the amplitude of the intensity fluctuations observed in Fig. 5 as a function of geotime for the experimental conditions. At a distance of 15 km from the source and using the estimated waveguide parameters calculated above, in the absence of ISWs a homogeneous intensity distribution would occur along the circular arc in Fig. 10. For the sector with central angle $\chi_0 \sim 8$ deg, the length of the arc is L $\chi_0 \sim 2$ km. For the focusing scenario the intensity in this area will concentrate between adjacent crests of the ISW. As noted above, this area has a length of ~400 m, so the intensity increases by approximately a factor of 5, or ~7 dB. For the defocusing scenario the ratio of intensities tends to infinity. The experimentally observed fluctuation values may be somewhat smaller than the focusing estimate because the acoustic track direction is not exactly parallel to ISW crests, and the source and receiver are not located between the same peaks of the train. In summary, the proposed mechanism of sound fluctuations is the focusing/defocusing of HRs, which provides synchronicity over depth, correlation with ISWs, and time-integrated intensity fluctuation features that are observed in the data.

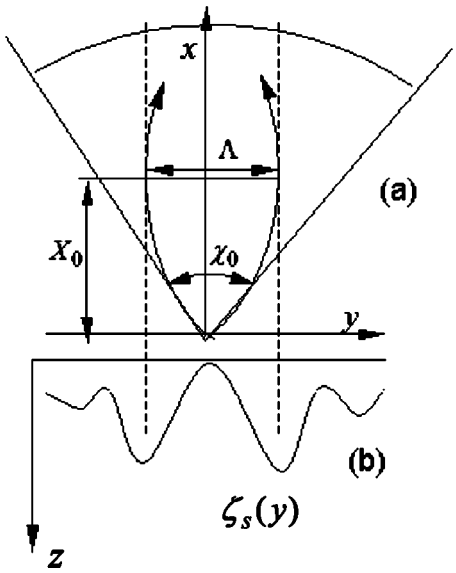

FIG. 10. Schematic diagrams showing: (a) patterns of horizontal rays with respect to the ISW amplitude, with dashed lines showing turning points of the rays focused within the critical angle χ_0 and curved lines representing horizontal rays with launch angles near χ_0; and (b) ISW amplitude in the yz plane.

By considering the experiment from the viewpoint of reciprocity, one can construct incoming HRs toward the receiver in order to describe the propagation. Examples of such HRs are presented for defocusing [Fig. 11(a)] and focusing [Fig. 11(b)] cases. As described previously for case (b), the source falls close to the shadow zone of HRs coming toward receiver, and so an intensity minimum should occur. Correspondingly for case (a), the sound intensity should increase.

B. Frequency dependence

As discussed in the previous section, HR trajectories and amplitudes depend on frequency through the eigenvalues q_l on the right side of Eq. (12). Therefore, in the integral of Eq.

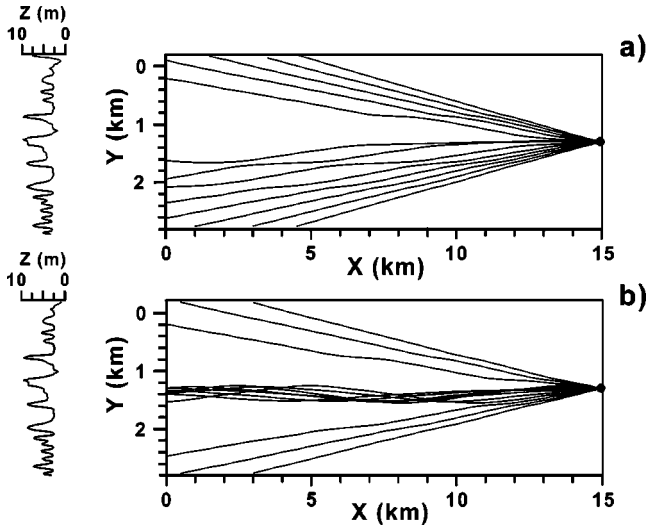

FIG. 11. Horizontal rays shown from the viewpoint of incoming rays at (a) 19:41, and (b) 19:47 GMT. Corresponding ISW positions are shown to the left of each plot. Note that the source position is at the origin for both cases.

(10), different contributions to the time-integrated intensity come from different frequencies. Recall that in Fig. 8 the magnitude of the refraction index is plotted versus frequency for five modes, with the vertical dashed lines representing the frequency band relevant to the SWARM airgun results.

To understand the propagation of broadband signals, the frequency dependence of the mode functions and of the HR, and their connections, need to be explained. From waveguide modal analysis,[23] at a fixed frequency the higher-order modes have their maximum amplitudes closer to the sea surface and hence to the layer containing the ISWs. The maximum amplitudes of lower modes are well below this layer. Hence, the higher modes have a greater chance of overlapping the thermocline.[15] As a function of increasing frequency, the maximum amplitude of each mode tends toward the sea bottom. Consequently, a frequency exists for which the amplitude of a particular mode overlaps with the internal wave layer. The existence of a maximum index of refraction at this frequency can be interpreted as having a number of HRs corresponding to a ''quasiresonant'' frequency, which increases their contributions to the sound field (in the case of focusing) and in turn provides higher intensity in comparison with other frequencies. Correspondingly in the case of defocusing, we should observe deeper minima for these quasiresonant frequencies. Away from this special frequency the effect of HRs reduces, as is shown clearly for modes 1 through 5 in Fig. 8. For some frequencies, an overlap occurs between the index of refraction of different modes. For example, in the band of interest in the SWARM experiment, (i.e., 30–160 Hz) the refraction indices for modes 1 and 4 are below those of modes 2 and 3, while the latter overlap. This phenomenon causes frequency-selective behavior of the refraction index and is similar to chromatic aberration in optics, where the focusing properties of a lens depends on the frequency/color of light.

To apply this theoretical result for interpretation of experimental data requires caution, since the single WVLA shown in Fig. 1 limits the ability to extract spatial information. However, it is possible to confirm the frequency dependence using the temporal behavior of the spectral time-integrated intensity. From the above reasoning the fluctuations due to the focusing/defocusing process increase with increasing refraction index. Thus, if separate frequency or modal components of the sound field are considered, these fluctuations will be greater for components having higher values of refraction index, which depends on mode number and frequency.

To illustrate this important point for SWARM, the spectrum of the received signals as a function of geotime for different modes is extracted from experimental data for the 30–160-Hz band. The following processing of experimental data was carried out. After frequency filtering the received pulses $P(z,t;T)$ with the sliding window $\Delta f = 10$ Hz for all geotime, a modal decomposition of the signal is performed

$$P_\omega(z,t,T) = \sum_l \psi_l(z) a_{l\omega}(t,T)\cos(\omega t + \theta_l), \tag{22}$$

where P_ω is a spectral component and θ_l is the phase shift. The modal time-integrated intensity for each frequency interval is calculated as

$$I_{l\omega}(T) = \tfrac{1}{2}\int_T^{T+\Delta t} a_{l\omega}^2(t,T)dt. \tag{23}$$

The results are shown in Fig. 12, which shows the fluctuation amplitude of each mode varying as a function of frequency, mode number, and geotime. For example, mode 1 has the largest fluctuations for the frequency band of 90–100 Hz, while mode 3 shows the largest fluctuations for 150–160 Hz. The character of the intensity fluctuation certainly differs for each mode as a function of frequency. Note that due to the frequency and mode number dependence of the refraction index, exact synchronicity of sound fluctuations for all modes and frequencies does not occur, as can be seen from Fig. 12. The synchronicity is revealed as a result of some averaging over frequency or space intervals.

To further interpret these results, we calculate the squared average value of the modal energy flux fluctuations after removing the mean. We use the concept of scintillation index (SI) defined for given mode number and frequency[24]:

$$SI_l^2(\omega) = \frac{\langle I_{l\omega}^2\rangle - \langle I_{l\omega}\rangle^2}{\langle I_{l\omega}\rangle^2}, \tag{24}$$

where $\langle F\rangle = 1/T_0 \int_0^{T_0} F(T)dT$. This quantity characterizes the average fluctuations for the entire $T_0 = 1$-h period in Fig. 13, which shows results on a dB scale for the three lowest modes. By comparing these dependencies with the refraction index behavior in Fig. 8, the averaged value of fluctuations is seen to depend on frequency. For example, the amplitude of the first mode undergoes less fluctuations than the second mode for all frequency bands, which corresponds to Fig. 8 where the refraction index for the second mode is always greater than the first. The fluctuations of the third mode for frequencies less than ~100 Hz are less than those of the second mode, while for frequencies greater than ~100 Hz the opposite behavior occurs. This behavior is also similar to the frequency dependence of the refraction index in Fig. 8.

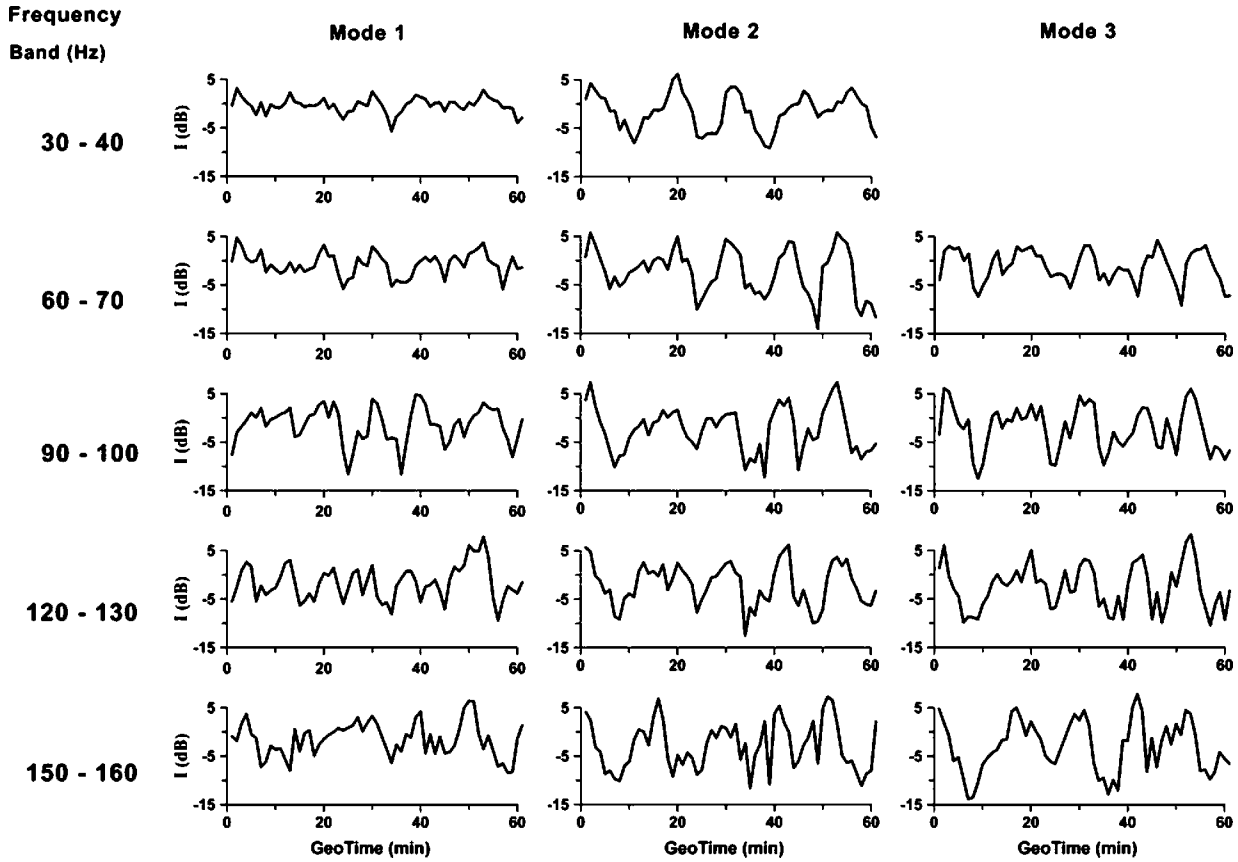

FIG. 12. Modal spectral time-integrated intensity $I_{i\omega}(T)$ in dB versus geotime for the three lowest modes and five spectral bands, calculated from data using Eq. (23).

Note the qualitative similarity between Figs. 8 and 13. Because of the frequency dependence, the curves in Fig. 13 will have the same shape at any receiver within the critical sector, because Eq. (20) depends on the unperturbed waveguide parameters only.

C. Parabolic equation calculations in the horizontal plane

The HR technique above provides a method to understand and interpret the basic features of sound propagation in the presence of horizontal refraction. However, HR calculations have the usual problems of ray caustics, so the theory is rarely applied for experimental comparisons. A more appropriate technique for this goal is the parabolic equation (PE).[25] A version of this method known as the adiabatic mode PE (AMPE) was developed for 3D calculations without mode coupling.[26]

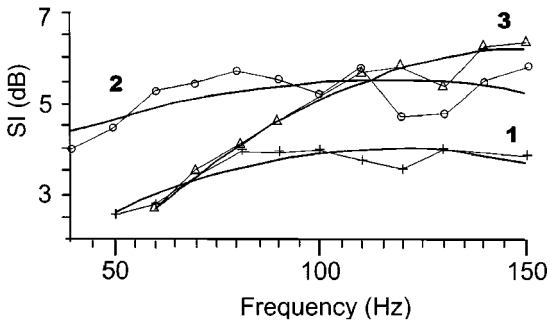

FIG. 13. Scintillation index, *SI* versus frequency for the three lowest modes; experimental values (points, joined by broken line) and their interpolation using mean square approximation (solid line).

In order to compare calculations with the observed experimental fluctuations using this PE, the starting point is the received field for a fixed frequency as a function of geotime T and source position $\Psi(\mathbf{r},z,\omega)$. Equation (7) is rewritten with the new variable $P_l^0(\mathbf{r}_r,\mathbf{r}_s)$ introduced

$$\Psi(\mathbf{r},z,\omega)=\sum_l \psi_l(\mathbf{r}_s,z_s)\psi_l(\mathbf{r},z)P_l^0(\mathbf{r},\mathbf{r}_s)e^{-(\gamma_l/2)|\mathbf{r}-\mathbf{r}_s|}, \tag{25}$$

where as before the source and receiver coordinates are $(\mathbf{r}_s,z_s)$ and $(\mathbf{r},z)$, and γ_l is the attenuation coefficient for mode l. This revision of Eq. (7), including the attenuation and source depth factors, is convenient for the PE solution. The solution of Eq. (9) is written in the form

$$P_l^0(\mathbf{r},\mathbf{r}_s)=F_l(x,y)\exp(iq_l^0x), \tag{26}$$

where $F_l(x,y)$ is a slowly varying function in the propagation direction for each mode. Considering $F_l(x,y)$ in the forward-scattering approximation ($\partial F_l/\partial x \ll q_l^0 F_l$) leads to a PE in the horizontal plane

$$\frac{\partial F_l}{\partial x}=\frac{i}{2q_l^0}\frac{\partial^2 F_l}{\partial y^2}+\frac{iq_l^0}{2}\mu_l F_l. \tag{27}$$

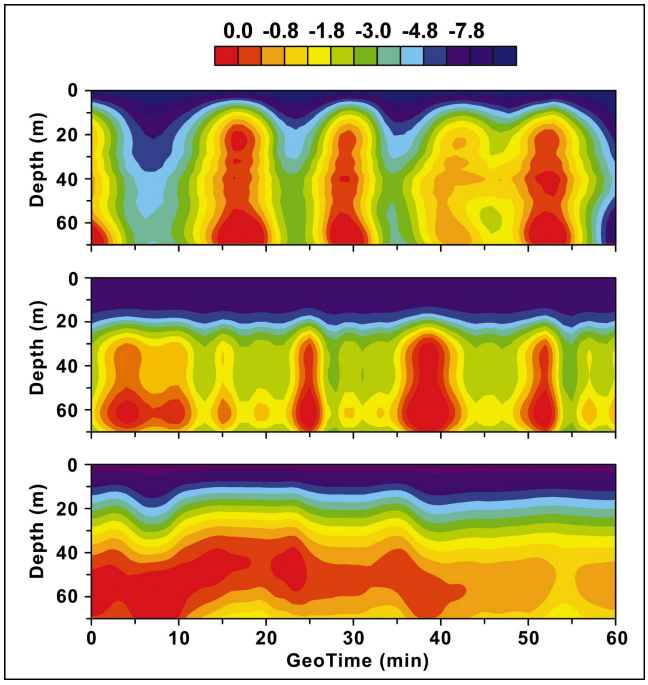

FIG. 14. Contour plots in depth and geotime for fluctuations of time-integrated intensity in normalized units: (a) experimental results [top]; (b) modeling results using horizontal PE and vertical modes [middle]; (c) modeling results using adiabatic modes without horizontal refraction [bottom]. The color unit is in dB.

The numerical solution of this equation can be produced with the standard split-step algorithm using the Fourier transform, although more accurate procedures[26] use other methods.

As an example of calculating the modal amplitude in a horizontal plane for fixed frequency, the solution of Eq. (27) is presented for the same case as done with the HR method earlier. The results are presented in Figs. 9(c) and (d) for comparison with the HR calculations in Figs. 9(a) and (b). These plots show the distribution of the second vertical mode amplitude for frequency 100 Hz. Excellent qualitative correspondence between results for the HR and PE methods is shown in depicting focusing and defocusing of the field, as is expected. To use this method for interpretation of and comparison with SWARM data, the spectral time-integrated intensity summed over all modes is calculated from the equation

$$I_\omega(\mathbf{r},z)=\frac{4\pi}{\rho c}|S(\omega)|^2\sum_l \psi_l^2(\mathbf{r}_s,z_s)\psi_l^2(\mathbf{r},z)|P_l^0(\mathbf{r},\mathbf{r}_s)|^2 \times e^{-\gamma_l|\mathbf{r}-\mathbf{r}_s|}. \tag{28}$$

For the geotime behavior of total time-integrated intensity, integrate Eq. (28) over frequency to obtain the analogue of Eq. (10)

$$I(\mathbf{r},z)=\int_0^\infty I_\omega(\mathbf{r},z)d\omega. \tag{29}$$

V. COMPARISON OF DATA AND MODEL RESULTS

A comparison between the experimental data and modeled results is shown in Fig. 14. Figure 14(a) shows contours of the total time-integrated intensity from Eq. (3) of the received acoustic signal on the WVLA from 19:00 to 20:00 GMT. This figure, which is constructed using all 16 hydrophones of the WVLA, clearly shows the 10- to 15-min periodicity of the intensity fluctuations versus geotime. In Fig. 14(b) the modeled results over the same geotime period are shown using calculations from the PE in Sec. IV-C. Five modes are used over the frequency band of 30–160 Hz, which is sufficient because nearly all the spectral energy is in the lowest part of this band and because higher-order modes contribute very little to the total acoustic field. Comparison of Figs. 14(a) and (b) confirms the 3D behavior of the waveguide in the presence of ISWs. The depth distribution of the time-integrated intensity, as well as the quasiperiodicity of the fluctuations, agrees well with the experimental data. Furthermore, very good agreement is shown for the depth locations of the intensity maxima, especially for the second half of the 1-h period. This is due to the passage of three large ISW peaks during this period. Differences between theoretical calculations and experimental data exist in the geotime arrivals of the maxima of the time-integrated intensity patterns (shifts of 3 to 5 min in arrival of the high-intensity bands near geotimes 19:25, 19:15, and 19:07 GMT in the calculated results). Other differences arise from the idealizations of the shallow-water waveguide model, such as the plane wavefront assumption for the ISW train. In the absence of detailed measurements of the ISW front curvature and other features, more precise matches with the experimental results are not expected. Moreover, the comparisons here between data and calculations are of one quantity, the total time-integrated intensity, which is expected to be more robust than others such as individual received pulses or their spectra.

The comparatively good agreement that is obtained for the positions of the last maxima in Fig. 14(b) can be discussed further. Within the framework of the plane wavefront assumption, three distinct small ISWs pass through the WVLA during the period 19:00 to 19:30 GMT, when large ISWs are detected at the source (see Fig. 9). From 19:30 to 20:00 GMT we have the opposite situation, with large ISWs at the receiver. The latter period can be modeled more realistically and naturally gives the predominant contributions to 3D effects. Moreover, the latter situation where the three maxima are visible at the receiver is well described by the incoming ray analogy (shown in Fig. 11). Some minor differences between the experimental data and the modeled results in Figs. 14(a) and (b) can be attributed to the lack of detailed environmental data along the acoustic track, including the bottom properties and the range-dependent sound-speed profile. However, it is noted that the modeling results presented here provide all the features of intensity fluctuations due to horizontal refraction.

Finally, Fig. 14(c) is presented to demonstrate conclusively the important role of horizontal refraction in the time-integrated intensity fluctuations. These contours represent the results of model calculations for the same experimental period but without taking into account horizontal refraction. This is accomplished by using the 2D adiabatic mode approximation,[21] which is valid because the sound-speed gradient along the acoustic track is relatively small, ~6

$\times 10^{-3}\,\mathrm{s}^{-1}$. In this case the expression for $F_l(x,y)$ in Eq. (26) is found from Eq. (27) by neglecting the refraction term and using the appropriate source normalization. The corresponding formula for the spectral time-integrated intensity differs from Eq. (28) by replacing $|P_l^0(\mathbf{r},\mathbf{r}_s)|^2$ with $1/(8\pi q_l L)$. The space-time intensity patterns in Fig. 14(c) are quite different from both the experimental results and the calculations including horizontal refraction. Figure 14(c) represents a 2D interference pattern with time-integrated intensity fluctuations of less than about 15%. For example, in the temperature record of Fig. 2 near geotime ~19:30 GMT, cold water occurs from a soliton displacement minimum. This thermocline rise broadens the effective sound channel and decreases intensity in the 2D calculations near ~19:34. At ~19:36 in Fig. 2 the water is warmer, the thermocline sinks corresponding to a soliton maximum, the sound channel narrows, and the sound intensity increases near ~19:41. This is opposite to predictions from the 3D modeling and the experimental data.

VI. CONCLUSIONS

When broadband acoustic signals propagate through ISWs, time-integrated intensity fluctuates with periods close to that of the ISW. Depending on the source–receiver geometry, the orientation of the internal wavefront with respect to the acoustic track, and other parameters of the waveguide such as the ratio between the thermocline layer thickness and the water depth, this effect could be significant (as large as 10 dB in the SWARM data presented here).

The experimental data in this paper indicate significant peak-to-peak total pulse-integrated intensity fluctuations of broadband signals. In addition, they are largely synchronous in water depth, so that the total signal energy in the water for a given geotime remains largely the same for all depths (below the thermocline). These features are interpreted as manifestations of 3D refraction in this shallow-water waveguide. To explain them, a theoretical model using horizontal rays and vertical modes is described. Results of the vertical mode and frequency spectrum decomposition of data are in strong agreement with model calculations. It is relevant to note that characteristics of the time-integrated intensity fluctuations can be qualitatively interpreted within the framework of ray theory. A direct comparison with integrated intensity data is facilitated using a horizontal plane PE model. The comparison between calculations and measured data shows good agreement, including the main features of the fluctuations. However, mismatches do occur, such as a time shift (up to ~3 min in Fig. 14) in the geotime dependence of integrated intensity. The differences result from idealizations in the waveguide model, which is based on data from thermistors at different depths along the receiver array. With only one point measurement, the ability to model properties, such as orientation, speed, and curvature, along the ISW wavefront is limited. It is noteworthy that, although small perturbations of the ISW speed and orientation angle modify the results, the synchronicity in depth and overall fluctuation amplitude is robust and does not vary significantly. Frequency-dependent focusing effects due to horizontal refraction are also found, with quite good agreement between theoretical and experimental results. This feature is analogous to chromatic aberration in optics.

Future work remains on this topic. Experimentally, a data set is needed that encompasses more frequencies, azimuthal angles, and ranges. Direct measurements of any ISW wavefronts would be extremely valuable. Theoretically, the structure of the horizontal ($x-y$ plane) modes, both trapped and continuous, that is created between the ISWs should be investigated. The ray and PE representations, as well as rough estimates[14] and numerical properties[18] of this structure, have been carried out, but more detailed analysis of the horizontal modes should produce additional insights into the physics of this fascinating ducting effect.

ACKNOWLEDGMENTS

The authors wish to thank the participants of the SWARM'95 experiment for their efforts. This work was supported by the Ocean Acoustics Program at the Office of Naval Research (ONR Grants N00014-01-1-0114 to U.D., and N00014-04-1-0016 to R.P.I.) and by the Russian Foundation For Basic Research (RFBR Grant 03-05-64568-a). This manuscript is also a WHOI contribution.

APPENDIX: Estimation of ISW speed V

The ISW speed V in the SWARM region can be estimated using some canonical models. For a water column with two layers, $H=h_1+h_2=20+50=70\,\mathrm{m}$, where each layer has constant temperature, select $\Delta T=T_2-T_1 \sim 13\,\mathrm{deg}$. It follows that $\Delta\rho\sim 1.7\ \mathrm{kg/m^3}$, so the buoyancy frequency is $N\sim 10\,\mathrm{cycles/h}$. If the ISW train consists of separate KdV solitons, for each of which

$$\zeta=\zeta_0\,\mathrm{sec}\,h^2[(y-VT)/\Delta],$$

where[26]

$$V=c_0+\zeta_0\tilde{\alpha}/3,\quad \Delta=\sqrt{12\tilde{\beta}/\tilde{\alpha}\zeta_0},$$

then

$$c_0=\sqrt{g\frac{\Delta\rho}{\rho}\frac{h_1h_2}{H}},\quad \tilde{\alpha}=c_0\frac{3(h_1-h_2)}{2h_1h_2},$$

$$\tilde{\beta}=c_0\frac{h_1h_2}{6}.$$

For SWARM conditions $c_0\sim 0.55\,\mathrm{m/c}$, $\tilde{\beta}\sim 90\,\mathrm{m^3/s}$, and $\tilde{\alpha}\sim 0.024\,\mathrm{s}^{-1}$. Furthermore, if $\zeta_0\sim 10\,\mathrm{m}$, then $\Delta\sim 70$ m and $V\sim 0.65\,\mathrm{m/s}$. The differences between the speeds of separate solitons of different amplitudes in the train are ignored, so the whole train is assumed to move with the same speed.

[1] J. R. Apel, M. Badiey, C.-S. Chiu, S. Finette, R. H. Headrick, J. Kemp, J. F. Lynch, A. E. Newhall, M. H. Orr, B. H. Pasewark, D. Tielburger, A. Turgut, K. von der Heydt, and S. N. Wolf, "An overview of the SWARM 1995 shallow-water internal wave acoustic scattering experiment," IEEE J. Ocean. Eng. **22**, 465–500 (1997).

[2] J. X. Zhou, X. S. Zhang, and P. H. Rogers, "Resonant interaction of sound waves with internal solitons in the coastal zone," J. Acoust. Soc. Am. **90**, 2042–2054 (1991).

[3] D. Rubenstein and M. N. Brill, "Acoustic variability due to internal waves and surface waves in shallow water," in *Ocean Variability and Acoustics*

Propagation, edited by J. Potter and A. Warn-Varnas (Kluwer Academic, Dordrecht, 1991), pp. 215–228.
[4] R. H. Headrick, J. F. Lynch, and the SWARM group, ''Acoustic normal mode fluctuation statistics in the 1995 SWARM internal wave scattering experiment,'' J. Acoust. Soc. Am. **107**, 201–220 (2000).
[5] R. H. Headrick, J. F. Lynch, and the SWARM group, ''Modeling mode arrivals in the 1995 SWARM experiment acoustic transmissions,'' J. Acoust. Soc. Am. **107**, 220–236 (2000).
[6] B. Pasewark, S. N. Wolf, M. H. Orr, and J. F. Lynch, ''Acoustic intensity variability in a shallow water environment,'' in *Impact of Littoral Environmental Variability on Acoustic Predictions and Sonar Performance*, edited by N. Pace and F. Jensen (Kluwer Academic, Dordrecht, 2002), pp. 11–18.
[7] M. Badiey, Y. Mu, J. F. Lynch, J. R. Apel, and S. N. Wolf, ''Temporal and azimuthal dependence of sound propagation in shallow water with internal waves,'' IEEE J. Ocean. Eng. **27**, 117–129 (2002).
[8] D. Rubenstein, ''Observations of cnoidal internal waves and their effect on acoustic propagation in shallow water,'' IEEE J. Ocean. Eng. **24**, 346–357 (1999).
[9] J. C. Preisig and T. F. Duda, ''Coupled acoustic mode propagation through continental shelf internal solitary waves,'' IEEE J. Ocean. Eng. **22**, 256–269 (1997).
[10] T. F. Duda and J. C. Preisig, ''A modeling study of acoustic propagation though moving shallow-water solitary wave packets,'' IEEE J. Ocean. Eng. **24**, 16–32 (1999).
[11] B. G. Katsnelson and S. A. Pereselkov, ''Resonance effects in sound scattering by internal wave packets in a shallow sea,'' Acoust. Phys. **44**, 684–689 (1998).
[12] S. D. Frank, M. Badiey, J. F. Lynch, and W. L. Siegmann, ''Analysis and modeling of broadband airgun data influenced by nonlinear internal waves,'' J. Acoust. Soc. Am. (to be published).
[13] Y. A. Kravtsov, V. M. Kuzkin, and V. G. Petnikov, ''Perturbation calculation of the horizontal refraction of sound waves in a shallow sea,'' Sov. Phys. Acoust. **30**, 45–47 (1984).
[14] B. G. Katsnelson and S. A. Pereselkov, ''Low-frequency horizontal acoustic refraction caused by internal wave solitons in a shallow sea,'' Acoust. Phys. **46**, 774–788 (2000).
[15] B. G. Katsnelson, S. A. Pereselkov, V. G. Petnikov, K. D. Sabinin, and A. N. Serebryanyi, ''Acoustic effects caused by high-intensity internal waves in a shelf zone,'' Acoust. Phys. **47**, 424–429 (2001).
[16] B. G. Katsnelson and S. A. Pereselkov, ''Space-frequency dependence of the horizontal structure of the sound field in the presence of intense internal waves,'' Acoust. Phys. **50**, 169–176 (2004).
[17] S. Oba and S. Finette, ''Acoustic propagation through anisotropic internal wave fields: Transmission loss, cross-range coherence, and horizontal refraction,'' J. Acoust. Soc. Am. **111**, 769–784 (2002).
[18] S. Finette and R. Oba, ''Horizontal array beamforming in an azimuthally anisotropic internal wave field,'' J. Acoust. Soc. Am. **114**, 131–144 (2003).
[19] D. Tielbuerger, S. Finette, and S. N. Wolf, ''Acoustic propagation through an internal wave field in a shallow waveguide,'' J. Acoust. Soc. Am. **101**, 789–808 (1997).
[20] S. M. Flatte, R. Dashen, W. M. Munk, K. M. Watson, and F. Zacharisen, Sound Transmission Through a Fluctuating Oceran, Cambridge Press, 1979.
[21] F. B. Jensen, W. A. Kuperman, M. B. Porter, and H. Schmidt, *Computational Ocean Acoustics* (Springer, New York, 2000).
[22] H. Weinberg and R. Burridge, ''Horizontal ray theory for ocean acoustics,'' J. Acoust. Soc. Am. **55**, 63–79 (1974).
[23] L. M. Brekhovskikh and Y. P. Lysanov, *Fundamentals of Ocean Acoustics* (Springer, New York, 1991).
[24] A. Ishimaru, Wave Propagation and Scattering in Random Media, Volume II, Academic Press, New York, 1978.
[25] F. D. Tappert, ''The Parabolic Equation Method,'' in *Wave Propagation and Underwater Acoustics*, edited by J. B. Keller and J. S. Papadakis (Springer, New York, 1977), pp. 224–287.
[26] M. D. Collins, ''The adiabatic mode parabolic equation,'' J. Acoust. Soc. Am. **94**, 2269–2278 (1993).
[27] K. Naugolnykh and L. Ostrovsky, *Nonlinear Wave Processes in Acoustics* (Cambridge University Press, Cambridge, 1998).

Geoacoustic inversion with ships as sources

Robert A. Koch[a] and David P. Knobles
Applied Research Laboratories, The University of Texas at Austin, P.O. Box 8029, Austin, Texas 78713-8029

(Received 7 June 2004; revised 10 November 2004; accepted 10 November 2004)

Estimation of geoacoustic parameters using acoustic data from a surface ship was performed for a shallow water region in the Gulf of Mexico. The data were recorded from hydrophones in a bottom mounted, horizontal line array (HLA). The techniques developed to produce the geoacoustic inversion are described, and an efficient method for geoacoustic inversion with broadband beam cross-spectral data is demonstrated. The performance of cost functions that involve coherent or incoherent sums over frequency and one or multiple time segments is discussed. Successful inversions for the first sediment layer sound speed and thickness and some of the parameters for the deeper layers were obtained with the surface ship at nominal ranges of 20, 30, or 50 water depths. The data for these inversions were beam cross-spectra from four subapertures of the HLA spanning a little more than two water depths. The subaperture beams included ten frequencies equally spaced in the 120–200 Hz band. The values of the geoacoustic parameters from the inversions are validated by comparisons with geophysical observations and with the parameter values from previous inversions by other invesigators, and by comparing transmission loss (TL) measured in the experiment with modeled TL based on the inverted geoacoustic parameters. [DOI: 10.1121/1.1848175]

PACS numbers: 43.30.Pc, 43.60.Gk [AIT] Pages: 626–637

I. INTRODUCTION

Sophisticated geoacoustic inversion techniques have been developed and applied to a variety of problems involving shallow water environments with both measured and simulated data.[1–10] Much of the previous work with measured acoustic data was done with transmission loss (TL),[1] arrivals from impulsive sources,[3,7,9] or other special wave forms.[2,5,6,8] There is a significant advantage to using broadband sources for geoacoustic inversions, and these previous analyses have given valuable insight into the requirements for performing successful shallow water inversions with controlled broadband sources. As potential broadband sources for geoacoustic inversions, surface ships in shallow water environments are abundant, but their output spectra are not under measurement control. Battle *et al.* (in Ref. 10, pp. 454–467) discuss inversion with cw lines received on a towed array but emitted at short ranges from the towing vessel. It is the purpose of this paper to consider techniques that can be used in shallow water with broadband data from uncontrolled sources of opportunity at many water depths in range.

To work with sources of opportunity, one issue that must be addressed is that the processing not be dependent on specific knowledge of the source spectrum. This affects the selection of a suitable cost function for optimization. A number of other issues must be addressed to obtain successful inversions in general for shallow water geoacoustic parameter values. Suitable frequency bands, receiver apertures, and source–receiver geometries need to be identified. A seabed description with an adequate level of complexity must be formulated, particularly for areas with soft sediments (sound speed at the top of the sediment less than the sound speed at the bottom of the water column) for which acoustic interaction with sediment sublayers may be significant. Parameter uncertainties need to be determined, and data collection schemes and processing algorithms should be developed to minimize parameter uncertainties in typical high noise shallow water environments. The processing must be robust, i.e., the values obtained for geoacoustic parameters from multiple inversions in the same area should be consistent if the environment does not change, and the signal-to-noise ratio required to achieve robustness needs to be established. The approach taken in the paper is to address these issues within the context of an actual inversion from measured data.

The acoustic data analyzed in this study were collected on a horizontal line array (HLA) deployed on the ocean bottom in the Gulf of Mexico during an experiment designed to support tests of various geoacoustic inversion methods.[9] The data processed for the analysis presented here were from an endfire radial traversed toward the HLA at 8 kt by the experimental platform, the R/V Longhorn. The auxiliary environmental data collected were water column sound speed profiles from measurements of conductivity and temperature as a function of depth (CTD), ship GPS recordings, and bathymetric soundings. Acoustic cw and impulsive sources were deployed on several tracks. Also, previous inversion results and numerous geophysical surveys in the area provide a basic description of the bottom as a soft layer overlying a harder, sand-like layer.[9,11] Table I is the starting geoacoustic profile for the inversions discussed in this paper. The values in Table I are not necessarily physically self-consistent. However, the starting values of the geoacoustic parameters need not be the actual values or consistent with any particular physically reasonable sediment because the solution from the inversion should be independent of the starting values.

[a]Electronic mail: koch@arlut.utexas.edu

TABLE I. Sediment geoacoustic parameter values used to initialize the inversions.

	Layer 1	Layer 2	Half-space
Top sound speed (m/s)	1483.77	1563.37	1697.92
Bottom sound speed (m/s)	1553.63	1680.42	
Density (g/cm^3)	1.72	1.81	1.845
Top attenuation (dB/m kHz)	0.021 54	0.023 66	0.3086
Bottom attenuation (dB/m kHz)	0.033 09	0.078 06	
Thickness (m)	45.1	78.58	

A range independent normal mode model was used to describe the forward propagation because the environment along the selected data track is close to being horizontally stratified.[12] Simulated annealing was chosen to sample the geoacoustic parameter space for the best data-model fit.[13] Both the normal mode and simulated annealing algorithms are well understood, and their selection involves no substantive issues, although practical systems for either range-dependent or real-time implementations may require more sophisticated modeling or inversion techniques for accuracy or efficiency.[10]

To accommodate the lack of knowledge concerning the frequency-dependent phase of the source spectrum, several variants of a cost function using cross-spectra from both elements and subaperture beams were tested.[14,15] Considerations involved in choosing cost functions with cross-spectra were discussed by Frazer and Sun in a geophysical context.[16] Previously, Musil *et al.*[5] investigated the performance of a cost function based on element cross-spectra from a vertical array for multiple time segments, i.e., time series samples on which a fast Fourier transform (FFT) to the frequency domain is performed. Matched field processing with beam data has been examined also.[17,18] The cost functions and uses of beam data for multiple time segments that are examined in the present paper differ in two main aspects from these previous works. First, this paper tests the use of a cost function formed by summing over the off-diagonal cross-spectral matrix elements only, which permits a coherent gain through the sum over frequency components and time segments.[14,15,19,20] For this paper inversions were obtained both from single time segment data and from multiple time segment data. Second, aside from the use of subaperture beam cross-spectra as data in the cost function, each subaperture is treated as a single receiver element with respect to forward model computations, which improves efficiency. In other words the subapertures provide some array gain, but they are still treated as a single omni-directional element in calculating the propagated field. The performance of inversions from single time segments are compared in this paper with inversions from multiple time segments, and inversions from beam data are compared with inversions from element data.

Several validations of the inversion results are presented. To examine the consistency of the values obtained for the geoacoustic parameters, a comparison of the results from inversions with data in different spectral bands and from different temporal segments were performed. Partial distributions of the cost function samples from the inversion were also used to characterize parameter uncertainties. Measured

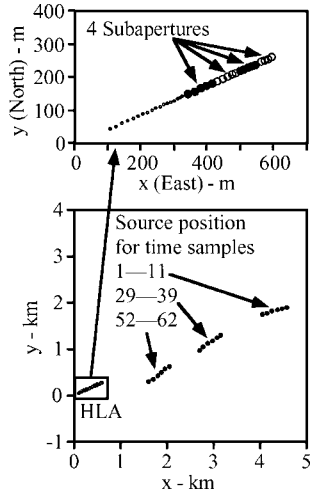

FIG. 1. Location of the HLA, the subapertures used for the inversions, and R/V Longhorn track positions from GPS during the intervals from which data were processed. The position is plotted at every other time sample for each of the three processing intervals.

TL was compared to TL computed using the geoacoustic parameters obtained from the inversion to provide an independent validation of the inversion procedure. The quality of source localizations based on the parameters from the inversions are examined. Finally, time series received from impulsive sources were simulated and compared with the measured data.

The issue with the greatest impact on the inversion results was the nature of the noise field. Although surface shipping is prevalent in the neighborhood of the experimental site, the presence of two seismic sources operating in the area dominated the low frequency bands. The noise field levels fluctuated significantly over tens of seconds and dictated the inclusion of multiple data time segments (temporal averaging) in the cost function to produce consistent results from the inversions.

The organization of the paper is as follows. Section II describes the experiment from which the surface ship data were obtained. Section III discusses the processing used to invert for the geoacoustic parameters from the recordings of surface ship data. Section IV summarizes the results obtained from inversions with single and multiple time segments.

II. EXPERIMENT

An experiment, designed to support shallow water geoacoustic inversion analyses, was conducted in the Gulf of Mexico in February 1998. Details of the experiment and results from geoacoustic inversions of impulsive sources in the area are available in Ref. 9. The data processed for this paper are 32K FFT spectra sampled at 2457.6 Hz. The data were recorded from a 52-element bottom-mounted HLA. The source of interest is the R/V Longhorn as it approached the HLA at 8 kt on one endfire approximately along the 110 m bathymetric contour from north of east. The array geometry and sample positions of the R/V Longhorn during the time segments analyzed in this paper are depicted in Fig. 1. The length of the array is about 530 m. For each of the HLA

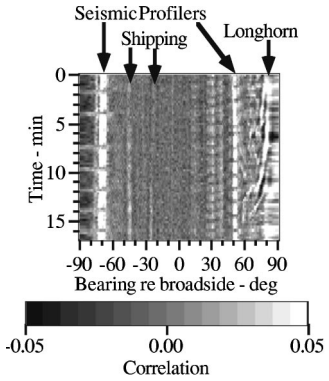

FIG. 2. Bearing-time display for the interval from which data were processed.

hydrophone elements FFT, spectra from 75 time segments were produced from a total interval of nearly 17 min.

During the selected data interval, a number of sources contribute to the acoustic field at the array, as shown in the bearing-time display (BTD) of Fig. 2, which was obtained by cross-correlating adaptively formed subaperture beams.[21–23] The BTD in Fig. 2 shows two seismic profilers, one off each endfire, operating in deeper water east–southeast and southwest of the array. In only a few of the 75 time segments are neither of the seismic sources active. Also evident in Fig. 2 are at least two sources at constant bearing. These sources are thought to be distant surface ships south–southwest of the array. For other frequency bands the BTDs show several other possible surface ship tracks. Finally, the approach of the R/V Longhorn from the east is heralded in the BTD at bearings 60°–90° by the diverging tracks characteristic of multipath arrival structure. (Individual vertical arrivals are manifest on the conical HLA beams as sources with distinct horizontal bearing and differentially become more vertical, i.e., diverge in horizontal bearing, as range decreases.) Endfire beam spectra, shown in Fig. 3, from the eastern subaperture exhibit both the seismic profiler bursts (horizontal bands) and striations (bands tilted from the horizontal) produced by interference between the multipath arrivals from the R/V Longhorn.

The water column sound speed profile shown in Fig. 4 was used for the forward model calculations[12] in the inversions for this paper. It is a coarsely depth sampled representation of the more finely sampled profiles taken in the neighborhood of the array shortly after deployment and at the

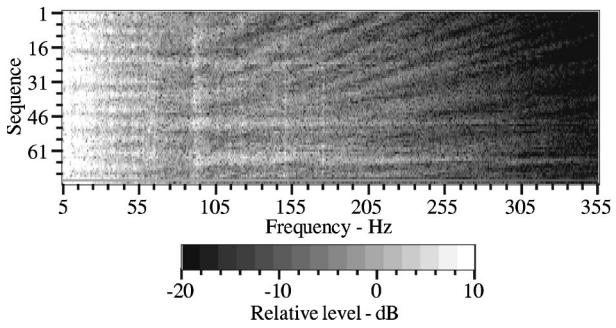

FIG. 3. Eastward endfire beam spectrum from the eastern 26-element subaperture for the interval from which data were processed.

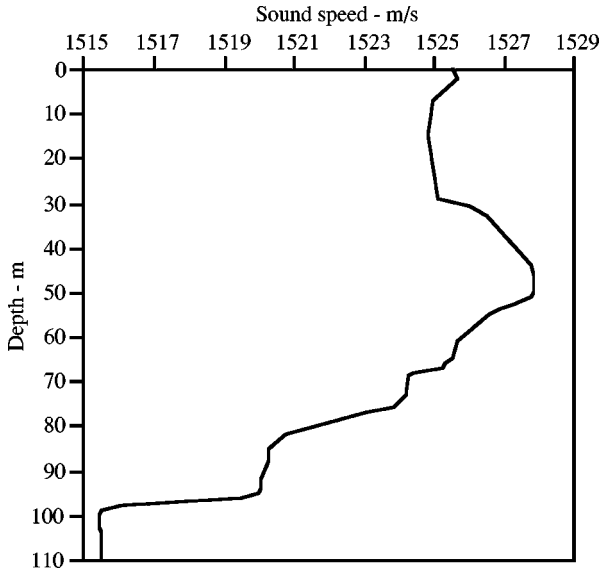

FIG. 4. Water sound speed profile used for the forward propagation model calculations.

eastern endfire 10 km from the array around the time of one of the implosive source deployments.[9] The measured profiles were made about 12 h before the experimental run that produced the data processed for this paper. No profiles from the time of the run are available because it was necessary to terminate the experiment prematurely due to adverse weather development. Inversions like those discussed in this paper were performed with other variants of the measured profiles. These inversions did not produce significantly different values for the well-determined geoacoustic parameters. Results from inversions with higher frequency data than those used in this work might be more dependent on the details of the water sound speed profile in the forward model.

III. PROCESSING SCHEME

A. Sediment parametrization

A previous inversion of data from an impulsive source deployed in the experiment at a range of 10 km was based on a fluid model. For the forward propagation model calculations[12] the fluid sediment description had two layers overlying a homogeneous half-space, which is a coarse realization of the geophysical data in the area. Only the water depth and the parameters for the top sediment layer were obtained.[9] For sources at shorter ranges, the received field may be sensitive to the deeper sediment layer structure. Hence, the inversions for this paper were performed for fluid model parameters in both sediment layers and in the half-space. It was expected that examining cost function distributions assembled from the optimization process would reveal which parameters are either not well determined or otherwise inaccessible.

In the fluid layer sediment description employed for the work described in this paper, the sediment layers each have a thickness, H_i, a linear depth dependent sound speed,

$$c_i(z) = c_{i0} + (z - z_i) g_i , \tag{3.1}$$

a constant density, ρ_i, and a linear depth dependent attenuation,

$$\alpha_i(z)=\alpha_{i0}+(z-z_i)\alpha_i', \tag{3.2}$$

where z_i is the depth of the top of sediment layer *i*. The surficial values of the sound speed and attenuation in the *i*th layer are c_{i0} and α_{i0}, respectively, and g_i and α_i' are the corresponding gradients. The half-space has constant sound speed, c_s, density, ρ_s, and attenuation, α_s. The parametrization selected for this paper uses the water depth, $H_0=z_1$, the layer thicknesses, the half-space and sediment layer densities, the attenuations at the top of the sediment and substrate layers, the sediment layer attenuation depth gradients, the sediment layer sound speed depth gradients, and the ratios of the sound speed at the top of each layer (sediment and half-space) to the speed at the bottom of the previous layer. These sound speed ratios are

$$R_1=c_{10}/c_w, \tag{3.3}$$

$$R_2=c_{20}/c_1(z_1+H_1)=c_{20}/c_1(z_2), \tag{3.4}$$

and

$$R_s=c_s/c_2(z_2+H_2), \tag{3.5}$$

where c_w is the sound speed at the bottom of the water column. Having the sound speed ratios and gradients be annealing parameters means that, for example, adjusting the sound speed at the top of the first layer affects the overall values in the sound speed profile, but preserves the impedance contrasts at the intervening layer interfaces.

B. Cost function

The general form of the cost function selected for the inversions reported in this paper is based on a correlation of hydrophone or beam cross-spectral data with corresponding modeled cross-spectra. Several variants of this general form were examined. These cost function variants tested the effect of frequency averaging over a few hertz about each center frequency, the dependence on the sample of center frequencies, and the effect of including multiple temporal samples. Cross-spectral values were used as data for processing ship noise because they are independent of source phase, which often varies with frequency if the dominant noise excitation processes are uncorrelated across frequency. (In contrast, the phases of the frequency components of an impulsive source wave form are correlated, and a cost function can be derived from the peak correlation of single element measured and modeled time series.[3,9,16])

The cost function variants analyzed for the work presented in this paper have the general form $C(\mathbf{X},\mathbf{Y})=1-c(\mathbf{X},\mathbf{Y})$, where $\mathbf{X}$ is source position at the initial sample time, t_0, and $\mathbf{Y}$ contains the inversion parameters. The data–model correlation of cross-spectra over center frequency, f_0, and time sample, *k*, is given by

$$c(\mathbf{X},\mathbf{Y})=\sum_{k,f_0,i,j} R_{ij}(k,f_0)M_i^*(k,f_0)M_j(k,f_0)/N, \tag{3.6}$$

where *N* is the normalization that gives $-1\leqslant c(\mathbf{X},\mathbf{Y})\leqslant 1$. The cost function $C(\mathbf{X},\mathbf{Y})$ is to be minimized, in which case the data-model correlation $c(\mathbf{X},\mathbf{Y})$ is greatest. In Eq. (3.6) and throughout this paper the dependence on $\mathbf{X}$ and $\mathbf{Y}$ of the modeled element fields, $M_i(k,f_0)$ will be suppressed. The cross-spectrum, $R_{ij}(k,f_0)$, normalized and averaged about f_0, is constructed from the beam data $B_i(k,f)$ and $B_j(k,f)$ for subapertures *i* and *j* at time t_k. For the inversion processing presented in this paper only conventional beams in the frequency domain were constructed. Single hydrophone subapertures are permitted, in which case the beam data reduce to single hydrophone spectra. Thus, the data cross-spectra are

$$R_{ij}(k,f_0)=\sum_{f\approx f_0} B_i(k,f)B_j^*(k,f), \tag{3.7}$$

where each $B_i(k,f)$ is normalized such that

$$1=\sqrt{\sum_i |B_i(k,f)|^2}. \tag{3.8}$$

The beam for B_i at time t_k is pointed from the *i*th subaperture phase center to the postulated source position at $\mathbf{X}+\mathbf{r}(t_k)-\mathbf{r}(t_0)$, where $\mathbf{r}(t_k)$ is the R/V Longhorn position from the GPS reconstruction at time t_k. The modeled field $M_i(k,f_0)$ is propagated from the source postulated at $\mathbf{X}+\mathbf{r}(t_k)-\mathbf{r}(t_0)$ to the phase center of the subaperture *i*, and the modeled fields for each subaperture are normalized such that

$$1=\sqrt{\sum_i |M_i(k,f_0)|^2}. \tag{3.9}$$

The use of cross-spectra in $c(\mathbf{X},\mathbf{Y})$ means that the unknown, frequency-dependent phases in the data from the source wave form can be ignored. The normalizations defined by Eqs. (3.8) and (3.9) were chosen to equally weight the contributions from each frequency, both in the sum over center frequencies in Eq. (3.6) and in the averaging that is performed about the center frequency to construct the cross-spectra $R_{ij}(k,f_0)$ via Eq. (3.7).

Several forms of $c(\mathbf{X},\mathbf{Y})$ were tested. Both single [only the index value $k=0$ in Eq. (3.6)] and multiple time sample inversions were performed, and inversions for cost functions with and without averaging about the center frequencies were made. In addition inversion results were generated for cost function variants in which the main diagonal ($i=j$ terms), or other diagonals offset from the main diagonal, were omitted from the sum in Eq. (3.6). These were compared with the result from an inversion using all of the cross-spectral terms. When all the cross-spectral terms are used, $c(\mathbf{X},\mathbf{Y})$ is a Bartlett-type processor for which the averaging over time samples and center frequencies may be termed *incoherent* in the sense that the contribution to $c(\mathbf{X},\mathbf{Y})$ from each center frequency and time sample is positive. In contrast, omitting the main diagonal terms produces *coherent* temporal and frequency averaging, in the sense that the contributions to $c(\mathbf{X},\mathbf{Y})$ from individual time samples and center frequencies may be positive or negative, i.e., they may constructively or destructively interfere. Previous work[15,19,20] had found that the coherent averaging increased the peak-to-background values of $c(\mathbf{X},\mathbf{Y})$ in matched field localization, which made attractive the present application to geoacoustic

inversion with ships of opportunity as sources. All of the inversion results explicitly displayed in this paper were produced with the cost function obtained by omitting the main diagonal terms. Comparisons of these inversion results with those using a cost function that included the main diagonal terms showed no difference in the parameters which were well determined, as defined in Sec. III F, i.e., the cost functions including and omitting the main diagonal have the same global minimum. Also, the difference between cost functions including and omitting the main diagonal terms decreases as the number of subapertures increases. This is because the ratio of the number of main diagonal to the number of off-diagonal terms, and the relative contribution of the main diagonal terms when included with the off-diagonal terms in the cost function, decreases inversely as the number of subapertures.

For the inversions described in this paper, at each call to the forward model with a new set of geoacoustic parameters, the cost function $C(\mathbf{X},\mathbf{Y})$ is computed for a source depth of 2 m, appropriate for the draft of the R/V Longhorn, on a grid of horizontal positions $\mathbf{X}$ centered at t_0 on the reconstruction position $\mathbf{r}(t_0)$. (Using other source depths from the interval 1–6 m had little impact on the geoacoustic values obtained from the inversion.) The value of the cost function that is returned to the simulated annealing algorithm is the grid minimum, $C(\mathbf{X}_{\min},\mathbf{Y}_{\min})$. The purpose of forming the spatial grid of $C(\mathbf{X},\mathbf{Y})$ is that the matched field localized position of the surface ship varies as the geoacoustic parameters are varied, and using too small a spatial search, e.g., a single point at the GPS position, would magnify the effect of any errors in the assumed position. Even if the ship GPS positions are accurate, errors could still arise due to uncertainty in the position and orientation of the HLA and due to offsets between the time on the clock in the array recording system and the GPS clock. Performing the grid search for the source position, rather than making annealing variables of the source coordinates, is also computationally more efficient for the forward model calculation. This approach may be viewed as a variant of the focalization technique developed by Collins and Kuperman.[24] The results in this paper were obtained using an 11×11 grid of initial positions in the coordinates shown in Fig. 1. The spacing of the grid points in both x and y was 25 m to produce a sample on a 250 m by 250 m horizontal square. For inversions with multiple data time samples, the propagation to the subaperture centers for temporal samples at time t_k is computed from a translation of each of the points in the initial grid by the displacement of the R/V Longhorn from time t_0, as determined from the GPS observations. In actual applications it may be necessary to determine the position, course, and speed of the ship of opportunity as part of the inversion. Thus, the inversion results in this paper have been obtained under optimal conditions with respect to knowledge of the source location. The uncertainties obtained for the geoacoustic parameters will likely be greater, and the requirements for consistency more stringent, when the source position parameters are less certain.

C. Frequency band selection

The spectra from the 52 hydrophones in the array were summed and averaged over frequency for several bands. Examination of the behavior of these averages over the data segment selected for processing showed that bands below 50 Hz are dominated by the seismic sources to such an extent that the approach of the R/V Longhorn is not apparent, whereas the 120–200 Hz band, and to a lesser degree the 50–120 Hz band, shows clearly increasing levels as the R/V Longhorn closes in range to the array. Therefore, it is not surprising that little success or, more important, consistency was obtained for inversions with data outside these two bands, and the best results were obtained with the 120–200 Hz data. All of the inversion results explicitly displayed in this paper were obtained with samples at ten center frequencies, each averaged over 0.4 Hz, equally spaced in the 120–200 Hz band. As discussed in Sec. IV, inversions performed with this frequency sampling from single time samples exhibited unacceptable variability and corresponding lack of robustness. The variability could be reduced somewhat, but insufficiently to achieve robustness, by substantially increasing the number of center frequencies from the same band.

D. Aperture selection

All of the inversion results explicitly displayed in this paper were obtained with beam cross-spectra from the four subapertures indicated in Fig. 1. The easternmost subaperture is comprised of four elements, and the other subapertures each have five elements. The use of subaperture data, instead of the individual element data, reduces the computational load, because model fields must be computed only for propagation from a source to estimated subaperture phase centers.

The subapertures provide some array gain against other, interfering sources. However, the use of subaperture data introduces two risks. One risk is that some multipaths from the source may be excluded from the subaperture beams that are formed, which will reduce the effective source strength and the information available about the bottom structure. The maximum vertical arrival angle spread, estimated from the water sound speed maximum and the sound speed in the bottom halfspace, is about 26° at ranges exceeding a few water depths, whereas the minimum endfire beamwidth, based on the longest subaperture and the highest frequency in the processing band, is about 9°. Another risk is that the modeled description of propagation from the source to a single element at the estimated position of the subaperture phase center may not correctly represent the signal captured in the subaperture beam, e.g., because the effective position of the subaperture is not at the estimated phase center. (The position of the subaperture phase center is estimated by the average of the element positions.)

Otherwise, the particular choice of subapertures exhibited in Fig. 1 is somewhat arbitrary, and the length and number of elements in the HLA permits a variety of possibilities with both shorter and longer total aperture. A few inversions with the same number of subapertures from both longer and shorter segments of the HLA were performed. Inversions with longer total aperture gave somewhat better results, and

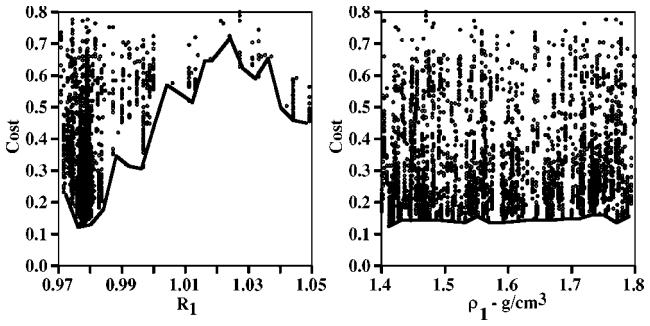

FIG. 5. Distributions of cost function values for the ratio of the surficial sediment to bottom water sound speed and the first layer density from a sample inversion.

inversions with shorter total aperture were less robust. Typically, the use of the total available aperture is desirable.

E. Annealing schedule

After some initial efforts to obtain geoacoustic inversions from various intervals of the selected data set, it was realized that the noise from the seismic profiling activity significantly altered the structure of the cost function on the space of geoacoustic parameter values. In fact, it became apparent that determining whether a sufficiently well-defined cost function minimum even existed was much more important than locating the exact position of a minimum in a cost function dominated by noise fluctuations. With that understanding, the appropriate choice of simulated annealing parameters is one that provides a sampling of the geoacoustic parameter space sufficient to reveal a broad minimum, and that does so efficiently. It was found that a total of 4800 cost function samples using a temperature reduction factor of 0.9 and 12 iterations per parameter per temperature from an initial temperature of 0.1 were sufficient to yield good representations of the cost function envelopes discussed in Sec. III F.[13,14] In addition, all of this paper's results are from inversions initialized from the same set of geoacoustic parameter values. Subsequent optimizations with more extensive searches and from other initializations confirmed the results from the abbreviated sampling.

F. Uncertainty characterization

The quantification of errors in the parameter values obtained from a geoacoustic inversion is necessary both to appreciate the significance of any of the values reported and to permit estimates of possible errors in predictions derived from those values. Some recent work has focused on a rigorous theoretical development of techniques for estimating parameter uncertainties and the application of these techniques to the analysis of experimental data.[8] For the restricted sampling approach taken in this work, a more qualitative approach was adopted.

The cumulative sample of the cost C as a function of the annealing parameters can be displayed as a distribution of values versus any one of the annealing parameters.[9] The inversion parameters for the distributions in Fig. 5 are the ratio of the surficial sediment and bottom water sound speeds, R_1 from Eq. (3.3), and the first layer density, ρ_1. Note that the same set of cost function values appear in each of the distributions in Fig. 5.

Also shown with each of the two distributions in Fig. 5 is the envelope of the distribution minima. In the figures that follow, just the envelope of the distribution minima for each inversion parameter will be displayed, instead of the whole distribution of cost function values. This will be sufficient to characterize the outcome of the inversion and will permit the results of several inversions to be shown simultaneously. For all of these displays, the envelopes were estimated by dividing the allowed range for each parameter during the inversion into 20 equal bins. Then, the minimum cost function value in each parameter bin is assigned to the envelope value at the bin center.

The two distributions of cost function values shown in Fig. 5 differ significantly. The cost function values between 0.1 and 0.2 that comprise the minimum around the ratio $R_1 \approx 0.975$ are spread almost uniformly across the whole range of the density, ρ_1. The reader should keep in mind that the distributions shown in Fig. 5 constitute a limited sample of the parameter space. The value obtained for R_1 at the minimum cost function value found during the annealing is likely to be close to the global minimum, whereas the value of ρ_1 at the global cost function minimum might differ significantly from the value obtained from the annealing process represented in Fig. 5. Thus, cost function distributions that have an envelope of minimum cost values like the one for ρ_1 suggest that the corresponding parameter values determined by the inversion are more uncertain than the values of parameters for which the envelope of minimum cost function values has a well-defined minimum, like the one for R_1.

A caveat applies to the interpretation of displays such as those in Fig. 5 and the remainder of this paper. The exhibition of a narrow minimum in a cost function distribution guarantees neither the presence of the global cost function minimum at that geoacoustic parameter value nor the agreement of the geoacoustic parameter value at that minimum with its actual value for the ocean sediment. In principle, the solution obtained by the annealing algorithm will be close to the global minimum if an appropriate annealing schedule is completed. However, as previously noted, the schedule used for the inversions presented in this paper are significantly abbreviated, and the solutions obtained thereby need not necessarily be the global minimum. Regarding the agreement of the geoacoustic parameter values at the global minimum of the cost function with the actual geoacoustic parameter values for the sediment, several factors may produce a global minimum for parameter values far from the true sediment values. These factors include errors in the assumptions that the bottom is flat, the true water sound speed profile is the one shown in Fig. 4, the actual array element locations are known, and the geoacoustic structure is range independent and is described by the parametrization given in Sec. III A. The results in Sec. IV suggest that the presence of significant noise from sources other than the surface ship is the most important factor accounting for the disagreements between true sediment parameter values and the location of global cost function minima that were identified in this work. A

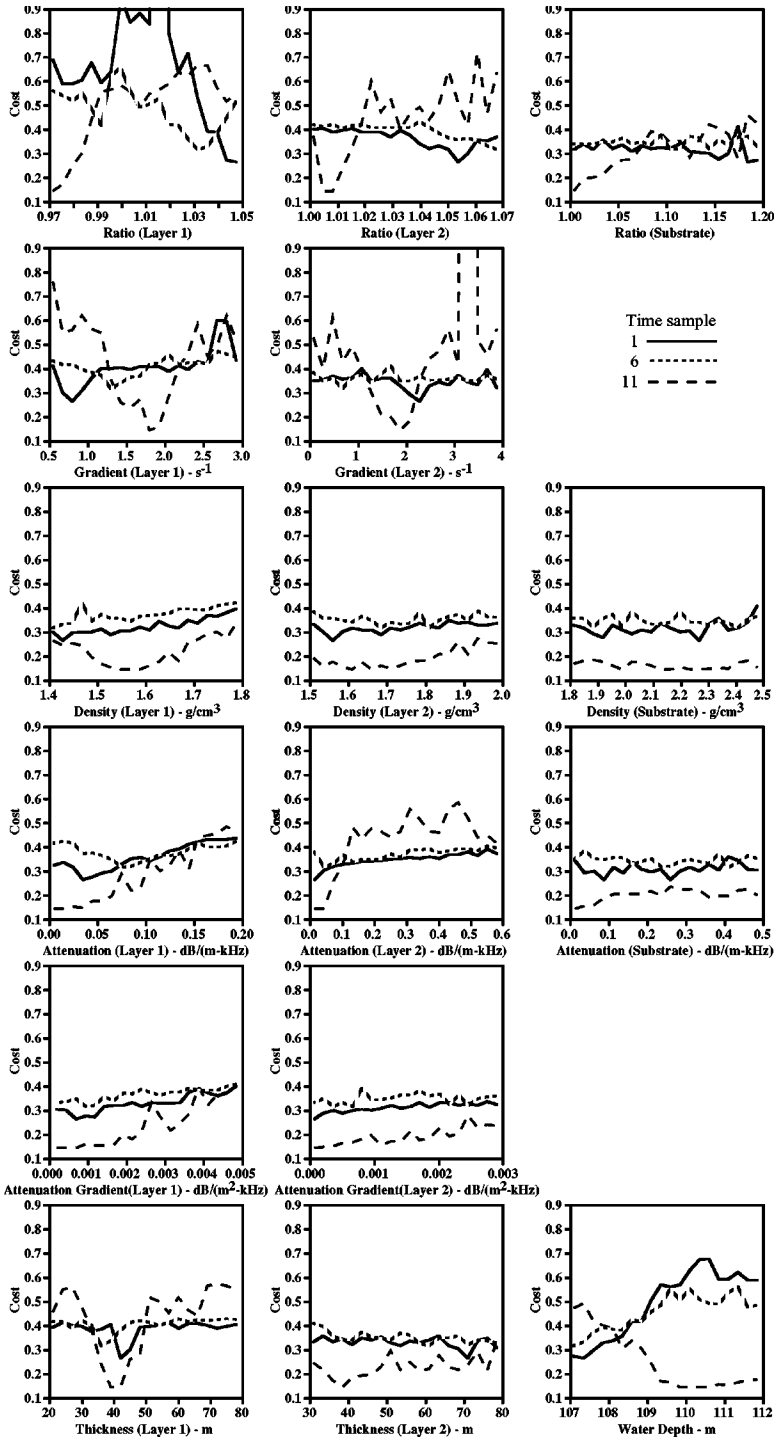

FIG. 6. Distributions of cost function values for each of the inversion parameters from separate inversions with time samples 1, 6, and 11.

technique that reduces the occurrence of this event is demonstrated in Sec. IV B.

IV. INVERSION RESULTS

A. Processing with single time samples

The initial stages of the analyses discussed in this paper emphasized the inversion of single data FFT time samples to examine the operation of the algorithm. After ascertaining that the algorithm was functioning correctly, considerable variability was observed among the geoacoustic parameter solutions from the inversion of different data samples. Especially disconcerting was the observation that solutions from consecutive data time samples might differ significantly, e.g., the sound speed ratio, R_1, might be less than unity in the solution with one data time sample, but the solution with the next data time sample would be significantly greater than unity. These solutions represent entirely different sediments, but neither could be accepted or rejected in the absence of supporting information.

The cost function distribution minimum envelopes in Fig. 6 illustrate the inconsistencies observed in the results

from inversions with single time samples. The envelopes of the distribution minima are from processing time samples 1, 6, and 11 independently. In each case, the R/V Longhorn is at a nominal range of 4 km (cf. Fig. 1 and the first 2 min of Fig. 2). The processing details are described in Sec. III. There is one column in the figure for each layer, except the water depth occupies the lower right slot instead of a substrate thickness. There is one row in the figure for each class of layer parameter, except the substrate is a half-space and has no gradient or thickness.

The general features of the inversion solutions from the data in these three time samples, as exhibited by the distribution envelopes in Fig. 6, are: (1) well-defined minima for most sound speed ratios, sound speed gradients, and layer thickness values; (2) ill-defined minima for most density and attenuation values. These observations are in qualitative agreement with results from previous inversion work; namely, surface sound speed ratios can usually be determined, but density and attenuation values tend to be less well defined, and half-space parameters are mostly inaccessible except at ranges for which there is significant energy from deeply penetrating sediment paths.[4,9] The inconsistencies among the solutions that are of greatest concern are seen in the envelopes for the first layer sound speed ratio and gradient, because these parameters have significant impact on TL predictions for soft sediments. The minima for time samples 1 and 6 are at sound speed ratios greater than unity, but for sample 11 the minimum is at a ratio less than unity. Also, for time sample 1 the cost function minimum is at a sound speed gradient less than unity, but for time sample 11 the gradient at the minimum is greater than unity. Similar variability was found in the solution for the first layer parameter values obtained from single time sample data from the time sample intervals 29–39 and 52–62.

Extensive tests with other frequency sampling, both for different sets of center frequencies, with and without averaging, and for a greater or fewer number of center frequencies, failed to make the inversion solutions of the single time sample data more robust. The number of independent (beam cross-spectral) data samples in the cost function $C(\mathbf{X},\mathbf{Y})$ for each inversion was $6\times10=60$, i.e., at each of the ten center frequencies there are six off-diagonal cross-spectra formed from pairs of the four subaperture beam spectra. Of concern is the fact that 60 independent data samples might be insufficient to determine 16 parameters should all of them be accessible. (Data independence is used here in the sense of sufficiently separated samples of the propagation in range and frequency.) To make the number of independent data samples comparable to that used for inverting with multiple time samples, as discussed in Sec. IV B, inversions with 67 center frequencies from the band 120 to 200 Hz were performed on the set of single time samples. With this increase in the number of independent data samples for each inversion to $6\times67=402$, the variation in the resulting solutions for the geoacoustic parameter values was reduced from that exhibited in Fig. 6, but unacceptable values for one or more of the first layer ratio, gradient, and thickness values were still obtained from the majority of the single time sample inversions.

Variations of the starting environment from that in Table I, variations of the annealing schedule, or variations in the composition of the annealing parameter sets also failed to produce relevant changes in the single time sample solutions. Likewise, using element data instead of beam data, changing the frequency band, including the diagonal terms in the cost function, or excluding other diagonals all failed to produce consistent solutions from one time sample to another. In short, the great variability in the solutions obtained from single time sample data appears to be representative of the variation of the actual global cost function minima for the acoustic fields that were present from one time sample to another. The BTD in Fig. 2 and the spectrum in Fig. 3 suggests the possibility that noise from the seismic profilers might be responsible for the variability in the inversion solutions of the single time sample data.

B. Processing with multiple time samples

Having exhausted the possible ways of performing inversions with single time sample data, inversions with multiple FFT time samples were performed. In the discussion that follows, results are presented for inversions with multiple time samples from the three sets identified in Fig. 1. Each of these sets of time samples spans a period of approximately 2.5 min. For the inversion with each time sample set 1–11, 29–39, and 52–62, subaperture beam cross-spectra for six time samples (every other FFT) were selected as data. Thus, the number of independent, complex beam cross-spectral data from the six time samples (independent in the sense of being distinct background noise samples) and ten center frequencies for each inversion is $6\times6\times10=360$. The cost function distribution minimum envelopes from the inversions with each of these sets of time samples are shown in Fig. 7. Table II gives the geoacoustic parameter values from the solution using time samples 29–39.

The general features of the multiple time sample inversions, as exhibited by the distribution envelopes in Fig. 7, are: (1) consistency among the solutions for the values of geoacoustic parameters for which the distribution envelopes for each of the time sample sets show a well-defined minima, e.g., the sound speed ratios and gradients for both sediment layers and the thickness of the first layer; (2) a well-defined minimum in the cost function distribution for the substrate to bottom sediment sound speed ratio is found at shorter ranges (time samples 52–62, nominally 1.5 km); (3) the development of a minimum in the cost function distribution for the first layer density and attenuation parameters at longer ranges (time samples 1–11, nominally 4 km).

The consistency among solutions for different source positions that the multiple time sample inversions provide is not due solely to the addition of data samples. Including more center frequencies in the processing of single time sample data did reduce some of the variability in the solutions but was insufficient to identify a single definitive value for any of the sediment parameters. Instead, the robustness of the multiple time sample inversions comes from processing the R/V Longhorn motion against the temporal variability of the noise. With single time sample data it is possible that components of the noise field can contribute to the cross-

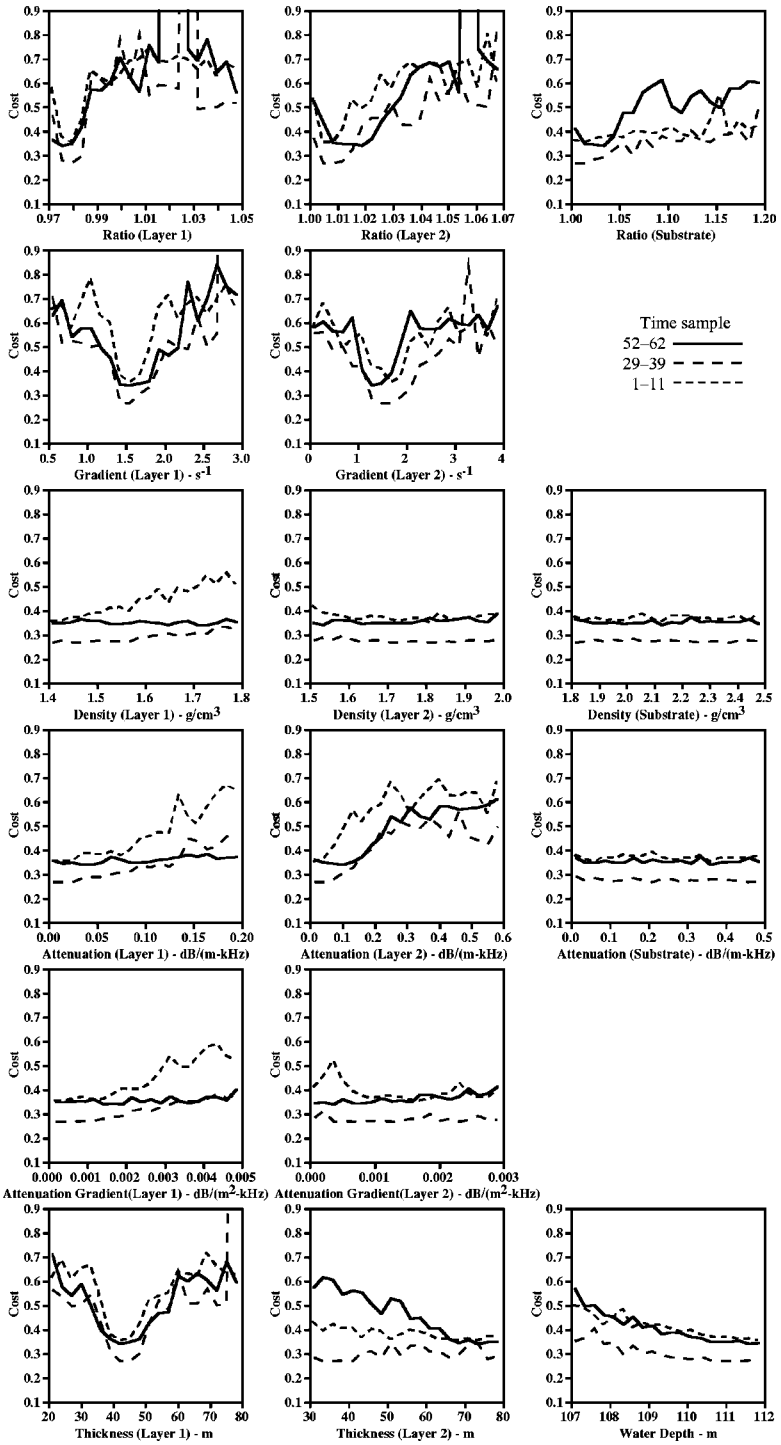

FIG. 7. Distributions of cost function values for each of the inversion parameters from separate inversions, each with multiple time samples. In each inversion every other time sample from the list in the legend is used.

spectral data in such a way as to mimic the field that the R/V Longhorn would produce if the sediment geoacoustic parameters had values significantly different from truth. On the other hand, the variability of the received field from the R/V Longhorn displacement can be modeled using the track reconstruction. With the correct bottom description, the resulting cross-spectral model components are much less likely to match the temporal variation produced in the measured cross-spectral data by the noise sources.

The solutions from the three multiple time sample inver-

TABLE II. Sediment geoacoustic parameter values from the inversion with time samples 29–39.

	Layer 1	Layer 2	Half-space
Top sound speed (m/s)	1486.4	1566.7	1638.7
Bottom sound speed (m/s)	1551.4	1619.6	
Density (g/cm^3)	1.41	1.71	2.26
Top attenuation (dB/m kHz)	0.016	0.039	0.465
Bottom attenuation (dB/m kHz)	0.035	0.062	
Thickness (m)	43.6	34.1	

TABLE III. Comparisons of selected geoacoustic parameters from first sediment layer with previously reported values for GEMINI location.

	Present	Knobles	Rubano	Lynch *et al.*	Collins *et al.*
Sound speed ratio	0.9808	0.9744	0.9820	0.9840	0.9710
Sound speed gradient (l/s)	1.49	1.74	···	2.25	2.03
Density (g/cm^3)	1.41	1.51	1.40	1.56	1.66
Top attenuation (dB/m kHz)	0.016	0.010	···	···	0.022

sions differ in the values for the parameters which do not exhibit a well-defined minima in the distribution envelopes shown in Fig. 7. The main differences among the solutions are in the density and attenuation profile for the first and second layers and in the thickness of the second layer. In contrast to the 34 m value shown in Table II, the inversions from time samples 1 to 11 and 52 to 62 both produced a value of 73 m for the thickness of the second layer. For the first and second layer densities, the inversion from time samples 52 to 62 produced values of 1.71 and 1.55 g/cm^3, respectively. However, the most significant differences among the solutions from the three sets of time samples are in the values of the first layer attenuation. The solution from time samples 1 to 11 for the attenuation at the top and bottom of the first layer are 0.006 and 0.020 dB/m/kHz, respectively, and the corresponding values in the solution from time samples 52 to 62 are 0.035 and 0.098 dB/m/kHz.

C. Validation

Several approaches can be taken to validate the inversion solutions. First, the layer sound speed ratios and thicknesses are in qualitative agreement with the geophysical observations.[11] Second, Table III shows that the result for the water–sediment sound speed ratio from the inversion with time samples 29–39 agrees with that obtained from previous inversions with other acoustic data collected in the area.[1,9,25,26] Third, TL modeled from the inversion solutions can be compared with the measured TL for the experimental site. Figure 8 shows such a comparison for the solution from the inversion with time samples 29–39. A corresponding comparison (not shown) for the result from time samples 1 to 11 shows less modeled loss from that solution, which produces better agreement with the data than seen in Fig. 8 for the three lower frequencies but underestimates the loss for the highest frequency. Not surprisingly, the modeled TL for the solution from time samples 52 to 62 (also not shown) is much too high. This variation in the overall modeled TL levels among the solutions from the three sets of time samples is almost entirely attributable to the differences in their attenuation values in the first sediment layer.

A fourth form of validation is to use data independent of that employed for the inversions to generate cost function ambiguity surfaces, representing localizations of the R/V Longhorn, for each of the multiple time sample inversion solutions. This was done for an ambiguity surface on the horizontal plane for a source depth of 2 m using element data, instead of subaperture data, with 0.83 Hz averages

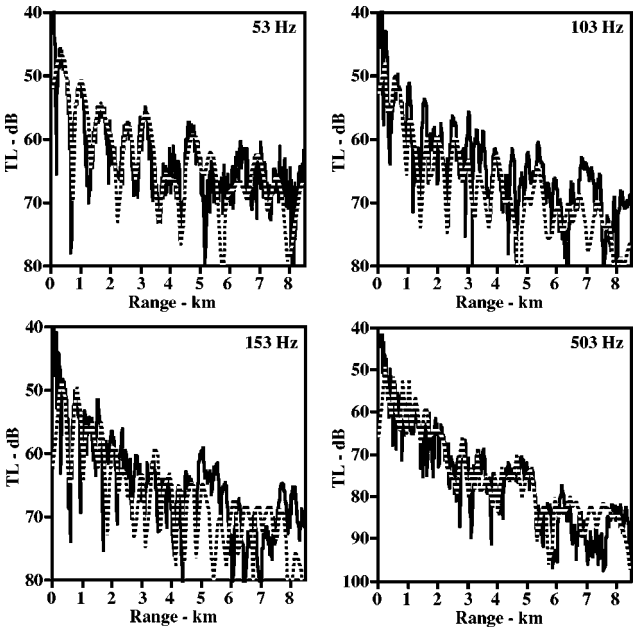

FIG. 8. Comparison of measured transmission loss (solid) with modeled transmission loss (dashed) using the geoacoustic solution from the inversion with time samples 29–39. Source depth is 29.5 m.

about 16 center frequencies from the 50 to 129 Hz band, and about 66 center frequencies from the 100 to 258 Hz band. Figures 9(a) and 9(b) show the ambiguity surfaces obtained in these two bands from the geoacoustic inversion solution with time samples 29–39. Similar results were obtained with the geoacoustic parameter solutions from time samples 1 to 11 and 52 to 62. The position of the R/V Longhorn from the GPS track reconstruction is at the center of each of the four displays in Fig. 9. For all three geoacoustic solutions from Fig. 7 and for both frequency bands, a minimum of the cost function over a rectangle 1700 m by 1200 m was within 250 m of the position of the R/V Longhorn given by the track

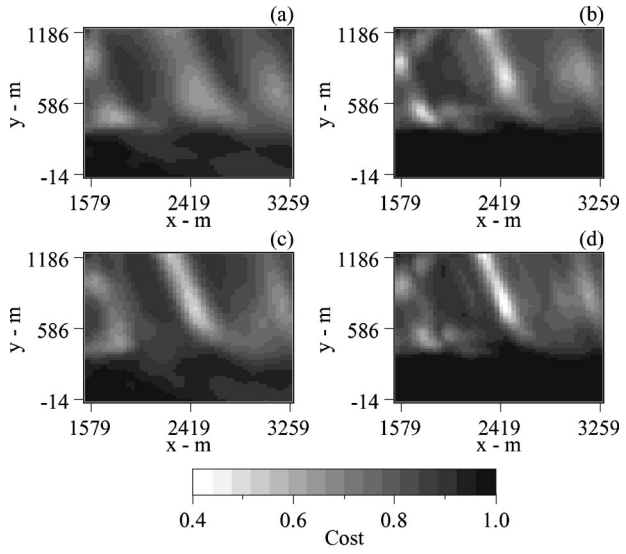

FIG. 9. Localizations with time samples 45–55. Source depth is 2 m. (a) 50–129 Hz with solution obtained from inversion with time samples 29–39. (b) 100–258 Hz with solution obtained from inversion with time samples 29–39. (c) 50–129 Hz with modified solution. (c) 100–258 Hz with modified solution.

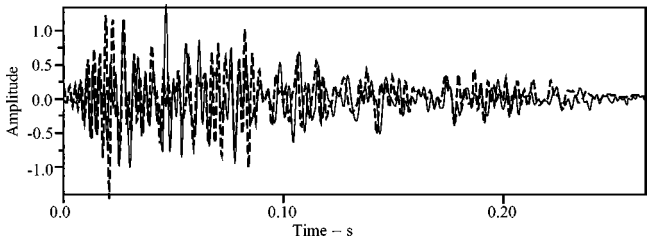

FIG. 10. Comparison of measured (solid) and simulated (dashed) time series. Source depth is 30 m.

reconstruction. Except for the result shown in Fig. 9(a), the positions of these cost function minima were within 50 m of each other. By modifying the geoacoustic solution obtained from time samples 29 to 39 this discrepancy was removed. The modification was to adjust the second layer thickness to the 73 m value in the other two solutions without changing the values of the other geoacoustic parameters in the solution from time samples 29 to 39. The localizations in the two frequency bands with this modified geoacoustic solution are shown in Figs. 9(c) and 9(d). It is interesting to note that this modification of the inversion solution produces no noticeable changes from Fig. 8 for the modeled TL.

A final form of validation is to compare measured time series data from the light bulb implosions that were used for inversions in previous work with simulated time series generated for geoacoustic parameter solutions.[9] The time series simulated from the geoacoustic solution with time samples 1–11 is compared in Fig. 10 with the measured time series from a light bulb imploded at a range of approximately 10 km along the eastern endfire of the array (cf. Fig. 1 and details in Ref. 9). Qualitatively, the measured and modeled time series both show several large amplitude arrivals within the first 0.1 s, followed by a larger number of arrivals with smaller and successively decreasing amplitudes over an interval of approximately 0.15 s. The latter set of arrivals are much more rapidly truncated in time series (not shown) generated with the solutions from time samples 29 to 39 and 52 to 62, because the attenuations in those solutions are too high.

V. CONCLUSION

A shallow water, broadband geoacoustic inversion technique for HLA data from a surface ship was demonstrated. The inversion technique was demonstrated with measured data and does not require knowledge of the spectrum of the surface ship. In addition a method was demonstrated for using data from multiple subaperture beams that is much more efficient for the forward model calculations than using all the corresponding individual hydrophone data. Performing a single inversion with multiple time samples and accounting for source motion was shown to give consistent results from different sections of the source track, whereas geoacoustic parameter values obtained from inversions of single time segments were inconsistent with each other. The inversion technique was demonstrated to permit the determination of the sediment geoacoustic structure through multiple layers, at least for the soft sediment present in the Gulf of Mexico environment in which the experiment was performed. The parameters that were determined most robustly from the inversions with multiple time samples were the sound speed ratio, sound speed gradient, and thickness for the first sediment layer. The values of the first sediment layer density and attenuation were not robust, but the cost function distributions suggest that inversions with sources at longer ranges may make these parameters more accessible. Values for the second layer sound speed ratio and sound speed gradient, though slightly less robust than for the corresponding first layer parameters, were also obtained. Obtaining robust values for the parameters of the deeper sediment layers requires data from sources at shorter ranges.

ACKNOWLEDGMENT

This work was supported by the Office of Naval Research.

[1] M. D. Collins, W. A. Kuperman, and H. Schmidt, ''Nonlinear inversion for ocean-bottom properties,'' J. Acoust. Soc. Am. **92**, 2770–2783 (1992). The references in this article summarize the earliest work on the topic.
[2] D. F. Gingras and P. Gerstoft, ''Inversion for geometric and geoacoustic parameters in shallow water: Experimental results,'' J. Acoust. Soc. Am. **97**, 3589–3598 (1995). This article summarizes the early work on combining localization with geoacoustic inversion.
[3] D. P. Knobles and R. A. Koch, ''A time series analysis of sound propagation in a strongly multipath shallow water environment with an adiabatic normal mode approach,'' IEEE J. Ocean. Eng. **21**, 1–13 (1996).
[4] ''Special Issue: Benchmarking Geoacoustic Inversion Methods,'' J. Comput. Acoust. **6**, 83–97 (1998). Papers from the Geoacoustic Inversion Workshop held in Vancouver, BC, 24–26 June, 1997. These articles survey then state-of-the-art geoacoustic inversion for range invariant environments with applications to simulated data.
[5] M. Musil, N. R. Chapman, and M. J. Wilmut, ''Range-dependent matched-field inversion of SWellEX-96 data using the downhill simplex algorithm,'' J. Acoust. Soc. Am. **105**, 3270–3281 (1999). This article summarizes the early work on geoacoustic inversion for range-dependent environments.
[6] M. R. Fallat, P. L. Nielsen, and S. E. Dosso, ''Hybrid geoacoustic inversion of broadband Mediterranean Sea data,'' J. Acoust. Soc. Am. **107**, 1967–1977 (2000).
[7] P. Pignot and N. R. Chapman, ''Tomographic inversion of geoacoustic properties in a range-dependent shallow-water environment,'' J. Acoust. Soc. Am. **110**, 1338–1348 (2001).
[8] S. E. Dosso and P. L. Nielsen, ''Quantifying uncertainty in geoacoustic inversion. II. Application to broadband, shallow-water data,'' J. Acoust. Soc. Am. **111**, 143–159 (2002).
[9] D. P. Knobles, R. A. Koch, L. A. Thompson, K. C. Focke, and P. E. Eisman, ''Broadband sound propagation in shallow water and geoacoustic inversion,'' J. Acoust. Soc. Am. **113**, 205–222 (2003).
[10] ''Special Issue on Geoacoustic Inversion in Range-Dependent Shallow-Water Environments,'' IEEE J. Ocean. Eng. **28**, (2003). Papers on state-of-the-art applications with simulated data from the Geoacoustic Inversion Technology Workshop held in Gulfport, MS, 14–17 May, 2001.
[11] H. L. Berryhill, Jr., *Late Quaternary Facies and Structure, Northern Gulf of Mexico*, AAPG Studies in Geology Vol. 23 (The American Association of Petroleum Geologists, Tulsa, Oklahoma, 1986).
[12] E. K. Westwood, C. T. Tindle, and N. R. Chapman, ''A normal mode model for acousto-elastic ocean environments,'' J. Acoust. Soc. Am. **100**, 3631–3645 (1996).
[13] W. L. Goffe, G. D. Ferrier, and J. Rogers, ''Global optimization of statistical functions with simulated annealing,'' J. Econometr. **60**, 65–99 (1994).
[14] R. A. Koch, D. P. Knobles, T. B. Neilsen, and M. S. Haire, ''Geoacoustic inversion using surface ship sources and HLA beam data,'' J. Acoust. Soc. Am. **109**, 2394 (2001).
[15] D. P. Knobles, R. A. Koch, and M. S. Haire, ''Geoacoustic inversion studies,'' Proceedings of MTS/IEEE Oceans 2001 Conference, Honolulu, HA, 2001, pp. 737–744.

[16] L. N. Frazer and X. Sun, ''New objective functions for waveform inversion,'' Geophysics **63**, 213–222 (1998).
[17] T. C. Yang and T. Yates, ''Matched-beam processing: Application to a horizontal line array in shallow water,'' J. Acoust. Soc. Am. **104**, 1316–1330 (1998).
[18] H. Cox, R. M. Zeskind, and M. Myers, ''A subarray approach to matched field processing,'' J. Acoust. Soc. Am. **87**, 168–178 (1990).
[19] E. K. Westwood, ''Broadband matched-field source localization,'' J. Acoust. Soc. Am. **91**, 2777–2789 (1992).
[20] D. P. Knobles and S. K. Mitchell, ''Broadband localization by matched-fields in range and bearing in shallow water,'' J. Acoust. Soc. Am. **96**, 1813–1820 (1994).
[21] H. Cox, R. M. Zeskind, and M. M. Owen, ''Robust adaptive beamforming,'' IEEE Trans. Acoust., Speech, Signal Process. **ASSP-35**, 1365–1376 (1987).
[22] T. R. Messerschmitt and R. A. Gramann, ''Evaluation of the dominant mode rejection beamformer using reduced integration times,'' IEEE J. Ocean. Eng. **22**, 385–392 (1997).
[23] T. M. Redheendran, ''Initial evaluation of the dominant mode rejection beamformer,'' J. Acoust. Soc. Am. **104**, 1331–1344 (1998).
[24] M. D. Collins and W. A. Kuperman, ''Focalization: Environmental focusing and source localization,'' J. Acoust. Soc. Am. **90**, 1410–1422 (1991).
[25] L. A. Rubano, ''Acoustic propagation in shallow water over a low-velocity bottom,'' J. Acoust. Soc. Am. **67**, 1608–1613 (1980).
[26] J. F. Lynch, S. D. Rajan, and G. V. Frisk, ''A comparison of broadband and narrow-band inversions for bottom geoacoustic properties at a site near Corpus Christi, Texas,'' J. Acoust. Soc. Am. **89**, 648–665 (1988).

The reflection of ultrasound from partially contacting rough surfaces

Ruth Thomas, Bruce W. Drinkwater,[a] and Dimosthenis Liaptsis
Department of Mechanical Engineering, University of Bristol, Bristol, BS8 1TA, United Kingdom

(Received 19 August 2004; revised 26 October 2004; accepted 27 October 2004)

Ultrasound is commonly used to detect and size cracks in a range of engineering components. Modeling techniques are well established for smooth and open cracks. However, real cracks are often rough (relative to the ultrasonic wavelength) and closed due to compressive stress. This paper describes an investigation into the combined effects of crack face roughness and closure on ultrasonic detectability. A contact model has been used to estimate the size and shape of scatterers (voids) at the interface of these rough surfaces when loaded. The response of such interfaces to excitation with a longitudinal ultrasonic pulse over a wide range of frequencies has been investigated. The interaction of ultrasound with this scattering interface is predicted using a finite-element model and good agreement with experiments on rough surfaces is shown. Results are shown for arrays of equi-sized scatterers and a distribution of scatterer sizes. It is shown that the response at high frequencies is dependent on the size, shape, and distribution of the scatterers. It is also shown that the finite-element results depart from the mass–spring model predictions when the product of wave number and scatterer half-width is greater than 0.4. © *2005 Acoustical Society of America.* [DOI: 10.1121/1.1835505]

PACS numbers: 43.35.Cg [YHB] Pages: 638–645

I. INTRODUCTION

Ultrasonic inspection is a useful tool in the nondestructive testing of structures, and the technique is well established. However, many engineering components can only be inspected when out of service, often when compressive stresses are present. The cracks will tend to close when compressive stresses are present, making detection more difficult. For example, aircraft wings are inspected when the aircraft is on the ground and the bottom skin of the wing is in compression. When in the air, the wing of the aircraft is subjected to cyclic tensile loads, allowing propagation of cracks. The detection and sizing of these types of cracks is not clearly understood and can result in an underestimation of the size of cracks and, in some cases, the presence of the cracks can be difficult to determine.

Current models of the interaction of ultrasound with cracks assume the cracks are smooth compared with the wavelength of the ultrasonic excitation. For example, Chapman[1] has developed a system model that can be applied in the ultrasonic inspection of smooth and open planar cracks that are at least 2 wavelengths in size. To date, researchers[2–10] have modeled the effect of compressive stress on the interface by assuming that the contacting surfaces behave in a spring-like manner. Such models are only valid if the wavelength of the ultrasound is considerably larger than the scatterer size.[10] For example, Baik and Thompson[2] developed a quasistatic mass–spring model to predict the interaction of ultrasound with interfaces consisting of embedded pores or inclusions. Margetan *et al.*[3] then measured the reflection from interfaces containing pores or inclusions with known characteristics and geometry, demonstrating good agreement with the mass–spring model. Haines[4] considered the interaction of ultrasound with a partially contacting solid–solid interface. He used statistical data from the surface roughness profile and an elastic contact model to predict the contact area at the interface, and thus obtained the reflection coefficient via a spring model. Nagy[5] used values of normal and transverse stiffness to distinguish between different types of imperfect interfaces such as kissing, partial, and slip bonds. A spring model approach was used by Thompson and Fiedler[6] to investigate the effects of crack closure on the ultrasonic measurements at a fatigue crack tip. Laverentyev *et al.*[7] predicted the response of two parallel interfaces, such as occurs in an adhesive bond, by modeling the interfaces as a series of springs. The description of the interface region as a thin ''effective'' layer with average effective properties has been investigated by Rokhlin and Wang.[8] They showed that in the low-frequency regime, such a layer model was equivalent to a spring model. Baltazar *et al.*[9] extended the spring model, using normal and transverse springs, to predict both the normal incidence and oblique incidence reflection coefficients of a rough contacting interface.

For the rough surfaces of a crack subjected to high-frequency ultrasonic excitation, when the void sizes at the interface are comparable to the wavelength of the ultrasonic wave, spring models are known to lose their validity.[2,10] Some researchers[11–15] have developed analytical models of the interaction of ultrasound with a range of scatterers, including single spherical cavities and penny-shaped cracks as well as arrays of cracks and spheres, valid at any frequency. Of most relevance to this paper, Rose[11] used an analytical independent scattering model to predict the reflection from uniform arrays of voids and inclusions in a diffusion bond. A number of authors[16,17] have also successfully used finite-element analysis as an alternative to these analytical scatter-

[a]Electronic mail: b.drinkwater@bristol.ac.uk

ing models, the main attractions being that the finite-element model is not restricted to one scatterer geometry and can be used in both the near- and far fields of the scatterers.

In this paper, a novel model of the interaction of ultrasound with a partially closed rough crack is described. This model is developed in two stages. First, a plastic contact model is used to predict the contact geometry at the solid–solid interface. Second, a finite-element model is used to predict the elastic interaction of ultrasound with the solid–solid interface. This model is valid beyond the low-frequency limitations of the previously used spring models. The limit of validity of the spring (or mass–spring) model of a solid–solid interface is explored and simple rules for its application defined. The results from the contact model and finite-element model are then used to explain experimental measurements of the reflection coefficient of partially contacting rough surfaces.

II. EXPERIMENTAL MEASUREMENT OF REFLECTION COEFFICIENT

Experiments that represent cracks under compressive load have been carried out to investigate the response of rough surfaces to ultrasonic excitation. The flat, machined surfaces of the mild steel specimens were treated with grit blasting to create the rough surfaces. The specimens had a Young's modulus of 207 GPa, a Poisson's ratio of 0.33, and a density of 7800 kgm^{-3}. The digitized surface profiles of both the rough surfaces were measured before testing using a stylus profilometer (Talyor Hobson Form Talysurf 50). Analysis of the surface profiles gave an approximate average roughness (R_a) of 3.5 μm. A review by Ekstrøm and Wåle[18] found that values of R_a for real fatigue cracks range from 3 to 12 μm. This indicates that the roughness of the surfaces tested in the experiments falls within the range of values for fatigue cracks, although it is at the smoother end of the range. Ekstrøm and Wåle reported that there was no crack branching for any of the fatigue cracks studied, and most of these cracks could be considered straight. From these investigations it would appear that the flat, machined, and grit-blasted surfaces of the experimental specimens are a reasonable representation of a fatigue crack.

The apparatus for the measurement of reflection coefficient from solid–solid partially contacting interfaces is shown in Fig. 1. Wide-bandwidth ultrasonic transducers were located in a water bath to ensure good transmission of the pulse through to the steel specimens. The transducers were operated in pulse–echo mode and carefully focused at the interface of the two surfaces. Transducers with nominal center frequencies of 5, 10, and 25 MHz were used for the experiments to cover the response over a wide range of frequencies. The load was applied using a tensile testing machine (Zwick 1478), using loads up to 45 kN. This corresponds to a nominal contact pressure of 255 MPa over the 15-mm-diameter contact region. A reference signal was recorded at the start of each test for a solid–air interface from which the reflection is assumed to be 100%.[19] All reflected signals were converted to the frequency domain using a Fast Fourier Transform (FFT). The reflection coefficient can then be defined as[10]

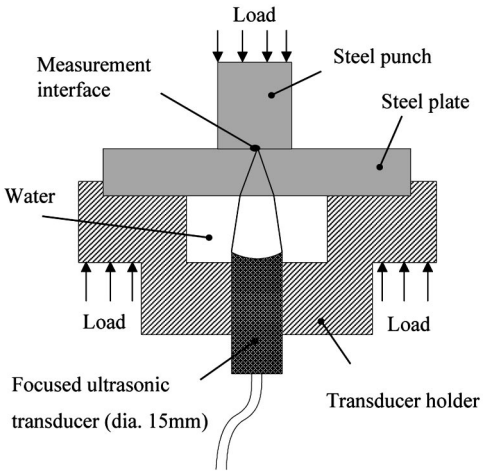

FIG. 1. Experimental apparatus for the measurement of reflection coefficient from rough surfaces.

$$R(f)=\frac{A_{\mathrm{meas}}(f)}{A_{\mathrm{ref}}(f)}, \tag{1}$$

where $A_{\mathrm{meas}}(f)$ is the amplitude of the wave reflected from the loaded steel–steel interface and $A_{\mathrm{ref}}(f)$ is the reference amplitude of the steel–air, both in the frequency domain.

Figure 2(a) shows the reflection coefficient variation with contact pressure at 10 MHz. It can be seen that the reflection coefficient decreases with increasing contact pressure. It can also be seen that, at a given contact pressure, the reflection coefficient is higher on the loading cycle than on

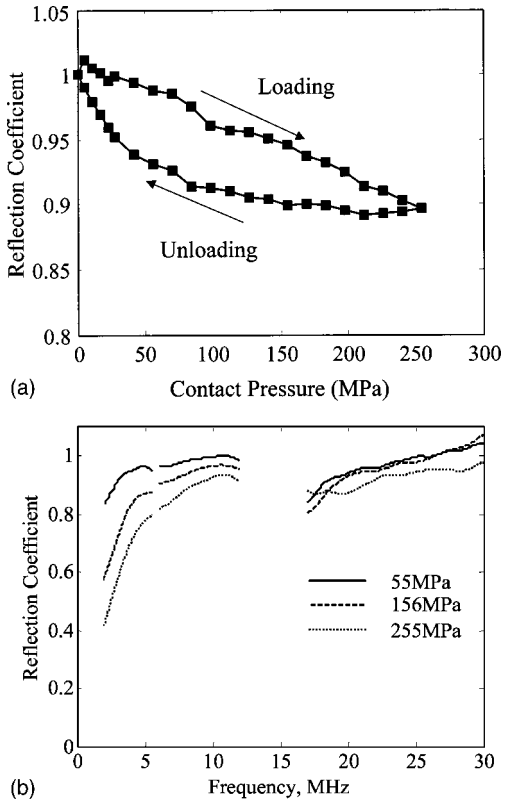

FIG. 2. Experimental results for grit-blasted surfaces (R_a=3.5 μm) showing (a) the reflection coefficient variation with contact pressure at 10 MHz and (b) the reflection coefficient variation with frequency for three contact pressures.

the unloading cycles. This effect was explained by Drinkwater *et al.*[10] as the difference between the mostly plastic loading and the mostly elastic unloading. The variation of reflection coefficient with frequency for contact pressures of 50, 150, and 250 MPa is shown in Fig. 2(b). The reflection coefficient of the interface is shown across the bandwidths of each of the transducers, indicating that, between 2 and 10 MHz, the reflection coefficient decreased as the pressure was increased. This is consistent with greater contact at the interface when higher pressures are applied and therefore more ultrasonic energy is transmitted through the interface. For frequencies up to approximately 10 MHz, the reflection coefficient increases as the frequency increases at all pressures. Note that a reduction in reflection coefficient is observed in the range 12–16 MHz. Also note that at frequencies greater than 17 MHz, the variation of reflection coefficient with both pressure and frequency is less smooth than at lower frequencies.

III. MODELING THE RESPONSE OF A ROUGH CRACK TO ULTRASOUND

A. Plastic contact model

Before an ultrasonic interaction model can be developed, it is important to model the contact at the interface of a rough surface (or crack). Various contact models have been developed by researchers to predict the contact parameters of a rough surface. Some models assume that the contact is elastic (e.g., Greenwood and Williamson[20] and Webster and Sayles[21]), while others assume an entirely plastic contact (e.g., Nayak[22]). When comparing the predictions from these contact models with experimental results from smooth surfaces via a spring model, Drinkwater *et al.*[10] have shown that the numerical model of Webster and Sayles gives parameters that produce reflection coefficient values that are the closest to experimental results, although this model predicts lower values of reflection coefficient than experimental measurements.

The general approach of existing contact models is to base the model on the statistical properties of the surface, generating average properties of the contact surfaces. However, the requirement for the contact model in this work is to produce details of the geometry of the scatterers at the interface. The numerical model of Webster and Sayles uses the digitized profile of the surface and assumes purely elastic behavior. When this technique was applied to the surfaces in this investigation, the stresses produced at the interface were considerably in excess of the yield stress of the steel, indicating that the model should consider plastic rather than elastic behavior.

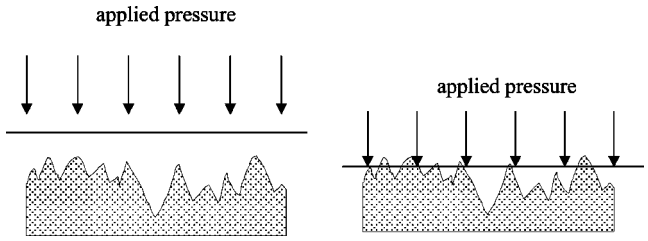

FIG. 3. Plastic random surface contact model to predict the interfacial geometry.

The plastic random surface contact model proposed by Nayak[22] has been extended to determine the interfacial geometry of the scatterers for the interfaces used in the experiments. It was thought that this model would be particularly appropriate for the first loading of an interface when the contact is known exhibit the most plasticity. The digitized surface profiles of the two surfaces are combined to give a composite surface of ordinates, $z(x)$, where z is the height of the roughness and x is the direction of the roughness profile. The two surfaces are loaded against each other as shown schematically in Fig. 3. The total pressure at the interface is calculated using the assumption that the pressure at each of the contact points is the flow pressure, p_f, of the material which was given by Nayak as

$$p_f = H_v g, \tag{2}$$

where H_v is the Vickers hardness number and g is the acceleration due to gravity. This was found to be equal to 1.334 GPa for the mild steel used in this paper. The contact model is described by Eq. (3) below, in which the contact pressure, P, is given by

$$P = \frac{1}{L}\int_0^L U(z(x)-h)p_f\,dx, \tag{3}$$

where h is the height of the flat surface above the mean line of the rough surface, L is the length of the profile in the x direction, and $U(x)$ is a unit step function defined as

$$U(x)=0 \quad \text{for } x<0,$$

and

$$U(x)=1 \quad \text{for } x\geqslant 0. \tag{4}$$

The output of this contact model is the deformed geometry of the plastic surface. If it is assumed that the points at the flow pressure are in contact and those at $P=0$ are out of contact, then the percentage contact and scatterer sizes can be extracted from the deformed geometry. The scatterer sizes and percentage contact areas generated using this contact model with the grit-blasted surface profiles tested in the ex-

TABLE I. Interfacial geometry for an interface with R_a approximately 3.5 μm.

Pressure at interface MPa	Average width of scatterers μm	Maximum width of scatterers μm	Percentage area of contact	Average aspect ratio of scatterers
50	166.3	429.5	3.7	0.12
150	91.0	379.8	11.0	0.16
250	63.7	260.5	18.5	0.18

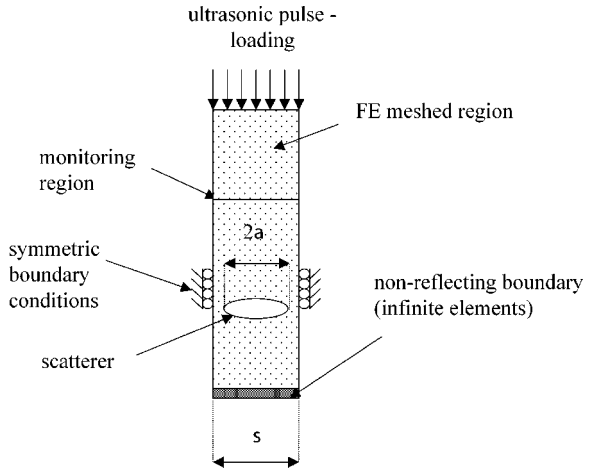

FIG. 4. Schematic diagram of the finite-element model (not to scale).

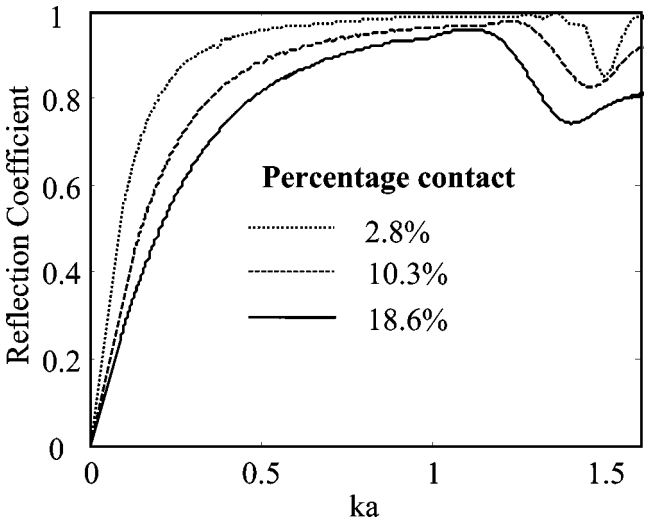

FIG. 5. Effect of change in percentage area of contact for an array of elliptical scatterers with an aspect ratio of $\frac{1}{4}$.

perimental work are shown in Table I. As the pressure at the interface increases, the model predicts that both the average and the maximum width of the scatterers decrease. The average scatterer width decreases from 166.3 μm at 50 MPa to 63.7 μm when the pressure is 250 MPa. A small reduction in aspect ratio (minor radius divided by major radius) of the scatterers as the pressure increases indicates that the average shape of the voids is more elongated at lower pressures. The model predicts that the area of contact at the interface is 3.7% with a pressure of 50 MPa, rising to 18.5% when the pressure reaches 250 MPa. It is interesting to compare these scatterer sizes with the ultrasonic wavelength in steel which is 1180 μm at 5 MHz and 236 μm at 25 MHz.

B. Finite-element scattering model

The commercial finite-element software package ABAQUS EXPLICIT 6.3 (ABAQUS UK Ltd., Warrington, UK) was used to generate a two-dimensional model of a solid–solid interface. The models used have been developed to simulate the experimental setup and the interfacial geometry was determined by the contact model described in Sec. III A and detailed in Table I. The finite-element method is applicable for any frequency (although the mesh would have to be refined at higher frequencies), and the effect of changes to the geometry or material properties used in the model can be investigated relatively easily. For simplicity, equi-sized, equi-spaced scatterers were used to investigate the effect of variations in size and shape on the reflection of an ultrasonic wave at the interface.

A range of scatterer shapes has been included in the analysis, varying from a circle through an ellipse to a slit. A schematic diagram of the model used in the finite-element analysis is shown in Fig. 4. Due to symmetry, only one scatterer needs to be modeled, with the edges of the mesh constrained in the horizontal degree of freedom to simulate the infinite array of scatterers. For all the finite-element models, 4-node bilinear plane strain elements (CPE4R) have been used, with an element size of 1.25 μm. A nonreflecting boundary of infinite elements was positioned on the bottom surface of the strip. This removed the complication of reflection from the bottom of the strip, ensuring that a clear reflection from the scatterers would be seen. The length of the modeled strip was 6 mm, with the center of the scatterer 0.5 mm from the bottom surface of the strip. A monitoring region was chosen 2.125 mm above the center of the scatterer. Measurements were taken at other points along the center line of the strip, and these confirmed that the reflection coefficient does not change as long as the measurement is taken some distance away from the scatterer.

A pulse of varying vertical displacement was used to simulate a longitudinal ultrasonic transducer on the top surface of the strip as shown in Fig. 4. Pulses with center frequencies in the range 5–50 MHz were used for the ultrasonic excitation of the model, ensuring that the response to a wide range of frequencies was analyzed. A FFT was performed on both the incident wave and the reflected wave to obtain the frequency spectrum for each trace. The reflection coefficient for each model can be calculated by dividing the amplitude of reflected signal by the incident signal over the bandwidth for each pulse.[4]

The response to ultrasonic excitation can be generalized by plotting the reflection coefficient against the term ka, which is the product of the wave number, k, and the half-width of the scatterer, a. The use of ka is common in the literature and is most useful when considering a single scatterer or when the scatterers are equi-sized, equi-spaced, and the same shape. For ''real'' interfaces, each different scatterer will have a different ka value. However, use of this normalized term allows the response to ultrasonic excitation to be obtained by varying either the frequency of excitation or the width of the scatterer.

IV. MODELING RESULTS

The variation of reflection coefficient with ka for an array of elliptical scatterers with an aspect ratio of $\frac{1}{4}$ is shown in Fig. 5 for 2.8%, 10.3%, and 18.6% area of contact at the interface. These values of percentage contact area were chosen to be as close as possible to those predicted by the contact model and shown in Table I. The discrete nature of the finite-element mesh means that sizes and shapes of scatterers

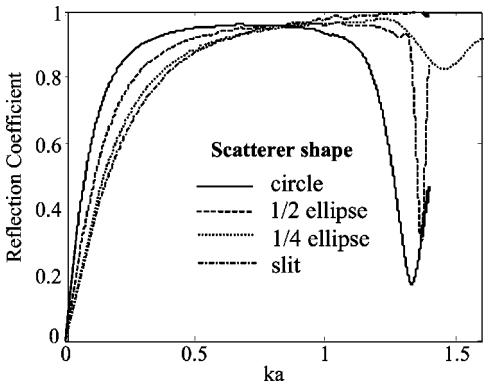

FIG. 6. Finite-element analysis results showing the effect of scatterer shape (10.3% contact area).

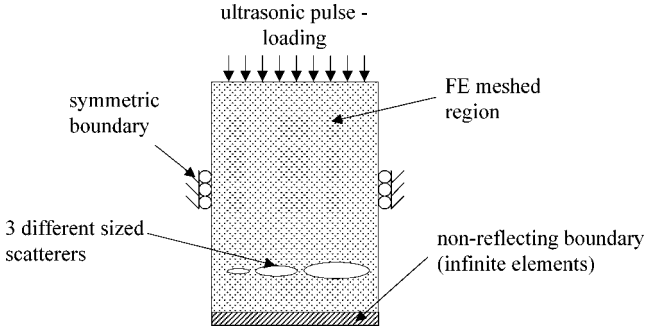

FIG. 7. Schematic diagram of a finite-element model with a repeating unit cell of three different-sized scatterers (not to scale).

can only be adjusted in one-element increments, which explains why the above percentage contact values are not exactly equal to those shown in Table I. As expected, an increase in percentage area of contact at the solid–solid steel interface shows a corresponding decrease in reflection coefficient for all values of ka. The response shows a significant reduction in reflection coefficient for values of ka between 1.2 and 1.6 and corresponds with a resonance of the elliptical scatterers.

Finite-element models have been analyzed with arrays of scatterers ranging from a circle to a slit, using values of ka up to 1.4 and with 10.3% contact at the interface (Fig. 6). For values of ka up to 0.8, the reflection coefficient increases as the scatterer shape changes from a slit through to a circle. When ka is 0.8, all the shapes have a similar reflection coefficient of approximately 0.9. At higher values of ka, all the shapes demonstrate a significant drop in reflection coefficient due to resonance of the scatterers, but this is more marked for the circle than for the crack. For the circle this effect occurs when ka is 1.35, while for the ellipse with the aspect ratio of $\frac{1}{4}$, this happens at a slightly higher ka of 1.45.

From the plastic contact model (Table I), the aspect ratio of the average scatterer was shown to range from 0.12 to 0.18, suggesting that the scatterer shape falls between the $\frac{1}{4}$ ellipse and the slit. The finite-element analysis shows that the reflections from arrays of these two shapes are similar and, therefore, the results from either geometry could be used to model the behavior of the solid–solid interfaces.

The equi-sized, equi-spaced models analyzed are a simplification of real cracks. To obtain a more realistic idea of the effect of different shapes and sizes on the reflection of an ultrasonic wave at an interface, models were considered with an array consisting of a repeating unit that contained three different-sized scatterers as shown in Fig. 7. An array of three $\frac{1}{4}$ elliptical voids was modeled with scatterer widths 131.3, 87.5, and 43.7 μm and symmetric boundary conditions applied to the outer edges of the three scatterer unit cell. The variation of reflection coefficient against frequency for this array is shown in Fig. 8, with 10% area of contact. For comparison, the behavior is shown for each of the scatterer sizes, assuming that the array consists of equi-sized scatterers. From these comparisons, it can be seen that the response of the array with three different-sized scatterers more closely follows the behavior of the equi-sized scatter-size models with the larger scatterer sizes. As expected, the resonant effects in the array of different-sized scatterers are less clearly defined than for the equi-sized scatterers. It is also worth noting that these results show that the experimental reflection coefficient is between the average and maximum scatterer lines, meaning that the larger scatterers have a significant influence on the result. This could mean that a particularly large scatter may tend to dominate the reflection behavior of an interface.

V. COMPARISON OF EXPERIMENTAL RESULTS WITH FINITE-ELEMENT ANALYSIS PREDICTIONS

The response to ultrasonic excitation of the interfaces used in the experimental work has been predicted using the finite-element analysis results. The interfacial geometry calculated from the plastic contact model was used as input to the finite-element scattering model to determine the reflection coefficient behavior over the range of frequencies used in the experiments. As discussed in the previous section, arrays modeled with three different-sized scatterers have indicated that the largest scatterers may tend to dominate the behavior, so the predictions for both the average and the largest scatterer sizes have been considered. The calculated average aspect ratio of the scatterers (Table I) suggests that, of the shapes modeled using finite-element analysis, the ellipse with the aspect ratio of $\frac{1}{4}$ is the shape that most closely

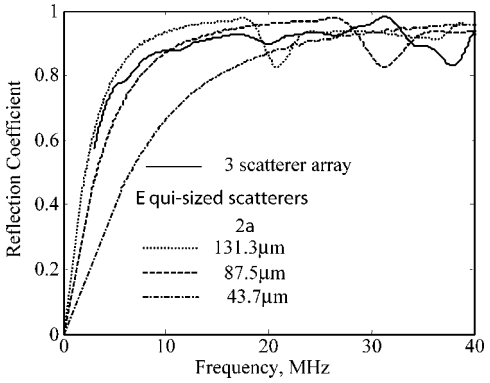

FIG. 8. Finite-element analysis results from a repeating unit cell with different-sized scatterers (10% area of contact).

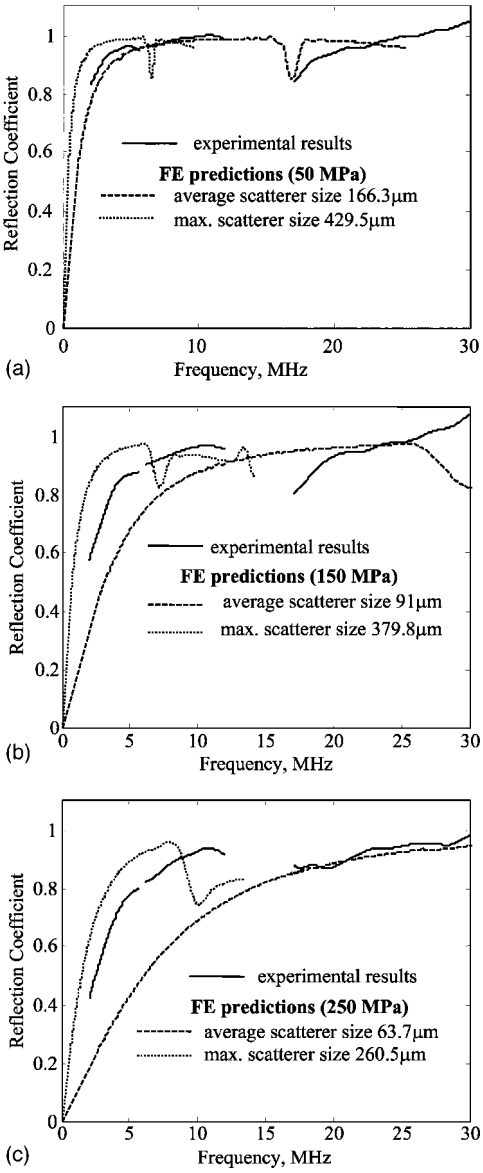

FIG. 9. Comparison of experimental results with finite-element analysis predictions at three different pressures (a) 50 MPa; (b) 150 MPa; and (c) 250 MPa.

represents the average shape of the scatterers present at the interface, although the difference between the $\frac{1}{4}$ ellipse and slit scatterers is small.

The predicted results using the finite-element analysis are compared with the experimental results in Fig. 9 for 50-, 150-, and 250-MPa contact pressure. The graphs show the predicted results assuming that the interface consists of an array of average-sized scatterers and also for an interface with an array with the maximum size of scatterer. Finite-element analysis results were computed for ka up to approximately 2. For frequencies up to approximately 6 MHz and at all pressures, the experimentally measured reflection coefficient is higher than the finite-element-predicted results, assuming an average-sized scatterer but lower than those predicted using finite-element analysis and assuming the maximum-sized scatterer. As the frequency increases to approximately 12 MHz, the experimental results are higher than those predicted using finite-element analysis for the average-sized scatterer, but there is no evidence of the resonant effect predicted using the maximum-sized scatterer. This is expected as the experimental surfaces consist of scatterers of different sizes and shapes, and so strong resonant effects are unlikely to be observed. Note that Figs. 9(a) and (b) show reasonable agreement above 17 MHz between the experimental results and the average-sized scatterer results, and Fig. 9(c) shows good agreement.

VI. COMPARISON BETWEEN THE FINITE ELEMENT AND THE SPRING AND SPRING–MASS MODELS

Previous work on the interaction of ultrasound with partially closed cracks was based on the assumption that the scatterers at the interface are small compared with the wavelength of the ultrasonic wave. Baik and Thompson[2] have shown that under these conditions, the reflection from an interface can be predicted by describing the interface as a series of springs and masses.

For elastic wave interaction,[23] the stiffness of the distributed spring representing the interface can be defined as

$$K = -\frac{d\sigma}{d\delta}, \tag{5}$$

where K is the interfacial stiffness per unit area, $d\sigma$ is the change in compressive stress, and $d\delta$ is the change in displacement at the interface. As the interface is represented by an array of voids, there is a change in density at the interface that Baik and Thompson suggested could be modeled as a mass per unit area given by

$$m = \int_{-l/2}^{l/2} (\rho_s - \rho_o)\, dx, \tag{6}$$

where l is the thickness of the ''interface layer'' containing the scatterers, ρ_s is the density of the interface layer, ρ_o is the density of the original material, and x is the direction across the interface. The mass per unit area will have a negative value when there are voids present at the interface, and will be positive if there are inclusions of higher density than the original material.

Applying the spring–mass model leads to the definition of reflection coefficient (R) as

$$R = \frac{i\omega(Z/2K - m/2Z)}{(1 - m\omega^2/4K) + i\omega(Z/2K + m/2Z)}, \tag{7}$$

where ω is the angular frequency, Z is the acoustic impedance, m is the mass per unit area, and i is $\sqrt{-1}$. This approximation assumes that the frequency (ω) is significantly less than the resonant frequency of the spring–mass combination, i.e., $\omega \ll (4K/m)^{1/2}$. Equation (7) reduces to the spring model when there are no inertia effects (i.e., $m = 0$).

Static finite-element analysis was used to determine the interfacial stiffness of an array of equi-sized scatterers. The case considered was an array of equi-sized scatterers corresponding to a contact pressure of 150 MPa, which can be seen from Table I to produce 11.0% contact and an average scatterer size of 91.0 μm. The static finite-element analysis predicted an interfacial stiffness of $0.919 \times 10^{15}\,\mathrm{Nm}^{-3}$ for the

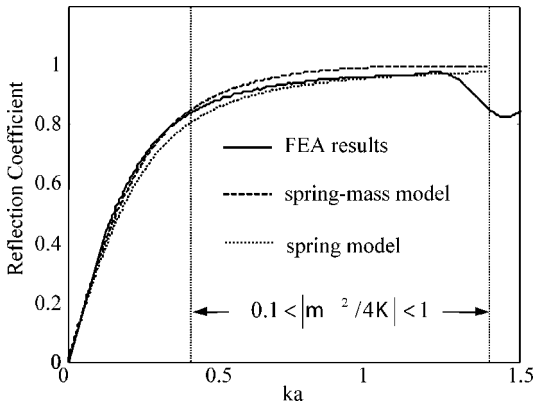

FIG. 10. Comparison of spring model and spring–mass model with finite-element analysis results for elliptical scatterers with $\frac{1}{4}$ aspect ratio and 10.3% contact area.

$\frac{1}{4}$ ellipse scatterers. The response of an interface to ultrasonic excitation, assuming spring–mass model behavior (using $m = -0.124\,\mathrm{kgm}^{-2}$), was then determined from Eq. (7). Comparison of the spring model, spring–mass model, and the results from the finite-element analysis are shown in Fig. 10 for an array of elliptical scatterers with an aspect ratio of $\frac{1}{4}$ and with 10.3% contact area. Comparing the spring model and the spring–mass model, inclusion of the mass factor gives slightly higher predicted reflection from the interface. The finite-element predictions can be seen to be in excellent agreement with the spring–mass model for ka values up to approximately 0.4 Beyond this, the agreement is not as good, although it is still reasonable up to ka values of 1.0. When ka is approximately 1.3, resonant effects are seen in the finite-element analysis results. Baik and Thompson suggested that the spring–mass model was likely to produce errors when $0.1 < |m\omega^2/4K|$ due to the resonance of the spring–mass system. This corresponds to $ka = 0.41$ for these surfaces and contact pressures, which is good in agreement with the departure of the mass–spring and finite-element model predictions seen in Fig. 10.

Calculated values of ka for the experimental results using average scatterer widths determined by the contact model are shown in Fig. 11. It can be seen that for each frequency, as the contact pressure increases, so the ka value decreases, and this is due to the reduction in scatterer size seen with load. The measurements at 5 MHz can be seen to be below ka values of 0.5, which from consideration of Fig. 5 indicates that mass–spring models would give reasonable accuracy for these interfaces. It can also be seen that when excitations of 25 MHz were used, the ka values were greater than 0.8 for all contact pressures, and so the mass–spring model would be expected to less accurate predictions for this case.

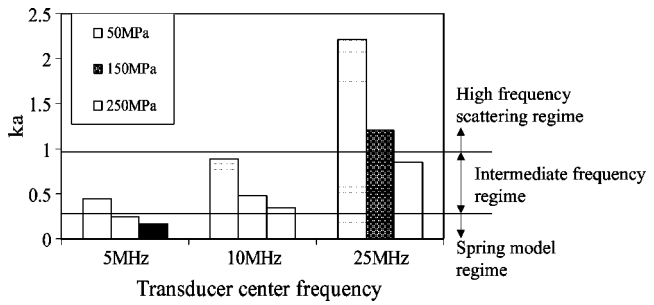

FIG. 11. Estimated ka values for the grit-blasted surface with R_a approximately 3.5 μm, based on the average scatterer size from the plastic contact model.

VII. CONCLUSIONS

Experimental measurements of reflection coefficient from rough, partially contacting interfaces with R_a approximately 3.5 μm over a range of frequencies have been compared with predictions from finite-element models.

A plastic random surface contact model has been used to determine the interfacial geometry of contacting the rough surfaces. This showed that for the surfaces considered (mild steel, grit blasted to $R_a = 3.5\,\mu$m) the scatterers at the interface were close to $\frac{1}{4}$ aspect ratio ellipses and the percentage contact varied up to 18.6% for an applied nominal contact pressure of 250 MPa. Finite-element analysis was then used to predict the interaction of longitudinal wave ultrasound with these partially contacting interfaces. Using an interface modeled as an array of equi-sized scatterers, the finite-element predictions were in good agreement with experimental results for frequencies from 4 to 30 MHz. It was also shown that arrays of equi-sized scatterers exhibited strong resonance effects, and that these were reduced when an array of varying scatterer size was present.

Comparisons between the finite-element model and the mass–spring model were made over a range of frequencies. The finite-element and mass–spring models were first seen to depart at ka values of 0.4, which is as expected from the work of Baik and Thompson.[2] However, the mass–spring model was seen to give surprisingly good results up to ka values as high as 1.0.

ACKNOWLEDGMENT

The authors would like to thank the Engineering and Physical Science Research Council, Swindon, U.K. for funding this research program.

[1] R. K. Chapman, "A system model for the ultrasonic inspection of smooth planar cracks," J. Nondestruct. Eval. **9**, 197–210 (1990).
[2] J.-M. Baik and R. B. Thompson, "Ultrasonic scattering from imperfect interfaces: A quasi-static model," J. Nondestruct. Eval. **4**, 177–196 (1984).
[3] N. F. Haines, "The theory of sound transmission and reflection at contacting surfaces," CEGB Berkeley Nuclear Laboratories, Report RD/B/N4744 (1980).
[4] F. J. Margetan, R. B. Thompson, J. H. Rose, and T. A. Gray, "The interaction of ultrasound with imperfect interfaces: Experimental studies of model structures," J. Nondestruct. Eval. **11**, 109–126 (1992).
[5] P. B. Nagy, "Ultrasonic classification of imperfect interfaces," J. Nondestruct. Eval. **11**, 127–139 (1992).
[6] R. B. Thompson and C. J. Fiedler, "The effects of crack closure on ultrasonic scattering measurements," Rev. Prog. Quant. Nondestr. Eval. **3A**, 207–215 (1984).
[7] A. I. Lavrentyev, A. Baltazar, and S. I. Rokhlin, "Ultrasonic spectroscopy of two parallel imperfect interfaces," Rev. Prog. Quant. Nondestr. Eval. **17**, 1379–1386 (1998).
[8] S. I. Rokhlin and Y. J. Wang, "Analysis of ultrasonic wave interaction with imperfect interface between solids," Rev. Prog. Quant. Nondestr. Eval. **104**, 185–192 (1991).
[9] A. Baltazar, S. I. Rokhlin, and C. Pecorari, "On the relationship between

ultrasonic and micromechanical properties of contacting rough surfaces,'' J. Mech. Phys. Solids **50**, 1397–1416 (2002).
[10] B. W. Drinkwater, R. S. Dwyer-Joyce, and P. Cawley, ''A study of the interaction between ultrasound and a partially contacting solid–solid interface,'' Proc. R. Soc. London **452**, 2613–2628 (1996).
[11] J. H. Rose, ''Ultrasonic reflectivity of diffusion bonds,'' Rev. Prog. Quant. Nondestr. Eval. **8B**, 1925–1931 (1989).
[12] J. Opsal, ''Theory of elastic wave scattering: Applications of the optimal truncation,'' J. Appl. Phys. **58**, 1102–1115 (1985).
[13] A. K. Mal, ''Interaction of elastic waves with a penny-shaped crack,'' Int. J. Eng. Sci. **8**, 381–388 (1970).
[14] J. D. Achenbach and M. Kitathara, ''Reflection and transmission of a an obliquely incident wave by an array of spherical cavities,'' J. Acoust. Soc. Am. **80**, 1209–1214 (1986).
[15] Y. C. Angel and J. D. Achenbach, ''Reflection and transmission by a periodic array of cracks,'' J. Appl. Mech. **52**, 33–41 (1985).
[16] O. Diligent, T. Grahn, A. Bostrøm, P. Cawley, and M. J. S. Lowe, ''The low frequency reflection and scattering of the s_o Lamb mode from a circular through-thickness hole in a plate: Finite element, analytical, and experimental studies,'' J. Acoust. Soc. Am. **112**, 2589–2601 (2002).
[17] M. J. S. Lowe, P. Cawley, J.-Y. Kao, and O. Diligent, ''The low frequency reflection characteristics of the fundamental antisymmetric Lamb wave a_o from a rectangular notch in a plate,'' J. Acoust. Soc. Am. **112**, 2612–2622 (2002).
[18] P. Ekstrøm and J. Wåle, ''Crack characterization for in-service inspection planning,'' SKI Report 95:70 (November 1995).
[19] J. Krautkramer and H. Krautkramer, *Ultrasonic testing of materials* (Springer, London, 1990).
[20] J. A. Greenwood and J. B. P. Williamson, ''Contact of nominally flat surfaces,'' Proc. R. Soc. London, Ser. A **299**, 300–319 (1966).
[21] M. N. Webster and R. S. Sayles, ''A numerical model for the elastic frictionless contact of real rough surfaces,'' Trans. ASME J. Tribol. **108**, 314–320 (1986).
[22] P. R. Nayak, ''Random process model of rough surfaces in plastic contact,'' Wear **26**, 305–333 (1973).
[23] J.-Y. Kim, A. Baltazar, and S. I. Rokhlin, ''Ultrasonic assessment of rough surface contact between solids from elastoplastic loading-unloading hysteresis cycle,'' J. Mech. Phys. Solids **52**, 1911–1934 (2004).

System for determination of ultrasonic wave speeds and their temperature dependence in liquids and *in vitro* tissues

William T. Yost
NASA-Langley Research Center, MS 231, Hampton, Virginia 23681-2199

Brandon R. Macias, Peihong Cao, Alan R. Hargens, and Toshiaki Ueno
Orthopaedic Surgery, University of California, San Diego, 350 Dickinson St #121, MC 8894, San Diego, California 92103-8894

(Received 3 June 2004; revised 15 November 2004; accepted 19 November 2004)

An interferometric technique capable of accurately measuring wave speed in liquids is reported. The hardware is adapted from a design to measure nonlinear responses of biological tissues to pressure changes (pressure derivatives) and temperature changes (temperature derivatives). It is used with the highly sensitive variable frequency pulsed phase-locked loop (VFPPLL) instrument. The system uses well-understood and well-characterized components and systems. The apparatus covers a temperature range from below 5 °C to above 45 °C. The system with the high-sensitivity VFPPLL is capable of measurement of wave speed to an uncertainty of less than 0.1%, and changes in wave speed to better than 0.001%. The transducer is an undamped temperature-characterized PZT-5A 500-kHz plate, whose output is corrected for off-resonance operation and for diffraction effects. To test the accuracy of the technique, measurement of ultrasonic compressional wave speed in water at temperatures from 10 °C to 45 °C are reported, with an estimated uncertainty of 0.07% and a temperature uncertainty of 0.15 °C. The agreement between mean values and literature values is better than 0.05%. [DOI: 10.1121/1.1848176]

PACS numbers: 43.35.Yb, 43.58.Dj [YHB] Pages: 646–652

I. INTRODUCTION

Recently, there has been an increase in the interest in the acoustic properties of liquids and biological tissues. For example, harmonic generation in tissue has been observed and even incorporated in some recently developed ultrasonic scanning systems. Additional interest has been shown in the temperature dependence of wave velocities in biological tissues. Because of the interest in the relationships among acoustical properties, their thermodynamic variables, and their thermodynamic derivatives, we developed an ultrasonic interferometric system capable of accurately measuring wave speeds in liquids and biological tissues.

This system is capable of measuring not only temperature dependence and pressure dependence of ultrasonic wave speeds in liquids and biological tissues, but also the absolute wave speeds in these materials with high accuracy. The apparatus uses well-understood and well-characterized components and electronics instrumentation. Its operational range covers a temperature range from 0 °C to above 45 °C, and a gauge pressure range from 0–2.5 atmospheres. For this work we test the apparatus accuracy in measurement of wave speed as a function of temperature from 10 °C to 45 °C at a gauge pressure of zero.

We use the previously reported variable frequency pulsed phase-locked loop (VFPPLL) device[1] as the electronics portion of the interferometer. This instrument is an automated version of a circuit first developed[2] by Blume as a high-resolution interferometric technique to measure small changes in wave speed. Heyman[3] later extended the idea to the development of the pulsed phase-locked loop used to measure bolt tensions in critical space shuttle applications.

Since the initial invention, there have been a number of measurement systems developed for use with the VFPPLL. In these applications the device is set up to monitor the change in wave speed in materials. Chern, Heyman, and Cantrell[4] used the device (pulse–echo) to determine material stress from changes in wave speed in aluminum alloys as a function of temperature. Allison, Heyman and Salama[5] (pulse–echo) used the device to measure the effects of carbon content in steels. Namkung *et al.*[6] developed techniques (pulse–echo) to measure changes in wave speeds with applied stress and applied magnetic fields in rail steels to determine stresses within the steels. Everbach and Apfel[7] developed apparatus to measure the pressure derivative in a number of liquids (in pitch–catch mode) including water and a variety of lipids.

In all of the above cases the results involve very small changes in wave speed, so the frequency changes are likewise very small. The device's sensitivity enables reproducible measurements of frequency changes to approximately 5 parts in 10^6 to parts in 10^7 (with averaging). Commercially available damped PZT-5 transducers were employed for the pulse–echo-based applications listed above. The pitch–catch application employed quartz plates. These applications work under an operational assumption that these small frequency changes do not require corrections for a consequent instrumental and transducer phase shift with frequency.

This system differs from the above applications in that it addresses the application of the VFPPLL as the electronics portion of the interferometer system to measure absolute wave speeds as opposed to measurements of changes in wave speed. The apparatus utilizes a pulse–echo arrangement of a reflector and an unbacked, well-characterized

PZT-5A plate whose off-resonance phase shift is calculated and results are corrected for off-resonance operation. The accurate measurement of the transducer's resonant frequency as a function of temperature is presented. This permits transducer corrections that are sufficient to assure overall measurement accuracy.

The apparatus is presented and the equations are derived. Methods for measuring the cycle count are presented. The system is then used to measure the wavelength in distilled water as a function of temperature. From the calculated wavelength and the measured wave frequency, we calculate the wave speed of distilled water at various temperatures. We compare these values with values obtained from the interpolation of literature values, and discuss sources of measurement uncertainty.

II. CALCULATION OF WAVE SPEED

As with any interferometer, the apparatus is used to determine the wavelength in the propagation medium. We take the simple case of a chamber consisting of a transducer placed a distance L from a reflector of infinite length. We consider what happens as the transducer is energized from a signal (tone burst) that originates from a reference oscillator. In response, the transducer feeds an ultrasonic wave into the medium. The wave is reflected and in turn received by the transducer, which develops an electrical signal to be phase compared with the reference oscillator.

While the ultrasonic wave propagation is taking place in the chamber, the reference oscillator develops a number of cycles, which are counted. Upon return the reference oscillator is phase compared to the electrical output from the transducer. This phase comparison permits the precise determination of the number of wavelengths between transmission and reception, and hence the number of wavelengths within the chamber. In summary we establish two paths: (1) the electrical oscillations of the reference oscillator, and (2) an ultrasonic propagation in a medium under investigation. The phase comparison between these two paths permits the calculation of the wavelength λ. A frequency counter measures the precise oscillator frequency f and hence the wave frequency. The product determines the wave speed in the medium

$$f\lambda = c, \tag{1}$$

where c is the wave speed. Thus, at each temperature we calculate the wave speed based on Eq. (1).

A. Determination of the cycle count, κ

We determine the number of cycles of oscillation between the ultrasonic tone-burst formation and the reception of its echo. Because the VFPPLL circuitry adjusts the reference oscillator to establish quadrature (phase difference of $\pi/2$ or $3\pi/2$) between the two paths when phase locked, we can expect κ to be approximately an integer $\pm 1/4$. Upon closer examination of the waveforms we find that this must be measured because of circuit vagaries. In Fig. 1(A) we show a schematic view of an oscilloscope screen showing the waveforms when the system is phase locked. The top trace is from the reference oscillator. The bottom traces

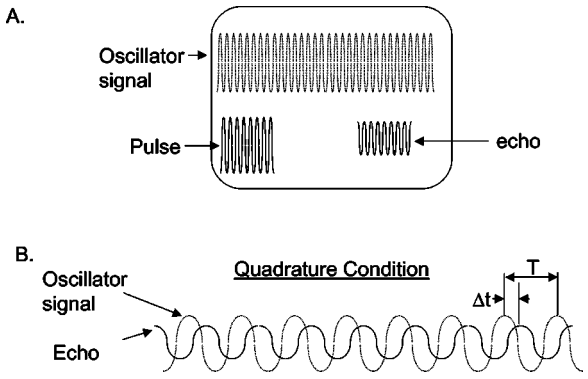

FIG. 1. (A), (B) A schematic diagram showing the quadrature condition between the oscillator and the significant transducer signals. (A) shows the oscillator and the transducer's signals (pulse and echo) as may appear on an oscilloscope screen. (B) shows the quadrature condition between the oscillator and the echo signals.

(pulse and echo) are taken from across the electrical terminals of the transducer. The screen is expanded to better show the phase relationship between the reference oscillator and the echo whose time axes are juxtaposed at quadrature in Fig. 1(B). The actual relationship when the system is phase locked typically gives a value that is nominally $\pm 1/4$ wave [this is a ratio of $\Delta t/T$, where Δt and T are labeled in Fig. 1(B)]. These values are measured carefully and added to the whole number of cycles between corresponding maxima of the pulse and the echo to determine κ.

B. The number of ultrasonic wavelengths in the cavity

We begin with an examination of phase shifts encountered from wave transmission to reception. For simplicity we calculate these in fractions of a wavelength. We assume that the wavelength in the cavity is λ. Since the distance traveled by the wave is $2L$, the number of waves in the cavity is

$$\kappa_\lambda = \frac{2L}{\lambda}. \tag{2}$$

During the transmission process there is a wave shift caused by the fact that the transducer is operated off its electrical antiresonant frequency[8] (that frequency where the transducer is precisely 1/2 wavelength in thickness). Similarly, the reception gives the same phase shift. Since the apparatus is constructed so that the reflector is long in the direction of wave propagation, the interface reflection contributes no phase shift.

Consider the interface between two contacting semi-infinite media of densities ρ_1 and ρ_2 with compressional wave speeds c_1 and c_2, respectively. Let a wave in medium 1 (specific acoustic impedance $Z_1 = \rho_1 c_1$) travel toward medium 2 (specific acoustic impedance $Z_2 = \rho_2 c_2$). At the interface between the two media, the wave is reflected with a reflection coefficient, R (Ref. 9) for pressure waves

$$\frac{A_r}{A_i} = R = \frac{Z_2 - Z_1}{Z_2 + Z_1}, \tag{3}$$

where A_r and A_i are the reflected and incident wave amplitudes, respectively. At the reflector, we have that $Z_2 > Z_1$. In

addition to a reduced amplitude, the reflection amplitude has the same sign of the incident wave.

The reflection at the transducer is more complicated.[10] We analyze the transducer (impedance $=Z_{\mathrm{PZT}}$) reflection as a transmission line segment of length, l. At $Z(0)$ the transducer is in contact with medium 1. At $Z(l)$ (the transducer's top surface) the transducer is in contact with air. If the impedance of air is given by Z_{air}, then the effective impedance of the transducer at the transducer–medium 1 interface is given by[11]

$$Z(0)=Z_{\mathrm{PZT}}\frac{Z_{\mathrm{air}}+iZ_{\mathrm{PZT}}\tan kl}{Z_{\mathrm{PZT}}+iZ_{\mathrm{air}}\tan kl}, \tag{4}$$

where $i=(-1)^{1/2}$, $k=2\pi/\lambda$ is the propagation constant, and λ is the wavelength in the transducer. Since air has a low acoustic impedance, Z_{air} is set to 0 and Eq. (4) reduces to

$$Z(0)=iZ_{\mathrm{PZT}}\tan kl. \tag{5}$$

Writing kl as $\pi f/f_r$, where f_r is the antiresonant frequency, and substituting $Z(0)$ of Eq. (5) for Z_2 into Eq. (3) gives

$$\frac{A_r}{A_i}=-\left(\frac{Z_1^2-Z_{\mathrm{PZT}}^2\tan^2\left(\pi\frac{f}{f_r}\right)}{Z_1^2+Z_{\mathrm{PZT}}^2\tan^2\left(\pi\frac{f}{f_r}\right)}-i\frac{2Z_1Z_{\mathrm{PZT}}\tan\left(\pi\frac{f}{f_r}\right)}{Z_1^2+Z_{\mathrm{PZT}}^2\tan^2\left(\pi\frac{f}{f_r}\right)}\right). \tag{6}$$

The phase angle between the reflected wave from the transducer, which is in step with the voltage across the transducer, and the incident wave amplitude is

$$\phi=\mathrm{Arc}\tan\frac{2Z_1Z_{\mathrm{PZT}}\tan\left(\pi\frac{f}{f_r}\right)}{Z_{\mathrm{PZT}}^2\tan^2\left(\pi\frac{f}{f_r}\right)-Z_1^2}. \tag{7}$$

ϕ is converted into fractional wave shift, Δ_T, by dividing Eq. (7) by 2π

$$\Delta_T=\frac{1}{2\pi}\mathrm{Arc}\tan\frac{2Z_1Z_{\mathrm{PZT}}\tan\left(\pi\frac{f}{f_r}\right)}{Z_{\mathrm{PZT}}^2\tan^2\left(\pi\frac{f}{f_r}\right)-Z_1^2}. \tag{8}$$

In the above analysis the transducer's antiresonant frequency is specified. In Sec. III A we outline its measurement as a function of temperature for use in the above equations.

As a wave is propagated from a circular transducer through a medium, dffraction related phase shifts also occur. Diffraction corrections[12] that allow for plane-wave analysis in pulse–echo applications from circular transducers were calculated from

$$D_L=1-e^{-i(2\pi/s)}\left[J_0\left(\frac{2\pi}{s}\right)+iJ_1\left(\frac{2\pi}{s}\right)\right], \tag{9}$$

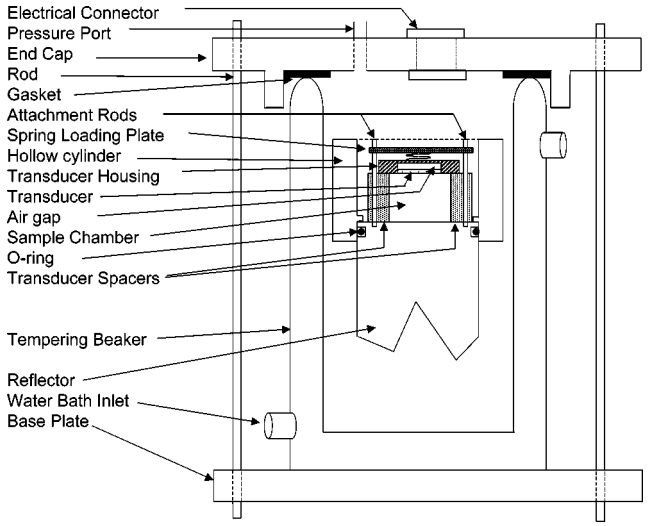

FIG. 2. Cross-sectional view of the apparatus.

where J_0 and J_1 are the first-order and second-order Bessel functions, respectively, s is the Seki parameter $(=z\lambda/a^2)$, $z(=2L)$ is the distance traveled by the wave, a is the transducer radius, and L is the cavity length determined by the spacers. The phase advance Δ_D in partial wavelengths is calculated by writing Eq. (9) in terms of its real and imaginary components and dividing by 2π

$$\Delta_D=\frac{1}{2\pi}\mathrm{Arc}\tan\frac{J_0\left(\frac{2\pi}{s}\right)\sin\left(\frac{2\pi}{s}\right)-J_1\left(\frac{2\pi}{s}\right)\cos\left(\frac{2\pi}{s}\right)}{1-J_0\left(\frac{2\pi}{s}\right)\cos\left(\frac{2\pi}{s}\right)-J_1\left(\frac{2\pi}{s}\right)\sin\left(\frac{2\pi}{s}\right)}. \tag{10}$$

When we equate the contributions between the acoustic wave path and the electronic path, we find that

$$\kappa=\kappa_\lambda-2\Delta_T+\Delta_D. \tag{11}$$

Solving Eq. (11) for κ_λ, substituting into Eq. (2) and Eq. (1) gives

$$c=\frac{2L}{\kappa+2\Delta_T-\Delta_D}f, \tag{12}$$

where

$$\frac{2L}{\kappa+2\Delta_T-\Delta_D}=\lambda. \tag{13}$$

C. Apparatus design

The apparatus consists of a specially constructed chamber attached to a cylinder of stainless steel that is lapped optically flat at one end, and used as a reflector as shown in Fig. 2. A hollow cylinder slides over the undercut reflector perimeter and seals against an O-ring to form the measurement chamber. Parallel to the axis and mounted every 120 deg in the reflector are threaded holes for stainless-steel attachment rods and precision-cut Pyrex glass spacers to serve as transducer attachment points. When the transducer is mounted on the spacers, the round-trip cavity path length is (5.080 ± 0.002) cm. The reflector is of sufficient length so

that the ultrasonic round-trip time within the reflector is longer than the pulse transit time in the sample. Thus, internal reflections from the opposite end of the reflector will not contribute to the phase measurement.

The chamber assembly is designed to fit within a stainless-steel tempering beaker used as a thermal jacket and pressure vessel. The tempering beaker fits between two stainless-steel end caps held securely in place with six threaded rods spaced every 60 deg around the end caps. The threaded rods are sufficiently tightened to assure good mechanical stability. The interior of the tempering beaker is sealed with the top end cap and gasket. In these measurements the port in the end cap is opened to the atmosphere. An electrical feed-through connector in the top end cap is used for electrical service to the ultrasonic transducer and to a thermistor, which is used as a thermometer.

The sample, commercially available distilled water, is placed between the reflector and the transducer. The transducer is mounted atop and spring loaded against the Pyrex spacers of equal length, which is 2.54 cm, by using a spring-loading system attached to threaded shafts to maintain alignment of the transducer on the spacers. The sample for measurement is placed between the reflector and the transducer in a way to assure parallelism between the transducer and reflector. A thermistor-based temperature circuit (Omega 44204 with Omega 44018 sensor packaged as a small sphere) is used to measure the sample temperature. It is placed so as to be out of the sound beam, and approximately halfway between the reflector and the transducer. The voltage supply for the thermistor circuit is a precision reference source (Analog Devices AD 780). The voltages from the precision divider circuit (supplied with the thermistor) are read to 5 digits with a digital voltmeter (Hewlett-Packard 3478). The temperature measurement uncertainty is less than $\pm 0.15\,^{\circ}\mathrm{C}$.

The transducer is a 2.54-cm diameter nominally 500-kHz coaxially plated PZT-5A compressional wave plate supplied by Boston Piezo-optics (2.12-cm diameter center electrode) fit into the transducer housing. Only the transducer edge is in contact with the housing, thus assuring a free (airgap) surface on the back. A small hole is drilled into the removable back cover plate for pressure relief. Care was taken in assembly to assure that the holder mount plane and the radiating transducer surface were aligned to better than 40 μm across the outer diameter (less than 1.5×10^{-3} radians of tilt). The ground connection to the transducer is epoxied to the outer ring. A spring-loaded copper foil pad maintains electrical contact with the center electrode to minimize interference with the transmission-line character of the transducer. This allows accurate computation of transducer corrections when the transducer is operated at an off-antiresonance condition. The transducer thickness is (4.1387 ± 0.0018) mm. According to information provided by the manufacturer, the antiresonant frequency is calculated to be $(5.2553 \pm 0.0022) \times 10^5$ Hz. We measured an antiresonant frequency of $(5.2925 \pm 0.0012) \times 10^5$ Hz at $(19.97 \pm 0.15)^{\circ}\mathrm{C}$.

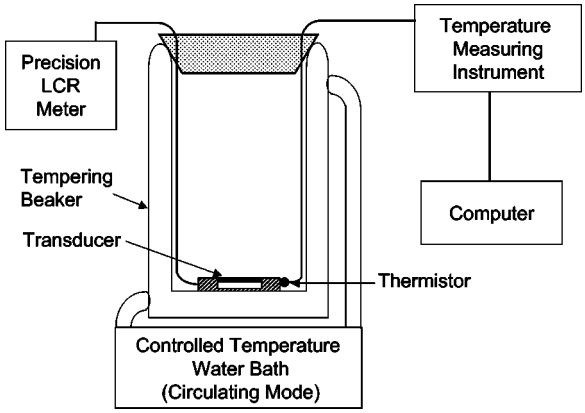

FIG. 3. Diagram showing the setup to measure the transducer's antiresonant frequency as a function of temperature.

III. MEASUREMENTS

A. Transducer antiresonant frequency as a function of temperature

In the above analysis the transducer's antiresonant frequency, f_r, must be accurately determined. We measure it by using an electrical technique. The transducer's electrical properties are calculated from Mason equivalent circuit of an ultrasonic transducer that has been treated in a number of references.[8] Since temperature affects the transducer's moduli and thickness, temperature changes affect f_r. We measured f_r as a function of temperature by measuring the transducer's electrical susceptance over a range of temperatures used in this study. A schematic of the setup for the measurement is shown in Fig. 3. The transducer in its mounting was placed inside a tempering beaker with its radiating surface pointed up, thus assuring that both front and back surfaces were acoustically unloaded. A thermistor was placed in thermal contact with the transducer housing. The tempering beaker was connected to a temperature-controlled water bath. At each temperature setting the system was allowed to equilibrate to a standard deviation of $\pm 0.001\,^{\circ}\mathrm{C}$ in the temperature measurement. The susceptance was measured with a precision LCR meter (Hewlett-Packard 4285A) by scanning through the transducer's f_r. The transducer's susceptance was plotted as a function of frequency. The susceptance null frequency $(=f_r)$ was calculated and recorded. Figure 4 shows the result of antiresonant frequency vs temperature. The uncertainty in temperature is approximately $\pm 0.15\,^{\circ}\mathrm{C}$, and the uncertainty in antiresonant frequency is approximately ± 120 Hz. The curve fit uncertainty is ± 69 Hz.

B. Water

The chamber was assembled and filled with distilled water free from visible air bubbles. The system was checked to be certain that any air bubbles accumulated by the transducer and reflector surfaces during transfer of the water to the chamber were removed. The system was lowered into the tempering beaker. A small amount of water was placed around the reflector base to improve thermal conductivity between the tempering beaker and the sample holding apparatus. Electrical connections were made between the trans-

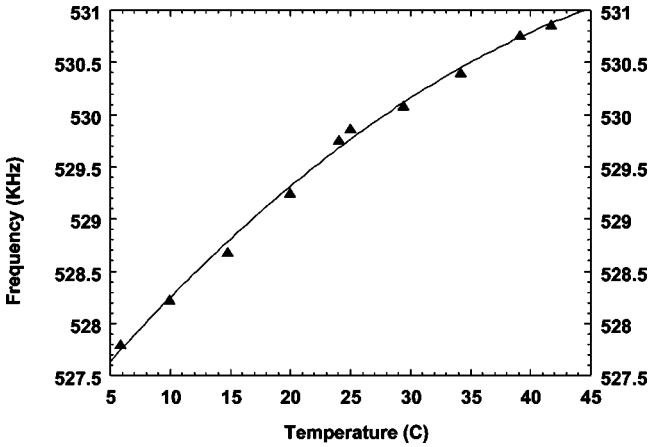

FIG. 4. A plot of the transducer antiresonant frequency as a function of temperature.

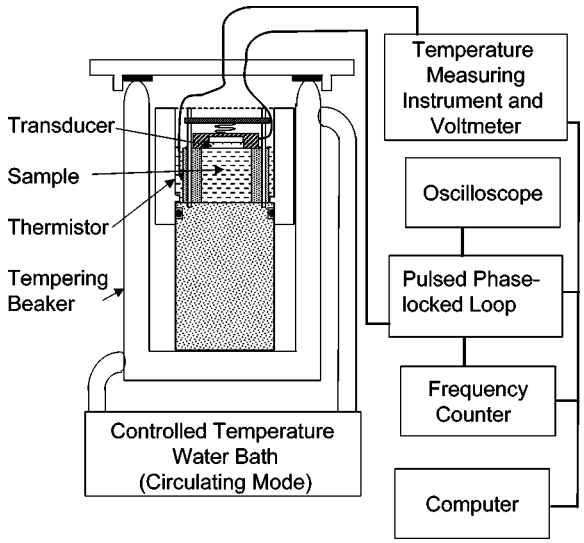

FIG. 5. Diagram showing the measurement setup for determining velocity in the sample (water).

ducer and the pulsed phase-locked loop, and between the thermistor and the temperature measuring system. The thermistor was placed approximately in the central plane of the water (sample), but completely outside the sound field. The end cap and the base plate were installed and the system was connected to instrumentation as shown in Fig. 5. The transducer lead was connected to the pulsed phase-lock loop, and the thermistor was connected to the temperature measuring circuit (resistive circuit, power supply, and voltmeter). The tempering beaker was connected to the temperature-regulated water bath for temperature control. The outputs from the pulsed phase locked loop were connected as shown. A frequency counter (Hewlett-Packard 53181A, resolution of 1 count in 10^6) was connected to the VFPPLL for frequency measurement. The oscilloscope was used for measurements and alignment of signals.

The pulsed phase-locked loop is covered elsewhere in detail.[1] For convenience an operational overview is included here. The voltage controlled oscillator (VCO) output is split into two paths. The first path is used to form a tone burst that is sent to the transducer. The second path goes to one leg of the phase comparator. In operation the tone burst forms an ultrasonic tone burst that propagates through the sample. The return ultrasonic signal is received by the same transducer, and converted into an electrical signal that is sent through an amplifier stage to the other leg of the phase comparator. The phase difference between the oscillator and the received signal causes the phase comparator to develop a voltage that is fed through the integrator to the VCO, thereby changing the VCO frequency until the phase comparator output is null and the integrator output stabilizes, thus stabilizing the VCO frequency. Under ideal operating conditions this results in quadrature between the oscillator signal and the received signal (i.e., phase difference nominally $\pm\pi/2$). In practice, however, this is not exactly the case. The oscilloscope is used to check for time alignment of the pulsed phase-locked loop apparatus parameters and the determination of the number of cycles between the transmitted and the received tone bursts at the quadrature condition.

For reasons including transducer antiresonance shifts with temperature, the system frequency most probably will be off-resonance of the transducer. Hence, the system was set up so that the frequency was always relatively far from transducer antiresonance.[13] For each run the lock is switched ''on'' and the system frequency equilibrates. The frequency is recorded and the temperature is incremented. When the temperature stabilizes the frequency is again recorded. There were at least 13 runs for each temperature setting. Temperature settings in the range from 5 °C to 45 °C were used, and data were taken at intervals of 5 °C.

1. Number of cycles between transmitted and received tone burst

When the phase-lock switch is in the locked position, one compares the number of cycles (from the oscillator) with the received output from the transducer by using the oscilloscope. For all of these measurements we use the signal from the first reflection. We measure the number of reference oscillator cycles κ between a peak in the initiating tone burst and the corresponding peak in the received echo. Because the loop is locked the oscillator is in quadrature at the chosen echo peak. Hence, the number of oscillator cycles, κ, between a point (peak) of the initiating tone burst and the corresponding point on the received tone burst can be determined. By using the high-resolution mode on the oscilloscope, κ can be determined to better than a degree or about 1/400 of a wavelength.

2. Relationship between κ and lock point

The lock point locates in time that portion of the phase signal chosen to control the phase-lock mechanism.[14] The lock point is counted down electronically from the beginning of the transmitted tone burst within the VFPPLL. As a consequence the cycle of the count down goes from the zeroth cycle to the selected cycle for application of the phase sampling. For these measurements the lock point is set close to the end of the received tone burst since the phase near the tone-burst ending is relatively easy to identify. Since the count to the lock point always begins at the beginning of the transmitted tone-burst cycle, the count to the lock point will always be a number larger than κ.

TABLE I. κ for the lock points used in this investigation.

Lock point	Temperature range (°C)	κ
1	10–20	18.3045±0.011
2	20–30	17.7293±0.003 8
3	30–45	17.3407±0.004 23

The value of κ is changed as the lock point is moved. Care in identification of correct cycle sampling must be taken in order to determine κ, and then to be certain that κ doesn't change during data collection at the different temperatures. We counted the whole number of cycles between the transmitted and received tone burst. To this number we added the phase difference between the overlapped oscillator signal and the first received signal. Typically, one expects κ to be near an integer $\pm 1/4$.[15] (For dispersive propagating media determination of κ may be more difficult, especially near the leading edges of the pulse.)

For each lock point we checked and refined the measurements of κ values by comparison with calculations based on the ultrasonic measurements in the temperature ranges as outlined below. The values of κ, the temperature range, and the three specific lock points used in this study are given in Table I, which are labeled as 1, 2, and 3 in the first column. We note that the values of κ are close to integers $\pm 1/4$, as predicted by the earlier analysis. The values in Table I support this point.

IV. RESULTS AND DISCUSSION

The data are shown in Table II. The first column gives the temperature at which the measurements were taken. The second column gives the transducer resonance frequency, while the third column gives the lock-point frequency at equilibration for each temperature. The transducer fractional wave shift Δ_T (fourth column) is calculated at each temperature from Eq. (8). The phase advance due to diffraction effects is shown in the fifth column, labeled ''diffraction fractional wave shift,'' and is calculated from Eq. (10). The acoustic path in the cavity is given as number of wavelengths in the sixth column, ''number of wavelengths in cavity κ_λ.'' Included in the acoustic path calculation are corrections for diffraction, off-resonance conditions in fractional wave shifts, and acoustic cavity thermal expansion.[16] The wavelength λ, given in the seventh column, is calculated by dividing cavity path length by the number of wavelengths in the cavity κ_λ. The wave speeds, given in column 8, are calculated from Eq. (1). The results are plotted and shown in Fig. 6. We compared the values that we obtained with values interpolated from data in the literature.[17] Table III shows a comparison of the values. We find that the difference is well within experimental uncertainty, which we estimate as no greater than $\pm 0.07\%$ in wave speed with an uncertainty of $\pm 0.15\,^{\circ}\mathrm{C}$ in temperature.

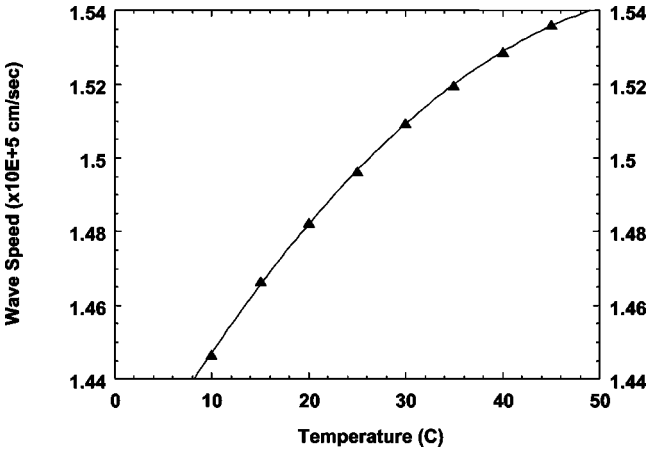

FIG. 6. A plot of the measured wave speed in water as a function of temperature.

The variable frequency pulse phase-locked loop gives good results when used with a measuring setup of fixed geometry utilizing a reflection from a single surface and well-characterized bare transducers. However, one must be careful to insure that the instrument is operated in a relatively stable

TABLE II. Terms and factors used in data reduction to calculate wave speed in water.

Temperature (°C)	Transducer resonance (MHz)	Lock point frequency, f (MHz)	Transducer fractional wave shift Δ_T	Diffraction fractional wave shift Δ_D	Number of wavelengths in cavity κ_λ	Wavelength λ (cm)	Wave speed ($\times 10^5$ cm/s)
10	0.528 248	0.511 139 3 ±0.000 558	−0.149 25	0.055 254	17.9437	0.283 11 ±0.000 4	1.4465
15	0.528 807	0.515 904 2 ±0.000 568	−0.188 65	0.055 373	17.8799	0.284 12 ±0.000 4	1.4665
20	0.529 313	0.508 370 5 ±0.000 803	−0.124 94	0.056 118	17.4230	0.291 57 ±0.000 3	1.4822
25	0.529 763	0.512 021 7 ±0.000 819	−0.144 98	0.056 178	17.3792	0.292 30 ±0.000 3	1.4964
30	0.530 160	0.515 170 0 ±0.000 813	−0.167 48	0.056 229	17.3414	0.292 94 ±0.000 3	1.5095
35	0.530 502	0.509 516 0 ±0.000 840	−0.124 96	0.056 594	17.0304	0.298 29 ±0.000 3	1.5195
40	0.530 789	0.511 853 6 ±0.000 837	−0.137 13	0.056 618	17.0072	0.298 70 ±0.000 3	1.5287
45	0.531 022	0.513 675 6 ±0.001 120	−0.148 15	0.056 641	16.9840	0.299 11 ±0.000 3	1.5361

TABLE III. A comparison of wave speeds of this work and interpolation from McSkimin's measurements (Ref. 17).

Temperature (°C)	Wave speed in water ($\times 10^5$ cm/s)	Wave speed in water (from Ref. 17) ($\times 10^5$ cm/s)	Difference %
10	1.4465	1.4471	0.04
15	1.4665	1.4657	−0.05
20	1.4822	1.4822	0.00
25	1.4964	1.4966	0.01
30	1.5095	1.5091	−0.01
35	1.5195	1.5198	0.02
40	1.5287	1.5288	0.007
45	1.5361	1.5364	0.02

temperature environment. Without such precautions the phase comparison at the lock point drifts. We also found that when operating the VFPPLL one must be certain that the oscilloscope measurements leading to the determination of κ must be made with electrical amplitudes that are close to the actual values encountered during measurements.

With care, small changes in the lock-point parameters (e.g., the cycle location of the sample/hold pulse timing relative to a long tone burst) does not strongly affect the measurement. However, major shifts of the sample/hold point especially close to the beginning of the tone burst result in large changes in frequency, and can lead to error. Additionally, one must observe caution when using this system (or any variable frequency-based ultrasonic system) to measure a highly dispersive[18] sample, such as may occur with stratified samples, as small shifts in frequency can result in relatively large changes in actual wave speeds. In these cases one would note a change in velocity with frequency.

V. CONCLUSIONS

We have described an interferometric ultrasonic system that is capable of highly accurate velocity measurements. To demonstrate this point we measured the speed of sound in distilled water. In order to make accurate transducer corrections we have presented temperature data on a PZT-5A transducer antiresonance frequency. By characterizing the temperature dependence of the transducer's antiresonant frequency as a function of temperature, we make more accurate corrections for the transducer phase shifts due to off-resonance operation. We have also shown that diffraction corrections have a much smaller effect, while also being relatively constant over the frequency range used in this study.

A larger effect is caused by the fact that ''quadrature'' as determined by the electronic circuitry in the VFPPLL contains small shifts associated with circuit-related imperfections. Examples of such are sample-and-hold droop, quadrature detector imbalance, preamplifier phase shifts, location of sample and hold point, etc. Many of these are impossible to remove from the circuit, but the experimental determination of κ removes their effects from the measurement.

We have shown that the apparatus described here is capable of accurate measurements as the temperature is varied over the range specified by measuring the wave speed in distilled water over the temperature range from 10 °C to 45 °C. The agreement with literature values is well within estimated measurement uncertainty.

[1] W. T. Yost, J. H. Cantrell, and P. W. Kushnick, ''Fundamental aspects of pulse phase-lock loop technology-based methods for measurement of ultrasonic velocity,'' J. Acoust. Soc. Am. **91**, 1456–1468 (1992).

[2] R. J. Blume, ''Instrument for continuous high resolution measurement of changes in the velocity of ultrasound,'' Rev. Sci. Instrum. **34**, 1400–1407 (1963).

[3] J. S. Heyman, ''Pulsed phase-locked loop strain monitor,'' U.S. Patent No. 4,363,242 (1982).

[4] E. J. Chern, J. S. Heyman, and J. H. Cantrell, Jr., ''Determination of material stress from the temperature dependence of the acoustic natural velocity,'' in *Proceedings IEEE Ultrasonics Symposium* (Institute of Electrical and Electronic Engineers, New York, 1981).

[5] J. S. Heyman, S. G. Allison, K. Salama, and S. L. Chu, ''Effects of Carbon Content on Stress and Temperature Dependences of Ultrasonic Velocity in Steels,'' ASM Proceedings, Nondestructive Evaluation: Application to Materials Processing, Philadelphia, PA., 3–4 October, 1984, pp. 177–184.

[6] M. Namkung, D. Utrata, and R. DeNale, ''Effect of uniaxial stress magnetic field-induced domain wall motion,'' Proc. IEEE Ultrasonics Symposium Vol. 2, 983 (1991).

[7] E. C. Everbach and R. E. Apfel, ''An interferometric technique for B/A measurement,'' J. Acoust. Soc. Am. **98**, 3428–3438 (1995).

[8] The relationship between the electrical properties of a thin disk resonator is covered well in V. M. Ristic, *Principles of Acoustic Devices* (Wiley, New York, 1983), pp. 142–145.

[9] J. Williams and J. Lamb, ''On the measurement of ultrasonic velocity in solids,'' J. Acoust. Soc. Am. **30**, 308–313 (1958).

[10] J. Williams and J. Lamb, ''On the measurement of ultrasonic velocity in solids,'' J. Acoust. Soc. Am. **30**, 308–313 (1958).

[11] W. C. Elmore and M. A. Heald, *The Physics of Waves* (McGraw-Hill, New York, 1969), pp. 101–102.

[12] P. H. Rodgers and A. L. Van Buren, ''An exact expression for the Lommel diffraction correction integral,'' J. Acoust. Soc. Am. **55**, 724–728 (1974). See also G. C. Benson and O. Kiyohara, ''Tabulation of some integral functions describing diffraction effects in the ultrasonic field of a circular piston source,'' J. Acoust. Soc. Am. **55**, 184–185 (1974).

[13] Initial frequency adjustment is normally made by observing the phase comparison signal from the pulsed phase-locked loop apparatus and adjusting the frequency until the signal's slope is zero. (This procedure places the operating frequency near transducer antiresonance.)

[14] The group delay in the phase signal filter causes a time shift in the phase signal. Hence, the choice of the portion of the tone burst to control the phase locking is offset in time from the received tone burst. Generally the tone-burst shape can be identified in the phase signal. We chose a lock point near the end of the phase signal that corresponded to the first received tone burst.

[15] This value is affected by circuit-related vagaries such as imbalance in the phase detector, sample and hold droop, bias current shifts in the integrator circuit, oscillator offsets, etc. The value of κ can be determined by a high-speed oscilloscope capable of phase measurements between the received signal from the cell and the voltage-controlled oscillator. Ideally, the points for wave retrieval (oscillator and echo wave) are at the phase detector in the circuit. See Ref. 1.

[16] The expansion includes the spacers (Pyrex) with a thermal expansion coefficient of approximately 3.6×10^{-6}/°C. The mounting frame for the transducer is made from Lucite (thermal expansion coefficient 70×10^{-6}/°C). We assume that because of the mounting geometry the transducer surface is held fixed to the front mounting plane. Therefore, we only considered the expansion coefficient of the pyrex spacers. See M. Bauccio, *ASM Engineering Materials Reference Book*, 2nd ed. (ASM International, Materials Park, OH (1994), pp. 322, 384, for thermal expansion data for Pyrex.

[17] H. J. McSkimin, ''Velocity of sound in distilled water for temperature range 20 degrees–75 degrees C,'' J. Acoust. Soc. Am. **37**, 325–328 (1965).

[18] The effect of dispersive systems on velocity and velocity measurements is covered well in G. B. Whitham, *Linear and Nonlinear Waves* (Wiley-Interscience, New York, 1974), Chaps. 11 and 12.

Analysis of the sandwich piezoelectric ultrasonic transducer in coupled vibration

Lin Shuyu
Institute of Applied Acoustics, Shaanxi Normal University, Xian, Shaanxi, 710062, People's Republic of China

(Received 8 January 2004; revised 23 November 2004; accepted 29 November 2004)

The coupled vibration of the sandwich piezoelectric transducer with a large cross-section is analyzed using an approximate analytic method. The resonance frequency equations of the transducer are derived and the effect of the geometrical dimensions on the resonance frequency is studied. It is illustrated that when the radial vibration in the transducer is considered, the vibration of the sandwich transducer becomes more complex. Apart from the longitudinal resonance frequency, the radial resonance frequency can also be obtained. For comparison, numerical methods are also used to simulate the coupled vibration; the resonance frequency and the vibrational displacement distribution are computed. Compared with one-dimensional longitudinal theory, the radial dimensions of the transducer are no longer limited because the coupled vibration is considered. Compared with numerical methods, the physical meaning of the analytic method is concise. It is illustrated that the resonance frequencies obtained from the coupled resonance frequency equations are in good agreement with those from numerical methods, and they are in better agreement with the measured results than those from one-dimensional theory. Since the radial and the coupled vibration are considered in the analysis, more resonance frequencies can be obtained. Therefore, using the coupled resonance frequency equations, the sandwich transducer with multifrequency or wide frequency bandwidth can be designed and used in ultrasonic cleaning, ultrasonic sonochemistry and other applications.
[DOI: 10.1121/1.1849960]

PACS numbers: 43.38.Fx, 43.38.Ar [AZ] Pages: 653–661

I. INTRODUCTION

Sandwich piezoelectric ultrasonic transducers are widely used in underwater acoustics and ultrasonics. According to traditional design theory of this type of transducer,[1–6] the vibration of the sandwich transducer is considered as one-dimensional with the Poisson effect and the radial vibration being ignored. Therefore, it is required that the radial dimensions of the transducer must be far less than the longitudinal dimension. Generally speaking, when the radial dimensions are less than a quarter of the longitudinal wavelength, one-dimensional theory can be used and the error between the measured and theoretical resonance frequencies is negligible. However, along with the development of ultrasonic technology, ultrasonic transducers are used in more and more new applications, such as high frequency ultrasonic metal and plastic welding and some practical applications concerning very large ultrasonic power. In these cases, the radial dimensions are usually larger than a quarter of a longitudinal wavelength. Therefore, one-dimensional longitudinal design theory of the sandwich transducers is no longer applicable; otherwise, large frequency error will be caused. Specifically speaking, one-dimensional longitudinal theory is not applicable for the following two types of sandwich piezoelectric ultrasonic transducers. (1) High frequency sandwich transducers such as those used in ultrasonic metal welding. When the resonance frequency of the sandwich transducer is increased, the longitudinal wavelength and geometrical dimension will accordingly decrease. According to the assumptions introduced in one-dimensional longitudinal theory, the radial dimensions of the transducer must also be decreased. Therefore, the cross-section of the transducer is small and the mechanical strength and the power capacity will be lowered. To raise the mechanical strength and the power capacity, the radial dimensions of the high frequency sandwich transducer must be increased; thus, the radial vibration in this kind of transducers must be considered in order not to bring about appreciable frequency design error. (2) High power sandwich transducers. In some new ultrasonic applications, such as ultrasonic metal and plastic welding, very large ultrasonic power is needed; therefore, the radial dimensions exceed a quarter of longitudinal wavelength and one-dimensional theory is also not applicable. In the above-mentioned two cases, the vibration of the transducer is a coupled one of longitudinal and radial vibrations. Therefore, new design theory must be developed in order to study the coupled vibration of the sandwich transducers with a large cross-section or high resonance frequency.

For the coupled vibration of sandwich piezoelectric ultrasonic transducers, numerical methods have been widely used to study the frequency characteristics and vibration modes.[7–10] Among the numerical methods, the finite element method seems to be the most promising. Nowadays, some commercial software is available in the analysis of vibrational systems, such as ANSYS software. Although numerical methods are widely used in engineering problems, the preprocessing of these methods is complex; the physical meaning of the results is not as concise as that in one-dimensional vibrational theory. On the other hand, compared

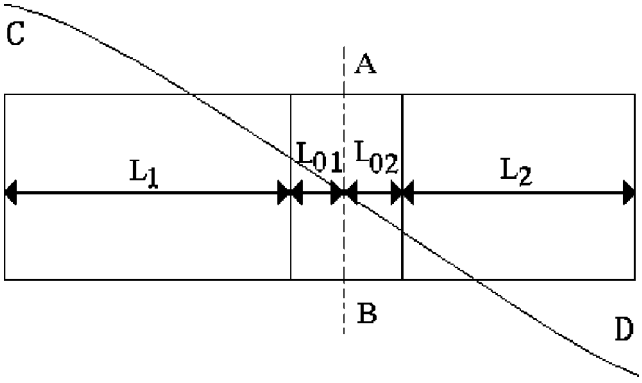

FIG. 1. Geometrical diagram of a sandwich piezoelectric ceramic ultrasonic transducer.

with some large engineering vibrational problems, the vibrational analysis of the sandwich transducers is comparatively simple. With the consideration of these factors, an approximate analytical method is presented in this paper and the coupled vibration of the sandwich transducer is studied analytically. In the following analysis, the equivalent elastic constants of the component parts of the transducer are introduced. The coupled vibration of the front and the back metal masses with a circular cross-section is first analyzed. Then the coupled vibration of the piezoelectric ceramic ring is studied, and then the coupled vibration of the sandwich transducer is analyzed. The resonance frequency equations are derived and the relationship between the resonance frequency and the geometrical dimensions is analyzed. Finally, the theoretical and experimental results are given.

II. COUPLED VIBRATION OF THE SANDWICH PIEZOELECTRIC TRANSDUCER WITH LARGE CROSS-SECTION AND HIGH FREQUENCY

Figure 1 illustrates a geometrical diagram and the vibrational displacement distribution of a sandwich piezoelectric ceramic ultrasonic transducer of a half wavelength. The transducer resonates at its fundamental mode and there is a displacement node in the transducer. In the figure, L_1 and L_2 are the lengths of the back and the front metal masses in the sandwich transducer; L_{01} and L_{02} are the lengths of the longitudinally polarized piezoelectric ceramic elements after and before the longitudinal displacement node line AB in the transducer, the curve CD represents the longitudinal displacement distribution. In the case of $L_1=L_2$ and $L_{01}=L_{02}$, the displacement node is located at the transducer's geometrical center. The radii of the three parts of the sandwich transducer are R_1, R_2, and R_0, respectively. In the figure, the displacement node line AB divides the half wavelength sandwich transducer into two vibrators of quarter wavelength. In the following analysis, the coupled vibration and the resonance frequency equations of the transducer will be analyzed.

The above-presented analytic method presented here can be defined as an equivalent elastic method and its basic principle can be explained as follows.[11,12] Since the structure of the sandwich transducer is usually axis-symmetrical, its vibration is also symmetrical; the vibration of the transducer can be regarded as a coupled one of longitudinal and radial vibrations. In this case, for the sandwich transducer, the shearing stress and strain in the transducer are ignored; the torsional and the flexural vibrations in the transducer are not taken into account, only the radial and the longitudinal extensional vibrations are considered. When a mechanical coupling coefficient is introduced, the complex coupled vibration of the sandwich transducer can be reduced to two equivalent extensional vibrations, one being the extensional vibration in the longitudinal direction, the other being the radial vibration in the radial direction. However, these two equivalent vibrations are not independent of each other; they are correlated by the mechanical coupling coefficient that is defined as the ratio of the longitudinal stress over the radial and tangential stresses. It should be noted that though the two introduced equivalent extensional vibrations in the transducer are similar to traditional one-dimensional vibrations, they are entirely different. The two equivalent extensional vibrations have different equivalent elastic constants. These equivalent elastic constants are not only dependable on the material parameters, but also on the geometrical dimensions and the coupling of the longitudinal and the radial vibrations.

According to the equivalent elastic analytic method, the coupled vibration of the transducer is regarded as the coupled vibration of two vibrations. One is the equivalent longitudinal vibration; the other the equivalent radial vibration. Therefore, the resonance frequency equations can be regarded as a combination of longitudinal and radial resonance frequency equations. For simplicity, the fundamental mode will be discussed in the following analysis. In this case, the sandwich transducer is a half wavelength vibrator. The displacements have maximum values at its two ends and in the middle of the sandwich transducer; there is a position of minimum displacement, which is defined as the displacement node.

As stated in the above analysis, the transducer is composed of two vibrators of a quarter wavelength. One consists of the metal mass of length L_1 and the piezoelectric ceramic element of length L_{01}, the other the metal mass of length L_2 and the piezoelectric ceramic element of length L_{02}. In the following analysis, the resonance frequency equations for radial vibrations in the transducer are first derived, and then the resonance frequency equations for a longitudinal vibration of the quarter wavelength vibrator are analyzed.

A. Radial resonance frequency equation of the metal mass in the sandwich transducer in coupled vibration

When the length and the radius do not satisfy the slender rod condition, one-dimensional theory is not applicable. In previous works,[13,14] the mechanical coupling coefficient is introduced and the coupled vibration of finite-dimension cylinders and disks is studied. The natural frequency equation is derived and some decoupled vibration modes are analyzed. According to the analytic method, the coupled vibration of the metal mass in the transducer can be reduced to two equivalent vibrations: one being the equivalent radial vibration, and the other the equivalent longitudinal vibration. These two equivalent vibrations can be represented by the

plane radial vibration of a thin disk and the longitudinal extensional vibration of a slender rod. For the equivalent radial vibration of the metal mass, when its outer side is free of external force, i.e., $T_{ri}|_{r=R_i}=0$, the resonance frequency equation for the equivalent radial vibration of the metal mass can be obtained as is shown in the following expression:[13]

$$k_{ri}R_iJ_0(k_{ri}R_i)(1-\nu_i n_i)-J_1(k_{ri}R_i)(1-\nu_i-2\nu_i n_i)=0. \tag{1}$$

In Eq. (1), $i=1,2$, which represents the back and the front metal masses, R_i is the radius of the metal mass; J_0 and J_1 are Bessel functions; ν_i is the Poisson's ratio of the metal mass; $k_{ri}=\omega/V_{ri}$, $V_{ri}=(E_{ri}/\rho_i)^{1/2}$, k_{ri}, V_{ri} are the equivalent radial wave number and sound speed; ρ_i is density of the back and front metal mass; $E_{ri}=E_i(1-\nu_i n_i)/(1+\nu_i)(1-\nu_i-2\nu_i n_i)$; E_i is Young's modulus of the back and the front metal mass; E_{ri} is defined as the radial equivalent elastic constant of the back and front metal mass; $n_i=T_{zi}/(T_{ri}+T_{\theta i})$; $T_{zi}, T_{ri}, T_{\theta i}$ are longitudinal, radial and tangential stresses; n_i is the introduced mechanical coupling coefficient in the back and front metal mass; ω is angular frequency. It can be seen from the above analysis that though the equivalent radial vibration in the back and front metal mass is similar to plane radial vibration of a thin metal disk, they are different. In this analysis, the mechanical coupling between longitudinal and radial vibrations is considered and the equivalent radial vibration depends on the longitudinal vibration.

B. Radial resonance frequency equations of the piezoelectric ceramic elements in the sandwich transducer in coupled vibration

Piezoelectric ceramic rings and disks are widely used in ultrasonic transducer, piezoelectric transformer, ceramic filter, vibration sensor and other applications. In traditional vibration analysis theory, the piezoelectric ceramic disk resonators are usually considered as one-dimensional and the coupling between longitudinal and radial vibrations is neglected. To satisfy the requirement of one-dimensional theory, the thickness of the disk resonator must be much larger or smaller than its radius, and these two types of geometrical shapes of the resonator are the limiting cases of the slender rod and the thin disk. The analysis theories for longitudinal vibration of the piezoelectric ceramic slender rod and radial vibration of the thin circular disk are well established and used in the design of resonators and measurement of piezoelectric ceramic material parameters. However, in practical applications, such as in the sandwich transducer, the disk resonator has finite dimensions of thickness and radius. The vibration of finite dimension disk resonator is complex; the coupling between different vibrational modes in the resonator must be taken into account, and one-dimensional theory is no longer applicable, especially for the disk whose thickness and radius have the same magnitude in dimension.

For coupled vibration of piezoelectric ceramic disk resonators of a finite dimension, a new analysis theory must be developed. Numerical methods have also been used to analyze the complex coupled vibration of piezoelectric ceramic circular disk resonators of finite dimension. The above-presented approximate analytic method for the coupled vibration analysis of an isotropic metal disk is also used for the coupled vibration of piezoelectric disk resonators.[15–19] In this method, the analysis of coupled vibration of the piezoelectric ceramic disk is similar to that of an isotropic metal disk. The difference is that the piezoelectric effect must be considered, and the analysis is a little more complex. Based on piezoelectric and motion equations, when shearing stress and strain are ignored and the mechanical coupling coefficient is introduced, the complex coupled vibration of the piezoelectric disk resonator is also reduced to two equivalent vibrations, one is the plane radial vibration of the piezoelectric ceramic disk, and the other is the longitudinal extensional vibration of the piezoelectric ceramic disk, these two equivalent vibrations have different elastic constants. When the piezoelectric ceramic disk is free of external force on its outside surface, we have $T_{r0j}|_{r=R_0}=0$. Here R_0 is the radius of the piezoelectric disk, T_{r0j} is the radial stress in the piezoelectric ceramic disk. Incorporating these boundary conditions, the equivalent radial resonance frequency equation of the piezoelectric ceramic resonator in coupled vibration is[15,16]

$$k_{r0j}R_0J_0(k_{r0j}R_0)(1-\nu_{13}n_{0j})-J_1(k_{r0j}R_0)(1-\nu_{12}-2\nu_{13}n_{0j})=0. \tag{2}$$

In Eq. (2), $j=1,2$ represents the piezoelectric ceramic elements after and before the displacement node. R_0 is the radius of the piezoelectric ceramic element, J_0 and J_1 are Bessel functions; $\nu_{12}=-s_{12}^E/s_{11}^E, \nu_{13}=-s_{13}^E/s_{11}^E$, s_{ij}^E is the elastic compliance constant at constant electric field of the piezoelectric ceramic material; $k_{r0j}=\omega/V_{r0j}$, $V_{r0j}=(E_{r0j}/\rho_0)^{1/2}$, k_{r0j}, V_{r0j} are the equivalent radial wave number and sound speed in the piezoelectric ceramic elements; ρ_0 is volume density;

$$\begin{aligned}E_{r0j}&=\frac{1}{2}\left(\frac{1}{s_{11}^E-s_{12}^E}+\frac{1}{s_{11}^E+s_{12}^E+2s_{13}^E n_{0j}}\right)\\&=\frac{s_{11}^E+s_{13}^E n_{0j}}{(s_{11}^E-s_{12}^E)(s_{11}^E+s_{12}^E+2s_{13}^E n_{0j})}\\&=\frac{1-\nu_{13}n_{0j}}{s_{11}^E(1+\nu_{12})(1-\nu_{12}-2\nu_{13}n_{0j})};\end{aligned}$$

E_{r0j} is defined as the equivalent elastic constant of radial vibration of the piezoelectric ceramic elements; $n_{0j}=T_{z0j}/(T_{r0j}+T_{\theta 0j})$; $T_{z0j}, T_{r0j}, T_{\theta 0j}$ are longitudinal, radial and tangential stresses; n_{0j} is the introduced mechanical coupling coefficient in the back and front piezoelectric ceramic elements; ω is angular frequency.

C. Longitudinal resonance frequency equations of back and front vibrators of quarter wavelength in the sandwich transducer in coupled vibration

According to the proposed approximate analytic method for the coupled vibration of the quarter wavelength sandwich transducer, the coupled vibration of the sandwich transducer is reduced to a combination of equivalent radial and longitudinal vibrations. Generally speaking, there are four equiva-

lent vibrations for the quarter wavelength sandwich transducer in coupled vibration. Among these four equivalent vibrations, two are equivalent radial vibrations corresponding to the metal mass and the piezoelectric ceramic disk; the other two are equivalent longitudinal vibrations for the two parts of the sandwich transducer. The two equivalent radial vibrations have been analyzed in the above analysis and the radial resonance frequency equations for the quarter wavelength sandwich transducer are derived. The quarter wavelength sandwich transducer consists of two parts, which are the metal mass and the piezoelectric ceramic elements. The longitudinal boundary conditions for the quarter wavelength sandwich transducer are as follows. (1). At the output end of the transducer (the metal mass end contacting with the external load), the longitudinal force is zero, i.e., $T_{zi}=0$. (2). At the interface between the metal mass and the piezoelectric ceramic elements, the longitudinal fore and the longitudinal displacement are continuous, i.e., $\xi_{zi}=\xi_{z0j}$ and $S_i T_{zi}=S_0 T_{z0j}$. Here ξ_{zi}, ξ_{z0j} are the longitudinal displacements in the metal mass and the piezoelectric ceramic elements. (3). At the displacement node of the quarter wavelength transducer (the displacement node of the transducer is in the piezoelectric ceramic elements and it divides the piezoelectric ceramic elements into two parts of length L_{01} and L_{02}), the boundary condition is that the displacement is zero. Incorporating these boundary conditions, for the equivalent longitudinal vibration of the quarter wavelength sandwich transducer, the resonance frequency equations of the quarter wavelength vibrators in the sandwich transducer can be obtained as[20]

$$\tan(k_{z0j}L_{0j})\cdot\tan(k_{zi}L_i)=(\rho_0 V_{z0j}S_0)/(\rho_i V_{zi}S_i). \tag{3}$$

In the above equation, L_{0j} is the length of the piezoelectric ceramic elements in the quarter wavelength vibrator; k_{z0j} is the equivalent longitudinal wave number, $k_{z0j}=\omega/V_{z0j}$, V_{z0j} is the equivalent longitudinal sound speed in the piezoelectric ceramic elements, $V_{z0j}=(E_{z0j}/\rho_0)^{1/2}$, E_{z0j} is the equivalent longitudinal elastic constant of the piezoelectric ceramic elements,

$$E_{z0j}=\left[s_{33}^E+\frac{s_{13}^E}{n_{0j}}-\frac{d_{33}}{\varepsilon_{33}^T}\left(d_{33}+\frac{d_{31}}{n_{0j}}\right)\right]^{-1}$$

$$=\frac{1}{s_{33}^E[1-\nu_{31}/n_{0j}-k_{33}^2(1-\lambda_{31}/n_{0j})]};$$

$\nu_{31}=-s_{13}^E/s_{33}^E$, $\lambda_{31}=-d_{31}/d_{33}$, d_{31} and d_{33} are piezoelectric constants, ε_{33}^T is the dielectric constant, $k_{33}^2=d_{33}^2/(s_{33}^E\varepsilon_{33}^T)$, k_{33} is the electro-mechanical coupling coefficient of a slender piezoelectric ceramic rod in longitudinal vibration; $S_0=\pi R_0^2$. L_i is the length of the back and front metal mass; k_{zi} is the equivalent longitudinal wave number, $k_{zi}=\omega/V_{zi}$, V_{zi} is the equivalent longitudinal sound speed in the back and front metal mass, $V_{zi}=(E_{zi}/\rho_i)^{1/2}$, E_{zi} is the equivalent longitudinal elastic constant of the back and front metal mass in the quarter wavelength vibrator, $E_{zi}=E_i/(1-\nu_i/n_i)$; $S_i=\pi R_i^2$ is the cross-sectional area of the back and front metal mass.

It can be seen that though Eq. (3) is similar to a traditional resonance frequency equation of a sandwich transducer in one-dimensional theory, the difference is obvious. For the coupled vibration of the sandwich transducer, the resonance frequency equation depends on the mechanical coupling coefficient. Therefore, in Eq. (3), the mechanical coupling between longitudinal and radial vibrations is considered.

In the above analysis, radial and longitudinal resonance frequency equations (1)–(3) for the quarter wavelength vibrators in the sandwich transducer in coupled vibration are derived. In these equations, there are three unknowns, which are n_i, n_{0j} and ω. Their solutions are definite. The three resonance frequency equations all have many roots; they correspond to different vibrational orders, such as fundamental mode or overtones. When the vibrational orders are determined, the resonance frequency can be obtained. For most practical applications in power ultrasonics and underwater sound, a fundamental vibrational mode is used. For this reason, only a fundamental vibrational mode is analyzed in the following analysis.

It can also be seen that the resonance frequency equations can be divided into two categories; one is for radial vibration and the other for longitudinal vibration. However, they are not independent, but are coupled to each other by the mechanical coupling coefficients. Therefore, the resonance frequencies obtained from these coupled radial and longitudinal resonance frequency equation are different from those from one-dimensional longitudinal theory, and since the radial vibrations are considered, more resonance frequencies can be obtained.

III. THEORETICAL RELATIONSHIP BETWEEN RESONANCE FREQUENCIES AND GEOMETRICAL DIMENSIONS OF THE SANDWICH TRANSDUCER IN COUPLED VIBRATION

In the above analysis, radial and longitudinal resonance frequency equations of the sandwich transducer in coupled vibration are derived. From the resonance frequency equations (1)–(3), the radial and the longitudinal resonance frequencies can be calculated when the material properties and the geometrical dimensions of the transducer are given. In order to analyze and design the sandwich transducer with a large cross-section and high resonance frequency, the relationship between the resonance frequency and the geometrical dimensions of the sandwich transducer in coupled vibration must be studied and the resonance frequency equations must be solved. Because the resonance frequency equations are transcendental ones and that their analytical solutions are impossible to find, numerical methods must be used. To simplify the computation, the sandwich transducer is assumed to be symmetrical. For symmetrical transducers, the quarter wavelength vibrators before and after the displacement node of the transducer are all the same, and we have $L_1=L_2$, $R_1=R_2$, $S_1=S_2$, $V_{z1}=V_{z2}$, $V_{r1}=V_{r2}$, $E_{z1}=E_{z2}$, $E_{r1}=E_{r2}$, $k_{z1}=k_{z2}$, $k_{r1}=k_{r2}$, $n_1=n_2$; $L_{01}=L_{02}$, $V_{z01}=V_{z02}$, $V_{r01}=V_{r02}$, $k_{z01}=k_{z02}$, $k_{r01}=k_{r02}$, $n_{01}=n_{02}$, $E_{z01}=E_{z02}$, $E_{r01}=E_{r02}$. Considering the symmetry of the sandwich transducer, only one vibrator of a quarter wavelength needs to be studied in the following analysis. In this case, there are three resonance frequency equations for the quarter wave-

TABLE I. Material property of the back and the front metal mass.

$\rho(\mathrm{kg/m^3})$	$E(\mathrm{N/m^2})$	ν
2.7×10^{3}	7.15×10^{10}	0.34

TABLE II. Material property of the piezoelectric ceramic elements.

$\rho_0(\mathrm{kg/m^3})$	$s_{11}^E(\mathrm{m^2/N})$	$s_{12}^E(\mathrm{m^2/N})$	$s_{13}^E(\mathrm{m^2/N})$	$s_{33}^E(\mathrm{m^2/N})$
7500	12.3×10^{-12}	-4.05×10^{-12}	-5.31×10^{-12}	15.5×10^{-12}
$d_{31}(C/N)$	$d_{33}(C/N)$	k_p	k_{33}	$\varepsilon_{33}^T/\varepsilon_0$
-123×10^{-12}	496×10^{-12}	0.58	0.70	1300

length transducer: two are for the radial vibrations and one is for the longitudinal vibration. In these three equations, there are three variables. They are the mechanical coupling coefficients n_i and n_{0j} for the metal mass and the piezoelectric ceramic elements and the resonance frequency. Since the number of the resonance frequency equations is the same as that of the variables, the solutions to the equations can be determined completely. It should be pointed out that only the mechanical coupling coefficients and the resonance frequency can be computed from the transcendental resonance frequency equations. The stresses in the transducer cannot be computed. This is the disadvantage of the developed approximate analytic method; that is to say, it cannot be used to compute the displacement distribution and the stress and strain in the transducer at present. Solutions to the frequency equations can be found by using a numerical method. In this paper, the MATHEMATICA software program is directly used to compute the mechanical coupling coefficients and the resonance frequency of the quarter wavelength transducer.

Based on the definition of the mechanical coupling coefficient, it is obvious that the mechanical coupling coefficient is dependent on the stresses in the transducer and the stresses are very important for the vibration of the transducer. However, it can be seen from the above analysis that it is the mechanical coupling coefficient not the stress that appears in the resonance frequency equations. Therefore, there is no need to consider the stress for the calculation of the resonance frequency. This does not mean that the stress has no effect on the resonance frequency; the effect of stress on the resonance frequency is reflected in the mechanical coupling coefficient in this approximate analytical method. On the other hand, it can be seen that when the material and the geometrical dimensions of the transducer are given, the resonance frequency is determined, and the mechanical coupling coefficient is also determined. This means that the resonance frequency and the mechanical coupling coefficient only depend on the material parameters and the geometrical dimensions of the transducer.

It should be pointed out that this is an approximation in the analysis. In practical cases, the resonance frequency is indeed only dependent on the material and geometrical dimensions. However, the stress is different at different positions in the transducer, and the mechanical coupling coefficient as a ratio of different stresses in the transducer may also be different at different positions in the transducer.

In the calculation, the material of back and front metal mass is hard aluminum; its standard material parameters are used and listed in Table I. The piezoelectric ceramic material is an equivalent of PZT-4 made in China. Its standard material parameters are also used and listed in Table II. Using these basic data, radial and longitudinal resonance frequencies of the sandwich transducer in coupled vibration are calculated. Because each of the three resonance frequency equations has a number of solutions that correspond to the fundamental mode and overtones of the transducer, many resonance frequencies can be obtained from the frequency equations. For simplicity, the fundamental vibrational mode is studied and the lowest resonance frequencies of the sandwich transducer are calculated. Based on the analysis and the computation results, it can be seen that for the fundamental vibrational mode of the sandwich transducer, three sets of solutions to the resonance frequency equations can be found, and they are represented by (f_{r1},n_{r1},n_{r01}), (f_{r2},n_{r2},n_{r02}) and (f_l,n_l,n_{0l}), respectively. They correspond to the radial vibration of the circular metal mass, the radial vibration of the piezoelectric ceramic elements, and the longitudinal vibration of the sandwich transducer, respectively. Figure 2 and Fig. 3 illustrate the calculated relationship between radial and longitudinal resonance frequency and geometrical dimensions of the sandwich transducer. In Fig. 2, the relationship between resonance frequency and length of the metal mass of the sandwich transducer is illustrated; in Fig. 3, the relationship between resonance frequency and radius of the sandwich transducer is illustrated.

From the theoretical results it can be seen that when the coupled vibration between longitudinal vibration and radial vibration in the sandwich transducer is considered, the vibration analysis of the sandwich transducer becomes complex compared with traditional one-dimensional longitudinal design theory. For each vibrational mode, apart from longitudinal resonance frequency, radial resonance frequencies can also be obtained. Since the transducer can be driven on either the fundamental mode or the overtones, many resonance frequencies can be found from the resonance frequency equations of the sandwich transducer.

From the theoretical analysis, it can be illustrated that

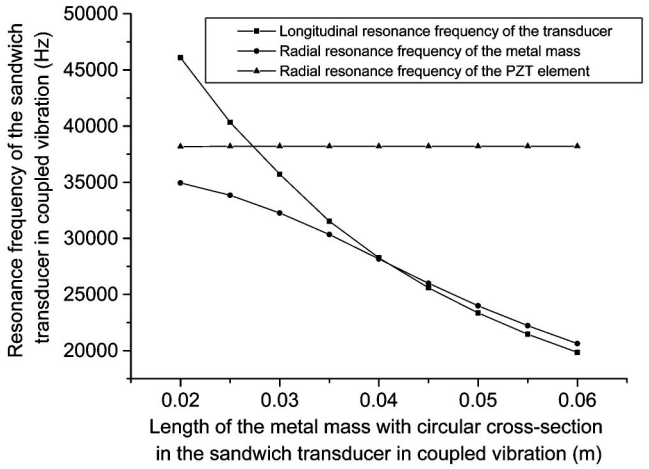

FIG. 2. Theoretical relationship between the resonance frequency and the length of the metal mass in the sandwich transducer in coupled vibration.

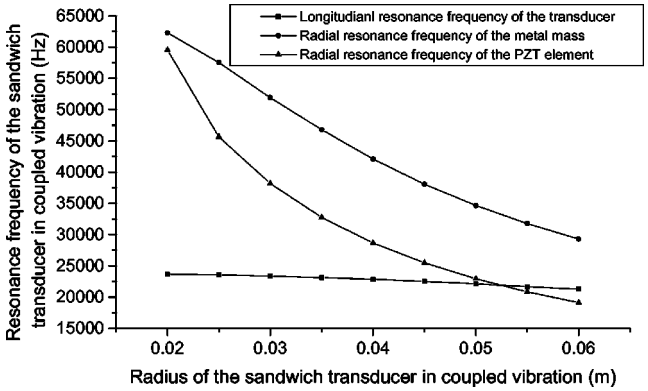

FIG. 3. Theoretical relationship between the resonance frequency and the radius of the sandwich transducer in coupled vibration.

both longitudinal and radial dimensions affect the resonance frequency of the transducer in coupled vibration. This is different from traditional one-dimensional longitudinal theory. According to one-dimensional longitudinal theory, only longitudinal resonance frequency can be obtained and radial dimension of the transducer has little effect on longitudinal resonance frequency.

It can be seen that for fundamental vibrational mode of the sandwich transducer of a quarter wavelength, there are three resonance frequencies which are radial resonance frequencies of the metal mass, radial resonance frequency of the piezoelectric ceramic elements and longitudinal resonance frequency of the sandwich transducer. They all depend on the geometrical dimensions of the sandwich transducer. When the dimensions of the piezoelectric ceramic elements are fixed, the resonance frequency of the transducer depends on the dimensions of the metal mass. When the length of the metal mass is increased, radial resonance frequency of the metal mass is decreased; radial resonance frequency of the piezoelectric ceramic elements remains unchanged and longitudinal resonance frequency is decreased. This can be explained as follows. For the metal mass, when its length is increased, the ratio of the length over the radius is increased, the longitudinal kinetic energy becomes large and the radial resonance frequency is therefore decreased. For the piezoelectric ceramic elements, its geometrical dimension remains unchanged and therefore its resonance frequency also remains unchanged. On the other hand, the radial dimension also affects the resonance frequency of the sandwich transducer. When the radius of the transducer is increased, the radial resonance frequencies of the metal mass and the piezoelectric ceramic elements are decreased and the longitudinal resonance frequency is also decreased. The reason for this phenomenon is that the radial resonance frequency is inversely proportional to the square of the radius. When the radius is increased, the radial kinetic energy for the sandwich transducer is increased and therefore the longitudinal resonance frequency is decreased because of Poisson's effect.

From the above analysis, it is clearly seen that both the length and radius affect the resonance frequency of the transducer according to the theory of coupled vibration. However, the effect of length and radius on the resonance frequency is not independent. When the lateral dimension is large compared with its length, the Poisson's effect cannot be ignored, and therefore the radial dimensions affect the resonance frequency. For the radial vibration, apart from the radius, the length also affects the radial resonance frequency. For the longitudinal vibration, apart from the length, the radius also affects the longitudinal resonance frequency. All these conclusions can be obtained from the calculated relationship between the dimension and the resonance frequency, and they are different from the conclusions drawn from one-dimensional theory.

It can be seen from the theoretical analysis that for the coupled vibration of the sandwich transducer, since the radial vibration and the coupling between longitudinal and radial vibrations are considered, many resonance frequencies can be obtained from the coupled resonance frequency equations. Therefore, by choosing the geometrical dimensions of the sandwich transducer properly, the sandwich transducer can be made to vibrate on many resonance frequencies or on a broad frequency bandwidth. Hence by using the coupled vibrational theory, multifrequency or wide bandwidth sandwich transducers can be designed and used in some applications such as ultrasonic cleaning and sonochemistry.

IV. NUMERICAL SIMULATION AND EXPERIMENTAL RESULTS

To verify the developed method for the design of sandwich transducers with a large cross-section and high frequency, two piezoelectric ceramic sandwich transducers with a large cross-section are designed and manufactured. The materials used for the trial-made transducers are the same as those used in the above theoretical calculations. The fundamental resonance frequencies of the trial-made transducers are measured using HP 4294A Precision Impedance Analyzer. The measured electric impedance characteristics of the trial-made sandwich transducers are illustrated in Fig. 4 and Fig. 5. In the figures, the frequencies corresponding to the minimum electric impedance are the resonance frequencies of the transducer. It can be seen that when the radius is increased, the impedance curve of the transducer becomes more complex, and more resonance frequency can be found. The trial-made half wavelength sandwich transducers are symmetrical, their geometrical dimensions, the calculated and the measured resonance frequencies are listed in Table III and Table IV. For comparison, the theoretical longitudinal resonance frequencies from one-dimensional theory are also calculated. At the same time, the resonance frequency and the vibrational displacement distribution of the sandwich transducers in coupled vibration are also computed using ANSYS software. The computed resonance frequencies using FEM are also listed in Table IV. In the table, f_{r1}, f_{r2} and f_l represent the radial resonance frequency of the metal mass and the piezoelectric ceramic elements, and the longitudinal resonance frequency of the sandwich transducer. f_m is the measured resonance frequency; f_c is the theoretical resonance frequency from the coupled theory of this paper; f_{1D} is the resonance frequency from one-dimensional theory. f_n is the theoretical resonance frequency from FEM. It can be seen that the resonance frequencies from the coupled vibrational theory are in good agreement with those from FEM, and they

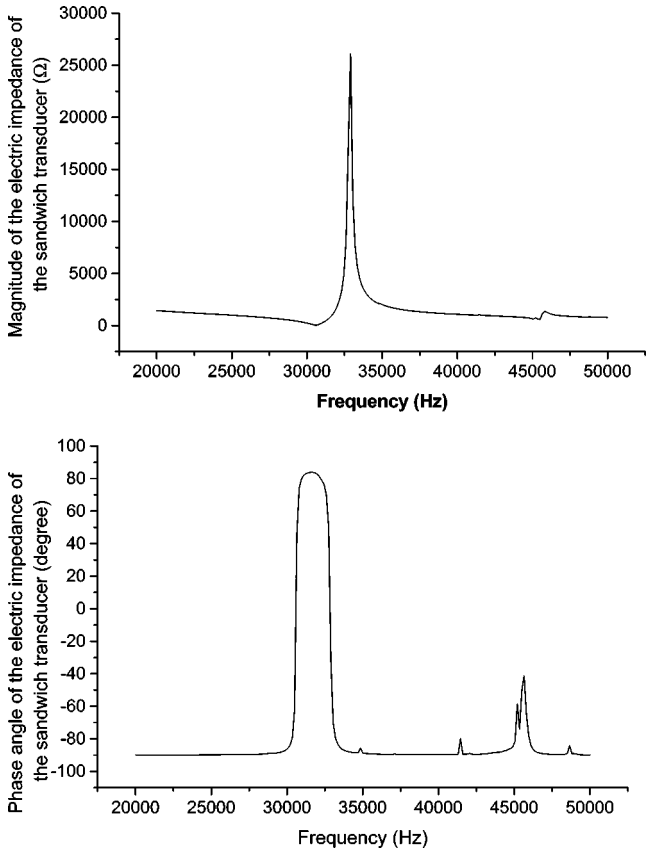

FIG. 4. Measured electric impedance and phase angle curves of the No. 1 sandwich transducer with a comparatively small cross-section.

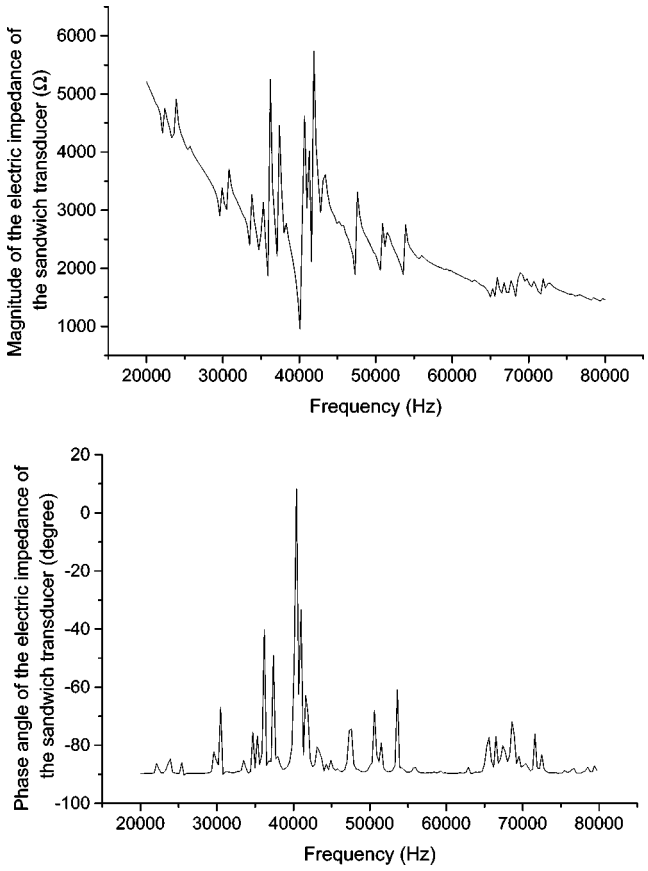

FIG. 5. Measured electric impedance and phase angle curves of the No. 2 sandwich transducer with a comparatively large cross-section.

are also in good agreement with the measured results. Compared with traditional one-dimensional theory, the results from the coupled vibrational theory are in better agreement with those from one-dimensional theory.

The vibrational displacement distributions of the transducer from FEM are illustrated in Fig. 6 and Fig. 7. Figure 6 illustrates the displacement distribution of the transducer in longitudinal resonance vibration; Fig. 7 illustrates the displacement distribution of the transducer in radial resonance vibration of the piezoelectric ceramic elements. In the figures, the dotted lines represent the undeformed shape of the sandwich transducer, (a) and (b) represent the No. 2 and No. 1 transducer, respectively.

It can also be seen from Fig. 4 and Fig. 5 that when the radius of the sandwich transducer is increased, the electric impedance characteristics of the transducers become complex, more vibrational modes can be found. The reason is that the radial vibration becomes large and its effect on the coupled vibration of the sandwich transducer becomes obvious. When the radius is small compared with the longitudinal wavelength, the radial vibration is weak, and the corresponding impedance peak is low. For example, the radial resonance frequency of the transducer with a comparatively small cross-section cannot be measured from the impedance curve measurement.

As for the frequency error, it is thought that two kinds of errors should be considered. One is the systematic error; the other the random error. The systematic error is caused by the approximate analytic method itself in which the shearing and the torsion are ignored, while the random error is determined by many uncertain factors. Sometimes the uncertain factors are more important, they affect the measured results. On account of the above factors, the following should be taken into account for the frequency error analysis: (1) The standard material parameters are different from the practical values. An error of 3%–5% can be caused by this factor. (2) The piezoelectric ceramic elements are considered as disks without inner holes. However, in practical cases, the piezoelectric ceramic elements are circular rings. (3) In this method, to simplify the analysis, the mechanical coupling coefficient is considered as a constant. However, the mechanical coupling coefficient is different at different positions in the sandwich transducer. (4) The longitudinal and the radial extensional

TABLE III. Geometrical dimensions of the trial-made sandwich transducers.

No.	L_1 (mm)	L_2 (mm)	L_{01} (mm)	L_{02} (mm)	R_1 (mm)	R_2 (mm)	R_0 (mm)
1	30	30	6	6	26	26	25
2	30	30	8	8	31	31	30

TABLE IV. Theoretical and measured resonance frequencies of the trial-made sandwich transducers.

No.	f_{r1} (Hz)					f_{r2} (Hz)				
	f_m	f_c	f_n	Δ1/%	Δ2/%	f_m	f_c	f_n	Δ1/%	Δ2/%
1	×	31692	×	×	×	34468	34124	35825	1.00	3.94
2	30517	29353	×	3.81	×	33428	32111	32565	3.94	2.58

No.	f_l (Hz)					
	f_m	f_c	f_n	f_{1D}	Δ1/%	Δ2/%
1	30575	31231	32102	33558	2.15	4.99
2	29372	28963	29019	31757	1.39	1.20

vibrations in the transducer are supposed. However, for the coupled vibration of the sandwich transducer, shearing, torsion and other strains may coexist in the resonator. (5) The trial-made transducer is clamped by an inner central bolt. In the theoretical calculation, the inner central bolt is not considered. This means the pre-stress of the sandwich transducer is ignored in the calculation. However, in fact, the pre-stress of the transducer affects the resonance frequency. (6) The analytical method presented in this paper is an approximate one. It can be used to analyze the resonance frequency of the sandwich transducer in coupled vibration; however, whether it can be used to calculate the vibrational displacement distribution remains to be studied further.

V. CONCLUSIONS

In this paper, the coupled vibration of the sandwich piezoelectric transducer with a large cross-section and high resonance frequency is analyzed by using an approximate analytic method. The resonance frequency equations are derived, the theoretical relationship between the resonance frequency and the geometrical dimensions is studied and the resonance frequencies of the trial-made sandwich transducer are measured. For comparison, numerical methods are also used to simulate the coupled vibration and compute the resonance frequency and displacement distribution. Based on the above analyses, the following conclusions can be drawn.

(a) Compared with numerical methods, the analytic method presented in this paper is a new analytic one. It is concise in physical meaning and simple in calculating the resonance frequencies of the sandwich transducers with large cross-section and high frequency.
(b) Compared with one-dimensional theory, the resonance frequencies obtained by means of the approximate analytic method presented in this paper are in better agreement with the measured frequencies.
(c) When radial vibration and coupling between longitudinal and radial vibrations are considered, more resonance frequencies can be obtained. Apart from longitudinal resonance frequency, radial resonance frequencies can also be obtained. It is expected that using this method the sandwich transducer with multifrequency or a wide bandwidth can be designed.
(d) Both radial and the longitudinal geometrical dimensions affect the resonance frequency of the sandwich transducer. When the length of the metal mass is increased and the piezoelectric ceramic elements are fixed, the radial resonance frequency of the metal mass is decreased, the radial resonance frequency of the piezoelectric ceramic elements remains unchanged and

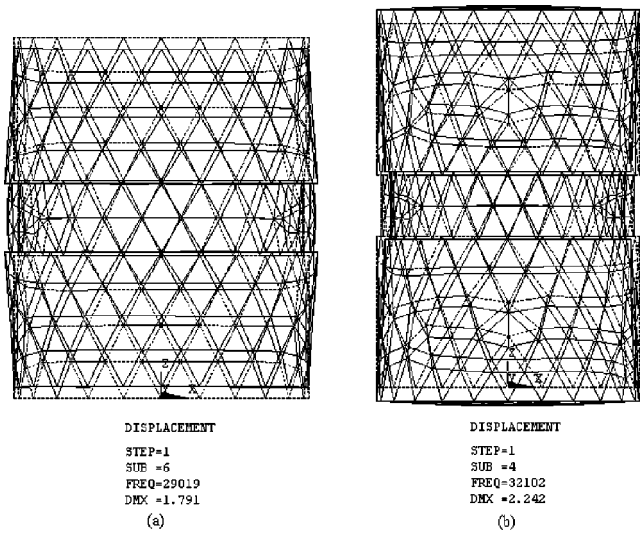

FIG. 6. Vibrational displacement distribution of the transducer in longitudinal resonance vibration of the sandwich transducer from FEM.

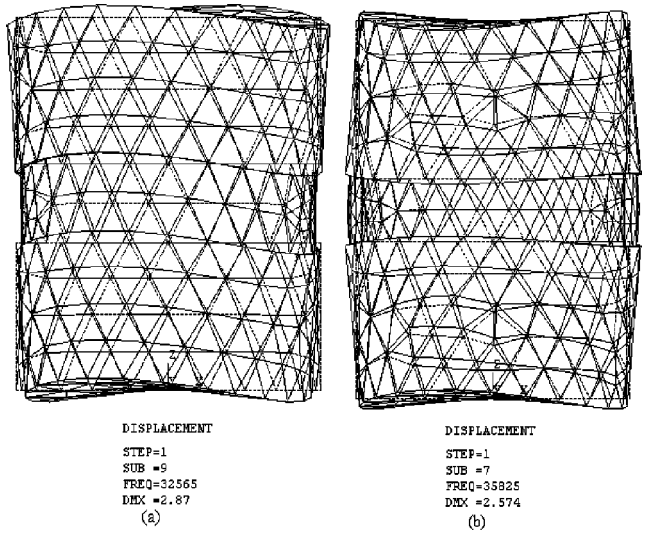

FIG. 7. Vibrational displacement distribution of the transducer in radial resonance vibration of the piezoelectric ceramic elements from FEM.

the longitudinal resonance frequency is decreased. The radial dimension also affects the resonance frequency of the sandwich transducer. When the radius of the transducer is increased, the radial resonance frequencies of the metal mass and the piezoelectric ceramic elements are decreased and the longitudinal resonance frequency is also decreased.

(e) The analysis on the coupled vibration design theory of the sandwich transducer with a large cross-section is based on the assumption that torsion and shearing strains are ignored. In practical cases, torsion, flexural and shearing strains can all be produced for the coupled vibration of the sandwich transducer.

(f) In this paper, the resonance frequency of the sandwich transducer with a large cross-section is studied by using the proposed analytic method. In later works, the displacement distribution, the stress and the strain distributions in the transducer with a large cross-section or high resonance frequency will be further studied according to the approximate analytic method.

ACKNOWLEDGMENT

The author acknowledges the financial support of the National Natural Science Foundation of China (Project No. 10274046).

[1] R. E. Horito, ''Free-flooding unidirectional resonators for deep-ocean transducers,'' J. Acoust. Soc. Am. **41**, 158–166 (1967).
[2] P. J. Michael, ''Velocity control and the mechanical impedance of single degree of freedom electromechanical vibrators,'' J. Acoust. Soc. Am. **84**, 1994–2001 (1988).
[3] R. Coates and R. F. Mathams, ''Design of matching networks for acoustic transducers,'' Ultrasonics **26**, 59–64 (1988).
[4] H. Minchenko, ''High-power piezoelectric transducer design,'' IEEE Trans. Sonics Ultrason. **SU-16**, 126–136 (1969).
[5] E. A. Neppiras, ''The pre-stressed piezoelectric sandwich transducer,'' *Ultrasonics International Conference Proceedings*, 1973, p. 295.
[6] T. J. Bulat, ''Macrosonics in industry: 3. Ultrasonic cleaning,'' Ultrasonics **12**, 59–68 (1974).
[7] Y. Kagawa and T. Yamabuchi, ''Finite element approach for a piezoelectric circular rod,'' IEEE Trans. Sonics Ultrason. , 262 (1976).
[8] R. Lerch, ''Simulation of piezoelectric devices by two- and three-dimensional finite elements,'' IEEE Trans. Ultrason. Ferroelectr. Freq. Control **37**, 233–247 (1990).
[9] H. A. Kunkel, S. Locke, and B. Pikeroen, ''Finite-element analysis of vibrational mode in piezoelectric ceramic disks,'' IEEE Trans. Ultrason. Ferroelectr. Freq. Control **37**, 316–327 (1990).
[10] N. Guo, and P. Cawley, ''Measurement and prediction of the frequency spectrum of piezoelectric disks by modal analysis,'' J. Acoust. Soc. Am. **92**, 3379–3388 (1992).
[11] E. Mori, K. Itoh, and A. Imamura, ''Analysis of a short column vibrator by apparent elasticity method and its applications,'' *Ultrasonics International Conference Proceedings* 1977, p. 262.
[12] E. Mori and Y. Tsuda, ''A new high power ultrasonic wave radiator for liquid medium,'' *Ultrasonics International Conference Proceedings*, Brighton, 1981, pp. 307–312.
[13] S. Y. Lin, ''Coupled vibration and natural frequency analysis of isotropic cylinders or disks of finite dimensions,'' J. Sound Vib. **185**, 193–199 (1995).
[14] S. Y. Lin, ''Frequency spectra of extensional vibration in isotropic short columns and thick circular disks,'' IEEE Trans. Ultrason. Ferroelectr. Freq. Control **41**, 573–576 (1994).
[15] S. Y. Lin, ''Coupled vibration analysis of piezoelectric ceramic disk resonators,'' J. Sound Vib. **218**, 205–217 (1998).
[16] S. Y. Lin, ''Analysis of the equivalent circuit of piezoelectric ceramic disk resonators in coupled vibration,'' J. Sound Vib. **231**, 277–290 (2000).
[17] S. Y. Lin, ''Coupled vibration in hollow cylinders of longitudinally polarize piezoelectric ceramics,'' J. Acoust. Soc. Am. **97**, 3599–3604 (1995).
[18] S. Ueha, S. Sakuma, and E. Mori, ''Measurement of vibration velocity distributions and mode analysis in thick disks of $Pb(Zr\cdot Ti)O_3$,'' J. Acoust. Soc. Am. **73**, 1842–1847 (1983).
[19] S. Y. Lin, ''The three-dimensional equivalent circuit and the natural frequencies of rectangular piezoelectric ceramic resonators,'' J. Acoust. Soc. Am. **96**, 1620–1626 (1994).
[20] S. Y. Lin, ''Design of piezoelectric sandwich ultrasonic transducers with large cross-section,'' Appl. Acoust. **44**, 249–257 (1995).

Sound-field reproduction in-room using optimal control techniques: Simulations in the frequency domain[a)]

Philippe-Aubert Gauthier[b)] and Alain Berry
Groupe d'Acoustique de l'Université de Sherbrooke, Université de Sherbrooke, 2500 boulevard de l'Université, Sherbrooke, Québec, J1K 2R1 Canada

Wieslaw Woszczyk
Center for Interdisciplinary Research in Music, Media, and Technology, McGill University, 555 Sherbrooke Street West, Montréal, Quebec, H3A 1E3 Canada

(Received 3 May 2004; revised 29 November 2004; accepted 29 November 2004)

This paper describes the simulations and results obtained when applying optimal control to progressive sound-field reproduction (mainly for audio applications) over an area using multiple monopole loudspeakers. The model simulates a reproduction system that operates either in free field or in a closed space approaching a typical listening room, and is based on optimal control in the frequency domain. This rather simple approach is chosen for the purpose of physical investigation, especially in terms of sensing microphones and reproduction loudspeakers configurations. Other issues of interest concern the comparison with wave-field synthesis and the control mechanisms. The results suggest that in-room reproduction of sound field using active control can be achieved with a residual normalized squared error significantly lower than open-loop wave-field synthesis in the same situation. Active reproduction techniques have the advantage of automatically compensating for the room's natural dynamics. For the considered cases, the simulations show that optimal control results are not sensitive (in terms of reproduction error) to wall absorption in the reproduction room. A special surrounding configuration of sensors is introduced for a sensor-free listening area in free field. [DOI: 10.1121/1.1850032]

PACS numbers: 43.38.Md, 43.60.Tj, 43.50.Ki [NX] Pages: 662–678

I. INTRODUCTION

This paper investigates the theoretical possibilities for sound-field reproduction using optimal control methods for potential audio applications. The major goals of this work are feasibility and parametric studies with questions: (1) The effect of a reflective acoustic environment on objective reproduction quality in comparison with free-field conditions; (2) the comparison of optimal control method with wave-field synthesis (WFS); and (3) the introduction of a practical configuration which can be, as mentioned later, related to WFS.

The simulations presented in this paper have been carried with a conventional least-square error formulation for the acoustical part of the problem (Elliott, 2001; Nelson *et al.*, 1992), while wave-field synthesis has been simulated using nonfocusing WFS operators for a general source array with a straight reference line (Verheijen, 1997). Simple and harmonic wave reproductions are considered in free-field or in-room conditions.

Historically, spatial sound reproduction has been a vivid and creative research domain involving artists, engineers, and scientists (Davis, 2003; Henriksen, 2002; Rumsey, 2001; Wilson, 2001). Numerous examples of historical systems, formats, patents, and advances concerning spatial audio have also been reported recently (Davis, 2003; Rumsey, 2001). With the relatively recent arrival of digital representation and multiple channels of audio, new possibilities of sound-field control and sound reproduction have been investigated. Commonly cited examples are: binaural techniques (Begault, 1994; Blauert, 1999), ambisonic formats (Rumsey, 2001), wave-field synthesis (WFS) (Berkhout, 1993; Verheijen, 1997), and stereo-dipole (SD) (Nelson *et al.*, 1997; Nelson, 2002; Watanabe *et al.*, 1999). In a broad sense, most of these techniques try to improve two aspects of the consumer level reproduction technology, with variable weighting and methods: (1) Achieve a large listening area for a given audience; (2) Create an appropriate 3D (or 2D) auditory scene.

A few words will be spent to introduce some of those techniques since they are mainly distinguished from traditional loudspeakers systems where the mixing engineer is entirely responsible for the channels' content, like for the 5.1 or 10.2 surround systems (Rumsey, 2001). (The $x \cdot y$ numbering convention for surround-sound system is used to describe a system with x broadband channels and y low-frequency channels for subwoofers.) The work presented here is more connected to *sound-field simulation* rather than to *perceptual simulation.* This short review will be devoted mainly to sound-field simulation, which may provide a broader listening area without any perceptual assumptions.

Although the ultimate goal of sound-field reproduction is an audio application, one must be aware that perfect reproduction of sound field does not necessarily lead to perfect auditory events reproduction, since multimodal sensory in-

[a)]Portions of this work were presented in "Sound reproduction using active control techniques: Simulations in the frequency domain," Proceedings of the 18th International Congress on Acoustics, Kyoto, Japan, April 2004, and "In-room sound reproduction using active control: Simulations in the frequency domain and comparison with wave field synthesis," 147th ASA meeting, New York, NY, May 2004.

[b)]Electronic mail: philippe_aubert_gauthier@hotmail.com

fluences and cognitive mechanisms both strongly influence sound localization and construction of a 3D auditory scene (Blauert, 1999; Bregman, 1990). In spite of this, it is assumed that, if not perfect, at least optimal sound-field reproduction will achieve optimal auditory impression if the audio system is not conflicting with visual indications or other sensory experiences. This assumption justifies the wave-field simulation approach.

A. Recent advances in spatial sound reproduction

The whole issue of reproduction of the spatial character of hearing may be divided in various complementary and hierarchic categories. The first fundamental division arises while introducing a distinction between *perceptual simulation* and *sound-field simulation*. To ensure a more general understanding, one can interpret the simulation of sound fields like the simulation of the physical stimulus, the sound field in this case. Any technology that implies a measure or knowledge of the spatial hearing mechanisms will belong to the perception simulation class. Examples of this type are binaural technologies which may include a measure of the perceptive chain, the external ear in this case (Begault, 1994; Blauert, 1999; Boulanger, 2001) and stereophonic productions [usually based on phantom imaging related to interaural time delay or interaural level difference auditory cues (Rumsey, 2001)]. With sound-field simulation, although possibly addressing the hearing system, one is not concerned with the perceptive mechanisms of spatial hearing in the technological development. Both perceptual simulation and sound-field simulation are subject of the research activities (Berkhout, 1993; Gardner, 1998; Kirkeby *et al.*, 1998; Nelson *et al.*, 1997; Nelson, 2002; Takeuchi *et al.*, 2002; Tokuno *et al.*, 1997; Verheijen, 1997; Ward *et al.*, 1999; Watanabe *et al.*, 1999). The simulation of sound fields can also be divided into two further approach types. The first is the *outer problem* (the creation of a synthetic directivity pattern around a set of acoustical sources; the reproduced sound field is surrounding the reproduction sources). The second is the *inner problem*. In this case the listening zone is surrounded by a loudspeaker array which is introduced to create a sound field within the interior of the surrounding array. The investigations reported here belong to this last type: inner problem of sound-field simulation. At the interface between outer and inner sound-field simulations, there is the *sound-field extrapolation*, where the reproduction sources are located on a plane separating the listening area (either virtual or real) from a space where a sound field must be extrapolated to the listening area.

1. Wave-field synthesis (WFS)

The work on the WFS originates from the theoretical analysis by Berkhout in the late 80s and in the early 90s (Berkhout, 1993; Verheijen, 1997). The underlying idea is rather simple. From the Kirchhoff–Helmholtz integral theorem, WFS operators are defined to ''link'' a given simple virtual source, fed by monophonic input, to an array of loudspeakers which should reproduce the virtual source acoustic field. The problem is usually concerned with reproduction in the horizontal plane by means of a finite number of discrete sources using appropriate simplifications of the integral formulation (Verheijen, 1997). Berkhout's theory seems to be a rigorous and up-to-date synthesis of some older ideas expressed by Camras (1968) and in the 30s, at the Bell Telephone Laboratory, by Steinberg and Snow (Davis, 2003; Rumsey, 2001).[1] With this WFS system, it is claimed that plane and spherical waves can be reproduced in a broad planar listening area surrounded by the loudspeaker array; it is thus a volume solution. Considerable amount of work on WFS has followed in Delft University of Technology and, later, in the CARROUSO European research project, where practical issues have been investigated and have been brought to a final prototype installed in a movie theater in Ilmenau (Germany). WFS researches have investigated spatial aliasing, source type, source directivity (Verheijen, 1997), multiactuator panel loudspeaker (de Vries *et al.*, 2003), room compensation (Spors *et al.*, 2003), scene composition with WFS, subjective evaluation (Verheijen, 1997), and more.

On one hand, the benefit of the current WFS prototype is its efficiency to transmit a spatial impression over a broad area surrounded by the loudspeakers. Actual prototypes also provide a convenient software tool for scene construction and kinetic spatial compositions. On the other hand, WFS drawbacks are more subtle and mainly related to the synthesis operators' definition, which makes assumptions on two points: (1) Synthesis operators are defined for a virtual free-field space. (2) Reproduction room's response is not considered in the process, except in specific applications including room compensation filters after the WFS filters (Spors *et al.*, 2003). The typical WFS system is consequently based on an open-loop architecture.

In the following simulations, a relation will be shown between WFS and some particular configuration of sensors using active control techniques.

2. Active sound control and adaptive filtering in audio reproduction

Classical active sound control techniques may be conceptually connected to sound reproduction from different view points. First, in its application, active control of sound is aimed at creating a controlling (secondary) pressure field which, locally or globally, cancels a disturbing (primary) pressure field. This task is nearly similar, except for a sign change, to the reproduction of a given sound field for audio applications. Second, from a temporal or spectral viewpoint, active control and corresponding adaptive filtering techniques may be used for single-point or multiple-point frequency response equalization. With this in mind, active sound field control may be applied to the spatial audio problem. This has already been done in the past using various approaches and solutions.

Adaptive multipoint equalization in various environments, such as room and car, have been, to our knowledge, studied and published by Elliot and Nelson first in 1985 and later in 1989 (Elliott and Nelson, 1989). At that time, the main objective was the realization of a better frequency response uniformity in a room enclosure. The equalization of room and loudspeakers is thus approached from a frequency

viewpoint more than from a standpoint of an extended spatially dependent sound-field reproduction. It is now more than interesting to note some conclusions from the previously cited authors. It clearly seems that appropriate multiple-point frequency equalization has been obtained by applying a proper modeling delay between the desired signals (at the error sensor locations) which were all deduced from a single monophonic signal. The introduction of these delays reproduces a wave somewhat similar to a traveling plane wave. This suggests that room and loudspeaker frequency equalization may thus benefit from proper spatial reproduction of a given virtual field.

Simulations have been introduced by Kirkeby and Nelson (1993) for plane-wave reproduction over a restricted area in free-field condition. Major differences between Kirkeby's paper and the present paper are related to the configurations considered, the presence of a reflective environment, and comparisons with WFS. Following Kirkeby's conclusion, a narrow-arc arrangement of loudspeakers in front of an equalization zone (a square of 0.5 meters) may create a progressive plane wave in free-field reproduction conditions.

Another important research about adaptive 3D sound systems is authored by Garas (1999). Most of Garas' work is related to various adaptive multichannel signal processing, including generic electroacoustical transfer functions, for a general design which can be applied to active noise control, cross-talk cancellation, and virtual imaging. In the case of adaptive virtual acoustics, the author suggests the use of error microphones inside listener's ears, a solution which may not be practical.

These previous examples form a part of the published works on active control in relation to sound reproduction. Other important papers concerning audio applications of active control and adaptive filtering which have been published more or less recently are listed in references (Elliott and Nelson, 1989, 1994; Kirkeby *et al.*, 1996; Nelson *et al.*, 1992; Nelson, 1994; Nelson *et al.*, 1995, 1996, 1997; Nelson, 2002; Uto *et al.*, 1995).

II. THEORETICAL MODEL

This section introduces the theoretical model on which the simulations are based. As was previously mentioned, the simulations are mainly concerned with sound-field reproduction. The reproduction system can be characterized by L monopole sources and M sound-pressure sensors. The radiation model for the sources is introduced first, while the optimal control formulation, the sound-field reproduction (or sound-field control), is presented next.

The proposed model is more appropriate for low frequencies, where the monopole may more adequately represent a closed-box loudspeaker. In all cases, the simulations are carried out up to 1.5 kHz. This frequency limit roughly corresponds to the auditory transition from an ITD (interaural time delay) auditory cue based on signals' fine structure of time differences to the one based on signals' envelope time differences (Blauert, 1999). Note that this upper-frequency limit seems to be shared by the WFS systems which integrate frequencies up to 1500 Hz or so (Verheijen, 1997). In our room simulations, this upper-frequency limit is lowered to 400 Hz for computational efficiency. However, the covered frequency range is still representative for the room considered in our simulations since it includes the Schroeder frequency (Nelson and Elliott, 1992), which dictates the progressive transition from a dominant-mode response to a diffuse response.

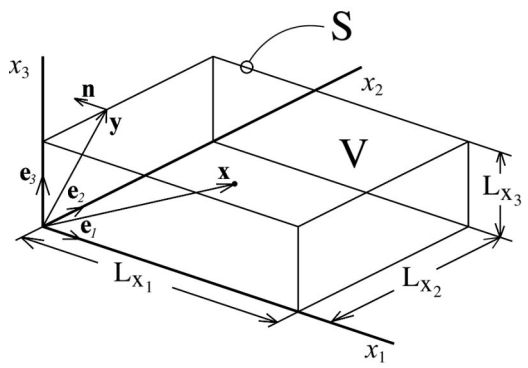

FIG. 1. Signs and symbols convention for the rectangular room. **x** describes an arbitrary point in volume V (or on the surface S), **y** describes an arbitrary point on S, **n** is a unitary vector normal to S and pointing outward, x_i is a set of Cartesian coordinates, and $\mathbf{e}_i$, a triad of unit base vectors.

A. Radiation modeling

The model is based on the Helmholtz equation for harmonic acoustic fields

$$\nabla^2 p(\mathbf{x}) + k^2 p(\mathbf{x}) = 0, \tag{1}$$

and on boundary conditions (homogeneous and mixed) for locally reacting surfaces

$$\nabla p(\mathbf{y}) \cdot \mathbf{n} = jk\beta(\mathbf{y}) p(\mathbf{y}), \tag{2}$$

where p is the space-dependent complex acoustic pressure [Pa], k the wave number [rad/m] ($k=\omega/c$), **x** the position in rectangular coordinates [m], **y** the position on walls [m], β the specific acoustic admittance dimensionless ratio for a given surface (normalized by ρc, with $\rho = 1.18$ kg/m^3 and $c = 343$ m/s), **n** a unit vector normal to the room surface (pointing outwards the room), ω the radial frequency [rad/s], and c the sound speed [m/s] at ambient temperature. A $e^{-j\omega t}$ time dependence is assumed for pressure and other harmonically varying variables. The system under study, with signs convention and parameter definition, is graphically introduced in Fig. 1.

Two different reproduction situations are investigated and compared: in a free field, and in a room. In all cases, the *reproduced sound field* is simply the sum of the individual sources' radiated sound field

$$p^{(\mathrm{rep})}(\mathbf{x}) = \sum_{l=1}^{L} G(\mathbf{x}|\mathbf{x}_l)(-j\omega\rho q_l), \tag{3}$$

where q_l is the complex strength of source l (located at $\mathbf{x}_l$) and $G(\mathbf{x}|\mathbf{x}_l)$ is the Green's function (Nelson and Elliott, 1992; Pierce, 1991). In free field, the Green's function is

$$G(\mathbf{x}|\mathbf{x}_l) = \frac{e^{jk|\mathbf{x}-\mathbf{x}_l|}}{4\pi|\mathbf{x}-\mathbf{x}_l|}. \tag{4}$$

While in a room, the following definition (which implicitly assumes modal expansion and the fact that eigenfunctions Ψ_n form an orthogonal set) is used (Morse *et al.*, 1968):

$$G(\mathbf{x}|\mathbf{x}_l)=\sum_{n=0}^{N}\frac{\Psi_n(\mathbf{x})\Psi_n(\mathbf{x}_l)}{V[k_n^2-k^2]}, \tag{5}$$

where, in Eq. (5), Ψ_n is the nth eigenfunction of Eq. (1) with boundary conditions Eq. (2), k_n the associated nth eigenvalue, and V the room volume. The eigenfunctions are amplitude normalized in such a manner that $\int_V \Psi_n \Psi_m dV = \delta_{nm}$. For the nonrigid case associated with Eq. (2), complex eigenfunctions and eigenvalues are expected. The eigenfunctions and eigenvalues are functions of the driving frequency, which is explicit in the boundary conditions [see Eq. (2)]. The modal scheme approximation for a rectangular room with nonrigid surfaces is taken from Morse and Ingard (1968) and is given by the following expressions:

$$\Psi_n(\mathbf{x})=\Psi_{n_{x1}}(x_1)\Psi_{n_{x2}}(x_2)\Psi_{n_{x3}}(x_3)/A_n, \tag{6}$$

$$A_n=\int_V \Psi_{n_{x1}}\Psi_{n_{x2}}\Psi_{n_{x3}}dV, \tag{7}$$

$$\Psi_{n_{xi}}(x_i)\approx\cos\left(q_{n_{xi}}\frac{\pi x_i}{L_{xi}}+j\beta\frac{kL_{xi}}{\pi q_{n_{xi}}}\right), \tag{8}$$

$$q_{0_{xi}}\approx\frac{1}{\pi j}\sqrt{2j\beta kL_{xi}}, \tag{9}$$

$$q_{n_{xi}}\approx n-\frac{2j\beta kL_{x1}}{\pi^2 n}, \tag{10}$$

$$k_n^2\approx\left(\frac{\pi q_{n_{x1}}}{L_{x1}}\right)^2+\left(\frac{\pi q_{n_{x2}}}{L_{x2}}\right)^2+\left(\frac{\pi q_{n_{x3}}}{L_{x3}}\right)^2. \tag{11}$$

This approximation is valid for a uniform admittance (which is the case since β is uniformly distributed over S in the simulations) and for low βkL_{xi}; it is thus limited to low admittance and more representative to low excitation frequency. Using matrix notation, Eq. (3) can be more compactly written

$$\mathbf{p}^{(\mathrm{rep})}=[p^{(\mathrm{rep})}(\mathbf{x}_1)\cdots p^{(\mathrm{rep})}(\mathbf{x}_m)\cdots p^{(\mathrm{rep})}(\mathbf{x}_M)]^T=\mathbf{Z}^{(m)}\mathbf{q}, \tag{12}$$

for a finite number of points, M, corresponding to receivers positions. In Eq. (12), $\mathbf{Z}^{(m)}$ is a transfer impedance matrix (from source strength to the reproduced sound pressure evaluated at $\{\mathbf{x}_1\cdots\mathbf{x}_m\cdots\mathbf{x}_M\}$ in the reproduction space) and $\mathbf{q}$, a complex source strength column vector defined as follows:

$$\mathbf{q}=[q_1\cdots q_l\cdots q_L]^T. \tag{13}$$

B. Control modeling

Now that the reproduced pressure field is defined in V subject to L simple monopole excitations, the optimal determination of $\mathbf{q}$ needs to be derived. The target wave field, or the *image field*, which has to be reproduced by the sources in V, is a plane wave of amplitude A

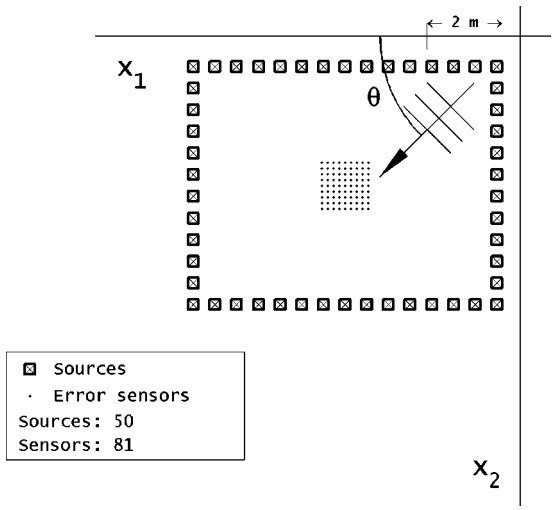

FIG. 2. First investigated configuration in free field. θ defines the propagation direction for a progressive plane-wave target field. The sensor array covers a 1×1-m area with a separation distance of 0.125 m along x_1 and x_2. The source array covers approximately a 7.5×6.4-m rectangle with a separation of approximately 0.46 m.

$$p^{(\mathrm{im})}(\mathbf{x})=Ae^{j\mathbf{k}\cdot\mathbf{x}}, \tag{14}$$

where $\mathbf{k}$ is the wave number vector. The plane wave is assumed to propagate in the horizontal (x_1,x_2) plane, with a direction defined by angle θ in Fig. 2. Alternatively, the image field can be a spherical wave

$$p^{(\mathrm{im})}(\mathbf{x})=A\frac{e^{jk|\mathbf{x}-\mathbf{x}_o|}}{|\mathbf{x}-\mathbf{x}_o|}. \tag{15}$$

In the last equation, the virtual source position is defined by $\mathbf{x}_o$.

Using Eq. (3), (14), or (15), a reproduction error function evaluated as a function of $\mathbf{x}$ is defined as follows:

$$e(\mathbf{x})=p^{(\mathrm{im})}(\mathbf{x})-p^{(\mathrm{rep})}(\mathbf{x}). \tag{16}$$

Perfect and ideal sound-field reconstruction would thus be obtained everywhere in the reproduction area while reaching $e(\mathbf{x})=0$ with properly adjusted source strengths $\mathbf{q}$. On a more practical ground, now assume that the reproduction system is not only made of L sources fed by an open-loop architecture but also of M error sensors, for which the errors between the target pressure defined and the reproduced pressure are evaluated at a set of M discrete points $\{\mathbf{x}_1\cdots\mathbf{x}_m\cdots\mathbf{x}_M\}$. The corresponding set of reproduction error amplitudes has to be minimized with respect to the control source strengths $\mathbf{q}$. With this in mind, an error vector $\mathbf{e}=[e_1\cdots e_m\cdots e_M]^T$ is introduced. For the mth term of $\mathbf{e}$

$$e_m(\mathbf{x}_m)=p^{(\mathrm{im})}(\mathbf{x}_m)-p^{(\mathrm{rep})}(\mathbf{x}_m). \tag{17}$$

This allows the following definition of a cost function (in terms of quadratic error $\mathbf{e}^H\mathbf{e}$), which corresponds to the quadratic Hermitian including Tikhonov regularization (that is, an effort penalty here expressed as $\gamma\mathbf{q}^H\mathbf{q}$) (Nelson, 2001):

$$J_M=\mathbf{e}^H\mathbf{e}+\gamma\mathbf{q}^H\mathbf{q}. \tag{18}$$

In Eq. (18), H superscript denotes the Hermitian transpose and γ the regularization parameter. The reproduction performance optimization is expressed as a function of the qua-

dratic reproduction errors because one wishes to bring the errors to zero as nearest as possible, that is, the ''least-square'' solution. Moreover, this is a common practice in active control of sound or vibration which found this correspondence with practical applications through adaptive filtering, which is often based on such type of quadratic cost function. On one hand, the regularization parameter γ can represent the possible trade-off between optimal reproduction and source strength minimization. On the other hand, γ introduces convenient regularization in the inverse problem (Nelson, 2001), as it will be seen in the next equation. This Tikhonov regularization, which is nothing more than the introduction of a γ-weighted source-strength penalty term in the cost function, is thus used to circumvent any ill-conditioning of the problem. The purposes and considerations of conditioning in regards to the sound-field reproduction are both addressed in Sec. III E. Within the context of active control practice, such a regularization is conceptually connected with the leaky adaptation of a feedforward system (Elliott, 2001). For a more detailed review of inverse problems and regularization, the reader is referred to the work of Nelson (2001).

Provided that $[\mathbf{Z}^{(m)H}\mathbf{Z}^{(m)}+\gamma\mathbf{I}]$ is positive definite, which is the case when $L<M$ (Nelson and Elliott, 1992), the cost function J_M has a unique minimum associated with

$$\mathbf{q}_{\text{opt}}=[\mathbf{Z}^{(m)H}\mathbf{Z}^{(m)}+\gamma\mathbf{I}]^{-1}\mathbf{Z}^{(m)H}\mathbf{p}^{(\text{im})}, \tag{19}$$

where $\mathbf{I}$ is the identity matrix and $\mathbf{p}^{(\text{im})}=[p^{(\text{im})}(\mathbf{x}_1)\cdots p^{(\text{im})}(\mathbf{x}_m)\cdots p^{(\text{im})}(\mathbf{x}_M)]^T$. By inspection of Eq. (19), it is apparent that the conditioning and hence invertibility of the matrix $[\mathbf{Z}^{(m)H}\mathbf{Z}^{(m)}+\gamma\mathbf{I}]$ will strongly influence the quality of the minimization results, and therefore the usefulness of the regularization parameter γ which adds a value to the diagonal terms of the matrix to be inverted in Eq. (19). Explained briefly and textually, such an addition increases all the matrix singular value from a given amount and consequently reduces the ratio of the largest to the smallest singular value. This ratio defines the condition number. While inverting any matrix, a very small singular value of the matrix results in very large values of the solution, and this may reduce the solution quality or even the numerical invertibility of the matrix (Nelson and Yoon, 2000). For this reason, the added diagonal value γ will stabilize the inversion of the matrix. By such means, the Tikhonov regularization thus circumscribes the solution values $\mathbf{q}_{\text{opt}}$ to a more acceptable range but, at the same time, it reduces, appreciably or not, depending on γ, the reproduction quality.

Substitution of Eq. (19) in J_M allows the definition of the residual normalized cost function (excluding the Tikhonov regularization term $\gamma\mathbf{q}^H\mathbf{q}$) when $\mathbf{q}$ is set to $\mathbf{q}_{\text{opt}}$

$$E_{LS}=\frac{J_M^{(\mathbf{q}=\mathbf{q}_{\text{opt}})}-\gamma\mathbf{q}_{\text{opt}}^H\mathbf{q}_{\text{opt}}}{J_M^{(\mathbf{q}=0)}}. \tag{20}$$

This parameter has been chosen for comparison and validation with past works from Kirkeby and Nelson (1993). The real scalar-valued E_{LS} here expresses the fitness between the image field and the reproduced field. A small E_{LS} value will thus demonstrate a good fit between the two fields and therefore express the effectiveness of the reproduction. Although one can monitor the spatial sound-field reproduction quality by means of the real scalar cost function J_M of Eq. (18), it would be difficult to use such a scalar for comparison purposes because it includes the effort penalty contribution (weighted by γ) and it varies with a varying number of error sensors since J_M includes the sum of the M quadratic errors. This motivates the E_{LS} definition for comparison purposes.

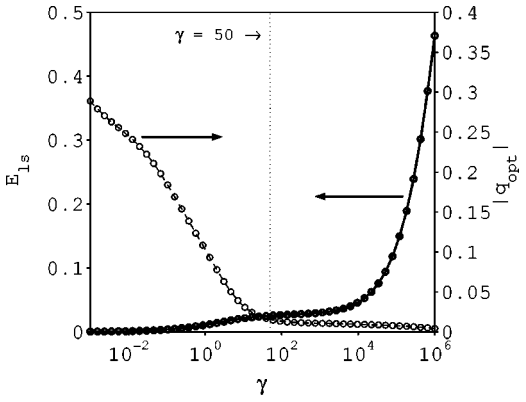

FIG. 3. E_{LS} (on left) and $|\mathbf{q}_{\text{opt}}|$ (on right) variation as a function of γ for the free-field case of Fig. 2 while reproducing a plane wave at 220 Hz with $\theta=30$ deg.

Using a small value of the regularization parameter γ can be sufficient, in terms of regularization, without reducing the reproduction quality. This idea is presented in Fig. 3 for the free-field configuration of Fig. 2 while reproducing a progressive plane wave at 220 Hz with $\theta=30$ deg. For a given regularization parameter, in this case roughly between 10 and 10^4, the total source strength amplitude $|\mathbf{q}_{\text{opt}}|$ is bounded to an acceptable value without important residual reproduction error increase [E_{LS} stays far below the suggested limit of $E_{LS}=0.5$ (Kirkeby and Nelson, 1993)]. Accordingly, a fixed value of $\gamma=50$ is used for all the simulations considered in this paper, although more rigorous determination rules have been introduced for the regularization of the inverse problem (Nelson, 2001). Moreover, Fig. 4 shows an alternative representation of Fig. 3 which is referred to as an L curve, where the chosen γ is near the corner

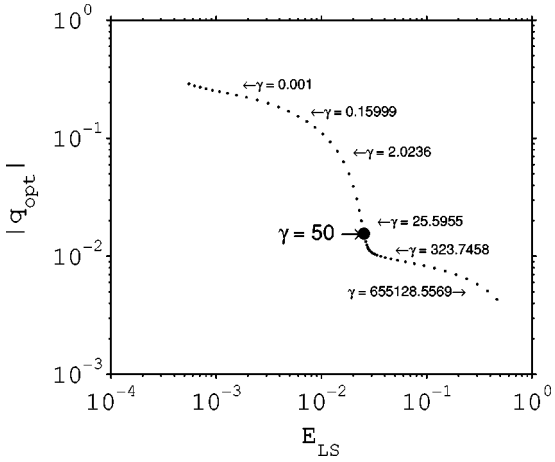

FIG. 4. Relation between $|\mathbf{q}_{\text{opt}}|$ and E_{LS}, with γ as a parameter (that is, the L-curve representation of Fig. 3 for the free-field case shown in Fig. 2).

region associated with the optimal regularization parameter (Nelson, 2001). Even if we use a frequency- and case-independent γ, it is, for our purposes, still sufficiently near the optimal corner of the case-dependent L curves. Some numerical experiments have shown better conditioning with values as small as $\gamma=0.1$ in comparison with absence of any regularization ($\gamma=0$). However, such small values usually lead to important error outside the sensor array, thus potentially introducing high sound pressure outside the reproduction area. This higher sound pressure is suggested in Fig. 3 by the $|q_{\text{opt}}|$ drastic increase with small γ. Although this increase introduces an E_{LS} reduction, it is at the costly expense of potentially disturbing high source strengths. A regularization parameter of $\gamma=50$ thus seems to be a good compromise between objective reproduction quality and source strength amplitude. When the regularization parameter is roughly kept in the flat regions of E_{LS} and $|q_{\text{opt}}|$ shown in Fig. 3, the results can be considered to be valid and revealing for our purposes. This region corresponds to the L curve's corner, where a higher concentration of points can be seen in Fig. 4 for a logarithmic variation of γ. As shown in both Figs. 3 and 4, this region is quite large and can support a γ variation, a tolerance which allows the use of a case-independent γ for our purposes.

Tikhonov regularization and regularization parameter choice have been extensively studied in the context of inverse source problem (Nelson, 2001) and for sound-reproduction filter design (Tokuno *et al.*, 1997). In our current theoretical problem, the idea is not to precisely define the source strength from a set of measurements (like for the inverse source problem) but more to physically reproduce a given wave field and evaluate the possibilities. For this simple reason, and for computational efficiency, the regularization parameter is not rigorously optimized in this work.

This entirely acoustical approach to the control problem is easily connected to feedforward control systems which usually try to reduce an estimated error by the adaptation of filters upstream of the actuators (Elliott, 2001). Using the optimal control approach in the frequency domain, simulations give some cues about the best possible situation and the involved control mechanisms. It is thus a preliminary evaluation and comparison tool which guides the understanding and the subsequent construction and configuration of such a system.

Since source power outputs may give some relevant indications about control mechanisms, each source acoustical power output is computed using $\Pi_l=(1/2)\Re(p^H(\mathbf{x}_l)q_l)$ (Elliott, 2001), where superscript H denotes complex conjugation (that is the Hermitian transpose of a scalar) and $\Re(z)$, the real part of z.

As will be presented in the next section, some comparisons with WFS are made. In this case, the source strengths are derived from straight application of WFS operators given by Verheijen (1997) for general source arrays, nonfocusing virtual image defined by a spherical wave, and a straight reference line through the source array center. For a given virtual spherical source, the reference line is perpendicular to a line from the virtual source position to the source array center. Some adjustments have been made to convert monopole amplitude to source strength representation (Pierce, 1991) using consistent time-dependence notation. In this case, the optimal source strength vector is replaced by the corresponding WFS sources strength.

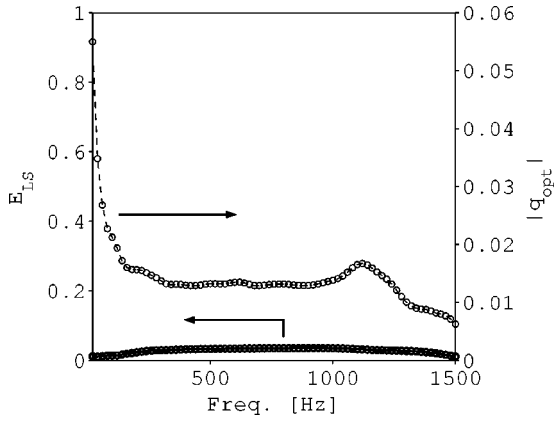

FIG. 5. Variation of E_{LS} (on left) and $|\mathbf{q}_{\text{opt}}|=\sqrt{\mathbf{q}_{\text{opt}}^H\mathbf{q}_{\text{opt}}}$ (on right) for progressive plane-wave ($\theta=30$ deg) reproduction in the (x_1,x_2) plane; see the configuration in Fig. 2.

III. RESULTS OF NUMERICAL SIMULATIONS

A. Feasibility study

The first question that should be addressed concerns the feasibility of a method such as active control in the context of sound-field reproduction. As a first investigation, Figs. 2 to 11 illustrate some results for the free-field case with given source and sensor configurations. The system configuration, which is depicted in Fig. 2, includes a 1-m-square sensor array. The target wave field is first defined as a progressive plane wave with a propagation direction of $\theta=30$ deg. Figure 5, which presents the minimization results, shows considerably low residual normalized cost function (E_{LS}) over the frequency range. Such a low residual error corresponds to a satisfactory quantitative reproduction of sound field, at least over the sensor array. (This is shown in further figures.) Also note in Fig. 5 that the reduction of $|\mathbf{q}_{\text{opt}}|$ with increasing frequency is related to low monopole radiation efficiency at low frequencies (for a frequency-independent source strength, which is volume velocity in this case).

Figure 6 shows the real part of the target wave field and the reproduced wave field for the same configuration at 220 Hz. Clearly, a low E_{LS} (below 0.1 as in Fig. 5 for 220 Hz) corresponds to a good wave-field reproduction over the sensor array and in its immediate vicinity. Kirkeby and Nelson

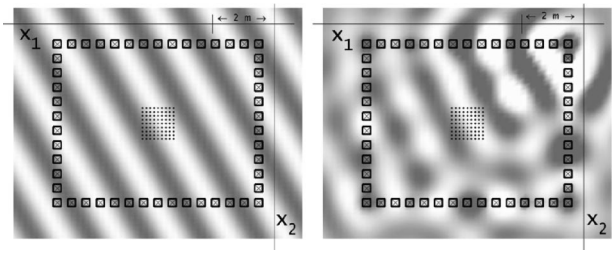

FIG. 6. On left, real part of the target wave field (plane wave) and, on right, the reproduced wave field at 220 Hz in free field.

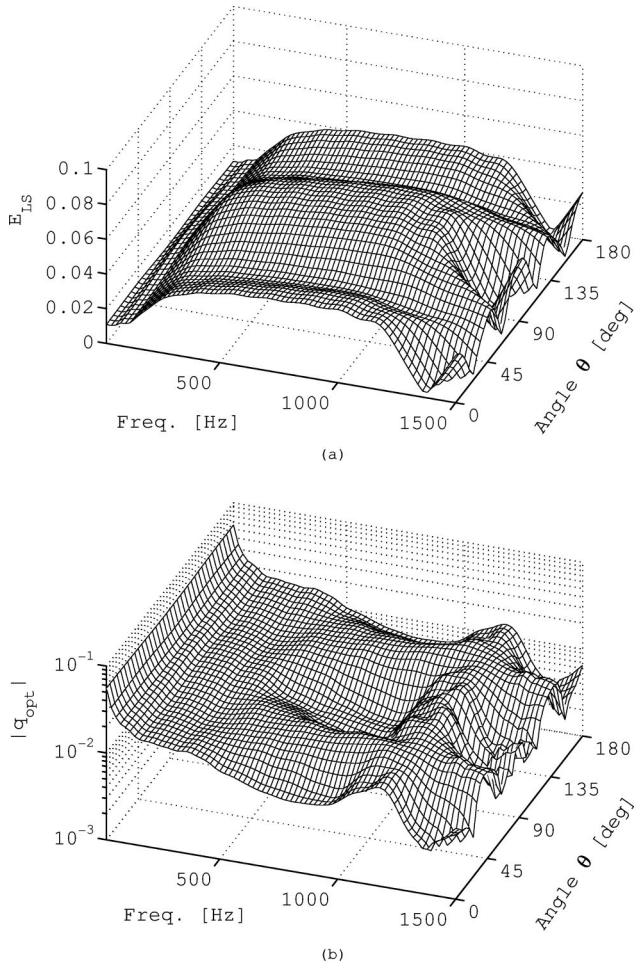

FIG. 7. Variation of E_{LS} (a) and $|q_{\text{opt}}|$ (b) with frequency and angle θ, for plane-wave reproduction in free field (see the configuration in Fig. 2).

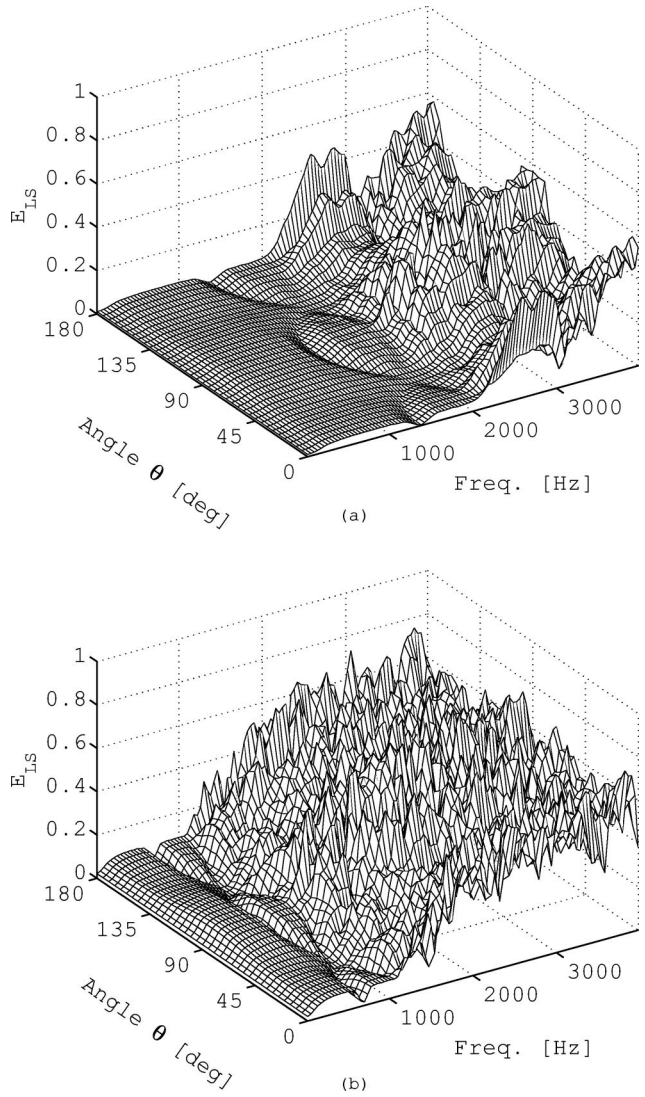

FIG. 8. Variation of E_{LS} with frequency and angle θ, for plane-wave reproduction in free field with: (a) a dense sensor array (see the configuration in Fig. 2) and (b) a sparse sensor array (double spaced in comparison with Fig. 2).

(1993) suggested 0.5 as a maximum acceptable value for E_{LS} for a similarly formulated reproduction problem. Although this simulation corresponds to an ideal situation, Figs. 5 and 6 allow us to conclude that it is possible to locally (in a 1-m^2 area) reproduce a plane wave using such a configuration in conjunction with active control techniques. This demonstrates that active control can thus be effective as a wave-field reconstruction system, like WFS. This was to be expected from previously published works for simple source configurations (Kirkeby and Nelson, 1993).

By analyzing Fig. 7, two simple phenomena can be observed for the free-field condition. First, slightly better objective reproduction, in terms of E_{LS}, is obtained for, roughly, 45- and 135-deg target plane-wave propagation directions. These directions correspond to the largest possible distance between reproduction source and sensor array for this configuration (consequently presenting a spherical wavefront of larger radius at the sensor array) and, according to Fig. 7(b), are associated with a $|\mathbf{q}_{\text{opt}}|$ increase. Second, depending on the target plane-wave propagation direction, a peculiar E_{LS} fluctuation can be observed around 1400 Hz. This fluctuation can be related to spatial aliasing which is function of sensor separation for this configuration. In this respect, Fig. 8(a) shows E_{LS} variations for a dense sensor array (which is the same as in Fig. 2) and Fig. 8(b) shows similar fluctuation for a sparse array (the same number of sensors with a spacing twice that of Fig. 2), both for a broader frequency span. Above 1400 Hz, E_{LS} rapidly increases for the dense array, which is characterized by a 0.125-m sensor spacing (corresponding approximately to a half-wavelength at 1400 Hz). When halving the sensor array density, this limiting frequency is also halved. This can be attributed to spatial aliasing by the sensor array. At least two sensors per wavelength have to be included for proper spatial sampling.

B. Comparison with WFS in free field

Since WFS systems have been shown to provide impressive subjective reproduction, a comparison between optimal control of sound-field reproduction and simple WFS is first presented in free field in Figs. 9 to 11. All these simulations have been carried out with a virtual spherical source located at $\mathbf{x}_o=[-2,-2,1.2]^T$ expressed in meters. The synthesis operators for an arbitrary source array and nonfocusing virtual

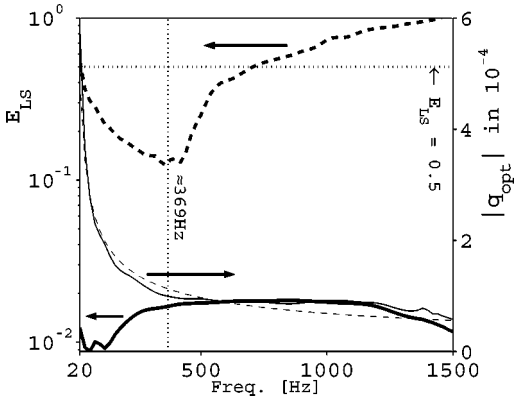

FIG. 9. Variation of E_{LS} and $|\mathbf{q}_{\text{opt}}|$ for spherical wave reproduction ($\mathbf{x}_o = [-2,-2,1.2]^T$ meters) in free field; see the configuration in Fig. 2. Solid lines: Optimal control. Dashed lines: WFS.

source are borrowed from Verheijen (1997) with a reference line across the sensor array center. This line is perpendicular to a line from the virtual source to the source array center. The virtual source's height, 1.2 m, is equal to source and sensor height. The inspection of E_{LS} in Fig. 9 shows that the reproduction error is lower for optimal control than for WFS over the considered frequency range at the sensor array. WFS provides an acceptable E_{LS} at low frequency. Above 369 Hz (see the broken vertical line in Fig. 9), the error for the WFS system increases drastically and monotonically. This result was to be expected since the sources' separation gives a spatial aliasing frequency of approximately 369 Hz for WFS in a first approximation (Verheijen, 1997; Nicol *et al.*, 1999). In

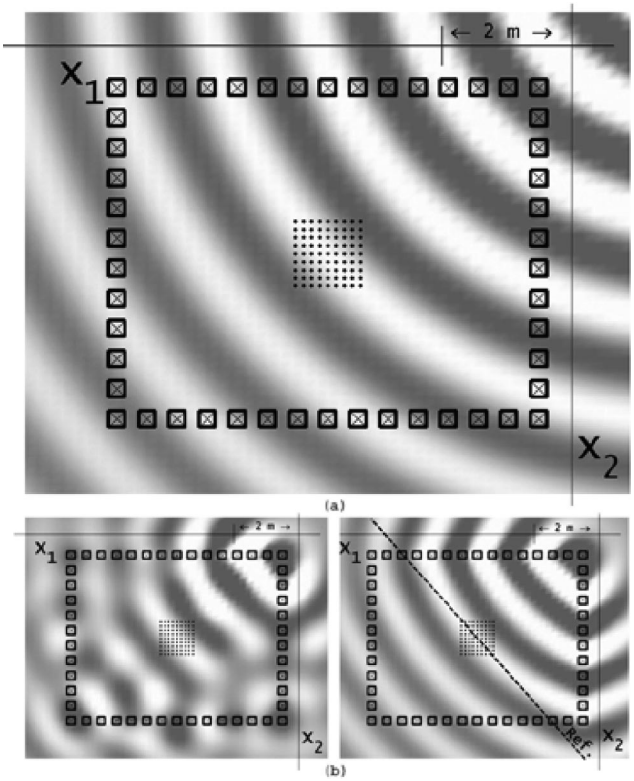

FIG. 10. (a) Real part of the target wave field at 220 Hz in free field. (b) Real part of the reproduced wave field at 220 Hz in free field using optimal control (on left) and using WFS (on right, the dashed line is the reference line).

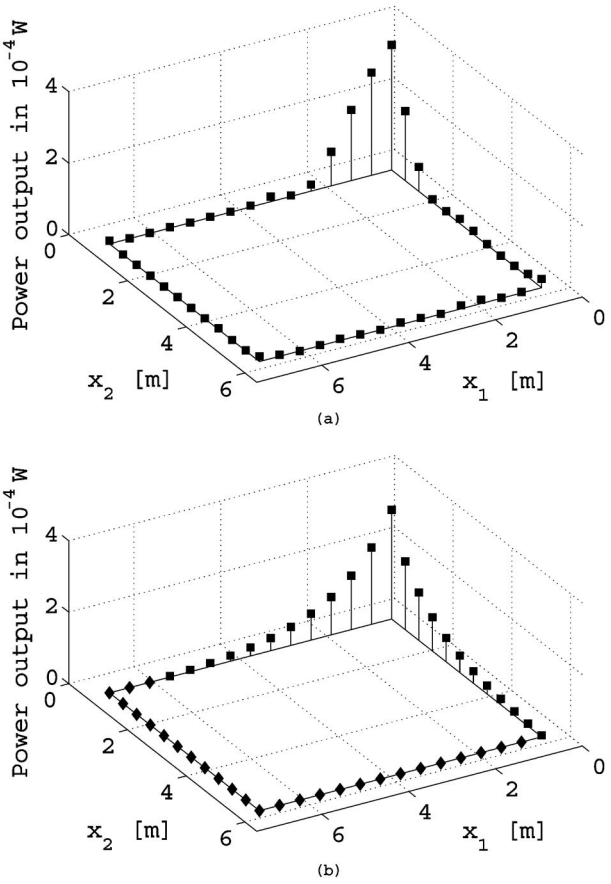

FIG. 11. Acoustical power output for: (a) optimal control and (b) WFS while reproducing a spherical wave at 220 Hz in free field; see Figs. 9 and 10.

fact, with such a source separation, WFS is penalized for higher frequencies. A denser source array would advantageously push this upper-frequency limit for WFS. WFS upper-frequency limit is actually defined by sources separation (Verheijen, 1997), while the optimal control frequency limit is defined by sensor separation, at least for this configuration. From a practical viewpoint, increasing microphone density is more easily achieved than increasing loudspeaker density, since microphones are usually smaller than loudspeaker cabinets. On the other side, from an auditory perception viewpoint, it may not be relevant to attempt physical sound-field reconstruction at frequencies larger than 1.5 kHz since our auditory mechanism of sound localization is dominated in the time domain, above this frequency, by ITD cues of signal envelope and not by ITD cues of signal's fine temporal structure (Blauert, 1999). Interaural level differences (ILD), however, are still effective for a higher frequency range (Blauert, 1999).

Even if the residual error is considerably lower for the optimal control solution, the wave field is correctly reproduced by WFS over a broader listening area at 220 Hz as demonstrated in Fig. 10. However, increasing the size of the listening area for optimal control using a broader sensor array may be desirable. The listening area aspect is further investigated in the next section of this paper.

Figure 11 shows the source power output for optimal control and for WFS. Clearly, similar power injection may be

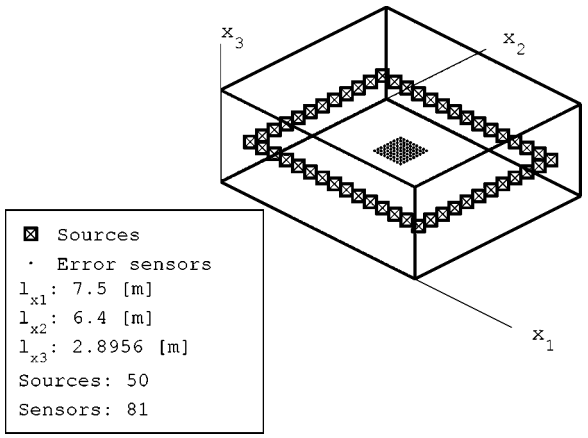

FIG. 12. Second investigated configuration: a room of 139 m^2 with a reverberation time of 0.28 s [as suggested by the AES (2001)].

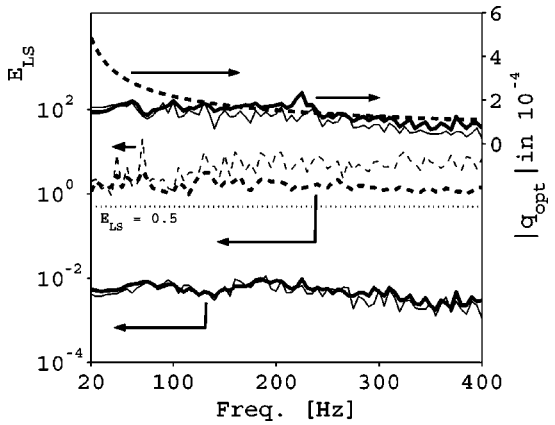

FIG. 13. Variation of E_{LS} (on left) and $|\mathbf{q}_{\mathrm{opt}}|$ (on right) for spherical wave reproduction in room. Solid lines: Optimal control. Dashed lines: WFS. Thick lines: Reverberation time of 0.28 s. Thin lines: Reverberation time of 2.8 s. $|\mathbf{q}_{\mathrm{opt}}|$ is independent of the reverberation time for WFS.

observed for both cases in free field. Somewhat lower power injection for optimal control is related to the smaller listening area, which corresponds to the sensor array in this case.

According to these simulations of the two methods, active control is able to achieve wave-field reproduction comparable to WFS in the free-field condition.

C. In-room reproduction, comparison with WFS and control mechanisms

The effect of a reflective environment on optimal reproduction at the sensor array position, in comparison with WFS, can now be evaluated. As shown previously, wave-field reproduction can be physically achieved in free field using active control technique. In the following, the comparison is conducted for a simple rectangular room.

The investigated configuration is depicted in Fig. 12. The room dimensions have been defined in accordance with the Audio Engineering Society (AES, 2001) and German Surround Sound Forum (Rumsey, 2001) recommendations for the optimal size of multichannel monitor rooms. For the given volume, $V=139\,\mathrm{m}^3$ (precisely $7.5\times6.4\times2.896$ m; source and sensor height: 1.2 m), a nominal reverberation time of approximately $T_{60}=0.28\,\mathrm{s}$ is suggested (Rumsey, 2001). Using the Eyring–Norris reverberation model for diffuse field without medium absorption (Kinsler *et al.*, 2000)

$$T_{60}=\frac{0.161V}{-S\ln(1-a)}, \tag{21}$$

an associated random-incidence energy absorption coefficient, a, is calculated and converted into an equivalent specific conductance ratio (normalized by the air characteristic impedance ρc) using an implicit relation (Kinsler *et al.*, 2000)

$$a=8\beta\left(1+\frac{\beta}{\beta+1}-2\beta\ln\left(\frac{\beta+1}{\beta}\right)\right). \tag{22}$$

The surface-specific conductance ratio β [see boundary conditions in Eq. (2) and modal scheme in Eqs. (6) to (11)] is set to 0.0651, which is real, frequency independent, and uniform on S. For the simulations, the number of modes in Eq. (5), N, is set to 6137. This proved sufficient to ensure convergence of the total time-averaged acoustical potential energy up to 400 Hz.

Figure 13 shows the comparison, for such a configuration, between optimal control and WFS. The target wave field is a spherical wave originating from $\mathbf{x}_o=[-2,-2,1.2]^T$ expressed in meters. E_{LS} for optimal control is below 0.02. Optimal control provides a small reproduction error over the whole frequency range. By comparison, WFS produces an E_{LS} larger than 1 for the same frequency range in the simulated room. According to Eqs. (16) to (20) an E_{LS} value of 1 corresponds to a reproduction error as important as perfect silence [$p^{(\mathrm{rep})}(\mathbf{x})=0$ and $e(\mathbf{x})=p^{(\mathrm{im})}(\mathbf{x})$] in the reproduction space; hence, large differences may be expected between the target wave field and the wave field reproduced by WFS with this room model. This is indeed supported by Figs. 14(a) to (c), where, this time, real and imaginary parts of pressure have been plotted to clearly differentiate propagating and standing waves. As shown in Fig. 14(b), the optimal control approach properly recreates the wave field at the position of the sensor array in the room. On the other hand, Fig. 14(c) reveals that WFS does not recreate the wave field in-room situation. Moreover, Fig. 14(d) shows that optimal control can reproduce a progressive wave field over a larger area in the room (2×2-m sensor array).

Similar simulations have been carried out for another configuration (where the surface-specific admittance ratio β has been replaced by 0.0059) corresponding to a reverberation time of approximately 2.8 s (that is, ten times longer than the AES recommendation for the given volume). The reproduction room is consequently regarded as a poor environment for audio applications since strong and distinct standing waves may appear both in space and frequency responses. The results are again shown in Fig. 13 for active control and WFS. From this figure, it is possible to conclude that active control automatically accounts for room dynamics, even for a highly reflective environment. This illustrates the usefulness of active control in sound-field reproduction.

The source acoustical power output for the 220-Hz spherical wave-field reproduction is shown in Fig. 15(a) for optimal control, and in Fig. 15(b) for WFS. The source output distributions are clearly different in each case. Power

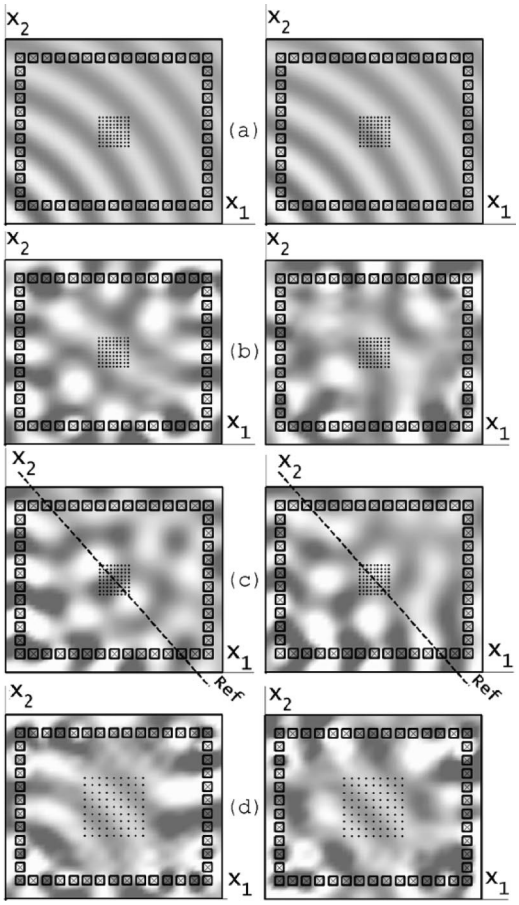

FIG. 14. Real (on left) and imaginary (on right) part of: (a) the target wave field at 220 Hz in-room ($T_{60}\approx 0.28$ s); (b) the corresponding reproduced wave field using optimal control; (c) the reproduced wave field in room using WFS; and (d) the reproduced wave field using optimal control in room for a larger sensor array.

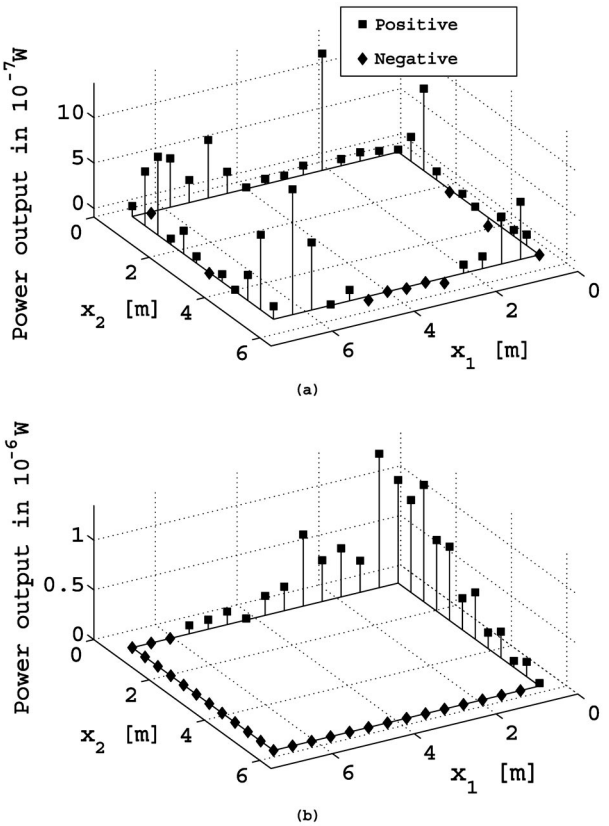

FIG. 15. Acoustical power output for: (a) optimal control and (b) WFS while reproducing a spherical wave at 220 Hz, in-room ($T_{60}\approx 0.28$ s).

absorption (negative power output) by acoustic sources is hardly visible in Fig. 15(a) for the active control of sound reproduction. This ensures reconstruction of a propagating wave field on a modal basis.

For such a frequency of 220 Hz [above the room's Schroeder frequency, which is approximately 94 Hz (Pierce, 1991)], where modal density and modal overlap are progressively more important, control mechanisms may be interpreted, in the limit of the present physical model, as a modal rearrangement where appropriate field reconstruction arises from the superposition and arrangement of modal responses at the driving frequency. Recalling that each room's oblique mode can be seen as a superposition of eight propagating plane waves, some superposition possibilities have to be expected when modal overlap increases. At lower frequencies, where the modal density is, by far, lower, acoustical power absorption by the reproduction sources becomes more important. This is illustrated in Figs. 16(a) and (b) for an image field at 70.5 Hz. For such low frequencies (below the room's Schroeder frequency) the spatial sound-pressure variations over the sensor array are small and the modal density is smaller. In this frequency range, the optimal control, again for this configuration, acts to create an acoustical energy flow over the sensor array and mainly prevents a pure standing-wave pattern. Acoustical power outputs are finally shown in Fig. 16(c) at 220 Hz for the same room with a longer reverberation time of approximately 2.8 s. In this case, power absorption by the reproduction sources is more effective in the optimal reproduction process above the Schroeder frequency. From these results and comparisons with WFS, it is clear that all the sources are active in contributing to progressive wave-field reconstruction in room. For this reason, wave-field reconstruction and room compensation may not be performed with only a fraction of the total number of reproduction sources. These sources that are inactive in WFS have to perform power absorption or modal rearrangement for better sound-field reproduction in-room.

D. Investigation of practical sensing configuration

In this section, a more practical microphone array is briefly introduced for sound-field reconstruction. The main objective is to investigate a potential sensor array which can reduce the total number of sensors and leave a listening zone (where the wave field must be reproduced) free of any sensor.

WFS is based on the Kirchoff–Helmoltz integral formulation (Verheijen, 1997; Morse *et al.*, 1968)

$$p(\mathbf{x}) = \int_{S'} (G(\mathbf{x}|\mathbf{y})\nabla p(\mathbf{y}) - p(\mathbf{y})\nabla G(\mathbf{x}|\mathbf{y}))\cdot \mathbf{n}\, dS', \quad (23)$$

which represents a mathematical formulation of the Huygens' principle where the normal pressure gradient on S' becomes a continuous monopole source and the pressure on S' becomes a continuous dipole source. Note that this ap-

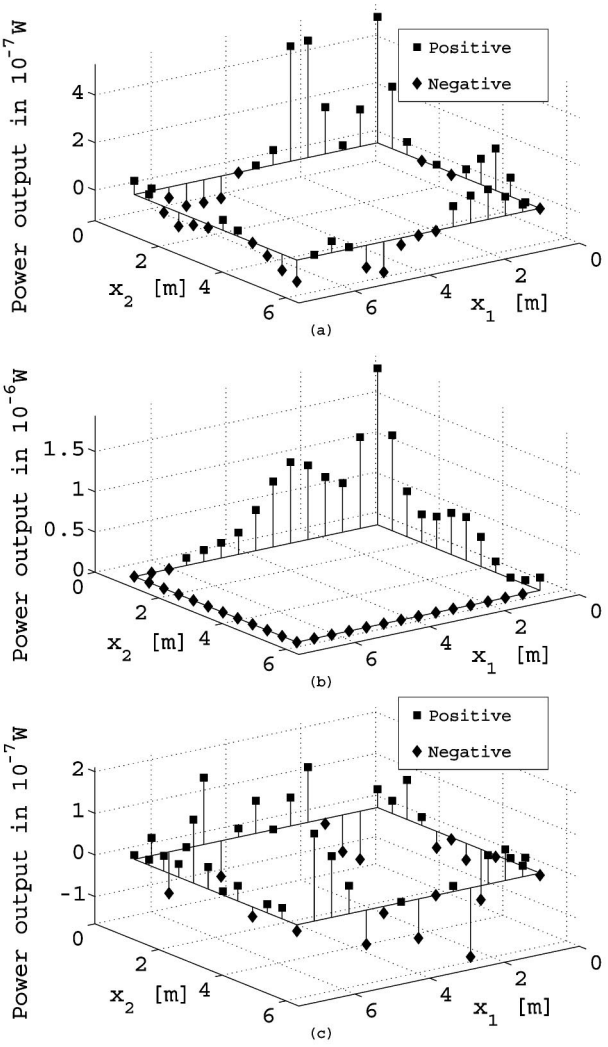

FIG. 16. Acoustical power output for: (a) optimal control and (b) WFS while reproducing a spherical wave at 70.5 Hz, in-room ($T_{60} \approx 0.28$ s). (c) Acoustical power output for optimal control while reproducing a spherical wave at 220 Hz, in-room with a lower admittance ($T_{60} \approx 2.8$ s).

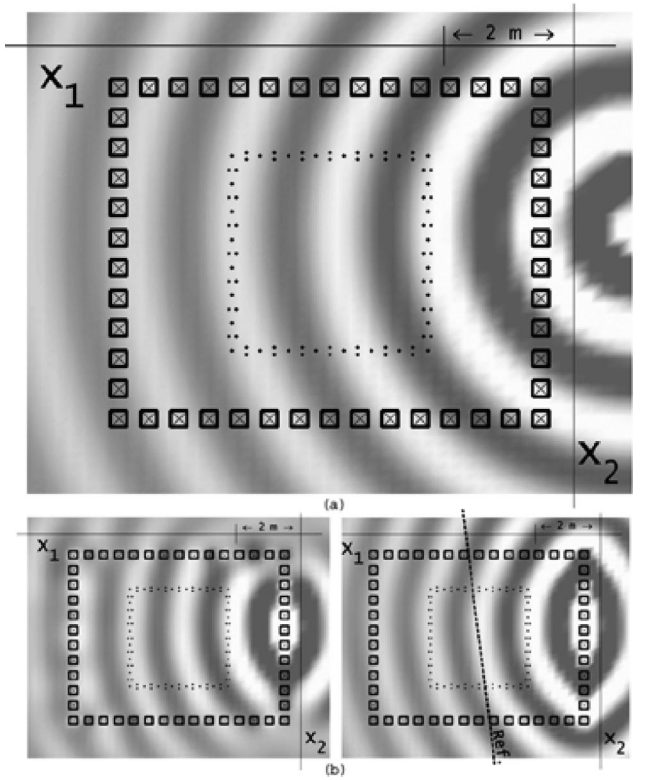

FIG. 17. (a) A linear sensor array in free field superposed to the real part of the target wave field (a spherical wave originating from $\mathbf{x}_o = [-1, 2.8, 1.2]^T$ m) at 220 Hz. (b) Real part of the corresponding reproduced wave fields in free field with optimal control (on left) and WFS (on right, the dashed line is the reference line).

plies only in the volume V' bounded by surface S' (see Fig. 1 for the chosen convention). Also note that S' may not correspond to a physical surface such as a room wall or source array. The WFS fundamental and theoretical interpretation of this formulation is that the wave field can be reconstructed using a surrounding and continuous distribution of appropriately driven monopoles and/or dipoles sources on S', where $p(\mathbf{y})$ is the target wave field on S'. Another interpretation of Eq. (23) is that any sound-pressure field inside V', which is assumed to be free of acoustic sources, is entirely and uniquely defined by its pressure and pressure gradient on the bounding surface S'. With this in mind, perfect wave-field reconstruction should be obtained if the pressure and the pressure gradient are continuously reconstructed on S' with reproduction sources outside V' and S'. Such interpretation has been previously pointed out by Ise (1999). Now, considering the fact that WFS, using a finite number of sources along a finite line replacing S', appropriately reproduces an approximation of the target wave field below the WFS aliasing frequency in free field (Berkhout, 1993; Verheijen, 1997), another sensor array for optimal control is introduced in Fig. 17(a). For this configuration, the sensors are distributed over the sides of a 3×3-m square, and consist of either single microphones or microphone pairs. For the microphone pair, the microphones are separated by 0.1071 m. There is a total of 84 sensors. With this linear sensor array, any reproduction error reduction will reconstruct an approximation of the sound pressure (single microphone) and sound-pressure gradient (microphone pairs) around the listening area. Depending on the situation, it is consequently expected that such a reconstruction will also imply wave-field reproduction inside the sensor array. The surrounding property of the linear array is chosen to ensure reproduction for all possible propagation directions in the horizontal plane. In free field, a simple layer, which only approximates sound pressure, could have alternatively been considered as sufficient for reproduction.

A similar type of reconstruction has been used by Corteel *et al.* (2002) for wave-field synthesis with panel loudspeakers. In their paper, the authors report the experimental usage of a simple linear sensor array in front of the panel sources to achieve filter design using adaptive filters. Adaptive filter design procedure is chosen since explicit WFS operators would be too difficult to theoretically define for such multiexciter panel loudspeakers.

Using the discrete approximation of reproduced pressure and pressure gradient around a listening area, in order to obtain an appropriate field inside the horizontal array, some revealing results about practical possibilities for such a sur-

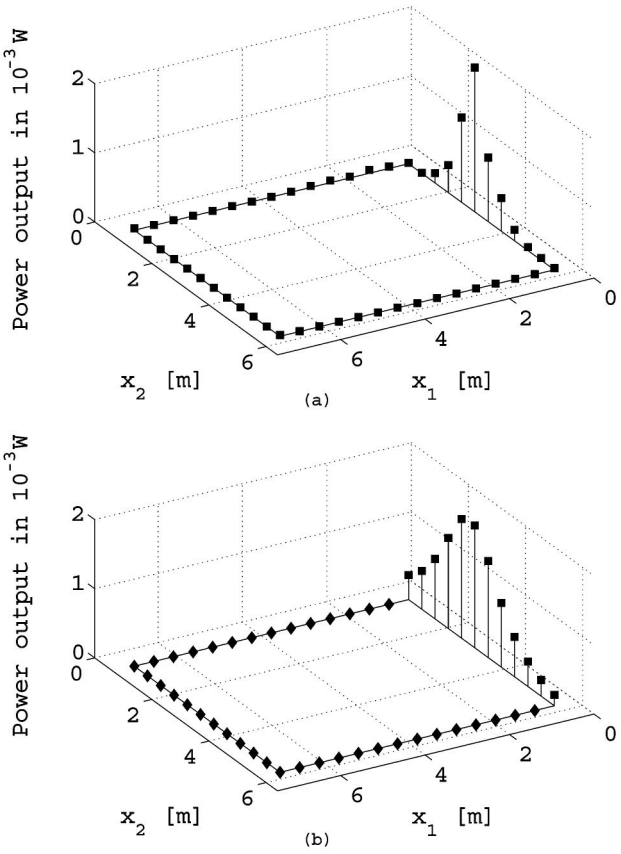

FIG. 18. Acoustical power output while reproducing a spherical wave at 220 Hz, in free field with (a) optimal control and (b) WFS (see Fig. 17). Diamond markers denote zero power output for WFS.

rounding array are provided. Optimal control application for a configuration in free-field situation is summarized in Figs. 17 and 18.

Wave-field reproduction is conveniently achieved in the listening zone, surrounded by this sensor array, using optimal control of error reproduction at these sensor locations. As illustrated in Fig. 17(b), optimal control results are comparable to WFS reproduction. Clearly, this simple preliminary result using a linear sensor array shows that active control leads to a sound-field reconstruction which is very similar to WFS reconstruction in a free-field reproduction space. This type of pressure and pressure gradient reconstruction constitutes a conceptual connection between WFS and active control of reproduction errors. Source power outputs are shown in Fig. 18. Again, sound-field control and WFS show similar power output distributions. The narrower power distribution for optimal control is related to the smaller dimensions of the reproduction area, as compared to the dimension of the WFS reference line in front of the sources. As expected for the free-field acoustics, there is no control mechanism that operates in this example other than wave interference. In comparison with the free-field results shown in Fig. 10, a larger listening zone is achieved. This difference is due to the larger extent of the sensor array that is more demanding in terms of securing a suitable reproduction area.

Being able to successfully use such an array in a room would be practically very attractive. Unfortunately, preliminary simulations using such a sensor array in a room situation show an inappropriate reproduction of sound field inside the surrounding array except for low frequencies. For low frequency, the sensor array is no longer a linear array since the dimensions of the sensor array are comparable to the acoustic wavelength. Such a difference between free-field and in-room situations was physically foreseeable. From the Kirchhoff–Helmholtz formulation, any distribution of sound pressure and sound-pressure gradient over S' will entirely define sound pressure $p(\mathbf{x})$ inside V'. Since our simulations are concerned with a planar listening area (that is, source distribution and sensors distribution in an horizontal plane), the free-field situation allows one to replace the surface integration by a line integration surrounding the listening area. The linear array of Fig. 17 is thus a free-field-specific interpretation of the Kirchhoff–Helmholtz integral simplified to a surrounding line. By marked contrast with the free-field situation, the room situation implies source reflections from the walls, ceiling, and floor, the sound-pressure field is thus defined by sound waves propagating with all possible directions through the closed surrounding surface S', which consequently cannot be replaced by a line array without loss of information. About this point, one can see a connection with the practical implementation of surrounding linear sensor array by Spors *et al.* (2003) used for plane-wave decomposition and room compensation. For the aforementioned reasons, a linear array such as the one introduced in Fig. 17 should be replaced by a surrounding sensor surface for the in-room context to achieve a more ideal correspondence with the Kirchhoff–Helmholtz integral formulation. In any case, further investigation should be carried out to evaluate both the effect and nature of such type of line approximation for in-room situation.

This linear sensor array gives only a frequency-dependent approximation of the continuous sound pressure and sound-pressure gradient around the listening space; the reproduction inside the array is consequently more sensitive to residual error and its quality is no more objectively evaluated by the unique consideration of E_{LS}. In spite of the need for further investigation of such a sensor array, the previous simulations suggest some potential and interesting applications. Moreover, this establishes a relation between wave-field synthesis and active control of sound reproduction. From a practical viewpoint, such a linear sensor array would be attractive for sound-field control since the quantity of sensors is seriously reduced (in comparison with a uniform rectangular array), and the listening area, which is considerably larger, is free of sensors. On the other hand, as mentioned earlier, some serious efforts should be devoted to the applicability and adaptation of such a type of sensor array in-room situation.

E. Conditioning of the reproduction system

This section deals with two other aspects of sound-field reproduction. The first is related to the effect and meanings of the Tikhonov regularization introduced earlier within the optimal control approach, while the second is a search for an ideal source and sensor configuration. Here, however, we do not seek an absolute solution to the quest for an ideal configuration, but general rules for practical elaboration of a

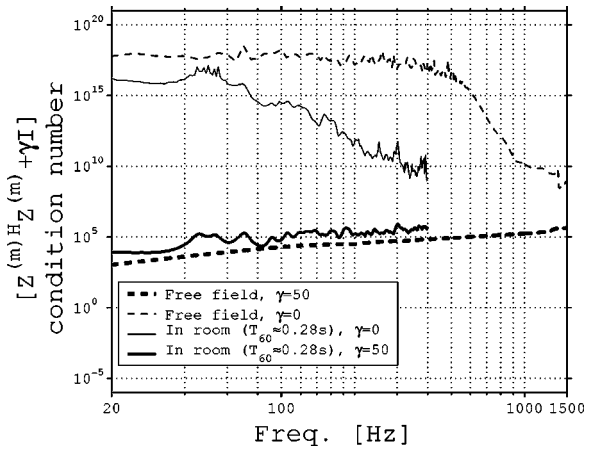

FIG. 19. Condition number of $[\mathbf{Z}^{(m)H}\mathbf{Z}^{(m)}+\gamma\mathbf{I}]$ [see the configurations in Figs. 2, 14(d), and 12].

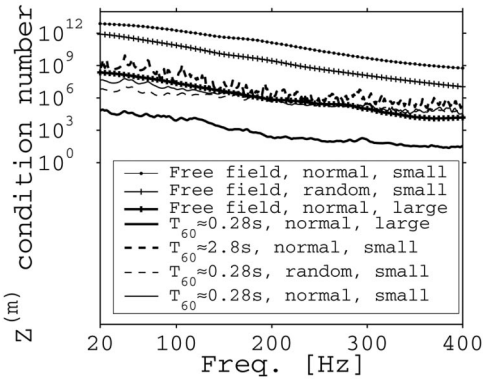

FIG. 20. Condition number of $\mathbf{Z}^{(m)}$ for various configurations (physical situation, the source configuration, and the sensor configuration). ''Normal'' refers to source position of Fig. 2. ''Random'' refers to source position of Fig. 2 with an additional ± 0.1-m randomization along the three axes. ''Small'' refers to sensor positions of Fig. 2, while ''large'' refers to a larger (3×3-m) array with 81 sensors.

sound-field reproduction system. For both aspects, conditioning of matrices is regarded as a source of relevant information.

Figure 19 introduces some aspects of sound-field reproduction in a room in comparison with a free-field situation from the matrix inversion viewpoint. Such considerations are first monitored by the condition number of $[\mathbf{Z}^{(m)H}\mathbf{Z}^{(m)}+\gamma\mathbf{I}]$, that is, the matrix to be inverted in Eq. (19) while achieving optimal control. The condition number of a matrix is formally defined as the ratio of the largest to the smallest nonzero singular values of the matrix. [See Golub *et al.* (1998) and Nelson and Yoon (2000) for a more detailed review of the potential meanings and applications of the condition number in relation with singular value decomposition, a topic which is beyond the scope of this paper.] A simple numerical interpretation of the condition number is that a higher condition number reveals an ill-conditioned matrix which, by means of numerical inversion, may lead to errors and fluctuations in the solution $\mathbf{q}_{\text{opt}}$. In the worst case of ill-conditioning, the solution may not be valid at all (showing an extremely sensitive reaction to numerical errors) and the matrix is nearly singular or singular, and thus prevents any significative matrix inversion. For our application and by inspection of Fig. 19, the condition number of the matrix which has to be inverted in the optimal control process is drastically reduced when the regularization parameter γ is introduced, as expected from Sec. II B. Since a large condition number characterizes an ill-conditioned problem, the Tikhonov regularization improves the conditioning and hence demonstrates its useful presence. Consequently, since this regularization corresponds to an effort penalty in the active control perspective, the beneficial effect of γ parameter suggests, for future works on sound field reproduction with optimal control, that a specific adaptation scheme such as the leaky adaptation[2] (Elliott, 2001) is to be considered for practical implementation to compensate for ill-conditioning of the problem, and by doing so avoid unacceptable large source strengths. Again from Fig. 19, the condition number shows strong variations with frequency in a room enclosure. In case of modal-dominated response (at lower frequency), the condition number increases at room resonances and thus suggests the effect of room dynamics on the optimal control problem conditioning. This will be more developed in the following comments.

We now consider effect of various parameters, such as: in-room versus free-field situation, admittance variation, sensor and source positions, on the condition number of the matrix $\mathbf{Z}^{(m)}$ to reach some guidelines for design purposes. This matrix is the plant matrix and it describes the reproduction system through the relation between $\mathbf{q}$ and $\mathbf{p}^{(\text{rep})}$ expressed by Eq. (12). Theoretically, the condition number of $\mathbf{Z}^{(m)}$ bounds the variations of $\mathbf{q}$ caused by $\mathbf{p}^{(\text{rep})}$ variations (Nelson, 2001) in the set of equations $\mathbf{q}=\mathbf{Z}^{(m)^{-1}}\mathbf{p}^{(\text{rep})}$ in such a manner that a well-conditioned matrix (with a small condition number) shows a small source strength variation caused by small pressure variations, while an ill-conditioned matrix (with a large condition number) implies important source strength variations for small pressure variations. Since for optimal control $\mathbf{p}^{(\text{rep})}$ is always trying to imitate in a ''least-square'' sense $\mathbf{p}^{(\text{im})}$, a high condition number for $\mathbf{Z}^{(m)}$ may thus lead to strong variations of $\mathbf{q}_{\text{opt}}$ associated with slight variations of $\mathbf{p}^{(\text{im})}$. Such a behavior is undesirable in practice because progressive or smooth time variations of the target wave field should necessarily be associated with a rather smooth variation of the source strength, since such abrupt change may be noticeable to an audience. For all these reasons, the condition number of $\mathbf{Z}^{(m)}$ provides some cues for the most appropriate reproduction configuration. Moreover, the condition number of $\mathbf{Z}^{(m)}$ alone allows us to compare the conditioning in various configurations without the influence of γ. It worth noting that optimal source distribution (OSD) systems for cross-talk cancellation have been developed on a similar theoretical basis about conditioning for a system including only two sources and two reproduction points (Takeuchi *et al.*, 2002; Ward *et al.*, 1999).

The computed $\mathbf{Z}^{(m)}$ condition numbers are introduced in Fig. 20 for various configurations in free field and in-room. The small sensor array refers to the one of Fig. 2. The large sensor array refers to a larger (3×3-m) square centered sensor array again including 81 sensors. Source positions are kept identical to Fig. 12, except for one case with random

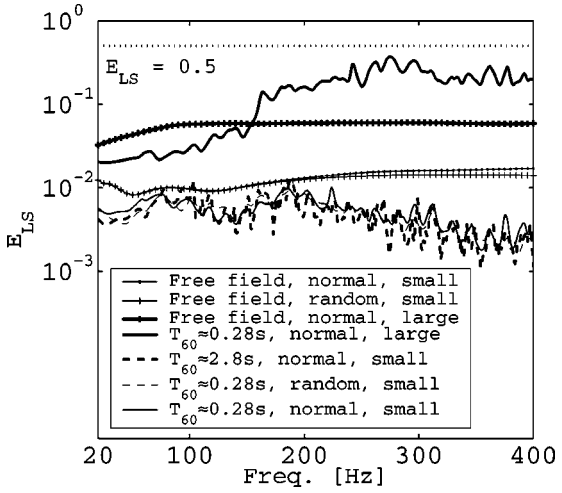

FIG. 21. E_{LS} values for the various cases presented in Fig. 20 while reproducing a spherical wave originating from $\mathbf{x}_o=[-2,-2,1.2]^T$ expressed in meters.

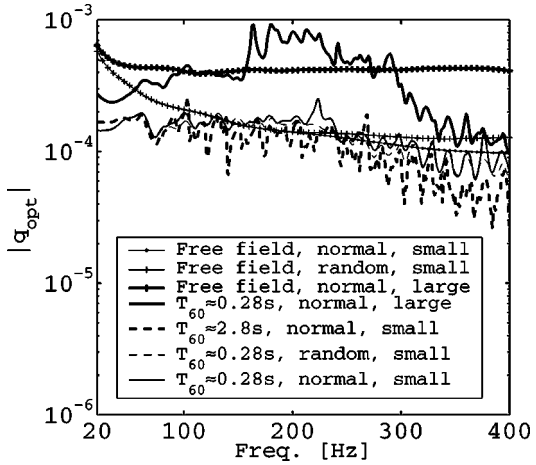

FIG. 22. $|\mathbf{q}_{\text{opt}}|$ values for the various cases presented in Fig. 20.

variations of the source positions limited to ± 0.1 m along the three axes. As introduced earlier, an admittance ratio of $\beta=0.0651$ is used in "normal" reverberation ($T_{60}\approx 0.28$ s) conditions (following the AES requirements), and an admittance ratio of $\beta=0.0059$ ($T_{60}\approx 2.8$ s) is used to evaluate the effect of less room absorption. All the corresponding J_M minimization results are shown in Figs. 21 and 22 for an image field defined by a spherical wave originating from $\mathbf{x}_o=[-2,-2,1.2]^T$ expressed in meters.

In all cases of Fig. 20, the condition number decreases with increasing frequency. This is caused by source and sensor separation distance in relation with decreasing wavelength. At low frequency, where the spatial variation of the sound pressure is small over the source and sensor arrays, the elements of $\mathbf{Z}^{(m)}$ tend to be identical and the transfer impedance matrix $\mathbf{Z}^{(m)}$ tends to be singular (hence presenting a more important condition number). This also explains the better conditioning associated with the large sensor array, that can more effectively observe longer wavelengths without the apparition of similar elements or linearly dependent lines or rows in the matrix $\mathbf{Z}^{(m)}$.

For both free-field and in-room situations, the slightly randomized source positions imply a better conditioning than the straightforward rectangular symmetrical array. Such alteration effectively breaks the potential symmetry and increases the differences between $\mathbf{Z}^{(m)}$ elements and, consequently, reduces the $\mathbf{Z}^{(m)}$ condition number and avoids a singular characteristic.

Let us now investigate the effect of the reproduction space on the condition number as function of frequency. From Fig. 20, the room situation with a shorter reverberation time shows a better conditioning than both the free-field situation and the longer reverberation room situation. (This is for the same source and receiver positions.) Consequently, although E_{LS} variation for various reverberation times were nearly unnoticeable in Fig. 13 using optimal control approach, the $\mathbf{Z}^{(m)}$ condition number increases when reverberation time is increased to $T_{60}=2.8$ s. This suggests that, although active control of sound may, in one unique operation, synthesize a wave field and overcome the room's natural dynamics, a less reflective environment, such as the one based on AES recommendations, is favorable in terms of conditioning and robustness of the inverse problem $\mathbf{q}=\mathbf{Z}^{(m)^{-1}}\mathbf{p}^{(\text{rep})}$. Hence, a more damped room, that is with a shorter reverberation time, will ensure less important $\mathbf{q}_{\text{opt}}$ variation for a given $\mathbf{p}^{(\text{im})}$ variation.

The previous observation that suggests that the in-room case (with $T_{60}=0.28$ s) is better conditioned than the free-field case may seem surprising at first glance. In fact, the major conditioning difference between free-field and in-room situations arises from free-field and in-room model differences. For the free-field model, a given frequency corresponds to a single acoustic wavelength, while the room model implies a modal expansion of the Green's function. Recalling that each mode has its own eigenvalue and corresponding wavelengths along axes, each mode present in the response will contribute differently to $\mathbf{Z}^{(m)}$ at a given frequency. The contribution of higher order modes in the room response therefore implies more differences in the $\mathbf{Z}^{(m)}$ coefficients, and ultimately a better conditioning of the problem. Even when $\mathbf{Z}^{(m)}$ is computed at low frequencies or for modal-dominated responses, such higher modes introduce a little regularization of the matrix which drastically improves the matrix conditioning.

Again from Fig. 20, the best conditioning situation is obtained for the large sensor array with rectangular source array in-room. However, such a sparse sensor array may reduce the upper-frequency effective limit which is, as seen previously, dictated by effective spatial sampling by the sensor array. Moreover, Figs. 21 and 22 show that both free-field and in-room situations including a large sensor array are associated with the largest source strengths and reproduction errors for spherical wave reproduction. However, in all cases introduced in Figs. 21 and 22, E_{LS} is still below 0.5. For these reasons, the most well-conditioned system may not suggest an ideal configuration. However, it is clear, from previous allegations about conditioning, that a broken symmetry and a reduced reverberation time will provide a better conditioned system which should be favored for practical applications.

Since these conditioning considerations have been for-

mulated for the transfer impedance matrix $\mathbf{Z}^{(m)}$, the remarks apply to a broader range of problems such as optimal control of noise and inverse problems in acoustics, since the usage of such transfer impedance matrix like $\mathbf{Z}^{(m)}$ is common to those problems. Moreover, even within a sound-reproduction context which is not based on optimal control, the conditioning observations give interesting insight into the relation between source strengths and reproduced pressure variations.

IV. DISCUSSION

From a practical perspective, loudspeakers can be relatively inexpensive, allowing their liberal use in multiple-loudspeaker arrays. On the other hand, a microphone array, such as the one introduced in Fig. 2 or 17, gives no practical advantages to an audience, and its physical presence may even be questionable in comparison with multiple-channel open-loop systems such as WFS. Indeed, one should consider that any attempt to introduce more complex reproduction systems (including more sources and, in this case, a supplementary set of sensors) in a real situation will have to overcome some resistance attributable to the nonpractical nature of a supplementary device located in the reproduction space intended for entertainment or virtual reality purposes. However, substantial benefits of the sensor array and active control are closely related to closed-loop and adaptive architectures for wave-field reproduction and room dynamics compensation as shown in Sec. III C. Moreover, the adaptive nature of a typical active control system implies that source (loudspeaker) frequency responses may not be perfectly matched since adaptive filter design will compensate for such discrepancies. This argument again points to the usefulness of sensors array in contrast with other open-loop systems. In this paragraph we briefly introduced the subtle and touchy compromise between high-fidelity objective reproduction and more practical and less critical applications. A compromise is needed which is a key factor for any further practical developments and which may suggest few different practical approaches to this problem.

A first type of method would thus be a straightforward, direct application of optimal control as simulated in this paper, that is providing the optimal control of sound-field reproduction on-line. Alternatively, one can think of optimal control including a sensor array as a setup procedure, that is, working off-line. In the latter case, a database of both possible virtual source positions and types may have to be stored. This database should also include the complete set of corresponding filters which would have been identified by means of adaptive signal processing, consistent with the optimal control theoretical analysis. Such a setup procedure could thus rapidly become a tedious one and may consequently be not so interesting in comparison with on-line applications. Moreover, the off-line application may introduce serious errors which come from the weakly time-variant acoustical nature of a room (Hatziantoniou *et al.*, 2004). In either the on-line or off-line case, the here-introduced observations and conclusions are still valid, except again for the remark about the nature of room acoustics, which may slightly change with time (Hatziantoniou *et al.*, 2004).

Considerations and decisions regarding the merits of on-line versus off-line solutions could be both further investigated and clarified in any corresponding practical studies.

From an adaptive active control viewpoint, the system includes a large number of inputs and outputs and may consequently become a computational burden, even for a 1.5-kHz frequency range. On the other hand, depending on the controller architecture and adaptation scheme (Elliott, 2001), some reduction in computation time can be achieved. If some practical aspects of current audio systems and sound control technology are taken into account, a reduced number of sensors should be considered in subsequent simulations and research.

In spite of this, the introduced configurations and the associated physical model have been used for investigation purposes, because they give indications about the physical possibility of creating a wave field (spherical or planar) in a given horizontal region with various closed-loop reproduction systems. These simple simulations have in fact revealed that it is possible to reproduce a progressive wavefront in a closed reflective environment, thus from a set of room modes, in a least-square sense.

Most of the presented simulations have been interpreted from an active control viewpoint, assuming an adaptive controller such as feedforward system with effort penalty. The simulations and results can also be considered from the inverse problem perspective. From this viewpoint, the questions are, is it physically possible to recreate a given wave field with a given set of sources, and what mechanisms are involved? As a response, the wave fields can be constructed, in the least-square sense, by a set of simple sources with source strengths totally different than WFS source strengths in a room situation. Some sources that are inactive in WFS are now active in the optimal control approach and may possibly perform power absorption. This suggests the need for WFS modifications in reflective environments. [See Spors *et al.* (2003) as an example of practical implementation.]

V. CONCLUSION

Active control techniques can be applied to sound-field reproduction with satisfactory quantitative reproduction results achieved in a room and in a free field. These methods provide more accurate sound-field reproduction than a standard open-loop WFS system operating in a room. Such benefits are related to source power absorption and compensation of room dynamics in a reflective environment. Moreover, the simulations show that all reproduction sources are active in the optimal control approach, thus suggesting a need for modifications of the standard WFS operators. It is also demonstrated that active sound control can simultaneously perform wave-field reproduction and room compensation in a unique error minimization task.

Other relevant conclusions are related to spatial aliasing and special sensor configuration. It has been shown that spatial aliasing in optimal control is dictated by sensor spacing in the case of a dense enough sensor array away from the sources, while it is source density which dominates spatial aliasing for WFS (Verheijen, 1997; Nicol *et al.*, 1999). For this reason, optimal control may be more interesting since a

dense microphone array is practically more convenient than a dense source array. However, one has to reduce the quantity of sensors for practical applications. Again from a practical viewpoint, an interesting configuration of sensors, namely a sensor layer around a listening area, provides satisfactory sound-field reproduction inside the array while keeping the listening region free of any sensors. Such a configuration, which implies pressure and pressure gradient reconstruction on a surrounding line, constitutes a conceptual link between active control and WFS. In this paper, the surrounding sensor configuration has not been optimized for all possible situations. Further research should address this point, since the sensor array introduced here is not performing sound-field reproduction in a room.

Other conclusions have been drawn on the conditioning of the reproduction system including sources, reproduction situation, and sensors. The results suggest that a large sensor area, a slightly randomized source positioning, and reproduction in closed space are favorable in terms of the problem conditioning. On the other hand, some well-conditioned configurations, like the large sensor area, imply larger reproduction errors. The introduction of a regularization parameter at this stage of the study suggests the needs for proper effort penalty consideration in any following practical work.

Future work should be devoted to control architecture, practical prototyping, and further objective evaluation of the suggested technique.

ACKNOWLEDGMENTS

This work has been supported by NSERC (Natural Sciences and Engineering Research Council of Canada), FQRNT (Fond Québecois de la Recherche sur la Nature et les Technologies), VRQ (Valorisation Recherche Québec), and Université de Sherbrooke.

[1]The historical origin of what is called wave-field synthesis in its current symbolism and formulation is attributable to Berkhout, although some descriptions and ideas—such as the ones introduced by Steinberg (Rumsey, 2001) and later by Camras (1968)—have been previously introduced. Interestingly, a similar theoretical concept has been introduced by Jessel as early as in 1973 (Jessel, 1973). Jessel's ''holophony'' is based on the same Kirchhoff–Helmholtz integral interpretation as WFS. Similar terminology is introduced about primary and secondary sources, which is borrowed from Huygens' principle. In his book, Jessel's idea was only theoretically developed in a generic way. In fact, WFS is a specific application (implying a finite set of discrete reproduction sources) of the holophony concept. A more recent publication has established a clear theoretical connection between ambisonic and holophony or WFS (Nicol *et al.*, 1999), where it is demonstrated that ambisonic is a special case of holophony or WFS.

[2]Leaky adaptation is the practical time-domain adaptive filtering method corresponding to the cost function introduced earlier by Eq. (18) (Elliott, 2001). The ''leaky'' qualifier arises from the introduction of an effort-penalty term in the cost function which make the solution leak toward zero when its possible.

AES Technical Comittee on Multichannel and Binaural Audio Technology (**2001**). *Multi-channel Sound Systems and Operation* (Audio Engineering Society, New York).

Begault, D. R. (**1994**). *3-D Sound for Virtual Reality and Multimedia* (AP Professional, Boston).

Berkhout, A. J., de Vries, D., and Vogel, P. (**1993**). ''Acoustic control by wave field synthesis,'' J. Acoust. Soc. Am. **93**, 2764–2778.

Blauert, J. (**1999**). *Spatial Hearing: The Psychophysics of Human Sound Localization* (MIT Press, Cambridge).

Boulanger, R. (**2001**). *The CSound book: Perspectives in Software Synthesis, Sound Design, Signal Processing, and Programming* (MIT Press, Cambridge).

Bregman, A. S. (**1990**). *Auditory Scene Analysis: The Perceptual Organization of Sound* (MIT Press, Cambridge).

Camras, M. (**1968**). ''Approach to recreating a sound field,'' J. Acoust. Soc. Am. **43**, 1425–1431.

Corteel, E., Horbach, U., and Pellegrini, R. S. (**2002**). ''Multichannel inverse filtering of multiexciter distributed mode loudspeakers for wave field synthesis,'' Convention paper 5611, Proceedings of the 112th AES Convention.

Davis, M. F. (**2003**). ''History of spatial coding,'' J. Audio Eng. Soc. **51**, 554–569.

Elliott, S. (**2001**). *Signal Processing for Active Control* (Academic, London).

Elliott, S. J., and Nelson, P. A. (**1989**). ''Multiple-point equalization in a room using adaptive digital filters,'' J. Audio Eng. Soc. **37**, 899–907.

Elliott, S. J., Bhatia, L. P., Deghan, F. S., Fu, A. H., Stewart, M. S., and Wilson, D. W. (**1994**). ''Practical implementation of low-frequency equalization using adaptive digital filters,'' J. Audio Eng. Soc. **42**, 988–998.

Garas, J. (**1999**). *Adaptive 3D Sound Systems* (Technische Universiteit Eindhoven, Eindhoven).

Gardner, W. G. (**1998**). *3-D Audio using Loudspeakers* (Kluwer Academic, Boston).

Golub, G. H. (**1996**). *Matrix Computations* (John Hopkins University Press, Baltimore).

Hatziantoniou, P. D., and Mourjopoulos, J. N. (**2004**). ''Errors in real-time room acoustics dereverberation,'' J. Audio Eng. Soc. **52**, 883–899.

Henriksen, F. E. (**2002**). *Space in Electroacoustic Music: Composition, Performance and Perception of Musical Space*, Ph.D. thesis (City University, London).

Ise, S. (**1999**). ''A principle of sound field control based on the Kirchhoff-Helmholtz integral equation and the theory of inverse systems,'' Acust. Acta Acust. **85**, 78–87.

Jessel, M. (**1973**). *Acoustique Théorique: Propagation et Holophonie (Theoretical Acoustics: Propagation and Holophony*) (Masson et Cie, Paris).

Kinsler, L. E., Frey, A. R., Coppens, A. B., and Sanders, J. V. (**2000**). *Fundamentals of Acoustics* (Wiley, New York).

Kirkeby, O., and Nelson, P. A. (**1993**). ''Reproduction of plane wave sound fields,'' J. Acoust. Soc. Am. **94**, 2992–3000.

Kirkeby, O., Nelson, P. A., and Hamada, H. (**1998**). ''The stereo-dipole—A virtual source imaging system using two closely spaced loudspeakers,'' J. Audio Eng. Soc. **46**, 387–395.

Kirkeby, O., Nelson, P. A., Orduña-Bustamante, F., and Hamada, H. (**1996**). ''Local sound field reproduction using digital signal processing,'' J. Acoust. Soc. Am. **100**, 1584–1593.

Morse, P. M., and Ingard, K. U. (**1968**). *Theoretical Acoustics* (McGraw-Hill, New York).

Nelson, P. A. (**1994**). ''Active control of acoustic fields and the reproduction of sound,'' J. Sound Vib. **177**, 447–477.

Nelson, P. A. (**2001**). ''A review of some inverse problems in acoustics,'' Int. J. Acous. Vib. **6**, 118–134.

Nelson, P. A. (**2002**). ''Active control for virtual acoustics,'' Proc. of Active 2002, pp. 67–89.

Nelson, P. A., and Elliott, S. J. (**1992**). *Active Control of Sound* (Academic, London).

Nelson, P. A., and Yoon, S. H. (**2000**). ''Estimation of acoustic source strength by inverse methods. I. Conditioning of the inverse problem,'' J. Sound Vib. **233**, 643–668.

Nelson, P. A., Hamada, H., and Elliott, S. J. (**1992**). ''Adaptive inverse filters for stereophonic sound reproduction,'' IEEE Trans. Signal Process. **40**, 1621–1632.

Nelson, P. A., Orduña-Bustamante, F., and Hamada, H. (**1995**). ''Inverse filter design and equalization zones in multichannel sound reproduction,'' IEEE Trans. Speech Audio Process. **3**, 185–192.

Nelson, P. A., Orduña-Bustamante, F., and Hamada, H. (**1996**). ''Multichannel signal processing techniques in the reproduction of sound,'' J. Audio Eng. Soc. **44**, 973–989.

Nelson, P. A., Kirkeby, O., Takeuchi, T., and Hamada, H. (**1997**). ''Sound fields for the reproduction of virtual acoustic images,'' J. Sound Vib. **204**, 386–396.

Nicol, R., and Emerit, M. (**1999**). ''3D-sound reproduction over an extensive listening area: A hybrid method derived from holophony and ambisonic,'' Proc. of the Audio Eng. Soc. 16th Int. Conf., pp. 436–453.

Pierce, A. D. (**1991**). *Acoustics: An Introduction to its Physical Principles*

and Applications (Acoustical Society of America, Woodbury, NY).
Rumsey, F. (**2001**). *Spatial Audio* (Focal, Oxford).
Spors, S., Kuntz, A., and Rabenstein, R. (**2003**). ''An approach to listening room compensation with wave field synthesis,'' Proc. of the AES 24th International Conference, pp. 70–82.
Takeuchi, T., and Nelson, P. A. (**2002**). ''Optimal source distribution for binaural synthesis over loudspeakers,'' J. Acoust. Soc. Am. **112**, 2786–2797.
Tokuno, H., Kirkeby, O., Nelson, P. A., and Hamada, H. (**1997**). ''Inverse filter of sound reproduction sytems using regularization,'' IEICE Trans. Fundamen. Electron. Commun. Comput. Sci. **80**, 809–820.
Uto, S., and Hamada, H. (**1995**). ''Transform domain adaptive audio equalizer for active control of sound field,'' Proc. of Active 95, pp. 1241–1246.
Verheijen, E. N. G. (**1997**). *Sound Reproduction by Wave Field Synthesis*, Ph.D. thesis (Delft University of Technology, Delft).
de Vries, D., and Boone, M. M. (**2003**). ''Experience with a wave field synthesis system based on multi-actuator panel loudspeakers,'' Proc. of the AES 24th International Conference, p. 29 (abstract only).
Ward, D. B., and Elko, G. W. (**1999**). ''Effect of loudspeaker position on the robustness of acoustic crosstalk cancellation,'' IEEE Signal Process. Lett. **6**, 106–108.
Watanabe, Y., Tokuno, H., Hamada, H., and Nelson, P. A. (**1999**). ''Sound reproduction for telecommunication system using auditory cues in virtual acoustic environment,'' Proc. of Active 99, pp. 1293–1304.
Wilson, S. (**2001**). *Information Arts: Intersection of Art, Science, and Technology* (MIT Press, Cambridge).

Mathematical model for characterizing noise transmission into finite cylindrical structures

Deyu Li and Jeffrey S. Vipperman[a)]
Department of Mechanical Engineering, 648 Benedum Hall, 3700 O'Hara Street, University of Pittsburgh, Pittsburgh, Pennsylvania 15261

(Received 23 May 2004; revised 8 October 2004; accepted 8 October 2004)

This work presents a theoretical study of the sound transmission into a finite cylinder under coupled structural and acoustic vibration. Particular attention of this study is focused on evaluating a dimensionless quantity, ''noise reduction,'' for characterizing noise transmission into a small cylindrical enclosure. An analytical expression of the exterior sound pressure resulting from an oblique plane wave impinging upon the cylindrical shell is first presented, which is approximated from the exterior sound pressure for an infinite cylindrical structure. Next, the analytical solution of the interior sound pressure is computed using modal-interaction theory for the coupled structural acoustic system. These results are then used to derive the analytical formula for the noise reduction. Finally, the model is used to predict and characterize the sound transmission into a ChamberCore cylindrical structure, and the results are compared with experimental data. The effects of incidence angle and internal acoustic damping on the sound transmission into the cylinder are also parametrically studied. [DOI: 10.1121/1.1828652]

PACS numbers: 43.40.Ey, 43.40.Fz, 43.20.Fn, 43.20.Ks [JGM] Pages: 679–689

I. INTRODUCTION

Thin composite cylindrical structures play an important role in the aerospace industry due to their lighter weight, higher strength, and larger stiffness when compared to their aluminum or steel counterparts.[1–5] Unfortunately, the noise transmission into such cylindrical enclosures is worse because of the light nature of composites.[1–4] As part of a noise transmission study for composite structures, a theoretical model to characterize the noise transmission into finite thin-wall cylindrical structures is developed.[1]

The problem of sound transmission through infinite, homogeneous, isotropic thin cylindrical structures has been investigated in some detail by several researchers. Tang *et al.* studied an infinite cylindrical sandwich shell with honeycomb core.[6,7] A simplified analysis of sound transmission through a finite, closed cylindrical shell was first proposed by White,[8] while the sound radiation into the acoustic cavity enclosed by a finite cylindrical shell with end plates was studied by Cheng.[9] Tso and Hansen derived a coupling loss factor for a cylindrical/plate structure using statistical energy analysis.[10] Their method, however, does not work well at low frequencies and further could not show the effects on sound transmission of the cavity resonances. Koval first presented a mathematical ''noise reduction'' (NR) model to account for the effects of cavity resonances on sound transmission into a thin cylindrical shell.[11] In his model, the axial modes of the cylindrical cavity are neglected, because both the cylindrical shell and the internal acoustic cavity are considered to be infinite in length. Actually, both structural and acoustic axial modes of a finite cylindrical structure are experimentally found to be very important modes for noise control in low frequencies.[1,4,12] Gardonio, Ferguson, and Fahy presented an expression of NR to characterize unit amplitude external incident sound transmission through a finite cylindrical shell.[13] However, the external sound pressure in their definition is considered to equate the incident, unit amplitude sound, and the effects of scattering sound from the cylindrical shell on the external sound field are ignored. Estève and Johnson included axial acoustic modes in a cylindrical model that predicted the performance of passive control schemes through the prediction of acoustic potential energy.[14]

This work presents a theoretical study of the sound transmission into a finite cylinder under coupled structural and acoustic vibration. The proposed model includes internal acoustic axial modes. Particular attention of this study is focused on evaluating a dimensionless quantity, noise reduction, for characterizing noise transmission into a small cylindrical enclosure. The paper is arranged as the follows. Section II presents the theoretical developments, which include analytical expressions of exterior and interior sound pressure for the finite cylindrical structure and the revisions to the definition of noise reduction. In Sec. III a numerical simulation for characterizing noise transmission into a ChamberCore cylinder is performed, which is accompanied by a comparison of analytical and experimental results. Some conclusions are given in the final section.

II. THEORY

The physics of the problem under study is described as follows: (1) an incident sound wave impinges upon the surface of a finite, cylindrical structure causing vibration of the shell; (2) the shell vibration induces sound-pressure fluctuations including scattering and radiation pressures; (3) the radiated pressure to the interior excites vibration of the air inside the cylinder; and (4) the noise of the interior cavity in turn interacts with the structure to affect the structural vibration and creates the coupled vibration. The purpose of this

a)Author to whom correspondence should be addressed.

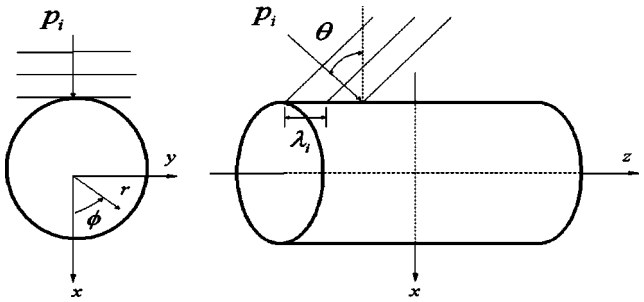

FIG. 1. Geometry and incident wave of an infinite cylindrical structure.

section is to find an analytical solution to describe the exterior and interior sound pressure of the cylinder under sound wave incident.

The calculation of exterior pressure over the outside shell is a near-field problem, which is difficult to analytically solve for a finite, elastic, cylindrical shell.[15] In this study, the near-field pressure of an infinite elastic cylindrical shell is used to approximate that of the finite one. The internal sound-pressure field is solved by means of the coupled structural and acoustic vibration under the input of the solved external pressure.[13,16–18] In order to simplify analysis, the impinging wave is selected to be an oblique plane wave, and time-dependent variables are assumed to be harmonic. The solutions of external and internal pressures are presented in the following sections.

A. Exterior pressure of an infinite elastic cylindrical shell

The specific problem studied is shown in Fig. 1. Consider an oblique plane wave impinging upon an infinite thin cylindrical shell approaching from the radial plane ($\phi=\pi$). The density of the fluid and the speeds of sound are ρ_1, c_1, and ρ_2, c_2, in the external and internal media, respectively. In the analysis of exterior pressure field, all waves will be assumed to have the same dependence on the axial coordinate z.

The incident plane sound wave can be represented as

$$p_i(x,z,t)=P_i e^{j(\omega t-k_{1x}x-k_{1z}z)}, \tag{1}$$

where P_i is the amplitude of incident sound pressure, k_{1x} and k_{1z} are the x component and z component of the wave number, respectively, and are computed from

$$\begin{cases} k_{1x}=k_1\cos\theta \\ k_{1z}=k_1\sin\theta, \end{cases} \tag{2}$$

where $k_1=\omega/c_1$ is the wave number in the external fluid medium, and θ is the incident angle. The expansion of Eq. (1) into a cylindrical coordinate system gives[11,15,19]

$$p_i(x,z,t)=P_i e^{j(\omega t-k_{1z}z)}\sum_{m=0}^{\infty}\varepsilon_m(-j)^m J_m(k_{1r}r)\cos m\phi, \tag{3}$$

where J_m is the Bessel function of the first kind of integer order m, $k_{1r}=k_{1x}$ the radial component of the wave number, and ε_m the Neumann factor given by

$$\varepsilon_m=\begin{cases} 1 & (m=0) \\ 2 & (m\geqslant 1) \end{cases}. \tag{4}$$

The total exterior sound-pressure field of the infinite cylindrical structure can be written as

$$p_{ext}=p_i+p_{se}, \tag{5}$$

where p_{ext} is the exterior pressure, p_i the incident pressure, p_{se} the scattered pressure by the elastic shell, which contains two parts

$$p_{se}=p_{s\infty}+p_{re}, \tag{6}$$

where $p_{s\infty}$ is the scattered pressure by a rigid cylinder with infinite acoustic impedance, and p_{re} is the pressure radiated by an elastic cylindrical shell. The general result of sound radiation from a vibrating structure is presented in the next section.

B. Radiation of a vibrating cylindrical shell

Assuming that an elastic cylindrical shell is vibrating with a surface-harmonic acceleration distribution $\ddot{w}(r=a,\phi,z,t)$, which can be expanded into a Fourier series as[11,15,19]

$$\ddot{w}(r=a,\phi,z,t)=e^{-jk_{1z}z}\sum_{m=0}^{\infty}\ddot{W}_m(t)\cos(m\phi), \tag{7}$$

where a is the radius of the midsurface, k_{1z} the z components of the wave number given by Eq. (2), and $\ddot{W}_m(t)$ the time-dependent part of the acceleration. Only the configuration in even ϕ is considered in Eq. (7). If the ϕ axis cannot be oriented to be consistent with this configuration, then a sine series is required using the same procedure presented here.

In a linear sound field without loss, the pressure (p) and the particle velocity ($\overline{u}$) satisfy wave equation[15]

$$\overline{\nabla}p=-\rho\frac{\partial\overline{u}}{\partial t}. \tag{8}$$

The boundary condition where the fluid meets the structure is governed in the normal direction by

$$\left.\frac{\partial p(r,\phi,z,t)}{\partial r}\right|_{r=a}=-\rho\ddot{w}(r=a,\phi,z,t), \tag{9}$$

where $\ddot{w}(r=a,\phi,z,t)$ is the fluid particle acceleration of the boundary. Note that the fluid particle vibration uses the same symbol as the shell vibration because it equates the shell vibration at structure–fluid boundaries. In order to satisfy the boundary condition, the radiation pressure field is therefore expressed as the series[11,15]

$$p_r(r,\phi,z,t)=e^{-jk_{1z}z}\sum_{m=0}^{\infty}P_m(t)H_m^{(2)}(k_{1r}r)\cos(m\phi), \tag{10}$$

where $H_m^{(2)}$ is a Hankel function of the second kind of m order. Substituting Eqs. (10) and (7) into (9), the coefficients $P_m(t)$ are solved from

$$P_m(t) = -\frac{\rho_1 \ddot{W}_m(t)}{k_{1r} H_m^{(2)'}(k_{1r}a)}, \tag{11}$$

where $(\ )'$ denotes the spatial derivative. The radiation pressure field is thus found to be

$$p_r(r,\phi,z,t) = -e^{-jk_{1z}z}\frac{\rho_1}{k_{1r}}\sum_{m=0}^{\infty}\frac{\ddot{W}_m(t)}{H_m^{(2)'}(k_{1r}a)} \times H_m^{(2)}(k_{1r}r)\cos(m\phi). \tag{12}$$

Because $W_m(t)$ is time harmonic, the surface pressure obtained from Eq. (12) can be written in terms of modal-specific acoustic impedance, z_m, as[15]

$$p_r(r=a,\phi,z,t) = e^{-jk_{1z}z}\sum_{m=0}^{\infty}\dot{W}_m(t) z_m \cos(m\phi), \tag{13}$$

where

$$\dot{W}_m(t) = -\frac{j\ddot{W}_m(t)}{\omega}, \tag{14}$$

$$z_m = -\frac{j\omega\rho_1 H_m^{(2)}(k_{1r}a)}{k_{1r} H_m^{(2)'}(k_{1r}a)}. \tag{15}$$

The scattered pressure from an infinite rigid and elastic cylindrical shell is solved in the next two sections using the results of this subsection.

C. Scattering from an infinite rigid cylindrical shell

When the boundary is rigid and there is no loss of air, the resultant particle acceleration at the boundary must have a zero component along the normal direction to the boundary

$$\ddot{w}_{s\infty}(r=a,\phi,z,t) + \ddot{w}_i(r=a,\phi,z,t) = 0, \tag{16}$$

where $\ddot{w}_{s\infty}(r=a,\phi,z,t)$ is the scattered fluid particle acceleration at boundary $(r=a)$, which is equal to the normal rigid surface acceleration, and $\ddot{w}_i(r=a,\phi,z,t)$ the normal incident fluid particle acceleration at the boundary, which is given by wave equation (8) or boundary condition Eq. (9)

$$\ddot{w}_i(r=a,\phi,z,t) = -\frac{1}{\rho_1}\left.\frac{\partial p_i(r,\phi,z,t)}{\partial r}\right|_{r=a}. \tag{17}$$

Combining Eqs. (3), (16), and (17), the rigid surface acceleration is obtained as

$$\ddot{w}_{s\infty}(r=a,\phi,z,t) = P_i(t)e^{-jk_{1z}z}\frac{k_{1r}}{\rho_1}\sum_{m=0}^{\infty}\varepsilon_m(-j)^m J_m'(k_{1r}a)\cos m\phi, \tag{18}$$

where ε_m is the Neumann factor given by Eq. (4). Comparing Eq. (18) with Eq. (7), the coefficient $\ddot{W}_{s\infty,m}(t)$ is solved for

$$\ddot{W}_{s\infty,m}(t) = P_i(t)\frac{k_{1r}}{\rho_1}\varepsilon_m(-j)^m J_m'(k_{1r}a). \tag{19}$$

Substituting Eq. (19) into Eq. (12), the scattered pressure from an infinite rigid cylindrical shell is obtained as

$$p_{s\infty}(r,\phi,z,t) = P_i(t)e^{-jk_{1z}z}\sum_{m=0}^{\infty}\varepsilon_m(-j)^m A_m \times H_m^{(2)}(k_{1r}r)\cos(m\phi), \tag{20}$$

where

$$A_m = -\frac{J_m'(k_{1r}a)}{H_m^{(2)'}(k_{1r}a)}. \tag{21}$$

The resultant pressure on the cylindrical surface required by analyzing the scattering action of elastic cylindrical shells is the sum of the incident and scattered waves of the rigid cylinder $(p = p_i + p_{s\infty})$. Considering the following relation:[1]

$$J_m(x)H_m^{(2)'}(x) - J_m'(x)H_m^{(2)}(x) = -j\frac{2}{\pi x}, \tag{22}$$

the resultant pressure is calculated from

$$p(r=a,\phi,z,t) = \frac{2P_i(t)}{\pi a k_{1r}}e^{-jk_{1z}z}\sum_{m=0}^{\infty}\varepsilon_m(-j)^{m+1}\frac{1}{H_m^{(2)'}(k_{1r}a)}\cos(m\phi). \tag{23}$$

D. Scattering from an infinite elastic cylindrical shell

The normal response of the elastic cylindrical shell under the influence of $(p = p_i + p_{s\infty})$ can be expressed in terms of modal mechanical and acoustic impedance as[15]

$$\dot{w}(r=a,\phi,z,t) = e^{-jk_{1z}z}\sum_{m=0}^{\infty}\frac{P_m(t)}{z_m + Z_m}\cos(m\phi), \tag{24}$$

where $P_m(t)$ can be obtained from Eq. (23) as

$$P_m(t) = \frac{2P_i(t)}{\pi a k_{1r} H_m^{(2)'}(k_{1r}a)}\varepsilon_m(-j)^{m+1}, \tag{25}$$

and z_m is the modal-specific acoustic impedance, and can be obtained from Eq. (15), Z_m is the modal mechanical impedance, and can be determined from Donnell–Mushtari equations with Flügge modifying constants[20] under the absence of fluid loading inside cylinder, which leads to the expression in the form[15]

$$Z_m = j\frac{c_p\rho_s h}{a}\frac{[\Omega^2 - (\Omega_m^{(1)})^2][\Omega^2 - (\Omega_m^{(2)})^2]}{\Omega(\Omega^2 - m^2)}, \tag{26}$$

where ρ_s is the volume density of the shell material, $c_p = \sqrt{E/\rho_p(1-\mu^2)}$ is the speed of sound propagating in the shell, a is the radius of midsurface, h is the thickness of the shell, $\Omega = \omega a/c_p$ is a dimensionless frequency parameter, $\Omega_m^{(1)}$, and $\Omega_m^{(2)}$ are the resonance frequencies of a thin cylindrical shell without axial components of displacement, and they are defined as[15]

$$\Omega_m^{(1)} = \tfrac{1}{2}[1 + m^2 + \beta m^4 - \sqrt{(1+m^2+\beta m^4)^2 - 4\beta m^6}], \tag{27}$$

$$\Omega_m^{(2)} = \tfrac{1}{2}[1 + m^2 + \beta m^4 + \sqrt{(1+m^2+\beta m^4)^2 - 4\beta m^6}], \tag{28}$$

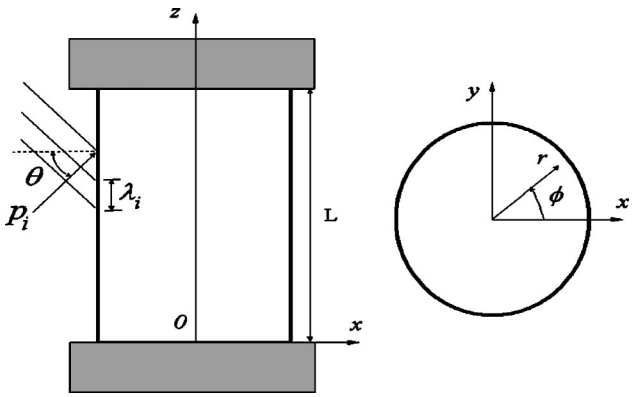

FIG. 2. Geometry and incident wave of a finite cylindrical structure.

where $\beta = h^2/12a^2$ is a dimensionless constant.

The coefficients of the surface-harmonic acceleration distribution can be obtained from Eq. (24)

$$\ddot{W}_m(t) = \frac{j\omega P_m(t)}{z_m + Z_m}. \tag{29}$$

Substituting Eq. (29) into Eq. (12), the radiation pressure from the infinite elastic cylindrical shell is

$$p_{re}(r,\phi,z,t) = P_i(t)e^{-jk_{1z}z}\sum_{m=0}^{\infty}\varepsilon_m(-j)^m B_m \times H_m^{(2)}(k_{1r}r)\cos(m\phi), \tag{30}$$

where

$$B_m = -\frac{2\rho_1\omega}{\pi a k_{1r}^2 (z_m + Z_m)[H_m^{(2)'}(k_{1r}a)]^2}. \tag{31}$$

Finally, the external pressure of the infinite elastic cylindrical shell is computed from

$$p_{ext}(r,\phi,z,t) = p_i(r,\phi,z,t) + p_{s\infty}(r,\phi,z,t) + p_{re}(r,\phi,z,t). \tag{32}$$

Substituting Eqs. (3), (20), and (30) into Eq. (32) yields

$$p_{ext}(r,\phi,z,t) = P_i(t)e^{-jk_{1z}z}\sum_{m=0}^{\infty}\varepsilon_m(-j)^m[J_m(k_{1r}r) + C_m H_m^{(2)}(k_{1r}r)]\cos(m\phi), \tag{33}$$

where $C_m = A_m + B_m$, and A_m and B_m are given by Eqs. (21) and (31), respectively.

When the incident pressure is time harmonic, i.e. $P_i(t) = P_i e^{j\omega t}$, the external pressure over the infinite flexible cylindrical shell is

$$p_{ext}(r=a,\phi,z,t) = P_i e^{j\omega t - jk_{1z}z}\sum_{m=0}^{\infty}\varepsilon_m(-j)^m[J_m(k_{1r}a) + C_m H_m^{(2)}(k_{1r}a)]\cos(m\phi), \tag{34}$$

where P_i is the magnitude of incident pressure. This concludes the derivation for the external pressure field.

E. Interior pressure of a finite elastic cylindrical shell

It is assumed that the end caps of the finite cylindrical structure are rigid, so that only the radial motion of the cylindrical shell excites the acoustic cavity (see Fig. 2). The modal-interaction approach[13,16–18] is used to calculate the sound pressure inside the cavity under the excitation of external pressure which is approximated by the one obtained from the infinite cylindrical shell [see Eq. (34)]. Only the even ϕ configuration is considered. Note that either odd [$\sin(m\phi)$ modes] or even [$\cos(m\phi)$ modes] can be chosen, since the $\phi = 0$ deg direction is arbitrary.

For a simply supported cylindrical structure without axial constraint, the harmonic radial displacement of the shell, subject to external pressure excitation, is described as a linear combination of the *in vacuo* normal modes as

$$w(r=a,\phi,z,t) = \sum_{o=0}^{\infty}\sum_{q=1}^{\infty} W_{oq}(t)\Phi_{oq}(\phi,z), \tag{35}$$

where o is the number of circumferential waves in the structural mode shapes, and q is the number of longitudinal half-waves in the structural mode shapes. The *in vacuo* structural normal mode shapes can be written as[21]

$$\Phi_{oq}(\phi,z) = \cos(o\phi)\sin\left(q\frac{\pi}{L}z\right), \tag{36}$$

where L is the length of the finite cylindrical shell. The natural frequencies for simply supported closed thin shells can be obtained from Leissa's book.[21]

The modal equation for the structure can then be derived by taking advantage of the orthogonal properties of the mode shapes as[16]

$$\ddot{W}_{oq}(t) + 2\xi_{oq}^s\omega_{oq}^s\dot{W}_{oq}(t) + (\omega_{oq}^s)^2 W_{oq}(t) = \frac{S}{\mathrm{M}_{oq}}\sum_{l,m,n=0}^{\infty} P_{lmn}(t)D_{oq,lmn} + \frac{p_{oq}(t)}{\mathrm{M}_{oq}}, \tag{37}$$

where the superscript s denotes "structure." In the right-hand side of Eq. (37), the first term is the cavity fluid loading, and the second term is the external distributed input, where M_{oq} is modal mass of the structure, $D_{oq,lmn}$ is the dimensionless structural–acoustic coupling coefficient, $p_{oq}(t)$ is the modal force from the external pressure field, $P_{lmn}(t)$ is the time-dependent portion of the interior pressure, l, m, and n are the number of radial nodes, diametric nodes, and longitudinal nodes in acoustic cavity mode shapes, respectively, and $S = 2\pi aL$ is the area of the midsurface of the cylindrical shell. M_{oq}, $D_{oq,lmn}$, and $p_{oq}(t)$ are given by the following equations, respectively:

$$\mathrm{M}_{oq} = \int_S m_s\Phi_{oq}^2(\phi,z)dS, \tag{38}$$

$$D_{oq,lmn} = \frac{1}{S}\int_S \Phi_{oq}(\phi,z)\Psi_{lmn}(r=a,\phi,z)dS, \tag{39}$$

$$p_{oq}(t) = \int_S p_{ext}(r=a,\phi,z,t)\Phi_{oq}(\phi,z)dS = P_i e^{j\omega t}E_{oq}, \tag{40}$$

where the structural mode shapes Φ_{oq} are given by Eq. (36), Ψ_{lmn} are the acoustic mode shapes, which are defined by Eq. (46), and the pressure p_{ext} is given by Eq. (34). For a uniform cylindrical shell with surface density m_s, coefficients M_{oq}, $D_{oq,lmn}$, and E_{op} become

$$\mathrm{M}_{oq}=\frac{1}{\varepsilon_o}m_s L a\pi, \tag{41}$$

$$D_{oq,lmn}=\begin{cases}\dfrac{aL}{S\varepsilon_m}J_m(k_{lm}a)\left[\dfrac{1-\cos(q+n)\pi}{q+n}+\dfrac{1-\cos(q-n)\pi}{q-n}\right], & (o=m \quad \text{and} \quad q\neq n)\\ 0, \quad \text{otherwise}\end{cases}, \tag{42}$$

$$E_{oq}=\begin{cases}(-j)^{o+1}aL\pi[J_o(k_{1r}a)+C_oH_o^{(2)}(k_{1r}a)], & \left(k_{1z}=q\dfrac{\pi}{L}\right)\\ (-j)^{o}aL\pi[J_o(k_{1r}a)+C_oH_o^{(2)}(k_{1r}a)]\left\{\left[\dfrac{-\cos(k_{1z}L+q\pi)+1}{k_{1z}L+q\pi}+\dfrac{\cos(k_{1z}L-q\pi)-1}{k_{1z}L-q\pi}\right]\right. & \\ \left.\quad +j\left[\dfrac{\sin(k_{1z}L+q\pi)}{k_{1z}L+q\pi}-\dfrac{\sin(k_{1z}L-q\pi)}{k_{1z}L-q\pi}\right]\right\}, & \text{otherwise}\end{cases} \tag{43}$$

where ε_o and ε_m are the Neumann factor given by Eq. (4).

If the cavity fluid loading is neglected, Eq. (37) becomes

$$\ddot{W}_{oq}(t)+2\xi_{oq}^s\omega_{oq}^s\dot{W}_{oq}(t)+(\omega_{oq}^s)^2W_{oq}(t)=\frac{P_iE_{oq}}{\mathrm{M}_{oq}}e^{j\omega t}. \tag{44}$$

The effects on the noise transmission into the cylinder due to ignoring cavity fluid loading will be discussed in Sec. III through comparing analytical and experimental results. Next, the cylindrical cavity acoustic effects induced by the elastic shell vibration are studied. The acoustic pressure in the cavity can be expressed as a linear combination of the rigid-wall acoustic cavity modes

$$p(r,\phi,z,t)=\sum_{l,m,n=0}^{\infty}P_{lmn}(t)\Psi_{lmn}(r,\phi,z). \tag{45}$$

The cylindrical acoustic cavity mode shapes are[21]

$$\Psi_{lmn}(r,\phi,z)=J_m(k_{lm}r)\cos(m\phi)\cos\left(n\frac{\pi}{L}z\right). \tag{46}$$

Note that l, m, and n cannot be zero at the same time, because the static pressure mode (0,0,0) is not considered in this study. k_{lm} is solved from $J'_{lm}(k_{lm}r)|_{r=a}=0$, and the acoustic natural frequencies are obtained from $\omega_{lmn}^f=c_2\sqrt{k_{lm}^2+(n\pi/L)^2}$, where the superscript f denotes "fluid."

Invoking the orthogonality condition for mode shapes and considering the damping term, the modal equation for the acoustic system is written as[16]

$$\ddot{P}_{lmn}(t)+2\xi_{lmn}^f\omega_{lmn}^f\dot{P}_{lmn}(t)+(\omega_{lmn}^f)^2P_{lmn}(t)=-\frac{\rho_2c_2^2S}{V_{lmn}}\sum_{o=0,q=1}^{\infty}\ddot{W}_{oq}(t)D_{oq,lmn}, \tag{47}$$

where V_{lmn} is the modal volume, and is calculated by

$$V_{lmn}=\int_V\Psi_{lmn}^2(r,\phi,z)dV, \tag{48}$$

where V is the acoustic cavity volume. For a cylindrical cavity with length L and midsurface radius a, the modal volume is computed from

$$V_{lmn}=\begin{cases}\dfrac{\pi a^2L}{2}, & l=m=0, n\in[1,\infty)\\ \dfrac{\pi a^2L}{\varepsilon_m\varepsilon_n}\left\{[J'_m(k_{lm}a)]^2+\left[1-\left(\dfrac{m}{k_{lm}a}\right)^2\right][J_m(k_{lm}a)]^2\right\}, & \text{otherwise}\end{cases}. \tag{49}$$

Because all time-dependent variables are assumed to be time harmonic, the displacement and pressure are expressed as $W_{oq}(t)=W_{oq}e^{j\omega t}$ and $P_{lmn}(t)=P_{lmn}e^{j\omega t}$. Solving Eqs. (44) and (47) for the modal pressure distribution, $P_{lmn}(t)$, yields

$$P_{lmn}(t)=P_ie^{j\omega t}\frac{F_{lmn}(\omega)}{[-\omega^2+j2\xi_{lmn}^f\omega_{lmn}^f\omega+(\omega_{lmn}^f)^2]V_{lmn}}, \tag{50}$$

where

$$F_{lmn}(\omega)=\rho_2 c_2^2 S \times \sum_{o=0,q=1}^{\infty}\left[\frac{E_{oq}D_{oq,lmn}}{\left\{\left[\left(\frac{\omega_{oq}^s}{\omega}\right)^2-1\right]+j2\xi_{oq}^s\frac{\omega_{oq}^s}{\omega}\right\}\mathrm{M}_{oq}}\right]. \tag{51}$$

Substituting Eq. (50) into Eq. (45), the internal pressure field is

$$p_{int}(r,\phi,z,t)=P_i e^{j\omega t}\sum_{l,m,n=0}^{\infty}\frac{F_{lmn}(\omega)}{[-\omega^2+j2\xi_{lmn}^f\omega_{lmn}^f\omega+(\omega_{lmn}^f)^2]V_{lmn}}\times\Psi_{lmn}(r,\phi,z). \tag{52}$$

The structural damping ξ^s and fluid medium damping ξ^f in Eq. (52) are determined by experimental modal identification.[1]

In order to derive an analytical solution for the noise reduction of the finite cylindrical structure, the modal pressure (P_{lmn}) is re-expressed as[1]

$$P_{lmn}(t)=P_i e^{j\omega t}(G_{lmn}^R+jG_{lmn}^I), \tag{53}$$

where G_{lmn}^R and G_{lmn}^I are the real part and imaginary part of $(F_{lmn}(\omega)/[-\omega^2+j2\xi_{lmn}^f\omega_{lmn}^f\omega+(\omega_{lmn}^f)^2]V_{lmn})$, respectively.[1] Then, the internal pressure field is rewritten as

$$p_{int}(r,\phi,z,t)=P_i e^{j\omega t}\sum_{l,m,n=0}^{\infty}(G_{lmn}^R+jG_{lmn}^I)\Psi_{lmn}(r,\phi,z). \tag{54}$$

Equations (34) and (54) are used in the calculation of noise reduction in the next section.

F. Noise reduction

The definition of transmission loss (TL) for an infinite flat panel assumes that the transmitted sound is totally absorbed, and only inward-propagating waves exist. However, the problem under consideration differs from the infinite flat panel, not only because of its finite dimension, but also because of the effects of internal acoustic cavity resonances in the closed cylindrical shell. Hence, it is not possible to define a transmission loss as is done for flat panels. For measurement of the sound transmission through cylindrical shells, Holmer and Heymann[22] defined the sound power transmission coefficient to be equal to the ratio of power radiated per unit surface area of the shell to the power passing axially through a unit area of cross section. In other references,[11,13,23–25] researchers suggested using the noise reduction instead of calculating TL, which was equal to the ratio of the outer time- and surface-averaged mean-square pressure and inner time- and volume-averaged mean-square pressure. In this study, the revised noise reduction for characterizing broadband sound transmission into a finite cylindrical structure is defined (where the external) surface-averaged mean-square pressure is used

$$\mathrm{NR}=-\log_{10}\frac{\langle p_{int}^2(r,\phi,z,t)\rangle}{\langle p_{ext}^2(r,\phi,z,t)\rangle}, \tag{55}$$

where $\langle p^2(r,\phi,z,t)\rangle$ is the mean-square pressure of $p(r,\phi,z,t)$ averaged over the midsurface area S, and a time period, T. It is defined as

$$\langle p^2(r,\phi,z,t)\rangle=\frac{1}{ST}\int_S\int_T p(r,\phi,z,t)p^*(r,\phi,z,t)dt\,dS, \tag{56}$$

where $(\,)^*$ denotes the complex conjugate. For a cylindrical shell, the expression of dS in Eq. (56) is $dS=r\,d\phi\,dz$, and the averaged mean-square external pressure is calculated from

$$\langle p_{ext}^2(r,\phi,z,t)\rangle=P_i^2\Pi(\omega), \tag{57}$$

$$\Pi(\omega)=\sum_{m=0}^{\infty}\varepsilon_m|J_m(k_{1r}a)+C_m H_m^{(2)}(k_{1r}a)|^2. \tag{58}$$

The averaged mean-square internal pressure is calculated from

$$\langle p_{int}^2(r,\phi,z,t)\rangle=\frac{1}{S}P_i^2\int_S\left\{\underbrace{\sum_{l,m,n=0}^{\infty}[(G_{lmn}^R)^2+(G_{lmn}^I)^2]\Psi_{lmn}^2}_{\text{term 1}}+\underbrace{\sum_{o=0,o\neq l}^{\infty}\sum_{l,m,n=0}^{\infty}(G_{lmn}^R G_{omn}^R+G_{lmn}^I G_{omn}^I)\Psi_{lmn}\Psi_{omn}}_{\text{term 2}}\right\}r\,d\phi\,dz. \tag{59}$$

The integration of the "term 1" in Eq. (59) over the midsurface yields

$$\int_S\sum_{l,m,n=0}^{\infty}[(G_{lmn}^R)^2+(G_{lmn}^I)^2]\Psi_{lmn}^2 r\,d\phi\,dz=aL\pi\sum_{n=1}^{\infty}[(G_{00n}^R)^2+(G_{00n}^I)^2]+aL\pi\sum_{l=0,m=1,n=0}^{\infty}\frac{1}{\varepsilon_n}[(G_{lmn}^R)^2+(G_{lmn}^I)^2]J_m^2(k_{lm}a)+2aL\pi\sum_{l=1,m=0,n=0}^{\infty}\frac{1}{\varepsilon_m\varepsilon_n}[(G_{lmn}^R)^2+(G_{lmn}^I)^2]J_m^2(k_{lm}a). \tag{60}$$

The integration of the "term 2" in Eq. (59) over the midsurface yields

$$\int_S \sum_{\substack{l,m,n,o=0 \\ o\neq l}}^{\infty} (G^R_{lmn}G^R_{omn}+G^I_{lmn}G^I_{omn})\Psi_{lmn}\Psi_{omn}r\,d\phi\,dz$$

$$= aL\pi \sum_{n,o=1}^{\infty} (G^R_{00n}G^R_{o0n}+G^I_{00n}G^I_{o0n})J_m(k_{om}a) + aL\pi \sum_{o=0,o\neq l}^{\infty}\ \sum_{l=0,m=1,n=0}^{\infty} \frac{1}{\varepsilon_n}(G^R_{lmn}G^R_{omn}+G^I_{lmn}G^I_{omn})$$

$$\times J_m(k_{lm}a)J_m(k_{om}a) + 2aL\pi \sum_{o=0,o\neq l}^{\infty}\ \sum_{l=1,m=0,n=0}^{\infty} \frac{1}{\varepsilon_m\varepsilon_n}(G^R_{lmn}G^R_{omn}+G^I_{lmn}G^I_{omn})J_m(k_{lm}a)J_m(k_{om}a). \quad (61)$$

Substituting Eqs. (60) and (61) and $S=2\pi aL$ into (59) yields

$$\langle p^2_{int}(r,\phi,z,t)\rangle = P_i^2\Theta(\omega), \quad (62)$$

where

$$\Theta(\omega) = \frac{1}{2}\sum_{n=1}^{\infty}[(G^R_{00n})^2+(G^I_{00n})^2] + \frac{1}{2}\sum_{l=0,m=1,n=0}^{\infty}\frac{1}{\varepsilon_n}[(G^R_{lmn})^2+(G^I_{lmn})^2]J^2_m(k_{lm}a) + \sum_{l=1,m=0,n=0}^{\infty}\frac{1}{\varepsilon_m\varepsilon_n}[(G^R_{lmn})^2$$

$$+(G^I_{lmn})^2]J^2_m(k_{lm}a) + \frac{1}{2}\sum_{n,o=1}^{\infty}(G^R_{00n}G^R_{o0n}+G^I_{00n}G^I_{o0n})J_m(k_{om}a) + \frac{1}{2}\sum_{o=0,o\neq l}^{\infty}\ \sum_{l=0,m=1,n=0}^{\infty}\frac{1}{\varepsilon_n}(G^R_{lmn}G^R_{omn}$$

$$+G^I_{lmn}G^I_{omn})J_m(k_{lm}a)J_m(k_{om}a) + \sum_{o=0,o\neq l}^{\infty}\ \sum_{l=1,m=0,n=0}^{\infty}\frac{1}{\varepsilon_m\varepsilon_n}(G^R_{lmn}G^R_{omn}+G^I_{lmn}G^I_{omn})J_m(k_{lm}a)J_m(k_{om}a). \quad (63)$$

Substituting Eqs. (57) and (62) into Eq. (55), the analytical formula for the calculation of noise reduction is obtained as

$$\mathrm{NR} = -10\log_{10}\frac{\Theta(\omega)}{\Pi(\omega)}. \quad (64)$$

The NR into a cylindrical structure under a plane wave impinging with an incident angle, θ, is only a function of frequency since the time variable disappeared from the integrations (as does spatial dependence), and the amplitude of incident plane wave was also canceled during the calculation of the internal and external mean-square pressure ratio. Note that the noise reduction given by Eq. (64) is only used to characterize the noise transmission into a finite, thin, cylindrical enclosure with two rigid ends, and also note that the equations are derived with the internal fluid loading ignored (assumed to be light) and with an oblique plane incident wave.

The definition of NR proposed in this paper is more similar to TL than previous definitions, and it is more amenable to comparing with experimental measurements. While only the radiation is considered in the transmitted wave for the TL, in the NR the transmitted sound includes both radiation and the scattered waves inside the acoustic cavity. Note that transmission loss and noise reduction are dimensionless quantities that are typically expressed in decibels.

III. NUMERICAL SIMULATION

Numerical results from Eq. (64) have been generated for the ChamberCore composite cylindrical shell with radius $a=255$ mm, effective thickness $h=20.1$ mm, and length $L=760$ mm. The physical parameters of the composite material have been homogenized and are Young's modulus $E=60$ GPa, Poisson's ratio $\mu=0.3$, effective density of the uniform shell is $\rho_s=315\ \mathrm{kg/m^3}$. The speed of sound and the density of air inside and outside the cylindrical shell are $c_1=c_2=346$ m/s (at 75 °F) and $\rho_1=\rho_2=1.21\ \mathrm{kg/m^3}$. The oblique incident plane wave is given by Eq. (1), where $\theta=30$ deg. In order to simplify analysis, the acoustic damping ratio was set to the same value for all modes and obtained by averaging the measured results (0.28%).[1,12] The structural damping ratio was also set to the same for all modes and obtained by averaging the identification results (4.64%).[1,12] The maximum order of acoustic and structural modes is set

TABLE I. First ten acoustic cavity modes and their natural frequencies.

Mode no.	Mode shape order (l,m,n)	Analytical frequency (Hz)
1	001	228
2	010	398
3	002	455
4	011	458
5	012	604
6	020	660
7	003	683
8	021	698
9	013	790
10	022	801

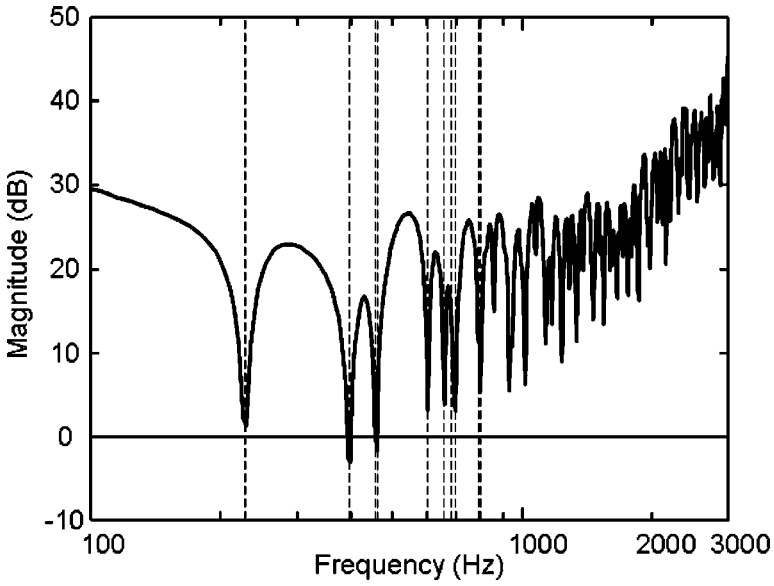

FIG. 3. Theoretical NR of a ChamberCore cylindrical fairing (θ=30°).

to six per each index in the simulation for a total of 36 structural modes and 216 acoustic cavity modes. The analytical results for the first ten acoustic modes and natural frequencies of the cavity formed by the closed cylindrical structure are listed in Table I.

Figure 3 shows the curves of the noise reduction given by Eq. (64) at θ=30 deg, with frequency range [0,3000] Hz and a logarithmic abscissa. The first ten acoustic cavity resonances are also indicated in the figure as dashed vertical lines. From Fig. 3 it is observed that there are sharp dips at all cavity resonances, which is consistent with previous experimental studies.[1,3,4,12] This phenomenon can be explained by examining Eqs. (52) and (55). From Eq. (52), there is a peak in the interior pressure–frequency curve at each acoustic cavity resonance frequency (ω_{lmn}^{f}), and these peaks become dips in the NR curve by the definition of NR in Eq. (55). It is concluded that the cavity resonances significantly reduce the noise reduction capability of the finite cylindrical structure, dominating the NR at low frequencies and even causing amplification (negative NR; also see Fig. 3) at 398, 455, and 458 Hz. From the figure it is also important to note that the pure longitudinal modes that were neglected in previous models, i.e. (001) at 228 Hz, (002) at 455 Hz, and (003) at 683 Hz, play a very important role in noise transmission of low frequencies. The structural resonances do not play a significant role in the NR results of Fig. 3 since they are higher than 4000 Hz. Table II lists the predicted structural resonance frequencies.[21]

TABLE II. First six structural modes and their natural frequencies.

Mode no.	Mode shape order (o,q)	Analytical frequency (Hz)
1	21	4141
2	31	4410
3	11	5546
4	41	5577
5	32	5827
6	42	6336

Figure 4 shows the effects of varying the internal acoustic damping on the NR for θ=30 deg. The solid curve is the NR curve with general acoustic damping ratio (0.28%), and the dashed curve is the NR curve with a ten-times increase in the general acoustic damping ratio (2.8%). From Fig. 4 it is observed that when increasing internal acoustic damping ratios the noise reduction obtains significant broadband improvement. Absorptive treatments would work well at providing increased damping at the higher frequencies, but not at low frequencies.

Figure 5 shows the effects of the sound incidence angle, θ, on the NR. In the following, the mechanism of how the incident angle affects the noise reduction is discussed in detail based on the normal incident sound (θ=0 deg) case. From Eq. (2) it can be observed that the x component of the wave number is $k_{1x}=\omega/c$, and the z component is $k_{1z}=0$ when θ=0 deg. Equation (43) then simplifies to

$$E_{oq}=\begin{cases}(-j)^{o+1}aL\pi[J_o(ka)+C_oH_o^{(2)}(ka)], & (q=0)\\ (-j)^o 4aL[J_o(ka)+C_oH_o^{(2)}(ka)]\dfrac{1}{q}, & \\ \qquad (q=\text{odd number}) & \\ 0, \quad (q=\text{even number}) & \end{cases}. \tag{65}$$

From Eqs. (42) and (65), it is observed that when the acoustic cavity modes are purely axial (i.e., $l=0$, $m=0$, and $n\neq 0$), the coupled structural and acoustic vibration loading in Eq. (51) becomes zero at these modes (i.e., $E_{oq}D_{oq,lmn}=0$), which will in turn cause the modal pressure, Eq. (51), to be zero [i.e., $F_{lmn}(\omega)=0$] at these modes. As a result, the purely axial cavity modes have no contribution to the internal pressure in Eq. (52) when the sound wave impinges normally upon the cylindrical shell. As the incidence angle increases, the extent of the contribution of the purely axial acoustic modes to the internal modal pressure increases, which in turn results in notches in the NR.. From inspecting

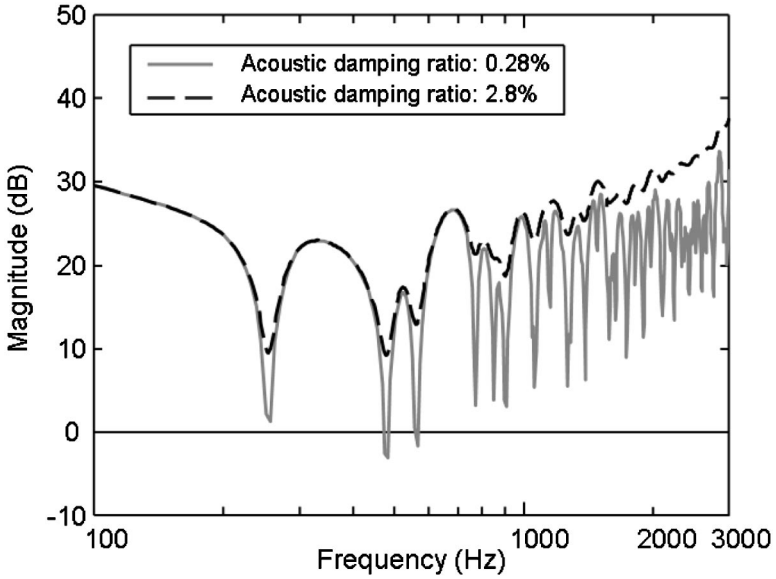

FIG. 4. Effects of the acoustic damping on NR (θ=30 deg).

Fig. 5, it is observed that the incident angle creates a significant influence on the NR at the vicinity of the resonance frequencies of purely axial acoustic cavity modes (001 mode at 228 Hz, 002 mode at 455 Hz, and 003 mode at 683 Hz).

Figure 6 is a comparison of analytical [Fig. 6(a)] and measured [Fig. 6(b)] results for the noise transmission into the ChamberCore cylindrical structure. As indicated in the legends of the figures, the analytical NR is calculated with a plane wave impinging at an incident angle, θ=30 deg, while the measured NR results are obtained in a approximately diffuse field.[1,3,4] The first ten acoustic cavity resonances are also shown in Fig. 6 as dashed vertical lines.

The measured noise reduction is calculated by an *in situ* method developed in previous studies.[1,3,4,12] First, the ChamberCore cylinder was installed in a diffuse sound field, and the autospectrum signals were measured over the outside and inside surface of the cylinder. Second, the noise reduction is computed by

$$\mathrm{NR} = -10 \log_{10} \frac{\langle p_{int}^2(\omega) \rangle}{\langle p_{ext}^2(\omega) \rangle}, \tag{66}$$

where $\langle p_{ext}^2(\omega) \rangle$ is the mean-square external pressure spectrum averaged over the outside shell surface, and $\langle p_{int}^2(\omega) \rangle$ is the mean-square internal pressure spectrum averaged over the inside shell surface. Note that because the shell is thin, both the internal and external areas are well approximated by the midsurface area, S.

From Fig. 6 it is observed that the general trends of the measured and analytical NR curves are very similar, while the absolute values of NR at low frequencies (smaller than 200 Hz) and high frequencies (larger than 1500 Hz) have some discrepancy. There are two main reasons for the difference between the experimental and analytical results. First, the analytical NR was calculated for a plane wave with an incident angle of (θ=30 deg), while the experimental results

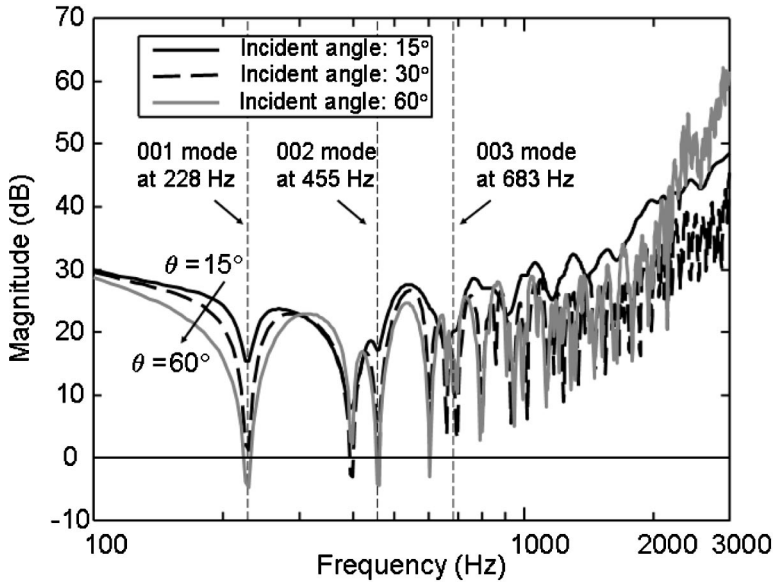

FIG. 5. Effects of the incident angle on NR.

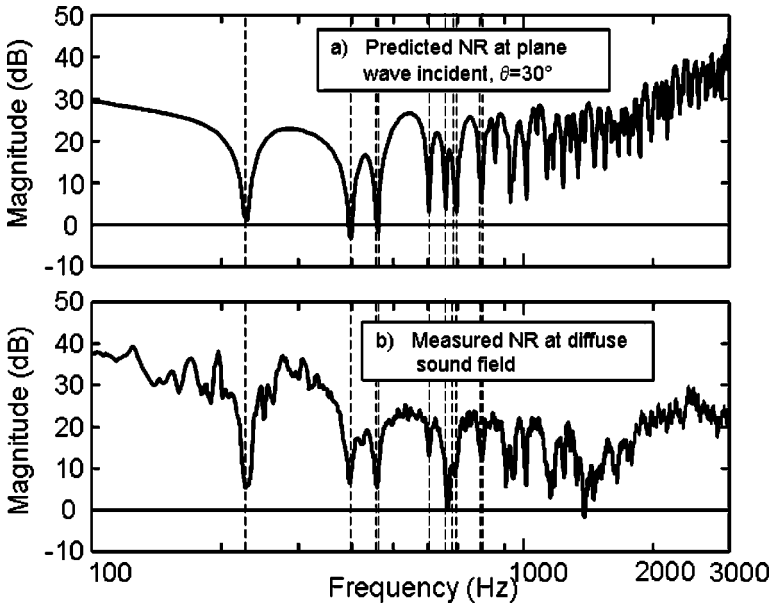

FIG. 6. Comparison of analytical (a) and measured (b) NR for a ChamberCore cylindrical fairing.

were measured in an approximately diffuse sound field. Second, the effects of the internal fluid loading on the NR are present in the experimental results, while the effects are neglected in the analytical model in order to simplify the derivation. The influence of the fluid loading on the NR is complex, and includes the change of both internal and external sound fields by the coupled acoustic and structural vibration. The effects of internal fluid loading and different sound fields on the NR would make a good topic for a future research endeavor.

IV. CONCLUSIONS

An extended model of the noise reduction for a finite uniform cylindrical shell was developed that includes axial structural–acoustic modes. The exterior near-field pressure was approximated with that for an infinite elastic cylindrical shell. The interior pressure distribution of a finite cylindrical structure was derived using a modal model. Donnel–Mushtari and Flügge's theories were used for the structural analysis, and were coupled to the rigid-wall acoustic modes using a modal-interaction approach. Analytical results were presented for a novel ChamberCore composite fairing and compared with experimentally obtained NR. Both the experimental and numerical results show that the cavity resonances have a significant effect on the noise transmission into the finite cylindrical structure. A parametric study found that higher internal acoustic damping provides improved broadband noise transmission reduction. In particular, the axial modes, which were not considered in previous studies, were found to provide significant decrease in the NR as the sound incident angle is increased.

[1] D. Li, ''Vibroacoustic Behavior and Noise Control Studies of Advanced Composite Structures,'' Ph.D. dissertation, School of Engineering, University of Pittsburgh, Pittsburgh, PA (2003).
[2] E. Herup, S. Huybrechts, S. Griffin, and S. Tsai, ''Method of making composite ChamberCore sandwich-type structure with inherent acoustic attenuation,'' U.S. Patent No. 6,231,710 B1 (2001).
[3] D. Li and J. S. Vipperman, ''Noise transmission control studies on a chamber core composite cylinder,'' IMECE02-33069, New Orleans, LA, 2002.
[4] J. S. Vipperman, D. Li, I. Avdeev, and S. A. Lane, ''Investigation of the sound transmission into an advanced grid-stiffened structure,'' J. Vibr. Acoust. **125**, 257–266 (2003).
[5] S. M. Huybrechts and T. E. Meink, ''Advanced grid stiffened structures for the next generation of launch vehicles,'' Proceedings of Aerospace Conference, IEEE, **1**, 263–270 (1997).
[6] Y. Y. Tang, J. H. Robinson, and R. J. Silcox, ''Sound transmission through two concentric cylindrical sandwich shells,'' 14th International Modal Analysis Conference, Dearbon, Michigan, Feb. 1996.
[7] Y. Y. Tang, J. H. Robinson, and R. J. Silcox, ''Sound transmission through a cylindrical sandwich shell with honeycomb core,'' 34th AIAA Aerospace Sciences Meeting and Exhibit, Reno, Nevada, AIAA Paper No. 96-0877 (1996).
[8] P. H. White, ''Sound transmission through a finite, closed, cylindrical shell,'' J. Acoust. Soc. Am. **40**, 1124–1130 (1966).
[9] L. Cheng, ''Fluid–structural coupling of a plate-ended cylindrical shell: Vibration and internal sound field,'' J. Sound Vib. **174**, 641–654 (1994).
[10] Y. K. Tso and C. H. Hansen, ''An investigation of the coupling loss factor for a cylinder/plate structure,'' J. Sound Vib. **199**, 629–643 (1997).
[11] L. R. Koval, ''Effects of cavity resonances on sound transmission into a thin cylindrical shell,'' J. Sound Vib. **59**, 23–33 (1978).
[12] D. Li and J. S. Vipperman, ''On the noise transmission and control for a cylindrical ChamberCore composite structure,'' J. Sound Vib. (to be published).
[13] P. Gardonio, N. S. Ferguson, and F. J. Fahy, ''A modal expansion analysis of noise transmission through circular cylindrical shell structures with blocking masses,'' J. Sound Vib. **244**, 259–297 (2001).
[14] S. J. Estève and M. E. Johnson, ''Reduction of transmission into a circular cylindrical shell using distributed vibration absorbers and Helmholtz resonators,'' J. Acoust. Soc. Am. **112**, 2840–2848 (2002).
[15] M. C. Junger and D. Feit, *Sound, Structures, and Their Interaction*, 2nd ed. (MIT Press, Cambridge, MA, 1986).
[16] F. Fahy, *Sound and Structural Vibration: Radiation, Transmission and Response* (Academic, London, 1993).
[17] Y. M. Huang and C. R. Fuller, ''The effects of dynamic absorbers on the forced vibration of a cylindrical shell and its coupled interior sound field,'' J. Sound Vib. **20**, 401–418 (1997).
[18] D. R. Thomas, P. A. Nelson, and S. J. Elliot, ''Active control of the transmission of sound through a thin cylindrical shell. II. The minimization of acoustic potential energy,'' J. Sound Vib. **167**, 113–128 (1993).
[19] N. M. McLachlan, *Bessel Functions for Engineers*, 2nd ed. (Oxford University Press, Oxford, 1955).
[20] R. D. Blevins, *Formulations for Natural Frequency and Mode Shape* (Van Nostrand Reinhold, New York, 1979).
[21] A. W. Leissa, ''Vibration of Shells,'' NASA-SP-288, 1973, pp. 43–46.

[22] C. I. Holmer and F. J. Heymann, "Transmission of sound through pipe walls in the presence of flow," J. Sound Vib. **70**, 275–301 (1980).
[23] C. R. Fuller, S. J. Elliott, and P. A. Nelson, *Active Control of Vibration* (Academic, London, 1989).
[24] C. R. Fuller and A. H. von Flotow, "Active control of sound and vibration," IEEE Control Syst. Mag. **15**, 9–19 (1995).
[25] C. H. Hansen and S. D. Scott D. Snyder, *Active Control of Noise and Vibration* (E & FN Spon, London, 1997).

Nonlinear vibrations of buried landmines

Dimitri Donskoy[a)]
Davidson Laboratory, Stevens Institute of Technology, 711 Hudson Street, Hoboken, New Jersey 07030

Alexander Reznik
Institute for Physics of Microstructures Russian Academy of Science (IPM RAS), GSP-105, Nizhny Novgorod, 603950, Russia

Andrei Zagrai and Alexander Ekimov
Davidson Laboratory, Stevens Institute of Technology, 711 Hudson Street, Hoboken, New Jersey 07030

(Received 10 October 2003; revised 29 November 2004; accepted 30 November 2004)

The seismo-acoustic method is one of the most promising emerging techniques for the detection of landmines. Numerous field tests have demonstrated that buried landmines manifest themselves at the surface through linear and nonlinear responses to acoustic/seismic excitation. The present paper describes modeling of the nonlinear response in the framework of the mass–spring model of the soil–mine system. The perturbation method used in the model allows for the derivation of an analytical solution describing both quadratic and cubic acoustic interactions at the soil–mine interface. This solution has been compared with actual field measurements to obtain nonlinear parameters of the buried mines. These parameters have been analyzed with respect to mine types and burial depths. It was found that the cubic nonlinearity could be a significant contributor to the nonlinear response. This effect has led to the development of a new intermodulation detection algorithm based on dual-frequency excitation. Both quadratic and intermodulation nonlinear algorithms were evaluated at the U.S. Army outdoor testing facilities. The algorithms appear to complement each other in improving the overall detection performance. [DOI: 10.1121/1.1850410]

PACS numbers: 43.40.Ga, 43.25.Ts, 43.28.En [ANN] Pages: 690–700

I. INTRODUCTION

In recent years, investigations at the University of Mississippi,[1,2] Stevens Institute of Technology,[3–5] and Georgia Institute of Technology[6,7] have demonstrated that seismic/acoustic techniques could deliver a high probability of detection with low false-alarm rate through the exploitation of the mechanical characteristic of soil–mine systems. It was shown that buried mines have very distinguishable vibrational ''signatures,'' which could be used for their successful and reliable detection and identification.

The seismo-acoustic technique excites low-frequency vibrations of buried mines and measures surface vibration above the mine using remote sensors. In this approach, the mine is excited with air-borne (acoustic) or soil-borne (seismic) waves. The resulting vibration is measured remotely with laser-Doppler vibrometers (LDVs), microwave or ultrasonic sensors. The level of soil vibration due to linear and nonlinear interaction of incident acoustic pressure with the buried mine could be represented in terms of spatially distributed vibration velocity profiles at the respective frequencies that uniquely define its ''linear'' or ''nonlinear'' vibrational signatures. The signature above the buried mine is different from the off-mine soil vibrational response because of the impedance (compliance) contrast and nonlinearity at the soil–mine interface. The first blind field test of the technique[8] demonstrated 95% probability of detection with a false-alarm rate of 0.03 m^2 for antitank (AT) mines. Nonlinear seismo-acoustic detection and discrimination further showed a high potential for even better performance for both AT and antipersonnel (AP) mines, because of its high selective sensitivity to mines, immunity to clutter,[5] and potentially high on/off mine contrast.

Practical application of the seismo-acoustic technique undoubtfully requires an adequate physical model to explain various phenomena observed in the field tests and to account for a diverse range of field conditions. The developed simple physical model describes the dynamics of the soil–mine system[3–5] by treating the mine and the soil as an integrated system where mine and soil interact at their physical interface. The model is based on a lump-element approach: the soil column on top of the mine is modeled as a mass (inertia), with compression and shear stiffnesses, and the mine is modeled as a dynamic mass and a stiffness associated with its upper diaphragm. This approach is justified as long as the acoustic wavelengths are greater than the size of the mine and the burial depth. The developed model provides insight into the physical mechanisms of seismo-acoustic detection and explains many experimental observations.

In this paper we further develop the lump-element model focusing on the nonlinear dynamics of the soil–mine system.

II. MECHANISM OF SOIL–MINE NONLINEARITY

The major reason for the strong nonlinearity at the soil–mine interface is the lack of bonding between the mine and the soil. The stress–strain dependence at the interface is

[a)]Electronic mail: ddonskoy@stevens.edu

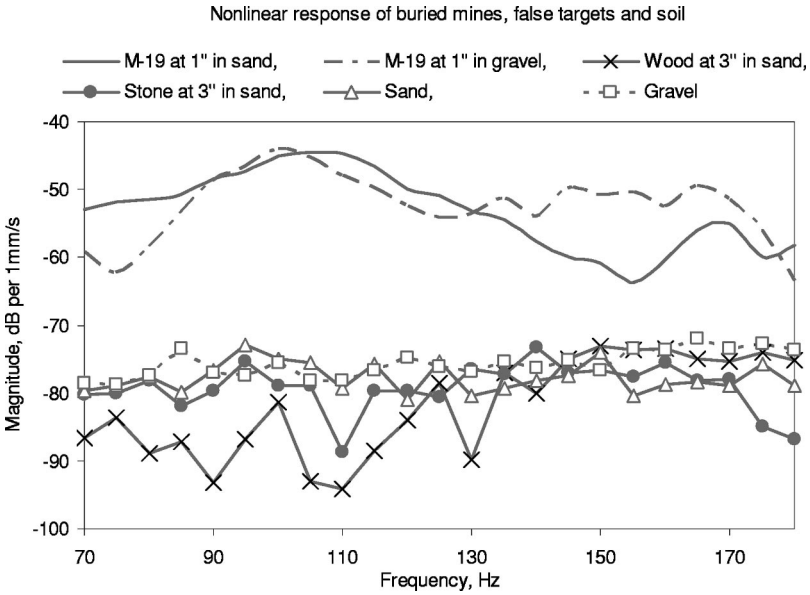

FIG. 1. Nonlinear responses of two types of soil (sand and gravel), false targets buried in sand, and antitank plastic mine M-19 buried in sand and gravel. Nonlinearities of sand and gravel represent averaged responses measured in 29 (gravel) and 3 (sand) off-mine locations.

quite different during the compressive and tensile phases of vibration: under tensile stress, separation of soil grains may occur at the soil–mine interface, whereas under compressive stress mine and soil are always in contact. This asymmetric response leads to noticeable nonlinear effects such as the generation of harmonics and signals with combination frequencies. There are two possible mechanisms for separation at the interface. In the first one, the level of applied vibrational force (stress) is higher than the weight of the soil on top of the mine. In this case, the soil will ''jump or bounce'' on top of the mine, leading to a very strong nonlinearity. This mechanism, however, should occur rarely considering the practical levels of vibrational excitation. Indeed, in most of the field tests we conducted, the soil surface acceleration was below the gravitational acceleration, implying that the vibrational force was smaller than the weight of the soil above the mine. Nevertheless, noticeable nonlinear effects were still observed, suggesting that there should be another mechanism of ''separation.''

Since both soil and mine are mechanical systems, each with their own inertia and stiffness, their respective phases of oscillation depend on the relative contributions of inertia and stiffness. If stiffness is the dominant contributor to the system's mechanical impedance, then the system will oscillate in phase with the applied external force. At higher frequencies, however, the inertial contribution becomes dominant and the system oscillates in opposite phase with respect to the external force. Therefore, the mine and soil may oscillate with opposite phases, and this will depend on the relative values of their mechanical impedances, leading to the phenomenon of soil grains separation at the interface. When this mechanism is dominant, separation will take place even at relatively low applied levels of vibrational force.

Measurements of the mechanical impedances of various mines[4,5] revealed that, in the frequency range below 1000 Hz, the stiffnesses of majority of the mines investigated were smaller than the stiffness of the surrounding soil, explaining high on/off mine impedance contrast. Such a low mine stiffness also has an important implication for nonlinear oscillations: mine stiffness contribution and respective phase are overtaken by the inertial effect at much lower frequencies leading to phase shift at the soil–mine interface and, as a result, to high nonlinearity at low frequencies. Typical nonlinear responses of buried mines are presented in Fig. 1. On the other hand, stiff objects such as rocks, metal pieces, etc., with dominant stiffness contribution oscillate in phase with soil in the frequency range of interest. This effect, coupled with much lower vibration amplitudes of stiff targets, explains weak nonlinearity above buried false targets[3–5] as illustrated in Fig. 1. Therefore, nonlinear response of the false targets is determined by the inherent nonlinearity of the soil rather than soil–target interaction.

Soil is a complex medium, the properties of which could be considerably affected by its composition, cohesiveness, and environmental factors. Although in seismo-acoustics soil is often considered as a homogeneous medium,[9] it should be remembered that essentially it consists of contacting grains. These microcontacts lead to nonlinear behavior at macro scale[9] and add to nonlinearity of the buried mine. One way of estimating contribution of soil nonlinearity into cumulative nonlinear response of the buried mine is measuring the nonlinear response of soil without mines. Figure 1 presents experimental data obtained at the sum frequency for two types of soil: gravel and sand. For convenience, soil nonlinearity is presented as two lines obtained by averaging 29 measurements in gravel and 3 measurements in sand. The measurements show that at low frequencies nonlinear response of soil is considerably lower than that of the buried mine. This observation is consistent with the results obtained by other researchers.[10,11] In the following sections, we present a model and estimations for both soil–mine interface and soil nonlinearities.

A. Quadratic (*Q*), and Cubic (*C*), nonlinear parameters

The interface nonlinearity can be described using a generic form of Hooke's law

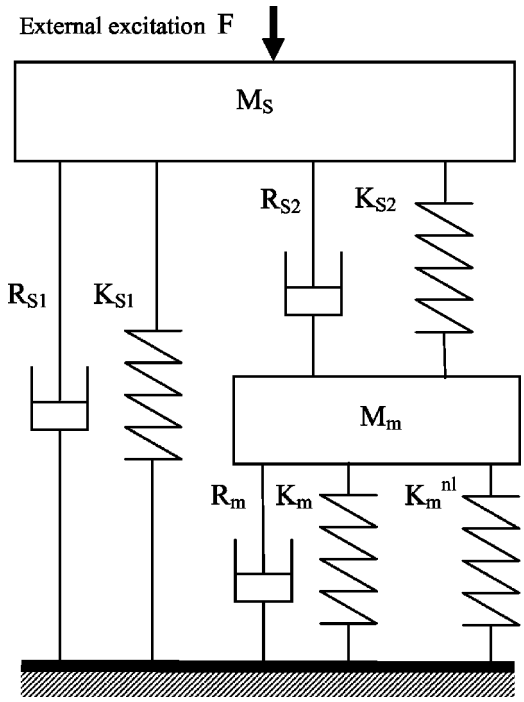

FIG. 2. Equivalent mechanical diagram for the nonlinear soil–mine system.

$$F(\xi)=\xi\cdot(k_m+k_m^{nl}(\xi)), \tag{1}$$

where ξ is the displacement, k_m is the linear stiffness coefficient, $k_m^{nl}(\xi)$ describes the nonlinear stiffness, and F is the applied force.

The mechanical mass–spring–dashpot diagram introduced in Donskoy *et al.*[4] was modified as shown in Fig. 2 by introducing the nonlinear spring,[12] $k_m^{nl}(\xi)$, instead of a diode. This approach is more consistent with the nonlinear stiffness concept introduced in Eq. (1).

The mathematical analogy between mechanical and electrical systems provides exceptional flexibility and convenience in the analysis of complex dynamical systems. Using this analogy,[13] we can conveniently represent mechanical parameters in terms of elements of the electrical circuit depicted in Fig. 3. The advantage of this approach is that the analysis of the nonlinear mechanical system shown in Fig. 2 is significantly simplified by considering a system of equations for the electrical circuit, which upon application of a perturbation technique[14] yields a solution for linear and nonlinear components.

Consider the electrical diagram presented in Fig. 3. The electrical elements in the circuit represent the following mechanical parameters: charge $Q\rightarrow$displacement ξ, current $I\rightarrow$velocity v, voltage $U\rightarrow$force F, inductance $L\rightarrow$mass m,

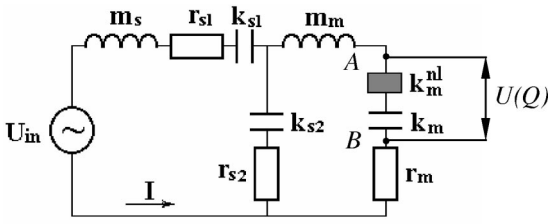

FIG. 3. Equivalent electrical diagram for the nonlinear soil–mine system.

capacitance $C\rightarrow$elastic compliance c, which is inversely proportional to stiffness k, resistance $R\rightarrow$damping factor r. Similar notations for the linear elements of the diagram (Fig. 3) are given in the previous publication.[4] According to the lump-element model presented in Fig. 2, we denote mass, stiffness, and internal losses of the mine as m_m, k_m, and r_m. The soil can be characterized by its added mass m_s, compression, k_{s2}, r_{s2}, and shear k_{s1}, r_{s1}, stiffnesses and damping factors, respectively.

The nonlinear nature of the acoustic interaction at the soil–mine interface is accounted for by the dependence of stiffness on ξ in Hooke's law as shown in Eq. (1). For small displacements, the contribution of the nonlinear effect can be approximated in terms of the first and second terms in the Taylor's expansion, i.e., $k_m^{nl}(\xi)\approx k_m(\alpha\xi+\beta^2\xi^2)$. Using the analogy between mechanical and electrical systems, we can therefore represent Hooke's law (1) in terms of electrical quantities as follows:

$$U(Q)=\frac{Q}{C_m}\cdot(1+\alpha Q+(\beta Q)^2), \tag{2}$$

where $U(Q)$ is the voltage drop across points A and B in Fig. 3 and capacitance C_m corresponds to $1/k_m$. This voltage drop is analogous to the force in the relationship (1) defined for the soil–mine interface, in which, assuming concave up monotonically increasing stress–strain relationship, α and β are the positive nonlinear coefficients of the mechanical system.

The parameters α and β characterize the quadratic and cubic nonlinearities of the system. Equation (2) shows that the first, second, and third terms on the right-hand side are equal when $Q=\alpha^{-1}=\beta^{-1}$, which indicates a very strong nonlinearity. In practice, the nonlinearity is usually weak, so that we assume

$$\alpha Q\ll 1 \quad \text{and} \quad \beta Q\ll 1. \tag{3}$$

Equation (2) suggests that the effect of the nonlinear interaction can be accounted for by introducing a nonlinear capacitance $C^{nl}(Q)=1/k_m^{nl}=1/[k_m(\alpha Q+(\beta Q)^2)]$ in the electric diagram. The nonlinear capacitance is intentionally expressed in two parts to emphasize the quadratic (parameter α) and the cubic (parameter β) nonlinearities of the system.

It should be noted that while the quadratic nonlinearity, α, is commonly used in acoustics, the cubic nonlinearity in Eq. (2), characterized by the coefficient β, is seldom considered for practical applications. The quadratic term in the nonlinear form of the Hooke's law, as a rule, dominates over the cubic term and the effects of the latter are usually neglected. In the case of a resonant system, however, the cubic nonlinearity could have appreciable effects. If the probing signal has excitation frequencies ω_1 and ω_2 close to the system's resonance frequency, the nonlinear response due to the cubic nonlinearity manifests itself at the intermodulation (IM) frequencies $2\omega_1-\omega_2$ and $2\omega_2-\omega_1$ (this term is widely used in electronic and rf engineering to describe similar cubic nonlinear effects). These intermodulation frequencies lie within the system's resonance and are effectively amplified by the resonance. In contrast, the quadratic nonlinear response observed at frequencies $\omega_1-\omega_2$, $\omega_1+\omega_2$, $2\omega_1$, $2\omega_2$ is not

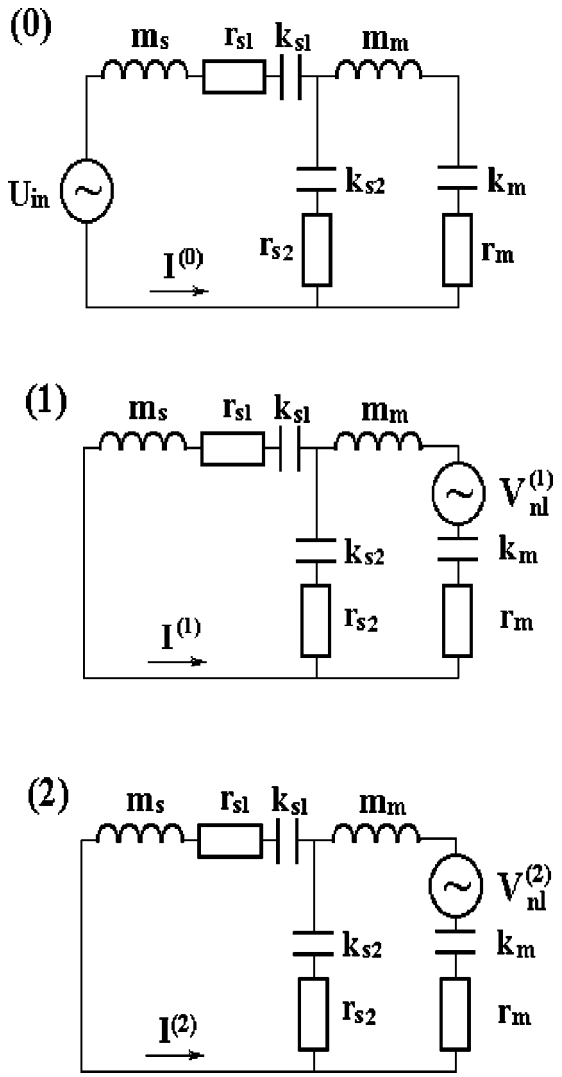

FIG. 4. Equivalent electrical diagrams for the soil–mine system in (0), (1), and (2) orders of the perturbation theory.

amplified since these frequencies are outside the resonance frequency band. As a result, even if the contribution of the cubic nonlinearity in Eq. (2) is weak, the response of the system at frequencies $2\omega_1-\omega_2$ and $2\omega_2-\omega_1$ could be of an amplitude comparable or even exceeding the response associated with the quadratic nonlinearity.

B. Analytical *Q* and *C* nonlinear solution

The analytical solution of a "weakly" nonlinear system can be obtained by a perturbation method. In the electric circuit shown in Fig. 3, the electric current can be represented as $I(t)=I^{(0)}(t)+I^{(1)}(t)+I^{(2)}(t)$, where indices 0, 1, 2 denote the order of the components in the perturbation steps. By definition, in a weakly nonlinear system, the contributions of the nonlinear terms $I^{(1)}$ and $I^{(2)}$ are rather small in comparison with the linear component, $I^{(0)}$, in accordance with condition (3).

The response of the system as measured by the current $I(t)$ is calculated for each order (step) of the perturbation method leading to the consideration of the three equivalent circuits presented in Fig. 4. As can be seen from the figure, this approach requires calculating currents $I^{(0)}(t)$, $I^{(1)}(t)$, $I^{(2)}(t)$ for the linear circuits with equivalent sources corresponding to each order of the perturbation solution.

In the zero-order approximation, the voltage source U_{in} supplies the linear circuit (0) in Fig. 4. The detailed investigation of this case was presented in the previous publication.[4] For the circuits of the first and second orders, the electromotive force (EMF) of the equivalent nonlinear sources (equivalent external forces) are expressed as follows:

$$V_{nl}^{(1)}(t)=-\alpha\cdot k_m Q_m^{(0)}(t)^2, \tag{4}$$

$$V_{nl}^{(2)}(t)=-k_m\cdot\lfloor 2\alpha Q_m^{(0)}(t)Q_m^{(1)}(t)+\beta^2 Q_m^{(0)}(t)^3\rfloor, \tag{5}$$

where $Q_m^{(0),(1)}(t)$ are the electric charges flowing in the m (mine) branch calculated for the zero- and first orders of perturbation, respectively. The EMF for each of the following orders is presented in terms of the solution obtained for the previous order. In other words, $V_{nl}^{(1)}(t)$ contains the zero-order term $Q_m^{(0)}$, and $V_{nl}^{(2)}(t)$ contains the zero- and first-order terms $Q_m^{(0)}$ and $Q_m^{(1)}$, respectively.

In order to proceed further with the analysis of the electric circuits depicted in Fig. 4, we consider the biharmonic excitation

$$U_{in}(t)=U_{01}e^{i\omega_1 t}+U_{02}e^{i\omega_2 t}+\text{cc}. \tag{6}$$

Such an excitation corresponds to the field-testing procedure previously described[3–5] for nonlinear landmine detection.

We are particularly interested in determining system response in terms of the following input currents: linear response $I_{1,2}$ at the probing frequencies ω_1, ω_2; quadratic nonlinear response I_Σ at the sum frequency $\omega_\Sigma=\omega_1+\omega_2$; and cubic nonlinear responses I_{IM1} and I_{IM2} at the corresponding intermodulation frequencies $\omega_{\text{IM1}}=2\omega_1-\omega_2$ and $\omega_{\text{IM2}}=2\omega_2-\omega_1$.

The complex amplitudes of the responses at these frequencies can be calculated using standard methods of circuit analysis and by considering the complex impedances of the circuits shown in Fig. 4. The resulting expressions for the linear responses at the probing frequencies and the quadratic nonlinear response can be expressed as

$$I_{1,2}=U_{01,02}/z_0(\omega_{1,2}), \tag{7}$$

$$I_\Sigma=\frac{2\alpha k_m}{\omega_1\omega_2}I_1 I_2\frac{z_\Sigma(\omega_1)z_\Sigma(\omega_2)}{z_m(\omega_1)z_m(\omega_2)}\frac{1}{z_1(\omega_\Sigma)}, \tag{8}$$

where the respective complex impedances are defined as $z_0=z_{S1}+z_\Sigma$, $z_\Sigma=z_{S2}z_m/(z_{S2}+z_m)$, $z_1=z_{S1}+z_m(1+z_{S1}/z_{S2})$, $z_2=z_m+z_{S2}/(1+z_{S2}/z_{S1})$, $z_m(\omega)=r_m+i(m_m\omega-k_m/\omega)$, $z_{S1}(\omega)=r_{S1}+i(m_S\omega-k_{S1}/\omega)$, $z_{S2}(\omega)=r_{S2}-ik_{S2}/\omega$.

It should be noted that both quadratic and cubic terms in Eq. (2) contribute to the intermodulation solution

$$I_{\text{IM1}}=I_{\text{IM1}}^Q+I_{\text{IM1}}^C. \tag{9}$$

I_{IM1}^Q represents the contribution of the quadratic nonlinearity and I_{IM1}^C that of the cubic nonlinearity

$$I^{Q}_{\mathrm{IM1}} = -\frac{2\alpha^2 k_m^2 I_1^2 I_2^*}{\omega_1^2 \omega_2}\left(\frac{z_\Sigma(\omega_1)}{z_m(\omega_1)}\right)^2\left(\frac{z_\Sigma(\omega_2)}{z_m(\omega_2)}\right)^*\frac{1}{z_1(\omega_{\mathrm{IM1}})} \times\left(\frac{2}{\omega_{\Delta 1} z_2(\omega_{\Delta 1})}+\frac{1}{2\omega_1 z_2(2\omega_1)}\right), \quad (10)$$

$$I^{C}_{\mathrm{IM1}} = i\frac{3\beta^2 k_m I_1^2 I_2^*}{\omega_1^2 \omega_2}\left(\frac{z_\Sigma(\omega_1)}{z_m(\omega_1)}\right)^2\left(\frac{z_\Sigma(\omega_2)}{z_m(\omega_2)}\right)^*\frac{1}{z_1(\omega_{\mathrm{IM1}})}, \quad (11)$$

where $\omega_{\Delta 1}=\omega_1-\omega_2$, and (...)* denotes the complex conjugate. The responses (9)–(11) were obtained for the intermodulation frequency ω_{IM1}. In the expression for the intermodulation response at ω_{IM2}, indices 1 and 2 in (9)–(11) should be interchanged. Note that this result suggests different dependencies of the IM response on the linear solution: $I_{\mathrm{IM1}}\sim I_1^2 I_2^*$ and $I_{\mathrm{IM2}}\sim I_2^2 I_1^*$.

It should be mentioned that in addition to the IM response described by Eqs. (10)–(11), many other combination frequency components, such as $3\omega_1$, $3\omega_2$, $2\omega_1+\omega_2$, $2\omega_2+\omega_1$, etc., are obtainable in the second order of perturbation. We devote particular attention to the intermodulation components because of their aforementioned amplification.

C. Example of analytical calculation of the nonlinear responses of AT mine

In this example we utilize mine and soil parameters presented previously[4] for the modeling of the linear response. The parameters for the plastic AT mine VS-1.6 were as follows: $k_m=2.5\cdot 10^7$ Pa/m, $m_m=12$ kg/m^2, $r_m=1.7\cdot 10^3$ kg/(m^2 s). Herein and throughout the paper, we use parameters normalized by the unit area of the mine upper surface. Soil parameters depend on many factors and can vary over a rather wide range. For the purpose of illustration, we have chosen gravel soil of 1-in. depth with the following estimated parameters: $k_{s1}=2.4\cdot 10^7$ Pa/m, $r_{s1}=3.9\cdot 10^3$ kg/(m^2 s), $m_s=40$ kg/m^2, $k_{s2}=10^8$ Pa/m, $r_{s2}=4\cdot 10^3$ kg/(m^2 s).

1. Q and C frequency responses

Figure 5 illustrates the results of calculations for the linear and nonlinear responses as a function of the frequency of the probing signal, $f_1=\omega_1/2\pi$. The linear response was obtained by setting the amplitude of the probing signal in Eq. (6) equal to $U_{01}=U_{02}=0.3$ Pa. This value corresponds to the amplitude of the acoustic pressure at the soil surface, which, according to field measurements, produces a soil surface velocity of $I_1\approx I_2\approx 5.7\cdot 10^{-5}$ m/s at the mine resonance frequency $f_0\approx 150$ Hz. The linear response is presented in Fig. 5 with a solid line and denoted as $\omega=\omega_{1,2}$. Figure 5 suggests that the resonance frequency band at -6 dB is approximately $\Delta f=20$ Hz. In order to observe the resonance amplification of the intermodulation frequencies, Δf should be greater than the difference between the frequencies of the probing signal, i.e., $\Delta f>\delta f=f_2-f_1$ and for this reason we have chosen $\delta f=5$ Hz.

The quadratic nonlinear response (curve Q in Fig. 5) features two distinctive maxima. The first, weaker in amplitude, occurs when the sum frequency f_Σ coincides with the resonance frequency f_0 (the probing signal frequencies $f_1\approx f_2\approx f_0/2$). The second maximum is stronger and it corresponds to the resonance at $f_1\approx f_2\approx f_0$. The sum frequency in this case is $f_\Sigma\approx 2f_0$. Figure 5 shows that for the chosen nonlinear parameter $\alpha=1$ μm^{-1}, curve Q reaches maximum value of $I_\Sigma\approx -54$ dB when the linear response is $I_1\approx -25$ dB relative to the level of vibrations 10^{-3} m/s. Using the modeling approach outlined for I_Σ, it is not difficult to calculate other nonlinear components at frequencies f_1-f_2, $2f_1$, $2f_2$. We omit an analysis of these components since their frequency responses generally follow the trends obtained for I_Σ.

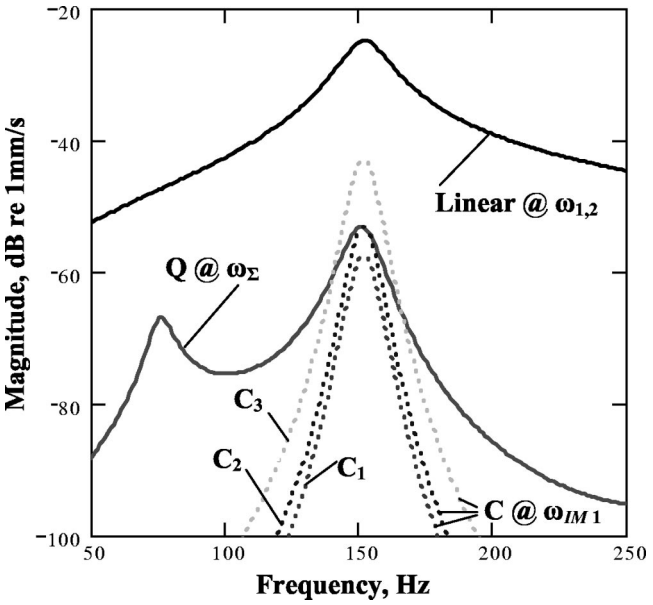

FIG. 5. Linear @ $\omega=\omega_{1,2}$, Q-nonlinear @ $\omega=\omega_\Sigma$, and C-nonlinear @ $\omega=\omega_{\mathrm{IM1}}$ responses of the soil–mine system versus frequency of the excitation signal. The intermodulation components are represented as follows: $C_1-\beta=0$ μm^{-1}; $C_2-\beta=1$ μm^{-1}; $C_3-\beta=2$ μm^{-1}.

The cubic nonlinear response, I_{IM1}, is depicted with the family of dotted curves (C curves) in Fig. 5. Maximum values are within the mine resonance band and the slopes rapidly decrease outside the resonance. Each C curve is obtained for the specific value of the cubic nonlinear parameter $\beta(C_1)=0$, $\beta(C_2)=1$ μm^{-1}, and $\beta(C_3)=2$ μm^{-1}. Curve C_1 shows the intermodulation response in terms of the quadratic nonlinear contribution I^Q_{IM1}, with a maximum by 12 dB lower than I_Σ.

Curves C_2 and C_3 demonstrate that the intermodulation response is dominated by the cubic nonlinear contributions I^C_{IM1}. Remarkably, for the parameter $\beta(C_2)=1$ μm^{-1}, I_{IM} is of the same order of magnitude as I_Σ, and for $\beta(C_3)=2$ μm^{-1} it even exceeds the maximum value of the Q-nonlinear response I_Σ.

2. Detection contrast

One of the critical factors in detecting buried landmines is the detection contrast. It is the contrast between the mine's vibrational "signature" measured at the soil surface above a buried mine and at off-mine locations (on/off detection contrast). The mine's vibrational signature can be linear (impedance or vibration velocity magnitude), nonlinear (Q and C),

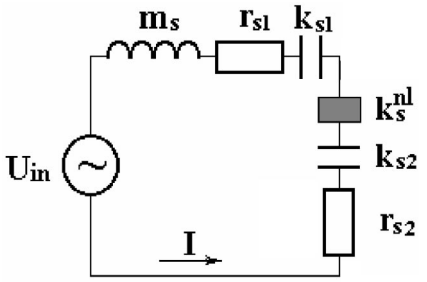

FIG. 6. Equivalent electrical diagram for the soil layer above stiff target.

or a combination of both. Essentially, it is the on/off detection contrast that determines the detectability of a buried landmine. With a background level (or, in other words, velocities measured off mine) of approximately -50 dB *re*: 1 mm/s,[1,5] typical values of the detection contrast for linear detection lie in the range of ~15–20 dB. The nonlinear background level is ~-80 dB *re*: 1 mm/s[5] and the nonlinear detection contrast is in the range of ~30–40 dB. This value is an order of magnitude larger than that the linear detection scheme could offer and, therefore, the nonlinear method has the potential of being very effective.

Immediate use of the nonlinear contrast gain, however, is constrained due to the relatively high noise floor of commercially available scanning LDVs. For example, the Polytec scanning LDV used in our field tests has a noise level of ~-60 dB *re*: 1 mm/s, thereby limiting the nonlinear contrast to ~10–20 dB only. At the same time, a single-point LDV with lower noise levels allowed for the measurements of background nonlinearity at -80 dB, thus, bringing up the nonlinear contrast to the predicted value of 40 dB.

D. Effect of soil nonlinearity

In porous soil the nonlinear behavior is associated with the microstructure of pores,[9] while the soil–mine nonlinearity is due to separation effect at the interface. Many mines are more compliant than soil and reveal resonances below 1 kHz. At the frequencies below the resonance, mine and soil oscillate in phase, but at the frequencies above the resonance, their phases could be different leading to separation of the mine casing and adjacent soil. A distinctively different situation occurs when a stiff target such as a stone or a piece of wood is buried into the soil. Stiff target always oscillates in phase with the soil, preventing separation at the interface. Therefore, we suggest that, in this case, nonlinear behavior is due to inherent nonlinearity of a soil layer above the target. Although according to Fig. 1 and previous studies[4,10,11] soil nonlinearity could be considerably lower than that of the buried mine, it is necessary to estimate its contribution into cumulative nonlinear response of the soil–mine dynamic system. For this purpose, we consider a buried stiff target, which exhibits nonlinearity in the upper soil layer, and employ the analytical approach described in the previous sections. The mechanical diagram presented in Fig. 2 is modified by eliminating elements that are responsible for mine parameters and by including soil nonlinear spring k_S^{nl}. The new mechanical diagram leads to the significantly simplified electrical diagram presented in Fig. 6. Using this diagram, it

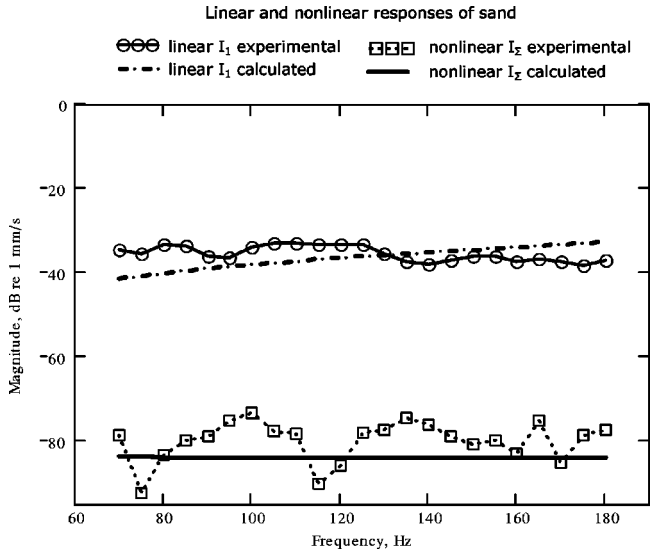

FIG. 7. Calculated and measured linear and nonlinear responses of sand, $\alpha_S = 0.02\ \mu\text{m}^{-1}$.

is not difficult to show that linear and quadratic nonlinear responses are governed by the following relationships:

$$I_{1,2} = U_{01,02}/z_S(\omega_{1,2}), \tag{12}$$

$$I_\Sigma = \frac{2\alpha_S k_S}{\omega_1 \omega_2} \cdot \frac{I_1 I_2}{z_S(\omega_\Sigma)}, \tag{13}$$

where $z_S = z_{S1} + z_{S2}$ is a complex soil impedance, $k_S = k_{S2} + k_{S1}$ is a total soil stiffness, and α_S corresponds to the quadratic nonlinear parameter of the soil.

In our estimations we considered two types of soil with the following parameters: for sand $m_s = 40\,\text{kg/m}^2$, $k_{s1} = 7 \cdot 10^7$ Pa/m, $r_{s1} = 8.4 \cdot 10^4\,\text{kg/(m}^2\,\text{s)}$, $k_{s2} = 7 \cdot 10^8$ Pa/m, $r_{s2} = 5 \cdot 10^4\,\text{kg/(m}^2\,\text{s)}$ and for gravel $m_s = 42.5\,\text{kg/m}^2$, $k_{s1} = 8 \cdot 10^7$ Pa/m, $r_{s1} = 7 \cdot 10^4\,\text{kg/(m}^2\,\text{s)}$, $k_{s2} = 9 \cdot 10^8$ Pa/m, $r_{s2} = 1.2 \cdot 10^5\,\text{kg/(m}^2\,\text{s)}$. Linear and nonlinear responses calculated with Eqs. (12) and (13) are presented in Fig. 7 and Fig. 8. Experimentally obtained dependencies are also shown

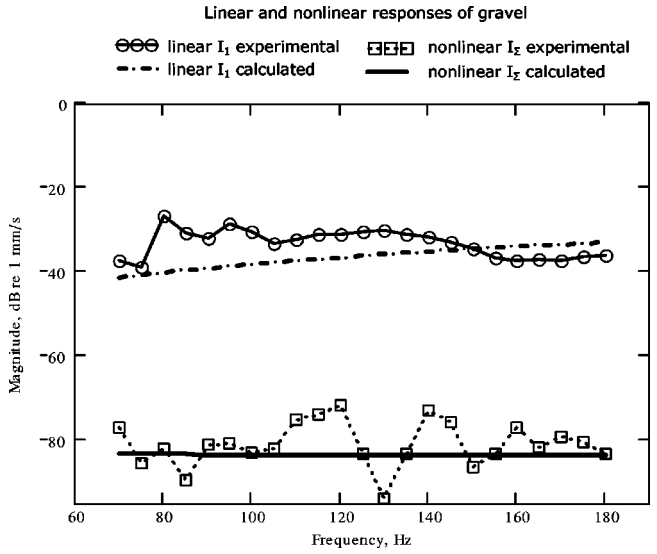

FIG. 8. Calculated and measured linear and nonlinear responses of gravel, $\alpha_S = 0.03\ \mu\text{m}^{-1}$.

FIG. 9. An experimental setup for the seismo-acoustic landmine detection.

in these figures. The data were collected in field at locations without mines. Quadratic nonlinear parameters α_S for sand and gravel were obtained as a best fit of experimental and calculated nonlinear responses that yielded $\alpha_S = 0.02\ \mu\text{m}^{-1}$ for sand and $\alpha_S = 0.03\ \mu\text{m}^{-1}$ for gravel. In the following section, we will show that nonlinear parameters of buried mines can be considerably larger. These results are in agreement with experimental dependencies in Fig. 1 that show more than a 20-dB difference between nonlinear responses of buried mines and soil. It should be noted that estimated nonlinear parameters is the first attempt to quantify soil nonlinearity off the buried mine and need further investigation, particularly for various soil conditions. Nonlinear interaction in soil is complex and includes many interesting phenomena at the mesoscopic scale. An improved model could be introduced by accounting for soil hysteresis due to effects associated with so-called mesoscopic nonlinearity.[15,16] This phenomenon is currently under investigation by Sabatier and Korman.[11] We believe that the developed approach provides adequate estimations for vibration velocities and frequency ranges used for the seismo-acoustic detection of landmines.

III. FIELD TEST VALIDATION OF THE ANALYTICAL MODEL

Field tests were conducted at the U.S. Army's outdoor test facilities in summer and fall of 2001 and 2002. The facilities offer an opportunity to perform measurements under a broad variety of conditions: several soil types and numerous types of live mines buried at different depths. The major objective of the tests was experimental validation of the developed nonlinear seismo-acoustic detection technique and the supporting physical model. We concentrated on two types of measurements: impedance measurements and nonlinear interaction of acoustic/seismic waves. These measurements were taken in gravel and sandy soil off and above buried mines. Two types of plastic AT mines (M-19, VS-1.6) buried at different depths were used in the test.

A. Experimental setup and procedure

The field measurement system used in this study is presented in Fig. 9. The system consists of two platforms: (a) a test cart which carries field instrumentation such as speakers,

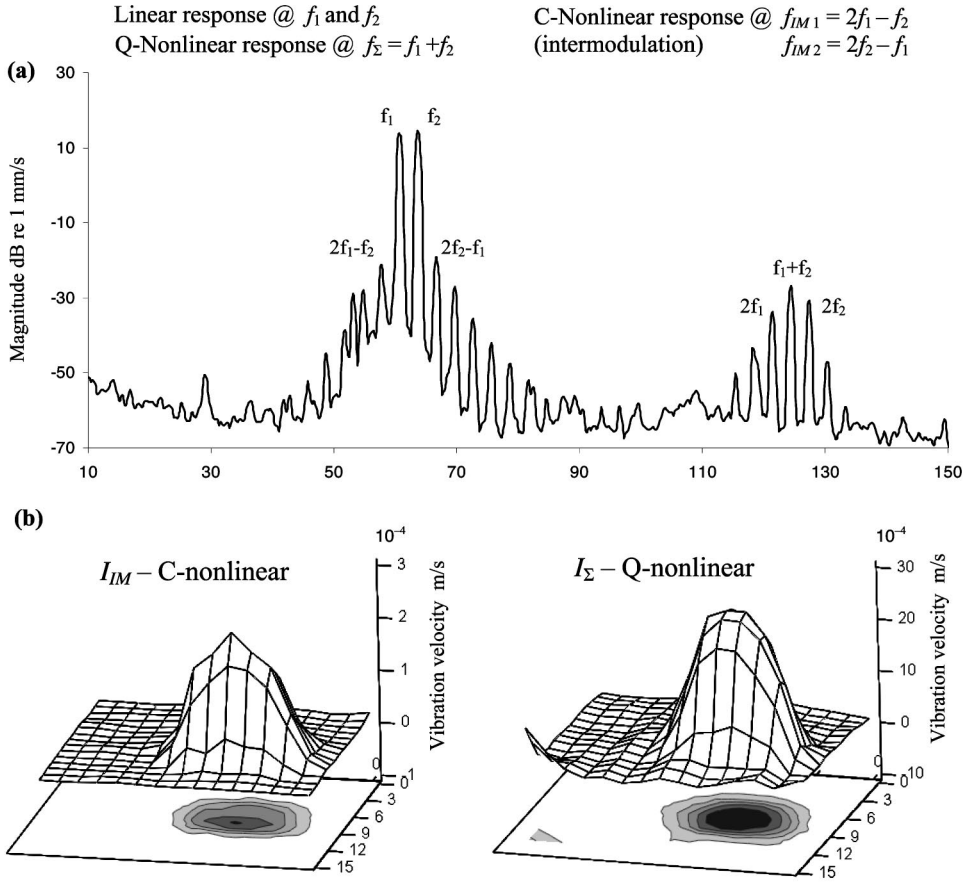

FIG. 10. (a) A vibration spectrum of the plastic mine simulant buried at $\frac{1}{2}$ in. showing the fundamental, sum, and intermodulation frequencies appeared due to Q and C nonlinearity; (b) Q and C nonlinear images for the AT mine VS-1.6 buried at 1 in. in sand; vertical axis is the vibration velocity (in m/s, linear scale) of the soil surface at f_Σ for Q response and the average of vibration velocities at f_{IM1} and f_{IM2} for C response; horizontal plane on images corresponds to the spatial position of the scanned point.

scanning and single-point LDVs, microphone, and may also accommodate a magnetostrictive shaker for seismic excitation; (b) a vehicle with signal generators, power amplifiers as well as control, data acquisition, and processing systems.

The test cart carries six speakers arranged in a hexagonal pyramid to insonify the soil within the pyramid footprint. The resulting soil vibration velocity (v) is measured by the LDV and the soil admittance (y) (or impedance $z=1/y$) is calculated as $y=v/p$, where p is the applied acoustic pressure measured with a microphone positioned near the soil surface.

In the 2002 implementation of the test procedure, we used two harmonic excitation signals with frequencies (f_1, f_2) close enough so that $\delta f = f_2 - f_1 \leqslant 20$ Hz. Twenty Hz is a typical resonance bandwidth of AT mines and the above condition allows for enhancing the intermodulation effect (C-nonlinearity) as both frequencies fit into the resonance band. This condition was confirmed in the laboratory testing of a plastic mine simulant buried at $\frac{1}{2}$ in. in sand. The spectrum of the simulant shown in Fig. 10(a) contains two fundamental frequencies ($f_1=60$ Hz and $f_2=63$ Hz), the intermodulation frequencies $f_{IM1}=2f_1-f_2=57$ Hz, $f_{IM2}=2f_2-f_1=66$ Hz, the sum frequency $f_\Sigma=123$ Hz, and higher harmonics.

In the field tests, the frequencies of the applied signals were swept in a wide frequency range (typically 50–1000 Hz) to yield both linear and quadratic nonlinear vibration responses. The sweep rate for both frequencies was the same, so that δf was constant for the entire sweep. The intermodulation effect was studied at fixed frequencies fitted into the resonance frequency band of a particular mine. LDV sensitivity threshold precluded us from obtaining the intermodulation frequency response outside the resonance.

This setup also allowed for scanning the soil surface to obtain linear and nonlinear spatial distribution of vibration velocities above the buried mine. The resultant velocity profiles enable imaging of buried mines with the prescribed scanning resolution (in the order of cm) and the determination of the detection contrasts. Figure 10(b) shows the nonlinear images for buried AT mine VS-1.6 obtained using C and Q nonlinear responses. The imaging was carried out within the mine's resonance frequency band by scanning over $15\times15=225$ points grid covering 0.58×0.60-m^2 rectangular area.

B. Linear and *Q*-nonlinear responses

As we further developed the model of the soil–mine interaction, the data collected during the 2001 field tests were re-examined. The 2001 test measurement procedure and the results of the experimental investigation were reported previously.[4] In this contribution, the same mine parameters[4] (mass, stiffnesses, and damping factors) were used to calculate linear [Eq. (7)] and nonlinear [Eq. (8)] responses of the soil–mine system under applied excitation $U_{01,02}$.

Figure 11 demonstrates good agreement between analytical calculations (dotted line) and experimental data (solid line) for linear responses of AT mines M-19 and VS-1.6 buried at 75 and 25 mm (a) and (b), respectively.

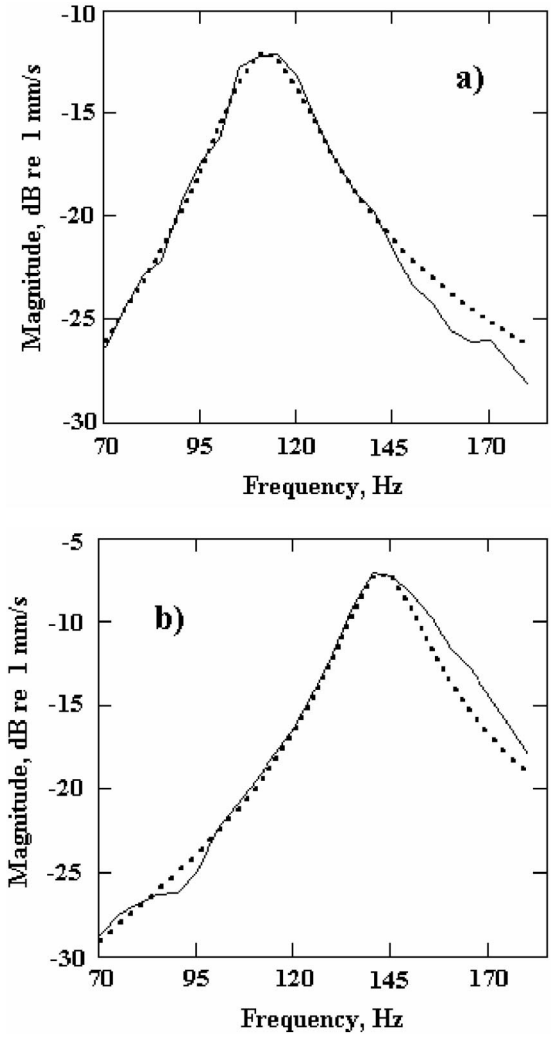

FIG. 11. Theoretically calculated (dotted line) and experimentally obtained (solid line) results for the linear response $I_1(f_1)$ of the soil–mine system: (a) M-19 buried in gravel at the depth of 3 in., $U_{01}=3.4$ Pa; (b) VS-1.6 buried in sand at the depth of 1 in., $U_{01}=2.5$ Pa.

Figure 12 shows a comparison between measured and calculated quadratic nonlinear responses I_Σ for AT mines M-19 and VS-1.6 buried at various depths in gravel and sand. The theoretical dependencies were determined for the parameters α which allowed for the best fit of theoretical and experimental results.

C. Intermodulation response and *C*-nonlinear parameter β

According to the analytical model presented in the preceding sections, both quadratic and cubic nonlinearities manifest themselves through the generation of two intermodulation signals, I_{IM1} and I_{IM2}, at the frequencies $f_{IM1}=2f_1-f_2$ and $f_{IM2}=2f_2-f_1$, respectively. The model suggests that if the amplitude of one probe signal (I_1) is kept constant, the amplitude dependences for two IM signals are different with respect to the amplitudes of the other probe signal (I_2), that is $I_{IM2}\sim I_2^2$ and $I_{IM1}\sim I_2^*$ as per Eqs. (10)

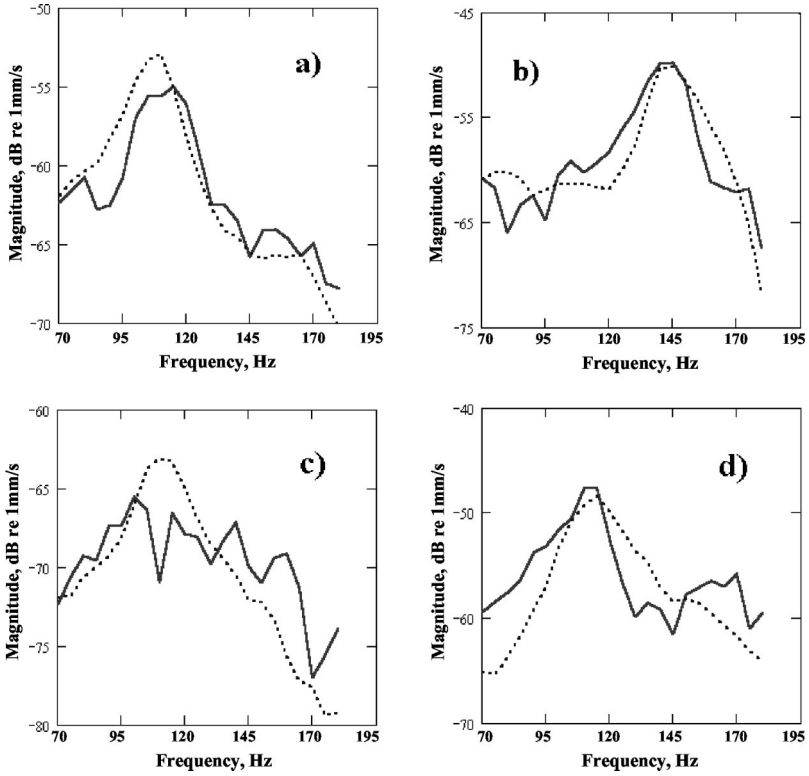

FIG. 12. Theoretically calculated (dotted line) and experimentally obtained (solid line) results for the quadratic nonlinear response I_Σ : (a) AT plastic mine M-19 buried in sand at the depth of 1 in., $\alpha=0.27\ \mu\text{m}^{-1}$; (b) AT plastic mine VS-1.6 buried in sand at the depth of 1 in., $\alpha=1\ \mu\text{m}^{-1}$; (c) M-19 buried in gravel at the depth of 5 in., $\alpha=3.23\ \mu\text{m}^{-1}$; (d) VS-1.6 buried in gravel at the depth of 3 in., $\alpha=0.91\ \mu\text{m}^{-1}$.

and (11). Furthermore, according to Eq. (8), quadratic nonlinear response $I_\Sigma \sim I_2$. As a first step in the validation of the model and its predictions, these dependences must be experimentally verified.

In the field test, two cw probe signals were broadcast at the fixed frequencies $f_1=90$ Hz and $f_2=110$ Hz (both within the mine's resonance frequency band). The amplitude $I_1(f_1)$ was kept constant, while the amplitude $I_2(f_2)$ was varied in a broad range by varying the voltage applied to the amplifiers. Quadratic nonlinear response I_Σ, intermodulation I_{IM1} and I_{IM2} responses were measured at their respective frequencies. Figure 13 shows the results of the experiment (dotted line) for (a) the quadratic nonlinear response I_Σ and (b) the intermodulation nonlinear response I_{IM1} and I_{IM2} obtained for the plastic AT mine VS-1.6 buried in sand at a 25-mm depth (July 2002 field test).

As can be seen from the figure, experimental results agree well with the theoretical calculations for the range of applied I_2, until the IM signals begin to decrease at relatively high amplitudes of I_2. This decrease, however, occurs at vibration levels far exceeding vibration levels typically measured above buried mines, and could be due to effect of the resonance frequency shift at higher amplitudes.[11] According to Fig. 13(b), the amplitude decreases after I_2 reaches -7 dB re: 1 mm/s, i.e., model predictions are valid below this level. This value roughly corresponds to 450 μm/s, which is considerably higher than vibration velocities used for detection of landmines. For example, according to the published data, typical vibration velocities measured above the buried mine are 40–250 μm/s in Ref. 2, 240 μm/s in Ref. 17, and 19–75 μm/s in Ref. 18). In our field tests,[5] typical vibration amplitudes used for landmine detection varied in the range of 180–220 μm/s.

The developed model proposes that the IM response consists of the contributions from quadratic, I_{IM}^{Q}, Eq. (10), and cubic I_{IM}^{C}, Eq. (11), nonlinearities. The relative contributions from both nonlinearities depend on the nonlinear parameters α and β. One approach to evaluate α and β is to use the measured amplitude for quadratic [Fig. 13(a)] and IM [Fig. 13(b)] dependences. First, we evaluate α from Fig. 13(a) using the best fit between experimental and analytical [Eq. (8)], amplitude dependences, which yields $\alpha=0.055$ μm^{-1}. Next, we substitute the obtained value for the nonlinear parameter α into Eq. (10) and compare the calculated quadratic IM contribution I_{IM}^{Q} with the experimental results in Fig. 13(b). The calculated quadratic IM contribution is approximately 20 dB below the experimental curve. This shows that the quadratic IM contribution is ten times smaller than the cubic IM contribution and can be neglected. This also demonstrates that the cubic nonlinearity indeed plays a noticeable role in the nonlinear dynamic response of the soil–mine system.

Since it has been determined that the dominant IM contribution is due to the cubic nonlinearity, the final step is to evaluate the nonlinear parameter β by fitting the solution (11) into the linear part of the experimental curve of Fig. 13(b). This exercise yields an average value of $\beta=0.15$ μm^{-1}.

It should be understood that the evaluated nonlinear parameters are the first attempt to quantify the nonlinearity of the soil–mine system. These parameters could vary substantially depending on mine and soil types, burial depth, soil condition, etc. The study of these effects should be the subject of future investigations.

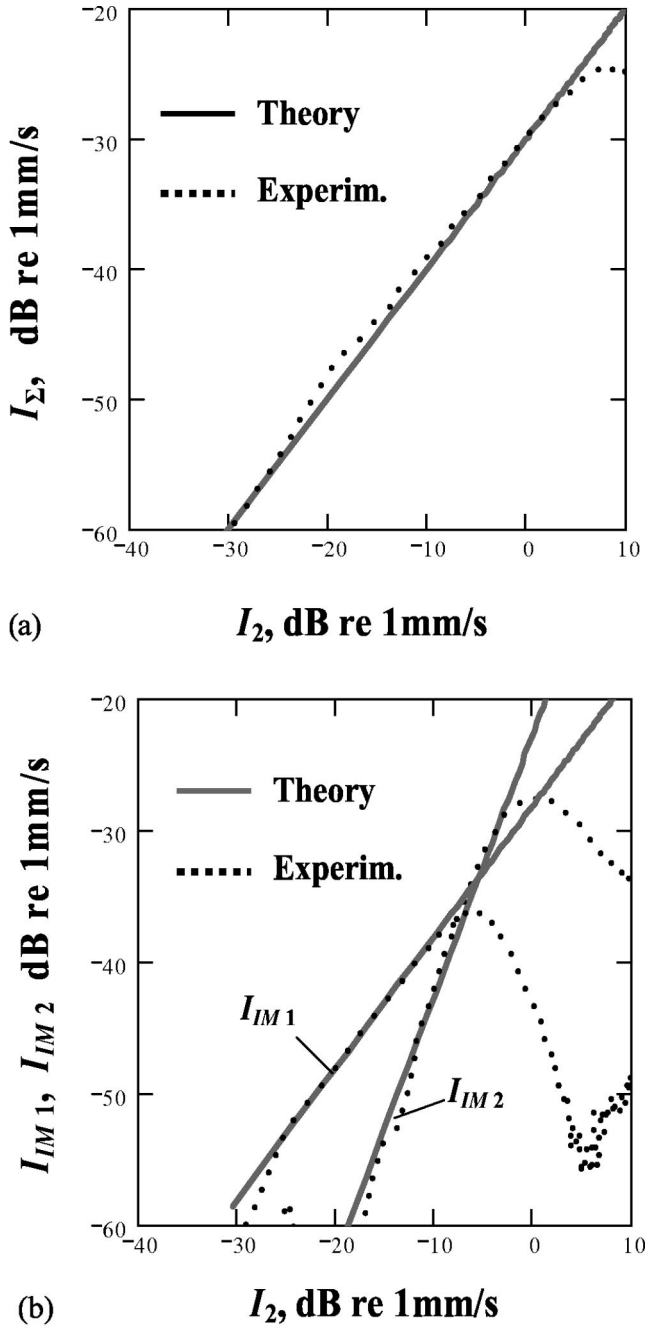

FIG. 13. Theoretically calculated (solid line) and experimentally measured (dotted line) Q and C nonlinear responses for the plastic AT mine VS-1.6 buried in sand at the depth of 1 in.: (a) quadratic nonlinear response I_Σ versus the linear response I_2 with fixed I_1; (b) intermodulation nonlinear responses I_{IM1} and I_{IM2} versus the linear response I_2 with fixed I_1.

IV. CONCLUSION

In this paper, we have further developed a physical model (first introduced in Refs. 3–5) describing the dynamics of soil–mine systems. In addition to the linear response, the model analytically describes quadratic and cubic nonlinear interaction at the soil–mine interface. Using equivalent electrical circuit analysis and a perturbation technique, we obtained analytical solutions for linear and nonlinear vibrations of the soil surface above the buried mine. The nonlinear analysis indicates that the vibrational responses at the sum and intermodulation frequencies offer the most promise for the detection of buried mines. Analysis of the solution explains the observed high contrast of the nonlinear detection method and provides an improved understanding of the effects of soil and mine parameters on detection performance.

The model was validated during field tests conducted in 2001–2002 with live mines buried in sand and gravel. These tests demonstrated good agreement with theoretically predicted frequency and amplitude dependencies.

For the first time, cubic nonlinear effects (intermodulation) in the soil–mine vibratory system were experimentally demonstrated and explained. The combination of strong nonlinearity of the soil–mine interface and the resonant nature of the soil–mine system explains the pronounced effect of the cubic nonlinearity. The measurements and analytical evaluation proved that the cubic nonlinearity could be a dominant contributor to the intermodulation response under certain conditions (resonance excitation and relatively low burial depth).

As a final remark, we would like to mention that the analytical model treats the soil–mine system as a system with discrete parameters (lumped element approximation). In general, a buried mine constitutes a distributed-parameter system. This observation means that more accurate models could be developed by considering the modal structure of mine's vibrations, the specific conditions for the excitation of particular modes, the complex spatial acoustic field distribution within soil, by treating soil as a poro-elastic medium, etc. All of these considerations will lead to more complex models including numerous unknown and often unmeasurable parameters and requiring elaborate and extensive numerical calculations. Without doubt, such an approach could further advance the analysis and understanding of the soil–mine dynamic problem. In contrast, our model with very few measurable parameters is simple to understand and to analyze, and it could serve as a reference for the numerical calculations using the distributed parameter model. As a practical matter, we believe that the developed model and derived analytical solutions could be quite useful for engineering analysis, prediction of detection performance for different mines and soils, utilization in signal processing, and serve as a guideline for further experimental research and development.

ACKNOWLEDGMENTS

The U.S. Army Communications-Electronics Command Night Vision and Electronics Sensors Directorate and the Office of Naval Research supported this work. The authors especially appreciate help and insights provided by Dr. Thomas Witten of NVESD and Dr. Clifford Anderson of ONR through the course of these studies.

[1] J. M. Sabatier and N. Xiang, "Laser-doppler based acoustic-to-seismic detection of buried mines," SPIE's Proceedings on Detection and Remediation Technologies for Mines and Minelike Targets IV, Vol. 3710, pp. 215–222 (1999).
[2] N. Xiang and J. M. Sabatier, "An experimental study on antipersonnel landmine detection using acoustic-to-seismic coupling," J. Acoust. Soc. Am. **113**(3), 1333–1341 (2003).
[3] D. M. Donskoy, "Nonlinear vibro-acoustic technique for land mine detection," SPIE's Proceedings on Detection and Remediation Technologies for

Mines and Minelike Targets III, Vol. 3392, pp. 211–217 (1998).
[4] D. Donskoy, A. Ekimov, N. Sedunov, and M. Tsionskiy, ''Nonlinear seismo-acoustic land mine detection and discrimination,'' J. Acoust. Soc. Am. **111**(6), 2705–2714 (2002).
[5] D. Donskoy, A. Ekimov, N. Sedunov, and M. Tsionskiy, ''Nonlinear seismo-acoustic land mine detection: Field test,'' SPIE's Proceedings on Detection and Remediation Technologies for Mines and Minelike Targets VII, Vol. 4742, pp. 685–695, 1–5 April (2002).
[6] W. R. Scott, Jr., S. H. Lee, G. D. Larson, J. S. Martin, and G. S. McCall II, ''Use of high-frequency seismic waves for the detection of buried land mines,'' SPIE's Proceedings on Detection and Remediation Technologies for Mines and Minelike Targets VI, Vol. 4394, pp. 543–552, 16–20 April (2001).
[7] S. H. Lee, W. R. Scott, Jr., J. S. Martin, G. D. Larson, and G. S. McCall II, ''Technical issues associated with the detection of buried land mines with high-frequency seismic waves,'' SPIE's Proceedings on Detection and Remediation Technologies for Mines and Minelike Targets VII, Vol. 4742, pp. 617–628, 1–5 April (2002).
[8] E. M. Rosen, K. D. Sherbondy, and J. M. Sabatier, ''Performance assessment of a blind test using the University of Mississippi's acoustic/seismic laser doppler vibrometer (LDV) mine detection apparatus at Fort A. P. Hill,'' SPIE's Proceedings on *Detection and Remediation* Technologies for Mines and Minelike Targets V, Vol. 4038, pp. 656–666, 24–28 April (2000).
[9] J. C. Santamarina, K. A. Klein, and M. A. Fam, *Soils and Waves* (Wiley, New York, 2001).
[10] J. M. Sabatier, M. S. Korman, and N. Xiang, ''Linear and non-linear acoustic velocity profiles over buried land mines,'' SPIE's Proceedings on Detection and Remediation Technologies for Mines and Minelike Targets VII, Vol. 4742, pp. 695–700, 1–5 April (2002).
[11] J. M. Sabatier and M. S. Korman, ''Nonlinear tuning curve vibration response of buried land mine,'' SPIE's Proceedings on Detection and Remediation Technologies for Mines and Minelike Targets VIII, Vol. 5089, pp. 476–486, 21–25 April (2003).
[12] R. M. Root and P. F. Cunniff, ''Shock spectrum of a two-degree-of-freedom nonlinear vibratory system,'' J. Acoust. Soc. Am. **60**(6), 1314–1318 (1976).
[13] E. Skudrzyk, *Simple and Complex Vibratory Systems* (University Press, University Park and London, 1968).
[14] J. J. Stoker, *Nonlinear Vibrations in Mechanical and Electrical Systems* (Wiley, New York, 1992).
[15] R. A. Guyer and P. A. Johnson, ''Nonlinear mesoscopic elasticity: Evidence for a new class of materials,'' Phys. Today, **52**(4), April, pp. 30–36, 1999.
[16] J. A. TenCate, E. Smith, and R. A. Guyer, ''Universal slow dynamics in granular solids,'' Phys. Rev. Lett. **85**(5), 1020–1023 (2000).
[17] D. Velea, R. Waxler, and J. M. Sabatier, ''An effective fluid model for landmine detection using acoustic to seismic coupling,'' J. Acoust. Soc. Am. **115**(5), 1993–2002 (2004).
[18] J. C. van den Heuvel, V. Klein, P. Lutzmann, F. J. M. van Putten, M. Hebel, and H. M. A. Schleijpen, ''Sound wave and laser excitation for acousto-optical landmine detection,'' SPIE's Proceedings on Detection and Remediation Technologies for Mines and Minelike Targets VIII, Vol. 5089, pp. 569–578, 21–25 April (2003).

On the choice of expansion functions in the Helmholtz equation least-squares method

Tatiana Semenova and Sean F. Wu
Department of Mechanical Engineering, Wayne State University, Detroit, Michigan 48202

(Received 31 August 2004; accepted 8 November 2004)

This paper examines the performance of Helmholtz equation least-squares (HELS) method in reconstructing acoustic radiation from an arbitrary source by using three different expansions, namely, localized spherical waves (LSW), distributed spherical waves (DSW), and distributed point sources (DPS), under the same set of measurements. The reconstructed acoustic pressures are validated against the benchmark data measured at the same locations as reconstruction points for frequencies up to 3275 Hz. Reconstruction is obtained by using Tikhonov regularization or its modification with the regularization parameter selected by error-free parameter-choice methods. The impact of the number of measurement points on the resultant reconstruction accuracy under different expansion functions is investigated. Results demonstrate that DSW leads to a better-conditioned transfer matrix, yields more accurate reconstruction than both LSW and DPS, and is not affected as much by the change in measurement points. Also, it is possible to obtain optimal locations of the auxiliary sources for DSW, LSW, and DPS by taking an independent layer of measurements. Use of these auxiliary sources and an optimal combination of regularization and error-free parameter choice methods can yield a satisfactory reconstruction of acoustic quantities on the source surfaces as well as in the field in the most cost-effective manner. [DOI: 10.1121/1.1841591]

PACS numbers: 43.40.Sk, 43.40.Rj, 43.60.Pt [JBS] Pages: 701–710

I. INTRODUCTION

Reconstructing acoustic quantities on the surface of a vibrating object has proven to be an effective way of identifying noise source and its transmission paths in automotive and aerospace applications.[1,2] The methods that have been used for this purpose include the Helmholtz integral equation[3] or single-layer potential[4] implemented through the boundary element method (BEM), and Helmholtz equation least-squares[5] (HELS) method. This paper focuses on the HELS method, which has been used successfully to reconstruct acoustic quantities on the spherical[6] and nonspherical (a long cylinder of spherical endcaps,[5] a four-cylinder engine block,[7] and a full-size vehicle front end[1]) surfaces in the low-to-medium frequency regime. Isakov and Wu[8] give a rigorous proof of existence of HELS solutions and their stability estimates.

Essentially, HELS is a series expansion method that uses the spherical waves as its basis functions. Such an expansion has been previously employed in acoustic scattering and prediction, with its expansion coefficients determined by at least three different methods: Rayleigh–Fourier method, point-matching method, and least-squares approximation method, which are collectively referred to as Rayleigh methods by some authors.[9,10] In HELS, the acoustic pressure is expressed as a linear combination of the outgoing spherical wave functions with its origin of coordinates located inside a vibrating object.[7] These outgoing spherical waves satisfy the Helmholtz equation and Sommerfeld radiation condition, and are linearly independent and complete in $L^2(S)$ for any sufficiently smooth surface S. Moreover, their normal derivatives are complete in $L^2(S)$. These properties of the expansion functions make it possible to depict the acoustic field generated by an arbitrarily shaped object.[11,8]

Note that the outgoing spherical waves are not the only system of functions that satisfies the above conditions. There are other systems of functions such as the localized spherical waves (LSW),[11] distributed spherical waves (DSW),[12] and distributed point sources (DPS)[13] that satisfy the Helmholtz equation and Sommerfeld radiation condition and that have been used in Rayleigh methods for acoustic diffraction and scattering.[14,15] Sometimes, they are collectively referred to as the discrete sources methods.[11]

In the discrete sources methods, the acoustic field from a source is approximated by that from one or more auxiliary sources. For LSW, the auxiliary source is located at the origin of the coordinate system. For DSW, the auxiliary sources are distributed on an auxiliary surface inside the object or on an axis of symmetry of this object. For DPS, the auxiliary sources are distributed on an auxiliary surface next to a source surface from the inside. The locations of these auxiliary sources may affect the rate of convergence of an expansion, and their optimal positions depend on the locations of singularities of analytic continuation of the solution to the Helmholtz equation across a source boundary, assuming that the boundary data and boundary surface are sufficiently smooth.[11] The impact of auxiliary sources and their locations is addressed in detail in Sec. V.

It is well known that the rate of convergence of any expansion depends on the complexity of the source boundary and frequency.[10,16–18] Although reconstruction of acoustic quantities can be done by HELS at any frequency,[8] its accuracy deteriorates with an increase in the frequency. This is because at high frequencies, the signal to noise (S/N) ratio is

very low such that the high-order terms in the HELS expansion may be contaminated. To avoid distortions in reconstruction due to noise contamination, we must truncate this expansion by eliminating the high-order terms. However, these high-order terms are critical in depicting acoustic quantities at high frequencies. Hence, an omission of the high-order terms in HELS will make it impossible to get the details of a reconstructed acoustic image right. It is emphasized that this high-frequency difficulty exists in other methods, e.g., BEM, whose computations can become prohibitively intensive.

Despite the fact that the discrete sources methods are extensively studied in the forward problems such as scattering and prediction of acoustic radiation, to the authors' best knowledge they have not been used in backward problems such as reconstruction of acoustic radiation, with the exception of HELS. The major difference between the forward and backward problem lies in the fact that the latter is ill posed and requires regularization.[8] Since the matrix involved in HELS is small, it is possible to employ a direct regularization method such as Tikhonov regularization (TR).[19] For large matrices, for example, those arising from 3D numerical simulations, an iterative regularization method may be a better alternative.

Success in regularization depends to a large extent on choice of regularization parameter. Based on the type of information available on a targeted solution, the parameter-choice methods (PCM) are classified as *a priori*, which is independent of the actual data, and *a posteriori*, which is dependent on the actual data.[20] The former includes heuristic[20] or error-free[21] methods that do not require the knowledge of the noise level in the input data and seek to predict this information from actual data. Note that for infinite-dimensional compact operators, error-free PCM may fail to yield a convergent regularization parameter, namely, to provide a regularized solution that will converge to the exact solution as the noise level tends to zero.[22]

In practice, there is always noise in the input data and often its level is unknown *a priori*. Hence, we must resort to an error-free PCM, even though it may occasionally fail to yield a convergent regularization parameter. Of course, if the noise level can be estimated, we can use Morozov's discrepancy principle to determine a regularization parameter and obtain satisfactory reconstruction.[23] Alternatively, we can impose constraints on the norm of a regularized solution[24] as suggested by Isakov and Wu[8] to specify a convergent regularization parameter. The trouble is that the right constraint on the norm of the exact solution is hard to acquire.

In this paper, we examine the performance of HELS using different expansion functions to reconstruct acoustic quantities generated by a speaker system that consists of a woofer, midranger, and tweeter in free space. Our previous studies have demonstrated that the reconstruction accuracy and efficiency of HELS are affected by the convergence rate of an expansion solution and condition number of the transfer matrix. The faster the convergence rate and the smaller the condition number are, the more efficient the numerical computations and the more accurate the HELS solutions become.

Needless to say, these factors depend on the choice of expansion functions. The objective of the present paper is to study the effects of various expansions on the resultant reconstruction and, more importantly, to identify the optimum expansion that can provide the best accuracy and efficiency of reconstruction. Specifically, we consider three expansions: LSW, DSW, and DPS in HELS to reconstruct acoustic quantities for frequencies up to 3275 Hz. Moreover, we employ TR and its modification plus damped singular value decomposition (DSVD) (Ref. 25) in regularization with the regularization parameters determined by various error-free PCMs such as generalized cross validation (GCV),[26] L-curve criterion,[27] and quasioptimality criterion (QOC).[28] Reconstructed acoustic quantities are validated with respect to benchmark data measured at the same locations as the reconstruction points.

Finally, we investigate the impact of measurement number on the resultant reconstruction accuracy of HELS using LSW, DSW, and DPS, respectively. The results of this comprehensive study are expected to provide a better understanding of HELS and gain an insight in selecting the optimal combinations of expansion functions, regularization strategies, and PCMs that will yield satisfactory reconstruction of acoustic radiation from an arbitrary source in free space in the most cost-effective manner.

II. HELS METHOD

We consider the complex amplitude u of a time-harmonic acoustic pressure that satisfies the Helmholtz equation and Sommerfeld radiation condition in the exterior of a vibrating object D in a free field

$$\nabla^2 u + k^2 u = 0, \tag{1}$$

$$\lim_{r\to\infty} r\left(\frac{\partial}{\partial r} - ik\right)u = 0, \tag{2}$$

where $r=|\mathbf{x}|$ for $\mathbf{x}$ in the exterior of D, $k=\omega/c$ is the acoustic wave number with ω being the angular frequency and c being the speed of sound of the fluid medium, i is the imaginary unit, and the origin of coordinates is chosen in D. In what follows, we refer to the complex amplitude of the acoustic pressure u as acoustic pressure for short.

The problem of reconstruction[29,8] is to describe u on a surface S that contains D based on the knowledge of the values of u specified on a sufficiently smooth surface Γ that encloses both S and D. Here, we refer to Γ as the measurement surface and the distance between Γ and S as the stand-off distance.

Let $\psi_j(\mathbf{x};\omega)$, $j=1,2,...$, be the system of functions that satisfies the Helmholtz equation (1) and Sommerfeld radiation condition (2). Let $\{\psi_j(\mathbf{x};\omega)\}_{j=1}^{\infty}$ be complete in $L^2(\Gamma)$, i.e., for any w in $L^2(\Gamma)$ and any $\varepsilon>0$, there is a $J=J(\varepsilon)$ and a set of coefficients $\{C_j^{(J)}\}_{j=1}^{J}$ such that

$$\int_\Gamma \left| w - \sum_{j=1}^{J} C_j^{(J)}\psi_j \right|^2 d\sigma < \varepsilon^2, \tag{3}$$

where $d\sigma$ denotes a surface element. Also, we require $\{\psi_j(\mathbf{x};\omega)\}_{j=1}^{\infty}$ to be linearly independent in $L^2(\Gamma)$. The com-

pleteness of $\{\psi_j(\mathbf{x};\omega)\}_{j=1}^{\infty}$ assures that any solution to the Helmholtz equation can be approximated in the mean-square sense on Γ by a superposition of $\psi_j(\mathbf{x};\omega)$, while its linear independence guarantees that the resultant matrix is of a full rank. Note that the latter does not imply good conditioning of a matrix.

In HELS, the solution u to Eq. (1) subject to condition (2) is approximated by a linear combination of the expansion functions $\psi_j(\mathbf{x};\omega)$

$$u_J(\mathbf{x};\omega)=\sum_{j=1}^{J} C_j^{(J)}\psi_j(\mathbf{x};\omega), \tag{4}$$

where $\psi_j(\mathbf{x};\omega)=h_n^{(1)}(kr)P_n^m(\cos\theta)e^{im\varphi}$, where $h_n^{(1)}(kr)$ are the first kind of the spherical Hankel functions of order n, $P_n^m(\cos\theta)$ are the associated Legendre functions, and the indices j, n, and m are governed by $j=n^2+n+m+1$, with n starting from 0 to N and m varying from $-n$ to $+n$. Therefore, for each n and m we have $j=1$ to J, where J implies the maximum number of expansion terms $J=(N+1)^2$.

The unknown coefficients $\xi=[C_1^{(J)},\ldots,C_J^{(J)}]^T$ can be specified by minimizing the least-squares error between the approximated solution (4) and the acoustic pressures measured on Γ

$$\xi=\arg\min\int_{\Gamma}|u-u_J|^2 d\sigma. \tag{5}$$

In general, the coefficients $C_j^{(J)}$ change with the number of expansion terms J. Since the value of J that can lead to a desired accuracy in reconstruction depends on the source geometry, type of expansion functions, measured data, and noise embedded in the input data, it is impossible to guess the smallest admissible number of expansion terms in (4).

Let $\{\mathbf{x}_m^{\Gamma}\}_{m=1}^{M}$ be a mesh on Γ and $\{\mathbf{x}_p^{S}\}_{p=1}^{P}$ be a mesh on S, where M, $P\geqslant J$. Then, using the following matrix notation, we can write:

$$[\Phi_{\Gamma}]_{mj}=\psi_j(\mathbf{x}_m^{\Gamma};\omega),\quad m=1,...,M;\quad j=1,...,J; \tag{6a}$$

$$[\Phi_S]_{pj}=\psi_j(\mathbf{x}_p^{S};\omega),\quad p=1,...,P;\quad j=1,...,J, \tag{6b}$$

and approximate the integral in (5) by the following discrete weighted least-squares problem:

$$\xi=\arg\min\|W_{\Gamma}(\Phi_{\Gamma}\xi-u_{\Gamma}^{M})\|_2^2, \tag{7}$$

where $u_{\Gamma}^{M}=[u(\mathbf{x}_1^{\Gamma}),\ldots,u(\mathbf{x}_M^{\Gamma})]^T$, W_{Γ} represents an $M\times M$ nonsingular diagonal weight matrix whose elements are determined by the quadrature formula and the mesh on Γ.

An unregularized solution of (7) can be written as the pseudoinverse[30] of Φ_{Γ} denoted by $\Phi_{\Gamma}^{+}:\tilde{\xi}=\Phi_{\Gamma}^{+}u_{\Gamma}^{M}$. Accordingly, the unregularized acoustic pressure on S is expressible through a matrix multiplication

$$\tilde{u}_{J,S}^{P}=\Phi_S\Phi_{\Gamma}^{+}u_{\Gamma}^{M}, \tag{8}$$

where $\Phi_S\Phi_{\Gamma}^{+}$ implies a $P\times M$ pressure-to-pressure transfer matrix of rank J. The reconstructed acoustic pressure given by (8) can be rewritten in terms of a reduced SVD (Ref. 31) of the transfer matrix $\Phi_S\Phi_{\Gamma}^{+}$

$$u_{J,S}^{P}=\sum_{j=1}^{\mathrm{rank}(\Phi_S\Phi_{\Gamma}^{+})}\frac{\hat{v}_{l,j}^{*}u_{\Gamma}^{M}}{\sigma_j}\hat{u}_{r,j}, \tag{9}$$

where $\hat{v}_{l,j}$ and $\hat{u}_{r,j}$ are the left and right singular vectors of $\Phi_S\Phi_{\Gamma}^{+}$, respectively, σ_j are nonzero singular values, and an asterisk denotes a conjugate transpose.

Ill-posedness of a reconstruction problem is reflected in the ill conditioning of the transfer matrix. It is seen from Eq. (9) that a small singular value σ_j can ruin the reconstructed acoustic pressure $u_{J,S}^{P}$ because any noise in the input data can be greatly amplified. Thus, the solution by pseudoinverse (8) is of little use because in practice the measured data are always incomplete and inaccurate. Accordingly, when expansion (4) is used to project the acoustic pressure from the measurement surface Γ toward a source surface S, it must be regularized.[8] In this paper, we use TR (Refs. 19, 24) to write ξ as a minimizer of a smoothing functional

$$\xi=\arg\min\left\{\int_{\Gamma}|u-u_J|^2 d\sigma+\lambda^2\int_S[|u_J|^2+|\partial_v u_J|^2]d\sigma\right\}, \tag{10a}$$

where $\lambda>0$ is a regularization parameter and its integral multiplier represents a penalty imposed on both the reconstructed acoustic pressure and normal velocity, namely, the energy norm of the solution.[32] It has been shown that imposing a penalty on the reconstructed acoustic pressure alone leads to a severe oversmoothing, and that on the reconstructed normal surface velocity alone, tends to be less oversmoothing, but that on both of these quantities yields an optimal reconstruction.[33]

A discrete version of (10a) can be written in the following form:

$$\xi=\arg\min\left\{\|W_{\Gamma}(\Phi_{\Gamma}\xi-u_{\Gamma}^{M})\|_2^2+\lambda^2\left\|W_S\begin{bmatrix}\Phi_S\\ \Psi_S\end{bmatrix}\xi\right\|_2^2\right\}, \tag{10b}$$

where $u_{\Gamma}^{M}=[u(\mathbf{x}_1^{\Gamma},\omega),\ldots,u(\mathbf{x}_M^{\Gamma},\omega)]^T$, W_S denotes a $P\times P$ nonsingular diagonal weight matrix whose elements depend on the quadrature formula and the mesh on S, and Ψ_S implies a normal derivative of $\psi_j(\mathbf{x}_p^{S};\omega)$, which is given by $[\Psi_S]_{pj}=\partial_v\psi_j(\mathbf{x}_p^{S};\omega)$, $p=1,...,P$, $j=1,...,J$.

For simplicity, we implement TR through the filter factors and generalized singular value decomposition (GSVD) (Ref. 25) of a matrix pair (A,L), where $A=W_{\Gamma}\Phi_{\Gamma}$ and $L=W_S\left[\begin{smallmatrix}\Phi_S\\ \Psi_S\end{smallmatrix}\right]$. The filter factors f_j are expressed in terms of the generalized singular values γ_j

$$f_j^{\mathrm{TR}}=\frac{\gamma_j^2}{\gamma_j^2+\lambda^2},\quad j=1,...,J. \tag{11}$$

A modification of Tikhonov filter factors, which gives less filtering, is referred to as the damped singular value decomposition (DSVD)[25]

$$f_j^{\mathrm{DSVD}}=\frac{\gamma_j}{\gamma_j+\lambda},\quad j=1,...,J. \tag{12}$$

Note that GSVD of (A,L) can be obtained from SVD of a corresponding matrix quotient AL^{+} by permutations. How-

ever, the resultant computational accuracy will depend on the condition number of the penalty matrix L and will be accurate only if L is well-conditioned.[34] Due to nonminimality of a system of expansion functions, we can expect L to be ill conditioned[35] for most reconstruction surfaces. Therefore, we should avoid computing GSVD by applying SVD to AL^{+}. A more efficient way of solving Eq. (10b) may be to use Elden's bidiagonalization,[36] rather than the filter factors at all.

Since the penalty matrix $L=W_S\left[\begin{smallmatrix}\Phi_S\\ \Psi_S\end{smallmatrix}\right]$ has more rows than columns with a full column rank, we may use a QR factorization first for $L=Q_L R_L$, and then calculate GSVD of the matrix pair (A,L), instead of calculating GSVD of (A,L) directly.

The regularization parameter λ in Eq. (10b) can be determined by one of the following error-free PCMs: GCV,[26] L-curve criterion,[27] and QOC.[28]

In GCV, the regularization parameter λ is obtained by minimizing the GCV function[26]

$$G(\lambda)=\frac{\|A\xi_\lambda-u_M^\Gamma\|_2^2}{[\mathrm{trace}(I_M-AA^{\#})]^2}, \tag{13a}$$

where $A^{\#}$ denotes the regularized pseudoinverse of A that produces ξ_λ, and I_M represents an $M\times M$ identity matrix.

The regularization parameter in QOC is obtained by minimizing the following function:[28]

$$Q(\lambda)=\lambda\left\|\frac{d\xi_\lambda}{d\lambda}\right\|_2. \tag{13b}$$

The L-curve criterion[27] is based on a parametric plot of the norm of a regularized solution $\|A\xi_\lambda-u_M^\Gamma\|_2$ versus the residual norm $\|L\xi_\lambda\|_2$ in a log–log scale with respect to λ. The corner of the L-curve (which is defined as a point of maximum curvature) separates the horizontal part (where regularization errors dominate) from the vertical part (where perturbation errors dominate), and thus represents a balance between the regularization and perturbation errors.

Once the regularization parameter is specified, the least-squares problem (10b) is solved and the expansion coefficients $C_j^{(J)}$ are determined. Obviously, the values of $C_j^{(J)}$ will depend on the number of expansion terms J and mesh sizes M and P. If Γ is sufficiently smooth and the mesh on Γ consists of equally spaced nodes using a rectangular rule in discretization, the weight matrix W_Γ is a constant multiple of an identity matrix and can be omitted. Further, if TR process is omitted, then Eq. (10b) reduces to the original HELS formulation.[7]

It is emphasized that if the nodes $\{\mathbf{x}_m^\Gamma\}_{m=1}^M$ are selected arbitrarily, the weight matrix W_Γ in Eq. (10b) cannot be omitted. To the best of the authors' knowledge, only the rectangular rule in discretization has been used with the least-squares method in reconstruction and scattering.

Using the notation defined in (10b), we can now write the reconstructed acoustic pressure on the source surface S as $u_{J,S}^P=\Phi_S\xi$, where $u_{J,S}^P=[u_J(\mathbf{x}_1^S,\omega),\ldots,u_J(\mathbf{x}_P^S,\omega)]^T$.[37,38]

III. CHOICE OF EXPANSION

In this section, we consider three expansions in HELS: LSW,[11] DSW,[12] and DPS,[13] all of which satisfy the Helmholtz equation and Sommerfeld radiation condition, and are complete and linearly independent in $L^2(\Gamma)$ for any sufficiently smooth Γ.

It is noted[11] that completeness can be proved for yet another system of functions, namely, the quasiplane waves. However, these quasiplane waves are difficult to compute; thus, they are excluded from our considerations.

In LSW, an approximate solution to the Helmholtz equation can be written as[11,39]

$$u_J(\mathbf{x};\omega)=\sum_{n=0}^{N}\sum_{m=-n}^{n}a_{nm}h_n^{(1)}(kr)P_n^{|m|}(\cos\theta)e^{im\varphi}, \tag{14}$$

where a_{nm} represent the expansion coefficients, (r,θ,ϕ) are the spherical coordinates of a point $\mathbf{x}=(x_1,x_2,x_3)$, N is an expansion order, and the total number of expansion terms is $J=(N+1)^2$. The auxiliary source for LSW is located at the origin of coordinate system.

Equation (14) shows that LSW is very similar to the original expansion in Eq. (4), except the index $|m|$ in the associated Legendre functions is always positive. From the definition of the associated Legendre functions,[40] we see that the functions with a negative index m differ only by a constant from the corresponding functions with a positive index m, which can be absorbed by the expansion coefficients a_{nm}. Hence, LSW is actually the same as the expansion in (4).

The auxiliary sources in DSW can be distributed on an auxiliary surface conformal to the boundary of D from the inside or on an axis of symmetry of D. For simplicity, we consider the latter with the z axis as the axis of symmetry on which $n_{\max}$ auxiliary sources are selected[12]

$$z_n=z_0\cos\beta_n,\quad n=1,\ldots,n_{\max}, \tag{15}$$

where z_0 is chosen such that all the sources are located in D (some of them may be close to the boundary of D), and $\beta_n=(\pi/2n_{\max})+([\pi(n-1)]/n_{\max})$, $n=1,\ldots,n_{\max}$.

The spherical coordinates of any point with respect to the z_nth auxiliary source $x-z_ne_3$, which are denoted by (r_n,θ_n,φ), can be expressed in terms of either the rectangular (x_1,x_2,x_3) or spherical (r,θ,φ) coordinates

$$r_n^2=x_1^2+x_2^2+(x_3-z_n)^2=r^2\sin^2\theta+(r^2\cos^2\theta-z_n)^2, \tag{16a}$$

$$\sin^2\theta_n=\frac{x_1^2+x_2^2}{r_n^2}=\frac{r^2\sin^2\theta}{r_n^2}. \tag{16b}$$

An approximate solution to the Helmholtz equation in DSW (Ref. 12) is then expressible as

$$u_J(\mathbf{x};\omega)=\sum_{n=1}^{n_{\max}}\sum_{m=-m_{\max}}^{m_{\max}}b_{nm}h_{|m|}^{(1)}(kr_n)P_{|m|}^{|m|}(\cos\theta_n)e^{im\varphi}, \tag{17}$$

where b_{nm} are the expansion coefficients, $n_{\max}$ is the number of auxiliary sources, and $m_{\max}$ is the order of expansion. The total number of expansion terms is $J=n_{\max}(2m_{\max}+1)$.

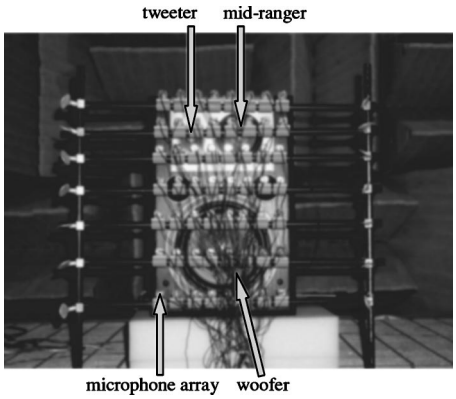

FIG. 1. An array of 56 microphones in front of a JBL speaker system.

Comparing Eq. (17) to Eq. (14) shows that DSW spreads an expansion with respect to several points rather than a single point as LSW does. This may give DSW certain special advantages in reconstructing acoustic quantities on an elongated body when auxiliary sources are distributed along the axis of elongation of the body, or on an arbitrary surface when the auxiliary sources are distributed over a conformal surface from the inside.

In DPS, the auxiliary sources are selected as a set of point sources $\{\mathbf{x}_j\}_{j=1}^{J}$ distributed on a sufficiently smooth surface inside D but close to its boundary.[13] Accordingly, we can express an approximate solution to the Helmholtz equation as

$$u_J(\mathbf{x};\omega)=\sum_{j=1}^{J} c_j h_0^{(1)}(k|\mathbf{x}-\mathbf{x}_j|), \tag{18}$$

where c_j are the expansion coefficients, J is the number of point sources, and $h_0^{(1)}(k|\mathbf{x}-\mathbf{x}_j|)$ is a fundamental solution to the Helmholtz equation.

These three expansions are adopted in HELS to reconstruct the acoustic quantities on the surface of a vibrating object in free space. The results thus obtained are validated with respect to the benchmark values measured at the same locations as the reconstruction points.

IV. EXPERIMENTAL SETUP

To examine the performance of HELS using these expansions, we conducted experiments on reconstructing acoustic radiation from a JBL® speaker that consisted of a woofer, midranger, and tweeter. This speaker system was driven by an HP 8904A multifunction synthesizer dc-600 kHz and McIntosh MC352 power amplifier to produce white noise inside a fully anechoic chamber in the Acoustics, Vibration, and Noise Control Laboratory at Wayne State University. The acoustic pressures were measured by an array of 56 PCB T130D21 free-field microphones (see Fig. 1). The input data were transferred to a personal computer through the Larson Davis digital sensor system model 100 for analog to digital conversion. All data acquisition and postprocessing were controlled by the computer.

The experimental procedures were as follows. First, the radiated acoustic pressures on a planar surface Γ_1 at 1-cm clearance in front of the speaker were measured. These data

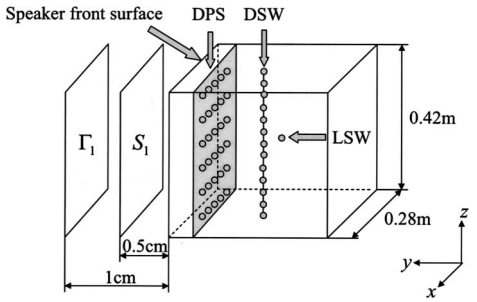

FIG. 2. Schematic of the experiment measurement locations in front of the speaker box.

were taken as input to HELS using LSW, DSW, and DPS, respectively, to reconstruct the acoustic pressures on a surface S_1 at 0.5-cm clearance in front of the speaker up to 3275 Hz (see Fig. 2). Next, the reconstructed acoustic pressures on S_1 were compared with those measured at the same locations as the reconstruction points for validation purpose. The measurement points on Γ_1 and S_1 were equidistant, and the origin of the coordinate system was set at the geometric center of the speaker. In particular, the auxiliary source for LSW was placed inside the speaker, those for DSW were distributed along a vertical axis between the front surface and center of the speaker box, and those for DPS were distributed on a plane next to the front surface of the speaker.

For simplicity yet without loss of generality, we only consider reconstruction of acoustic radiation from the speaker front surface. Accordingly, we set the characteristic dimension $a=\sqrt{(0.28/2)^2+(0.42/2)^2}=0.28$ m as the characteristic dimension. Thus, for a frequency range of 200 to 3275 Hz, the dimensionless acoustic wave number was from $ka\approx 1.0$ to 16.6, where the speed of sound in the air at room temperature was $c=344$ m/s and the density of the air $\rho=1.16$ kg/m^3.

From Eq. (14) we learn that the total number of expansion terms for LSW is $J=(N+1)^2$, where N is the order of expansion determined by the highest frequency of interest. In general, we may set $N=(ka)_{\max}\approx 17$, so $J=324$. Hence, we need at least 324 measurements on Γ_1 to cover the specified frequency range. In practice, we may have to truncate an expansion to reduce distortion caused by a low S/N. In this experiment, we set $N=9$, so $J=100$.

The number of expansion terms in DSW is $J=n_{\max}(2m_{\max}+1)$, where $n_{\max}$ is the number of auxiliary sources, and $m_{\max}$ is the order of expansion, which is smaller than N in LSW. There are no known theories or methodologies that we can utilize to estimate the optimum values of $n_{\max}$ and $m_{\max}$ for an arbitrarily shaped object. In general, the values of $n_{\max}$ and $m_{\max}$ depend on the complexities of source geometry and the highest frequency of interest. To achieve the best result, it may be a good idea to set distances among neighboring auxiliary sources to be less than one wavelength of the highest frequency of interest and distribute the auxiliary sources evenly on a conformal surface inside the source boundary. For example, the front surface of the speaker is a plane of 0.28×0.42 m^2, the highest frequency is $f_{\max}=3275$ Hz, its wavelength is $\lambda_{\min}\approx 0.104$ m, so $n_{\max}=(0.28/0.104)\times(0.42/0.104)\approx 11$. In this experiment we set $m_{\max}=4$, so the number of expansion terms is $J=99$. There-

fore, we need to take about 100 measurements of the acoustic pressures on Γ_1 to guarantee satisfactory reconstruction over the specified frequency range.

In DPS, the auxiliary sources are distributed uniformly on a surface conformal to a source boundary from the inside. However, as in the case of DSW, the optimal number and locations of these auxiliary sources are unknown *a priori*; their determination is a topic of research by itself and will not be considered here. Since the front surface of the speaker is planar, it is sufficient to distribute the auxiliary sources on a plane and set $J=n_x n_z$, where n_x and n_z are the numbers of sources in the x- and z directions, respectively. Here, we set $n_x=10$ and $n_z=10$, so $J=100$.

In this experiment, 112 measurements of the acoustic pressures were taken on Γ_1 and S_1, respectively, which were close to the estimated numbers of measurements for LSW, DSW, and DPS. It is emphasized that the number of measurement points may not be as critical as it seems. The controlling factor is S/N value. If S/N is low, there is no way of getting good reconstruction no matter how many measurements are taken.

In Sec. V, we examine the effects of locations of auxiliary sources, condition numbers of the transfer matrices in HELS, number of measurements, and regularization scheme and PCM on the resulting accuracy in reconstruction.

V. RESULTS AND DISCUSSIONS

A. Locations of the auxiliary sources

Selection of the auxiliary source locations can be crucial to the success of reconstruction. Although there is no known theory that can depict exactly the inter-relationship between locations of auxiliary sources and rate of convergence of resultant expansion and reconstruction accuracy, the following guideline is clear: The analytic continuation of solution to the Helmholtz equation requires that the surface on which auxiliary sources are distributed must enclose all singularities of an acoustic field.[11]

However, the singularities for a given acoustic field are unknown *a priori*. To circumvent this difficulty in studying the effect of an auxiliary surface location, we start from an arbitrarily selected auxiliary surface, and measure acoustic pressures on surfaces Γ_1 and S_1, respectively. Then, we substitute the data measured on Γ_1 to Eq. (10b) to reconstruct acoustic pressures on S_1, and calculate mean relative errors in reconstruction with respect to the benchmark data on S_1. Next, we move the auxiliary surface to a different location, reconstruct the acoustic pressures on S_1, and calculate the mean relative errors of reconstruction with respect to those measured on S_1 again. Note that there is no need to remeasure acoustic pressures on S_1. This process is repeated until mean relative errors in reconstruction are minimized, which leads to the optimal location of an auxiliary surface for a given frequency and a set of measurements.

It is emphasized that in practice we only measure acoustic pressures on a surface Γ_1. The reason for taking an additional set of measurements on S_1 is to develop a guideline for selecting an optimal location of an auxiliary surface for a specific expansion function. Needless to say, the impact of an auxiliary surface location for different expansions is different. Hence, by taking an independent set of measurements on S_1, we can validate the reconstructed acoustic pressures, determine the optimal location of an auxiliary surface for a given expansion function, and study the sensitivity of the auxiliary surface on the reconstruction accuracy using this expansion.

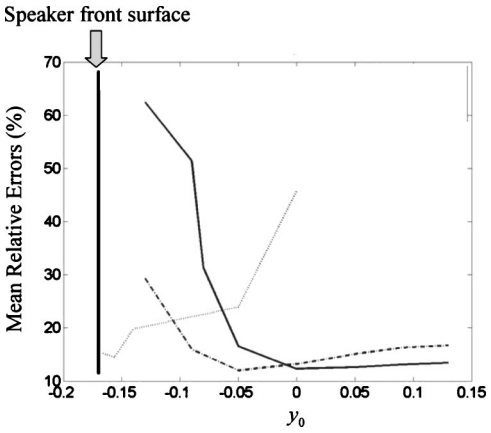

FIG. 3. Comparison of the auxiliary surface locations at 1690 Hz. ——— for LSW; -·- DSW; and ··· DPS.

Figure 3 depicts the mean relative errors in reconstructing acoustic pressures on S_1 using LSW, DSW, and DPS, respectively, with respect to auxiliary sources located on a plane $y=-y_0$, where y_0 varies from -0.17 to 0.13 m, at a fixed frequency 1690 Hz. In particular, the auxiliary sources are uniformly distributed on a plane for DPS, along a line for DSW, and at a single point for LSW. The results show that DSW is relatively insensitive to the auxiliary surface locations as compared to LSW and DPS. At the optimum auxiliary surfaces, LSW and DSW yield nearly the same level of accuracy in reconstruction, whereas DPS produces a slightly lower accuracy in reconstruction.

It is interesting to observe that LSW places its optimum location of an auxiliary surface near the origin of the coordinate system, DSW moves its optimum auxiliary surface away from the origin of the coordinate system toward the front surface, and DPS puts its optimum auxiliary surface right behind the front surface of the speaker system.

Note that the stand-off distance and frequency can also affect the reconstruction accuracy. However, their effects are negligibly small as compared to those of an auxiliary source surface location. Hence, we focus on the determination of optimal locations of auxiliary source surfaces by minimizing the mean relative errors in reconstruction with respect to an independent set of measurements on S_1.

B. Condition number of the transfer matrices

Reconstruction of acoustic radiation from any source is an ill-posed problem. As a result, the transfer matrix in HELS may be ill conditioned. Ill conditioning of any matrix is measured by the 2-norm condition number, defined as the ratio of the largest to smallest singular values of the matrix.[25] This can be done prior to taking any measurements, if the frequency and measurement and reconstruction locations are specified. In many cases, if the condition number is of the

order of $O(10^3)$ or higher, the matrix may be ill conditioned; if the condition number is of the order of $O(10^2)$ or lower, the matrix is more or less well conditioned. Regularization may be omitted if a transfer matrix is well conditioned, but must be implemented if the matrix is ill conditioned.

In our experiments, the condition numbers of the transfer matrices for a selected stand-off distance and frequency are as follows: $O(10)$ for DSW, $O(10^2)$ to $O(10^3)$ for LSW, and $O(10^5)$ for DPS. Therefore, for the same frequency and measurement and reconstruction locations, DSW provides the best-conditioned transfer matrix among all three expansions. This is expected because DSW uses a lower-order spherical Hankel function ($m_{\max}=4$) than LSW does ($N=9$). The small singular values are always associated with high-order terms, and the condition number of a transfer matrix containing the high-order terms is much larger than that of a transfer matrix containing the low-order terms. The reason DPS produces an ill-conditioned transfer matrix may be attributed to the fact that the sound field produced by the present speaker system cannot be adequately described by a distribution of point sources. Consequently, the resultant transfer matrix in DPS becomes rank deficient and ill conditioned.

From the condition numbers of the transfer matrices, we see that regularization is needed for DPS and LSW, but unnecessary for DSW. Note that condition numbers are calculated before measurements are taken; hence, no information on noise level in the input data is available. As a result, we have to resort to an error-free PCM in regularization.

One of our main objectives in this paper is to examine the performance of HELS by using various expansions to reconstruct acoustic radiation from an arbitrary source. To this end we first calculate an ideal regularization parameter by minimizing reconstruction error with respect to the benchmark data on S_1. This benchmark solution allows for assessing not only the reconstruction accuracy, but also the impact of reducing measurement number on reconstruction using various expansions. This latter is of great importance since in practice fewer measurements mean bigger savings in costs and manpower.

C. Effect of measurement number

The effect of the number of measurements on reconstruction accuracy is examined in this section. Figures 4–6 depict the mean relative errors in reconstructing the acoustic pressure using LSW, DSW, and DPS, respectively, based on different numbers of measurements. Apparently, in this frequency range the more the measurements are taken, the higher the accuracy of regularized reconstruction becomes. This is usually true when the S/N in the measured data is high.

Secondly, regularization can significantly enhance the reconstruction accuracy, especially at higher frequencies. This is obvious in Figs. 4 and 6 since the transfer matrices for LSW and DPS are ill conditioned. However, the impact of regularization on reconstruction accuracy for DSW is not as drastic (see Fig. 5), because its transfer matrix is more or less well conditioned. Note that we have used ideal regularization parameters for all three expansions to maximize this

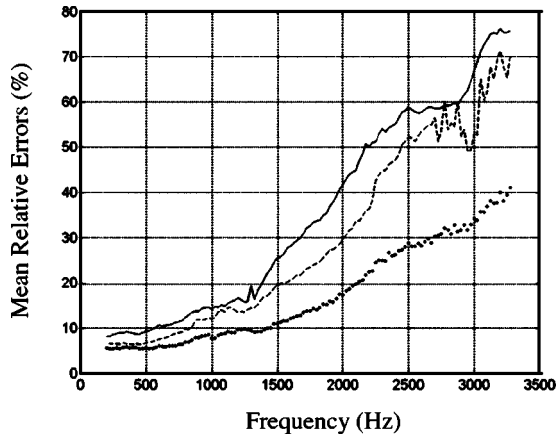

FIG. 4. Comparison of the mean relative errors in reconstructing acoustic pressures by LSW. ——— 56 measurements with an ideal regularization parameter; --- 112 measurements with no regularization; ··· 112 measurements with an ideal regularization parameter.

effect. The calculated regularization parameters for LSW and DPS increased monotonically with frequency from 0.002 to 0.05, whereas it remained negligibly small at 0.0008 for DSW. This implied that there was almost no need for regularization in DSW within this frequency range.

Thirdly, results show that even with an ideal regularization parameter, DPS failed to yield a compatible level of accuracy with DSW and LSW under the same set of input data. Moreover, DPS is more sensitive to PCM than DSW and LSW are.

Finally, it is important to mention that for ill-conditioned transfer matrices, increasing the numbers of measurements and expansion terms in HELS without implementing regularization will only increase distortions in reconstruction. This is seen in DPS expansion. As the number of measurements was doubled, the mean relative errors in nonregularized reconstruction exceeded 200% (the corresponding curve was omitted in Fig. 5 for clarity). The reason for that was that the high-order terms in DPS expansion were contaminated by noise embedded in measured data, and these disturbances were significantly amplified as the acoustic pressures were

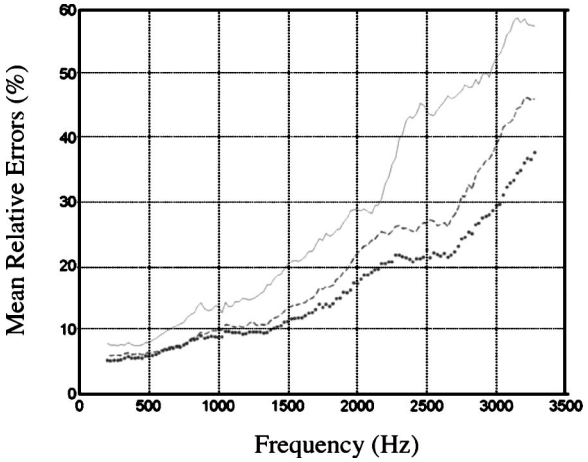

FIG. 5. Comparison of the mean relative errors in reconstructing acoustic pressures by DSW. ——— 56 measurements with an ideal regularization parameter; --- 112 measurements with no regularization; ··· 112 measurements with an ideal regularization parameter.

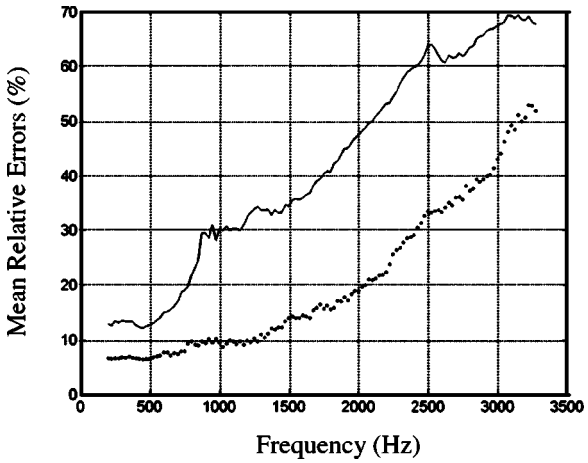

FIG. 6. Comparison of the mean relative errors in reconstructing acoustic pressures by DPS. ——— 56 measurements with an ideal regularization parameter; ··· 112 measurements with an ideal regularization parameter.

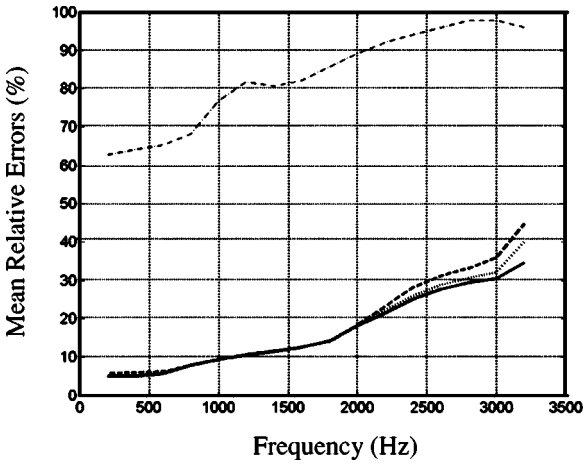

FIG. 7. Comparison of the mean relative errors in reconstructing acoustic pressures using LSW in HELS with TR and various error-free PCM. -·- QOC; --- L-curve; ··· GCV; ——— ideal case.

projected back toward a source surface. When the transfer matrix is not very highly ill conditioned, as in LSW, increasing the measurement number can improve reconstruction accuracy up to certain frequency without regularization (see Fig. 4). When the transfer matrix is more or less well conditioned, for example, in DSW, increasing the measurement number allows for an increase in the number of expansion terms, which can enhance the reconstruction accuracy even without regularization (see Fig. 5).

D. Choice of regularization

In many engineering applications, the noise level embedded in the input data is unknown *a priori*. Thus, we must rely on an error-free PCM in regularization. In this study, we want to find out if there exists an optimal regularization with an error-free PCM for each of DSW, LSW, and DPS expansions in HELS. To this end, we examine performances of all possible combinations of TR and its modification implemented through GSVD and DSVD, together with various penalty functions with respect to pressure, normal velocity, or both, and error-free PCM such as GCV, L-curve, and QOC to select the best regularization parameter. It is seen that for some expansions, it is possible to find the optimal regularization with an error-free PCM that can produce an almost ideal regularization parameter over a wide frequency range, but for other expansion such optimal combinations are not possible. For brevity, we summarize the most important results here.

(1) The optimal regularization for DSW is modified TR implemented by DSVD, and the best regularization parameter can be provided by L-curve together with an energy norm as its penalty function.

(2) The optimal regularization for LSW is TR implemented by GSVD with its regularization parameter determined by GCV and with an energy norm as its penalty function. Depicted in Fig. 7 is a comparison of the mean relative errors in reconstruction using LSW and TR, with its regularization parameter determined by different error-free PCMs. It is clear that the regularization parameter given by GCV is almost identical to the ideal value over the specified frequency range, that provided by L-curve is close to an ideal one, but those produced by QOC are way off the target. Figure 8 indicates the regularization parameters given by GCV, L-curve, and QOC for TR in LSW versus the frequency. Results illustrate that GCV yields nearly the ideal regularization parameters, L-curve gives a regularization parameter close to the ideal one, but the regularization parameter provided by QOC is off by at least two orders of magnitude of an ideal value.

(3) For DPS, it is not possible to find one regularization scheme that can produce satisfactory reconstruction over a wide frequency range. In fact, we must utilize different combination of regularization, penalty function, and error-free PCM to select an optimal regularization parameter for different frequency.

Figure 9 summarizes the results of this investigation on optimal choices of regularization schemes for DSW, LSW, and DPS expansions in HELS. Comparing Fig. 9 with Figs. 4 and 5 reveals that using the optimal regularization schemes, for example, TR implemented by DSVD with its regulariza-

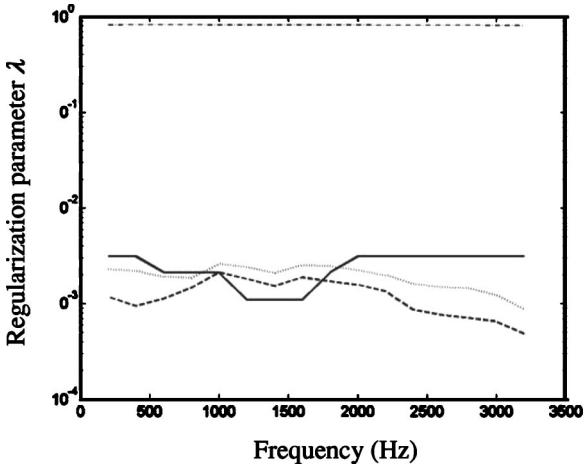

FIG. 8. Comparison of regularization parameters calculated by various error-free PCMs for reconstruction of the acoustic pressure using LSW in HELS. -·- QOC; --- L-curve; ··· GCV; ——— ideal case.

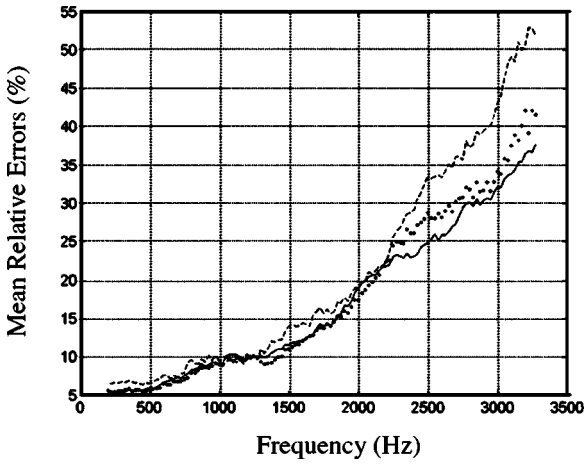

FIG. 9. Comparison of the mean relative errors in reconstructing the acoustic pressure with regularization. ——— DSW using DSVD and L-curve; ··· LSW using TR and GCV; --- DPS using TR and GCV.

tion parameter determined by L-curve for DSW, and TR with its regularization parameter determined by GCV for LSW, we can get the same level of reconstruction accuracy as that produced by ideal regularization. On the other hand, when we rely on a single regularization scheme, for example, TR and GCV for DPS, the mean relative reconstructions errors can be very large, especially at higher frequencies. This can be seen by comparing the mean relative errors in Fig. 9 with those in Fig. 5.

It must be emphasized that there is no single regularization strategy that can yield the best reconstruction for all sources under all circumstances. For example, although TR and DSVD plus L-curve work well for DSW in the present case, it may not work well in a different scenario or in a different frequency range. The best regularization strategy is always case dependent. Also, we must keep in mind that an error-free PCM can fail to yield a convergent regularization parameter at all. On the other hand, it is always advantageous to take double-layer measurements whenever possible. These double-layer measurements can help us to device optimal regularization schemes and produce the best reconstruction of the acoustic quantities.

VI. CONCLUSION

The performance of HELS using expansions of DSW, LSW, and DPS to reconstruct the acoustic pressures radiated from a general sound source is examined. The effects of locations of auxiliary surfaces for various expansions, regularization schemes together with error-free PCMs, and penalty functions on the resultant reconstruction accuracy are investigated.

Results show that DSW leads to the best-conditioned transfer matrix, is the least sensitive to choices of auxiliary surfaces locations, and yields the most satisfactory reconstruction over a wide frequency range. LSW is the next best choice of expansion for HELS, its transfer matrix may be weakly ill conditioned, and its optimal auxiliary source location is close to the geometric center of a source. If the optimal location for the auxiliary source is selected, LSW can yield nearly the same level of accuracy in reconstruction as DSW does. Moreover, it is possible to improve the reconstruction accuracy in LSW by increasing the measurements taken at very close range to the source surface, even without regularization. DPS gives a highly ill-conditioned transfer matrix and is very sensitive to an auxiliary surface location. The reason for that may be due to the fact that the acoustic pressure radiated from an arbitrary source may not be adequately described by a distribution of point sources. When DPS expansion is used in HELS, it is necessary to implement regularization in order to obtain a convergent reconstruction.

The optimal regularization for DSW is modified TR implemented by DSVD plus L-curve to determine a regularization parameter with an energy norm as its penalty function. The optimal regularization for LSW is TR implemented by GSVD plus GCV to determine its regularization parameter with an energy norm as its penalty function. There is no single optimal regularization scheme that can produce satisfactory reconstruction over a wide frequency range for DPS. In this case, different regularization schemes must be used at different frequencies in order to produce satisfactory reconstruction.

It is emphasized that, although it is possible to find the optimal regularization schemes for DSW and LSW, they may not hold in different scenarios or frequency regimes. In other words, there is no single regularization strategy that can guarantee good reconstruction for all sources under all conditions.

Finally, it is always a good idea to take double-layer measurements. Such measurements can help us to determine the optimal auxiliary surface location for particular expansion functions in HELS and to select the optimal regularization scheme that includes choosing penalty functions and error-free PCMs to yield the best regularization parameter.

ACKNOWLEDGMENTS

The authors would like to express sincere thanks to Mr. Manmohan Moondra for setting up the experiments and collecting all measurements. This work was supported by the NSF Grant CMS-0245587.

[1] N. Rayess and S. F. Wu, "Experimental validation of the HELS method for reconstructing the acoustic radiation from a complex vibrating structure," J. Acoust. Soc. Am. **107**, 2955–2964 (2000).
[2] E. G. Williams, B. H. Houston, P. C. Herdic, S. T. Raveendra, and B. Gardner, "Interior near-field acoustical holography in flight," J. Acoust. Soc. Am. **108**, 1451–1463 (2000).
[3] M. R. Bai, "Application of BEM (boundary-element method)-based acoustic holography to radiation analysis of sound sources with arbitrary shaped geometries," J. Acoust. Soc. Am. **92**, 533–549 (1992).
[4] T. Delillo, V. Isakov, N. Valdivia, and L. Wang, "The detection of the source of acoustical noise in two dimensions," SIAM (Soc. Ind. Appl. Math.) J. Appl. Math. **61**, 2104–2121 (2001).
[5] Z. Wang and S. F. Wu, "Helmholtz equation least-squares method for reconstructing the acoustic pressure field," J. Acoust. Soc. Am. **102**, 2020–2032 (1997).
[6] S. F. Wu, N. Rayess, and X. Zhao, "Visualization of acoustic radiation from a vibrating bowling ball," J. Acoust. Soc. Am. **109**, 2771–2779 (2001).
[7] S. F. Wu, "On reconstruction of acoustic pressure field using the Helmholtz equation least-squares method," J. Acoust. Soc. Am. **107**, 2511–2522 (2000).
[8] V. Isakov and S. F. Wu, "On theory and application of the Helmholtz

equation least-squares method in inverse acoustics,'' Inverse Probl. **18**, 1147–1159 (2002).
[9] I. P. Lysanov, ''Theory of the scattering of waves at periodically uneven surfaces,'' Sov. Phys. Acoust. **4**, 1–10 (1958).
[10] P. M. van den Berg, ''Reflection by a grating: Rayleigh methods,'' J. Opt. Soc. Am. **71**, 1224–1229 (1981).
[11] A. Doicu, Y. Eremin, and T. Wriedt, *Acoustic and Electromagnetic Scattering Analysis using Discrete Sources* (Academic, New York, 2000).
[12] Y. A. Eremin, ''Complete systems of functions for the study of boundary value problems in mathematical physics,'' Sov. Phys. Dokl. **32**, 635–637 (1987).
[13] V. D. Kupradze, ''On the approximate solutions of problems in mathematical physics,'' Suc. Math. Sci. **22**, 58–108 (1967).
[14] Y. I. Bobrovnitskii and T. M. Tomilina, ''General properties and fundamental errors of the method of equivalent sources,'' Acoust. Phys. **41**, 649–660 (1995).
[15] Y. A. Eremin, N. V. Orlov, and A. G. Sveshnikov, ''The analysis of complex diffraction problems by the discrete source method,'' Comput. Maths Math. Phys. **35**, 731–743 (1995).
[16] A. Wirgin, ''On Rayleigh's theory of sinusoidal diffraction gratings,'' Opt. Acta **27**, 1671–1692 (1980).
[17] T. Namioka, T. Harada, and K. Yasuura, ''Diffraction gratings in Japan,'' Opt. Acta **26**, 1021–1034 (1979).
[18] D. Agassi and T. F. George, ''Convergent scheme for light scattering from an arbitrary deep metallic grating,'' Phys. Rev. B **33**, 2393–2400 (1986).
[19] A. N. Tikhonov, ''Regularization of incorrectly posed problems,'' Sov. Math. Dokl. **4**, 1624–1627 (1963).
[20] H. Engl, M. Hanke, and A. Neubauer, *Regularization of Inverse Problems*, Mathematics and its Applications, Vol. 375 (Kluwer Academic, Dodrecht, 1996).
[21] M. Hanke and P. C. Hansen, ''Regularization methods for large-scale problems,'' Surv. Math. Ind. **3**, 253–315 (1993).
[22] A. B. Bakushinskii, ''Remarks on choosing a regularization parameter using the quasioptimality and ration criterion,'' Comput. Math. Math. Phys. **24**, 181–182 (1984).
[23] V. A. Morozov, ''On the solution of functional equations by the method of regularization,'' Sov. Math. Dokl. **7**, 414–417 (1966).
[24] A. N. Tikhonov and V. Y. Arsenin, *Solutions of Ill-posed Problems* (Winston Washington, D.C., Wiley, New York, 1977).
[25] P. C. Hansen, *Rank-deficient and Discrete Ill-posed Problems* (SIAM Monographs on Mathematical Modeling and Computation, SIAM, Philadelphia, PA, 1998).
[26] G. H. Golub, M. T. Heath, and G. Wabha, ''Generalized cross-validation as a method for choosing a good ridge parameter,'' Technometrics **21**, 215–223 (1979).
[27] C. L. Lawson and R. J. Hanson, *Solving Least-squares Problems* (Prentice-Hall, Englewood Cliffs, NJ, 1974).
[28] V. A. Morozov, *Methods for Solving Incorrectly Posed Problems* (Springer, New York, 1984).
[29] Y. I. Bobrovnitskii, ''The problem of vibration field reconstruction: Statement and general properties,'' J. Sound Vib. **247**, 145–163 (2001).
[30] G. H. Golub and C. F. Van Loan, *Matrix Computations* (The John Hopkins University Press, Baltimore, MD, 1996).
[31] L. N. Trefethen and D. Bau III, *Numerical Linear Algebra* (SIAM, Philadelphia, PA, 1997).
[32] J. T. Marti, *Introduction to Sobolev Spaces and Finite Element Solution of Elliptic Equations* (Academic, New York, 1986).
[33] T. Semenova, ''On the behavior of the Helmholtz equation least-squares method for acoustic radiation and reconstruction,'' Ph.D. dissertation, Department of Mechanical Engineering, Wayne State University, Detroit, MI, 2004.
[34] P. C. Hansen, ''Relations between SVD and GSVD of discrete regularization problems in standard and general form,'' Linear Algebr. Appl. **141**, 165–176 (1990).
[35] G. F. Crosta, ''Complete families and Rayleigh obstacles,'' J. Comput. Acoust. **9**, 611–622 (2001).
[36] L. Elden, ''Algorithms for the regularization of ill-conditioned least-squares problems,'' BIT **17**, 134–145 (1977).
[37] C. L. Lawson and R. J. Hanson, *Solving Least-Squares Problems* (Prentice-Hall, Englewood Cliffs, NJ, 1974).
[38] V. A. Morozov, *Methods for Solving Incorrectly Posed Problems* (Springer, New York, 1984).
[39] I. N. Vekua, ''On completeness of the system of methaharmonic functions,'' Dokl. Akad. Nauk SSSR **90**, 715–718 (1953).
[40] E. G. Williams, *Fourier Acoustics: Sound Radiation and Nearfield Acoustical Holography* (Academic, San Diego, 1999).

Krylov subspace iterative methods for boundary element method based near-field acoustic holography

Nicolas Valdivia[a] and Earl G. Williams
Code 7130, Naval Research Laboratory, Washington, DC 20375

(Received 29 June 2004; revised 15 October 2004; accepted 8 November 2004)

The reconstruction of the acoustic field for general surfaces is obtained from the solution of a matrix system that results from a boundary integral equation discretized using boundary element methods. The solution to the resultant matrix system is obtained using iterative regularization methods that counteract the effect of noise on the measurements. These methods will not require the calculation of the singular value decomposition, which can be expensive when the matrix system is considerably large. Krylov subspace methods are iterative methods that have the phenomena known as ''semi-convergence,'' i.e., the optimal regularization solution is obtained after a few iterations. If the iteration is not stopped, the method converges to a solution that generally is totally corrupted by errors on the measurements. For these methods the number of iterations play the role of the regularization parameter. We will focus our attention to the study of the regularizing properties from the Krylov subspace methods like conjugate gradients, least squares QR and the recently proposed Hybrid method. A discussion and comparison of the available stopping rules will be included. A vibrating plate is considered as an example to validate our results. [DOI: 10.1121/1.1841511]

PACS numbers: 43.40.Sk, 43.20.Rz, 43.40.Yq [MO] Pages: 711–724

I. INTRODUCTION

Near-field acoustic holography (NAH) is a technique that uses near-field measurements for the reconstruction of the acoustic field (pressure, normal velocity, and intensity). This technique has had a tremendous success analyzing sources with geometries which conform closely to one of the separable geometries of the acoustic wave equation. In particular, considerable work has been performed to analyze sources in planar, spherical, and cylindrical geometries.[1,2] The limitation on source geometry is eliminated by using a reconstruction process that is based on the boundary element method (BEM). The BEM is a numerical technique which uses an integral representation, to the solution of the governing equation, to produce the *Green's transfer* functions. These transfer functions relate the pressure measurements with the acoustic field. The solution to NAH is given by an inversion of the transfer functions by special *regularization* methods, which will reduce the effect of measurement errors. This methodology of NAH is called the inverse boundary element method (IBEM). The IBEM is broken into two classes, depending on the integral formulations: the direct formulations,[3–7] which spring from the Helmholtz–Kirchhoff integral equation (HIE), and the indirect formulations,[8–13] which manipulate the HIE and solve for a fictitious source distribution. The conventional technique uses these formulations to produce an *explicit representation* of the Green's transfer function, which requires the inversion of matrices. Later a new technique, which was implemented in Refs. 14–16, avoids these inversion of matrices using an implicit representation to the Green's transfer functions. The common implementation procedure of regularization, for all the previous formulations and representation techniques, is based on the calculation of the singular value decomposition (SVD). The calculation of the SVD considerably increases the computation time and storage requirements of the regularization method. As an alternative to these problems, regularization methods can be implemented via iterative procedures.

The classical iterative method for the solution of ill-posed problems is called Landweber (see Ref. 17) and was proposed in 1951. This method has been extensively used over the years,[18–20] although its convergence to the optimal solution is very slow. Efforts were made to accelerate Landweber iterations by Hanke in Ref. 21, which produced the so called ν-methods. More recently the use of some Krylov subspace iterative methods, like conjugate gradients,[22] has received most of the attention from the mathematical community. Conjugate gradients rapidly converge to the optimal regularization solution which is its most attractive property (see Ref. 23). This iterative method was successfully used for the solution to NAH (see Refs. 15 and 24), and it was found that the rapid convergence (attractive for the reduction of the computation time) will create difficulties for the development of a reliable stopping rule. Another important Krylov subpace iterative method is least squares QR (LSQR).[25] This particular iterative method is equivalent to conjugate gradients, with the advantage of producing an orthogonal basis at each iteration. This orthogonal basis is used for a recently proposed method called the hybrid method,[26] which implements an ''inner'' regularization at each iteration. The hybrid method combines the computational efficiency of iterative methods with reliable stopping rules.

We present in this paper a study of the regularization properties of the Krylov subspace iterative methods like conjugate gradients and LSQR. We will pay particular attention

[a]Electronic mail: valdivia@pa.nrl.navy.mil

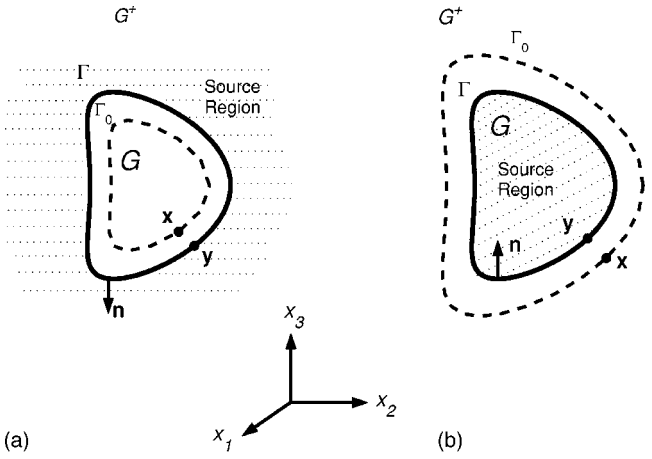

FIG. 1. Formulation for (a) interior NAH and (b) exterior NAH.

to LSQR since we will show that the orthogonal basis, which this method produces at each iteration, can be used to create a partial SVD. The partial SVD is used to explain the semi-convergence phenomena of Krylov subspace methods in the NAH problem. Similarly the partial SVD is a key element for the understanding of the recently proposed hybrid methods. There are several open questions about these methods, and perhaps the most relevant for us will refer to the proper ''inner'' regularization to be used with the partial SVD. Our study will be done for the explicit and implicit approaches as in Ref. 16.

II. BOUNDARY ELEMENT REPRESENTATION

Let G be a domain in $\mathbb{R}^3$, interior to the boundary surface Γ where we assume that Γ is allowed to have edges and corners. Similarly, we will denote as G^+ the region outside of G that shares the same boundary Γ. As shown by Fig. 1, in interior(exterior) NAH the acoustical sensors are placed on a surface Γ_0 inside (outside) the domain G. These are used to measure the pressure p and the fundamental problem is to recover the acoustic field (pressure, normal velocity, and normal intensity) on Γ.

For a time-harmonic ($e^{-i\omega t}$) disturbance of frequency ω the sound pressure p can be represented by the *direct formulation* (also known as the Helmholtz–Kirchhoff integral) for $\mathbf{x}=(x_1,x_2,x_3)\in G^+$ as

$$p(\mathbf{x})=(Dp)(\mathbf{x})-i\omega\rho(Sv)(\mathbf{x}) \quad \text{(exterior NAH)}, \tag{1}$$

or for $\mathbf{x}\in G$ as

$$p(\mathbf{x})=i\omega\rho(Sv)(\mathbf{x})-(Dp)(\mathbf{x}) \quad \text{(interior NAH)}, \tag{2}$$

where the operator notation S and D is used as in[27,28]

$$(S\phi)(\mathbf{x}):=\int_\Gamma \Phi(\mathbf{x},\mathbf{y})\phi(\mathbf{y})dS(\mathbf{y}), \tag{3}$$

$$(D\phi)(\mathbf{x}):=\int_\Gamma \frac{\partial\Phi(\mathbf{x},\mathbf{y})}{\partial\mathbf{n}(\mathbf{y})}\phi(\mathbf{y})dS(\mathbf{y}), \tag{4}$$

and

$$\Phi(\mathbf{x},\mathbf{y})=\frac{\exp(ik|\mathbf{x}-\mathbf{y}|)}{4\pi|\mathbf{x}-\mathbf{y}|}. \tag{5}$$

In Eqs. (1) and (2), ρ is the mean fluid density and in Eq. (4) $\mathbf{n}$ is the unit normal with direction shown in Fig. 1. In Eq. (5), $k=\omega/c$ is the wave number and c the constant for the speed of sound. In addition to the integral representation in Eq. (1) or (2) we will consider the *indirect formulation*, as suggested by Refs. 14 and 15, for $\mathbf{x}\in G$ (or G^+)

$$p(\mathbf{x})=(S\varphi)(\mathbf{x}), \tag{6}$$

where φ is a density function.

The solution to NAH by the direct or indirect formulation will use the jump relations (Ref. 27, Theorems 2.13 and 2.19) for Eq. (4) and the normal derivative of Eq. (3) when $\mathbf{x}\in\Gamma$,

$$(D\phi)^{\pm}(\mathbf{x}):=\int_\Gamma \frac{\partial\Phi(\mathbf{x},\mathbf{y})}{\partial\mathbf{n}(\mathbf{y})}\phi(\mathbf{y})dS(\mathbf{y})\pm\Omega(\mathbf{x})\phi(\mathbf{y}), \tag{7}$$

$$\left(\frac{\partial S}{\partial\mathbf{n}}\phi\right)^{\pm}(\mathbf{x}):=\int_\Gamma \frac{\partial\Phi(\mathbf{x},\mathbf{y})}{\partial\mathbf{n}(\mathbf{x})}\phi(\mathbf{y})dS(\mathbf{y})\mp\Omega(\mathbf{x})\phi(\mathbf{x}), \tag{8}$$

where $\Omega(\mathbf{x})$ is the solid angle coefficient given by the integral formula

$$\Omega(\mathbf{x})=-\int_\Gamma \frac{\partial}{\partial\mathbf{n}(\mathbf{y})}\left(\frac{1}{4\pi|\mathbf{x}-\mathbf{y}|}\right), \quad \mathbf{x}\in\Gamma. \tag{9}$$

The superscript sign ''+'' in Eqs. (7) and (8) is used for exterior NAH and ''−'' for interior NAH. This notation will be kept through the rest of this work. $\Omega(\mathbf{x})$ will be $\frac{1}{2}$ for all $\mathbf{x}\in\Gamma$, when Γ is a smooth surface.

For the numerical solution of NAH, the boundary surface Γ is decomposed into triangular elements with three nodes or quadrilateral elements with four nodes. In this paper (as recommended in Refs. 16 and 15), iso-parametric linear functions are selected for interpolating the geometric and acoustical quantities. Let $\mathbf{p}$ be a column vector that represents M pressure measurements on Γ_0, and the column vector $\mathbf{p}^s$, $\mathbf{v}^s$ respectively represents N pressure and normal velocity points on Γ. As in Ref. 16, Eqs. (3) and (4) are reduced to the $M\times N$ complex matrices $[\mathbf{S}]$ and $[\mathbf{D}]$ when $\mathbf{x}\in\Gamma_0$. Similarly, when $\mathbf{x}\in\Gamma$, Eqs. (3), (7), and (8) are reduced to the $N\times N$ complex matrices $[\mathbf{S}^s]$, $[\mathbf{D}^{\pm}]$, and $[\mathbf{K}^{\pm}]$, respectively.

As explained in Ref. 16, the *direct-explicit* (DE) approach (the traditional approach for the solution of NAH) is based on the explicit creation of the *Green's transfer* functions. That means that the DE approach creates the $M\times N$ complex matrices $[\mathbf{G}_\mathbf{d}^{\pm}]$, $[\mathbf{G}_\mathbf{n}^{\pm}]$ such that

$$[\mathbf{G}_\mathbf{d}^{\pm}]\mathbf{p}^s=\mathbf{p}, \tag{10}$$

$$[\mathbf{G}_\mathbf{n}^{\pm}]\mathbf{v}^s=\mathbf{p}. \tag{11}$$

Matrices $[\mathbf{G}_\mathbf{d}^{\pm}]$, $[\mathbf{G}_\mathbf{n}^{\pm}]$ are formed explicitly using representation in Eq. (2) and the jump relation in Eq. (7):

$$[\mathbf{G}_\mathbf{d}^{\pm}]=\pm([\mathbf{D}]-[\mathbf{S}][\mathbf{S}^s]^{-1}([\mathbf{D}^{\pm}]\mp[\mathbf{I}])), \tag{12}$$

$$[\mathbf{G}_\mathbf{n}^{\pm}]=\pm i\omega\rho([\mathbf{D}]([\mathbf{D}^{\pm}]\mp[\mathbf{I}])^{-1}[\mathbf{S}^s]-[\mathbf{S}]). \tag{13}$$

As an alternative to the DE approach, this inverse problem can also be solved with an *indirect-implicit* (IM) ap-

proach as in Refs. 14–16. The indirect formulation in Eq. (6) is used to solve

$$[\mathbf{S}]\boldsymbol{\varphi}=\mathbf{p} \tag{14}$$

for the column vector of N entries $\boldsymbol{\varphi}$. Then the normal velocity will be obtained using Euler's equation and Eq. (8),

$$\mathbf{v}^s=\frac{1}{i\omega\rho}[\mathbf{K}^{\pm}]\boldsymbol{\varphi}. \tag{15}$$

Similarly the pressure on Γ will be obtained using

$$\mathbf{p}^s=[\mathbf{S}^s]\boldsymbol{\varphi}. \tag{16}$$

III. NUMERICAL REGULARIZATION

For the experimental problem, the exact pressure $\mathbf{p}$ is perturbed by measurement errors. We denote the measured pressure as $\tilde{\mathbf{p}}$. If the elements of the perturbation $\mathbf{e}=\tilde{\mathbf{p}}-\mathbf{p}$ are Gaussian (unbiased and uncorrelated) with covariance matrix $\sigma_0^2[\mathbf{I}]$, then $E(\|\mathbf{e}\|_2^2)=M\sigma_0^2$, where $\|\cdot\|_2$ is the two-norm. It is well known that the linear systems on Eqs. (10), (11), and (14) are ill-posed, i.e., the errors in $\tilde{\mathbf{p}}$ will be amplified on the solutions $\mathbf{p}^s$, $\mathbf{v}^s$, or $\boldsymbol{\varphi}$, and in most of the cases the recovery will be useless. For that reason special *regularization methods* are required to find the solution of these linear systems.

Consider the solution of the generic ill-posed linear matrix system

$$[\mathbf{A}]\mathbf{z}=\tilde{\mathbf{p}}, \tag{17}$$

where $\mathbf{z}$ is a column vector of N entries and $[\mathbf{A}]$ is an $M\times N$ complex matrix [as in Eqs. (10), (11), and (14)]. As explained in Ref. 29, regularization methods for the solution $\mathbf{z}$ of Eq. (17) can be divided into two types: *direct* and *iterative*.

A. Direct regularization

For the direct regularization, the matrix $[\mathbf{A}]$ of the linear system in Eq. (17) will be decomposed using the singular value decomposition (SVD). The SVD of $[\mathbf{A}]$ will be

$$[\mathbf{A}]=[\mathbf{U}][\boldsymbol{\Sigma}][\mathbf{V}]^H, \tag{18}$$

where $[\mathbf{U}]$ and $[\mathbf{V}]$ are unitary matrices of dimensions $M\times M$ and $N\times N$, respectively, and $[\mathbf{V}]^H$ is the conjugate transpose of $[\mathbf{V}]$. $[\boldsymbol{\Sigma}]$ is a diagonal matrix with values $\sigma_1\geqslant\cdots\geqslant\sigma_{N*}\geqslant 0$ and $N^*\equiv\mathrm{rank}([\mathbf{A}])$. The values σ_i are called *singular values*.

Denote as $\mathbf{u}_i$, $i=1,...,M$, and $\mathbf{v}_i$, $i=1,...,N$, the columns of $[\mathbf{U}]$ and $[\mathbf{V}]$, respectively. For NAH, $\mathbf{u}_i$, $\mathbf{v}_i$ will be an approximation to the acoustic field by basic acoustic waves or *mode shapes* (see Ref. 7). In particular when $[\mathbf{A}]=[\mathbf{G}_\mathbf{n}]$ [as in Eq. (11)], $\mathbf{u}_i$ will be the modes of the measured pressure on Γ_0 and $\mathbf{v}_i$ will be the modes of the normal velocity on Γ. These modes are organized in such a way that the first modes are related with the nonevanescent waves and the last modes will be related with the evanescent waves. The numerical solution of Eq. (17) by conventional methods $\mathbf{z}_{LS}$ can be represented using the SVD as

$$\mathbf{z}_{LS}=[\mathbf{V}][\boldsymbol{\Sigma}]^{\dagger}[\mathbf{U}]^H\tilde{\mathbf{p}}=\sum_{i=1}^{N^*}\left(\frac{\mathbf{u}_i^H\tilde{\mathbf{p}}}{\sigma_i}\right)\mathbf{v}_i, \tag{19}$$

where $[\boldsymbol{\Sigma}]^{\dagger}\equiv\mathrm{diag}(1/\sigma_1,\ldots,1/\sigma_{N*})$ is the Pseudo-inverse of $[\boldsymbol{\Sigma}]$. Notice that this solution will include modes $\mathbf{u}_i$, $\mathbf{v}_i$ that are related to both nonevanescent and evanescent waves. It is well known that the modes related to the evanescent waves will produce the fine details of the reconstruction $\mathbf{z}_{LS}$, but at the same time will amplify the noise in $\tilde{\mathbf{p}}$. Regularization methods for the solution to this inverse acoustic problem will need to include enough of these modes in order to obtain the desired resolution, and at the same time exclude some of these modes that are totally corrupted with noise.

Regularization methods can be implemented using the SVD and the filter matrix $[\mathbf{F}^\alpha]=\mathrm{diag}(f_1^\alpha,...,f_{N*}^\alpha)$ by modifying Eq. (19) as

$$\mathbf{z}_\alpha=[\mathbf{V}][\mathbf{F}^\alpha][\boldsymbol{\Sigma}]^{\dagger}[\mathbf{U}]^H\tilde{\mathbf{p}}=\sum_{i=1}^{N^*}f_i^\alpha\left(\frac{\mathbf{u}_i^H\tilde{\mathbf{p}}}{\sigma_i}\right)\mathbf{v}_i, \tag{20}$$

where α is the regularization parameter and f_i^α, $i=1,...,N^*$, are the *filter factors* (see Refs. 30 and 29). The parameter α will control the inclusion of modes related to evanescent waves into the solution $\mathbf{z}_\alpha$. The best known regularization method is Tikhonov and will be implemented using the filter factors

$$f_i^\alpha=\frac{\sigma_i^2}{\sigma_i^2+\alpha}. \tag{21}$$

The topic of direct regularization methods for linear matrix systems have been extensively studied in the last few decades. There are many other approaches depending on the particular problem, such as the use of Tikhonov regularization with a high-pass filter (see Ref. 31) which uses the physical behavior of the evanescent waves to produce an optimal filter.

B. Iterative methods

Iterative regularization methods for the linear system (17) are based on iteration schemes that access the coefficient matrix $[\mathbf{A}]$ only via matrix-vector multiplications with $[\mathbf{A}]$ and $[\mathbf{A}]^H$. They produce a sequence of iteration vectors $\mathbf{z}_{(l)}$, $l=1,2,3,...$, that converge to $\mathbf{z}_{LS}$ in Eq. (19). For ill-posed linear systems like Eqs. (10), (11), and (14), these methods produce the phenomena of ''semi-convergence,'' i.e., the vector $\mathbf{z}_{(l)}$ approaches the optimal regularization solution after a few iterations l. If the iteration is not stopped, the method converges to the least squares solution $\mathbf{z}_{LS}$ in Eq. (19) which is generally totally corrupted by the noisy data $\tilde{\mathbf{p}}$. In this case each iteration vector $\mathbf{z}_{(l)}$ can be considered as a regularized solution, with the iteration number l playing the role of the regularization parameter. These iterative methods are preferable to direct methods when the matrix $[\mathbf{A}]$ is so large that it is too time consuming or too memory-demanding to work with the SVD of $[\mathbf{A}]$. In the next section we will discuss a special type of iterative method called the Krylov subspace methods.

IV. KRYLOV SUBPACE ITERATIVE METHODS

In this section we present some general features of the Krylov subspace methods, and restrict our exposition for two

TABLE I. Algorithm for conjugate gradients for the normal equations.

starting vector $\mathbf{z}_{(0)}=0$
$\mathbf{r}_{(0)}=\tilde{\mathbf{p}}$
$\mathbf{d}_{(0)}=[\mathbf{A}]^H\mathbf{r}_{(0)}$
for $l=1,2,...(\leqslant N^*)$
$\alpha_{(l)}=\|[\mathbf{A}]^H\mathbf{r}_{(l-1)}\|_2^2/\|[\mathbf{A}]\mathbf{d}_{(l-1)}\|_2^2$,
$\mathbf{z}_{(l)}=\mathbf{z}_{(l-1)}+\alpha_{(l)}\mathbf{d}_{(l-1)}$,
$\mathbf{r}_{(l)}=\mathbf{r}_{(l-1)}-\alpha_{(l)}[\mathbf{A}]\mathbf{d}_{(l-1)}$
$\beta_{(l)}=\|[\mathbf{A}]^H\mathbf{r}_{(l)}\|_2^2/\|[\mathbf{A}]^H\mathbf{r}_{(l-1)}\|_2^2$,
$\mathbf{d}_{(l)}=[\mathbf{A}]^H\mathbf{r}_{(l)}+\beta_{(l)}\mathbf{d}_{(l-1)}$,

of these methods: conjugate gradients for the normal equations (CGNE) and least squares QR (LSQR). Consider the normal equations of Eq. (17),

$$[\mathbf{A}]^H[\mathbf{A}]\mathbf{z}=[\mathbf{A}]^H\tilde{\mathbf{p}}. \tag{22}$$

The solution to Eq. (22) is equal to the least squares solution $\mathbf{z}_{LS}$ given in Eq. (19). The CGNE iterative algorithm (given in Table I) produces, for each iteration l, the vector $\mathbf{z}_{(l)}$ that approximates the least squares solution $\mathbf{z}_{LS}$ to Eq. (22). Notice from Table I, line 6, that on iteration $l=1$ of CGNE, $\mathbf{z}_{(1)}$ is formed by the vector $[\mathbf{A}]^H\tilde{\mathbf{p}}$ multiplied by a constant. On iteration $l=2$, $\mathbf{z}_{(2)}$ is formed by $c_1[\mathbf{A}]^H\tilde{\mathbf{p}}+c_2([\mathbf{A}]^H[\mathbf{A}])\times[\mathbf{A}]^H\tilde{\mathbf{p}}$, where c_1, c_2 are constants. Similarly, for each l, a vector $\mathbf{z}_{(l)}$ can be expressed as

$$\mathbf{z}_{(l)}=\sum_{i=0}^{l-1} c_i([\mathbf{A}]^H[\mathbf{A}])^i[\mathbf{A}]^H\tilde{\mathbf{p}}, \tag{23}$$

where c_i, $i=0,...,l-1$ are constants. In mathematical notation, this combination of vectors is called the *Krylov subspace* l, and is denoted as $\mathcal{K}^{(l)}([\mathbf{A}]^H\tilde{\mathbf{p}},[\mathbf{A}]^H[\mathbf{A}])$. We write, instead of Eq. (23), $\mathbf{z}_{(l)}\in\mathcal{K}^{(l)}([\mathbf{A}]^H\tilde{\mathbf{p}},[\mathbf{A}]^H[\mathbf{A}])$. There are a variety of iterative methods that, for each iteration l, produce vectors $\mathbf{z}_{(l)}$ that belong to the Krylov subspace l [at each iteration $\mathbf{z}_{(l)}$ can be written as Eq. (23)]. For that reason these methods are called *Krylov subspace methods* (see Ref. 23). It is not obvious, but it can be shown that in general the Krylov subspace methods will approximate the least squares solution $\mathbf{z}_{LS}$ to Eq. (22) as l increases (see Appendix A). CGNE is the most representative Krylov subspace method for the solution to the normal equations in Eq. (22). There is also a wide variety of well-known Krylov subspace methods like Landweber or generalized minimal residual (GMRES) (see Ref. 23 for more information). When the matrix $[\mathbf{A}]$ in Eq. (17) is square (the dimensions $M=N$), then Krylov subspace methods like GMRES are more commonly used. These methods are based directly on the solution to Eq. (17) where $\mathbf{z}_{(l)}\in\mathcal{K}^{(l)}(\tilde{\mathbf{p}},[\mathbf{A}])$ (see Refs. 32–34).

Despite the simplicity of the CGNE algorithm, each iterate $\mathbf{z}_{(l)}$ has minimal residual in $\mathcal{K}^{(l)}([\mathbf{A}]^H\tilde{\mathbf{p}},[\mathbf{A}]^H[\mathbf{A}])$, i.e., $\mathbf{z}_{(l)}$ satisfies

$$\|[\mathbf{A}]\mathbf{z}_{(l)}-\tilde{\mathbf{p}}\|_2\leqslant\|[\mathbf{A}]\mathbf{h}-\tilde{\mathbf{p}}\|_2, \tag{24}$$

for all vectors $\mathbf{h}\in\mathcal{K}^{(l)}([\mathbf{A}]^H\tilde{\mathbf{p}},[\mathbf{A}]^H[\mathbf{A}])$. Another important property of the CGNE algorithm is that

$$\|[\mathbf{A}]\mathbf{z}_{(l)}-\tilde{\mathbf{p}}\|_2\leqslant\|[\mathbf{A}]\mathbf{z}_{(l-1)}-\tilde{\mathbf{p}}\|_2, \quad \|\mathbf{z}_{(l-1)}\|_2\leqslant\|\mathbf{z}_{(l)}\|_2. \tag{25}$$

TABLE II. Algorithm for Lanczos bidiagonalization.

initial step
$\beta_{(1)}=\|\tilde{\mathbf{p}}\|_2$, $\mathbf{u}_{(1)}=\beta_{(1)}^{-1}\tilde{\mathbf{p}}$, $\mathbf{v}_{(0)}=0$.
for $l=1,2,...(\leqslant N^*)$
$\mathbf{r}_{(l)}=[\mathbf{A}]^H\mathbf{u}_{(l)}-\beta_{(l)}\mathbf{v}_{(l-1)}$

for $j=1,...,(l-1)$
$\mathbf{r}_{(l)}=\mathbf{r}_{(l)}-(\mathbf{v}_{(j)})^H\mathbf{r}_{(l)}\mathbf{v}_{(j)}$ (Reorthogonalization)
$\alpha_{(l)}=\|\mathbf{r}_{(l)}\|_2$
$\mathbf{v}_{(l)}=\mathbf{r}_{(l)}/\alpha_{(l)}$
$\mathbf{q}_{(l)}=[\mathbf{A}]\mathbf{v}_{(l)}-\alpha_{(l)}\mathbf{u}_{(l)}$

for $j=1,...,(l-1)$
$\mathbf{q}_{(l)}=\mathbf{q}_{(l)}-(\mathbf{u}_{(j)})^H\mathbf{q}_{(l)}\mathbf{u}_{(j)}$ (Reorthogonalization)
$\beta_{(l+1)}=\|\tilde{\mathbf{q}}_{(l)}\|_2$
$\mathbf{u}_{(l+1)}=\mathbf{q}_{(l)}/\beta_{(l+1)}$

The proof of these properties is rather technical, so we recommend Refs. 30 and 23 for more details.

Although CGNE has been used previously for deriving solutions in NAH (see Refs. 15 and 24), we strive for physical understanding of the resultant iteration vectors $\mathbf{z}_{(l)}$, similar to the understanding obtained from the SVD in direct regularization methods (see Ref. 7). The key to the physical understanding of CGNE lies on the physical meaning of the Krylov subspace $\mathcal{K}^{(l)}([\mathbf{A}]^H\tilde{\mathbf{p}},[\mathbf{A}]^H[\mathbf{A}])$, which is not obvious. To gain this understanding we pursue the LSQR algorithm (see Refs. 25 and 35), a Krylov subspace method that has the advantage of creating a basis of orthonormal vectors for $\mathcal{K}^{(l)}([\mathbf{A}]^H\tilde{\mathbf{p}},[\mathbf{A}]^H[\mathbf{A}])$, a more favorable property for our further discussion. We will also discuss an important connection between CGNE and LSQR in the next subsections.

A. Lanczos bidiagonalization and LSQR

The Lanczos bidiagonalization algorithm (given in Table II) with starting vector $\tilde{\mathbf{p}}$ produces a bidiagonal $(l+1)\times l$ real matrix $[\mathbf{B}^{(l)}]$ and two complex matrices $[\mathbf{U}^{(l+1)}]$ and $[\mathbf{V}^{(l)}]$ of dimensions $M\times(l+1)$ and $N\times l$, respectively, with orthonormal columns such that

$$[\mathbf{A}][\mathbf{V}^{(l)}]=[\mathbf{U}^{(l+1)}][\mathbf{B}^{(l)}]. \tag{26}$$

The bidiagonal matrix $[\mathbf{B}^{(l)}]$ is given by

$$[\mathbf{B}^{(l)}]=\begin{pmatrix} \alpha_{(1)} & & & \\ \beta_{(2)} & \alpha_{(2)} & & \\ & \beta_{(3)} & \ddots & \\ & & \ddots & \alpha_{(l)} \\ & & & \beta_{(l+1)} \end{pmatrix}.$$

We denote as $\mathbf{v}_{(j)}$, $j=1,...,l$, the columns of $[\mathbf{V}^{(l)}]$, and as $\mathbf{u}_{(j)}$, $j=1,...,l+1$, the columns of $[\mathbf{U}^{(l+1)}]$.

Looking at the Lanczos bidiagonalization algorithm in Table II, notice that on iteration $l=1$, $\mathbf{v}_{(1)}$ is formed by the vector $[\mathbf{A}]^H\tilde{\mathbf{p}}$ multiplied by a constant. On iteration $l=2$, $\mathbf{v}_{(1)}$, $\mathbf{v}_{(2)}$ are formed by $c_1[\mathbf{A}]^H\tilde{\mathbf{p}}+c_2([\mathbf{A}]^H[\mathbf{A}])[\mathbf{A}]^H\tilde{\mathbf{p}}$, where c_1, c_2 are constants. Then, as in the explanation of the CGNE algorithm, we have $\mathbf{v}_{(1)},\ldots,\mathbf{v}_{(l)}\in\mathcal{K}^{(l)}\times([\mathbf{A}]^H\tilde{\mathbf{p}},[\mathbf{A}]^H[\mathbf{A}])$. Moreover, $\mathbf{v}_{(1)},\ldots,\mathbf{v}_{(l)}$ form an orthonormal basis for $\mathcal{K}^{(l)}([\mathbf{A}]^H\tilde{\mathbf{p}},[\mathbf{A}]^H[\mathbf{A}])$. In numerical com-

putations, the columns of $[\mathbf{U}^{(l+1)}]$ and $[\mathbf{V}^{(l)}]$ can fail to be orthonormal, which will be an undesirable effect. The Lanczos algorithm in Table II includes a reorthogonalization step (as suggested in Ref. 36) for the columns of $[\mathbf{U}^{(l+1)}]$, $[\mathbf{V}^{(l)}]$, in order to avoid this complication.

The LSQR algorithm uses Lanczos bidiagonalization given by Eq. (26) to define the iteration vector

$$\mathbf{z}_{(l)}=[\mathbf{V}^{(l)}][\mathbf{B}^{(l)}]^{\dagger}[\mathbf{U}^{(l+1)}]^{H}\tilde{\mathbf{p}}, \tag{27}$$

where $[\mathbf{B}^{(l)}]^{\dagger}\equiv([\mathbf{B}^{(l)}]^{H}[\mathbf{B}^{(l)}])^{-1}[\mathbf{B}^{(l)}]^{H}$ is the pseudoinverse of $[\mathbf{B}^{(l)}]$. It is well known that $\mathbf{z}_{(l)}$ in Eq. (27) has the property given in Eq. (24) (see Ref. 36). Since both LSQR and CGNE produce a vector $\mathbf{x}_{(l)}$ with minimal residual norm $\|[\mathbf{A}]\mathbf{z}_{(l)}-\tilde{\mathbf{p}}\|_2$ over the Krylov subspace $\mathcal{K}^{(l)}\times([\mathbf{A}]^{H}\tilde{\mathbf{p}},[\mathbf{A}]^{H}[\mathbf{A}])$, then it follows that the vector $\mathbf{z}_{(l)}$ produced by iteration l of LSQR is the same as the one produced by iteration l of CGNE. In practice, LSQR is not implemented as explicitly written in Eq. (27), instead the algorithm is based on an efficient update of $\mathbf{z}_{(l-1)}$ into $\mathbf{z}_{(l)}$, at the cost of one additional iteration vector of length N, and neither $[\mathbf{U}^{(l+1)}]$ nor $[\mathbf{V}^{(l)}]$ needs to be stored (see Refs. 25 and 35).

B. The link between the Krylov subspace and the SVD

Let us define the SVD of $[\mathbf{B}^{(l)}]$,

$$[\mathbf{B}^{(l)}]=[\tilde{\mathbf{U}}^{(l)}][\tilde{\mathbf{\Sigma}}^{(l)}][\tilde{\mathbf{V}}^{(l)}]^{H}, \tag{28}$$

where $[\tilde{\mathbf{U}}^{(l)}]$, $[\tilde{\mathbf{V}}^{(l)}]$ are $(l+1)\times(l+1)$, $l\times l$ real matrices, respectively. $[\tilde{\mathbf{\Sigma}}^{(l)}]=\mathrm{diag}(\theta_1^{(l)},...,\theta_l^{(l)})$, and $\theta_1^{(l)}\geqslant\cdots\geqslant\theta_l^{(l)}$ are called the Ritz values (as in Ref. 37). The Ritz values have the property that for a fixed j, $\theta_j^{(l)}$ increases as l increases. Combine Eqs. (26) and (28) to obtain

$$[\mathbf{A}][\hat{\mathbf{V}}^{(l)}]=[\hat{\mathbf{U}}^{(l)}][\tilde{\mathbf{\Sigma}}^{(l)}], \tag{29}$$

where $[\hat{\mathbf{U}}^{(l)}]=[\mathbf{U}^{(l+1)}][\tilde{\mathbf{U}}^{(l)}]$ and $[\hat{\mathbf{V}}^{(l)}]=[\mathbf{V}^{(l)}][\tilde{\mathbf{V}}^{(l)}]$. Denote as $\hat{\mathbf{u}}_j^{(l)}$, $j=1,...,l+1$, and $\hat{\mathbf{v}}_j^{(l)}$, $j=1,...,l$, the columns of $[\hat{\mathbf{U}}^{(l)}]$ and $[\hat{\mathbf{V}}^{(l)}]$, respectively. It is proven in Appendix B that $[\hat{\mathbf{U}}^{(l)}]$ and $[\hat{\mathbf{V}}^{(l)}]$ have orthonormal columns, and that $\hat{\mathbf{v}}_j^{(l)}$ form an orthonormal basis for the Krylov subspace $\mathcal{K}^{(l)}\times([\mathbf{A}]^{H}\tilde{\mathbf{p}},[\mathbf{A}]^{H}[\mathbf{A}])$.

With the new decomposition, given in Eq. (29), we represent each iteration $\mathbf{z}_{(l)}$, $l=1,2,3,...$, from the LSQR algorithm given in Eq. (27) by

$$\mathbf{z}_{(l)}=[\hat{\mathbf{V}}^{(l)}][\tilde{\mathbf{\Sigma}}^{(l)}]^{\dagger}[\hat{\mathbf{U}}^{(l)}]^{H}\tilde{\mathbf{p}}=\sum_{i=1}^{l}\left(\frac{(\hat{\mathbf{u}}_i^{(l)})^{H}\tilde{\mathbf{p}}}{\theta_i^{(l)}}\right)\hat{\mathbf{v}}_i^{(l)}. \tag{30}$$

Notice that Eq. (30) is similar to the least squares solution given in Eq. (19), with the difference that in Eq. (30) we use $\theta_j^{(l)}$, $\hat{\mathbf{u}}_j^{(l)}$, $\hat{\mathbf{v}}_j^{(l)}$ instead of σ_j, $\mathbf{u}_j$, $\mathbf{v}_j$ from Eq. (19). As we might expect, the quantities $\theta_j^{(l)}$, $\hat{\mathbf{u}}_j^{(l)}$, $\hat{\mathbf{v}}_j^{(l)}$ will converge to σ_j, $\mathbf{u}_j$, $\mathbf{v}_j$ as l increases. Some topics related to this convergence are found in the papers of van der Sluis, van der Vorst and Sleijpen.[38–43,37] In Ref. 40 there is a detailed study that shows that the Ritz values $\theta_j^{(l)}$ approximate rapidly the biggest singular values σ_j after a few iterations of CGNE. Further results can be found in Ref. 37. We will include a similar study in the following subsection, but in addition there is a study on the convergence of the vectors $\hat{\mathbf{v}}_j^{(l)}$ into $\mathbf{v}_j$.

For the purposes of the regularization theory, the most significant result from the previous collection of cited paper is given in Ref. 38. In this paper it was found that the LSQR iteration vector $\mathbf{z}_{(l)}$ can be represented using the SVD as

$$\mathbf{z}_{(l)}=[\mathbf{V}][\mathbf{F}^{(l)}][\mathbf{\Sigma}]^{\dagger}[\mathbf{U}]^{H}\tilde{\mathbf{p}}=\sum_{i=1}^{N^*}f_i^{(l)}\left(\frac{\mathbf{u}_i^{H}\tilde{\mathbf{p}}}{\sigma_i}\right)\mathbf{v}_i, \tag{31}$$

where $[\mathbf{F}^{(l)}]=\mathrm{diag}(f_1^{(l)},...,f_{N^*}^{(l)})$ and

$$f_i^{(l)}=1-\prod_{i=1}^{l}\frac{(\theta_i^{(l)})^2-\sigma_i^2}{(\theta_i^{(l)})^2}. \tag{32}$$

The representation in Eqs. (31) and (32) is important for the understanding of the regularizing effect of the LSQR iterations, but will not be the proper way to implement this algorithm. The proper implementation of LSQR (as described through this section) avoids the creation of the SVD of $[\mathbf{A}]$, which can be expensive when $[\mathbf{A}]$ is large. We will use Eqs. (31) and (32) just to show the behavior of the filter $[\mathbf{F}^{\alpha}]$ for our NAH problem.

C. Numerical experiment

For the numerical example of this subsection, we will consider the interior problem of reconstructing $\mathbf{v}^s$ on the surface Γ, a sphere of radius 1 with 1026 points decomposed onto 2048 triangular elements (as shown in Fig. 2 of Ref. 16), using pressure measurements $\mathbf{p}$ over Γ_0, a sphere of radius 0.95 with 1026 points distributed as in Γ. We will use a point source located at $(0,-1.3,0)$. The vector $\tilde{\mathbf{p}}$ is created by adding to $\mathbf{p}$ the vector $\mathbf{e}$ with a SNR of 35 dB. The figures that will be shown in this subsection over the sphere Γ depend on the spherical coordinates (r,ϕ,θ), and hence will be transformed using interpolation into the plane (ϕ,θ) for better visualization purposes.

Consider $[\mathbf{U}]$, $[\mathbf{\Sigma}]$, $[\mathbf{V}]$, the SVD decomposition of $[\mathbf{A}]=[\mathbf{G_n}]$ [given in Eq. (11)], and the decomposition $[\hat{\mathbf{U}}^{(l)}]$, $[\tilde{\mathbf{\Sigma}}^{(l)}]$, $[\hat{\mathbf{V}}^{(l)}]$ obtained using the bidiagonalization algorithm for $[\mathbf{A}]=[\mathbf{G_n}]$ and SVD of $[\mathbf{B}^{(l)}]$ (as explained in the previous subsection). The vectors $\mathbf{v}_1,\ldots,\mathbf{v}_{36}$ (the first 36 columns of $[\mathbf{V}]$) are the modes of the surface velocity $\mathbf{v}^s$, and are plotted in Fig. 2. The first columns of Table III show the singular values $\sigma_1,\ldots,\sigma_{20}$ and the following columns shows the Ritz values $\theta_1^{(l)},\ldots,\theta_l^{(l)}$ for $l=5$, $l=10$, $l=15$, and $l=20$, respectively. We proceed as in Ref. 40 for the analysis of the convergence of the Ritz values. For $l=5$, we clearly notice that $\theta_1^{(5)}\approx\sigma_1$. Similarly $\theta_2^{(5)}$ and $\theta_3^{(5)}$ approximate the first three digits of σ_2 and σ_4, respectively. At $l=10$, $\theta_1^{(10)}\approx\sigma_1,\ldots,\theta_4^{(10)}\approx\sigma_4$ and $\theta_5^{(10)}$ approximate the first three digits of σ_6. A similar convergence behavior will be found for $l=15$ and $l=20$. It is important to recall the property that $\theta_j^{(l)}$ increases for fixed j as l increases. The sequence of Ritz's values $\theta_5^{(5)}$, $\theta_5^{(10)}$, $\theta_5^{(15)}$, and $\theta_5^{(20)}$ increasingly converge to σ_5. We can conclude from these observations (as in Ref. 40) that the Ritz values $\theta_j^{(l)}$ will have the tendency to approximate the biggest singular values (the first singular values) after a few iterations. These analyses can be extended

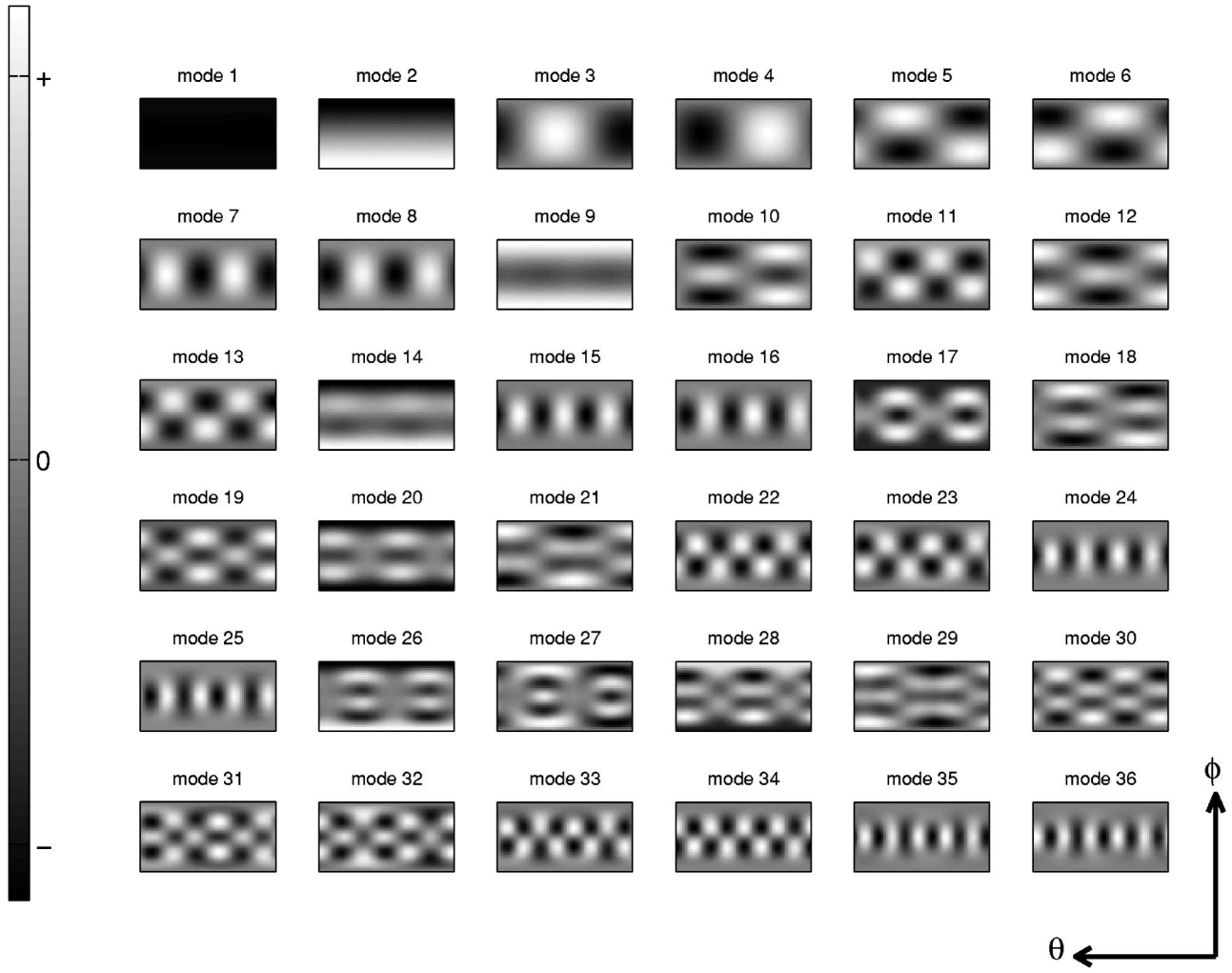

FIG. 2. Columns $\mathbf{v}_1,\ldots,\mathbf{v}_{36}$ of $[\mathbf{V}]$, which is obtained from the SVD of $[\mathbf{G}_\mathbf{n}]$. The matrix $[\mathbf{G}_\mathbf{n}]$ is calculated for the spherical surfaces Γ_0 and Γ. The columns $\mathbf{v}_j$ are the modes for the normal velocity in Γ that are ordered from biggest to smallest singular value. The frequency is 50 Hz.

TABLE III. Ritz values $\theta_i^{(l)}$ approximation to the singular values σ_i for iterations l of the LSQR method.

i	σ_i	$\theta_i^{(5)}$	$\theta_i^{(10)}$	$\theta_i^{(15)}$	$\theta_i^{(20)}$
1	3.483 039	3.483 039	3.483 039	3.483 039	3.483 039
2	1.162 439	1.161 336	1.162 439	1.162 439	1.162 439
3	1.160 067	1.157 138	1.160 067	1.160 067	1.160 067
4	1.158 283	0.479 882	1.158 283	1.158 283	1.158 283
5	0.482 024	0.260 270	0.481 162	0.481 383	0.482 024
6	0.481 294		0.478 698	0.480 924	0.481 294
7	0.479 646		0.291 522	0.479 349	0.479 646
8	0.479 203		0.204 556	0.474 368	0.479 203
9	0.474 365		0.160 850	0.291 920	0.474 365
10	0.292 096		0.104 207	0.290 667	0.291 950
11	0.291 938			0.202 518	0.290 902
12	0.291 807			0.151 322	0.290 441
13	0.291 795			0.125 302	0.202 805
14	0.290 777			0.098 628	0.201 669
15	0.290 719			0.060 318	0.150 603
16	0.290 177				0.134 431
17	0.203 392				0.116 084
18	0.202 927				0.089 954
19	0.202 921				0.064 369
20	0.202 998				0.036 788

to the convergence of the modes $\hat{\mathbf{v}}_j^{(l)}$, $j=1,...,l$, as shown by Fig. 3. The first modes $\hat{\mathbf{v}}_j^{(l)}$ converge rapidly to the first modes $\mathbf{v}_j$, after a few iterations. Figure 3 shows the vectors $\hat{\mathbf{v}}_j^{(l)}$, $j=1,...,l$, that form a basis for $\mathcal{K}^{(5)}([\mathbf{A}]^H\tilde{\mathbf{p}},[\mathbf{A}]^H[\mathbf{A}])$, $\mathcal{K}^{(10)}([\mathbf{A}]^H\tilde{\mathbf{p}},[\mathbf{A}]^H[\mathbf{A}])$ and $\mathcal{K}^{(15)}([\mathbf{A}]^H\tilde{\mathbf{p}},[\mathbf{A}]^H[\mathbf{A}])$, respectively.

Figure 4 shows the plot of the relative error between the exact normal velocity $\mathbf{v}^s$ and the reconstructed velocity $\mathbf{v}_l^s$ from l iterations of CGNE (implemented by LSQR). Notice that after 15 iterations the relative error is optimal (about 11%). If the iteration procedure is not stopped, then the relative error increases. This is the ''semi-convergence'' phenomena, which is found in Krylov subspace iterative methods for the solution of ill-posed problems. Our previous analysis on the convergence of the Ritz values and Eq. (30) can be used to explain this phenomena. On the first iterations of CGNE, the modes $\hat{\mathbf{v}}_j^{(l)}$ in Eq. (30) will approximate the modes $\mathbf{v}_j$ in Eq. (18) associated with the biggest singular values (nonevanescent waves). If the CGNE iteration procedure is not stopped, then the modes $\hat{\mathbf{v}}_j^{(l)}$ will approximate the modes $\mathbf{v}_j$ associated with smaller singular values (evanescent waves), which amplify the effect of noise. As an alternative explanation to the ''semi-convergence'' phenomena we can

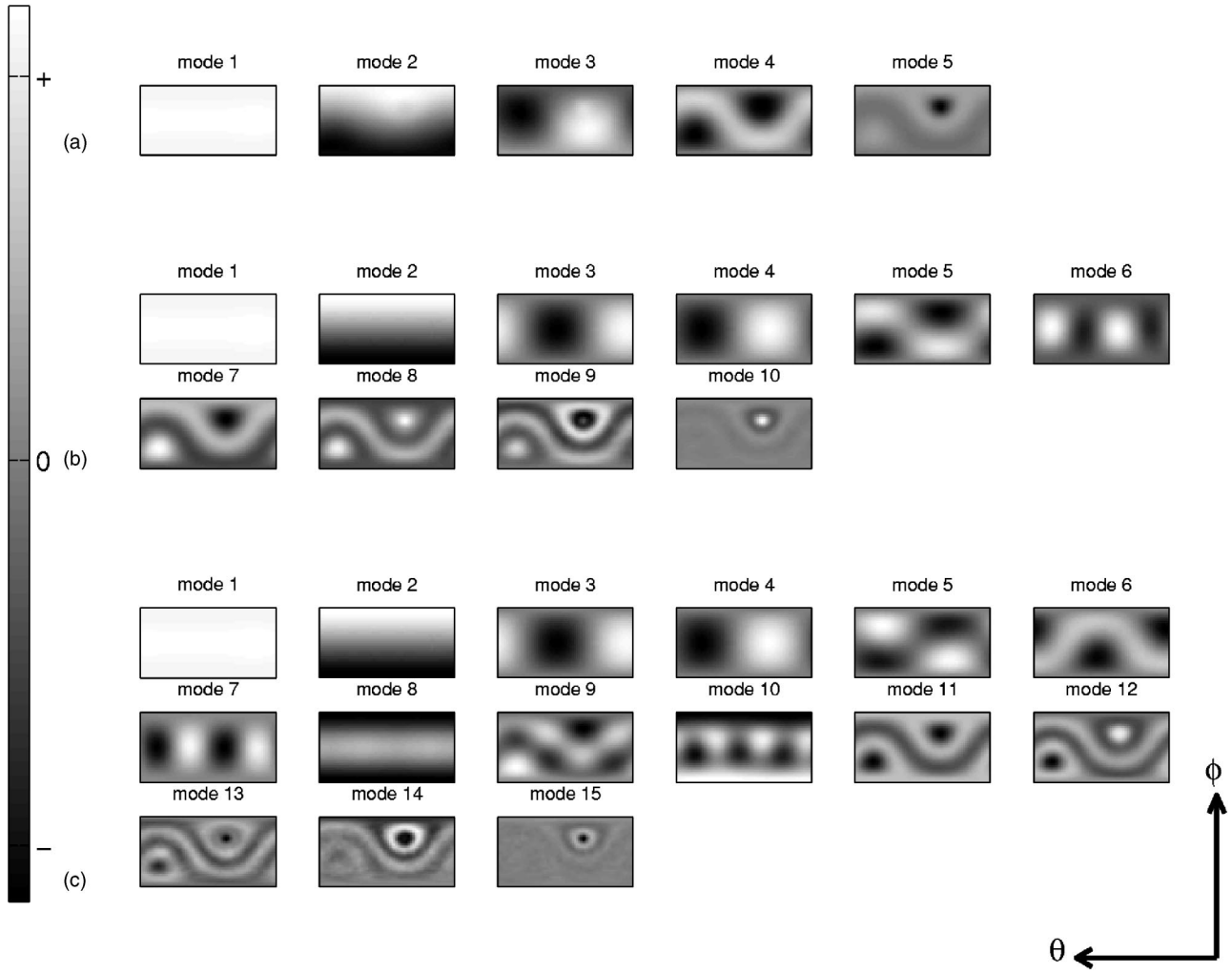

FIG. 3. The columns $\hat{\mathbf{v}}_1,\ldots,\hat{\mathbf{v}}_l$ of $[\mathbf{V}^{(l)}]$ obtained by the Lanczos bidiagonalization algorithm for $[\mathbf{G}_\mathbf{n}]$ and SVD of $[\mathbf{B}^{(l)}]$ (as explained in Sec. IV B). These columns form a basis for the Krylov subspaces (a) $\mathcal{K}^{(5)}([\mathbf{A}]^H\tilde{\mathbf{p}},[\mathbf{A}]^H[\mathbf{A}])$, (b) $\mathcal{K}^{(10)}([\mathbf{A}]^H\tilde{\mathbf{p}},[\mathbf{A}]^H[\mathbf{A}])$ and (c) $\mathcal{K}^{(15)}([\mathbf{A}]^H\tilde{\mathbf{p}},[\mathbf{A}]^H[\mathbf{A}])$. The frequency is 50 Hz.

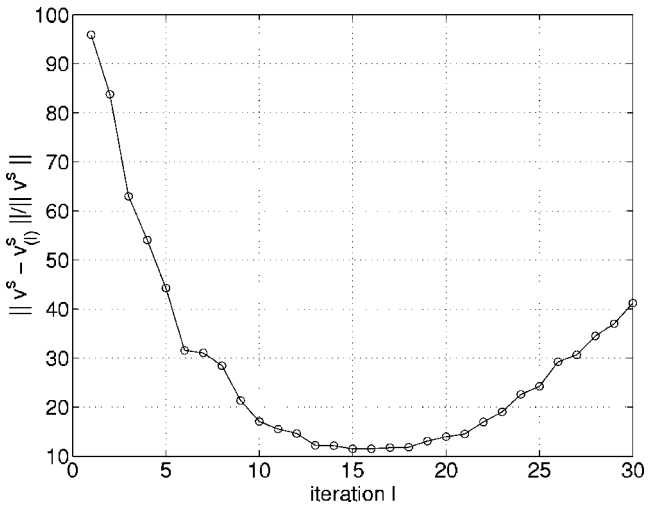

FIG. 4. Plot of the relative error between the exact normal velocity $\mathbf{v}^s$ and the recovered normal velocity $\mathbf{v}_l^s$ given by l iterations of the LSQR method. The vertical axis is the error % and the horizontal axis corresponds to the iterations l.

use the explicit expression for the CGNE filter given in Eq. (32). In Fig. 5 the filter factors are plotted for iterations $l=5$, 10, 15, 20. Notice how the filter includes more modes $\mathbf{v}_j$ as l increases. An undesirable property of this filter [observed in Fig. 5(b)] is that some of the filter factors $f_i^{(l)}$ can be greater than 1.

The phenomena of ''semi-convergence'' (as seen in Fig. 4) require us to stop the CGNE iterations before the solution $\mathbf{z}_{(l)}$ becomes corrupted by the noise in the data $\tilde{\mathbf{p}}$. In the next section we will discuss briefly some of the known stopping rules for the CGNE iterations, and propose a new technique that seems to be promising for our particular NAH problem.

V. THE CHOICE OF OPTIMAL NUMBER OF CGNE ITERATIONS

As mentioned in the previous section, when CGNE is used for NAH, the phenomena of ''semi-convergence'' is observed (see Fig. 4). It is crucial to obtain a reliable stopping rule (choose the optimal regularization parameter) for the CGNE iterations. In this section we will survey some of the best known methods currently used as stoping rules for

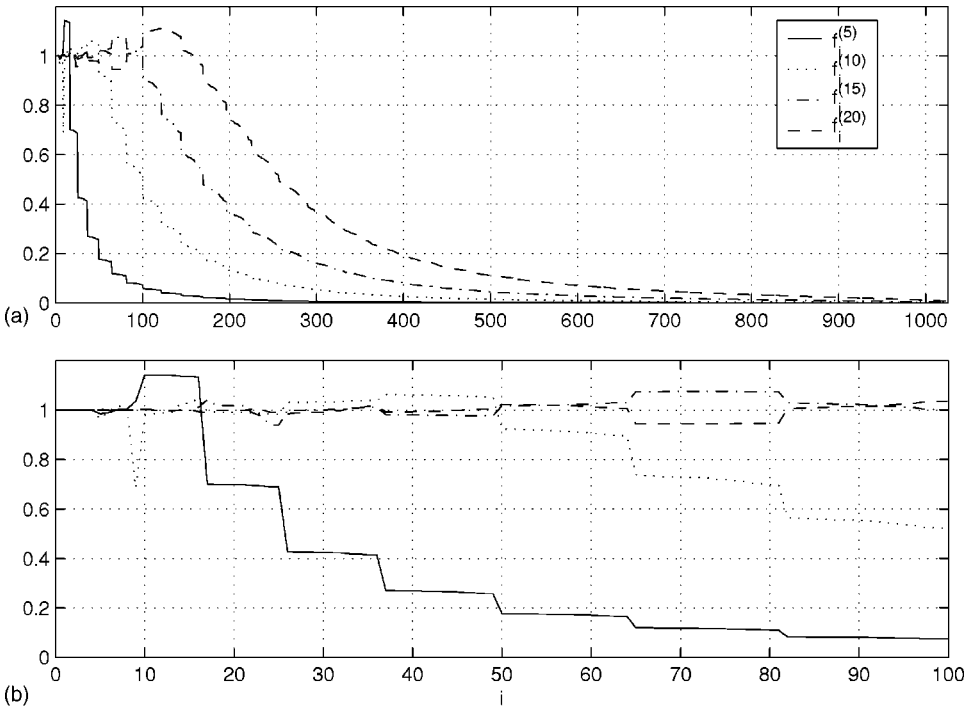

FIG. 5. The filter $[\mathbf{F}^{(l)}] = \mathrm{diag}(f_1^{(l)},...,f_{1026}^{(l)})$ for LSQR iteration $l=5$, 10, 15, 20. On (a) the filter factors are shown for $i=1,...,1026$ and on (b) the filter factors are shown for $i=1,...,100$.

CGNE: generalized cross-validation (GCV), L-curve and the Hanke–Raus method. Later we will discuss a hybrid method, which is a newer approach, that relies on the relation between the LSQR solution given in Eq. (30) and the solution in Eq. (21) computed using the SVD.

A. Stopping rules

To apply GCV for GCNE, as suggested in Ref. 29, we use the approximation to the function $\mathcal{G}$

$$\mathcal{G}(l)=\frac{\|[\mathbf{A}]\mathbf{z}_{(l)}-\tilde{\mathbf{p}}\|_2^2}{(M-l)^2}=\frac{\|\mathbf{r}_{(l)}\|_2^2}{(M-l)^2}, \tag{33}$$

where $\mathbf{r}_{(l)}$ is obtained for each iteration l of the CGNE algorithm. The optimal iteration l_{opt} is the iteration for which $\mathcal{G}$ will has its minimum value.

For L-curve,[44] we plot the coordinates

$$x(l)=\log(\|\mathbf{r}_{(l)}\|_2), \quad y(l)=\log(\|\mathbf{z}_{(l)}\|_2), \tag{34}$$

which gives a curve that resembles an L-shape. The optimal iteration l_{opt} is the iteration with coordinates $(x(l_{opt}),y(l_{opt}))$ which are closer to the point of maximum curvature of the L-shaped curve.

Finally we discuss the rule designed by Hanke and Raus.[45] In the CGNE algorithm (Table I), for iteration l we include the sequence

$$\gamma_{(l)}=\left(\frac{\alpha_{(l)}\beta_{(l-1)}}{\alpha_{(l-1)}}+1\right)\gamma_{(l-1)}-\left(\frac{\alpha_{(l)}\beta_{(l-1)}}{\alpha_{(l-1)}}\right)\gamma_{(l-2)}+\alpha_{(l)}, \tag{35}$$

where $\gamma_{(0)}=\gamma_{(-1)}=0$. The optimal iteration l_{opt} is the iteration for which the function

$$\mathcal{H}(l)=|\gamma_{(l)}|^{1/2}\|\mathbf{r}_{(l)}\|_2 \tag{36}$$

has its minimum value.

B. The hybrid method

The hybrid method was introduced by O'Leary and Simmons (see Ref. 26). In each iteration l of LSQR, instead of Eq. (30), we use

$$\mathbf{z}_{(l)}=[\hat{\mathbf{V}}^{(l)}][\mathbf{F}_{(l)}^{\alpha}][\tilde{\boldsymbol{\Sigma}}^{(l)}]^{\dagger}[\hat{\mathbf{U}}^{(l)}]^{H}\tilde{\mathbf{p}}, \tag{37}$$

where $[\mathbf{F}_{(l)}^{\alpha}]=\mathrm{diag}(f_1^{\alpha},...,f_l^{\alpha})$ and f_j^{α}, $j=1,...,l$, are the filter factors. The choice of the optimal filter factors for Eq. (37) is still an open question (see Refs. 26 and 46). For our particular problem we found that the use of the Tikhonov filter factors will yield better results.

Notice that the filter matrix $[\mathbf{F}_{(l)}^{\alpha}]$ depends on two parameters: the iteration l and α of the "inner filtering." This second parameter can be found using some of the well-known methods of obtaining the optimal parameter like Morozov, L-curve or GCV. We found that the better suited method was GCV, where the optimal parameter α is the minimum of the function

$$\mathcal{G}(\alpha)=\frac{\|[\hat{\mathbf{U}}^{(l)}][\mathbf{F}_{(l)}^{\alpha}][\hat{\mathbf{U}}^{(l)}]^{H}\tilde{\mathbf{p}}\|_2^2}{(M-\Sigma_{i=1}^{l}f_i^{\alpha})^2}. \tag{38}$$

As an advantage to CGNE, the hybrid method will not have the "semi-convergence" phenomena, since an "inner" regularization (produced by the matrix $[\mathbf{F}_{(l)}^{\alpha}]$) is used at each step l. The hybrid method will be stop when $\|\mathbf{x}_{(l)}-\mathbf{x}_{(l-1)}\|/\|\mathbf{x}_{(l)}\|<\epsilon$, where $\epsilon>0$ is a chosen tolerance.

In the next section we will use a vibrating plate data to reconstruct the normal velocity for CGNE with the stopping rules described iterations in Sec. V A and the proposed hybrid method.

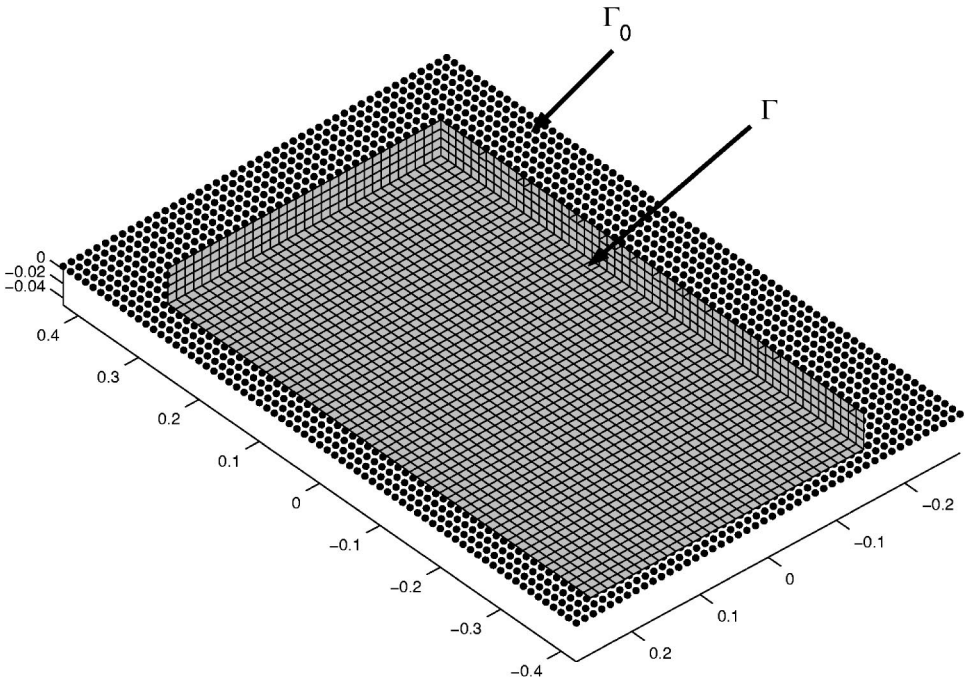

FIG. 6. The parallelepiped Γ and array Γ_0 used for the physical experiment. In case 1, Γ_0 had 805 measurement points and Γ was decomposed into 1072 linear quadrilateral elements with 1074 points. In case 2, Γ_0 had 3174 measurement points and Γ was decomposed into 4288 linear quadrilateral elements with 4290 points.

VI. PHYSICAL EXPERIMENTS

The experimental configuration for the holographic measurement is similar to Ref. 47. A steel rectangular plate (of 55.9×26.7 cm^2 and thickness of 1.6 mm) was driven by a Wilcoxon F3/F9 inertial shaker (0 to 3000 Hz) fixed in the underneath corner of the plate in order to generate a broad spectrum of spatial wave numbers. The resulting applied force was used to normalize the pressure measured with a ACO 7046 $\frac{1}{2}$-in. microphone above the plate. The scan is conducted in an automated point-by-point fashion. The microphone is initially positioned by the x-y scanner at a corner of the scan area, where the data is then acquired. Next, the microphone is moved to an adjacent point, and data is again acquired. This process is continued until the full scan area is measured. Synchronization between the source shaker, the data acquisition, and the scanner has proven to have high stability, yielding coherent data that can be thought of as having been acquired simultaneously. The pressure was measured on a grid of 69 points along the longer dimension and 46 points along the shorter dimension in a plane 0.4 cm above the plate surface. The step size in both the x and y directions was 1.25 cm, providing an overall scan dimension of 85×57.5 cm. The plate surface is located at the center of this area.

We consider two cases for the reconstruction of the acoustic field. In case 1 the points on the planar surface Γ_0 (35 points along the x direction and 23 points along the y direction) correspond to $\frac{1}{4}$ the original pressure measurements (and a spacing in both x and y directions of 2.5 cm). In case 2 the points on the planar surface Γ_0 (69 points along the x direction and 46 points along the y direction) correspond to the original pressure measurements (and a spacing in both x and y directions of 1.25 cm). In both cases Γ will be a rectangular parallelepiped of 70×40 cm^2 and height of 2.5 cm, located 0.4 cm below Γ_0 as shown in Fig. 6. The surface Γ contains the actual plate on its upper x-y plane. A uniform spacing of 2.5 cm was used for all points on Γ in case 1 and a spacing of 1.25 cm in case 2. The spacings over points on Γ_0 and Γ satisfy the minimal requirements to avoid aliasing when working with frequencies up to 2 kHz. Γ_0 and Γ have center over the origin (see Fig. 6). On the calculation of the BEM, we use meters instead of centimeters, and all the plots will be in MKS units.

In the results which follow, the ''exact'' normal velocity $\mathbf{v}^s$ on the plate were determined by standard planar NAH reconstruction[2] using the full 69×46-point array. It has been demonstrated that the reconstructions with the over-scanned hologram are extremely accurate.[2] The use of the BEM discussed in Sec. III with the iterative regularization discussed in Sec. V will give the reconstructed normal velocity $\mathbf{v}_r^s$ over Γ for 24 frequencies distributed equally from 100 Hz to 1.223 kHz, but all the comparisons and calculation of errors will be taken over the upper x-y plane of Γ.

A. Case 1

In Fig. 7 we show the relative error of the reconstructed normal velocity $\mathbf{v}_r^s$, i.e., $\|\mathbf{v}^s-\mathbf{v}_r^s\|_2/\|\mathbf{v}^s\|_2\times100\%$ for 24 frequencies. In (a) the DE approach (use transfer function $[\mathbf{G_n}]$ given in Eq. (11)) was used, while in (b) the IM approach [given in Eqs. (14)–(16)] was used. The ''optimal'' refers to the CGNE iteration that produces the minimal relative error. This ''optimal'' solution can be found, since the ''exact'' normal velocity is known. In the IM approach (b) the reconstruction given by the optimal iterations gives slightly smaller errors than the DE approach in (a). We notice that the GCV and L-curve stopping rules provide higher relative errors than Hanke–Raus for frequencies below 600 Hz. Moreover, it can also be observed that on the first frequency the relative error is over 40%. This behavior is explained in Fig. 8. In this figure, for each frequency, we plot the number of optimal iterations and iterations obtained by the GCV, L-curve, and Hanke–Raus stopping rules. Notice that GCV

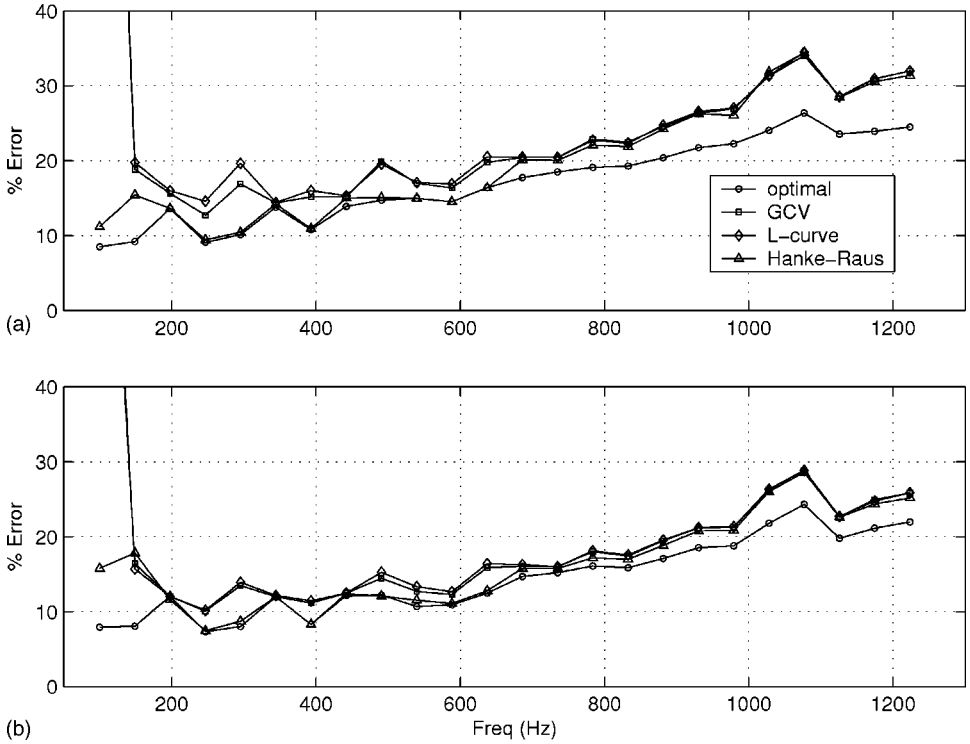

FIG. 7. Relative error comparison for the reconstructed normal velocity $\mathbf{v}_r^s$, obtained by CGNE and three different stopping rules. On (a) the DE approach (transfer function $[\mathbf{G_n}]$ given in Eq. (11)) was used, and on (b) the IM approach [single source representation given in Eq. (14)] was used. The vertical axis is the error % and the horizontal axis corresponds to the frequencies (Hz).

and L-curve required over 50 iterations for all frequencies. Hanke–Raus gave a number of iterations closer to, and sometimes smaller than, the optimal. In both cases the optimal number of iterations is below 30, which is one of the attractive characteristics of CGNE (for 100–600 Hz), since a small number of iterations will require a small amount of computational work. For the reconstruction of $\mathbf{v}_r^s$, a number of iterations less than the optimal gives an oversmooth reconstruction (the reconstruction will be smoother than required). A larger number of iterations than the optimal gives an undersmooth reconstruction (the reconstruction will amplify the noise). Based on the previous figures, it follows that an undersmooth reconstruction of $\mathbf{v}_r^s$ (caused by GCV and L-curve stopping rules) can lead to high amounts of relative error for lower frequencies. At higher frequencies, an undersmooth reconstruction is not that much of a serious problem with respect to the error, but at the cost of a useless amount of extra work done by the extra iterations.

Figure 9 shows the relative error plots of the reconstructed normal velocity obtained by the hybrid method (LSQR and Tikhonov with GCV given in Sec. IV) for 24 frequencies over the plate. As in Figs. 7 and 8, in (a) the DE

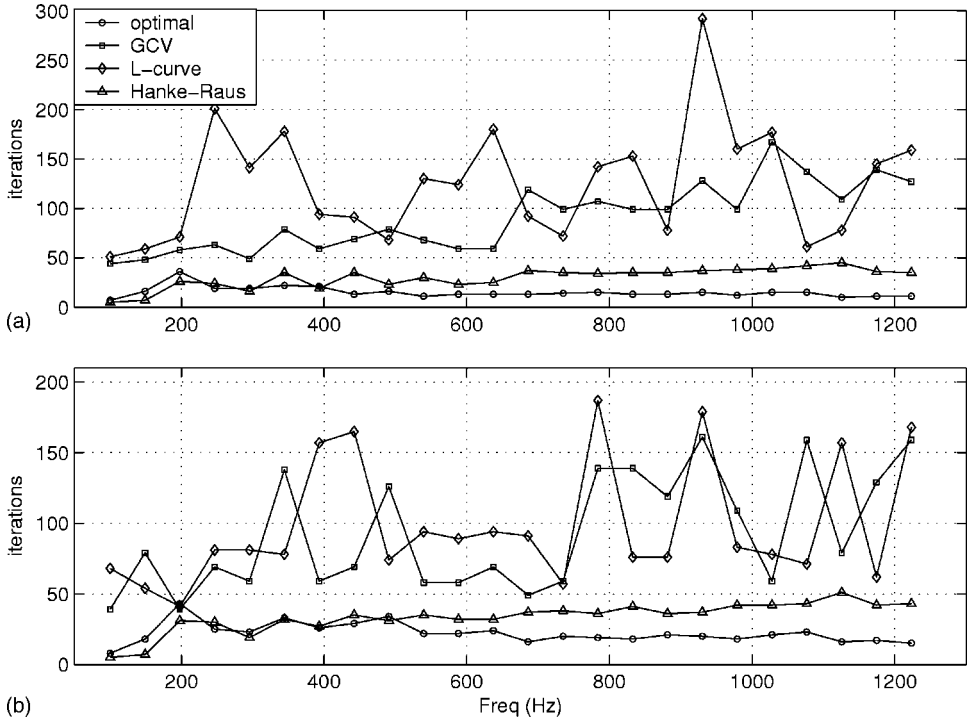

FIG. 8. Number of CGNE iterations used for the reconstruction of the normal velocity $\mathbf{v}_r^s$. The number of iterations were obtained using three different stopping rules: GCV, L-curve and Hanke-Raus. On (a) the DE approach (transfer function $[\mathbf{G_n}]$ given in Eq. (11)) was used, and on (b) the IM approach [single source representation given in Eq. (14)] was used. The vertical axis is the number of iterations and the horizontal axis corresponds to the frequencies (Hz).

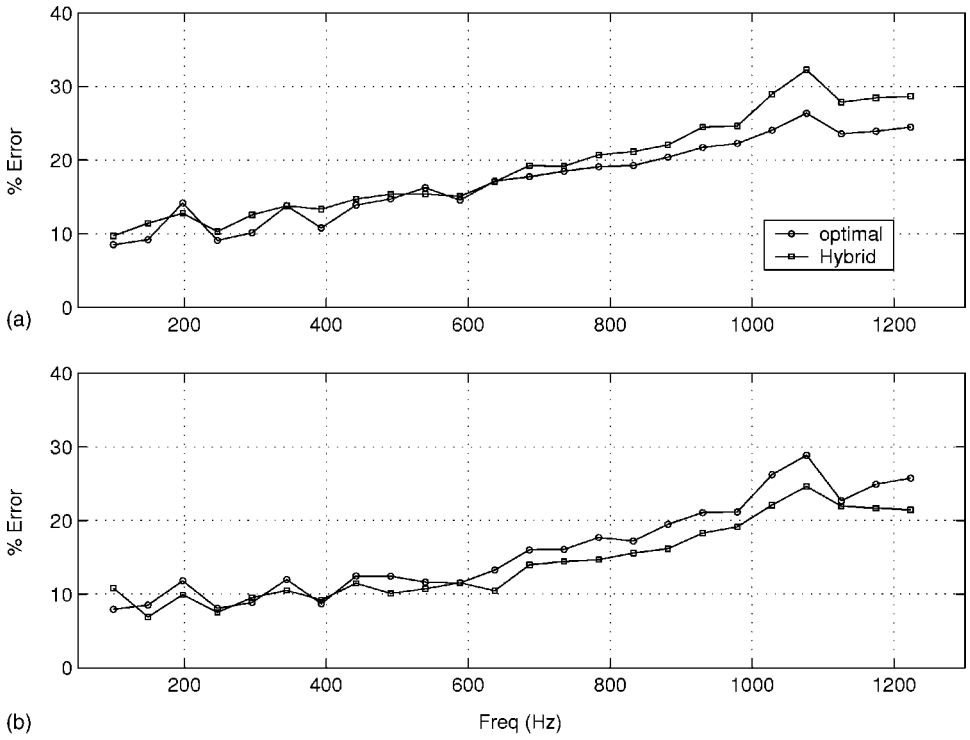

FIG. 9. Relative error comparison for the reconstructed normal velocity $\mathbf{v}_r^s$, obtained by regular CGNE optimal iterations and the Hybrid method. On (a) the DE approach (transfer function $[\mathbf{G_n}]$ given in Eq. (11)) was used, and on (b) the IM approach [single source representation given in Eq. (14)] was used. The vertical axis is the error % and the horizontal axis corresponds to the frequencies (Hz).

approach is used and in (b) the IM approach is used. As mentioned in the previous section, different from the regular CGNE iterations, the hybrid method will not depend crucially on a stopping rule to obtain the optimal number of iterations. This is the result of the ''inner'' Tikhonov regularization made on each step of the LSQR solution in Eq. (37). After a certain number of iterations l, the solution $\mathbf{z}_{(l)}$ will not differ much from $\mathbf{z}_{(l-1)}$. For that reason, the iteration is stopped when $\|\mathbf{z}_{(l)}-\mathbf{z}_{(l-1)}\|_2/\|\mathbf{z}_{(l-1)}\|_2<0.001$. For the given 24 frequencies the hybrid method needed between 40 and 80 iterations to satisfy this stoping criterion. The hybrid method will require more computational work than regular CGNE iterations, but this extra work will guarantee that the resultant solution $\mathbf{v}_r^s$ will be close to the optimal. In some cases the hybrid method yields smaller relative error than the optimal CGNE iterations (see Fig. 9).

B. Case 2

For a large number of measurement points the DE approach becomes computationally expensive because of the matrix inversion in Eqs. (12) and (13). For this case the creation of a matrix $[\mathbf{G_n}]$ with $M=3174$ and $N=4290$ will require the inversion of a 4290×4290 complex matrix $[\mathbf{D}^+]-[\mathbf{I}]$. The inversion itself will be as computationally expensive as the calculation of the SVD of $[\mathbf{G_n}]$ (which we want to avoid). On the other hand, the IM approach does not require this inversion and so will be computationally more efficient. For that reason the reconstruction for case 2 will be obtained using only the IM approach.

In Fig. 10(a) we show the relative error of the reconstructed normal velocity $\mathbf{v}_r^s$ obtained by CGNE, and in Fig. 10(b) we plot the respective number of iterations required by the GCV, L-curve, and Hanke–Raus stopping rules. We will observe the same behavior as in case 1, where GCV and L-curve will require more iterations than optimal, and Hanke–Raus will be closer to the optimal number of iterations. Figure 11 shows a gray-scale rendition on the real value of the reconstructed normal velocity $\mathbf{v}_r^s$ for the 24 frequencies, obtained by the hybrid method. As shown in the error plot of these reconstructions in Fig. 12, the errors are relatively small so the reconstructed $\mathbf{v}_r^s$ will look similar to the ''exact'' normal velocity. Notice that as in case 1, the relative error of the reconstruction for the hybrid method is sometimes smaller that the relative error from regular CGNE with optimal iterations.

VII. CONCLUSION

We have shown that two Krylov subspace methods and a hybrid method can be used as regularization methods for the reconstruction of the acoustic field using NAH. The iterative methods avoid the calculation of the SVD that can be computationally expensive for big matrix systems.

In Secs. IV A and IV B we explained the physical meaning of the Krylov subspace using orthonormal basis that result from the LSQR iterations. In Sec. IV C we study the convergence of the LSQR iterations into the least squares solution $\mathbf{z}_{LS}$ in Eq. (19). This convergence explains the ''semi-convergence'' phenomena found in iterative methods for ill-posed problems.

In Sec. VI our experiment with the plate data showed that CGNE iterations can be used as an effective implementation of regularization methods. These iterative methods were successfully used with the DE approach and the IM approach, producing similar reconstruction errors. In particular the IM approach was used when the matrix system in Eq. (17) was so big that the creation of the transfer function $[\mathbf{G_n}]$ was computationally expensive. The hybrid method yields

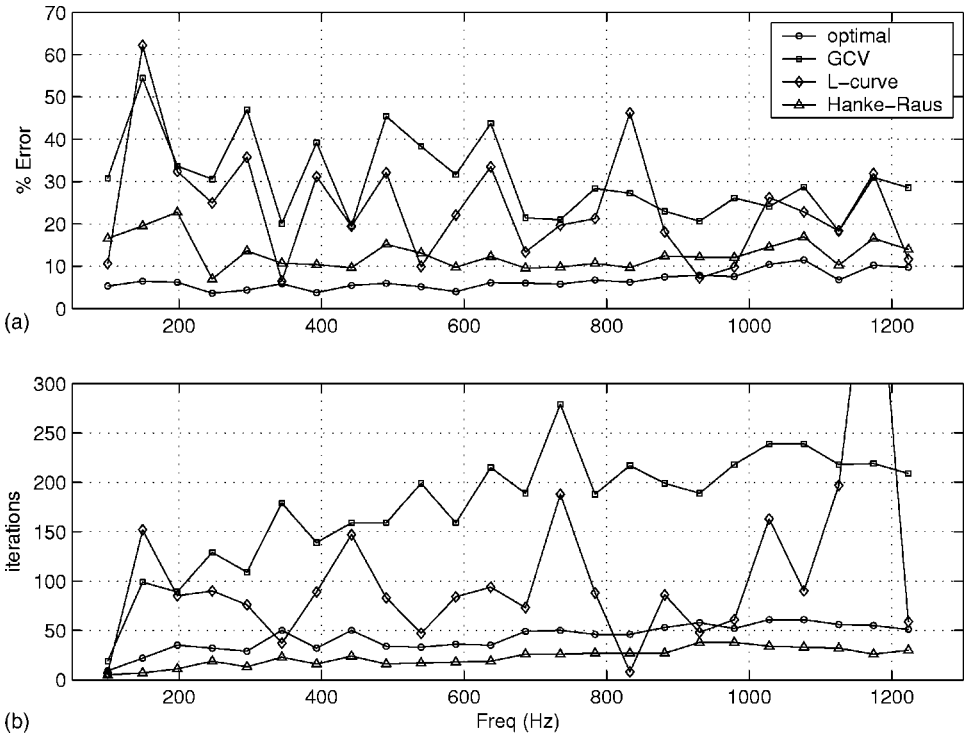

FIG. 10. Comparison of three different stopping rules of CGNE iterations for the IM approach [single source representation given in Eq. (14)]. (a) shows the relative error for the reconstructed normal velocity $\mathbf{v}_r^s$ and (b) Shows the number of CGNE iterations used for the reconstruction of the normal velocity $\mathbf{v}_r^s$. The horizontal axis corresponds to the frequencies (Hz).

reconstructions with the smaller relative error, but it usually requires more iterations than CGNE.

ACKNOWLEDGMENTS

The experimental measurement data from the planar hologram was provided by Brian Houston and Peter Herdic from the Naval Research Laboratory. This work was supported by ONR and NRC.

APPENDIX A

The formal proof to the convergence of the Krylov subspace methods into the least squares solution $\mathbf{z}_{LS}$ of Eq. (22) will require some advances techniques from functional analysis. For that reason, in this appendix, instead of a formal mathematical proof, we present a sketch of the formal proof that will help the reader understand some of the basic ingredients. We suggest the reader see Refs. 48, 49, and 30 for the formal proof.

The evaluation of a function f over the matrix $[\mathbf{A}]^H[\mathbf{A}]$ can be represented, using the SVD of $[\mathbf{A}]$, as

$$f([\mathbf{A}]^H[\mathbf{A}])=[\mathbf{V}]f(|\Sigma|^2)[\mathbf{V}]^H, \quad |\Sigma|^2=[\mathbf{\Sigma}]^H[\mathbf{\Sigma}], \tag{A1}$$

where $f(|\Sigma|^2)=\mathrm{diag}(f(\sigma_1^2),\ldots,f(\sigma_{N*}^2))$ (see Ref. 49). With this notation, the solution $\mathbf{z}_{LS}$ to Eq. (22) can be written as

$$\mathbf{z}_{LS}=([\mathbf{A}]^H[\mathbf{A}])^{-1}[\mathbf{A}]^H\tilde{\mathbf{p}}=[\mathbf{V}]f(|\Sigma|^2)[\mathbf{\Sigma}]^H[\mathbf{U}]^H\tilde{\mathbf{p}}, \tag{A2}$$

with $f(x)=1/x,\ x\in[\sigma_{N*},\sigma_1]$.

The SVD and the function notation in Eq. (A1) will be used to write a vector $\mathbf{y}\in\mathcal{K}^{(l)}([\mathbf{A}]^H\tilde{\mathbf{p}},[\mathbf{A}]^H[\mathbf{A}])$ as

$$\begin{aligned}\mathbf{y}&=a_0[\mathbf{A}]^H\tilde{\mathbf{p}}+a_1([\mathbf{A}]^H[\mathbf{A}])[\mathbf{A}]^H\tilde{\mathbf{p}}\\&\quad+\cdots+a_{l-1}([\mathbf{A}]^H[\mathbf{A}])^{l-1}[\mathbf{A}]^H\tilde{\mathbf{p}},\\&=[\mathbf{V}](a_0+a_1|\Sigma|^2+\cdots+a_{l-1}|\Sigma|^{2(l-1)})[\mathbf{\Sigma}]^H[\mathbf{U}]^H\tilde{\mathbf{p}},\\&=[\mathbf{V}]P^{(l)}(|\Sigma|^2)[\mathbf{\Sigma}]^H[\mathbf{U}]^H\tilde{\mathbf{p}},\end{aligned} \tag{A3}$$

where

$$P^{(l)}(x)=a_0+a_1x+a_2x^2+\cdots+a_{l-1}x^{l-1}. \tag{A4}$$

The above paragraph implies that any vector $\mathbf{y}$ that belongs to $\mathcal{K}^{(l)}([\mathbf{A}]^H\tilde{\mathbf{p}},[\mathbf{A}]^H[\mathbf{A}])$ can be represented as in Eq. (A1) using a polynomial $P^{(l)}$ of degree $l-1$ given in Eq. (A4). A key feature of the Krylov subspace methods is that for each iteration l, the coefficients $a_0,\ldots,a_{l-1}$ are chosen in such a way that the polynomial $P^{(l)}(x)$ approximates the function $1/x$ over $\sigma_{N*}\leqslant x\leqslant\sigma_1$. As we increase the number of iterations l, the Krylov subspace will be composed of polynomials with higher degree, so we might expect that the approximation $P^{(l)}$ to $1/x$ will become more accurate. In fact, this is a classic result known as the Stone–Weirstrass theorem (Ref. 48, Theorem IV.3). Then it can be concluded that the Krylov subspace methods applied to Eq. (22) will approximate the least squares solution $\mathbf{z}_{LS}$ in Eq. (19).

APPENDIX B

The multiplication of $[\mathbf{V}^{(l)}]$ by an $l\times l$ real matrix $[\tilde{\mathbf{V}}^{(l)}]$ will produce a resulting matrix with columns that are linear combinations of $\mathbf{v}_j^{(l)}$. Since $\mathbf{v}_j^{(l)}$, $j=1,\ldots,l$, form a basis for $\mathcal{K}^{(l)}([\mathbf{A}]^H\tilde{\mathbf{p}},[\mathbf{A}]^H[\mathbf{A}])$, then the columns $\hat{\mathbf{v}}_j^{(l)}$, $j=1,\ldots,l$, of $[\hat{\mathbf{V}}^{(l)}]$ form a basis for the same Krylov subspace. Moreover, it is not surprising to find that $[\hat{\mathbf{V}}^{(l)}]$ has orthonormal columns, since

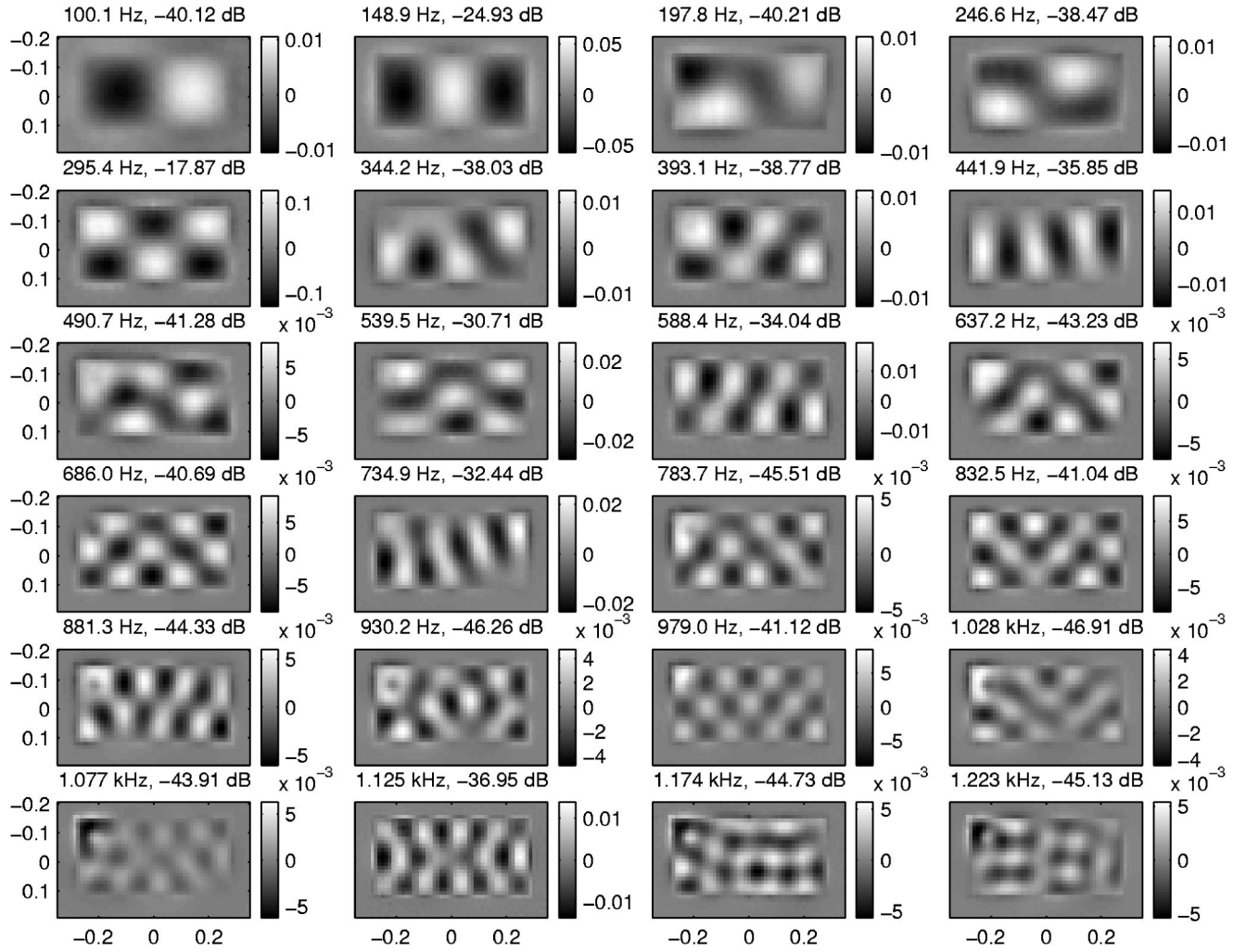

FIG. 11. Gray scale rendition of the real part of the normal velocity recovered using the IM approach [single source representation given in Eq. (14)] for 24 equally distributed frequencies between 100 Hz and 1.22 kHz. At each frequency we show the maximum dB level over plate.

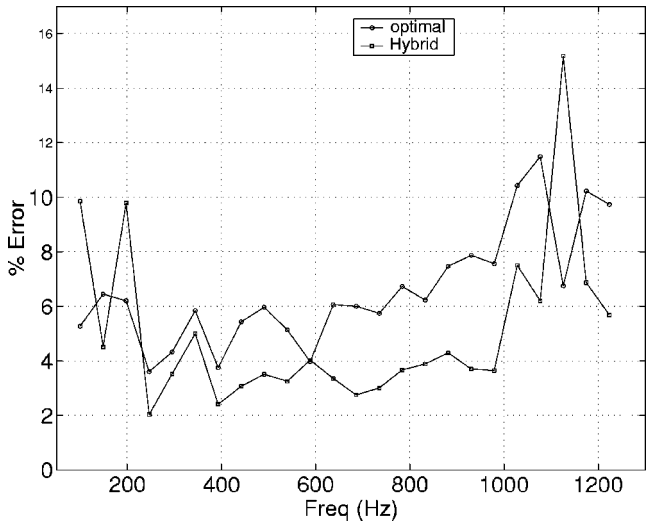

FIG. 12. Relative error comparison for the reconstructed normal velocity $\mathbf{v}_r^s$, obtained by regular CGNE optimal iterations and the hybrid method. The IM approach [single source representation given on Eq. (14)] was used. The vertical axis is the error % and the horizontal axis corresponds to the frequencies (Hz).

$$[\hat{\mathbf{V}}^{(l)}]^H[\hat{\mathbf{V}}^{(l)}] = ([\mathbf{V}^{(l)}][\tilde{\mathbf{V}}^{(l)}])^H[\mathbf{V}^{(l)}][\tilde{\mathbf{V}}^{(l)}]$$
$$= [\tilde{\mathbf{V}}^{(l)}]^H[\mathbf{V}^{(l)}]^H[\mathbf{V}^{(l)}][\tilde{\mathbf{V}}^{(l)}]$$
$$= [\tilde{\mathbf{V}}^{(l)}]^H[\tilde{\mathbf{V}}^{(l)}] = [\mathbf{I}^{(l)}],$$

where $[\mathbf{I}^{(l)}]$ is the $l \times l$ identity matrix. Similarly we can find that $[\hat{\mathbf{U}}^{(l)}]$ has orthonormal columns.

[1] E. G. Williams, "On Green functions for a cylindrical cavity," J. Acoust. Soc. Am. **102**, 3300–3307 (1997).
[2] E. G. Williams, *Fourier Acoustics: Sound Radiation and Nearfield Acoustical Holography* (Academic, London, UK, 1999).
[3] J. D. Maynard, "Acoustic holography for wideband, odd-shaped noise sources," in *Proceedings Inter-noise '88*, Avignon, France, September 1988, Vol. I, pp. 223–231.
[4] W. A. Veronesi and J. D. Maynard, "Digital holographic reconstruction of sources with arbitrarily shaped surfaces," J. Acoust. Soc. Am. **85**, 588–598 (1989).
[5] G.-T. Kim and B.-H. Lee, "3-d sound source reconstruction and field reprediction using the helmholtz integral equation," J. Sound Vib. **136**, 245–261 (1990).
[6] M. R. Bai, "Application of bem (boundary element method)-based acoustic holography to radiation analysis of sound sources with arbitrarily shaped geometries," J. Acoust. Soc. Am. **92**, 533–549 (1992).
[7] E. G. Williams, B. H. Houston, P. C. Herdic, S. T. Raveendra, and B. Gardner, "Interior nah in flight," J. Acoust. Soc. Am. **108**, 1451–1463 (2000).

[8] S. T. Raveendra, N. Vlahopoulos, and A. Glaves, ''An indirect boundary element formulation for multi-valued impedance simulation in structural acoustics,'' Appl. Math. Model. **22**, 379–393 (1998).
[9] N. Vlahopoulos and S. T. Raveerdra, ''Formulation, implementation and validation of multiple connection and free edge constraints in a indriect boundary element formulation,'' J. Sound Vib. **201**, 137–152 (1998).
[10] F. Augusztinovicz, ''Application and extension of acoustic holography techniques for tire noise investigations,'' J. Acoust. Soc. Am. **105**, 1373 (1999 (A)).
[11] Z. Zhang, N. Vlahopoulos, S. T. Raveendra, T. Allen, and K. Y. Zhang, ''A computational acoustic field reconstruction process based on an indirect boundary element formulation,'' J. Acoust. Soc. Am. **108**, 2167–2178 (2000).
[12] Z. Zhang, N. Vlahopoulos, T. Allen, and K. Y. Zhang, ''A source reconstruction process based on a indirect variational boundary element formulation,'' Eng. Anal. Boundary Elem. **25**, 93–114 (2001).
[13] A. Schuhmacher, J. Hald, K. B. Rasmussen, and P. C. Hansen, ''Sound source reconstruction using inverse boundary element calculations,'' J. Acoust. Soc. Am. **113**, 114–126 (2003).
[14] T. K. DeLillo, V. Isakov, N. Valdivia, and L. Wang, ''The detection of the source of acoustical noise in two dimensions,'' SIAM (Soc. Ind. Appl. Math.) J. Appl. Math. **61**(6), 2104–2121 (2001).
[15] T. K. DeLillo, V. Isakov, N. Valdivia, and L. Wang, ''The detection of surface vibrations from interior acoustical pressure,'' Inverse Probl. **19**(3), 507–524 (2003).
[16] N. Valdivia and E. G. Williams, ''Implicit methods of solution to integral formulations in boundary element methods based near-field acoustic holography,'' J. Acoust. Soc. Am. **116**, 1559–1572 (2004).
[17] L. Landweber, ''An iteration formula for fredholm integral equations of the first kind,'' Am. J. Math. **73**, 615–624 (1951).
[18] O. N. Strand, ''Theory and methods related to the singular-function expansion and landweber's iteration for integral equations of the first kind,'' SIAM (Soc. Ind. Appl. Math.) J. Numer. Anal. **11**(4), 798–825 (1974).
[19] J. Graves and P. M. Prenter, ''Numerical iterative filters applied to first kind fredholm integral equations,'' Numer. Math. **30**, 281–299 (1978).
[20] H. E. Fleming, ''Equivalence of regularization and truncated iteration in the solution of ill-posed image reconstruction,'' Linear Algebr. Appl. **130**, 133–150 (1990).
[21] M. Hanke, ''Accelerated landweber iterations for the solution of ill-posed equations,'' Numer. Math. **60**(3), 341–373 (1990).
[22] M. R. Hestenes and E. L. Stiefel, ''Method of conjugate gradients for solving linear systems,'' J. Res. Natl. Bur. Stand. **49**, 409–436 (1952).
[23] M. Hanke, *Conjugate Gradient Methods for Ill-Posed Problems* (Kluwer Academic, Boston, 1995).
[24] T. K. DeLillo, T. Hrycak, and N. Valdivia, ''Iterative regularization methods for inverse problems in acoustics,'' in Proceedings of ASME2002, New Orleans, LA, November 2002.
[25] C. C. Paige and M. A. Saunders, ''LSQR: An algorithm for sparse linear equations and sparse least squares,'' ACM Trans. Math. Softw. **8**(1), 43–71 (1982).
[26] M. E. Kilmer and D. P. O'Leary, ''Choosing regularization parameters in iterative methods for ill-posed problems,'' SIAM J. Matrix Anal. Appl. **22**(4), 1204–1221 (2001).
[27] D. Colton and R. Kress, *Integral Equation Methods in Scattering Theory* (Wiley-Interscience, New York, 1983).
[28] D. Colton and R. Kress, *Inverse Acoustics and Electromagnetic Scattering Theory* (Springer-Verlag, New York, 1992).
[29] P. C. Hansen, *Rank-Deficient and Discrete Ill-Posed Problems* (SIAM, Philadelphia, PA, 1998).
[30] H. W. Engl, M. Hanke, and A. Neubauer, *Regularization of Inverse Problems* (Kluwer Academic, Boston, 1996).
[31] E. G. Williams, ''Regularization methods for near-field acoustical holography,'' J. Acoust. Soc. Am. **110**, 1976–1988 (2001).
[32] D. Calvetti, B. Lewis, and L. Reichel, ''On the choice of subspace for iterative methods for linear discrete ill-posed problems,'' Int. J. Appl. Math Comput. Sci. **11**(5), 1069–1092 (2001).
[33] D. Calvetti, B. Lewis, and L. Reichel, ''GMRES, L-curves, and discrete ill-posed problems,'' BIT **42**(1), 44–65 (2001).
[34] D. Calvetti, B. Lewis, and L. Reichel, ''On the regularizing properties of GMRES,'' Numer. Math. **91**(4), 605–625 (2002).
[35] Å. Björck, ''A bidiagonalization algorithm for solving large and sparse ill-posed systems of linear equations,'' BIT **28**, 659–670 (1988).
[36] Å. Björck, ''An implicit shift bidiagonalization algorithm for ill-posed systems,'' BIT **34**, 510–534 (1994).
[37] G. L. G. Sleijpen and A. van der Sluis, ''Further results on the convergence behavior of conjugate-gradients and Ritz values,'' Linear Algebr. Appl. **246**, 233–278 (1996).
[38] A. van der Sluis and H. A. van der Vorst, ''The rate of convergence of conjugate gradients,'' Numer. Math. **48**, 543–560 (1986).
[39] A. van der Sluis, ''The convergence behaviour of conjugate gradients and Ritz values in various circumstances,'' Iterative Methods Linear Algebra, **48**, 543–560 (1992).
[40] A. van der Sluis and H. A. van der Vorst, ''The convergence behaviour of Ritz values in the presence of close eigenvalues,'' Linear Algebr. Appl. **88/89**, 651–694 (1987).
[41] A. van der Sluis and H. A. van der Vorst, ''SIRT- and CG-type methods for the iterative solution of sparse linear least-squares problems,'' Linear Algebr. Appl. **130**, 257–302 (1990).
[42] H. A. van der Sluis, ''The convergence behaviour of conjugate gradients and Ritz values in various circumstances,'' in *Iterative Methods in Linear Algebra*, edited by R. Beauwens and P. de Groen (Elsevier Science, North-Holland, Amsterdam, 1992).
[43] H. A. van der Vorst, ''Conjugate gradient type methods for nonsymmetric linear systems,'' in *Iterative Methods in Linear Algebra*, edited by R. Beauwens and P. de Groen (Elsevier Science, North-Holland, Amsterdam, 1992).
[44] P. C. Hansen and D. P. O'Leary, ''The use of the 1-curve in the regularization of discrete ill-posed problems,'' SIAM J. Sci. Comput. (USA) **14**(6), 341–373 (1993).
[45] M. Hanke and T. Raus, ''A general heuristic for choosing the regularization parameter in ill-posed problems,'' SIAM J. Sci. Comput. (USA) **17**(4), 956–972 (1996).
[46] M. Hanke and P. C. Hansen, ''Regularization methods for large-scale problems,'' Surv. Math. Ind. **3**, 253–315 (1993).
[47] E. G. Williams and B. Houston, ''Fast Fourier transform and singular value decomposition for patch nearfield acoustical holography,'' J. Acoust. Soc. Am. **114**, 1322–1332 (2003).
[48] M. Reed and B. Simon, *Functional Analysis* (Academic, New York, 1980).
[49] G. H. Golub and C. Van Loan, *Matrix Computations* (Johns Hopkins U.P., Baltimore, MD, 1996).

Helmholtz resonator lined with absorbing material

A. Selamet,[a] M. B. Xu, and I.-J. Lee
Department of Mechanical Engineering and The Center for Automotive Research, The Ohio State University, Columbus, Ohio 43210

N. T. Huff
Owens Corning, Novi, Michigan 48377

(Received 21 May 2004; revised 25 August 2004; accepted 4 November 2004)

A closed-form, two-dimensional analytical solution is developed to investigate the acoustic performance of a concentric circular Helmholtz resonator lined with fibrous material. The effect of density and the thickness of the fibrous material in the cavity is examined on the resonance frequency and the transmission loss. With the expressions for the eigenvalue and eigenfunction in the cavity, the transmission loss is obtained for a piston-driven model by applying a pressure/velocity matching technique. The results from the analytical methods are compared to the numerical predictions from a three-dimensional boundary element method and the experimental data obtained from an impedance tube setup. It is shown that the acoustic performance of a Helmholtz resonator may be modified considerably by the density and thickness of the fibrous material without changing the cavity dimensions. © *2005 Acoustical Society of America.* [DOI: 10.1121/1.1841571]

PACS numbers: 43.50.Gf, 43.20.Mv [ANN] Pages: 725–733

I. INTRODUCTION

Their continuous strands combined with broadband acoustic attenuation characteristics make fibrous materials desirable for silencer applications. In terms of the bulk-reacting model, Scott[1] presented an analysis of the sound transmission in infinite rectangular and circular ducts; Ko[2] discussed the characteristics of sound attenuation of infinite rectangular, annular, and circular ducts; and Nilsson and Brander[3] and Cummings and Chang[4] investigated the effects of a perforate screen and mean flow on the modal attenuation rates, respectively. Cummings and Chang[5] further analyzed a finite length dissipative expansion silencer including mean flow by a mode-matching technique. Peat[6] developed a transfer matrix formulation for a dissipative expansion chamber from the match of the average acoustic pressure and volume velocity across the chamber discontinuities. Since only the fundamental mode was included, the model's accuracy was confined to low frequencies. By including additional terms in the series expansions for the Bessel and Neumann functions, Kirby[7] determined transmission loss for a circular dissipative duct filled with fibrous material which was separated from the mean flow path by a perforated screen. Due to the inherent limitation of expansions, the approach remains confined to relatively low frequencies. Selamet *et al.*[8] developed a one-dimensional (1D) analytical and three-dimensional (3D) boundary element method (BEM) approaches for sound attenuation in single-pass concentric perforated dissipative silencers. They further investigated numerically and experimentally the acoustic behavior of a specific type of hybrid silencer, consisting of two single-pass perforated dissipative chambers combined with a Helmholtz resonator.[9] Xu *et al.*[10] developed a two-dimensional (2D) analytical solution to examine the acoustic performance of dissipative expansion chambers. Selamet *et al.*[11] further investigated the effect of perforated ducts on the sound attenuation in dissipative silencers.

While the fibrous material is known to be typically effective at relatively high frequencies, the reactive Helmholtz resonators are widely used to control noise at low frequencies. Such resonators consist of a volume communicating to main duct through a neck and produce narrow bands of high acoustic attenuation. The resonance frequency modeled by an equivalent spring-mass analogy is $f_r=(c_0/2\pi)\sqrt{S_n/(V_c L_n)}$ with c_0 being the speed of sound and S_n, L_n, and V_c being the neck cross-sectional area, the neck length, and the resonator volume, respectively. However, due to the higher modes excited on both sides of the neck, the neck length is usually ''corrected'' by adding a term (end correction δ_n) to improve the accuracy.[12,13] Ingard[12] investigated the effect of neck geometry, such as cross-sectional area shape, location, and size, on the resonance frequency of a Helmholtz resonator with a circular or rectangular cavity cross section. Alster[13] extended the spring-mass analogy and presented a semiempirical formula for resonators of various shapes. Although various expressions of end correction have been suggested, the correction at the junction remains somewhat unclear because of the three-dimensional structure.[14] In order to predict resonator response accurately, a multi-dimensional analysis of the connector-volume interface is usually required. For the reactive Helmholtz resonators, the effect of cavity volume, cavity shape, neck location, and neck extension have been recently investigated with different approaches.[15–18] In addition to the effect of length-to-diameter ratio of the volume on the resonance frequency and transmission loss characteristics by using lumped and 1D approaches,[15] a number of circular concentric configurations have been studied with lumped, 1D radial and axial, 2D analytical, and 3D BEM approaches.[16] A 3D analytical approach is proposed to investigate the effect of neck offset on the

[a]Electronic mail: selamet.1@osu.edu

behavior of circular asymmetric Helmholtz resonators.[17] The effect of neck extension into the cavity of a circular Helmholtz resonator has also been examined.[18]

While the fibrous materials have been used to enhance the attenuation of another reactive silencer, the expansion chamber, they have not been closely examined in connection with Helmholtz resonators, except for some early claims.[19] Therefore, the basics of the impact of fibrous material on the Helmholtz resonator are yet to be explored. Thus, the objective of the present study is, in the absence of mean flow in the main duct, to (1) investigate theoretically, numerically, and experimentally the acoustic attenuation performance of a concentric circular Helmholtz resonator with the cavity lined with fibrous material, and (2) examine the effect of the density and thickness of this material on the resonator behavior. A 2D analytical solution is developed to investigate the acoustic performance. With the eigenvalue and eigenfunction determined from the governing eigenequation, the transmission loss is obtained by applying a pressure/velocity matching technique to the piston-driven model. The results from the analytical approach are compared to the predictions from a 3D boundary element method and the experimental data obtained from an impedance tube setup.

Following this Introduction, Sec. II obtains the expressions for the eigenvalue and eigenfunction in the cavity by solving the governing eigenequation, and develops a two-dimensional analytical approach by applying a pressure/velocity matching technique to the piston-driven model. Following a brief summary of the 3D boundary element method in Sec. III, Sec. IV discusses the effect of the fibrous material on the transmission loss, and compares the analytical results with numerical predictions and experiments. The study is concluded with final remarks in Sec. V.

II. TWO-DIMENSIONAL ANALYTICAL APPROACH

A piston-driven circular Helmholtz resonator is shown in Fig. 1(a), with a cavity volume of circular cross-section of radius r_3 lined with fibrous material of thickness $h=r_3-r_2$, and a neck of radius r_1 and length L_n. The neck, the airway, and the fibrous material in the cavity are denoted by domains I, II_a, and II_b, respectively.

A. Wave propagation for circular neck (domain I)

For a two-dimensional axisymmetric wave propagation in the neck (domain I), the Helmholtz equation is given by

$$\frac{\partial^2 P}{\partial r^2}+\frac{1}{r}\frac{\partial P}{\partial r}+\frac{\partial^2 P}{\partial x^2}+k_0^2 P=0 \tag{1}$$

with P being the acoustic pressure and $k_0=2\pi f/c_0$ being the wave number of the air with c_0 being the speed of sound and f the frequency. The acoustic pressure can be expressed as

$$P_A(r,x)=\sum_{n=0}^{\infty}(A_n^+ e^{-jk_{x,A,n}x}+A_n^- e^{jk_{x,A,n}x})\psi_{A,n}(r), \tag{2}$$

where the subscripts x, A, n denote axial direction, domain I, and mode number, respectively. A_n^+ and A_n^- are the modal amplitudes corresponding to components traveling in the positive and negative x directions, respectively;

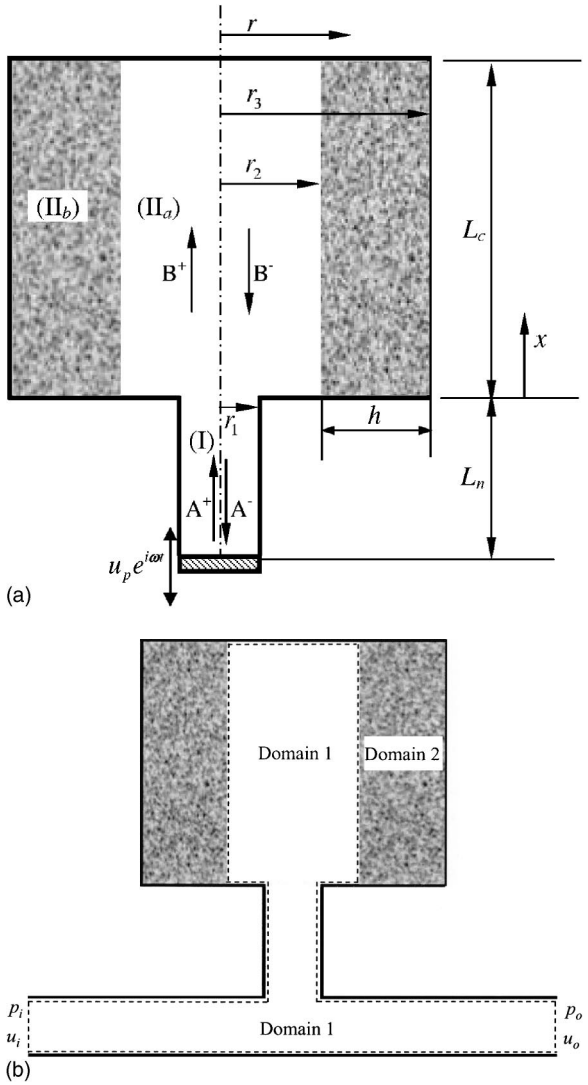

FIG. 1. (a) Wave propagation in a piston-driven Helmholtz resonator with the cavity volume lined with fibrous material. (b) Pipe-mounted Helmholtz resonator with the cavity volume lined with fibrous material.

$$\psi_{A,n}(r)=J_0(k_{r,A,n}r) \tag{3}$$

is the eigenfunction where J_0 is the zeroth-order Bessel function of the first kind, $k_{r,A,n}$ is the radial wave number satisfying the rigid wall boundary condition of

$$J_0'(k_{r,A,n}r_1)=0, \tag{4}$$

and

$$k_{x,A,n}=\begin{cases}\sqrt{k_0^2-k_{r,A,n}^2}, & k_0>k_{r,A,n},\\ -\sqrt{k_0^2-k_{r,A,n}^2}, & k_0<k_{r,A,n},\end{cases} \tag{5}$$

is the wave number in the axial direction.

In terms of the linearized momentum equation, the particle velocity in the x direction may then be obtained from Eq. (2) as

$$u_{x,A}(r,x)=\frac{1}{\rho_0\omega}\sum_{n=0}^{\infty}k_{x,A,n}(A_n^+ e^{-jk_{x,A,n}x}-A_n^- e^{jk_{x,A,n}x})\times\psi_{A,n}(r) \tag{6}$$

with ρ_0 being the density of air and ω the angular velocity.

B. Wave propagation for cavity volume (domains II_a and II_b)

The cavity volume (domains II_a and II_b) of circular cross section is covered by fibrous material of thickness h. The filling material is assumed to be homogeneous and isotropic, and characterized by the complex speed of sound $\tilde{c}$ and density $\tilde{\rho}$. Similar to the preceding section, the two-dimensional sound wave propagation in cylindrical coordinates (r,x) is governed by

$$\frac{\partial^2 P}{\partial r^2}+\frac{1}{r}\frac{\partial P}{\partial r}+\frac{\partial^2 P}{\partial x^2}+\kappa^2 P=0, \tag{7}$$

where

$$\kappa=\begin{cases} k_0, & 0\leqslant r\leqslant r_2, \\ \tilde{k}, & r_2\leqslant r\leqslant r_3, \end{cases} \tag{8}$$

with $\tilde{k}=2\pi f/\tilde{c}$ denoting the wave number of the fibrous material (domain II_b).

The airway and the fibrous material have the common axial wave number $k_{x,B,n}$ and different radial wave numbers $k_{r,B,n}$ (for the air) and $\tilde{k}_{r,B,n}$ (for the fibrous material) related by

$$k_{r,B,n}^2+k_{x,B,n}^2=k_0^2 \tag{9}$$

and

$$\tilde{k}_{r,B,n}^2+k_{x,B,n}^2=\tilde{k}^2. \tag{10}$$

The acoustic pressure and axial and radial particle velocities are then expressed as

$$P_B(r,x)=\sum_{n=0}^{\infty}(B_n^+e^{-jk_{x,B,n}x}+B_n^-e^{jk_{x,B,n}x})\psi_{B,n,P}(r), \tag{11}$$

$$u_{x,B}(r,x)=\frac{1}{\rho_0\omega}\sum_{n=0}^{\infty}k_{x,B,n}(B_n^+e^{-jk_{x,B,n}x}-B_n^-e^{jk_{x,B,n}x})\psi_{B,n,u_x}(r), \tag{12}$$

and

$$u_{r,B}(r,x)=\frac{j}{\rho_0\omega}\sum_{n=0}^{\infty}(B_n^+e^{-jk_{x,B,n}x}+B_n^-e^{jk_{x,B,n}x})\psi_{B,n,u_r}(r). \tag{13}$$

Here

$$P_B(r,x)=\begin{cases} P_{II_a}(r,x), & 0\leqslant r\leqslant r_2, \\ P_{II_b}(r,x), & r_2\leqslant r\leqslant r_3, \end{cases} \tag{14a}$$

$$u_{x,B}(r,x)=\begin{cases} u_{x,II_a}(r,x), & 0\leqslant r\leqslant r_2, \\ u_{x,II_b}(r,x), & r_2\leqslant r\leqslant r_3, \end{cases} \tag{14b}$$

$$u_{r,B}(r,x)=\begin{cases} u_{r,II_a}(r,x), & 0\leqslant r\leqslant r_2, \\ u_{r,II_b}(r,x), & r_2\leqslant r\leqslant r_3, \end{cases} \tag{14c}$$

$$\psi_{B,n,P}(r)=\begin{cases} \psi_{II_a,n,P}(r), & 0\leqslant r\leqslant r_2, \\ \psi_{II_b,n,P}(r), & r_2\leqslant r\leqslant r_3, \end{cases} \tag{14d}$$

$$\psi_{B,n,u_x}(r)=\begin{cases} \psi_{II_a,n,u_x}(r)=\psi_{II_a,n,P}(r), & 0\leqslant r\leqslant r_2, \\ \psi_{II_b,n,u_x}(r)=\dfrac{\rho_0}{\tilde{\rho}}\psi_{II_b,n,P}(r), & r_2\leqslant r\leqslant r_3, \end{cases} \tag{14e}$$

$$\psi_{B,n,u_r}(r)=\begin{cases} \psi_{II_a,n,u_r}(r)=\dfrac{\partial\psi_{II_a,n,P}(r)}{\partial r}, & 0\leqslant r\leqslant r_2, \\ \psi_{II_b,n,u_r}(r)=\dfrac{\rho_0}{\tilde{\rho}}\dfrac{\partial\psi_{II_b,n,P}(r)}{\partial r}, & r_2\leqslant r\leqslant r_3, \end{cases} \tag{14f}$$

where subscripts B, II_a, II_b, and r denote the cavity, domain II_a (the central airway), domain II_b (the fibrous material), and radial direction, respectively; B_n^+ and B_n^- the modal amplitudes; and $\psi_{B,n,P}$, ψ_{B,n,u_x}, and ψ_{B,n,u_r} the transverse modal eigenfunctions for the pressure and axial and radial particle velocities, respectively. Substituting Eqs. (9)–(11) into (7) gives

$$\frac{\partial^2\psi_{B,n,P}(r)}{\partial r^2}+\frac{1}{r}\frac{\partial\psi_{B,n,P}(r)}{\partial r}+\kappa_{r,B,n}^2\psi_{B,n,P}(r)=0. \tag{15}$$

The solution for Eq. (15) is expressed as

$$\psi_{B,n,P}(r)=\begin{cases} C_1J_0(k_{r,B,n}r)+C_2Y_0(k_{r,B,n}r), & 0\leqslant r\leqslant r_2, \\ C_3J_0(\tilde{k}_{r,B,n}r)+C_4Y_0(\tilde{k}_{r,B,n}r), & r_2\leqslant r\leqslant r_3, \end{cases} \tag{16}$$

where Y_0 denotes the zeroth-order Neumann function; C_1-C_4 are the coefficients related by the following four boundary conditions at $r=0$, r_2, and r_3:

(1) At $r=0$, the pressure is finite, thus Eqs. (11) and (16) yield

$$C_2=0. \tag{17}$$

(2) From Eqs. (13), (14), and (16), the rigid wall boundary condition at $r=r_3$ gives

$$C_3J_1(\tilde{k}_{r,B,n}r_3)+C_4Y_1(\tilde{k}_{r,B,n}r_3)=0 \tag{18}$$

with J_1 and Y_1 being the first-order Bessel and Neumann functions, respectively.

(3) From Eqs. (13), (14), and (16), the continuity of radial particle velocity at $r=r_2$ gives

$$\frac{k_{r,B,n}}{\rho_0}[C_1J_1(k_{r,B,n}r_2)+C_2Y_1(k_{r,B,n}r_2)]=\frac{\tilde{k}_{r,B,n}}{\tilde{\rho}}[C_3J_1(\tilde{k}_{r,B,n}r_2)+C_4Y_1(\tilde{k}_{r,B,n}r_2)]. \tag{19}$$

(4) At $r=r_2$, the continuity of the acoustic pressure in Eq. (11) yields

$$C_1 J_0(k_{r,B,n} r_2) + C_2 Y_0(k_{r,B,n} r_2) = C_3 J_0(\tilde{k}_{r,B,n} r_2) + C_4 Y_0(\tilde{k}_{r,B,n} r_2). \tag{20}$$

The foregoing boundary conditions [Eqs. (17)–(20)] yield the following characteristic equation:

$$\frac{\rho_0 \tilde{k}_{r,B,n}}{\tilde{\rho} k_{r,B,n}} \frac{J_0(r_2 k_{r,B,n})}{J_1(r_2 k_{r,B,n})} = \frac{J_0(r_2\tilde{k}_{r,B,n}) Y_1(r_3\tilde{k}_{r,B,n}) - Y_0(r_2\tilde{k}_{r,B,n}) J_1(r_3\tilde{k}_{r,B,n})}{J_1(r_2\tilde{k}_{r,B,n}) Y_1(r_3\tilde{k}_{r,B,n}) - Y_1(r_2\tilde{k}_{r,B,n}) J_1(r_3\tilde{k}_{r,B,n})}. \tag{21}$$

The transverse eigenfunctions for the pressure and the axial velocity can then be determined as

$$\psi_{B,n,P}(r) = \begin{cases} J_0(k_{r,B,n} r), & 0 \leqslant r \leqslant r_2, \\ C_5 \left[J_0(\tilde{k}_{r,B,n} r) - \dfrac{J_1(\tilde{k}_{r,B,n} r_3)}{Y_1(\tilde{k}_{r,B,n} r_3)} Y_0(\tilde{k}_{r,B,n} r) \right], & r_2 \leqslant r \leqslant r_3, \end{cases} \tag{22a}$$

$$\psi_{B,n,u_x}(r) = \begin{cases} J_0(k_{r,B,n} r), & 0 \leqslant r \leqslant r_2, \\ C_5 \dfrac{\rho_0}{\tilde{\rho}} \left[J_0(\tilde{k}_{r,B,n} r) - \dfrac{J_1(\tilde{k}_{r,B,n} r_3)}{Y_1(\tilde{k}_{r,B,n} r_3)} Y_0(\tilde{k}_{r,B,n} r) \right], & r_2 \leqslant r \leqslant r_3, \end{cases} \tag{22b}$$

with

$$C_5 = \frac{J_0(k_{r,B,n} r_2) Y_1(\tilde{k}_{r,B,n} r_3)}{J_0(\tilde{k}_{r,B,n} r_2) Y_1(\tilde{k}_{r,B,n} r_3) - J_1(\tilde{k}_{r,B,n} r_3) Y_0(\tilde{k}_{r,B,n} r_2)}. \tag{23}$$

Equations (11), (12), (14), and (22) yield the pressure and the particle axial velocity in the cavity as

$$P_B(r,x) = \begin{cases} \displaystyle\sum_{n=0}^{\infty} (B_n^+ e^{-jk_{x,B,n}x} + B_n^- e^{jk_{x,B,n}x}) J_0(k_{r,B,n} r), & 0 \leqslant r \leqslant r_2, \\ \displaystyle\sum_{n=0}^{\infty} C_5 (B_n^+ e^{-jk_{x,B,n}x} + B_n^- e^{jk_{x,B,n}x}) \left[J_0(\tilde{k}_{r,B,n} r) - \dfrac{J_1(\tilde{k}_{r,B,n} r_3)}{Y_1(\tilde{k}_{r,B,n} r_3)} Y_0(\tilde{k}_{r,B,n} r) \right], & r_2 \leqslant r \leqslant r_3, \end{cases} \tag{24a}$$

and

$$u_{x,B}(r,x) = \begin{cases} \dfrac{1}{\rho_0 \omega} \displaystyle\sum_{n=0}^{\infty} k_{x,B,n} (B_n^+ e^{-jk_{x,B,n}x} - B_n^- e^{jk_{x,B,n}x}) J_0(k_{r,B,n} r), & 0 \leqslant r \leqslant r_2, \\ \dfrac{1}{\tilde{\rho} \omega} \displaystyle\sum_{n=0}^{\infty} k_{x,B,n} C_5 (B_n^+ e^{-jk_{x,B,n}x} - B_n^- e^{jk_{x,B,n}x}) \left[J_0(\tilde{k}_{r,B,n} r) - \dfrac{J_1(\tilde{k}_{r,B,n} r_3)}{Y_1(\tilde{k}_{r,B,n} r_3)} Y_0(\tilde{k}_{r,B,n} r) \right], & r_2 \leqslant r \leqslant r_3. \end{cases} \tag{24b}$$

The expressions for the pressure and particle velocity are similar to those in the neck if the cavity contains only the air or the fibrous material.

C. Boundary conditions

With the expressions of the pressure and particle velocity in both the cavity and neck [Eqs. (2), (6), and (24)], the unknown coefficients are then determined by using the boundary conditions at $x=0$ and $x=L_c$. In view of Eq. (24), the rigid boundary condition at $x=L_c$, $u_{x,B}(r,x=L_c)=0$, gives

$$B_n^- = B_n^+ e^{-2jk_{x,B,n}L_c}, \quad n=0,1,2,...,\infty. \tag{25}$$

At $x=0$, the continuity of the acoustic pressure and axial particle velocity across the interface gives

$$P_A = P_B, \quad 0 \leqslant r \leqslant r_1, \tag{26}$$

and

$$u_B = \begin{cases} u_A, & 0 \leqslant r \leqslant r_1, \\ 0, & r_1 \leqslant r \leqslant r_3, \end{cases} \tag{27}$$

or, in view of Eqs. (2), (6), and (24),

$$\sum_{n=0}^{\infty} (A_n^+ + A_n^-) \psi_{A,n}(r) = \sum_{n=0}^{\infty} (B_n^+ + B_n^-) \psi_{B,n,P}(r), \quad 0 \leqslant r \leqslant r_1, \tag{28}$$

and

$$\sum_{n=0}^{\infty} k_{x,B,n}(B_n^+ - B_n^-)\psi_{B,n,u_x}(r)$$

$$= \begin{cases} \sum_{n=0}^{\infty} k_{x,A,n}(A_n^+ - A_n^-)\psi_{A,n}(r), & 0 \leqslant r \leqslant r_1, \\ 0, & r_1 \leqslant r \leqslant r_3. \end{cases} \tag{29}$$

In order to solve Eqs. (28) and (29), the infinite series of unknown amplitudes must be truncated to a suitable number, and the equations of the same number solved for the amplitudes of the acoustic waves. An analytical approach originated in Ref. 20 is used to match the sound field between the neck and cavity. Imposing the continuities of the integral of the pressure and axial velocity over discrete zones of the neck-cavity interface ($x=0$), Eqs. (28) and (29) yield the pressure and velocity matching conditions

$$\sum_{n=0}^{N} (A_n^+ + A_n^-) \int_0^{r_{m,P}} \psi_{A,n}(r)dr$$

$$= \sum_{n=0}^{N} (B_n^+ + B_n^-) \int_0^{r_{m,P}} \psi_{B,n,P}(r)dr, \tag{30}$$

$$\sum_{n=0}^{N} k_{x,B,n}(B_n^+ - B_n^-) \int_0^{r_{m,u}} \psi_{B,n,u_x}(r)dr$$

$$= \begin{cases} \sum_{n=0}^{N} k_{x,A,n}(A_n^+ - A_n^-) \int_0^{r_{m,u}} \psi_{A,n}(r)dr, & 0 \leqslant r_{m,u} \leqslant r_1, \\ \sum_{n=0}^{N} k_{x,A,n}(A_n^+ - A_n^-) \int_0^{r_1} \psi_{A,n}(r)dr, & r_1 \leqslant r_{m,u} \leqslant r_3, \end{cases} \tag{31}$$

with

$$r_{m,P} = \frac{m}{N+1} r_1, \quad m = 1,...,N+1, \tag{32}$$

$$r_{m,u} = \frac{m}{N+1} r_3, \quad m = 1,...,N+1. \tag{33}$$

D. Resonance frequency and transmission loss

Assuming decay of the higher order modes through neck from $x=0$ to $x=-L_n$, the acoustic impedance at $x=-L_n$ can be calculated with the amplitudes determined from Eqs. (25), (30), and (32) as[18]

$$Z_H = \frac{P_A}{\rho_0 c_0 u_p} \tag{34}$$

with u_p being the axial velocity at $x=-L_n$, leading to the evaluation of resonance frequency. With an anechoic termination at the exit of the main duct and plane wave propagation through the main duct, transmission loss for a pipe-mounted Helmholtz resonator maybe determined by[18]

$$\mathrm{TL} = 10 \log_{10} \left| 1 + \frac{S_n}{2S_p} \frac{1}{Z_H} \right|^2, \tag{35}$$

where S_n and S_p are the cross-sectional areas of the neck and main pipe, respectively.

III. BOUNDARY ELEMENT METHOD

The wave propagation is governed by the Helmholtz equation in Cartesian coordinates,[18]

$$\nabla^2 P(x,y,z) + k^2 P(x,y,z) = 0, \tag{36}$$

with its integral form for an acoustic domain given, using the Green's theorem, by

$$C(q_1)P(q_1) = \int_\Gamma \left[G(q_1,q_2) \frac{\partial P(q_2)}{\partial \vec{n}} - P(q_2) \frac{\partial G(q_1,q_2)}{\partial \vec{n}} \right] d\Gamma(q_2), \tag{37}$$

where q_1 and q_2 are points on the boundary surface Γ, $C(q_1)$ coefficient, and $G(q_1,q_2)$ is the Green's function or fundamental solution given, for a three-dimensional acoustic domain, by

$$\mathrm{G}(q_1,q_2) = \frac{e^{-jk|q_1-q_2|}}{4\pi|q_1-q_2|}. \tag{38}$$

For the pipe-mounted model depicted in Fig. 1(b), the Helmholtz resonator can be divided into two acoustic domains: unfilled 1 and filled 2. The impedance matrices for each domain are obtained by discretizing the boundaries and then applying Eqs. (37) and (38). These matrices are then combined using the boundary conditions for pressure and particle velocity continuities at the interface between two domains. Finally, the transfer matrix, which expresses the relationship between the acoustic pressure and particle velocity at the inlet and outlet of the main duct, is given by

$$\begin{bmatrix} P_{in} \\ \rho_0 c_0 u_{in} \end{bmatrix} = \begin{bmatrix} T_{11} & T_{12} \\ T_{21} & T_{22} \end{bmatrix} \begin{bmatrix} P_{out} \\ \rho_0 c_0 u_{out} \end{bmatrix}, \tag{39}$$

where T_{ij} designates the transfer matrix element, and subscripts *in* and *out* indicate the inlet and outlet of the main duct, respectively. Assuming a main duct with constant cross-sectional area, transmission loss can then be calculated from the transfer matrix by

$$\mathrm{TL} = 20 \log_{10}\left(\tfrac{1}{2}|T_{11} + T_{12} + T_{21} + T_{22}|\right). \tag{40}$$

For detailed descriptions of the boundary element method, refer to Refs. 8, 9, and 18.

IV. RESULTS AND DISCUSSION

A cylindrical Helmholtz resonator has been fabricated with $r_1 = 2$ cm, $r_3 = 7.62$ cm, $L_c = 20.32$ cm, and $L_n = 8.5$ cm. The main duct is built of square cross-section (4.3 cm×4.3 cm) for clear identification of the geometric neck length. The square main duct is then connected to the circular impedance tube with smooth transitions that retain a constant cross-sectional area development. The characteristic impedance $\tilde{Z} = \tilde{\rho}\tilde{c}$ and wave number $\tilde{k}$ of the absorbing material in the present study are given as[21]

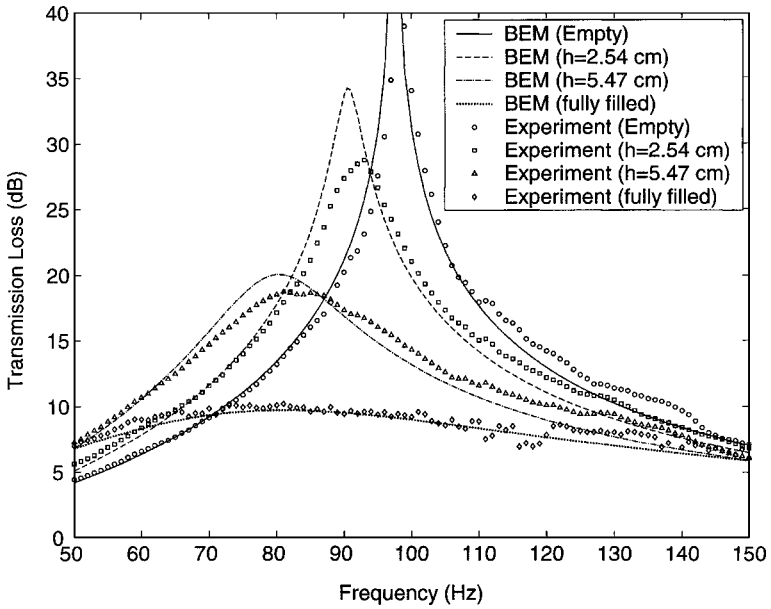

FIG. 2. Measured transmission loss for Helmholtz resonators with cavity lined with fibrous material ($R=4896$ Rayls/m).

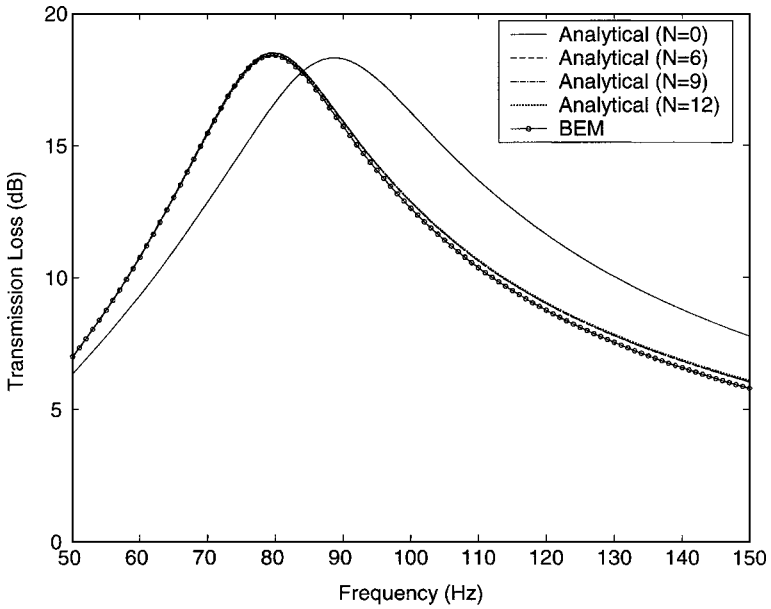

FIG. 3. Transmission loss comparisons of analytical predictions with BEM results for a Helmholtz resonator with $h=5.62$ cm ($=r_3-r_1$) and $R=4896$ Rayls/m.

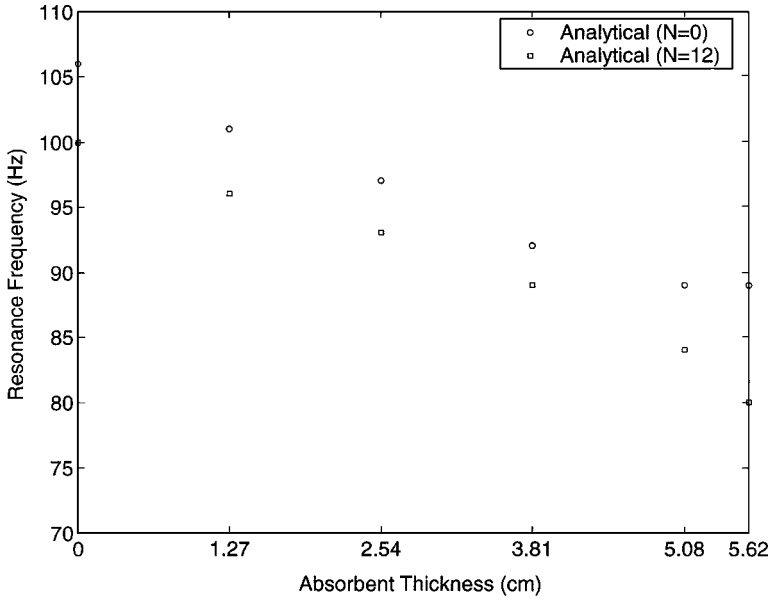

FIG. 4. Resonance frequency predictions for Helmholtz resonators with different absorbent thickness ($R=4896$ Rayls/m).

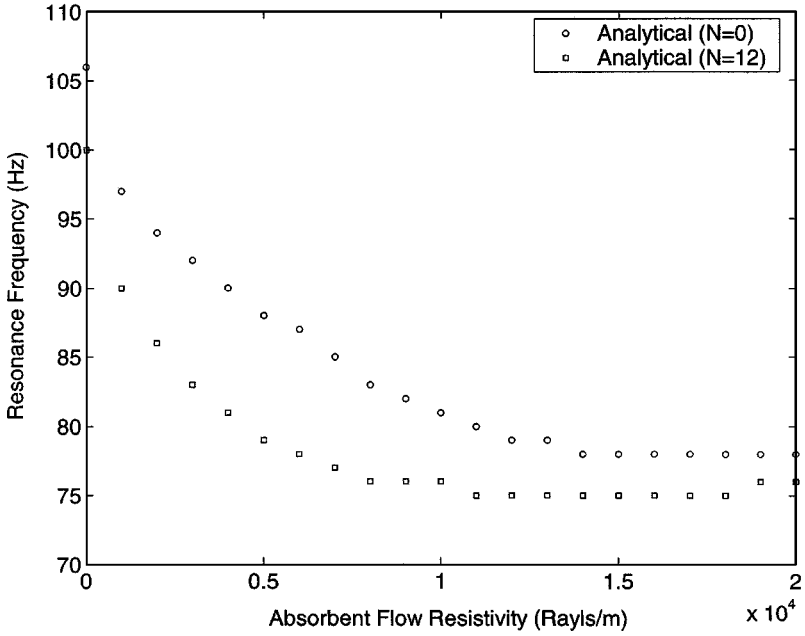

FIG. 5. Resonance frequency predictions for Helmholtz resonators with different flow resistivity of fibrous material [$h = 5.62$ cm $(= r_3 - r_1)$].

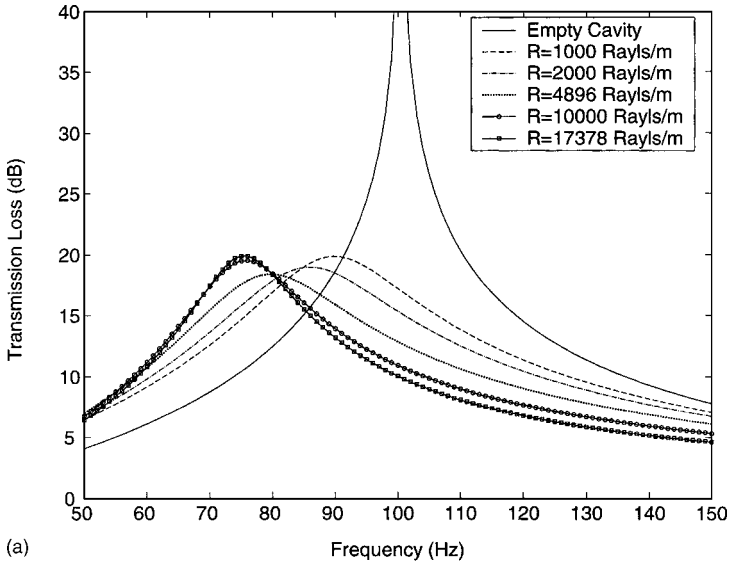

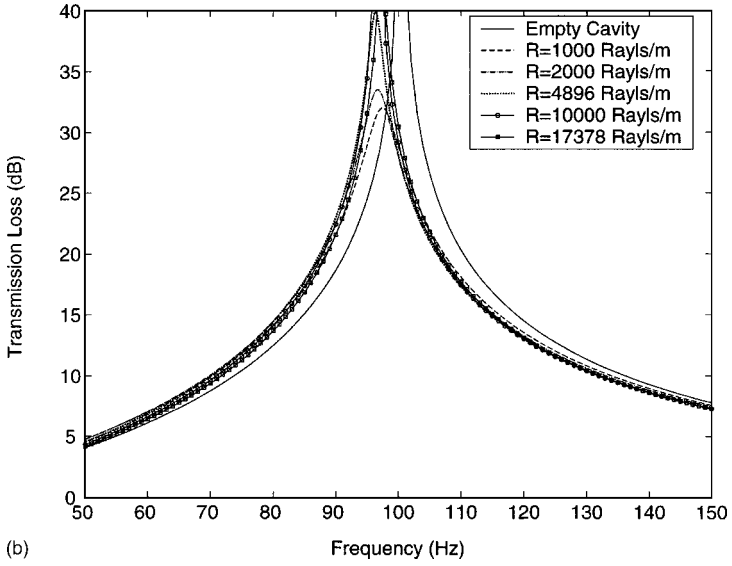

FIG. 6. Transmission loss predictions for Helmholtz resonators with different flow resistivity of fibrous material for (a) $h = 5.62$ cm $(= r_3 - r_1)$ and (b) $h = 1.27$ cm.

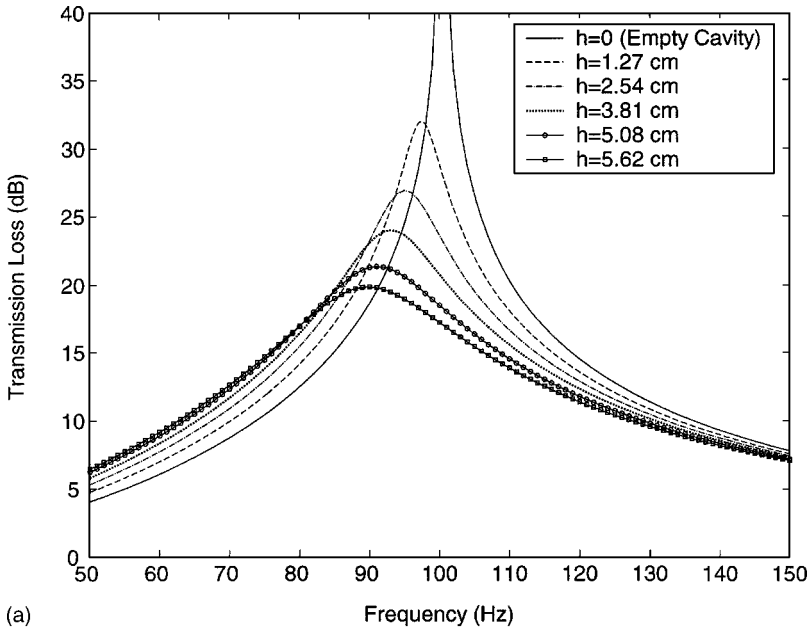

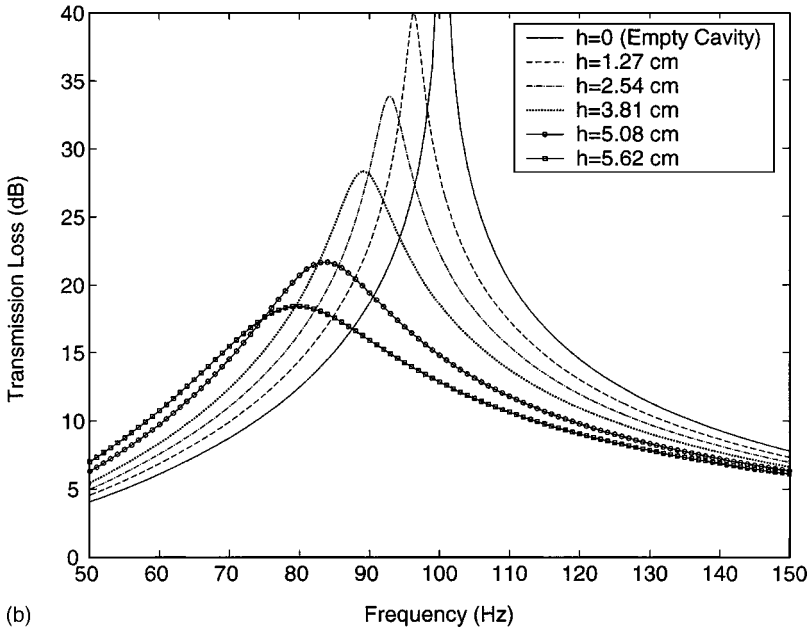

FIG. 7. Transmission loss predictions for Helmholtz resonators with different absorbent thickness for (a) $R=1000$ Rayls/m and (b) $R=4896$ Rayls/m.

$$\frac{\tilde{Z}}{Z_0}=[1+0.0511(f/R)^{-0.75}]+j[-0.0768(f/R)^{-0.73}], \tag{41}$$

$$\frac{\tilde{k}}{k}=[1+0.0858(f/R)^{-0.70}]+j[-0.1749(f/R)^{-0.59}], \tag{42}$$

where $Z_0=\rho_0 c_0$ is the characteristic impedance of the air and R [mks Rayls/m] denotes the absorbent flow resistivity. The measured flow resistivities are 4896 and 17 378 Rayls/m for 100 and 200 g/l material densities, respectively. For the fibrous materials used in this study, Eqs. (41) and (42) yield more representative transmission loss results at lower frequencies than empirical formulations applied in Refs. 9–11.

An impedance tube test setup[14] is used to obtain transmission loss of pipe-mounted resonators applying the two-microphone technique. Figure 2 shows the measured transmission loss for a cavity which is empty ($h=0$), filled with two different thicknesses of fibrous material ($h=2.54$ and 5.47 cm), and fully filled, while maintaining the overall volume. Also included in Fig. 2 are the corresponding BEM predictions, exhibiting a reasonable agreement with the experimental results. As the absorbent thickness increases to $h=5.47$ cm, both the resonance frequency and the peak value of the transmission loss decrease. The fully filled cavity shows further reduction in the peak transmission loss combined with a nearly diminishing resonance behavior. The experimental peak transmission loss for the empty resonator is 38.9 dB at 99 Hz, which is lowered 15 Hz by the filled cavity of $h=5.47$ cm. The frequency width in which the transmission loss is, for example, 10 dB, is 65 (73–138), 66 (66–132), and 63 Hz (58–121) for $h=0$, 2.54, and 5.47 cm, respectively.

To examine the accuracy, the analytical results with dif-

ferent numbers of higher order waves [varying N in Eqs. (31) and (33)] are compared with BEM predictions in Fig. 3 for a Helmholtz resonator with $h=5.62\,\text{cm}$ $(=r_3-r_1)$ and $R=4896\,\text{Rayls/m}$. Setting $N=0$ in Eqs. (31) and (33) leads to the overestimation of the resonance frequency. Figure 3 shows that, for the current geometry and frequency range, the analytical predictions are accurate and remain the same for $N\geqslant 12$, thus $N=12$ is used hereafter. Although the resonance frequency from the analytical method is close to that from BEM, the analytical results shift from the BEM predictions by up to 0.3 dB at times due presumably to the neglect of higher order modes at the neck and main duct interface in the former model.

Figures 4 and 5 examine the resonance frequencies as a function of absorbent thickness h and flow resistivity R, respectively. With $R=4896\,\text{Rayls/m}$, the resonance frequency decreases from 100 to 80 Hz as h increases from 0 to 5.62 cm (Fig. 4). The resonance frequency with $h=5.62\,\text{cm}$ $(=r_3-r_1)$ decreases from 100 to 76 Hz as the flow resistivity increases to about 8000 Rayls/m (Fig. 5). However, the resonance frequency remains nearly the same (slightly higher) for the flow resistivity above 8000 Rayls/m.

Figure 6 gives the transmission loss as a function of absorbent flow resistivity with (a) $h=5.62\,\text{cm}$ $(=r_3-r_1)$ and (b) $h=1.27\,\text{cm}$. Figure 6(a) shows with increasing flow resistivity that the resonance frequency shifts to lower frequencies and the overall transmission loss decreases relative to the empty chamber. Figure 6(b) shows only small changes.

Figure 7 compares the transmission loss for different absorbent thickness with (a) $R=1000\,\text{Rayls/m}$ and (b) $R=4896\,\text{Rayls/m}$. Both the resonance frequency and the peak value of the transmission loss decrease with increasing absorbent thickness, consistent with the trends in the earlier subset of Fig. 2. For low frequencies below the resonance, the transmission loss with thicker absorbent is slightly higher, whereas this behavior is reversed on the other side of resonance.

V. CONCLUDING REMARKS

Acoustic characteristics of a Helmholtz resonator with the cavity lined with acoustically absorbing material have been studied analytically, numerically, and experimentally. Predictions from 2D analytical approach for a piston-driven model show good agreement with BEM. For a pipe-mounted configuration, the BEM predictions of the transmission loss show reasonable agreement with the experiments. The fibrous material in the cavity has been found to lower the resonance frequency and the peak transmission loss. The effects of both the thickness and resistivity of fibrous material on the resonance frequency and acoustic attenuation have been illustrated.

[1] R. A. Scott, "The propagation of sound between walls of porous material," Proc. Phys. Soc. **58**, 358–368 (1946).
[2] S. H. Ko, "Theoretical analyses of sound attenuation in acoustically lined flow ducts separated by porous splitters (rectangular, annular and circular ducts)," J. Sound Vib. **39**, 471–487 (1975).
[3] B. Nilsson and O. Brander, "The propagation of sound in cylindrical ducts with mean flow and bulk reacting lining. I. Modes in an infinite duct," IMA J. Appl. Math. **26**, 269–298 (1980).
[4] A. Cummings and I. J. Chang, "Internal mean flow effects on the characteristics of bulk-reacting liners in circular ducts," Acustica **64**, 169–178 (1987).
[5] A. Cummings and I. J. Chang, "Sound attenuation of a finite length dissipative flow duct silencer with internal mean flow in the absorbent," J. Sound Vib. **127**, 1–17 (1988).
[6] K. S. Peat, "A transfer-matrix for an absorption silencer element," J. Sound Vib. **146**, 353–360 (1991).
[7] R. Kirby, "Simplified techniques for predicting the transmission loss of a circular dissipative silencer," J. Sound Vib. **243**, 403–426 (2001).
[8] A. Selamet, I. J. Lee, Z. L. Ji, and N. T. Huff, "Acoustic attenuation performance of perforated absorbing silencers, SAE Noise and Vibration Conference and Exposition," SAE Paper No. 2001-01-1435, Traverse City, MI, 30 April–3 May (2001).
[9] A. Selamet, I. J. Lee, and N. T. Huff, "Acoustic attenuation of hybrid silencers," J. Sound Vib. **262**, 509–527 (2003).
[10] M. B. Xu, A. Selamet, I. J. Lee, and N. T. Huff, "Sound attenuation in dissipative expansion chambers," J. Sound Vib. **272**, 1125–1133 (2004).
[11] A. Selamet, M. B. Xu, I. J. Lee, and N. T. Huff, "Analytical approach for sound attenuation in perforated dissipative silencers," J. Acoust. Soc. Am. **115**, 2091–2099 (2004).
[12] U. Ingard, "On the theory and design of acoustic resonators," J. Acoust. Soc. Am. **25**, 1037–1061 (1953).
[13] M. Alster, "Improved calculation of resonant frequencies of Helmholtz resonators," J. Sound Vib. **24**, 63–85 (1972).
[14] R. C. Chanaud, "Effects of geometry on the resonance frequency of Helmholtz resonators," J. Sound Vib. **178**, 337–348 (1994).
[15] N. S. Dickey and A. Selamet, "Helmholtz resonators: one-dimensional limit for small cavity length-to-diameter ratios," J. Sound Vib. **195**, 512–517 (1996).
[16] A. Selamet, P. M. Radavich, N. S. Dickey, and J. M. Novak, "Circular concentric Helmholtz resonator," J. Acoust. Soc. Am. **101**, 41–51 (1997).
[17] A. Selamet and Z. L. Ji, "Circular asymmetric Helmholtz resonators," J. Acoust. Soc. Am. **107**, 2360–2369 (2000).
[18] A. Selamet and I. J. Lee, "Helmholtz resonator with extended neck," J. Acoust. Soc. Am. **113**, 1975–1985 (2003).
[19] U. Schmidt, "Sound muffling device," United States Patent 2,101,460, 1937.
[20] M. B. Xu, X. M. Zhang, and W. H. Zhang, "The effect of wall joint on the vibrational power flow propagation in a fluid-filled shell," J. Sound Vib. **224**, 395–410 (1999).
[21] M. E. Delany and E. N. Bazley, "Acoustical properties of fibrous absorbent material," Appl. Acoust. **3**, 105–116 (1970).

A study of active tonal noise control for a small axial flow fan

J. Wang, L. Huang,[a] and L. Cheng
Department of Mechanical Engineering, The Hong Kong Polytechnic University, Kowloon, Hong Kong

(Received 2 July 2004; revised 9 November 2004; accepted 11 November 2004)

Sound radiated by a computer cooling fan consists of tones which are phase locked with the rotation, and other less deterministic tones and broadband random noise. This paper demonstrates the feasibility of globally eliminating the rotation-locked tones by applying a very simple destructive interference to a modified cooling fan with the number of struts equal to the number of rotor blades. The rig consists of a miniature electret microphone used as a rotation sensor, an ordinary loudspeaker, and a bandpass filter with adjustable amplitude and phase delay. The microphone is located at the inlet bellmouth of the fan to pick up the fluctuating aerodynamic pressure caused by the passing rotor blades. The pressure spectrum is rich in the blade passing frequency (BPF) and its low-order harmonics. It provides much better performance than a pulse-generating tachometer. Analysis of the original fan noise shows that about 90% of the radiated tonal sound is phase locked with rotation, and this portion is almost completely eliminated in all directions. The reductions of the radiated sound power in the first two BPFs are 18.5 and 13.0 dB, respectively, and the overall sound power reduction is 11.0 dB. © *2005 Acoustical Society of America.*
[DOI: 10.1121/1.1848072]

PACS numbers: 43.50.Ki, 43.28.Ra, 43.50.Ed [SFW] Pages: 734–743

I. INTRODUCTION

Knowledge of generic fan noise mechanisms exists but it may be said that the abatement of noise from a specific fan application remains a tough job. This study is concerned with the feasibility of applying the technique of destructive acoustic interference to a computer cooling fan, and the primary motivation for the study is to maximize the simplicity and the global effectiveness of the technique so that it might become economic enough to be applied in practice. In this section, the general fan noise mechanisms are given a brief review, together with efforts to reduce the fan noise. This is then followed by the rationale for the choice of the specific fan configuration and the active control technique.

A. General fan noise mechanisms

Fans are but one member of the turbomachinery family and, as far as the acoustics is concerned, the family may also include helicopter rotors and propellers. The study of the propeller noise caused by the steady loading was the topic of Gutin's (1936) research. In the application of fan noise, Gutin noise is negligible. The dominant noise source is the dipole caused by the fluctuating pressure on the rotating blades. The study of Tyler and Sofrin (1962) was significant in that it revealed the paramount importance of the matching or mismatching of the numbers of the rotor and stator blades for the noise caused by the rotor–stator interaction. A rather formal theoretical platform was established by Lighthill's (1952) acoustic analogy for the aerodynamic noise caused by a compact turbulent jet, and its elegant extension by Ffowcs Williams and Hawkings (1969) to applications where the presence of a solid structure in arbitrary motion is a primary feature. Since then the use of the so-called Ffowcs Williams and Hawkings equation has served well the community of turbomachinery noise research although alternative approaches also exist. In fact, search for the knowledge of a specific fan noise mechanism has never ceased since Gutins time, and reviews of the topic at large were written by authors such as Sharland (1964) and Morfey (1973). The work of Lowson (1965, 1970) on the point source formulation for the unducted rotors was, in the opinion of the current authors, quite useful and illuminating. These formulations were recently adapted to characterize the specific application of computer cooling fans (Huang, 2003) where the numbers of rotor and stator blades are small. Focusing on computer cooling fans, the important mechanisms of fan noise are summarized below.

- Tip leakage flow. The flow leaks through the blade tip due to the pressure difference developed between the pressure and suction sides of a blade. The leakage flow may manifest itself into jetlike, unstable shear layers and roll up into vortices in the blade passage. It may even hit a neighboring blade. Details can be found in the work of Fukano *et al.* (1986), among others.
- Nonuniform inlet flow condition. A nonuniform inlet flow is seen as unsteady flow by rotating blades and unsteady pressure ensues on the blade surfaces. This is perhaps one of the most efficient dipole sources of fan noise. The noise thus radiated is often a combination of broadband and tones (Trunzo *et al.*, 1981; Majumdar and Peake, 1998).
- Turbulent and/or separated flow condition on a rotor. Flow separation occurs whenever the incidence angle is large, and most realistic flows through a fan are more or less always turbulent. Large scale flow turbulence, such as that caused by a fan working at a loading much higher than the condition it is designed for, can be very noisy, and most of the noise created is broadband in nature [see, for example, Sharland (1964) and Longhouse (1976)].

[a]Author to whom correspondence should be addressed. Electronic mail: mmlhuang@polyu.edu.hk

- Trailing edge noise. When unstable convection waves inside a developing boundary layer are disrupted by the trailing edge of a blade, part of the energy is scattered into sound waves (Ffowcs Williams and Hall, 1970). The resulting sound power is proportional to the fifth power of the representative flow speed when the source is noncompact, and the dependency becomes the sixth power when the source is compact (Howe, 1998; Blake, 1986).
- Rotor-stator interaction. When the wake of a rotor impinges on the stator blades, forces on the stator blades fluctuate rapidly. Empirical models for such interaction (Kemp and Sears, 1953, 1955) have still served the purpose of noise estimation. This is often the dominant noise source in turbomachinery. Recently, Huang (2003) speculated that the back reaction towards the upstream blade row could be more important when the downstream stator is a bluff body like a circular strut used in computer cooling fans. The unsteady force generated on the upstream rotor is caused by the periodic flow blockage by the downstream struts.

B. Fan noise abatement

Sound absorption is often the most reliable and effective measure of noise abatement, but this is not true for unducted fan applications. Most efforts of fan noise abatement have been directed towards improving the flow conditions pertinent to noise source mechanisms, such as the inlet flow uniformity, and the reduction of the strength of wake interactions which depend crucially on the distance between the rotor and stator blades. Fitzgerald and Lauchle (1984) demonstrated a collection of modifications for reducing the axial flow fan noise, such as the use of a bellmouth to smooth out the inlet flow distortions, the leaning design of the downstream struts to reduce rotor-stator flow interactions, and the correction of the cupped trailing edge to prevent flow separation and vortex shedding. The method of leaning strut design was also discussed by Envia and Nallasamy (1999). They also showed that a positive sweep angle can reduce the tone level due to the additional cancellation caused by phase differences in the axial direction. Longhouse (1978) also attempted to eliminate the tip leakage flow by using a rotating shroud, a feature which may cause structural vibration problems if the shroud is not properly balanced.

In the area of active noise control (ANC), the technique has been tried for ducted fan with some success. The cut-on of the spinning pressure modes is first described by Tyler and Sofrin (1962) and the acoustics is essentially identical to that of duct acoustics. To cancel the sound of higher order modes propagating in a duct, Gerhold (1997) used a delicate ring of 48 microphones and many control sources in a duct. Thomas *et al.* (1993, 1994) controlled the plane wave mode in a duct by 12 electromagnetic compression sound drivers, and used three-channel feedforward method to create a 30° quiet zone for an operational turbofan engine. For unducted fan noise, ANC has not been tested as extensively. The main reason could be as follows. Noise from an unducted fan has complex modal composition in space, and it is rather hard to match such distribution with a limited number of secondary sources. Lauchle *et al.* (1997) and Quinlan (1992) have both had some success in suppressing the BPF tones of a fan in isolation except that a baffle was used on the rotational plane and that might have significantly changed the acoustic directivity of the fan. The work of Lauchle *et al.* (1997) is also remarkable in that the fan itself was shaken in the axial direction to serve as a control source. Apparently it was hoped that the vibrating fan would produce a good directivity match with the original noise pattern. The acoustic radiation from an oscillating fan can be thought of as follows. First, a vibrating fan assembly radiates noise much like a loudspeaker in the absence of flow. Second, the fact that the fan also shakes the flow means that it would induce additional fluid loading hence dipole radiation from the fan. Details of such flow modification by the fan oscillation are apparently beyond the scope of Lauchle *et al.* (1997). Generally speaking, it can be said that the modification could reduce or eliminate the unsteady loading on the fan structure caused by the wake interactions. It may also generate an antisound which matches with the original noise without directly interfering with the source of the original noise. Nauhaus *et al.* (2003) placed small flow obstructions around the blade tips, and blew air jets into the tip clearance. An active aerodynamic control algorithm was used to counter the rotating instability and suppress the BPF noise originating from the wake interactions. Similar aerodynamic control was also demonstrated by Rao *et al.* (2001) and Simonich *et al.* (1993). The work reported here shares the acoustic feature of the active noise control described above, but the use of formal control algorithms is deemphasized in favor of simplicity and the use of knowledge of specific source mechanisms.

C. Rationale for the current work

Instead of following the strategy of complex aerodynamic control, or using complex secondary loudspeaker arrays, this study aims to explore the feasibility of a very simple destructive acoustic interference technique for typical computer cooling fans which consist of a rotor and a set of downstream struts. The technique involves a redesign of the fan struts so that the primary noise becomes a simple dipole in the axial direction. A miniature microphone is used to pick up the information of blade rotation, much like a traditional tachometer, and the signal is filtered, phase shifted, and amplified to drive a single loudspeaker placed just beneath the fan casing. There is no error microphone and the setup can be regarded as a simple feedforward, open-loop control. The secondary noise is a simple dipole with its axis aligned with that of the fan rotation. The key questions asked are as follows. (a) How effective is the manipulation of the fan noise directivity? (b) Can the simplified noise be cancelled by the simple open-loop arrangement? The rationale for using such a simple scheme is based on practical considerations. One cannot afford to have a sophisticated control algorithm and complex detection and error microphones for applications like computer cooling. The same applies to many other situations.

In what follows in Sec. II, the noise made by the sample fan is analyzed thoroughly. The analysis shows the directivity, the components of noise that can be controlled, and those lying beyond the scope of the current scheme. It would also

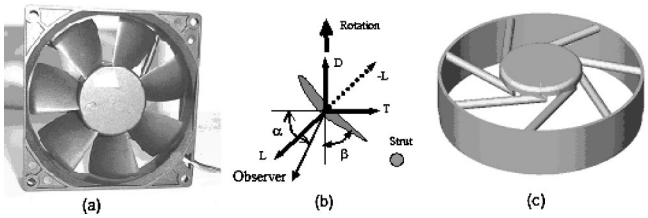

FIG. 1. Computer cooling fan and its noise sources. (a) is the front view of a typical fan, (b) is the cross-sectional view of a blade with forces acting on the surrounding air ($-L$) decomposed into thrust (T) and drag (D) components, and (c) is the strut design for the coincident configuration of $B=S=7$.

assess whether such a specially designed configuration with a dipole sound radiation is worthwhile for practical use. In Sec. III, details of the experimental configuration will be disseminated before the results of noise reduction are given. Such details include the sensor signal, loudspeaker performance, and the characteristics of the filters. At the end, results of the noise reduction and the limitations of the method are presented.

II. ANALYSIS OF THE ORIGINAL NOISE

A. Noise mechanisms of the sample cooling fan

As shown in Fig. 1(a), the sample fan for the study is a computer cooling fan of 92 mm in diameter, consisting of seven blades and four struts at the back for holding the motor. At the design point, the rotational speed is 3200 rpm. With such low blade tip speed, noise generated by the Gutin mechanisms is totally negligible. The acoustic spectrum consists of a broadband noise and discrete tones at the multiples of the blade passing frequency (BPF). As described by Wong and Huang (2003), the dominant noise source for such a fan is the aerodynamic interactions induced by two noticeable features. One is the interaction between the rotor blades and the downstream struts; another is the interaction between the distorted inlet flow pattern and the rotor, the inlet flow being a four-lobe distortion caused by the four sharp edges of the incomplete bellmouth cut short by the square outer frame. The dominant noise source is the fluctuating force induced by the two interaction processes on the rotor blades. If one compares the noises made by these two interactions, it is possible that the inlet flow distortion is louder. However, this feature can be avoided by using a complete and smooth bellmouth. As a result, the current study focuses on the noise radiated by the interaction between the rotor and its downstream struts, the latter being regarded as an essential structural feature that cannot be removed or drastically modified.

It has to be said that noise emanates from both blade surfaces and all other stationary surfaces experiencing unsteady pressure. However, the lift-generating nature of the rotor blade makes it the largest source of noise. Figure 1(b) is the cross-sectional view of a blade, and the unsteady force exerted on the surrounding air, which is the reaction of the lift, $-L$, is divided into two components: drag D and thrust T. The component of drag should be better named the driving force in this case but the term is kept here in step with literature. If the blade has a significant lean, a radial force component may also exist (not shown). The reason why the force is divided this way is that noise radiated by each of these components has its own distinct characters which can be used for the source characterization purpose. If the unsteady force on the blades is represented by a point force of thrust component T and drag component D, the rotary noise at the frequency of the mth harmonic of the fundamental BPF is given below in terms of its complex pressure amplitude c_{mB} (Lowson, 1965, 1970):

$$c_{mB}=\frac{imB\omega}{2\pi c_0 r_0}\sum_{k=-\infty}^{\infty} i^{-\nu}\left(T_{kS}\cos\alpha-\frac{\nu}{mBM}D_{kS}\right)\times J_\nu(mBM\sin\alpha),\quad \nu=mB-kS, \tag{1}$$

where B and S denote the numbers of the rotor blades and struts, respectively, ω is the angular rotating speed, mB is the frequency index of the observed sound, kS is the frequency index in the spectrum of the unsteady force, the dimensional frequency being the product of these indices and the rotational frequency, rps=rpm/60, r_0 is the distance between the fan center and the observer, α is the angle between the rotational axis and the observer direction, as shown in Fig. 1(b), c_0 is the speed of sound, M is the Mach number of the source point motion, and T_{kS}, D_{kS} are, respectively, the kS components of the spectra of the source forces T and D. Note that both m and k can be any integer. The frequency index differential, $\nu=mB-kS$, or the index of spinning pressure mode (Tyler and Sofrin, 1962) is the most important parameter. The source frequency index is kS because each blade experiences blockage by S struts during one cycle of rotation. The observed noise has frequency indices of mB because the noise of other frequency components is cancelled among themselves since B rotor blades all radiate sound with a fixed phase relation determined by the rotation. In fact, the phase relation is an important assumption which is not satisfied completely in reality. For example, there might be unsteady forces arising from vortex shedding from the cylinder and its timing could be very different from the fan rotation. Noise from such dynamic process cannot be modeled easily but can be measured and analyzed to some extent. Here, the part of noise that is phase locked to or synchronized with the rotation is denoted rotary noise, while the rest is denoted as random noise although the underlying mechanism could well be deterministic. The acoustic interference designed in this study deals solely with the rotary noise.

When the two indices coincide, $mB=kS$, the noise is rather loud since noises radiated by all blade-strut interaction events simply add up. This radiation is denoted here as the coincident mode, and the special design of $B=S$ allows such coincident radiation for all harmonics, $m=1,2,3,\ldots$. The coincident configuration is the one being tested in this study. The reason why noise is also made when the two frequency indices do not match, $\nu=mB-kS\neq 0$, is due to the Doppler effect of the source motion with the rotating blade. The strength of the Doppler effect is governed by the Bessel function $J_\nu(z)$ of order ν and argument $z=mBM\sin\alpha$. For the small cooling fan operating at low speed, normally BM

<0.2, the Bessel function can be simplified: $J_0|_{z\to 0}\to 1$, $J_{\pm 1}|_{z\to 0}\to 0.54z$.

It is clear that the thrust noise is loudest when $\nu=0$. However, examination of the drag noise term in Eq. (1) reveals a different phenomenon. The noise at $\nu=0$ is annulled by the presence of ν in the numerator, but the noise with $\nu=\pm 1$ is not proportional to z due to the presence of $mBM\propto z$ in the denominator. In fact, the loudest drag noise is heard when $\nu=\pm 1$ and the amplitude of the drag noise is of the same order (z^0) as that of the thrust noise in terms of the small argument z. This mode of drag noise radiation can be called the leading-order radiation, which is, in principle, equally noisy as the coincident mode thrust noise. This shift in coincident radiation mode originates from the artificial decomposition of the total fluctuating lift into D and T. The drag force D changes direction once per cycle and this changes the actual frequency perceived on the ground from kS to $kS\pm 1$, hence the loud noise at $\nu=\pm 1$. The reason why drag noise vanishes at $\nu=0$ is also rooted in its changing force direction, and detailed explanation is given by Huang (2003). Ideally, a quiet fan should be designed in such a way that the index $|\nu|$ is at least 2 or above for all integer numbers k. But a simple analysis of $\nu=mB-kS$ shows that this is almost impossible for the leading BPF harmonics, say $m=1, 2, 3$, when B and S are both small as might be limited by aerodynamic and structural considerations.

B. Acoustics of the coincident configuration

The knowledge of loud noise radiation with $\nu=0$ seems to be well known for most engineering designers of cooling fans, but that loud noise is also made with a design of $\nu=\pm 1$ does not seem to be as commonly known. This perhaps explains why the most popular design is $B=7$ with $S=4$, as shown in Fig. 1(a). The dominant BPF noise ($m=1$) occurs for $k=2$, $\nu=-1$, which is a loud drag noise. The drag noise radiated by such a mode has its peaks on the rotational plane, as indicated by the directivity factor of $\sin(\alpha)$ in Eq. (1), where α is the angle between the rotational axis and the source-observer vector. The drag source is in fact a rotating dipole which changes the axis constantly on the rotational plane. In contrast, a thrust noise is a dipole with a fixed axis which coincides with the rotational axis, for which the sound pressure directivity is $\cos(\alpha)$. If conventional loudspeakers are used to construct antisound, a ring of loudspeakers with delicate phase relation may be required to cancel the drag noise, while one fixed loudspeaker is all it takes for the thrust noise. This is the reason why a coincident design of $B=S$ is chosen for the current study. Figure 1(c) shows the design of struts. Note that, for such a configuration, all drag noise is cancelled out by the rotating blades and does not need any attention.

It has to be acknowledged that the increased number of struts increases the time-mean blockage of the flow, and the aerodynamic performance of the fan may suffer. In fact, the actual amount of noise radiated by this coincident design of $B=S=7$ would also be higher than the leading order drag noise radiation of the original design, $B=7$, $S=4$. A specific estimate of the sound powers from the two configurations was made in (Wong and Huang, 2003) and a general analysis

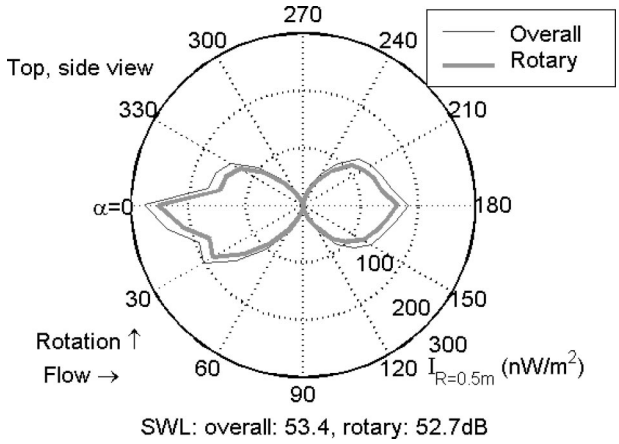

FIG. 2. Directivity of the sound intensity measured at $r_0=0.5$ m when the sample fan operates at 3200 rpm.

is given for the effect of S by Huang (2003), both concluding that S is a very dominant factor when the size of each strut is fixed. However, the conclusion changes if the size of each strut is allowed to decrease. For $S=7$, the strut size could be cut down to $\frac{4}{7}$ of the original. In such a case, one strut may not be able to contain all the electrical wires, and two struts might be involved for wiring. This issue of practical design complication is put aside for the moment. Wong and Huang (2003) also found that the lift fluctuation T_{kS} is almost proportional to d^x where d is the strut diameter and $x>2$. So the reduction in strut size by a factor of $\frac{4}{7}$ would give a noise reduction of at least $20\log_{10}(\frac{7}{4})^2=9.7$ dB. This would, to a large extent, compensate for the difference between the coincident thrust noise and the leading-order drag noise radiation from $S=4$. In addition to this justification, there are cooling fans which feature fewer rotor blades, such as $B=3$ or 4. In such applications, the coincident design of $S=B$ may well be the best choice for structural reasons. In short, the design of $B=S$ is not unrealistic for a fan with few rotor blades, and the original strut size is used for demonstration purpose.

The directivity measured in the full anechoic chamber for the coincident configuration is shown in Fig. 2 in the form of sound intensity distribution when the fan operates at 3200 rpm. The intensity is calculated by the far field approximation, $I=p_{rms}^2/(\rho_0 c_0)$, where p_{rms} is the local rms value of the measured sound which contains the near field contribution. The exact intensity is $I=1/2\,\mathrm{Re}(pu_r^*)$, where u_r^* is the conjugate of the radial component of the acoustic particle velocity. For the sound field produced by a simple dipole, formulas for p and u_r can be found in Dowling (1998) for simulation purpose. When the sound power integration is carried out over a sphere of radius $r=0.5$ m from the fan center, the error caused by the sound intensity approximation is 9%, which means $10\log(1.09)=0.37$ dB. Due to the low sound pressure level in some part of the fan noise pattern, use of a large radius r would give a very poor microphone signal. Therefore $r=0.5$ m is used in measurement as a compromise. Comparing with sound pressure level, the use of intensity I in the directivity plot amplifies any nonuniformity existing in the actual acoustic field. The thin outer curve in

Fig. 2 is the intensity of the overall noise, the thicker inner line is the rotary component found by synchronous averaging with the help of a tachometer [see Wong and Huang (2003) for details]. The sound power level (SWL) is the result of integration of the sound intensity I, and details are given in Eq. (15) of Huang (2003). The total sound power levels (SWL ref. 10^{-12} W) for the two intensity distributions are indicated in the lower label. Note that the rotary noise dominates in this case. Note also that, when the inlet flow condition is smoothed out, the original fan with four struts shown in Fig. 1(a) has a sound power of around 47 dB, while the current coincident configuration has 53.4 dB, which is not too noisy considering the use of $S=7$ struts with its original size.

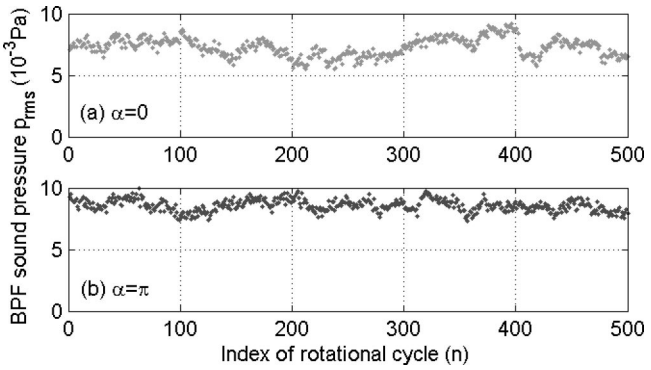

FIG. 3. The cycle-to-cycle variation of the BPF sound pressure amplitude in (a) the front and (b) the back of the fan.

C. Analysis of the noise components

Ideally, the sound radiated by the fan is a perfect thrust dipole with an intensity directivity of $I(\alpha)\propto\cos^2\alpha$, and the radiation is perfectly stable with a constant rpm. A single loudspeaker is then able to radiate a perfect antisound to cancel the fan noise. The reality deviates from this in many ways, and the part of noise that does conform to the ideal assumption is here called controllable noise. Major deviations are analyzed below.

First, the actual sound radiation does not feature T and D with equal strength on every blade with a perfect time difference locked with the rotation. Unsteady forces can hardly be deterministic given the high Reynolds number flow which is inevitably turbulent. If the force on one blade is different from the average of the seven blades, the difference can be seen as the effect of having an additional single strut, $S=1$, for which the noise of all sorts of spinning pressure mode ν exists including the drag noise. Second, the rotational speed varies from one cycle to the next slightly. Since the active control technique can only use the information from one cycle to construct antisound to cancel the noise of the next cycle, the imperfection of noise radiation caused by rotational speed variation is another source of uncontrollable noise. Since the directivity shown in Fig. 2 is taken by using a single microphone traversing the whole horizontal plane of 360°, its deviation from a perfect $\cos^2(\alpha)$ distribution is also partly attributed to the temporal variation of rotational speed and rotor-strut interaction. The extent to which the measured directivity $I(\alpha)$ conforms to the ideal distribution of, say, $I_T\cos^2\alpha$, may be measured by the following correlation calculation,

$$I_T=\int_0^{\pi} I(\alpha)\cos^2\alpha\, d\alpha \Big/ \int_0^{\pi}\cos^4\alpha\, d\alpha, \tag{2}$$

and the sound power from the ideal component with amplitude I_T is given as

$$P_T=\int_0^{\pi}(I_T\cos^2\alpha)2\pi r_0^2\sin\alpha\, d\alpha=\frac{I_T}{3}(4\pi r_0^2). \tag{3}$$

The estimated intensity amplitude I_T for Fig. 2 is 1.70×10^{-7} W/m^2 for the observer radius of $r_0=0.5$ m, and the thrust sound power P_T is found to be 1.78×10^{-7} W, or SWL$=10\lg(P_T/10^{-12}\,\mathrm{W})=52.5$ dB. The difference between this sound power level and the actual rotary sound power level of 52.7 dB is 0.2 dB. The difference must be caused by an additional noise for which the sound power level is estimated as $10\lg(10^{5.27}-10^{5.25})=39.2$ dB. This additional noise is deemed to be uncontrollable. The difference between the overall noise and the synchronously averaged noise also represents the uncontrollable noise by the current method, but this part of the noise is mainly broadband and is not the focus of the present study.

The variation of sound radiation from one cycle to the next is studied by taking the Fourier transform for each cycle of the measured sound, which contains $B=7$ pressure oscillations for the BPF component. The temporal borders of each cycle are indicated by the tachometer signal taking into account the time required for sound propagation over a distance of $r_0=0.5$ m. The rms value of the BPF sound pressure varies with the cycle index n and is denoted as $p_{rms}(n)$, which is shown in Fig. 3 for the front, $\alpha=0°$, and the back of the fan, $\alpha=180°$. One possible reason for such variation is the change of local rpm with n. Assuming that the radiated sound power follows the usual sixth power law for dipoles, p_{rms} is proportional to $(\mathrm{rpm})^3$. The value of p_{rms} shown in Fig. 3 has already taken this into account by multiplying a factor of $(\mathrm{rpm}_0/\mathrm{rpm})^3$, where rpm_0 is the mean rpm and rpm is the actual rotational speed for cycle n. Thus corrected, the variation shown in Fig. 3 is believed to derive solely from the random aerodynamic events. The amplitude of noise from such random events is estimated as follows. If the random event contributes to the BPF noise with an rms amplitude A_r and the deterministic noise has an amplitude A_d, the range of the amplitude for the actual noise is, statistically, $[A_d-A_r, A_d+A_r]$. Here, A_d is found easily as the mean of the $p_{rms}(n)$ pattern shown in Fig. 3, i.e., $A_d=\overline{p_{rms}(n)}$, while A_r is found as $std(p_{rms})\sqrt{2}$. A_r is found to be roughly uniform over the whole measurement plane, so the sound power associated with the random events is calculated as $P_r=A_r^2 4\pi r_0^2/(\rho_0 c_0)$, which is found to be 38.4 dB, very close to the result of directivity pattern analysis shown in Eqs. (2) and (3). To summarize, the amount of uncontrollable rotary noise is about 39 dB and the maximum expected rotary sound power reduction is 52.7–39.0=13.7 dB. In terms of the percentage in sound power, the uncontrollable part represents $10^{-13.7/10}=0.043$ or 4.3%.

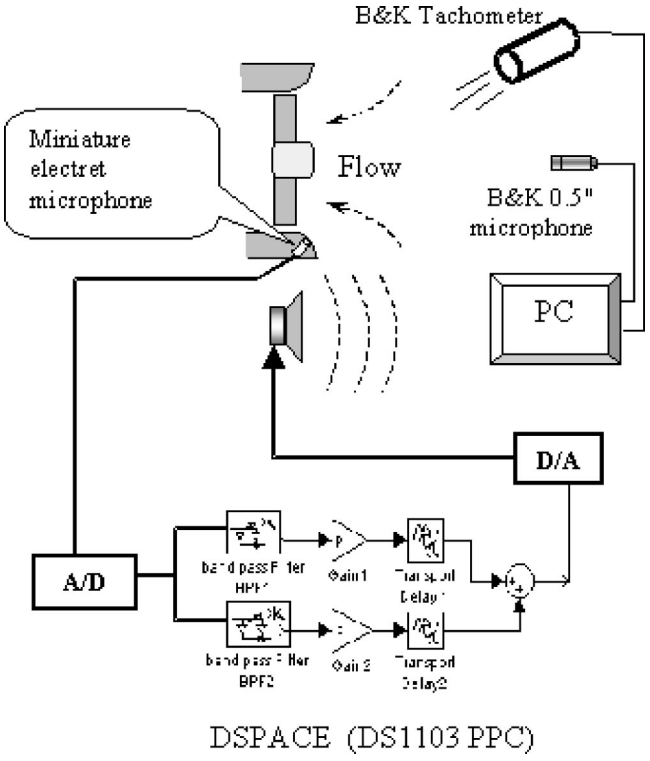

FIG. 4. Experimental setup in the anechoic chamber. The fan is isolated and unbaffled, and the secondary louderspeaker is put beneath the fan.

III. EXPERIMENTAL STUDIES

An open-loop, feed-forward control is used for the sample fan being investigated here. The system simply consists of three components. First, a nonacoustic reference from a miniature electret microphone, of which the details are described below, located on the bellmouth of the fan provides the clock information of the rotating fan blades. To some extent, the amplitude of the signal is also weakly related to the rotational speed. Second, the signal is bandpass filtered to keep the components of BPF and a few chosen harmonics, and further conditioned in terms of amplitude and phase delay. Third, the conditioned signal drives the loudspeaker attached just beneath the fan to produce the anti-sound to cancel out the noise made by the fan at the earliest possible blade passage cycle, which is $1/B$ of a rotational cycle. Note that for deterministic sound from the fan, the acoustic signal repeats B times during one rotational cycle. The total time delay of the system is found to be such that the signal from one moment is actually used to cancel noise at the next blade passage. Such a short time delay means that the limitation of the system performance is mainly rooted in the randomness of the aeroacoustic source. In what follows, the three elements of the control rig are discussed before the results are presented.

A. Experimental setup

The schematic diagram of the experiment is shown in Fig. 4. Illustrated at the upper-right corner are a $\frac{1}{2}$-in. survey microphone (B&K type 4187) and a tachometer (B&K type M004) connected to a PC equipped with signal analysis software MATLAB® and an A/D card. The survey microphone is not used as error sensor here but is merely for the purpose of evaluating the results. Note that this part of the experimental setup can be easily absorbed into the controller block shown in Fig. 4. It is kept as a separate part purely for operational convenience. The rig is built around a dSPACE (DS1103 PPC) controller, which is a real-time system with multiple A/D and D/A channels, and a Motorola PowerPC 604e microprocessor running at 333 MHz. The input signal derives from the rotation sensor and the output goes to the secondary sound source. The digital controller is connected to a personal computer through an ISA bus. The control algorithm is simply based on IIR filters constructed by the SIMULINK function in MATLAB® assembled in the host personal computer. A real-time interface (RTI) is used to build the code downloaded to and executed on the dSPACE hardware. The rotation sensor signal is sampled at 10 kHz, and the output analog signal is also constructed at an updating rate of 10 kHz, both deemed sufficient for the range of frequencies encountered in the current study. The control is concentrated on the most outstanding peaks on the fundamental BPF and its first harmonic, $m=1$, 2, at which the noise level exceeds the broadband by 17 and 14 dB, respectively. Two filters are constructed as parallel channels, one for each peak, to extract the rotational information at the two frequencies. Each channel has its own phase delay and amplification variables which can be adjusted manually in the computer to optimize the results. The outputs from the two channels are added together before the DA conversion.

The experiment is conducted in a full anechoic chamber with a cutoff frequency of 80 Hz, and the acoustic directivity is measured by the survey microphone fixed at one position 0.5 m away from the fan center, while the fan and loudspeaker rotate on a tripod to traverse all directions on the horizontal plane at an angular interval of 10°. The pulse signal from the optical tachometer is sampled together with that of the electret microphone by a 24-bit AD card using a sampling rate of 16 kHz. More details of the sensor microphone and other elements in the rig are discussed below.

B. Description of rig components

Normally, a photoelectric tachometer provides the information of the instantaneous position of the rotor by generating a pulse at each passing of a marked blade. Since the spectral energy of an ideal pulse (delta function) spreads out over a very wide frequency range, the amount of signal energy in one narrow band of frequency, such as that around the BPF, would be necessarily low in proportion. This makes it less ideal for the current purpose. In addition to this drawback, the height of the pulse is independent of the rotational speed, and it requires some kind of frequency to amplitude conversion if more antisound needs to be constructed to cancel the noise of the fan running at momentarily higher speed. In this study, a miniature electret microphone is used as the alternative rotation sensor. The microphone used is a 151 series from Tibbetts industries. It has a cylindrical head 0.1 in. in diameter and 3 mm in height, with a flat frequency response of 0.018 V/Pa from 300 Hz to 5 kHz. A photoelectric tachometer (B&K type MM0024) is also used in the rig and is located at some 30 cm upstream of the fan, while the

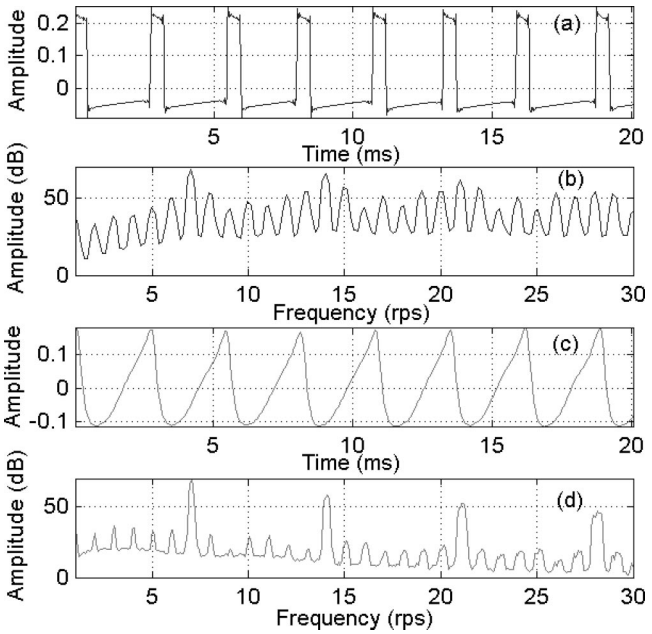

FIG. 5. Signals from two rotation sensors. (a) is for the photoelectric tachometer and (b) is the spectrum of signal in (a). (c) is the signal from the miniature microphone, and (d) its spectrum.

electret microphone is flush mounted on the inlet bellmouth of the fan just upstream of the blades. Signals from the photoelectric tachometer and the electret microphone are compared in Fig. 5. The photoelectric tachometer signal is shown in Fig. 5(a) and its spectrum in Fig. 5(b). Here, the ripples around the edges of the pulses are caused by the high-pass filter installed in the data acquisition system to avoid excessive electronic noise that exists at low frequencies. When the optical reflex paper is attached to all seven blades of the fan, the main peaks are found at the BPF and its harmonics. The appearance of the peaks at the rotational frequency (rps) and its non-BPF harmonics is caused by the difference among the pulses due to either the variation of tachometer or the changing fan rotational speed. The difference between the first BPF and its two neighboring non-BPF peaks is 16 dB.

Figure 5(c) shows the saw-tooth-like waveform from the electret microphone, and its spectrum is shown in Fig. 5(d). The BPF peak is cleared of its nearest non-BPF peaks by 35 dB. What is measured here is the aerodynamic pressure variation on the bellmouth surface caused by the constant sweeping of the blades, which is a source of far field sound but not all sound by itself. The effect of the blade rotation on the upstream flow is mainly a potential flow blockage, and its magnitude should be of the order of the dynamic pressure head associated with the velocity change during the sweeping. A brief test shows that the measured peak-to-peak pressure variation is 0.140, 0.154, and 0.162 Pa for the rotational speeds of 3000, 3100, and 3200 rpm, respectively. One suspected drawback of using the miniature microphone is that, in principle, the fan noise and antisound can also be sensed leading to a feedback loop in the system. But this worry is unfounded since the near-field amplitude of the loudspeaker sound is found to be around 5×10^{-3} Pa, which is much lower than the aerodynamic pressure amplitude, 162×10^{-3} Pa.

When the two signals in Figs. 5(a) and (c) are compared in terms of BPF energy contents, the tachometer has 23% while the electret microphone has 83%. The large spectral clearance between the BPF and its non-BPF neighbors for the electret microphone means that the passband of the filter does not have to be too narrow in order to extract the BPF signal. In fact, a very wide band of 200–500 Hz is used in the current study for the BPF around 373 Hz. This way, the time delay caused by the filtering is minimal, and the effect of noise cancellation is expected to be much better than that based on the photoelectric tachometer. In addition to this crucial time-delay factor, the use of a miniature microphone is also more economical and convenient. A much broader bandpass filter also allows simpler analog construction in future applications. In terms of the secondary source, a 4-in. loudspeaker is used, and its dipole directivity is confirmed by the measurement without the fan. Also, the loudspeaker is found to have a time delay of 0.4 ms at the frequency of the BPF for which the period is 2.7 ms.

The overriding consideration for the filter design is the time delay caused by the filter. A time delay here means that the signal of the rotational sensor at present is used to construct antisound for the future. The random variation of the BPF amplitude with respect to the rotational cycle shown in Fig. 3 means that such delay should be minimized in order to achieve the best result. Since an infinite-impulse-response (IIR) filter has much smaller time delay than a finite-impulse-response (FIR) filter with equivalent bandpass performance, the former is chosen. In making this choice, the factor of signal distortion by the IIR filter is not much a factor for the following reason. There is no reason to assume that the time delay between the component of BPF in the rotational signal shown in Fig. 5(c) and the radiated sound is the same as that for the second BPF component. In other words, the required time delays for the fundamental ($m=1$) and first harmonic ($m=2$) may well be different. In fact, due to the variation of the rotational speed of the fan, the ideal antisound should maintain a fixed phase angle of 180° with respect to the original noise at its varying BPF and higher harmonics. The varying phase relation between the sensor signal and the final antisound for various frequencies means a nonlinear phase response might well be ideal. In this study, such nonlinear phase response is not studied, nor is the varying amplitude response that might be beneficial.

As shown in Fig. 5, the sharp BPF peak allows a wide passband to be used together with a wide transitional band. This allows a low-order filter to be constructed to achieve a flat response. For the fan operating at 3200 rpm, 373 Hz is the fundamental BPF, and 200–550 Hz is chosen as the passband with its center at 375 Hz. The band of 600 to 900 Hz is chosen for the first harmonic with its center at 750 Hz. A six-order Chebyshev IIR filter is constructed by using the least *p*-norm optimal IIR filter design in the SIMULINK of MATLAB®, and the responses of the two filters are shown in Fig. 6. Based on these filters, a further gain and phase delay are required to construct the antisound, as shown in the lower part of Fig. 4. These are achieved by manual tuning for the two channels independently, although there is no reason why a formal procedure of system identification cannot be

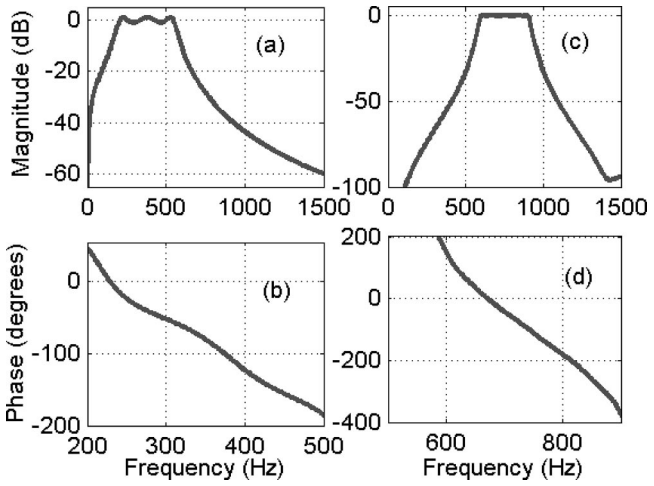

FIG. 6. The responses of the two filter channels. (a) and (b) are the magnitude and phase response for the first BPF, respectively, (c) and (d) are for the second.

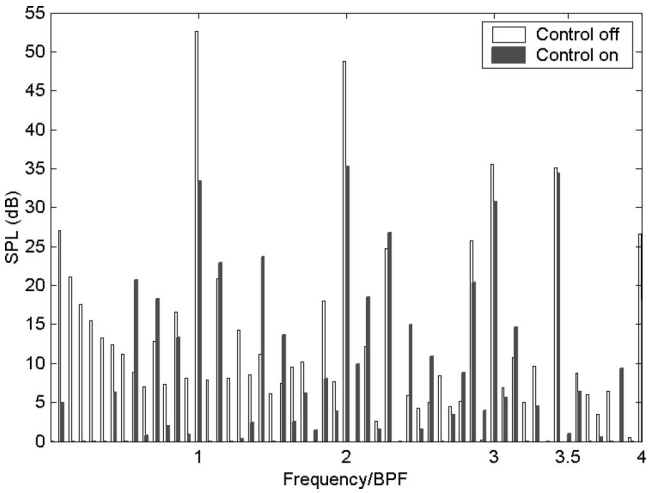

FIG. 7. Sound pressure spectra at the on-axis peaks of dipole with control off (open bar) and on (filled bar).

followed to achieve the goal of noise minimization. The manual tuning is based on the display of sound picked up by the survey microphone on the rotational axis, $\alpha=0$.

C. Results and error analysis

The loudspeaker is put underneath the fan to minimize its influence on the incoming flow stream. The dipole sound from the fan and that from the loudspeaker are coupled as an effective lateral quadrupole with a perpendicular separation distance of $d=10$ cm between the two parallel dipole axes. The ratio of the quadrupole sound power to the dipole sound power can be shown to be $(kd)^2/5$ (Dowling, 1998), where $k=2\pi f/c_0$ is the wave number. For frequency $f=373$ Hz, the ratio turns out to be 0.096, which means a maximum reduction of sound power of $-10\lg(0.096)=10.2$ dB. This is a serious limiting factor. Ideally, a ring of small loudspeakers should be placed around the fan circumference in order to create a better coincidence of the centers of the two noise sources. In practice, two or four loudspeakers might be adequate. Using simple numerical simulation of linear superposition of sounds from two antisound speakers placed at the top and the bottom of the fan, which is itself modeled by seven-point dipoles on a ring of 4.5-cm radius, it is found that the best cancellation is improved to become 24.1 dB, which is quite satisfactory. So, the issue of the relatively large fan-loudspeaker separation distance is temporarily set aside by the following heuristic method. The parameters of the antisound are tuned only on the horizontal plane level with the fan center, and the finalized result is also measured on the same plane. In terms of the separation of the primary and secondary sources, the method of shaking the fan itself as a secondary source (Lauchle *et al.*, 1997) may have achieved a rather perfect collocation. The only limitation factor for the performance becomes the issue of whether the primary and secondary sources have the same dipole composition and acoustic directivity pattern.

The spectra of synchronous sound measured with and without the loudspeaker for $\alpha=0$ are presented in Fig. 7. It is found that 18.5-dB noise reduction is achieved for the first BPF, and 13.0 dB for the second BPF. There is also a peak at approximately 3.5 BPF, for which there is virtually no change in sound pressure level. This source of this peak is beyond the scope of the current investigation. Acoustic directivity is also measured on the horizontal plane level with the center of the fan, and the control on–off comparison of sound intensity is made in Fig. 8. Figure 8(a) compares the total synchronous sound pressure levels in decibel units, with the total sound powers labeled on the horizontal axis. Figure 8(b) gives the details of the control-on directivity, which includes the overall noise, rotary noise, and the random noise derived from, respectively, the original signal measured from the survey microphone, the synchronous average of the measured signal, and the power difference between the original

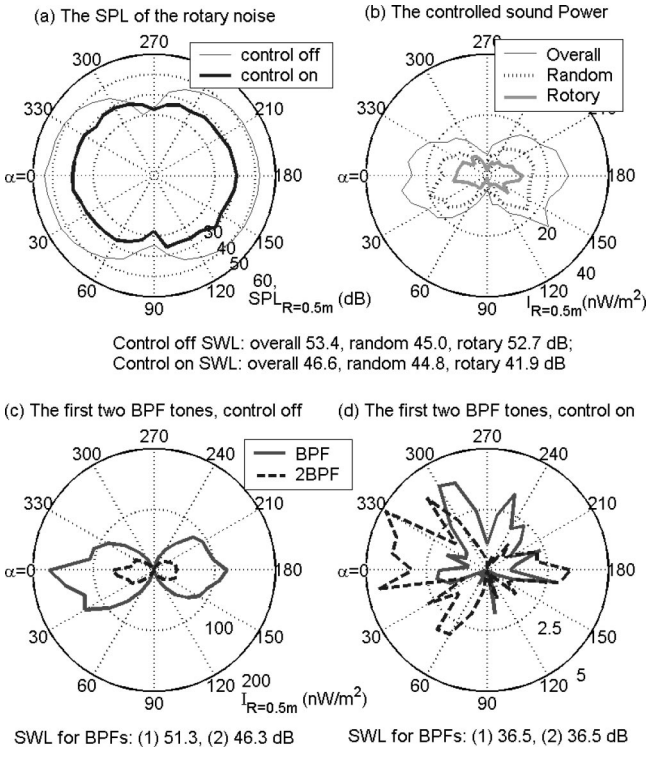

FIG. 8. Sound power level comparisons for with and without control.

and synchronous signals. Note that the rotary noise includes sound at frequencies other than the harmonics of BPF, such as 3.5 BPF shown in Fig. 7. The total reduction in the rotary noise power is $52.7-41.9=10.8$ dB. The overall noise reduction is $53.4-46.3=7.1$ dB while the random noise, about 50.0 dB, is essentially unchanged.

Figures 8(c) and (d) show the sound intensity directivity of the BPF and 2 BPF noise for control-off and control-on, respectively. While the control-off pattern is clearly an axial dipole with some limited distortions, the control-on pattern is quite irregular and the scale for this figure is amplified by 40 times when compared with Fig. 8(c). The irregular shape indicates that most harmonic noise that can be controlled by the simple scheme has already been suppressed successfully. The sound power reductions for the two frequencies are 14.8 and 9.8 dB, respectively.

The result of this simple control scheme is determined by many factors, and the main one has been recognized earlier as the random variation of sound radiation by the rotating fan (see Fig. 3). The standard deviation of sound pressure amplitude is 15.9% while that for the rpm is 0.4%. If the radiated sound pressure grows with rpm by the third power law, the variation in the sound pressure amplitude would have been only $3\times0.4=1.2\%$. The difference between this prediction and the actual 5.6% change in the radiated sound amplitude means that the variation is rather independent of the rotational speed change. In fact, the correlation study between one-cycle p_{rms} and rpm^3 shows a peak correlation of only 20%. The deterministic error of using the rotational signal from one blade passage to control the noise radiated by the next blade passage is also analyzed in terms of the phase error due to the response characteristics of the filter shown in Fig. 6(b). The error of 0.4% BPF period means a frequency error of $0.004\times373=1.5$ Hz, or a phase response difference of $\delta\theta=1.5°$ based on the phase response curve in Fig. 6(b). This phase angle error can only lead to an error of $\delta\theta$ in radian units, which is 0.026 or a limit of noise reduction of $-20\lg(0.026)=31.7$ dB, which is also unlikely to be a bottleneck of the performance.

IV. CONCLUSIONS

The reported scheme of active acoustic interference demonstrates that the sound locked with the rotation from the typical computer cooling fan can be significantly attenuated by a simple design. More specifically, the following conclusions are drawn.

(1) The noise of the sample computer cooling fan is sufficiently deterministic to allow a meaningful implementation of the proposed scheme. For the dominant BPF sound, it is shown that the noise associated with the seemingly random variation of sound radiation with respect to the fan rotation is about 13.7 dB below that of the deterministic part. In other words, 95.7% of sound energy is deterministic, and the maximum expected noise reduction is 13.7 dB. The experimental rig deals with the first and second BPF frequencies. The reductions in the total sound power for these frequencies are 10.4 and 9.8 dB, respectively, while the total synchronous sound is reduced by 10.8 dB. The reduction of the sound power in the experiment for the BPF, 10.8 dB, is close enough to the limit of 13.7 dB forecasted for the deterministic acoustic interference.

(2) The cause of the random variation could have a complex origin in turbulent fluid dynamics, and the limitation imposed by this factor is much more stringent than those imposed by the known phase delay and amplitude mismatch problems associated with the inevitable variation of the fan rotational speed from one cycle to the next. In fact, this variation is rather small since the total time delay involved in the current study is only about half of the blade passage, or $\frac{1}{14}$ of the rotational cycle. A more stringent limitation appears to be the separation distance between the fan center and the single loudspeaker, but this problem would be alleviated if two loudspeakers are used.

(3) If the rotation signal is provided by a traditional photoelectric tachometer, the pulse signal does not carry sufficient BPF content and it would limit the performance of the method. In this study, a miniature electret microphone is used to provide the unsteady pressure arising from the blade rotation just upstream of the rotor. The signal is found to be very rich in BPF content and is rather smooth. Spectral analysis shows that the peak at the BPF is well above the neighboring rps harmonics. As a result, a broad passband can be used to extract the BPF signals to drive the loudspeaker. The time delay for the filter is thus minimized. Apart from this technical advantage, the miniature microphone is also relatively cheap and small to allow the implementation of the technique in practice.

(4) The sample fan used in this study is a modified version of a typical computer cooling fan. In a typical fan, the number of struts differs from the number of rotor blades, $S\neq B$. It is pointed out in this study that this seemingly correct design avoids the worst coincident mode sound radiation by the unsteady flow thrust, but it is almost impossible to avoid the equally efficient radiation of drag noise. Since drag noise originates from a rotating dipole with a changing dipole axis, the modification from the usual design with drag noise domination to the coincident design of $S=B$ with thrust noise domination carries the following important technical advantage: a simple loudspeaker can be used as the secondary source for the thrust noise but the same cannot be done easily for the drag noise.

ACKNOWLEDGMENTS

The first author thanks the Hong Kong Polytechnic University for the Ph.D. research studentship. The support by the Research Grants Council of the Government of HKSAR (Grant No. PolyU 1/02C) is also gratefully acknowledged.

Blake, W. K. (**1986**). *Mechanics of Flow-induced Sound and Vibration* (Academic, Orlando, FL).

Dowling, A. P. (**1998**). "Steady-state radiation from sources," in *Handbook of Acoustics*, edited by M. J. Crocker (Wiley, New York), Chap. 8.

Envia, E., and Nallasamy, M. (**1999**). "Design selection and analysis of a swept and leaned stator concept," J. Sound Vib. **228**, 793–836.

Ffowcs Williams, J. E., and Hall, L. H. (**1970**). ''Aerodynamic sound generation by turbulent flow in the vicinity of a scattering half plane,'' J. Fluid Mech. **40**, 657–670.
Ffowcs Williams, J. E., and Hawkings, D. L. (**1969**). ''Sound generation by turbulence and by surfaces in arbitrary motion,'' Philos. Trans. R. Soc. London, Ser. A **264**, 321–342.
Fitzgerald, J. M., and Lauchle, G. C. (**1984**). ''Reduction of discrete frequency noise in small, subsonic axial-flow fans,'' J. Acoust. Soc. Am. **76**, 158–166.
Fukano, T., Takamatsu, Y., and Kodama, Y. (**1986**). ''The effects of tip clearance on the noise of low pressure axial and mixed flow fans,'' J. Sound Vib. **105(2)**, 291–308.
Gerhold, C. H. (**1997**). ''Active control of fan-generated tone noise,'' AIAA J. **35**, 17–22.
Gutin, L. (**1936**). ''On the sound field of a rotating propeller,'' Zh. Tekh. Fiz. **6**, 899–909.
Howe, M. S. (**1998**). *Acoustics of Fluid-structure Interaction* (Cambridge U.P., Cambridge).
Huang, L. (**2003**). ''Characterizing computer cooling fan noise,'' J. Acoust. Soc. Am. **114**, 3189–3199.
Kemp, N. H., and Sears, W. R. (**1953**). ''Aerodynamic interference between moving blade rows,'' J. Aeronaut. Sci. **20**, 583–598.
Kemp, N. H., and Sears, W. R. (**1955**). ''Unsteady forces due to viscous wakes in turbomachines,'' J. Aeronaut. Sci. **22**, 478–483.
Lauchle, G. C., Macgillivray, J. R., and Swanson, D. C. (**1997**). ''Active control of axial-flow fan noise,'' J. Acoust. Soc. Am. **101**, 341–349.
Lighthill, M. J. (**1952**). ''On sound generated aerodynamically. I. Genera theory,'' Proc. Annu. Tech. Meet., Tech. Assoc. Graphic Arts **211**, 564–587.
Longhouse, R. E. (**1976**). ''Noise mechanism separation and design considerations for low tip-speed, axial-flow fans,'' J. Sound Vib. **48**, 461–474.
Longhouse, R. E. (**1978**). ''Vortex shedding noise of low tip speed, axial flow fan,'' J. Sound Vib. **53**, 25–46.
Lowson, M. V. (**1965**). ''The sound field for singularities in motion,'' Proc. R. Soc. London, Ser. A **286**, 559–572.
Lowson, M. V. (**1970**). ''Theoretical analysis of compressor noise,'' J. Acoust. Soc. Am. **47**, 371–385.
Majumdar, S. J., and Peake, N. (**1998**). ''Noise generation by the interaction between ingested turbulence and a rotating fan,'' J. Fluid Mech. **359**, 181–216.
Morfey, C. L. (**1973**). ''Rotating blades and aerodynamic sound,'' J. Sound Vib. **28**, 587–617.
Nauhaus, L., Schulz, J., Neise, W., and Moser, M. (**2003**). ''Active control of the aerodynamic performance and tonal noise of axial trubomachines,'' Proc. Inst. Mech. Eng., Part A: J. Power and Energy **217**, 375–383.
Quinlan, D. A. (**1992**). ''Application of active control to axial flow fans,'' Noise Control Eng. J. **39**, 95–101.
Rao, N. M., Feng, J. E., Burdisso, R. A., and Ng, W. F. (**2001**). ''Experimental demonstration of active flow control to reduce unsteady stator-rotor interaction,'' AIAA J. **39**, 458–464.
Sharland, I. J. (**1964**). ''Sources of noise in axial flow fan,'' J. Sound Vib. **I(3)**, 302–322.
Simonich, J., Lavrich, P., Sofrin, T., and Topol, D. (**1993**). ''Active aerodynamic control of wake-airfoil interaction noise—experiment,'' AIAA J. **31**, 1761–1768.
Thomas, R. H., Burdisso, R. A., Fuller, C. R., and O'Brien, W. F. (**1993**). ''Preliminary experiments on active control of fan noise from a turbofan engine,'' J. Sound Vib. **161(3)**, 532–537.
Thomas, R. H., Burdisso, R. A., Fuller, C. R., and O'Brien, W. F. (**1994**). ''Active control of fan noise from a turbofan engine,'' AIAA J. **32**, 23–30.
Trunzo, R., Lakshminarayana, B., and Thompson, D. E. (**1981**). ''Nature of inlet turbulence and strut flow disturbances and their effect on turbomachinery rotor noise,'' J. Sound Vib. **76(2)**, 233–259.
Tyler, J. M., and Sofrin, T. G. (**1962**). ''Axial flow compressor noise studies,'' SAE Trans. **70**, 309–332.
Wong, J., and Huang, L. (**2003**). ''Identification and control of noise sources in a small axial-flow cooling fan,'' Symposium on Fan Noise 2003, Senlis, France, 23–25 September.

Inverse method predicting spinning modes radiated by a ducted fan from free-field measurements[a)]

Serge Lewy[b)]
CFD and Aeroacoustics Department, ONERA (National Aerospace Research Agency), MB 72, 92322 Chatillon, France

(Received 21 June 2004; revised 3 November 2004; accepted 29 November 2004)

In the study the inverse problem of deducing the modal structure of the acoustic field generated by a ducted turbofan is addressed using conventional farfield directivity measurements. The final objective is to make input data available for predicting noise radiation in other configurations that would not have been tested. The present paper is devoted to the analytical part of that study. The proposed method is based on the equations governing ducted sound propagation and free-field radiation. It leads to fast computations checked on Rolls-Royce tests made in the framework of previous European projects. Results seem to be reliable although the system of equations to be solved is generally underdetermined (more propagating modes than acoustic measurements). A limited number of modes are thus selected according to any *a priori* knowledge of the sources. A first guess of the source amplitudes is obtained by adjusting the calculated maximum of radiation of each mode to the measured sound pressure level at the same angle. A least squares fitting gives the final solution. A simple correction can be made to take account of the mean flow velocity inside the nacelle which shifts the directivity patterns. It consists of modifying the actual frequency to keep the cut-off ratios unchanged. [DOI: 10.1121/1.1850208]

PACS numbers: 43.50.Lj, 43.20.Mv, 43.60.Pt [EGW] Pages: 744–750

I. INTRODUCTION

Free-field radiation from a turbofan at a given frequency is primarily determined by the modal structure of the acoustic waves which may propagate inside the nacelle. Modal analysis has been made for a long time, since the paper of Tyler and Sofrin.[1] Several ways to do that have been implemented, using either rakes of rotating microphones or arrays of fixed microphones. Tests however require an expensive setup, and remain rather long even if data processing is now entirely digital. They are generally made inside the duct.[2,3] Some experiments have also been performed in front of the intake to avoid intrusive probes whose wakes could interact with the rotor blades. Measurements then have to be duplicated at several distances from the duct exit to scan the modal content at various angles of radiation.[4,5]

Another issue is thus addressed now in several laboratories. If one measures a conventional farfield directivity, can the generating modal components be deduced? Of course, that modal splitting has to be made (like the modal analyses) for the various rotational speeds, and for each tone because the duct acts on modes like a low-pass filter which becomes wider when the frequency increases. On the other hand, this would be very interesting because available acoustic computer codes could then predict the radiated field in other configurations (for instance, other duct shapes, or other duct linings), and optimize them. The only hypothesis would be that there is no coupling between the sources and the ducted sound field, but this seems to be generally valid.[6]

The inverse problem is ill-posed *a priori*.[7,8] There is indeed no reason why there should exist only one set of propagating modes generating a given free-field directivity. Moreover, let us call (m,μ) a spinning mode, m being the circumferential wave number and μ the radial mode ($\mu \geqslant 1$). The root mean square (rms) value of the radiated sound pressure, P_{rms}, at a fixed radial distance from the duct exit and at a given frequency, f, writes for incoherent modes (see Lewy *et al.*[9] for a justification of this assumption)

$$P_{\mathrm{rms}}^2(\varphi) = \sum_{m,\mu} \frac{A_{m\mu}^2}{2} |F_{m\mu}(\varphi)|^2, \tag{1}$$

where φ is the radiation angle, the $F_{m\mu}$ are the known eigenfunctions, and $A_{m\mu}$ are the amplitudes of modes (m,μ). Pressure P_{rms} is measured at L locations φ_l, and the $A_{m\mu}$ are the unknowns. We get a system of L linear equations that is underdetermined if there are more than L modes (m,μ). For instance, $L=18$ if measurements are made from 5° to 90° every 5°, and more than 18 modes may propagate as soon as the reduced frequency $KR>11$ (R is the duct radius, and K is the wave number), or $f \geqslant 1400$ Hz if the diameter is 0.864 m (see the tests in Secs. III and IV).

It is shown in the paper how the above question can be solved. Only the feasibility of a solution is discussed, and the problems related to the numerical reconstruction of the source pressure will be addressed in a subsequent study. Several regularization techniques are available to get a better conditioned radiation operator,[10] mainly in the domain of acoustical holography for back-propagation of a sound field generated by a vibrating structure.[11,12]

Equations related to acoustic ducted propagation and farfield radiation are reiterated in the next section. In Secs. III and IV some first results applied to tests made by Rolls-

[a)]Portions of this work were presented at ICA 2004, 18th International Congress on Acoustics, Kyoto, Japan, 4–9 April 2004.
[b)]Electronic mail: Serge.Lewy@onera.fr

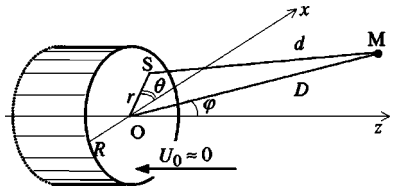

FIG. 1. Definition of the coordinates for the computation of sound radiation.

Royce within the framework of the previous European projects FANPAC (*Fan Noise Prediction And Control*)[13] and RESOUND (*Reduction of Engine Source Noise through Understanding and Novel Design*)[3,14] are presented. It is assumed in Sec. III that there is no flow inside the duct, but Sec. IV suggests a simple means of taking into account the effect of fluid velocity on the directivity patterns.

II. THEORETICAL BACKGROUND

A. In-duct propagation

Let us consider a cylindrical duct of radius R (Fig. 1). Flow velocity is neglected up to Sec. IV. The in-duct cylindrical coordinates are (r,θ,z). The acoustic pressure field at an angular frequency $\omega=2\pi f$ is split into modes (m,μ), such that

$$p(r,\theta,z,t)=\sum_{m,\mu} p_{m\mu}(r,\theta,z,t). \tag{2}$$

If reflected waves on the duct exit are neglected (this is rather valid, except for modes close to cutoff):[15,16]

$$p_{m\mu}(r,\theta,z,t)=A_{m\mu}J_m(k_t r)e^{i(\omega t-m\theta-k_z z+\psi)}, \tag{3}$$

J_m being the Bessel function of the first kind and of order m, and ψ being an arbitrary phase. The transverse wave number, k_t, depends on the boundary conditions. If the duct wall is perfectly rigid, then

$$k_t=\chi_{m\mu}/R, \quad \text{such that } J'_m(\chi_{m\mu})=0. \tag{4}$$

The axial wave number, k_z, is related to the total wave number, $K=\omega/a$ (where a is the speed of sound), and to k_t through the dispersion relationship:

$$K^2=k_z^2+k_t^2. \tag{5}$$

For propagating modes, $K\geqslant k_t$ and k_z is real. A maximum of the sound pressure level, SPL, for a mode (m,μ) is reached on the duct wall:

$$\mathrm{SPL}_{\mathrm{wall}}=20\log\left[\frac{A_{m\mu}|J_m(\chi_{m\mu})|}{\sqrt{2}p_{re}}\right], \quad \text{with } p_{re}=20\,\mu\mathrm{Pa}. \tag{6}$$

The calculation of in-duct sound power starts from the momentum equation:

$$\rho_0\frac{\partial \mathbf{v}}{\partial t}+\nabla p=0 \quad \text{or} \quad i\rho_0 aK\mathbf{v}+\nabla p=0. \tag{7}$$

Let us call u the axial component of the acoustical velocity $\mathbf{v}$:

$$\rho_0 a u_{m\mu}(r,\theta,z,t)=\frac{i}{K}\frac{\partial p_{m\mu}}{\partial z}=\frac{k_z}{K}p_{m\mu}(r,\theta,z,t). \tag{8}$$

The axial sound intensity of a propagating mode (m,μ) is

$$i_{m\mu}=\frac{1}{2}\Re\mathrm{e}(p_{m\mu}u^*_{m\mu})=\frac{A^2_{m\mu}}{2\rho_0 a}\frac{k_z}{K}J^2_m(k_t r), \tag{9}$$

where $\Re\mathrm{e}$ means "*real part*," and the star is the complex conjugate. The sound power per mode is deduced from integration on the duct cross section:

$$w_{m\mu}=\int_0^{2\pi}\int_0^R i_{m\mu}r\,dr\,d\theta$$

$$=\frac{A^2_{m\mu}}{2\rho_0 a}\frac{k_z}{K}2\pi\int_0^R J^2_m(k_t r)r\,dr. \tag{10}$$

The radial integral is a Lommel integral. If the duct wall is perfectly rigid, then $J'_m(k_t R)=0$, and

$$w_{m\mu}=\frac{A^2_{m\mu}}{2\rho_0 a}\frac{k_z}{K}2\pi\frac{R^2}{2}\left(1-\frac{m^2}{k_t^2R^2}\right)J^2_m(k_t R). \tag{11a}$$

In the special case of a plane wave, $m=0$, $k_t=0$, and

$$\int_0^R J_0^2(0)r\,dr=\frac{R^2}{2}.$$

Reference of sound power levels, PWL, is $W_{re}=1\ \mathrm{m}^2\times I_{re}=1\ \mathrm{m}^2\times p^2_{re}/(\rho_0 a)$, and

$$\mathrm{PWL}_{\mathrm{in}}=10\log(w_{m\mu}/W_{re}). \tag{11b}$$

B. Farfield radiation

The free space is referred to spherical coordinates (D,θ,φ), the origin being on the center of the duct exit (Fig. 1). Angle θ is the same as inside the duct. Angle $\varphi=0$ is on the fan centerline, and $\varphi=90°$ is in the intake plane. According to the model of Tyler and Sofrin[1] (a Rayleigh integral[17]), the farfield sound pressure is

$$P^{(\mathrm{TS})}_{m\mu}(D,\varphi,t)=i^{m+1}\frac{A_{m\mu}Rk_z}{2D/R}e^{i(\omega t-KD+\psi)}$$

$$\times J_m(k_t R)\Phi(\varphi), \tag{12a}$$

where the directivity $\Phi(\varphi)$ is given by

$$\Phi(\varphi)=\frac{2KR\sin\varphi}{(k_t R)^2-(KR\sin\varphi)^2}J'_m(KR\sin\varphi), \tag{12b}$$

with $xJ'_m(x)=mJ_m(x)-xJ_{m+1}(x)$. If $\sin\varphi=k_t/K$, then

$$\Phi(\varphi)=\left(1-\frac{m^2}{k_t^2R^2}\right)J_m(k_t R). \tag{13}$$

The more general Kirchhoff integral is nearly equivalent for computing farfield radiation:[18]

$$P^{(K)}_{m\mu}(D,\varphi,t)=\left(\frac{1}{2}+\frac{K\cos\varphi}{2k_z}\right)P^{(\mathrm{TS})}_{m\mu}(D,\varphi,t). \tag{14}$$

This equation should be better than Eqs. (12a) and (12b) for lateral radiation ($\varphi\approx 90°$) because the hypothesis of flanged inlet is not required here.

For the plane wave,

$$\Phi(\varphi)=\frac{2J_1(KR\sin\varphi)}{KR\sin\varphi}, \tag{15}$$

and, if $\varphi\approx 0$, $\Phi(\varphi)\approx 1$. It is the only case where $P_{m\mu}(D,\varphi,t)\neq 0$ for $\varphi=0$. The sound level on the centerline can thus only be generated by the plane wave $(m,\mu)=(0,1)$.

The sound intensity of spherical waves simply is

$$I_{m\mu}=\frac{\overline{P_{m\mu}^2}}{\rho_0 a}=\frac{A_{m\mu}^2}{2\rho_0 a}\left(\frac{Rk_z}{2D/R}\right)^2 J_m^2(k_t R)\Phi^2(\varphi). \tag{16}$$

Sound power radiated in the half-space $0\leqslant\varphi\leqslant\pi/2$ is

$$W_{m\mu}=\int_0^{2\pi}\int_0^{\pi/2} I_{m\mu}D^2\sin\varphi\, d\varphi\, d\theta$$

$$=2\pi D^2\int_0^{\pi/2} I_{m\mu}\sin\varphi\, d\varphi,$$

or

$$\frac{W_{m\mu}}{W_{re}}=2\pi D^2\int_0^{\pi/2}\frac{\overline{P_{m\mu}^2}}{p_{re}^2}\sin\varphi\, d\varphi, \tag{17a}$$

and

$$\mathrm{PWL}_{\mathrm{out}}=10\log(W_{m\mu}/W_{re}). \tag{17b}$$

Computations are made at angles $\varphi_j=j\,\Delta\varphi(j=0,1,...,J)$ with a step $\Delta\varphi=\pi/(2J)$, and sound power is deduced from a trapezoidal integration.

Equations of Secs. II A and II B are used to compute the spinning modes (m,μ) radiating into the free field, and their levels. The basic idea is to calculate a farfield directivity due to the propagating modes at a given frequency, using arbitrary amplitudes $A_{m\mu}$ (say, $A_{m\mu}=1$ Pa). A first estimate (overprediction) is obtained by equaling the maximum radiated level computed for each mode, and the measured level at the same angle. The values are then adjusted to get the best fit to the measured directivity pattern by minimizing a standard deviation, σ, defined below in Eq. (19). Of course, any *a priori* knowledge on the modes being generated is taken into account. The following section explains how the method can be implemented, using available experimental data from previous European programs.

III. EXPERIMENTAL ASSESSMENT

The proposed method has been checked on the RESOUND tests made by Rolls-Royce in its Ansty Noise Compressor Test Facility (ANCTF).[14] Let us consider the test series on the low noise rotor LNR1 with a hard-walled intake duct. The fan diameter was $2R=0.864$ m. There were $B=26$ rotor blades and $V=58$ outlet guide vanes (B and V are the numbers of blades and vanes, respectively). The design rotation speed was $N_d=8664$ rpm. The forward acoustic farfield was measured in the large anechoic room at $D=18.5$ m every $\Delta\varphi=5°$.

There is no interaction mode propagating on the blade passing frequency (BPF) at subsonic tip speeds, and only $m=-6$ is theoretically propagating on the first harmonic at 2BPF. The sign of m is of no interest in this study because both modes $(+m,\mu)$ and $(-m,\mu)$ generate exactly the same directivity pattern.

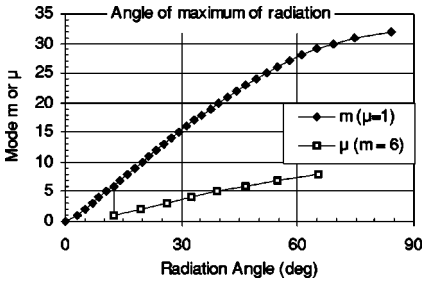

FIG. 2. An estimate of the angles of maximum radiation: Fan LNR1, $N=5027$ rpm, 2BPF=4357 Hz. (Solid lines are just connections between data points.)

A. Rotor–stator interaction modes for a low-speed run

First analyses are relative to 2BPF at a low rotational speed, $N=5027$ rpm. A crude estimate of the angles of maximum radiation is deduced from the approximation of geometric acoustics:[16]

$$\sin\varphi_{\max}\approx k_t/K, \tag{18}$$

$\xi=k_t/K$ being the cut-on ratio ($0\leqslant\xi\leqslant 1$). The previous equation provides basic information to make a first guess of the main modes radiating in a given direction. It can be seen in Fig. 2 that there are eight cut-on modes $|m|=6$, from $\mu=1$ to $\mu=8$, radiating in the range 10° to 65°. Also shown are the 33 modes with $\mu=1$. Notice that the reduced frequency is $KR=34.8$, and that there are 166 possible propagating modes $(|m|,\mu)$.

The two upper curves in Fig. 3(a) are the test data, $\mathrm{SPL}_{\mathrm{test}}$, and the total computed sound pressure level, $\mathrm{SPL}_{\mathrm{calc}}$,

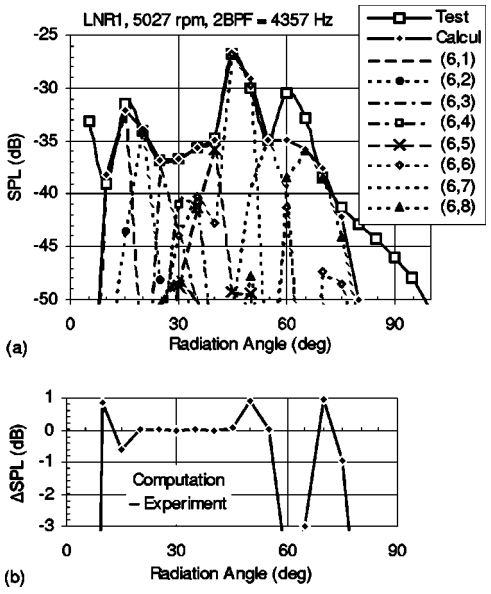

FIG. 3. Computation of sound radiation using rotor–stator interaction modes: Fan LNR1, $N=5027$ rpm, 2BPF=4357 Hz. (a) Computation of free-field directivity. (b) Difference between computed and measured sound pressure levels.

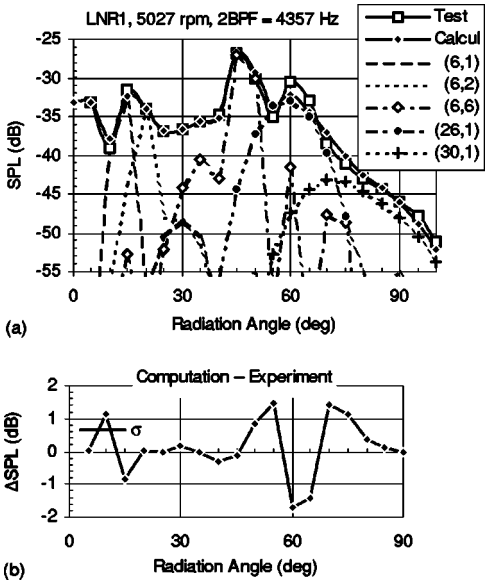

FIG. 4. Computation of sound radiation using 21 modes: Fan LNR1, $N=5027$ rpm, 2BPF=4357 Hz. (a) Computation of free-field directivity. (b) Difference between computed and measured sound pressure levels.

due to the eight modes $|m|=6$ at 2BPF (reference level is arbitrary, but 0 dB is the same in all the results). Directivities of the modes contributing to $\mathrm{SPL}_{\mathrm{calc}}$ are also plotted. Figure 3(a) proves that the amplitudes of the spinning modes $|m|=6$ can be adjusted such that prediction fits test data. Differences between computed and measured levels, $\mathrm{SPL}_{\mathrm{calc}}-\mathrm{SPL}_{\mathrm{test}}$, are better seen in Fig. 3(b) with an enlarged dB scale. Agreement is excellent in the range where modes $|m|=6$ radiate (see Fig. 2), but actual levels cannot be retrieved at low and large angles, and also around $\varphi=60°$.

Some other modes thus need to be generated. According to Fig. 2, these levels can only be due to low-order modes (for $\varphi\approx 0$), and to modes near cut off (for $\varphi\approx 90°$). Modes $m=0$ to 5 thus are also taken for radiation toward low angles, and modes $m=26$ to 32 for radiation above 55°, all with $\mu=1$. There are 21 modes, more than the 18 measurement locations. The same fit as in Fig. 3(a) is done in Fig. 4(a), and the differences are plotted in Fig. 4(b) [like Fig. 3(b)]. The horizontal bar on the left hand side of Fig. 4(b) is a kind of standard deviation, σ. It is defined by the following mean value over the radiation angle, φ:

$$10^{\sigma/10}=\langle 10^{|\mathrm{SPL}_{\mathrm{calc}}-\mathrm{SPL}_{\mathrm{test}}|/10}\rangle_{\varphi}. \tag{19}$$

This is the parameter to be minimized in the least squares fitting. The result is rather good. The errors are less than ± 2 dB, and are better than ± 1 dB at most angles. It must also be reiterated that measurements are used as a comparison basis, but they are not perfectly exact, and these data are submitted to some inaccuracy. Figure 5 shows the sound levels of the modes, ordered by their radial wave number (i.e., their angle of maximum radiation). Three curves are plotted: the sound pressure level on the duct wall, $\mathrm{SPL}_{\mathrm{wall}}$ [Eq. (6)], and sound power levels inside the duct and in the free field, $\mathrm{PWL}_{\mathrm{in}}$ and $\mathrm{PWL}_{\mathrm{out}}$ [Eqs. (11b) and (17b)], respectively. It is assessed that these two last values are the same. A fourth curve is also shown (black triangles), corresponding to

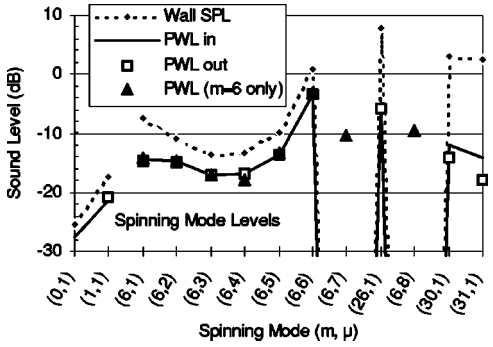

FIG. 5. Sound levels of the modes generating the 2BPF tone in Fan LNR1 at $N=5027$ rpm.

the PWL found in Fig. 3. Wall SPL tends to increase for modes near cutoff (their radial profile is more and more concentrated near the duct wall), but sound power level, PWL, is more uniform.

Several interesting features are worth being outlined. (i) Measured radiation can finally be explained by using only 11 modes out of the 21 modes. (ii) The plane wave (0,1) is included to get a smooth directivity at low angles toward the centerline, as is generally found experimentally, but there is no measurement at $\varphi=0°$. In fact, the curve of Fig. 4(b) would not be modified if that mode were deleted. (iii) Mode (26,1) is very strong, and generates the hump around 60°. One can notice that $26=B$, but there is no theoretical reason why this mode should be present on 2BPF. (iv) Modes (6,7) and (6,8) with many radial lobes were present in Fig. 3, but have become useless in Fig. 4, where they are replaced by the mode (26,1). (v) Modes (6,1) to (6,6) exactly have the same levels in Figs. 3 and 4, and they are higher than modes (0,1), (1,1), (30,1), and (31,1). This tends to assess the robustness of the method.

It can be checked that the system of Eqs. (1) is equivalent to the above fitting if the number of modes is equal to the number of measurement locations. Let us take the modes (6,1) to (6,6), and test data at 15°, 20°, 25°, 35°, 40°, and 45°. Solutions are accurate because the highest terms of the matrix $\|F_{m\mu}\|$ lie on the diagonal, or are close to it (see Fig. 2). Table I compares the amplitudes $A_{m\mu}$ (in dB) to those from the least squares fitting. The main difference is on mode (6,1). It is shown in Fig. 4(b) that the least squares fitting is a compromise between the levels measured at 10° and 15°. The solution of Eqs. (1) exactly reproduces the level at 15°, but would overestimate that at 10° by 2 dB.

Figure 6 shows the variation of the overall standard deviation, σ, as defined in Eq. (19), if the level of one of the strongest modes, (6,6) or (26,1), slightly varies. It is found that the parameter σ is well sensitive to mode levels, a variation of the order of 1 dB modifies σ by about 0.1 dB. This

TABLE I. A comparison of modal amplitudes from least squares fitting and from Eqs. (1).

$A_{m\mu}$ (dB)	(6,1)	(6,2)	(6,3)	(6,4)	(6,5)	(6,6)
Least squares fitting	1.1	1.1	−0.1	1.4	5.8	16.2
System of Eqs. (1)	2.4	1.1	0.0	0.8	5.7	17.0

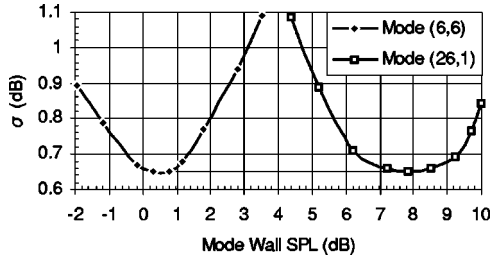

FIG. 6. Effect of mode levels on standard deviation: Fan LNR1, $N=5027$ rpm, 2BPF=4357 Hz. Horizontal line at $\sigma=0.65$ connects the two sound pressure levels found in Figs. 4 and 5.

confirms that the method seems to be rather robust, and the sound levels can be successively optimized for each mode.

B. Example at another rotational speed

It is important to check the method on 2BPF at another subsonic rotational speed, say $N=7013$ rpm. There are 13 propagating modes $|m|=6$ ($\mu=1$ to 13). The last mode (6,13) is closer to the cutoff limit than in the previous case, and radiates toward large angles. There are 46 modes ($m=0$ to 45) propagating with $\mu=1$, but only the first five ($m=0$ to 4) seem to be sufficient to predict the directivity toward the low angles.

Figure 7 shows the result using the 18 above modes, this value being equal to the number of measurement angles. The sound levels of the modes are given in Fig. 8. Two comments can again be made. (i) The 18 modes are needed to get a good fit to the experimental data, except the plane wave, which is only used as before to get a smooth directivity around the fan centerline. The main modes which contribute to the humps of directivity are plotted in Fig. 7(a). (ii) Agreement between computation and test data again is very good; errors are less than ± 2 dB and close to 0 dB up to angles of 45°. The difference at the large angle of 55° can be due to a

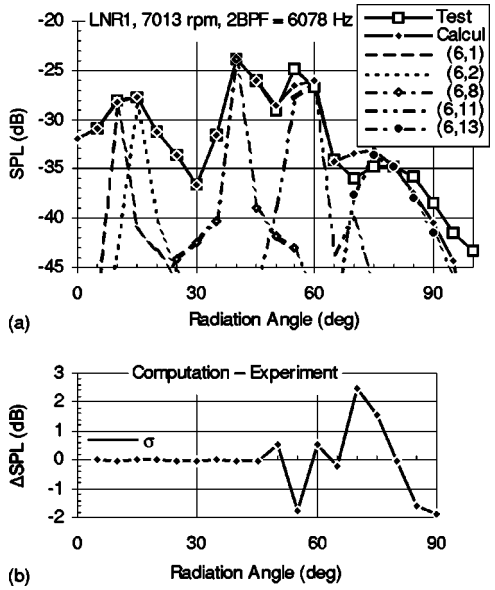

FIG. 7. Computation of sound radiation: Fan LNR1, $N=7013$ rpm, 2BPF =6078 Hz. (a) Computation of free-field directivity. (b) Difference between computed and measured sound pressure levels.

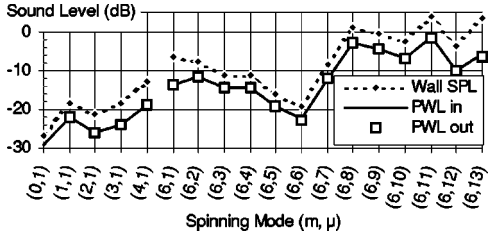

FIG. 8. Sound levels of the modes generating the 2BPF tone in Fan LNR1 at $N=7013$ rpm.

slight shift of the computed directivity of mode (6,11) because flow velocity is not taken into account (see Sec. IV).

C. Tone without any propagating interaction mode

One more analysis is shown at the blade passing frequency, BPF, on which no interaction mode can propagate. The same speed as above is considered, $N=7013$ rpm.

The prediction of radiation is shown in Fig. 9, along with some curves for the main modes in Fig. 9(a). The modes initially used are the 22 propagating modes with $\mu=1$, plus modes (13,2) and (15,2) to try to better fit to the small humps measured at 55° and 65°. In fact, these two modes do not lead to any improvement, and Fig. 10 shows that only 13 modes out of the 24 modes are necessary. The accuracy is very good [Fig. 9(b)], lying inside ± 1 dB. Of course, this does not mean that another set of modes with $\mu\neq 1$ could not give similar results, but modes $\mu=1$ often are higher. It can be noted that the plane wave (0,1) tends here to improve the directivity at small angles, and that its sound power level is the lowest of the 13 modes (like in the two previous examples).

IV. IN-DUCT FLOW EFFECT ON FREE-FIELD RADIATION

Up until now, the ducted flow Mach number, M_{ax}, has been neglected. If the velocity is assumed to be uniform, Eq. (4) is replaced by

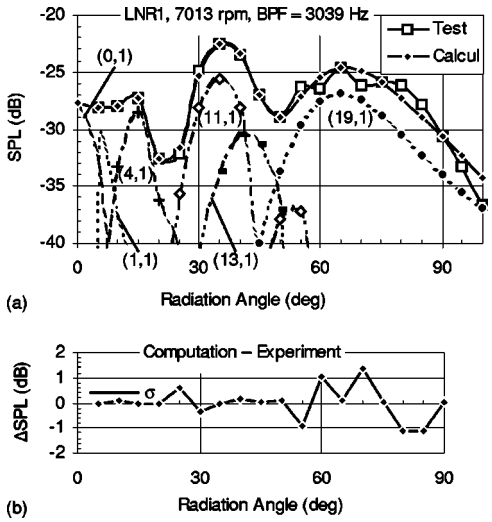

FIG. 9. Computation of sound radiation: Fan LNR1, $N=7013$ rpm, BPF =3039 Hz. (a) Computation of free-field directivity. (b) Difference between computed and measured sound pressure levels.

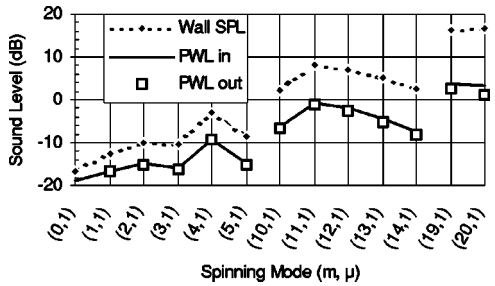

FIG. 10. Sound levels of the modes generating the BPF tone in Fan LNR1 at $N=7013$ rpm.

$$k_t=\sqrt{1-M_{ax}^2}\chi_{m\mu}/R=\sqrt{1-M_{ax}^2}k_{t0}, \tag{20}$$

where $k_{t0}=\chi_{m\mu}/R$, subscript 0 reminding us that Eq. (4) applies to $M_{ax}=0$. In a first approximation, Eq. (18) remains valid using this modified value of k_t. The difference between $\varphi_{0\,\max}$ (at $M_{ax}=0$) and $\varphi_{\max}$ (at $M_{ax}\neq 0$) is roughly given by

$$\varphi_{0\,\max}-\varphi_{\max}=\arcsin\left(\frac{k_{t0}}{K}\right)-\arcsin\left(\sqrt{1-M_{ax}^2}\frac{k_{t0}}{K}\right), \tag{21}$$

which is plotted in Fig. 11 as a function of $\varphi_{0\,\max}$. The hypothesis neglecting the flow inside the duct is rather valid up to axial Mach numbers $M_{ax}=0.2-0.3$ (except at large angles, i.e., for modes near cutoff), but M_{ax} can reach 0.5 in front of the blades at high speeds.

It has appeared that the main parameter of free-field radiation is the cut-on ratio $\xi=k_t/K$. If we want to keep fast computations, equations of Sec. II without flow can still be used, but it is noted that

$$\xi=\frac{k_t}{K}=\sqrt{1-M_{ax}^2}\frac{k_{t0}}{K}=\frac{k_{t0}}{K'}. \tag{22}$$

This means that the actual frequency, f, could be simply replaced by a higher frequency, f':

$$K'=\frac{K}{\sqrt{1-M_{ax}^2}}\quad\text{or}\quad f'=\frac{f}{\sqrt{1-M_{ax}^2}}. \tag{23}$$

The change of frequency of course modifies the estimated amplitudes, $A_{m\mu}$.

A case of supersonic tip speed is considered now because the axial Mach number is high. The rotor mode due to steady loading can then propagate, and generally dominates

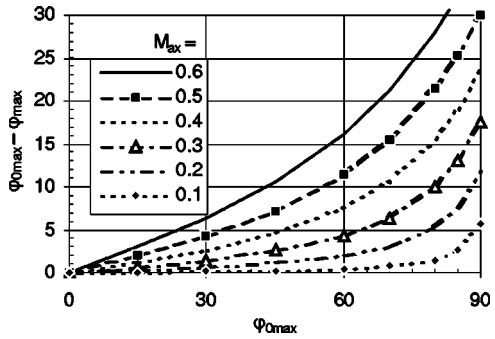

FIG. 11. In-duct flow effect on the angle of maximum radiation.

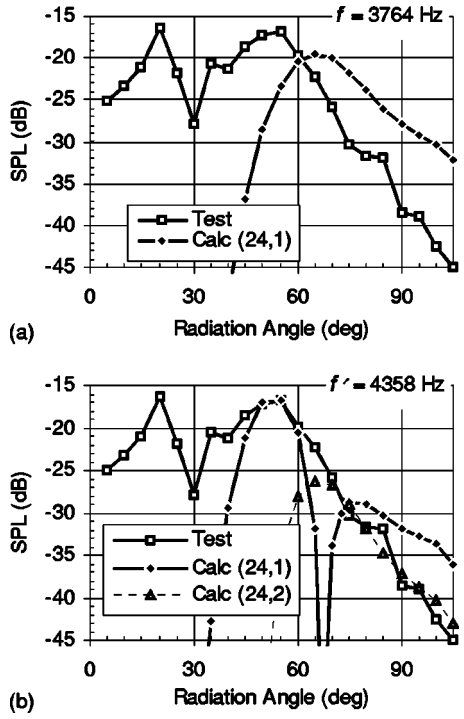

FIG. 12. Computation of sound radiation by mode P=%=24 on BPF of the FANPAC fan at a supersonic tip speed: $N=9411$ rpm. (a) Computation at the actual frequency: $f=3764$ Hz. (b) Computation at modified frequency: $f'=4358$ Hz.

the radiated acoustic field. The main azimuthal mode, m, is thus equal to the harmonic order of the rotation frequency: $m=B$ on BPF.

LNR1 tests are not appropriate since that fan is just transonic at the design speed. Let us thus consider previous Rolls-Royce tests made in the framework of the European project FANPAC with a rigid-walled duct.[19] Experimental conditions were similar to those given at the beginning of Sec. III. The fan diameter also was $2R=0.864$ m, but the number of rotor blades was $B=24$ instead of 26. The main difference was the design rotation speed, 15% higher than LNR1, i.e., $N_d=10\,100$ rpm, which corresponds to a tip Mach number of 1.34.

Figure 12 is relative to BPF at a supersonic rotational speed $N=9411$ rpm (the tip Mach number is 1.25). Figure 12(a) shows the radiation of mode $m=B=24$ computed at the actual frequency, $f=3764$ Hz. This does not agree with the measured directivity. The axial Mach number is $M_{ax}=0.504$, and the frequency given by Eq. (23) is $f'=4358$ Hz. Figure 12(b) shows that the maximum around 55° then is well retrieved. Only the first radial mode (24,1) is propagating in the case of Fig. 12(a), and its sound power level is the same in both graphs. The second radial mode (24,2) also propagates in the case of Fig. 12(b), but it does not seem to contribute to radiation.

Some other modes of lower order are required to predict the radiation at smaller angles, mainly around 20°. Figure 13 displays as before the results using the 33 propagating modes with $\mu=1$ at the modified BPF. Prediction is again very good except at large angles, but experimental levels seem to be rather low in this run (see the gap between 85° and 90°).

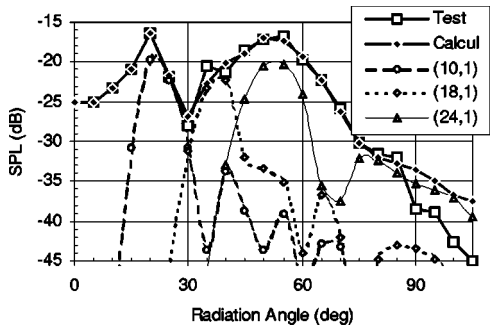

FIG. 13. Computation of sound radiation: FANPAC fan, $N=9411$ rpm, corrected BPF=4358 Hz.

Figure 14 shows that only 11 spinning modes contribute to radiation. The rotor mode (24,1) is the highest, but some neighboring modes nearly have the same level. The peak at 20° is due to strong modes (8,1), (9,1), and (10,1).

V. CONCLUSIONS

It has been found that the basic theory of ducted propagation and free-field radiation well describes the actual fan directivity measured in an anechoic chamber. This leads to a fast computer code that can easily be used to predict the spinning modes generating a given tone. The flow axial Mach number inside the duct can be simply introduced by modifying the actual frequency, and this correction must be done at high speeds to find valid directivities. The examples discussed in this article have shown that the method seems to be robust.

The next step will be the implementation of an automatic procedure to numerically determine the acoustic levels of the modes. The system of linear equations written in the Introduction gives us the amplitudes of the modes if we take as many modes as measurement locations in the free field. The solution can be accurate since the square matrix of coefficients looks like a diagonal matrix, i.e., the main terms are on the diagonal or near it if modes are ordered according to their transverse wave number. A least squares fitting has however to be made in a more general case when the numbers of modes and of measured sound levels are not equal. The standard deviation that has been defined appears to be a valid parameter to be minimized.

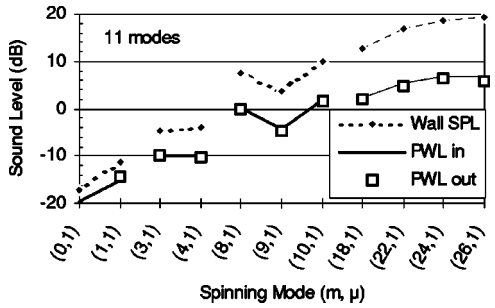

FIG. 14. Sound levels of the modes generating the BPF tone in the FANPAC fan at $N=9411$ rpm.

The proposed method will be assessed during the model engine fan tests planned within the European Integrated Platform SILENCE®, which will include both in-duct modal analyses and free-field acoustic measurements. The final objective is to deduce the modal structure generated by the acoustic sources from free-field measurements without requiring any in-duct modal analysis. These data can then be used as inputs in computer codes to optimize the nacelle shape and lining.

ACKNOWLEDGMENTS

This work has been done within the European Integrated Platform SILENCE®, and has been partly funded by the European Union.

[1] J. M. Tyler and T. G. Sofrin, "Axial flow compressor noise studies," SAE Trans. **70**, 309–332 (1962).
[2] U. Bolleter and M. J. Crocker, "Theory and measurement of modal spectra in hard-walled cylindrical ducts," J. Acoust. Soc. Am. **51**, 1439–1447 (1972).
[3] E. R. Rademaker and P. Sijtsma, "*Mode detection with an optimised array in a model turbofan engine intake at varying shaft speeds*," 7th AIAA/CEAS Aeroacoustics Conference, Maastricht, The Netherlands, 28–30 May, 2001, AIAA Paper No. 2001-2181.
[4] S. Lewy and H. Gounet, "Experimental study of the acoustic spinning modes generated by a helicopter turboshaft engine," *18th Congress of the International Council of the Aeronautical Sciences*, Beijing, 20–25 September, 1992, ICAS-92-1.5.1, ICAS Proceedings 1992, ICAS & AIAA, Vol. 1, pp. 898–906.
[5] F. Farassat, D. M. Nark, and R. H. Thomas, "The detection of radiated modes from ducted fan engine," *7th AIAA/CEAS Aeroacoustics Conference*, Maastricht, The Netherlands, 28–30 May, 2001, AIAA Paper No. 2001-2138.
[6] F. Farassat and P. L. Spence, "Noise radiation from ducted fans with realistic duct-rotor coupling," J. Acoust. Soc. Am. **92**, 2456 (1992).
[7] P. A. Nelson, "A review of some inverse problems in acoustics," Int. J. Acoust. Vib. **6**, 118–134 (2001).
[8] M. B. S. Magalhães and R. A. Tenenbaum, "Sound sources reconstruction techniques: A review of their evolution and new trends," Acta Acust. **90**, 199–220 (2004).
[9] S. Lewy, J. Lambourion, C. Malarmey, M. Perulli, and B. Rafine, "*Direct experimental verification of the theoretical model predicting rotor noise generation*," AIAA 5th Aeroacoustics Conference, Seattle, WA, 12–14 March, 1979, AIAA Paper No. 79-0658.
[10] R. W. Schaffer, R. M. Mersereau, and M. A. Richards, "Constrained iterative restoration algorithm," Proc. IEEE **69**, 432–450 (1981).
[11] E. G. Williams, "Regularization methods for near-field acoustical holography," J. Acoust. Soc. Am. **110**, 1976–1988 (2001).
[12] T. Semenova and S. F. Wu, "The Helmholtz equation least-squares method and Rayleigh hypothesis in near-field acoustical holography," J. Acoust. Soc. Am. **115**, 1632–1640 (2004).
[13] P. J. G. Schwaller, B. J. Tester, and D. G. Henshaw, "The effects on fan noise of inlet steady flow distortion," *3rd AIAA/CEAS Aeroacoustics Conference*, Atlanta, GA, 12–14 May, 1997, AIAA Paper No. 97-1590-CP.
[14] C. L. Bewick, M. J. Adams, P. J. G. Schwaller, and L. Xu, "Noise and aerodynamic design and test of a low tip speed fan," *7th AIAA/CEAS Aeroacoustics Conference*, Maastricht, The Netherlands, 28–30 May, 2001, AIAA Paper 2001–2268.
[15] E. Lumsdaine, "Calculation of pressure reflection ratio," J. Sound Vib. **52**, 145–147 (1977).
[16] E. J. Rice, "Multimodal far field acoustic radiation pattern using mode cutoff ratio," AIAA J. **16**, 906–911 (1978).
[17] E. G. Williams and J. D. Maynard, "Numerical evaluation of the Rayleigh integral for planar radiators using the FFT," J. Acoust. Soc. Am. **72**, 2020–2030 (1982).
[18] S. Lewy, "Computation of broadband noise radiated by a ducted fan in a uniform flow," Int. J. Acoust. Vib. **8**, 211–218 (2003).
[19] S. Lewy, "Experimental study of upstream fan broadband noise radiated by a turbofan model," Int. J. Acoust. Vib. **6**, 65–75 (2001).

Effective impedance spectra for predicting rough sea effects on atmospheric impulsive sounds[a)]

Patrice Boulanger and Keith Attenborough[b)]
Department of Engineering, The University of Hull, Hull HU6 7RX, United Kingdom

(Received 18 October 2003; revised 2 November 2004; accepted 5 November 2004)

Two methods of calculating the effective impedance spectra of acoustically hard, randomly rough, two-dimensional surfaces valid for acoustic wavelengths large compared with the roughness scales have been explored. The first method uses the complex excess attenuation spectrum due to a point source above a rough boundary predicted by a boundary element method (BEM) and solves for effective impedance roots identified by a winding number integral method. The second method is based on an analytical theory in which the contributions from random distributions of surface scatterers are summed to obtain the total scattered field. Effective impedance spectra deduced from measurements of the complex excess attenuation above 2D randomly rough surfaces formed by semicylinders and wedges have been compared to predictions from the two approaches. Although the analytical theory gives relatively poor predictions, BEM-deduced effective impedance spectra agree tolerably well with measured data. Simple polynomials have been found to fit BEM-deduced spectra for surfaces formed by intersecting parabolas corresponding to average roughness heights between 0.25 and 7.5 m and for five incidence angles for each average height. Predicted effects of sea-surface roughness on sonic boom profiles and rise time are comparable to those due to turbulence and molecular relaxation effects.
[DOI: 10.1121/1.1847872]

PACS numbers: 43.50.Vt, 43.28.Fp [LCS] Pages: 751–762

I. INTRODUCTION

Effects on continuous outdoor sound result from ground porosity and surface roughness. Roughness leads to specular and nonspecular scatter and changes the effective impedance of the ground.[1–3] The main effect of the finite surface impedance of the ground on sonic boom propagation is on each side of the carpet edge and in the shadow zone.[4] There are less important effects in the primary carpet, where the incidence angle varies quite significantly. To reduce the noise impact of sonic booms from civil supersonic flights, it is likely that, wherever possible, the aircraft will pass through the sound barrier over the sea. This means that prediction of sonic boom characteristics in coastal areas will be important and will involve propagation over the sea as well as over land. Given that the specific impedance of seawater is greater than that of air by four orders of magnitude, the sea surface may be considered to be acoustically hard. Nevertheless, it is likely that boom characteristics are modified during near-grazing propagation above a rough sea surface. Such propagation is likely to be of interest also when predicting sound propagation from near-ground explosions. Although the sea surface is continuously in motion associated with winds and currents, so that the scattered field is not constant, a sonic boom or blast waveform is sufficiently short compared with the period of the sea-surface motion that the roughness may be considered to be static. If the incident acoustic wavelengths are large compared with the water wave heights and periods, the effect of the diffraction of sound waves by roughness may be modeed by an effective impedance, and this is a convenient way to incorporate the acoustical properties of a rough sea surface into sonic boom and blast sound propagation models. The objective of this work is to develop models for the effective impedance spectra of rough, hard surfaces corresponding to different sea states. Several theories have been developed to describe the effective impedance of rough surfaces when the roughness scale is small compared to the acoustic wavelength. The boss theory attributed to Biot and Tolstoy (see Ref. 3) models rough surfaces of finite impedance but does not account for nonspecular scattering (sometimes called incoherent scattering). Inclusion of effects of nonspecular scattering has been found necessary when comparing predicted results with measurements.[3] Lucas and Twersky[5] have developed a theory that incorporates a nonspecular scattering term in the effective admittance. When used to model 2D periodic and random hard roughness, this theory has been found to give reasonable agreement with measured ground effect.[2] This model has been extended heuristically[3] to finite impedance roughness, and the resulting predictions have given good agreement with ground effect measured over rough sand surfaces in the laboratory and with data obtained over outdoor ground surfaces.

There have been several studies of the derivation of effective impedance from excess attenuation (EA) measurements.[6] A novel component of the work reported here is to use a winding number integral method[7] to identify the impedance roots of the classical expression for the sound field due to a point source above a smooth impedance plane. In addition, a boundary element method (BEM) is used to predict EA spectra that are compared with predictions from

[a)]Parts of this paper were presented at the 10th LRSPS Grenoble 2002 and at Forum Acusticum, Seville 2002.
[b)]Electronic mail: k.attenborough@hull.ac.uk

Lucas and Twersky's theory and measurements. Complex excess attenuation spectra obtained from measurements and BEM simulations are used to deduce effective impedance spectra, and the results are compared to Lucas and Twersky's analytical theory. The BEM has proved capable of accurate predictions of sound-pressure level for propagation from a point source over mixed impedance[8] and rough, hard ground.[2] However, the real part of impedance predicted by Lucas and Twersky's theory for a hard, rough surface does not conform to the low-frequency limit (infinite real) that is expected from physical considerations. Moreover, it is found to give less satisfactory agreement with hard, rough surface data than the BEM. For these reasons, BEM calculations have been used to derive effective impedance spectra for hypothetical rough surfaces corresponding to certain sea states and several incidence angles. Intersecting parabolas are used to represent rough sea surfaces. Simple frequency-dependent polynomial fits of BEM-deduced spectra are used for the effective impedance evaluations. Coefficients are obtained that enable prediction of the effective surface impedance for six rough-sea states and for five incidence angles. As they result from fitting averages of several BEM predictions using deterministic profiles with randomly generated roughness heights, the polynomials offer a ''shortcut'' to use of multiple BEM predictions.

Section II describes the boundary element method for predicting complex excess attenuation (EA) and Lucas and Twersky's analytical boss theory for effective admittance. Section III describes the winding number integral method to obtain the effective impedance for rough surfaces from the measured or BEM-predicted complex EA. Section IV tests the validity of the model's predictions by comparing results with measured data for semicylindrical and wedge-shaped roughness. Polynomial fits of the BEM-deduced effective impedance are also presented. Section V shows an example of BEM EA and deduced effective impedance for one average height of parabolically shaped roughness and for one grazing angle. The effective impedance fit coefficients obtained for six average roughness sizes and five incidence angles are shown to be dependent on both average roughness sizes and incidence angles, and an interpretation is presented in section VI A–B. Section VI C gives a brief analysis of the inaccuracies in the effective impedance fit-coefficient estimations. Section VII shows that the BEM-predicted EA fluctuations may be due to roughness-induced surface waves, and Sec. VIII presents predictions of the rough-sea surface effect on sonic boom profiles. Conclusions are drawn in Sec. IX.

II. THE MODELS

A. The boundary element numerical model

Chandler-Wilde[9,10] has developed a boundary integral equation method for solving the Helmholtz equation for the pressure at the receiver due to a line source above an impedance plane. The resulting boundary integral equation is solved approximately by assuming a constant pressure over each boundary element of the ground surface and using the (point) collocation method. The latter approximates the solution by weighted residuals and sets the residual function to zero at a series of points. These equations for each point plus the discretization of the integral equation give a system of equations whose dimension is the number of collocation points. It is possible to model either a flat or a profiled ground surface since the discretizing points can be chosen out of the horizontal plane. To save computation time, an equivalent two-dimensional problem is solved, i.e., only ground and sound sources that show no variation along one axis are modeed. Source, receiver, and specular reflection point are assumed to be in a vertical plane perpendicular to the roughness axis, and a line integral is solved instead of a surface integral. The acoustic impedance can be chosen independently for each surface element of the profile. The BEM is used to predict sound levels over rough surfaces by including the roughness profile in the form of node coordinates input to the program. In the models used in this work, acoustically hard surfaces are modeled by setting admittance $\beta=0$.

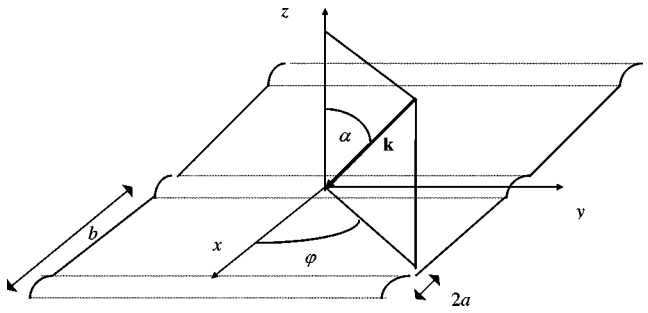

FIG. 1. A plane wave obliquely incident on a surface containing semicylindrical bosses.

B. Twersky's analytical theory

Lucas and Twersky have developed a boss model[5] to describe coherent reflection from a hard (or a pressure-release) surface containing semicylindrical or semielliptical roughness in which the contributions of the scatterers are summed to obtain the total scattered field. Sparse and closely packed distributions of bosses have been considered and interactions between neighboring scatterers have been included. The model predicts a real part of the effective admittance of the rough, hard surface, which may be attributed to nonspecular scattering.

1. Semicircular cylinders

Consider a plane wave incident on an array of semicylinders of radius a and mean center-to-center spacing b on an otherwise plane hard boundary (see Fig. 1). The angle of incidence with respect to the normal is α and the angle (azimuthal angle) between the projection of the wave vector on the horizontal plane and the axis perpendicular to the cylindrical roughness elements is φ. Twersky's result for the effective specific acoustic admittance β relative to air of a rough, hard surface (zero admittance of the rough material) containing randomly spaced 2D circular semicylinders is

$$\beta = \eta - i\xi, \tag{1}$$

where

$$\xi(\alpha,\varphi)\approx kV[-1+(\delta\cos^2(\varphi)+\sin^2(\varphi))\sin^2(\alpha)]+O(k^3), \quad (2)$$

$$\eta(\alpha,\varphi)\approx \frac{nk^3\pi^2a^4}{8}(1-W)^2\left\{(1-\sin^2\alpha\sin^2\varphi)\times\left[1+\left(\frac{\delta^2}{2}\cos^2\varphi-\sin^2\varphi\right)\sin^2\alpha\right]\right\}+O(k^5) \quad (3)$$

The term $V=n\pi a^2/2$ is the raised cross sectional area per unit length, n is the number of semicylinders per unit length $(=1/b)$, $\delta=2/(1+I)$ is a measure of the dipole coupling between the semicylinders, and $I=(a^2/b^{*2})I_2$. The integral I_2 is evaluated in Ref. 5. $(1-W)^2$ is a packing factor introduced for random distributions, $W=nb^*=b^*/b$, b^* is the minimum (center-to-center) separation between two cylinders, and $k=2\pi f/c$ is the wave number with f the frequency and c the speed of sound. Note that, in Ref. 2, the factor $(1-W^2)$ in the expression for η should be $(1-W)^2$, and the factor b in the denominator of the definition of I should be b^*.

2. Semielliptical cylinders

According to Lucas and Twersky,[5] if semielliptical cylinders have ratio K between the major (Ka) and minor (a) axes such that $V=n\pi a^2K/2$, the dipole coupling between the semicylinders is $\delta=1+K/(1+I[K(1+K)/2])$. Note that K is defined erroneously as the eccentricity in Ref. 2. The source height h_s, n, Ka, a, and b^* are varied to obtain the best least-square fit with the effective impedance obtained from BEM predictions or from measured data. The frequency dependence of the admittance, $\beta=\mathrm{Re}(\beta)+i\,\mathrm{lm}(\beta)$, is given by $\mathrm{Re}(\beta)=\chi f^3+\mathrm{O}(f^5)$ and $\mathrm{Im}(\beta)=\gamma f+\mathrm{O}(f^3)$, where χ is a positive coefficient and the sign of the coefficient γ depends on the semiwidth/height of the semielliptical cylinders but is mostly negative for near-semicylindrical roughness shapes. When f tends to zero, $\mathrm{Re}(\beta)$ decreases much faster than $\mathrm{lm}(\beta)$ and the effective specific acoustic impedance Z tends to ∞ as $-i/(\gamma f)$. This implies that, when f tends to zero, $\mathrm{Re}(Z)$ tends towards zero and $-\mathrm{lm}(Z)$ goes to $-\infty$. This result is confirmed by the effective impedance graphs presented in Sec. IV.

III. EFFECTIVE IMPEDANCE OBTAINED FROM MEASURED AND BEM-BASED EXCESS ATTENUATION

A. Computation method for excess attenuation

The magnitude of excess attenuation (EA), which is the attenuation of the sound wave in excess of that from spherical spreading, is defined for both models and measurements by

$$\mathrm{EA}=20\lg\left|\frac{P}{P_1}\right|. \quad (4)$$

Here, the direct wave is given by

$$P_1=P_0\frac{\exp(ikR_1)}{R_1}. \quad (5)$$

The total pressure P for the model based on Twersky's theory is computed from[11]

$$P=P_0\frac{\exp(ikR_1)}{R_1}+QP_0\frac{\exp(ikR_2)}{R_2}. \quad (6)$$

The distances R_1 and R_2 are the direct and specularly reflected path lengths. The spherical wave reflection coefficient is defined by $Q=R+[1-R]F(w)$.

The plane-wave reflection coefficient $R=(\cos\alpha-\beta)/(\cos\alpha+\beta)$, the boundary loss factor $F(w)=1+i\sqrt{\pi}we^{-w^2}\,\mathrm{erfc}(-iw)$, and the numerical distance $w=\sqrt{\frac{1}{2}ikR_2}(\beta+\cos\alpha)$. For semicylindrical hard, rough surfaces, the effective admittance β relative to air that appears in the above expressions for R and w is obtained from Eqs. (1)–(3).

B. Effective impedance from BEM-predicted or measured excess attenuation

1. The admittance root equation

The complex pressure ratio, P/P_1, evaluated numerically using the BEM and by measurements, corresponds to the attenuation due to the interference between the direct wave and the surface reflected wave. Both parts of the complex pressure ratio are needed to evaluate the complex effective impedance relative to air. To estimate the effective impedance of a rough surface, it is postulated that the complex pressure ratio predicted by the BEM (or measured) is produced by a smooth surface with effective admittance β_{eff} relative to air. Use is made of the classical expression for the sound field due to a point source above an impedance boundary. The problem becomes a search for complex roots β_{eff} of the equation

$$1+\frac{R_1}{R_2}e^{ik(R_2-R_1)}\left\{\frac{\cos\alpha-\beta}{\cos\alpha+\beta}+\left(1-\frac{\cos\alpha-\beta}{\cos\alpha+\beta}\right)\times(1+i\sqrt{\pi}w(\beta)e^{-w(\beta)^2}\,\mathrm{erfc}[-iw(\beta)])\right\}-\frac{P}{P_1}=0. \quad (7)$$

This equation is solved for each frequency point and for input values of R_1, R_2, $\cos\alpha$, P, and P_1. Since it does not have a readily available analytical solution, numerical methods must be used. Among the standard numerical methods for finding the roots of complex variable equations, the Newton–Raphson method has been used previously in effective impedance estimations,[6] but produces only one root per frequency point. Another method, Müller's algorithm, is found in the IMSL library routine "ZANLY"[12] but is limited to two roots for each frequency point. If several roots are in the same complex admittance neighborhood for a given frequency, such single-root methods may pick up a root belonging to another root spectrum and follow that for subsequent frequencies, giving mixed root spectra as a result. Indeed, this has been observed in several test cases when solving Eq. (7). To avoid this problem, a third, more thorough, root search method based on winding number integral has been developed.

2. The winding number integral method

The winding number integral is a contour integral around a closed path in the complex plane. It is used to determine the presence of zeros and poles in the enclosed area. Having determined that a closed area in the complex plane contains roots, the location of those roots can be deduced with a high degree of accuracy by using higher moments of the winding integral. The method has been applied by Brazier-Smith *et al.*[7] to the determination of the roots of dispersion equations. Assume that it is desired to determine the roots of a function F, analytic everywhere inside a closed contour Γ. The difference between the number of zeros n_Z and the number of poles n_P of F inside Γ can be computed from the integral

$$\frac{1}{2\pi i}\oint_\Gamma \frac{F'}{F}dz = n_z - n_p. \tag{8}$$

The complex integral can be evaluated by the winding number $\mathrm{wnd}(F(\Gamma),0)$ of $F(\Gamma)$ around the origin in an anticlockwise path such that

$$n_Z - n_P = \mathrm{wnd}(F(\Gamma),0). \tag{9}$$

Once the image of the closed contour Γ is computed by the function F, it is simple to divide the path into a series of chords and examine whether each chord takes $\ln(F)$ across the negative real axis. If it crosses from above, the winding number is increased by 1. If it crosses from below, it is reduced by 1. When the number of zeros inside a contour is established, the roots need to be identified. If, as in this work, there is a search for two roots at a time in a contour, only the first two moments of the winding integral are required. The moment of order n is given by

$$I_n = -\frac{1}{2\pi i}\left\{[z^n \ln F] - n\oint_\Gamma z^{n-1}\ln F\,dz\right\}$$

$$= \sum_i (z_z^i)^n - \sum_j (z_p^j)^n, \tag{10}$$

where z_z^i is the location of the ith zero and where z_p^j is the location of the jth pole. Equation (7) shows only one pole for $\beta = -\cos(\theta)$; therefore, the expressions for the moments are simplified and contain only z_z^i in most of the complex plane. When the winding number is equal to 1, the single zero is given by I_1 and, when the winding number is equal to 2, the two zeros are determined by the roots of the quadratic equation

$$z^2 - I_1 z + 0.5(I_1^2 - I_2) = 0. \tag{11}$$

If three roots are sought at a time, the third moment of the winding number integral is needed and it should be noted that the constant term, $-(I_1^2)/6$ in Eq. (9) of Ref. 8, should be $-(I_1^3)/6$. The integral [Eq. (10)] is computed numerically with a Riemann sum. Great care must be exercised when computing the function $\ln(F)$ because ln is not analytical across the negative real axis and the argument F of ln might cross this branch cut. This potential discontinuity in $\ln(F(z))$ is solved using an analytical continuation of ln across the branch cut. Thus, instead of considering ln as a simple function, it is viewed as a family of ln functions, each defined on a separate Riemann sheet. This allows continuity of the $\ln(F(z))$ family function at each branch cut. A branch cut is viewed as a seam between two successive Riemann sheets.

In general, the relative calculation errors of the moments I_n increase with the order n. For finding the roots of Eq. (7), the method uses a series of square contours Γ in which to search for the roots. The square is the most convenient and efficient geometrical shape with which to cover the β plane in the areas of interest. If more than two roots are detected with the winding number count inside each square contour Γ, a smaller contour must be chosen. An important computational constraint is the number of points N used to discretize a given contour size. This number is crucial as it determines also the relative error of the numerical integration used to evaluate the first and second moments I_1 and I_2 of the winding integral on which the root search is based. If N is too small, the estimation of the root values is so approximate that they do not satisfy the root condition $F(z)=0$. It was found that 2^N points with $N=12$ for a 2×2 square contour of Γ would give a root relative error of 0.01 on known roots of a test function. As a consequence, the search area has been divided into a series of small 2×2 square contours in the complex β plane. Using such contours, an 800-MHz processor takes 10 min to run a root search for one frequency point in a 1000×100 array of β values.

Although the winding number integral method is more demanding computationally than the Newton–Raphson or Müller method, it allows complete root searches when the classical methods fail to converge. It has been found that, for some roughness profiles, there are frequency ranges with only negative real effective impedance roots. This unphysical behavior may result from the enhanced EA levels (>6 dB) (Ref. 13) possibly caused by surface waves (see Secs. IV–VII). To avoid this difficulty, several BEM EA spectra corresponding to various roughness profiles of same average roughness height have been averaged, and the effective impedance relative to air has been evaluated from the averaged complex EA above a raised smooth plane representing the ground surface. The following section gives more details of the method and compares the results with measurements made above arrays of 2D random hard semicylinders and wedge roughness profiles.

IV. RESULTS FOR HARD, RANDOMLY SPACED SEMICYLINDRICAL AND WEDGE ROUGHNESS

In the following, d denotes the source–receiver separation distance, h represents the (equal) source and receiver heights, h_{eff} is the effective source and receiver height, l is the semicylinder diameter, and Z is the impedance. In the measurements, $d=1$ m, $h=0.1$ m, and the semicylinder and wedge roughness axes were perpendicular to the source–receiver propagation path. Since the experimental procedure has been described in detail elsewhere,[2] only the results are reported here. Since the measured data and BEM predictions of excess attenuation spectra are rather sensitive to the roughness condition at the point of specular reflection between source and receiver, EA data and predictions have been averaged over several random distributions. This at-

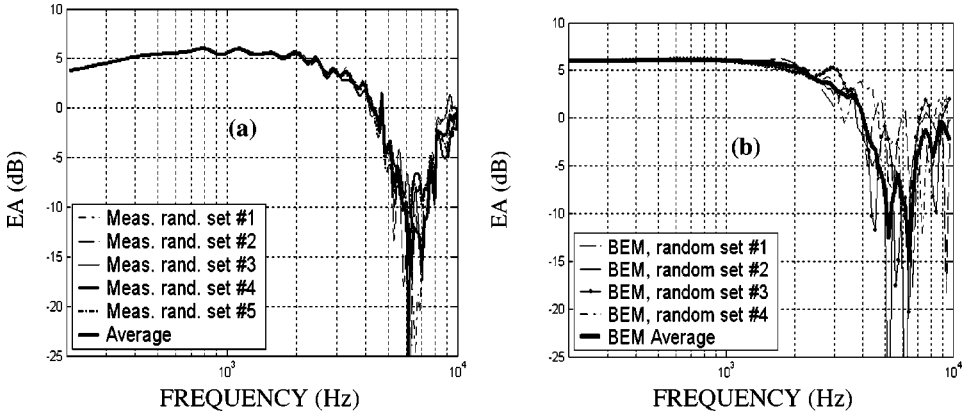

FIG. 2. Measured (a) and BEM-predicted (b) excess attenuation spectra above a surface containing small, identical semicylindrical roughness elements.

tempts to obtain an average result appropriate to particular random profiles. The averaging process can be justified further since, during the propagation of the boom over the sea, the roughness profile at the specular reflection point will vary with time and location.

A. Excess attenuation and effective impedance results for surfaces including small, hard, randomly spaced semicylinders

The averaged BEM-predicted excess attenuation spectrum above surfaces formed by 20 hard, randomly spaced semicylinders with $l=0.0135\,\mathrm{m}$ [Fig. 2(b)] compares favorably with averaged measured data [Fig. 2(a)]. It should be noted that these measured data are unreliable below 700 Hz as a result of the limited frequency response of the loudspeaker used in the measurements. Note also that the frequency of the threshold of reliability varies between experiments. When using BEM predictions and the nominal ground plane height, then, at some frequency points, the winding number integral method results in unphysical negative real impedance roots [of Eq. (7)]. Calculations reported elsewhere[14] suggest that the negative values of Re(Z) are due to the oscillations of the EA magnitude around 6 dB. Section VII investigates whether surface waves can explain instances of BEM-predicted EA>6dB. The results are improved when the effective impedance is computed with the effective height of the ground plane set to the top of the random roughness ($h_{\mathrm{eff}}=0.093\,\mathrm{m}$). Raising the effective impedance plane above the lowest point in the roughness profile has been suggested before.[15,16] Consequently a raised effective impedance plane has been employed when calculating effective impedance spectra from BEM predictions. In addition, any negative values of Re(Z) are set to zero. The latter step produces very little discrepancy between the nominal and deduced EA. The effective impedances deduced from measured data and BEM predictions are shown in Figs. 3(a) and (b), respectively. The predictions resulting from a five-parameter least-square fit with Lucas and Twersky's theory are compared also to

$$\mathrm{Re}(Z)=\alpha f^{-1}+\delta, \tag{12}$$

and

$$\mathrm{Im}(Z)=\alpha' f^{-1/2}+\delta', \tag{13}$$

respectively. These polynomial forms are chosen empirically, but they resemble the two-parameter model for the surface impedance of rigid porous ground in which the porosity decreases with depth.[17–19] However, in this ground impedance model, the real part is proportional to $1/\sqrt{f}$ and the imaginary part contains terms proportional to $1/\sqrt{f}$ and $1/f$. The forms of these polynomials ensure that the real part dominates at low frequency. This is consistent with the BEM results and expected from physical considerations. The effective impedance spectra obtained from measured data agree fairly well with the BEM results in the frequency range 700–7000 Hz for the real part and in the frequency range 2000–5000 Hz for the imaginary part. Note, however, that an unexpected resonance at 8000 Hz in the deduced impedance is obtained from measurements. Such high-frequency resonance is seen frequently in the impedance spectra deduced from measured complex EA for small roughness and in BEM predictions of

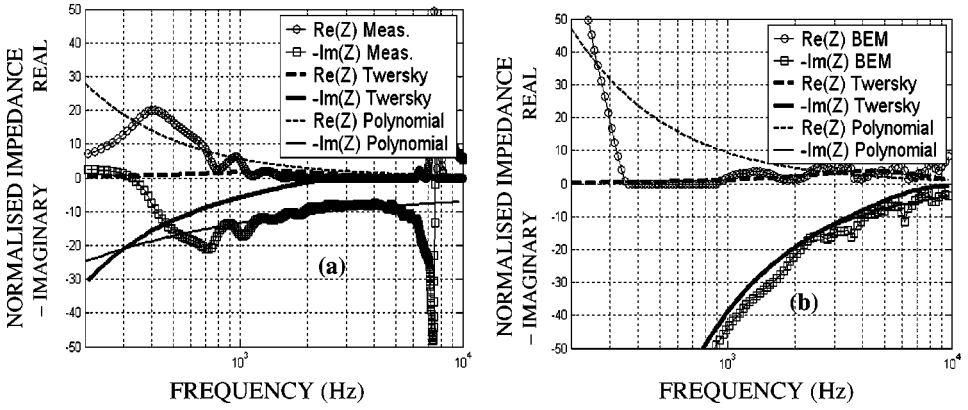

FIG. 3. Effective impedance from measured (a) and BEM-predicted (b) complex excess attenuation above small, identical semicylindrical roughness elements.

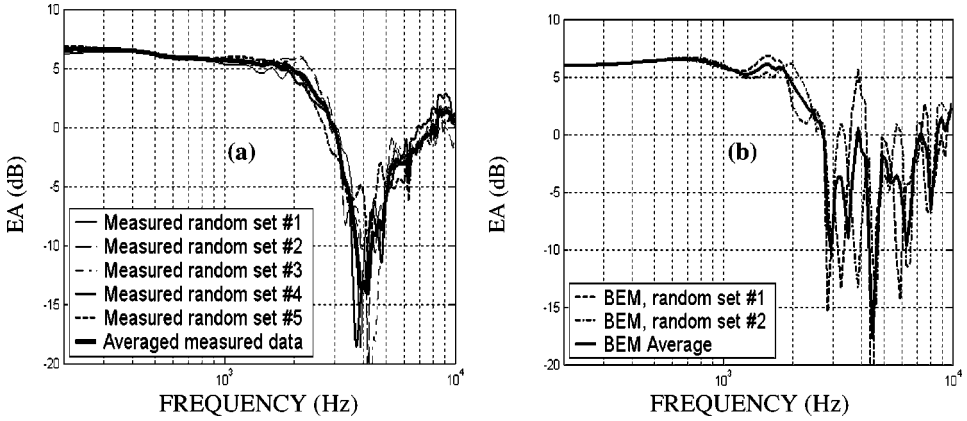

FIG. 4. Measured (a) and BEM-predicted (b) excess attenuation magnitude spectra above a surface containing identical wedge-shaped roughness elements.

the effective impedance for surfaces with parabolically shaped roughness, but their cause is unknown. In the BEM predictions, the magnitude of these resonances is found to depend on the location of the effective impedance plane. Additional measurements with larger semicylindrical roughness have been compared to theory and the results, not reported here, show greater discrepancies.

B. Excess attenuation and effective impedance results for triangular wedge roughness

Measurements and BEM predictions have been made for profiles formed by random distributions of 15 hard rods with identical triangular cross sections. The base and height of the triangle are 0.03 and 0.015 m, respectively. The averaged EA spectrum from the BEM predictions [Fig. 4(b)] compares favorably with averaged measured data [Fig. 4(a)]. It should be noted that the measured data are unreliable below 400 Hz. The effective impedance computed from the measured data and BEM EA predictions are shown in Figs. 5(a) and (b), respectively. The agreement between effective impedance obtained from measured and predicted data is good for frequencies in the range 400–6000 Hz. As mentioned in Sec. II B, using the Lucas and Twersky analytical results, the low-frequency predictions of the real part of effective impedance found for all roughness sizes considered tend toward zero, although increasing values are expected and predicted from the BEM simulations. Table I summarizes the parameter values obtained by fitting the Lucas and Twersky model to the BEM predictions and to the measured data for all of the roughness forms considered in Sec. IV. The polynomial fit coefficients obtained from the measurements and BEM predictions are summarized in Table II. The Lucas and Twersky theory is based on the approximation $ka<1$ that is valid for the small semicylindrical and wedge roughness for frequencies below 8000 and 5100 Hz, respectively. Despite being in the nominal frequency domain of validity, the low-frequency predictions of Lucas and Twersky's theory are poor. Consequently, only BEM calculations have been used to predict sound levels over profiles formed from intersecting parabolas and intended to represent the rough sea surface.

V. PARABOLIC ROUGHNESS RESULTS

Random intersecting parabolic profiles have been used to model acoustically hard, rough random surfaces corresponding to the various sea states. Parabolic wave crests are sharper and the wave troughs are flatter than in the usual sinusoidal profiles.[14] The height H and wavelength λ of the parabolic roughness are related by the ratio $H/\lambda=0.1$. This value is chosen to be below the value 0.14, beyond which the water waves break.[13] Random parabolic wave surfaces have been generated using a random number generator while constraining the height of the parabolas to within a chosen range. An example random-height parabolic roughness profile with wave heights in the range between 0.2 and 0.6 m is shown in Fig. 6. The source–receiver separation distance is 8 m in this example. The discretization step in the roughness

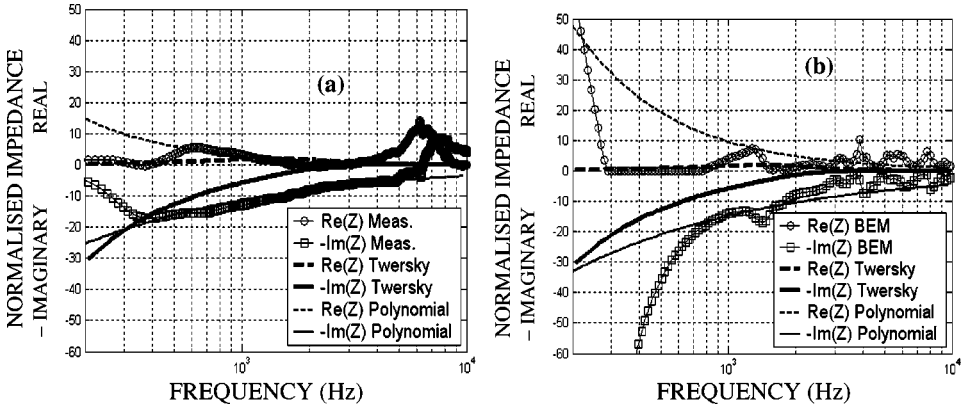

FIG. 5. Effective impedance from measured (a) and BEM-predicted (b) complex excess attenuation above identical wedge-shaped roughness elements.

TABLE I. Least-square fit parameters for Lucas and Twersky's effective impedance.

	n (1/m)	Ka (m)	a (m)	b^* (m)	h_s (m)
BEM small cyl.	5	0.071	0.005	0.202	0.1
Meas. small cyl.	3	0.137	0.005	0.336	0.1
BEM wedges	1	0.104	0.024	0.208	0.1
Meas. wedges	3	0.137	0.005	0.336	0.1

profile is chosen to be one-third of the smallest roughness wavelength (2 m), i.e., 0.66 m. The length of rough ground modeled is limited to 20 m to keep BEM run time for the whole spectrum under 20 min on a Pentium III 800-MHz processor. The rough surface is extended by 90 m of flat, hard surface on each side of source and receiver to avoid edge effects. This means that the total surface length modeled is 200 m.

It is necessary to consider the meaning of the ''angle of incidence'' θ on a randomly rough surface. It should be noted that the choice of horizontal plane from which the incident angle is evaluated is arbitrary as the surface is rough. The local angle of incidence depends on the point of the profile being considered. The reference plane from which the incidence angle is evaluated in this work is chosen as that at the average roughness height. For example, the incidence angle for the source height $h=0.93$ m, average roughness height $\langle H\rangle=0.25$ m, and propagation distance $d=8$ m is obtained using $\arctan(2(0.93-0.25)/8)=0.17$ rad (the factor 2 occurs because source and receiver have the same vertical heights above the horizontal). Excess attenuation spectra have been predicted using BEM for grazing incidence angles of 0.012, 0.04, 0.065, 0.17, and 0.23 radians, corresponding respectively to 0.7, 2, 4, 10, and 13 deg. Five example EA spectra obtained for roughness cusp heights randomly generated in the range 0.1 and 0.4 m, and their average at grazing incidence angle 0.012 radian ($h=0.3$ m) are presented in Fig. 7(a). The effective impedance spectrum [corresponding to the average EA in Fig. 7(a)] and the associated polynomial fit are shown in Fig. 7(b). Comprehensive details of EA, effective impedance spectra, and polynomial fit coefficients for all the roughness scales and geometries studied in this work are available elsewhere.[13,20] Only a few illustrations and the main results are presented here. The frequency range used for the polynomial impedance fit computation is shown in the legend of Fig. 7(b). The angle dependence of the fit coefficients α (or α') and δ (or δ') defined in Eqs. (12) and (13) are represented by circles and error bars in Figs. 8 and 9, respectively. The error bars indicate the inherent inaccuracies of the method (see Sec. VI C). The angle-dependent fit coefficients $\alpha(\theta)$, $\alpha'(\theta)$, $\delta(\theta)$, $\delta'(\theta)$, and their error bars have been fitted by eye using Gaussian curves (see Sec. VI). Figure 8 shows the example of a Gaussian fit with infinite semiwidth, indicating that the best fit is a horizontal straight line. The Gaussian-fitted impedance fit coefficients in cases of average roughness heights 0.25, 0.4, 0.6, 1.5, 3.5, and 7.5 m corresponding to sea states 2–7, respectively, have been computed and are discussed in the next section.

TABLE II. Coefficients of the polynomial fits to measured and BEM-predicted effective impedance spectra.

	$\mathrm{Re}(Z_m)$	$\mathrm{Im}(Z_m)$	$\mathrm{Re}(Z_{\mathrm{BE}})$	$\mathrm{Im}(Z_{\mathrm{BE}})$
$\alpha_{\text{small cyl.}}$	4620	291	9471	38276
$\delta_{\text{small cyl.}}$	0	4.2	0	0
α_{wedge}	2970	360	9610	467
δ_{wedge}	0	0	0	0

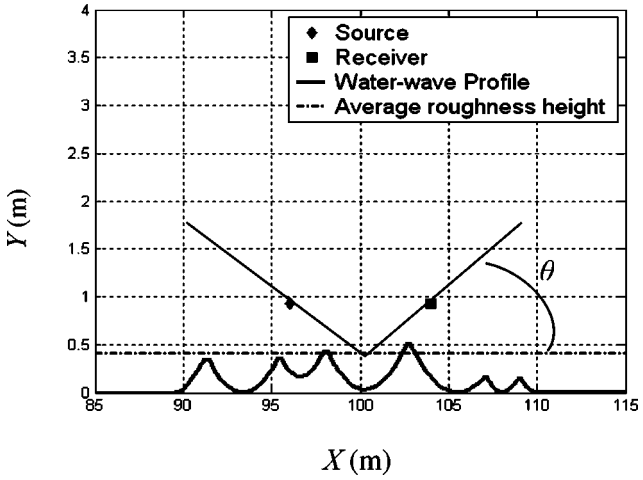

FIG. 6. Example of randomly rough parabolic surface model with cusp heights $0.2<H<0.6$ m.

VI. INTERPRETATION AND DISCUSSIONS

A. Dependence of fit coefficients on incidence angle at constant average roughness height

Five angle-dependent values have been obtained for each of the fit coefficients $\alpha(\theta)$, $\alpha'(\theta)$, $\delta(\theta)$, and $\delta'(\theta)$ [see Eqs. (12) and (13)]. To enable extrapolation of the fit coefficients to other grazing angles of incidence, in particular to grazing angles near to zero, fits have been attempted through the data points plus their error bars. Tolerable success is obtained with Gaussian curves of the type $\gamma+\gamma_m\exp[-\theta^2/\sigma]$, in which the parameters γ, γ_m, and σ are varied to obtain the best visual fit with the ''data'' points. The incidence angle and roughness size dependence of the best fit coefficients α, α', δ, and δ' are summarized in the 3D Figs. 10(a), 10(b), 11(a) and 11(b), respectively. These results show that $\alpha(\theta)$, $\alpha'(\theta)$, $\delta(\theta)$, and $\delta'(\theta)$ are either nearly constant or decrease with increasing incidence angle. It should be noted that the values of δ do not have as great an influence as values of α at low frequencies. These results are consistent with the expected decrease of the effective impedance (and hence of the coefficients) of a rough, hard surface with increasing grazing angle for a given average roughness height.

B. Dependence of fit coefficients on average roughness height at constant incidence angle

Figures 10(a) and (b) show that, for constant grazing incidence angles in the range between $\theta=0.17$ and 0.23 rad, the coefficients α and α' generally decrease with increasing average roughness height, while for lower grazing angles, between $\theta=0.02$ and 0.06 rad, the maximum values are found for roughness heights $\langle H\rangle=0.4$ m. As α (or α') gov-

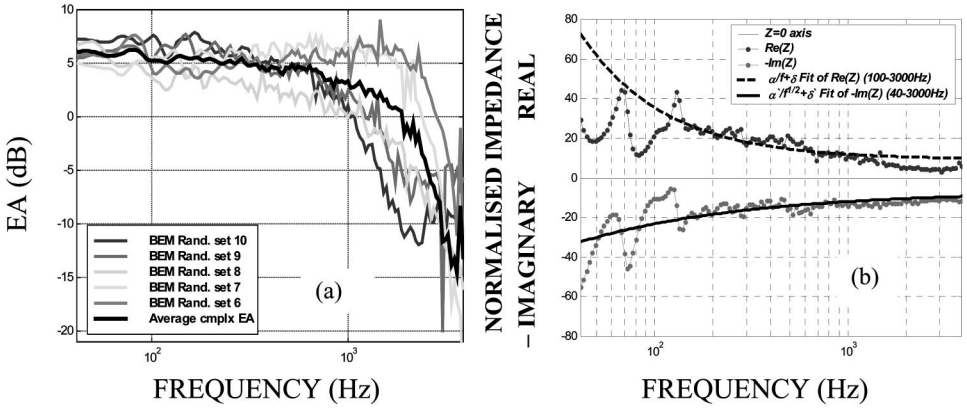

FIG. 7. (a) BEM-predicted excess attenuation spectra for a point source 0.3 m above the lowest points in five realizations of a 2D surface formed by intersecting parabolas with mean height 0.25 m and cusp heights between 0.1 and 0.4 m. This corresponds to a grazing angle of 0.012 rad with respect to the horizontal mean height plane. (b) Real and imaginary parts of the effective impedance spectrum deduced from the mean excess attenuation spectrum and corresponding polynomial fits.

erns the effective impedance at low frequency, it is expected that its values should be greater for small roughness heights as the wavelength is much greater than the roughness size, and therefore the surface is nearer a smooth, hard surface. When the roughness size increases and becomes comparable to the larger acoustic wavelengths (at low frequency), it is expected that the effect of the rough surface will be larger and depart most from that of a smooth, hard surface. In general, this is consistent with Figs. 10(a) and (b), where the coefficients α and α' are found to decrease with increasing roughness sizes except for the smallest roughness at the smallest grazing angles. The surface with mean roughness height 0.4 m appears harder at low frequency and at a grazing angle of 0.02 rad than that with mean roughness height of 0.25 m ($\alpha[0.4\text{ m}]>\alpha[0.25\text{ m}]$). There is no obvious explanation for this result.

The coefficients δ and δ', summarized in Figs. 11(a) and (b), respectively, show a tendency to decrease with increasing average roughness height at constant incidence angle. As δ and δ' dominate Eqs. (12) and (13), respectively, at high frequency, it can be concluded that the effectie impedance at high frequency decreases with increasing roughness heights. Note that the coefficients δ and δ' do not vary as monotonically as α and α' at constant incidence angle due to the increased uncertainty in the effective impedance fits (see Sec. VI C) created by the high-frequency resonance peaks in the deduced impedance spectra. Since the impedance is dominated by the α (or α'), small departures from monotonic trend in δ (or δ') are not particularly important except at very high frequencies.

Overall, the effective impedance fit coefficients vary monotonically with incidence angle and average roughness heights. The local nonmonotonic variations result from uncertainties in the fit coefficient values due to the method followed to estimate the effective impedance (see Sec. VI C). The local nonmonotonic coefficient variations with angle dependence at constant average roughness height have been removed by the use of the Gaussian best fits. However, local nonmonotonic variations with average roughness heights at constant incidence angle remain. Inaccuracies in the effective impedance coefficient values result from (a) the frequency range used for the fits and (b) the dependence on the five specific rough-surface realizations used for the BEM calculations. A brief analysis of these two factors is given in the next section.

C. Inaccuracies in estimating effective impedance fit coefficients

In principle, there would not need to be any freedom in the choice of frequency range if the effective impedance roots varied monotonically with frequency and displayed the expected decrease with increasing frequency. Unfortunately, the apparent high-frequency resonance-like peaks and the unphysical low-frequency behavior of the effective impedance spectra mean that this is not always the case. Therefore, the frequency range where the effective impedance roots are physically meaningful has to be selected. This choice introduces some uncertainty in the values of the coefficients, as it is difficult to estimate the point at which the effective impedance departs from the expected increase with decreasing frequency due to numerical artifacts. From the examples studied, the net effect is an uncertainty of the order of 25% in the value of α (or α') and 17% in the value of δ (or δ').

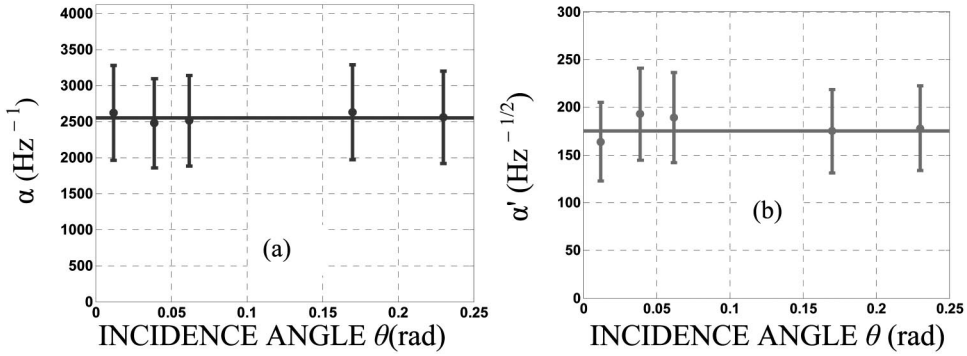

FIG. 8. Dependence of the coefficients α (a) and α' (b) on incidence angle for roughness mean height 0.25 m and cusp heights between 0.1 and 0.4 m. Continuous lines represent Gaussian curve fits to the respective angle dependence.

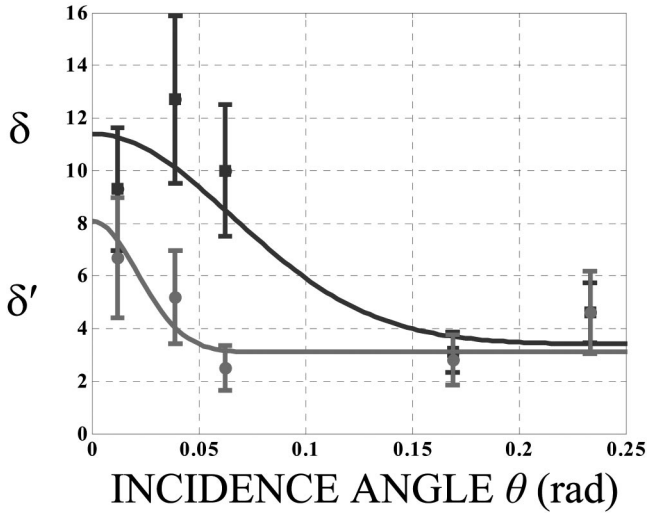

FIG. 9. Dependence of the coefficients δ (squares) and δ' (circles) on incidence angle for roughness mean height 0.25 m. Continuous lines represent Gaussian curve fits to the respective angle dependence.

The effective impedance results depend on the specific roughness profiles used, even though the impedance roots are determined from the complex pressure ratio averages over five profiles. Consequently, some inaccuracy in the best-fit coefficients is introduced by the choice of the five roughness profiles involved in the average. Based on the few examples studied, the net effect is an inaccuracy of the order of 25% in the value of α (or α') and 50% in the value of δ (or δ'). The combination of both sources of inaccuracies is estimated to give total inaccuracies on the order of 50% and 70% in α (or α') and δ (or δ'), respectively. These worst-case estimates are used to give the error bars shown in Figs. 8 and 9. Despite the errors, the polynomials offer a shortcut compared with making several BEM predictions for random or deterministic profiles and averaging them.

VII. THEORY FOR SURFACE WAVE AMPLITUDE AND COMPARISON WITH BEM RESULTS

In this section an approximate analytical prediction of surface wave magnitudes is compared with BEM predictions. Medwin and D'Spain[21] have argued that the otherwise unlimited increase in the boundary wave amplitude predicted by Tolstoy should be modified by attenuation. They have introduced the attenuation factor Λ, which is dominant at low frequency and short propagation range r, and the attenuation factor μ, which is dominant at high frequency and long range. By extending Tolstoy's results, they have suggested that the relative boundary wave amplitude above a rough surface is given by

$$P_B/P_D(r,k,H)=\epsilon(H)(2\pi r)^{1/2}k^{3/2} \times \exp\{-\Lambda(k,H)r-\mu(k,H)r^2\}, \quad (14)$$

where P_B is the amplitude of the cylindrically diverging boundary wave, P_D is the amplitude of the spherically diverging wave, ϵ is the scattering parameter, and r is the propagation range. The term $\epsilon(H)(2\pi r)^{1/2}k^{3/2}$ requires small spacing compared with wavelength, $kb<1$, and small roughness height compared with wavelength, $kH<1$. The scattering parameter can be expressed as $\epsilon=\tau([(1+\Delta)/\upsilon]-1)$, where Δ is the virtual mass coefficient of the scatterer, υ is the dipole interaction factor,[22] and $\tau=20\langle H\rangle^2N/3$ and N is the number of roughness elements per unit length. A 2D version of the attenuation factor Λ can be deduced from the expression given as Eq. (45) in Tolstoy[22]

$$\Lambda_{2D}=\frac{\langle\tau\rangle^3}{2N}\left\{\frac{1+\Delta}{\upsilon}-1\right\}\left[1+\frac{(1+\Delta)^2}{2}\right]k^5, \quad (15)$$

where $\langle\tau\rangle$ is the average area of random roughness elements per unit length. The value of the dipole interaction factor ν is close to 1 for the parabolic roughness. Using Tolstoy's[22] Eqs. (A4) and carrying out a numerical evaluation of his integral (A6), a value for the virtual mass coefficient $\Delta=0.116$ is obtained for the parabolic roughness of interest here. The BEM-predicted EA magnitudes at frequency 70 Hz for the lowest grazing angle are compared to the low-frequency approximate theory [Eq. (14) with $\mu=0$] for varying roughness height and for a given range. Using P_R to represent the amplitude of the reflected wave, this frequency is sufficiently low to insure the validity of the approximation $(P_R+P_D)/P_D=2$ such that EA magnitude$=20\log[2+P_B/P_D]$. The large spacing between parabolically shaped roughness elements ($b\sim20\langle H\rangle$), means that 70 Hz is significantly above the upper frequencies (11, 7, and 5 Hz) that satisfy $kb<1$ for average roughness heights $\langle H\rangle=0.25$, 0.4, and 0.6 m, respectively. However, it is below the upper frequencies (220, 140, and 90 Hz) for the validity of the approximation on roughness height ($kH<1$) for average roughness heights $\langle H\rangle=0.25$, 0.4, and 0.6 m, respectively. The BEM-predicted EA magnitudes, shown as circles, squares, and diamonds in Fig. 12 at 8-m range for average roughness heights $\langle H\rangle$

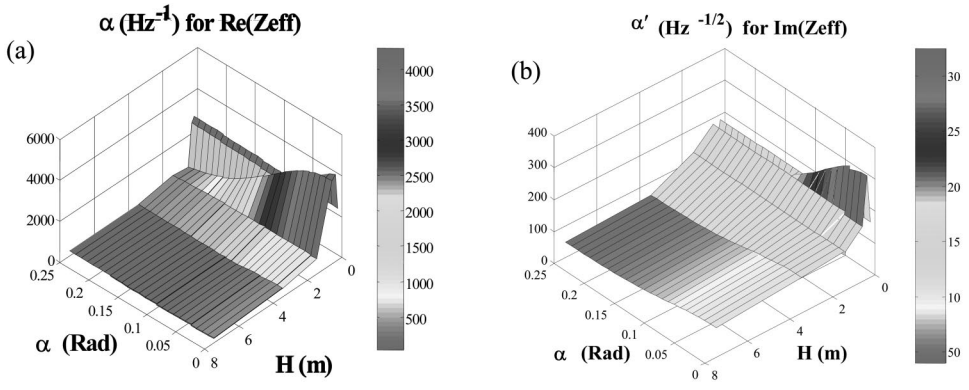

FIG. 10. Dependence of the coefficient α for $\mathrm{Re}(Z_{\mathrm{eff}})$ (a) and α' for $\mathrm{Im}(Z_{\mathrm{eff}})$ (b) on incidence angle and mean roughness height.

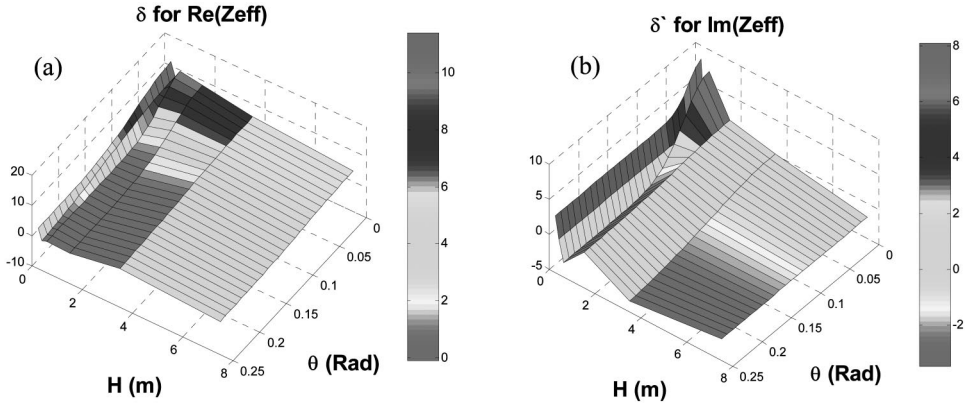

FIG. 11. Dependence of the coefficient δ for $\mathrm{Re}(Z_{\mathrm{eff}})$ (a) and δ' for $\mathrm{Im}(Z_{\mathrm{eff}})$ (b) on incidence angle and mean roughness height.

$=0.25$, 0.4, 0.6 m, respectively, compare favorably with the analytical theory (red line). The enhancement predicted by the analytical theory is at most 0.4 dB above the 6 dB that is expected when no surface wave is present, although the BEM predicts larger enhancements up to 2 dB. Therefore, the results obtained from analytical theory fit the BEM predictions no better than the 6-dB horizontal line. The approximate theory at 40 Hz for an 18-m range and 1.5-m average roughness height (dotted-dashed line) does not predict enhancement above 6 dB; this in agreement with the BEM predictions. Including the term $\exp\{-\mu(k,H)\mathrm{r}^2\}$ in Eq. (14) would not modify the results since, at the low frequency and propagation range studied, $\exp\{-\mu(k,H)\mathrm{r}^2\}\sim 1$. However, it should be noted that the approximate theory Eq. (14) considers source and receiver to be embedded in the rough surface. Despite the small grazing incidence angles (0.7 deg) studied with the parabolic roughness, this is not the case with the geometry assumed for the BEM predictions and may be a cause of the discrepancy in Fig. 12. Although small surface wave enhancements are predicted by the Tolstoy/Medwin approximate theory at the frequency and for the roughness heights studied, the results of the BEM-predicted EA magnitudes neither support nor contradict the hypothesis that the BEM-predicted enhancements over parabolically shaped roughness are due to surface waves.

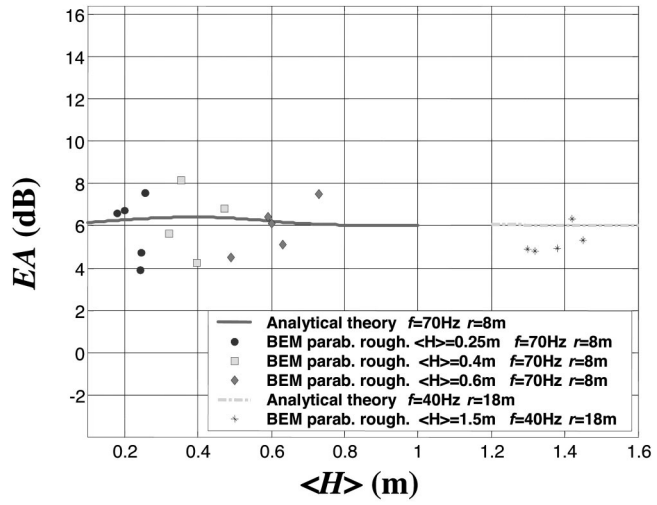

FIG. 12. EA predicted at 70 Hz by the BEM and the Medwin/Tolstoy theory at grazing angle and 8-m range for varying parabolically shaped roughness heights.

Nevertheless, there have been many laboratory measurements of surface waves over rough surfaces[19,23,24] and recent measurements of outdoor blast noise[25] propagation over a rough-sea surface show enhanced sound-pressure levels consistent with surface wave propagation at long range. These results, together with some of the numerical results in this paper, suggest that it might be necessary to consider the propagation of surface waves when studying grazing sound propagation over a sea surface.

VIII. PREDICTED ROUGH-SEA SURFACE EFFECT ON SONIC BOOMS

The effective impedance model for rough-sea surfaces has been used to estimate the effect of such surfaces on sonic boom propagation. Previous work[4] has shown that ground impedance has a strong effect on boom propagation at the so-called carpet cutoff where creeping sound waves are launched along the earth surface. Consequently, the effective impedance fit coefficients $(\alpha,\delta,\alpha',\delta')$ deduced from the Gaussian fit at zero incidence angle are used for a fixed sea-wave height. Sonic boom profiles have been predicted at the sea surface for a standard atmosphere (no wind, 15 °C at sea level, and a constant temperature gradient of -6.5 K/km up to 11 km).[26] The incident signal on the rough-sea surface has been assumed to be an ideal N wave with a total duration 0.27 s (typical for Concorde cruising at Mach 2) and a peak overpressure normalized to 1. The rise time is defined as the time interval required by the overpressure to increase from 10% to 90% of the peak overpressure. Figure 13 displays the computed pressure waveforms at the carpet cutoff for seven mean sea-wave heights ($\langle H\rangle$) in the range 0 to 7.5 m. For $\langle H\rangle=0$ m, corresponding to a smooth rigid surface, the model predicts an N-wave normalized peak overpressure of 1.4 as expected from diffraction theory. With the exception of the smallest height (0.25 m), Fig. 13 shows that increasing the mean sea-wave height decreases the peak overpressure and increases the rounding of the sonic boom wave profile, indicating increased wave absorption. The most significant effect is obtained for the rise time. The predicted values of 4–16 ms can be larger than those induced by molecular relaxation[27] or atmospheric turbulence.[28] This suggests that sonic boom predictions in coastal areas should take sea-roughness effects into account.

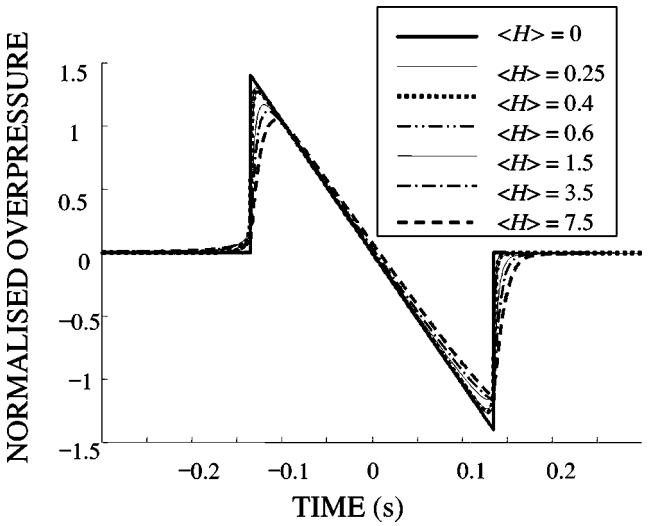

FIG. 13. Sonic boom profiles predicted for various mean sea-wave heights up to 7.5 m.

IX. CONCLUSIONS

Tolerable agreement has been found between measured data and BEM predictions of excess attenuation using averaged data sets, particularly in the case of wedge-shaped roughness. The effective impedance spectra of randomly rough surfaces have been deduced from complex excess attenuation obtained from either BEM predictions or measurements by finding the impedance roots of the classical expression for the total sound pressure due to a point source above an impedance plane. These effective impedance spectra can be used in the classical expression to reproduce the measured or BEM-predicted excess attenuation. The deduced impedance spectra are found to be very sensitive to the roughness profiles in the specular reflection area corresponding to the geometries used for the BEM calculations. Also, they show large fluctuations for relatively small (<1 dB) fluctuations in the excess attenuation magnitudes. The winding number integral method has been used to conclude that for some roughness profiles there are frequency ranges with only negative real effective impedance roots. As a consequence the complex excess attenuation has been calculated for several random distributions and averaged. Moreover, it is found for BEM simulations with semicylindrical and parabolically shaped roughness that the effective impedance plane has to be raised by between a fifth and the whole of the average roughness height depending on the average roughness height and the incident angle.

An analytical technique based on Lucas and Twersky boss theory has been used also to fit the effective impedance deduced from measurements and BEM predictions above small semicylindrical roughness. However, the asymptotic low-frequency dependence of Twersky's theory impedance for hard surfaces does not predict the large real values expected from physical considerations. An alternative boss theory models the effective admittance of a hard surface containing porous roughness and introduces an additional attenuation leading to the correct low-frequency dependence. This model will be investigated in further work.

Empirical polynomial fits of BEM-deduced impedance spectra have been derived for the effective impedance evaluations corresponding to roughness profiles formed by intersecting parabolas and intended to model sea waves. Values of the coefficients have been computed for six average roughness heights (sea states) and five angles of incidence. There are inaccuracies in the estimates of the effective impedance fit coefficients due to the particular choices of roughness profiles used for the BEM EA simulations and the particular choice of frequency ranges for the polynomial fits. The angle-dependent coefficients at constant roughness height and their error bars are fitted successfully with Gaussian curves and these allow extrapolation to lower angles of incidence. It may be concluded that the general trends for the effective impedance fit coefficients of hard, rough surfaces are consistent with the expected decrease in effective impedance with increasing grazing incidence angles (at constant roughness scale) and with increasing roughness scale (at constant incidence angle). The resulting effective impedance polynomials are convenient for implementation in sonic boom propagation codes. Preliminary predictions indicate that the effect of the sea-surface roughness on sonic boom profiles and rise time is comparable to that due to turbulence and molecular relaxation effects.

ACKNOWLEDGMENT

This investigation has been carried out under a contract awarded by the European Commission, ''Sonic Boom European Research Program: Numerical and Laboratory-Scale Experimental Simulation'' (SOBER), Contract Number G4RD-CT-2000-00398.

[1] K. Attenborough and S. Taherzadeh, ''Propagation from a point source over a rough finite impedance boundary,'' J. Acoust. Soc. Am. **98**(3), 1717–1722 (1995).
[2] P. Boulanger, K. Attenborough, S. Taherzadeh, T. Waters-Fuller, and K. M. Li, ''Ground effect over hard rough surfaces,'' J. Acoust. Soc. Am. **104**, 1474–1482 (1998).
[3] K. Attenborough and T. Waters-Fuller, ''Effective impedance of rough porous ground surfaces,'' J. Acoust. Soc. Am. **108**(3), 949–956 (2000).
[4] F. Coulouvrat, ''Sonic boom in the shadow zone: A geometrical theory of diffraction,'' J. Acoust. Soc. Am. **111**(2), 499–508 (2002).
[5] R. J. Lucas and V. Twersky, ''Coherent response to a point source irradiating a rough plane,'' J. Acoust. Soc. Am. **76**, 1847–1863 (1984).
[6] S. Taherzadeh and K. Attenborough, ''Deduction of ground impedance from measurements of excess attenuation spectra,'' J. Acoust. Soc. Am. **105**, 2039–2042 (1999).
[7] P. R. Brazier-Smith and J. F. M. Scott, ''On the determination of the roots of dispersion equations by use of winding number integrals,'' J. Sound Vib. **145**, 503–510 (1991).
[8] P. Boulanger, K. Attenborough, T. Waters-Fuller, and K. M. Li, ''Models and measurements of sound propagation from a point source over mixed impedance ground,'' J. Acoust. Soc. Am. **102**, 1432–1442 (1997).
[9] S. N. Chandler-Wilde and D. C. Hothersall, ''Efficient calculation of the green function for acoustic propagation above a homogeneous impedance plane,'' J. Sound Vib. **180**, 705–724 (1995).
[10] S. N. Chandler-Wilde and D. C. Hothersall, ''A uniformly valid far-field asymptotic expansion of the Green function for two-dimensional propagation above a homogeneous impedance plane,'' J. Sound Vib. **182**, 665–675 (1995).
[11] C. F. Chien and W. W. Soroka, ''Sound propagation along an impedance plane,'' J. Sound Vib. **43**(1), 9–20 (1975).
[12] IMSL Math Library User's Manual, Version 3.0, Visual Numerics, Inc., Houston, TX (1994).
[13] P. Boulanger and K. Attenborough, ''Effective Impedance of Rough Sea

Surfaces,'' D8 SOBER Report, Project No. GRD1-2000-25189 University of Hull (2002).
[14] M. Rousseau and F. Coulouvrat, ''Scattering of a high frequency acoustic wave by a sinusoidal swell: Asymptotic formulation, numerical simulation and fluid motion influence,'' Acustica **86**, 821–829 (2000).
[15] J. P. Chambers, J. M. Sabatier, and R. Raspet, ''Grazing incidence propagation over a soft rough surface,'' J. Acoust. Soc. Am. **102**, 55–59 (1997).
[16] J. F. Allard, L. Kelders, and W. Lauriks, ''Ultrasonic surface waves above a doubly periodic grating,'' J. Acoust. Soc. Am. **105**, 2528–2531 (1999).
[17] K. Attenborough, ''Acoustical impedance models for outdoor ground surfaces,'' J. Sound Vib. **99**(4), 521–544 (1985).
[18] K. Attenborough, ''Ground parameter information for propagation modeling,'' J. Acoust. Soc. Am. **92**, 418–427 (1992); see also R. Raspet and K. Attenborough, ''Erratum: 'Ground parameter information for propagation modeling,'' J. Acoust. Soc. Am. **92**, 3007 (1992).
[19] R. Raspet and J. M. Sabatier, ''The surface impedance of grounds with exponential porosity profiles,'' J. Acoust. Soc. Am. **99**(1), 147–152 (1996).
[20] P. Boulanger and K. Attenborough, ''Effective impedance of rough sea surfaces for varying incidence angle and roughness scale,'' Task3.4 SOBER Report, EC FP5 Project No. GRD1-2000-25189 University of Hull (2002).
[21] H. Medwin and G. D'Spain, ''Near-grazing, low-frequency propagation over randomly rough, rigid surfaces,'' J. Acoust. Soc. Am. **79**(3), 657–665 (1986).
[22] I. Tolstoy, ''Smooth boundary conditions, coherent low-frequency scatter, and boundary modes,'' J. Acoust. Soc. Am. **75**(1), 1–22 (1984).
[23] H. Medwin, G. L. D'Spain, E. Childs, and S. J. Hollis, ''Low frequency grazing propagation over periodic steep-sloped rigid roughness elements,'' J. Acoust. Soc. Am. **76**(6), 1774–1790 (1984).
[24] H. Medwin, J. Baillie, J. Bremhorst, B. J. Savage, and I. Tolstoy, ''The scattered acoustic boundary wave generated by grazing incidence at a slightly rough rigid surface,'' J. Acoust. Soc. Am. **66**(4), 1131–1134 (1979).
[25] D. J. James and G. Kerry, ''The Propagation of Blast Noise Across Acoustically Hard Surfaces,'' Proceedings of Internoise 2000.
[26] Airbus France SA (AM-B), Final Technical Report on Project No. GRD1-2000-25189 SOBER (2004).
[27] F. Coulouvrat and T. Auger, ''Influence of molecular relaxation on the rise time of sonic booms,'' Proceedings of the 7th International Symposium on Long Range Sound Propagation, Ecole Centrale de Lyon, 25–26 July (1996), 177–191.
[28] P. Boulanger, R. Raspet, and H. Bass, ''Sonic boom propagation through a realistic turbulent atmosphere,'' J. Acoust. Soc. Am. **98**, 3412–3417 (1995).

The effect of a periodic absorptive strip arrangement on an interior sound field in a room

Joo-Bae Park
Center for Noise and Vibration Control (NOVIC), Department of Mechanical Engineering, Korea Advanced Institute of Science and Technology (KAIST), Science Town, Daejon-shi, 305-701, South Korea

Karl Grosh
Mechanical Engineering and Applied Mechanics, University of Michigan, 2250 G. G. Brown Building, 2350 Hayward Street, Ann Arbor, Michigan 48109-2125

Yang-Hann Kim[a)]
Center for Noise and Vibration Control (NOVIC), Department of Mechanical Vibration, Korea Advanced Institute of Science and Technology (KAIST), Science Town, Daejon-shi, 305-701, South Korea

(Received 10 December 2002; accepted 26 October 2004)

In this paper we study the effect of periodically arranged sound absorptive strips on the mean acoustic potential energy density distribution of a room. The strips are assumed to be attached on the room's surface of interest. In order to determine their effect, the mean acoustic potential energy density variation is evaluated as the function of a ratio of the strip's arrangement period to wavelength. The evaluation demonstrates that the mean acoustic potential energy density tends to converge. In addition, a comparison with a case in which absorptive materials completely cover the selected absorptive plane shows that a periodic arrangement that uses only half of the absorptive material can be more efficient than a total covering, unless the frequency of interest does not coincide with the room's resonant frequencies. Consequently, the results prove that the ratio of the arrangement period to the wavelength plays an important role in the effectiveness of a periodic absorptive strip arrangement to minimize a room's mean acoustic potential energy density. © *2005 Acoustical Society of America.* [DOI: 10.1121/1.1852547]

PACS numbers: 43.55.Dt, 43.55.Ka [MK] Pages: 763–770

I. INTRODUCTION

Much research has been performed regarding how the size and arrangement of absorptive materials affect sound absorption. Parkinson[1] measured the absorption coefficients of absorptive materials in different patterns and different arrangements. His experiments showed that there is a maximum effective spacing that depends on a wavelength; longer waves appear to have a wider spatial influence. He explained that this is mainly because of diffraction. Sabine[2] also noticed this diffraction effect. He noted that there is some discrepancy between what is predicted based on reverberation assumptions and what is actually measured, and showed that a localized absorption often produces this discrepancy due to diffraction. Chrisler[3] experimentally studied the effect of the size of the sample on the absorption coefficient measurement. His experiments show that the measured absorption coefficient of a small sample is greater than the coefficient of a large sample, and the measured absorption coefficient converges as the sample size increases. Ramer[4] experimentally studied the effect of varying the width of an absorbing strip and the effect of its location in a reverberation chamber. He concluded that the narrower the strip, the greater the absorption coefficient. Harris[5] reported that absorption characteristics vary, depending on where absorptive patches are placed. He experimentally showed that absorption is greatest if the patches are placed where the pressure is greatest. Investigations on sound absorption by patches (or strips) conducted by Pellam,[6] Levitas and Lax,[7] Cook,[8] and Northwood, Geisaru, and Medcof[9] had similar conclusions. These studies showed analytically that as the absorption coefficient increases, the absorptive patch (or strip) is made smaller. Daniel[10] experimentally showed that not only does absorption increase proportional to the size of the absorptive material, but also that its edges tend to be longer. Mechel[11,12] used an iterative method and variational formulation[7,13] to construct two approximate solutions to evaluate absorption for finite-sized absorbers. With the approximate solutions, he built expressions for the radiation impedance of the absorbing strip and rectangles. Thomasson[14] derived a general statement about the absorption of a locally reacting patch with an arbitrary shape. He evaluated the pressure on the absorber by using the variational principle, and then constructed a new statistical absorption coefficient of which the magnitude is always less than 1. The absorption coefficient, instead of using incident power related to the infinite absorber, is defined as the ratio between absorbed and available power.

Especially important to this research are the studies by Bruijn,[15,16] Takahashi,[17] and Mechel[18] that investigated the effect of periodically arranged absorptive materials on sound reduction and analytically evaluated excess absorption properties by considering both a periodically absorbing uneven surface and a flat surface. Takahashi's experimental result

[a)]All correspondences must be sent to Yang-Hann Kim (yanghannkim@kaist.ac.kr)

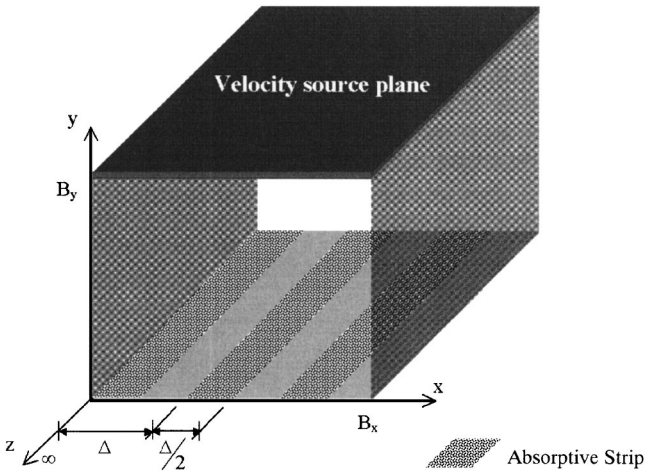

FIG. 1. A parallelepiped enclosure of an infinite length in the z direction. On the plane at $y=0$, absorptive strips of infinite length and width $\Delta/2$ are arranged periodically. The arrangement period is defined as Δ.

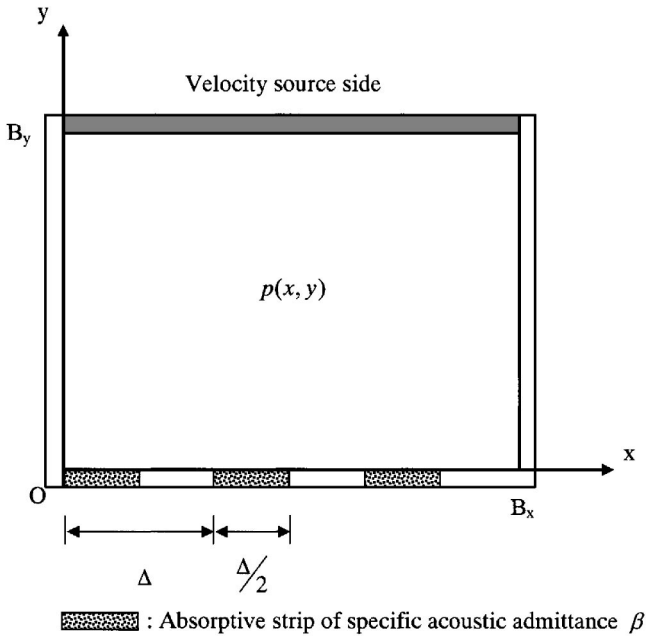

FIG. 2. Cross sectional view of Fig. 1. The source side at $y=B_y$ vibrates in the velocity of $u_y=f(x)e^{j\omega t}$. In this case, there are three absorptive strips on the absorptive plane at $y=0$.

complemented analytical evaluations for the periodic absorber on the flat surface. Mechel,[18] by introducing Hartree harmonics to distinguish the scattered field from the periodic absorbers, evaluated the absorption, the reflection coefficient, the directivity and field pressure patterns of various surfaces, such as plates with periodic grooves filled with absorber material, empty grooves with an absorbing ground, and perforated covers on porous absorbers. In these studies, Bruijn, Takahashi, and Mechel[18] assume that the extensions of the absorbers are infinite. Holmberg, Hammer, and Nilsson[19] used a variational formulation to evaluate the combined absorption characteristics of a finite-size absorber of arbitrary shape with subareas that are arranged in a specific pattern. As a result, in their study, separating the subareas increases the statistical absorption coefficient, which is a function of both the surface impedance of the absorbers and the radiation impedance. They verified their evaluation by a comparison with the measurement result.

These previous researches mainly studied how the absorption of a surface varies due to the shape and arrangement of the absorptive material. However, they did yet explore to understand how the arrangement affects the acoustic potential energy density of an enclosure. In this paper we seek to address this important practical consideration. This study's theoretical result indicates how the sound absorptive material can best be arranged to obtain the desired acoustic potential energy reduction.

II. PROBLEM STATEMENT

The objective of this study is to investigate the effect of periodic absorptive strip arrangement on an interior sound field. Periodic absorptive strip arrangement on a wall is depicted in Fig. 1. Mathematically, this means that we have to solve a mixed boundary value problem.[20] The analytic solution for a general sound field, which has a mixed boundary condition, cannot be obtained easily. It is significant that our aim is to see the effect of the absorptive strip arrangement on an acoustic potential energy density, not to find a general three-dimensional solution that describes details of the interior sound field. So, we attempt to use a two-dimensional analytic solution for studying the relation. Figure 1 shows a parallelepiped enclosure where absorptive strips, with a specific acoustic admittance β of 1, are arranged periodically on the rigid plane at $y=0$. This specific acoustic admittance β is defined as the ratio of the normal particle velocity to the sound pressure on the absorptive material, times ρc, where ρ is the density and c is the speed of sound. The plane at $y=B_y$ vibrates harmonically in a prescribed manner. The other two vertical planes at $x=0$, B_x are assumed to be rigid. The parallelepiped enclosure's z-directional length is assumed to be infinite so that the interior sound field does not vary in the z direction. Accordingly, the interior sound field can be considered to be two-dimensional, as depicted in Fig. 2.

Figure 2 shows a two-dimensional rectangular enclosure; there are two rigid sides at $x=0$, B_x: a source side at $y=B_y$, and an absorptive side at $y=0$. The arrangement period Δ can be written as

$$\Delta=\frac{B_x}{L}, \tag{1}$$

where L is the total number of absorptive material strips. Consequently, L is always an integer variable. The width of the absorptive strip is assumed to be $\Delta/2$. Therefore, regardless of L, the following relation always holds:

$$\frac{total\ \ width\ \ of\ \ absorptive\ \ strip}{B_x}=\frac{1}{2}. \tag{2}$$

It is noteworthy that the constraint of Eq. (2) essentially preserves the total absorptive material usage, regardless of period changes in the absorptive strip's arrangement. This enables us to observe the acoustic potential energy density variation due to the Δ change.

Then let us define dimensionless variables as $\tilde{\rho}=\rho/\rho_0$, $\tilde{c}=c/c_0$, $\tilde{p}=p/\rho_0 c_0^2$, $\tilde{x}=x/\lambda$, $\tilde{y}=y/\lambda$, $\tilde{B}_x=B_x/\lambda$, $\tilde{B}_y=B_y/\lambda$, $\tilde{k}=k\cdot\lambda$ (i.e., $\tilde{k}=2\pi$), and $\tilde{\Delta}=\Delta/\lambda$, where c_0 and ρ_0 are phase speed and density of air, respectively. Here, c and ρ are phase speed and density of air so that $\tilde{\rho}=1$ and $\tilde{c}=1$. In order to verify the effect of the wavelength on a sound field with a periodic absorptive strip arrangement, the wavelength λ scales every length variable, such as coordinates and wave number.

Substituting these dimensionless variables into the Helmholtz equation and boundary conditions yield

$$\left(\frac{\partial^2}{\partial\tilde{x}^2}+\frac{\partial^2}{\partial\tilde{y}^2}+\tilde{k}^2\right)\tilde{p}(\tilde{x},\tilde{y})=0, \tag{3}$$

$$\frac{\partial\tilde{p}}{\partial\tilde{x}}=0, \quad \text{at } \tilde{x}=0, \tag{4}$$

$$\frac{\partial\tilde{p}}{\partial\tilde{x}}=0, \quad \text{at } \tilde{x}=\tilde{B}_x, \tag{5}$$

$$\frac{\partial\tilde{p}}{\partial\tilde{y}}=\tilde{g}(\tilde{x}), \quad \text{at } \tilde{y}=0, \tag{6a}$$

where

$$\tilde{g}(\tilde{x})=\begin{cases} j2\pi\beta\tilde{p}, & l\tilde{\Delta}<\tilde{x}\leqslant(l+0.5)\tilde{\Delta},\ l=0,1,2,...,L, \\ 0, & (l+0.5)\tilde{\Delta}<\tilde{x}\leqslant(l+1)\tilde{\Delta},\ l=0,1,2,...,L, \end{cases} \tag{6b}$$

$$\frac{\partial\tilde{p}}{\partial\tilde{y}}=-j2\pi\tilde{\rho}\tilde{c}\cdot\tilde{f}(\tilde{x}), \quad \text{at } \tilde{y}=\tilde{B}_y, \tag{7}$$

where the function $\tilde{f}(\tilde{x})$ expresses the dimensionless velocity that is defined as $\tilde{f}(\tilde{x})=f(\tilde{x})/c_0$. The function $\tilde{g}(\tilde{x})$ describes the periodic absorptive strip arrangement on the rigid side at $y=0$. These dimensionless forms of the governing equation and boundary conditions completely describe the problem we want to study. The next step is to solve this mathematical problem and obtain useful information that can provide us with guidelines for obtaining the desired acoustic energy reduction by using a periodic sound absorptive strip arrangement.

III. SOLUTION METHOD

A solution that completely describes the enclosure's interior sound field can be obtained by summing the modal functions that satisfy the prescribed boundary conditions. It is, however, essential to first get the modal functions. For example, a mixed boundary condition, which is illustrated in Fig. 1, makes it difficult to find normal modes in the y direction. In the following section we explain how to get an approximate solution that meets our objectives.

A. Truncated approximate solution

First, we apply the method of separation of variable to Eq. (3). This gives the following general solution:

$$\tilde{p}(\tilde{x},\tilde{y})=(Ce^{-j\tilde{k}_x\tilde{x}}+De^{j\tilde{k}_x\tilde{x}})(Ee^{-j\tilde{k}_y\tilde{y}}+Fe^{j\tilde{k}_y\tilde{y}}), \tag{8}$$

where C, D, E, F are arbitrary constants. The propagation constants $\tilde{k}_x$ and $\tilde{k}_y$ satisfy the following relation:

$$\tilde{k}_x^2+\tilde{k}_y^2=\tilde{k}^2, \tag{9}$$

where the dimensionless wave number is $\tilde{k}=2\pi$.

The homogeneous Neumann boundary condition, on the sides of $x=0$ and $x=B_x$, determines the eigenvalue and eigenfunctions in the x direction; substituting Eq. (8) for $\tilde{p}$ in Eqs. (4) and (5) gives the following eigenvalues:

$$\tilde{k}_{xn}=\frac{n\pi}{\tilde{B}_x}, \quad n=0,1,2,.... \tag{10}$$

The corresponding eigenfunctions are

$$\phi_n(\tilde{x})=\epsilon_n\cos(\tilde{k}_{xn}\tilde{x}), \quad n=0,1,2,..., \tag{11a}$$

where

$$\epsilon_n=\begin{cases} 1, & n=0, \\ \sqrt{2}, & n=1,2,3,.... \end{cases} \tag{11b}$$

Therefore, the general solution (8) can be rewritten as

$$\tilde{p}(\tilde{x},\tilde{y})=\sum_{n=0}^{\infty}\phi_n(x)(E_ne^{-j\tilde{k}_{yn}\tilde{y}}+F_ne^{j\tilde{k}_{yn}\tilde{y}}), \tag{12a}$$

where

$$\tilde{k}_{xn}^2+\tilde{k}_{yn}^2=(2\pi)^2. \tag{12b}$$

Because $\tilde{p}(\tilde{x},\tilde{y})$, given by Eq. (12), always satisfies the governing equation (3) and the rigid boundary conditions at $\tilde{x}=0$ and $\tilde{x}=\tilde{B}_x$, all that remains is to find the unknown coefficients E_n and F_n that satisfy the boundary conditions $\tilde{y}=0$ and $\tilde{y}=\tilde{B}_y$, respectively. It is noteworthy that we have to somehow limit our summation of Eq. (12) to a finite number N. This can be simply done by limiting the sum until it converges; in other words, when E_n and F_n tend to zero as n goes to $N-1$. Therefore, Eq. (6) can be rewritten as

$$\sum_{n=0}^{N-1}\phi_n(\tilde{x})[j\tilde{k}_{yn}(-E_n+F_n)]=\tilde{g}(\tilde{x}). \tag{13}$$

Here $\tilde{g}(x)$ [Eq. (6b)] has to be rewritten as

$$\tilde{g}(\tilde{x})=\begin{cases} j2\pi\beta\sum_{n=0}^{N-1}\phi_n(\tilde{x})(E_n+F_n), & l\tilde{\Delta}<\tilde{x}\leqslant(l+0.5)\tilde{\Delta},\ l=0,1,2,...,L, \\ 0, & (l+0.5)\tilde{\Delta}<\tilde{x}\leqslant(l+1)\tilde{\Delta},\ l=0,1,2,\ldots,L. \end{cases} \tag{14}$$

Also, substituting the finite form of Eq. (12) to another boundary condition, Eq. (7), yields

$$\sum_{n=0}^{N-1}\phi_n(\tilde{x})[j\tilde{k}_{yn}(-E_n e^{-j\tilde{k}_{yn}\tilde{B}_y}+F_n e^{j\tilde{k}_{yn}\tilde{B}_y})] = -j2\pi\tilde{\rho}\tilde{c}\cdot\tilde{f}(\tilde{x}). \tag{15}$$

It is also noteworthy that the $\phi_n(\tilde{x})$ and $\tilde{f}(\tilde{x})$ in Eqs. (13) and (15) are prescribed; therefore, we have $2N$ number of unknowns E_n and F_n. Henceforth, $2N$ number of linear algebraic equations are required to determine unknown coefficients E_n and F_n. Applying the method of weighted residual[21] to Eqs. (13) and (15) provides the set of $2N$ linear algebraic equations. If the approximate solution (a finite sum instead of an infinite sum) exactly satisfies the boundary condition at $\tilde{y}=0$ and $\tilde{y}=\tilde{B}_y$, then Eqs. (13) and (15) can be rewritten as

$$\int_0^{\tilde{B}_x}\left(\sum_{n=0}^{N-1}\phi_n(\tilde{x})[j\tilde{k}_{yn}(-E_n+F_n)]-\tilde{g}(\tilde{x})\right)w_i(\tilde{x})d\tilde{x}=0, \tag{16}$$

$$\int_0^{\tilde{B}_x}\left(\sum_{n=0}^{N-1}\phi_n(\tilde{x})[j\tilde{k}_{yn}(-E_n e^{-j\tilde{k}_{yn}\tilde{B}_y}+F_n e^{j\tilde{k}_{yn}\tilde{B}_y})] + j2\pi\tilde{\rho}\tilde{c}\cdot\tilde{f}(\tilde{x})\right)h_i(\tilde{x})d\tilde{x}=0, \tag{17}$$

where $w_i(\tilde{x})$ and $h_i(\tilde{x})$ are the weight functions that are defined in the range of $0\leqslant\tilde{x}\leqslant\tilde{B}_x$. It is noteworthy that Eq. (16) essentially has $2L$ different integral intervals due to the periodic absorptive strip arrangement. Therefore, if we apply the weighting function $w_i(\tilde{x})$ into Eq. (16), then we have $2L$ linear algebraic equations. Those weighting functions, which are linearly independent, can be defined as

$$w_i(\tilde{x})=\sin\left(\frac{2(i+1)\pi}{\Delta}\tilde{x}\right),\quad i=0,1,2,\cdots\left(\frac{N}{2L}-1\right), \tag{18}$$

$$h_i(\tilde{x})=\epsilon_i\cos(\tilde{k}_{xi}\tilde{x}),\quad i=0,1,2,...(N-1), \tag{19}$$

where ϵ_i is the same as that used in Eq. (11b). In order to use the orthogonal property of the eigenfunction when we calculate Eq. (17), $h_i(\tilde{x})$ is written in the same form of eigenfunction $\phi_n(\tilde{x})$. Finally, solving the set of $2N$ linear algebraic equations gives E_n and F_n, which make the approximate solution satisfy the boundary conditions at $\tilde{y}=0$ and $\tilde{y}=\tilde{B}_y$.

B. Accuracy of the approximate solution

The approximate solution, which is a truncated form of Eq. (12), has an error because it does not exactly satisfy the boundary conditions [Eqs. (13) and (15)]. Equation (15), which expresses the boundary condition at $\tilde{y}=\tilde{B}_y$, essentially decomposes $\tilde{f}(\tilde{x})$ in terms of eigenfunctions $\{\phi_n(\tilde{x})\}_{n=0}^{N-1}$. Therefore, if we select the function $\tilde{f}(\tilde{x})$ as a combination of eigenfunctions $\{\phi_n(\tilde{x})\}_{n=0}^{N-1}$, then it satisfies the boundary condition at $\tilde{y}=\tilde{B}_y$ and we have an error only on the absorptive side at $\tilde{y}=0$. This error determines the solution's accuracy.

The error is defined in two different ways. One definition evaluates the relative error due to the admittance discrepancy. That is,

$$\bar{\beta}_{\text{error}}=\frac{1}{0.5\tilde{B}_x|\beta_{in}|}\sum_{l=0}^{L-1}\int_{l\tilde{\Delta}}^{(l+0.5)\tilde{\Delta}}|\beta(\tilde{x})-\beta_{in}|d\tilde{x}, \tag{20}$$

where β_{in} is the given constant admittance and $\beta(\tilde{x})$ is the admittance reconstructed based on the approximate solution. Therefore, $\bar{\beta}_{\text{error}}$ refers to how well the approximate solution, compared to β_{in}, satisfies the boundary condition on the absorptive strip. It is important that Eq. (20) is applied only to surfaces where absorptive strips are attached.

The other definition is for the error where no absorptive strips are arranged. That is,

$$\bar{R}_{\text{error}}=\frac{1}{0.5\tilde{B}_x|\tilde{U}_0|}\sum_{l=0}^{L-1}\int_{(l+0.5)\tilde{\Delta}}^{(l+1)\tilde{\Delta}}|\tilde{u}_y(\tilde{x})|d\tilde{x}, \tag{21}$$

where $\tilde{U}_0$ is the given dimensionless source velocity magnitude [i.e. $|\tilde{f}(\tilde{x})|$] and $\tilde{u}_y(\tilde{x})$ is the reconstructed dimensionless y-direction velocity on the rigid wall. Therefore, $\bar{R}_{\text{error}}$ refers to how well the approximate solution, compared to the source velocity magnitude $|\tilde{U}_0|$, satisfies the rigid wall condition between absorptive strips. These two measures of error essentially evaluate the performances of the truncated approximate solutions in two ways: one has to do with admittance and the other is related to the rigid boundary condition.

We now have a solution method and measures that evaluate how well the solution method works for the nondimensional mixed boundary value problem. Therefore, the next step is to find practical guidelines for quieting an enclosure using the periodic absorptive strip arrangement.

IV. DIMENSIONLESS PARAMETER STUDY

In order to determine the effect of a periodic absorptive strip arrangement, the dimensionless mean acoustic potential energy density of the entire cross section, which is illustrated in Fig. 2, is evaluated while changing the absorptive strip's arrangement period but while preserving the constraint of Eq. (2). As explained, the constraint of Eq. (2) means that the total area of the absorptive material is fixed as a constant.

In order to investigate the effect of the cross sectional shape, the side length ratio $\delta(=B_y/B_x)$ is introduced. Then,

for δ=0.01, 0.1, 1, 10, and 100 the effect of the arrangement period change is investigated for each. The area of the cross section, for each δ, is considered to be $1 \leqslant \tilde{A} \leqslant 100$, where $\tilde{A}=\tilde{B}_x\tilde{B}_y$. Consequently, $\tilde{A}$ means the dimensionless area that is normalized by λ^2. It is also noteworthy that the length ratio δ can be any positive value for the same area $\tilde{A}$. The total number of the basis functions of Eq. (12) is selected in such a way as to make the solution sufficiently accurate and considers computational capability, namely, $N=800$. The source side velocity $\tilde{f}(\tilde{x})$, to make a numerical evaluation simple, is defined as a constant (i.e, $\tilde{f}(\tilde{x})=0.001$). There can be many possible choices for selecting the admittance of the absorptive material. However, the specific acoustic admittance of the absorptive strip is defined as $\beta=1$ (i.e., as an impedance matching boundary condition). This choice maximizes the absorption difference between the absorptive strip and the rigid wall so that we can clearly observe the effect of the periodic arrangement.

A. Cost function and parameters

The cost function, which depends on the absorptive material arrangement change, is defined as the dimensionless mean acoustic potential energy density $\tilde{e}_p$. Specifically, the cost function $\tilde{e}_p$ of an entire rectangular cross section with a normalized area of $\tilde{A}$, using the truncated approximate solution of Eq. (12), can be defined as

$$\begin{aligned}\tilde{e}_p &= \frac{1}{4\tilde{A}\tilde{\rho}\tilde{c}^2}\int_0^{\tilde{B}_y}\int_0^{\tilde{B}_x}|\tilde{p}(\tilde{x},\tilde{y})|^2 d\tilde{x}\,d\tilde{y} \\ &= \frac{1}{4\tilde{A}\tilde{\rho}\tilde{c}^2}\sum_{n=0}^{N-1}\left[\tilde{B}_y(|E_n|^2+|F_n|^2)\right. \\ &\quad \left. +2\int_0^{\tilde{B}_y}\mathrm{Re}(E_n^* F_n e^{j2\tilde{k}_{yn}\tilde{y}})d\tilde{y}\right], \end{aligned} \tag{22}$$

where* is the complex conjugate. This means that the total dimensionless acoustic potential energy is divided by the dimensionless area: an average acoustic potential density in the rectangular cross section.

The parameters are a dimensionless variable $\tilde{A}$ that refers to a normalized room volume of a unit length in the z direction, and a dimensionless integer variable $L(=B_x/\Delta)$ that refers to the number of absorptive strips on the absorptive side at $\tilde{y}=0$. The larger L is, for a constant B_x, the smaller is the absorptive strip's arrangement period Δ. It is significant that a noninteger L violates the constraint of Eq. (2). On the contrary, integer values of L mean that the total usage of absorptive materials is always half of an absorptive area defined at $y=0$, independent of the arrangement period Δ change.

B. Results and discussion

Figures 3, 4, 5, 6, and 7 show the cost function $\tilde{e}_p$ variation for δ=0.01, 0.1, 1, 10, and 100, respectively. Here, the periodic arrangement change is represented by L, i.e., by the number of absorptive strips on $y=0$. In Figs. 3–7, the normalized acoustic potential energy density level E_L is defined as

$$E_L = 10\log_{10}\left(\frac{\tilde{e}_p}{\tilde{e}_{po}}\right), \tag{23}$$

where $\tilde{e}_{po}$ means $\tilde{e}_p$ when the absorptive material totally covers the plane at $y=0$. Therefore, in the case of $\tilde{e}_{po}$, the total absorptive material usage is double that of the periodic arrangement. Due to the constraint of Eq. (2), regardless of the period change, the periodic arrangement covers only half of the plane at $y=0$. In order to determine the efficiency of the periodic arrangement with respect to an extreme case, the acoustic potential energy density is normalized by $\tilde{e}_{po}$. Also, there are additional contour lines of $E_L=0$ in Figs. 3–7, which make it easy to find where the region has $\tilde{e}_p$ that is smaller than $\tilde{e}_{po}$.

Figure 3 shows the case of δ=0.01, in which E_L variation is a function of $\tilde{A}$ and L ($1 \leqslant \tilde{A} \leqslant 100$ and $1 \leqslant L \leqslant 20$). In Fig. 3(b), zero level contour lines divide the result into two regions: the darker region of $E_L>0$ and the brighter region

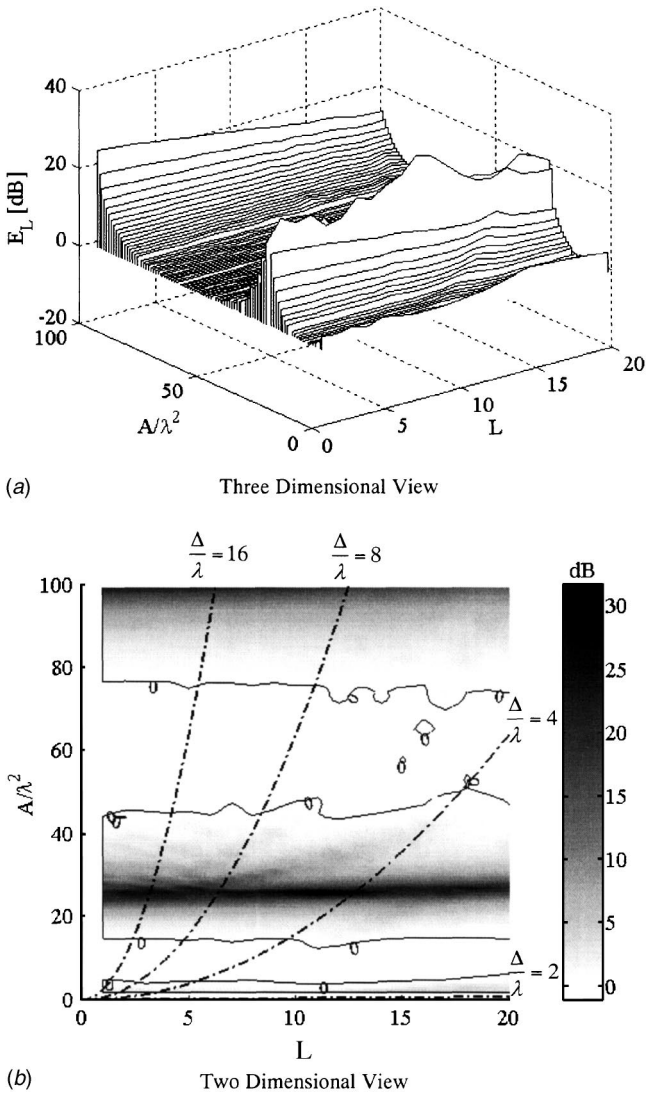

FIG. 3. Normalized acoustic potential energy density level E_L variation as the function of both $\tilde{A}$ and L when δ=0.01.

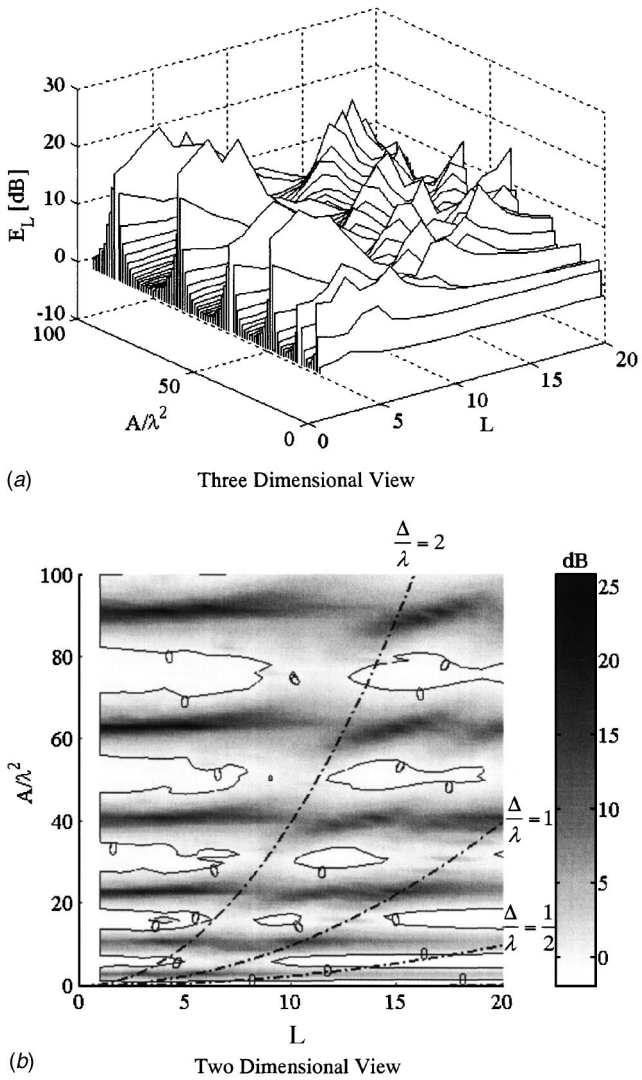

FIG. 4. Normalized acoustic potential energy density level E_L variation as the function of both $\tilde{A}$ and L when $\delta=0.1$.

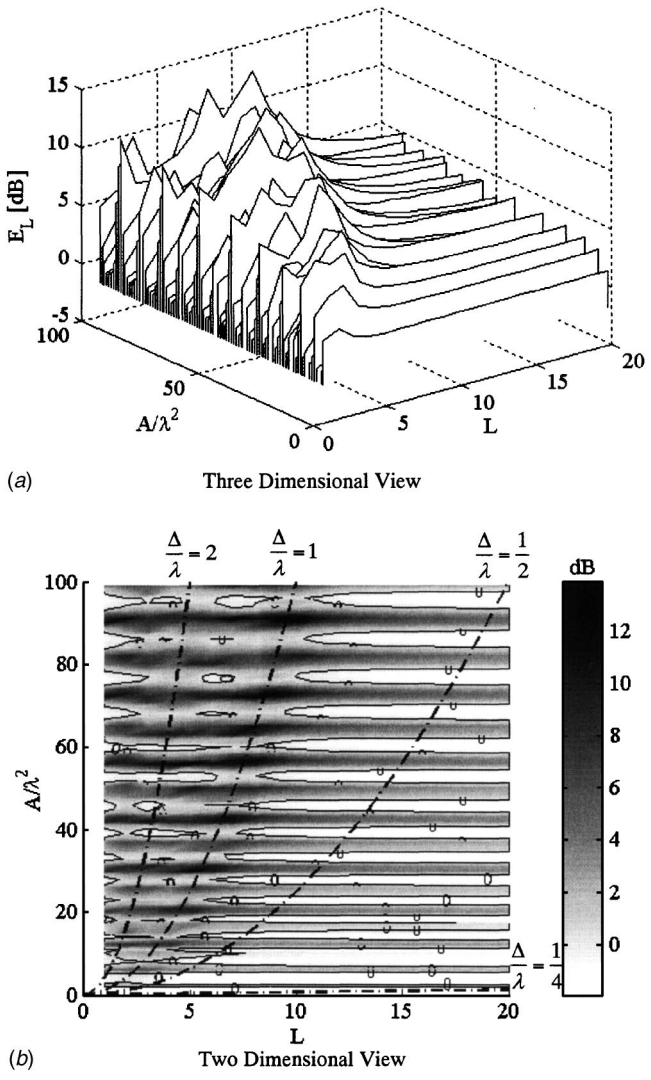

FIG. 5. Normalized acoustic potential energy density level E_L variation as the function of both $\tilde{A}$ and L when $\delta=1$.

of $E_L<0$. The region of $E_L<0$ proves that as long as the sound field is not a case of resonance, a periodic arrangement can be more efficient than a fully covered case. Even though the difference from $\tilde{e}_{po}$ is not large, the regions of $E_L<0$ are distinctly observed. Dark bands in Fig. 3, which mean higher E_L, are shown near the case of $B_y/\lambda=n/2$, where n is a nonzero integer. This corresponds to the case in which the side length B_y of the enclosure is in integer multiples of half wavelengths, i.e., resonances. In order to observe the effect of a Δ/λ change in the periodic absorptive material arrangement, three dash–dotted lines of constant Δ/λ are added to Fig. 3. Here, Δ/λ means the ratio between the absorptive strip arrangement period and the wavelength. It is also noteworthy that L and $\tilde{A}$ have a quadratic relation of $\tilde{A}=\delta\cdot(\Delta/\lambda)^2\cdot L^2$. Therefore, the relations of constant $\Delta/\lambda=16$, 8, 4, and 2 are expressed as individual quadratic curves in Fig. 3. Here, Fig. 3 does not show explicitly any dependency of E_L on the Δ/λ change. However, in the consecutive evaluations of $\delta=0.1$, 1, 10, and 100, we can observe that Δ/λ is a major parameter on the E_L variation.

Figure 4 depicts the case of $\delta=0.1$. This case is similar to that in Fig. 3 as the region of $E_L<0$ and the darker bands of the resonance region are again observed. Unlike Fig. 3, however, due to the change of δ, there are a greater number darker bands and a region of $E_L<0$ appears between them. Specifically, due to the enlarged δ, for the same range of $\tilde{A}$, the domain of B_y is increased but the domain of B_x is decreased. In addition, Fig. 4 clearly shows the dependency on the Δ/λ change. The dash-dotted lines of $\Delta/\lambda=2$ and $\Delta/\lambda=1$, which are different from Fig. 3, break the regions of $E_L<0$. This result assures that the ratio of the arrangement period to the wavelength, i.e. Δ/λ, affects the variation of the acoustical potential energy density.

Next, in Fig. 5, which shows $\delta=1$ (i.e, a square cross section), the number of darker bands is greater and the region of $E_L<0$ is denser than in Figs. 3 and 4, but the overall trend is similar to that in Fig. 4. The lines of $\Delta/\lambda=2$ and $\Delta/\lambda=1$ break the region of $E_L<0$, and the region between $\Delta/\lambda=2$ and $\Delta/\lambda=1$ seems to be a transition region. In addition, compared to Figs. 3 and 4, Fig. 5 shows more distinctly the E_L dependency on Δ/λ. The line of $\Delta/\lambda=1$ acts as a borderline that divides the variation trend of E_L. The region where $\Delta/\lambda<1$, the overall E_L variation due to L change regardless

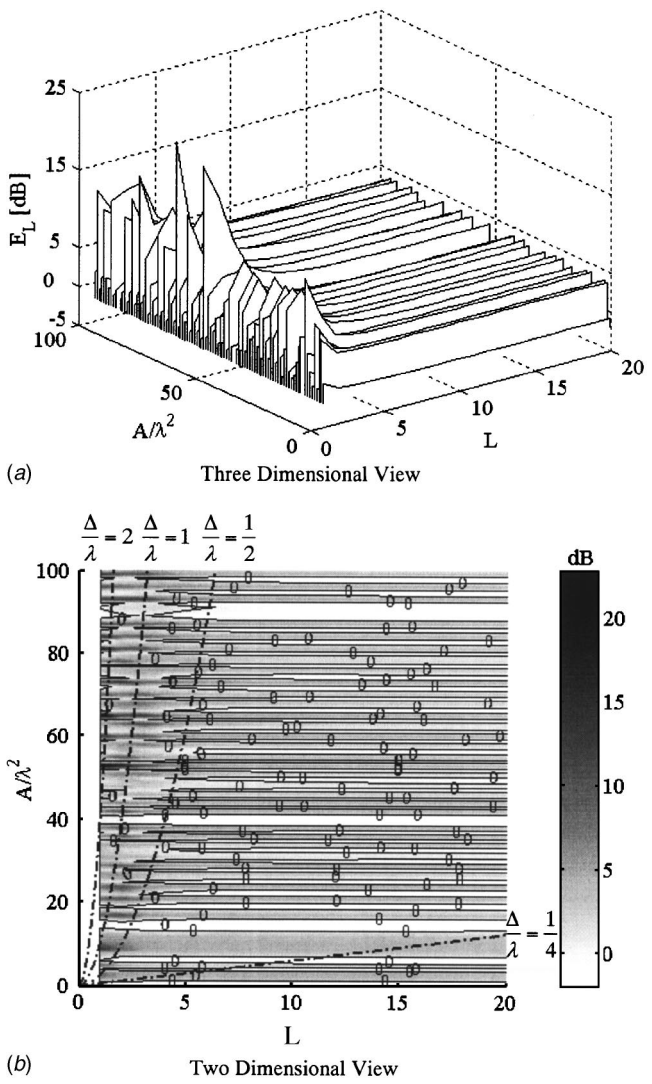

FIG. 6. Normalized acoustic potential energy density level E_L variation as the function of both $\tilde{A}$ and L when δ=10.

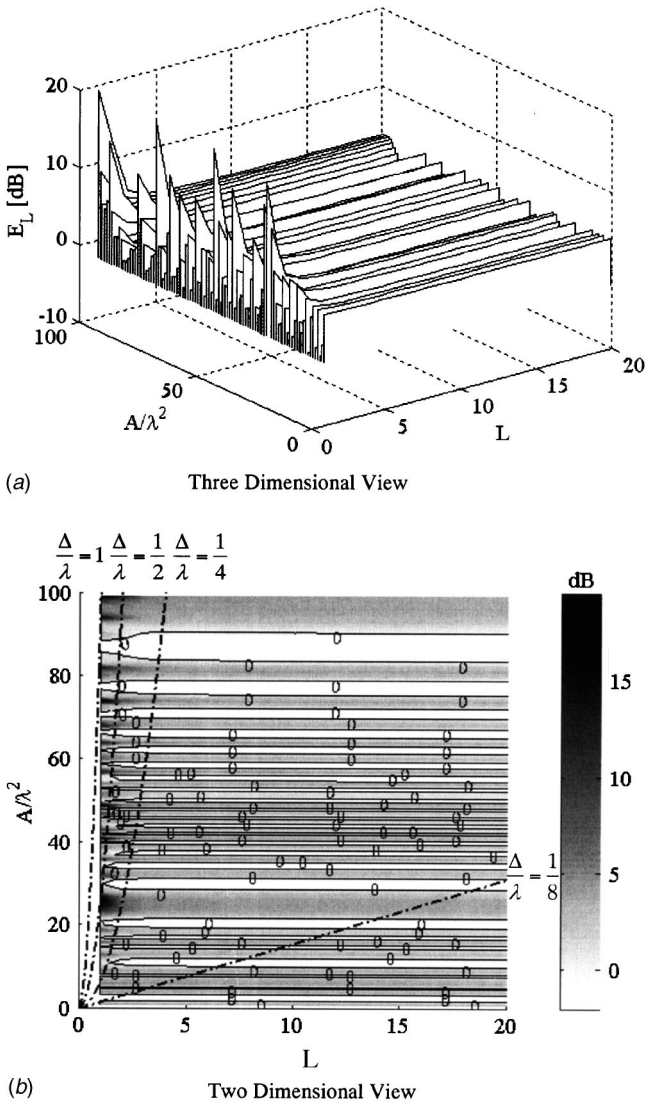

FIG. 7. Normalized acoustic potential energy density level E_L variation as the function of both $\tilde{A}$ and L when δ=100.

of $\tilde{A}$ converges to some constant value. Whether $\tilde{A}$ is resonance or not, this stable condition is applied in the same way.

Figure 6 shows the case of δ=10 and has a similar result. Even though the region of $E_L<0$ is denser than the case of δ=1, the line of $\Delta/\lambda=1$ divides the E_L variation as in Fig. 5. As explained in Fig. 4, the larger is δ, the longer is B_y. Therefore, compared to the case of the smaller δ, more resonance lines are observed in the same range of $1\leqslant\tilde{A}\leqslant100$.

Finally, Fig. 7 shows the case where δ=100. In this case, as depicted in Fig. 7(b), all the evaluation cases correspond where $\Delta/\lambda<1$. As a result, except for the region near $L=1$, the variation of E_L converges rapidly. The consecutive results of Figs. 5–7 stress that two conditions should be satisfied to make $\tilde{e}_p$ less than $\tilde{e}_{po}$ through the periodic absorptive material arrangement: the sound field should not be resonance, and the ratio should be $\Delta/\lambda<1/2$.

The accuracy of Figs. 3–7 is evaluated by Eqs. (20) and (21). Table I shows mean errors for the five different cases of δ=0.01, 0.1, 1, 10, and 100. The range of the admittance boundary condition reconstruction error is $1.4\times10^{-02}\leqslant\overline{\beta}_{\text{error\_mean}}\leqslant2.3\times10^{-02}$, and the range of the rigid wall boundary condition reconstruction error is $2.1\times10^{-02}\leqslant\overline{R}_{\text{error\_mean}}\leqslant2.9\times10^{-02}$. Therefore, $\max(\beta_{\text{error\_mean}})$ is 2.3% and $\max(R_{\text{error\_mean}})$ is 2.9%. These errors are assumed to be acceptable.

V. CONCLUSION

In this study we focus on how the periodic absorptive strip arrangement affects an interior sound field's mean acoustic potential energy density. Specifically, throughout a

TABLE I. Mean admittance and rigid wall bondary condition reconstruction error for five different cross sectional shapes with side ratio δ=0.01, 0.1, 1, 10, and 100, respectively.

δ	$\overline{\beta}_{\text{error\_mean}}$	$\overline{R}_{\text{error\_mean}}$
0.01	2.3×10^{-02}	2.9×10^{-02}
0.1	2.2×10^{-02}	2.9×10^{-02}
1	1.5×10^{-02}	2.0×10^{-02}
10	1.5×10^{-02}	2.1×10^{-02}
100	1.4×10^{-02}	2.1×10^{-02}

parameter study for five different cross sectional shapes with side ratios of δ=0.01, 0.1, 1, 10, and 100, the relation between the ratio Δ/λ of the arrangement period to the wavelength and the enclosure's mean acoustic potential energy density $\tilde{e}_p$ is investigated. Also, in order to determine the efficiency of the periodic absorptive strip arrangement, every $\tilde{e}_p$ of the periodic arrangement is compared to a case in which the surface was fully covered by strips. As a result, the parameter study shows that the sound absorption performance is not simply a function of how much absorptive material is used. It demonstrates that the periodic absorptive strip arrangement is more efficient, if the frequency of interest is not one of the room's resonance frequencies and if the ratio of the arrangement period Δ to wavelength λ is less than 0.5, i.e. $\Delta/\lambda<1/2$. On the contrary, at resonance, $\tilde{e}_p$ of the periodic arrangement is always larger than in the totally covered case.

ACKNOWLEDGMENTS

This study was partially supported by the NRL (National Research Laboratory) of KISTEP (Korea Institute of Science & Technology Evaluation and Planning) and by BK21 (Brain Korea 21), the Ministry of Education & Human Resources Development of Korea.

[1] J. S. Parkinson, ''Area and pattern effects in the measurements of sound absorption,'' J. Acoust. Soc. Am. **2**, 112–122 (1930).
[2] P. E. Sabine, ''What is measured in sound absorption measurement,'' J. Acoust. Soc. Am. **6**, 239–245 (1935).
[3] V. L. Chrisler, ''Dependence of sound absorption upon the area and distribution of the absorbent material,'' J. Res. Natl. Bur. Stand. **13**, 169–187 (1934).
[4] L. G. Ramer, ''The absorption of strips, effects of width and location,'' J. Acoust. Soc. Am. **12**, 323–326 (1941).
[5] C. M. Harris, ''The effect of position on the acoustical absorption by a patch of material in a room,'' J. Acoust. Soc. Am. **17**, 242–244 (1946).
[6] J. R. Pellam, ''Sound diffraction and absorption by a strip of absorbing material,'' J. Acoust. Soc. Am. **11**, 396–400 (1940).
[7] A. Levitas and M. Lax, ''Scattering and absorption by an acoustic strip,'' J. Acoust. Soc. Am. **23**, 316–322 (1951).
[8] R. K. Cook, ''Absorption of sound by patches of absorbent materials,'' J. Acoust. Soc. Am. **29**, 324–329 (1957).
[9] T. D. Northwood, M. T. Geisaru, and M. A. Medcof, ''Absorption of sound by a strip of absorptive material in a diffuse sound field,'' J. Acoust. Soc. Am. **31**, 595–599 (1959).
[10] E. D. Daniel, ''On the dependence of absorption coefficients upon the area of the absorbent material,'' J. Acoust. Soc. Am. **35**, 571–573 (1963).
[11] F. P. Mechel, ''Iterative solutions for finite-size absorbers,'' J. Sound Vib. **134**, 489–506 (1989).
[12] F. P. Mechel, ''On sound absorption of finite-size absorbers in relation to their radiation impedance,'' J. Sound Vib. **135**, 225–262 (1989).
[13] P. M. Morse and K. U. Ingard, *Thoretical Acoustics* (McGraw-Hill, New York, 1968), pp. 454–463.
[14] S.-I. Thomasson, ''On the absorption coefficient,'' Acustica **44**, 266–273 (1980).
[15] A. de Bruijn, ''The sound absorption of an absorbing periodically uneven surfaces,'' Acustica **18**, 123–131 (1967).
[16] A. de Bruijn, ''Anomalous effects in the sound absorption of periodically uneven surfaces,'' Acustica **24**, 75–84 (1971).
[17] D. Takahashi, ''Excess sound absorption due to periodically arranged absorptive materials,'' J. Acoust. Soc. Am. **86**, 2215–2222 (1989).
[18] F. P. Mechel, ''Sound fields at periodic absorbers,'' J. Sound Vib. **136**, 379–412 (1990).
[19] D. Holmberg, P. Hammer, and E. Nilsson, ''Absorption and radiation impedance of finite absorbing patches,'' Acustica **89**, 406–415 (2003).
[20] I. N. Sneddon, *Mixed Boundary Value Problems in Potential Theory* (Wiley, New York, 1966), Chap. I, pp. 1–25.
[21] M. A. Celia and W. G. Gray, *Numerical Methods For Differential Equations* (Prentice–Hall, Englewood Cliffs, NJ, 1992), pp. 115–134.

A scale value for the balance inside a historical opera house

Nicola Prodi[a] and Sylvia Velecka
Dipartimento di Ingegneria, Università degli Studi di Ferrara, via Saragat 1, 44100 Ferrara, Italia

(Received 28 May 2003; revised 26 July 2004; accepted 10 November 2004)

In the framework of opera house acoustics, the term ''balance'' refers to the acoustical competition between the singer on the stage and the orchestra in the pit. The mechanism allowing the operatic singers to be heard over the orchestra has to do with their skill in enhancing the vocal emission by a peculiar use of the formant frequencies. This vital factor is sensed by the listeners and, apart from the obvious sound power ratio of the stage and the pit sources, is the main cue that helps to formulate a subjective impression of the balance. To achieve its objective qualification, two calibrated sound sources can be placed on the stage and in the pit, respectively, and their sound level difference is measured at the listeners' seats. The scope of this work is to investigate the relationship between the subjective impression and the objective indicator of the balance and to develop a scale value for the parameter in the case of a historical opera house. For this scope a set of acoustical data from the Teatro Comunale in Ferrara will be used to create synthetic sound fields with controlled conditions of the balance between the stage and the pit. This methodology employs an anechoic piece for soprano (with piano accompaniment) and is implemented in a dead room equipped with an acoustical rendering system. The sound fields are used to investigate the appropriate balance values by means of listening tests. The results of the scaling exercise show that a suitable range of values can be extracted and that the sound from the stage and the pit is perceived as balanced when the loudness difference between the two is comprised within −2.0 dBA and +2.3 dBA. [DOI: 10.1121/1.1842774]

PACS numbers: 43.55.Hy, 43.55.Fw, 43.55.Gx [MK]. Pages: 771–779

I. INTRODUCTION

Inside opera houses the sound level at the listeners' position is typically the sum of two separate contributions. The former is produced by a sound source, the singer, which is located on the stage, and the latter by a sound source in the pit, the orchestra. For the appraisal of the opera the listener must be able to discern both sources and the interplay of the orchestra and the singer must be such that none of them overwhelms the other. Meyer[1] clarified this system in acoustical terms and introduced the subjective impression ''balance'' as the acoustical competition between the singer and the orchestra experienced by the listener in the opera house. He pointed out that the orchestra and the singer have different sound powers, namely 102 dB for an average *forte* by a singer and 114 dB for a ''Verdi'' orchestral grouping playing *forte*. Despite this apparent disparity the singer can compete with the orchestra thanks to a peculiar use of the formant frequencies of the singing voice.

In particular, in the region close to 3 kHz, where most of the orchestral instruments have sound components even 20 dB or more below their strongest components, the bass, baritone, tenor, and alto voices are able to cluster the F3, F4, and F5 formants so that they create the so-called singer's formant, revealed as an unusually high spectrum peak close to 3 kHz.[2] Its exact frequency and level can change according to the singer proficiency, the wovel, the fundamental frequency and also the vocal loudness is important, so that increasing 10 dB in the overall level can increase the formant amplitude up to 16 dB.

For the sopranos the procedure seems more complicated since, due to the high fundamental frequencies, they tend to make separate use of the resonance properties of formants F3 and F4 so that a wider range of partials can be covered uniformly.[3] In addition, the sopranos extensively use a mechanism of formant tracking to boost the projecting power of their voices: this happens when the fundamental frequency of singing (F0) is higher than the first formant (F1). Matching F1 to F0 greatly improves the voice emission without extra effort.[2,4]

Thanks to the outlined principles of clustering or tracking of the formant frequencies the singers can rise their voices above the sound power of the orchestra. At present there is no evidence of other basic cooperating or constrasting physical factors that may play a role of comparable importance.

After the subjective impression of the balance was defined, an experimental procedure to achieve a related objective paramenter was first proposed by Barron.[5] He measured the difference of the sound levels (long time averages) emitted by a directional source on the stage and by an omnidirectional one in the pit, both fed with stationary random noise. To comply with Meyer's indications the two sound sources were calibrated to have the same sound power output. This level difference was given the same name ''balance'' and was indicated as *B*. The author employed this type of set-up inside a group of opera houses and reported an average value for *B* of nearly 2 dB in favor of the singer. Since no problems with the balance were reported by users

[a]Corresponding author: Nicola Prodi, Dipartimento di Ingegneria, Università degli Studi di Ferrara, Via Saragat 1, 44100 Ferrara, Italy. Electronic mail: prodi@ing.unife.it

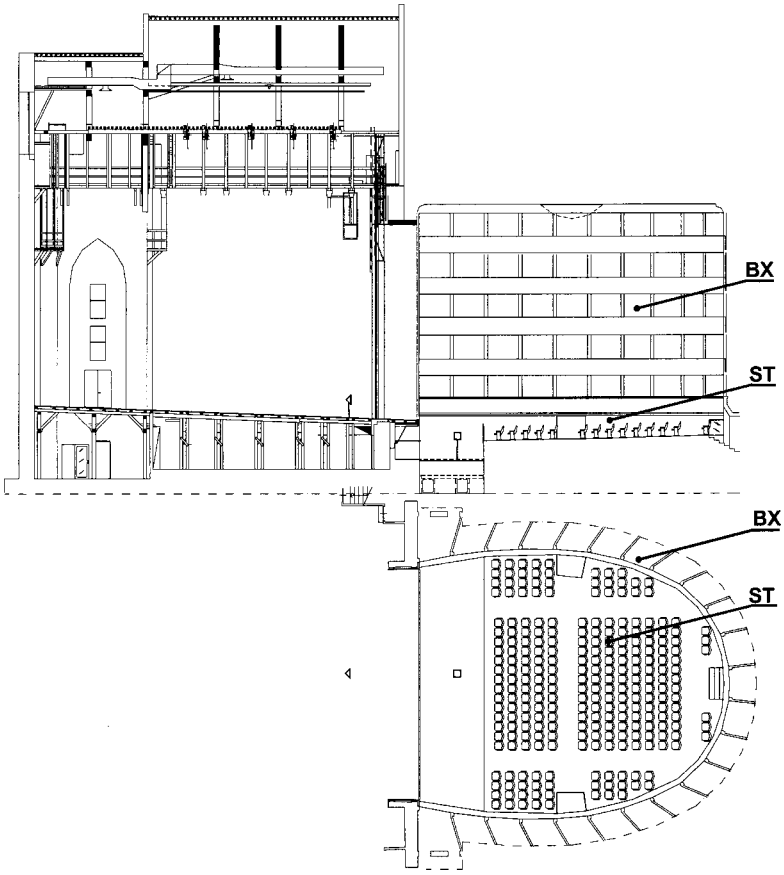

FIG. 1. Plan and section of the Teatro Comunale di Ferrara, Italy. The positions used for later implementing the virtual sound fields are indicated. The location ST is close to the central area of the stalls whereas BX is in a lateral box of the third order. In the graphic also the location on the omnidirectional source (open square) and of the directional source (open triangle) are reported.

of the measured opera houses, he concluded that such a value could probably be appropriate for the parameter.

Later O'Keefe[6] proposed a specific indicator in the form of an energetic ratio with a time limit set at 50 ms, and called it $B50$. In this case the measurement technique involved one omnidirectional source in the pit and the directional source on the stage was obtained by sealing all speakers but one in the dodecaedric source. A 1/3 octave band analysis was performed and some differences between the low and high frequency ranges were shown, but the significance of such data is still an open question.

At present both an objective indicator for the subjectively perceived balance and the procedures to measure it are still not included in the technical norms for room-acoustical measurements.[7]

Within the described context, the present work will focus on the subjective evaluation of the parameter balance (B) according to the objective definition given by Barron. In particular a major open point is the lack of a scale value for the indicator to match the listeners' impression with the measured indicator B. With such a reference scale available the balance could be assessed by field measurements. In this work such a scale will be obtained by means of psychoacoustics tests inside a controlled room. The procedure, which is explained in detail, consisted at first in measuring some impulse responses in two typical positions inside a historical opera house. With these basic data and with the available anechoic signals, many virtual sound fields were generated with different balance ratios between the stage and the pit sources. Then two psychoacoustics scaling experiments were implemented to rate the sound fields according to the attribute under study. After statistical processing the scale value for the balance was achieved.

II. *IN-SITU* MEASUREMENTS

The task of the measurements was to collect impulse responses, which later served to implement virtual sound fields in a controlled room. The measurement campaign took place inside the Teatro Comunale di Ferrara, Italy.[8] The theatre has 800 seats and has an elliptical plan shape with four tiers of boxes surmounted by a gallery. The hall has a volume of nearly 5000 m^3 and the stagehouse has a volume of 8500 m^3. During the measurements there was no stage set and also the pit there was free from music stands, chairs and instruments. The measurements regarded two positions, one in the center of the stalls (called ST) and the other in a lateral box of the 3rd order (BX). The plan and section of the theatre with the locations ST and BX is shown in Fig. 1. The receiver was a B&K4100 binaural head with a torso. The chosen positions should represent some of the most common listening conditions found inside a historical opera house. In particular in the stalls the orchestra is not visible due to the screening effect of the pit rail, while in the box position the sight line to the pit is free.

Two different sound sources, one omni-directional and one directional, were placed at 1 m off the symmetry axis of the hall in the orchestra pit and on the stage, respectively. The location of the sources is also reported in Fig. 1. The omnidirectional dodecaedric source (Lookline model by

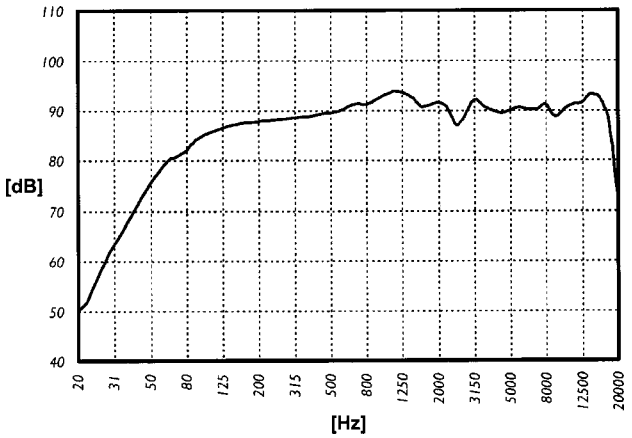

FIG. 2. The frequency response of the directional loudspeaker employed to simulate the singer in the field measurements. The reported dB values are obtained in anechoic conditions at 1 m in front of the loudspeaker.

Claber s.n.c. manufacturer) in the pit was at 2 m from the rail and its center was at 1.3 m above the floor. This sound source is equalized to have a flat frequency response and its directional characteristics comply with the requirements indicated in the norm.[7] On the stage a two-way active directional source (Lem SP Media model by Generalmusic s.p.a. manufacturer) was located 2 m from the fire curtain facing towards the hall, and stood 1.5 m above the floor. As shown in Fig. 2 (taken from the technical specifications of the device) the frequency response for the frontal direction of this sound source is sufficiently flat and for this reason no equalization processing was implemented during the measurements. The directivity pattern of the directional sound source in the horizontal plane was also measured under anechoic conditions and the obtained polar plots are reported in Fig. 3. As can be seen, the directivity is increased in the frontal direction when passing from low to high frequency bands. As regards the vertical plane, the employed sound source has a marked frontal directionality with an angle aperture of about 50° to 60° centered frontally (0° elevation) at 500 Hz and 1 kHz and inclined upwards by 10° at 2 kHz and 4 kHz. The measured directionality data for the two-way loudspeaker can be compared with the similar available data for a soprano voice reported by Parati and Otonto.[9] Some discrepancies are found and discussed[10] (mainly in the 1 KHz and 4 kHz oct. bands for the horizontal plane and in the 500 Hz and 2 kHz for the vertical plane) but this sound source seems appropriate to emulate the singer. In this respect it is believed that only the introduction of a new antropometric sound source would probably improve the similarity further.

Once the listening positions were fixed, the measurements consisted of the emission of an exponential sweep signal, which was delivered sequentially from both the directional and the omnidirectional sound sources. The recorded signals were later post-processed in the laboratory to obtain impulse responses for the left and right ear of the dummy head.

The acoustic parameters measured in ST and in BX are shown in Fig. 4 where they are plotted as averages of the two ear values. The reverberation time RT20 has values of about 1.2 s at mid frequencies, which are quite typical for this type

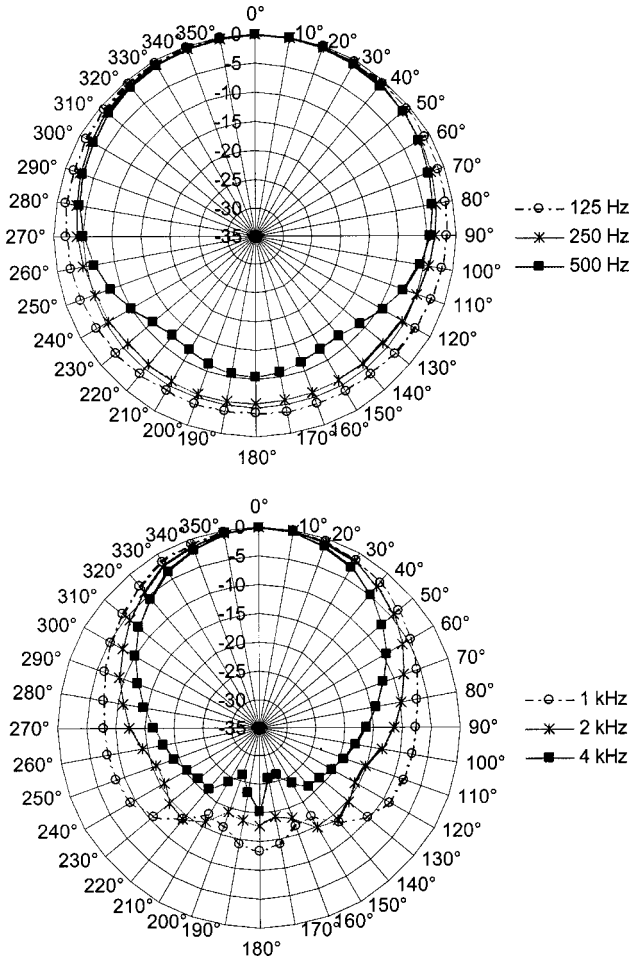

FIG. 3. The measured directivity pattern of the directional loudspeaker used to simulate the singer in the field measurements. The polar plots show octave band dB levels measured under anechoic conditions on a horizontal plane with 10° steps. The band values were scaled to the respective maximum at 0°.

of historical opera house. This parameter shows also a marked frequency dependence so that its value is halved when passing from 125 Hz to 4 kHz. Table I reports the S/N ratios of the measured impulse responses. It is shown that the evaluation of the RT20 parameter was done safely in the range −5 dB to −25 dB whereas the calculation of RT30 could be not as easy. In fact in the 125 Hz band some S/N values would be too close to or smaller than the required 35 dB value. For this reason it was decided to adopt the reverberation time RT20 all through the work.

Moreover the parameter has limited variations for different sources and receivers. Apart from the ''ST Direc.'' combination, the all pass values (indicated as ''Lin'') are within the 5% to 10% limen, which is indicated as the ''just noticeable difference'' limit (JND) for the quantity.[11] On the contrary, remarkable differences, bigger than the respective JNDs, are found both for the center time (TS) and the interaural cross-correlation (IACC) parameters. In fact, the directional source produces in the stalls a set of very peaked first reflections with an almost frontal direction, and this affects the energy ratios and the correlation between the two ears. On the other hand, the pit source creates a sound field with

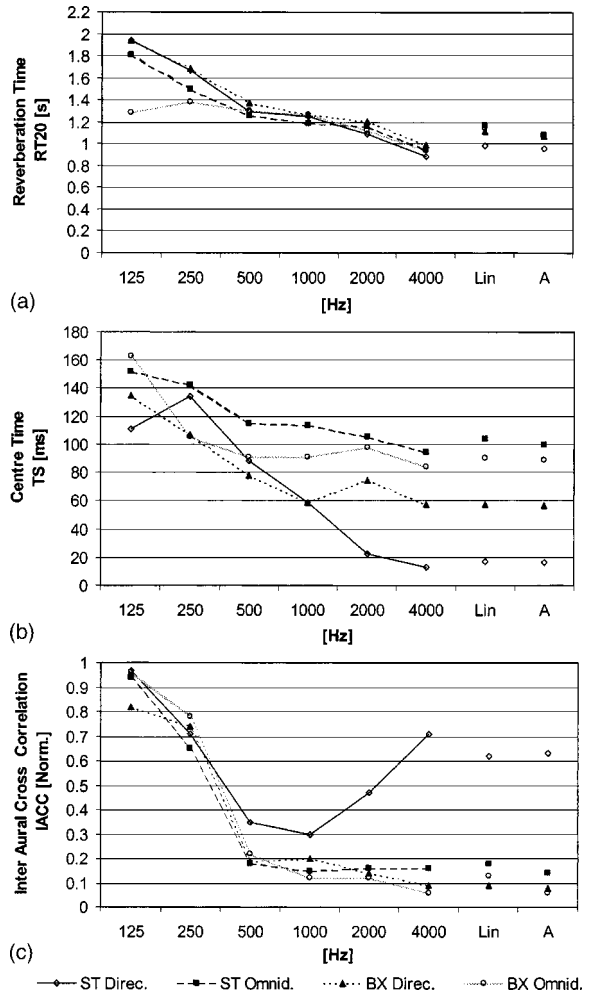

FIG. 4. Acoustical parameters inside the Teatro Comunale of Ferrara, Italy measured for various combinations of sources and receivers. Each plot is the average of left and right values. ''Direc.'' and ''Omnid.'' are the directional and omnidirectional sound source, respectively. From top to bottom: (a) reverberation time RT20; (b) center of gravity of energy, known as center time TS, and (c) interaural cross correlation IACC.

longer TS and slightly lower IACC, and this is also due to the screening effect of the pit rail.

III. THE DEVELOPMENT OF THE LISTENING TESTS

A. Signal processing procedures

Once the impulse responses for the two measured positions in the opera house were available, a set of virtual sound fields was prepared and rendered inside a controlled room. During this part of the work the impulse responses were separately scaled in amplitude to achieve the best possible signal-to-noise ratio. By doing so the information on the real field value of B, which was not essential in the development of the tests, was dropped. All of the listening tests were prepared from the song ''Tormento'' by Tosti (XIX century) for soprano and piano. The music motif has *Andante* speed and is in E minor tonality. Its duration is 16 s and the strength of the motif is *mezzo forte* (mf). This piece was sung by a professional soprano singer and was recorded in the free field (under anechoic conditions).

TABLE I. The S/N ratios of the measured impulse responses expressed as the arithmetical average of the left and the right ear values dB.

Impulse response	125 Hz	250 Hz	500 Hz	1 kHz	2 kHz	4 kHz	Lin	A
ST direc.	36.4	41.2	47.8	52.4	48.5	49.8	44.7	47.1
ST omnid.	36.7	47.1	49.6	48.4	51.9	49.2	44.4	48.0
BX direc.	41.0	43.1	50.9	55.7	58.1	61.1	53.8	56.7
BX omnid.	33.0	48.9	50.5	52.7	55.7	51.7	46.8	51.2

The recorded piece consisted in a stereo file with sampling frequency 44.1 kHz with the vocal line on the left channel and an electric piano (called simply a keyboard from now on) on the right channel. Unfortunately it was not possible to use an anechoic recording with a score for voice and orchestra, since, to the knowledge of the authors, a recording of this kind is still lacking.

In Fig. 5 the two long time average spectra of the voice and keyboard anechoic signals are reported. As it can be seen the voice spectra clearly reveals two separated spectrum peaks in the 1/3 oct. bands centered at 1250 Hz and at 3150 Hz. The peaks are, respectively, 2 dB and 12 dB lower than the highest level, which can be found in the band centered at 630 Hz. This finding complies with Ref. 3 and it witnesses the various formants' resonances in this case.

The process of preparation and rendering of the virtual sound fields was performed at 44.1 kHz and can be described by the following steps.

(1) Convolution of the mono vocal line with the binaural impulse responses measured with the directional source on the stage.
(2) Convolution of the mono keyboard line with the binaural impulse responses measured with the omnidirectional source in the pit.
(3) The mixing of vocal and keyboard source files to achieve sound fields with different balance ratios.
(4) Cross-talk canceling and inverse filtering according to the stereo-dipole processing[12] with 20° of loudspeakers opening with respect to the listener.

Both for the stalls and the box locations the prepared virtual sound fields were characterized by changing the amplitude of the stage impulse responses in 3 dB steps from -7 dB to $+8$ dB, so that six sound fields were created in each case. It is to be noted that no other processing on the impulse responses was implemented. That is to say that the investigation did not take into account other possible factors influencing the balance apart from the level difference between the stage and the pit sources.

The level differences were later measured at the ears of the dummy head, which was placed at the listener position inside the controlled room. This was accomplished by playing back separately the singer and keyboard lines after the entire procedure was completed. The obtained B values for the six sound fields of both ST and BX are resumed in Table II.

Then the mixing procedure at point (3) above was used to produce two separate groups of sound fields. In the former group the overall level of the mixed sound fields changed from one sound field to the next (variable level group—VL). Their overall level ranged from 77.8 dBA to 83.4 dBA in the

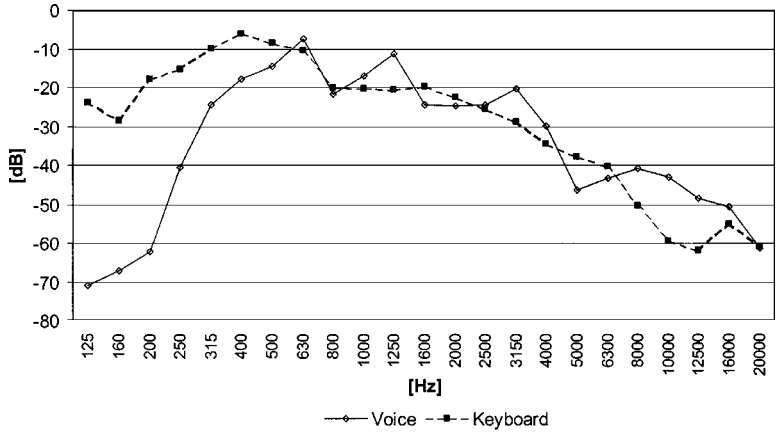

FIG. 5. Emission spectra of the anechoic signals of voice and keyboard. The values are measured as long term time average energies with an arbitrary reference.

ST position and from 77.0 dBA to 82.8 dBA in the BX position. On the contrary, in the latter group the overall level was always kept fixed (fixed level group—FL). This was obtained by setting the level of the sound fields in the first group to exactly 80.0 dBA. This adjustment allowed us to maintain the balance values unaltered between the two groups of sound fields. The value of 80 dBA, which can be regarded as a preferred condition for the listeners to music,[13] is also typical for the performances inside historical opera houses. For instance, this can be demonstrated for the Municipal Theatre in Modena,[14] a historical house quite similar to the one under study in this work. In that house one of the authors measured a space averaged strength value G (according to Annex A of Ref. 7) equal to 8 dB (with a spatial standard deviation—S.D.—equal to 2 dB) in the stalls and 5 dB (S.D. 2 dB) in the boxes. Given the *forte* of the Verdi full orchestra at 114 dB, the resulting level is, respectively, 91 dB (S.D. 2 dB) in the stalls and 88 dB (S.D. 2 dB) in the boxes. Since, when passing to dBA, one can expect a decrease of these levels by 1 to 3 dB, the *forte* at the listeners can be set, respectively, at 89 dBA and 86 dBA (with the same S.D.). It follows that most of the score, usually close to mf, would be around 80 dBA at the listener if a doubling in the perceived piece strength can be reasonably assimilated to a change of about 10 dB in the sound energy.

The final step in the preparation of the listening experiments was the processing of the two obtained families of sound fields, VL and FL, according to the stereo-dipole technique. The rendering technique was implemented in a listening room with almost anechoic characteristics by placing the two loudspeakers (F11 monitors by Quested manufacturer) at 2 m symmetrically in front of the listener with 20° of an angular opening. The frequency response of the monitors is from 65 Hz to 20 kHz (± 3 dB).

The system is able to create phantom sources with good accuracy. Takeuchi[15] tested a similar system (but with a 10° angular span of loudspeakers instead of the 20° employed here) and measured the correlation coefficients between the presented and the perceived directions of the phantom sources equal to 0.93 for the azimuth and 0.70 for the elevation. That system showed some back-to-front confusion, which is not relevant in the present application. In fact, all of the sound fields are designed to have the sound sources in the frontal position, though with a slight elevation difference.

Furthermore, the stereo dipole system implemented in this research is capable of reproducing virtual sound fields where all of the relevant acoustic parameters are not distinguishable from the original ones measured *in-situ*. This aspect was deeply investigated in the past[16] and it was shown that the difference between the real field parameters and the virtually reproduced one is well within one JND.

TABLE II. The B values in the virtual sound fields measured as the arithmetical average of the left and the right ear values expressed in dBA.

Sound field	A	B	C	D	E	F
ST—stalls	−8.7	−5.7	−2.7	0.3	3.3	6.3
BX—box	−9.7	−6.7	−3.7	−0.7	2.3	5.3

B. Psychoacoustics formulation

The implemented tests aimed at fixing a scale value for the balance indicator. To achieve this goal it was decided to employ a statistical methodology known as ''unidimensional scaling.''[17] In particular, the formulation used is known as the ''Thurstone method of categorical judgement.'' To apply this method it was assumed that the psychoacoustic attribute to be qualified had a fundamental dimension corresponding to the level difference between the stage and the pit signals. This assumption obviously complies with the definition of the balance under study.

In order to implement the method it was first decided to produce a rating scale consisting of five items. They were named, respectively, ''voice too low (VTL),'' ''voice rather low (VRL),'' ''voice and keyboard balanced (VKB),'' ''voice rather high (VRH)'' and ''voice too high (VTH).'' Only one of these items had to be selected by checking a box when the listener judged a sound field. In Fig. 6 the obtained checkbox for a sound field is shown. This method allowed us both to achieve a scale value for each of the presented sound fields, and to set the category boundaries between the items selected to rate the balance.

Each test session consisted in the playback of one group of six sound fields, which were randomly ordered. During

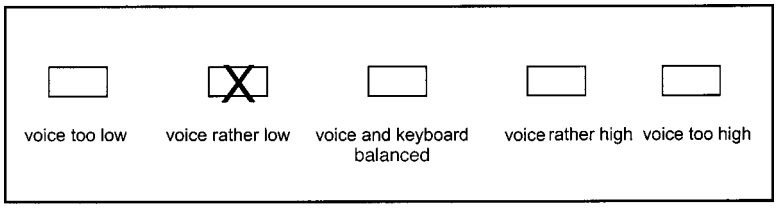

FIG. 6. The checkbox employed for collecting the judgements of sound fields during the listening tests.

one session five seconds of silence were inserted between successive sound fields to give the tester the time to judge the listened sound field. A complete experiment consisted first in a practice session where the listener familiarized with the six sound fields and then of two proper test sessions with different orders of presentation. Only these two latter sessions were used in the statistical processing. A complete experiment was prepared for each position.

The whole test procedure was repeated twice: first the sound fields with a variable overall level were used (VL) and then those with a fixed overall level (FL).

Each listening experiment was introduced by a brief explanation about the system consisting of the singer on stage and the orchestra in the pit. It was pointed out that each source produces a different loudness level at the listener ears and that the balance was introduced to evaluate and then to assess the optimal mixing of the music from the pit and of the singing voice from the stage. Then testers were instructed to focus on the loudness difference and to formulate a subjective judgment based on their personal experience and musical taste. Then, based on their impression, they had to fill in the prepared checkbox of rating items. All of the testers were young men and women (aged between 20 and 40 years) with normal hearing acuity. Some of them reported musical skills and operatic knowledge, but a regular opera-going experience was not required to participate in the experiments.

A selection based on reliability was implemented to validate the testers. In fact those who judged three or more sound fields under the same item were dropped since this was considered the proof that they had not had sufficient listening skills. The number of validated testers ranged from 10 to 13 so that each sound field had at least 20 reliable judgements, that is 10 to 13 for each session. The 50% of the validated testers had a background in classical music as instrument players.

IV. RESULTS

The data collected during the tests were elaborated according to the algorithms of the Thurstone categorical judgement. For each complete experiment there were two main results expressed in statistical terms: the scale values for the presented sound fields and the category boundaries for the rating items. Since the statistical formulation provided results basically in terms of standard deviation units, it was necessary to transfer them back into the level scale used in preparing the sound fields. This step was accomplished by calculating the linear regression between the obtained scale values for the presented sound fields and the respective level scale fixed during the preparation stage (see Table II). The results of this operation are reported in Fig. 7. In each case the regression coefficient was high ($R^2 > 0.94$) and a suitable linear relationship could be established. Actually this was considered the first evidence that the scaling experiment was successful, since a functional dependence of the balance from the level difference was established. By means of the regression equations and using the scale values of the category boundaries as inputs, the respective level values of the category boundaries were calculated too.

The results of these operations are shown in the Tables III and IV. The tables report, respectively, the boundary values and the amplitude of the intervals of the items used to rate the balance in the presented sound fields. Table III shows that there are some differences in the boundary values obtained with the two groups of sound fields, that is, VL and FL. In particular the absolute average difference of the obtained boundary values between VL and FL experiments is 0.8 dB in the case of ST and 0.7 dB in the case of BX. Only two discrepancies are bigger than 1 dB, as can be seen in Table II in the columns VTL−VRL by subtracting rows one and two and under column VKB−VRH by subtracting at rows four and five.

The differences between VL and FL sound fields can be accounted for by some expected interference of the judge-

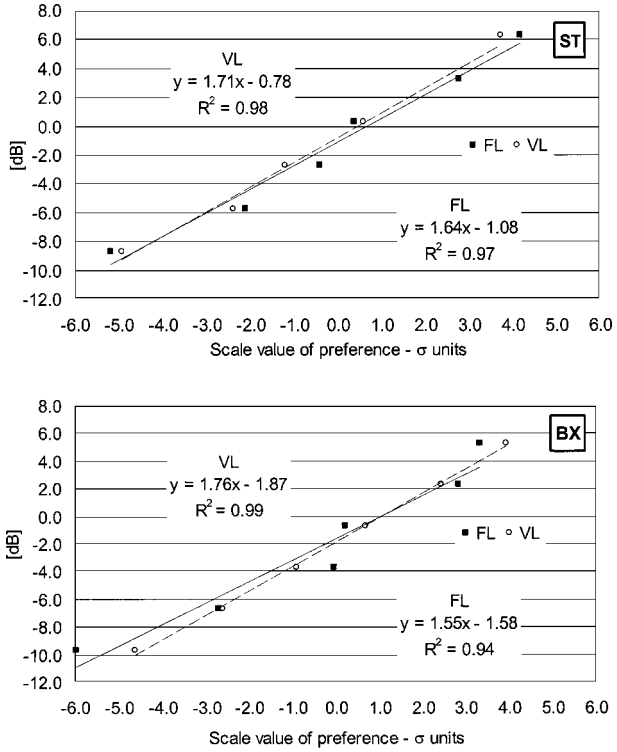

FIG. 7. The linear relationships between the obtained scale values and the level scale used in preparing the sound fields both for the VL and FL experiments. Top: position ST; bottom: position BX. The R^2 coefficients for each regression are also reported.

TABLE III. The obtained boundary values for the items used in the rating of the balance. Units are dBA. VTL is ''voice too low,'' VRL is ''voice rather low,'' VKB is ''voice and keyboard balanced,'' VRH is ''voice rather high'' and VTH is ''voice too high.'' The average values are rounded to the first decimal position.

Position	Field	VTL–VRL	VRL–VKB	VKB–VRH	VRH–VTH
ST—stalls	VL	−5.27	−1.67	3.21	5.19
	FL	−6.63	−2.40	2.60	4.51
	Avg. ST	−6.0	−2.0	2.9	4.9
BX—box	VL	−6.47	−2.13	1.10	4.17
	FL	−5.53	−1.67	2.21	3.97
	Avg. BX	−6.0	−1.9	1.7	4.1
	AVG.	−6.0	−2.0	2.3	4.5

ments with the subjects' preference for a higher or lower level of sound fields. Actually, some of the testers reported that formulating the judgment in the FL experiment was more difficult than in the VL one. This was because some of them probably also used the overall level for judging the sound fields.

The discrepancies of the obtained boundary values should be compared to the JND for the loudness of a music piece. A suitable reference is the value of approximately 0.5 ±0.2 dB, which can be found[18] as the JND for a sinusoidal signal with an intensity level at 80 dB. In the present case, with a nonstationary musical signal, it can be surely assumed that such a JND would cover the above discrepancies of 0.7 dB and 0.8 dB. This is the basic reason why the two sets of results from the VL and the FL experiments can be considered consistent with each other despite the overall level change.

As a consequence of this argument in Table III, the respective averages for ST (row three) and BX (row six) are calculated. Comparing these two averaged boundary values it is seen that they have now only a 1.2 dBA gap under the column VKB–VRH, while the other boundaries are quite in agreement. This means that the balance is judged in a very similar way in the stalls and in the box. Only the median interval (VKB) is slightly bigger in the stalls, as can be verified in Table III by comparing row three with row six under the VKB column.

From all the above results it seems appropriate to describe the global requirements for the opera house as the average of the two sets of values for ST and BX. The averaged boundary values are reported in the last row of Table III. It is seen that the averaged VKB region extends from −2 dBA to +2.3 dBA. The 4 dBA interval on the left of it, that is from −6 dBA to −2 dBA is regarded as VRL and below −6 dBA the voice is heard as too low. On the other side the region VRH has just a 2.2 dBA interval and is not symmetric to the VRL. Above 4.5 dBA the voice is perceived as too high.

TABLE IV. The amplitudes of the item intervals. Units are dBA. VRL is ''voice rather low,'' VKB is ''voice and keyboard balanced,'' VRH is ''voice rather high.'' The extreme items have boundaries going, respectively, to minus and plus infinity and their amplitude cannot be reported. The average values are rounded to the first decimal position.

Position	Field	VRL	VKB	VRH
ST—stalls	VL	3.60	4.88	1.98
	FL	4.23	5.00	1.91
	Avg. ST	3.9	4.9	1.9
BX—box	VL	4.34	3.23	3.07
	FL	3.86	3.88	1.76
	Avg. BX	4.1	3.6	2.4
	AVG.	4.0	4.2	2.2

TABLE V. Test of the goodness of fit. Difference between the measured probabilities and those predicted *a posteriori*.

Δp	VL	FL
ST—stalls	0.001	0.004
BX—box	0.015	0.015

To validate the statistical results also, the goodness of fit was evaluated according to the procedure expounded by Edwards and Thurstone.[19] This approach assesses the statistics by checking the averaged differences Δp between the experimentally measured probabilities and those estimated *a posteriori* by means of the obtained distribution parameters. The results of the goodness of fit are reported in Table V. According to Ref. 19 both the results are quite statisfactory, and the ST yelds a more robust fit.

V. DISCUSSION

The scale values of the balance achieved for the stalls and for the box are substantially in agreement. This finding confirms that the level difference between the pit and the stage is by far the most important attribute governing the perceived balance. The other characteristics of the impulse responses in the two positions play a minor role.

In fact, as reported above, the acoustical parameters showed quite different courses between the ST and BX locations, so that the respective listening conditions are substantially distinct. Actually these characteristics were also nicely reproduced in the virtual sound fields. The position ST sounded quite clear, focused and intimate to the listener whereas the BX sound field was neither focused nor intimate. The testers seldom reported both these facts even if a specific judgment was not requested. Anyway, it has to be pointed out here that the present experiments were not suitable to investigate the further dependence of B on each room-acoustical parameter. For this task a wider group of impulse responses and sound fields would be needed.

The averaged boundary values have been obtained from two different types of experiments and the VL ones had a potential trade-off due to the simultaneous change of the balance and of the overall level. Notwithstanding this, the VL approach has two basic advantages. First it allows an easier relative judgment of the singer level with respect to the fixed keyboard level and, second, it could better reproduce some typical listening conditions found inside opera houses. In fact, the VL sound fields could be appropriate, for instance, to describe different combinations of singers and musicians. In particular each singer will have a peculiar sound power output depending on many factors such as the type of voice, the personal ability, and training. On the other hand, during

the executions also the musicians will adjust their sound power output to some extent under the supervision of the conductor. That is why the VL condition can reproduce this common variability better than the FL one which, on the contrary, is independent of the testers' preference for sound fields of a higher or lower level. The results for the two types of experiments showed a discrepancy, which could be compared with the JND for the sound level. Based on this argument a common set of *B* values was extracted.

Moreover the sound fields in the listening tests were characterized by different balance ratios expressed in terms of dBA values. This weighting procedure has the great advantage of better focusing on the frequency region where the use of the formants by the singers is most effective. As explained above, in fact, both male and female singers (though with some peculiarities typical of each voice register) make use of the formant frequencies in order to enhance their vocal emission. That is why the findings of this work should in principle apply to all of the operatic singing voices.

To employ dBA values it was assumed that the level differences occurring out of the region of interest were not as important for the assessment of the balance as those being inside that range. To confirm this choice it is recalled that the other masking effects from the orchestral sounds (or in this case from the piano) are concentrated primarily in the lower frequency range. It is known in fact that the long term spectral envelope of orchestral sound, peaked at around 450 Hz, can easily mask the singing voice at lower frequencies.[2] The A-weighting allowed us to control the masking at lower frequencies and it was also possible to partially compensate for the use of an electric piano rather than of a proper orchestra, whose behavior had to be reproduced only in the frequency range of interest. It has to be remarked here that the use of the A-weighting differs from the approach of Barron, who used long time average values but without weighting.

Actually the usage of long time averages seems to conflict with the nature of music and singing, both being nonstationary phenomena, and with the nature of the human auditory system which operates on a short-time basis. The above approach is directly derived by the room acoustical measurement procedures described in Annex A of Ref. 7, whose aim is to objectively qualify the acoustics of a room. As recalled by Barron[20] the objective indicator for the loudness, called strength (*G*), was first derived by assessing recordings made at orchestral rehearsals in actual concert halls. It is clear then that this approach gained increasing success over the years among researchers and practitioners due to its simplicity and effectiveness, but the optimization of the loudness calculation scheme for both music and singing is still an open question.

Another point to be discussed is how the findings can be transferred to other opera houses. In the present case the results showed limited discrepancies between ST and BX positions, and it can be predicted that the appropriate *B* values should not depend so much on the position inside a given hall. In particular the results achieved here should apply to historical opera houses whose listening attributes are very similar to those in the investigated theater. It seems that the fine structure of the impulse responses should play a minor role in the assessment of *B*, since the level difference clearly governs the perception of the attribute. Nevertheless a change in the above scale for *B* could perhaps occur in opera houses with a reverberation time, deviating substantially from the present case. In those houses the strong impact of reverberation on the intelligibility of the singing voice should be considered.

Finally, it has to be remarked that the values used here were the measured level differences of the singer and the keyboard lines played separately in the listening room after the whole processing was implemented. This kind of direct virtual measurement was forced, since the power output of the two sources in the free-field conditions of recording was unknown and surely not equal in the range of interest. Anyway, for the evaluation of *B* the obtained scale values must be compared with the field values measured when operating two calibrated sound sources. Experimentally those data can be achieved either by means of separate measurements with a sound level meter or by post-processing of suitable impulse responses. Unfortunately, discrepancies between the two measurement techniques were reported in the last years.[21,22]

VI. CONCLUSIONS

In this work a reference scale for the evaluation and the assessment of the balance between the singer and the orchestra inside a historical opera house was first developed. Based on the fundamental mechanisms allowing the singer to acoustically compete with the orchestra, which stem from the peculiar usage of the formant frequencies of the singing voice, the concept and physical background of the balance was outlined. This perceived attribute was investigated by means of listening tests, which gave statistically reliable results. In particular the boundary values of the parameter, measured as the dBA level differences between the stage and the pit sources, and the item intervals were derived by unidimensional scaling experiments. The main findings of the work were the following.

(1) An accurate scaling can be achieved by means of the level difference. The scale values of the sound fields and the balance values are linked by a linear relationship with high correlation coefficients.
(2) The other room-acoustical indicators play a minor role since a limited discrepancy between the two investigated positions in the stalls and in the box was found.
(3) Judgements of sound fields with variable and fixed levels were performed and a common set of boundary values could be extracted.
(4) From this scale it was found that the balance region extends on average from -2 dBA to $+2.3$ dBA and for *B* above $+4.5$ dBA the voice level is judged as too high.

Some further researches are necessary to clarify the influence of reverberation time on the balance, because this attribute could affect the intelligibility of the singing voice.

ACKNOWLEDGMENTS

This work was funded by the Marie Curie Host Fellowship of the European Union. The authors are grateful to Ing.

Linda Parati for the collaboration in the experimental measurements in the theater and for the directivity measurements. Professor Roberto Pompoli is acknowledged for his continuous support and interest in the present research. Furthermore the authors wish to express their sincere thanks to all the testers taking part in the listening experiments.

[1] J. Meyer, ''Some problems of opera house acoustics,'' *Proceedings of the 12th I.C.A.*, Vancouver, 1986.
[2] J. Sundberg, ''The acoustics of the singing voice,'' Sci. Am. **236**, 82–91 (1977).
[3] J. Sundberg, ''Level and center frequency of the singer's formant,'' J. Voice **15**, 176–186 (2001).
[4] J. Sundberg, ''Research on the singing voice in retrospect,'' *Speech, Music and Hearing*, KTH Stockholm TMH-QPSR, 2003, Vol. 45, pp. 11–22.
[5] M. Barron, *Auditorium Acoustics and Architectural Design* (E & FN Spon, London, 1993), p. 333.
[6] J. O'Keefe, ''Measurement of stage to pit balance in four proscenium arch theatres,'' *Proceedings of IOA—Auditorium Design at the Millennium*, Belfast, 1997.
[7] ISO/DIS 3382, *Measurement of Reverberation Time With Reference to Other Acosutical Parameters* (International Organization fo Standardization, Geneve, 1997).
[8] Theater's site: http://www.teatrocomunaleferrara.it/
[9] L. Parati and F. Otonto, ''Comparison of directional sources in simulating a soprano voice,'' *Proceedings of SMAC2003*, August 2003, Stockholm, Sweden.
[10] L. Parati, ''Acoustical balance between singer on the stage and orchestra in the pit,'' Cap. 3, Ph.D. thesis, Facoltà di Ingegneria, Università degli Studi di Ferrara, A. Y. 2002, 2003.
[11] J. Cox, W. J. Davies, and Y. W. Lam, ''The sensitivity of listeners to early sound field changes in auditoria,'' Acustica **79**, 27–41 (1993).
[12] O. Kirkeby, P. A. Nelson, and H. Hamada, ''Local sound field reproduction using two closely spaced loudspeakers,'' J. Acoust. Soc. Am. **104**, 1973–1981 (1998).
[13] Y. Ando, *Architectural Acoustics: Blending Sound Sources, Sound Fields and Listeners* (Springer-Verlag, New York, 1998), p. 34.
[14] N. Prodi, R. Pompoli, and L. Parati, ''The acoustics of the Municipal Theatre in Modena,'' *Proceedings of the Forum Acusticum 2002*, Seville, September 2002.
[15] T. Takeuchi and P. A. Nelson, ''Subjective evaluation of the Optimal Source Distribution system for virtual acoustic imaging,'' *Proc. of the AES 19th International Conference*, Schloss Elmau, Germany, June 2001.
[16] N. Prodi and S. Velecka, ''The evaluation of playback systems for virtual sound fields,'' Appl. Acoust. **64**, 147–161 (2003).
[17] W. S. Torgerson, *Theory and Methods of Scaling*, 7th printing (Wiley, New York, 1967), Chap. 10.
[18] W. Yost and D. W. Nielsen, *Fundamentals of Hearing, an Introduction* (Italian edition) (Piccin, Padova, 1986), p. 147.
[19] A. L. Edwards and L. L. Thurstone, ''An internal consistency check for scale values determined by the method of successive intervals,'' Psychometrika **17**, 169–180 (1952).
[20] M. Barron, ''The value of ISO3382 for research and design,'' *Proceedings of IOA—Auditorium Acoustics*, London, 2002, Vol. 24, Part 4.
[21] G. Iannnace, C. Ianniello, L. Maffei, and R. Romano, ''The measurement of G in auditoria: comparing two techniques,'' *Proceedings of the 23rd Congress of the Italian Acoustics Association*, Genova, May 1999 (in Italian).
[22] D. G. Ciric and M. A. Milosevic, ''Inaccuracies in sound level determination from room impulse response,'' J. Acoust. Soc. Am. **111**, 210–216 (2002).

Intersymbol interference in underwater acoustic communications using time-reversal signal processing

Daniel Rouseff
Applied Physics Laboratory, College of Ocean and Fishery Sciences, University of Washington, 1013 NE 40th Street, Seattle, Washington 98105

(Received 26 April 2004; revised 1 November 2004; accepted 4 November 2004)

Coherent underwater communication is hampered by the time spread inherent to acoustic propagation in the ocean. Because time-reversal signal processing produces pulse compression, communications has been suggested as a natural application of the technique. Passive versions of time-reversal processing use a receive-only array to do combined temporal and spatial matched filtering. It can be shown, however, that the pulse compression it achieves is not perfect and that an equalizer that relies solely on time-reversal processing will have an error floor caused by uncompensated intersymbol interference (ISI). In the present paper, a physics-based model is developed for the uncompensated ISI in a passive time-reversal equalizer. The model makes use of a normal-mode expansion for the acoustic field. The matched-filtering integral is approximated and the intermediate result interpreted using the waveguide invariant. After combining across the array and sampling, formal statistical averages of the soft demodulation output are calculated. The results show how performance scales with bandwidth, with the number and position of array elements, and with the length of the finite impulse response matched filters. Good agreement is obtained between the predicted scaling and that observed in field experiments. © *2005 Acoustical Society of America.*
[DOI: 10.1121/1.1841692]

PACS numbers: 43.60.Tj, 43.60.Dh, 43.30.Bp [DRD] Pages: 780–788

I. INTRODUCTION

Time-reversal signal processing was first prominently demonstrated in underwater acoustics by Parvulescu.[1] An acoustic source transmitted a short burst. The response, observed several kilometers away, exhibited significant time spread as late-arriving energy interacted multiple times with both the sea surface and the bottom. The received signal was sent back via a radio link, then retransmitted from the source but in a time-reversed fashion. With the slowest paths now sent first, the backpropagated field recombined to produce a sharp response at the receiver. In a later theoretical study, Jackson and Dowling[2] considered a scenario with an active array that was capable of both reception and transmission. They showed how the time-reversed field backpropagated from such an array would focus both in time and in space at the location of the original source. Dowling later showed how analogous pulse compression could also be achieved using a passive, receive-only array.[3] Active time reversal using a vertical source–receiver array was demonstrated by Kuperman *et al.*[4]

The ability of time-reversal processing to produce pulse compression suggests its attractiveness for use in underwater communications. The time spread so typical of propagation in the ocean makes acoustic communication a challenging problem.[5,6] The standard approach is to design an equalizer that attempts to correct for these propagation effects. The equalizer must adapt to the constantly changing ocean environment. If an appropriate form of time-reversal processing could be developed, it might be possible to simplify the processing dramatically. Ideally, adequate pulse compression would be achieved with the ocean acting implicitly as its own equalizer. The open research questions of how and when time-reversal processing might best be applied involves aspects of wave propagation theory, signal processing and experimental design.

As befitting an interdisciplinary topic, time-reversal processing for communications has been viewed from a variety of perspectives. From a mathematical physics standpoint, it has been shown how communications performance can actually improve as the scattering in a complicated environment increases.[7] Statistical stability of a communications link has been examined as a function of bandwidth.[8,9] From the standpoint of communications theory, time reversal has been compared to other more explicit equalization techniques.[10–12] If there is low signal to noise, time reversal produces performance comparable to an explicit equalizer at a fraction of the computational cost. These papers have also showed, however, that an equalizer that relies purely on time reversal will ultimately be limited by uncompensated intersymbol interference (ISI). From the standpoint of doing experiments, both active[13–15] and passive[16–22] versions of time-reversal communications have been implemented.

The present paper synthesizes these various approaches to time-reversal communications. A physics-based model for the performance of a passive time-reversal equalizer is developed. The model, derived in Sec. II, includes basic communications design parameters such as the bandwidth and the array geometry, but also basic propagation physics such as embodied in the waveguide invariant. Formal statistical averages of the equalizer's soft demodulation output are performed. The numerical calculations in Sec. III demonstrate the effects of residual ISI on performance. The calculations show how performance scales with bandwidth, with the number and spacing of array elements, and with the length of

the finite impulse response matched filters. Model predictions for the scaling are shown to be in good agreement with results from field experiments in Sec. IV.

II. MODEL

The limiting factor for time-reversal communications in the ocean is uncompensated intersymbol interference. This section develops a physics-based model for this inherent error. To define the terminology and mathematical notion in a simple setting, an idealized correlation demodulator[23] is first reviewed. If there is no noise, no multipathing, and perfect synchronization, a sequence of symbols can be recovered using a correlation demodulator without interference. A passive time-reversal equalizer operating in the ocean waveguide is then considered. An analytical expression for this processor's intersymbol interference is derived in terms of ocean waveguide parameters. A formal statistical average then yields the mean-squared error.

A. Correlation demodulator

Consider the phase-encoded data stream $s_d(t)$ operating at the radian center frequency ω_0

$$s_d(t)=\sum_{n'} s(t-n'T_s)\cos(\omega_0 t+\phi_{n'}), \tag{1}$$

where $s(t)$ is the envelope and $f_s=1/T_s$ is the symbol rate. For simplicity, encoding is restricted to binary phase shift keying (BPSK), implying $\phi_{n'}$ is either 0 or π; generalization to higher order constellations is straightforward.

Suppose $s_d(t)$ could be measured at a receiver. A correlation demodulator is one technique for extracting the discrete symbols $\cos(\phi_{n'})$ from the measurement. The technique can be illustrated with an idealized example. Letting

$$s_i(t)=s(t)\cos(\omega_0 t) \tag{2}$$

be known at the receiver, the cross correlation with the data stream is

$$\begin{aligned} S(t)&=\int_{-\infty}^{\infty} s_i(t')s_d(t'+t)dt' \\ &=\frac{1}{2\pi}\int_{-\infty}^{\infty}\tilde{s}_i(\omega)\tilde{s}_d^*(\omega)e^{-i\omega t}d\omega. \end{aligned} \tag{3}$$

The secondary form in Eq. (3) uses Fourier transforms, denoted by tildes. Operating in either the time or frequency domain, one can show that

$$S(t)=\frac{1}{2}\sum_{n'} C(t-n'T_s)\cos(\omega_0 t+\phi_{n'}), \tag{4}$$

where $C(t)$ is the autocorrelation of the envelope

$$C(t)=\frac{1}{2\pi}\int_{-\infty}^{\infty}|\tilde{s}(\omega)|^2 e^{-i\omega t}d\omega, \tag{5}$$

and where high-frequency terms that can be removed by filtering are neglected. Through standard processing techniques the phase can be synchronized, and Eq. (4) can be sampled at the symbol rate $t=nT_s$. For mathematical convenience, $\omega_0 T_s$ is taken to be a multiple of 2π, yielding

$$S[n]\equiv S(nT_s)=\frac{1}{2}\sum_{n'} C((n-n')T_s)\cos(\phi_{n'}). \tag{6}$$

Inspecting Eq. (6), it is clear that the transmitted symbols can be recovered exactly for this noise-free case when the sampled envelope autocorrelation satisfies

$$C((n-n')T_s)=\begin{cases}1, & n=n'\\ 0, & n\neq n'.\end{cases} \tag{7}$$

A function that satisfies Eq. (7) is a form of the raised cosine

$$C(t)=\frac{\sin(\pi K_B f_s t)}{\pi K_B f_s t}, \tag{8}$$

where K_B is a nonzero integer. The described procedure gives perfect recovery of the transmitted binary data at f_s symbols per second. One can show that the bandwidth of Eq. (8) is $K_B f_s$. Consequently, the ratio of the data rate to the bandwidth—a measure of communications efficiency—is $1/K_B$. For this idealized case, choosing $K_B>1$ simply increases the bandwidth without improving the data throughput.

Time-reversal communications in the ocean borrows from the basic concept of a correlation demodulator. The above development has ignored issues like phase synchronization and sampling that must be solved in practice. Certain choices have been made to illustrate the concept in a simple mathematical setting; it is not necessary in practice, for example, to constrain the bandwidth to be an integer multiple K_B of the data rate. When considering the underwater communications in subsequent sections, K_B will be referred to as the *bandwidth factor*. It will be shown how bandwidth combines with array geometry, and knowledge of the channel response to quantify the performance of a time-reversal equalizer.

B. Time-reversal equalizer

Consider an underwater acoustics scenario where the direction of communication is from an isolated source to a distant receive-only array. Applying passive time-reversal processing to this problem combines temporal and spatial matched filtering. The temporal filtering step is developed following the notation of the previous section. In analogy with Eq. (1), let $p_d(t;\mathbf{r_m})$ be the phase-encoded data stream as observed at position $\mathbf{r_m}$ far from the transmitter. Let $p_i(t;\mathbf{r_m})$ be the corresponding known probe response. Form the cross correlation as in Eq. (3)

$$\begin{aligned} R_{id}(t;\mathbf{r_m})&=\int_{-\infty}^{\infty} p_i(t';\mathbf{r_m})p_d(t'+t;\mathbf{r_m})dt' \\ &=\frac{1}{2\pi}\int_{-\infty}^{\infty}\tilde{p}_i^*(\omega;\mathbf{r_m})\tilde{p}_d(\omega;\mathbf{r_m})e^{-i\omega t}d\omega. \end{aligned} \tag{9}$$

Assume that there are M elements in the receiving array, and that the cross correlation Eq. (9) is calculated at each. Combining yields the output of the time-reversal processor

$$P(t)=\sum_{m=1}^{M} R_{id}(t;\mathbf{r_m}). \tag{10}$$

In this section, an expression for $P(t)$ is derived in terms of the number of receiving elements M, the spacing between the elements, the bandwidth factor K_B, and the ocean waveguide geometry. The expression is then sampled at the symbol rate yielding the soft demodulation output. The soft demodulation output exhibits the effects of intersymbol interference. The reader less interested in mathematical details is referred to the final result, Eqs. (28) and (29).

To begin the derivation, it is most convenient to analyze Eq. (9) in the Fourier domain. Assuming a range-independent waveguide, the observed data stream is expanded in its normal modes[24]

$$\tilde{p}_d(\omega;\mathbf{r_m}) = \tilde{s}_d(\omega) \sum_{\mu} (\xi_\mu x_m)^{-1/2} \Psi_\mu(z_0) \Psi_\mu(z_m) \times e^{-\alpha_\mu x_m} e^{i\xi_\mu x_m}. \quad (11)$$

In Eq. (11), Ψ_μ represents the depth-dependent normal modes (eigenfunctions) with ξ_μ the corresponding horizontal wave numbers (eigenvalues) and α_μ the associated modal attenuation. The source is at range zero and depth z_0, and certain unimportant scaling factors have been suppressed. To simplify the geometry, assume each receiving array element is in the same vertical plane so $\mathbf{r_m}=(x_m,z_m)$. The phase-encoded data stream is embedded in $\tilde{s}_d(\omega)$, the Fourier transform of Eq. (1). An analogous expression for the probe response $\tilde{p}_i(\omega;\mathbf{r_m})$ can be written with $\tilde{s}_i(\omega)$ replacing $\tilde{s}_d(\omega)$.

Normal-mode expansions are more typically used at lower frequencies. At the frequencies relevant to acoustic communications, the waveguide may support several hundred modes. The modal expansion is useful for present purposes because ultimately one is not calculating the propagating acoustic field but rather the output from the time-reversal equalizer.

Returning to the cross correlation, the modal expansions are substituted into Eq. (9) and the frequency integration can be evaluated in principle. The integration is complicated by the fact that all the mode-dependent quantities, including the number of propagating modes, are implicit functions of frequency. To simplify the analysis, what is essentially a stationary phase approximation is made. Frequency dependence is ignored everywhere except in the phase. Retaining the frequency dependence in the phase is important because that is where the BPSK data are encoded. In a subsequent section, experimental data are used to test the validity of the approximation. Equation (9) becomes

$$R_{id}(t;\mathbf{r_m}) \approx \sum_{\mu,\nu} A_{\mu\nu m} I_{\mu\nu}(t), \quad (12)$$

where

$$A_{\mu\nu m} = (\xi_\mu \xi_\nu x^2)^{-1/2} \Psi_\mu(z_0) \Psi_\mu(z_m) \Psi_\nu(z_0) \times \Psi_\nu(z_m) e^{-(\alpha_\mu+\alpha_\nu)x}, \quad (13)$$

with each of the mode-dependent quantities evaluated at the center frequency ω_0. The time dependence is embedded in

$$I_{\mu\nu}(t) = \frac{1}{2\pi} \int_{-\infty}^{\infty} \tilde{s}_i^*(\omega) \tilde{s}_d(\omega) e^{i\theta_{\mu\nu}} e^{-i\omega t} d\omega, \quad (14)$$

where the phase depends on the wave number difference

$$\theta_{\mu\nu} = (\xi_\mu - \xi_\nu)x. \quad (15)$$

In the preceding, a vertical receiving array is assumed so that each of the M array elements is at the same range $x_m = x$. This assumption can be relaxed at the cost only of leaving $\theta_{\mu\nu}$ a function of the sensor index m.

Equation (14) differs from the idealized Eq. (3) by the presence of the additional complex exponential with phase $\theta_{\mu\nu}$. When the two mode indices are equal, $\theta_{\mu\mu}=0$ and Eq. (14) reduces to Eq. (4). For $\mu \neq \nu$, $\theta_{\mu\nu}$ can be expanded about the center frequencies $\pm\omega_0$

$$\theta_{\mu\nu}(\omega) \approx \theta_{\mu\nu}(\omega_0) + (\omega-\omega_0)\frac{d\theta_{\mu\nu}}{d\omega} = \omega_0 x(1/v_\mu - 1/v_\nu) + (\omega-\omega_0)x(1/u_\mu - 1/u_\nu). \quad (16)$$

In Eq. (16), u and v are the group and phase velocities, respectively, of the subscripted modes evaluated at the center frequency. It is useful to define the ratio

$$\beta_{\mu\nu} \equiv -\frac{1/v_\mu - 1/v_\nu}{1/u_\mu - 1/u_\nu}. \quad (17)$$

The quantity $\beta_{\mu\nu}$ is the finite-difference version[25,26] of the so-called waveguide invariant.[27] Often $\beta_{\mu\nu}$ is only a weak function of the mode indices and can be replaced by a constant; the canonical shallow water value is $\beta=1$.[27,28] Defining the group slowness difference $g_{\mu\nu}=1/u_\mu - 1/u_\nu$, the phase velocity terms in Eq. (16) can be eliminated, yielding

$$\theta_{\mu\nu} \approx -\omega_0 \beta_{\mu\nu} g_{\mu\nu} x + (\omega-\omega_0) g_{\mu\nu} x. \quad (18)$$

The presence of the waveguide invariant in Eq. (18) merits some comment. Generally regarded as a low-frequency concept, it arises in the present context because of the temporal matched filtering step. At high frequencies, the acoustic waveguide supports many acoustic modes. Because each mode propagates with its own velocity, the modes interfere with one another when the field is match filtered. The timing of these interference terms is dictated by the difference in group slowness between the modes taken in pairs. The difference in phase slowness between the modes is relevant because BPSK coding has been used. The phase and group slowness differences are related via the waveguide invariant. The waveguide invariant is a weak function of frequency[29] consistent with the stationary phase approximation.

To evaluate Eq. (14), the Fourier transforms $\tilde{s}_d(\omega)$ and $\tilde{s}_i(\omega)$ are calculated from Eq. (1) and Eq. (2), respectively. The integral is then broken into positive- and negative-frequency components, and the phase expansion Eq. (18) is applied to each. Evaluating the two integrals, recombining, and neglecting high-frequency terms yields

$$I_{\mu\nu}(t) = \frac{1}{2}\sum_{n'} C(t - n'T_s - g_{\mu\nu}x) \times \cos(\omega_0 t + \omega_0 \beta_{\mu\nu} g_{\mu\nu} x + \phi_{n'}), \quad (19)$$

where we recall $C(t)$ is the autocorrelation of the envelope, Eq. (5).

Together with Eq. (12), Eq. (19) represents the output of the time-reversal processor. As with the correlation demodulator in the previous section, it is assumed that perfect phase synchronization can be achieved by separate means. Sampling at $t=nT_s$ and rearranging terms gives

$$P[n]\equiv P(nT_s)=\sum_{\mu,\nu} A_{\mu\nu}I_{\mu\nu}(nT_s), \tag{20}$$

where the weights

$$A_{\mu\nu}=\sum_{m=1}^{M} A_{\mu\nu m}=(\xi_\mu\xi_\nu x^2)^{-1/2}\Psi_\mu(z_0)\Psi_\nu(z_0) \times e^{-(\alpha_\mu+\alpha_\nu)x}\sum_{m=1}^{M}\Psi_\mu(z_m)\Psi_\nu(z_m), \tag{21}$$

contain the dependence on the number M of elements in the receiving array and their positions. The transmitted data stream is embedded in

$$I_{\mu\nu}(nT_s)=\frac{1}{2}\sum_{n'} C((n-n')T_s-g_{\mu\nu}x) \times\cos(\omega_0\beta_{\mu\nu}g_{\mu\nu}x+\phi_{n'}). \tag{22}$$

Equations (20)–(22) should be compared to the correlation demodulator result, Eq. (6). The time shift $g_{\mu\nu}x$ in Eq. (22) means that the processor output at time nT_s is contaminated by the other symbols, $n'\neq n$. This intersymbol interference (ISI) fundamentally limits the performance of the time-reversal equalizer.[10–12] Note that the ISI can be reduced through spatial diversity. This can be deduced from Eq. (21) for the limiting case of a densely populated array spanning the water column: the summation is replaced by an integration over depth and, since the acoustic modes are orthogonal, the weights are zero except when the mode indices are equal, $\mu=\nu$. Since $g_{\mu\mu}=0$ by definition, there is no ISI from the remaining terms. In practice, this limit would be difficult to achieve;[22] with a shorter array and a reduced number of elements, there will be some residual ISI.

To study the ISI, Eq. (22) is evaluated for the specific envelope correlation function given in Eq. (8). Applying standard trigonometric identities, one can show that

$$C((n-n')T_s-g_{\mu\nu}x)=\delta_{\mu\nu}\delta_{nn'}+(1-\delta_{\mu\nu}) \cdot\frac{(-1)^{K_B(n-n')+1}\sin(\pi K_B f_s g_{\mu\nu}x)}{\pi K_B(n-n'-f_s g_{\mu\nu}x)}, \tag{23}$$

where Kronecker delta functions have been used to isolate the special case where the mode indices are equal. Equation (22) can be further simplified for BPSK modulation. Since $\phi_{n'}$ is constrained to be either 0 or π

$$\cos(\omega_0\beta_{\mu\nu}g_{\mu\nu}x+\phi_{n'})=\cos(\phi_{n'})\cos(\omega_0\beta_{\mu\nu}g_{\mu\nu}x). \tag{24}$$

Combining Eqs. (20)–(24), the sampled output of the time-reversal processor is

$$P[n]=\frac{1}{2}\cos(\phi_n)\sum_{\mu} A_{\mu\mu}+\frac{1}{2}\sum_{\mu\nu,\mu\neq\nu} D_{\mu\nu} \times\sum_{n'}\frac{(-1)^{K_B(n-n')+1}\cos(\phi_{n'})}{\pi K_B(n-n'-f_s g_{\mu\nu}x)}, \tag{25}$$

where

$$D_{\mu\nu}=A_{\mu\nu}\sin(\pi K_B f_s g_{\mu\nu}x)\cos(\omega_0\beta_{\mu\nu}g_{\mu\nu}x). \tag{26}$$

The first term in Eq. (25) is proportional to the desired data stream $\cos(\phi_n)$, while the second represents the ISI. Making this more explicit, define

$$C_N\equiv\left(\sum_{\nu} A_{\nu\nu}\right)^{-1}. \tag{27}$$

Then, the normalized soft demodulation output is

$$\bar{P}[n]\equiv 2C_N P[n]=\cos(\phi_n)+\varepsilon[n], \tag{28}$$

where the error from ISI is

$$\varepsilon[n]=C_N\sum_{\mu\nu,\mu\neq\nu} D_{\mu\nu}\sum_{n'}\frac{(-1)^{K_B(n-n')+1}\cos(\phi_{n'})}{\pi K_B(n-n'-f_s g_{\mu\nu}x)}. \tag{29}$$

In practice, the soft demodulation output is fed into a decision device that produces the final estimate for the transmitted symbol.

C. Statistics for time-reversal equalizer

The BPSK data are encoded in the phases ϕ_n as in Eq. (1). The derivation of Eq. (28) showed how $\cos(\phi_n)$ could be recovered after propagating through the idealized ocean waveguide using time-reversal equalizer. The recovery is not perfect, however, as reflected by the error term $\varepsilon[n]$ defined in Eq. (29). The error is due to the intersymbol interference from other symbols in the data stream. In this section, a formula for the mean-squared error (MSE) induced by the interference is derived.

Treat the phases ϕ_n as being random variables. For BPSK data, the phase is constrained to be either 0 or π. Assuming that these two values are equally likely implies $\langle\cos(\phi_n)\rangle=0$, where the angle brackets denote an ensemble average. It follows immediately from Eq. (29) that the mean error is zero. To calculate the MSE, different pairs of symbols are assumed to be uncorrelated. It follows that

$$\langle\varepsilon^2[n]\rangle=C_N^2\sum_{\mu\nu,\mu\neq\nu}\sum_{\mu'\nu',\mu'\neq\nu'} D_{\mu\nu}D_{\mu'\nu'}(\pi K_B)^{-2} \cdot\sum_{n'}[(n-n'-f_s g_{\mu\nu}x)(n-n'-f_s g_{\mu'\nu'}x)]^{-1}. \tag{30}$$

To simplify Eq. (30), ignore any transient effects from the finite length of the data stream. The limits on the summation over the symbol index n' are extended and a formula attributed to Euler[30]

$$\sum_{n'=-\infty}^{\infty} \frac{1}{(\xi-n')(\eta-n')} = \frac{\pi}{\eta-\xi}[\cot(\pi\xi)-\cot(\pi\eta)], \tag{31}$$

is used. Applying Eq. (31) and standard trigonometric identities yields

$$\langle \varepsilon^2[n]\rangle = C_N^2 \sum_{\mu\nu,\mu\neq\nu} \sum_{\mu'\nu',\mu'\neq\nu'} \frac{D_{\mu\nu}D_{\mu'\nu'}}{\pi K_B^2 f_s(g_{\mu\nu}-g_{\mu'\nu'})x} \cdot \frac{\sin(\pi f_s(g_{\mu\nu}-g_{\mu'\nu'})x)}{\sin(\pi f_s g_{\mu\nu}x)\sin(\pi f_s g_{\mu'\nu'}x)}. \tag{32}$$

Note that the MSE is independent of the output symbol index n, as one would expect when transient effects near the beginning or end of a long data stream are ignored.

Equation (32) for the MSE can be further simplified. The equation features a fourfold summation over the mode indices. The individual terms in the summation may be positive or negative, but their sum is the positive MSE. It is asserted, and later demonstrated by numerical example, that the dominant contribution to the summation in Eq. (32) occurs when the mode indices $\mu=\mu'$ and $\nu=\nu'$. Retaining only these terms

$$\sigma^2 \equiv \langle \varepsilon^2[n]\rangle = C_N^2 \sum_{\mu\nu,\mu\neq\nu} \frac{D_{\mu\nu}^2}{K_B^2 \sin^2(\pi f_s g_{\mu\nu}x)}. \tag{33}$$

Rearranging terms using Eq. (26) yields the final result for the MSE

$$\sigma^2 = C_N^2 \sum_{\mu\nu,\mu\neq\nu} A_{\mu\nu}^2 S_{\mu\nu}^2, \tag{34}$$

where

$$S_{\mu\nu}^2 = \frac{\sin^2(\pi K_B f_s g_{\mu\nu}x)\cos^2(\omega_0\beta_{\mu\nu}g_{\mu\nu}x)}{K_B^2 \sin^2(\pi f_s g_{\mu\nu}x)}. \tag{35}$$

In this partitioning, $S_{\mu\nu}^2$ contains the dependence on the signal bandwidth, as expressed in K_B, and the symbol rate f_s. The term also reflects the fact that different acoustic modes propagate with different group velocities, as expressed in $g_{\mu\nu}$, and different phase velocities. The phase and group velocities for the ocean waveguide are related via the waveguide invariant $\beta_{\mu\nu}$. The weightings $A_{\mu\nu}^2$ contain the dependence on the experimental geometry, in particular on the number M of receiving array elements and their depths; see Eq. (21). In other words, the effects of frequency diversity are contained in $S_{\mu\nu}^2$ while the effects of spatial diversity are contained in $A_{\mu\nu}^2$. The individual terms in Eq. (34) are summed over the mode indices and normalized.

III. NUMERICAL RESULTS

To illustrate the analytical results of the previous section, a particular model for the ocean waveguide is chosen. Consider an isovelocity water column with sound speed c_0 and depth d above an acoustically fast sediment. Dirichlet boundary conditions are enforced at both the sea surface and the water–sediment interface. The acoustic modes and wave numbers for this scenario are, respectively

$$\Psi_\mu(z) = \sqrt{2/d}\sin(\mu\pi z/d), \tag{36}$$

$$\xi_\mu = \sqrt{k_0^2-(\mu\pi/d)^2}, \tag{37}$$

where $k_0=\omega_0/c_0$. Associated with mode μ is the propagation angle with respect to the horizontal

$$\chi_\mu = \pm\sin^{-1}(\mu\pi/(k_0 d)). \tag{38}$$

At communications frequencies, the Dirichlet boundary condition is a reasonable approximation at the water–sediment interface provided attention is restricted to the lower order modes. Higher order modes, propagating at steeper angles, eventually exceed the critical grazing angle and are lost into the sediment. This effect is approximated by fixing the maximum number of acoustic modes $\mu_{\max}$ based on an assumed critical angle. For $\omega_0/2\pi=15$ kHz, $c_0=1500$ m/s, and $d=50$ m, a 30 deg critical angle has $\mu_{\max}=500$. Unless otherwise noted, these parameter values are used in the numerical simulations that follow. The range is fixed at 3 km, the source depth at 12 m, and the symbol rate $f_s=2500$ symbols/s.

As presently formulated, the proposed model's biggest apparent limitation is that it ignores variability in the geometry or the medium. The source or receiving array could drift with the motion changing the effective geometry. Oceanographic phenomena like surface waves, internal waves, and turbulence introduce temporal and spatial variability. When scattering from the sea surface is important, it is not unusual for the acoustic field to decorrelate in less than a second.[16,31] To reduce the difficulties imposed by a time-varying medium, Flynn *et al.*[17,18] proposed an adaptive version of time-reversal processing. In this decision-directed approach, past symbol estimates are used in a feedback loop to update the matched filters and compensate for changes in the environment. The updated matched filters are used to process the next block of data. The procedure then repeats with the matched filters updated many tens of times per second as the algorithm marches through the data stream. Both real[18] and simulated[32] data have been used to test the algorithm.

Consequently, with adaptive processing the chief limitation is not time variability *per se* but rather the fact that there is always some error in the matched filters. It is often difficult for the matched filters to represent accurately the late-arriving energy as these paths have had multiple interactions with the sea surface. The effects of imperfect channel knowledge can be approximated within the model. If there are $\mu_{\max}$ propagating modes, a reduced number of modes $\nu_{\max}$ is used to represent the matched filter. By setting $\nu_{\max}<\mu_{\max}$, the effective length of the finite impulse response matched filter is truncated, creating a mismatch between the filter and the data. Notice that as $\nu_{\max}$ is reduced, the normalization factor C_N defined in Eq. (27) increases. As a result, the error Eq. (29) also increases. Using Eq. (38), $\nu_{\max}$ can be related to an effective angle for the matched filter.

The performance of the time-reversal processor can now be quantified. Of particular interest is how the performance scales as a function of the three principle parameters: the bandwidth as expressed through K_B, the number of elements M in the receiving array, and the length of the matched filter.

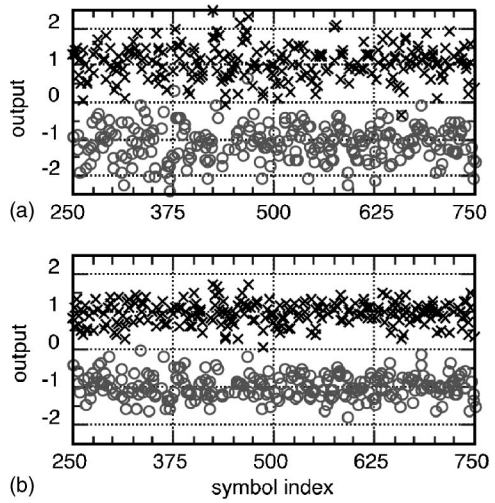

FIG. 1. Scatter plot of soft demodulation output. (a) Bandwidth equals symbol rate, $K_B=1$. (b) Bandwidth increased to twice the symbol rate, $K_B=2$. See the text for other simulation parameters.

Realizations of the processor output can be generated using Eqs. (27)–(29). The ensemble MSE can be calculated using Eq. (34)–(35).

Figure 1 shows scatter plots of the soft demodulation output. Transmitted symbols $\phi_n=0$ are mapped by an "x" and transmitted $\phi_n=\pi$ are mapped by a circle. An "x" mapped into the lower half-space of the scatter plot indicates an error, as does a circle in the upper half-space. Qualitatively, the plots are similar to those produced with experimental data.[16] The plots begin with symbol $n=250$ to avoid transients near the beginning of the data stream. For both panels, $M=10$, $\mu_{\max}=200$, and $\nu_{\max}=50$. In Fig. 1(a), the bandwidth equals the data rate so $K_B=1$. For this example, there are four errors and the sample variance is -6.5 dB. In Fig. 1(b), the bandwidth has been doubled and $K_B=2$. There are no errors and the sample variance is reduced to -10.2 dB. These sample variances can be compared to ensemble calculations. For the two cases shown, Eqs. (34)–(35) produce -7.0 and -10.0 dB, respectively. The similarity between the sample and ensemble results lends credence to the approximations made in replacing Eq. (32) with Eq. (33).

If the matched filter is a good representation of the propagation channel, time-reversal processing can be successful even in complicated environments. Figure 2 assumes a perfect matched filter with $\nu_{\max}=\mu_{\max}$. The ensemble MSE is plotted versus critical angle for various bandwidth factors K_B. In each case, there are $M=4$ array elements. The error generally increases with critical angle when there are a severely limited number of propagating modes. As the critical angle increases, the performance eventually stabilizes; adding additional propagating modes has no detrimental effect on performance provided that they are also included in the matched filter.

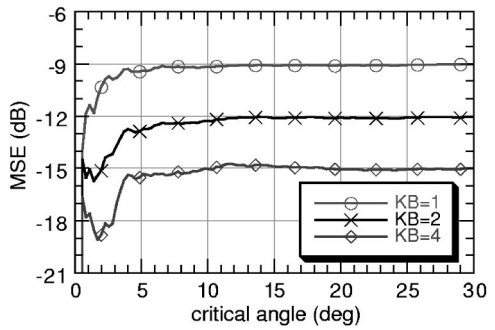

FIG. 2. Effect of critical angle on communications performance. Critical angle dictates number of propagating acoustic modes via Eq. (38). Ideal matched filter uses same number of modes. Results plotted for $M=4$ elements in receiving array and various values of the bandwidth factor K_B.

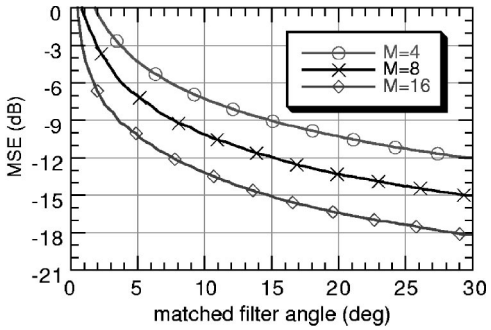

FIG. 3. Effect of matched filter truncation on communications performance. Matched filter truncated to retain energy propagating at angles less than or equal to the critical angle of 30 deg. Results plotted for bandwidth factor $K_B=2$ and M array elements.

In Fig. 2, perfect knowledge is assumed for the matched filter. In Fig. 3, the more realistic scenario of a truncated matched filter is considered. The critical angle is fixed at 30 deg and the MSE is calculated as a function of the matched filter angle. The bandwidth factor $K_B=2$ and the calculation is made for various M array elements. Note that an approximately 3-dB improvement in performance is achieved by either doubling the number of array elements or doubling the length of the matched filter. The result suggests how in practice one can compensate for imperfect channel knowledge by increasing the number of array elements.

In Fig. 4, the MSE is plotted as a function of the number of array elements for various K_B. The matched filter angle is 5 deg. Doubling either the number of array elements or the bandwidth improves the performance by approximately 3 dB. In practice, bandwidth may be a precious commodity, particularly if there are multiple users trying to communicate simultaneously. The result suggests how one could compen-

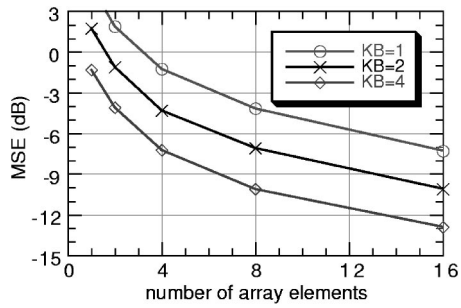

FIG. 4. Effect of number of array elements on communications performance. Calculation has critical angle 30 deg and matched filter angle 5 deg. Various values for bandwidth factor K_B.

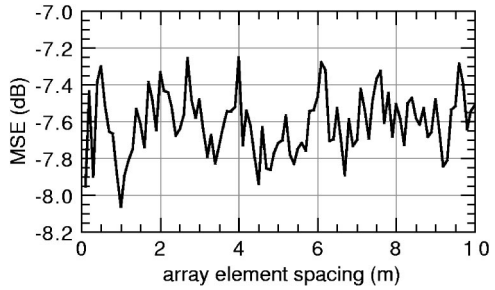

FIG. 5. Effect of element spacing on communications algorithm performance. Calculation has critical angle 30 deg and matched filter angle 5 deg. $M=3$ array elements centered in water column with uniform spacing between elements. Bandwidth factor $K_B=6$.

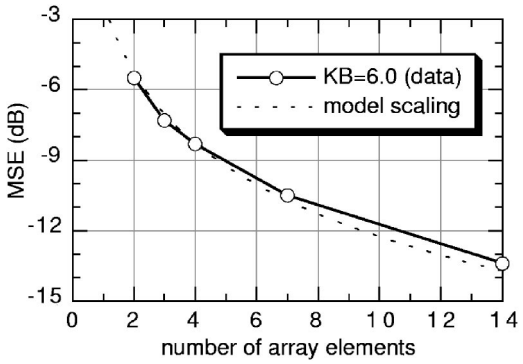

FIG. 6. Experimental results showing effect of number of array elements on communications performance. Dashed line shows scaling predicted by model. See the text for details of experiment.

sate for a reduction in the available bandwidth by increasing the number of array elements.

In Figs. 1–4, the calculations were made with an array spanning the water column and uniform spacing between the elements. To study the effects of element spacing, consider Fig. 5. The $M=3$ element vertical array is centered in the water column and the separation between the elements is varied. The bandwidth is fixed with $K_B=6$ and the matched filter angle is 5 deg. The results fluctuate by a fraction of a decibel, suggesting a weak dependence on array spacing. This result can have important implications for designing a communications system based on time-reversal processing: it is not necessary to have an array spanning the water column, as similar performance might be achieved using a much shorter aperture.[22] The number of array elements is more important than their distribution in depth. An important caveat is that these calculations assumed an isovelocity water column. For a more complicated environment, one obviously would not want a small aperture to be in a shadow zone of the source.

IV. COMPARISON WITH EXPERIMENTS

The model of the previous sections predicts how the performance of the time-reversal processor scales with parameters like bandwidth, matched filter length, and array geometry. Some of these predictions can be tested using archival data from field experiments. The present emphasis is on how the measured performance scales with experimental parameters that can be readily varied; no attempt is made in these initial model-data comparisons to predict the absolute performance level. To be consistent with the assumptions made in developing the model, only data with high ambient SNR are used.

The model is tested using data taken during an experiment in Puget Sound near Seattle in May 2000.[16] A 14-element receiving array was deployed in waters between 30 and 50 m deep. Probe pulses and simple PSK data streams, 5 s in duration, were sent at ranges up to 5 km. The center frequency was 11.5 kHz and the -40-dB bandwidth was 13 kHz. Data were transmitted at 2174 symbols/s. Note that, unlike in the analysis, the bandwidth in the experiment was not constrained to be an integer multiple of the symbol rate; the corresponding equivalent bandwidth factor is $K_B=6.0$. Grab samples showed the bottom to be a sand/silt sediment. The measured sound speed in the water column was nearly depth independent with nominal value 1480 m/s.

Figure 6 shows an example of how communications performance scales with the number of array elements. For this deployment, the array was vertical with 2-m spacing between the elements. The range to the transmitter was 0.9 km and the ambient SNR was 38.5 dB. The finite impulse response matched filter was 108 symbols long and updated using the decision-directed algorithm every 100 symbols.[18] Various subsets of the full 14-element array were used and plotted results represent averages. For example, the seven-element result is an average of using the top, middle, and bottom seven elements in the array. The points connected by a solid line show the averaged data, while the dashed line shows the scaling predicted by the model. Consistent with the model, the data show the performance improving by approximately 3 dB as the number of array elements is doubled.

With some exceptions,[33] studies of time-reversal processing in the ocean have emphasized vertical arrays. The vertical array calculation in Fig. 5 showed that the spacing between the elements had only a minimal effect on the communications performance. As an additional test of the model, consider field data taken when the array was deliberately curved away from the vertical.[34] Figure 7 is a scale diagram

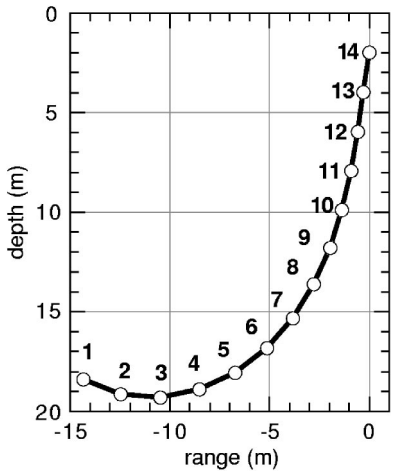

FIG. 7. Scale diagram of curved receiving array deployed during experiment. Fourteen array elements shown as function of depth and range. See the text for details of experiment.

TABLE I. Effect of element spacing on communications algorithm performance. Results for curved array experiment.

Aperture	MSE (dB)
(2,3,4)	−7.33
(6,7,8)	−7.73
(11,12,13)	−7.71
(1,7,14)	−7.60
All 14 elements	−13.27

showing the location in depth and relative range of the 14 elements during the curved array deployment. The transmitter was located 1.0 km away at bearing, approximately 10 deg relative to array endfire.

Table I shows performance results for one 5-s transmission using different subapertures of the full array. Using just three array elements to do the processing, the triplet of elements (6,7,8) near the middle of the water column produced results similar to the shallow group (11,12,13). The results are also similar to the widely spaced triplet (1,7,14). Interestingly, the nearly horizontal triplet (2,3,4) performs within 0.4 dB of the other, more vertical apertures. The variability between the different triplets in Table I is within the levels suggested by Fig. 6. The weak dependence on array geometry that is observed in both the data and the simulations may be a result of the high-frequency acoustic field having a short spatial correlation length in shallow water.[35]

V. CONCLUDING REMARKS

Passive time-reversal acoustic signal processing produces pulse compression. Because this compression is not perfect, an underwater communications algorithm that relies on time reversal to achieve equalization will have an error floor that limits performance. The error floor is caused by uncompensated intersymbol interference. In the present paper, a physics-based model for this interference is developed. The calculation is taken ''through the sensor'' to predict the mean-squared error caused by the interference at the output of the processing algorithm. To a limited extent, the model has been compared to archival experimental results with good agreement.

Numerical results show how the communications performance scales with the three principle parameters: the bandwidth, the number of array elements, and the length of the finite impulse response matched filters. In practice, each of these parameters is controlled at a different stage in the processing. The ratio of the bandwidth to the data rate is set at the transmitter. The number of elements in the array is set at the receiver. The stability of the intervening ocean effectively dictates the length of the matched filter that is feasible. In designing a communications system based on passive time reversal, one could imagine making trade-offs between bandwidth, array size, and the achievable filter length based on local conditions. The numerical results also show that the communications performance depends only weakly on the details of the array geometry, at least for vertical arrays. This suggests that a practical system might be designed using a spatially compact array; it is not necessary for the receiving array to span the water column. The analysis in this paper has been limited to vertical arrays, but it should be straightforward to consider more general configurations.

The goal of this paper has been to develop a physics-based model for uncompensated intersymbol interference in a time-reversal equalizer. The simple model for the environment used in the numerical calculations was adequate for testing the broader model and for predicting how performance should scale with the principal parameters. A more rigorous test would be to predict not just how the performance scales but to predict the absolute performance level that could be achieved at a particular site. To make these predictions, it would be necessary to use a better model for the environment. A better model for how the acoustic modes attenuate would probably be needed as well. The effects of ambient noise and reverberation could also be included. It is hoped that the present work will prove useful in developing a predictive model for communications system performance.

ACKNOWLEDGMENTS

John Flynn analyzed the field experiment data that were used to test the model in Sec. IV. The author thanks Darrell Jackson and Warren Fox for several useful conversations in the development of this work. The anonymous reviewers made many helpful suggestions. The Office of Naval Research supported this work under the ARL Program.

[1] A. Parvulescu, ''Matched-signal (MESS) processing by the ocean'' J. Acoust. Soc. Am. **98**, 943–960 (1995).
[2] D. R. Jackson and D. R. Dowling, ''Phase conjugation in underwater acoustics,'' J. Acoust. Soc. Am. **89**, 171–181 (1991).
[3] D. R. Dowling, ''Acoustic pulse-compression using passive phase-conjugate processing,'' J. Acoust. Soc. Am. **95**, 1450–1458 (1994).
[4] W. A. Kuperman, W. S. Hodgkiss, H. C. Song, T. Akal, and D. R. Jackson, ''Phase conjugation in the ocean: Experimental demonstration of an acoustic time-reversal mirror,'' J. Acoust. Soc. Am. **103**, 25–40 (1998).
[5] M. Stojanovic, J. A. Catipovic, and J. G. Proakis, ''Phase-coherent digital communications for underwater acoustic channels,'' IEEE J. Ocean. Eng. **19**, 100–111 (1994).
[6] D. B. Kilfoyle and A. B. Baggeroer, ''The state of the art of underwater acoustic telemetry,'' IEEE J. Ocean. Eng. **25**, 4–27 (2000).
[7] A. Derode, A. Tourin, J. de Rosny, M. Tanter, S. Yon, and M. Fink, ''Taking advantage of multiple scattering to communicate with time-reversal antennas,'' Phys. Rev. Lett. **90**, 014301–014304 (2003).
[8] P. Blomgren, G. Papanicolaou, and H. Zhao, ''Super-resolution in time-reversal acoustics,'' J. Acoust. Soc. Am. **111**, 230–248 (2002).
[9] A. D. Kim, P. Kyritsi, P. Blomgren, and G. Papanicolaou, ''Low probability of intercept and intersymbol interference in multiple-input/single-output time reversal communication systems,'' IEEE J. Ocean Eng. (submitted). Available from adkim@math.stanford.edu
[10] J. A. Flynn, J. A. Ritcey, W. L. J. Fox, and D. Rouseff, ''Performance of reduced-complexity multi-channel equalizers for underwater acoustic communications,'' in *Thirty-Sixth Asilomar Conference on Signals, Systems and Computers* (IEEE, New York, 2002), Vol. 1, pp. 453–460.
[11] M. Stojanovic, ''Spatio-temporal focusing for elimination of multipath effects in high rate acoustic communications,'' in *High Frequency Ocean Acoustics*, edited by M. B. Porter, M. Siderius, and W. A. Kuperman (AIP, New York, 2004).
[12] J. Preisig, ''The impact of underwater acoustic channel structure and dynamics on the performance of adaptive coherent equalizers,'' in *High Frequency Ocean Acoustics*, edited by M. B. Porter, M. Siderius, and W. A. Kuperman (AIP, New York, 2004).
[13] T. Akal, G. Edelmann, S. Kim, W. S. Hodgkiss, W. A. Kuperman, and H. C. Song, ''Low and high frequency ocean acoustic phase conjugation experiments,'' in Proceedings Fifth European Conference on Underwater Acoustics (EC 2000), pp. 989–994.
[14] G. F. Edelmann, T. Akal, W. S. Hodgkiss, S. Kim, W. A. Kuperman, and H. C. Song, ''An initial demonstration of underwater acoustic communication using time reversal,'' IEEE J. Ocean. Eng. **27**, 602–609 (2002).

[15] M. Heinemann, A. Larraza, and K. B. Smith, ''Experimental studies of applications of time-reversal acoustics to noncoherent underwater communications,'' J. Acoust. Soc. Am. **113**, 3111–3116 (2003).
[16] D. Rouseff, D. R. Jackson, W. L. J. Fox, J. A. Ritcey, and D. R. Dowling, ''Underwater acoustic communications by passive phase conjugation: Theory and experimental results'' IEEE J. Ocean. Eng. **26**, 821–831 (2001).
[17] J. A. Flynn, J. A. Ritcey, W. L. J. Fox, D. R. Jackson, and D. Rouseff, ''Decision-directed passive phase conjugation: equalisation performance in shallow water,'' Electron. Lett. **37**, 1551–1553 (2001).
[18] J. A. Flynn, J. A. Ritcey, D. Rouseff, and W. L. J. Fox, ''Multichannel equalization by decision-directed passive phase conjugation: experimental results,'' IEEE J. Ocean. Eng. **29**, 824–836 (2004).
[19] P. Hursky, M. B. Porter, J. A. Rice, and V. K. McDonald, ''Passive phase-conjugate signaling using pulse-position modulation,'' in *Oceans '01* (IEEE, New York, 2001), Vol. 4, pp. 2244–2249.
[20] A. Silva, S. Jesus, J. Gomes, and V. Barroso, ''Underwater acoustic communication using a 'virtual' electronic time-reversal mirror approach,'' in Proceedings Fifth European Conference on Underwater Acoustics (EC 2000), pp. 531–536.
[21] A. J. Silva and S. M. Jesus, ''Underwater communications using virtual time reversal in a variable geometry channel,'' in *Oceans '02* (IEEE, New York, 2002), Vol. 4, pp. 2416–2421.
[22] T. C. Yang, ''Temporal resolutions of time-reversal and passive-phase conjugation for underwater acoustic communications,'' IEEE J. Ocean. Eng. **28**, 229–245.
[23] J. G. Proakis, *Digital Communications*, 3rd ed. (McGraw-Hill, New York, 1995).
[24] F. B. Jensen, ''Wave theory modeling: A convenient approach to cw and pulse propagation modeling in low-frequency acoustics,'' IEEE J. Ocean. Eng. **13**, 186–197 (1988).
[25] V. M. Kuz'kin, ''The effect of variability of ocean stratification on a sound field interference structure,'' Acoust. Phys. **41**, 300–301 (1995).
[26] D. Rouseff and R. C. Spindel, ''Modeling the waveguide invariant as a distribution,'' in *Ocean Acoustic Interference Phenomena and Signal Processing*, edited by W. A. Kuperman and G. L. D'Spain (AIP, New York, 2002), Chap. 5, pp. 137–148.
[27] S. D. Chuprov, ''Interference structure of a sound field in a layered ocean,'' in *Ocean Acoustics. Current State*, edited by L. M. Brekhovskikh and I. B. Andreevoi (Nauka, Moscow, 1982), pp. 71–91.
[28] L. M. Brekhovskikh and Y. P. Lysanov, *Fundamentals of Ocean Acoustics*, 2nd ed. (Springer, New York, 1991), pp. 140–145.
[29] G. L. D'Spain and W. A. Kuperman, ''Application of waveguide invariants to analysis of spectrograms from shallow water environments that vary in range and azimuth,'' J. Acoust. Soc. Am. **106**, 2454–2468 (1999).
[30] T. J. I'A. Bromwich, *An Introduction to the Theory of Infinite Series*, 2nd ed. rev. (Macmillan, London, 1926), p. 225.
[31] M. Badiey, Y. Mu, J. A. Simmen, and S. E. Forsythe, ''Signal variability in shallow-water channels,'' IEEE J. Ocean. Eng. **25**, 492–499 (2000).
[32] D. Rouseff, J. A. Flynn, W. L. J. Fox, and J. A. Ritcey, ''Acoustic Communication Using Time-Reversal Signal Processing: Spatial and Frequency Diversity,'' in *High Frequency Ocean Acoustics*, edited by M. B. Porter, M. Siderius, and W. A. Kuperman (AIP, New York, 2004).
[33] M. R. Dungan and D. R. Dowling, ''Orientation effects on linear time-reversing array retrofocusing in shallow water,'' J. Acoust. Soc. Am. **112**, 1842–1852 (2002).
[34] D. Rouseff, J. A. Flynn, W. L. J. Fox, and J. A. Ritcey, ''Decision-directed passive phase conjugation for underwater acoustic communication: Experimental results,'' in *Oceans '02* (IEEE, New York, 2002), Vol. 4, pp. 2422–2424.
[35] P. D. Dahl, ''Forward scattering from the sea surface and the van Cittert–Zernike theorem,'' J. Acoust. Soc. Am. **115**, 589–599 (2004).

Characterization of subwavelength elastic cylinders with the decomposition of the time-reversal operator: Theory and experiment

Jean-Gabriel Minonzio and Claire Prada
Laboratoire Ondes et Acoustique, Université Denis Diderot, UMR CNRS 7587 ESPCI, 10 rue Vauquelin, 75231 PARIS Cedex 05, France

David Chambers[a)]
Department of Electrical and Computer Engineering, University of California Santa Barbara, Santa Barbara, California

Dominique Clorennec and Mathias Fink
Laboratoire Ondes et Acoustique, Université Denis Diderot, UMR CNRS 7587 ESPCI, 10 rue Vauquelin, 75231 PARIS Cedex 05, France

(Received 9 January 2004; revised 6 September 2004; accepted 9 September 2004)

The decomposition of the time-reversal operator provides information on the scattering medium. It has been shown [Chambers and Gautesen, J. Acoust. Soc. Am. **109**, 2616–2624 (2001)] that a small spherical scatterer is in general associated with four eigenvalues and eigenvectors of the time-reversal operator. In this paper, the 2D problem of scattering by an elastic cylinder, imbedded in water, measured by a linear array of transducers is considered. In this case, the array response matrix has three nonzero singular values. Experimental results are obtained with linear arrays of transducers and for wires of different diameters smaller that the wavelength. It is shown how the singular value distribution and the singular vectors depend on the elastic velocities c_L, c_T, the density ρ of each wire, and on the density ρ_0 and velocity c_0 of the surrounding fluid. These results offer a new perspective towards solution of the inverse problem by determining more than scattering contrast using conventional array processing like that used in medical ultrasonic imaging. © *2005 Acoustical Society of America.* [DOI: 10.1121/1.1811471]

PACS numbers: 43.60.Pt, 43.28.We, 43.20.Fn [DRD] Pages: 789–798

I. INTRODUCTION

The analysis of acoustic scattering is an important tool for object identification. It has applications among nondestructive evaluation, medical imaging, or underwater acoustics. The DORT method is a new approach to scattering analysis that was developed in 1994. It was derived from the theoretical analysis of acoustic time-reversal mirror (TRM) used in the pulse echo mode. DORT is the French acronym for Décomposition de l'Opérateur de Retournement Temporel. It consists of the determination of the invariants of the time-reversal operator (TRO). It was applied to detection and selective focusing through nonhomogeneous multiple targets media.[1,2] It has also been applied to nondestructive evaluation,[3] and characterization of a cylindrical shell through the analysis of the circumferential Lamb modes.[4] While the time-reversal mirror has been shown to be very interesting for spatial and temporal focusing in shallow water,[5–7] the DORT method has also shown high potential for highly resolved detection in a water waveguide.[8–10] This method applies to all type of linear waves and it appears to be interesting for electromagnetic scattering and inverse problem.[11,12]

For all these applications, a good understanding of the invariants of the time-reversal operator is required. Some experimental results obtained in a former study revealed the multiplicity of the invariant of the time-reversal operator for a rigid cylinder immersed in water.[13] In the present paper, we study these invariants for elastic cylinders theoretically and experimentally. In Sec. II, we derive an expression for the array response matrix **K** in two dimensions for the case of a linear array and an elastic cylinder in a fluid medium. The singular value decomposition (SVD) is applied to **K** to determine the number of singular values generated by the cylinder. For the particular case of low frequency (small cylinder), analytic expressions for the singular values and singular vectors are obtained and used to interpret the acoustic scattering mechanism that generates each eigenstate of the time-reversal operator. We use the approach found in recent analyses of time reversal for spheres.[14,15] We will develop the theory for a discrete array at a single frequency ω and then give the final results. In Sec. III, experimental results for thin steel and nylon cylinders are described. It is shown that the analysis of singular values and singular vectors of the transfer matrix **K** offers the possibility to characterize cylinders of subwavelength diameter.

[a)]Correspondence address: Lawrence Livermore National Laboratory, P.O. Box 808, L-154, Livermore, CA 94551.

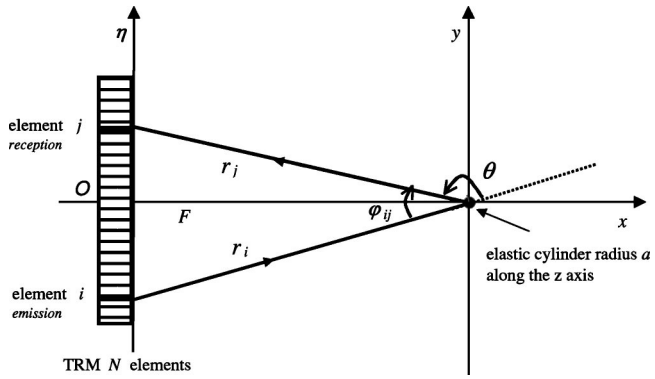

FIG. 1. Geometry of the experiment: F is the distance between the elastic cylinder and the array. The cylinder is perpendicular to the plane insonified by the N-elements array.

II. THEORY

A. Reduced array response matrix for an isotropic scatterer

First of all, an array of N transmit–receive transducers insonifying a static scattering medium is considered as a linear, time-invariant system of N inputs and N outputs. It is characterized at each frequency ω by the array response matrix $\mathbf{K}(\omega)$. The matrix $\mathbf{K}^*(\omega)\mathbf{K}(\omega)$ is called the time-reversal operator,[1] TRO (the notation* means complex conjugate). Its eigenvectors can be interpreted as invariants of the time-reversal process.

As discussed in several papers,[16] if the scattering medium contains a single isotropic scatterer, the array response matrix is easily written as the product of three elements:

(i) a propagation vector of size $N\times 1$, written $\mathbf{H}$, that describes the transmission and the propagation from the N transducers to the scatterer. The coefficient H_i of the vector corresponds to the Fourier transform of the impulse response from transducer number i to the scatterer.
(ii) a scattering coefficient c, which corresponds to the reflectivity of the scatterer.
(iii) a backpropagation vector which is ${}^t\mathbf{H}$ due to the reciprocity principle. The notation ^{t} is used for the transpose operation.

The array response matrix is then

$$\mathbf{K}=\mathbf{H}c\,{}^t\mathbf{H}. \tag{1}$$

We see that in the case of a single isotropic scatterer, things are very simple: the expression above provides directly the singular value decomposition (SVD) of $\mathbf{K}$. In this particular case, there is one nonzero singular value c, and one singular vector $\mathbf{H}$.

We now introduce a reduced array response matrix that will be used in the following analysis. Assuming $k_0F\gg 1$, where F is the distance between the scatterer and the array, and k_0 is the wave number in water (Fig. 1), we can use the far-field form (large argument) of the propagation Green's function in two dimensions in the expression for element number i of the propagation vector

$$H_i(\omega)=\sqrt{\frac{2}{i\pi k_0}}\frac{e^{ik_0r_i}}{\sqrt{r_i}}. \tag{2}$$

For that case, the 2D cylindrical Green's function is the Hankel function. Note that r_i is the distance from the scatterer to the transducer number i. Each element of the array response matrix is then

$$K_{ij}(\omega)=p_0\frac{2}{i\pi k_0}\frac{e^{ik_0r_i}}{\sqrt{r_i}}\frac{e^{ik_0r_j}}{\sqrt{r_j}}c, \tag{3}$$

where p_0 is the amplitude of the pressure emitted by a transducer. We introduce the matrix of the phase terms $\mathbf{T}$. It contains the N phase element $e^{ik_0r_i}$ corresponding to the propagation between the transducer number i and the scatterer, i.e., a diagonal coefficient is $T_{ii}=e^{ik_0r_i}$. $\mathbf{T}$ is unitary and diagonal. It is possible to write the array response matrix as

$$\mathbf{K}(\omega)=p_0\frac{2}{i\pi k_0}\mathbf{T}\mathbf{K}^{\text{reduced}}(\omega)\mathbf{T}. \tag{4}$$

An element of the reduced array response matrix is then written

$$K_{ij}^{\text{reduced}}(\omega)=\frac{c}{\sqrt{r_ir_j}}. \tag{5}$$

In the case of a single isotropic scatterer, this reduced matrix is real and symmetrical. Thus, the singular value decomposition is reduced to diagonalization. We shall see that this reduction is always possible in the far-field approximation and we shall use it for simplicity in the case of anisotropic scatterer.

B. Reduced array response matrix for an elastic cylinder

The pressure field scattered by an elastic cylinder, even for a small cylinder, is not isotropic. In far-field conditions, the field scattered from a plane wave is given, in polar coordinates r and θ, by a sum of partial waves[18,19]

$$P_{\text{sca}}(r,\theta)=p_0\sqrt{\frac{2}{i\pi k_0r}}e^{ik_0r}\sum_{n=0}^{\infty}\epsilon_nR_n\cos(n\theta), \tag{6}$$

where R_n are the scattering coefficients, θ is the angle at the origin between the field point and direction of the incident plane wave, and r is the distance between the scatterer and the field point (Fig. 1). The Neumann coefficients are $\epsilon_0=1$ and $\epsilon_n=2$ for $n\geqslant 1$. As before, we have used the far-field form of the field, replacing the Hankel functions with their asymptotic expressions for large arguments. The scattering coefficients are the coefficients found in Flax *et al.*[18] These are functions of the physical parameters of the cylinders, density ρ_1, radius a, transverse and longitudinal wave speeds (c_T and c_L), and the physicals parameters of the fluid surrounding, velocity c_0 and density ρ_0.

Each term of the sum corresponds to a partial wave, or normal mode. The first term R_0 produces a monopole wave that is circularly symmetric. The second term $2R_1\cos(\theta)$ produces a dipole partial wave, the third term $2R_2\cos(2\theta)$ a quadrupole partial wave, and so on. Thus, the values of the

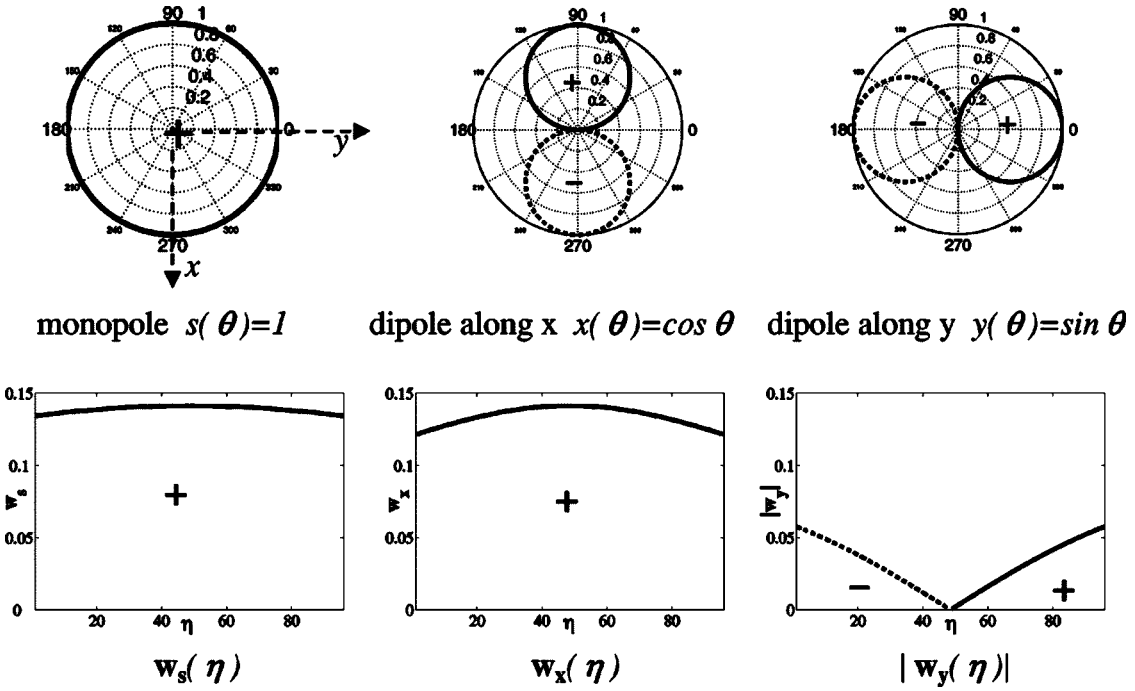

FIG. 2. Normal modes in polar coordinates and their projections onto the array: The normal modes *s*, *x*, and *y* are orthogonal, whereas the projections $\mathbf{w}_s$, $\mathbf{w}_x$, and $\mathbf{w}_y$ are not. The projected modes $\mathbf{w}_s$ and $\mathbf{w}_x$ are symmetric around the *x* axis, whereas $\mathbf{w}_y$ is antisymmetric.

R_n coefficients determine the shape of the scattered field. Let η denote the position along the axis of the array, with η_i the position of transducer number *i*. The position vectors for transducers *i* and *j* are $\mathbf{r}_i=\begin{bmatrix}-F\\ \eta_i\end{bmatrix}$ and $\mathbf{r}_j=\begin{bmatrix}-F\\ \eta_j\end{bmatrix}$, with the angle between them given by $\cos(\varphi_{ij})=(\mathbf{r}_i\cdot\mathbf{r}_j)/r_ir_j=(F^2+\eta_i\eta_j)/r_ir_j$. If the radius *a* of the cylinder is much smaller than the distance to the array ($a\ll F$), the field emitted from transducer *i* is a plane wave at the cylinder, and the scattered field received by transducer *j* will be given by Eq. (6) with $\theta=\pi-\varphi_{ij}$. Using $\cos(n\theta)=(-1)^n\cos(n\varphi_{ij})$, the reduced array response matrix for the case of a single elastic scattering cylinder can be written as

$$K_{ij}^{\text{reduced}}(\omega)=\frac{1}{\sqrt{r_ir_j}}\sum_{n=0}^{\infty}\epsilon_nR_n(-1)^n\cos(n\varphi_{ij}). \tag{7}$$

We notice that the expressions for the reduced array response matrices for isotropic or anisotropic scatterers are similar, in far-field conditions. We introduce the scattering coefficient C_{ij} equal to the sum $\Sigma_{n=0}^{\infty}\epsilon_nR_n(-1)^n\cos(n\varphi_{ij})$, where C_{ij} is an element of the $N\times N$ matrix $\mathbf{C}$. Thus, the general form for an element of the reduced array response matrix is

$$K_{ij}^{\text{reduced}}(\omega)=\frac{C_{ij}}{\sqrt{r_ir_j}}. \tag{8}$$

Note that the matrix $\mathbf{C}$ reduces to a scalar *c* in the case of an isotropic scatterer. It is independent of the positions of the transducers *i* and *j* with respect to the scatterer and $\mathbf{K}^{\text{reduced}}$ is rank 1. For the elastic cylinder, $\mathbf{C}$ is a matrix defined by the infinite sum. The rank of $\mathbf{K}^{\text{reduced}}$ depends on the number of significant R_n. We shall see that if only R_0 and R_1 are significant, $\mathbf{K}^{\text{reduced}}$ is rank 3.

C. Reduced array response matrix for a small elastic cylinder

Though the sum is formally over an infinite number of terms, the coefficients for $n\gg k_0a$ are exponentially small and the sum can be truncated with little error.[15] For the case of a thin cylinder ($k_0a\ll1, k_La\ll1, k_L=\omega/c_L$), the scattering for $n\geqslant2$ can be ignored[18] and the scattered pressure becomes

$$P_{\text{sca}}(r_j,\varphi_{ij})=p_0\sqrt{\frac{2}{i\pi k_0r_j}}e^{ik_0r_j}\left(R_0-2R_1\cos\varphi_{ij}+o\left(2\pi\frac{a}{\lambda}\right)\right). \tag{9}$$

The two first scattering coefficients are[20]

$$R_0=i\frac{\pi k_0^2a^2}{4}\left(\frac{\rho_0c_0^2}{\rho_1(c_L^2-c_T^2)}-1\right)=i\frac{\pi k_0^2a^2}{4}\left(\frac{B_0}{\lambda+\mu}-1\right), \tag{10}$$

$$R_1=-i\frac{\pi k_0^2a^2}{4}\frac{\rho_1-\rho_0}{\rho_1+\rho_0}. \tag{11}$$

In this approximation an element of the reduced scattering matrix becomes (omitting the term $-i[\pi k_0^2a^2/4]$)

$$K_{ij}^{\text{reduced}}(\omega)=\frac{1}{\sqrt{r_ir_j}}\left(\alpha+\beta\frac{F^2+\eta_i\eta_j}{r_ir_j}\right). \tag{12}$$

The constants α and β are[20]

$$\alpha=\left(1-\frac{B_0}{\lambda+\mu}\right),\quad \beta=2\frac{\rho_1-\rho_0}{\rho_1+\rho_0}, \tag{13}$$

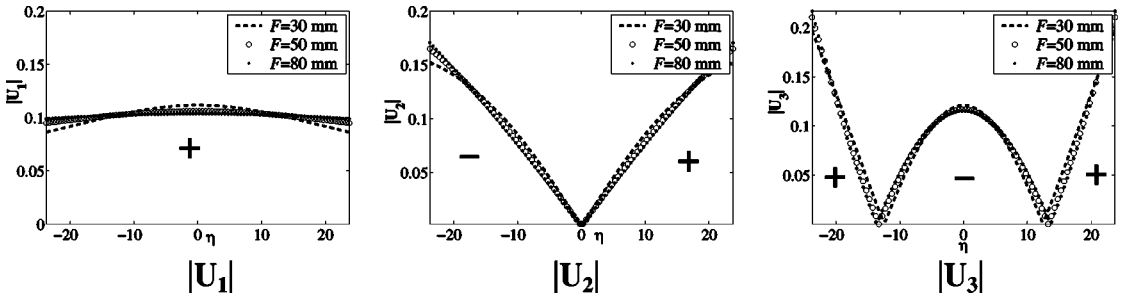

FIG. 3. The three singular vectors $\mathbf{U_1}$, $\mathbf{U_2}$, and $\mathbf{U_3}$ are calculated analytically with the small cylinder approximation along the array (η coordinate). Their modulus are ploted for different distances F between the scatterer and the array: 30 mm (--), 50 mm (○), and 80 mm (*). The variations with the distance are weak.

where λ and μ are the Lamé elastic constants of the cylinder, and B_0 is the bulk modulus (inverse of compressibility) of the fluid. For a 2D-elastic medium, the bulk modulus is $B=\lambda+\mu$ [$B=\lambda+(2/3)\mu$ for a 3D-elastic medium]. The term proportional to α represents scattering by the compressibility contrast. It produces a monopolar radiation pattern that is circularly symmetric. The term proportional to β represents scattering by the density contrast, which produces dipolar radiation pattern (Fig. 2).

D. Analysis of reduced array response matrix for a small elastic cylinder

An element of the matrix can be rewritten as the sum of three separable terms

$$K_{ij}^{\text{reduced}}=\alpha\frac{1}{\sqrt{r_i}}\frac{1}{\sqrt{r_j}}+\beta\frac{F}{r_i^{3/2}}\frac{F}{r_j^{3/2}}+\beta\frac{\eta_i}{r_i^{3/2}}\frac{\eta_j}{r_j^{3/2}}. \tag{14}$$

Let $\mathbf{w_s}$, $\mathbf{w_x}$, and $\mathbf{w_y}$ be the three vectors which correspond to the projection of the normal modes on the TRM (Fig. 2). The elements number i of these vectors, corresponding to the transducer number i, are

$$w_s(\eta_i)=\frac{1}{r_i^{1/2}},\quad w_x(\eta_i)=\frac{F}{r_i^{3/2}},\quad w_y(\eta_i)=\frac{\eta_i}{r_i^{3/2}}. \tag{15}$$

We see that $\mathbf{K}^{\text{reduced}}=\alpha\mathbf{w_s}\,{}^t\mathbf{w_s}+\beta\mathbf{w_x}\,{}^t\mathbf{w_x}+\beta\mathbf{w_y}\,{}^t\mathbf{w_y}$, is the sum of three $N\times N$ matrices of rank 1 which implies that the rank of $\mathbf{K}^{\text{reduced}}$ is 3 as long as α and β are nonzero.

Whatever the emitted signal, the measurement of the scattered field is a linear combination of these three projected vectors. The array response matrix can then be expressed in this new basis and the singular vectors $\mathbf{U_i}$ ($\mathbf{i}=1,2,3$) are linear combinations of the $\mathbf{w_n}$ ($\mathbf{n}$ and $\mathbf{m}$ are used for the indexes $\mathbf{s}$, $\mathbf{x}$, or $\mathbf{y}$), $\mathbf{U_i}=\chi_s\mathbf{w_s}+\chi_x\mathbf{w_x}+\chi_y\mathbf{w_y}$. We denote W_{nm} the scalar product between the vectors $\mathbf{w_n}$ and $\mathbf{w_m}$: $W_{nm}=\langle\mathbf{w_n}|\mathbf{w_m}\rangle=\Sigma_{i=1}^{N}w_n(i)w_m(i)={}^t\mathbf{w_n}\cdot\mathbf{w_m}$. In general, the SVD of $\mathbf{K}$ reduces to solving for the eigenvalues and eigenvectors of a 3×3 matrix, expressed in the new basis of the $\mathbf{w_n}$

$$\begin{bmatrix}\alpha W_{ss} & \alpha W_{sx} & \alpha W_{sy}\\ \beta W_{sx} & \beta W_{xx} & \beta W_{xy}\\ \beta W_{sy} & \beta W_{xy} & \beta W_{yy}\end{bmatrix}\begin{bmatrix}\chi_s\\ \chi_x\\ \chi_y\end{bmatrix}=\lambda\begin{bmatrix}\chi_s\\ \chi_x\\ \chi_y\end{bmatrix}. \tag{16}$$

If the position of the cylinder is symmetrical with respect to the array, the matrix simplifies to

$$\begin{bmatrix}\alpha W_{ss} & \alpha W_{sx} & 0\\ \beta W_{sx} & \beta W_{xx} & 0\\ 0 & 0 & \beta W_{yy}\end{bmatrix}\begin{bmatrix}\chi_s\\ \chi_x\\ \chi_y\end{bmatrix}=\lambda\begin{bmatrix}\chi_s\\ \chi_x\\ \chi_y\end{bmatrix}. \tag{17}$$

Thus, the reduced array response matrix for a thin cylinder may have as many as three distinguishable singular values and singular vectors. If the density contrast β is zero, there is only one singular value. The interpretation of the

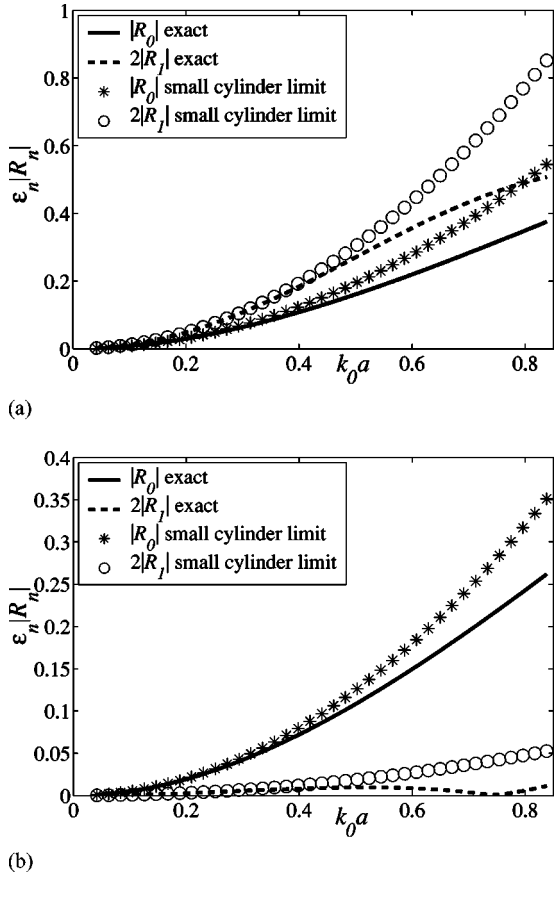

FIG. 4. Coefficients of normal modes $\epsilon_n R_n$ (no dimension) versus k_0a: comparison between the exact value and the approximation for small objects (only the two first coefficients are taken into account). The approximation is valid for k_0a less than 0.5. In the case of steel (a), the two coefficients R_0 and $2R_1$ are of the same order, whereas, in the case of nylon (b), the second coefficient $2R_1$ is small because of the small density contrast.

TABLE I. Physical parameters of steel and nylon.

	ρ (g·cm^{-3})	c_L (mm·μs^{-1})	c_T (mm·μs^{-1})	α	β	β/α
Steel	7.8	5.75	3	0.99	1.55	1.56
Nylon	1.15	2.5	1.05	0.62	0.14	0.23
Water	1	1.48				

singular values is analogous to that for the sphere studied by Chambers and Gautesen.[14] Three singular values are possible because there are three independent scattering modes: a monopole mode from the compressibility contrast, and two dipole modes from the density contrast. The three singular states of the array response matrix represent three orthogonal combinations of the projected scattering modes.

If the aperture of the array is symmetric around the x axis, the matrix elements W_{sy} and W_{xy} are zero, and simple analytic expressions can be found for the singular values

$$\lambda_{1,3}=\frac{1}{2}(\alpha W_{ss}+\beta W_{xx}) \times\left(1\pm\sqrt{1-4\alpha\beta\frac{W_{ss}W_{xx}-W_{sx}^2}{(\alpha W_{ss}+\beta W_{xx})^2}}\right), \tag{18}$$

$$\lambda_2=\beta W_{yy}. \tag{19}$$

Since $W_{ss}W_{xx}\geqslant W_{sx}^2$ by the Schwarz inequality, the quantity under the radical is always positive[14] and thus, the singular values are real, as required. For our applications $(W_{ss}W_{xx}-W_{sx}^2)/(\alpha W_{ss}+\beta W_{xx})^2\ll 1$, and we can approximate the singular value numbers 1 and 3 as

$$\lambda_1^{\text{app}}\approx\alpha W_{ss}+\beta W_{xx}, \tag{20}$$

$$\lambda_3^{\text{app}}\approx\alpha\beta\frac{W_{ss}W_{xx}-W_{sx}^2}{\alpha W_{ss}+\beta W_{xx}}. \tag{21}$$

Note that the singular values are ordered: $\lambda_1\geqslant\lambda_2\geqslant\lambda_3$. The singular vectors can be written in terms of the $\mathbf{w_n}$

$$\mathbf{U_{1,3}}=\alpha W_{sx}\mathbf{w_s}+(\lambda_{1,3}-\alpha W_{ss})\mathbf{w_x},\quad \mathbf{U_2}=\mathbf{w_y}. \tag{22}$$

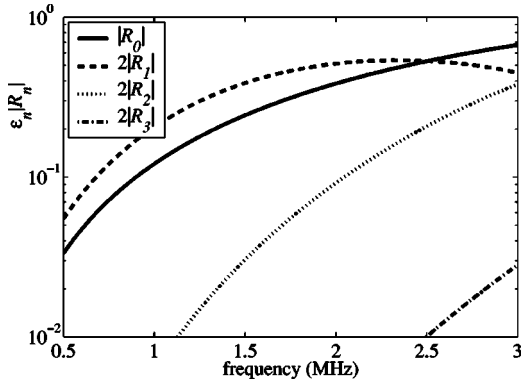

FIG. 5. Coefficients $\epsilon_n R_n$ (no dimension) of the normal modes (logarithm scale) for a steel cylinder of diameter 0.2 mm versus frequency between 0.5 and 3 MHz. The two first coefficients R_0 (monopole) and $2R_1$ (dipole) are predominant in the frequency range. The third one, $2R_2$ (quadrupole), is small and non-negligible for frequencies above 1 MHz. The small object approximation is not valid for that case.

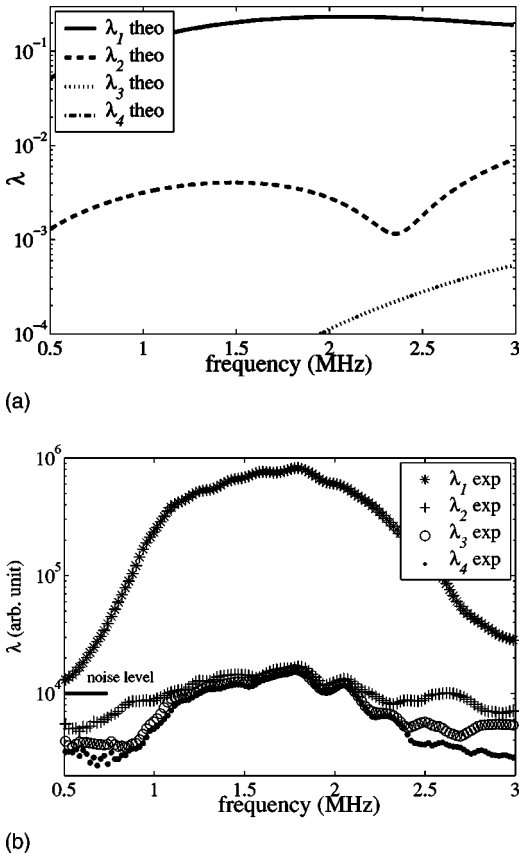

FIG. 6. Singular values λ_n (logarithm scale) for a steel cylinder of diameter 0.2 mm versus frequency: (a) theoretical, the first singular value λ_1 varies slowly in the frequency range. The ratio λ_2/λ_1 lies between 1% and 3%; (b) experimental: the first singular value λ_1 is clearly measured. The second one, λ_2, and the noise are of same order (about 1%).

The two singular vectors $\mathbf{U_1}$ and $\mathbf{U_3}$ are symmetric around the x axis, while $\mathbf{U_2}$ is antisymmetric. Thus, for a symmetric experiment, one singular state represents a dipole oriented parallel to the array, while the other two are orthogonal combinations of the monopole and a dipole oriented normal to the array (Fig. 3).

III. EXPERIMENTAL RESULTS

Experiments have been carried out in a water tank on two materials, steel and nylon, and for different cylinders of

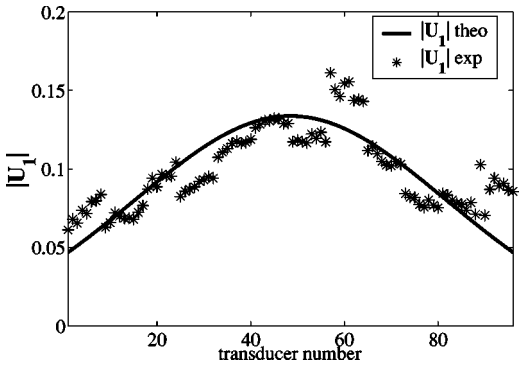

FIG. 7. Modulus of the first singular vector $|\mathbf{U_1}|$ along the array at 1.5 MHz. The difference between theory (continuous line) and experiment (*) is due to the reception level dispersion of the array elements.

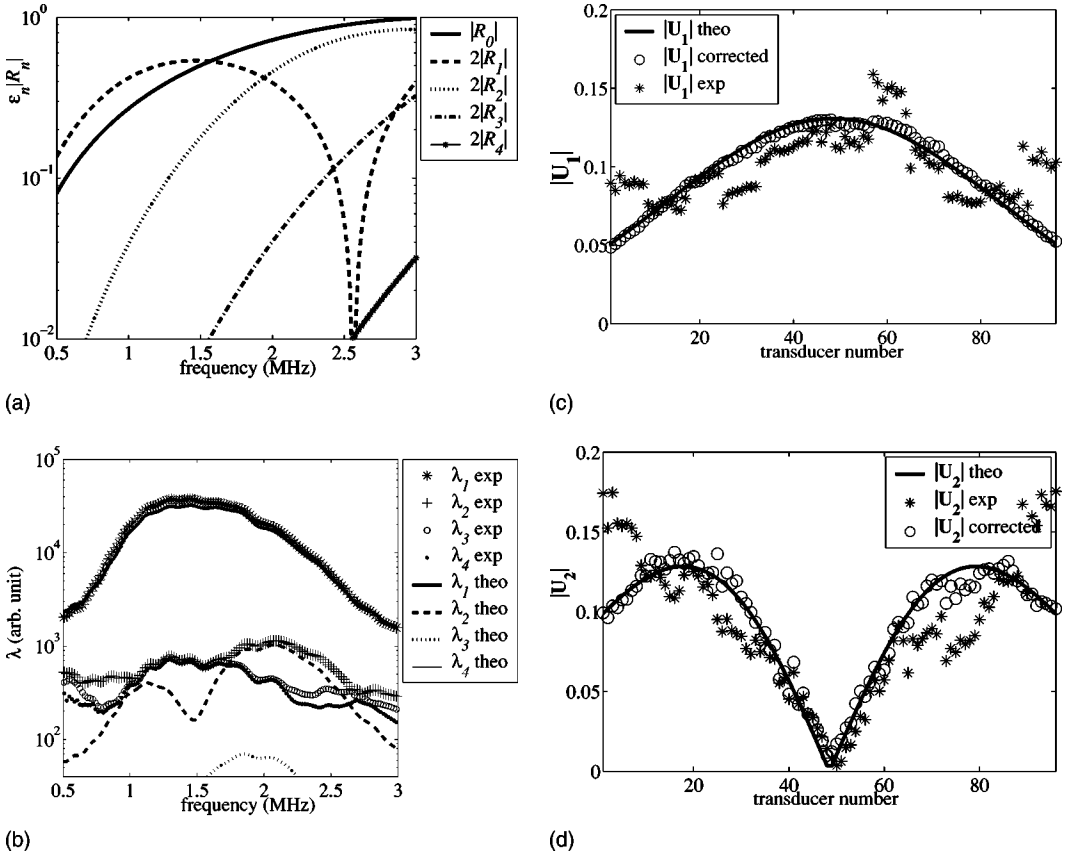

FIG. 8. Results for steel 0.32 mm: (a) coefficients $\varepsilon_n|R_n|$ of normal modes (logarithm scale) versus frequency. The five first coefficients are taken into account in the simulation; (b) simulated (with frequency response) and experimental singular values λ_n (logarithm scale) versus frequency. The experimental second singular value is visible between 1.7 and 2.5 MHz; modulus of the first singular vector $|\mathbf{U_1}|$ (c) and of the second singular vector $|\mathbf{U_2}|$ (d) along the array at 2 MHz: theoretical (continuous line), experimental (*), and reception sensitivity corrected values (○).

diameters between 0.2 and 0.5 mm. The transducer array has 96 elements with central frequency 1.5 MHz, and the array pitch is 0.5 mm. For each experiment, the distance F between the wire and the array is 50 mm. As the cylinder diameters are less than half a wavelength, they have a low scattering power. In order to get a reasonable signal to noise ratio we used the Hadamard–Walsh basis to acquire the array response matrix as explained by Folégot *et al.*[10] This emission basis is very convenient and, in principle, it increases the signal level by a factor of $\sqrt{N}$, N being the number of elements. We also used chirps in order to use the whole bandwidth of the transducers (0.9–2.5 MHz).

The two first coefficients $\varepsilon_n R_n$ for steel and for nylon are shown in Fig. 4. The exact value and the small object approximation of $\epsilon_n R_n$ are compared for $k_0 a$ under 0.8. The expression of approximate coefficients are

$$|R_0|_{\text{app}} = \frac{\pi k_0^2 a^2}{4}\alpha, \quad 2|R_1|_{\text{app}} = \frac{\pi k_0^2 a^2}{2}\beta. \tag{23}$$

The above parabolic approximation [terms are proportional to $(k_0 a)^2$] is valid for $k_0 a$ lower than 0.5. For bigger values of $k_0 a$ the deviation increases. We also remark that in the case of nylon, the β coefficient is small because of the small density contrast (Table I). The frequency band of our system lies between 0.9 and 2.5 MHz, which corresponds to $0.4 < k_0 a < 1.9$. Thus, for the simulations of singular values and vectors, the values of $\epsilon_n R_n$ are calculated with the exact formula given by Flax *et al.*[18] The physical parameters of the cylinders are given in Table I. For comparison to experimental results, the simulation also takes into account the frequency response on transmit and receive and the directivity of each transducer element. The directivity has been measured with a needle probe, and taken into account in the simulations.

A. Steel cylinder, diameter 0.2 mm, a quasi-isotropic scatterer

The first experiment was carried out on the thinnest steel cylinder (diameter 0.2 mm). The coefficients of the normal modes $\varepsilon_n R_n$ for such a cylinder are shown (Fig. 5). The two first coefficients R_0 and $2R_1$ are predominant in the frequency range. The third one, $2R_2$, is small and the others are negligible. We cannot consider that wire as a small object because of the weight of the quadrupole term $2R_2$. In Fig. 6(a), we can see the theoretical singular values calculated for the experimental geometry. The first singular value λ_1 is predominant, the second one λ_2 is very small, and the others are negligible. The ratio λ_2/λ_1 lies between 1% and 3%, in the frequency range [Fig. 6(a)]. In the experimental results the second singular value represents the noise level and we can see in Fig. 6(b) that the noise level is about 3% at the central frequency. So, it is impossible to measure properly the second singular vector.

As the theoretical first singular value varies slowly in the

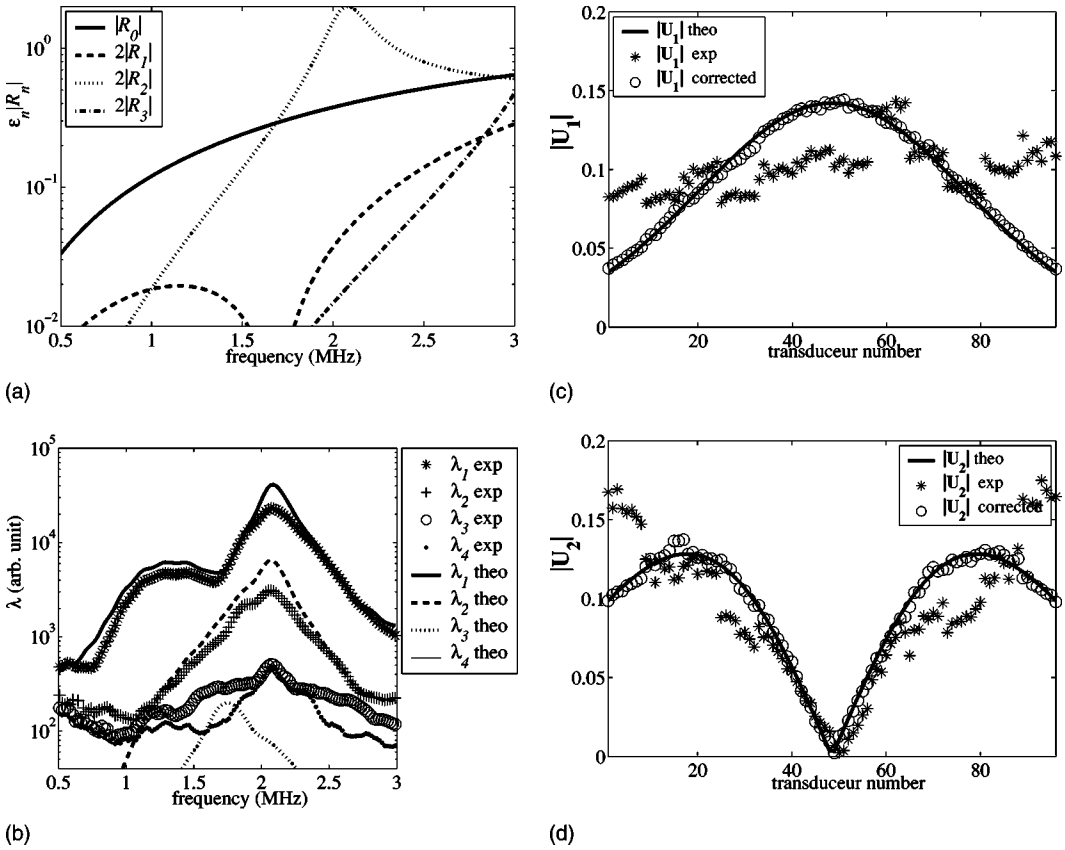

FIG. 9. Results for nylon 0.24 mm: (a) coefficients $\varepsilon_n|R_n|$ of normal modes (logarithm scale) versus frequency; (b) simulated (with frequency response) and experimental singular values λ_n (logarithm scale) versus frequency; modulus of the first singular vector $|\mathbf{U_1}|$ (c) and of the second singular vector $|\mathbf{U_2}|$ (d) along the array at 2.1 MHz.

frequency range, we choose to use this experiment to calibrate our system. The ratio between experimental and theoretical first singular values is used to characterize the frequency response of the system. For the measurement on the other cylinders, the theoretical singular values are multiplied by this ratio to compare them to the experimental ones. We also correct for element sensitivity variations in the array. As we can see for the amplitude of the first singular vector $\mathbf{U_1}$ (Fig. 7), the reception sensitivity varies from one transducer to another. At each frequency, we determine a correction factor from the experimental and theoretical first singular vectors. For the other cylinders, this correction factor was applied frequency by frequency to the array response matrix before computing the SVD.

B. Steel cylinder, diameter 0.32 mm

The second measurement has been carried out on a steel cylinder of diameter 0.32 mm. As we can see in Fig. 8(a), we cannot consider the object as a small scatterer because of the weight of the quadrupole term $2R_2$. The good agreement between the experimental and simulated first singular values λ_1 shows that the frequency response obtained with the smaller steel cylinder is acceptable [Fig. 8(b)]. Figure 8(c) shows the first singular vector $\mathbf{U_1}$. The experimental data (*) show the same reception sensitivity variation as the case of the first steel cylinder (Fig. 7). The corrected data (0) are in good agreement with the simulated singular vector. Thus, the reception correction factor is also acceptable. Figure 8(b) shows that the second experimental singular value λ_2 is generally below the noise level. However, between 1.7 and 2.5, it is clearly above noise, so that we can see the second experimental singular vector $\mathbf{U_2}$ at 2 MHz [Fig. 8(d)].

C. Nylon cylinder, diameter 0.24 mm

The next experiment was carried out on a nylon cylinder of diameter 0.24 mm. We can see in Fig. 9(a) the coefficient of normal modes. The dipole mode coefficient $2|R_1|$ is very small, due to the small density contrast. The quadrupole term $2|R_2|$ has a peak at 2.1 MHz. The peak of the first simulated singular value at 2.1 MHz corresponds to a combination of the monopole, the symmetrical dipole, and quadrupole, the quadrupole contribution being dominant [Fig. 9(b)]. The second experimental singular value λ_2 is clearly above the noise level between 1.2 and 2.5 MHz. So, it is possible to calculate the first two singular vectors $\mathbf{U_1}$ and $\mathbf{U_2}$ [Figs. 9(c) and (d)]. The reception correction is as efficient as for the steel 0.32-mm cylinder.

D. Nylon cylinder, diameter 0.35 mm

The next experiment was carried out on a nylon cylinder of diameter 0.35 mm. We can see in Fig. 10(a) the coefficient of normal modes. The dipole mode coefficient $2|R_1|$ is still very small, due to the small density contrast. The quadrupole term $2|R_2|$ has a peak at 1.52 MHz. The following term $2R_3$

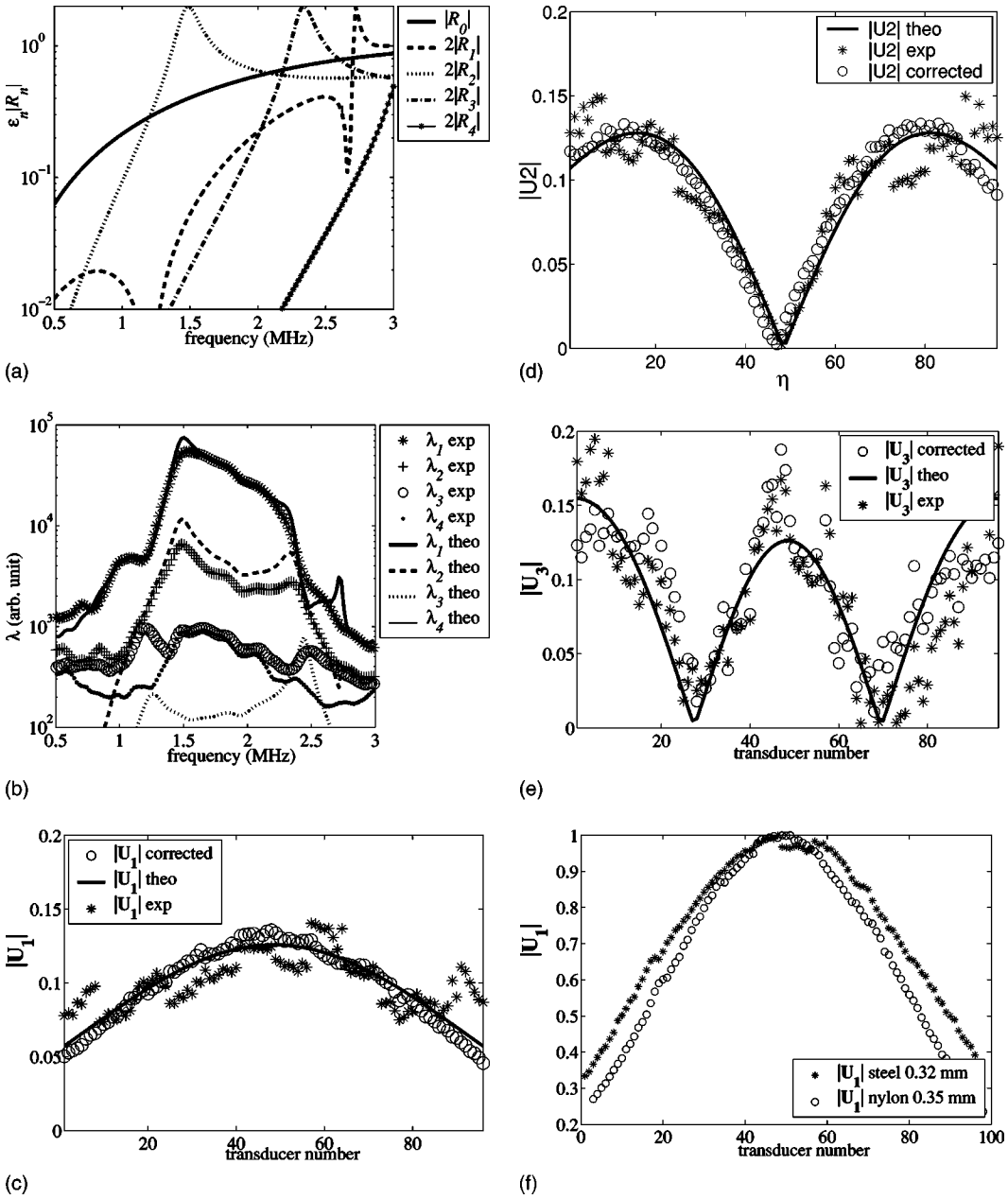

FIG. 10. Results for nylon 0.35 mm: (a) coefficients $\varepsilon_n|R_n|$ of normal modes (logarithm scale) versus frequency; (b) simulated (with frequency response) and experimental singular values λ_n (logarithm scale) versus frequency. The experimental third singular value is above noise around 1 and 2.5 MHz; modulus of the first singular vector $|\mathbf{U_1}|$ (c), of the second singular vector $|\mathbf{U_2}|$ (d) and of the third singular vector $|\mathbf{U_3}|$ (e) along the array at 1.05 MHz; (f) comparison of the modulus of the first singular vector $|\mathbf{U_1}|$ at 1.5 MHz, for a steel wire (0.32 mm:*) and a nylon wire (0.35 mm: ○). Curves are normalized; maxima of the vectors are equal to 1. For a equivalent diameter, the shape difference is due to the coefficients of normal modes. The nylon vector is sharper than the steel one because of the predominant weight of the quadrupole.

is not negligible. The peak of the first simulated singular value at 1.52 MHz corresponds to the quadrupole dominant peak [Fig. 10(b)]. For the two nylon cylinders, that peak corresponds to the same value of k_0a equal to 1.12. But, in that case the peak lies in the middle of the frequency window. The difference between experimental and theoretical peak levels is about 30%, and may be due to a dissipation phenomenon, which is not taken into account in the theory.

We can see in Figs. 10(c) and (d) that there is good agreement between corrected and simulated values for the first two singular vectors $\mathbf{U_1}$ and $\mathbf{U_2}$. The third singular value λ_3 is barely above noise around 1.2 MHz. We observe in Fig. 10(e) that the third singular vector $|\mathbf{U_3}|$ after correction is still noisy, but has a reasonable shape. In Fig. 10(f), we compare the first singular vector for steel (0.32 mm) and nylon (0.35 mm) at 1.5 MHz. The nylon vector is sharper than the steel one because of the predominant weight of the quadrupole. The first singular vector $\mathbf{U_1}$ is a combination of the monopole, the symmetrical dipole, and quadrupole. In the case of nylon at that frequency, the quadrupole contribution is dominant.

E. Nylon cylinder, diameter 0.46 mm

The last experiment was carried out on a nylon cylinder of diameter 0.46 mm. We can see in Fig. 11(a) the coefficient

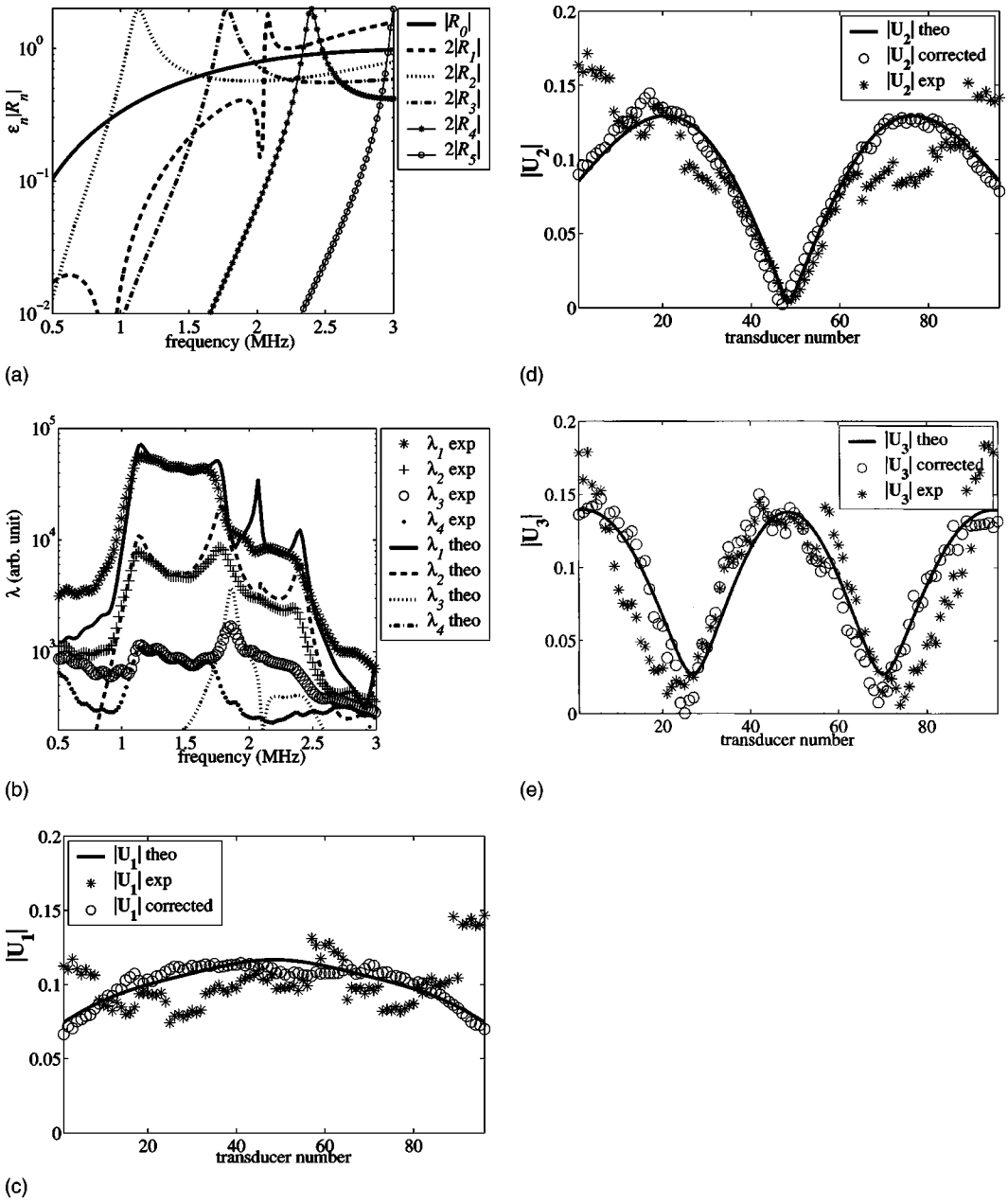

FIG. 11. Results for nylon 0.46 mm: (a) coefficients $\varepsilon_n|R_n|$ of normal modes (logarithm scale) versus frequency; (b) simulated (with frequency response) and experimental singular values λ_n (logarithm scale) versus frequency. The experimental third singular value is above noise around 1.9 MHz; modulus of the first singular vector $|\mathbf{U_1}|$ (c), of the second singular vector $|\mathbf{U_2}|$ (d), of the third singular vector $|\mathbf{U_3}|$ (e) along the array at 1.9 MHz.

of normal modes. The dipole mode coefficient $2|R_1|$ presents a resonance at 2 MHz (π phase jump). The quadrupole term $2|R_2|$ has a peak at 1.14 MHz, corresponding to k_0a equal to 1.12. The following term $2|R_3|$ has a peak at 1.8 MHz. The experimental singular values are in good agreement with simulated ones [Fig. 11(b)], except for the little peaks at 1.17 and 1.74 MHz. Again, the disagreement is probably due to the dissipation phenomenon, which was not taken into account in the simulation.

We can see in Figs. 11(c), (d), and (e) the three singular vectors $\mathbf{U_1}$, $\mathbf{U_2}$, and $\mathbf{U_3}$. There is a good agreement between corrected and simulated values. The third singular value λ_3 is barely above the noise at 1.9 MHz. Figure 12 shows the first three singular values λ_n for the three nylon wires versus k_0a. There is a good agreement between experiment and

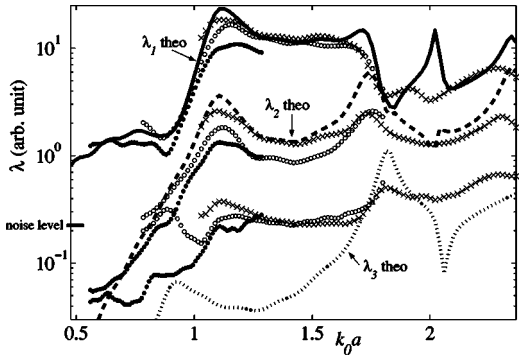

FIG. 12. The first singular values λ_n ($n=1,2,3$) for the three nylon wires are plotted versus k_0a. Experimental values: 0.24-mm diameter wire (·), 0.35-mm diameter wire (°), 0.46-mm diameter wire (×). Theoretical values: first singular value (continuous line), second singular value (dashed line), the third singular values (dotted line). It appears that, if the material of the cylinder is known, its diameter can be deduced from the singular values.

simulation for the three wires. As the noise level is about 1%, we can see that the second experimental singular value is clearly measured for k_0a above 1, and the third one is clearly measured for k_0a above 1.8. Furthermore, it appears that if the material of the cylinder is known, its diameter can be deduced from the singular values.

IV. CONCLUSION

Initially, the DORT method was used assuming a one-to-one correspondence between point-like scatterers and singular vectors of the array response matrix. In Sec. II, we have shown that a subwavelength elastic cylinder is associated with at least three singular vectors and singular values. The singular vectors are a linear combination of normal modes projected onto the array. These combinations are given analytically in the small cylinder limit: the three singular vectors are a combination of the cylindrical mode and two dipolar modes.

In Sec. III, this paper presents the first experimental results showing the multiple singular values for subwavelength scatterers. Five different scatterers were compared at frequencies between 0.9–2.5 MHz: a 0.2- and a 0.32-mm steel cylinder and 0.24-, 0.35-, and 0.46-mm nylon cylinders. Experimental results are in good agreement with theory when several normal modes were taken into account. Different behaviors of nylon and steel are clearly shown. For the steel cylinders, the second eigenvalue was much smaller than the first and contributed little to the scattering. For the nylon cylinders, the second eigenvalue was significant but was generated by a combination of the monopole and quadrupole terms. The dipole term was negligible since the density contrast was small. These results show how the material properties of the cylinder affect the decomposition of the TRO. This opens a new approach to target characterization and the inverse problem based on the analysis of the TRO.

[1] C. Prada and M. Fink, ''Eigenmodes of the time reversal operator: a solution to selective focusing in multiple-target media,'' Wave Motion **20**, 151–163 (1994).

[2] C. Prada, S. Manneville, D. Spoliansky, and M. Fink, ''Decomposition of the time reversal operator: Application to detection and selective focusing on two scatterers,'' J. Acoust. Soc. Am. **99**, 2067–2076 (1996).

[3] E. Kerbrat, C. Prada, D. Cassereau, R. K. Ing, and M. Fink, ''Detection and imaging in complex media with the D.O.R.T. method,'' IEEE Ultrasonic Symposium Proceedings, 779–783 (2000).

[4] C. Prada and M. Fink, ''Separation of interfering acoustic scattered signals using the invariant of the time-reversal operator. Application to Lamb waves characterization,'' J. Acoust. Soc. Am. **104**(2), 801–807 (1998).

[5] D. R. Jackson and D. R. Dowling, ''Phase conjugation in underwater acoustics,'' J. Acoust. Soc. Am. **89**(1), 171–181 (1991).

[6] W. A. Kuperman, W. S. Hodgkiss, H. C. Song, T. Akal, C. Ferla, and D. R. Jackson, ''Phase conjugation in the ocean: Experimental demonstration of an acoustic time-reversal mirror,'' J. Acoust. Soc. Am. **103**(1), 25–40 (1998).

[7] S. R. Khosla and D. R. Dowling, ''Time-reversing array retrofocusing in noisy environments,'' J. Acoust. Soc. Am. **109**(2), 538–546 (2001).

[8] N. Mordant, C. Prada, and M. Fink, ''Highly resolved detection and selective focusing in a waveguide using the D.O.R.T. method,'' J. Acoust. Soc. Am. **105**, 2634–2642 (1999).

[9] T. Yokoyama, T. Kikuchi, T. Tsuchiya, and A. Hasegawa, ''Detection and selective focusing on scatterers using decomposition of time reversal operator method in Pekeris waveguide model,'' Jpn. J. Appl. Phys. **40**, 3822–3828 (2001).

[10] T. Folégot, C. Prada, and M. Fink, ''Resolution enhancement and separation of reverberation from target echo with the time reversal operator decomposition,'' J. Acoust. Soc. Am. **113**, 3155–5160 (2003).

[11] H. Tortel, G. Micolau, and M. Saillard, ''Decomposition of the time reversal operator for electromagnetic scattering,'' J. Electromagn. Waves Appl. **13**, 687–719 (1999).

[12] G. Micolau, M. Saillard, and P. Borderies, ''DORT as applied to ultrawideband signals for detection of buried objects,'' IEEE Trans. Geosci. Remote Sens. **41**(8), 1813–1820 (2003).

[13] S. Komilikis, C. Prada, and M. Fink, ''Characterization of extended objects with the D.O.R.T. method,'' IEEE Ultrasonic Symposium Proceedings, 1401–1404 (1996).

[14] D. H. Chambers and A. K. Gautesen, ''Time reversal for a single spherical scatterer,'' J. Acoust. Soc. Am. **109**, 2616–2624 (2001).

[15] D. H. Chambers, ''Analysis of the time-reversal operator for scatterers of finite size,'' J. Acoust. Soc. Am. **112**, 411–419 (2002).

[16] C. Prada, ''Detection and imaging in complex media with the D.O.R.T. method,'' in *Imaging of Complex Media with Acoustic and Seismic Waves*, Topics Appl. Phys. Vol. 84 (Springer, Berlin, 2002), pp. 107–133.

[17] W. F. Walker, ''C- and D-weighted ultrasonic imaging using the translating aperture algorithm,'' IEEE Trans. Ultrason. Ferroelectr. Freq. Control **48**(2), 452–461 (2001).

[18] L. Flax, G. Gaunard, and H. Überall, ''Theory of resonance scattering,'' *Physical Acoustics*, edited by W. Mason and R. Thurston (Academic Press, New York, 1976), Vol. XV, pp. 191–294.

[19] A. Derem, ''N. Gespa La diffusion acoustique par des cibles géométriques de forme simple Théories et expériences,'' Cedocar Chap. 9, 196–200 (1987).

[20] R. Doolittle and H. Überall, ''Sound scattering by elastic cylindrical shells,'' J. Acoust. Soc. Am. **39**, 272–275 (1965).

Gibbs sampling for time-delay-and amplitude estimation in underwater acoustics

Zoi-Heleni Michalopoulou[a)]
Department of Mathematical Sciences, New Jersey Institute of Technology, Newark, New Jersey 07102

Michele Picarelli[b)]
Department of Mathematics, St. Peter's College, 2641 Kennedy Boulevard, Jersey City, New Jersey 07306

(Received 27 August 2004; revised 12 November 2004; accepted 12 November 2004)

Multipath arrivals at a receiving sensor are frequently encountered in many signal-processing areas, including sonar, radar, and communication problems. In underwater acoustics, numerous approaches to source localization, geoacoustic inversion, and tomography rely on accurate multipath arrival extraction. A novel method for estimation of time delays and amplitudes of arrivals with maximum *a posteriori* (MAP) estimation is presented here. MAP estimation is optimal if appropriate statistical models are selected for the data; implementation, requiring maximization of a multidimensional function, is computationally demanding. Gibbs sampling is proposed as an efficient means for estimating necessary posterior probability distributions, bypassing analytical calculations. The Gibbs sampler includes as unknowns time delays, amplitudes, noise variance, and number of arrivals. Through Monte Carlo simulations, the method is shown to have a performance very close to that of analytical MAP estimation. The method is also shown to be superior to expectation-maximization, which is often applied to time-delay estimation. The Gibbs sampling approach is demonstrated to be more informative than other time-delay estimation methods, providing complete posterior distributions compared to just point estimates; the distributions capture the uncertainty in the problem, presenting likely values of the unknowns that are different from simple point estimates. [DOI: 10.1121/1.1847894]

PACS numbers: 43.60.Pt, 43.60.Jn [AIT] Pages: 799–808

I. INTRODUCTION

In underwater acoustics, matched-field processing approaches[1,2] are frequently employed for the estimation of the source location of a sound-emitting source. Such methods produce estimates by numerically calculating the full acoustic field to obtain a measure of correlation between the computed field (replica) and received data; they are inherently dependent on assumptions necessary for the acoustic field computations.

A good match and, consequently, accurate estimates, between full replica and true fields are difficult to attain. Even when uncertainty on environmental factors is integrated in matched-field methods, as is often the case, when the propagation medium is complex and challenging to mathematically describe, the task is challenging. Under such circumstances, simple approaches that do not rely on full-field calculations can be implemented with excellent results. Such approaches depend on identification of individual arrivals (paths) in the received field. Source location, bottom depth, sediment depths, and sound-speed information can be extracted from the arrival times of these paths. The amplitudes of the arrivals provide information on geoacoustic properties of the sediments. In Refs. 3–11, it has been shown that arrival information can be employed for efficient and accurate source and receiver localization and tracking and environmental parameter estimation. The quality of the estimates, however, is interwoven with the quality of time-delay-and amplitude estimation of the explored arrivals. It is, therefore, of great interest to develop methods for the extraction of accurate information on distinct arrivals. In a noisy received time series, however, arrival time differences between distinct paths and corresponding amplitudes can be difficult to identify.

A matched filter between source waveform and received time series is the simplest time-delay-and amplitude estimation approach, but suboptimal, especially for closely spaced arrivals.[12] Many other methods, several focusing on high-resolution approaches, have been presented in the literature. (For a thorough presentation of different methods and applications, the reader is referred to Refs. 13, 14.)

In this work interest is on multipath propagation of deterministic signals. As shown in Ref. 12, an optimal approach for time-delay-and amplitude estimation is maximization of the posterior probability distribution function of delays and amplitudes. This maximization, given the observed data, leads to an analytical expression for amplitudes; using those estimates, time delays can be obtained by identifying the maximum of an M-dimensional function, where M is the (known) number of paths at the receiver.[12] When M is large, these calculations can become a computationally cumbersome task.

A simpler method, which also requires M-dimensional optimization and approximates maximum *a posteriori* (MAP) estimation, has been proposed in Ref. 15. Approximate maximum likelihood approaches have been proposed in Refs. 16, 17. Simulated annealing as a tool for optimization

[a)]Electronic mail: michalop@njit.edu
[b)]Electronic mail: mpicarelli@optonline.net

of the time-delay estimation problem was suggested in Ref. 18.

To reduce the computational requirements of MAP estimation of time delays and amplitudes, expectation-maximization (EM) has been implemented.[19,20] EM is an efficient way of maximizing log likelihoods (equivalent under certain assumptions to posterior probability distributions), when the exact likelihood function is difficult to compute. A drawback is that EM is a hill-climbing algorithm, generally converging to *local* maxima.

Here, we propose implementation of a MAP approach for time delay and amplitude estimation using Gibbs sampling for the efficient computation of full, joint posterior distributions.[21] The method was first introduced in Ref. 22 and is in this paper evaluated and studied in terms of convergence. Results from this approach are compared to estimates obtained with the analytical maximum *a posteriori* approach, which is feasible to implement when M is small and the exhaustive search over time delays for distribution maximization is manageable.

Section II discusses the derivation of the joint posterior probability distribution of time delays and amplitudes, and what is entailed in its maximization. Section III introduces Gibbs sampling and derives conditional marginal distributions of the unknown parameters necessary for the operation of the Gibbs sampler for time-delay-and amplitude estimation. Section IV presents a performance evaluation of the Gibbs sampling approach, comparing it to the analytical MAP method. Section V evaluates the novel approach through a comparison to EM. Section VI discusses the case of an unknown number of arrivals. Section VII addresses convergence issues for the Gibbs sampler. Section VIII presents Gibbs sampling estimates obtained for arrival times and amplitudes in a realistic ocean environment. Conclusions are presented in Sec. IX.

II. THE ANALYTICAL MAXIMUM *A POSTERIORI* ESTIMATOR

Estimates of unknown parameters of a statistical model can be obtained through the maximization of the posterior probability distribution of these parameters, given the observed data and quantitatively described prior knowledge. Assuming a received signal $r(n)$, consisting of M multipaths $s(n-n_i)$ [where $s(n)$ is the transmitted signal] and noise in a nondispersive medium, we can write

$$r(n)=\sum_{i=1}^{M} a_i s(n-n_i)+w(n), \tag{1}$$

where $n=1,...,N$ (N is the duration of the received signal), a_i is the amplitude of the ith path, and n_i is the arrival time of the ith path. Quantity $w(n)$ is additive, white, normally distributed noise with zero mean and variance σ^2. It is assumed that the number of arrivals is known. Initially, it is also assumed that σ^2 is known as well. The amplitudes are real numbers (positive or negative, the sign indicating polarity of the arrivals). The assumption of lack of dispersion is reasonable for moderately high frequencies in many underwater environments. When significant dispersion is present, the model of Eq. (1) would not be adequate for delay and amplitude estimation.[18]

One might assume that prior information is available for the arrival amplitudes. For example, in multipath propagation, the paths that undergo multiple reflections off the boundaries are attenuated; an exponential decay model might be a suitable representation for the amplitudes. However, any such model does not always describe sufficiently the problem at hand. When source and receiver are at the same depth, for example, some paths arrive simultaneously. The two simultaneous arrivals appear as a single arrival with a doubled amplitude, which is larger than that of the preceding arrival; a model of decay would then be unsuitable. Here, to avoid erroneous assumptions, we consider no prior information on the amplitudes. We assign to them uniform, improper prior distributions[23]

$$p(a_i)=1, \quad -\infty<a_i<\infty, \quad i=1,...,M. \tag{2}$$

We set uniform priors for the delays

$$p(n_i)=\frac{1}{N}, \quad 1\leqslant n_i\leqslant N, \quad i=1,...,M. \tag{3}$$

We can write the posterior probability distribution function of all amplitudes and delays (n_i and a_i for $i=1,...,M$) as follows:

$$p(n_1,n_2,\ldots,n_M,a_1,a_2,\ldots,a_M|r(n))=K\frac{1}{N^M}\frac{1}{(\sqrt{2\pi})^N\sigma^N}$$
$$\times\exp\left(-\frac{1}{2\sigma^2}\sum_{n=1}^{N}\left(r(n)-\sum_{i=1}^{M}a_i s(n-n_i)\right)^2\right). \tag{4}$$

Quantity K is a constant. Also $(1/N^M)[1/(\sqrt{2\pi})^N\sigma^N]$ is a constant, being independent of all unknowns. All constants can be consolidated into one; Eq. (4) becomes

$$p(n_1,n_2,\ldots,n_M,a_1,a_2,\ldots,a_M|r(n))$$
$$=C\exp\left(-\frac{1}{2\sigma^2}\sum_{n=1}^{N}\left(r(n)-\sum_{i=1}^{M}a_i s(n-n_i)\right)^2\right). \tag{5}$$

Once the joint posterior distribution of all unknowns is described, MAP estimates of those parameters can be obtained through its maximization. Maximizing the distribution in Eq. (5) over the unknown amplitudes and delays is equivalent to maximization of the likelihood function of Eq. (5) in Ref. 12 in the discrete case. This problem seems to require a search in a $2\times M$-dimensional space. As shown in Ref. 12, however, amplitude estimates can be analytically obtained, and subsequently a search in an M-dimensional space is required for delay estimation.

In order to justify results that will follow, it is here essential to point out what is involved in the maximum likelihood (or MAP, in this case) amplitude-and time-delay estimation. By obtaining derivatives of the likelihood function with respect to amplitudes and borrowing notation from Ref. 12, we can write

$$A=\Lambda^{-1}\phi, \tag{6}$$

where $A=[a_1\,a_2\ldots a_M]^T$, $\phi=[\phi_1\,\phi_2\ldots\phi_M]^T$, $\phi_i=\Sigma_{n=1}^{N}s(n-n_i)r(n)$, and $i=1,...,M$. Matrix Λ is defined as

$$\Lambda=\begin{pmatrix}\lambda_{11} & \lambda_{12} & \cdots & \lambda_{1M}\\ \lambda_{21} & \lambda_{22} & \cdots & \lambda_{2M}\\ . & . & . & .\\ . & . & . & .\\ \lambda_{M1} & \lambda_{M2} & \cdots & \lambda_{MM}\end{pmatrix}, \tag{7}$$

where $\lambda_{ij}=\Sigma_{n=1}^{N}s(n-n_i)s(n-n_j)$, $i=1,...,M$, $j=1,...,M$.

Estimates for the time delays can be subsequently obtained by maximizing over time delays function $f(n_1,n_2,\ldots,n_M)$, where

$$f(n_1,n_2,\ldots,n_M)=\phi^T\Lambda^{-1}\phi. \tag{8}$$

For a problem involving M arrivals, the estimation process involves a search in an M-dimensional space.

III. BUILDING THE GIBBS SAMPLER

Gibbs sampling is an iterative Monte Carlo sampling process where realizations from a joint distribution are obtained by cycling through conditional distributions that are typically easier to sample from than the joint distribution.[21] The first step is to derive the necessary conditional distributions. This will be achieved using the distributions of Sec. II; the analysis of Sec. II is now extended to include noise variance as an unknown.

A noninformative prior distribution is considered for the variance as in Ref. 24

$$p(\sigma^2)\propto\frac{1}{\sigma^2}, \tag{9}$$

typical of a variable taking only positive values. Including the prior for the unknown variance, and consolidating constants, the joint posterior distribution is as follows:

$$p(n_1,n_2,\ldots,n_M,a_1,a_2,\ldots,a_M,\sigma^2|r(n))=C\frac{1}{\sigma^{N+2}}\exp\left(-\frac{1}{2\sigma^2}\sum_{n=1}^{N}\left(r(n)-\sum_{i=1}^{M}a_i s(n-n_i)\right)^2\right). \tag{10}$$

The conditional posterior distribution for the variance is identified as an inverse χ^2 distribution

$$p(\sigma^2|n_1,n_2\ldots,n_M,a_1,a_2\ldots,a_M,r(n))\propto\frac{1}{\sigma^{N+2}}\exp\left(-\frac{1}{2\sigma^2}\sum_{n=1}^{N}\left(r(n)-\sum_{i=1}^{M}a_i s(n-n_i)\right)^2\right). \tag{11}$$

Samples from such a distribution can be drawn readily.

From the joint posterior function of Eq. (10), the marginal posterior probability distributions for time delays and amplitudes of arrivals are obtained. Assuming that all amplitudes a_j, $j=1,...,M$ and $j\neq i$, and delays n_k, $k=1,...,M$ are known, we can derive the following conditional distribution for amplitude a_i:

$$p\left(a_i\middle|n_1,n_2,\ldots,n_M,a_1,a_2,\ldots,a_M,\sigma^2,r(n)\right)=C\frac{1}{\sigma^{N+2}}\exp\left(-\frac{1}{2\sigma^2}\left(a_i-\left(\sum_{n=1}^{N}r(n)s(n-n_i)-\sum_{j=1(j\neq i)}^{M}a_j s(n-n_i)s(n-n_j)\right)\right)^2\right). \tag{12}$$

The argument of the exponential of Eq. (12) reveals a normal distribution for amplitude a_i with mean

$$\left(\sum_{n=1}^{N}r(n)s(n-n_i)-\sum_{j=1(j\neq i)}^{M}a_j s(n-n_i)s(n-n_j)\right),$$

and variance σ^2.

The marginal posterior distributions for delays n_i, $i=1,...,M$, are obtained on a grid (between 1 and N with unit spacing, where N is the length of the received sequence). Using the distribution of Eq. (10), the conditional posterior distribution of n_i for known a_j, $j=1,...,M$, n_k, $k=1,...,M$, $k\neq i$, and σ^2 is

$$p(n_i|n_1,n_2\ldots,n_M,a_1,a_2\ldots,a_M,\sigma^2,r(n))=G\exp\left(-\frac{1}{2\sigma^2}\sum_{n=1}^{N}\left(r(n)-\sum_{i=1}^{M}a_i s(n-n_i)\right)^2\right). \tag{13}$$

The conditional distributions derived above will be used as building blocks in the Gibbs sampler for the estimation of the posterior probability distribution of time delays and amplitudes.

In the present context we are concerned with obtaining the joint posterior distribution for amplitudes a_i, time delays n_i, $i=1...,M$, and variance σ^2. Conditional on all time delays and amplitudes of the arrivals as well as noise variance, the marginal conditional posterior distribution of each amplitude is analytically tractable in a closed form as shown in Eq. (12). So is the marginal conditional posterior distribution of σ^2 [Eq. (11)]. The marginal posterior distributions for time delays are not analytically tractable; we thus proceed with a grid-based approximation using the distributions of Eq. (13) (griddy Gibbs[25]).

Gibbs sampling begins with a set of initial conditions for all $2M+1$ unknown parameters (a_i and n_i, $i=1,...,M$, and σ^2). The process as implemented here first draws a sample from the inverse χ^2 distribution of Eq. (11); this is the new, updated value of the variance for the first iteration. Subsequently, a sample is drawn from the normal marginal conditional posterior of a_1 [Eq. (12)]. Given the new values of σ^2, a_1, and the initial values for $a_3,\ldots,a_M$, n_1, $n_2,\ldots,n_M$, a sample is then drawn in the same way for a_2. We continue this procedure, drawing samples for all unknown parameters from their respective marginal conditional posterior distributions. For a large number of iterations, the obtained sample sequences eventually converge to the true joint posterior distribution of σ^2, a_i, and n_i, $i=1,...,M$.[21,26,27]

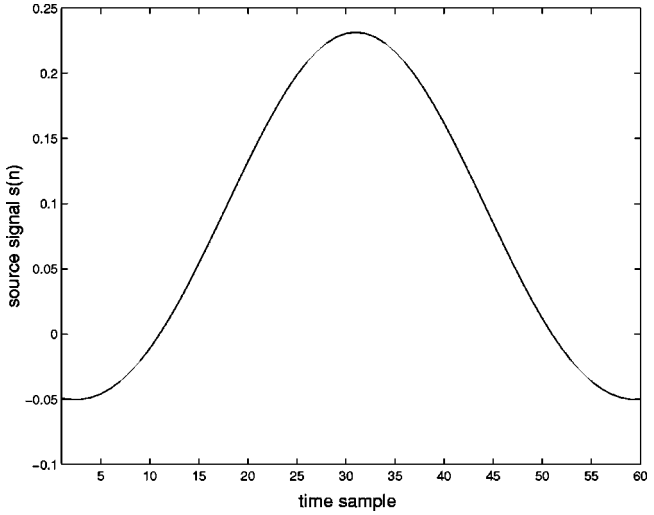

FIG. 1. Transmitted signal.

IV. PERFORMANCE EVALUATION

To evaluate the proposed Gibbs sampling MAP approach, a two-arrival problem was simulated. The Gibbs sampler was evaluated through a comparison to the analytical calculation of the maximum of the joint posterior distribution. The transmitted signal $s(n)$ for the simulations is shown in Fig. 1. The first arrival time (delay) n_1 was always considered to be at the 50th sample. The second arrival time n_2 varied between the 52nd and 160th sample. Amplitudes a_1 and a_2 were always 100 and -90, respectively. The evaluation was performed for 200 noisy data realizations. The initial conditions were 10 and 20 for the two arrival times; the initial condition for both amplitudes was 30. The initial value for σ^2 was 0.05. In most cases the Gibbs sampler was run for 5000 iterations (this issue will be revisited in a subsequent section).

Figures 2 and 3 present errors for time delays and amplitudes, respectively, for noise variance $\sigma^2=0.01\|r_s(n)\|^2$ [where $r_s(n)=\Sigma_{i=1}^{M}a_i s(n-n_i)$] as obtained from the analytical MAP estimator (solid line with "○") and the Gibbs sampler (solid line with "+"). Delay error error e_d was calculated as

$$e_d=\sqrt{(1/2)(\Sigma_{j=1}^{200}(\hat{n}_{1j}-n_1)^2/200+\Sigma_{i=j}^{200}(\hat{n}_{2j}-n_2)^2/200)}.$$

Delays 1 and 2 are denoted by n_1 and n_2, respectively; quantities $\hat{n}_{j1}$ and $\hat{n}_{j2}$ denote the estimates obtained from the jth realization for n_1 and n_2. Similarly, the amplitude error e_a is calculated as

$$e_a=\sqrt{(1/2)(\Sigma_{j=1}^{200}(\hat{a}_{1j}-a_1)^2/200+\Sigma_{j=1}^{200}(\hat{a}_{2j}-a_2)^2/200)}.$$

Here, a_1 and a_2 stand for the first and second amplitude; $\hat{a}_{1j}$ and $\hat{a}_{2j}$ are the estimates for a_1 and a_2 obtained for the jth realization.

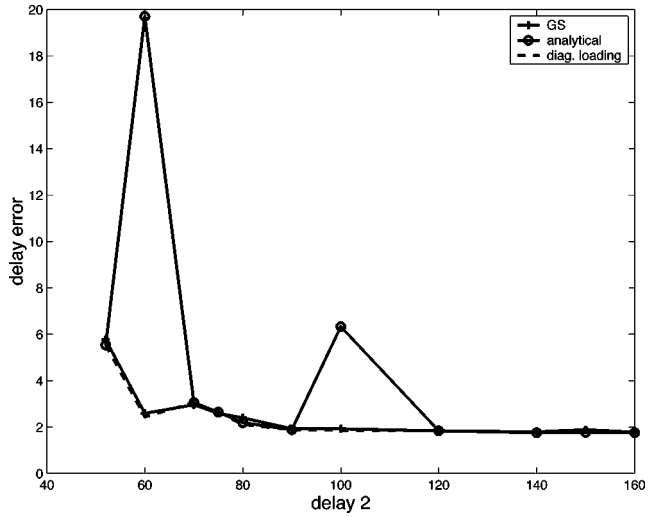

FIG. 2. Delay error e_d for the analytical processor (without and with diagonal loading) and the Gibbs sampler as a function of the second arrival time: $\sigma^2=0.01\|r_s(n)\|^2$.

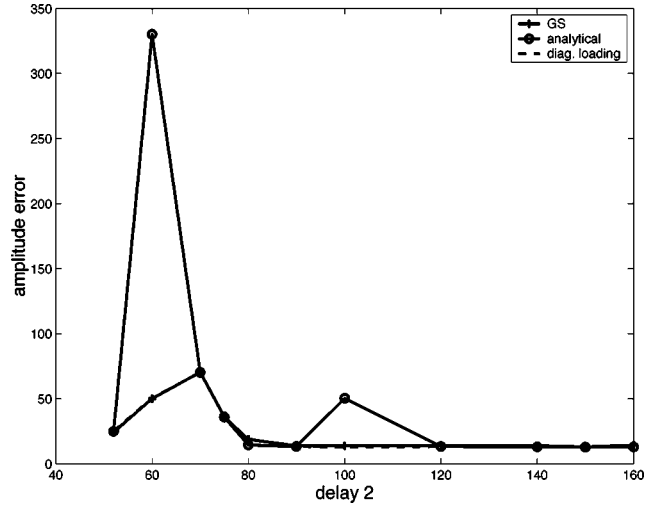

FIG. 3. Amplitude error e_a for the analytical processor (without and with diagonal loading) and the Gibbs sampler as a function of the second arrival time: $\sigma^2=0.01\|r_s(n)\|^2$.

The results were initially surprising; the Gibbs sampler appears to outperform the analytical processor, yielding smaller errors for both delays and amplitudes. The analytical MAP process was seen as a benchmark for good performance. The Gibbs sampler, estimating the posterior distribution that the analytical processor maximizes, was expected to approach the performance of that but not to exceed it (as, theoretically, it cannot). Equations (6) and (8) reveal the source of the discrepancy. These equations make use of matrix inversion for calculation of the estimates; when the matrix has a large condition number, the estimation becomes less robust with highly varying results from one case to the next (large variance in the estimates). As a consequence of the lack of stability, some estimates are affected more than others.

The analytical processing was repeated using diagonal loading for matrix Λ. Diagonal loading stabilizes the inversion and, consequently, estimation of time delays and amplitudes; it reduces the variance in the estimates but also introduces biases.[28] The new (with loading) analytical MAP estimates are shown in Figs. 2 and 3 with dashed lines; the results show a very good agreement between the analytical MAP process and the Gibbs sampling approximation to the analytical approach. A practically important result is that, because the Gibbs sampler does not make use of any matrix

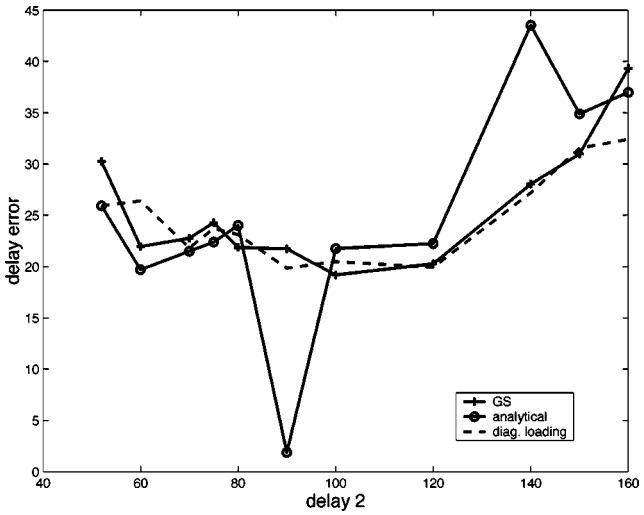

FIG. 4. Delay error e_d for the analytical processor (without and with diagonal loading) and the Gibbs sampler as a function of the second arrival time: $\sigma^2 = 0.05\|r_s(n)\|^2$.

inversions, it does not suffer from instabilities. The comparatively large delay and amplitude errors observed in both sets of results for delay spacings less than 30 samples are attributed to the difficulty of both processors in resolving the closely spaced arrivals.

Simulations were also run for noise variance $\sigma^2 = 0.05\|r_s(n)\|^2$. Figures 4 and 5 present the delay and amplitude results for the analytical MAP processor without and with loading and the Gibbs sampler. Again, substantial variance characterizes the analytically obtained results. A closer match between the two processors is achieved with diagonal loading for matrix Λ; especially in the case of time delays, the two processors perform very similarly. It should be pointed out here that the variance of the analytical processor estimates (and, consequently, the error) is artificially reduced with the loading process.

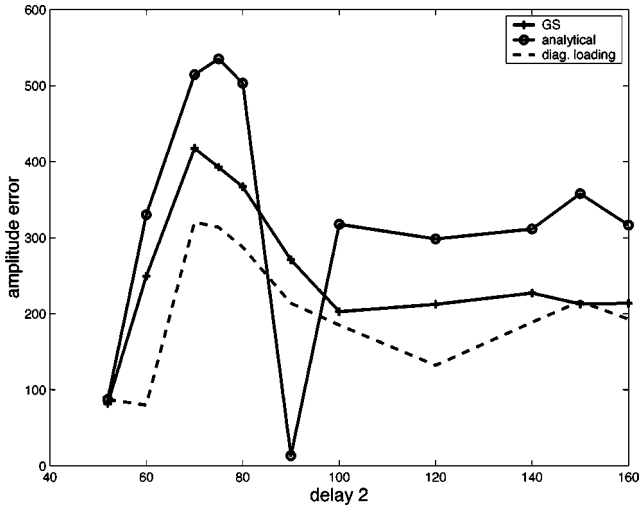

FIG. 5. Amplitude error e_a for the analytical processor (without and with diagonal loading) and the Gibbs sampler as a function of the second arrival time: $\sigma^2 = 0.05\|r_s(n)\|^2$.

TABLE I. Medians of delay estimates from 200 realizations for the analytical MAP method, Gibbs sampling (GS), and EM for noise variance $\sigma^2 = 0.01\|r_s(n)\|^2$.

True delay	Anal. MAP	GS	EM
50	50	50	50
80	80	80	51

V. GIBBS SAMPLING VS EXPECTATION-MAXIMIZATION

To circumvent the calculations required for the analytical MAP (or maximum-likelihood) process, Feder and Weinstein applied the EM method for time delay and amplitude estimation.[20] The method, being elegant and fast, became an important tool for time-delay estimation.

EM is a two-step process: starting from randomly picked initial values for the unknown parameters, the expectation of the log likelihood is formed (expectation step). The expectation is, subsequently, maximized (maximization step) over the unknowns, and estimates of those are produced. The two-step procedure is repeated for a few iterations (typically, less than ten) until convergence to a maximum is achieved. This maximum, however, could be a local extremum, since, in many cases, likelihood functions (and posterior distributions) are multimodal. EM performs a local search and the estimates critically depend on the initial conditions. As discussed in Ref. 20, it is imperative that the process is run with several sets of initial conditions for inferences to be made on whether convergence to the global maximum has been achieved.

Tables I and II present the medians of time-delay-and amplitude estimates, respectively, from 200 realizations for one of the examined cases. For the estimation we used analytical MAP estimation (with diagonal loading), the proposed Gibbs sampler, and EM. Gibbs sampling and EM required selection of initial conditions. For both methods and all runs the same initial conditions were selected: 10 and 20 for the two delays, and 30 and 30 for the two amplitudes. The analytical processor and Gibbs sampling estimates are very close to the true values both in delay and amplitude. The poor EM performance, although startling at first sight, is not surprising. As mentioned earlier in the paper, EM is a local, hill-climbing technique, its performance highly dependent on initial conditions. All results reported in the previous section were generated with a single set of initial conditions. For EM to explore the search space more globally, as mentioned previously, it is recommended that several sets of initial conditions be employed and the process applied several times.

TABLE II. Medians of amplitude estimates from 200 realizations for the analytical MAP method, Gibbs sampling (GS), and EM for noise variance $\sigma^2 = 0.01\|r_s(n)\|^2$.

True amplitude	Anal. MAP	GS	EM
100	101.13	102.72	54.21
−90	−92.50	−95.43	54.37

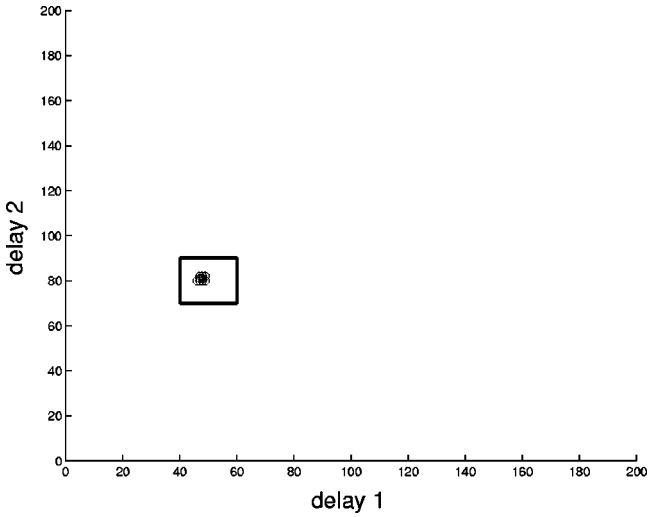

FIG. 6. Scatter plot for delays obtained via Gibbs sampling for 100 different initial conditions.

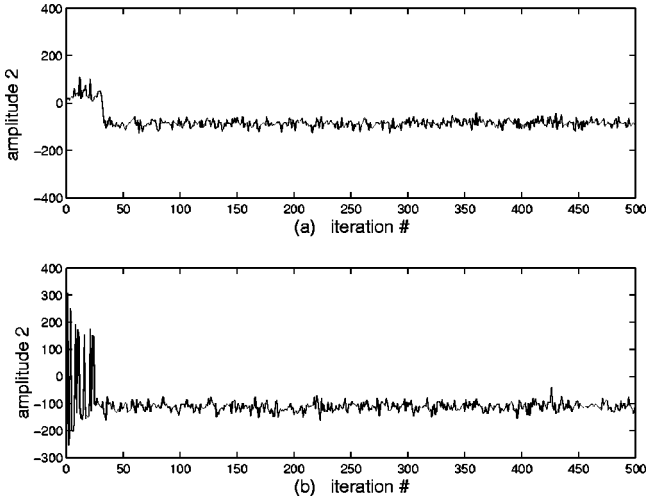

FIG. 8. Samples for the second amplitude drawn by the Gibbs sampler for two sets of initial conditions.

When such an approach is followed, EM typically gives good results in time-delay estimation.

To illustrate this point, we selected a single noisy realization for the two-arrival case. We performed time-delay- and amplitude estimation for this realization employing EM for 100 different sets of randomly selected initial conditions. At the same time, we applied the Gibbs sampler to the same realization with the same set of initial conditions. The true delays were at 50 and 80; the amplitudes were 100 and -90. The Gibbs sampler results, regardless of the initial conditions, yielded MAP estimates very close to the true values; those are shown in Figs. 6 and 7, demonstrating small deviations. Figure 8 shows samples drawn by the Gibbs sampler for the second amplitude vs iteration for two different initial conditions. The samples differ during the first few iterations but concentrate around the value of -90 after approximately 40 iterations in both cases.

Figures 9 and 10 show scatter plots of EM time-delay- and amplitude estimates for the first and second arrivals for the different initial conditions. The boxes in the plots demonstrate areas around the true parameter values. Only 14 sets of estimates fall inside the boxes (within 10 units of the true delays and 20 units of the true amplitudes).

A further test demonstrated a weakness of EM for closely spaced arrivals, which was not present in Gibbs sampling. A case with arrivals at samples 50 and 52 was selected; the amplitudes were 100 and -90. Initial conditions for EM were set at 49 and 53 for delays and 110 and -80 for amplitudes (all very close to the true values). EM was run on one noisy realization for 100 iterations. The delay estimates did not change from the initial conditions (49 and 53). The EM amplitude estimates versus iteration are shown in Fig. 11. The figure demonstrates that there is a divergence in the amplitude estimates; as the iterations progress, the amplitude estimates deviate further away from the true values. Such behavior is not present in EM results obtained for delays

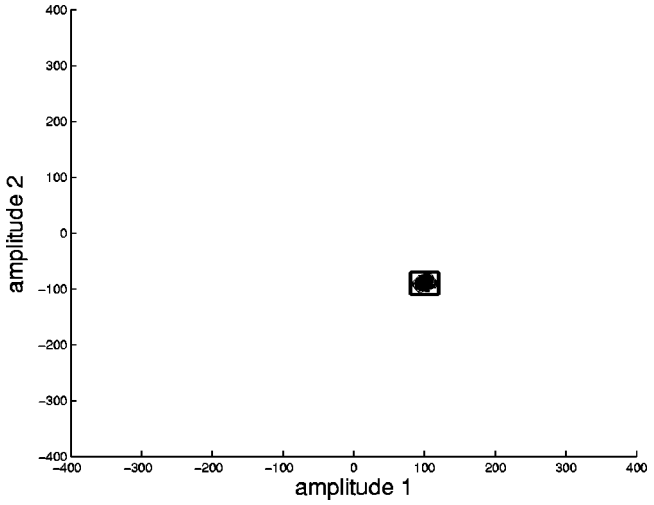

FIG. 7. Scatter plot for amplitudes obtained via Gibbs sampling for 100 different initial conditions.

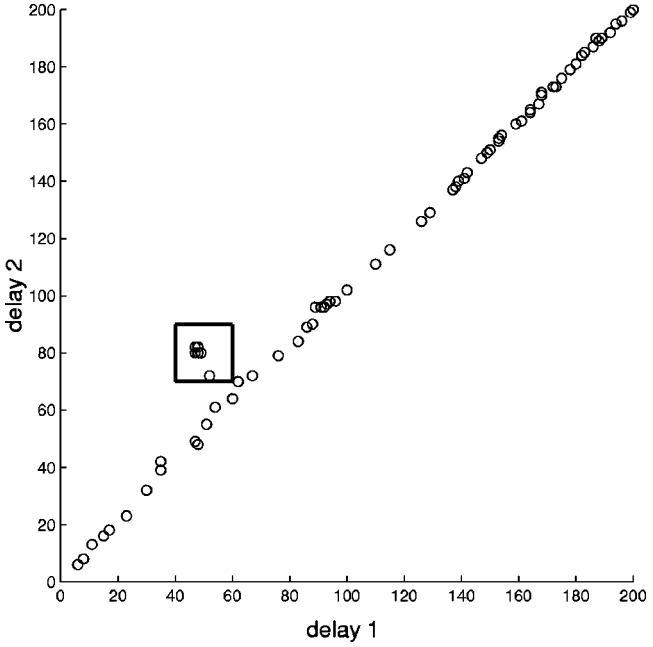

FIG. 9. Scatter plot for delays obtained via EM for 100 different initial conditions.

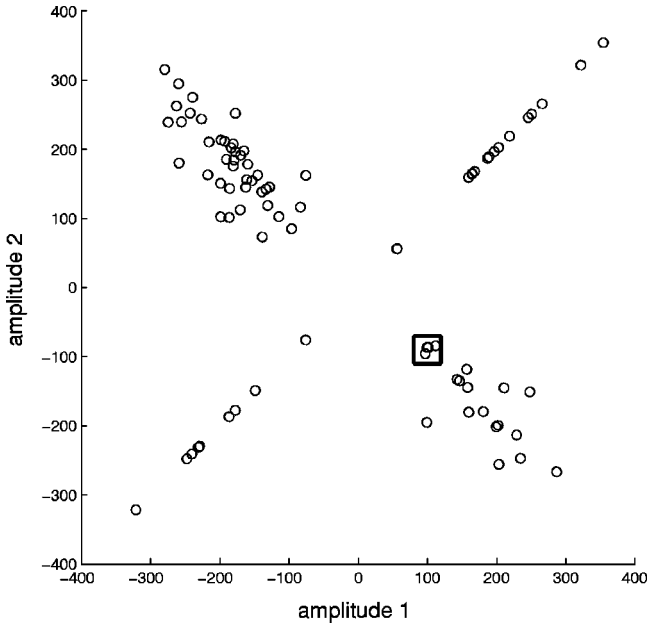

FIG. 10. Scatter plot for amplitudes obtained via EM for 100 different initial conditions.

with wider separation. Figure 12 shows EM amplitude estimates vs iteration for a case with delays at 50 and 80; true amplitudes were 100 and −90. Initial conditions were 49 and 83 for delays, and 110 and −80 for amplitudes. The amplitudes converged within less than ten iterations to values 101 and −86 (the delays stabilized to values 48 and 82 in one iteration). The divergence issue for the closely spaced arrivals did not appear in the Gibbs sampling results.

EM and several other methods applied to the task of time delay and amplitude estimation yield point estimates (single values), while the Gibbs sampler provides estimates of full posterior probability distributions of the parameters. These are particularly useful since they include a substantial amount of information that is naturally absent from point estimates; point estimates do not offer insight into variance structure or multimodality, which would explain the vulnerability of point estimators in finding a global maximum.

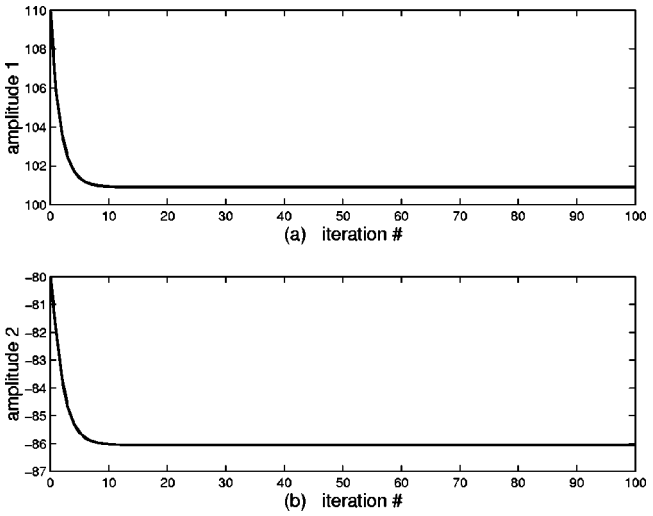

FIG. 12. EM: Amplitudes vs iteration for arrivals at samples 50 and 80.

As an example, Fig. 13 illustrates the two-dimensional posterior probability distributions over (a) delay 1 and amplitude 1 and (b) delay 2 and amplitude 2 for a two-arrival problem. The true arrival times are at samples 50 and 80; the true amplitudes are 100 and −90. Initial conditions for both amplitudes were set at 30; initial conditions for delays 1 and 2 were 10 and 20, respectively. Noise variance was equal to $0.05\|r_s(n)\|^2$. The Gibbs sampler gives the following estimates: 44 for the first delay, 100 for the first amplitude, 193 for the second delay, and 82 for the second amplitude. Although the first arrival is quite accurately characterized, the second arrival is erroneously estimated; concentration of probability around the erroneous set of values for the second arrival is an artifact generated by the presence of noise. However, observing Fig. 13(b), we can see that there is significant probability concentration around the correct values of 80 and −90 (corresponding to delay and amplitude) for the second arrival. Thus, although in terms of point estimates the second arrival is not correctly recovered by the Gibbs

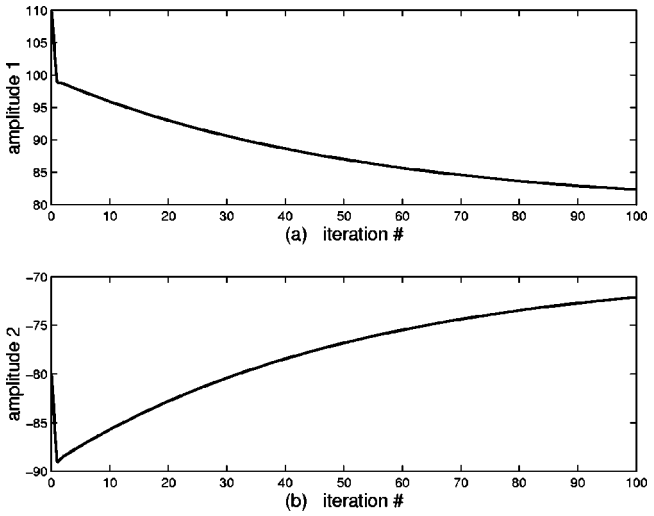

FIG. 11. EM: Amplitudes vs iteration for closely spaced arrivals (at samples 50 and 52).

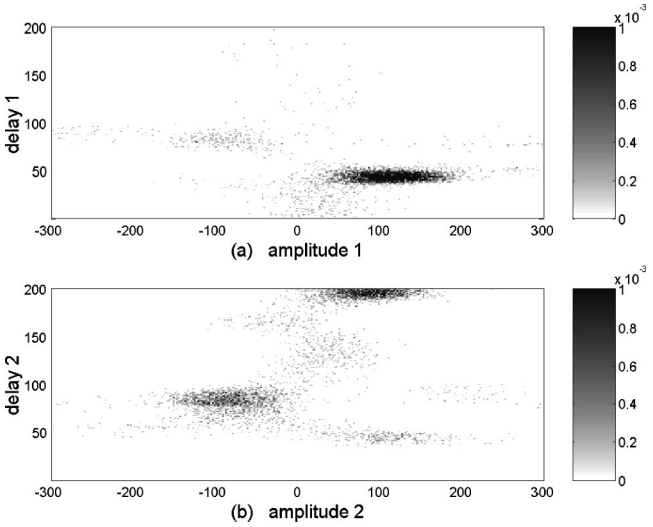

FIG. 13. Estimated posterior probability distributions of time delays and amplitudes via Gibbs sampling: (a) first arrival; (b) second arrival.

sampler (or other point estimators), the uncertainty introduced by the second peak of the posterior distribution strongly suggests that an alternative set of estimates may be relevant, and that further exploration is necessary for a better identification of the second arrival.

VI. UNKNOWN NUMBER OF ARRIVALS

In the preceding section, the number of arrivals was assumed known and equal to two. Typically, there is no precise information on the number of arrivals, which depends on the propagation medium. Here, the assumption of a known arrival number is relaxed; along with the amplitudes, delays, and noise variance, the number of arrivals is estimated.

According to the analysis presented in this paper, the joint probability distribution we have so far estimated with Gibbs sampling is in reality a conditional distribution, conditioning being on the number of arrivals M: $p(a_1,\ldots,a_M,n_1,\ldots,n_M,\sigma^2|r(n),M)$. Following the Bayesian paradigm, a prior distribution can be specified for M. In the absence of specific information on M, we select a uniform prior

$$p(M)=\frac{1}{M_2-M_1+1}, \quad M_1\leqslant M\leqslant M_2, \tag{14}$$

where M_1 and M_2 are lower and upper bounds for the expected arrival number.

For the uniform prior of Eq. (14), estimation of the number of arrivals, M, can be achieved using the Schwartz–Rissanen criterion for model selection.[29] According to the criterion, M is chosen in order to minimize

$$-\log p(r(n)|\hat{a}_i(i=1,\ldots,M),\hat{n}_i(i=1,\ldots,M),\hat{\sigma}^2) = -\frac{1}{2\sigma^2}\sum_{n=1}^{N}\left(r(n)-\sum_{i=1}^{M}\hat{a}_i s(n-\hat{n}_i)^2\right) - M\log(N), \tag{15}$$

where N is the length of the received signal, and $\hat{a}_i$ and $\hat{n}_i$ are the amplitude and delay estimates, respectively, obtained from the Gibbs sampler for a selected value of M between M_1 and M_2; $\hat{\sigma}^2$ is the estimate of the unknown variance. The Schwartz–Rissanen criterion uses estimates of amplitudes, delays, and variance to eventually calculate M. The criterion can be suitably altered in case of priors for M other than the uniform of Eq. (14).

Two hundred runs were generated to test the estimation of the number of arrivals; the variance was set to $0.01\|r_s(n)\|^2$. Three arrivals were present (at samples 50, 75, and 150 with amplitudes 100, −80, and 60, respectively). Using prior knowledge, it was assumed that M could vary between 2 and 5. Using the Schwartz–Rissanen criterion, M was estimated correctly to be three 138 out of the 200 times.

VII. CONVERGENCE OF THE GIBBS SAMPLER

There is not a straightforward manner with which to choose an optimal number of samples necessary for the Gibbs sampler to converge. Monitoring convergence is a topic of open research. Several approaches are recommended for testing the convergence of the estimated distribution to the true joint posterior.[21] In this work, the Gibbs sampler was originally tested by initializing the process with different parameter values. This is a standard procedure used to test convergence of Monte Carlo methods in general.[21,30] As shown in Sec. V (Figs. 6 and 7), the Gibbs sampler results were insensitive to initial conditions, indicating convergence of the process to the true posterior distribution.

TABLE III. Modes of the posterior distributions for amplitudes vs iteration groups.

Iterations	a_1	a_2	a_3
1 001–2 000	455	−405	75
2 001–3 000	135	−125	75
3 001–4 000	395	−475	75
4 001–5 000	1175	−1175	75
5 001–6 000	1255	−1215	75
6 001–7 000	85	−75	65
7 001–8 000	95	−85	65
8 001–9 000	105	−85	65
9 001–10 000	95	−85	65

Running several parallel Gibbs samplers initialized in different ways is an effective monitor for convergence but is computationally demanding. As an alternative convergence test, we monitored the modes of the marginal posterior distributions of the parameters (which can be readily calculated from the Gibbs sampling results[27] for a single set of initial conditions. Table III demonstrates the process for a three-arrival problem. The table includes modes for the distributions of the three amplitudes (true values: 100, −80, 60) for groups of 1000 iterations. The modes for the first two amplitudes vary significantly for different groups of iterations up to iteration 6000. Following that, the modes stabilize close to 100 and −85. After stabilization has been observed, the Gibbs sampler is stopped.

It was observed that, as expected, the number of necessary iterations for convergence increased with the number of arrivals M. The necessary number of iterations increased with noise variance as well. A closed-form relationship, however, relating convergence and factors affecting the estimation process was not derived. For the two arrival problem that we investigated in Sec. IV, we found that 5000 iterations were adequate for most realizations.

VIII. TIME-DELAY-AND AMPLITUDE ESTIMATION IN A REALISTIC ENVIRONMENT

To further validate the Gibbs sampling approach and simulate a realistic underwater propagation problem, we generated synthetic signals at two receiving hydrophones. The source signal, a *sinc* waveform with frequency content between 500 and 900 Hz, propagated in a shallow-water waveguide. The sampling rate was 2 kHz. The source was located at 55 m in depth; the receivers were 300 m away from the source, with two phones placed at 10 and 70 m in depth. The sound-speed profile in the 200-m-deep water column was an isovelocity one set at 1482 m/s. A sketch of the environment, which is similar to that of the Haro Strait experiment,[10] is shown in Fig. 14.

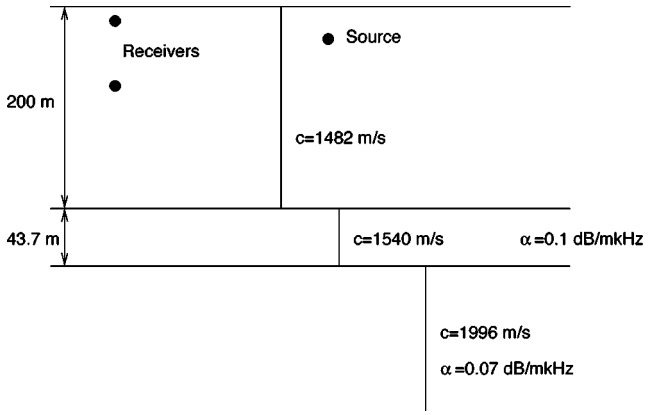

FIG. 14. The propagation environment.

Time series were generated at the two receiving phones using a broadband normal-mode approach.[31] Under the assumptions underlying the simulations experiment, two paths (direct and surface reflection) are observed at the two receivers (other arrivals are severely attenuated and hardly present at the selected phone depths). Figure 15 presents the two noise-free received time series. The same time axis is used for both time series. We assume that the source instant is unknown (as is usually the case); we are, thus, estimating arrival times relative to an arbitrarily selected initial time $t=0$ and are actually interested in relative arrival times between distinct paths. The two paths (direct and surface reflection) overlap at the first phone and are visibly separated at the second phone. For the assumed isovelocity profile and the source–receiver geometry, sound is expected to arrive at the top receiver in 0.2047 s. The surface reflection is expected at 0.2071 s. The difference between the two arrival times for the first phone is 0.0024 s or, equivalently, 5 samples for a 2-kHz sampling rate. For the second phone, the two arrival times are calculated as 0.2027 and 0.2193 s for the direct and surface paths, respectively, corresponding to an arrival time difference of 33 samples.

A set of 200 noisy realizations was then generated for each phone for noise variance of $0.01\|r_s(n)\|^2$, where $r_s(n)$ was the noise-free time series. The Gibbs sampler was applied to the noisy data for the estimation of the two arrival times and amplitudes for each phone (the number of arrivals was assumed known). Initial conditions were set to samples 10 and 20 for the two arrival times, and to 30 for both amplitudes. It should be emphasized that the time series were generated using a normal-mode model, while the estimation process models the time series via Eq. (1). The estimates for delays and amplitudes are given in Tables IV and V, respectively; time series 1 is the time series at the top receiver (10 m in depth) and time series 2 is that corresponding to the receiver at 70 m in depth. The time-delay estimates of Table IV show an excellent match with our previous calculations; the two arrival times differ by 4 samples (our calculation was 5), and the two arrival times for the second time series differ by 33 samples (our calculation was 33). Taking into account the very close arrivals in time series 1 and the problems typically encountered when paths are close in time, the Gibbs sampler offers excellent estimates of the delays (and delay differences). The amplitudes (Table V) also seem to follow expectations; the direct arrival and surface reflection are found to have opposite polarities for both time series. A larger standard deviation in the amplitude of the second arrival of time series 1 is likely the result of trying to resolve two overlapping paths.

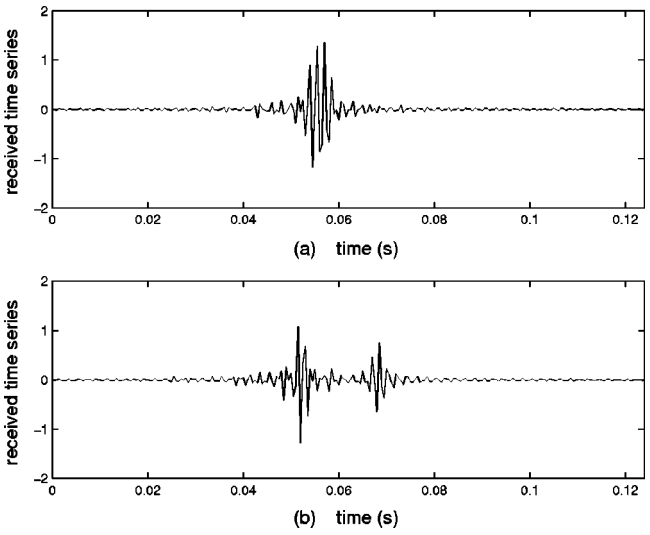

FIG. 15. Received times series at two vertically separated phones at a horizontal distance of 300 m from a sound source. The phones are placed at depths of (a) 10 m and (b) 70 m.

TABLE IV. Medians and standard deviations of Gibbs sampling delay estimates from 200 realizations for the two time series generated for an ocean environment.

Time series 1 median	Times series 1 st. dev.	Time series 2 median	Time series 2 st. dev.
80	1.53	75	0.24
84	0.58	108	5.06

IX. CONCLUSIONS

A novel approach for time-delay-and amplitude estimation in multipath environments was presented. The technique estimates joint posterior distributions using Gibbs sampling; once an estimate of the posterior distribution of time delays and amplitudes is available, its maximum yields estimates for the unknowns. The proposed method differs from other approaches typically used in time-delay estimation in that, in addition to point estimates, it offers full posterior distributions for the parameters of interest. Those distributions could potentially highlight information (such as a missed arrival), which would have otherwise remained obscure.

The method performs well compared to the analytical MAP estimator. It is also stable with respect to initial condi-

TABLE V. Medians and standard deviations of Gibbs sampling amplitude estimates from 200 realizations for the two time series generated for an ocean environment.

Time series 1 median	Times series 1 st. dev.	Time series 2 median	Time series 2 st. dev.
4.46	1.73	3.94	1.40
−0.25	4.68	−1.82	2.18

tions and is not adversely affected in the case of closely spaced arrivals. Convergence is monitored through an examination of the stability of statistics (modes, in our case) of marginal posterior distributions.

ACKNOWLEDGMENTS

This work was funded by the Office of Naval Research through Grants N00014-01-1-0085 and N00014-97-1-0600.

[1] A. Tolstoy, *Matched Field Processing for Underwater Acoustics* (World Scientific, Singapore, 1993).
[2] A. Baggeroer, W. Kuperman, and H. Schmidt, ''Matched field processing: Source localization in correlated noise as an optimum parameters estimation problem,'' J. Acoust. Soc. Am. **83**, 571–587 (1988).
[3] H. Bucker, ''Matched-field tracking in shallow water,'' J. Acoust. Soc. Am. **96**(6), 3809–3811 (1994).
[4] S. E. Dosso, M. R. Fallat, B. J. Sotirin, and J. L. Newton, ''Array element localization for horizontal arrays via Occam's inversion,'' J. Acoust. Soc. Am. **104**(2), 846–859 (1998).
[5] S. E. Dosso, G. H. Brooke, S. J. Kilistoff, B. J. Sotirin, V. K. McDonald, M. R. Fallat, and N. E. Collison, ''High-precision array element localization for vertical line arrays in the Arctic Ocean,'' IEEE J. Ocean. Eng. **23**, No. 4, 365–379 (1998).
[6] S. E. Dosso and B. Sotirin, ''Optimal array element localization,'' J. Acoust. Soc. Am. **106**, 3445–3459 (1999).
[7] E. K. Westwood and D. P. Knobles, ''Source track localization via multipath correlation matching,'' J. Acoust. Soc. Am. **102**, 2645–2654 (1997).
[8] P. Pignot and R. Chapman, ''Tomographic inversion for geoacoustic properties in a range dependent shallow water environment,'' J. Acoust. Soc. Am. **110**(3), 1338–1348 (2001).
[9] L. Jaschke, ''Geophysical inversion by the freeze bath method with an application to geoacoustic ocean bottom parameter estimation,'' M.S. thesis, University of Victoria, 1997.
[10] L. Jaschke and R. Chapman, ''Matched field inversion of broadband data using the freeze bath method,'' J. Acoust. Soc. Am. **106(4)**, 1838–1851 (1999).
[11] X. Ma, ''Efficient inversion methods in underwater acoustics,'' Ph.D. thesis, New Jersey Institute of Technology, May 2001.
[12] J. E. Ehrenberg, T. E. Ewart, and R. D. Morris, ''Signal processing techniques for resolving individual pulses in a multipath signal,'' J. Acoust. Soc. Am. **63**, 1861–1865 (1978).
[13] G. C. Carter, ''Time delay estimation for passive sonar signal processing,'' IEEE Trans. Acoust., Speech, Signal Process. **29**, 463–470 (1981).
[14] *Coherence and Time Delay Estimation*, edited by G. C. Carter (IEEE, New York, 1993).
[15] R. J. Tremblay, G. C. Carter, and D. W. Lytle, ''A practical approach to the estimation of amplitude and time delay parameters of a composite signal,'' IEEE J. Ocean. Eng. **OE-12**, 273–278 (1987).
[16] I. Kirsteins, ''High resolution time delay estimation,'' in ICASSP-87, pp. 451–453, 1987.
[17] S. Umesh and D. W. Tufts, ''Estimation of parameters of exponentially damped sinusoids using fast maximum likelihood estimation with application to NMR spectroscopy data,'' IEEE Trans. Signal Process. **44**, 2245–2259 (1996).
[18] A. D. Blackowiak and S. D. Rajan, ''Multi-path arrival estimates using simulated annealing: Application to crosshole tomography experiment,'' IEEE J. Ocean. Eng. **20**, 157–165 (1995).
[19] A. P. Dempster, N. M. Laird, and D. B. Rubin, ''Maximum likelihood from incomplete data via the EM algorithm,'' J. R. Stat. Soc. Ser. B. Methodol. **39**, 1–38 (1977).
[20] M. Feder and E. Weinstein, ''Parameter estimation of superimposed signals using the EM algorithm,'' IEEE Trans. Acoust., Speech, Signal Process. **36**, No. 4, 477–489 (1988).
[21] W. R. Gilks, S. Richardson, and D. J. Spiegelhalter, *Markov Chain Monte Carlo in Practice*, 1st ed. (Chapman and Hall, London CRC, 1996).
[22] Z.-H. Michalopoulou and M. Picarelli, ''A Gibbs sampling approach to maximum a posteriori time delay and amplitude estimation,'' in ICASSP-02, Vol. 3, pp. 3001–3004, 2002.
[23] J. O. Berger, *Statistical Decision Theory and Bayesian Analysis*, 2nd ed. (Springer, Berlin, 1985).
[24] G. Box and G. Tiao, *Bayesian Inference in Statistical Analysis* (Addison-Wesley, Reading, MA, 1973).
[25] M. A. Tanner, *Lecture Notes in Statistics: Tools for Statistical Inference*, 2nd ed., Observed Data and Data Augmentation Methods, Vol. 67 (Springer, Berlin, 1992).
[26] S. Geman and D. Geman, ''Stochastic relaxation, Gibbs distributions, and the Bayesian restoration of images,'' IEEE Trans. Pattern Anal. Mach. Intell. **PAMI-6**, 721–741 (1984).
[27] A. E. Gelfand and A. F. Smith, ''Sampling-based approaches to calculating marginal densities,'' J. Am. Stat. Assoc. **85**, 398–409 (1990).
[28] R. Aster, B. Borchers, and C. Thurber, *Parameter Estimation and Inverse Problems* (Elsevier, Amsterdam, 2004).
[29] M. Wax and T. Kailath, ''Detection of signals by information theoretic criteria,'' IEEE Trans. Acoust., Speech, Signal Process. **32**, 387–392 (1985).
[30] S. Dosso, ''Quantifying uncertainty in matched field inversion. I A fast Gibbs sampler approach,'' J. Acoust. Soc. Am. **111**, No. 1, 129–142 (2002).
[31] M. B. Porter, ''The KRAKEN normal mode program,'' SACLANT Undersea Research Centre Memorandum (SM-245) and Naval Research Laboratory Mem. Rep. 6920, 1991.

Inversion of sonobuoy data from shallow-water sites with simulated annealing

Dennis Lindwall[a)]
Naval Research Laboratory, Seafloor Sciences Branch, Stennis Space Center, Mississippi 39529

John Brozena
Naval Research Laboratory, Marine Physics Branch, 4555 Overlook Avenue SW, Washington, D.C. 20375-5320

(Received 15 April 2004; revised 4 November 2004; accepted 30 November 2004)

An enhanced simulated annealing algorithm is used to invert sparsely sampled seismic data collected with sonobuoys to obtain seafloor geoacoustic properties at two littoral marine environments as well as for a synthetic data set. Inversion of field data from a 750-m water-depth site using a water-gun sound source found a good solution which included a pronounced subbottom reflector after 6483 iterations over seven variables. Field data from a 250-m water-depth site using an air-gun source required 35 421 iterations for a good inversion solution because 30 variables had to be solved for, including the shot-to-receiver offsets. The sonobuoy derived compressional wave velocity–depth (V_p-Z) models compare favorably with V_p-Z models derived from nearby, high-quality, multichannel seismic data. There are, however, substantial differences between seafloor reflection coefficients calculated from field models and seafloor reflection coefficients based on commonly used V_p regression curves (gradients). Reflection loss is higher at one field site and lower at the other than predicted from commonly used V_p gradients for terrigenous sediments. In addition, there are strong effects on reflection loss due to the subseafloor interfaces that are also not predicted by V_p gradients. [DOI: 10.1121/1.1850405]

PACS numbers: 43.60.Pt, 43.30.Ma [RAS] Pages: 809–817

I. INTRODUCTION AND FIELD DATA

The purpose of the sonobuoy-based data collection procedure and modified simulated annealing (SA) inversion technique described here is to rapidly determine seafloor geoacoustic parameters, primarily subbottom layer thicknesses and compressional wave velocities, using inexpensive and easily deployed equipment from ships and (potentially) aircraft. The modified SA inversion technique has been previously used by Wood and Lindwall (1996) on high-frequency normal-incidence acoustic profiles of the seafloor, by Lindwall *et al.* (1995) on deep-tow multichannel seismic data, and by Lindwall (1995) on normal-incidence acoustic profiles, deep-tow multichannel data, and simulated seismic refraction data.

Data preparation for the inversion used a series of FORTRAN and Seismic Unix (SU; Cohen and Stockwell, 2003) programs. Shot-to-receiver offsets were calculated from the direct wave arrival time at the receivers, which we first picked automatically and then adjusted manually. Accurate measurements of the water sound velocity, water depth, and source and receiver depths were made in the field when possible; however, if these environmental variables are poorly known, they must be included in the inversion calculation, making computation times much greater.

The modified SA inversion is first applied to synthetic data and then to two sets of field data. Inverting synthetic data tests the inversion algorithm, since the earth model is known exactly and the data can be generated at any desired quality. The field data were collected in the STRATA FORmation on Margins (STRATAFORM) area near the mouth of the Eel River in California (Fig. 1). The STRATAFORM program is a coordinated multi-investigator study of continental-margin stratigraphy initiated by the Office of Naval Research (Nittrouer, 1999). This area was selected as the West Coast STRATAFORM site because of the high rate of sediment deposition. Extensive shallow geological and geoacoustic studies have been done here (Nittrouer, 1999) as well as two multichannel seismic exploration surveys (C. Fulthorpe, personal communication, 1997; J. Yun, personal communication, 1997; Yun *et al.*, 1999). The geological studies only cover the upper few meters of sediment, while the multichannel seismic surveys penetrated approximately the same 200- to 300-m depths as reached in this sonobuoy study.

The quality of the field data presented here is low in terms of amplitude dynamic range, frequency bandwidth, and spatial sampling, but that is the main challenge for this inversion application. Our original plan was to collect and invert data from a few receivers and sources at each location, but the plan changed to inverting data from a single receiver and multiple sources. We deployed six to ten sonobuoys at each site and shot to them during two or three passes from the ship. The field data had too many variables to allow an inversion using data from several sonobuoys simultaneously. Each sonobuoy had a different sensitivity and, given the limited dynamic ranges of the buoys, each had a different recovery response from the direct water-wave signal. Correcting for each receiver response as well as solving for each sonobuoy and shot position in three dimensions would add a

[a)]Electronic mail: lindwall@nrlssc.navy.mil

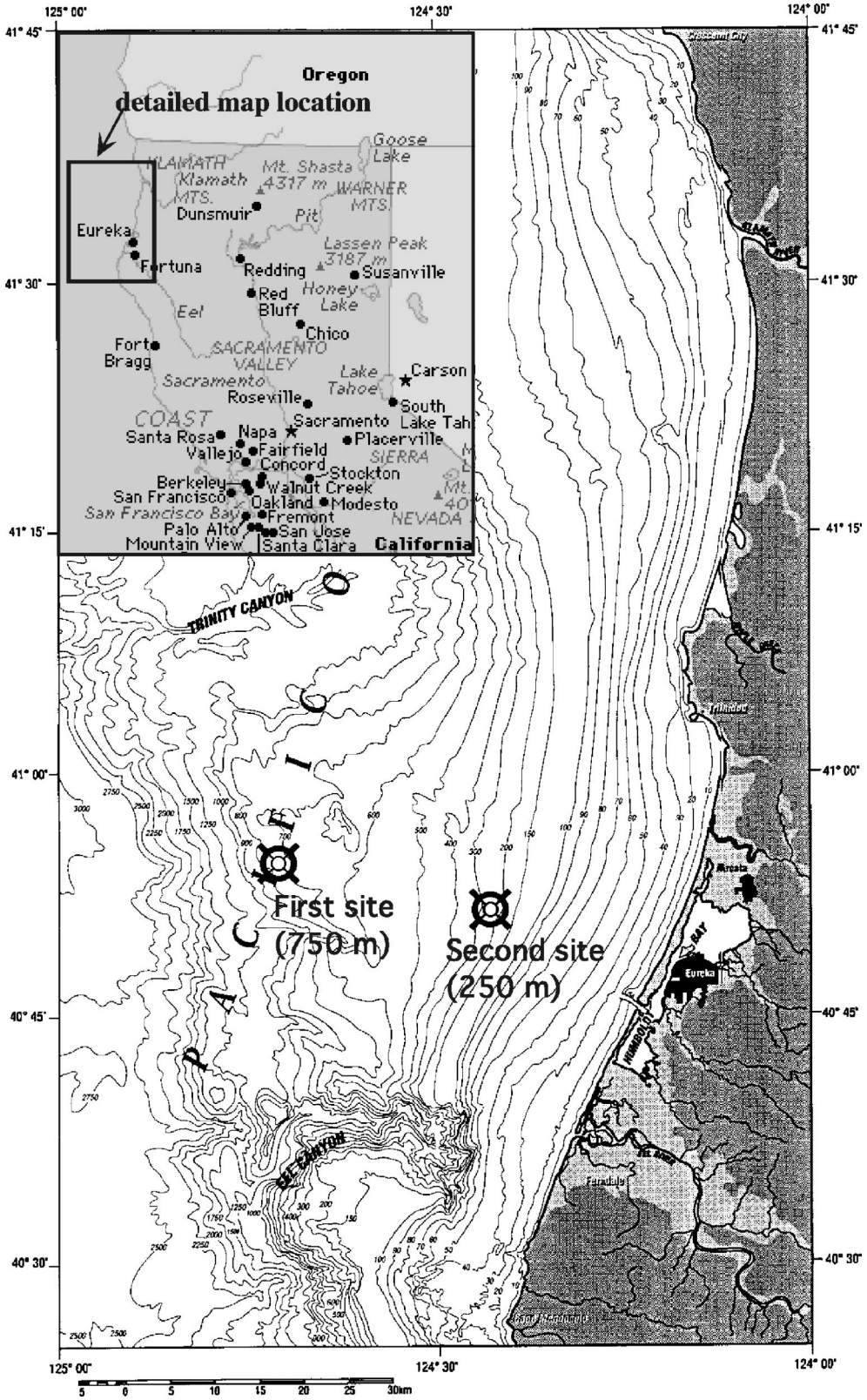

FIG. 1. Location map for the field data. Both field sites are located in the West Coast STRATAFORM area, which is on the sediment fan of the Eel River. There have been extensive coring studies, acoustic seafloor classification surveys, and seismic exploration surveys in this area. The first site has a water depth of 750 m and the second site has a depth of 250 m. The ship tracks were parallel to the isobaths. The data from these two sites (out of eight) were the deepest and shallowest sites where we had good data.

large number of additional variables to the inversion problem. Continued development of our inversion algorithm will eventually allow the use of multiple sonobuoy recordings, but here, we limit our effort to the level of difficulty of multiple shots to a single sonobuoy.

U.S. Navy AN/SSQ-57B ambient-noise sonobuoys were

deployed from a ship while steaming along an isobath, firing an acoustic source (water gun or air gun) every 30 s. The sonobuoys employ a calibrated omnidirectional hydrophone set for a depth of 18 m. The telemetered hydrophone signals were received at the ship by a U.S. Navy ARR-72 16-channel sonobuoy receiver. The acoustic signals were digitized and stored on tape for the full audio bandwidth of the buoys (20 kHz) and later filtered and downsampled to a 2-kHz sample rate for processing and analysis. An additional audio channel on the data acquisition system recorded ''shot time'' data from a microphone located near the stern of the ship. Start times for processing of the sonobuoy arrivals were determined from the microphone signal. Sonobuoy deployment and shot locations were tagged with differential GPS positions for an initial estimate of offset distances.

II. INVERSION METHOD

The rapid inversion method described here is adapted from the SA method. The original SA algorithm is by Metropolis *et al.* (1953), who used it to describe atoms in thermal equilibrium. Kirkpatrick *et al.* (1983) showed how SA can be used as a method for multivariate optimization, i.e., inversion. Basu and Frazer (1990) first applied SA inversion to velocity estimations from seismic waveform data, with later developments by Sen and Stoffa (1991). The very fast simulated annealing (VFSA) modification of Ingber (1989) accelerates convergence by progressively focusing the model search space onto the better-fitting solutions. The SA algorithm used in this study is an extension of all of these methods.

SA inversion uses synthetic data from a forward-modeling algorithm and an evolutionary test criterion, the cost or objective function, to determine the best-fitting physical model (environmental parameters) for a given data set. SA inversion is used in cases where the physical model cannot be directly determined from the data and the model space is too complex for the best solution to be found by moving by iterative improvement from a random starting solution. To calculate the synthetic data for this study, we used a ray-trace code with a one-dimensional environmental model that includes shear wave conversion losses, but does not include compressional wave multiples or the sea-surface reflections (Chapman, 1976; Cerveny *et al.*, 1977). This forward algorithm was chosen because it is extremely fast relative to full wave-field methods, such as reflectivity (Fuchs and Müller, 1971), used by Lindwall (1995) and Wood and Lindwall (1996).

The SA algorithm used here has the option of using a different temperature (or convergence criteria) for each layer in the earth model. By using lower temperatures for the upper layers, the model parameters for these layers can be fit before fitting the lower layers. This is similar to the technique of ''layer stripping'' (Slotnick, 1950). The upper layers, especially the seafloor, usually give stronger reflections than lower layers. Fitting the stronger features from the upper layers is usually easy and can be done quickly. With the upper structure constrained, the lower model parameters are easier to fit. The second significant new option is for fitting the waveform envelope rather than the waveforms. Fitting the waveform envelope greatly smoothes the residual function, particularly for high-frequency and limited bandwidth signals, making the inversion much faster (Wood and Lindwall, 1996).

III. VP MODELING OF SHELF SEDIMENTS

The first inversion example uses synthetic data [Fig. 2(a)] from an environmental model having 15 layers with six variables for each layer. These variables are: thickness, density, compressional wave velocity (V_p), shear wave velocity (V_s), compressional attenuation, and shear attenuation. The search was done only over V_p and layer thickness for the upper three sediment layers in order to reduce computation time. All other model variables were set to their true values. Within a limited time (877 iterations) the inversion found the solution shown in Fig. 2(d). The residual amplitude [Fig. 2(c)] is less than 10% of the data amplitude. This first inversion solution fit the waveforms well, since we used the same forward algorithm to calculate both the synthetic data and the inversion solutions. The field data waveforms were converted to envelopes to minimize problems with sea-surface reflections, source signal deconvolution, and receiver response.

The first of the marine data sets [Fig. 3(a)] was collected from a 750-m water-depth site (Fig. 1) using a water-gun sound source. The water gun produced a very sharp impulse, so we did not need to use source deconvolution. The data were smoothed with a 50-Hz low-pass filter (from the 2-kHz sample rate) to allow for simpler models and an easier inversion at the expense of spatial resolution. Source-to-receiver offsets were carefully determined from the unfiltered (to retain resolution) direct wave arrival times. We fit the envelope rather than the waveform, since the forward-modeling algorithm does not include important parts of the waveform in the calculation, specifically the sea-surface multiples and interbed multiples from the detailed structures near each of the major interfaces. Fitting the waveform envelope allows for a much faster inversion with nearly the same precision as a full waveform fit (Wood and Lindwall, 1996). The residual from the inversion solution shown has 51% of the amplitude of a random solution, which we feel is a good result for field data. Sen and Stoffa (1991) achieved a correlation of about 0.5 while inverting synthetic data with 30% noise and came very close to the true model. When Sen and Stoffa (1991) inverted field data, their highest correlation was 0.759. This inversion used 6483 iterations and took 32 min on a Sun SPARC 10.

Only two features in the data from the first site [Fig. 3(a)] were modeled, the seafloor reflection and a subsurface reflection about 0.2 s after the seafloor reflection. The seafloor depth, as determined by the inversion fit of the reflection hyperbola, is 756 m deep and the water velocity is 1.498 km/s. The V_p of the upper sediments is 1.538 km/s. The subsurface reflector interface is 147 m below the seafloor with a V_p of 1.558 km/s below that horizon. The V_p of the lower sediment is poorly constrained since only the relative amplitude of the reflection is known, and that value is dependent on the unknown density contrast as well as V_p. V_p measurements from nearby multichannel seismic lines (C. Fulthorpe, personal communication, 1997; J. Yun, personal

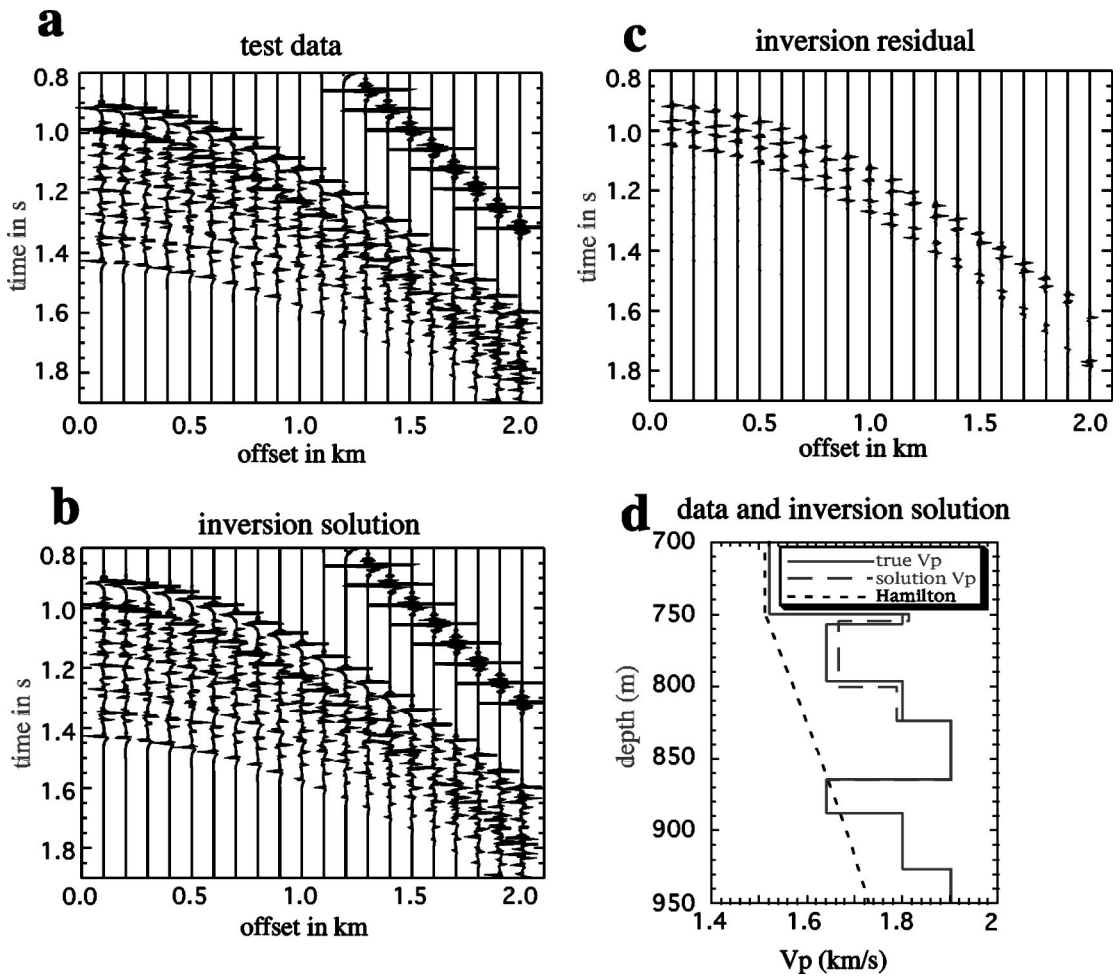

FIG. 2. Synthetic data (a) calculated using a realistic marine sediment model are inverted using simulated annealing (SA) to find a good fit with limited computational resources (877 iterations and 110 min on a Sun SPARC10). The solution synthetic is in panel (b) for comparison. The residual (a)–(b) is shown in (c) and has only 9.6% of the amplitude of the data (summed over the time window), demonstrating that the fit is very good. Panel (d) compares the known physical model (solid line) to the inversion solution (long dashes). The velocity search window was from 1.5 to 2.5 km/s and the layer thickness window was ±33% of the true value. A commonly used curve for terrigenous sediments (Hamilton, 1980) is shown for comparison (short dashes).

communication, 1997) have similar subbottom velocities [Fig. 3(d)]. The MCS data are adjusted so that the seafloor depth is the same as our SA inversion solution. The sediment V_p determined from the sonobuoy data is equal to the lowest value obtained from the MCS data, and all but one of the MCS profiles show a significant reflector within 50 m of the depth of the reflection horizon identified by the SA inversion. Most of the MCS data came from a 168-channel, 2.5-km-long streamer which collected higher quality data than the sonobuoys used for the SA inversion.

We tested the reliability of the ray-traced synthetics by calculating reflectivity synthetics for the final solution, and also tested the sensitivity of the solution to shear wave velocity [Figs. 3(e) and (f)]. The lower reflection in the ray-traced synthetics has a cutoff at about 0.8 km that is not present in the reflectivity synthetics. The synthetics from the high V_s model has a slightly weaker seafloor reflection at the larger offsets than the low V_s calculations. Considering the level of noise in the data [Fig. 3(a)], we do not believe that the inversion is sensitive to the shear wave velocities. The reliability of the SA inversion using sonobuoy data is also supported by the overall agreement between the sonobuoy-derived and the MCS-derived V_p models.

A second field data set was collected at a shallower site (~250-m water depth, Fig. 1) using an 82-ml air-gun source. The air gun produces a lower frequency signal and has a narrower bandwidth than the water gun used at the 750-m-depth site. Source-to-receiver offsets were initially determined from the direct water wave arrival times, but these were not accurate enough for a good inversion. It was necessary to include the offsets as inversion variables, adding 20 variables to the existing 10 model variables. Solving for 30 rather than 10 variables means not only that each sweep (once through all variables) takes three times as many calculations, but the cooling process must also be done much more slowly. There have been no studies of how many more iterations are needed for each new variable added to an inversion, but experience suggests that it is a power law rather than linear function. This third inversion case used 35 421 iterations for 30 variables, while the data inversion for the 750-m site required 6483 iterations for 7 variables. Again, we fit the envelope rather than the waveform. The lower frequency of the air-gun signal reduced some of the complications of having a limited bandwidth and the lack of surface reflections in the synthetic calculations. The shallower water depth at this site complicates the analysis, since the seafloor

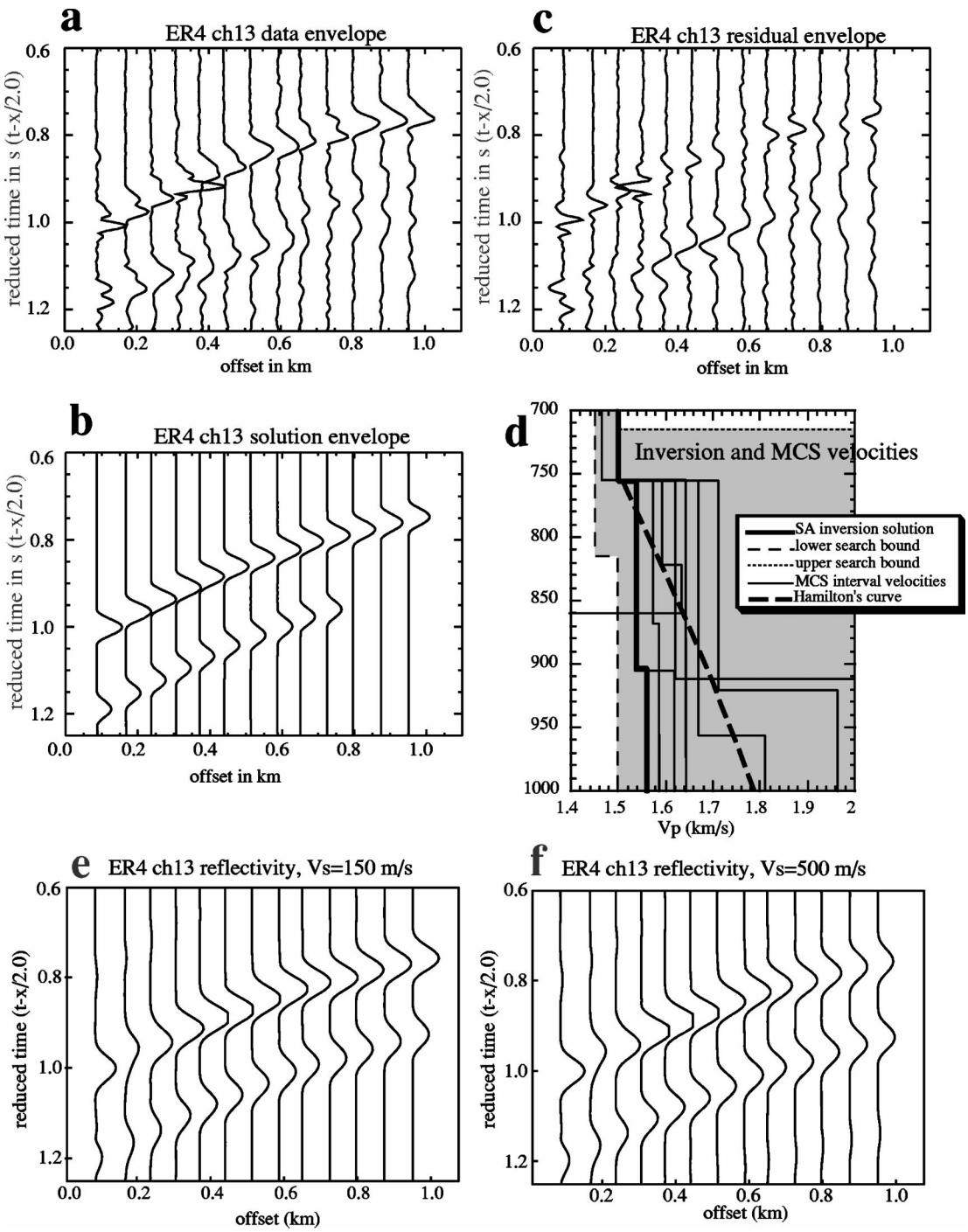

FIG. 3. Inversion of field data collected in the Eel River STRATAFORM area at a water depth of 756 m. The field data [panel (a)] shows the seafloor reflection as the large-amplitude reflection ranging from 1.0 s reduced time at 0.1 km to 0.75 s at 0.95 km. The subseafloor reflector noted in the text appears in (a) at 1.2 s at 0.1 km and decreases rapidly in amplitude with increasing offset. Synthetic data using the solution model determined by the simulated annealing (SA) inversion (6483 iterations and 32 min on a Sun SPARC10) is in panel (b) for comparison. The residual (a)–(b) is shown in panel (c) and has 51% of the amplitude of a random solution. Panel (d) compares the compressional wave (V_p) inversion solution (thick line) to V_p determined from several high-resolution multichannel seismic (MCS) data (thin lines) collected at nearby sites and adjusted so that the seafloor depths are the same. The SA inversion solution is identical to the lowest MCS solution (the two lines are superimposed down to 905 m), and three other MCS sites have a similar reflector between 900- and 920-m depth. This approximate agreement with the MCS data indicates that the SA inversion gives reliable results. The gray area in panel (d) covers the search range for the V_p and depth variables used by the SA algorithm. A commonly used curve for terrigenous sediments (Hamilton, 1980) is shown for comparison (dashed line). Synthetic sections calculated using reflectivity are shown in panels (e) and (f). The synthetic data in panel (f) were made with a high shear wave velocity and have a relatively weaker seafloor reflection at the larger offsets than the low V_s calculation. Using the reflectivity code for the inversion is not practical, since one forward iteration took 93 s largely due to the very fine sampling required over the wave number to avoid aliasing at the smallest offsets.

and subbottom reflections are perilously close to the direct arrivals which saturated the sonobuoy receivers. Sonobuoy data do not have the correct amplitudes or waveforms when they are saturated, and the sonobuoy electronics take several tenths of a second to recover. The distorted amplitudes of the seafloor reflections and the overlapping, decaying direct signal make reliable inversions more difficult.

Features in the data modeled for the 250-m-depth site

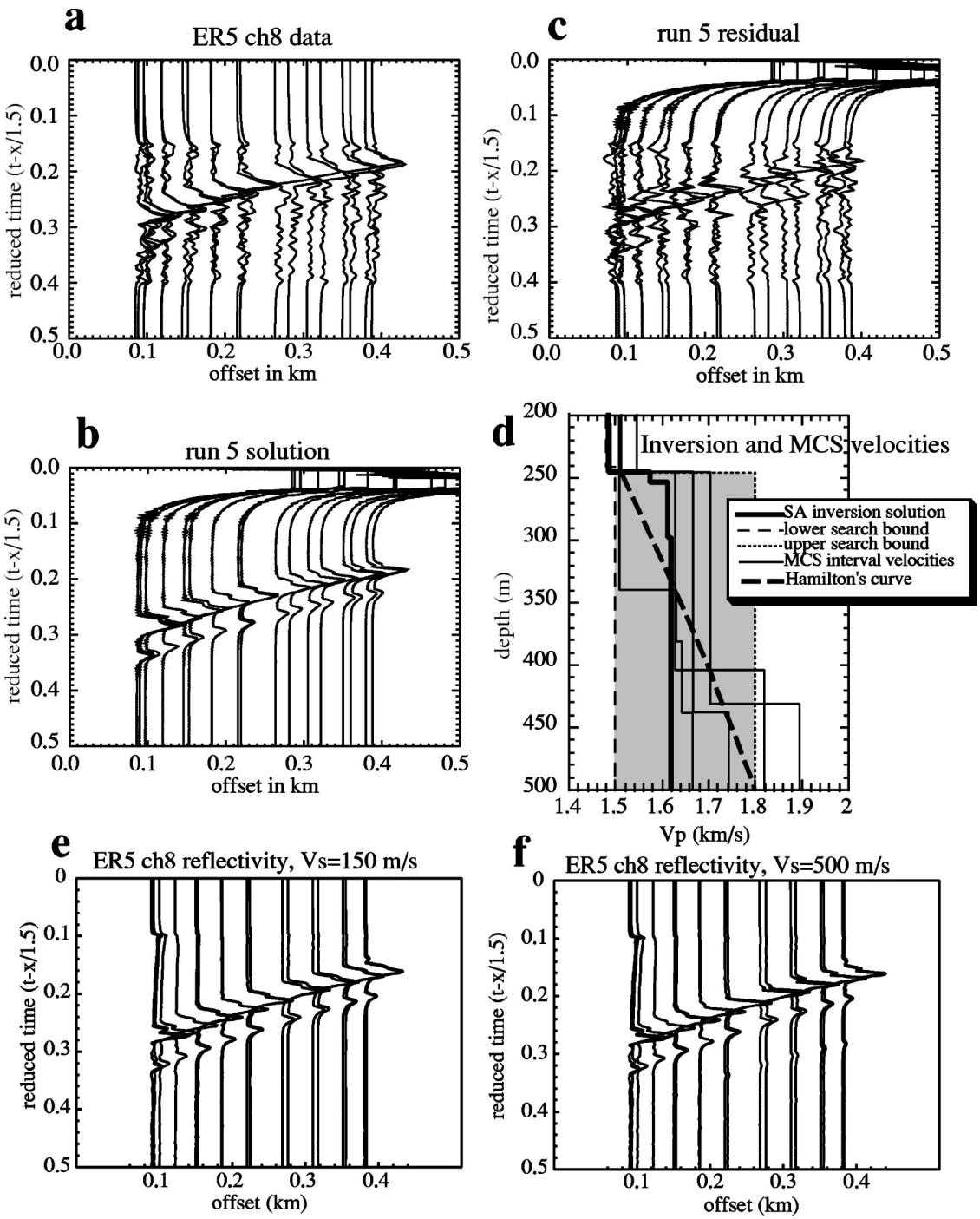

FIG. 4. Inversion of field data collected in the Eel River STRATAFORM area at a water depth of 245 m. The field data are shown in panel (a). The SA inversion solution used 35 421 iterations and took 9.6 h on a Sun SPARC10. The solution synthetic is in panel (b) for comparison. The residual (a)–(b) is shown in panel (c) and has 80% of the amplitude of a random solution. The first 0.15 s of the data (a) are muted because the sonobuoy electronics were saturated by the direct wave. The very high amplitudes for the first 0.1 s in (b) is the direct wave as calculated by the synthetic program. Panel (d) compares the inversion solution (thick line) to velocities determined from several high-resolution multichannel seismic (MCS) data (thin lines) collected nearby and adjusted so that the seafloor depths correspond. The V_p values for the upper 150 m of sediment from the SA inversion are in the middle of the MCS derived values, indicating a reliable result from the inversion. The prominent reflector in the MCS data at a depth range of 380–440 m is obscured in the sonobuoy data by the sea-surface multiple and so is not modeled in the SA inversion. The gray area in panel (d) covers the search range for the V_p and depth variables used by the SA algorithm. A commonly used curve for terrigenous sediments (Hamilton, 1980) is shown for comparison (dashed line). Synthetic sections calculated using reflectivity are shown in panels (e) and (f). Using the reflectivity code for the inversion is not practical, since one forward iteration took 142 s largely due to the very fine sampling required over the wave number to avoid aliasing at the smallest offsets.

[Fig. 4(a)] include a complex seafloor reflection and a subsurface reflection arriving about 0.04 s after the seafloor reflection. The inversion solution gives a seafloor depth of 245 m and a water sound velocity of 1.482 km/s (from the seafloor reflection hyperbola). The measured V_p of the first 9 m of sediment is 1.573 km/s and 1.612 km/s for the underlying 43-m-thick layer. The V_p below this is modeled at 1.618 km/s, but this value is poorly constrained because it is based

on amplitude rather than a well-developed reflection hyperbola. V_p models from nearby multichannel seismic lines (C. Fulthorpe, personal communication, 1997; J. Yun, personal communication, 1997) have similar subbottom V_p values [Fig. 4(d)]. The MCS data are adjusted so that the seafloor depth is the same as the SA inversion solution. Our sediment V_p measurements are in the middle of the multichannel seismic (MCS) measured values for the upper 100 m. All of the MCS data show a significant interface at the 400–440-m-depth range, but the reflection arrival times are the same as the seafloor reflection multiple in the sonobuoy data so it is not visible. The SA inversion solution is consistent with the MCS data.

We again tested the reliability of the ray-traced synthetics by calculating reflectivity synthetics for the final solution, and also tested the sensitivity of the solution to shear wave velocity [Figs. 4(e) and (f)]. There is a slight decrease in the strength of the seafloor reflection at the larger reflections. Considering the level of noise in the data [Fig. 4(a)], we don't believe that the inversion is sensitive to the shear wave velocities.

IV. DISCUSSION

Each of the three data sets presented in this paper has a set of issues critical for a successful inversion. Perhaps the most important factor for all three data sets is which portion (i.e., frequency band, waveform, or envelope) of the data to model. Other issues, which are detailed below, are of differing importance to inverting each data set and include which forward code to use, measuring offsets, and sonobuoy limitations. Last, we discuss the advantages of using field measurements of subbottom velocities rather than velocities from regression curves fit to a data base.

Selecting the portion of the data to use for an inversion involves more than just selecting the appropriate time and offset windows. For an efficient inversion, it is essential to simplify the data so that it contains only information necessary for the model fit. Simplifying the data means removing not just noise and unwanted data, but reducing the resolution of the data to an optimal level. The inversion algorithm used here fits a synthetic waveform to a data waveform. The data can be filtered to a desired frequency band or converted to the waveform envelope by calculating the quadrature trace using a Hilbert transform. Using the envelope as the waveform reduces the resolution from the wavelength of the signal to the size of the wavelet.

For a forward code, we chose a fast, simple ray-tracing method (ray1D) over more accurate but slower methods. Ray1D does not include surface multiples. The sea surface is a nearly perfect reflector, so for shallow receivers or sources, the surface multiples will be as strong as the primary. An inversion with a forward code that does not include surface reflections will try to solve for these multiples as part of the seafloor reflection response and will put strong interfaces where none exist. This effect was minimized by using the envelope which combines the sea-surface reflections with direct waves into a positive low-frequency signal (Wood and Lindwall, 1996). This approach worked because the sources and receivers were close enough to the surface so that the multiples were within the envelope of the primary arrivals. A future version of ray1D will include sea-surface reflections.

Ray1D can be further enhanced with the addition of dip and gradients as model variables. Inclusion of dip is straightforward in ray-trace forward codes and allows running field lines at any azimuth, thereby reducing the logistics of the field experiment. The data used in this demonstration were acquired along strike (parallel to bathymetry lines), a restriction that need not remain in future versions of this inversion code. Velocity and density gradients are also straightforward to include in ray-trace codes and are commonly observed over the scales of the layer thicknesses that we modeled at our two sites. Each new aspect, dips and gradients, adds more variables to the inversion problem as well as complicates the forward calculation.

The offsets between source and receivers must be measured to within half a wavelength (1 m for the data shown here) for accurate inversions, and these offsets must be determined from the data itself using the direct wave. The direct wave is not a simple pulse but a complex waveform that changes due to complex paths through the water and the nonlinear response of the sonobuoys to the overly strong signals. The sonobuoy's nonlinear overload response is a significant limitation. For these reasons, the direct wave response changes enormously with offset, so the offsets cannot be measured by picking the peak amplitude or the first swing in the signal. For these experiments, the offsets were manually picked for the final offsets (first site) or for the initial model (second site). Future processing can be enhanced by measuring the offsets by cross correlating the direct waves over a moving window that follows the moveout (arrival time change due to changing offset) hyperbola.

The sonobuoys limited our resolution, minimum depth, and minimum offsets because of their high sensitivity and limited dynamic range. Saturating the amplifiers and transmitters in the buoys was avoided by using weak sources at the small offsets. As it was, the direct arrival waves saturated the buoys for over 0.1 s [the muted zone in Fig. 4(a)]. This recovery time limits the minimum water depth in which useful geoacoustic measurements can be made with sonobuoys of this type. Although we collected data at several other sites down to as little as 90-m depth, the 250-m site was the shallowest where we obtained useful data. At shallower sites, the seafloor reflection arrivals overlapped with the recovery from the direct wave. Using an even weaker source to lessen the saturation problem would reduce the signal strength to below the noise levels. The sensitivities of several sonobuoys were reduced by inserting modified amplifiers attenuated by 25 dB; but, these sonobuoys were either unreliable or not sensitive enough to detect the subbottom reflectors. Ideal sonobuoys would have enough dynamic range so that larger sources such as SUS charges could be used even at small offsets. If sonobuoys were improved only by having a faster recovery from saturation, these experiments could be done in shallower water.

The advantage of making field measurements for predicting the acoustic response of the seafloor is shown by comparing our discontinuous velocity–depth functions with curves calculated from Table IV (for terrigenous sediments)

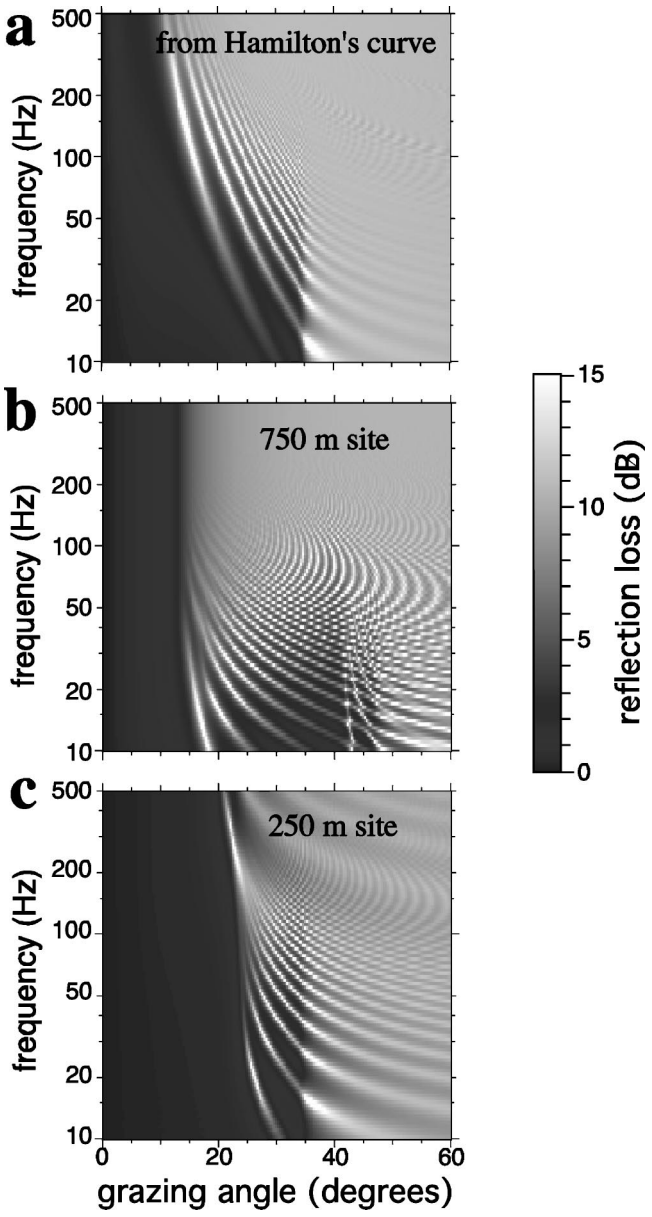

FIG. 5. These three images compare reflection coefficients calculated using the compressional wave velocity regression curve of Hamilton (1980) for terrigenous sediments (a) and the measured velocities from the 750-m water-depth site (b) and the 250-m water-depth site (c). Both sites are over terrigenous sediments yet have markedly different reflection coefficients than Hamilton's curve. This show the usefulness of using measured layer velocities instead of an average velocity function for a general sediment. The different V_p at the seafloor (1.538 km/s for 750 m, 1.573 km/s for 250 m, and 1.511 from Hamilton's regression curve) cause higher grazing angles for nearly perfect reflections in the measured models. The layered structure in the measured models also causes complex interference structures in the reflection loss plots.

of Hamilton (1980) [Figs. 3(d) and 4(d)]. Hamilton fit a smooth polynomial curve through V_p values from 20 sites. The measurements from the two field sites may be approximately consistent with Hamilton's V_p values, but the time to reflector depth is underpredicted by Hamilton's curve at the 750-m site by 0.066 s (more than 3% error) and overpredicted at the 250-m site by 0.005 s (more than 7% error). Also, discrete reflectors and discontinuous V_p–depth functions dominate the geoacoustic responses at these two sites. Figure 5 compares reflection coefficients calculated from Hamilton's V_p regression fit (a) with measured velocities at the 750-m water depth site (b) and at the 250-m water depth site (c). Hamilton's regression curve has a 1.511-km/s V_p at the seafloor while the measured V_p is 1.538 km/s at the 750-m site and 1.565 km/s at the 250-m site with a 1.60-km/s layer only 8.7 m below the seafloor. This difference in V_p, although small, increased the maximum angle for less than 2-dB reflection loss from 2 deg to nearly 20 deg (at 200 Hz) at the 250-m site. Both field sites are over terrigenous sediments, yet have markedly different reflection coefficients than those calculated from Hamilton's curve. This shows the advantage of using measured layer V_p values rather than an averaged V_p curve for a general sediment type. Hamilton's V_p–depth curves are useful for estimating the two-way travel time to reflectors, but the layered structure in the measured models causes complex interference structures in the reflection loss plots that are not predicted by Hamilton's smooth V_p regression fit.

V. SUMMARY

Two sonobuoy refraction lines collected at the Eel River STRATAFORM site were inverted for layer thicknesses and V_p using a modified simulated annealing (SA) algorithm. This SA inversion algorithm is robust and has been used on other, diverse geoacoustic data sets. Each SA inversion application requires modifications and additions to the old algorithm to either make the inversion achievable or practical. For these inversions we used a very fast ray-tracing code for the forward model, fit the envelope of the waveforms, and solved for seven variables at one site and 30 at the second site.

The inversion solutions for V_p and layer thicknesses compare favorably with measurements from nearby multichannel seismic lines. Although the V_p values here are consistent with Hamilton's (1980) regression curve fit for terrigenous sediments, our stratified seafloor V_p models have significantly different acoustic responses than Hamilton's gradients; thus, field tests are necessary for good site-specific acoustic predictions.

ACKNOWLEDGMENTS

Warren Wood of NRL-SSC provided ray1D, the forward algorithm, and helped with informal discussions of the project. L. Neil Frazer of the University of Hawaii and Mrinal Sen of the University of Texas have made major contributions to the inversion efforts through many years of discussions about simulated annealing, forward synthetic algorithms, and many discussions about seismology in general. Thanks to C. Fulthorp, J. Yun, Amoco, and Jebco for providing the MCS velocities. D. Small of ONR provided the sonobuoys. Dr. Joseph Gettrust and Dr. Fred Bowles of NRL-SSC reviewed early drafts of the manuscript and contributed to the focus and clarity of this paper. This research was supported by the Office of Naval Research through the Naval Research Laboratory, Program Element 62435N.

Basu, A., and Frazer, L. N. (**1990**). ''Rapid determination of the critical temperature in simulated annealing inversion,'' Science **249**, 1409–1412.
Cerveny, V., Molotkov, I. A., and Psencík, I. (**1977**). *Ray Method in Seismology* (Univerzita Karlova, Praha).
Chapman, C. H. (**1976**). ''Exact and approximate generalized ray theory in vertically inhomogenous media,'' Geophys. J. R. Astron. Soc. **46**, 201–233.
Cohen, J. K., and Stockwell, Jr., J. W. (**2003**). ''CWP/SU: Seismic Unix Release 37: A free package for seismic research and processing,'' Center for Wave Phenomena, Colorado School of Mines. http://www.cwp.mines.edu/cwpcodes
Fuchs, K., and Müller, G. (**1971**). ''Computation of synthetic seismogram with the reflectivity method and comparison with observations,'' Geophys. J. R. Astron. Soc. **23**, 417–433.
Hamilton, E. L. (**1980**). ''Geoacoustic modeling of the sea floor,'' J. Acoust. Soc. Am. **68**, 1313–1340.
Ingber, L. (**1989**). ''Very fast simulated reannealing,'' Math. Comput. Modell. **12**, 967–973.
Kirkpatrick, S., Gelatt, Jr., C. D., and Vecchi, M. P. (**1983**). ''Optimization by simulated annealing,'' Science **220**, 671–680.
Lindwall, D. A. (**1995**). ''Simulated annealing inversion of several types of high resolution marine seismic data,'' Abstract, EOS (Wash. D.C.) **76**, 369.
Lindwall, D. A., Sen, M. K., and Gettrust, J. F. (**1995**). ''Detection of High Shear Wave Velocities in Marine Sediment by Inversion with Simulated Annealing,'' in *Full Field Inversion Methods in Ocean and Seismo-Acoustics*, edited by O. Diachok, A. Cati, P. Gerstoft, and H. Schmidt (Kluwer Academic, Dordrecht), pp. 383–388.
Metropolis, N., Rosenbluth, A., Rosenbluth, M., Teller, A., and Teller, E. (**1953**). ''Equation of state calculations by fast computing machines,'' J. Chem. Phys. **21**, 1087–1092.
Nittrouer, C. A. (**1999**). ''STRATAFORM: Overview of its design and synthesis of its results,'' Mar. Geol. **154**, 3–12.
Sen, M. K., and Stoffa, P. L. (**1991**). ''Nonlinear one-dimensional seismic waveform inversion using simulated annealing,'' Geophysics **56**, 1624–1638.
Slotnick, M. M. (**1950**). ''A graphical method for the interpretation of refraction profile data,'' Geophysics **15**, 163–180.
Wood, W. T., and Lindwall, D. A. (**1996**). ''Full waveform inversion of field sonar returns for a visco-acoustic earth: A comparison of linearized and fully nonlinear methods,'' IEEE J. Ocean. Eng. **21**, 423–431.
Yun, J. W., Orange, D. L., and Field, M. E. (**1999**). ''Subsurface gas offshore of northern California and its link to submarine geomorphology,'' Mar. Geol. **154**, 357–368.

Simultaneous recording of stimulus-frequency and distortion-product otoacoustic emission input–output functions in human ears[a)]

Kim S. Schairer[b)] and Douglas H. Keefe
Center for Hearing Research, Boys Town National Research Hospital, 555 N. 30th Street, Omaha, Nebraska 68131

(Received 20 August 2004; revised 22 November 2004; accepted 1 December 2004)

Stimulus frequency otoacoustic emission (SFOAE) input–output (I/O) functions were elicited in normal-hearing adults using unequal-frequency primaries in equal-level and fixed-suppressor level (L_s) conditions. Responses were repeatable and similar across a range of primary frequency ratios in the fixed-L_s condition. In comparison to equal-frequency primary conditions [Schairer, Fitzpatrick, and Keefe, J. Acoust. Soc. Am. **114**, 944–966 (2003)], the unequal-frequency, fixed-L_s condition appears to be more useful for characterizing SFOAE response growth and relating it to basilar-membrane response growth, and for testing the ability to predict audiometric thresholds. Simultaneously recorded distortion-product OAE (DPOAE) I/O functions had higher thresholds than SFOAE I/O functions, and they identified the onset of the nonlinear-distortion mechanism in SFOAEs. DPOAE threshold often corresponded to nonmonotonicities in SFOAE I/O functions. This suggests that the level-dependent nonmonotonicities and associated phase shifts in SFOAE I/O functions were due to varying degrees of cancellation of two sources of SFOAE, such as coherent reflection and distortion mechanisms. Level-dependent noise was observed on-band (at the frequencies of the stimuli) but not off-band, or in the DPOAEs. The variability was observed in ears with normal hearing and ears with cochlear implants. In general, these results indicate the source of the variability is biological, possibly from within the middle ear. © *2005 Acoustical Society of America.* [DOI: 10.1121/1.1850341]

PACS numbers: 43.64.Jb, 43.64.Ri, 43.64.Kc [BLM] Pages: 818–832

I. INTRODUCTION

Cochlear-mechanical response growth in normal mammalian ears (for a review of cochlear mechanics, see Robles and Ruggero, 2001) has a compressive nonlinearity, with nearly linear growth at low stimulus levels and more compressive growth at moderate stimulus levels. This characterization is mainly derived from basilar-membrane (BM) and auditory-nerve input–output (I/O) functions (i.e., response level as a function of stimulus level) recorded in animals. Nonlinear response growth is spatially localized, at least at higher frequencies, such that only responses to frequencies near the characteristic frequency (CF, or place from which recordings are being made) grow nonlinearly with stimulus level. Responses to frequencies remote from CF grow more linearly with stimulus level. The nonlinearity is attributed to outer hair cell (OHC) function, is present in normal-hearing ears, and is decreased or absent in ears with hearing loss, presumably due to OHC loss. This compressive nonlinearity produces the large dynamic range of hearing in normal ears, and is thought to be involved in perceptual phenomena such as loudness growth, intensity discrimination, and forward masking (for reviews of cochlear compression effects on auditory perception, see Moore and Oxenham, 1998; Oxenham and Bacon, 2003).

However, BM response growth measurements are invasive, and cannot be performed in human ears. Attempts have been made to relate a noninvasive measure of cochlear function, otoacoustic emissions (OAE), to the compressive nonlinearity of the cochlear mechanics and to its perceptual consequences in humans (e.g., Buus *et al.*, 2001; Neely *et al.*, 2003; Schairer *et al.*, 2003). Several studies characterize distortion product OAE (DPOAE) I/O functions and response growth in normal-hearing human ears (Boege and Janssen, 2002; e.g., Buus *et al.*, 2001; Dorn *et al.*, 2001; Gorga *et al.*, 2002; Gorga *et al.*, 1994; Kummer *et al.*, 1998; Lonsbury-Martin *et al.*, 1990; Whitehead *et al.*, 1995), while one study systematically characterizes stimulus frequency OAEs (SFOAE) I/O functions in a large group of normal-hearing human ears (Schairer *et al.*, 2003). SFOAEs may provide a more frequency-specific response than DPOAEs, and may be easier to relate to BM I/O measurements and perceptual phenomena.

SFOAEs are recorded at the frequency (f_p) of a probe stimulus presented at level L_p in the presence of a suppressor stimulus of frequency f_s and level L_s. SFOAEs can be elicited with $f_s = f_p$ or with f_s/f_p ratios close to 1, and with various L_s to L_p relationships, for example, equal level, or fixed L_s with L_p varied (Schairer *et al.*, 2003). In that study, it was demonstrated that when $f_s = f_p$ in a fixed-L_s condition, the noise or variability of the response associated with the

[a)]Portions of this work were presented in: K. S. Schairer and D. H. Keefe, "SFOAE input/output functions elicited by slightly off-frequency suppressors," Presented at the 143rd Meeting of the Acoustical Society of America, 3–7 June 2002, Pittsburgh, PA. J. Acoust. Soc. Am. **111**, 2356 (2002).

[b)]Electronic mail: schairerk@boystown.org

fixed L_s was large and approximately constant across the I/O function (as L_p was varied). This on-band level-dependent response variability (i.e., the SFOAE variability recorded at f_p) limited the detection of the SFOAE, and elevated its threshold, which was defined as the lowest L_p at which the SFOAE was separated from the noise. The SFOAE threshold was lower in the equal-level than the fixed-L_s condition. However, the signal-to-noise ratio (SNR) between the 25th percentile of the SFOAE and 75th percentile of the noise was restricted in the equal-level tests. This may limit the utility of the response for clinical purposes, such as separating normal-hearing from hearing-impaired ears.

The current study follows up on Schairer *et al.* (2003) by investigating the effect of a different stimulus paradigm on SFOAE response growth. Unequal-frequency primaries (i.e., $f_s \neq f_p$ with f_s/f_p close to 1) were used to construct SFOAE I/O functions in a group of normal-hearing adults. It was predicted that unequal-frequency primaries would produce a larger SNR over a larger L_p range in both conditions (i.e., fixed-L_s and equal-level) than the equal-frequency primaries used by Schairer *et al.* (2003) because the response variability recorded at f_p would be separated from the response variability at f_s. If this is the case, it would improve the ability to relate SFOAE response growth to BM response growth, particularly in the fixed-L_s condition for which SFOAE detection was poor in the $f_s = f_p$ condition (Schairer *et al.*, 2003). In the fixed-L_s case, the suppression of the SFOAE at f_p would be clearer and it would be easier to test for full suppression of the probe by comparing the response amplitude in the presence of a range of fixed suppressor levels. Furthermore, with a larger SNR over an extended stimulus range, it might improve the ability to use SFOAE I/O functions to characterize response growth in ears with hearing impairment or to predict hearing threshold. Describing this relationship with SFOAEs would extend the data already available regarding the same issues with DPOAE I/O functions (e.g., Boege and Janssen, 2002; Dorn *et al.*, 2001; Gorga *et al.*, 2003; Kummer *et al.*, 1998). Because the primary stimuli and responses are very closely spaced in frequency for SFOAEs, they may represent cochlear functioning from a more localized area on the BM than DPOAEs recorded using more widely spaced primary frequencies ($f_2/f_1 \approx 1.2$) for which the DPOAE is at a more remote response frequency.

Cubic-distortion (CDT) DPOAEs elicited by primaries with frequency ratios $0.95 < f_2/f_1 < 1.05$ (with $f_1 < f_2$) have been described as place-fixed (Knight and Kemp, 2000; 2001), because their latencies were much longer than the so-called wave-fixed latencies of DPOAEs with frequency ratios $f_2/f_1 > 1.1$. The generator of wave-fixed DPOAEs is in the region of the peak of the f_2 traveling wave and it acts via intermodulation distortion of the spatially overlapping traveling waves at the f_1 and f_2 frequencies. A long-latency generator has been described as a coherent linear-reflection source of emissions (Zweig and Shera, 1995). The terminology of place-fixed emission may be somewhat misleading for DPOAEs—the place-fixed DPOAEs described by Knight and Kemp may arise through a coherent nonlinear-reflection process (Talmadge *et al.*, 1998; 2000) based on intermodulation distortion, unlike the coherent linear-reflection process that does not involve intermodulation distortion. For f_2/f_1 ratios close to 1, there is substantial overlap of the f_1, f_2, $2f_1 - f_2$, and $2f_2 - f_1$ traveling waves. Thus, CDT DPOAEs with $0.95 < f_2/f_1 < 1.05$ arise in such a model via intermodulation distortion, but nonetheless have long latencies similar to SFOAEs at the f_p place. If the appearance of CDT DPOAEs signals the onset of intermodulation distortion in cochlear mechanics, and if SFOAEs are generated by a mixture of coherent-emission and distortion mechanisms at higher levels, then the appearance of DPOAEs in an SFOAE paradigm may signal the onset of nonlinear-distortion mechanisms in SFOAEs.

An advantage of using unequal f_s and f_p is that it is possible to simultaneously record SFOAEs along with the pair of CDT DPOAEs at $2f_s - f_p$ and $2f_p - f_s$. Thus, a goal of the present study was to compare SFOAE and DPOAE responses in the same ear elicited by identical primary tones. While SFOAE generation is dominated by linear coherent reflection at low levels (Shera and Guinan, 1999; Talmadge *et al.*, 1998; Zweig and Shera, 1995), there is evidence for a second generator mechanism at higher stimulus levels that sometimes produces minima in their I/O functions (Schairer *et al.*, 2003). This second generator may be intermodulation distortion (Shera and Guinan, 1999; Talmadge *et al.*, 2000). Since DPOAEs only arise via intermodulation distortion, the threshold of DPOAE I/O functions can be used to identify the presence of nonlinear distortion, which would also be expected to influence the SFOAE I/O function at suprathreshold levels.

A novel feature observed in Schairer *et al.* (2003) was level-dependent notches in SFOAE I/O functions that occurred at different frequencies and levels in some of the subjects. These level-dependent notches were associated with approximately 180-deg phase shifts. It was hypothesized that the notches were due to interaction of two sources. More examples of notches observed in individual I/O functions are presented in this report to demonstrate that notches occur under more general stimulus conditions (unequal probe and suppressor frequencies) with better SNRs. This is further evidence that the notches were not an artifact related to the poorer SNRs associated with the equal-frequency primary conditions used by Schairer *et al.* (2003). The second generator revealed by the presence of notched SFOAE I/O functions might be due to intermodulation distortion, or to a zero in the mechanical motion at an OHC location that produces a notched receptor potential (Allen, 1980; Lin and Guinan, 2000; Zwislocki, 1980). If the thresholds of simultaneously recorded DPOAE I/O functions occur at the same level as notches in SFOAE I/O functions (and if SFOAE notches do not occur at levels at which DPOAEs are absent), it would support the hypothesis that the second source is due to nonlinear distortion rather than to a zero in the local mechanical motion on the BM. Notches in both of the SFOAE and DPOAE I/O functions would favor the theory that a zero in mechanical motion occurs.

Another novel feature of the SFOAE I/O functions reported by Schairer *et al.* (2003) was level-dependent variability in the SFOAE SPL. Response variability increased in

ears as a function of stimulus level for SFOAEs, but not for DPOAEs or in a test cavity. It was noted that the increase in noise level occurred only in the bin of the response, referred to as on-band noise, and not in the surrounding frequency bins, referred to as off-band noise. The source of the variability is unknown, but Schairer *et al.* (2003) proposed that it might be due to variability in the middle-ear muscle activation. If the source of variability were the middle ear, then on-band, level-dependent variability would be detectable in the SFOAE at f_p under the new unequal-frequency test conditions, but it would be reduced. This is because the variability becomes more detectable above the system noise floor as the energy in the stimulus increases. In the equal-frequency condition, the energy of both primaries is present at the frequency of the response. In the unequal-frequency conditions used in the current study, the variability with only one primary is associated with the frequency of the response.

The theory that the source of the response variability is due to variability in middle ear muscle contractions, rather than variability in the cochlear mechanics, was also examined by testing ears with cochlear implants. Schairer *et al.* (2003) estimated system distortion at f_p by presenting the protocol in a test cavity and in ears with cochlear implants in which responses due to active mechanisms would not be expected. While the distortion was less in the test cavity recordings, the distortion increased as a function stimulus level in ears with cochlear implants, and exceeded the 75th percentile of responses from normal-hearing ears in some cases. It is unknown why this occurred. The present report presents new results in ears with cochlear implants using the unequal suppressor and probe frequency protocol to further investigate this effect.

In summary, the following hypotheses were tested: (1) SFOAE I/O functions obtained with unequal-frequency primaries produce larger SNRs over a larger stimulus range than equal-frequency primaries in both fixed-L_s and equal-level conditions; (2) the thresholds of CDT DPOAE I/O functions identify the thresholds of the nonlinear-distortion mechanism in SFOAEs elicited by the same primaries; (3) level-dependent notches and associated phase shifts occur in SFOAE I/O functions measured using unequal-frequency primaries; (4) SFOAE I/O functions elicited with unequal frequency primaries are repeatable; (5) on-band, but not off-band, noise is level dependent, indicative of an origin in the variability of middle-ear function; and (6) use of unequal-frequency primaries yields improved separation compared to equal-frequency primaries between distortion recorded in normal-hearing ears, and in ears with cochlear implants and a test cavity. Hypotheses 1 through 5 were addressed by collecting SFOAE I/O functions in a group of 32 normal-hearing listeners. Hypotheses 5 and 6 were addressed by collecting data an IEC 711 standard ear simulator and in two ears with cochlear implants.

II. METHODS

A. Subjects

1. Subjects with normal hearing

Thirty-two adults with normal hearing were recruited from a local university and from the clinical staff (see the demographic information in Table I). Data were collected in 16 left ears and 16 right ears. All subjects were informed of the procedures and purpose of the study, and signed a consent form prior to participation. Hearing thresholds in the test ear were at or better than 15 dB HL at audiometric test frequencies of 250 to 8000 Hz, as assessed using conventional procedures and a GSI-16 or GSI-61 clinical audiometer (American National Standards Institute, 1996). Tympanometry was used to screen for normal middle-ear function using a GSI-33 middle-ear analyzer and a 226-Hz probe tone. Normal middle-ear function was defined as peak pressure in the test ear between -40 and $+45$ daPa and peak static admittance between 0.3 and 1.4 mL. Subjects were seated in a sound-attenuated booth during SFOAE testing, and were allowed to sleep or read quietly during data collection. The time to collect all data, including hearing screening and tympanometry, was limited to approximately 2 to $2\frac{1}{2}$ h.

TABLE I. Summary demographic information.

	Left ears		Right ears	
	Male	Female	Male	Female
N	5	11	3	13
Minimum age	19	19	19	18
Maximum age	29	36	22	35
Mean age	23.6	23.5	20	22.46
SD	4.2	5.6	1.7	5.6

Four subjects returned for repeat tests. The time between tests for each subject was 1 year and 5 months for subject SFS04 (left ear), and 1 year and 4 months for subjects SFS05 (right ear), SFS14 (right ear), and SFS21 (left ear).

2. Subjects with cochlear implants

Two subjects with cochlear implants were tested using the same stimulus generation and recording parameters as with subjects with normal hearing. Subject SFSCI01 was a 45-year-old male with a cochlear implant on his right ear. Subject SFSCI02 was a 58-year-old female with a cochlear implant on her right ear. Both subjects were tested with their processors turned off and transmitters removed.

3. Ear simulator

Distortion and noise were measured in a Brüel & Kjær ear simulator, type 4157 (IEC 711 standard) for each condition to assess system distortion. Coupler measurements were recorded with the same stimulus generation and recording parameters as for normal and implanted ears.

B. Stimulus conditions

In the DPOAE literature, stimuli are referred to as f_2 presented at L_2 for the higher frequency stimulus, and f_1 presented at L_1 for the lower frequency stimulus. However, in order to be consistent with discussions of SFOAEs measured using a suppression paradigm, the stimuli are referred to as f_s and f_p in the current paper. It should be noted that f_s is not always the higher frequency, and results are reported for varying f_s/f_p ratios. In different conditions, f_p was approximately equal to 1000, 2000, or 4000 Hz. For all f_p

TABLE II. Stimulus conditions. All frequencies are rounded to integers (in Hz).

f_p = 1000 Hz (Actual f_p = 991 Hz)		f_p = 2000 Hz (Actual f_p = 1981 Hz)		f_p = 4000 Hz (Actual f_p = 4005 Hz)	
f_s (Hz)	f_s/f_p	f_s (Hz)	f_s/f_p	f_s (Hz)	f_s/f_p
		1938	0.98	3919	0.98
948	0.96	1895	0.96	3833	0.96
		1852	0.93	3747	0.94
		2024	1.02	4091	1.02
1034	1.04	2067	1.04	4177	1.04
		2110	1.07	4264	1.06

frequencies, responses were measured using nominal f_s/f_p ratios of 0.96 and 1.04. At $f_p = 2000$ Hz, responses were measured for additional f_s/f_p ratios of 0.93, 0.98, 1.02, and 1.07. At $f_p = 4000$ Hz, responses were measured for f_s/f_p of 0.94, 0.98, 1.02, and 1.06, with the ratio differences (e.g., 0.93 at 2000 Hz and 0.94 at 4000 Hz) accounted for by the choice of discrete f_s and f_p frequencies at the given sample rate (22 050 Hz) and buffer size (512 samples) of the discrete Fourier transform. The actual f_s and f_p frequencies, and their frequency ratios, are listed in Table II. For clarity in the text and figures, each f_p was rounded to the nearest octave frequency (i.e., 1000, 2000, and 4000 Hz).

The two primary-level conditions were fixed-L_s and equal-level. In the fixed-L_s condition, L_s was fixed at 80 dB SPL and L_p decreased from 75 to 0 dB SPL in 5-dB steps. A fixed-level condition of $L_s = 70$ dB SPL was also used, in which L_p decreased from 65 to 0 dB SPL in 5-dB steps. This condition was presented at a subset of the f_s/f_p ratios to one subject (SFS04) for comparison in order to determine whether full suppression was obtained. If the SFOAE responses were similar with 70- and 80-dB SPL suppressors, then it was concluded that full suppression was achieved with the 80-dB SPL suppressor used in the main experiment. In the equal-level condition, the primary levels were varied from 85 to 0 dB SPL in 5-dB steps, with $f_s/f_p = 0.96$.

C. Stimulus generation and OAE recording

Stimuli were generated by an in-house software program, using a 24-bit Card Deluxe sound card (Digital Audio Labs) with a sample rate of 22 050 Hz for digital-to-analog (DAC) and analog-to-digital (ADC) conversion. Stimuli were transmitted to an Etymotic ER-10C low-noise probe that was modified to provide an extended 20-dB range of output. Two channels of DAC stimuli were delivered to separate receiver ports of the probe. The probe assembly was coupled to the ear canal using Etymotic foam probe tips. The sound-pressure signal recorded by the probe microphone in the ear canal was sampled by the ADC, digitally high-pass filtered with a cutoff frequency of 500 Hz, and tested for artifact rejection as described in Schairer *et al.* (2003). The double-evoked (2E) method of extraction, which yields a nonlinear residual based on responses to a set of these stimuli (see Keefe, 1998; Schairer *et al.*, 2003 for details), was used and responses at f_p, f_s, $2f_s - f_p$, $2f_p - f_s$ were extracted for analysis. It should be noted that in theory, in the fixed-L_s condition, the SFOAE at f_p is present in the interval in which f_p is presented alone (because it is unsuppressed), and absent in the interval in which both primaries are presented (assuming full suppression by f_s and no other nonlinearity). By contrast, the DPOAEs are present only in the interval in which both primaries are presented. In this sense, the SFOAEs at f_p and the DPOAEs may not be present simultaneously. However, because both types of emissions are extracted in the same manner from the same stimulus set in the 2E method, they are recorded simultaneously during the presentation of each stimulus set. Further, in cases of less than full suppression, such as in the equal-level conditions at lower L_ps, the interval in which both primaries are presented most likely produces SFOAEs and DPOAEs. Therefore, we refer to SFOAEs and DPOAEs as ''simultaneously recorded.''

D. Analysis

Summary data of distortion and on-band noise are presented as medians and percentiles (25th to 75th). In addition, median response variability in the frequency bins on either side of f_p was averaged as an estimate of off-band noise (Schairer *et al.*, 2003). To quantify repeatability of the responses for the four subjects who returned, the root-mean-square (rms) difference of the SFOAE SPL at f_p between the two runs was calculated.

III. RESULTS

A. Subjects with normal hearing

1. Median SFOAE I/O functions

The SFOAE SPL and on-band noise SPL results for the fixed-L_s conditions at 80 and 70 dB SPL for subject SFS04 are presented in the top row of Fig. 1 for the $f_s/f_p = 0.96$ condition, and in the bottom row for the $f_s/f_p = 1.04$ condition. The similarity in the SFOAE levels recorded at f_p at the two suppressor levels suggests that full suppression was achieved by 70 dB SPL for this subject. Thus, the 80-dB SPL suppressor used in the main experiment was considered sufficient for full suppression in all other subjects.

Median distortion and on-band noise (across ears and subjects) recorded at f_p in all f_s/f_p conditions in the fixed-L_s condition are presented in Fig. 2. On-band noise increased as a function of L_p. The responses across the different f_s/f_p conditions were nearly identical across the L_p range for which the signal is well above the noise, that is, the fully suppressed SFOAE at f_p was insensitive to the choice of f_s.

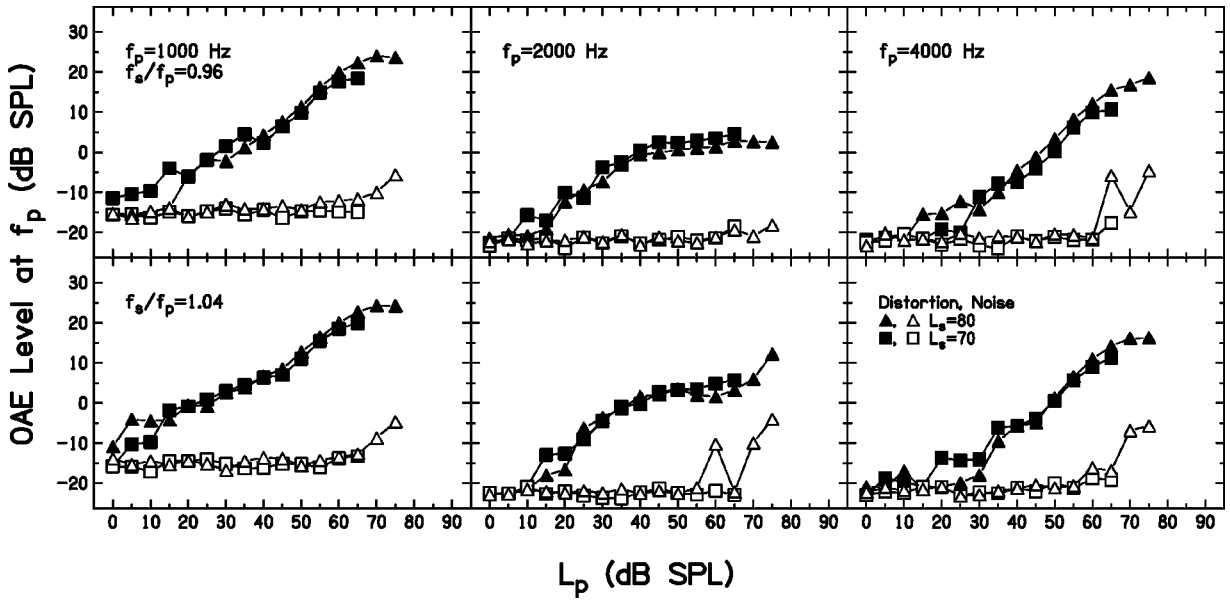

FIG. 1. SFOAE (filled) and on-band noise (open) SPL (in dB) vs L_p recorded with fixed L_s of 80 dB SPL (triangles) and 70 dB SPL (squares), and with $f_s/f_p=0.96$ (top row) and 1.04 (bottom row) for normal-hearing subject SFS04 (left ear). The $f_p=1000$-, 2000-, and 4000-Hz conditions are presented in the left, middle, and right columns. SFOAE levels were similar in the presence of 80- and 70-dB SPL suppressors at all f_p and in both f_s/f_p conditions.

Thus, the $f_s/f_p=0.96$ condition that was common to all three f_p frequencies (see Table II) was selected for presentation in the remaining figures, unless otherwise specified.

The median SFOAE SPL and on-band noise at f_p with the 25th to 75th percentile range are presented in Fig. 3 in the fixed-L_s (top row) and equal-level (bottom row) conditions. In general, SFOAEs separated from the on-band noise at a lower L_p and had a greater SNR in the moderate L_p range in the fixed-L_s condition in comparison to the equal-level condition. This is because, in the equal-level condition, the SFOAE levels were lower and the on-band noise increased at a lower L_p than in the fixed-L_s condition. In the fixed-L_s condition (top row), the off-band noise did not increase as a function of L_p, even at the highest levels. In the equal-level condition, off-band noise increased at the two highest stimulus levels ($\geqslant$80 dB SPL) in the $f_p=2000$- and 4000-Hz conditions. In the $f_p=1000$ Hz equal-level condition, off-band noise began to increase at a similar L_p as the on-band noise. However, it did not grow at the same rate and did not achieve the same absolute level. In the $f_p=1000$ Hz, fixed-L_s condition, the off-band noise was constant across all L_p. At 1000 Hz, the level-dependent off-band noise in the equal-level condition, and the constant, but elevated, off-band noise in the fixed-L_s condition were due to the fact that the frequency bin adjacent to the f_p bin, which was included in the calculation of off-band noise, was the suppressor. Thus, the on-band noise associated with the suppressor contaminated the average off-band noise associated with the probe in Fig. 3, but only at 1000 Hz.

Figure 4 shows the median OAE level in the f_p, f_s, $2f_p-f_s$, and $2f_s-f_p$ frequency bins in the fixed-L_s and equal-level conditions. In this case, $2f_p-f_s$ is the same as the $2f_2-f_1$ frequency described in the DPOAE literature (because $f_p>f_s$), and $2f_s-f_p$ is the same as $2f_1-f_2$. SFOAEs at f_s in the fixed-L_s condition are not plotted, because they were limited by the high noise associated with the fixed 80-dB SPL stimulus (similar to the $f_s=f_p$ responses described in Schairer *et al.*, 2003), and were approximately constant across the I/O function (e.g., see Fig. 9, top row). In

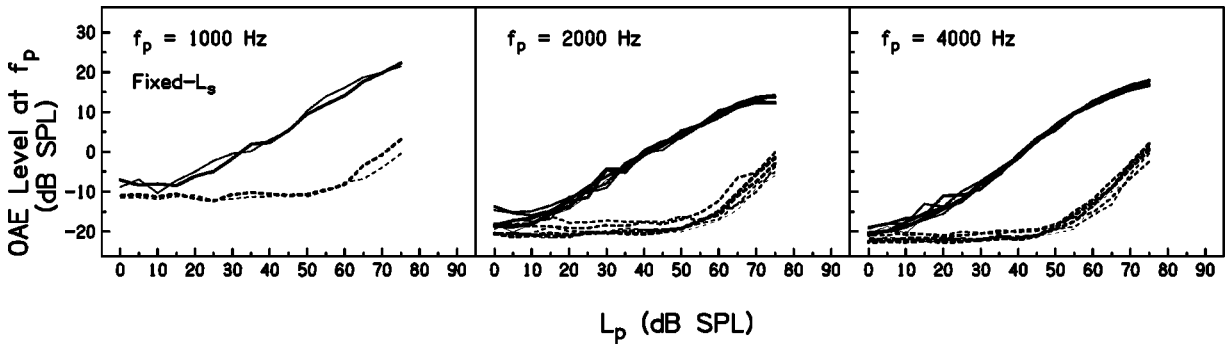

FIG. 2. Median SFOAE (solid lines) and on-band noise (dashed lines) SPL (in dB) recorded at f_p for 32 normal-hearing ears in the fixed-L_s condition with f_s/f_p as the parameter (see Table II). The f_p conditions of 1000, 2000, and 4000 Hz are presented in the left, middle, and right panels. The f_s/f_p conditions are represented by increasingly thicker lines from the smallest to largest ratio. This f_s/f_p range was 0.93 to 1.07 at f_p of 2000 and 4000 Hz, and 0.96 to 1.04 at 1000 Hz.

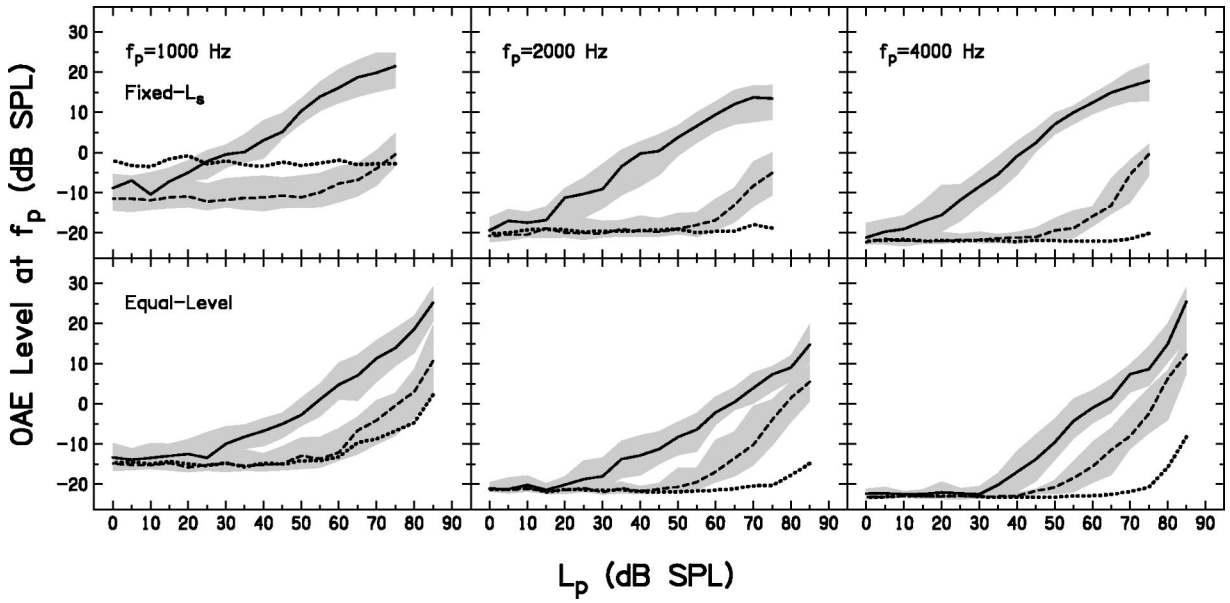

FIG. 3. Median SFOAE (solid lines) and on-band noise (dashed lines) SPL with the 25th to 75th percentile range (shaded areas) recorded at f_p in the $f_s/f_p=0.96$ condition in the fixed-L_s (top row) and equal-level (bottom row) conditions. The f_p conditions of 1000, 2000, and 4000 Hz are presented in the left, middle, and right columns. The data for the $f_s/f_p=0.96$, fixed-L_s condition were also presented in Fig. 2, but are reproduced here to show dispersion (25th to 75th percentile range), and for comparison with the equal-level condition. Off-band noise (dotted lines) was calculated as the average of the median noise in the two bins immediately adjacent to the f_p bin.

the fixed-L_s condition, the SFOAE responses at f_p had a lower threshold and were larger than the DPOAE responses across most of the L_p range. In addition, the $2f_s-f_p$ responses were larger than the $2f_p-f_s$ responses. Although it is not directly identified in this plot, a larger SNR over the largest L_p range was achieved at f_p in this fixed-L_s condition than in the equal-level condition. In the equal-level condition, the SFOAEs at f_s were larger in level than the SFOAEs at f_p for L_p up to approximately 65 dB SPL. The SFOAEs at f_s and f_p were similar at higher levels, which is most likely due to either similar increases in on-band noise at those levels or spread of excitation. DPOAEs in the equal-level condition were generally similar to each other and to the SFOAEs at f_p, although there is a midlevel region at 2000 and 4000 Hz in which the DPOAE SPL at $2f_p-f_s$ is larger than the DPOAE at $2f_s-f_p$. Although not evident in this plot, the largest SNR for the equal-level condition in the moderate L_p range occurred for the SFOAE at f_s. However, above $L_s=60$ dB SPL, the SNR at both DPOAE frequencies either equaled or exceeded the SFOAE SNR at f_s and f_p due to the level-dependent increase in SFOAE variability. The responses at f_s+f_p were examined as examples of quadratic

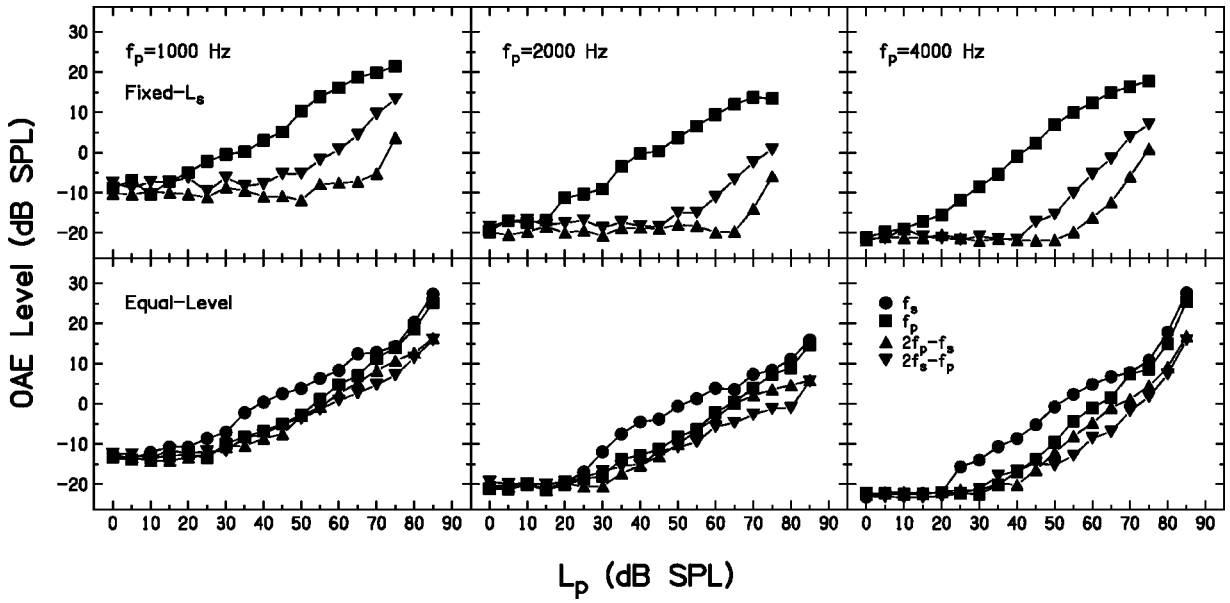

FIG. 4. Median OAE SPL in the $f_s/f_p=0.96$ condition, in the fixed-L_s (top row) and equal-level (bottom row) conditions, recorded at f_s (circles), f_p (squares), $2f_p-f_s$ (upward triangles), and $2f_s-f_p$ (downward triangles). SFOAEs at f_s in the fixed-L_s condition were constant across the I/O function because they were limited by the noise associated with the fixed 80-dB SPL stimulus, and are therefore not plotted in the top row.

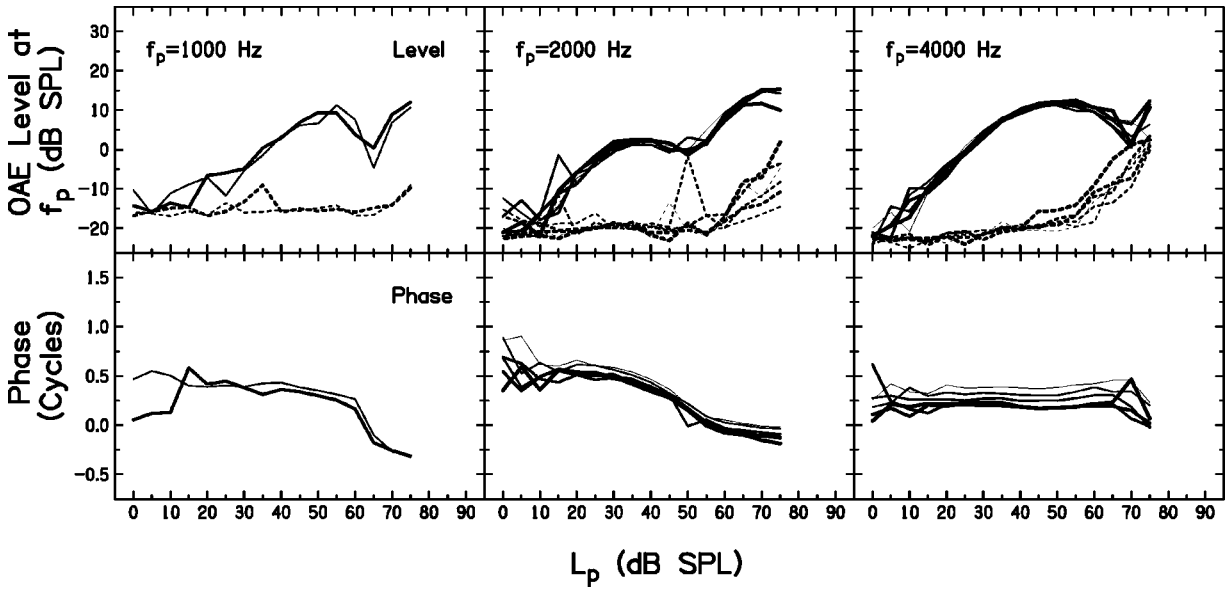

FIG. 5. SFOAE and on-band noise (solid and dashed lines, respectively; top row) SPL and phase (bottom row) recorded at f_p in the fixed-L_s condition for subject SFS19 (right ear). The f_s/f_p conditions are represented as in Fig. 2.

DPOAEs. However, responses were contaminated by system distortion measured in the coupler, possibly due to intermodulation distortion in the pair of probe loudspeakers.

2. Individual SFOAE I/O functions

SFOAE level and phase are shown in Figs. 5 and 6 for two subjects (SFS19 and SFS27, respectively) who had notched I/O functions. These figures also demonstrate the shift in phase that accompanied the level-dependent notches observed in some individual I/O functions. For subject SFS19 (Fig. 5), a sharp notch in the I/O function occurred at $f_p=1000$ Hz around $L_p=65$ dB SPL, and a more shallow notch or plateau was observed at $f_p=2000$ Hz around $L_p=45$ to 50 dB SPL. Although there appeared to be a notch at $f_p=4000$ Hz around $L_p=70$ dB SPL, this was not regarded as a ''true'' notch because the SNR was poor, and because the possibility of acoustic reflex involvement at 70 dB SPL could not be ruled out. The notches were repeatable, inasmuch as they were observed in all f_s/f_p conditions at both $f_p=1000$ Hz and 2000 Hz. The corresponding phase I/O functions rotated by approximately half a cycle in the same L_p range as that of the notches. The phase did not change in the moderate L_p range in which there was no OAE level notch at $f_p=4000$ Hz.

Subject SFS27 (Fig. 6) had a nonmonotonic I/O function at $f_p=4000$ Hz around $L_p=45$ dB SPL. It occurred in all f_s/f_p conditions, although the depth ranged from a sharp notch to a more gradual plateau across conditions. A half-cycle phase shift occurred at approximately the same L_p. No level notches or changes in phase were observed at $f_p=2000$ Hz, or at $f_p=1000$ Hz until $L_p=65$ dB SPL. The more gradual phase change at $f_p=1000$ Hz at 65–70 dB SPL was clearly less than half a cycle, and perhaps was contaminated by the spike in noise (i.e., poorer SNR), at least for the

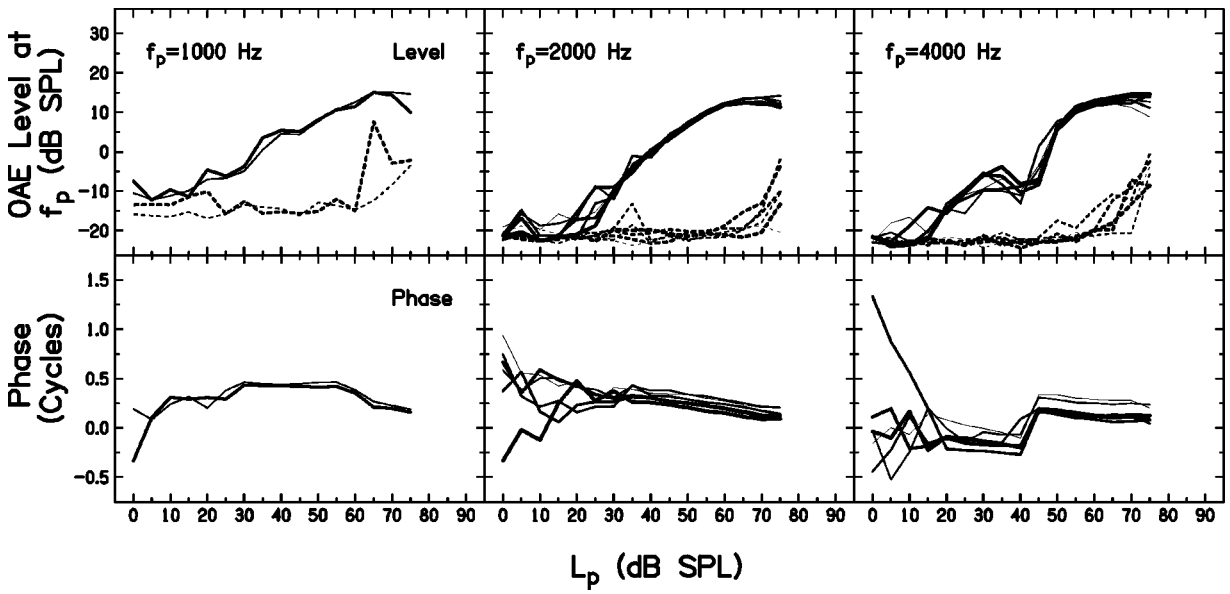

FIG. 6. As in Fig. 5 for subject SFS27 (right ear).

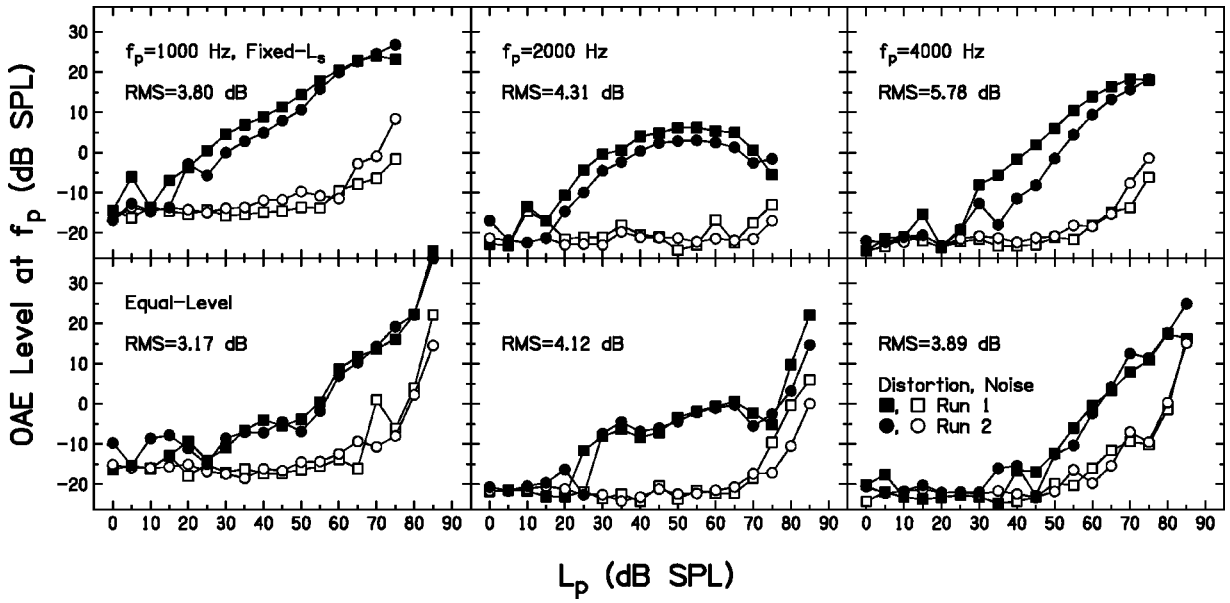

FIG. 7. Repeatability of SFOAE (filled) and on-band noise (open) SPL in select conditions for subject SFS04 (left ear). The L_s and f_p conditions are represented in the frames as in Fig. 3. The first and second repetitions are represented by squares and circles, respectively. The time between first and second repetitions was approximately 1 year and 5 months. The rms difference in SPL for distortion between the two repetitions is displayed in each frame.

$f_s/f_p=1.04$ condition. The phase shift at this f_p in the $f_s/f_p=0.96$ condition, which had an adequate SNR, differs from the half-cycle phase shifts observed in other notched responses, although no clear notch was evident in its level.

As an example of repeatability, Fig. 7 shows the two runs and the rms difference in SPL between the runs in select conditions for subject SFS04. The average rms difference across frequency and subject for the equal-level condition was 4.97 dB (range 3.17–6.67 dB). The average rms difference across frequency, f_s/f_p, and subject for the fixed-L_s condition was 5.04 dB (range 2.27–15.11 dB).

B. Ear simulator and subjects with cochlear implants

Figure 8 shows the distortion SPL (akin to the SFOAE SPL) and noise level recorded in the two ears with cochlear implants, as well as in the coupler. The 25th to 75th percentiles of distortion and noise for normal-hearing ears are plotted for comparison (as in Fig. 3) as the upper and lower gray backgrounds, respectively. The data for implant subject SFSCI02 at $f_p=1000$ Hz are not shown because they were contaminated by high noise levels. In the fixed-L_s condition, there is a clear separation between the 25th percentile of

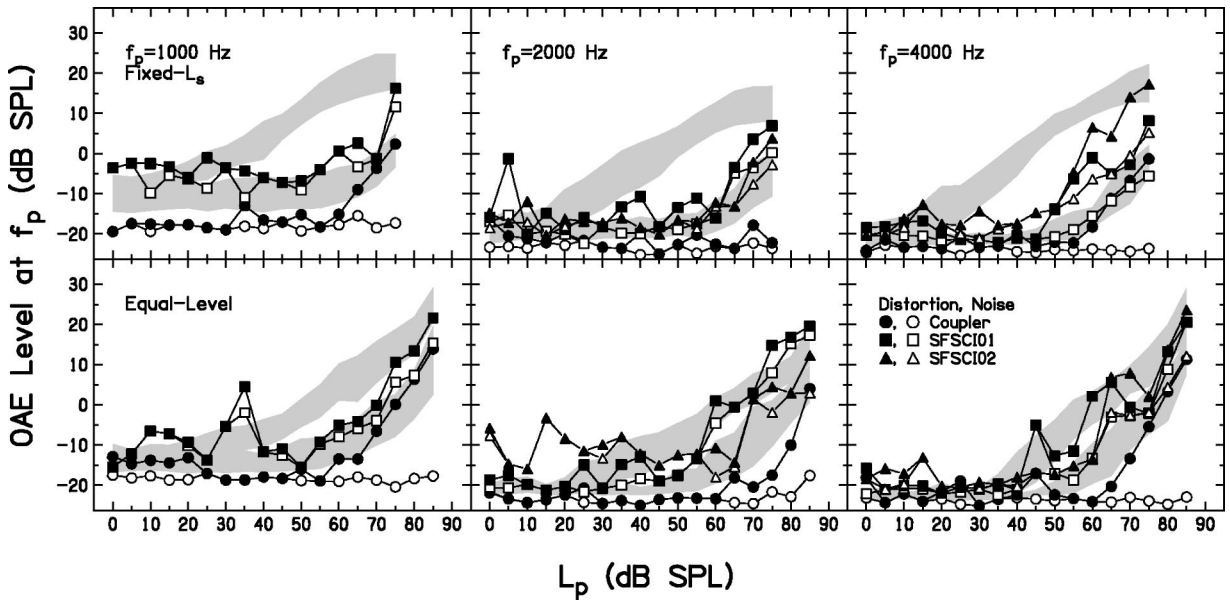

FIG. 8. SFOAE (filled symbols) and on-band noise (open symbols) SPL recorded in SFSCI01 (squares), SFSCI02 (triangles), and an IEC 711 standard coupler (circles) superimposed on the 25th to 75th percentiles for SFOAE (upper shaded band) and on-band noise (lower shaded band) in normal-hearing ears for the $f_s/f_p=0.96$ condition. The L_s and f_p conditions are arranged as in Fig. 3. Responses at $f_p=1000$ Hz are not shown for SFSCI02 because they were contaminated by high noise levels. Both subjects had cochlear implants in their right ears from which these data were recorded. The processors were turned off and removed during testing, and the opposite ear was unaided.

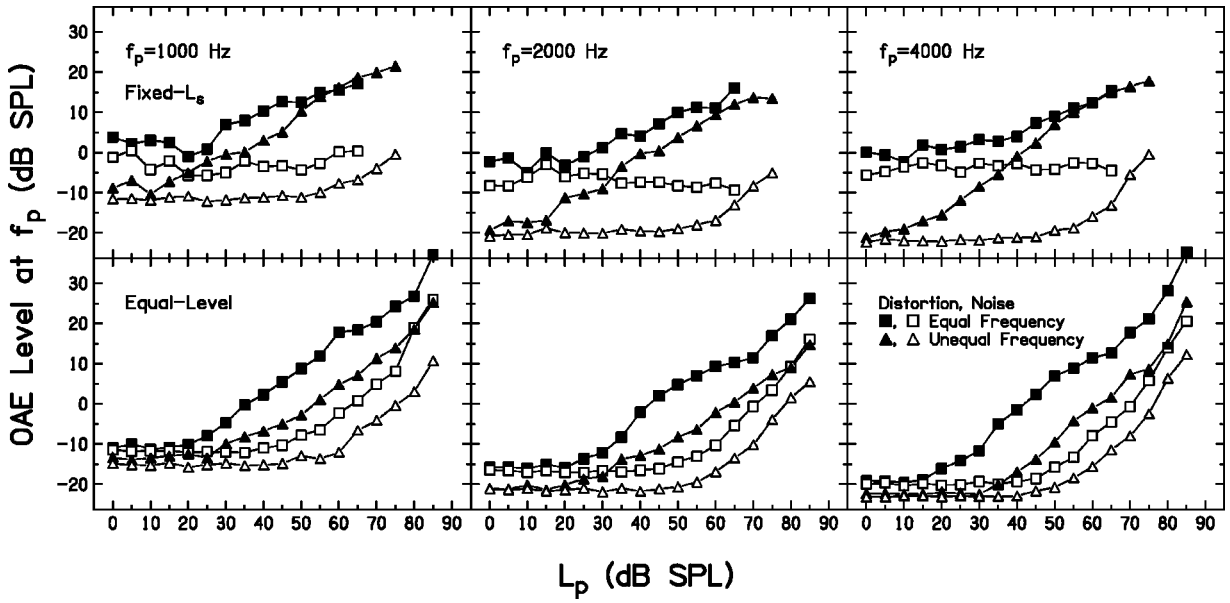

FIG. 9. Median SPL of the SFOAE (filled symbols) and the on-band noise (open symbols) recorded in the equal-frequency primary condition (squares) from Schairer *et al.* (2003) and in the unequal-frequency primary condition (triangles) from the current study. Responses from the current study were recorded at f_p, in the $f_s/f_p=0.96$ condition.

distortion in normal-hearing ears and the lower distortion level recorded in ears with cochlear implants in the moderate L_p range. At the highest L_p (75 dB SPL), the distortion recorded in SFSCI01's ear approached the 25th percentile in the $f_p=1000$- and 2000-Hz conditions, and the distortion recorded in SFSCI02's ear exceeded the 25th percentile in the $f_p=4000$ Hz condition. In the equal-level condition, however, there was only a small separation between responses from ears with cochlear implants and the 25th percentile in normal-hearing ears over a small range at $f_p=1000$ Hz. The distortion recorded in SFSCI01's ear equaled or exceeded the 25th percentile of responses from normal-hearing ears over most of the L_p range at $f_p=2000$ and 4000 Hz. This overlap of responses from normal-hearing and implanted ears in the equal-level condition is due in part to the higher threshold and variability of the SFOAEs in normal-hearing ears. On-band variability increased as a function of L_p in ears with cochlear implants (similar to results in ears with normal hearing), but not in the coupler.

IV. DISCUSSION

A. SFOAE I/O functions obtained with unequal- vs equal-frequency primaries

Hypothesis 1 stated that slightly off-frequency primaries would elicit SFOAE I/O functions with larger SNR than equal-frequency primaries over a larger L_p range in both the fixed-L_s and equal-level conditions. Figure 9 shows the median SFOAE level and on-band noise level elicited with unequal-frequency primaries in the current study (with $f_s/f_p=0.96$), in comparison to the median responses elicited with equal-frequency primaries in the Schairer *et al.* (2003) study. In the fixed-L_s case from Schairer *et al.* (2003), L_s was fixed at 70 dB SPL.

1. Fixed-L_s condition

In the fixed-L_s condition (top row Fig. 9), the level-dependent on-band noise was lower at each f_p in the unequal-frequency condition in comparison to the equal-frequency condition across the I/O function. This is because the level-dependent variability associated with the high SPL of the fixed-L_s condition was removed from the f_p bin in the unequal-frequency primary case, but present in the equal-frequency primary case. In the $f_p=1000$- and 4000-Hz conditions, the median SFOAE levels were nearly identical at approximately $L_p=50$ dB SPL and above. This suggests that on average, unequal- and equal-frequency primaries elicited similar response levels for L_p at and above 50 dB SPL once the SFOAE level exceeded on-band variability, and that a similar amount of suppression was provided by the 70-dB SPL on-frequency (Schairer *et al.*, 2003) and 80-dB SPL off-frequency (current) suppressors. The unequal-frequency primaries provided less suppression than the equal-frequency primaries at $f_p=2000$ Hz.

In comparison, Souter (1995, Fig. 5) presented a fixed-L_p condition in which SFOAEs were elicited with $L_p=60$ dB SPL, $f_p=2800$ Hz, and f_s and L_s varied around these values (including an equal-frequency condition) in a guinea pig and a human (only the human data are referred to here). The f_s/f_p range was 1.8 to 0.6, a much wider range of f_s/f_p ratios than in the present study. Souter noted that the largest residual was produced in the equal-frequency condition with L_s equal to or above L_p in the human data. The condition in Souter (1995) in which $f_s=2660$ Hz ($f_s/f_p=0.95$) is the closest analog to the unequal-frequency primary condition in the current data. At $f_p=2000$ Hz, our fixed-L_s, unequal-frequency ($f_s/f_p=0.96$) condition produced lower SFOAE amplitudes in comparison to the equal-frequency primary condition. This is consistent with Souter's data.

TABLE III. SFOAE thresholds in fixed-L_s conditions for equal- and unequal-frequency primaries.

L_s	f_p	Primary frequency condition	Threshold in dB SPL based on medians	Threshold in dB SPL based on 25th percentile of signal minus 75th percentile of noise
Fixed	1000	Equal	10	55
		Unequal	15	35
	2000	Equal	25	50
		Unequal	20	30
	4000	Equal	15	55
		Unequal	15	25
$=L_p$	1000	Equal	25	35
		Unequal	30	55
	2000	Equal	25	35
		Unequal	30	45
	4000	Equal	20	35
		Unequal	40	50

In the fixed-L_s condition, due to the reduced noise in the current data, the median SNR was larger in the unequal-frequency condition than the equal-frequency condition at $f_p=1000$ Hz for $L_p=50$ dB SPL and above, and at $f_p=2000$ and 4000 Hz for $L_p=20$ dB SPL and above. The largest difference in SNR between the two conditions was at $f_p=4000$ Hz. The SFOAE threshold was defined in two ways: (1) the lowest L_p at which the median SFOAE level was at least 3 dB greater than the median on-band noise, and (2) the lowest L_p at which the 25th percentile of the SFOAE level was at least 3 dB greater than the 75th percentile of the on-band noise. Thresholds calculated by these two rules for both primary frequency conditions for the fixed-L_s condition are shown in the top half of Table III. When only the median data were considered (rule 1), the thresholds were within 5 dB across the primary frequency conditions. However, once the variability of the data was taken into consideration (rule 2), the thresholds in both primary frequency conditions increased, but were 20 or 30 dB lower in the unequal-frequency primary case. Rule 2 was more successful at quantifying the threshold differences evident in the SFOAE data in Fig. 9.

2. Equal-level condition

In the equal-level condition (bottom half of Fig. 9), the on-band noise was lower in the unequal-frequency condition than in the equal-frequency condition across the I/O function. As for the fixed-L_s condition, this is because the variability associated with one of the primaries was removed from the probe frequency bin in the unequal-frequency primary condition. The SFOAE level was also decreased, and by a greater amount than the noise, in the unequal-frequency primary case. This is because SFOAE level is a nonlinear residual that reflects how much the emission is reduced by the presence of the suppressor. When the suppressor is at f_p, it produces more suppression than when it is more distant in frequency from f_p.

The SNR was larger in the equal-frequency than the unequal-frequency condition at $f_p=1000$ Hz for $L_p \geqslant 30$ dB SPL, at $f_p=2000$ for $L_p \geqslant 40$ dB SPL, and at $f_p=4000$ Hz for $L_p \geqslant 20$ dB SPL. However, the improvement in SNR was greatest in the moderate L_p region (i.e., the SNRs were more similar between the two primary frequency conditions at the low and high probe levels). Thresholds calculated by the two rules described above for both primary frequency conditions for the equal-level condition are shown in the bottom portion of Table III. When only the median data were considered (rule 1), thresholds for the two primary frequency conditions were within 5 dB at $f_p=1000$ and 2000 Hz, but threshold was 20 dB lower in the equal-frequency primary case at $f_p=4000$ Hz. Once the variability of the data was taken into consideration (rule 2), thresholds were 10 to 20 dB lower in the equal-frequency primary case. Again, rule 2 is preferred for assessing the threshold differences.

This trend between primary frequency conditions in the equal-level condition is the opposite of that in the fixed-L_s condition. This is due in part to the level-dependent variability that decreased as L_p decreased in the equal-level case, but remained high and stable in the fixed-L_s case when primary frequencies were equal. Thresholds elicited with unequal-frequency primaries were higher in the equal-level than the fixed-level condition. This may be due to the following effects: in the unequal-frequency primary condition, mutual suppression effects (between the probe and suppressor tones) produced lower SFOAE levels in general in the equal-level condition, whereas full suppression of the probe was achieved in the fixed-L_s condition with less suppression by the probe tone on the suppressor tone.

3. Summary of unequal and equal-frequency primary comparison

These results confirm hypothesis 1 and have the following implications. First, the condition with fixed L_s and unequal-frequency primaries would be the better measure for characterizing SFOAE response growth and relating it to BM response growth or to predict threshold in hearing-impaired ears. This is because the condition with fixed-L_s and equal-frequency primaries was contaminated by level-dependent noise, which reduced the SNR and increased the threshold. The unequal-frequency condition also has the advantage that it was possible to test for full suppression of the SFOAE at f_p (e.g., see Fig. 1), whereas the equal-level condition (regardless of the primary frequency condition) may be confounded by mutual and incomplete suppression. Second, the condition with equal levels and equal frequencies is more easily interpreted for modeling purposes as described by Schairer *et al.* (2003), because a single frequency is used to elicit the SFOAE. In contrast, the unequal-frequency primary case (regardless of the primary level condition) requires a more complex, two-tone suppression model.

Although it is not shown, there was little difference for the unequal-frequency conditions between the SFOAE distortion extracted by the 2E method and the difference method (Dreisbach, 1999; Guinan, 1990; Kemp and Brown, 1983; Shera and Guinan, 1999), except at low stimulus levels where the response levels decreased into the noise floor. In the difference method, f_p is presented in one interval, and f_p and f_s are presented simultaneously in a second interval. The SFOAE is calculated as the difference between the responses

TABLE IV. CDT DPOAE response growth slopes.

f_p	CDT	Slope (dB/dB)	Ratio of slopes
1000	$2f_s-f_p$	0.74	2.4
	$2f_p-f_s$	1.79	
2000	$2f_s-f_p$	0.64	2.5
	$2f_p-f_s$	1.61	
4000	$2f_s-f_p$	0.64	2.2
	$2f_p-f_s$	1.38	

in both intervals. As long as the suppressor contains no energy at f_p, the SFOAE residuals from the 2E and difference methods should be the same in the limit of no noise. Because the difference method uses two buffers and the 2E method uses three buffers, the noise in the difference method should be 10* log(2/3), or 1.8 dB lower. The 2E method for the equal-frequency condition does not have a difference-method analog.

B. CDT DPOAE I/O functions and SFOAE level-dependent notches

Hypothesis 2 stated that CDT DPOAE I/O functions reflect the threshold of the nonlinear-distortion mechanism in SFOAEs elicited by the same unequal-frequency primary tones. This is because distortion is the source mechanism for DPOAEs, and, if present, would also contribute to the generation of SFOAEs. This is consistent with the OHC receptor potential nonlinearity model of Lukashkin and Russell (1998), in which distortion contributes both to SFOAE and DPOAE generation. Hypothesis 3 stated that level-dependent notches and associated phase shifts should occur in SFOAE I/O functions measured using unequal-frequency primary conditions. These two hypotheses are related in that Schairer *et al.* (2003) suggested that notched I/O functions may be produced by an interaction of two sources, such as nonlinear distortion and linear coherent reflection. If this is the case, and if simultaneously elicited DPOAEs reflect the onset of nonlinear distortion, then the DPOAE threshold should correspond to a stimulus level close to the level at which the SFOAE notches occur.

1. Fixed-L_s condition

In the fixed-L_s condition, with $f_s/f_p=0.96$, the $2f_p-f_s$ CDT (which corresponds to $2f_2-f_1$ in DPOAE terminology) is predicted to have 2:1 growth rate, and the $2f_s-f_p$ (which corresponds to $2f_1-f_2$) is predicted to have 1:1 growth rate with L_p (Withnell and Yates, 1998). This prediction is based on a simple cubic nonlinearity model, but does not take account of cochlear compression and suppression effects in the traveling wave within the region of generation. Therefore, an exact slope relationship between the two CDTs of 2:1 might not be expected. Response growth slopes in the fixed-L_s condition that are listed in Table IV were calculated using the OAE levels at the highest pair of L_p levels, 70 and 75 dB SPL. The slope estimate was restricted to these two highest stimulus levels because, at least in the $f_p=1000$- and 2000-Hz conditions, the $2f_p-f_s$ response either was not present or did not start to grow until these levels (e.g., see the top row of Fig. 4). The slopes are less than predicted for each DPOAE. However, the relationship of slopes between the two DPOAEs ranges from 2.2 to 2.5, which is close to the predicted slope ratio of 2.

Other previous works have addressed the relationship of DPOAE growth rate. For example, the slopes reported here for $2f_s-f_p$ (0.64–0.74) are lower than the slopes reported by Gaskill and Brown (1990) of approximately 0.87, averaged across fixed-L_1 (corresponding to fixed L_s in this case) conditions of 55, 60, and 65 dB SPL (see their Table IVb, p. 828). The difference in slopes may be accounted for by the different primary frequency ratios used. Gaskill and Brown used an f_p/f_s ratio of 1.225, which was demonstrated to be the optimal ratio for eliciting DPOAEs, but is much larger than the ratio used in the current study.

Kemp *et al.* (1990, Fig. 1) described a simple nonlinear model that predicts that when L_s is fixed and L_p is varied below L_s (as in the current data), the output at f_p increases at a rate of about 1 dB/dB as L_p increases. The model also predicts that the output at $2f_s-f_p$ should increase at a similar rate then start to decrease as $L_s=L_p$ is approached, whereas the output at $2f_p-f_s$ should increase more rapidly, at a rate of approximately 2:1 as $L_s=L_p$ is approached. When $L_s=L_p$, the output at $2f_s-f_p$ and $2f_p-f_s$ should be equal. This model does not take into consideration such assumptions as place- and wave-fixed sources, which would lead to more complex predictions, and it does not depend on the primary frequency ratio, which is important in real ear measurements. Kemp *et al.* caution that in a real ear, the OAE source of generation varies with stimulus parameters. However, the model predictions are consistent in general with the current results, in that the rate of growth is more rapid at $2f_p-f_s$ than at $2f_s-f_p$ (Fig 4, top row, fixed-L_s condition with L_p varied below L_s), and that levels of these two distortion products are nearly equal when $L_s=L_p$ (Fig. 4, bottom row).

Souter (1995) showed a plot from a human ear in which $2f_s-f_p$ and SFOAE I/O functions were simultaneously recorded [Fig. 12(b)]. The SFOAEs were elicited with $f_p=2800$ Hz, $L_p=60$ dB SPL, $f_s=2240$ (for an $f_s/f_p=0.8$, or f_p/f_s of 1.25), and L_s varied. The data for this example ear appear to be similar to the averaged current data in that the $2f_s-f_p$ growth was steeper than the f_p growth, the $2f_s-f_p$ levels were much lower than the f_p levels, and $2f_s-f_p$ threshold was higher than for f_p. The $2f_s-f_p$ growth rate was approximately 2:1, which is in contrast to the 1:1 growth rate observed in the current data. This may be due to the fact that Souter's experiment used a different f_s/f_p and varied L_s with constant L_p, whereas the current experiment varied L_p with constant L_s.

2. Equal-level condition

In the equal-level condition, the response growth was similar for f_p, $2f_s-f_p$, and $2f_p-f_s$ (Fig. 4). When primary frequencies are closely spaced, such as the $f_s/f_p=0.96$ condition shown in Fig. 4, the traveling waves for the primaries have substantial overlap, and the place-fixed sources of the CDT DPOAEs are also close together. Knight and Kemp (2001) demonstrated that with equal-level primaries of 70 dB

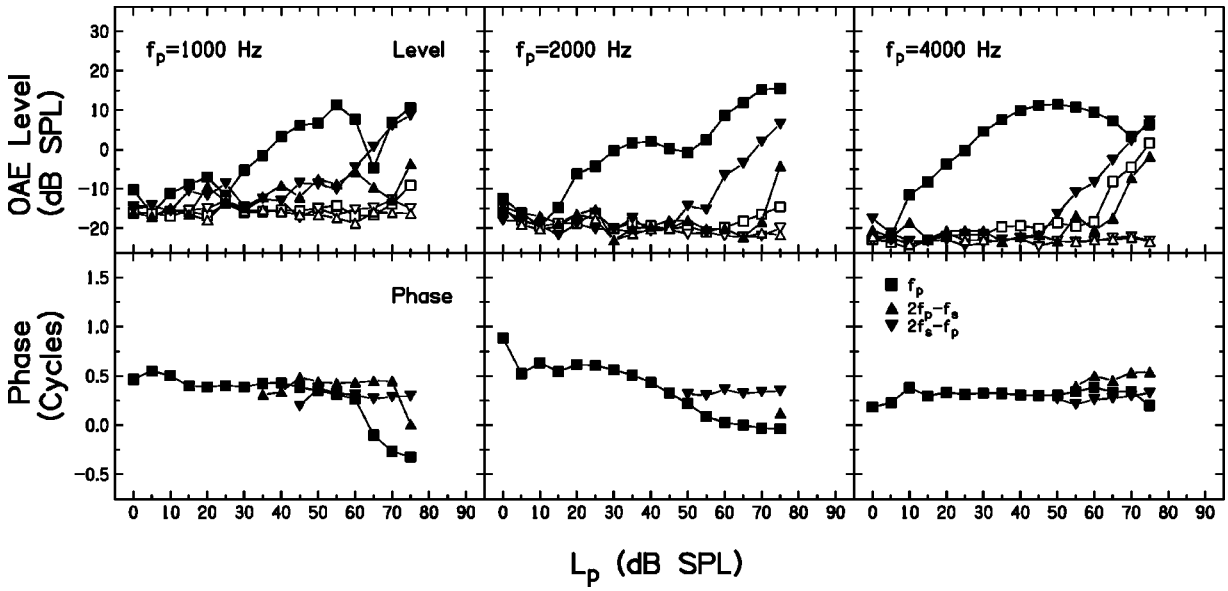

FIG. 10. Comparison of SFOAE notched I/O functions and DPOAE I/O functions. OAE level (top row) and phase (bottom row) recorded in the $f_s/f_p = 0.96$, fixed-L_s condition. Symbols represent frequency bins as described in Fig. 4 (in the top row, open symbols represent on-band noise, filled symbols represent distortion). Data are for subject SFS19.

SPL and closely spaced primaries ($f_2/f_1 < 1.1$), both the upper sideband region ($2f_2 - f_1$) and lower sideband ($2f_1 - f_2$) of the DPOAEs were dominated by place-fixed components. A wave-fixed component also was observed in the lower-sideband response. Taken together, these results suggest that a distortion source is present in simultaneously recorded SFOAEs. Additionally in the current data, the SFOAE level was greater at f_s than at f_p. This suggests that when the primaries were equal or close in level, the higher frequency tone (f_p in this case) suppressed the lower-frequency tone (f_s in this case) to a greater degree than the reverse.

3. Level-dependent notches

Level-dependent notches occurred in SFOAE I/O functions elicited with unequal-frequency primaries in both the equal-level and fixed-L_s conditions. Sharp notches were associated with sharp phase transitions (e.g., Fig. 5, $f_p = 1000$ Hz), whereas more gradual notches were associated with more gradual phase transitions (e.g., Fig. 5, $f_p = 2000$ Hz). Lukashkin *et al.* (2002) observed a similar relationship between level-dependent notch sharpness and the rate and size of phase transitions in CDT DPOAEs in guinea pigs. In the current data, two classes of nonmonotonic SFOAE functions were identified, and the prevalence of each type was assessed in both primary level conditions elicited with $f_s/f_p = 0.96$ at $f_p = 2000$ Hz. The L_p range was restricted to 20 to 70 dB SPL in order to avoid potential acoustic reflex contribution at higher stimulus levels and poor SNR at lower stimulus levels.

An SFOAE function was considered to have a sharp notch if the following conditions were satisfied: (1) as L_p increased toward the lower-level side of the notch, distortion decreased by 3 dB or more at one L_p step or over two successive L_p steps, and (2) as L_p increased on the higher-level side of the notch, distortion increased by at least 6 dB within two consecutive increases in L_p. An SFOAE function was considered to have a plateau if the following conditions were satisfied: (1) as L_p increased toward the lower-level side of the notch, distortion changed by 2 dB or less at two or more consecutive increases in L_p; (2) as L_p increased on the higher-level side of the notch, distortion increased by at least 6 dB within three consecutive increases in L_p. In addition, the following conditions had to be satisfied for both classes: (1) the SNR was at least 6 dB at adjacent stimulus levels, and (2) there was no abrupt increase (by 10 dB or more) in noise at the lower-level L_p side of the notch, indicative of an artifact in recording. Of the 32 subjects, there were six subjects in the equal-level and fixed-L_s conditions that had sharp notches. Three of these subjects had sharp notches in both level conditions. There were four subjects who had plateaus in the equal-level condition, and three subjects who had plateaus in the fixed-L_s condition. None of these subjects had notches in both level conditions. These classifications are not mutually exclusive within and across subjects and conditions. For example, subject SFS27 (Fig. 6) had a combination of a sharp notch and a plateau at $f_p = 4000$ Hz across the different f_s/f_p ratio conditions.

Figure 10 shows the OAE distortion level, noise level, and phase at f_p, $2f_s - f_p$, and $2f_p - f_s$ in the $f_s/f_p = 0.96$, fixed-L_s condition for subject SFS19 (the f_p responses are repeated from Fig. 5). For the DPOAEs, only the phase values for which the SNR was at least 3 dB at stimulus levels above 30 dB SPL are plotted. In terms of response growth, the $2f_s - f_p$ DPOAE (i.e., $2f_1 - f_2$) had a threshold at a L_p close to the L_p of the notch at $f_p = 1000$ and 2000 Hz. In all the nonmonotonic SFOAE functions examined, sharp notches and plateaus at f_p were always associated with the presence of $2f_s - f_p$ DPOAEs. However, the presence of DPOAEs was not always associated with a nonmonotonic SFOAE I/O function at f_p. This is explained if the relative phase in the ear-canal signal between the coherent reflection and distortion sources varies between constructive and de-

structive interference. The presence of DPOAEs at L_p values near a notch is consistent with the hypothesis that the same distortion source responsible for DPOAEs is also responsible for the second SFOAE source. In the L_p range in which the SFOAE notches or plateaus occurred at f_p, the corresponding phase at f_p rotated by approximately a half cycle or more, whereas the phase at $2f_s-f_p$ varied slowly with frequency (Fig. 10).

This suggests that notches and plateaus in the SFOAEs are the result of the interaction of two sources, most likely the linear coherent reflection that dominates SFOAEs at low to moderate stimulus levels and the distortion that dominates DPOAEs. Whether the nonmonotonicity is a sharp notch or a plateau depends on the varying degrees of cancellation of the relative phase and level or strength of the two components. In three of the subjects, notches occurred in both the fixed-L_s and equal-level conditions. On the other hand, more shallow notches were observed in fewer subjects, and in no case did the notch repeat in both primary level conditions, which suggests a lesser degree of cancellation. The varying degrees of cancellation might also explain why notches were not observed in every subject and condition. The two sources might not always be perfectly out of phase, and the precise combination of primary frequencies and levels that produces enough destructive interference to be observed in the ear canal may be highly variable across ears. Further, the fact that the emissions do not decrease completely into the noise floor even in sharp notches suggests that the sources do not completely cancel one another.

The fact that the $2f_s-f_p$ phase varied slowly within the bandwidth of the SFOAE notch frequency, while the SFOAE phase varied rapidly, is evidence against a multimodal resonance in the microstructure of the organ of Corti. Any mechanical resonance producing a cancellation in the BM velocity near a particular location on the organ of Corti would produce a notch in both the SFOAE I/O function at f_p and DPOAE I/O function at $2f_s-f_p$, at least in the limit of a spatially localized source region. The absence of such a notch in the corresponding DPOAE I/O function supports a two-source model of notched I/O functions in which the high-level source is due to distortion. This conclusion does not imply that multimodal resonances may not contribute to responses measured under other experimental conditions.

Liberman *et al.* (2004) demonstrated the presence of DPOAEs at high stimulus levels in mutant mice that lacked prestin (the protein that is associated with outer hair cell motility). They attributed this second, high-level source of DPOAE generation to nonlinear stereocilia transduction. The DPOAEs recorded in the ear canal in the knock-out mice in that study had very high thresholds, between 75 and 80 dB SPL (see their Fig. 2 for $f_2=22.6$ kHz). However, the SFOAE notches observed in the current human ear canals occurred at much lower levels. Thus, it is unlikely that the stereocilia transduction source of DPOAEs, if it exists in human ears, contributes to the notches in SFOAE I/O functions observed in the current data.

C. SFOAE I/O function repeatability

It was hypothesized that the SFOAE I/O functions elicited with unequal frequency primaries would be repeatable. The average rms errors in the two level conditions for SFOAEs in four subjects elicited with unequal-frequency primaries were 4.97 dB in the equal-level condition, and 5.04 in the fixed-L_s condition. This general level of agreement confirms that responses were repeatable. In Schairer *et al.* (2003), repeatability for equal-frequency, equal-level conditions at primary frequencies was examined using correlations in four subjects at 2000 and 4000 Hz, and in two subjects at 1000 Hz. However, it was noted that correlations may not adequately reflect the systematic differences between responses. Thus, the average rms error was calculated for comparison with the current error estimates. The average rms error in the equal-level conditions of Schairer *et al.* (2003) was 3.39 dB. It is unknown why the error was smaller in those subjects in comparison to the errors in the current data. One possible source is the difference in time between the data collection sessions. In the Schairer *et al.* repeatability study, there was a delay of 1 to 3 months between runs, whereas the delay in the current study was over 1 year.

D. Level-dependent on-band noise

It was hypothesized that with unequal-frequency primaries, on-band, but not off-band, noise would be level dependent if the source of the noise is variability in middle-ear transmission. This is demonstrated in Fig. 3 in the $f_p=2000$- and 4000-Hz conditions. Off-band noise was constant across L_p in the fixed-L_s condition, whereas on-band noise increased as a function of L_p. Results for the current unequal-frequency, equal-level primary condition were consistent with the equal-frequency, equal-level condition reported by Schairer *et al.* (2003). That is, off-band noise increased only at the highest stimulus levels, whereas on-band noise began to increase at lower stimulus levels. On-band noise only increased slightly at the highest L_p at the DP frequencies (not shown), and it was constant as a function of L_p in the coupler (Fig. 8).

Confirmation of this hypothesis supports the theory that the source of SFOAE variability is within the middle ear, as suggested by Schairer *et al.* (2003). A middle-ear source of variability at the frequencies present in the stimulus would be present in ears with normal hearing, hearing loss, or cochlear implants. It would not be present in a coupler, or at DPOAE frequencies because there is no stimulus energy at the DPOAE frequencies. The increase in off-band variability at higher levels in the equal-frequency condition may have been due to an occasional activation of the acoustic reflex. If this is the case, SFOAE variability could be used to examine variability of stimulus transmission through the middle ear. However, the presence of an acoustic reflex shift was not independently assessed in this experiment.

The middle-ear muscle activity has three components: a random activity in the absence of any specific acoustic cue, a reflex response to an acoustic stimulus, and contractions related to other somatic motor activity (Simmons, 1964). The first random component is present as variability in the tonus

of both the tensor tympani and stapedius muscles. The observed on-band SFOAE noise is consistent with the actions of such a source of middle-ear variability, in which fluctuations in muscle tone would produce fluctuations in forward and reverse transmission through the middle ear. The SFOAE noise is present on-band as a result of the stimulus energy at f_p. The middle ear may produce variability over a wide range of frequencies, but the on-band biological noise recorded in the ear canal may not be measurable at the stimulus frequency until the stimulus intensity is high enough to increase the response variability or noise above the system noise floor. This on-band noise may be influenced by middle-ear variability at the eardrum in the form of a fluctuating component to the eardrum impedance. The relative level of the on-band noise to the stimulus SPL characterizes the noise-to-signal level, and is on the order of -70 dB in the fixed-L_s SFOAE responses in Figs. 2 and 3 (i.e., the level difference between the SFOAE on-band noise SPL and the on-band stimulus level L_p). This theory predicts that the noise-to-signal level should increase linearly with L_p, and the data in Fig. 2 are consistent with this prediction. It is possible that other physiological noise sources may contribute to the SFOAE on-band noise level, for example, noise related to blood flow or respiration may also affect the eardrum impedance.

The relative contributions of the tensor tympani and stapedius muscle are unknown, but any occasional activation of a middle-ear muscle reflex shift would reflect the activity of the stapedius muscle alone (Pang and Peake, 1985). Such an occasional reflex activation would also influence the measured time-averaged responses and, thus, the measured noise.

The off-band SFOAE noise would be insensitive to a stimulus-related middle-ear source of transmission variability because there is no stimulus energy present at off-band frequencies (except for isolated conditions at $f_p = 1000$ Hz described in the Results section, in which the off-frequency band unavoidably included the suppressor tone). Similarly, the on-band DPOAE noise would be insensitive to this source of middle-ear variability because the DPOAE bin has no stimulus energy present, and the relative noise-to-signal level associated with the reverse-transmitted DPOAE would be far below the noise of the measurement system. This accounts for the absence of a level-dependent increase in on-band DPOAE noise. An alternate view is that SFOAE variability may arise from the cochlea rather than the middle ear, but no cochlear model of SFOAE variability in the absence of DPOAE variability has been proposed.

E. Distortion in ears with cochlear implants and in a test cavity

In comparison to the equal-frequency primary conditions used in Schairer *et al.* (2003), it was hypothesized that the unequal-frequency primary conditions would yield improved separation between distortion recorded in normal-hearing ears, and distortion recorded in ears with cochlear implants and in a test cavity. Figure 8 shows that in the equal-level, $f_s/f_p = 0.96$ condition (bottom row), the distortion recorded in the implanted ear of subject SFSCI01 overlapped the range of responses recorded in normal-hearing ears at $f_p = 2000$ and 4000 Hz. These results are similar to Schairer *et al.* (2003, Fig. 4). The hypothesis was confirmed for the fixed-L_s condition in the current data. Only two responses at the highest stimulus levels exceeded the 25th percentile of normal-hearing responses at $f_p = 4000$ Hz in SFSCI02. The distortion recorded in the coupler did not equal or exceed the 25th percentile of responses in the normal-hearing ears at any of the f_p frequencies in either level condition. Based on the comparison of the current and previous Schairer *et al.* data, the preferred condition for separation of normal from impaired ears would be the unequal-frequency, fixed-L_s condition.

Although the current data extend the findings to a broader set of stimulus conditions, they do not answer the question of the origin of the distortion in ears with cochlear implants. The fact that the distortion is observed in implant ears in all conditions lends further support to the theory that the distortion in implant ears is biological. Recently, Liberman *et al.* (2004) demonstrated that at high stimulus levels in mutant mice lacking prestin, a small, physiologically vulnerable DPOAE was present in the absence of OHC somatic motility. They attributed these emissions to mechanical nonlinearity of stereocilia transduction. It is possible that this mechanism contributes to the generation of SFOAEs at high levels in ears with hearing loss. However, this hypothesis cannot be confirmed or rejected with the current data.

V. CONCLUSIONS

SFOAE I/O functions elicited with a range of f_s/f_p ratios of approximately 0.93 to 1.07 in a fixed-L_s condition were similar and repeatable. The fixed-L_s, unequal-frequency primary combination produced the largest SNR over a larger dynamic range in normal-hearing ears, and greater separation between responses in normal-hearing ears and distortion in ears with cochlear implants. Further, this condition was not confounded by mutual suppression effects as was the equal-level condition, and it can be used to test for full suppression. Thus, the fixed-L_s condition is advantageous for the purposes of characterizing SFOAE response growth, relating SFOAE response growth to BM response growth, and testing the ability to predict audiometric thresholds from SFOAE I/O function.

CDT DPOAE I/O functions reflected the threshold of the nonlinear-distortion mechanism in SFOAEs elicited by the same primaries, and the DPOAE threshold often corresponded to nonmonotonicities in SFOAE I/O functions at f_p. This suggests that the level-dependent notches and plateaus in SFOAEs, which were also associated with phase shifts, were due to varying degrees of cancellation of two sources, most likely the coherent linear reflection source, which dominates SFOAEs at lower levels, and the nonlinear distortion source that also is responsible for DPOAE generation.

In general, level-dependent SFOAE noise was observed on-band (i.e., at the frequencies of the stimuli) but not off-band. On-band SFOAE noise was observed in ears with normal hearing and in ears with cochlear implants. Because the SFOAE variability was observed in ears with cochlear im-

plants, a possible source is variability in the middle-ear mechanics, such as variability in the middle-ear muscle tonus.

ACKNOWLEDGMENTS

This research was supported by Grants R01 DC003784, T32 DC00013, R03 DC006342, and P30 DC04662 from the National Institute on Deafness and Other Communication Disorders of the National Institutes of Health. We appreciate the helpful comments made by two anonymous reviewers.

Allen, J. B. (**1980**). ''Cochlear micromechanics—a physical model of transduction,'' J. Acoust. Soc. Am. **68**, 1660–1670.

American National Standards Institute (**1996**). ''American National Standard S3.6: Specification for Audiometers,'' (American National Standards Institute, New York).

Boege, P., and Janssen, T. (**2002**). ''Pure-tone threshold estimation from extrapolated distortion product otoacoustic emission I/O functions in normal and cochlear hearing loss ears,'' J. Acoust. Soc. Am. **111**, 1810–1818.

Buus, S., Obeling, L., and Florentine, M. (**2001**). ''Can basilar-membrane compression characteristics be determined from distortion-product otoacoustic-emission input–output functions in humans?'' in *Proceedings of the 12th International Symposium on Hearing: Physiological and Psychophysical Bases of Auditory Function*, edited by D. J. Breebaart, A. J. M. Houtsma, A. Kohlrausch, V. F. Prijs, and R. Schoonhoven (Shaker, Maastricht, Netherlands), pp. 373–381.

Dorn, P. A., Konrad-Martin, D., Neely, S. T., Keefe, D. H., Cyr, E., and Gorga, M. P. (**2001**). ''Distortion product otoacoustic emission input/output functions in normal-hearing and hearing-impaired human ears,'' J. Acoust. Soc. Am. **110**, 3119–3131.

Dreisbach, L. E. (**1999**). ''Characterizing the $2f_1-f_2$ distortion-product otoacoustic emission and its generators measured from 2 to 20 kHz in humans,'' doctoral dissertation, Northwestern University.

Gaskill, S. A., and Brown, A. M. (**1990**). ''The behavior of the acoustic distortion product, $2f_1-f_2$, from the human ear and its relation to auditory sensitivity,'' J. Acoust. Soc. Am. **88**, 821–839.

Gorga, M. P., Neely, S. T., Bergman, B. M., Beauchaine, K. L., Kaminski, J. R., and Liu, Z. (**1994**). ''Towards understanding the limits of distortion product otoacoustic emission measurements,'' J. Acoust. Soc. Am. **96**, 1494–1500.

Gorga, M. P., Neely, S. T., Dorn, P. A., and Hoover, B. M. (**2003**). ''Further efforts to predict pure-tone thresholds from distortion product otoacoustic emission input/output functions,'' J. Acoust. Soc. Am. **113**, 3275–3284.

Gorga, M. P., Neely, S. T., Dorn, P. A., and Konrad-Martin, D. (**2002**). ''The use of distortion product otoacoustic emission suppression as an estimate of response growth,'' J. Acoust. Soc. Am. **111**, 271–284.

Guinan, J. J., Jr. (**1990**). ''Changes in stimulus frequency otoacoustic emissions produced by two-tone suppression and efferent stimulation in cat,'' in *The Mechanics and Biophysics of Hearing*, edited by P. Dallos, C. D. Geisler, J. W. Matthews, M. A. Ruggero, and C. R. Steele (Springer, New York), pp. 170–177.

Keefe, D. H. (**1998**). ''Double-evoked otoacoustic emissions. I. Measurement theory and nonlinear coherence,'' J. Acoust. Soc. Am. **103**, 3489–3498.

Kemp, D. T., Brass, D., and Souter, M. (**1990**). ''Observations on simultaneous SFOAE and DPOAE generation and suppression,'' in *The Mechanics and Biophysics of Hearing*, edited by P. Dallos, C. D. Geisler, J. W. Matthews, M. A. Ruggero, and C. R. Steele (Springer, New York), pp. 202–209.

Kemp, D. T., and Brown, A. M. (**1983**). ''A comparison of mechanical nonlinearities in the cochleae of man and gerbil from ear canal measurements,'' in *Hearing Physiological Basis and Psychophysics*, edited by R. Klinke and R. Hartmann (Springer, Berlin), pp. 82–88.

Knight, R. D., and Kemp, D. T. (**2000**). ''Indications of different distortion product otoacoustic emission mechanisms from a detailed f_1, f_2 area study,'' J. Acoust. Soc. Am. **107**, 457–473.

Knight, R. D., and Kemp, D. T. (**2001**). ''Wave and place fixed DPOAE maps of the human ear,'' J. Acoust. Soc. Am. **109**, 1513–1525.

Kummer, P., Janssen, T., and Arnold, W. (**1998**). ''The level and growth behavior of the $2f_1-f_2$ distortion product otoacoustic emission and its relationship to auditory sensitivity in normal hearing and cochlear hearing loss,'' J. Acoust. Soc. Am. **103**, 3431–3444.

Liberman, M. C., Zuo, J., and Guinan, Jr., J. J. (**2004**). ''Otoacoustic emissions without somatic motility: Can stereocilia mechanics drive the mammalian cochlea?,'' J. Acoust. Soc. Am. **116**, 1649–1655.

Lin, T., and Guinan, Jr., J. J. (**2000**). ''Auditory-nerve-fiber responses to high-level clicks: Interference patterns indicate that excitation is due to the combination of multiple drives,'' J. Acoust. Soc. Am. **107**, 2615–2630.

Lonsbury-Martin, B. L., Harris, F. P., Stagner, B. B., Hawkins, M. D., and Martin, G. K. (**1990**). ''Distortion product emissions in humans. I. Basic properties in normally hearing subjects,'' Ann. Otol. Rhinol. Laryngol. Suppl. **147**, 3–14.

Lukashkin, A. N., Lukashkina, V. A., and Russell, I. J. (**2002**). ''One source for distortion product otoacoustic emissions generated by low- and high-level primaries,'' J. Acoust. Soc. Am. **111**, 2740–2748.

Lukashkin, A. N., and Russell, I. J. (**1998**). ''A descriptive model of the receptor potential nonlinearities generated by the hair cell mechanoelectrical transducer,'' J. Acoust. Soc. Am. **103**, 973–980.

Moore, B. C., and Oxenham, A. J. (**1998**). ''Psychoacoustic consequences of compression in the peripheral auditory system,'' Psychol. Rev. **105**, 108–124.

Neely, S. T., Gorga, M. P., and Dorn, P. A. (**2003**). ''Cochlear compression estimates from measurements of distortion-product otoacoustic emissions,'' J. Acoust. Soc. Am. **114**, 1499–1507.

Oxenham, A. J., and Bacon, S. P. (**2003**). ''Cochlear compression: Perceptual measures and implications for normal and impaired hearing,'' Ear Hear. **24**, 352–366.

Pang, X. D., and Peake, W. T. (**1985**). ''How do contractions of the stapedius muscle alter the acoustic properties of the ear?,'' in *Peripheral Auditory Mechanisms*, edited by J. Allen, J. Hall, A. Hubbard, S. Neely, and A. Tubis (Springer, New York).

Robles, L., and Ruggero, M. A. (**2001**). ''Mechanics of the mammalian cochlea,'' Physiol. Rev. **81**, 1305–1352.

Schairer, K. S., Fitzpatrick, D., and Keefe, D. H. (**2003**). ''Input–output functions for stimulus-frequency otoacoustic emissions in normal-hearing adult ears,'' J. Acoust. Soc. Am. **114**, 944–966.

Shera, C. A., and Guinan, Jr., J. J. (**1999**). ''Evoked otoacoustic emissions arise by two fundamentally different mechanisms: A taxonomy for mammalian OAEs,'' J. Acoust. Soc. Am. **105**, 782–798.

Simmons, F. B. (**1964**). ''Perceptual theories of middle ear muscle function,'' Ann. Otol. Rhinol. Laryngol. **73**, 724–739.

Souter, M. (**1995**). ''Stimulus frequency otoacoustic emissions from guinea pig and human subjects,'' Hear. Res. **90**, 1–11.

Talmadge, C. L., Tubis, A., Long, G. R., and Piskorski, P. (**1998**). ''Modeling otoacoustic emission and hearing threshold fine structures,'' J. Acoust. Soc. Am. **104**, 1517–1543.

Talmadge, C. L., Tubis, A., Long, G. R., and Tong, C. (**2000**). ''Modeling the combined effects of basilar membrane nonlinearity and roughness on stimulus frequency otoacoustic emission fine structure,'' J. Acoust. Soc. Am. **108**, 2911–2932.

Whitehead, M. L., Stagner, B. B., McCoy, M. J., Lonsbury-Martin, B. L., and Martin, G. K. (**1995**). ''Dependence of distortion-product otoacoustic emissions on primary levels in normal and impaired ears. II. Asymmetry in $L1$, $L2$ space,'' J. Acoust. Soc. Am. **97**, 2359–2377.

Withnell, R. H., and Yates, G. K. (**1998**). ''Onset of basilar membrane nonlinearity reflected in cubic distortion tone input–output functions,'' Hear. Res. **123**, 87–96.

Zweig, G., and Shera, C. A. (**1995**). ''The origin of periodicity in the spectrum of evoked otoacoustic emissions,'' J. Acoust. Soc. Am. **98**, 2018–2047.

Zwislocki, J. J. (**1980**). ''Five decades of research on cochlear mechanics,'' J. Acoust. Soc. Am. **67**, 1679–1685.

On the binding of successive sounds: Perceiving shifts in nonperceived pitches[a)]

Laurent Demany[b)] and Christophe Ramos
Laboratoire de Neurophysiologie, CNRS and Université Victor Segalen (UMR 5543), 146 rue Leo-Saignat, F-33076 Bordeaux, France

(Received 12 August 2004; revised 3 November 2004; accepted 30 November 2004)

It is difficult to hear out individually the components of a ''chord'' of equal-amplitude pure tones with synchronous onsets and offsets. In the present study, this was confirmed using 300-ms random (inharmonic) chords with components at least 1/2 octave apart. Following each chord, after a variable silent delay, listeners were presented with a single pure tone which was either identical to one component of the chord or halfway in frequency between two components. These two types of sequence could not be reliably discriminated from each other. However, it was also found that if the single tone following the chord was instead slightly (e.g., 1/12 octave) lower or higher in frequency than one of its components, the same listeners were sensitive to this relation. They could perceive a pitch shift in the corresponding direction. Thus, it is possible to perceive a shift in a nonperceived frequency/pitch. This paradoxical phenomenon provides psychophysical evidence for the existence of automatic ''frequency-shift detectors'' in the human auditory system. The data reported here suggest that such detectors operate at an early stage of auditory scene analysis but can be activated by a pair of sounds separated by a few seconds.
[DOI: 10.1121/1.1850209]

PACS numbers: 43.66.Mk, 43.66.Hg [JHG] Pages: 833–841

I. INTRODUCTION

The understanding of speech or the identification of a melody requires a perceptual binding of successive sounds that differ from each other. Little is known about the neural machinery responsible for this binding in the human brain. Remarkably, a melody retains its perceptual identity when it is transposed in the frequency domain, i.e., when the frequencies of the successive tones are multiplied by a common factor (Attneave and Olson, 1971; Divenyi and Hirsh, 1978). This shows that human listeners perceive melodies as patterns rather than mere concatenations of independent tones. From that point of view, a melody may not be completely equivalent to a sequence of tones varying in intensity rather than frequency: Curiously, binary sound sequences with a complex structure (e.g., ABAAABBAAB) are identified more accurately when their two components (A and B) differ in frequency than when they differ in intensity, independently of the magnitude of the difference (McFarland and Cacace, 1992). In order to account for the propensity of melodies to be perceived as patterns, it has been speculated by some authors (Deutsch, 1969; van Noorden, 1975; Anstis and Saida, 1985; Okada and Kashino, 2003) that the human auditory system contains automatic ''frequency-shift detectors'' which are sensitive to the direction of such shifts and can be activated by a pair of successive sounds even when these sounds are separated by a silent delay. The existence of shift detectors operating in the frequency or pitch domain might also account for an informal observation made by Davis *et al.* (1951) and Bilsen (2001) during their investigations of the weak pitch sensations produced by certain binaural interactions (Bilsen, 2001) or evoked by the periodicity of stimuli consisting of high-rank harmonics of a missing fundamental (Davis *et al.*, 1951). These authors noted that the audibility of pitch in a given sound can be markedly improved if, instead of being presented alone repeatedly, this sound alternates with a similar sound liable to evoke a somewhat different pitch.

In the auditory cortex of cats or monkeys, the response of many neurons to a pure tone can be strongly influenced by a preceding pure tone with a different frequency (Brosch and Schreiner, 1997, 2000; Weinberger and McKenna, 1988; McKenna *et al.*, 1989). However, this sensitivity to discrete frequency shifts seems to hold only when the interstimulus interval (ISI) is relatively short—less than 1 s. By contrast, the hypothesis that will be considered here is the existence of shift detectors (possibly more complex than single neurons) functioning even for ISIs lasting a few seconds. The hypothesis in question is consistent with the fact that the human ability to detect consciously small frequency shifts between temporally remote tones, and to identify the direction of such shifts, does not depend on the subject's mental activity or focus of attention during the ISI (Demany *et al.*, 2001; Clément, 2001). It is also worthy to note that this ability differs from the ability to detect intensity shifts with respect to their dependence on the ISI (Clément *et al.*, 1999).

The present paper stems from our accidental discovery of a paradoxical perceptual phenomenon which seems to lend strong support to the idea that automatic frequency-shift detectors exist in the human auditory system. This phenomenon is elicited by the successive presentation of: (i) a sum of N synchronous pure tones with equal amplitudes, forming an inharmonic ''chord;'' (ii) a single pure tone (''T''). The

[a)]Portions of this work were presented at the 147th meeting of the Acoustical Society of America, New York, NY, May 2004.
[b)]Electronic mail: laurent.demany@psyac.u-bordeaux2.fr

chord's components may have randomly drawn frequencies, but must be at least a few semitones apart in order to be separated in the cochlea (Plomp, 1964; Moore and Ohgushi, 1993; Shera *et al.*, 2002). Even so, if the chord is rather brief and N exceeds 2 or 3, it will be difficult for the listener to perceive the pitches of the chord's components. This difficulty reflects an ''informational masking'' effect (Neff and Green, 1987; Kidd *et al.*, 1994). A ''fusion'' (Bregman, 1990) of the chord's components takes place at a central level of the auditory system, so that typically the whole chord is heard as a single sound, with a tonal quality but only a vague global pitch. We observed indeed that if the following tone, T, is identical to one component of the chord, this identity generally goes unnoticed. However, we also observed that if T is instead slightly lower or higher in frequency than one component of the chord, many listeners are able, after a little practice, to perceive a pitch shift in the corresponding direction. To their surprise, they find that it is possible to hear an upward or downward shift in a pitch which was not heard in the chord (and is not heard retroactively when T is presented). Moreover, it appears that the direction of the melodic interval formed by T and its neighbor in the chord can be identified even when the chord and T are separated by a silent ISI of a few seconds. The experiments described below substantiate these counterintuitive observations.

II. EXPERIMENT 1

A. Method

On each trial run in this experiment (and the subsequent ones), the listener was presented with a chord consisting of five synchronous pure tones, spaced by intervals which were four independent random variables. The probability distribution of each interval was rectangular on a log-frequency scale and ranged from 6 semitones (1/2 octave) to 10 semitones (5/6 octave). The chord was randomly positioned within a 4-octave frequency range, 200–3200 Hz, and was followed by a single pure tone, T. The aim of experiment 1 was to compare perceptual performances in two conditions, respectively termed ''up/down'' and present/absent.''

In the up/down condition, schematized in the leftmost panel of Fig. 1, T was positioned 1 semitone above or below one of the chord's three intermediate components. The component in question and the direction of the 1-semitone shift were selected at random on each trial. The listener knew that and had to judge if the 1-semitone frequency shift was made upward or downward.

In the present/absent condition (Fig. 1, central panel), T was equiprobably (i) identical to one of the chord's three intermediate components or (ii) positioned halfway in frequency between two components (frequency being scaled logarithmically). In either case, a random choice was made between the three or four possible options. The listener also knew that and had to judge if T was present in the chord or not.

In both conditions, the chord and T had a total duration of 300 ms and were gated on and off with 20-ms raised-cosine amplitude ramps. They were separated by a 500-ms

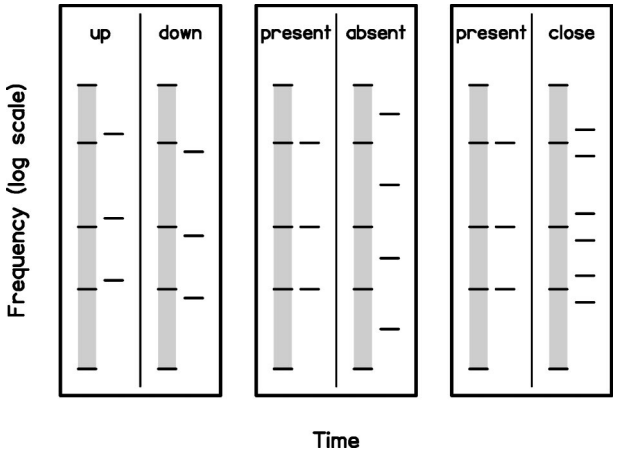

FIG. 1. Illustration of the stimulus configurations used in the ''up/down,'' ''present/absent,'' and ''present/close'' conditions. Each horizontal segment represents a pure tone and the shaded areas represent a possible chord. For a given chord, the frequency of the following tone, T, could take 6, 7, or 9 possible values, depending on the experimental condition. In this figure, for visual reasons, the T tones have been horizontally positioned close to the chords. In the experiments, actually, the time interval separating T from the chord always exceeded the duration of both stimuli.

silent ISI. Each T tone and component of the chord had a nominal sound-pressure level of 65 dB. The stimuli were heard binaurally (diotically), via earphones (Sennheiser HD265). They were generated via a 24-bit digital-to-analog converter (Echo Gina), at a sampling rate of 44.1 kHz. Each trial began with the presentation of a 2.1-s random melody, serving as a warning signal and consisting of seven 300-ms pure tones with frequencies drawn independently between 200 and 3200 Hz.[1] The chord was presented 600 ms after this melody. The listener, sitting in a double-walled sound-attenuating booth, had an unlimited response time after the presentation of T. His or her response, given by making a mouse-click on one of two labeled zones of a monitor screen, automatically triggered the next trial within blocks of 50 trials. Responses were not followed by an immediate feedback, but listeners were informed of their performance between successive blocks of trials. Each block was carried out in a fixed condition (up/down or present/absent); the two conditions alternated from block to block. Listeners were tested in three or four sessions, on different days, until 500 trials had been run in each condition.

The experiment was conducted on 11 normal-hearing listeners between the ages of 22 and 50 years. Two of them were the authors. Most of them had received a significant musical education. Six listeners had previously participated in other experiments concerning pitch perception (Demany *et al.*, 2001, 2004). For each listener, the experiment proper was preceded by a few training sessions—generally not more than two. The chords initially used in these training sessions consisted of only three pure tones, with a duration of 700 ms instead of 300 ms; they were similar to those employed by Demany *et al.* (2004). In addition to the 11 listeners who finally constituted the experimental group, three other listeners participated in training sessions. They were not included in the experimental group because of their apparent inability to exceed the chance level of performance in any condition.

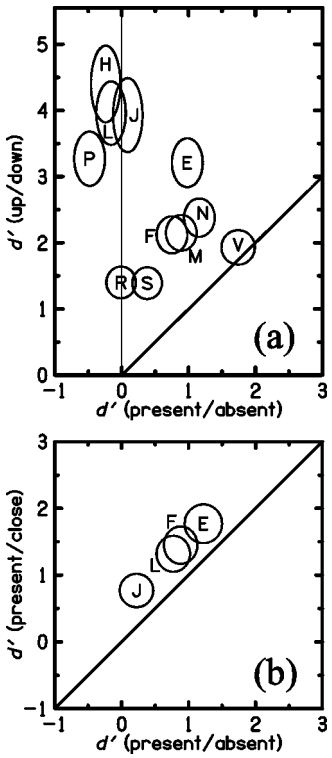

FIG. 2. Results of experiment 1 [panel (a)] and experiment 2 [panel (b)]. Each ellipse (or circle) is centered on the d' values measured in the two conditions for a given listener, and its surface represents a 95% confidence area. Oblique lines indicate where the ellipses could be centered if d' was identical in the two conditions. Listeners are identified by capital letters. Confidence intervals around d' were computed as suggested by Macmillan and Creelman (1991).

B. Results

Performance was measured in terms of d' (Green and Swets, 1974). The results are displayed in the upper panel of Fig. 2, where 11 ellipses represent the 11 listeners' data. Each ellipse (actually a circle in some cases) is centered on the d' values measured in the two conditions for a given listener, and its surface represents a 95% confidence area. Listeners are identified by capital letters in order to permit within-subject comparisons of performance across experiments; "E" and "F" are the authors.

There was a considerable interindividual variability in performance. For each listener, however, d' was larger in the up/down condition than in the present/absent condition, and the corresponding difference was generally quite pronounced. Commonly, a sensory signal is said to be detectable if $d'>1$. It can be seen that this threshold was exceeded by all listeners in the up/down condition, but by only two listeners in the present/absent condition. Four listeners (H, J, L, P) made only few errors (1.4–6.6 %) in the up/down condition while performing at the chance level, or even slightly below it, in the present/absent condition. Only one listener (V) had statistically equivalent performance levels in the two conditions. Perhaps not fortuitously, this was also the only listener endowed with "absolute pitch" (Ward and Burns, 1982).

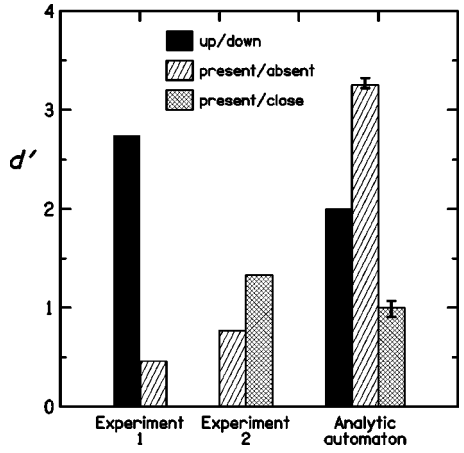

FIG. 3. Comparison of the average d' values measured in experiments 1 and 2 (left and center) with the d' values expected from the analytic automaton described in Sec. II C (right). The two small error bars represent a variability of d' resulting from the use of different values of δ_k by the automaton. The lowest and highest values of δ_k considered here (1.9–2.4 semitones for the present/absent condition, and 0.7–1.3 semitones for the present/close condition) are consistent with the largest response biases actually observed in experiments 1 and 2.

C. Discussion

Each participant in this experiment stated that the chords' components were very difficult or impossible to hear out individually. Let us consider, however, an "analytic automaton" Λ for which this is not the case. In both conditions, Λ takes on each trial an explicit (but relatively imprecise) measurement of the chord's component frequencies, and then relates these data to the frequency of T. In the up/down condition, the task of Λ is to determine if the musical interval formed by T and the closest component of the chord is equal to $+1$ or -1 semitone. In the present/absent condition, on the other hand, the task is to determine if the corresponding interval is equal to 0 or at least 3 semitones (given that the chords' components are separated by at least 6 semitones). Since the difference between $+1$ and -1 is smaller than the difference between at least 3 and 0, the performance of Λ in the present/absent condition should logically exceed its performance in the up/down condition. We confirmed this in a Monte Carlo simulation assuming that the strategy of Λ is optimal and that its performance is limited only by a source of noise in the frequency measurements. Our simulation specifically supposed that the measured frequency of each component of the chord is a Gaussian random variable with a mean equal to the true frequency and a standard deviation of 1 semitone. On each trial, Λ computes the differences between log transforms of the frequency of T and the measured frequencies of the chord's three intermediate components. Its response is then based on the difference δ which has the smallest absolute value. In the up/down condition, Λ responds "up" if and only if $\delta>0$. In the present/absent condition, Λ responds "present" if and only if $|\delta|<\delta_k$, δ_k being a positive constant. The d' scores of Λ can be compared in Fig. 3 to the average d' values measured in experiment 1. In the present/absent condition, the d' score of Λ is somewhat dependent on δ_k, because $|\delta|$ is not a Gaussian variable; but, the influence of δ_k is small as long as this

criterion takes reasonable values. Figure 3 makes clear that Λ is a completely inadequate model of real listeners: Whereas real listeners are much more successful in the up/down condition than in the present/absent condition, the opposite is true for Λ.

The analytic automaton Λ that we have just considered is an ideal listener, in several respects. In particular, there are no systematic errors (i.e., biases) in its frequency measurements, and its response criteria—especially δ_k—are strictly invariant across trials. In theory, the poor performance of real listeners in the present/absent condition could partly be ascribed to the difficulty of behaving like an *ideal* analytic listener rather than to an inability to hear out the individual components of the chords. This issue will be examined in the next section. Meanwhile, another issue should be considered. Although the bandwidths of the chords exceeded 2 octaves, each chord evoked as a whole a global pitch sensation, presumably related to its ''center of gravity'' in the frequency domain. This global pitch was imprecise, but it noticeably varied from trial to trial together with the chord itself. In the up/down condition, a conceivable strategy was to respond ''up'' if the pitch of T was higher than the global pitch evoked by the chord, and to respond ''down'' otherwise. To what extent was this holistic strategy profitable? The answer is that it could not be very efficient, even for a theoretical listener perceiving the global pitch in an optimal manner. Its use would have led to systematic errors when T was 1 semitone above the lower neighbor of the chord's median component, or 1 semitone below its higher neighbor. If the global pitch of a chord corresponded exactly to the geometric mean of its five component frequencies, and if the holistic strategy was used exclusively and perfectly, the d' value expected in the up/down condition was equal to 0.70. Much higher d' values were actually measured in experiment 1. For most listeners, the difference between the d' values obtained in the up/down and present/absent conditions was too large to be accounted for by the availability of holistic pitch cues in the up/down condition. It can actually be supposed that such cues were never used because each listener was initially instructed to ignore the global pitches of the chords.

III. EXPERIMENT 2

A. Rationale and method

Introspectively, the difficulty of the present/absent condition of experiment 1 originated from the fact that the chords' components were very hard to perceive individually. In this condition, there were no obvious perceptual cues permitting to give correct responses without perceiving consciously the individual components of the chords (whereas the opposite was true for the up/down condition). In theory, however, the difficulty of the present/absent condition could be accounted for otherwise. Due to the inherent inaccuracy of any perceptual measurement, and also due to the possible existence of small contextual effects in the perception of pure tone pitch (e.g., Terhardt, 1970), a chord component physically identical to T might nevertheless be perceived as different from T. This implies that, in the present/absent condition, an ''analytic'' listener had to use a response rule involving a difference criterion, as discussed in the previous section. The difference criterion, δ_k, had to be larger than 0 and stable across trials. Crucially, δ_k had to be defined by the listener him-/herself since it was an *internal* reference. In the up/down condition, on the other hand, an internal reference was not *a priori* needed by an analytic listener; it could be sufficient to determine if T was higher or lower than the closest component of the chord (an ''external'' reference). A conceivable hypothesis, therefore, was that the difficulty of the present/absent condition stemmed from the need, in this condition, of a stable internal reference serving as a response criterion for the assessment of pitch differences.

In experiment 2, this hypothesis was tested by comparing the performances of four listeners in the present/absent condition and a new condition, termed ''present/close'' (Fig. 1, rightmost panel). In both conditions, T was equiprobably present or not present in the chord and the listener had to make a two-alternative judgment in this regard. The two conditions differed from each other only when T was not present in the chord. On the corresponding trials in the present/close condition, T was positioned exactly 1.5 semitone (1/8 octave) above or below one of the chord's three intermediate components; the six possible options were equiprobable. Note that, in this condition, T was always much closer in frequency to one component of the chord than to any other component since the components were spaced by intervals of at least 6 semitones. In contrast, when T was absent from the chord in the present/absent condition, T was at least 3 semitones away from any component since it was positioned halfway between two components. Thus, for an analytic listener, the present/close condition was more difficult than the present/absent condition. In Fig. 3, this is confirmed for the analytic automaton Λ defined in Sec. II C; its d' score in the present/close condition is about 1.0, much worse than its score of about 3.3 in the present/absent condition. Clearly, if the hypothesis that we intended to test in the present experiment were correct, performance could not be better in the present/close condition than in the present/absent condition, since the alleged problem of the internal reference serving as a response criterion existed in both conditions and was not less critical in the present/close condition. However, our prediction was on the contrary that performance would be better in the present/close condition than in the present/absent condition. This prediction rested on the assumption that, in the present/close condition, a clear upward or downward pitch shift would be generally audible on ''close'' trials, but not or less so on ''present'' trials. In contrast, the difficulty of the present/absent condition suggested that ''absent'' trials could not be reliably discriminated from ''present'' trials on the basis of the audibility of a pitch shift.

The procedure used in experiment 2 was essentially the same as that employed in experiment 1, except for the replacement of the up/down condition by the present/close condition. There was again a 500-ms ISI between each chord and the following T tone. Eight blocks of 50 trials were run in each of the two conditions; this required only two sessions. The experiment proper was preceded by a single and short training session. The four listeners who acted as sub-

jects included the authors. Each listener had been previously tested in experiment 1.

B. Results and discussion

The individual d' scores obtained in each condition are displayed in the lower panel of Fig. 2, and their average values are plotted in Fig. 3. Each listener was significantly more successful in the present/close condition than in the present/absent condition. This outcome is consistent with our prediction and contradicts the hypothesis tested in the experiment. It seems clear that the difficulty of the present/absent condition did not stem from a difficulty to use an adequate response criterion in this condition. A more plausible explanation is that it was difficult to hear out the individual components of the chords, as suggested by the listeners' introspective reports.

Yet, d' had an average value of only 1.33 in the present/close condition, and was not dramatically lower in the present/absent condition. The modest values of d' in the present/close condition imply that it was not extremely easy to discriminate ''close'' trials from ''present'' trials on the basis of the audibility of a pitch shift. One might infer from this that pitch shifts were not easily heard on ''close'' trials. However, such a conclusion would be inconsistent with the listeners' introspective reports. From these reports, it appears instead that a pitch shift was, to some extent, liable to be heard on any type of trial—even a ''present'' trial. The fact that d' was lower in the present/close condition than in the up/down condition of experiment 1 is not, *per se*, surprising insofar as, in the present/close condition, the directions of the pitch shifts heard were not valid cues. In the absence of valid directional cues, the listeners had to base their judgments only on the salience and/or the magnitude of the pitch shifts heard.

IV. EXPERIMENT 3

If, in the present/absent condition, performance was poor owing to a difficulty to use an adequate response criterion and not because the chords' components were hard to hear out individually, then performance should be poor not only when T follows the chord but also when T precedes the chord. By contrast, it could be expected that presenting T before the chord rather than after it would increase performance by improving the audibility of T within the chord on ''present'' trials. This rationale led us to perform a short experiment testing listeners in two variants of the present/absent condition: a ''chord-T'' variant, replicating what had been done in experiments 1 and 2, and a ''T-chord'' variant in which T preceded the chord instead of following it. In both variants, there was a 500-ms ISI between the chord and T. For each subject, in the experiment proper, eight blocks of 50 trials were run in each of the two variants, alternating from block to block. The four listeners who acted as subjects had previously participated in experiment 1; two of them were the authors. Before the experiment proper, each listener received some training in the T-chord variant.

The results are displayed in Fig. 4. For three listeners, d' was much higher in the T-chord variant than in the chord-T variant; the fourth listener (S) performed at the chance level in the two variants.[2] Overall, these data confirm the view that, in the present/absent condition of experiments 1 and 2, performance was limited by an informational masking effect rather than by a difficulty to use an adequate response criterion. For at least some listeners, the informational masking of T within the chord can be efficiently opposed by presenting T before the chord rather than after it. The source of this benefit is presumably a focusing of the listener's attention on the appropriate spectral region of the chord during the chord presentation.

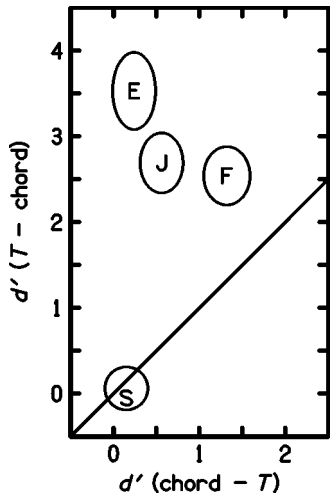

FIG. 4. Results of experiment 3, in the same format as Fig. 2.

V. EXPERIMENT 4

This final experiment was an extension of experiment 1. Its aim was to determine if the up/down condition remains easier than the present/absent condition when the ISI separating T from the chord is made much longer than the 500-ms ISI used in experiment 1. A positive answer was expected because preliminary listening sessions revealed that the 1-semitone frequency shifts occurring in the up/down condition were still liable to evoke sensations of pitch shift for an ISI of a few seconds.

Four listeners served as subjects. Two of them were the authors, and all of them had previously served as subjects in experiment 1. Each listener was at first tested only in the up/down condition, using ISIs of 0.5, 1, 2, 4, and 8 s. Each of these ISIs was used in a single block of 50 trials per session, until 400 trials had been run for every ISI; the order in which the ISIs were used was counterbalanced across sessions. Then, two final sessions included a total of 400 trials in the present/absent condition with an ISI fixed at 4 s.

Figure 5 shows the results. In the up/down condition, as the ISI increased, d' decreased with a negative acceleration. When the ISI was 4 s, d' was still well above 0 in this condition; its average value was 0.94. For the same ISI, in the present/absent condition, d' was definitely lower; its average value was 0.33.

These data call for comments relating to a hypothesis put forth by van Noorden (1975; see also Anstis and Saida, 1985) on the perception of pitch shifts between successive

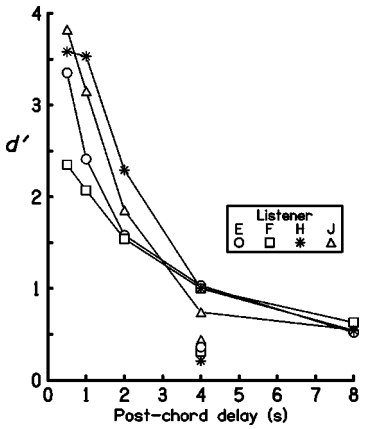

FIG. 5. Results of experiment 4: d' values measured in the up/down condition (symbols connected by lines) and the present/absent condition (nonconnected symbols), as a function of the silent interval separating the chord from T.

tones. van Noorden argued that such shifts are perceived in the same way as discontinuous displacements of visual objects. In the visual domain, a discontinuous displacement is able to evoke a sensation of motion, called ''phi'' motion, when the ISI amounts to 100–300 ms, but not when the ISI is much longer. Likewise, according to van Noorden, a pair of successive tones with different frequencies can evoke a sensation of ''pitch motion'' when the ISI is, e.g., 200 ms, but not when the ISI is much longer. If this idea is correct, then the present data imply that the mechanism underlying listeners' good performance in the up/down condition is independent of the neural processing of rapid frequency shifts. However, van Noorden's hypothesis may be wrong. To the best of our knowledge, whereas there are objective psychophysical data (i.e., measures of performance) supporting the distinction between percepts of ''succession with motion'' and ''succession without motion'' in the visual domain (Palmer, 1986), this is not the case in the domain of pitch.

VI. GENERAL DISCUSSION

A. Summary of the findings

For at least some fraction of human listeners,[3] it is possible to identify the direction of a discrete frequency shift in an informational masking context preventing a conscious perception of the initial frequency. This was demonstrated using sound sequences consisting of a random chord of pure tones followed by a single pure tone. When the single tone was positioned slightly above or below a randomly selected component of the chord, a pitch shift in the corresponding direction could be heard by 11 listeners. The position of the single tone relative to the closest component of the chord could be reliably identified even when the chord and the single tone were separated by a silent ISI of a few seconds. However, for most of the tested listeners, it was very difficult to discriminate between sequences in which the single tone was respectively identical to one component of the chord or halfway in frequency between two components. The pattern of listeners' performances in the three discrimination tasks employed was very different from the pattern expected from an ideal ''analytic'' discriminator, hearing out the individual components of the chords. Moreover, the listeners' pattern of performance could not be produced either by a nonideal analytic discriminator, hearing out the individual components of the chords but using a defective response criterion.

B. A schematic model of frequency-shift detectors

Our results can be understood by assuming the existence, in the human auditory system, of automatic ''frequency-shift detectors'' playing a role in the binding of successive sounds and sensitive to memory traces left in some primitive ''echoic store'' (Kubovy and Howard, 1976). More specifically, we hypothesize that these detectors have the following properties: (i) some of them are activated only by upward frequency shifts, while others are activated only by downward shifts; (ii) within each subset, the detectors' response is stronger for small shifts than for large shifts, but some minimum magnitude of shift is required to elicit a response; (iii) when detectors of upward shifts and downward shifts are simultaneously activated—this was presumably the case in our experiments—the dominantly perceived shift is in the direction preferred by the subset of detectors with the stronger activation. According to the corresponding model, performance in our up/down condition ought to be relatively good because ''up'' and ''down'' trials dominantly activated different subsets of shift detectors. By contrast, on ''present'' trials as well as on ''absent'' trials, the two subsets of detectors were in theory activated with approximately the same strength, which explains why it was more difficult to discriminate between these two types of trial. Finally, regarding the present/close condition, the model implies that one subset of detectors tended to be more strongly activated than the other subset on ''close'' trials, whereas this was less true on ''present'' trials; thus, performance in this condition ought to be better than in the present/absent condition, but still poorer than in the up/down condition.

It should be noted that the three hypotheses presented above tally with those proposed by Allik *et al.* (1989) in order to account for data concerning the perception of complex sequences of chords.[4] A more precise and quantitative model is certainly desirable, but probably premature at present. Further psychophysical studies are needed to this aim.

C. Physiological considerations

In the visual cortex of mammals, continuous motions of objects are detected by direction-selective neurons. In the auditory cortex, similarly, certain neurons selectively respond to either upward or downward frequency glides (Whitfield and Evans, 1965; Zhang *et al.*, 2003). It has been hypothesized that, in humans, such neurons govern the perceptual experience of rapid and continuous frequency modulations (Gardner and Wilson, 1979; Tansley and Regan, 1979; Wilson *et al.*, 1994; Shu *et al.*, 1993), and also play a role in the perception of successive steady tones separated by a short ISI (van Noorden, 1975; Okada and Kashino, 2003). At present, however, both of these points remain speculative (Wakefield and Viemeister, 1984; Moody *et al.*, 1984). Whereas several studies showed that the responses of indi-

vidual visual neurons to motion provide information which determines the subject's ability to identify behaviorally the direction of motion (e.g., Ditterich *et al.*, 2003), analogous demonstrations have not been reported in the auditory domain. According to Weinberger and McKenna (1988) and McKenna *et al.* (1989), the response of a single cortical neuron to a given tone preceded by a higher- or lower-frequency tone can depend on the direction of the shift even if the two tones are separated by more than 500 ms; but, the corresponding evidence is limited. At least for ISIs exceeding 500 ms, it is possibly erroneous to search for a physiological substratum of the perceptual sensitivity to frequency shifts in the discharge rates of individual neurons. This substratum might in fact lie in the cross correlations of separate neurons' responses, as suggested by Espinosa and Gerstein (1988). In other words, the shift detectors might not be reducible to single neurons and consist instead of neuronal assemblies.

Functional imaging (fMRI) studies have recently indicated that, in humans, the cerebral activity induced by melodies differs from that induced by repetitions of a single tone (Griffiths *et al.*, 2001; Patterson *et al.*, 2002; Warren *et al.*, 2003) or by sequences of sounds with changing spatial locations (Warren and Griffiths, 2003). However, these studies suggest that melodies engage specific neural processes only beyond the primary auditory cortex. More precisely, on the basis of both functional imaging data (Patterson *et al.*, 2002) and behavioral data relating to the consequences of brain lesions on pitch perception (Johnsrude *et al.*, 2000), it has been surmised that the lateral part of Heschl's gyrus, in the right hemisphere, is crucially involved in the perception of frequency shifts. The special sound sequences used in the present investigation could be profitably reemployed in future imaging and lesion studies: they seem to be particularly appropriate tools for the localization of brain structures responsible for the sensitivity to frequency shift *per se*.

We argue here that the human auditory system is equipped with automatic detectors of frequency shifts. From a more general point of view, the idea that modifications in a sound can be detected automatically within the auditory system has already been supported by a large amount of research concerning an event-related brain potential termed ''mismatch negativity'' or MMN (Näätänen and Winkler, 1999; Schröger, 1997). This brain potential, elicited by any type of acoustic novelty or ''deviance'' in a sound sequence, is observable when the subject does not pay attention to the sequence. However, Cowan *et al.* (1993) reported that no MMN can be elicited by a sequence of only two sounds, which would imply that the change-detection process reflected by the MMN differs from the one investigated here. Recently, Jääskeläinen *et al.* (2004) claimed that a sequence of only two sounds is actually able to elicit an MMN. According to these authors, and also May *et al.* (1999), the MMN does not originate from a neural structure responding to auditory change *per se*, contrary to a commonly held idea; instead, it is produced by the neural population responding to the deviant stimulus itself and is due to transient adaptation of feature-specific neurons. Note that a change detector based on adaptation phenomena should logically lead its possessor to be more successful in our present/absent condition than in our up/down condition, whereas the opposite is true for real listeners. Thus, the thesis advocated by Jääskeläinen *et al.* and May *et al.* would still imply that the change-detection mechanism reflected by the MMN differs from the one investigated here.

D. Change detection and scene analysis

The change-detection mechanism investigated here appears to be more primitive than the one reflected by the MMN. An MMN originates from the processing of high-level sound representations which are quite similar to the conscious percepts evoked by the stimuli. Indeed, it has been shown that the MMN is sensitive to the perceptual fission of rapid melodic sequences into separate and concomitant sound streams (Sussman *et al.*, 1999), to the auditory continuity illusion (Micheyl *et al.*, 2003), to a change in the virtual pitch of complex tones with randomly varying spectral contents (Winkler *et al.*, 1995), and even to the listener's linguistic background (Näätänen *et al.*, 1997). In our up/down condition, by contrast, the *T* tone was put in relation with a tone which could not be consciously perceived because it was grouped with synchronous tones producing an informational masking effect. A representation of the masked tone's frequency existed at the cochlear level and certainly beyond in the auditory pathway. However, there was no representation of this specific frequency in the outcome of auditory scene analysis since the corresponding pitch could not be heard.

It would be unwarranted to infer from the latter point that the perceptual phenomenon described here is unrelated to auditory scene analysis. On the contrary, we suppose that the auditory system makes use of automatic frequency-shift detectors in the global scene analysis process. They are probably useful for the creation of links between temporally separate acoustic events which differ from each other in spectral content, but were nonetheless produced by one and the same sound source and should thus be integrated into a common perceptual stream.

ACKNOWLEDGMENTS

The authors thank R.P. Carlyon, A. de Cheveigné, J.M. Edeline, C. Lorenzi, D. Pressnitzer, C. Semal, N. Versfeld, and especially A. Gorea and C. Micheyl for helpful discussions or comments on the manuscript. This work was supported by a grant from the CNRS (Programme Interdisciplinaire ''Cognition et Traitement de l'Information'').

[1]This random melody not only served as a warning signal: It was also intended to ''erase'' the memory trace of the *T* tone used on the previous trial. Without the melody, in the up/down condition, a given *T* tone was liable to be mistakenly compared with the previous *T* tone rather than with a component of the chord. Informal pilot studies suggested to us that such confusions were indeed easily made. In contrast, when each trial began with a random melody, we felt that the *T* tone was not liable to be mistakenly compared with the last component tone of the melody, because all the component tones of the melody were perceptually grouped into a separate entity. This was not formally checked, however. The ideal procedure would be to replace the melody by a visual warning signal and to insert a very long silent interval between consecutive trials in order to minimize the disrupting effect of irrelevant memory traces.

[2]In the chord-*T* variant, Listener E was significantly less successful here than during experiments 1 and 2. By contrast, F and J were slightly more successful than before. In view of these changes in performance, it is worthy to note that experiment 3 was conducted 1 year after experiment 2 (and actually after the experiment numbered 4 in the present paper).

[3]It was mentioned in Sec. II A that three volunteers for experiment 1 were eventually dismissed because they did not succeed at all in either condition. These listeners might have been more successful in the up/down condition after a longer, and/or different, training phase. However, the converse is also true: Some normal-hearing people may be completely unable to experience the perceptual phenomenon permitting success in the up/down condition. In this respect, the influence of musical education is still unclear. The three listeners that we had to dismiss were not more impervious to music than those who provided the data. Indeed, one of them was a professional orchestra conductor.

[4]In the experiments of Allik *et al.* (1989), the subjects' task was to identify the direction of pitch motion in stochastic sequences of chords made up of either pure or complex tones (with frequency ratios which were generally much smaller than those employed in the present research). The results were accounted for by a ''dipole contribution model.'' This model is not directly usable here but it is based on assumptions similar to those we make. Essentially, Allik *et al.* argued that the perceived direction of pitch motion was determined by the sum of the contributions of direction-sensitive dipoles consisting of pairs of consecutive tones *close in pitch*.

Allik, J., Dzhafarov, E.N., Houtsma, A.J.M., Ross, J., and Versfeld, H.J. (**1989**). ''Pitch motion with random chord sequences,'' Percept. Psychophys. **46**, 513–527.

Anstis, S., and Saida, S. (**1985**). ''Adaptation to auditory streaming of frequency-modulated tones,'' J. Exp. Psychol. Hum. Percept. Perform. **11**, 257–271.

Attneave, F., and Olson, R.K. (**1971**). ''Pitch as a medium: A new approach to psychophysical scaling,'' Am. J. Psychol. **84**, 147–166.

Bilsen, F.A. (**2001**). ''The case of the missing central spectra,'' in *Physiological and Psychophysical Bases of Auditory Function*, edited by D.J. Breebart, A.J.M. Houtsma, A. Kohlrausch, V.F. Prijs, and R. Schoonoven (Shaker, Maastricht, The Netherlands), pp. 145–152.

Bregman, A.S. (**1990**). *Auditory Scene Analysis* (MIT Press, Cambridge, MA).

Brosch, M., and Schreiner, C.E. (**1997**). ''Time course of forward masking tuning curves in cat primary auditory cortex,'' J. Neurophysiol. **77**, 923–943.

Brosch, M., and Schreiner, C.E. (**2000**). ''Sequence sensitivity of neurons in cat primary auditory cortex,'' Cereb. Cortex **10**, 1155–1167.

Clément, S. (**2001**). ''La mémoire auditive humaine : Psychophysique et neuroimagerie fonctionnelle,'' Ph.D. dissertation (Université Victor Segalen, Bordeaux, France).

Clément, S., Demany, L., and Semal, C. (**1999**). ''Memory for pitch versus memory for loudness,'' J. Acoust. Soc. Am. **106**, 2805–2811.

Cowan, N., Winkler, I., Teder, W., and Näätänen, R. (**1993**). ''Memory prerequisites of mismatch negativity in the auditory event-related potential (ERP),'' J. Exp. Psychol. Learn. Mem. Cogn. **19**, 909–921.

Davis, H., Silverman, S.R., and McAuliffe, D.R. (**1951**). ''Some observations on pitch and frequency,'' J. Acoust. Soc. Am. **23**, 40–42.

Demany, L., Clément, S., and Semal, C. (**2001**). ''Does auditory memory depend on attention?,'' in *Physiological and Psychophysical Bases of Auditory Function*, edited by D.J. Breebart, A.J.M. Houtsma, A. Kohlrausch, V.F. Prijs, and R. Schoonoven (Shaker, Maastricht, The Netherlands), pp. 461–467.

Demany, L., Montandon, G., and Semal, C. (**2004**). ''Pitch perception and retention: two cumulative benefits of selective attention,'' Percept. Psychophys. **66**, 609–617.

Deutsch, D. (**1969**). ''Music recognition,'' Psychol. Rev. **76**, 300–307.

Ditterich, J., Mazurek, M.E., and Shadlen, M.N. (**2003**). ''Microstimulation of visual cortex affects the speed of perceptual decisions,'' Nat. Neurosci. **6**, 891–898.

Divenyi, P.L., and Hirsh, I.J. (**1978**). ''Some figural properties of auditory patterns,'' J. Acoust. Soc. Am. **64**, 1369–1385.

Espinosa, I.E., and Gerstein, G.L. (**1988**). ''Cortical auditory neuron interactions during presentation of 3-tone sequences: Effective connectivity,'' Brain Res. **450**, 39–50.

Gardner, R.B., and Wilson, J.P. (**1979**). ''Evidence for direction-specific channels in the processing of frequency modulation,'' J. Acoust. Soc. Am. **66**, 704–709.

Green, D.M., and Swets, J.A. (**1974**). *Signal Detection Theory and Psychophysics* (Krieger, New York).

Griffiths, T.D., Uppenkamp, S., Johnsrude, I.S., Josephs, O., and Patterson, R.D. (**2001**). ''Encoding of the temporal regularity of sound in the human brainstem,'' Nat. Neurosci. **4**, 633–637.

Jääskeläinen, I.P., Ahveninen, J., Bonmassar, G., Dale, A.M., Ilmoniemi, R.J., Levänen, S., Lin, F.H., May, P., Melcher, J., Stufflebeam, S., Tiitinen, H., and Belliveau, J.W. (**2004**). ''Human posterior auditory cortex gates novel sounds to consciousness,'' Proc. Natl. Acad. Sci. U.S.A. **101**, 6809–6814.

Johnsrude, I.S., Penhune, V.B., and Zatorre, R.J. (**2000**). ''Functional specificity in the right human auditory cortex for perceiving pitch direction,'' Brain **123**, 155–163.

Kidd, G., Mason, C.R., Deliwala, P.S., Woods, W.S., and Colburn, H.S. (**1994**). ''Reducing informational masking by sound segregation,'' J. Acoust. Soc. Am. **95**, 3475–3480.

Kubovy, M., and Howard, F.P. (**1976**). ''Persistence of a pitch-segregating echoic memory,'' J. Exp. Psychol. Hum. Percept. Perform. **2**, 531–537.

Macmillan, N.A., and Creelman, C.D. (**1991**). *Detection Theory: A User's Guide* (Cambridge University Press, Cambridge, MA).

May, P., Tiitinen, H., Ilmoniemi, R.J., Nyman, G., Taylor, J.G., and Näätänen, R. (**1999**). ''Frequency change detection in human auditory cortex,'' J. Comput. Neurosci. **6**, 99–120.

McFarland, D.J., and Cacace, A.T. (**1992**). ''Aspects of short-term acoustic recognition memory: Modality and serial position effects,'' Audiology **31**, 342–352.

McKenna, T.M., Weinberger, N.M., and Diamond, D.M. (**1989**). ''Responses of single auditory cortical neurons to tone sequences,'' Brain Res. **481**, 142–153.

Micheyl, C., Carlyon, R.P., Shtyrov, Y., Hauk, O., Dodson, T., and Pullvermüller, F. (**2003**). ''The neurophysiological basis of the auditory continuity illusion: A mismatch negativity study,'' J. Cogn Neurosci. **15**, 747–758.

Moody, D.B., Cole, D., Davidson, L.M., and Stebbins, W.C. (**1984**). ''Evidence for a reappraisal of the psychophysical selective adaptation paradigm,'' J. Acoust. Soc. Am. **76**, 1076–1079.

Moore, B.C.J., and Ohgushi, K. (**1993**). ''Audibility of partials in inharmonic complex tones,'' J. Acoust. Soc. Am. **93**, 452–461.

Näätänen, R., Lehtokoski, A., Lennes, M., Cheour-Luhtanen, M., Huotilainen, M., Iivonen, A., Vainio, M., Alku, P., Ilmoniemi, R.J., Luuk, A., Allik, J., Sinkkonen, J., and Alho, K. (**1997**). ''Language-specific phoneme representations revealed by electric and magnetic brain responses,'' Nature (London) **385**, 432–434.

Näätänen, R., and Winkler, I. (**1999**). ''The concept of auditory stimulus representation in cognitive neuroscience,'' Psychol. Bull. **125**, 826–859.

Neff, D.L., and Green, D.M. (**1987**). ''Masking produced by spectral uncertainty with multicomponent maskers,'' Percept. Psychophys. **41**, 409–415.

Okada, M., and Kashino, M. (**2003**). ''The role of spectral change detectors in temporal order judgment of tones,'' NeuroReport **14**, 261–264.

Palmer, J. (**1986**). ''Mechanisms of displacement discrimination with and without perceived movement,'' J. Exp. Psychol. Hum. Percept. Perform. **12**, 411–421.

Patterson, R.D., Uppenkamp, S., Johnsrude, I.S., and Griffiths, T.D. (**2002**). ''The processing of temporal pitch and melody information in auditory cortex,'' Neuron **36**, 767–776.

Plomp, R. (**1964**). ''The ear as a frequency analyzer,'' J. Acoust. Soc. Am. **36**, 1628–1636.

Schröger, E. (**1997**). ''On the detection of auditory deviations: a preattentive activation model,'' Psychophysiology **34**, 245–257.

Shera, C.A., Guinan, J.J., and Oxenham, A.J. (**2002**). ''Revised estimates of human cochlear tuning from otoacoustic and behavioral measurements,'' Proc. Natl. Acad. Sci. U.S.A. **99**, 3318–3323.

Shu, Z.J., Swindale, N.V., and Cynader, M.S. (**1993**). ''Spectral motion produces an auditory after-effect,'' Nature (London) **364**, 721–723.

Sussman, E., Ritter, W., and Vaughan, H.G. (**1999**). ''An investigation of the auditory streaming effect using event-related brain potentials,'' Psychophysiology **36**, 22–34.

Tansley, B.W., and Regan, D. (**1979**). ''Separate auditory channels for unidirectional frequency modulation and unidirectional amplitude modulation,'' Sens Processes **3**, 132–140.

Terhardt, E. (**1970**). ''Oktavspreizung und Tonhöhenverschiebung bei Sinustönen,'' Acustica **22**, 345–351.

van Noorden, L.P.A.S. (**1975**). ''Temporal coherence in the perception of tone sequences,'' Ph.D. dissertation (Technische Hogeschool, Eindhoven, The Netherlands).

Wakefield, G.H., and Viemeister, N.F. (**1984**). ''Selective adaptation to linear frequency-modulated sweeps: Evidence for direction-specific FM channels?,'' J. Acoust. Soc. Am. **75**, 1588–1592.
Ward, W.D., and Burns, E.M. (**1982**). ''Absolute pitch,'' in *The Psychology of Music*, edited by D. Deutsch (Academic, New York), pp. 431–451.
Warren, J.D., and Griffiths, T.D. (**2003**). ''Distinct mechanisms for processing spatial sequences and pitch sequences in the human auditory brain,'' J. Neurosci. **23**, 5799–5804.
Warren, J.D., Uppenkamp, S., Patterson, R.D., and Griffiths, T.D. (**2003**). ''Separating pitch chroma and pitch height in the human brain,'' Proc. Natl. Acad. Sci. U.S.A. **100**, 10038–10042.
Weinberger, N.M., and McKenna, T.M. (**1988**). ''Sensitivity of single neurons in auditory cortex to contour: Toward a neurophysiology of music perception,'' Music Percept. **5**, 355–390.
Whitfield, I.C., and Evans, E.F. (**1965**). ''Responses of auditory cortical neurons to stimuli of changing frequency,'' J. Neurophysiol. **28**, 655–672.
Wilson, J.P., Frost, D., and Wilkes, G.D. (**1994**). ''Adaptation to unidirectional sweeping spectral peaks,'' in *Advances in Hearing Research*, edited by G.A. Manley, G.M. Klump, C. Koppl, H. Fastl, and H. Oeckinghaus (World Scientific, Singapore), pp. 452–461.
Winkler, I., Tervaniemi, M., Huotilainen, M., Ilmoniemi, R., Ahonen, A., Salonen, O., Standertskjöld-Nordenstam, C.G., and Näätänen, R. (**1995**). ''From objective to subjective: Pitch representation in the human auditory cortex,'' NeuroReport **6**, 2317–2320.
Zhang, L.I., Tan, A.Y.Y., Schreiner, C.E., and Merzenich, M.M. (**2003**). ''Topography and synaptic shaping of direction selectivity in primary auditory cortex,'' Nature (London) **424**, 201–205.

The role of visual speech cues in reducing energetic and informational masking

Karen S. Helfer and Richard L. Freyman
Department of Communication Disorders, University of Massachusetts, Arnold House, Amherst, Massachusetts 01003

(Received 16 June 2004; revised 26 October 2004; accepted 2 November 2004)

Two experiments compared the effect of supplying visual speech information (e.g., lipreading cues) on the ability to hear one female talker's voice in the presence of steady-state noise or a masking complex consisting of two other female voices. In the first experiment intelligibility of sentences was measured in the presence of the two types of maskers with and without perceived spatial separation of target and masker. The second study tested detection of sentences in the same experimental conditions. Results showed that visual cues provided more benefit for both recognition and detection of speech when the masker consisted of other voices (versus steady-state noise). Moreover, visual cues provided greater benefit when the target speech and masker were spatially coincident versus when they appeared to arise from different spatial locations. The data obtained here are consistent with the hypothesis that lipreading cues help to segregate a target voice from competing voices, in addition to the established benefit of supplementing masked phonetic information. © *2005 Acoustical Society of America.* [DOI: 10.1121/1.1836832]

PACS numbers: 43.66.Pn, 43.66.Dc, 43.66.Qp, 43.71.Gv [GDK] Pages: 842–849

I. INTRODUCTION

People often converse in environments with more than one person talking simultaneously. In this type of listening situation an individual must focus on a target talker's message while ignoring the distracting speech of other people. In such situations listening can be easier than in steady-state noise because gaps in the masking signal produce silent intervals in which portions of the target message will be audible (e.g., Bronkhorst and Plomp, 1992; Takahashi and Bacon, 1992). However, under some circumstances listening in the presence of competing talkers actually can be more difficult than with a steady-state masking noise of equivalent energy. The excess masking that is produced by speech (above and beyond the masking from a steady-state noise of the same energy) has been referred to as perceptual masking (Carhart *et al.*, 1969) or informational masking (Freyman *et al.*, 1999, 2001, 2004; Brungart, 2001; Arbogast *et al.*, 2002). Informational masking in speech recognition appears to be due to both target/masker uncertainty and similarity of target and masker along several (as yet largely unspecified) dimensions. This is in contrast to energetic masking, which occurs when a signal is inaudible in the presence of noise because the peripheral neural elements that would normally encode the signal are responding to the masker.

Masking in a competing speech situation is reduced when the target source is in a different location from the maskers. Traditionally, reduction in masking from separation of a target from a masking signal has been attributed to binaural interaction in the low frequencies and head shadow in the high frequencies (e.g., Zurek, 1993). These spatial advantages often are reduced in real rooms because of the presence of reflections (e.g., Hirsh, 1950; MacKeith and Coles, 1971; Plomp, 1976) leading to reduction in spatial release from energetic masking. Nevertheless, in tasks where it is assumed that there is a great deal of informational masking spatial separation is still effective, even in the presence of single simulated reflections (Freyman *et al.*, 1999, 2001, 2004), or actual reverberation (Kidd *et al.*, submitted). In reverberant environments the benefit from spatial separation may be due to the fact that the target and masker are perceived in different locations because of the precedence effect. Perceived separation of target and speech masker may reduce informational masking because it helps the listener to focus on the target voice in the presence of the masking voice(s). The apparent spatial separation does not improve performance when the masker consists of steady-state noise or noise modulated with the envelope of a speech signal (Freyman *et al.*, 2001).

In this paper we theorize that individuals may also use visual cues from the target talker to reduce informational masking. It is clear that lipreading improves speech recognition in adverse listening conditions by providing supplementary phonetic information missing in the auditory signal. For example, place-of-articulation cues (which are easily masked by noise) can be conveyed quite accurately via lipreading (e.g., Sumby and Pollack, 1954). This supplementation is likely to occur whether the target speech is presented in a background of steady noise or within a complex mixture of voices. However, in the latter case we propose that visual cues play an additional important role: helping to overcome informational masking. A major component of informational masking in speech recognition is confusability of the target voice with the masking voice(s). Lipreading cues (which are synchronized with the target auditory signal) may help the listener to pull the target message out of a complex mixture and maintain attention on the talker's voice.

The studies described in this paper were designed to compare how beneficial visual speech cues are in situations in which the target speech is masked by other speech versus

by steady-state noise. Several previous studies have found visual cues to be beneficial in speech-on-speech masking tasks (Reisberg, 1978; Summerfield, 1979; Vitkovitch and Barber, 1994; Spence *et al.*, 2000; Rudmann *et al.*, 2003). However, it is not known how the degree of visual benefit found for speech maskers compares with that obtained in the presence of steady-state noise. Lipreading should help supplement masked phonetic information in the presence of either of these types of maskers, although the nature of that supplementation may differ. We propose that visual cues will provide greater benefit in a speech-masking situation known to produce informational masking than when the masker is steady-state noise. Moreover, we anticipate that visual cues will be most beneficial when the target and masker are spatially coincident, and less helpful when they are perceived to emanate from different spatial locations (and therefore are less confusable).

II. EXPERIMENT 1: SPEECH RECOGNITION IN STEADY-STATE NOISE VERSUS IN A SPEECH MASKER

A. Method

1. Stimuli

The target stimuli for this study consisted of lists of syntactically simple sentences aggregated by topic. Sentences were developed under 12 topics (clothing/jewelry, food, animals, hobbies/arts/entertainment, health, crime/law, furniture/house/cleaning, gardening/farming/weather, money, sports, school/learning, and travel). Two sets of 15 sentences were generated under each topic, with each sentence having three key words (underlined in the following example) used for scoring. For example, the sentence, ''I wish that hood had some fur'' was included in the clothing/jewelry category.

The sentence lists were videotaped in a double-walled audiometric sound room (IAC #1604) measuring 2.76 $\times$2.55 m. A Sylvania VKC 242 video camera was used to record an adult female with no discernible regional dialect speaking the target sentences. The video camera was adjusted to produce a life-sized facial image on a 19 in. television screen. A Shure 560 microphone placed below the talker's mouth (so as not to block lipreading cues) picked up the audio portion of the stimuli. The talker viewed a VU meter to help monitor her vocal intensity. She was instructed to speak in a conversational manner but to keep her vocal level constant throughout each sentence. The stimuli were recorded onto analog videotape with an interval of approximately 7 s between sentences.

Two types of maskers were used in this study. The first masker consisted of the voices of two other female talkers reciting sentences unrelated to any of the topics used in the target sentences. A two-talker masker was chosen because it has been shown to produce a robust effect of perceived spatial separation between target and masker (Freyman *et al.*, 1999, 2001, 2004). The masking sentences were recorded with the same apparatus and procedure used to generate the target stimuli, although only the audio portion of the signal was used in the present experiment. The analog output of the video recorder was low-pass filtered at 8.5 kHz, sampled at 22.05 kHz using a 16-bit analog-to-digital converter (TDT AD1), and stored on a computer hard drive. Masking sentences from each of the two talkers were concatenated with pauses between sentences eliminated. The two masking files (one from each talker) were equalized in rms level and then combined to produce a 56-s loop of the two-talker masker complex. A steady-state noise masker was created by shaping white noise by the long-term average spectrum of the two-talker masker. Two-channel versions of both the two-talker complex and the noise masker were generated with one channel delayed by 4 ms relative to the other channel.

2. Experimental conditions

Data were collected in the double-walled IAC chamber described above. The reverberation time in this chamber was between 0.12 s (at 6300 and 8000 Hz) and 0.24 s (at 125 Hz). Calibration was performed periodically using a sound-level meter with the microphone placed at the position of the subject's head. The target speech sentences were calibrated using a standard phrase played from the videotaped stimuli. The maskers were calibrated using the speech-shaped noise masker which had been equated in rms amplitude to the two-talker masker. Postrecording analysis of the peak levels of individual target sentences found a $\pm$3-dB range between the 20th and 80th percentiles.

Each subject received all possible combinations of two loudspeaker conditions, three S/N ratios, two types of maskers, and auditory-only (A-only) versus auditory-visual (AV) presentation. In one type of condition (F-F) both the target speech and the masker emanated from a 4 in. RCA loudspeaker directly in front of the subject. The loudspeaker was placed on top of a television monitor and was at a height of 1.24 m from the floor and a distance of 1.37 m from the subject. In the second condition (F-RF) the target speech was presented from the front loudspeaker only while the masker was presented simultaneously from the front and from a loudspeaker placed 60 deg to the right of the subject's head, at the same distance and height as the front speaker. The maskers were presented with the delayed channel from the front loudspeaker and the nondelayed channel from the right loudspeaker. Due to the precedence effect, the masker was perceived to be located near the right loudspeaker, well separated from the target.

The target speech signal was routed from the audio output of a videotape player (Mitsubishi U61) to a programmable attenuator (TDT PA4) and then to a mixer (TDT SM3). The two-channel masker was sent from a computer's sound card to separate programmable attenuators. One channel of this competition was mixed with the speech target (TDT SM3), routed through a headphone buffer (TDT HB5), amplified (TOA P75D), and then delivered to the front loudspeaker. The other channel was fed from the programmable attenuator through the headphone buffer to the amplifier and was then routed to the right loudspeaker.

The precise S/N ratios, which were determined via pilot listening, varied with experimental conditions, with the target speech presented at 50 dBA (*re*: speech peaks) in all conditions. For A-only presentation, data were collected at -8, -4, and 0 dB S/N. The S/N ratios for the AV mode were

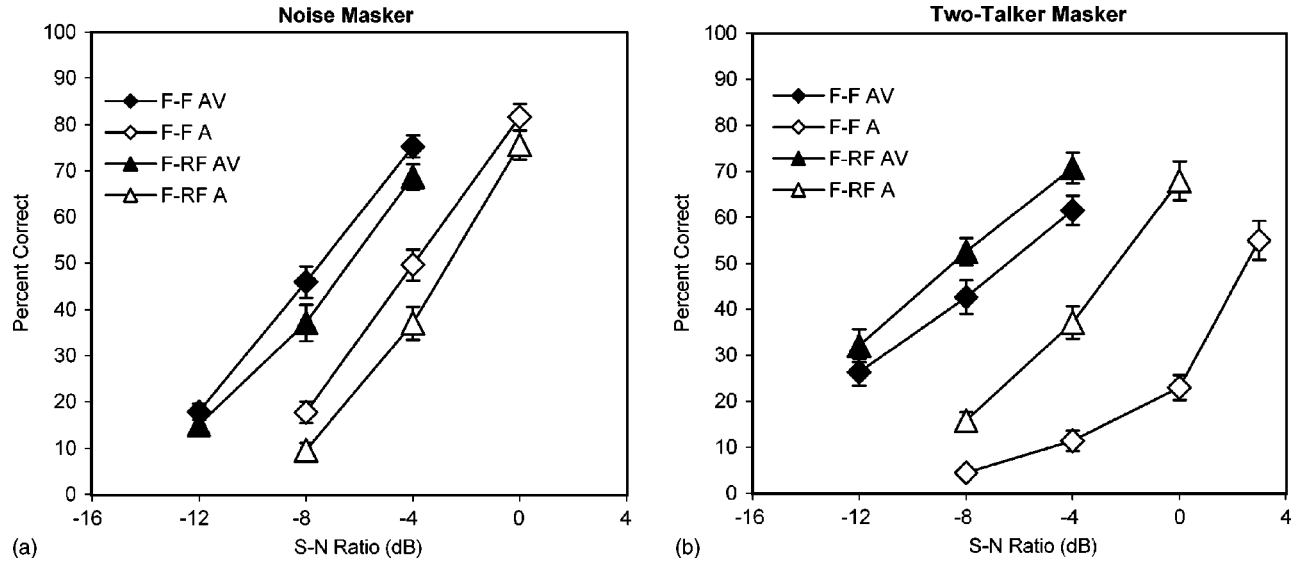

FIG. 1. Mean percent-correct recognition of words in steady-state noise (left panel) and in two-talker competition (right panel) as a function of S/N ratio, spatial condition (F-F versus F-RF), and presentation condition (auditory-only: A or auditory-visual: AV). Error bars represent the standard error.

−12, −8, and −4 dB. Data also were collected at +3-dB S/N for the F-F condition with the speech masker because performance was very poor at less advantageous S/N ratios. This necessitated the repetition of one stimulus list, as there were 25 conditions and only 24 lists available. The repeated list varied by subject and was always the one used for the most difficult condition with the noise masker (F-F, A-only, −8-dB S/N ratio) where the mean performance was 8% correct recognition. This condition's list was chosen to minimize the possibility that subjects would recognize a word that had previously been presented.

3. Procedures

A within-subjects Latin-square design was used in the present study in order to minimize the effect of list differences. Each subject was presented with all 24 topic-based sentence lists once in random order, with a different list for each condition. The assignment of lists to conditions was different for each subject so that, across the entire data set, all 360 sentences were presented in each condition. Each subject also listened to one repeated list (in the +3-S/N F-F speech-masker condition) as described above.

An experimenter sat in the sound-treated room with the subject in order to control the timing of the experiment and to score the subject's responses. During the experiment the videotape of the target stimuli was presented continuously. An investigator controlled the presentation of the masker by gating it on in the range of 1–3 s prior to each target sentence, varying the precise interval at random. The masker was gated off after the end of each target utterance, at which time the subject responded by repeating as much of this sentence as possible.

Twenty-four college-aged adults participated in this study. Each subject passed a pure-tone threshold screening at 15 dB HL (*re*: ANSI, 1996) in each ear. A brief practice session was completed during which subjects were given experience responding to the stimuli in each experimental condition at one S/N ratio. Subjects were informed of the topic (with both oral and orthographic cues) before each list and were instructed to use this information to try to differentiate the target talker from the masking talkers. During auditory-only presentation the subject's eyes were covered with a blindfold. Data for each of the 24 subjects were collected in one session lasting approximately 1.5 h.

B. Results

1. Group psychometric functions

Results for the noise-masking conditions and the two-talker speech masking conditions are shown in panels (a) and (b) of Fig. 1, respectively. Each data point represents the percent-correct recognition of 1080 key words (360 sentences × 3 key words/sentence) across 24 subjects. In steady-state noise, perception in the F-F condition was slightly better than in the F-RF condition for both A-only and AV presentations. Most likely this was a consequence of the increase in masking energy in the latter situation from the addition of the masking signal from the right loudspeaker. This result is consistent with our analysis of this slight energetic masking effect reported in Freyman *et al.* (1999). Overall, our data show that perception of the masking noise near the right loudspeaker and well-separated from the target does not improve recognition relative to when the target and masker are spatially coincident.

With speech maskers, performance in the F-RF condition was better than in the F-F condition. Unlike the noise-masking data shown in panel (a) of Fig. 1, where the triangles (F-RF) are below the diamonds (F-F), the reverse is true for speech maskers [panel (b)]. This effect is especially apparent in the A-only condition (open symbols). The improvement in the F-RF condition relative to performance in the F-F condition is consistent with previous results from this lab (Freyman *et al.*, 1999, 2001, 2004) and is assumed to be due to release from informational masking produced by perceived spatial separation. The shallower slopes evident in the

TABLE I. S/N ratios for 50%-correct recognition of keys words in sentences for conditions with (F-RF) and without (F-F) apparent spatial separation in the presence of two types of maskers (noise and speech).

Condition	S/N ratio in dB for 50%-correct recognition
Noise: Auditory only/F-F	−3.96
Noise: Auditory-visual/F-F	−7.45
Noise: Auditory only/F-RF	−2.65
Noise: Auditory-visual/F-RF	−6.37
Speech: Auditory only/F-F	2.36
Speech: Auditory-visual/F-F	−6.44
Speech: Auditory only/F-RF	−2.33
Speech: Auditory-visual/F-RF	−8.50

psychometric functions for the two-talker masking condition (relative to the noise-masking conditions) also are consistent with these earlier reports as well as with nonspeech studies of informational masking (e.g., Kidd *et al.*, 1998).

The advantage of providing lipreading cues along with the auditory target can be seen by comparing filled and unfilled symbols in Fig. 1. Performance was better for all conditions when visual speech cues were provided. Improvement from the provision of visual cues is most apparent in panel (b) (two-talker masker), especially in the F-F condition. In terms of percent-correct identification of key words, the amount of benefit from visual supplementation ranged from 25.65 percentage points in the F-F condition/noise masker to 50.15 percentage points for the F-F/two-talker masker condition. The amount of visual benefit for the noise-masking data in the present study agrees in general with that shown in previous studies of auditory-visual speech perception, where a 20–40 percentage point increase in recognition of speech in noise has been reported across a variety of speech materials and noise maskers (e.g., Sumby and Pollack, 1954; Bench *et al.*, 1995; Helfer, 1997; Grant and Seitz, 2000a; Gagne, Rochette, and Charest, 2002).

Auditory-only and auditory-visual data were analyzed separately using repeated-measures analyses of variance (ANOVA) with masker type (speech versus noise), spatial position (F-F versus F-RF), and S/N ratio as independent variables. All main effects and interactions were significant (beyond the 0.001 level) in the A-only data. For the AV data, the only significant main effect was for S/N ratio [$F(2,22) = 422.62$, $p < 0.001$]. The interaction of masker type × spatial position [$F(1,23) = 24.61$, $p < 0.001$] and masker type × S/N ratio [$F(1,23) = 26.93$, $p < 0.001$] also were significant in the analysis of the AV data.

2. S/N ratio for criterion performance

The psychometric functions were examined to find the S/N ratio required for 50% correct performance in each condition. These S/N ratios (which are presented in Table I) were determined by interpolating linearly from the two data points in each function that bracketed the 50%-correct point. Figure 2 shows the effect of providing visual cues on the criterion S/N ratio. The figure shows clearly that visual speech cues were more beneficial in speech-masking conditions than with noise as the masker. The advantage of supplying visual speech cues was approximately 3.5 dB for noise maskers in both the F-F and F-RF conditions. When the masker was competing speech, visual cues provided close to 9 dB of benefit in the F-F condition and approximately 6 dB of benefit in the F-RF condition. Thus, even when informational masking was presumably released (in the F-RF condition) there was still greater visual benefit for speech maskers than for noise maskers.

Figure 3 shows the effect of presenting the masker from the front and the right loudspeakers as compared to from the front loudspeaker only (F-RF versus F-F). With noise as the masker, the S/N ratio for criterion performance was approximately 1 dB poorer in the F-RF condition (versus the F-F condition) for both AV and A-only presentation. In competing speech conditions the S/N ratio for 50%-correct performance was reduced by approximately 2 dB in the AV condition and by 4–5 dB in the A-only mode. It should be noted that because of variations in slopes of the psychometric functions obtained in conditions using the two-talker masker, the amount of benefit from visual and spatial cues was dependent on the level of performance. For example, at the 25%-correct performance level visual benefit was approximately

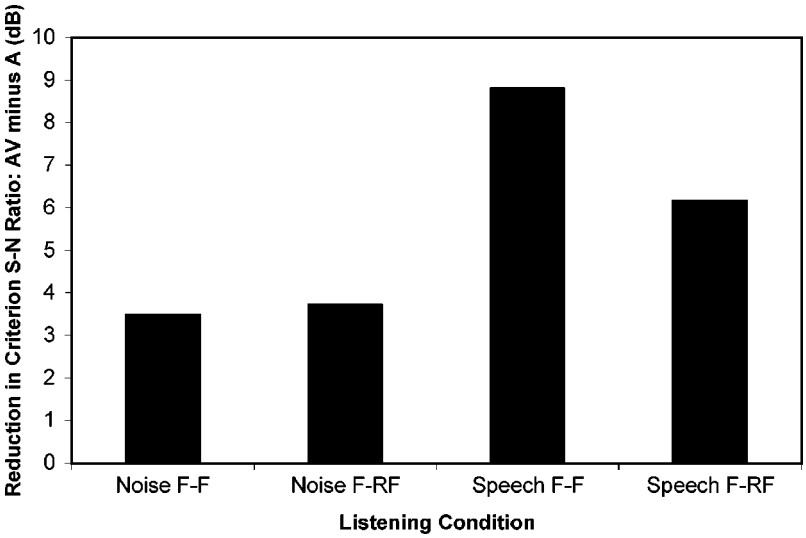

FIG. 2. Amount of benefit from the provision of visual speech cues as a function of listening condition. Benefit is expressed as the difference in S/N ratio in auditory-visual (AV) versus auditory-only (A) conditions for 50%-correct recognition of speech.

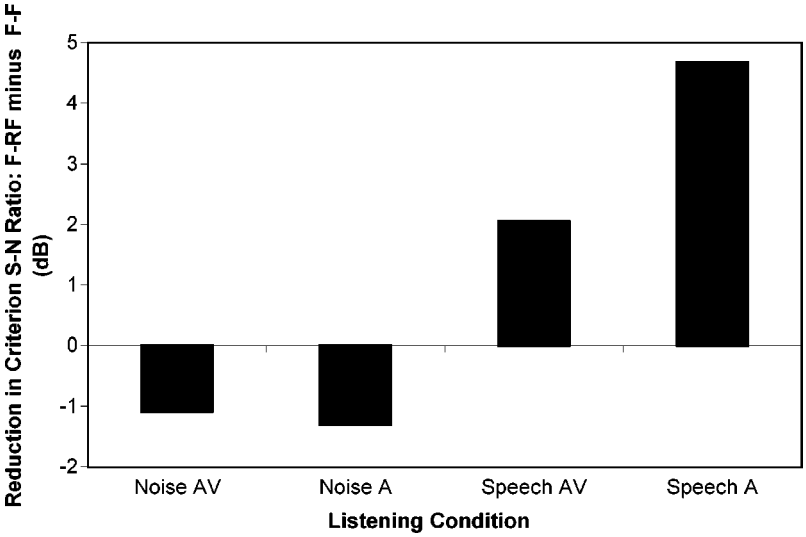

FIG. 3. Amount of benefit from perceived separation of target and masker as a function of listening condition. Benefit is expressed as the difference in S/N ratio in conditions with perceived spatial separation (F-RF) versus conditions with no spatial separation (F-F) for 50%-correct recognition of speech.

12 dB, as compared to 8.8 dB at the criterion level of 50%-correct recognition.

The results of experiment 1 demonstrate that visual cues are maximally beneficial when the target and masker are highly confusable. In the presence of either a noise masker or a speech masker, visual cues in the target provide phonetic information that aids in recognition. However, we theorize that when the masker is speech, lipreading plays an additional role of helping to separate the target voice from a complex mixture of voices. An alternative explanation is that there is a difference in the type and/or degree of phonetic supplementation for AV targets presented in the two types of maskers. In experiment 2 we used a speech detection task in an attempt to differentiate these two potential visual benefits.

III. EXPERIMENT 2: DETECTION OF AUDITORY-ONLY AND AUDITORY-VISUAL SPEECH

Previous research on the impact of lipreading on detection of an auditory message suggests that visual speech cues provide minimal or no advantage in helping to detect speech in the presence of steady-state noise (Grant and Seitz, 2000b; Grant, 2001) or in signal-correlated noise (Repp *et al.*, 1992). This is probably because the phonetic supplementation that makes lipreading advantageous for speech *understanding* in the presence of masking noise is of only limited usefulness for speech *detection*. Hence, using a detection task (in which phonetic supplementation provides little benefit) should help elucidate why the visual advantage is greater for a speech masker than for a noise masker. If visual speech cues give significantly greater benefit for speech detection in the presence of a speech masker (versus a noise masker), particularly in a condition where the speech target is highly confusable with the speech masker, it will support our argument that lipreading helps to ''pull out'' a target voice from within a mixture of other voices.

A. Method

1. Stimuli and experimental conditions

The target stimuli for this experiment consisted of the same 45 sentences for each condition. The target sentences were selected by examining the data by list, across conditions, from experiment 1. The set of sentences used in experiment 2 (30 sentences from the Gardening–Farming–Weather category and 15 sentences from the Health category) was chosen because it yielded close to average performance in experiment 1. The same two maskers used in experiment 1 (speech-spectrum noise and two-talker interference) also were used for experiment 2. A new set of 12 young, normal-hearing subjects (verified via pure-tone screening) participated in this experiment.

Each subject completed the detection task in all possible combinations of the following variables: noise versus speech masker; F-F versus F-RF masker configuration; and auditory-only versus auditory-visual presentation of the target stimuli. The equipment and experimental setup was identical to that used for experiment 1.

2. Procedure

Data were collected using a single-interval yes–no procedure. As in experiment 1 each trial began and ended with the onset and offset of the masker. The timing of the target presentation within an interval was varied as in experiment 1. During each AV trial the subject watched the visual image of the talker saying a target sentence. The subjects were blindfolded during A-only presentation. On a given trial there was a 50% probability of the target sentence being presented auditorily. Subjects were instructed to indicate whether they heard the target voice within the noise or speech maskers. In the two-talker masking condition subjects were told to listen for ''another person talking.'' Participants could use any available cues to determine whether the target voice was present in a given trial. A 3-down, 1-up adaptive procedure was used to estimate the 79.4% detection threshold (Levitt, 1971) with the masker presented at 55 dBA and the target level varied in 2-dB steps. The beginning presentation level of the target voice was 41 dBA, yielding an initial S/N ratio of −14 dB. Practice was not given but subjects were familiarized with the target voice in quiet before the initiation of data collection. Subjects completed 45 trials per condition. Detection thresholds were computed by aver-

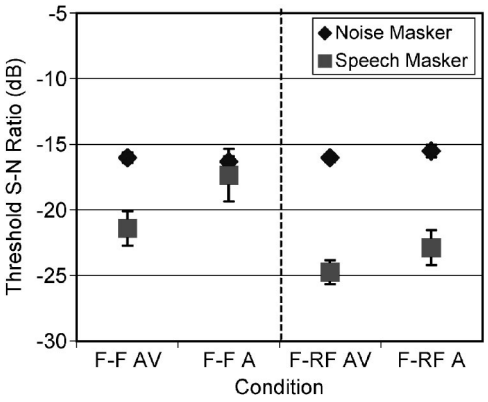

FIG. 4. Results for detection of speech in a noise masker versus in two-talker competition as a function of listening condition. Data are plotted as S/N ratio for 79.4% detection of the target voice.

aging target levels for all but the first reversal. Threshold was calculated based on a mean of nine reversals averaged across all conditions and subjects.

B. Results

Mean detection thresholds averaged across subjects are shown in Fig. 4. These data were analyzed using repeated-measures analysis of variance with masker type (noise versus speech), spatial condition (F-F versus F-RF), and presentation condition (A-only versus AV) as within-subjects factors. Results of this analysis indicated that all main effects and most interactions were significant [masker type: $F(1,11) = 27.22$, $p < 0.001$; spatial condition: $F(1,11) = 7.83$, $p = 0.017$; presentation condition: $F(1,11) = 5.59$, $p = 0.037$; masker type $\times$ presentation condition: $F(1,11) = 5.02$, $p = 0.047$; masker type $\times$ spatial condition: $F(1,11) = 15.45$, $p = 0.002$; masker type $\times$ presentation condition $\times$ spatial condition: $F(1,11) = 5.20$, $p = 0.044$].

Overall, speech detection was better for conditions with the two-talker masker than when the masker consisted of continuous speech-shaped noise, although the difference was minimal for the F-F A-only condition. The pattern of better performance in the presence of the speech masker is likely due to subjects' use of temporal and spectral fluctuations in this masking complex that aided in detecting the target. Intersubject variability in performance (as revealed by the standard error of the mean) was substantially larger for conditions with the two-talker masker than with the noise masker. For noise-masking conditions the amount of visual benefit was small (less than 1 dB) and did not vary between F-F and F-RF presentation modes. Benefit from visual cues was greater for speech-masking conditions, particularly when the target and masker were spatially coincident (F-F), where visual benefit was 4.1 dB. This can be seen in Fig. 4 by comparing the two square symbols on the left side of the graph. A similar trend was found for the benefit of adding the masking signal from the right loudspeaker (F-RF versus F-F). Less than 1 dB of advantage was found for noise maskers, but the improvement was 3.4 and 5.5 dB in the AV and A-only conditions, respectively, when the masker was speech.

IV. DISCUSSION

The results of the present study demonstrate that visual speech cues are particularly helpful in competing speech situations. Provision of visual speech cues gave an 8.8-dB advantage in S/N ratio for 50%-correct recognition when the speech target and speech masker were presented from the same spatial position. This is substantially greater than the 3–4-dB advantage seen for noise maskers. We propose that in conditions in which informational masking is presumably present, visual cues provide both phonetic supplementation and assistance in extracting and attending to the target voice. As described by Summerfield (1987), seeing the target talker's face allows the listener to tell which acoustic intensity changes are part of the target signal and which belong to the masker, since the degree of mouth opening is related to the overall amplitude contour of the target talker's message. The time-varying lip/jaw movements corresponding to the target talker match the target's auditory message, but not that of the masking talkers. Listeners can use these visual cues to help identify the target talker and focus on the target message.

Although the F-F results suggest that visual cues can help reduce informational masking, the data in the F-RF condition point to another contribution that lipreading might make toward resolving complex listening situations. In the present study visual speech cues provided a 6.2-dB advantage in the F-RF speech masker condition and approximately 3.5 dB of benefit with the noise masker. Assuming that there is little or no informational masking in the presence of either steady-state noise or in the F-RF speech-masking condition, this implies that visual cues are more effective in reducing energetic masking in the speech masker than in the noise masker. Visual phonetic supplementation might be different for steady-state noise than for a fluctuating masker like speech in which there are spectral and temporal valleys. This difference in phonetic supplementation between maskers also is likely to play a role in performance in spatially coincident conditions.

Another potential explanation is that visual cues provide additional benefit in speech masking (versus noise masking) conditions because they reduce the uncertainty about when to listen within the observation interval. Summerfield (1979) addressed this question by examining the benefit of provision of a visual timing cue. He compared speech recognition in conditions with full-face visual cues versus a condition where subjects were provided with a visual display of amplitude envelope information from the speech signal on an oscilloscope. The data showed no benefit from the latter condition, suggesting that the provision of only timing information was not useful for speech recognition. However, it is possible that the nature of the visual stimulus used in this study might have influenced its outcome. Existing data suggest that auditory and visual information must be perceived to originate from a common object in order to provide useful information about one another (Vroomen and De-Gelder, 2000). It is possible that the auditory and visual signals in the Summerfield (1979) study cited above were not integrated because they were not perceived to arise from the same object or event.

Results from experiment 1 demonstrated that perceived

spatial separation led to substantial benefit in speech-masking conditions for both auditory-only (4.7 dB) and auditory-visual (2.1 dB) presentation. The smaller benefit of perceived spatial separation found for auditory-visual presentation is consistent with the idea that spatial cues are less important when other cues can be used to segregate a signal from a masker (Noble and Perrett, 2002). Research has identified factors such as harmonicity, temporal asynchrony, and fundamental frequency as tools used to group auditory objects together (e.g., Darwin and Carlyon, 1995). Visual information that is synchronized with the auditory signal also may serve this purpose. In the present study, when visual speech cues provided information that allowed the listener to perceive the target message, spatial separation took on a less prominent role. However, it should be noted that the difference between S/N ratios required for criterion recognition in the most difficult condition (F-F A-only) and in the condition with both visual cues and spatial separation (F-RF AV) was 10.9 dB, greater than the benefit provided from either visual cues or spatial separation alone. This suggests that visual speech cues and spatial separation both provide important (and at least partially complementary) means of improving speech recognition.

Although speech recognition research is usually concerned with how well individuals can understand a target message, the ability to ignore unwanted auditory information is invariably important in complex listening situations. Previous studies have demonstrated that, in situations with multiple talkers, it is more difficult to ignore a message when one is looking in the direction from which it is perceived (e.g., Reisberg *et al.*, 1981; Spence *et al.*, 2000). This phenomenon could play a role in why performance in the F-RF condition (in which the subject is looking toward the target but not toward the perceived location of the masker) is superior to that obtained in the F-F condition (where the subject's visual focus is in the direction of both masker and target). In other words, creating perceived spatial separation not only makes it easier to understand the message, it also makes it easier to ignore the maskers.

The detection results from experiment 2 provide additional evidence that lipreading plays a role above and beyond phonetic supplementation when the masker consists of other voices. Visual speech cues led to less than 1 dB of advantage in noise-masking conditions, but provided 4 dB of benefit when the speech masker was spatially coincident with the target. The present study's results for noise maskers are consistent with those of Grant and Seitz (2000b), who found that visual cues gave only a small (an average of 1.6 dB) improvement in the detection of sentences in the presence of steady-state noise. The fact that substantial visual benefit was found for speech *recognition* within a noise masker but not for speech *detection* supports our premise that phonetic supplementation from visual cues is not useful or necessary in a detection task. We believe the greater visual advantage for detection in the speech-masking conditions (relative to when the masker was noise) reflects the contribution that lipreading makes to helping separate a masking voice from a target voice. This argument is supported by the fact that the greatest visual benefit was obtained when the target and masker were maximally confusable (that is, when both originated from the front loudspeaker).

The data obtained in the present experiments show that visual speech cues are especially beneficial in competing speech situations. A large body of evidence has shown that lipreading helps fill in phonetic information that is masked by steady-state noise. The data described in this paper suggest that this visual supplementation might be different for speech maskers versus noise maskers. Moreover, the present results support the theory that visual cues also play a role in segregating or pulling out an auditory target from a complex mixture of voices. The data demonstrate that visual speech cues are effective in reducing both energetic and informational masking; visual benefit was demonstrated in all conditions but was maximal when informational masking was presumed to exist. This beneficial effect occurs for both threshold-level (detection) and suprathreshold (recognition) processing.

ACKNOWLEDGMENTS

We thank Uma Balakrishnan, Bethany Butler, Kristie Dion, Wendy Levesque, Natalie Sitko, Joni Skinner, Nate Whitmal, and Danielle Winheim for their assistance on this project. This research was supported by a grant from NIDCD (DC01625).

ANSI (**1996**). ANSI 3.6-1996, ''Specifications for Audiometers'' (American National Standards Institute, New York).

Arbogast, A. L., Mason, C. R., and Kidd, G. (**2002**). ''The effect of spatial separation on informational and energetic masking of speech,'' J. Acoust. Soc. Am. **112**, 2086–2098.

Bench, J., Doyle, J., Daly, N., and Lind, C. (**1995**). ''Audiovisual, auditory, and visual perception of BKB/A sentence lists (speechreading version) by normally hearing subjects: Practice effects across presentation modes,'' Aust. J. Audiol. **17**, 115–121.

Bronkhorst, A. W., and Plomp, R. (**1992**). ''Effect of multiple speech-like maskers on binaural speech recognition in normal and impaired hearing,'' J. Acoust. Soc. Am. **92**, 3132–3139.

Brungart, D. S. (**2001**). ''Informational and energetic masking effects in the perception of two simultaneous talkers,'' J. Acoust. Soc. Am. **109**, 1101–1109.

Carhart, R., Tillman, T., and Greetis, R. (**1969**). ''Perceptual masking in multiple sound backgrounds,'' J. Acoust. Soc. Am. **45**, 694–703.

Darwin, C. J., and Carlyon, R. P. (**1995**). ''Auditory Grouping,'' in *The Handbook of Perception and Cognition (Hearing)*, edited by B. C. J. Moore (Academic, London), pp. 387–424.

Freyman, R. L., Helfer, K. S., McCall, D. D., and Clifton, R. K. (**1999**). ''The role of perceived spatial separation in the unmasking of speech,'' J. Acoust. Soc. Am. **106**, 3578–3588.

Freyman, R. L., Balakrishnan, U., and Helfer, K. S. (**2001**). ''Spatial release from informational masking in speech recognition,'' J. Acoust. Soc. Am. **109**, 2112–2122.

Freyman, R. L., Balakrishnan, U., and Helfer, K. S. (**2004**). ''Effect of number of masking talkers and auditory priming on informational masking in speech recognition,'' J. Acoust. Soc. Am. **115**, 2246–2256.

Gagne, J. P., Rochette, A. J., and Charest, M. (**2002**). ''Auditory, visual and audiovisual clear speech,'' Speech Commun. **37**, 213–230.

Grant, K. W. (**2001**). ''The effect of speechreading on masked detection thresholds for filtered speech,'' J. Acoust. Soc. Am. **109**, 2272–2275.

Grant, K. W., and Seitz, P. F. (**2000a**). ''The recognition of isolated words and words in sentences: Individual variability in the use of sentence context,'' J. Acoust. Soc. Am. **107**, 1000–1011.

Grant, K. W., and Seitz, P. F. (**2000b**). ''The use of visible speech cues for improving auditory detection of spoken sentences,'' J. Acoust. Soc. Am. **108**, 1197–1208.

Helfer, K. S. (**1997**). ''Auditory and auditory-visual perception of clear and conversational speech,'' J. Speech Lang. Hear. Res. **40**, 432–443.
Hirsch, I. J. (**1950**). ''Relation between localization and intelligibility,'' J. Acoust. Soc. Am. **22**, 196–200.
Kidd, G., Jr., Mason, C. R., Brughera, A., and Hartmann, W. M., ''The role of reverberation in release from masking due to spatial separation of sources for speech identification,'' Acust. Acta Acust. (submitted).
Kidd, G., Jr., Mason, C. R., Rohtla, T. L., and Deliwala, P. S. (**1998**). ''Release from masking due to spatial separation of sources in the identification of nonspeech auditory patterns,'' J. Acoust. Soc. Am. **104**, 422–431.
Levitt, H. (**1971**). ''Transformed up–down methods in psychoacoustics,'' J. Acoust. Soc. Am. **49**, 467–477.
MacKeith, N. W., and Coles, R. R. (**1971**). ''Binaural advantages in the hearing of speech,'' J. Laryngol. Otol. **85**, 213–232.
Noble, W., and Perrett, S. (**2002**). ''Hearing speech against spatially separate competing speech versus competing noise,'' Percept. Psychophys. **64**, 1325–1336.
Plomp, R. (**1976**). ''Binaural and monaural speech intelligibility of connected discourse in reverberation as a function of azimuth of a single competing sound source (speech or noise),'' Acustica **34**, 200–211.
Reisberg, D. (**1978**). ''Looking where you listen: Visual cues and auditory attention,'' Acta Psychol. **42**, 331–341.
Reisberg, D., Scheiber, R., and Potemken, L. (**1981**). ''Eye position and the control of auditory attention,'' J. Exp. Psychol. Hum. Percept. Perform. **7**, 318–323.
Repp, B. H., Frost, R., and Zsiga, E. (**1992**). ''Lexical mediation between sight and sound in speechreading,'' Q. J. Exp. Psychol. A **45**, 1–20.
Rudmann, D. S., McCarley, J. S., and Kramer, A. F. (**2003**). ''Bimodal displays improve speech comprehension in environments with multiple speakers,'' Hum. Factors **45**, 329–336.
Spence, C., Ranson, J., and Driver, J. (**2000**). ''Cross-modal selective attention: On the difficulty of ignoring sounds at the locus of visual attention,'' Percept. Psychophys. **62**, 410–424.
Sumby, W. H., and Pollack, I. (**1954**). ''Visual contribution to speech intelligibility in noise,'' J. Acoust. Soc. Am. **26**, 212–215.
Summerfield, Q. (**1979**). ''Use of visual information for phonetic perception,'' Phonetica **36**, 314–331.
Summerfield, Q. (**1987**). ''Some preliminaries to a comprehensive account of audio-visual speech perception,'' in *Hearing by Eye: The Psychology of Lipreading*, 1st ed., edited by B. Dodd and R. Campbell (Erlbaum, London), pp. 3–51.
Takahashi, G. A., and Bacon, S. P. (**1992**). ''Modulation detection, modulation masking, and speech understanding in noise in the elderly,'' J. Speech Hear. Res. **35**, 1410–1421.
Vitkovitch, M., and Barber, P. (**1994**). ''Effects of video frame rate on subjects' ability to shadow one of two competing verbal passages,'' J. Speech Hear. Res. **37**, 1204–1210.
Vroomen, J., and de Gelder, B. (**2000**). ''Sound enhances visual perception: Cross-modal effects of auditory organization on vision,'' J. Exp. Psychol. Hum. Percept. Perform. **26**, 1583–1590.
Zurek, P. M. (**1993**). ''Binaural advantages and directional effects in speech intelligibility,'' in *Acoustical Factors Affecting Hearing Aid Performance*, edited by G. A. Studebaker and I. Hockberg (Allyn and Bacon, Boston), pp. 255–276.

Voice responses to changes in pitch of voice or tone auditory feedback[a)]

Mahalakshmi Sivasankar
Department of Communication Sciences and Disorders, Northwestern University, 2240 Campus Drive, Evanston, Illinois 60208

Jay J. Bauer
Department of Communication Sciences and Disorders, University of Wisconsin—Milwaukee, P.O. Box 413, Milwaukee, Wisconsin 53201-0413

Tara Babu
5403 MacArthur Boulevard, Washington, D.C. 20016

Charles R. Larson[b)]
Department of Communication Sciences and Disorders, Northwestern University, 2240 Campus Drive, Evanston, Illinois 60208

(Received 14 May 2004; revised 29 October 2004; accepted 26 November 2004)

The present study was undertaken to examine if a subject's voice F_0 responded not only to perturbations in pitch of voice feedback but also to changes in pitch of a side tone presented congruent with voice feedback. Small magnitude brief duration perturbations in pitch of voice or tone auditory feedback were randomly introduced during sustained vowel phonations. Results demonstrated a higher rate and larger magnitude of voice F_0 responses to changes in pitch of the voice compared with a triangular-shaped tone (experiment 1) or a pure tone (experiment 2). However, response latencies did not differ across voice or tone conditions. Data suggest that subjects responded to the change in F_0 rather than harmonic frequencies of auditory feedback because voice F_0 response prevalence, magnitude, or latency did not statistically differ across triangular-shaped tone or pure-tone feedback. Results indicate the audio–vocal system is sensitive to the change in pitch of a variety of sounds, which may represent a flexible system capable of adapting to changes in the subject's voice. However, lower prevalence and smaller responses to tone pitch-shifted signals suggest that the audio–vocal system may resist changes to the pitch of other environmental sounds when voice feedback is present.
[DOI: 10.1121/1.1849933]

PACS numbers: 43.70.Aj, 43.75.Bc [AL] Pages: 850–857

I. INTRODUCTION

Despite the importance of vocalization for speech and singing, and the prevalence of disorders affecting the voice, neural mechanisms controlling the voice are poorly understood. As with other types of motor behaviors, researchers have speculated on the role of central neural mechanisms including sensory feedback for voice control. Data from studies using nerve stimulation and anesthetization techniques suggest that kinesthetic receptors are important in fine control of voice fundamental frequency (F_0) (Jürgens and Kirzinger, 1985; Ludlow *et al.*, 1992; Sundberg *et al.*, 1993). However, there is considerably more evidence for audition as an important form of sensory feedback in vocal control, as seen by increased variability in voice F_0 and intensity following post-lingual deafness (Cowie and Douglas-Cowie, 1992), when speaking in noisy environments (Lane and Tranel, 1971), and under conditions where auditory feedback is delayed (Lechner, 1979) or masked with noise (Elliott and Niemoeller, 1970; Mürbe *et al.*, 2002; Ternström *et al.*, 1988).

The noninvasive pitch-shifting technique is a powerful method of assessing the role of auditory feedback in real-time vocal control. Using this technique, researchers have demonstrated that auditory feedback helps in the stabilization of voice F_0 through a closed-loop negative feedback mechanism with latencies between 100–150 ms (Burnett *et al.*, 1998; Hain *et al.*, 2000; Larson *et al.*, 2001). When the perceived voice pitch is greater than the intended pitch, voice F_0 is reduced to compensate for the disparity. Conversely, when the feedback pitch is perceived lower, voice F_0 is increased. A compensatory pitch-shift response has been demonstrated following pitch perturbations during sustained vocalizations (Burnett *et al.*, 1998; Hain *et al.*, 2000; Jones and Munhall, 2002; Kawahara, 1995; Larson *et al.*, 2000), whistling (Anstis and Cavanagh, 1979), glissandos (Burnett and Larson, 2002), and nonsense syllables (Donath *et al.*, 2002; Natke *et al.*, 2003; Natke and Kalveram, 2001). The pitch-

[a)]Material originally presented in "Comparison of vocal responses to changes in pitch of voice, triangular, and sinusoidal tone feedback," The 3rd International Conference for Vocal Fold Physiology and Biomechanics, Denver, Colorado, September 2002. Portions of this manuscript were also presented as "Voice responses to changes in pitch of voice or tone feedback," at the Speech Motor Control Conference, Williamsburg, VA, March, 2002.

[b)]Electronic mail: clarson@northwestern.edu

shifting technique is a useful method to manipulate auditory feedback in real time, and provides a means to directly investigate the relationship between auditory feedback and voice F_0 control during ongoing vocalizations.

Changes in voice F_0 have also been observed in response to nonvocal sounds such as claps (Baer, 1979) and clicks (Sapir *et al.*, 1983b), suggesting that the audio–vocal system may be sensitive to other sounds besides the subject's voice. However, these studies had limitations in that the stimuli were short in duration and were presented suddenly. Nevertheless, the question remains as to which specific acoustical properties of the stimuli elicited the vocal responses. Moreover, the response latencies to nonvocal sounds (50–60 ms) were shorter than those observed with the pitch-shift technique for voice auditory feedback perturbations (100–200 ms) (Burnett *et al.*, 1998; Donath *et al.*, 2002; Hain *et al.*, 2000; Larson *et al.*, 2000; Natke and Kalveram, 2001), suggesting that the mechanisms underlying the auditory–laryngeal reflex may be different than those underlying the pitch-shift response.

Exploring the potential influence of nonvocal sounds on voice F_0 regulation is important for at least two reasons. First, considering that auditory feedback has a regulatory function in voice control (Burnett *et al.*, 1998; Hain *et al.*, 2000), knowing whether certain ranges of F_0 or specific harmonic frequencies of the feedback signal are involved in this regulatory process would enable us to understand how the auditory system interacts with laryngeal and respiratory motor systems for vocal control. Second, understanding the influence of nonvocal sounds on voice control is important for learning how the voice is controlled in a noisy environment while singing or speaking. Depending on the task, singers either maintain their intended vocal pitch by ignoring auditory feedback from other vocalists and instruments, or by matching their pitch to auditory feedback.

In the present study we compared pitch-shift responses elicited by perturbations in pitch of either voice feedback or nonvoice sounds to ascertain whether pitch-shift responses are sensitive only to the voice or to other periodic sounds as well. A secondary question was whether the audio–vocal system was sensitive primarily to the F_0 of the signal or a combination of the F_0 and harmonic components. To address these questions we compared pitch-shift responses elicited by perturbed voice feedback, perturbed triangular-shaped waves, and perturbed sinusoidal waves across two experiments. We hypothesized that the audio–vocal system would be more sensitive to the subject's own voice feedback compared to the tone feedback, as reflected in greater response prevalence and magnitudes for voice compared to the tone signals. Moreover, we predicted that the triangular signal, with its many harmonics and thus greater similarity to the voice, would elicit greater response prevalence and magnitudes than the sinusoidal signal.

II. METHODS

Experiment 1 compared responses to pitch-shifted voice and pitch-shifted complex tone (triangle) auditory feedback. Experiment 2 compared responses to pitch-shifted voice and pitch-shifted pure-tone (sinusoidal) auditory feedback.

A. Experiment 1

1. Subjects

Nineteen healthy female subjects (21–36 years of age; mean age=25.5 years) participated in this study. Previous studies using perturbed voice auditory feedback have revealed no differences in voice F_0 response measures between male and female subjects (unpublished observations). In order to maintain a similar relationship between voice F_0 and harmonics of the voice and tone feedback across all subjects, only female subjects were tested in this experiment. All subjects passed a hearing screening at 15-dB SPL (octave frequencies between 500–8000 Hz), and reported no history of neurological deficits, speech, language, or voice disorders. None of the subjects were trained singers.

2. Apparatus and procedures

Subjects were seated comfortably in a sound-treated booth and instructed to vocalize /u/ vowel sounds at a comfortable and steady habitual pitch while listening in near-real time to pitch-shifted voice and/or tone auditory feedback over headphones. Subjects were instructed to maintain their voice pitch regardless of any auditory feedback disturbance they might hear. Subjects sustained each vocalization for approximately 5 seconds at 77 dB SPL (self-monitored visually with a Dorrough loudness monitor model 40-A). Each subject produced 48 vocalizations across four blocks of 12 consecutive vocalizations. Vocalizations were transduced with an AKG boom-set microphone (HSC 200; microphone-to-mouth distance of 5 cm), and then amplified by a Mackie mixer (model 1202). A 534-Hz triangular tone (*TT*) produced by a function generator (Wavetek model 188) served as the external auditory tone. A 534-Hz tone was selected as the nonvoice sound after pilot study data. These data revealed very little overlap between the fundamental and harmonic frequencies of the 534-Hz tone with the harmonics of a female voice produced at habitual pitch. Voice and tone signals were processed for pitch shifting using an Eventide Ultraharmonizer (SE 3000) controlled by Musical Instrument Digital Interface software (MAX v3.5.9 by Opcode). During each vocalization beginning 500–1000 ms after vocal onset, the Ultraharmonizer was triggered five times in succession to increase or decrease voice or tone feedback pitch by 100 cents (equal to one semitone) each for a duration of 300 ms with a minimum interstimulus interval of at least 600 ms between perturbations. The onset of each pitch-shift stimulus was rapid, with a rise time of approximately 10 ms. To partially mask bone-conducted feedback and reduce potential binaural beating with tone feedback, voice and tone signals were mixed (Mackie mixer model 1202-VLZ), with 70-dB SPL pink noise (Goldline Audio Noise Source, model PN2; spectral frequencies 1 to 5000 Hz). Feedback signals were amplified with a Crown audio amplifier (D75-A), routed through HP decibel attenuators (model 350D), and fed back to the subjects via circumaural AKG headphones (model HSC 200). Voice and tone loudness feedback, when amplified, were perceptually equalized at about 88 dB SPL. Acoustical equipment was calibrated with a Brüel & Kjær 2203 sound-level meter (weighting A) prior to data collec-

tion. The ''A''-weighting scale was used because of low-level hum of the ventilation system and rack-mounted equipment in the building and laboratory immediately adjacent to the sound-attenuated booth.

Each subject participated in four experimental conditions in a randomized order. Subjects vocalized sustained /u/ vowels and heard

(1) only their amplified voice feedback, which was subsequently pitch shifted (V_{ps}).
(2) only amplified triangle tone feedback, which was subsequently pitch shifted (TT_{ps}). In this case, the subject's voice feedback was not amplified or pitch shifted, so the primary source of auditory feedback was the tone. However, subjects may have been able to perceive the voice signal through the bone-conducted pathway.
(3) both their amplified voice feedback and triangle tone feedback, but only their voice feedback was pitch shifted ($V_{ps}+TT$).
(4) both their amplified voice feedback and triangle tone feedback, but only the triangle tone feedback was pitch shifted ($V+TT_{ps}$).

B. Experiment 2

1. Subjects

Nineteen healthy female subjects (19–30 years of age; mean age=23 years) who did not participate in experiment 1, were tested in this study. Subject selection criteria were identical to experiment 1.

2. Apparatus and procedures

The methodology was similar to experiment 1; however, the external auditory tone was a 534-Hz pure-tone (PT) stimulus (Wavetek function generator model 188). Four conditions were tested for each subject in a random order: V_{ps}, PT_{ps}, $V_{ps}+PT$, $V+PT_{ps}$.

3. Data analysis

In each experiment for each condition, the subject's vocal signal, auditory feedback, control pulse indicating direction of the pitch shift, and TTL trigger pulse indicating onset of the pitch-shift stimulus were recorded. Signals were digitized on-line onto a laboratory computer at a 12-bit sampling rate of 10 kHz (5-kHz antialias filtering) using A/D conversion software (MACLAB CHART v3.5 by AD Instruments).

In off-line analysis (IGOR PRO software, version 4.0 by Wavemetrics, Inc.) the voice signal was low-pass filtered at 200 Hz, differentiated, and then smoothed with a five-point binomial, sliding window so as to remove high-frequency harmonics from the audio signals. A wave representing temporal fluctuations in voice F_0 (where voltage corresponded to F_0 in hertz) was then extracted from these preprocessed signals using a custom software algorithm in IGOR PRO. This algorithm detected positive-going threshold-voltage crossings, interpolated the time fraction between the two sample points that constituted each crossing, and calculated the reciprocal of the period defined by the center points. These F_0 signals were then converted to a cents scale using the following equation: $\text{cents}=100(12(\log_{10}(f2/f1))/\log_{10}(2))$, where $f1$ equals an arbitrary reference note at 195.997 Hz (G4) and $f2$ equals the voice signal in hertz. The conversion of voltage signals to cents permitted a relative comparison of the extent of change in the F_0 in response to a pitch modulation across all conditions, regardless of baseline F_0 (Baken and Orlikoff, 2000). Voice signals were then low-pass filtered at 20 Hz to remove sharp discontinuities associated with each glottal cycle. Event-related averages were generated for each subject and for each experimental condition by time-aligning the voice signals with pitch-shift stimulus onset (TTL control pulse). Event-related averages consisted of a minimum of 15 trials, each with a 400-ms prestimulus baseline and a 600-ms poststimulus response window. A pitch-shift response was automatically identified using a custom software algorithm, and the pitch-shift response magnitude and latency were concurrently measured from each event-related average. Pitch-shift responses were identified as valid or invalid responses according to the criteria below. A valid response was defined as a deviation from the averaged F_0 baseline trace with a magnitude $\geqslant$2 standard deviations (SDs) of the prestimulus baseline, a peak time $\geqslant$120 ms and a latency $\geqslant$50 ms but $\leqslant$400 ms after stimulus onset.

4. Statistical analysis

The total number of trials in each experiment equaled 152 (19 subjects $\times$4 feedback conditions $\times$2 pitch-shift stimulus directions). To determine if the total number of valid responses (response prevalence) differed across conditions, nonparametric Cochran's Q was calculated separately for each experiment across the four conditions collapsed across stimulus direction. Previous studies have indicated that responses to downward pitch shifts do not differ quantitatively from responses elicited by upward pitch-shifts (Burnett *et al.*, 1998; Hain *et al.*, 2000; Larson *et al.*, 2001). Statistical analyses for pitch-shift response magnitude and latency were calculated only for valid responses in each experiment. Raw data for response magnitude and latency did not fulfill assumptions of normality (non-normal distribution, small sample size, and unequal samples per cell) and therefore Bonferoni corrected nonparametric repeated Friedman's ANOVAs were calculated for each variable (Siegel and Castellan, 1988). Additionally, all valid responses were categorized according to whether they changed in the opposite direction (compensatory response) or the same direction as the pitch-shift stimulus (''following'' response) (Burnett *et al.*, 1998). The proportion of compensatory and following responses was then compared across all conditions in each experiment and submitted to significance testing using a chi-square analysis. Furthermore, response prevalence for pitch-shifted triangular (experiment 1) and pure tone (experiment 2) feedback were compared using a chi-square analysis. Response magnitude and latency were compared across experiments with Wilcoxon Mann–Whitney U tests.

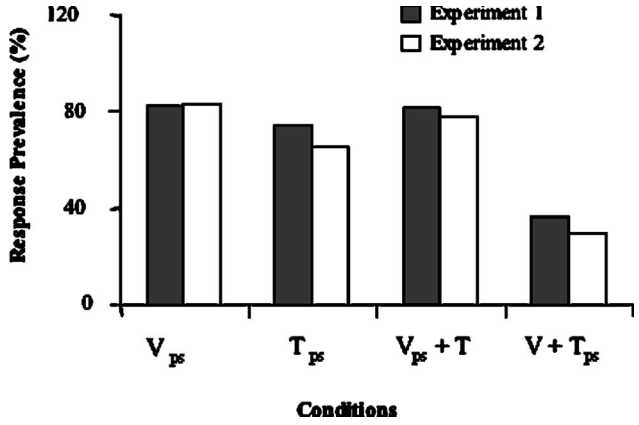

FIG. 1. Bar graph displaying response prevalence (%) across four conditions for both experiment one (triangle tone) and two (pure tone). Filled bars represent mean % of response prevalence for subjects in experiment 1. Unfilled bars represent mean % of response prevalence for subjects in experiment 2. Abbreviations: V_{ps}=voice feedback with voice pitch shifted; T_{ps}=tone feedback with tone pitch shifted; $V_{ps}+T$=voice and tone feedback with only voice pitch shifted; $V+T_{ps}$=voice and tone feedback with only tone pitch shifted.

III. RESULTS

A. Experiment 1

1. Response prevalence

Response prevalence differed significantly across the four conditions (Fig. 1). More valid pitch-shift responses were elicited for voice feedback pitch shifts (V_{ps}) than for perturbed triangular tone feedback (TT_{ps}) (Cochran's $Q=12.66$, df=3, $p<0.05$). Response prevalence for voice feedback pitch shifts (V_{ps}), and voice feedback pitch shifts in the presence of tone feedback ($V_{ps}+TT$) were significantly greater than that for tone feedback pitch shifts in the presence of voice ($V+TT_{ps}$) (McNemar's *post hoc* tests: $\chi^2=5.56$, df=1, $p<0.05$; $\chi^2=4.96$, df=1, $p<0.05$, respectively).

2. Response magnitude and latency

Response magnitude differed significantly across voice and tone feedback pitch-shift conditions (Friedman's $F=7.11$, $k=3$, $p<0.05$, Fig. 2). *Post hoc* testing indicated response magnitude for voice feedback pitch shifts (23±13 cents) and voice feedback pitch shifts in the presence of tone (20±11 cents) were significantly greater than that for tone feedback pitch shifts (12±6 cents; $p<0.05$). The response magnitudes for tone feedback pitch shifts in the presence of voice (10±4 cents) were lower than that for the other three conditions, but were excluded from statistical analysis due to poor response prevalence (small proportion of valid responses). Response latency did not differ across experimental conditions (Friedman's $F=1.34$, $k=3$, $p>0.05$, Fig. 3). Mean response latency varied from 106 ms (voice feedback pitch shifts) to 113 ms (tone feedback pitch shifts). Mean response latency was lowest for tone feedback pitch shifts in the presence of voice (95 ms), but again this condition was excluded from analysis due to low response prevalence.

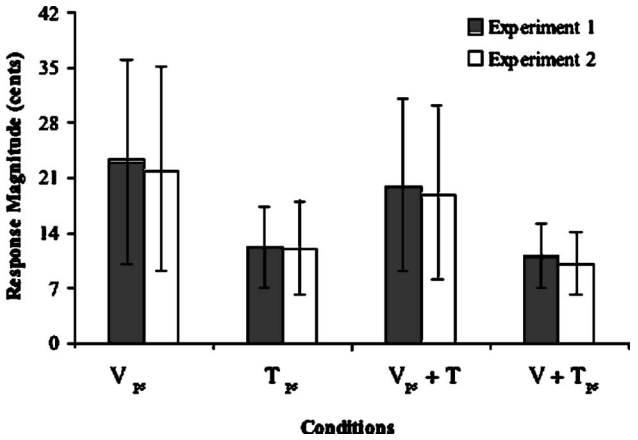

FIG. 2. Bar graph displaying mean response magnitude (cents) across four conditions for experiment one (triangle tone) and two (pure tone). Filled bars represent mean response magnitude ±1 SD across conditions for subjects in experiment 1. Unfilled bars represent mean response magnitude ±1 SD across conditions for subjects in experiment 2. Abbreviations: same as Fig. 1.

3. Response type

The proportion of compensatory and following responses did not vary across conditions as seen in Fig. 4 ($\chi^2=1.11$, df=1, $p>0.05$). Across all four conditions, the majority of valid pitch-shift responses (81%) was compensatory. That is, the responses were in the opposite direction of the pitch-shift stimulus. A few responses (19%) were ''following'' or in the same direction as the pitch-shift stimulus. Although statistically nonsignificant, a greater proportion of following responses was observed for tone feedback pitch shifts in the presence of voice (29%) than for any other condition (less than 20%).

B. Experiment 2

1. Response prevalence

Results from experiment 2 using a pure tone as the external auditory stimulus were similar to experiment 1. The number of valid responses differed significantly across all

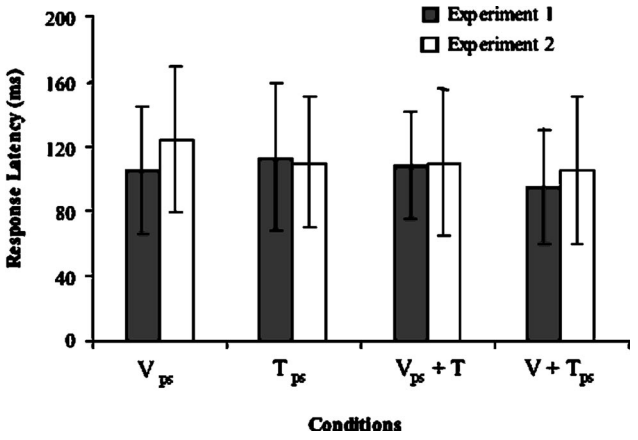

FIG. 3. Bar graph displaying mean response latency (ms) across four conditions for both experiment one (triangle tone) and two (pure tone). Filled bars represent mean response latency ±1 SD across conditions for subjects in experiment 1. Unfilled bars represent mean response latency ±1 SD across conditions for subjects in experiment 2. Abbreviations: same as Fig. 1.

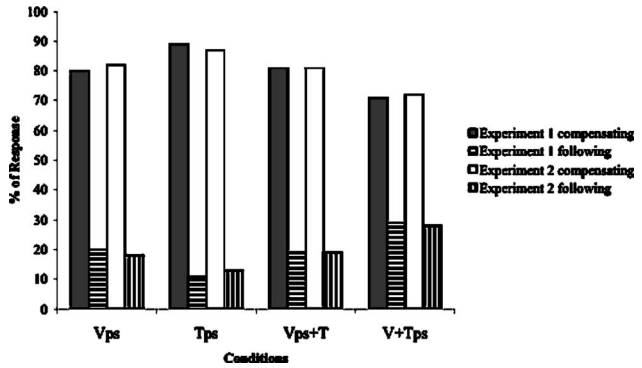

FIG. 4. Bar graph displaying response type (%) across four conditions for both experiment one (triangle tone) and two (pure tone). Filled bars represent % of compensatory responses in experiment 1. Filled horizontal striped bars represent % of following responses in experiment 1. Unfilled bars represent % of compensatory responses in experiment 2. Unfilled vertical striped bars represent % of following responses in experiment 2. Abbreviations: same as Fig. 1.

four conditions (Cochran's $Q=11.76$, df$=3$, $p<0.05$, Fig. 1), indicating that the pitch-shift response was not equally prevalent for voice and pure-tone feedback pitch shifts. Response prevalence for voice feedback pitch shifts and voice feedback pitch shifts in the presence of pure-tone feedback were significantly greater than that for pure-tone feedback pitch-shifts in the presence of voice (McNemar's *post hoc*: $\chi^2=6.32$, df$=1$, $p<0.01$ and $\chi^2=4.99$, df$=1$, $p<0.05$, respectively).

2. Response magnitude and latency

Response magnitude differed significantly across conditions as seen in Fig. 2 (Friedman's $F=6.73$, $k=3$, $p<0.05$), indicating that the extent of pitch-shift response magnitude varied for voice and pure-tone pitch-shifts. Response magnitude for voice feedback pitch shifts (22 ± 13 cents) and voice feedback pitch shifts in the presence of pure tone (19 ± 13 cents) were significantly greater than that for pure-tone feedback pitch shifts (12 ± 6 cents; $p<0.05$). The response magnitude for pure-tone feedback pitch shifts in the presence of voice (9 ± 4 cents) was lower than that for the other three conditions, but was excluded from statistical analysis due to the significantly greater proportion of invalid responses. As seen in Fig. 3, response latency did not differ across experimental conditions (Freidman's $F=2.01$, $k=3$, $p>0.05$). Mean response latency varied from 110 ms (pure-tone feedback pitch shifts) to 121 ms (voice feedback pitch shifts). Mean response latency was lowest for pure-tone feedback pitch shifts in the presence of voice (105 ms).

3. Response type

The proportion of compensatory and following responses did not vary across conditions as seen in Fig. 4 ($\chi^2=1.21$, df$=1$, $p>0.05$). Across all four conditions, the majority of the pitch-shift responses (81%) was compensatory, but a few responses (19%) were following. Additionally, a greater proportion of following responses was observed for pure-tone feedback pitch shifts in the presence of voice (28%) than any other condition (less than 18%).

C. Experiment 1 and experiment 2

Pitch-shift response prevalence did not vary with the nature of external auditory tone (triangular or pure tone; see Table I). That is, between-experiment comparisons demonstrated comparable response prevalence for triangular and pure-tone feedback pitch shifts ($\chi^2=1.19$, df$=1$, $p>0.05$). Similarly, response prevalence did not differ for voice feedback pitch shifts in the presence of tone (triangular or sinusoidal $\chi^2=1.01$, df$=1$, $p>0.05$) or when tone (triangular or sinusoidal) was shifted in the presence of voice ($\chi^2=0.96$, df$=1$, $p>0.05$). The finding of reduced response prevalence for $V+T_{ps}$ condition across both experiments suggests that the audio–vocal system may rely more on voice feedback than on tone feedback for maintaining vocal F_0 stability. Response magnitude and response latency did not vary with triangular or pure tone (Wilcoxon Mann–Whitney statistic, $p>0.05$), indicating that similar patterns of responses were elicited regardless of the type of external auditory tone. Furthermore, the proportion of compensatory and following responses was similar across both experiments, suggesting that the audio–vocal system responds in a similar fashion to complex and simple nonverbal external stimuli (Table I).

TABLE I. Comparisons of response characteristics: % of response prevalence, mean response magnitude (cents±SD), mean response latency (ms±SD), and % of response direction across the four conditions of V_{ps} (voice feedback with voice pitch shifted), T_{ps} (triangular or sinusoidal tone feedback with tone pitch-shifted), $V_{ps}+T$ (voice and tone feedback with only voice pitch shifted), and $V+T_{ps}$ (voice and tone feedback with only tone pitch shifted) in each of two experiments [triangle tone stimulus (TT), or pure-tone stimulus (PT)].

Conditions	V_{ps}		T_{ps}		$V_{ps}+T$		$V+T_{ps}$	
Experiment	TT	PT	TT	PT	TT	PT	TT	PT
Prevalence	82%	83%	74%	66%	82%	79%	34%	30%
Mean mag.	23	22	12	12	20	19	10	9
(±1 SD)	(±13)	(±13)	(±6)	(±6)	(±11)	(±13)	(±4)	(±4)
Mean latency	105	124	113	110	108	110	95	105
(±1 SD)	(±39)	(±45)	(±45)	(±40)	(±33)	(±45)	(±35)	(±45)
Compensatory Responses	80%	82%	89%	87%	81%	81%	71%	72%
Following Responses	20%	18%	11%	13%	19%	19%	29%	28%

IV. DISCUSSION

The role of the pitch-shift response in stabilizing voice F_0 by correcting for pitch perturbations has been widely recognized (Burnett *et al.*, 1998; Burnett and Larson, 2002; Donath *et al.*, 2002; Hain *et al.*, 2000; 2001; Larson *et al.*, 2001; 2000; Natke *et al.*, 2003; Natke and Kalveram, 2001). Additionally, there has been preliminary evidence for the presence of reflexive changes in voice F_0 in response to short-duration nonverbal sounds such as claps (Baer, 1979) and clicks (Sapir *et al.*, 1983b). Others have reported that when the pitch of whistle is altered, subjects produce a compensatory response that is similar to the pitch-shift response (Anstis and Cavanagh, 1979). Compensatory voice F_0 responses have also been elicited by sinusoidal modulations of saw-tooth tones, suggesting the presence of a short latency brainstem auditory–laryngeal reflex pathway (Sapir *et al.*, 1983a). Whether the audio–vocal system responds to pitch changes in nonvoice tones in the presence of unperturbed voice feedback has not been examined before. The present study demonstrates a compensatory vocal response to pitch changes in external nonverbal auditory tones in the presence of amplified, unaltered voice feedback.

Regardless of the ability of the system to respond to both voice or nonvoice feedback, the audio–vocal system appears to depend more on voice feedback than tone feedback to stabilize voice F_0. This was demonstrated by greater response prevalence and magnitude for conditions where voice feedback was pitch shifted ($V_{ps}, V_{ps}+T$). Conversely, response prevalence was lowest in the condition where voice feedback was not pitch shifted ($V+T_{ps}$). That is, voice feedback but not tone feedback appears to be used as the guiding referent to correct for perceived changes in voice F_0. Similarly, response magnitude was greatest for conditions where voice feedback was available and pitch shifted ($V_{ps}, V_{ps}+T$), and lowest for the condition where voice feedback was absent (T_{ps}) or unperturbed ($V+T_{ps}$). This increased sensitivity and dependence on voice would be necessary to prevent a person's voice from varying excessively with fluctuations in external environmental sounds. The lower response magnitude to pitch fluctuations in conditions where tone was shifted could reflect a mechanism employed by the audio–vocal system to avoid phonatory instability. If the audio–vocal system were equally sensitive to changes in voice and tone feedback, a person's voice would fluctuate with changes in the pitch of sounds in the surrounding environment. This selective sensitivity of the audio–vocal system to voice over tone may help explain how singers in a choir are able to maintain their vocal pitch in the presence of conflicting auditory feedback from adjacent singers or instruments. However, future studies are needed to address the role of unrelated voice auditory feedback on elicitation of voice F_0 responses. Nevertheless, our finding that subjects responded to pitch perturbations in the tone demonstrates that when a subject vocalizes in the presence of another acoustical signal, pitch perturbations in the external sound could destabilize voice F_0. In other words, subjects would have greater difficulty holding a steady voice F_0 in the presence of external periodic sounds. Results from the present study suggest that the magnitude of the instability is small (e.g., 9–10 cents), but under some circumstances (perhaps extremely noisy conditions or underlying vocal pathology), the instability could be greater.

The difference in sensitivity to the voice and tone feedback signals may reflect developmental or environmental factors important for voice control. Humans are dependent on voice for speech, and the dominance of voice over tone may be an inherent feature of the audio–vocal system adapted to enhance communication effectiveness.

Although it is important to understand why responses to the two types of signals (voice and tone) differed, it is equally important to understand factors that led to similarities in responses. That is, subjects produced compensatory responses to both the voice and tone-shifted signals with similar response latency, even though the magnitude and prevalence to the tone-shifted signals were reduced. These similarities suggest that the audio–vocal system may respond to a common property of both simple and complex tones. The most likely candidate for such an acoustical property is F_0. However, the 200–300-Hz difference in frequency between the tone (534 Hz) and the voice F_0 of the subjects would seem to be dissimilar enough, to obviate confusion of the tone for the subject's own voice feedback. All subjects verbally reported that the tone signal sounded much different than their voice. Moreover, results of pitch perception experiments indicate that people can detect differences in tone frequencies as small as 3 to 4 Hz (Wier *et al.*, 1977), suggesting that the 200- to 300-Hz difference between the voice and the tone signals in the present experiment should have been easy to discriminate. It is unlikely that overlap in harmonic frequencies of the tone and harmonics of the voice feedback accounted for the similarities in results reported here, because similar results were obtained with the pure-tone signal (no harmonic frequencies).

An alternative consideration is whether an overlap between harmonic frequencies of the voice signal and the F_0 of the tone signals accounted for the similarities in results. As a test of this possibility, we subjected 30% of our data to FFT analysis to determine if there was a pattern of overlap between the F_0 and harmonics, of the voice and the tones. By comparing the frequency components of voice output with that of the tone feedback, regions of overlap could be easily identified. The results of these FFT analyses showed that there was no systematic overlap between voice harmonics and tone frequencies for all 30% of data. Thus, overlap in frequency content (or masking of tone by voice) between the voice and tone signals does not appear to explain our data.

Since it seems unlikely that similarities in F_0 of the signals or overlaps of harmonic content of the signals can easily explain the similarity in responsiveness to the voice and tone signal, other explanations are needed. One possibility is that the audio–vocal system is a very adaptable system and will respond to changes in the voice as well as changes in frequency of any tone while a subject is vocalizing. Thus, the audio–vocal system may utilize a nonselective ''pitch change detector'' to respond to perturbations in pitch of periodic types of auditory feedback. Such adaptability would be advantageous in that it would allow the system to respond to the subject's voice regardless of the F_0. Through a pro-

cess of development, the system could learn to respond to a subject's voice at many different frequencies, and this could result in a system that is not selective to precise acoustical properties of feedback signals, only a change in frequency *per se*. One could also argue that since the control of whistling frequency is sensitive to perturbed pitch feedback (Anstis and Cavanagh, 1979), the system is capable of a motor response to perturbations in pitch of any frequency-modulating device that a person has learned to control. Such an outcome would predict that control of frequency in any musical instrument might also be sensitive to perturbations in pitch as well (Parlitz and Bangert, 1999). It is unlikely that startle responses could account for the results since upward and downward pitch-shift stimuli led to compensatory responses (71%–89% of the time) with an average latency between 95–124 ms. If the subjects were startled by the stimuli, one would expect short-latency, noncompensatory responses due to a contraction of laryngeal adductor and respiratory muscles resulting only in increases in subglottal pressure and voice F_0. Moreover, startle responses habituate to repeated stimulation (Shalev *et al.*, 1992), while responses to pitch-shifted voice feedback do not.

Finally, in previous reports using the pitch-shifting technique, we have reported that some responses ''follow'' the stimulus direction while most oppose the perturbation direction (compensation). Such compensatory behavior and error correction have also been observed in other sensory and motor systems including the visual, auditory, and articulatory systems (Baum *et al.*, 1996; Cole and Abbs, 1988; Gracco and Abbs, 1985; Held, 1965; Shaiman and Gracco, 2002). In an investigation on the role of auditory adaptation in the speech domain, human subjects were provided auditory feedback in which the vowel formants being produced were shifted slowly over time (Houde and Jordan, 1998). Over 4220 trials, subjects adjusted vowel production to compensate for the vowel's perturbed identity. In the present study we observed that most responses were compensatory and a small minority of them were of the following type. Moreover, there was a nonsignificant increase in numbers of following responses in conditions where the tone was shifted rather than the voice. It was previously noted that more following responses were observed with large magnitude stimuli (Burnett *et al.*, 1998), and it was speculated that feedback signals that differ from the voice could lead subjects to change their choice of referent and follow the stimulus direction (Hain *et al.*, 2000). The larger numbers of following responses with tone stimuli in the present study support this speculation, but more data are needed before we can adequately explain such responses.

V. CONCLUSION

The present study tested the responses of the audio–vocal system to pitch perturbations in voice and external nonvoice sounds. Results demonstrate that the system responds with a robust compensatory response to pitch changes in both voice and external nonvoice sounds (triangular and pure tones). However, greater response magnitudes were observed to pitch-shifted voice feedback compared to pitch-shifted tone feedback, suggesting that the audio–vocal system depends chiefly on voice feedback to stabilize voice F_0. Even in the presence of simultaneous voice and tone feedback signals, the system appears to rely more on voice feedback than external nonvoice feedback. Furthermore, the presence of a pitch-shift response to pitch perturbations in either a nonverbal complex or pure tone, suggests that the audio–vocal system is sensitive to changes in fundamental frequency of tonal feedback rather than the harmonic energy. The ability of the audio–vocal system to respond to both the subject's voice and external tone stimuli may reflect a flexible system capable of adapting to behavioral and developmental changes in vocal behavior.

ACKNOWLEDGMENT

This research was supported by NIH Grant No. DC006243-01A1.

Anstis, S. M., and Cavanagh, P. (**1979**). ''Adaptation to frequency-shifted auditory feedback,'' Percept. Psychophys. **26**, 449–458.
Baer, T. (**1979**). ''Reflex activation of laryngeal muscles by sudden induced subglottal pressure changes,'' J. Acoust. Soc. Am. **65**, 1271–1275.
Baken, R. J., and Orlikoff, R. F. (**2000**). *Clinical Measurement of Speech and Voice*, 2nd ed. (Singular, San Diego).
Baum, S. R., McFarland, D. H., and Diab, M. (**1996**). ''Compensation to articulatory perturbation: Perceptual data,'' J. Acoust. Soc. Am. **99**, 3791–3794.
Burnett, T. A., and Larson, C. R. (**2002**). ''Early pitch shift response is active in both steady and dynamic voice pitch control,'' J. Acoust. Soc. Am. **112**, 1058–1063.
Burnett, T. A., Freedland, M. B., Larson, C. R., and Hain, T. C. (**1998**). ''Voice $f0$ responses to manipulations in pitch feedback,'' J. Acoust. Soc. Am. **103**, 3153–3161.
Cole, K. J., and Abbs, J. H. (**1988**). ''Grip force adjustments evoked by load force perturbations of a grasped object,'' J. Neurophysiol. **60**, 1513–1522.
Cowie, R., and Douglas-Cowie, E. (**1992**). ''Postlingually acquired deafness,'' in *Trends in Linguistics, Studies and Monographs* (Mouton de Gruyter, New York).
Donath, T. M., Natke, U., and Kalveram, K. T. (**2002**). ''Effects of frequency-shifted auditory feedback on voice f_0 contours in syllables,'' J. Acoust. Soc. Am. **111**, 357–366.
Elliott, L., and Niemoeller, A. (**1970**). ''The role of hearing in controlling voice fundamental frequency,'' Int. Aud. **IX**, 47–52.
Gracco, V. L., and Abbs, J. H. (**1985**). ''Dynamic control of the perioral system during speech: Kinematic analyses of autogenic and nonautogenic sensorimotor processes,'' J. Neurophysiol. **54**, 418–432.
Hain, T. C., Burnett, T. A., Larson, C. R., and Kiran, S. (**2001**). ''Effects of delayed auditory feedback (daf) on the pitch-shift reflex,'' J. Acoust. Soc. Am. **109**, 2146–2152.
Hain, T. C., Burnett, T. A., Kiran, S., Larson, C. R., Singh, S., and Kenney, M. K. (**2000**). ''Instructing subjects to make a voluntary response reveals the presence of two components to the audio–vocal reflex,'' Exp. Brain Res. **130**, 133–141.
Held, R. (**1965**). ''Plasticity in sensory-motor systems,'' Sci. Am. **213**(5), 84–94.
Houde, J. F., and Jordan, M. I. (**1998**). ''Sensorimotor adatation in speeech production,'' Science **279**, 1213–1216.
Jones, J. A., and Munhall, K. G. (**2002**). ''The role of auditory feedback during phonation: Studies of mandarin tone production,'' J. Phonetics **30**, 303–320.
Jürgens, U., and Kirzinger, A. (**1985**). ''The laryngeal sensory pathway and its role in phonation. A brain lesioning study in the squirrel monkey,'' Exp. Brain Res. **59**, 118–124.
Kawahara, H. (**1995**). ''Hearing voice: Transformed auditory feedback effects on voice pitch control,'' 'Computational Auditory Scene Analysis'

and 'International Joint Conference on Artificial' Intelligence,'' Montreal.
Lane, H., and Tranel, B. (**1971**). ''The Lombard sign and the role of hearing in speech,'' J. Speech Hear. Res. **14**, 677–709.
Larson, C. R., Burnett, T. A., Kiran, S., and Hain, T. C. (**2000**). ''Effects of pitch-shift onset velocity on voice $f0$ responses,'' J. Acoust. Soc. Am. **107**, 559–564.
Larson, C. R., Burnett, T. A., Bauer, J. J., Kiran, S., and Hain, T. C. (**2001**). ''Comparisons of voice f_0 responses to pitch-shift onset and offset conditions,'' J. Acoust. Soc. Am. **110**, 2845–2848.
Lechner, B. (**1979**). ''The effects of delayed auditory feedback and masking on the fundamental frequency of stutterers and non-stutterers,'' J. Speech Hear. Res. **22**, 243–253.
Ludlow, C., Van Pelt, F., and Koda, J. (**1992**). ''Characteristics of late responses to superior laryngeal nerve stimulation in humans,'' Ann. Otol. Rhinol. Laryngol. **101**, 127–134.
Mürbe, D., Pabst, F., Hofmann, G., and Sundberg, J. (**2002**). ''Significance of auditory and kinesthetic feedback to singers' pitch control,'' J. Voice **16**, 44–51.
Natke, U., and Kalveram, K. T. (**2001**). ''Effects of frequency-shifted auditory feedback on fundamental frequency of long stressed and unstressed syllables,'' J. Speech Lang. Hear. Res. **44**, 577–584.
Natke, U., Donath, T. M., and Kalveram, K. T. (**2003**). ''Control of voice fundamental frequency in speaking versus singing,'' J. Acoust. Soc. Am. **113**, 1587–1593.
Parlitz, D., and Bangert, M. (**1999**). ''Short and medium motor responses to auditory pitch shift: Latency measurements of the professional musician's audio-motor loop for intonation,'' J. Acoust. Soc. Am. **105**, 1298.
Sapir, S., McClean, M., and Luschei, E. S. (**1983a**). ''Effects of frequency-modulated auditory tones on the voice fundamental frequency in humans,'' J. Acoust. Soc. Am. **73**, 1070–1073.
Sapir, S., McClean, M. D., and Larson, C. R. (**1983b**). ''Human laryngeal responses to auditory stimulation,'' J. Acoust. Soc. Am. **73**, 315–321.
Shaiman, S., and Gracco, V. L. (**2002**). ''Task-specific sensorimotor interactions in speech production,'' Exp. Brain Res. **146**, 411–418.
Shalev, A. Y., Orr, S. P., Peri, T., Schreiber, S., and Pitman, R. K. (**1992**). ''Physiologic responses to loud tones in Israeli patients with posttraumatic stress disorder,'' Arch. Gen. Psychiatry **49**, 870–875.
Siegel, S., and Castellan, N. J. (**1988**). *Nonparametric Statistics for the Behavioral Sciences* (McGraw-Hill, New York).
Sundberg, J., Iwarsson, J., and Billström, A.-M. H. (**1993**). ''Significance of mechanoreceptors in the subglottal mucosa for subglottal pressure control in singers,'' 22nd Annual Symposium Care of the Professional Voice, Philadelphia.
Ternström, S., Sundberg, J., and Colldén, A. (**1988**). ''Articulatory $f0$ perturbations and auditory feedback,'' J. Speech Hear. Res. **31**, 187–192.
Wier, C. C., Jesteadt, W., and Green, D. M. (**1977**). ''Frequency discrimination as a function of frequency and sensation level,'' J. Acoust. Soc. Am. **61**, 178–184.

Lip kinematics in long and short stop and fricative consonants[a)]

Anders Löfqvist[b)]
Haskins Laboratories, 270 Crown Street, New Haven, Connecticut 06511and Department of Logopedics, Phoniatrics and Audiology Lund University, Lund, Sweden

(Received 23 February 2003; revised 22 October 2004; accepted 29 October 2004)

This paper examines lip and jaw kinematics in the production of labial stop and fricative consonants where the duration of the oral closure/constriction is varied for linguistic purposes. The subjects were speakers of Japanese and Swedish, two languages that have a contrast between short and long consonants. Lip and jaw movements were recorded using a magnetometer system. Based on earlier work showing that the lips are moving at a high velocity at the oral closure, it was hypothesized that speakers could control closure/constriction duration by varying the position of a virtual target for the lips. According to this hypothesis, the peak vertical position of the lower lip during the oral closure/constriction should be higher for the long than for the short consonants. This would result in the lips staying in contact for a longer period. The results show that this is the case for the Japanese subjects and one Swedish subject who produced non-overlapping distributions of closure/constriction duration for the two categories. However, the peak velocity of the lower lip raising movement did not differ between the two categories. Thus if the lip movements in speech are controlled by specifying a virtual target, that control must involve variations in both the position and the timing of the target. [DOI: 10.1121/1.1840531]

PACS numbers: 43.70.Aj, 43.70.Bk [PFA] Pages: 858–878

I. INTRODUCTION

This paper examines lip and jaw kinematics in the control of lip closure/constriction duration in labial stop and fricative consonants, where the duration of the oral closure/constriction is varied for linguistic purposes. Based on earlier work on lip movements (Löfqvist and Gracco, 1997), it was hypothesized that speakers could vary the duration of the oral closure by shifting the position of a virtual target for the lips. For example, the target for the lower lip would be at a higher vertical position for a long than for a short consonant. Such a strategy would make the lips stay in contact for a longer time. Preliminary evidence for such a strategy for controlling closure duration was provided for one Swedish speaker by Löfqvist (2000). In addition, Löfqvist and Gracco (1997) found a positive correlation between closure duration and the peak vertical position of the lower lip during the oral closure, but the range of closure durations was not very large in their study.

The results presented by Löfqvist and Gracco (1997) showed that the lips were moving at close to their peak velocities at the instant of labial closure. The high velocity at the impact resulted in tissue compression making the airtight seal for the stop consonant. In addition, mechanical interactions between the lips were observed, with the lower lip pushing the upper lip upward due to its higher velocity. These results were compatible with the idea of a virtual target for the lips that would have them move beyond each other. Such a control strategy would ensure that the lips will make a closure irrespective of variations in their onset positions.

Although there are several acoustic studies of long and short consonants, e.g., Finnish (Lehtonen, 1970), Bengali and Turkish (Lahiri and Hankamer (1988), Swedish (Elert, 1964), and Japanese (Beckman, 1982; Han, 1994), not much is known about possible differences in the articulation of long and short consonants. Electropalatographic studies of Italian stops have shown that the amount of tongue palate contact is larger for geminate than for single stops, and also that there is a general increase in the extent of tongue-palate contact with increasing closure duration (Farnetani, 1990); similar results for American English have been presented by Byrd (1995). An x-ray study of French consonants by Vaxelaire (1995) suggested that the area of tongue palate contact was larger for the long (abutted) stops than for the short ones. Lehiste *et al.* (1973) recorded the activity of the upper lip muscles in a subject producing long and short labial consonants in Estonian, and found that the long cognate was generally produced with two successive peaks in the EMG signal. Dunn (1993) studied lip movements in long and short consonants in Italian and Finnish. Using a derived measure of lip aperture, she found that the lips stayed in contact for a longer period of time for the long sounds; however, the movement kinematics were not consistently different for the long and short consonants. A related study by Smith (1995) examined lip and tongue movements in single and geminate consonants in Japanese and Italian. Of particular interest for the present study, Smith found that the closing movements of the lips were slower for the geminate than for the single consonant.

Although Löfqvist and Gracco (1997) proposed the idea of a virtual target for lip movements, they also noted that it might be applicable to other articulators as well, since whenever two articulators make contact, at least one of them consists of soft tissue. Moreover, recent work on tongue move-

[a)]Parts of this paper were presented at the First Pan-American/Iberian Meeting on Acoustics, Cancun, Mexico, 2–6 December, 2002.
[b)]Electronic mail: lofquist@haskins.yale.edu

ments in speech has explored a similar idea. In this case, the argument has been made that the virtual target for the tongue in the production of a velar stop consonant is above the hard palate in the nasal cavity. Empirical studies of tongue movement kinematics, showing that the tongue can be moving at a high velocity at the instant of oral closure (Fuchs *et al.*, 2001; Löfqvist and Gracco, 2002), and modeling work using a virtual target (Perrier *et al.*, 2003) have shown some support for this idea. It should be pointed out that this study does not address the broader issue of the potential role of virtual targets in speech motor control. The current experiment was only designed to examine a specific hypothesis about virtual targets for the lips.

The hypothesis to be explored in the present study is that a temporal property in speech, i.e., the duration of a labial closure/constriction for stops and fricatives, is governed by varying a spatial control parameter, i.e., lip target position. Although the coordinate system for speech motor control is not known, one proposal views the proper control regime as tract variables, e.g., lip aperture which is implemented jointly by movements of the upper and lower lips and the jaw (e.g., Saltzman and Munhall, 1989). Thus, it is possible that the kinematics of both the upper lip, the lower lip, and the jaw will differ for long and short consonants. Due to the mechanical interactions between the lips discussed above and further elaborated below, measurements will primarily be made of the lower lip movements. However, the peak velocity of the closing movement of the upper lip and the closing movement of a derived measure of lip aperture will be also examined, since they occur before the lips meet. This focus on the lower lip is methodological and should not be taken as evidence that the control is limited to the lower lip.

In its simplest form, the hypothesis about a change in virtual position only considers the movement displacement and assumes that other aspects of the movement, e.g., timing, remain unchanged. For epistemological reasons, such a simple and restricted hypothesis is most easily refuted and thus helpful for a further understanding of lip aperture control in speech. In terms of motor control, the theoretical framework is similar to the model proposed by Gottlieb *et al.* (1989), where the magnitude and the duration of the underlying force pulse can be controlled. In the present case, the assumption is that only the magnitude of the pulse is changed to produce a long consonant.

If the hypothesis that speakers vary the position of a virtual target for the lower lip to produce long and short consonants is correct, the following predictions can be made of the lip movements in long and short consonants:

(1) The peak position of the lower lip is higher for a long than for a short consonant. If this is true, the following additional predictions can also be made:
(2) There is a positive correlation between the vertical positions of the upper and lower lips at the point in time when the lower lip reaches its highest vertical position. This follows from the previously observed mechanical interactions between the two lips with the lower lip pushing the upper lip upward (Löfqvist and Gracco, 1997). With the lower lip reaching a higher vertical position for a long consonant, it would push the upper lip further upward. Hence, the upper lip position at this point in time is higher for a long than for a short consonant.
(3) A long consonant is produced with a larger lower lip closing displacement than a short consonant. Furthermore, this is due to a difference in the vertical end position of the lower lip and not to a difference in its starting position.
(4) A long consonant is produced with a higher peak closing velocity of the lower lip. This follows from the strong correlation between movement displacement and peak velocity that has been observed in both speech and nonspeech movements (e.g., Cooke, 1980; Ostry *et al.* 1983; Kelso *et al.*, 1985; Vatikiotis-Bateson and Kelso, 1993; Hertrich and Ackermann, 1997; Löfqvist and Gracco, 1997). One exception to this pattern can occur when a movement of one articulator is truncated by a following gesture, so that its movement displacement is decreased (e.g., Munhall *et al.*, 1992; Harrington *et al.*, 1995; Byrd *et al.*, 2000). Interestingly, a different kind of truncation is shown in the lip data presented by Löfqvist and Gracco (1997), when the lowering movement of the upper lip is checked by the rising lower lip. The same phenomenon is observed in the present study.

We should note from the outset that any observed differences will be in the order of a few mm, since the lip movements in labial consonants are usually 1 cm or less, depending on the vowel context (e.g., Löfqvist and Gracco, 1997). To test the hypothesis of variations of the position of a virtual to control closure/constriction duration, speakers of Japanese and Swedish were studied. Both these languages have a contrast between long and short consonants, although the structure of the length contrast differs in the two languages. In Swedish, there is a durational relationship between a vowel and a following consonant. That is, a short vowel is followed by a long consonant, while a long vowel is followed by a short consonant. In addition, there may be differences in vowel quality between the long and short vowels in Swedish (cf., Hadding-Koch and Abramson, 1964; Fant, 1973). Most likely due to these additional components of the length contrast for Swedish consonants, the difference in duration between a long and short consonant is often quite small, and there may be a substantial overlap between the distributions of the closure durations of long and short consonants (Elert, 1964). In Japanese, the difference in closure duration is much larger than in Swedish, with the long ones being about twice as long as the short ones (e.g., Beckman, 1982; Han, 1994).

II. METHOD

A. Subjects

Four female native speakers of Japanese and two native speakers of Swedish, one male and one female, served as subjects. They reported no speech, language, or hearing problems. They were naive as to the purpose of the study. Before participating in the recording, they read and signed a

consent form. (The experimental protocol was approved by the IRB at the Yale University School of Medicine.)

B. Linguistic material

The linguistic material consisted of Japanese and Swedish words, occurring in a short carrier sentence. To keep the phonetic context of the labial consonants as similar as possible, the consonant was placed between the open vowel /a/, whenever possible. The specific reason for keeping the context similar was the predicted larger lower lip vertical displacement for the long than for the short consonants. Unless the position of the lower lip at the start of the closing movement was very similar for the long and short consonants, the observed result might simply be due to differences between the onset positions for the long and short consonants. As a consequence, differences in peak velocity might also be due to differences in displacement related to different onset positions. As will be discussed below, the attempt to control the onset position of the lower lip was not always successful, however.

In Japanese, the following words were used: ''napa,'' ''nappa,'' ''sama,'' ''samma,'' ''tofuru,'' and ''daffuru.'' The labial consonant in the two last words is a bilabial fricative /Φ/. The Swedish subjects produced the following words: ''rapa,'' ''rappa,'' ''Saba,'' ''sabba,'' ''rama,'' ''ramma,'' ''slafa,'' and ''haffa.'' The linguistic material was organized into randomized lists and presented to the subjects in Swedish and Japanese writing, with the words occurring in a short frame sentence with sentence stress on the test word. Fifty repetitions of each word were recorded.

C. Movement recording

The movements of the lips and jaw were recorded using a three-transmitter magnetometer system (Perkell *et al.*, 1992); when proper care is taken during the calibration, the spatial resolution of the system is in the order of 0.5 mm. Receivers were placed on the vermilion border of the upper and lower lip, and on the lower incisors at the gum line. Two additional receivers placed on the nose and the upper incisors were used for the correction of head movements. All receivers were attached using Isodent, a dental adhesive. Care was taken during each receiver placement to ensure that it was positioned at the midline with its long axis perpendicular to the sagittal plane. Two receivers attached to a plate were used to record the occlusal plane by having the subject bite on the plate for a brief interval during the recording. All data were subsequently corrected for head movements and rotated to bring the occlusal plane into coincidence with the *x* axis. This rotation was performed to obtain a uniform coordinate system for all subjects (cf., Westbury, 1994); the origin of the coordinate system was the receiver placed on the upper incisors.

The articulatory movement signals (induced voltages from the receiver coils) were sampled at 500 Hz after low-pass filtering at 200 Hz. The resolution for all signals was 12 bits. After voltage-to-distance conversion, the movement signals were low-pass filtered using a 25-point triangular window with a 3-dB cutoff at 14 Hz; this was done forwards and backwards to maintain phase. A measure of lip aperture was obtained by calculating the difference between the upper and lower lip vertical receivers. To obtain instantaneous velocity, the first derivative of the position signals was calculated using a three-point central difference algorithm. The velocity signals were smoothed using the same triangular window. Movement onsets and offsets were defined algorithmically at zero-crossings in the velocity signal. The peak movement velocity was also labeled algorithmically. Signal averages were obtained using the onset of oral closure, defined in the acoustic signal, as the line-up point, and with a temporal window extending 100 ms before and 150 ms after the line-up point; these averages were only used for visualization purposes and all measurements were based on the individual tokens. All the signal processing was made using the Haskins Analysis Display and Experiment System (HADES) (Rubin and Löfqvist, 1996).

The acoustic signal was preemphasized, low-pass filtered at 4.5 kHz, and sampled at 10 kHz. The onset and release of the oral closure for the stops and nasals were identified in waveform and spectrogram displays of the acoustic signal. The onset of the closure was identified by the decrease in the signal amplitude. For the fricatives, the cessation and reappearance of voicing were used to identify the constriction phase.

The duration of the oral closure/constriction was measured in the acoustic signal. The vertical receiver positions of the lips and the jaw were measured at the onset and offset of the oral closing movement. The peak vertical velocity of the closing movement was also measured. Finally, the vertical position of the upper lip was measured at the point in time when the lower lip reached its peak vertical position. The displacement of the closing movement was calculated as the difference between the onset and offset vertical positions. The measurements of the upper lip closing movement were problematic due to interactions between the upper and lower lips. This is illustrated in Fig. 1, showing a short (left panel) and a long (right panel) nasal consonant produced by Japanese subject NY. The shaded areas in the left and right panels show the lip movements during the nasal consonant. In the production of the short nasal in ''sama'' (left panel), there is only one zero-crossing in the upper lip velocity signal during the consonant. However, in the production of the long nasal in ''samma'' (right panel), there are three zero-crossings in the upper lip velocity signal during the consonant. They occur because the lower lip checks the descent of the upper lip and pushes it upward, as can be seen in the upper lip position signal [see Löfqvist and Gracco (1997) for a detailed analysis of these patterns]. Thus, the upper lip displacement could not be reliably measured, in particular for the long consonants where most of these interactions occurred. The peak velocity of the upper lip closing movement was measured, however, since it occurs before the lips meet; the arrows in Fig. 1 show the peak velocities of the upper and lower lip closing movements. Similarly, the peak closing velocity of the lip aperture signal was measured.

T-tests were used to assess differences between the long and short consonants for each subject. With 50 repetitions of each word, the tests have 98 degrees of freedom. To adjust

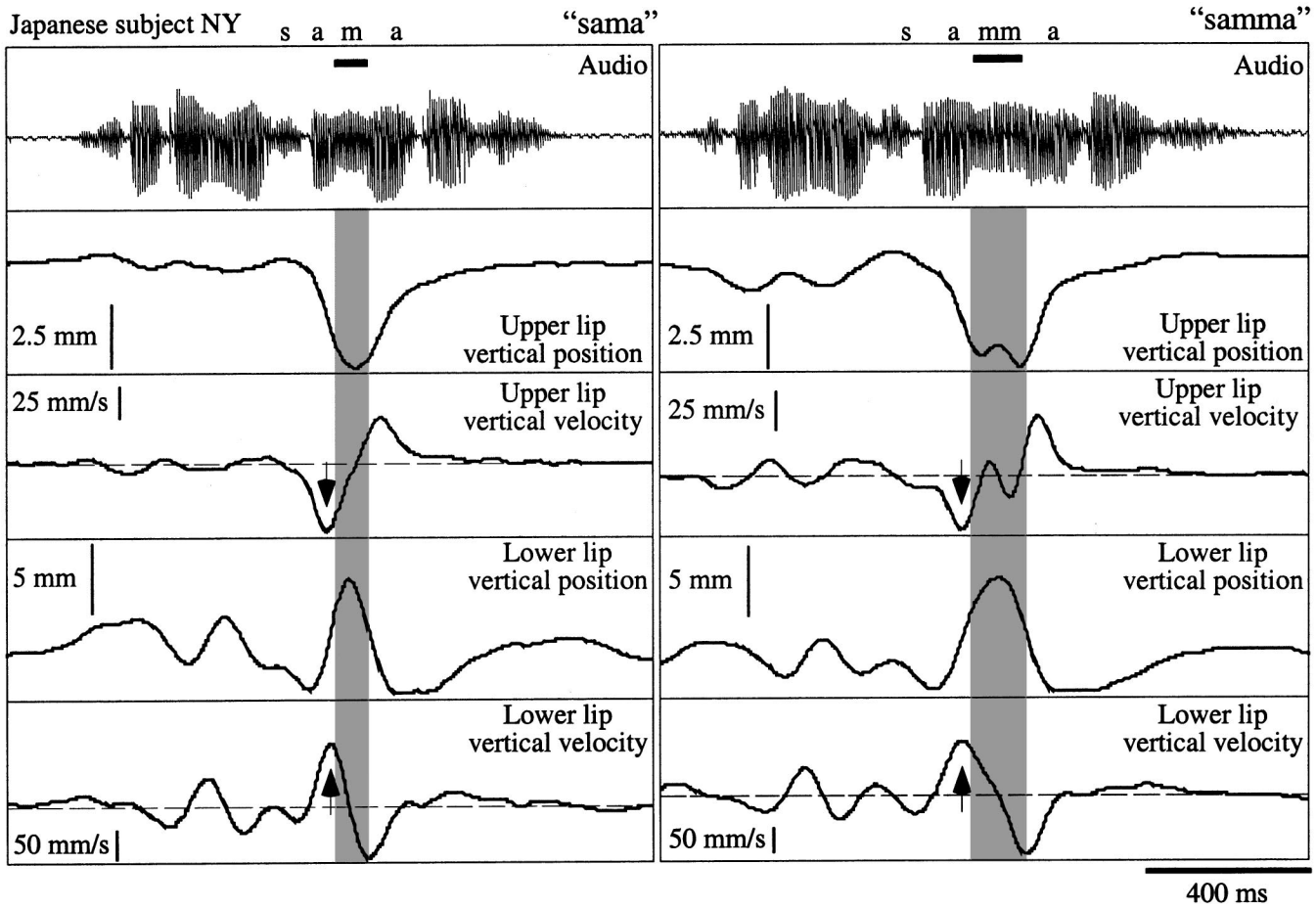

FIG. 1. A short (left panel) and a long (right panel) nasal consonant produced by Japanese subject NY. The shaded area in each panel shows the oral closure for the consonant. The arrows point at the peak velocities of the upper and lower lip closing movements.

for an elevated type I error rate due to multiple comparisons, a conservative α-level of 0.001 was adopted.

III. RESULTS

A. Closure duration

Figure 2 presents the duration of the oral closure/constriction for the Swedish subjects. In Fig. 2, there is considerable overlap between the closure durations for the long and short consonants, in particular for subject AG. The statistical analysis revealed that subject AG did not reliably distinguish the closure durations of the long and short voiceless consonant /p/, $t(98)=2.23$, ns, but did so for the voiced stop /b/, $t(98)=5.01$, $p<0.001$, the nasal /m/, $t(98)=7.87$, $p<0.001$, and the fricative /f/, $t(98)=9.98$, $p<0.001$. In contrast, Swedish subject NR reliably used different closure/constriction durations for all the consonants, $t(98)=15.57$, 7.79, 7.52, and 20.21, for /p,b,m,f/, respectively, with $p<0.001$ in all cases. Figure 3 plots the same results for the Japanese subjects. Here, and in contrast to the Swedish results, there is no overlap between the closure/constriction durations for the long and short consonants for any of the subjects or consonants. The closure/constriction duration of the long consonant is about twice as long as that for the short ones. The statistical analysis showed that all the Japanese subjects produced highly significantly different closure/constriction durations for the long and short consonants, $t(98)=41.44$, 24.99, 29.38, and 34.18 for the labial stop /p/ for subjects HI, Y, NY, and SS, respectively. The corresponding t values for the labial nasal /m/ were 38.12, 24.89, 29.84, and 32.35 for subjects HI, MY, NY, and SS, respectively, and 34.79, 42.12, 29.7, and 31.2 for the bilabial fricative for subjects HI, MY, NY, and SS, respectively.

B. Movement kinematics

Figure 4 shows signal averages (aligned to the beginning of the acoustic closure) of the lip and jaw movements for the four Japanese subjects, since many of the subsequent analyses will be focused on these subjects. The arrows show the direction of the movement (they have been left out for the jaw since its movement was very small). Note that the window used for signal averaging includes movements during the vowels before and after the short consonants. Since the lip receivers were placed at the vermilion border of the upper and lower lips, the lip receivers are about 0.5–1.5 cm apart vertically when the lips are closed. With one exception, the lower lip of Japanese subject HI in Fig. 4(a), all the lip movements predominantly occur in the vertical dimension. Thus, the focus on the vertical movement dimension is justified. A comparison of the lower lip movement patterns for the long and short consonants in Fig. 4 shows that the lower lip tends to reach a higher vertical position for the long

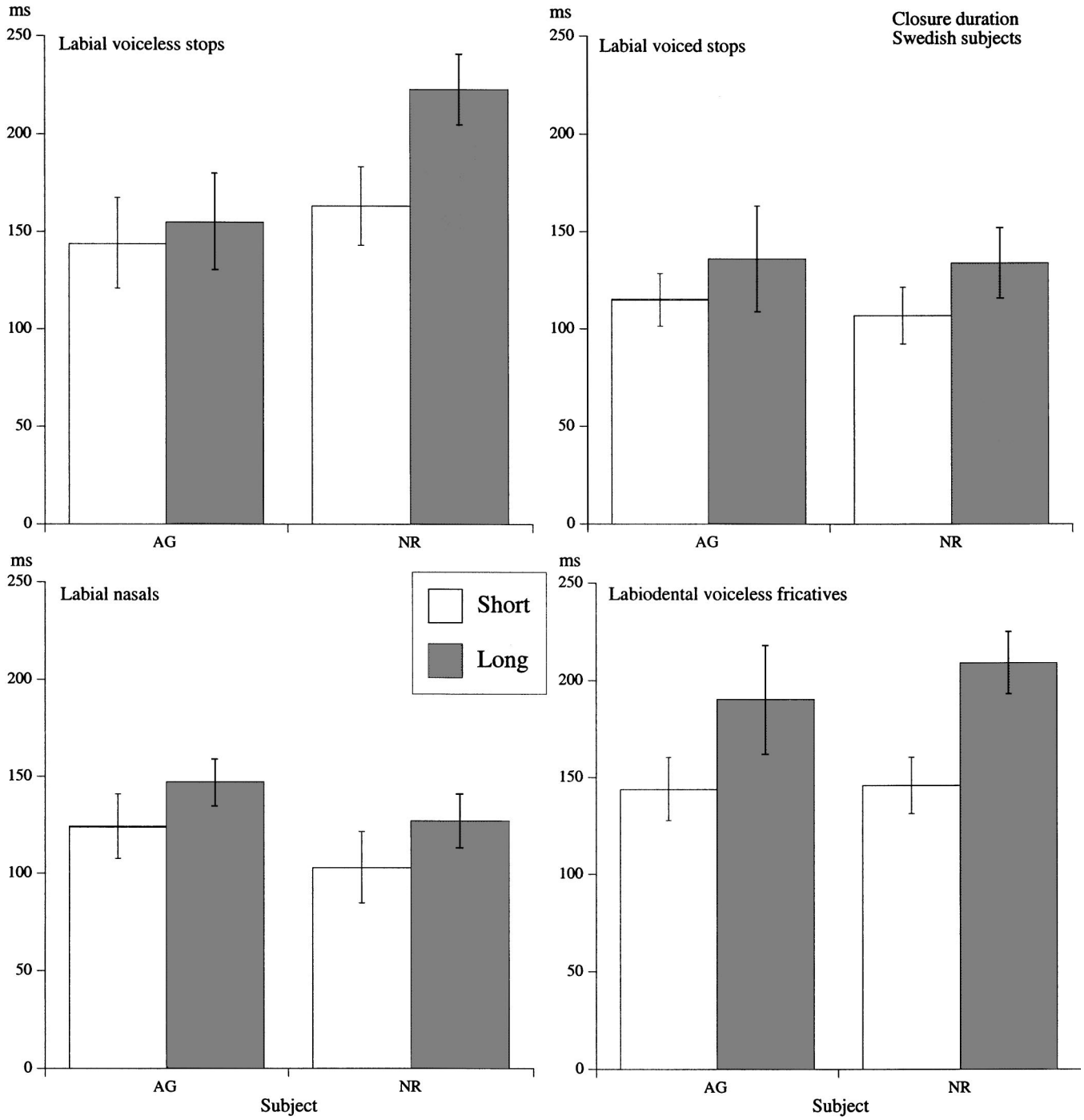

FIG. 2. Closure duration (mean and standard deviation) for the Swedish subjects.

(dashed lines) than for the short ones (solid lines) for all subjects, although the magnitude of the difference varies between subjects. The difference is in the order of a few mm, in particular for Japanese subjects MY, NY, and SS. It is also evident in Fig. 4 that the lip movements differ for the stop and the nasal, on the one hand, and the fricative, on the other; the fricative is bilabial. In particular, the lower lip reaches a lower vertical position for the fricative than for the stop and the nasal, while the upper lip has a higher position during the fricative than during the stop and the nasal.

The main focus of this study is on the kinematics of the lower lip. An analysis of jaw movements revealed no consistent differences between the long and short consonants; the jaw movements were very similar. As mentioned above, the analysis of upper lip movements is complicated by interactions between the upper and lower lips. That is, the upper lip lowering movement was often checked by the lower lip raising movement. These interactions also depend on the positions of the lip receivers (cf., Löfqvist and Gracco, 1997, for a more detailed analyses of such interactions). Figure 5 presents the results of the peak upper lip lowering velocity for the Swedish and Japanese subjects' productions of the short and long stop and nasal consonants; for the fricatives, the upper lip movement was very small and often less than 1

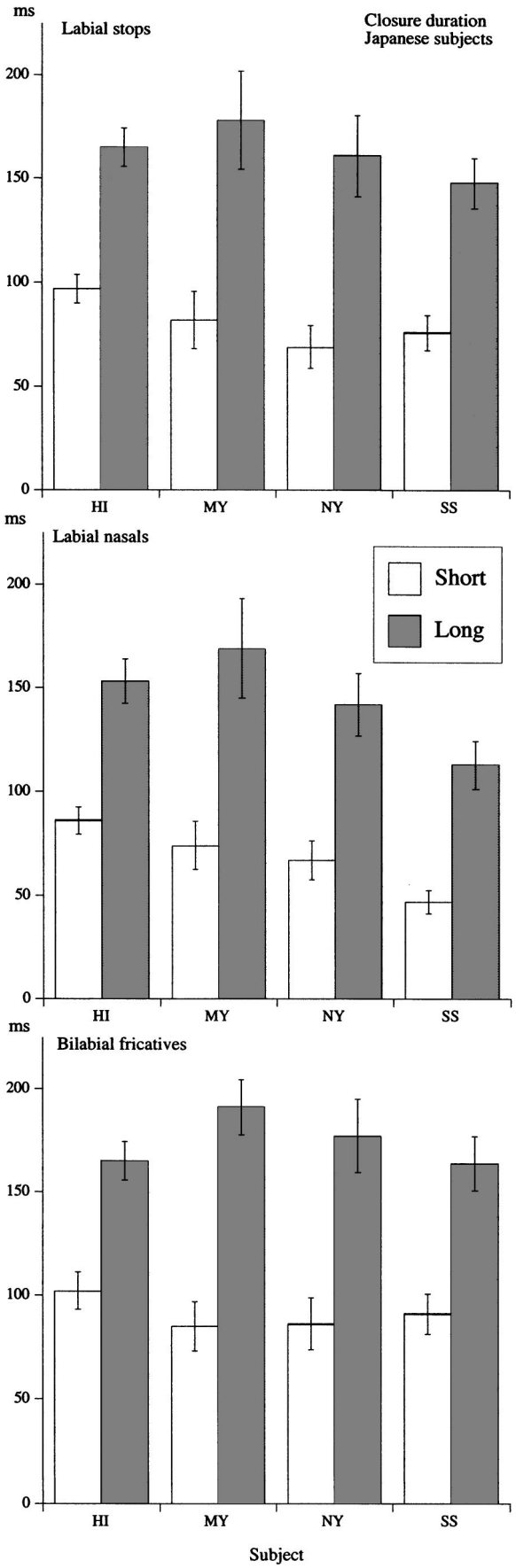

FIG. 3. Closure duration (mean and standard deviation) for the Japanese subjects.

mm. From Fig. 5, it is evident that there is no overall pattern for the speakers. The Swedish speaker AG produced the short and long consonant with almost identical velocities of the upper lip. On the other hand, Swedish speaker NR produced all the long consonants with a significantly higher velocity of the upper lip than the short ones [$t(98)=10.87$, 12.62, and 12.34 for /p,b,m/, respectively, $p<0.001$]. In contrast, the Japanese speakers tended to use higher upper lip velocities for the short consonants than for the long ones. For the labial stops, the upper lip velocity difference was significant for subjects HI, NY, and SS, $t(98)=7.12$, 4.56, and 3.34, $p<0.001$. For the nasals, the diference was significant for subjects HI, MY, and SS, $t(98)=15.61$, 6.65, and 6.01, $p<0.001$.

C. Peak vertical lower lip position during the closure

Figure 6 plots the peak lower lip vertical position for the Swedish subjects. According to the hypothesis, the lower lip should reach a higher vertical position for the long than for the short consonants. The results for the two subjects differ, however. A comparison between the peak lower lip position for the long and short consonants showed no significant difference for Swedish subject AG, $t(98)=2.01$, 1.61, 1.61, and 0.39 for /p,b,m,f/, but significant differences for Swedish subject NR, with the lower lip reaching a slightly higher position for the long consonants., $t(98)=6.8$, 4.9, 7.56, and 5.18 for /p,b,m,f/, with $p<0.001$ in all cases.

Figure 7 plots the same results for the Japanese subjects. Here, the peak lower lip position was significantly higher for the long than for the short consonants for all four Japanese subjects. For HI, $t(98)=4.22$, 8.4, and 15.58 for the stop, nasal, and fricative, respectively, with $p<0.001$. The corresponding t statistics for Japanese subject MY were 10.7, 11.99, and 8.51, for Japanese subject NY 17.55, 21.77, and 12.25, and for Japanese subject SS 26.62, 23.38, and 15.12.

These results thus mostly agree with the prediction of a higher peak lower lip vertical position during the closure for the long than for the short consonants. All the Japanese subjects and one of the Swedish subjects produced the long consonants with a higher lower lip vertical position during the closure/constriction for the long than for the short consonants. Due to the overlap in closure/constrictions durations for the Swedish consonants and their more restricted ranges than those of the Japanese subjects, the Swedish data are not particularly useful for testing the original hypothesis. Thus, in the following, the focus will be on the Japanese results.

D. Interactions between the lips

Table I presents the vertical position of the upper lip at the point in time when the lower lip reaches its highest vertical position for the Japanese subjects. As predicted, the upper lip vertical position at the point in time when the lower lip reaches its highest vertical position was significantly higher for the long than the short consonants for subject HI [$t(98)=3.45$, 7.04, and 7.09, for the stop, nasal, and fricative, respectively, with $p<0.001$], the stops and nasals of subjects MY [$t(98)=3.54$, and 5.94] and SS [$t(98)=11.28$ and 4.61], and the stops of subject NY [$t(98)=9.07$]. How-

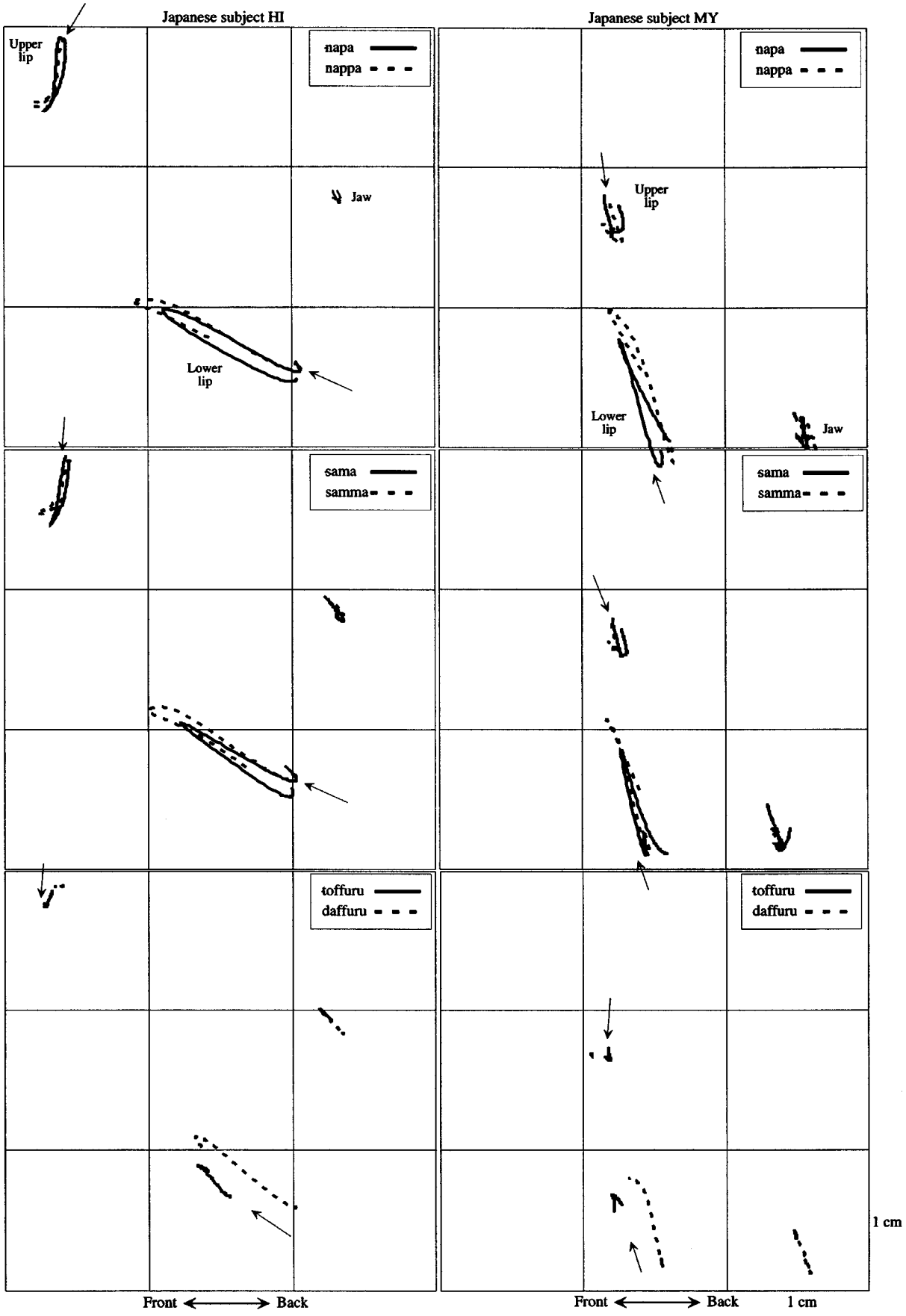

FIG. 4. Average lip and jaw signals for the Japanese subjects HI and MY. The arrows show the direction of movement. The subjects are facing to the left. Average lip and jaw signals for the Japanese subjects NY and SS. The arrows show the direction of movement. The subjects are facing to the left.

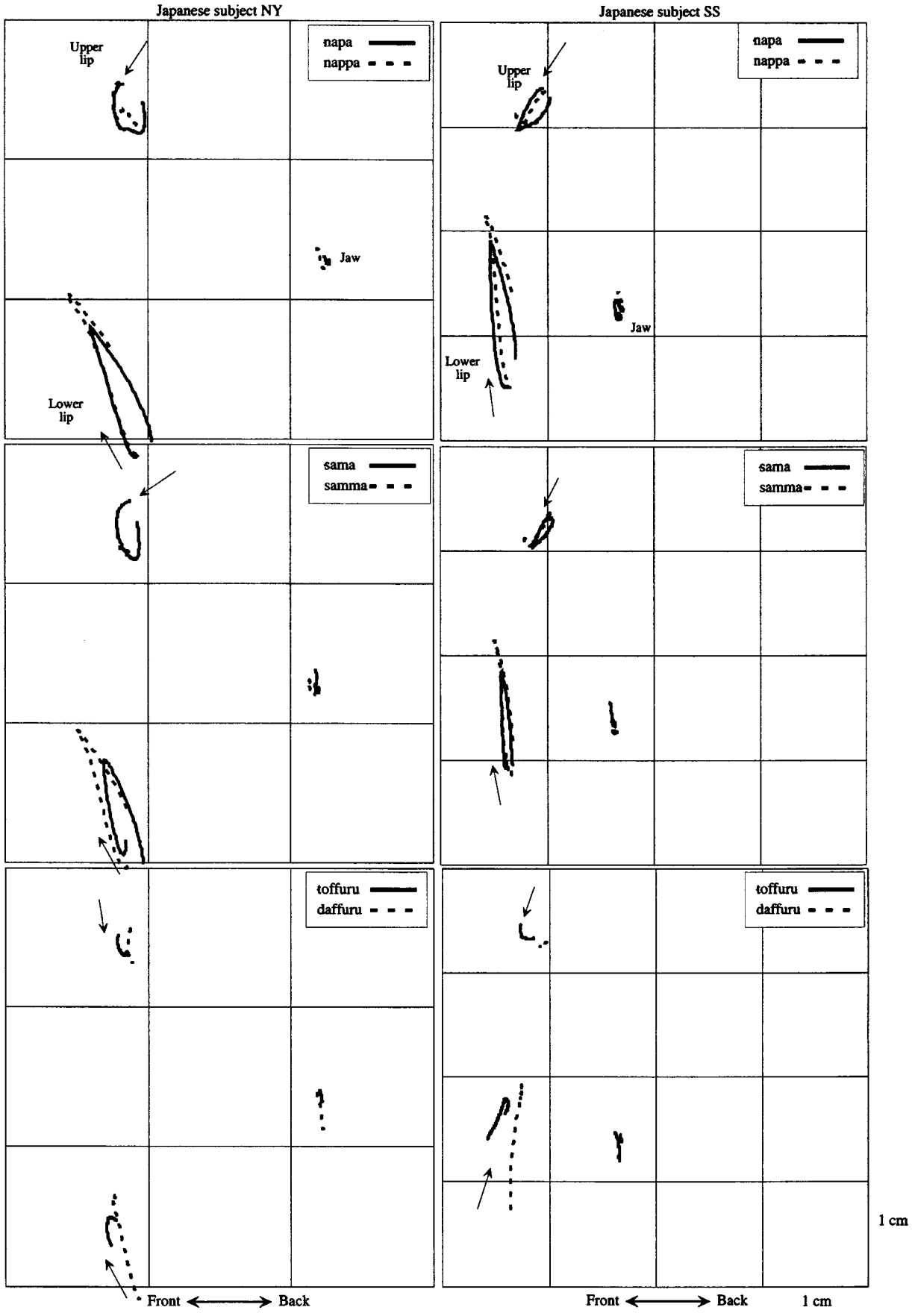

FIG. 4. (*Continued*.)

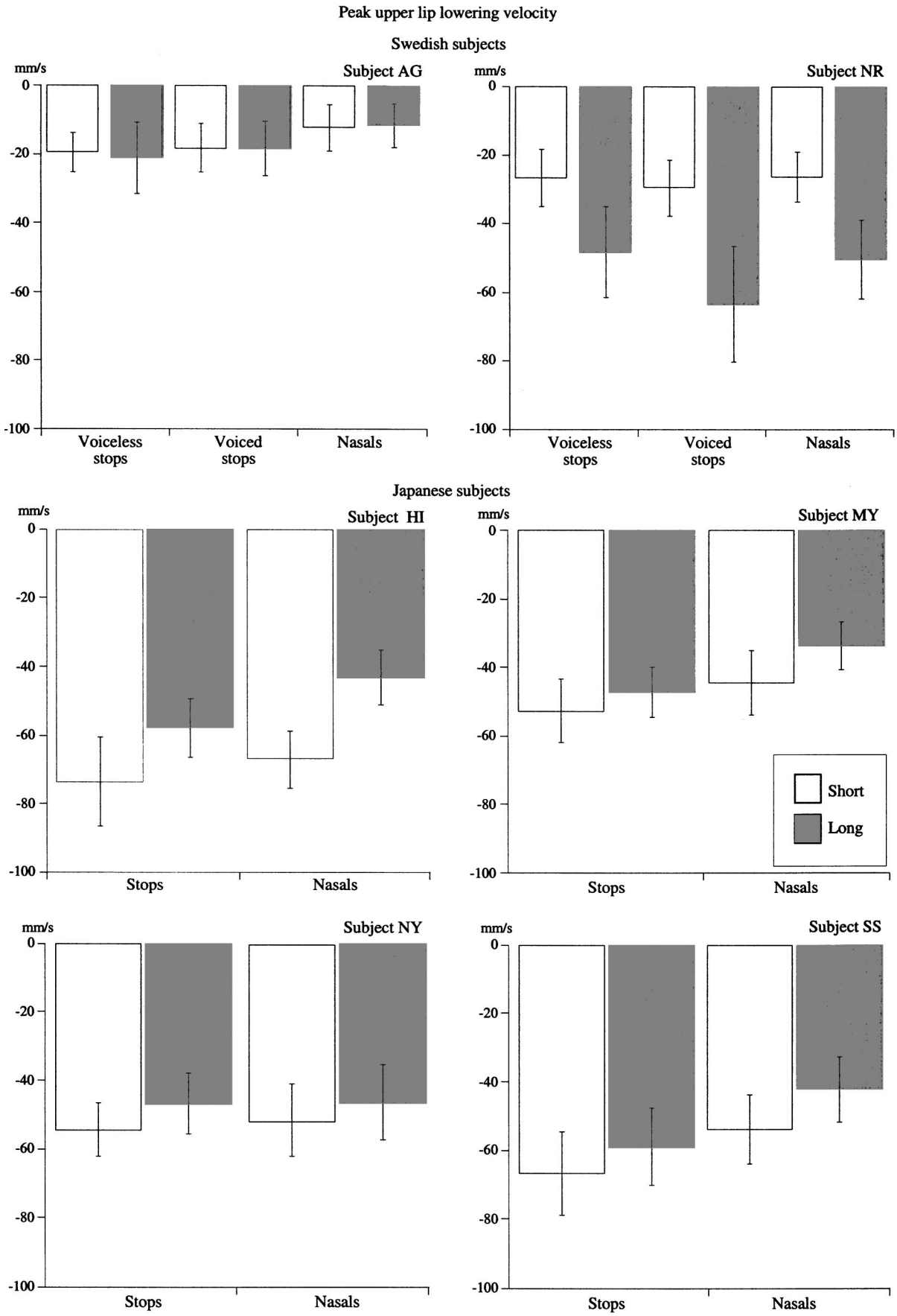

FIG. 5. Peak upper lip lowering velocity for the Swedish and Japanese subjects (mean and standard deviation).

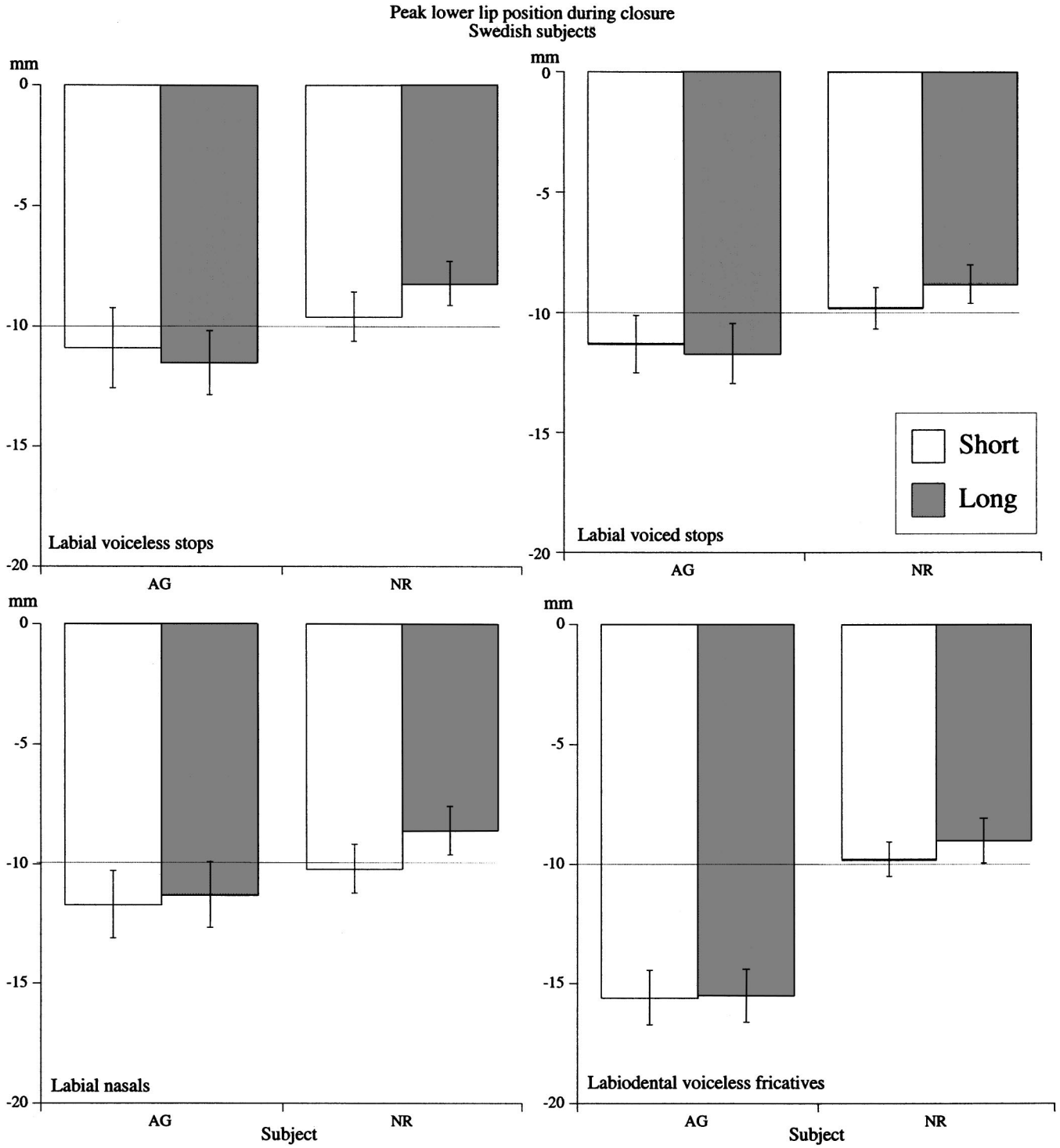

FIG. 6. Peak lower lip vertical position (mean and standard deviation) for the Swedish subjects.

ever, the fricatives of subjects NY and SS showed significant higher upper lip positions for the short than for the long consonant [$t(98)=4.41$, and 3.32, $p<0.001$]. There was no difference for the fricative of Japanese subject MY [$t(98=2.34)$], and for the nasals of subject NY [$t(98)=2.5$].

E. Lower lip closing displacement

The third hypothesis predicts that the lower lip closing displacement is larger for the long than for the short consonants. In an attempt to make the vertical onset position of the lower lip closing movement as similar as possible, the vowel context of the labial consonants were made similar. However, both the Swedish subjects produced the long and short consonants with different onset positions of the lower lip. It was always lower for the long consonants, most likely reflecting the more open vowel quality of the preceding short vowel and with higher first and, often, second formant frequencies than its long cognate (Fant, 1973). Thus, the hypotheses about larger lower lip closing displacements and velocities in long consonants could not be assessed for the

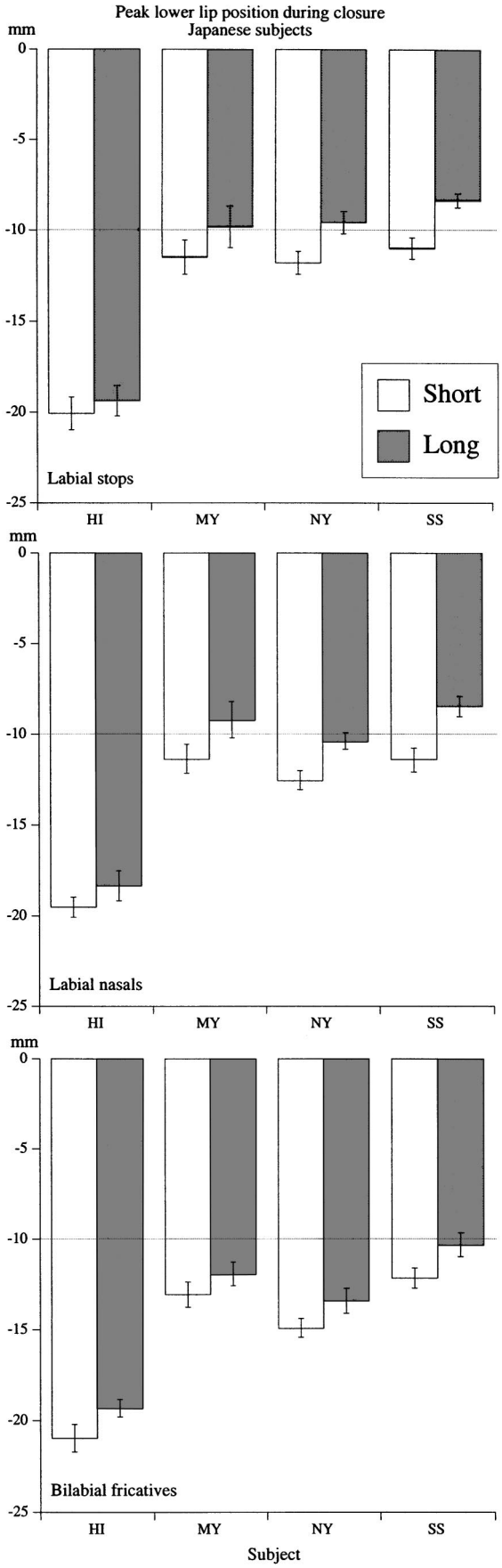

FIG. 7. Peak lower lip vertical position (mean and standard deviation) for the Japanese subjects.

TABLE I. Japanese subjects' upper lip vertical position at the point in time of lower lip peak vertical position (mm). The standard deviation is shown within parentheses.

Subject	p	pp	m	mm	f	ff
HI	−5.9	−5.4	−5.3	−4.3	−2.0	−1.2
	(0.81)	(0.8)	(0.6)	(0.84)	(0.71)	(0.42)
MY	−4.7	−4.0	−4.7	−3.7	−3.1	−3.3
	(1.13)	(0.97)	(0.72)	(0.95)	(0.42)	(0.5)
NY	2.2	3.4	2.0	2.5	3.8	3.2
	(0.49)	(0.84)	(0.73)	(1.04)	(0.69)	(0.7)
SS	−0.3	1.1	0.3	1.1	3.2	2.8
	(0.8)	(0.4)	(0.7)	(0.97)	(0.61)	(0.62)

Swedish subjects. Similarly, all four Japanese subjects produced the long bilabial fricative with a significantly lower lip onset position than its short cognate, so these two hypotheses could not be verified for this consonant in the Japanese material.

Table II summarizes the lower lip closing displacement for the stops and nasals for the Japanese subjects. For all subjects, the lower lip displacement is larger for the long than for the short consonants. The *t*-tests showed all the differences between the lower lip displacement for the long and short stops to be significant [Japanese subject HI: $t(98) = 3.83$; Japanese subject MY: $t(98) = 4.89$; Japanese subject NY: $t(98) = 11.02$; Japanese subject SS: $t(98) = 9.66$, with $p < 0.001$ in all cases]. The same was true for the nasals [Japanese subject HI: $t(98) = 7.33$; Japanese subject MY: $t(98) = 8.35$; Japanese subject NY: $t(98) = 17.41$; Japanese subject SS: $t(98) = 18.12$, with $p < 0.001$ in all cases].

Since this result could be due to a difference in onset position, offset position, or both, Table III shows the vertical onset position of the lower lip closing movement. The *t*-tests revealed no significant differences in the lower lip onset position between long and short consonants except for the nasals of subjects NY [$t(98) = 6.61, p < 0.001$] and SS [$t(98) = 18.12, p < 0.001$], which had a lower position for the long than for the short consonants.

The hypothesis about a larger lower lip raising displacement for the long than for the short consonants was supported by the results for the Japanese productions of stops and nasals. Moreover, there was no difference in the onset position of the lower lip closing movement between the long and short consonants, with two exceptions. However, inspection of Fig. 7 and Table III shows that the difference in the peak lower lip position for the nasals is 2.1 and 2.9 mm for subjects NY and SS, respectively, while the difference in the

TABLE II. Japanese subjects' lower lip raising displacement (mm). The standard deviation is shown within parentheses.

Subject	p	pp	m	mm
HI	4.5	5.1	4.2	5.3
	(0.78)	(0.73)	(0.58)	(0.87)
MY	9.7	11.3	7.6	9.9
	(1.53)	(1.65)	(1.22)	(1.5)
NY	9.6	11.6	6.8	10.0
	(0.99)	(0.82)	(0.85)	(0.95)
SS	13.9	16.5	9.4	13.1
	(0.5)	(1.46)	(1.02)	(1.03)

TABLE III. Japanese subjects' lower lip verical position at the onset of the closing movement. The standard deviation is shown within parenthesis.

Subject	p	pp	m	mm
HI	−24.6	−24.5	−23.7	−23.6
	(0.78)	(0.83)	(0.5)	(0.46)
MY	−21.7	−21.1	−19.0	−19.1
	(1.37)	(1.09)	(1.01)	(0.93)
NY	−21.4	−21.1	−19.4	−20.4
	(1.01)	(0.75)	(0.63)	(0.84)
SS	−24.9	−24.9	−20.8	−21.6
	(1.12)	(1.39)	(0.88)	(1.09)

onset position is 1.0 and .8 mm. Thus, the difference in the peak lower lip position is greater than the difference in the lower lip onset position. Hence, the results the nasals of subjects NY and SS are compatible with the original hypothesis about a larger closing displacement of the lower lip for the long than for the short consonants.

F. Lower lip peak closing velocity

The next hypothesis to be evaluated predicts that the peak closing velocity of the lower lip is higher for the long than for the short consonants. This is based on the commonly found strong relationship between movement displacement and peak velocity (e.g., Cooke, 1980; Ostry *et al.*, 1983; Kelso *et al.*, 1985; Vatikiotis-Bateson and Kelso, 1993; Hertrich and Ackermann, 1997; Löfqvist and Gracco, 1997). Figure 8 plots the peak velocity of the lower lip closing movement for the Japanese subjects' production of stops and nasals. Contrary to the prediction, there were no significant differences between the peak closing velocity of the lower lip between the long and short consonants except for the stops of subject MY $[t(98)=3.44, p<0.001]$, but here the short stops were produced with a higher lower lip closing velocity. Thus, this particular prediction was not supported by the data. This is puzzling given the commonly observed very strong correlation between movement displacement and peak velocity. To provide a closer view of this particular relationship, Fig. 9 plots the lower lip displacement and peak velocity separately for the long and short consonants, the stops in Fig. 9(a) and the nasals in Fig. 9(b). Interestingly, the expected positive relationship only holds within the long and short consonants, but not between them. All the correlations are significant and all are above 0.9, with the exception of the long stops and nasals of subject NY (lower left panels in Fig. 9). The predicted results would have the data points for the long and short consonants form a continuous function, with the long ones, the open triangles, being higher than the short ones, the filled squares. Thus, these results strongly suggest that these subjects do not control the duration of the oral closure in long and short consonants by only varying the position of a virtual target of the lower lip during the oral closure: The long and short consonants have different control regimes. The original hypothesis is thus wrong. So, how do these subjects control the duration of the oral closure? One potential answer is provided by the slopes of the regressions shown in Fig. 9. This slope is one representation of the stiffness of the movement (cf. Kelso *et al.*, 1985). For all subjects except HI (where the slopes are almost identical), the slopes are higher for the short than for the long consonants, thus suggesting that the short consonants are produced with stiffer movements. However, examination of the 95% confidence intervals for the slopes of the long and short consonants only showed no overlap for subject MY.

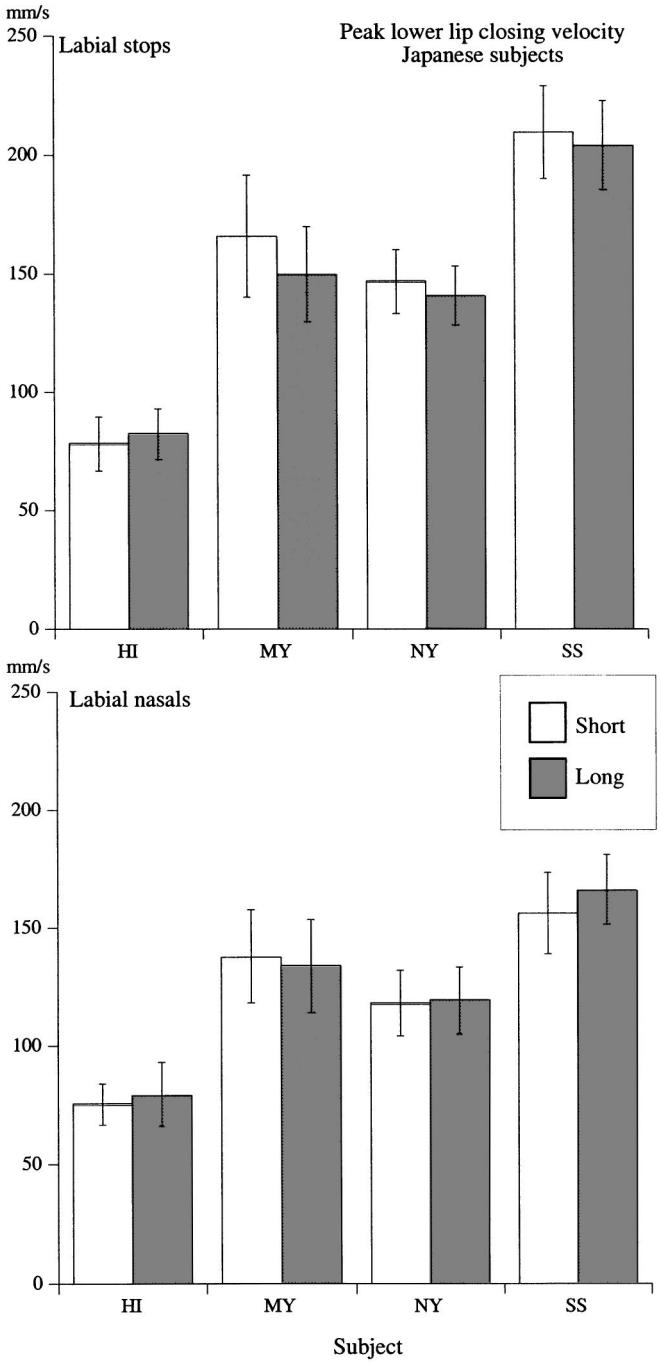

FIG. 8. Peak velocity of the lower lip closing movement (mean and standard deviation) for the Japanese subjects.

Before examining movement stiffness in more detail, we will look at the peak closing velocity of the derived lip aperture signal. The results are shown in Table IV. The first thing to note is that in most of the cases, the short consonant is produced with a higher lip aperture closing velocity; the only exceptions are the nasals of subject SS, where the long consonant has a higher velocity, and of subject NY, where

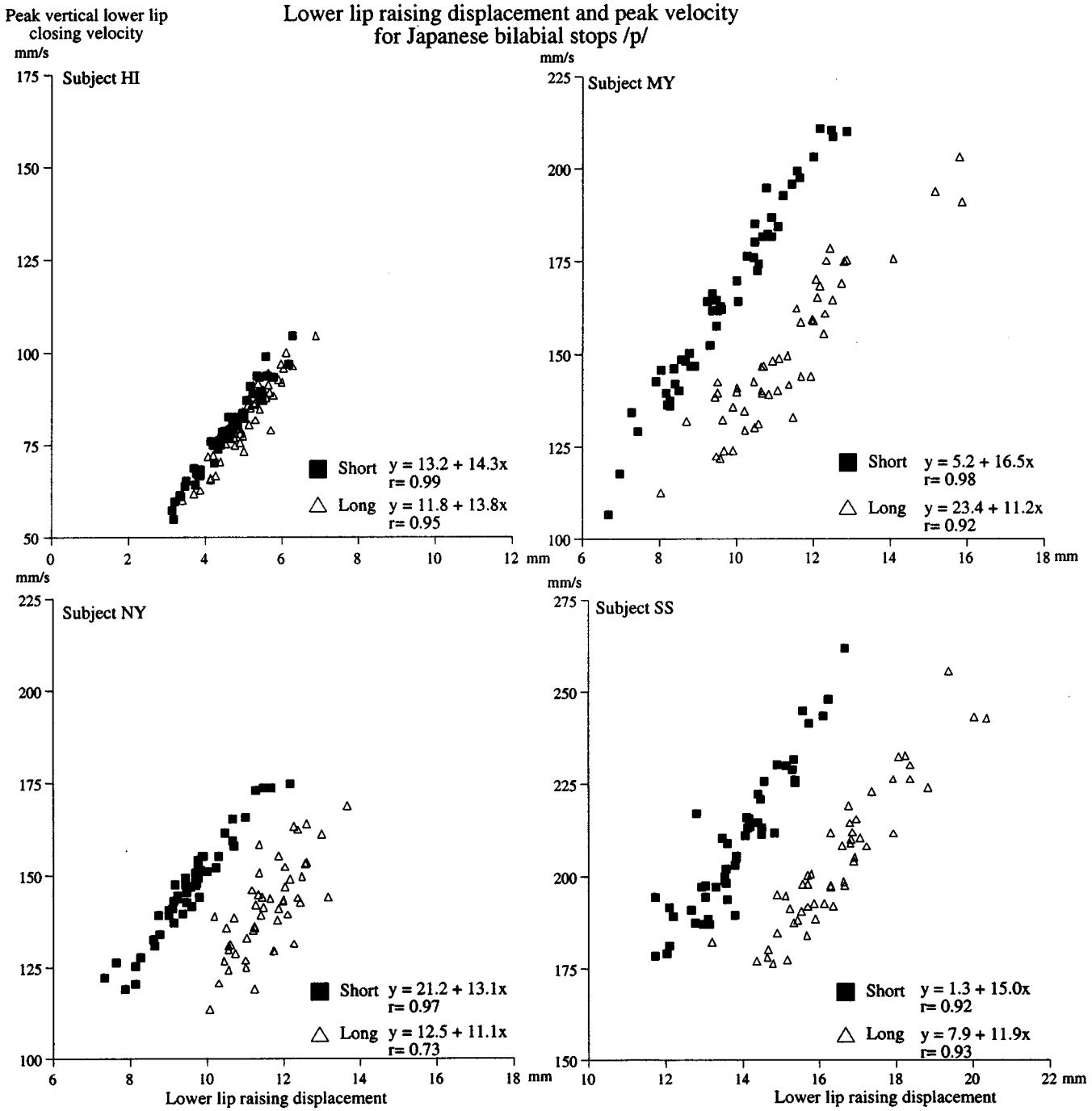

FIG. 9. Lower lip raising displacement and peak velocity for the Japanese subjects' production of labial stops. Lower lip raising displacement and peak velocity for the Japanese subjects' production of labial nasals.

there is no difference. Overall, the difference is not very large, however, and the statistical analysis only showed three of the differences to be significant: the stops for subjects MY [$t(98)=3.93, p<0.001$] and NY [$t(98)=3.38, p<0.001$], and the nasals of subject HI [$t(98)=7.01$, $p<.001$].

G. Velocity and acceleration of the lower lip

Figures 10 and 11 plot averages (aligned to the beginning of the acoustic closure) of the lower lip position, velocity, and acceleration signals for the Japanese subjects' productions of labial stops and nasals, respectively; Fig. 10 shows the stops and Fig. 11 the nasals. The long consonants are shown by the dashed lines. Several observations can be made about these results. First, the position signals show that the peak position of the lower lip does not occur at the same point in time for the long and short consonants. Only for the stops of subject HI is there a similarity in the timing of the peaks in the position signals for the long and short consonants. For all other cases, the peak lower lip position occurs later in the long than in the short consonant. Second, the lower lip raising velocity signals for the short consonant show the bell-shaped characteristic of simple movements. However, for the long consonants, the velocity of the lower lip shows a change around the second zero crossing, just

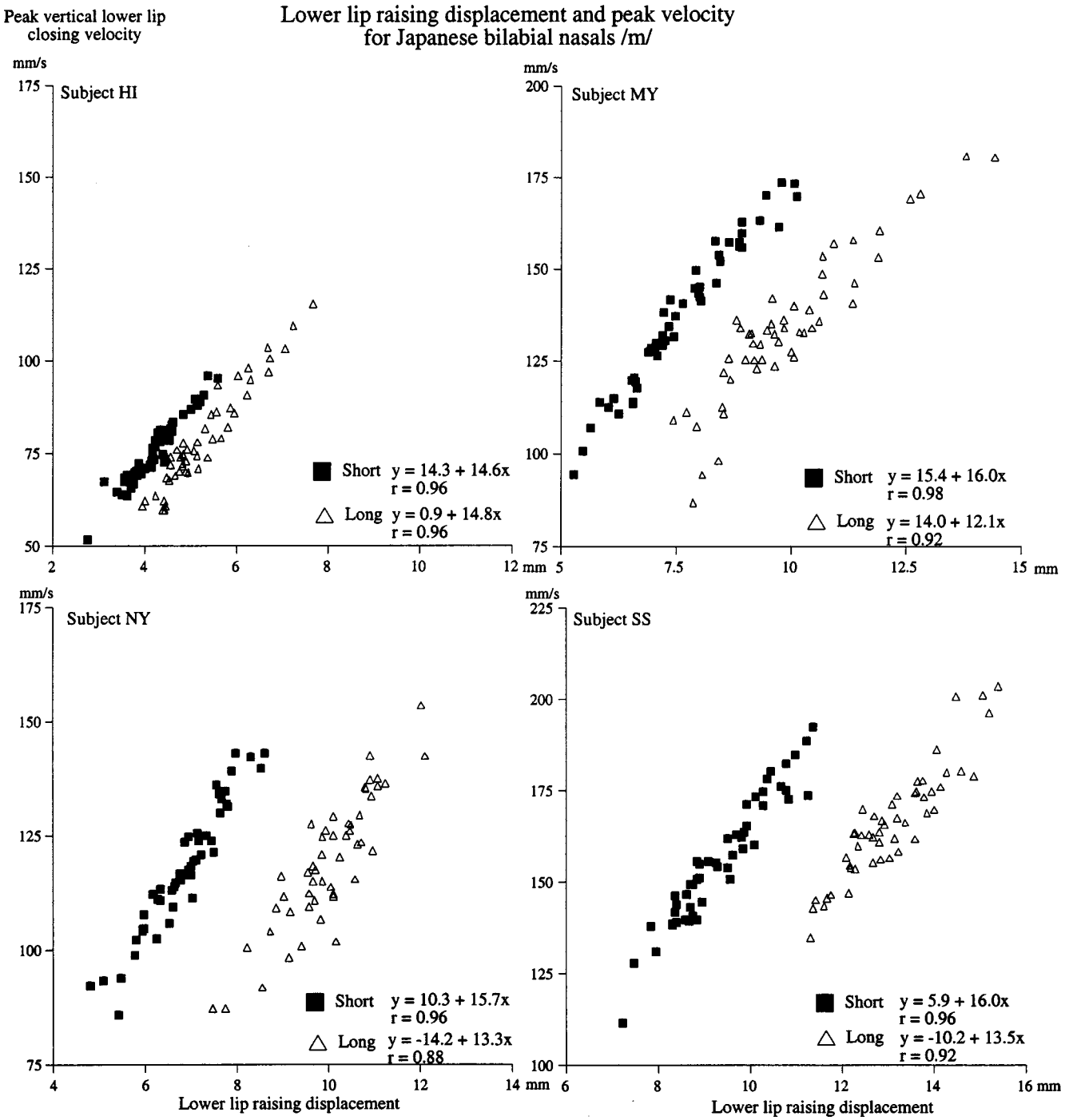

FIG. 9. (*Continued.*)

before it for subjects MY, NY, and SS, and just after it for subject HI, so that the velocity curve is not symmetric. Third, the acceleration signals indicate that the deceleration of the lower lip is momentarily reduced for the long consonants. This adjustment is apparently made to maintain the lower lip in a high position (subject HI) or keep it moving upwards (subjects MY, NY, and SS) and thus in contact with the upper lip for a longer period of time. For the long stops of subject HI, the deceleration almost reaches zero [lower left panel in Fig. 10(a)].

TABLE IV. Peak closing velocity of the lip aperture signal. The standard deviation is shown within parenthesis.

Subject	p	pp	m	mm
HI	−139.2	−128.8	−131.6	−113.5
	(13.79)	(10.04)	(11.16)	(14.53)
MY	−189.8	−173.3	−157.8	−149.0
	(23.11)	(18.67)	(17.69)	(17.44)
NY	−183.4	−173.2	−157.0	−157.1
	(14.75)	(15.24)	(19.51)	(20.38)
SS	−255.6	−243.9	−191.0	−195.5
	(24.44)	(25.03)	(18.9)	(18.2)

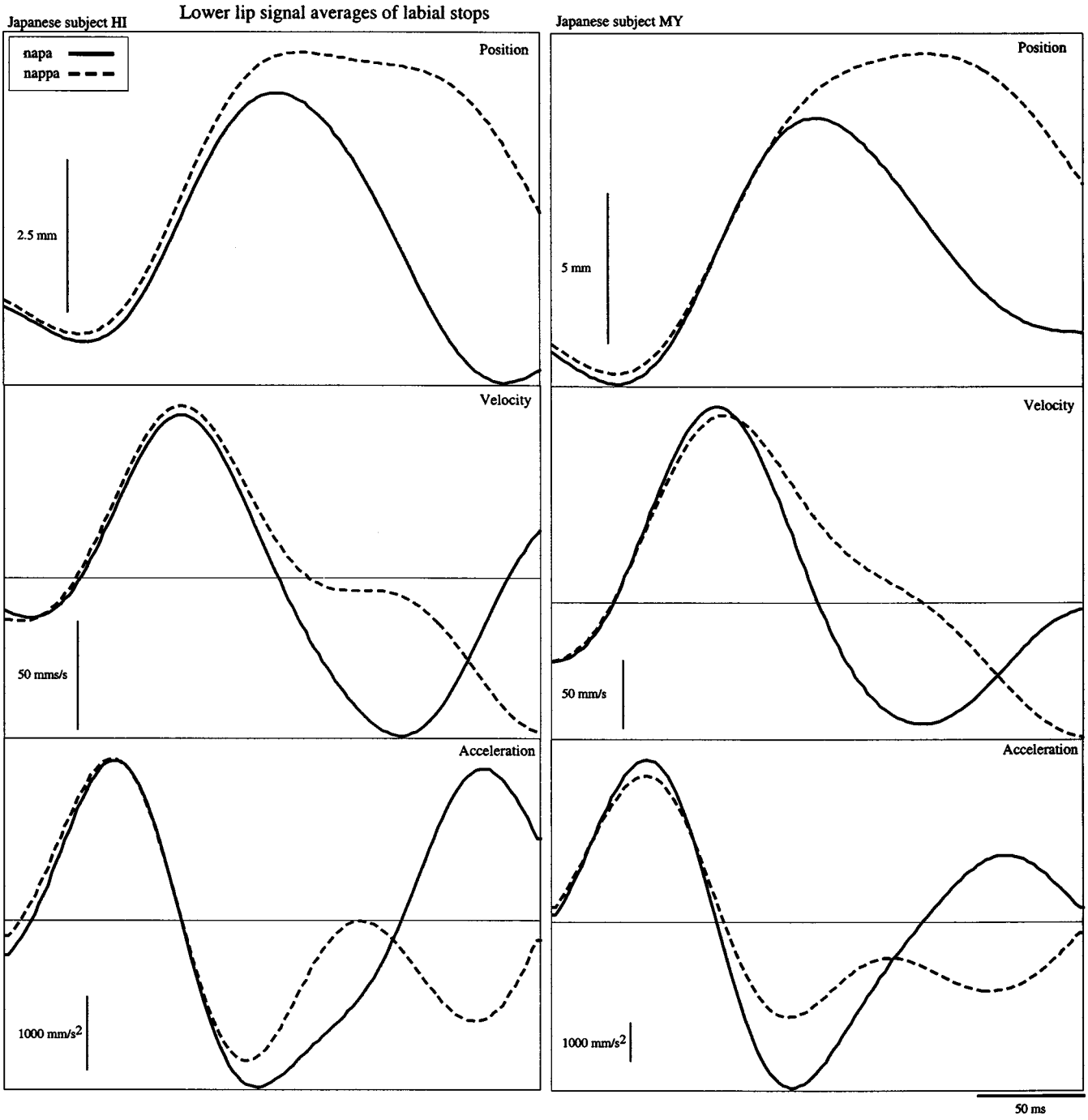

FIG. 10. Signal averages of lower lip position, velocity, and acceleration for the labial stops produced by the Japanese subjects HI and MY. The vertical line in the velocity and acceleration panels represents zero velocity and acceleration. Signal averages of lower lip position, velocity, and acceleration for the labial stops produced by the Japanese subjects NY and SS. The vertical line in the velocity and acceleration panels represents zero velocity and acceleration.

H. Movement stiffness

The regressions shown in Fig. 9 between the displacement and peak velocity of the lower lip closing movement suggest that there might be a difference in the stiffness of the movements for the long and short consonants. To pursue this issue in more detail, another measure of stiffness was calculated as the temporal interval between movement onset and peak velocity (cf. Adams *et al.*, 1993; Hertrich and Ackermann, 1997). This was applied to both the lower lip and lip aperture closing movements. The results are shown in Fig. 12. In all cases, this interval is shorter for the short than for the long consonants, suggesting a stiffer movement for the short than for the long ones. The statistical analysis showed this difference to be significant for the lower lip and the stops [Fig. 12(a)], $t(98) = 3.15$, 10.65, 9.36, and 9.42 for Japanese subjects HI, MY, NY, and SS, respectively, with $p < 0.001$ in all cases. The same was true for the lower lip and the nasals, $t(98) = 16.59$, 6.67, 17.63, and 9.33 for Japanese subjects HI, MY, NY, and SS, respectively, with $p < 0.001$ in all cases. For the lip aperture, shown in Fig. 12(b), this interval was

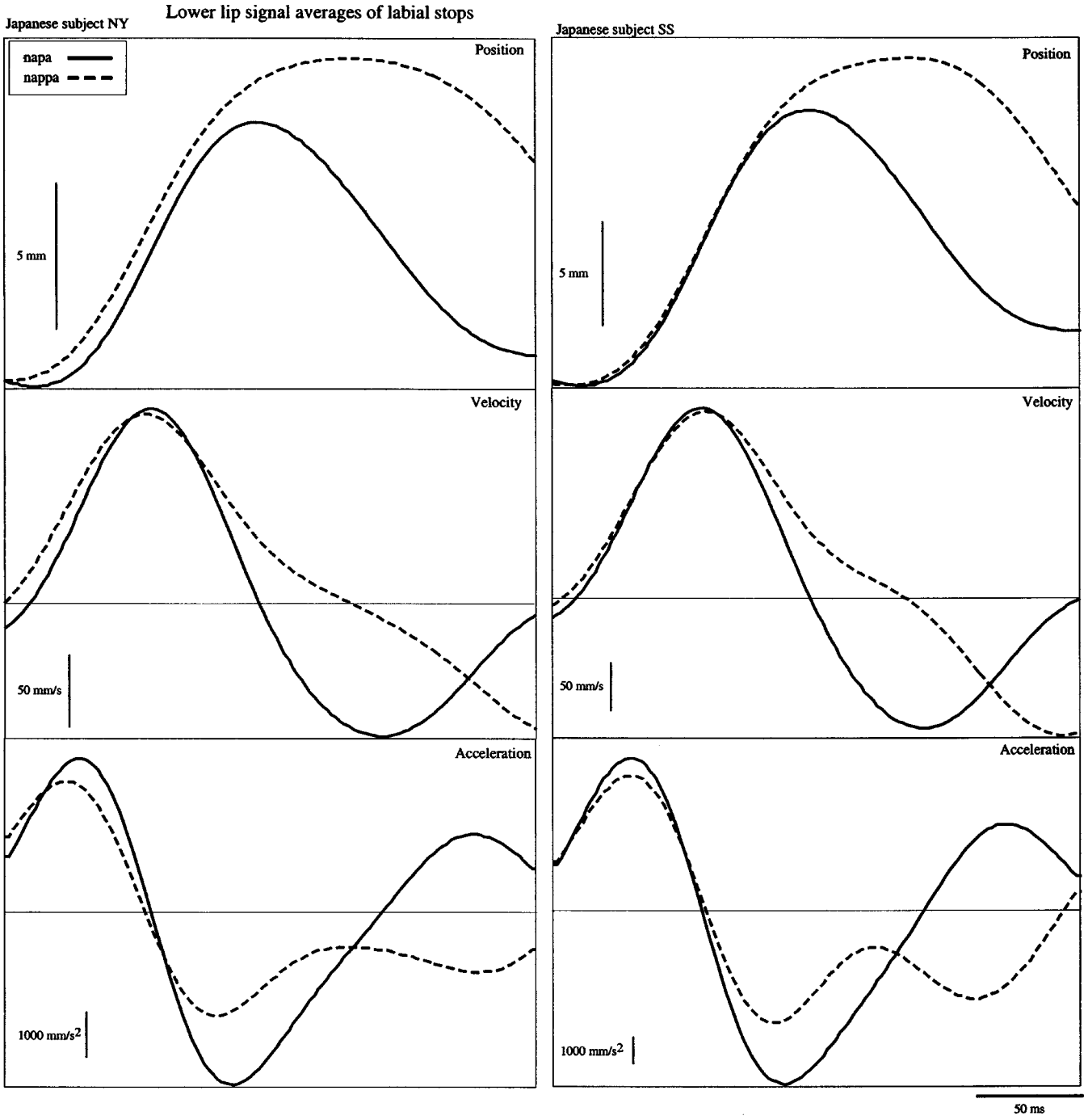

FIG. 10. (*Continued.*)

reliably shorter for the short than for the long stops in the three subjects MY, NY, and SS [$t(98)=6.4$, 6.87, and 9.47, with $p<0.001$ in all cases]. The large standard deviation for subject HI is due to the fact that it was sometimes hard to find a proper zero crossing in her lip aperture velocity signal. For the nasals, the interval was again shorter in the short than in the long consonants in three subjects HI, NY, and SS [$t(98)=8.16$, 10.96, and 8.25, with $p<0.001$ in all cases]. Subject MY did not show a statistical difference for the nasals.

IV. DISCUSSION

Consistent with the different structure of the length contrast in Swedish and Japanese, the distributions of closure/constriction duration for long and short consonants showed considerable overlap in the Swedish data but not in the Japanese data. As a consequence, the distributions of closure/constriction durations spanned a smaller temporal range in Swedish than in Japanese, making the Japanese data more suitable for testing the original hypothesis about virtual targets. As noted, in Swedish, there are variations in the duration and quality of the preceding vowel (cf. Hadding-Koch and Abramson, 1964; Fant, 1973). Overall the results for closure/constriction duration in Swedish and Japanese found in the present study are in close agreement with those obtained in other studies.

The results for all four Japanese speakers, and most of

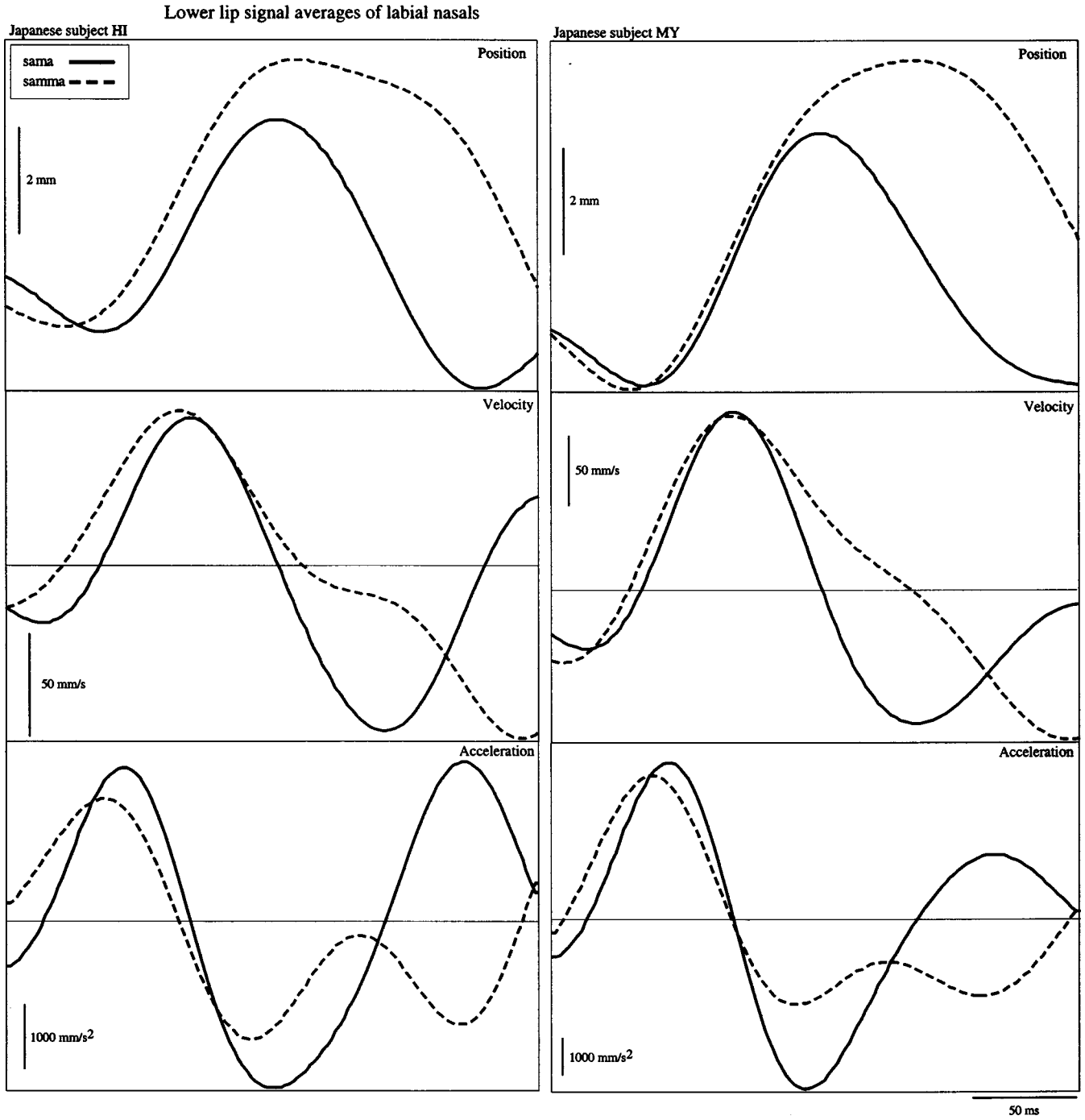

FIG. 11. Signal averages of lower lip position, velocity, and acceleration for the labial nasals produced by the Japanese subjects HI and MY. The vertical line in the velocity and acceleration panels represents zero velocity and acceleration. Signal averages of lower lip position, velocity, and acceleration for the labial nasals produced by the Japanese subjects NY and SS. The vertical line in the velocity and acceleration panels represents zero velocity and acceleration.

them for one of the Swedish speakers (NR), confirm three of the four predictions stated in the introduction: The lower lip reaches a higher vertical position during the closure for long than for short labial consonants (see the results for Swedish subject NR in the right half of the panels in Fig. 6, and all the results for the Japanese subjects in Fig. 7). As shown in Table I, the vertical position of the upper lip is higher at the point in time when the lower lip is at its highest position during the closure for the long stops and nasals, but generally not for the fricatives. This is most likely due to the complete oral closure for the stops and the nasal, whereas the fricative requires a narrow constriction. The closing movement of the lower lip has a larger displacement for long than for short consonants (Table II) which is generally due to a difference in the end position (Fig. 7) and not in the onset position (Table III). Crucially, however, the final prediction was not supported by the empirical results. That is, the predicted higher peak closing velocity of the lower for the long than for the short consonants was not found (Fig. 8). Thus, the observed differences in lower lip movement between long

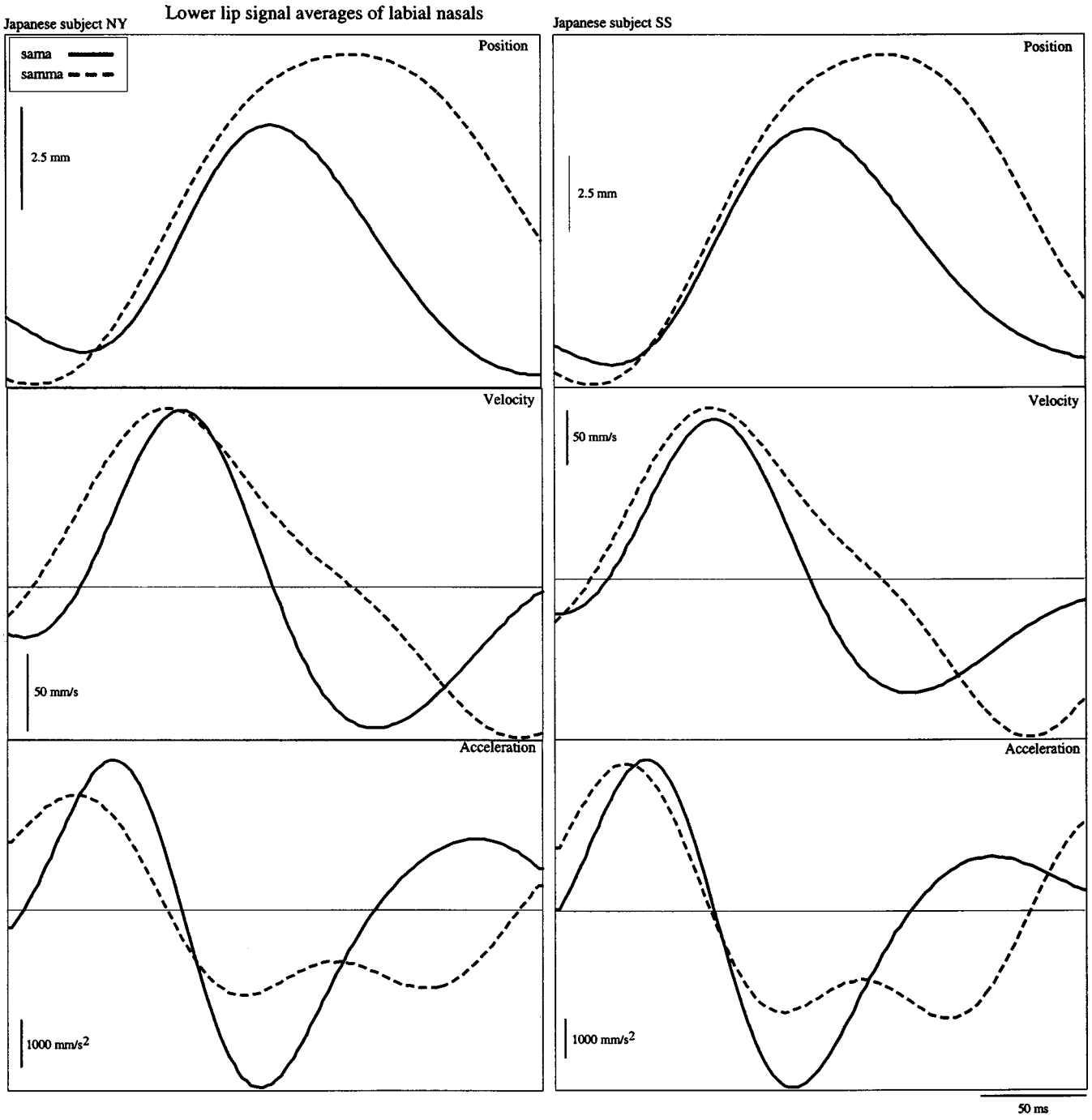

FIG. 11. (*Continued*.)

and short consonants are not due to a change only in virtual target position. Interestingly, the expected close relationship between movement displacement and peak velocity was only found to hold within the long and short consonants separately (Fig. 9) but not across them, as originally predicted. Assuming that speakers use virtual targets for consonant movements, these results suggest that the subjects did not produce the different closure/constriction durations by only changing the position of a virtual target, but rather by changing both its position and timing. In particular, they modified the deceleration of the lower lip movement to keep it in contact with the upper lip for a longer period of time (Figs. 10 and 11). The original hypothesis assumed a change only in the displacement of the underlying excitation pulse (cf. Gottlieb *et al.*, 1989), but the results also suggest that the duration of the pulse is changed. Although no electromyographic recordings were attempted in this study, such recording might show a longer duration of activity in the lower lip muscles for the long than for the short consonants (cf. Lehiste *et al.* 1973). At the same time, the lower lip movement pattern during the closure is affected by its contact with the upper lip. Recordings of the contact pressure between the lips could help in further clarifying their interactions.

The results shown in Fig. 2 for the Japanese subjects indicate that the lip movements predominantly occur in the vertical dimension, except for subject HI. Interestingly, the

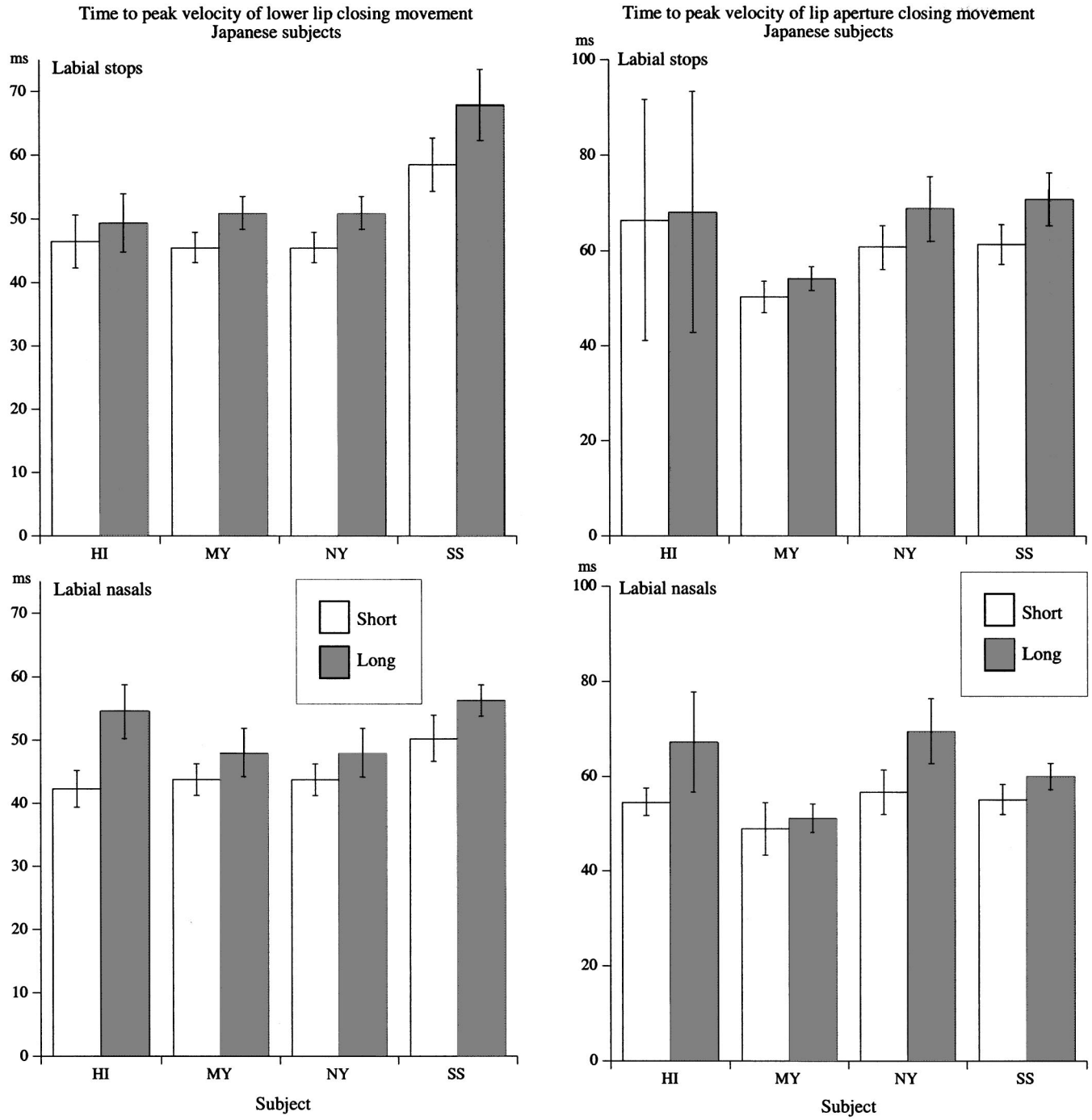

FIG. 12. The interval from movement onset to peak velocity (mean and standard deviation) of the lower lip closing movement for the Japanese subjects. The interval from movement onset to peak velocity (mean and standard deviation) of the lip aperture closing movement for the Japanese subjects.

movement pattern of her lower lip [shown in the left panels of Figs. 10(a) and 11(a)] shows that its peak position occurred approximately at the same time for the long and short consonants; for the other Japanese subjects the lower lip reached its highest position later for the long than for the short consonants. The results for subject HI also differed from those of the other three Japanese subjects in the upper lip movement pattern during the oral closure when the two lips interact. Specifically, all the upper lip movement patterns of subject HI were similar to the one shown in the left panel of Fig. 1, i.e., the lip kinematics during the production of a short labial nasal; this was also true for the long consonants. In contrast, the other three subjects generally showed a pattern like the one shown in the right panel of Fig. 1, where there is more than one zero-crossing in the upper lip velocity signal during the closure for a long consonant. Possibly, anatomical differences in bite type may explain these differences between the subjects. The movement trajectories shown in Fig. 4 indicate that the vertical separation between the upper and lower lip receivers during the oral closure is slightly larger for subject HI than for the other subjects. Although differences in receiver position will influence the nature and amount of observed lip interaction during the oral closure, the results shown in Table I do not indicate that subject HI

generally shows a different pattern of upper and lower lip interaction that might be due to different receiver placement.

Although no systematic differences in jaw kinematics were found between the long and short consonants, the upper lip lowering movement peak velocity was higher for the short than for the long consonants in the Japanese subjects (Fig. 5), but not always statistically significant. Similarly, the lip aperture closing velocity tended to be higher for the short than the long consonants, although the differences were only significant in three cases (Table IV). These trends are similar to the results presented by Smith (1995). At the same time, the Swedish subject who produced the long and short consonants with different durations (NR) produced the long ones with a higher upper lip closing velocity than the short ones, cf. Fig. 5. Interestingly, Smith (1995) found a similar difference between Japanese and Italian.

The lip movements of the short consonants tended to be made with higher stiffness, measured both in the lower lip and in the lip aperture signal (Fig. 12). This might be due to the shorter movement times of the lips for the short consonants, since movement stiffness tends to decrease with movement duration, at least when such durational changes have been due to changes in speaking rate (e.g., Adams *et al.*, 1993).

In summary, the present results suggest that the original hypothesis about only a change in the position of a virtual target for the lips in the control of closure duration needs to be modified. Clearly, and as shown in Figs. 10 and 11, both the position and the timing of the target is changed. At the same time, the idea of a spatial control of a durational property in speech is interesting and receives some qualified support in the present study. That is, a speaker can use variations in lip displacement to make changes in closure duration for labial consonants.

To further understand the production of long and short consonants, some additional studies can be considered. One is to study the development of this contrast in children's speech, since lip movements can be recorded using noninvasive procedures (e.g., Green *et al.*, 2000). Another interesting issue in the production of long and short labial consonants is the coordination of lip and tongue movements. Löfqvist and Gracco (1999) showed that more than 50% of the tongue movement from the first to the second vowel in a VCV sequence with a labial stop occurred during the stop closure. The material presented by Smith (1995) suggests that the tongue movement might be altered so that the tongue moves slower during the closure for a long consonant in Japanese. Finally, since the tongue is moving during the closure for a lingual stop consonant (e.g., Löfqvist and Gracco, 2002), one might predict that the tongue movement during the closure is slower for a long than for a short consonant in order to maintain the contact between the tongue and the palate. Löfqvist (2003, 2004) presents evidence that this is indeed the case.

ACKNOWLEDGMENTS

The author is grateful to Mariko Yanagawa for help with the Japanese material, and to Peter Assman, Dani Byrd, and an anonymous reviewer for comments on an earlier version of the manuscript. This work was supported by Grant No. DC-00865 from the National Institute on Deafness and Other Communication Disorders, National Institutes of Health.

Adams, S., Weismer, G., and Kent, R. (**1993**). ''Speaking rate and speech movement velocity profiles,'' J. Speech Hear. Res. **36**, 41–54.

Beckman, M. (**1982**). ''Segment duration and the mora in Japanese,'' Phonetica **39**, 113–135.

Byrd, D. (**1995**). ''Articulatory characteristics of single and blended lingual gestures,'' in *Proceedings of the XIIIth International Congress of Phonetic Sciences*, edited by K. Elenius and P. Branderud, Stockholm, Vol. 2, pp. 438–441.

Byrd, D., Kaun, A., Narayanan, S., and Saltzman, E. (**2000**). ''Phrasal signatures in articulation,'' in *Papers in Laboratory Phonology V: Acquisition and the Lexicon*, edited by M. B. Broe and J. B. Pierrehumbert (Cambridge U.P., Cambridge), pp. 70–87.

Cooke, J. (**1980**). ''The organization of simple, skilled movements,'' in *Tutorials in Motor Behavior*, edited by G. Stelmach and J. Requin (North-Holland, Amsterdam), pp. 199–212.

Dunn, M. H. (**1993**). ''The Phonetics and Phonology of Geminate Consonants: A Production Study,'' unpublished doctoral dissertation, Yale University.

Elert, C.-C. (**1964**). *Phonologic Studies of Quantity in Swedish* (Almqvist & Wiksell, Uppsala).

Fant, G. (**1973**). ''Acoustic description and classification of phonetic units,'' in *Speech Sounds and Features*, edited by G. Fant (Ed.) (MIT, Cambridge, MA), pp. 32–83.

Farnetani, E. (**1990**). ''V-C-V lingual coarticulation and its spatiotemporal domain,'' in *Speech Production and Speech Modelling*, edited by W. Hardcastle and A. Marchal (Kluwer, Dordrecht), pp. 93–130.

Fuchs, S., Perrier, P., and Mooshammer, C. (**2001**). ''The role of the palate in tongue kinematics: An experimental assessment in VC sequences,'' *Proc. Eurospeech 2001*, Aalborg, pp. 1487–1490.

Gottlieb, G., Corcos, D., and Agarwal, G. (**1989**). ''Strategies for the control of voluntary movements with one mechanical degree of freedom,'' Behav. Brain. Sci. **12**, 189–250.

Green, J. R., Moore, C. A., Higashikawa, M., and Steeve, R. (**2000**). ''The physiologicl development of speech motor control: Lip and jaw coordination,'' J. Speech Lang. Hear. Res. **43**, 239–255.

Hadding-Koch, K., and Abramson, A. (**1964**). ''Duration versus spectrum in Swedish vowels: Some perceptual experiments,'' Studia Linguistica **18**, 94–107.

Han, M. (**1994**). ''Acoustic manifestations of mora timing in Japanese,'' J. Acoust. Soc. Am. **96**, 73–82.

Harrington, J., Fletcher, J., and Roberts, C. (**1995**). ''Coarticulation and the accented/unaccented distinction; Evidence from jaw movement data,'' J. Phonetics **23**, 305–322.

Hertrich, I., and Ackermann, H. (**1997**). ''Articulatory control of phonological vowel length contrasts: Kinematic analysis of labial gestures,'' J. Acoust. Soc. Am. **102**, 523–536.

Kelso, J. A. S., Vatikiotis-Bateson, E., Saltzman, E., and Kay, B. (**1985**). ''A qualitative dynamic analysis of reiterant speech production: Phase portraits, kinematics, and dynamic modeling,'' J. Acoust. Soc. Am. **77**, 266–280.

Lahiri, A., and Hankamer, J. (**1988**). ''The timing of geminate consonants,'' J. Phonetics **16**, 327–338.

Lehtonen, J. (**1970**). *Aspects of Quantity in Standard Finnish*, K. J. Gummerus Jyväskylä.

Lehiste, I., Morton, K., and Tatham, M. (**1973**). ''An instrumental study of consonant gemination,'' J. Phonetics **1**, 131–148.

Löfqvist, A. (**2000**). ''Control of closure duration in stop consonants,'' in *Proceedings of the 5th Seminar on Speech Production: Models and Data* (Institut für Phonetik und Sprachliche Kommunikation, Munich), pp. 29–32.

Löfqvist, A. (**2003**). ''Control of closure/constriction duration in lingual consonants,'' J. Acoust. Soc. Am. **114**, 2397(A).

Löfqvist, A. (**2004**). ''Making a vocal tract closure longer and shorter,'' in *From Sound to Sense: Fifty+Years of Discoveries in Speech Communication*, edited by J. Slifka, S. Manuel, and M. Matthies (Res. Lab. Electronics, MIT, Cambridge, MA), pp. C169–C174.

Löfqvist, A., and Gracco, V. (**1997**). ''Lip and jaw kinematics in bilabial stop consonant production,'' J. Speech Lang. Hear. Res. **40**, 877–893.

Löfqvist, A., and Gracco, V. (**1999**). ''Interarticulator programming in VCV sequences: Lip and tongue movements,'' J. Acoust. Soc. Am. **105**, 1864–1876.

Löfqvist, A., and Gracco, V. (**2002**). ''Control of oral closure in lingual stop consonant production,'' J. Acoust. Soc. Am. **111**, 2811–2827.
Munhall, K., Hawkins, S., Fowler, C. A., and Saltzman, E. (**1992**). ''Compensatory shortening' in monosyllables of spoken English,'' J. Phonetics **20**, 225–239.
Ostry, D., Keller, E., and Parush, A. (**1983**). ''Similarities in the control of speech articulators and the limbs: Kinematics of tongue dorsum movements during speech,'' J. Exp. Psychol. Hum. Percept. Perform. **9**, 622–636.
Perkell, J., Cohen, M., Svirsky, M., Matthies, M., Garabieta, I., and Jackson, M. (**1992**). ''Electromagnetic midsagittal articulometer (EMMA) systems for transducing speech articulatory movements,'' J. Acoust. Soc. Am. **92**, 3078–3096.
Perrier, P., Payan, P., Zandipour, M., and Perkell, J. (**2003**). ''Influence of tongue biomechanics on speech movements during the production of velar stop consonants: A modeling study,'' J. Acoust. Soc. Am. **114**, 1582–1599.
Rubin, P., and Löfqvist, A. (**1996**). ''HADES: Haskins Analysis Display and Experiment System,'' *Haskins Laboratories Status Report on Speech Research* (available at www.haskins.yale.edu/HASKINS/SR/sr.html).
Saltzman, E., and Munhall, K. (**1989**). ''A dynamical approach to gestural patterning in speech production,'' Ecological Psychol. **1**, 333–382.
Smith, C. L. (**1995**). ''Prosodic patterns in the coordination of vowel and consonant gestures,'' in *Laboratory Phonology IV: Phonology and Phonetic Evidence*, edited by B. Connell and C. Arvaniti (Cambridge U.P., Cambridge), pp. 205–222.
Vatikiotis-Bateson, E., and Kelso, J. A. S. (**1993**). ''Rhythm type and articulatory dynamics in English, French, and Japanese,'' J. Phonetics **21**, 231–265.
Vaxelaire, B. (**1995**). ''Single vs. double (abutted) consonants across speech rate: X-ray and acoustic data for French,'' *Proc. XIII Int. Conf. Phonetic Sci.*, Stockholm, Vol 1, pp. 384–387.
Westbury, J. (**1994**). ''On coordinate systems and the representation of articulatory movements,'' J. Acoust. Soc. Am. **95**, 2271–2273.

Effects on the glottal voice source of vocal loudness variation in untrained female and male voices

Johan Sundberg[a] and Ellinor Fahlstedt
Department of Speech Music Hearing, Royal Institute of Technology (KTH), SE-120044 Stockholm, Sweden

Anja Morell
Assistive Technology Resource Center, SE-22100 Lund, Sweden

(Received 24 March 2004; revised 18 September 2004; accepted 8 November 2004)

Subglottal pressure is one of the main voice control factors, controlling vocal loudness. In this investigation the effects of subglottal pressure variation on the voice source in untrained female and male voices phonating at a low, a middle, and a high fundamental frequency are analyzed. The subjects produced a series of /pae/ syllables at varied degrees of vocal loudness, attempting to keep pitch constant. Subglottal pressure was estimated from the oral pressure during the /p/ occlusion. Ten subglottal pressure values, approximately equidistantly spaced within the pressure range used, were identified, and the voice source of the vowels following these pressure values was analyzed by inverse filtering the airflow signal as captured by a Rothenberg mask. The maximum flow declination rate (MFDR) was found to increase linearly with subglottal pressure, but a given subglottal pressure produced lower values for female than for male voices. The closed quotient increased quickly with subglottal pressure at low pressures and slowly at high pressures, such that the relationship can be approximated by a power function. For a given subglottal pressure value, female voices reached lower values of closed quotient than male voices. [DOI: 10.1121/1.1841612]

PACS numbers: 43.70.Gr, 43.70.Aj [AL] Pages: 879–885

I. INTRODUCTION

Variation of vocal loudness is normally achieved by changes of subglottal pressure P_S. Such changes affect the voice source not only by increasing its amplitude, but also by changing other of its waveform parameters. The effect of variation of the P_S on the voice source flow waveform, or the flow glottogram, has been studied in several investigations of untrained voices (Holmberg *et al.*, 1988, 1989; Sulter and Wit, 1996; Stathopoulos and Sapienza, 1993; Hertegård and Gauffin, 1991) and professional singers (Sundberg *et al.*, 1999). The results have demonstrated that P_S significantly affects several flow glottogram parameters, such as closed quotient (Q_{closed}), maximum flow declination rate (MFDR), peak-to-peak pulse amplitude ($\hat{U}$), leakage, the level difference H_1-H_2 between partials 1 and 2 of the source spectrum, and the speed quotient. These observations have mostly been based on measurements from three or four pressure values. Also, in most of these investigations voice $F0$ has been allowed to vary freely. Holmberg *et al.* (1989) found that a variation of fundamental frequency $F0$ did not significantly affect any of the flow glottogram parameters that they studied. On the other hand, a clear effect of $F0$ has been found in professional singers (Sundberg *et al.*, 1999).

While it is clear that P_S significantly affects certain flow glottogram parameters, it is not possible to specify in quantitative terms the relationship between P_S and flow glottogram parameters in untrained voices on the basis of three or four pressure values. Yet, such approximations should be relevant to attempts to improve the naturalness of synthesized speech. They should also provide a useful basis for improving the theory of the glottal voice source. The aim of the present investigation was to investigate, in quantitative terms, the relation between P_S and a set of acoustically relevant voice source parameters in untrained voices. To realize this aim, a wide range of pressures was studied at low, middle, and high $F0$.

II. METHOD

Fifteen females and 14 males, age range 20–40 years, volunteered as subjects. None of them had any formal voice training, although some had a modest experience of singing in amateur choirs. None were smokers, none had any history of voice disorders or pulmonary disease, and none had any cold at the time of the experiment. None of them reported a hearing loss.

The recording consisted of two parts. First, a 30-s sample of the subjects' normal speaking pitch was secured by asking them to describe a picture that was shown to them and their mean $F0$ during this task was determined. Second, the subjects were presented with a real-time phonetogram display showing SPL versus $F0$ and a cursor adjusted to the subject's mean $F0$ (FOG program, Hitech Development AB, Sweden). The subjects were then asked to repeatedly pronounce the syllable [pae:] at a gradually varying degree of vocal loudness that ranged from loudest to softest possible, while trying to keep $F0$ constant. Three fundamental frequencies were selected, one corresponding to the subject's mean speaking $F0$, one 6 semitones higher, and one 12 semitones higher. This task was greatly facilitated by the real-

[a]Author to whom correspondence should be addressed.

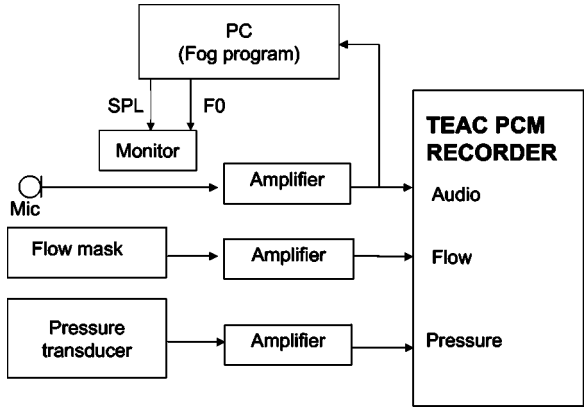

FIG. 1. Block diagram of the experimental setup used for the recordings. The feedback on $F0$ and SPL was used to make it easier for the subjects to keep pitch constant while varying vocal loudness.

time visual feedback offered by the phonetogram program. Indeed, all subjects but four (one female and three male) managed to keep their $F0$ constant within ± 2 semitones. Each subject performed this task at least three times for each $F0$. No instructions were given regarding register, and while all male subjects used modal register for all $F0$ values, some of the female subjects seemed to produce the highest $F0$ in a different register. The experimental setup is shown in Fig. 1. The flow signal was captured by means of a flow mask (Glottal Enterprises). Oral pressure during the p-occlusions was measured by a pressure transducer attached to a thin plastic tube, inner diameter 4 mm, that the subjects held in the corner of their mouths. The flow and pressure signals were recorded on a multichannel TEAC RD-200T PCM data recorder together with an audio signal recorded at 30 cm from the mouth. Calibration was undertaken on two occasions, before the first recording and before recording the 11th subject. The flow transducer was calibrated by recording on the same PCM recorder airflow obtained from a pressure tank and measured by a rotameter. Likewise, the pressure transducer was calibrated by recording various pressures as determined by a manometer. SPL was calibrated by sustaining a vowel sound of which the SPL was measured by means of a B&K sound-level meter, the microphone of which was held next to the audio microphone.

The analysis was performed using the SWELL SIGNAL Workstation program package (Hitech Development AB, Sweden). Each recording on the tape was digitized, one file for each $F0$ condition. The total number of files was 87 (for each subject 3 $F0$ conditions, 14 male and 15 female subjects). Each file comprised three channels, one for audio, one for flow, and one for pressure sampled at 20, 10, and 10 kHz, respectively.

For each $F0$ condition, ten pressure values were selected that were approximately equidistantly spaced between the highest and lowest pressures. Thereby, deviations up to ± 2 semitones from the target $F0$ were accepted. Wherever possible, pressure peaks with a flat plateau were chosen, since such peaks indicate a constant subglottal pressure. In cases where such peaks were not available, the pressure was measured at the end of the peak, just at the end of the occlusion.

The inverse filtering was accomplished by means of the custom-made DECAP program written by Granqvist. The program requires manual setting of poles with variable frequencies and bandwidths, and displays the original plus the resulting inverse filtered waveform and spectrum. For optimizing the filter frequencies and bandwidths, a flat closed phase and an even source spectrum envelope were applied as criteria. If needed, different filter settings were used for different syllables in the same file.

The vowels following the selected pressure values were analyzed. As the flow glottogram typically changed immediately after the initial consonant [p], a period appearing after these changes, i.e., in the quasi-steady-state part of the vowel, was selected for measurement. The following characteristics were determined for each of the ten syllables selected under each condition; see Fig. 2: (1) period T; (2) closed phase T_{closed}; (3) peak-to-peak amplitude $\hat{U}$; (4) U_{dc} flow, i.e., the mean airflow during the closed phase or the glottal leakage; and (5) flow U_{mean}, measured as the mean flow amplitude during the open phase. The instant of closure was assumed to correspond to the discontinuity in the flow waveform that appeared at the end of the closing phase. In addition (6) MFDR, i.e., the negative peak amplitude of the differentiated glottogram was measured, as well as (7) the level difference H_1-H_2 between the first and second partials of the source spectrum obtained from a FFT analysis of the inverse filtered waveform. From T and T_{closed} the closed quotient Q_{closed} was computed, $Q_{\text{closed}}=T_{\text{closed}}/T$. Glottal adduction is an important aspect of phonation, affecting the ratio between the air volume displaced in a glottal airflow pulse and the associated P_S. This ratio can be regarded as the glottal compliance C_{Gl}, which was approximated as

$$C_{\text{Gl}}=(U_{\text{pulse}}-U_{\text{dc}})*T_{\text{op}}/P_{\text{s}}, \tag{1}$$

where U_{pulse} is the mean air flow during the open phase, U_{dc} is the mean airflow during the closed phase, i.e., the leakage, and T_{op} is the duration of the open phase, i.e., $T_{\text{op}}=T-T_{\text{closed}}$. As proposed by Titze (1992), the pressure values P_{s} were expressed in terms of the normalized excess pressure P_{SEN}

$$P_{\text{SEN}}=(P_{\text{s}}-P_{\text{thr}})/P_{\text{thr}}, \tag{2}$$

where P_{thr} is the threshold pressure measured for the softest phonation observed for each $F0$ condition.

III. RESULTS

Figure 3 shows the means of the maximum and minimum P_S used by the female and male subjects. The pressures tended to increase with $F0$ both for softest and loudest phonation. The mean $F0$ for the female and male subjects was 219.2 and 117.1 Hz (SD 15.7 and 17.7 Hz, respectively). The dependence in softest phonation is similar to that expected for the phonation threshold pressure (Titze, 1992), even though the averaged minimum pressure for the male subjects' phonation at low $F0$ was slightly higher than that observed for their 6-semitones-higher $F0$.

For each of the 29 subjects the relationship between P_{SEN} and the various flow glottogram parameters was analyzed and approximated with equations, mostly linear regressions. For each parameter, the constants in these equations

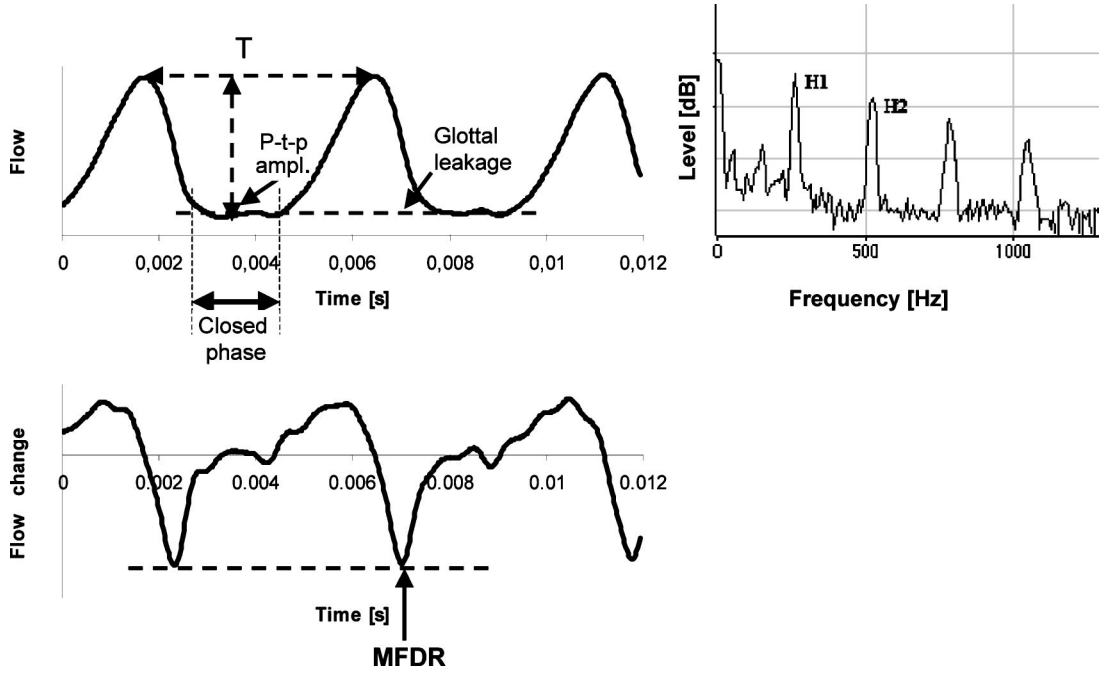

FIG. 2. Example of flow glottogram (upper left panel), its derivative (lower left panel), and its spectrum (right panel), and the voice source characteristics measured.

were averaged across subjects such that a mean relationship was obtained; see Table I. In calculating the means for the linear regressions, only cases with a correlation of $r \geqslant 0.5$ were included, random variation seemingly being of limited interest. The table also lists the correlation, averaged across subjects for each condition for these regressions. It should be noted that the means thus only refer to subjects who showed a correlation greater than 0.5. The table also lists the number of subjects included in the calculation of the averages.

Q_{closed} tended to increase quickly at low pressures and to approach an asymptote at high pressures, and could be approximated by a power function of the type

$$Q_{\text{closed}} = A - e^{(-\alpha * P_{\text{SEN}}) + B}, \tag{3}$$

where A is the asymptote, α is the curvature, and $B = \ln(A)$. For each $F0$ and each subject these constants were optimized using as criterion the mean of the squared difference between the subject's data points and the corresponding values calculated with the equation. Figure 4(a) illustrates the average relationship for the female and male subjects. The asymptote was higher for the male than for the female voices. The difference was particularly great at the high $F0$ where the females reached a mean of no more than $Q_{\text{closed}} = 0.3$, while the corresponding value for the males was 0.44. The α con-

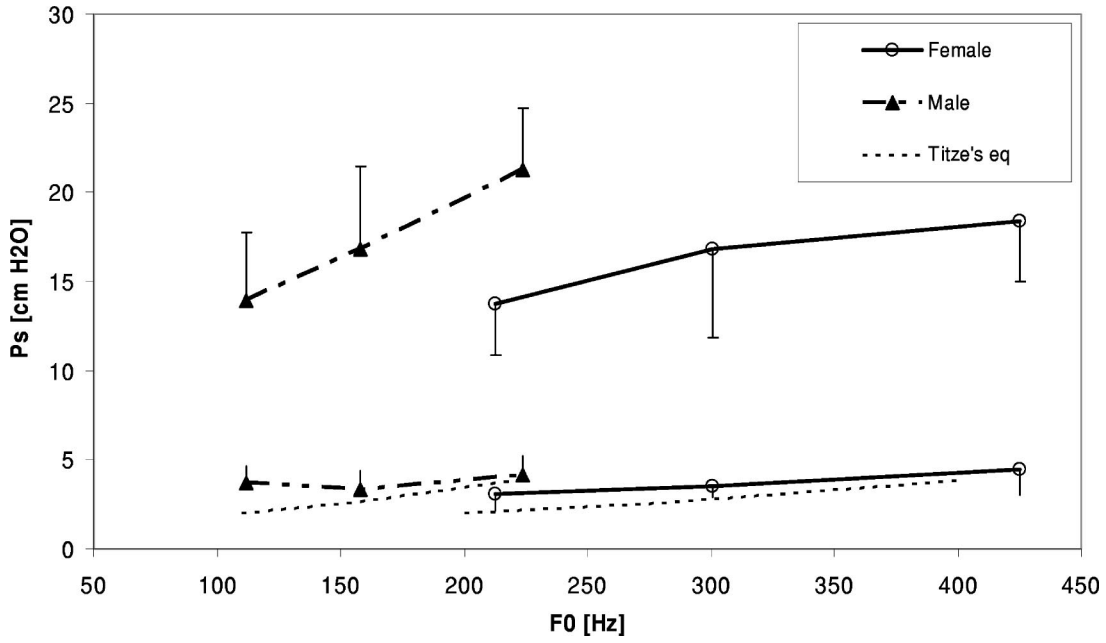

FIG. 3. Maximum and minimum subglottal pressure averaged across subjects as function of $F0$. The bars represent 1 SD.

TABLE I. Top lines: Means and standard deviations (SD) of the constants A, alpha, and B in the equation approximating the relationship between P_{SEN} and Q_{closed} [Eq. (3)] for 15 female and 14 male untrained voices and observed at mean $F0$ in spontaneous speech (MV $F0$), and at an $F0$ 6 and 12 semitones above this $F0$ (MV $F0+6$ and MV $F0+12$); Diff^2 represents the mean of the squared difference between data points and the corresponding values calculated with the equation. Lower lines: Corresponding means and standard deviations of slope (C), intercept (Icpt), and correlation (r) between P_{SEN} and MFDR, $\hat{\mathbf{U}}$, glottal compliance, and DC airflow and between H1-H2 and Q_{Closed}, between MFDR and AC and between MFDR and Q_{Closed}. In the calculation of all these means only the N cases with $r>0.5$ were included. The relationship between P_{SEN} and DC airflow has been divided into two groups depending on whether or not the airflow increased or decreased with increasing P_{SEN}.

		MV $F0$							MV $F0+6$							MV $F0+12$						
		N	A	SD	Alpha	SD	B	Diff^2	*N*	A	SD	Alpha	SD	B	Diff^2	*N*	A	SD	Alpha	SD	B	Diff^2
P_{SEN} and Q_{closed}	Females	*15*	0.49	0.12	0.56	0.3	−0.74	0.07	*15*	0.44	0.17	0.65	0.47	−0.94	0.04	*15*	0.32	0.13	0.76	0.46	−1.26	0.04
	Males	*14*	0.49	0.09	1.09	0.78	−0.73	0.09	*14*	0.52	0.08	0.83	0.94	−0.66	0.11	*14*	0.44	0.14	1.43	1.13	−0.88	0.15
		C		Icpt		*r*			C		Icpt		*r*			C		Icpt		*r*		
		Mean	SD	Mean	SD	Mean	SD		Mean	SD	Mean	SD	Mean	SD		Mean	SD	Mean	SD	Mean	SD	
P_{SEN} and MFDR	Females	*15*	142.8	46	−44.7	111	0.967	0.016	*15*	145	50.4	24.2	86	0.919	0.067	*15*	177.9	57.1	49.1	88.9	0.934	0.06
	Males	*14*	140.6	61.1	105.9	108	0.889	0.112	*14*	232.3	79.8	64.7	143	0.925	0.086	*14*	343.5	105	95.6	103	0.949	0.039
P_{SEN} and $\hat{U}$	Females	*15*	0.051	0.01	0.49	0.25	0.934	0.051	*14*	0.053	0.02	0.51	0.23	0.884	0.095	*15*	0.077	0.03	0.57	0.36	0.91	0.106
	Males	*14*	0.085	0.03	0.31	0.21	0.892	0.088	*14*	0.12	0.04	0.4	0.19	0.937	0.065	*14*	0.164	0.06	0.43	0.17	0.953	0.029
P_{SEN} and compliance	Females	*14*	−0.005	0	0.065	0.02	−0.73	0.211	*11*	−0	0	0.038	0.01	−0.59	0.482	*11*	0	0	0.023	0.01	0.036	0.682
	Males	*14*	−0.028	0.02	0.253	0.15	−0.83	0.189	*13*	−0.02	0.02	0.172	0.09	−0.78	0.17	*12*	−0.01	0.02	0.09	0.05	−0.61	0.499
P_{SEN} and DC	Females	*3*	−0.01	0.02	0.04	0.05	0.726	0.18	*2*	0.04	0.02	0.13	0.04	0.832	0.04	*7*	0.04	0.03	0.05	0.06	0.776	0.18
		7	−0.05	0.04	0.1	0.1	0.767	0.13	*3*	−0.03	0.03	0.1	0.1	0.771	0.13	*4*	−0.03	0.03	0.06	0.07	0.706	0.14
	Males	*3*	0.05	0.05	0.09	0.03	0.733	0.14	*2*	0.03	0.02	0.04	0	0.926	0.04	*4*	0.1	0.04	0.18	0.19	0.83	0.08
		3	−16	0.11	0.27	0.15	0.679	0.07	*4*	−0.11	0.12	0.29	0.25	0.765	0.14	*1*	−0.06		0.4		0.753	
*H*1-*H*2 and Q_{closed}	Females	*15*	−40.7	12.3	24.6	5	0.878	0.094	*13*	−40.6	13.4	24.2	4.3	0.907	0.1	*10*	−39.3	17.6	25.6	5.1	0.783	0.12
	Males	*13*	−30	11.5	21.8	5.9	0.928	0.071	*14*	−25.9	6.9	19.8	2.9	0.912	0.1	*13*	−23.5	5.9	17.6	2.6	0.886	0.09
MFDR and AC	Females	*15*	2548	658	−159	105	0.954	0.047	*15*	2663	549	−130	70.2	0.944	0.065	*15*	2364	933	−74	145	0.963	0.063
	Males	*14*	1492	372	−222	140	0.952	0.063	*14*	1962	553	−310	266	0.972	0.019	*14*	2164	695	−299	175	0.973	0.023
MFDR and Q_{closed}	Females	*15*	1760	483	−163	149	0.872	0.06	*13*	1676	694	−51.5	163	0.852	0.086	*13*	2053	1288	25.7	142	0.753	0.117
	Males	*14*	1745	864	−149	369	0.829	0.099	*14*	1944	903	21.1	301	0.848	0.088	*13*	2866	943	63.1	400	0.834	0.071

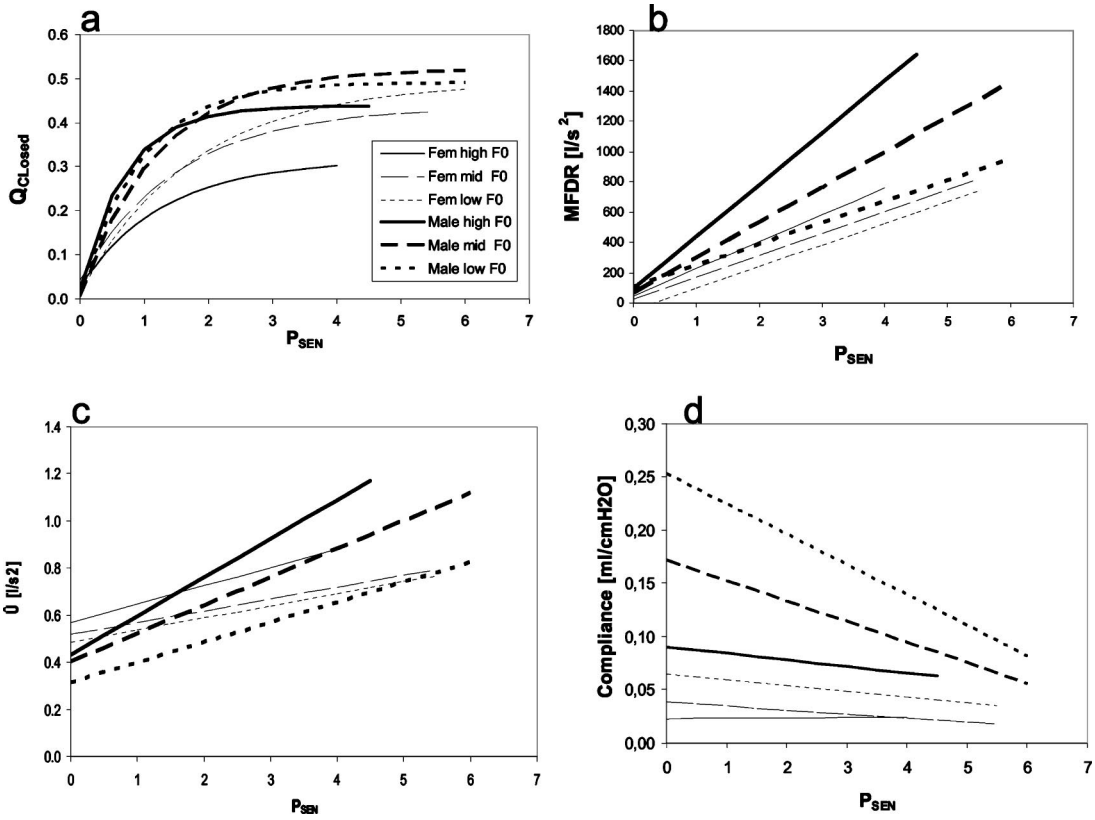

FIG. 4. Average relationship at low, mid, and high $F0$ (dotted, dashed, and solid lines, respectively) between the means of the indicated flow glottogram characteristics and the mean normalized excess pressure P_{SEN} for the female and male subjects (thin and heavy lines, respectively).

stant was much lower for the females, particularly at the high $F0$, indicating that their Q_{closed} increased considerably slower with increasing pressure than for the male subjects.

MFDR showed a strong linear correlation with P_{SEN}, $r=0.940$, and $r=0.921$ for the female and male subjects, respectively. The mean relationship is illustrated in Fig. 4(b). MFDR for the females was much lower than for the males. Thus, for a given P_{SEN} the males obtained two or three times higher values of MFDR than the females. Moreover, the males tended to gain a greater increase of MFDR for a given increase of P_{SEN}, particularly at high $F0$.

The mean relationship between $\hat{U}$ and P_{SEN} is illustrated in Fig. 4(c). The relationship was rather strong, $0.953 \geqslant \text{mean } r \geqslant 0.884$. At low P_{SEN} values the females showed higher values than the males. For high P_{SEN} the males' high $F0$ showed the highest $\hat{U}$ values. The slope was considerably steeper and increased more with $F0$ for the male than for the female voices.

At the two lower $F0$ values the *compliance* tended to decrease linearly with increasing P_{SEN}, but for the highest $F0$ it remained almost constant. With increasing $F0$ the slope and the intercept decreased for female and male subjects alike. However, compliance was substantially lower for the female than for the male subjects. In other words, a given P_{SEN} yielded a much smaller compliance for the female than for the male subjects.

The *dc flow* showed a correlation with P_{SEN} in some subjects only; see Table I. Most female subjects showed no systematic variation at mid $F0$, and a majority of the males showed no systematic variation at any $F0$. With increasing P_{SEN} the dc flow increased in some subjects and decreased in others.

The H_1-H_2 measure showed a negative relationship with Q_{closed}. Figure 5 shows the mean H_1-H_2 for different values of Q_{closed}, Thus, the H_1-H_2 values were computed using the averages across subjects of the slope and intercept, listed in Table I. For the females the slope and intercept were similar for the three $F0$ values, while for the males both slope and intercept tended to decrease with increasing Q_{closed}. For a given value of Q_{closed}, the males showed lower values of H_1-H_2 than the females.

IV. DISCUSSION

Our findings are mostly in agreement with those reported in earlier investigations. Thus, Holmberg and associates (1988) also found that the maximum Q_{closed} was lower for female than for male voices. Likewise, Holmberg and co-workers' (1989) finding of lower values of maximum Q_{closed} at high as compared to mid and low $F0$. Also with respect to the MFDR, our data are in agreement with those reported by earlier investigations (Holmberg *et al.*, 1995; Sulter and Wit, 1996; Stathopoulos and Sapienza, 1993; Titze and Sundberg, 1992), though higher than those reported by Hertegård and Gauffin (1991). For the approximation of the linear relationship MFDR to P_S, a mean slope of 215 and an intercept of 156 have been observed for baritone singers (Sundberg *et al.*, 1999). Analyzing two degrees of vocal loudness, comfortable and loud, as produced by 20 untrained female subjects, Holmberg *et al.* (1995) found a

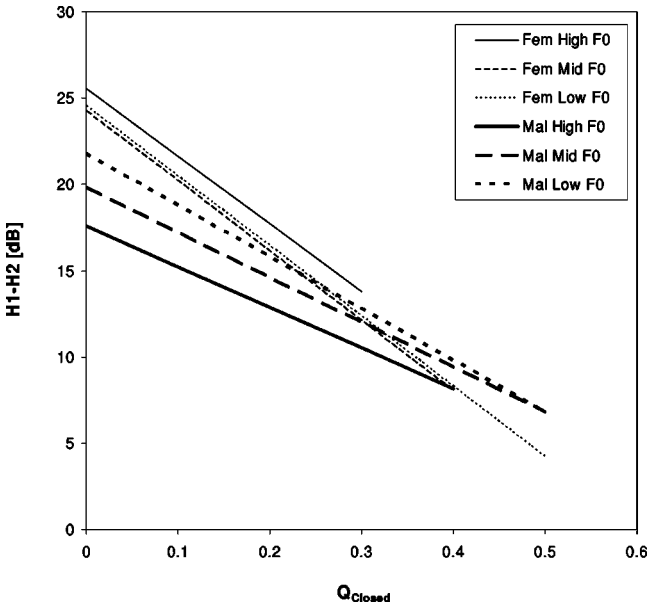

FIG. 5. Average relationship at low, mid, and high $F0$ (dotted, dashed, and solid lines, respectively) between mean $H1$-$H2$ and Q_{closed} for the female and male subjects (thin and heavy lines, respectively).

correlation of -0.69 for the relationship between H_1-H_2 and Q_{closed}. Our correlation for the H_1-H_2 and the Q_{closed} amounted to -0.88, -0.81, and -0.64 for the female subjects' low, middle, and high $F0$, respectively. Our higher correlation value may be due to the greater number of P_S values.

Hanson (1997) measured H_1-H_2 in spectra of speech produced by 22 female untrained voices. She found an average H_1-H_2 of about 3 dB for emphasized versions of the vowels [ae,ɛ,ʌ], produced within a carrier phrase. As the effects of formants on the H_1-H_2 values were compensated for, her data should be comparable to ours. We related H_1-H_2 to Q_{closed}, which varied greatly with P_S. Using the constants listed in Table I for the relationship between H_1-H_2 and Q_{closed}, our results yield an H_1-H_2 of 6.8, 3.1, and 2.3 dB for low, mid, and high $F0$, respectively, produced at an intermediate vocal loudness ($P_{\text{SEN}}=3$). If the emphasis in Hanson's experiment resulted in an elevated $F0$, our values agree well with her.

With respect to leakage averaged across $F0$, our data for female subjects were somewhat lower than those found by Holmberg and associates (1994) and by Sulter and Wit, 1996, but similar to those reported by Hertegård and Gauffin (1991). The leakage was considerably higher in the male than in the female subjects, which may reflect the longer vocal folds in males. Our values are higher for the male subjects as compared with values reported in previous investigations (Holmberg *et al.*, 1994; Hertegård and Gauffin, 1991; Sulter and Wit, 1996). This discrepancy might be due to differences in the experimental conditions. Hertegård and Gauffin found that the dc flow decreased with pressure at low $F0$. We observed this trend in some of our subjects. In the investigation of baritone singers no relationship with pressure was observed. The increased leakage at higher $F0$ that we found for our male subjects is in accordance with observations reported by Hertegård *et al.* (1992).

Thus, while our results are mostly similar to those reported in earlier investigations, the great number of P_S values allowed us to describe also in analytic form the relationship between P_S and various flow glottogram characteristics.

Our material also allows comparisons of voice source characteristics in female and male untrained voices. As compared with male voices the female voices had a lower Q_{closed}, particularly at high $F0$. This would, at least in part, be due to the fact that some female subjects apparently failed to produce the highest $F0$ in the same vocal register as the two lower $F0$ values. Moreover, the female subjects showed a lower MFDR for a given P_{SEN} and a smaller increase of MFDR with increasing P_{SEN}. $\hat{U}$ was higher and increased more with P_{SEN} for the males. Probably these differences can be ascribed to the shorter female vocal folds and the associated smaller glottal area; for a given P_{SEN} a smaller glottis would allow less airflow, i.e., a lower $\hat{U}$ than a longer glottis. The lower female MFDR values may appear somewhat surprising, since MFDR increases with $F0$, but the low $\hat{U}$ at high $F0$ should produce the opposite effect.

Thick vocal folds should be associated with a greater phase lag between the upper and lower layers of the vocal folds which, in turn, should result in a longer closed phase (Sundberg and Högset, 2001). This may be the explanation why Q_{closed} was lower for high than for low $F0$; the vocal folds are elongated and hence thinner at high than at low $F0$. If females have thinner vocal folds than males, also the lower values of Q_{closed} for a given P_{SEN} is understandable. $H1$-$H2$ showed a strong correlation with Q_{closed}. For low values of Q_{closed}, the females showed a more dominant fundamental than the males, suggesting a more sinusoidal flow glottogram. The reason for this is not clear.

Apart from the above comparisons between female and male untrained voices, our results for the male subjects can also be compared with those previously observed for professional operatic baritone soloists (Sundberg *et al.*, 1999). This comparison is facilitated by the fact that the same experimental method was used in both investigations.

While the average minimum pressures were similar, the singers' maximum P_{SEN} was clearly higher than those of the untrained voices, particularly at high $F0$ where the mean difference amounted to more than 40%. To some small extent this difference may be due to the fact that the singers' high $F0$ was about 280 Hz, which is about 3 semitones higher than that of the untrained voices. The main reason would be related to the phonatory mechanism. Recalling that all these pressures are much lower than the highest pressure that can be produced by the human pulmonary system, the great difference suggests a vocal fold difference. Probably, the singers train their vocal folds such that they can cope with higher pressures than what is appropriate for untrained voices.

The nonsingers gained more MFDR for a given increase of P_{SEN} than the singers. At mid $F0$ the singers reached higher maximum MFDR values than the untrained male voices, and at their maximum P_{SEN} they reached considerably higher MFDR values than the untrained males.

Q_{closed} affects voice timbre in the sense that it determines how great a portion of the cycle will contain a formant

ringing. With respect to the relationship between P_{SEN} and Q_{closed}, the singers showed less random variation than the nonsingers, the overall mean squared departure from an optimized power function being 0.12 for the nonsingers and 0.007 for the singers. Disregarding the nonsingers' greater random variation, Q_{closed} showed a similar dependence on P_{SEN} for the singers and the nonsingers, but Q_{closed} changed less with $F0$ in the singers. In this sense, then, the singers' voice timbre changed less with $F0$ and loudness than in the untrained voices.

The sound level of a vowel typically equals the level of the first formant which, in turn, is determined mainly by MFDR, other things being equal (Fant, 1960; Gramming and Sundberg, 1988). Two flow glottogram properties contribute to the variation of MFDR, $\hat{U}$ and Q_{closed}. Thus, both an increase of $\hat{U}$ and an increase of Q_{closed} caused by an earlier glottal closure relative to the flow pulse will cause MFDR to increase. As can be seen in Table I, MFDR was strongly correlated with $\hat{U}$, $0.973 \geqslant \text{mean } r \geqslant 0.944$, and slightly less with Q_{closed}, $0.872 \geqslant \text{mean } r \geqslant 0.753$. The lower correlation for Q_{closed} would at least partly depend on the fact that Q_{closed} does not increase with pressure increases in the high-pressure range. In other words, MFDR and hence the sound level will increase because of an increase of Q_{closed} mainly at low P_{SEN} values. At higher P_{SEN} values the increase of MFDR is caused by an increase of $\hat{U}$.

The compliance measure reflects the relation between transglottal air volume and P_S. It has been found to be related to the perceived degree of hyperfunction (Sundberg *et al.*, 2004). It should thus increase with increasing glottal adduction and hence should be relevant to vocal hygiene. However, it was found to vary considerably with both P_{SEN} and $F0$. While it may seem likely that untrained subjects tend to increase glottal adduction with $F0$ and vocal loudness, it is also possible that compliance varies with P_s and $F0$ for purely aerodynamic reasons.

Our results demonstrate the paramount relevance of P_s to phonation. P_s variation may cause Q_{closed} to vary between 0 and about 0.5, MFDR between almost zero to 700 or 1600 l/s^2 for female and male voices, and $\hat{U}$ between about 0.15 and more than 1 l/s. Likewise, $H1$-$H2$ may vary between 10 or 20 dB. Also, $F0$ affects most flow glottogram parameters substantially. Thus, comparisons between flow glottogram characteristics should be made under conditions of identical P_s and $F0$.

V. CONCLUSIONS

Subglottal pressure has a major influence on many voice source parameters in untrained female and male voices. MFDR and $\hat{U}$ tend to increase and compliance to decrease linearly with normalized excess pressure, while the variation of Q_{closed} with this pressure can be approximated by a power function. Q_{closed}, MFDR, and compliance are lower for females than for males. The results indicate that meaningful comparisons of Q_{closed} and other flow glottogram characteristics should refer to identical values of P_s and $F0$.

ACKNOWLEDGMENTS

This investigation, originally a master thesis work in logopedics at the Lund University, was carried out by coauthors E.F. and A.M. with coauthor J.S. as supervisor. The kind cooperation of the subjects is gratefully acknowledged. The authors are also indebted to two anonymous reviewers and to editor Anders Löfqvist for many valuable comments and suggestions on the manuscript.

Fant, G. (**1960**). *Acoustic Theory of Speech Production* (Mouton, The Hague).

Gramming, P., and Sundberg, J. (**1988**). "Spectrum factors relevant to phonetogram measurement," J. Acoust. Soc. Am. **83**, 2352–2360.

Hanson, H. (**1997**). "Glottal characteristics of female speakers: Acoustic correlates," J. Acoust. Soc. Am. **101**, 466–481.

Hertegård, S., and Gauffin, J. (**1991**). "Insufficient vocal fold closure as studied by inverse filtering," in *Vocal Fold Physiology: Acoustic, Perceptual and Physiological Aspects of Voice Mechanisms*, edited by J. Gauffin and B. Hammarberg (Singular, San Diego), Chap. 31.

Hertegård, S., Gauffin, J., and Karlsson, I. (**1992**). "Physiological correlates of the inverse filtered flow waveform," J. Voice **6**, 224–234.

Hirano, M., Kiyokawa, K., and Kurita, S. (**1988**). "Laryngeal muscles and glottal shaping," in *Vocal Fold Physiology: Voice Production, Mechanisms and Functions*, edited by O. Fujimura (Raven, New York), Chap. 5.

Holmberg, B., Hillman, R. E., and Perkell, J. S. (**1988**). "Glottal airflow and transglottal air pressure measurement for male and female speakers in soft, normal, and loud voice," J. Acoust. Soc. Am. **84**, 511–529.

Holmberg, B., Hillman, R. E., and Perkell, J. S. (**1989**). "Glottal airflow and transglottal air pressure measurement for male and female speakers in low, normal, and high pitch," J. Voice **3**, 295–305.

Holmberg, E. B., Hillman, R. E., Perkell, J. S., and Gress, C. (**1994**). "Relationships between intra-speaker variation in aerodynamic measures of voice production and variation in SPL across repeated recordings," J. Speech Hear. Res. **37**, 484–495.

Holmberg, E. B., Hillman, R. E., Perkell, J. S., Guiod, P. C., and Goldman, S. L. (**1995**). "Comparisons among aerodynamic, electroglottographic, and acoustic spectral measures of female voice," J. Speech Hear. Res. **38**, 1212–1223.

Stathopoulos, H., and Sapienza, C. (**1993**). "Respiratory and laryngeal function of women and men during intensity variation," J. Speech Hear. Res. **36**, 64–75.

Sulter, A. M., and Wit, H. P. (**1996**). "Glottal volume velocity waveform characteristics in subjects with and without vocal training, related to gender, sound intensity, fundamental frequency, and age," J. Acoust. Soc. Am. **100**, 3360–3373.

Sundberg, J., and Högset, C. (**2001**). "Voice source differences between falsetto and modal registers in counter tenor, tenor, and baritone singers," Logoped. Phoniat. Vocol. **26**, 26–36.

Sundberg, J., Andersson, M., and Hultqvist, C. (**1999**). "Effects of subglottal pressure variation on professional baritone singers' voice sources," J. Acoust. Soc. Am. **105**, 1965–1971.

Sundberg, J., Thalén, M., Alku, P., and Vilkman, E. (**2004**). "Estimating perceived phonatory pressedness in singing from flow glottograms," J. Voice **18**, 56–62.

Titze, I. R. (**1992**). "Phonation threshold pressure: A missing link in glottal aerodynamics," J. Acoust. Soc. Am. **91**, 2926–2935.

Titze, I. R., and Sundberg, J. (**1992**). "Vocal intensity in speakers and singers," J. Acoust. Soc. Am. **91**, 2936–2946.

Synthesis fidelity and time-varying spectral change in vowels

Peter F. Assmann[a] and William F. Katz[b]
School of Behavioral and Brain Sciences and Callier Center for Communication Disorders, The University of Texas at Dallas, Box 830688, Richardson, Texas 75083

(Received 13 September 2002; revised 4 October 2004; accepted 2 December 2004)

Recent studies have shown that synthesized versions of American English vowels are less accurately identified when the natural time-varying spectral changes are eliminated by holding the formant frequencies constant over the duration of the vowel. A limitation of these experiments has been that vowels produced by formant synthesis are generally less accurately identified than the natural vowels after which they are modeled. To overcome this limitation, a high-quality speech analysis-synthesis system (STRAIGHT) was used to synthesize versions of 12 American English vowels spoken by adults and children. Vowels synthesized with STRAIGHT were identified as accurately as the natural versions, in contrast with previous results from our laboratory showing identification rates 9%–12% lower for the same vowels synthesized using the cascade formant model. Consistent with earlier studies, identification accuracy was not reduced when the fundamental frequency was held constant across the vowel. However, elimination of time-varying changes in the spectral envelope using STRAIGHT led to a greater reduction in accuracy (23%) than was previously found with cascade formant synthesis (11%). A statistical pattern recognition model, applied to acoustic measurements of the natural and synthesized vowels, predicted both the higher identification accuracy for vowels synthesized using STRAIGHT compared to formant synthesis, and the greater effects of holding the formant frequencies constant over time with STRAIGHT synthesis. Taken together, the experiment and modeling results suggest that formant estimation errors and incorrect rendering of spectral and temporal cues by cascade formant synthesis contribute to lower identification accuracy and underestimation of the role of time-varying spectral change in vowels. [DOI: 10.1121/1.1852549]

PACS numbers: 43.71.An, 43.70.Ep, 43.71.Es [RLD] Pages: 886–895

I. INTRODUCTION

A. Time-varying spectral change

Recent studies have shown that American English vowels are identified more accurately when time-varying changes in the formant frequencies are preserved rather than eliminated. This effect has been demonstrated in experiments in which portions of the waveforms of natural vowels are deleted (Strange *et al.*, 1983; Nearey and Assmann, 1986), and in experiments with synthesized vowels that hold the frequencies of the formants constant over time (Hillenbrand and Nearey, 1999; Assmann and Katz, 2000). Time-varying changes in spectral shape occur (1) as a natural consequence of coarticulation with adjacent consonants (Stevens and House, 1963; Hillenbrand *et al.*, 2001b) and (2) as an inherent property of vowel quality, described in phonetic terms as diphthongization, which persists even when vowels are spoken in isolation (Nearey and Assmann, 1986; Nearey, 1989; Andruski and Nearey, 1992). Spectral variation over time provides a dimension of phonetic contrast that helps to differentiate pairs of vowels with similar formant patterns, such as /ɪ/ and /e/.

Time-varying spectral change might be expected to play an important role when the fundamental frequency (F_0) is high, as in children's voices. In children's vowels, information about the spectral envelope (such as the frequencies of formant peaks) can be difficult to recover from the power spectrum, because the transfer function of the vocal tract is sparsely ''sampled'' by the harmonics of the fundamental, compared to adult vowels. This is referred to as the ''sparse sampling'' problem (Ryalls and Lieberman, 1982; Diehl *et al.*, 1996). Change in F_0 over the time course of the vowel could help to solve the sparse sampling problem by shifting the frequencies of the harmonics, thereby ''filling in'' the spectral envelope (Carlson *et al.*, 1975; Marin and McAdams, 1991; Diehl *et al.*, 1996; Katz and Assmann, 2001). However, Katz and Assmann (2001) found that vowels synthesized with time-varying changes in F_0 were no better identified than vowels with stationary F_0.

Formant frequency movement over the course of the vowel could also provide a solution to the sparse sampling problem. That is, formant frequency movement leads to correlated changes in the pattern of harmonic amplitudes over time, and these changes may facilitate the tracking of formant frequencies when F_0 is high. However, Assmann and Katz (2000) found that the benefits provided by time-varying changes in the center frequencies of the formants were no greater for identifying the high-pitched vowels of children than for identifying the vowels of adults with lower F_0's. No evidence was found for an increased role of formant-frequency flattening in the vowels of children compared to adults, nor was there a correlation between F_0 and the effects of formant flattening. Assmann and Katz concluded that for-

[a]Electronic mail: assmann@utdallas.edu
[b]Electronic mail: wkatz@utdallas.edu

mant frequency movement does not solve the sparse sampling problem either; instead, it contributes through its role in the phonetic specification of vowels. One concern, however, is that this conclusion was based on vowels synthesized using the cascade formant model, and such vowels are identified with lower accuracy than natural spoken vowels (Hillenbrand and Nearey, 1999; Assmann and Katz, 2000; Hillenbrand *et al.*, 2001a). The aim of the current study was to reexamine the role of time-varying spectral change in vowel identification using a high-quality speech synthesizer to produce stimuli that are closer to natural vowels.

B. Synthesis fidelity

A basic assumption guiding speech synthesis experiments is that listeners' responses to stimulus manipulations will accurately reflect their sensitivity to those properties when they occur in natural speech. This assumption may not be valid when the synthesizer distorts or fails to preserve important features of natural speech so that the synthesized signal is less intelligible than the original. Inaccuracies in synthetic speech may cause listeners' attention to focus on stimulus properties that have low salience in natural speech, leading to an inflated estimate of their perceptual importance. Alternatively, distortions of the signal may draw attention away from stimulus properties that are normally highly salient, leading to underestimation of their cue value. Hillenbrand and Nearey (1999) and Assmann and Katz (2000) reported lower accuracy for vowels produced by cascade formant synthesis compared to the original spoken vowels. Hillenbrand *et al.* (2001a) found that the importance of duration as a cue to vowel identity varied as a function of synthesis quality, with a reduced effect of vowel duration differences when the stimuli were generated by a high-quality sinusoidal speech coder compared to formant synthesis. These findings raise the possibility that the effects of time-varying spectral change may be different when the synthesizer does a better job of preserving spectro-temporal details that are used to identify natural vowels.

The present study addressed this issue by replicating several of the experimental manipulations conducted by Assmann and Katz (2000) and Katz and Assmann (2001) using a high-quality vocoder called STRAIGHT (Kawahara, 1997; Kawahara *et al.*, 1999). The STRAIGHT vocoder uses an effective strategy for decomposing the speech signal to recover the separate contributions of the laryngeal source and vocal tract filter, and thus provides a basis for independent manipulations of source and filter properties. The aim of this study was to reexamine the effects of time-varying spectral change in vowel identification by (1) holding the natural time-varying changes in the spectral envelope (including the formant frequencies) constant over time, and (2) holding F_0 constant over time. The STRAIGHT vocoder was chosen for this purpose because the synthesized speech it generates is often indistinguishable from natural speech. To facilitate comparisons of STRAIGHT and cascade formant synthesis, the experimental methods (i.e., subject inclusion criteria, stimulus presentation procedures, response collection and scoring) were the same as those used previously (Assmann and Katz, 2000; Katz and Assmann, 2001). A statistical pattern recognition model was used to relate acoustic measurements of the stimuli to listeners' vowel identification responses.

II. EXPERIMENT

A. Method

1. Stimuli

The stimuli were natural and synthesized versions of 12 vowels of American English, /i ɪ e ɛ æ ʌ ɑ ɔ o ʊ u ɝ/, spoken in /hVd/ context (''heed,'' ''hid,'' ''hayed,'' ''head,'' ''had,'' ''hud,'' ''hod,'' ''hawed,'' ''hoed,'' ''hood,'' ''who'd,'' ''herd'') taken from the vowel database described in Assmann and Katz (2000) and Katz and Assmann (2001). All talkers were native speakers of American English from the Dallas, Texas area. The vowels were extracted from the /hVd/ syllables, where the vowel onset was defined as the first pitch period of the voiced portion of the syllable, and the offset as the last pitch period before the stop closure associated with the final /d/. Natural and synthesized versions of the vowels were included in the five conditions described below. The synthesized vowels were constructed using a custom version of the STRAIGHT program (Kawahara, 1997). The STRAIGHT program includes separate stages of source analysis (voicing detection and F_0 estimation) and spectral envelope analysis. By manipulating the outputs of these stages, modifications of the estimated source and filter properties could be introduced, as described below. Liu and Kewley-Port (2004) have shown that spectral envelope manipulations using STRAIGHT provide an effective tool for investigating formant frequency discrimination in vowels. In the present study, we used STRAIGHT to construct separate versions of the vowels with F_0 held constant (*flat* F_0) or allowed to vary naturally (*variable* F_0), and with the spectral envelope held constant (i.e., flattened formant frequencies, *flat FF*) or allowed to vary naturally (*variable FF*). Following Hillenbrand and Nearey (1999) we chose a point early in the vowel (20% of the duration of the vocalic segment) at which to hold the F_0 and spectral envelope constant.

All of the stimuli (both natural and synthesized vowels) were recorded or synthesized at a sample rate of 48 kHz, and were scaled to the maximum peak-to-peak amplitude of the 16-bit quantization range. A 10.7-ms Kaiser window was used to shape the onset and offset of each stimulus to minimize the effects of gating transients.

F_0 flattening. For this manipulation, vowels were synthesized on a monotone pitch, with the measured F_0 held constant near its starting value. The F_0 estimation function of the STRAIGHT program provides estimates of F_0 at fixed (1-ms) intervals in all voiced frames (which included *all* of the frames in these vowel stimuli, since they were voiced throughout). F_0 flattening was carried out in two steps. First, the median F_0 was obtained from a 25-ms window (i.e., 25 frames), whose onset was positioned at 20% of the duration between vowel onset and offset. Second, each of the F_0 estimates throughout the vowel was replaced by this constant value, as illustrated in the top panel of Fig. 1.

Formant flattening. Formant frequency variation over the course of the vowel was eliminated by holding the spec-

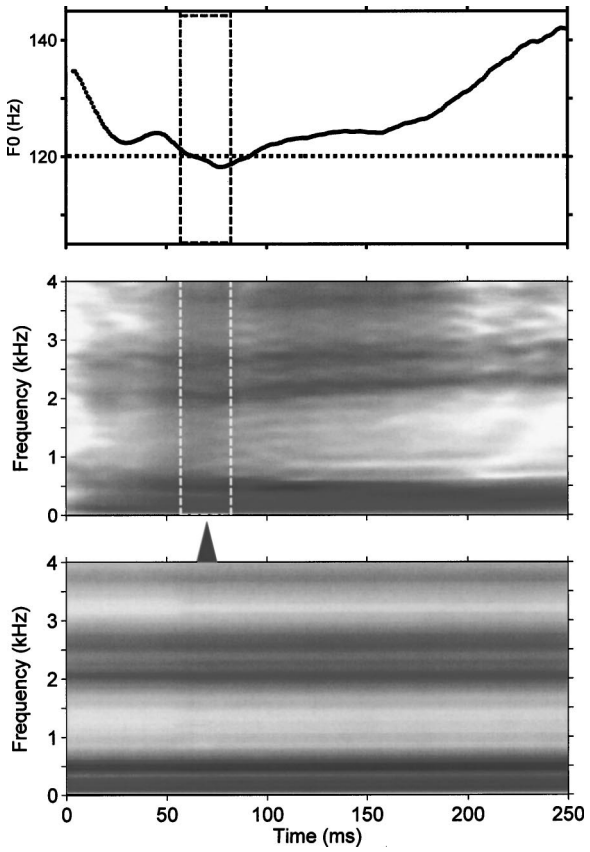

FIG. 1. Illustration of the F_0 and formant-flattening manipulations. The thick solid line in the upper panel shows the natural F_0 trajectory of the vowel from the syllable /hed/, spoken by an adult male. The flattened version is shown with the horizontal dashed line. The rectangle enclosed by dashed lines illustrates the 25-ms time window from which the flattened F_0 value was derived. The onset of the window was positioned at 20% of the vowel's duration. The middle panel shows the smoothed envelope spectrogram of the natural vowel. The bottom panel shows the smoothed envelope spectrogram of the same vowel with its formants flattened by averaging across the time window indicated by the dashed lines in the upper panel.

trum constant across the entire vowel, again sampling from a 25-ms window whose onset was positioned at 20% of the vowels duration. This strategy eliminates formant movement by fixing the spectral envelope at a point near the vowels onset, rather than by holding the frequencies of the formants constant using a formant synthesizer, as in previous studies by Hillenbrand and Nearey (1999) and Assmann and Katz (2000). The spectral envelope estimation stages of the STRAIGHT program provides a matrix of spectral magnitudes (N time frames $\times M$ frequency channels). A 1-ms frame update rate is used, and the number of frequency channels is determined by the length of the FFT (fast Fourier transform) (513 channels in this implementation). The output of this stage provides an estimate of the vocal tract transfer function, and resembles a smoothed spectrogram of the original signal, as illustrated in the middle panel of Fig. 1. The flattened version is shown in the bottom panel.

The experiment included five stimulus conditions: the original ''natural'' vowels and four synthesized versions, as described below.

Natural. A set of 180 vowels [three talkers×five groups (adult males, adult females, and children ages 3, 5, and 7 years)×12 vowels] was selected for the *natural* vowel condition. These were the same vowels used in experiments reported previously (Assmann and Katz, 2000; Katz and Assmann, 2001).

Variable FF, variable F_0. Synthesized versions of the *natural* vowels were constructed using the STRAIGHT vocoder, preserving the natural time variation in F_0 and in the spectral envelope without any parameter modifications.

Variable FF, flat F_0. The STRAIGHT vocoder was used to hold F_0 constant across the vowel, while preserving natural variations in the spectral envelope over time.

Flat FF, variable F_0. The STRAIGHT vocoder was used to hold the spectral envelope constant across the vowel, while preserving natural variations in F_0.

Flat FF, flat F_0. The STRAIGHT vocoder was used to hold both F_0 and the spectral envelope constant across the vowel.

2. Listeners

The listeners were ten young adults who had previously enrolled in a phonetics course at the University of Texas at Dallas. All were monolingual speakers of American English with no reported history of speech, hearing, or language disorders. The majority (eight of ten) were longstanding residents of the Dallas, Texas region.

3. Procedure

Stimuli were presented on-line at 48 kHz, low-pass filtered at 10 kHz (Tucker-Davis Technologies FT5), attenuated (TDT PA4), amplified (TDT HB5), and presented diotically via headphones (Sennheiser HD-414). All stimuli were adjusted to the same peak amplitude, resulting in levels between 65 and 72 dB SPL(A).

Listeners were tested individually in a sound-treated booth. Prior to the experiment, listeners completed three brief practice sets using vowels derived from a different set of talkers (three adult males, three adult females, and three 5-year-old children) than those used in the main experiment. In the first practice set, they listened to examples of the 12 natural vowels without responding. In the second practice set, they heard 36 vowels and identified them by selecting 1 of 12 response panels on the computer screen, labeled with phonetic symbols along with the following keywords: ''weed,'' ''did,'' ''made,'' ''bed,'' ''dad,'' ''mud,'' ''cawed,'' ''pod,'' ''bird,'' ''toad,'' ''wood,'' ''rude.'' Feedback was provided after each response indicating the correct (intended) vowel response, and listeners repeated the set until they reached a score of 31/36 (85% or better). In the third practice set, they listened without responding to 12 synthesized vowels, with three vowels randomly selected from each of the four synthetic speech conditions of the experiment. In the main experimental condition, listeners identified 900 vowel stimuli (12 vowels×5 conditions×5 talker groups×3 talkers) in a single block of trials, with all conditions, vowels, and talkers randomly interspersed. They entered their responses using the 12-panel response screen, but did not receive feedback. The experiment was self-paced, with an approximate 4-s delay between their response and the

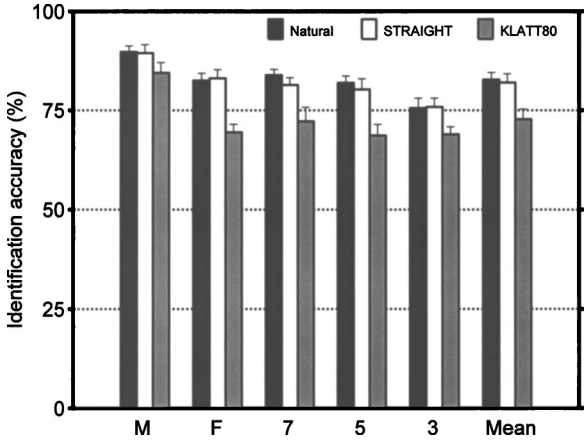

FIG. 2. Mean identification accuracy for natural and STRAIGHT synthesized vowels in experiment 1. Black bars show the mean accuracy for natural vowels, and white bars show the results for vowels synthesized with STRAIGHT in the variable F_0, variable FF condition. For comparison, the gray bars show the identification accuracy for vowels generated with the Klatt (1980) cascade formant synthesizer from Assmann and Katz (2000; Experiment 2). Error bars show the standard errors across the ten listeners.

presentation of the next vowel. Experimental sessions (including practice) were completed in about 90 min.

B. Results and discussion

1. Natural versus synthesized vowels

Figure 2 shows that listeners identified the vowels synthesized using STRAIGHT (white bars) as accurately as the natural versions (black bars). For comparison, the gray bars show the substantially lower identification accuracy for formant-synthesized vowels found by Assmann and Katz (2000, experiment 1). The pattern of identification accuracy was similar for natural and STRAIGHT-synthesized vowels across the five talker groups.

A three-way repeated measures analysis of variance on the identification data from the present experiment was carried out on the factors condition (natural versus STRAIGHT), talker group, and vowel. No significant differences between natural and STRAIGHT-synthesized vowels were obtained, nor were there significant two-way or three-way interactions of condition (natural versus synthesized) $\times$vowel$\times$talker group. There was a significant main effect of talker group, $F(4,36)=17.55$; $p<0.01$, with higher accuracy for the males compared to the females and children, and lower accuracy for the 3-year olds compared to the older children and adults (Scheffé test, $p<0.05$). The correlation between identification accuracy and F_0 was near zero ($r=0.01$; $N=180$; $p=0.34$), similar to the pattern reported by Assmann and Katz (2000).

2. Comparison of STRAIGHT and cascade formant synthesis

Vowels synthesized using STRAIGHT were identified as well as the original spoken vowels after which they were modeled, and were more accurately identified than the same vowels produced using the Klatt (1980) cascade formant synthesizer in our previous study (Assmann and Katz, 2000). To look for systematic vowel and/or group-specific differences in synthesis fidelity, we compared identification accuracy for corresponding pairs of natural and synthesized vowels. Three types of synthesis were considered: STRAIGHT synthesis (data from the current study) and two types of cascade formant synthesis, one using hand-tracked formants (Assmann and Katz, 2000, experiment 1) and the other using semi-automatic formant-tracking (Assmann and Katz, 2000, experiment 2).

Synthesis fidelity was summarized by difference scores (i.e., the difference, in percent, between the identification scores for natural and synthesized vowels) for each of the 180 vowel tokens in the three experiments, broken down in terms of vowel, talker group, and synthesis method. The same set of 180 natural vowels was used in each of the three experiments, but the listeners were different. Table I shows the number of vowel tokens showing a drop in identification accuracy of 25% or greater. There were 38 such cases for formant synthesis with hand-tracked formants, 35 for the semi-automated formant tracking, and 4 cases for STRAIGHT synthesis. Errors were not uniformly distributed across the vowels: some showed substantial declines while others were unaffected. Within each vowel category, the distribution across talkers and talker groups was also nonuniform. Vowels that were poorly identified when spoken by a given talker were often well identified when produced by another talker.

Comparison of error rates for vowels synthesized using hand-tracked formants and semi-automatic formant tracking revealed that different tokens caused the drop in these two conditions. A plausible interpretation is that different types of formant tracking errors are responsible. The correlation between the difference scores across these two conditions was small, but significant ($r=0.24$; $N=180$; $p<0.01$). The presence of a significant correlation suggests that sources of error common to the two types of formant estimation may be responsible for the drop in identification accuracy relative to natural vowels. However, the low magnitude of the correlation suggests that problems specific to each formant tracking method make a larger contribution. The overall conclusion is that no explicit combinations of vowel, talker group, or formant tracking method can be identified as the source of the problem. Rather, the broad distribution of error patterns appears to be due to token-specific types of formant tracking errors, combined with more general shortcomings of the synthesis procedure. A model of vowel identification was developed to further investigate this possibility and is described in Sec. III below.

3. Effects of F_0 and formant flattening

Figure 3 shows that holding F_0 constant using STRAIGHT synthesis did not reduce identification accuracy significantly, $F(1,9)=1.65$; $p=0.23$, while holding the spectral envelope constant had a substantial effect, $F(1,9)=725.44$; $p<0.01$. *Post-hoc* (Scheffé) tests revealed that 7 of the 12 vowels (/o/, /e/, /ʊ/, /ɪ/, /u/, /ɛ/, and /ɜ˞/, ranked in order of effect size) were significantly less accurately identified in the flat FF condition compared to variable FF.

The effects of F_0 flattening were negligible overall compared to the FF flattening effect, but there was a signifi-

TABLE I. Identification errors by vowel and talker group for three synthesis methods. Table entries are the numbers of synthesized vowels (from $N=3$ talkers) showing identification accuracy declines of 25% or greater from natural to synthesized conditions. Formant (H): cascade formant synthesis with hand-tracked formants (Assmann and Katz, 2000; experiment 1); Formant (A): cascade formant synthesis with semi-automatic formant tracking (Assmann and Katz, 2000; experiment 2).

	i	ɪ	e	ɛ	æ	ʌ	ɝ	ɑ	ɔ	o	ʊ	u	Total
						Formant (H)							
Males		1			2	1	1		2		1		8
Females	1	1		2	2			1			2	1	10
7-year olds		1	1	1	1	1			1		1	2	9
5-year olds			2		1	2			1			1	7
3-year olds		1					1	1		1			4
Total	1	4	3	3	6	4	2	2	4	1	4	4	38
						Formant (A)							
Males				2	1				1				4
Females	1		1	2	1	1		3			1		10
7-year olds				1	1	2							4
5-year olds	2	1	1	1		2			2	1		2	12
3-year olds	1					2		1				1	5
Total	5	1	2	6	3	7	0	4	3	1	1	3	35
						STRAIGHT							
Males													0
Females													0
7-year olds				1	1	1							3
5-year olds													0
3-year olds		1											1
Total	0	1	0	1	1	1	0	0	0	0	0	0	4

cant three-way interaction of $F_0 \times$FF flattening$\times$vowel, $F(11,99)=2.69$; $p<0.01$. This interaction is plotted in Fig. 4, which shows the mean effects of F_0 and FF flattening separately for each vowel. F_0 flattening produced only minor deviations from the pattern of FF flattening for individual vowels described above. Moreover, F_0 flattening had inconsistent effects, producing small increases in accuracy for some vowels but lower accuracy in others. In comparison, the effects of formant flattening showed a high degree of consistency across the two F_0 conditions.

The effect of formant flattening using STRAIGHT was twice the size of the effect found in our previous study that used formant synthesis (a decline of 23% compared to 11.5%; Assmann and Katz, 2000, experiments 1 and 2). This suggests that important details of time-varying spectral change are preserved by STRAIGHT but are lost in formant synthesis. This interpretation is supported by the finding that vowels synthesized with STRAIGHT were better recognized than vowels synthesized with cascade formant synthesis

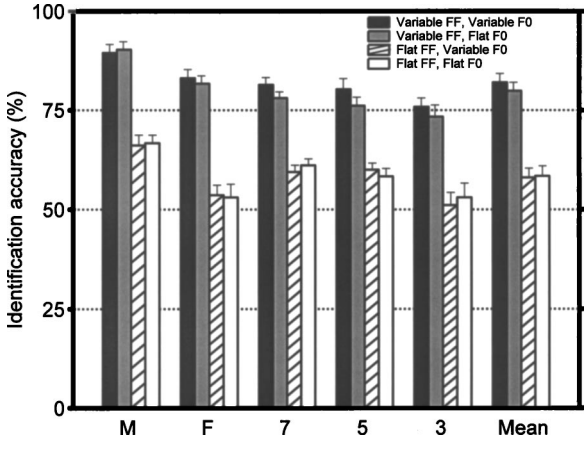

FIG. 3. Mean identification accuracy by talker group for conditions with variable and flattened F_0 and formant frequencies created using STRAIGHT synthesis in experiment 1. Error bars show the standard errors across the ten listeners.

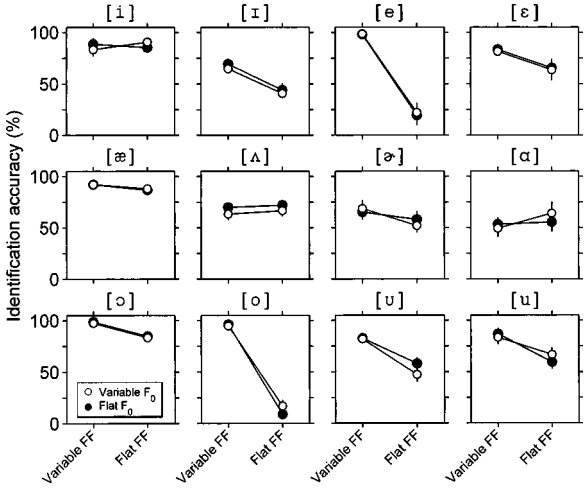

FIG. 4. Mean identification accuracy by vowel in conditions with variable and flattened F_0 and formant frequencies in experiment 1. Error bars show the standard errors across the ten listeners.

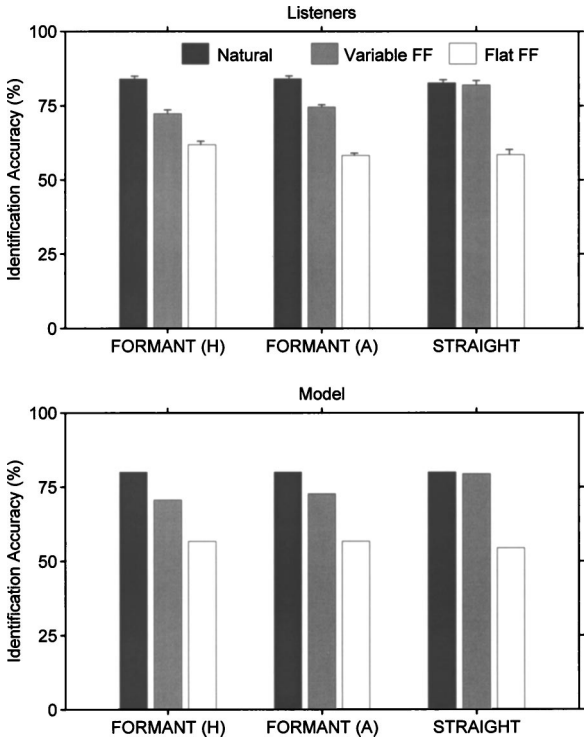

FIG. 5. The upper panel shows the mean identification accuracy for natural vowels (black bars) and synthesized vowels with time-varying formants (gray bars) or flattened formants (white bars). Formant (H): cascade formant synthesis with hand-tracked formants (Assmann and Katz, 2000; experiment 1); Formant (A): cascade formant synthesis with semi-automatic formant tracking (Assmann and Katz, 2000; experiment 2); STRAIGHT: vowels constructed using the STRAIGHT synthesizer in experiment 1. Error bars are standard errors across the listeners. The lower panel shows the predictions of the model for the same stimuli.

when time-varying spectral changes were preserved, but not when these changes were eliminated. This pattern is shown in the upper panel of Fig. 5, which summarizes the effects of FF flattening using formant synthesis (Assmann and Katz, 2000, experiments 1 and 2), and STRAIGHT synthesis in the present study. Most of the difference between the two synthesis methods was due to the higher performance with STRAIGHT for the variable FF vowels (82.0% for STRAIGHT, 71% for formant synthesis) rather than lower performance with flat FF vowels (58.4% for STRAIGHT, 59.5% for formant synthesis). Overall, the results suggest that formant flattening has a larger effect when STRAIGHT is used rather than formant synthesis because STRAIGHT does a better job of rendering the time-varying properties of vowels.

III. STATISTICAL PATTERN RECOGNITION MODEL

A. Acoustic measurements

To determine the acoustic basis for the drop in identification accuracy with formant synthesis, we carried out a series of comparisons between the natural and synthesized vowels, combining informal listening with acoustic measurements of the stimuli which showed a drop in identification accuracy of 25% or more (Table I). Inspection of these measurements failed to reveal any single acoustic property that might explain the poorer performance. However, careful listening to corresponding pairs of natural and formant-synthesized vowels revealed differences in phonetic quality that appeared, in some cases, to be related to systematic errors in formant tracking. We therefore suspected that formant synthesis errors in our previous study might have been at least partly responsible for the reduced performance. To address this issue, we analyzed the 180 stimuli from each of four conditions (natural vowels and the three synthesis types discussed in Sec. II B 2) using a new automatic technique for formant frequency measurement developed by Nearey (Nearey *et al.*, 2002), along with the STRAIGHT-TEMPO procedure for F_0 estimation (Kawahara *et al.*, 1999). The formant estimation algorithm uses autocorrelation linear predictive coding (LPC) to obtain formant candidates (F1,F2,F3) by solving for the roots of the predictor polynomial. Each utterance is analyzed at several different sampling rates with coordinated F3 cutoff frequencies and a fixed LPC order to obtain independent sets of candidates that are postprocessed by a simple tracking algorithm. The best matching set of formant candidates is determined by a measure of the similarity between the spectrogram of the original signal and one resynthesized from the estimated track set, in combination with other heuristic figures of merit (including formant continuity, ranges, and bandwidths).

Estimates of the formant frequencies (F1, F2, and F3) and F_0 were obtained at 2-ms intervals over the vocalic portion of the /hVd/ syllables for four sets of 180 vowels: (1) natural vowels; (2) vowels synthesized with the cascade formant model using hand-tracked formant frequencies [experiment 1 in Assmann and Katz (2000), designated formant (H)]; (3) formant-synthesized vowels using a semi-automated tracking procedure [experiment 2 in Assmann and Katz (2000), designated formant (A)]; and (4) vowels synthesized using STRAIGHT from the experiment described above. Frame-by-frame comparisons of the tracks indicated that F1, F2 and F3 frequencies were closer (i.e., absolute frequency distances were smaller) between the natural and STRAIGHT-synthesized vowels than between the natural and either type of formant-synthesized vowels. For example, the mean absolute frequency deviation between corresponding pairs of vowels in the natural and formant (H) conditions, measured between the 20% and 80% points in the vowel, was 60 Hz in F1, 109 Hz in F2, and 218 Hz in F3. In comparison, the average frequency difference between natural and STRAIGHT synthesis for the same 180 vowel pairs was 17 Hz in F1, 39 Hz in F2, and 62 Hz in F3. This analysis indicates that the formant frequencies of vowels synthesized using STRAIGHT were in fact closer to the natural vowels than those synthesized using cascade formant synthesis.

B. Model description

To determine whether the acoustic differences described above could account for the patterns of identification accuracy for natural vowels and three types of synthesized vowels, we implemented a version of the statistical pattern recognition model described by Hillenbrand and Nearey (1999). The aims of the modeling were (1) to study the basis for the increased effect of formant flattening with STRAIGHT synthesis compared to formant synthesis, and (2) to identify

TABLE II. Correlations of predicted APPi scores and observed mean identification accuracy across listeners. Formant (H): cascade formant synthesis with hand-tracked formants; Formant (A): cascade formant synthesis with semi-automatic formant tracking.

	Variable FF			Flat FF		
	Formant (H)	Formant (A)	STRAIGHT	Formant (H)	Formant (A)	STRAIGHT
Pearson *r*	0.51	0.56	0.27	0.73	0.52	0.55
R^2	0.26	0.31	0.07	0.53	0.27	0.30
N	180	180	180	180	180	180

acoustic properties that are preserved by STRAIGHT but not by formant synthesis that might explain the lower identification of vowels of the latter.

1. Training and testing stages

The model included two stages: a training phase and a testing phase. The training data consisted of acoustic measurements of a set of 3301 vowels, drawn from a larger set of 5040 vowels. The complete set included between 6 and 12 repetitions of each of the 12 vowels in /hVd/ words produced by 10 men, 10 women and 30 children, ages 3, 5, and 7 years, all from the north Texas region. Additional details of the vowel database are described in Assmann and Katz (2000). Tokens were omitted from the set if the recordings were low in amplitude, or if any acoustic measurements were missing or incomplete, or if they were judged to be mispronunciations during informal phonetic screening by one of the authors.

The test data were acoustic measurements of the stimuli from the experiment described above, along with measurements of the corresponding stimuli from experiments 1 and 2 in Assmann and Katz (2000). None of the vowels in the test set were included in the training set. For both training and test sets, formant frequency estimates were obtained using the automatic formant tracking method developed by Nearey *et al.* (2002).

The acoustic measures used to represent the vowels were the same as those used by Hillenbrand and Nearey (1999): the formant frequencies F1, F2, and F3 sampled at the 20% and 80% points in the vowel, mean F_0, and duration. All frequency measures were log-transformed. Linear discriminant analyses of the training data using this set of eight measures revealed that 85.9% of the 3301 tokens were correctly classified. Nearly half (206/465) of the classification errors involved /ɑ/ and /ɔ/, two vowels that were frequently confused by the listeners as well.

2. Predictions of synthesis fidelity and formant flattening

The lower panel of Fig. 5 shows the classification results from linear discriminant analyses of the test data. Comparison with listeners' data in the upper panel shows that the pattern recognition model captures three important aspects of the results: the lower accuracy for formant-synthesized vowels compared to STRAIGHT (for the variable FF stimuli); the decline in scores when formant frequency movement is eliminated; and the larger decline when formant frequency movement is eliminated from vowels generated using STRAIGHT compared to formant synthesis. Indeed, the close correspondence in the pattern of the means suggests that differences in the formant pattern (and possibly F_0, but not duration, which did not vary across the four conditions) might be responsible for the lower identification accuracy with formant synthesis compared to STRAIGHT.

This result must be interpreted cautiously, however, since a high degree of correspondence between the overall correct classification scores does not necessarily reflect accurate predictions for individual vowel tokens in the test set. To compare the performance of the model and listeners on a token-by-token basis, we adopted the approach described by Hillenbrand and Nearey (1999) and computed the *a posteriori* probability (APP) of group membership for each vowel token from linear discriminant function analysis. APP scores provide an index of the relative strength of group membership which can be compared to the mean identification accuracy scores for individual vowel tokens (Nearey and Assmann, 1986). Pearson product-moment correlation coefficients were used to measure the correspondence between *a posteriori* probabilities for the intended vowel (APPi) and the mean observed identification accuracy from the listeners. A high correlation would support the hypothesis that listeners and model rely on the same information.

Table II shows the correlation coefficients for the variable and flat FF conditions with each of the three synthesis types. Correlations were all significant by randomization tests (Nearey and Assmann, 1986) but explained only a modest proportion of the variance (7%–31% for variable FF stimuli and 27%–53% for the flat FF stimuli). In general, correlations were lower in conditions where mean accuracy was higher (i.e., for STRAIGHT synthesis), indicating that ceiling effects may place limits on the strength of the correlations. Consistent with previous findings (Hillenbrand and Nearey, 1999), these results suggest that F_0 and formant frequency measurements can account for some, but not all, of the variance in listeners' identification responses.

A further test of the model is provided by comparing the change in performance across key conditions, such as the identication accuracy drop from natural to synthesized vowels, or from variable FF to flat FF conditions. To determine how well the model predicts these patterns, we computed difference scores between the predicted *a posteriori* probabilities for natural and synthesized vowels and compared them with the observed difference scores for individual vowel tokens, with identification accuracy pooled across listeners. Similar comparisons were made for variable and flat FF conditions (Table III).

Columns in the left half of Table III indicate small but

TABLE III. Correlations of predicted APPi and observed identification accuracy difference scores. Left side: effects of synthesis fidelity (natural–synthesized). Right side: effects of formant flattening (variable FF–flat FF). Formant (H): cascade formant synthesis with hand-tracked formants; Formant (A): cascade formant synthesis with semi-automatic formant tracking.

	Natural–synthesized			Variable FF–flat FF		
	Formant (H)	Formant (A)	STRAIGHT	Formant (H)	Formant (A)	STRAIGHT
Pearson *r*	0.25	0.22	0.02	0.62	0.51	0.69
R^2	0.06	0.05	0.00	0.38	0.26	0.48
N	180	180	180	180	180	180

significant correlations between predicted and observed difference scores representing the effects of synthesis fidelity (natural–synthesized) for the two types of formant synthesis, but not for STRAIGHT-synthesized vowels. A significant correlation was not expected for the STRAIGHT condition, since there was no decline in identification accuracy with this type of synthesis. The correlations indicate that a small but significant proportion of the decline in identification accuracy from natural to synthesized vowels may be attributable to errors in the specification of the formant frequencies and F_0.

The three columns on the right in Table III list difference correlations for the effects of formant flattening. The correlations were moderate in size, and all were significant, accounting for between 26% and 48% of the variance in listeners' responses. This suggests that the drop in performance due to formant flattening can be explained to some degree by a model based on F_0 and formant frequency measurements of the vowel taken at 20% and 80% of its duration. Consistent with Hillenbrand and Nearey (1999), the present modeling results confirm that the effects of formant flattening can be simulated, to a first approximation, by neutralizing the second spectral sample in a two-target representation of the vowel. In addition, the model predicts the larger decline in identification accuracy when formant frequency movement is eliminated from vowels generated using STRAIGHT compared to formant synthesis.

IV. GENERAL DISCUSSION

Using a high-quality vocoder, experiment 1 replicated three key findings reported in our previous studies (Assmann and Katz, 2000; Katz and Assmann, 2001): (1) vowel identification accuracy was unaffected by holding F_0 constant over the duration of the vowel; (2) identification accuracy was lowered by holding the formant frequencies constant; and (3) there were no systematic differences in the effects of formant frequency flattening as a function of F_0 or talker group. The findings provide little support for the idea that time-varying spectral change helps to solve the sparse sampling problem that arises when F_0 is high, as in children's voices. The correlation between F_0 and identification accuracy was close to zero. One possibility is that the impact of sparse sampling is minimized by the presence of other (nonspectral) cues to vowel identity in natural speech.

In contrast to our earlier findings using cascade formant synthesis, which showed significantly lower performance compared to natural vowels, the current experiment showed no drop in identification accuracy for vowels synthesized using STRAIGHT. Vowel identification accuracy as a function of vowel category and talker group was similar to the pattern found with natural vowels. These findings suggest that STRAIGHT may provide a useful method for investigating vowel and talker group differences, particularly for women and children's voices which are generally harder to render using cascade formant synthesis (Klatt and Klatt, 1990).

Formant flattening showed an effect of nearly twice the magnitude when the STRAIGHT synthesizer was used to produce the stimuli rather than cascade formant synthesis. A comparison of the effects of formant flattening for the two synthesis types indicated that performance was much higher for STRAIGHT synthesis when formant frequency movement was preserved (reaching the level of accuracy found for natural vowels). In comparison, identification accuracy for vowels with flattened formants was similar for the two synthesis methods. Thus, the increased effect of formant flattening may arise because STRAIGHT synthesis does a better job of preserving time-varying spectral change in vowels.

Acoustic analyses were carried out to establish the basis for the effects of synthesis fidelity and formant flattening. These analyses confirmed that the formant frequencies were more accurately preserved in vowels synthesized with STRAIGHT than with cascade formant synthesis used in our previous studies. A statistical pattern recognition model was implemented to determine the extent to which formant frequency measurement errors could explain the drop in performance. The model was trained on formant frequency and F_0 measurements from a large sample of vowels spoken by men, women, and children. It provided accurate predictions of mean identification accuracy as a function of stimulus type (cascade formant synthesis, STRAIGHT synthesis, and natural vowels). The decline in identification accuracy for vowels synthesized with cascade formant synthesis compared to natural vowels (and the absence of this effect with STRAIGHT synthesis) was well predicted by the model, suggesting that formant measurement error makes a significant contribution to the effects of synthesis fidelity. The difference between STRAIGHT and formant synthesis was more pronounced for stimuli with time-varying than flattened formants, and this was also well predicted by the model, suggesting that factors related to time-varying spectral change contribute to the drop in identification accuracy.

The relatively small proportion of variance explained by the model suggests that factors other than formant measurement error may contribute to synthesis fidelity. On average,

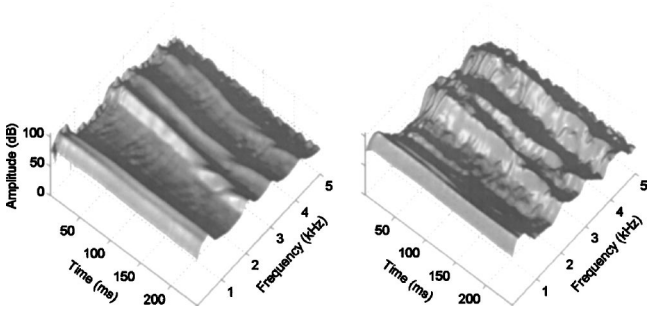

FIG. 6. The 3-D surface plots of the smoothed spectrogram generated by the STRAIGHT analysis-synthesis algorithm. The right panel shows the natural version of the vowel in /hɪd/ spoken by an adult female talker; the left panel shows the cascade formant synthesis version.

there was a 9%–12% drop in identification accuracy for vowels synthesized using cascade formant synthesis compared to the original recordings (Assmann and Katz, 2000). However, there was substantial variability across the vowel set, with some tokens showing little change and others showing a large drop in identification accuracy. We examined the subset of vowels for which cascade formant synthesis led to a large drop in identification accuracy (compared to the natural version) and the STRAIGHT version was well identified. Within this subset, vowels that showed similar formant patterns for the two synthesis types (cascade, STRAIGHT) were of particular interest. For instance, the estimated formant frequencies for the syllable /hɪd/ spoken by one of the adult female talkers were nearly identical for the natural and cascade formant synthesis versions. The natural vowel was identified as /ɪ/ with 100% accuracy, and the formant synthesis version was consistently misidentified as /u/. In this case, the reduced identification of the formant-synthesized version appears to be due to factors other than formant frequency estimation error.

Figure 6 shows 3-D surface plots of the smoothed spectrograms generated by STRAIGHT for this example. We chose the STRAIGHT spectral representation rather than a standard spectrogram because it (1) eliminates the ripple in the spectrogram introduced by vocal fold vibration, (2) forms the basis for high-quality synthesis, and (3) highlights aspects of the time-varying spectrum envelope that may be linked to the drop in identification accuracy. The natural vowel is shown in the right panel and the formant-synthesized version on the left. The STRAIGHT-synthesized vowel was not included in this comparison because its spectral representation was virtually identical to that of the natural vowel. While the frequency locations of the formant peaks are similar, there are additional details in the smoothed spectrogram of the natural vowel that are not preserved by formant synthesis. For example, the amplitudes of the higher formants are reduced in the synthesized version, and additional (nonformant) peaks occur in the natural version that are not preserved in the synthesized version. In addition to formant frequency measurement error (considered above) we have explored various measures to predict the identification accuracy drop, including formant amplitude. However, measured differences in formant amplitude between natural and formant-synthesized vowels were not significantly correlated with differences in vowel identification accuracy, and so far no *single* acoustic property has emerged as a strong candidate.

In comparison with the effects of synthesis fidelity, the model did a better job of predicting the effects of formant flattening, including the larger decline in accuracy when formant frequency flattening was implemented using STRAIGHT compared to formant synthesis. The findings extend previous modeling results reported by Hillenbrand and Nearey (1999) to high-quality synthetic speech in which the formant frequencies are not explicitly manipulated as synthesis control parameters. When the effects of formant flattening were expressed as identification accuracy difference scores between variable and flattened formant conditions, the model accounted for up to 48% of the variance in the difference scores. Overall, the results provide further evidence of the importance of formant frequency movement for vowel identification (Hillenbrand and Nearey, 1999; Assmann and Katz, 2000) and support the idea that the increased effects of formant flattening with high-fidelity synthesis are due to more accurate rendering of time-varying spectral change.

ACKNOWLEDGMENTS

Thanks to Lucy Liu for assistance in testing the subjects, Terry Nearey for helpful discussions, Hideki Kawahara for providing the STRAIGHT synthesis software, and Randy Diehl, Winifred Strange and an anonymous reviewer for helpful comments on the manuscript. Portions of this work were reported at the 142nd meeting of the Acoustical Society of America, 4 December 2001, Fort Lauderdale, FL [J. Acoust. Soc. Am. **110**(5), 2658 (2001)]. This work was supported by a National Science Foundation grant (#0318451) to author PA.

Andruski, J., and Nearey, T. M. (**1992**). ''On the sufficiency of compound target specification of isolated vowels and vowels in /bVb/ syllables,'' J. Acoust. Soc. Am. **92**, 390–410.

Assmann, P. F., and Katz, W. F. (**2000**). ''Time-varying spectral change in the vowels of children and adults,'' J. Acoust. Soc. Am. **108**, 1856–1866.

Carlson, R., Fant, G., and Granstrom, B. G. (**1975**). ''Two-formant models, pitch, and vowel perception,'' in *Auditory Analysis and Perception of Speech*, edited by G. Fant and M. A. A. Tatham (Academic, London), pp. 55–82.

Diehl, R. L., Lindblom, B., Hoemeke, K. A., and Fahey, R. P. (**1996**). ''On explaining certain male-female differences in the phonetic realization of vowel categories,'' J. Phonetics **24**, 187–208.

Hillenbrand, J. M., and Nearey, T. M. (**1999**). ''Identification of resynthesized /hVd/ utterances: Effects of formant contour,'' J. Acoust. Soc. Am. **105**, 3509–3523.

Hillenbrand, J. M., Clark, M. J., and Houde, R. A. (**2001a**). ''Some effects of duration on vowel recognition,'' J. Acoust. Soc. Am. **108**, 3013–3022.

Hillenbrand, J. M., Clark, M. J., and Nearey, T. M. (**2001b**). ''Effects of consonant environment on vowel formant patterns,'' J. Acoust. Soc. Am. **109**, 748–763.

Katz, W. F., and Assmann, P. F. (**2001**). ''Identification of children's and adults' vowels: Intrinsic fundamental frequency, fundamental frequency dynamics, and presence of voicing,'' J. Phonetics **29**, 23–51.

Kawahara, H. (**1997**). ''Speech representation and transformation using adaptive interpolation of weighted spectrum: Vocoder revisited,'' *Proceedings of the ICASSP*, pp. 1303–1306.

Kawahara, H., Masuda-Katsuse, I., and de Cheveigné, A. (**1999**). ''Restructuring speech representations using a pitch-adaptive time-frequency smoothing and an instantaneous-frequency-based F0 extraction,'' Speech Commun. **27**, 187–207.

Klatt, D. H. (**1980**). ''Software for a cascade/parallel formant synthesizer,'' J. Acoust. Soc. Am. **67**, 971–995.
Klatt, D. H., and Klatt, L. C. (**1990**). ''Analysis, synthesis, and perception of voice quality variations among female and male talkers,'' J. Acoust. Soc. Am. **87**, 820–857.
Liu, C., and Kewley-Port, D. (**2004**). ''STRAIGHT: A new speech synthesizer for vowel formant discrimination,'' ARLO **5**, 31–36.
Marin, C. M. H., and McAdams, S. (**1991**). ''Segregation of concurrent sounds. II. Effects of spectral envelope tracing, frequency modulation coherence, and frequency modulation width,'' J. Acoust. Soc. Am. **89**, 341–351.
Nearey, T. M. (**1989**). ''Static, dynamic, and relational properties in vowel perception,'' J. Acoust. Soc. Am. **85**, 2088–2113.
Nearey, T. M., and Assmann, P. F. (**1986**). ''Modeling the role of inherent spectral change in vowel identification,'' J. Acoust. Soc. Am. **80**, 1297–1308.
Nearey, T. M., Hillenbrand, J. M., and Assmann, P. F. (**2002**). ''Evaluation of a strategy for automatic formant tracking,'' J. Acoust. Soc. Am. **112**, 2323.
Ryalls, J. H., and Lieberman, P. (**1982**). ''Fundamental frequency and vowel perception,'' J. Acoust. Soc. Am. **72**, 1631–1634.
Stevens, K. N., and House, A. S. (**1963**). ''Perturbation of vowel articulations by consonantal context: An acoustical study,'' J. Speech Hear. Res. **6**, 111–128.
Strange, W., Jenkins, J. J., and Johnson, T. L. (**1983**). ''Dynamic specification of coarticulated vowels,'' J. Acoust. Soc. Am. **74**, 695–705.

Lexical frequency and neighborhood density effects on the recognition of native and Spanish-accented words by native English and Spanish listeners[a)]

Satomi Imai[b)]
Division of Speech and Hearing Sciences, University of Alabama at Birmingham, 1530 Third Avenue South, Birmingham, Alabama, 35294

Amanda C. Walley
Department of Psychology, University of Alabama at Birmingham, 1530 Third Avenue South, Birmingham, Alabama, 35294

James E. Flege
Division of Speech and Hearing Sciences, University of Alabama at Birmingham, 1530 Third Avenue South, Birmingham, Alabama, 35294

(Received 5 May 2004; revised 28 September 2004; accepted 5 October 2004)

This study examined the effect of presumed mismatches between speech input and the phonological representations of English words by native speakers of English (NE) and Spanish (NS). The English test words, which were produced by a NE speaker and a NS speaker, varied orthogonally in lexical frequency and neighborhood density and were presented to NE listeners and to NS listeners who differed in English pronunciation proficiency. It was hypothesized that mismatches between phonological representations and speech input would impair word recognition, especially for items from dense lexical neighborhoods which are phonologically similar to many other words and require finer sound discrimination. Further, it was assumed that L2 phonological representations would change with L2 proficiency. The results showed the expected mismatch effect only for words from dense neighborhoods. For Spanish-accented stimuli, the NS groups recognized more words from dense neighborhoods than the NE group did. For native-produced stimuli, the low-proficiency NS group recognized fewer words than the other two groups. The-high proficiency NS participants' performance was as good as the NE group's for words from sparse neighborhoods, but not for words from dense neighborhoods. These results are discussed in relation to the development of phonological representations of L2 words. (200 words).
[DOI: 10.1121/1.1823291]

PACS numbers: 43.71.Es, 43.71.Gv [RLD] Pages: 896–907

I. INTRODUCTION

Speech perception becomes attuned to native or first language (L1) sounds during infancy and childhood (e.g., Best, 1995; Jusczyk, 1993; Werker and Polka, 1993). Because of differences in the phonetic inventories between any two languages, individuals who learn a second language (L2) in adulthood may have L2 speech representations that are affected by their L1 phonology, and so differ from those of native speakers (cf. Flege, 1995; Kuhl and Iverson, 1995). A failure to reattune speech representations to specific features of the L2 explains, in part, why L2 learners often display poor speech recognition performance, especially in nonideal listening conditions (e.g., Bradlow and Bent, 2002; Meador, Flege, and MacKay, 2000). However, the word recognition difficulty that L2 listeners sometimes experience may be the result of insufficient higher-level knowledge of the L2, including weaker lexical constraints, in addition to differences in bottom-up processing. The overall purpose of the present study was to provide a better understanding of the interface between the phonological and lexical levels in L2 word recognition.

To date, most L2 speech perception research has focused on demonstrating differences in the processing of phonemic and/or phonetic information by L2 listeners (for review, see Strange, 1995). At the phonemic level, it has been well documented that L2 listeners do not perceive certain sounds in the same way as L1 listeners in categorical identification and discrimination tasks (e.g., Best, McRoberts, and Goodell, 2001; Flege, Munro, and Fox, 1994). According to Best (1995), foreign language (or L2) phonemes that can be assimilated to a single L1 phonemic category present the greatest discrimination difficulty (e.g., native Spanish speakers categorize both English /i/ and /ɪ/ as instances of Spanish /i/), a claim that is generally supported across different languages. More recently, Pallier, Colome, and Sebastian-Galles (2001) showed that in a repetition priming task, some Spanish-dominant bilinguals of Catalan and Spanish processed nonwords containing phonemes that were contrastive

[a)]Portions of this study were presented at the 144th Meeting of the Acoustical Society of America, Nashville, TN, May 2003, and in ''Spoken word recognition of accented and native speech: Lexical factors affecting native and non-native listeners,'' Proceedings from the 15th International Congress of Phonetics Sciences, Barcelona, Spain, August 2003.

[b)]Electronic mail: imais@uab.edu

only in Catalan as if they were Spanish phonemes, without distinguishing the two Catalan phonemes.

At the phonetic level, two languages may exhibit subtle variations, and previous research has demonstrated that adult L2 learners are often not sensitive to the relevant differences. For example, word-initial /p/, /t/, and /k/ are produced with more aspiration in English than Italian, and word-final stops are less likely to be released in English. Thus, native Italian speakers who have learned English as an L2 have difficulty identifying English stop consonants in noise (MacKay, Meador, and Flege, 2001). In a gating experiment using nonwords, Sebastian-Galles and Soto-Faraco (1999) showed that Spanish-dominant bilinguals required more phonetic information to identify Catalan-specific phonemes than Catalan-dominant bilinguals did.

One limitation of previous L2 speech perception research is that we currently know little about how differences in phonemic and phonetic perception between native and non-native listeners impact higher or later levels of speech processing—specifically, word recognition. Several recent studies have examined L2 word recognition in sentence context and found poorer performance by non-native listeners as compared to native listeners (Bradlow and Bent, 2002; Mayo, Florentine, and Buus, 1997; Meador *et al.*, 2000; van Wijngaarden, 2001; van Wijngaarden, Steeneken, and Hougast, 2002). However, in these studies, characteristics of the stimulus words to be identified (e.g., word frequency) and the carrier sentences have not been controlled or systematically manipulated. Thus, the extent to which non-native listeners' poorer performance is due to inaccurate segmental perception or insufficient semantic/syntactic knowledge is unclear.

In addition to the lack of empirical evidence regarding the interface between the phonological and lexical levels in L2 perception, there has been a paucity of theoretical attention directed toward this issue. In the L1 acquisition literature, it has been suggested that young children first establish holistic (e.g., syllable-based) representations of words, and only gradually develop phonological representations that include more detailed, segmental information (e.g., Ferguson and Farwell, 1975; Metsala and Walley, 1998). A major impetus for this developmental shift is vocabulary growth. On this view, an increasing number of items overlap with one another as the lexicon expands, and more fine-grained representations are needed for fast, accurate word recognition (see also Charles-Luce and Luce, 1990). Perhaps with greater L2 exposure and additional word learning, L2 learners' lexical representations may also become more fine-grained or fully specified *vis-à-vis* their new language.

There is some evidence relating L2 learners' segmental perception and word recognition. In Meador *et al.*'s (2000) study, early and late Italian-English bilinguals were asked to repeat semantically unpredictable English sentences that were presented in different levels of noise. The number of correctly repeated words was analyzed and compared to identification scores for vowels and consonants (assessed in other experiments). Regression analyses showed that accuracy scores for segment identification accounted for 17% of the variance in the number of words correctly repeated after demographic variables (e.g., age of arrival, use of the L1, length of residence in Canada) were partialled out. Although these results are correlational, they suggest that accurate perception of L2 vowels and consonants contributes to differences in word recognition among bilinguals.

A study by Bradlow and Pisoni (1999) provided a fuller picture of the lexical factors that influence word recognition. These researchers presented ''easy'' and ''hard'' words to native and non-native English speakers of varying L1 backgrounds. The easy words had a high frequency of occurrence and were from sparse neighborhoods (i.e., were phonologically similar to few other words); the hard words had a low frequency of occurrence and were from dense neighborhoods (i.e., were confusable with many other words). In addition, the neighbors of the easy words were, on average, of low frequency, and those of the hard words were of high frequency. The results showed that both listener groups recognized fewer hard than easy words, primarily because words from dense neighborhoods are confusable with one another (e.g., Luce and Pisoni, 1998). However, the difference between the hard and easy words was larger for the non-native group (cf. Takayanagi, Dirks, and Moshfegh, 2002). Bradlow and Pisoni therefore concluded that non-native listeners may have reduced sensitivity to some of the phonetic details that are necessary for lexical discrimination.

The present study extended the Bradlow and Pisoni (1999) study in several ways. First, we compared the performance of native English (NE) speakers and two groups of native Spanish (NS) speakers who differed in pronunciation proficiency (as defined by overall degree of foreign accent). Second, the participants of this study were tested on English words that were spoken by both a NE and a NS speaker. The two NS groups and two types of speech input (native-produced and foreign-accented stimuli) were included to assess how the representation/processing of lexical items might vary at different stages of L2 acquisition.

We assumed that our NS participants' phonological representations would not be optimally matched to English speech input, especially those of the less proficient NS participants (''the phonological mismatch hypothesis''). We expected NS participants to be better able to recognize English words spoken with a Spanish accent than words spoken by a native English speaker. That is, a better match should exist between the NS participants' phonological representations and the acoustic phonetic specification of English words as spoken by other NS speakers, in part because they often hear such renditions and because the NS participants themselves pronounce English words in a similar manner. We assumed that L2 phonological representations are initially affected by the L1 sound system, but that as L2 learning proceeds and L2 pronunciation proficiency increases, these representations become more attuned to the L2 and thus more similar to those of native speakers. Any advantage for Spanish-accented stimuli should therefore be smaller for more proficient NS participants than less proficient ones. If such a phonological mismatch effect were found, L2 learners' phonological representations could be understood as being organized differently than those of native speakers.

There is, in fact, some evidence that L2 listeners benefit

from hearing L2 speech produced with L1 accent. In a study by Bent and Bradlow (2003), NE and non-native listeners of different L1 backgrounds listened to English sentences (all embedded in white noise) that were spoken by a NE talker and by proficient and nonproficient Chinese and Korean talkers. The researchers assumed that L2 learners develop a shared knowledge base for the L2 sound system which helps them understand the L2 speech of other talkers of the same language background (the ''matched interlanguage speech intelligibility benefit'') and even of different language backgrounds (the ''mismatched interlanguage speech intelligibility benefit''). In support, it was found that NE listeners recognized more words in the sentences spoken by the NE talker than by the L2 talkers, whereas Chinese and Korean listeners' performance was as good for sentences spoken by proficient talkers of their L1 as it was for sentences spoken by the NE talker. Further, another group of non-native listeners from various language backgrounds (ten different languages) recognized as many words in the sentences spoken by proficient Chinese and Korean talkers as by the NE talker.

Similar results were obtained by van Wijngaarden (2001), who examined the recognition of both native-produced and English-accented Dutch sentences by native Dutch listeners and by native English listeners. The native English listeners had spoken Dutch as an L2 for an average of 20 years and were highly proficient. Using a speech reception threshold method, it was found that the native Dutch listeners generally tolerated a higher level of noise than the English listeners did, and they tolerated more noise for native-produced than English-accented speech. However, the native English listeners tolerated noise for English-accented speech to the same extent as for the native Dutch speech. Thus, non-native speech was less intelligible to native listeners, but it was as intelligible as native speech to non-native listeners.

In a subsequent study (van Wijngaarden *et al.*, 2002), native Dutch participants were asked to identify words in Dutch, English, and German sentences that were produced by native talkers of each language, as well as by native Dutch talkers (thus including Dutch-accented English and German sentences). Again using a speech reception threshold method, the researchers found that the Dutch listeners, who were more proficient in English than German, tolerated more noise for native-produced as compared to Dutch-accented English sentences, whereas more noise was tolerated for Dutch-accented vs native-produced German sentences.

The results from the three studies just cited are, however, only suggestive with respect to our phonological mismatch hypothesis. Lexical characteristics such as word frequency were not controlled or examined in these studies. In addition, the proficiency of non-native listeners in the L2 varied substantially across studies and/or was not systematically evaluated. Further, sentence recognition is affected by various suprasegmental factors including prosody and speaking rate (e.g., Bradlow, Torretta, and Pisoni, 1996; Cohen, Douaire, and Elsabbagh, 2001; Cutler and van Donselaar, 2001), but the influence of these factors was not considered either. As a result, it is not clear how any advantage in perceiving foreign-accented speech might be related specifically to L2 listeners' segmental representations for spoken words.

According to the phonological mismatch hypothesis evaluated in the present study, the accuracy or efficiency of spoken word recognition should be reduced when listeners' lexical representations do not match input speech stimuli. Thus, our hypothesis bears not only on listeners' perception of L2 words, but also on the perception of foreign-accented speech by native listeners. The NE participants in our study were expected to recognize more English words spoken by another NE speaker than English words spoken with a Spanish accent. Apart from the findings already reviewed, the only other relevant research on foreign-accented speech perception by native listeners has used sentence stimuli to show reduced performance as compared to native-produced speech—a difference that has been attributed to normalization processes (Derwing and Munro, 1997; Munro and Derwing, 1995) and processing cost (Derwing and Munro, 2001; Munro, 1998; Munro and Derwing, 2001). If our hypothesis were upheld, it could offer a further explanation at the level of segmental representations for the difficulty that native speakers have in perceiving non-native speech.

Like Bradlow and Pisoni (1999), we examined the effect of word frequency and neighborhood density on word recognition. However, our study differs from that of Bradlow and Pisoni in a third important respect. In Bradlow and Pisoni's study, lexical factors covaried—i.e., easy words were of high frequency and were from sparse neighborhoods, whereas hard words were of low frequency and were from dense neighborhoods. As the researchers themselves acknowledged, their non-native listeners' recognition of fewer hard than easy words might have reflected the influence of word frequency, apart from any effect of neighborhood density. Indeed, in contrast to native listeners, the non-native listeners also rated hard words as less familiar than easy words. Bradlow and Pisoni used a 7-point familiarity scale, but only a rating of ''7'' (''I know this word'') was taken as clear evidence that a word was known (see Balota, Pilotti, and Cortese, 2001, for discussion). A follow-up analysis examining the subset of lexical items given a rating of ''6'' or ''7'' yielded essentially the same results as the analysis of all items. It is nevertheless possible that the non-native participants actually knew fewer hard than easy words, and that this contributed to their difficulty in recognizing hard words.

To address these limitations, the stimulus set examined in the present study consisted entirely of known English words that varied orthogonally in word frequency and neighborhood density.[1] Our results should therefore help pinpoint the causes of any word recognition difficulty by non-native listeners. We hypothesized that the effects of word frequency and neighborhood density would be greater when there is a mismatch between phonological representations and incoming speech stimuli. NE participants should thus display larger effects of these lexical factors for Spanish-accented speech than for native-produced stimuli, whereas NS participants should show larger effects for native-produced speech than Spanish-accented stimuli. Specifically, the impact of frequency (better recognition for high- than low-frequency words) and neighborhood density (better recognition for words from sparse than dense neighborhoods, or a ''compe-

tition effect'') should be greater in the mismatch than the match conditions.

Finally, we also collected subjective frequency estimates for the test words from both NE and NS participants to further explore differences in lexical organization. Specifically, we wanted to examine how strongly subjective and objective word frequency measures might be correlated, and whether or not subjective frequency is related to word recognition performance. Experienced word frequency has typically been operationalized by reference to the number of occurrences of lexical items in written corpora such as that of Kučera and Francis (1967), which is based on written materials. However, several previous studies have indicated that such estimates of word frequency may be confounded with age of acquisition and other dimensions of word familiarity that affect various stages of word recognition (e.g., Connine *et al.*, 1990; Garlock, Walley, and Metsala, 2001; Morrison and Ellis, 1995). In addition, objective frequency counts are subject to sampling biases, including the under-representation of low-frequency words and restricted range effects (Carroll, 1971; Lachman, Shaffer, and Hennrikus, 1974). For these reasons, subjective estimates may actually be better predictors of psychological familiarity, and thus word recognition performance (Gernsbacher, 1984; Gordon, 1985). Past research has also revealed modality-specific effects for subjective frequency estimates, suggesting that people can differentiate between auditory and visual experiences with particular words (Amano, Kondo, and Kakehi, 1995; Balota *et al.* 2001; Gaygen and Luce, 1998). In our study then, we asked participants to provide estimates for the relative frequency with which the test words were spoken and/or heard.

In summary, the present study differed from previous studies in several ways: (i) two lexical factors, word frequency and neighborhood density, were orthogonally varied; (ii) native-produced and foreign, Spanish-accented stimuli were presented to listeners; (iii) our non-native listeners had similar L1 backgrounds, but varied in English pronunciation proficiency; (iv) steps were taken to ensure that all the test words were known to the listeners; and (v) subjective frequency ratings were collected.

The specific aims of this study were (a) to determine if there is an advantage for recognizing words when listeners' presumed phonological representations match incoming speech stimuli; (b) to determine how such an advantage might change as L2 pronunciation proficiency increases; (c) to examine the separate effects of word frequency and neighborhood density on L2 word recognition; and (d) to evaluate the relation between subjective and objective word frequency for NE and NS participants, as well as the effect of subjective frequency on recognition performance.

II. EXPERIMENT

A. Method

1. Stimuli and design

a. Stimulus selection. To ensure that all participants, including those in the NS groups, knew all the test words, we began by developing a list of 365 words that were likely to be acquired by adults in the early stages of learning English as an L2. All were one syllable in length, and most had a CVC structure (e.g., *bird, cake, love*). In a pilot test, six NS-speaking listeners (none of whom subsequently participated in the study) indicated if they knew each word and, if so, rated it for subjective familiarity using a scale that ranged from 1 (''least familiar'') to 7 (''most familiar'').

TABLE I. Mean word frequency and neighborhood density of test words (ranges are in parentheses). Note. WF: word frequency, or occurrence per million words (Kučera and Francis, 1967); ND: neighborhood density, or number of words that differ by a one segment, addition, deletion, or substitution (Luce and Pisoni, 1998).

	High WF		Low WF	
ND	Dense	Sparse	Dense	Sparse
Example	''bed''	''bring''	''bell''	''boss''
WF	169.5 (54-500)	177.8 (58-591)	18.0 (3-37)	22.4 (1-41)
ND	23.5 (17-39)	10.0 (3-15)	23.8 (19-30)	10.4 (4-14)

Four sets of 20 words that differed orthogonally in text word frequency (Kučera and Francis, 1967) and neighborhood density (Luce and Pisoni, 1998) were formed from the 332 items that were known by at least five of the six pilot listeners and that received a familiarity rating greater than 5.0. All 80 test words are listed in the Appendix. The four sets of test words consisted of: (a) words with relatively high text frequency from dense neighborhoods; (b) high-frequency words from sparse neighborhoods; (c) low-frequency words from dense neighborhoods; and (d) low-frequency words from sparse neighborhoods. As shown in Table I, words differing in frequency had comparable neighborhood density values, and words differing in neighborhood density had comparable frequency values.[2]

b. Recording. The 80 test words were recorded by a male NE talker who was born and raised in the Midwest but had lived in Birmingham, Alabama for 21 years. The stimuli produced by this talker are referred to as the ''native-produced'' (or simply ''native'') stimuli. The test words were also recorded by an adult male speaker of Spanish who was born in Chile, had resided in the U.S. for 2 months, and was judged by the authors to speak English with a strong foreign accent. These stimuli are referred to as ''Spanish-accented'' (or ''accented'') stimuli. The words produced by both talkers were digitized at 22.05 kHz and normalized for peak intensity (50% of full scale).

The NE talker read the test words from a list, one at a time. For accented stimuli, in order to generate a range of tokens to select from, the NS talker produced the 80 test words four times each using different elicitation methods (see Flege, Munro, and MacKay, 1995). The four tokens of each test word produced by the NS talker were auditorily evaluated by the third author, a NE speaker with extensive training in phonetics. A few tokens contained a segmental substitution that resulted in a perceived change in lexical identity (e.g., a *hide* token that sounded like *hi*, a *bed* token that sounded like *Beth*). These tokens were eliminated and the token of each word that was judged to have the strongest foreign accent among the remaining tokens was retained for the study.

A single NE pilot listener listened to the 80 native

stimuli in the clear and recognized all of them. Three NE pilot listeners evaluated the 80 Spanish-accented stimuli. At least one listener recognized 69 stimuli. Of the 11 stimuli not recognized by any listener, three stimuli were misheard in the same way. Specifically, all three listeners heard the accented *fish* stimulus (pronounced /fiʧ/) as *feet* /fit/; the accented *voice* stimulus (pronounced /bɔɪs/) as *boy*s /bɔɪz/; and the accented *boss* stimulus (pronounced /bɔɪs/) as *bus* /bʌs/. These misperceptions by the native English pilot listeners do not indicate that the aforementioned Spanish-accented stimuli were inappropriately chosen. The *fish, voice,* and *boss* stimuli were correctly recognized by 57% of the NS-speaking listeners when presented in noise in the experiment proper. This suggested that while the Spanish-accented stimuli might not have been realized in such a way as to promote correct lexical access by NE-speaking listeners, their phonetic realization was sufficient for lexical access by at least some people who themselves spoke English with a Spanish accent.

The third author carried out a broad phonetic transcription of the 80 Spanish-accented stimuli. A total of 17 segmental substitutions was noted, the most common being /s/ for /z/ (in *cheese, noise, nose*), /tʃ/ for /ʃ/ (in *push, shake, shine*), and /ɔ/ for /ɑ/ (in *boss, lost, sock*). The substitutions were somewhat more common in words drawn from sparse than dense neighborhoods (12 vs 5), but about equally common in high- and low-frequency words (8 vs 9). The imbalance in number of substitutions between high- and low-neighborhood word stimuli is probably due to the fact that segmental substitutions result in a perceived change in lexical identity less often for sparse word stimuli than dense word stimuli. As expected from previous research (e.g., Flege and Munro, 1994), all stimuli contained subsegmental divergences from the phonetic norms of English and therefore conveyed foreign accent. These included the shortening of voice-onset time in word-initial tokens of /p t k/, the partial devoicing of word-final tokens of voiced obstruents, the prolongation of initial /h/ tokens, and the weakening of final /n/ segments.

The stimuli were measured for duration and the duration values were submitted to a 2 (talker)$\times$2 (neighborhood density)$\times$2 (word frequency) ANOVA. Words from dense neighborhoods were significantly shorter than words from sparse neighborhoods ($M=473$ vs 528 ms), $F(1,76)=8.4$, $p<0.01$, and the Spanish-accented stimuli were shorter than the native-produced stimuli ($M=448$ vs 552 ms), $F(1,76)=80.0$, $p<0.01$. The effect of frequency was nonsignificant, however; $F(1,76)=1.1$, $p>0.10$, and no significant interactions were found.

The 160 stimuli (80 test words$\times$2 talkers) were mixed with noise to bring word recognition scores off ceiling. Multitalker babble was created by adding the voices of six NE and six NS talkers. The noise segment was set to 10% of full scale of peak intensity, and then added to the 160 stimuli described earlier (which had been normalized at 50% peak intensity of full scale). This yielded stimuli having S/N ratios of approximately 14 dB.

c. Counterbalancing procedure. Two blocks of 40 test words, designated ''A'' and ''B'' (with ten items randomly selected from each of the four lexical sets in which word frequency and neighborhood density varied) were formed. The order of words was randomized within each block. Blocks A and B were presented as both native and Spanish-accented stimuli, and the order of presentation for stimulus type (native vs Spanish-accented) was counterbalanced. Thus, the participants were randomly assigned to one of four counterbalanced conditions: A-native/B-accented, A-accented/B-native, B-native/A-accented, or B-accented/A-native. Across participants, each test word was presented in both native and Spanish-accented form. A given listener heard each of the 80 test words (half native, half Spanish-accented) only once.

2. Procedure

Participants were tested individually in a sound booth in a session lasting about 1 h. They completed three primary tasks in the following order: a word recognition task, a written lexical knowledge test, and a sentence production task. These tasks were preceded by a pure-tone hearing screening and followed by a language background questionnaire in which demographic information such as age of arrival and length of residence in the United States, and use of English and Spanish was collected (see Table II).

In the word recognition task, the stimulus words were presented one at a time via loudspeakers. The participants were asked to write down each word on a prepared answer sheet. They were given a short demonstration of the task, and a 16-item practice session preceded each of the two blocks. The participants were encouraged to adjust loudness to a comfortable level during the practice session. The practice words differed from the 80 test words. They were recorded by a female NE and a female NS talker and presented with the same multitalker babble as the test stimuli. Each test block began with five extra items which were not analyzed.

In the lexical knowledge test, participants were asked to indicate whether or not they knew each of the 80 test words, which were presented in written form. Five nonword foils were included to ensure that participants would veridically report any test items they did not know. If they knew an item, participants provided an estimate of frequency of usage on a scale that ranged from 1 (''seldom hear/say this word'') to 7 (''often hear/say this word''). To encourage them to use the entire rating scale when rating the 80 items, participants were given examples of seven words that were presumed to span the full 7-point scale (e.g., *dog* is heard/said much more often than *octopus*). Thus, our rating scale emphasized the relative frequency of word usage. Next, two 7-item practice sets were presented. When participants demonstrated an understanding of the instructions, the test items were presented.

The sentence production task involved saying five simple English sentences three times each using a delayed repetition technique (see Flege *et al.*, 1995). The sentences were later used to assign NS participants to subgroups differing in English pronunciation proficiency. Only the third, fluent repetition of each sentence was used for group assignment (see below).

Participants' written responses in the word recognition task were scored ''correct'' when they exactly matched the

TABLE II. Demographic information for the HP and LP groups. Shown for each characteristic are means (standard deviations and ranges are in parentheses). Note. HP: high pronunciation proficiency group; LP: low pronunciation proficiency group. FA (foreign accent) ratings are based on a 9-point scale from 1 (strongest accent) to 9 (least accent). AOA: age-of-arrival in the U.S. in years; LOR: length of U.S. residence in years. Estimates of hours of English and Spanish use per day are based on a 6-point scale from 1 (none), 2 (0.5 h), 3 (1 h), 4 (2 h), 5 (4 h), and 6 (6 h or more). Estimates of hearing Spanish-accented speech are based on a scale from 1 (very seldom) to 7 (very often). Estimates of ability to speak and understand English and Spanish are based on a 7-point scale (1—poor; 4—OK; 7—good).

	HP	LP
Chronological age	30 (8.3; 19–46)	33 (8.5; 20–47)
FA rating	6.3 (1.8; 3.6–8.8)	2.1 (0.5; 1.4–2.9)
AOA	19.8 (8.8; 1.9–38.5)	29.0 (8.2; 13.4–41.9)
LOR	9.7 (6.7; .9–24.2)	4.1 (3.4; 0.02–1.2)
Age English study began	8.9 (4.3; 0–16)	10.4 (2.6; 6–14)
Years of English study	6.5 (4.5; 0–14)	6.5 (4.1; 0.1–13)
Education in home country	13.5 (5.8; 3–22)	15.8 (4.9; 4–25)
Education in US	5.2 (4.6; 0–14)	1.5 (1.8; 0–5)
Spoken English use	5.9 (0.3; 5–6)	4.6 (1.4; 2–6)
Spoken Spanish use	5.1 (1.2; 2–6)	5.4 (1.1; 2–6)
Hearing Spanish-accented speech	2.4 (1.7; 1–6)	3.3 (2.5; 0–7)
Ability to speak English	5.9 (0.9; 4–7)	4.3 (1.1; 2–6)
Ability to speak Spanish	6.8 (0.5; 5–7)	6.9 (0.3; 6–7)
Ability to understand English	6.0 (0.8; 4–7)	4.8 (1.2; 3–7)
Ability to understand Spanish	6.8 (0.5; 5–7)	7.0 (0; 7)

target words. However, we anticipated that the NS participants might misspell some words. Given that our interest was in spoken word recognition rather than in spelling ability, the experimenter examined each participant's written responses after practice sessions and after each block of 40 test stimuli. She asked for clarification if the handwriting was not legible. For responses that were not exact, she asked what word the participant had intended to write. If the explanation corresponded to the target (e.g., ''being noisy'' for the written response ⟨laud⟩ for the stimulus *loud*), the written response was scored as correct.

3. Participants

Sixty NS speakers living in or near Birmingham, AL and 16 NE speakers, who were born and raised in Alabama, were recruited through advertisements in a university paper and through personal contacts. The NS participants were required to have been born in a predominantly Spanish-speaking country, to have learned Spanish as their L1 from native Spanish-speaking parents, and to be between the ages of 19–50 years. Nine of the 60 NS participants were excluded: two failed the pure-tone hearing screening; one did not complete the experiment; three failed to report three or more nonword foils in the lexical knowledge test as unknown words; and three knew fewer than 96% (77/80) of the test words.

As mentioned earlier, participants recorded sentences after the lexical knowledge test. Three sentences produced by each of the 51 retained NS participants and the 16 NE participants were digitized (22.05 kHz), and then randomly presented to seven NE listeners from Alabama. Sentences produced by the NS and NE speakers who had recorded the stimuli for the word recognition task were also presented. The NE listeners rated the sentences using a scale that ranged from 1 (''strong accent'') to 9 (''no accent'').

An average foreign accent (FA) rating was computed for each NS participant. The 16 NS participants with the mildest foreign accents were assigned to a ''high pronunciation proficiency'' (HP) group, with the restriction that there were four participants from each of the four counterbalancing conditions in this group. The 16 NS participants with the strongest foreign accents were assigned to a ''low pronunciation proficiency'' (LP) group with the same restriction. The average age, in years, of the NE, HP, and LP groups was 34 (range: 22–47), 30 (range: 19–46), and 33 (range: 20–47), respectively, and the average FA rating was 8.67 (range: 7.5–9.0), 6.34 (range: 3.6–8.8), and 2.13 (range: 1.4–2.9). Demographic information for the two NS groups is shown in Table II.

B. Results

1. Word recognition scores

Percent-correct scores for the ten items in each of the eight conditions of the stimulus design were obtained for each participant and submitted to a 3(group: NE, HP, LP)×2 (stimulus type: native, Spanish-accented)×2 (word frequency: high, low)×2 (neighborhood density: dense, sparse) ANOVA. Group served as a between-subjects factor, and stimulus type, word frequency and neighborhood density as within-subjects factors. Only significant main effects or interactions will be reported. Significant interactions were followed up by simple effects tests with Bonferroni's correction ($p<0.05$).

The ANOVA yielded significant main effects of group, $F(2,45)=15.27$, $p<0.001$, stimulus type, $F(1,45)=98.82$, $p<0.001$, and neighborhood density, $F(1,45)=67.06$, $p<0.001$. Both the NE and HP groups performed better than the LP group (66.6% and 65.0% vs 53.0%). Also, more native than accented stimuli were correctly recognized (70.4% vs 52.8%), as were more words from sparse than dense neighborhoods (66.6% vs 56.6%).

The two-way group×stimulus type interaction was significant, $F(2,45)=29.73$, $p<0.001$. The NE and HP groups performed better for native than accented stimuli, whereas

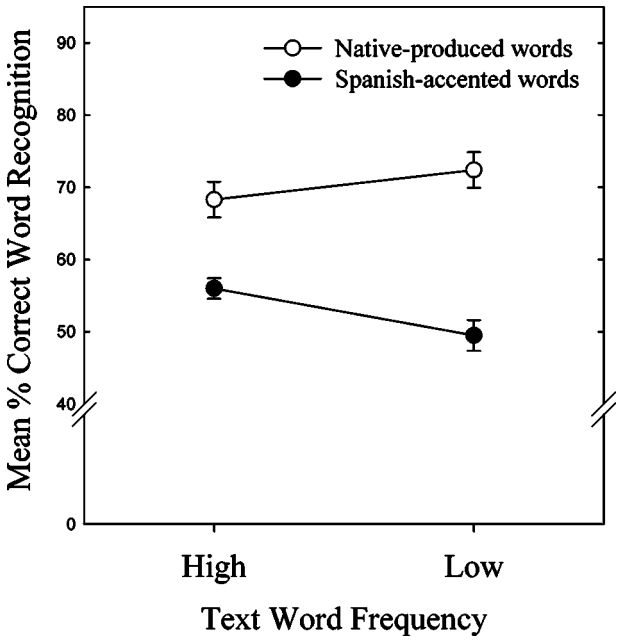

FIG. 1. Mean percent-correct word recognition scores as a function of stimulus type (native, accented speech) and text word frequency. Error bars represent one standard error of the mean.

the LP group's performance was similar for the two types of stimuli. This finding only partially supported the phonological mismatch hypothesis. That is, although the NE group did recognize more native than accented stimuli, the LP group did not recognize more Spanish-accented than native stimuli.

The two-way stimulus type×word frequency interaction was also significant, $F(2,45)=14.99$, $p<0.001$. This was the only significant effect involving word frequency (see Fig. 1). *Post hoc* tests revealed that more high- than low-frequency words were recognized in the accented condition, $F(1,47)=9.03$. The opposite trend for native stimuli did not reach significance when Bonferroni's correction was applied, $F(1,47)=5.11$. This result might reflect subtle differences in the way the NE and the NS talker produced the stimuli. The NE talker might have produced the low-frequency words more clearly than the high-frequency words (e.g., Geffin and Luszcz, 1983; Wright, 1979), whereas the NS talker might have produced the high-frequency words more accurately (with less foreign accent because of the frequent use) than low-frequency words. However, as noted in the Method section, when duration and segmental substitutions were analyzed, no differences were found for high- vs low-frequency words by either the NE or NS talker.

The significant three-way group×stimulus type ×neighborhood density interaction, $F(2,45)=5.56$, $p<0.01$, is shown in Fig. 2. For words from sparse neighborhoods (right panel), there was no difference between the NE, HP, and LP groups' performance when the stimuli were accented (59.4%, 59.1%, and 57.8%, respectively), $F(2,45)=0.04$, whereas both the NE and HP groups performed better than the LP group for native stimuli (83.4% and 82.2% vs 57.5%), $F(2,45)=36.54$. For words from dense neighborhoods (left panel), the HP and LP groups performed better than the NE group when the stimuli were accented (51.6% and 48.1% vs 40.6%), $F(2,45)=5.82$. In contrast, for native-produced stimuli, the NE group performed better than the HP group, who performed better than the LP group (83.1% vs 67.5% vs 48.4%), $F(2,45)=43.64$. Thus, for both native and accented words from sparse neighborhoods, the NE and HP groups performed similarly. Interestingly, however, for words from dense neighborhoods, the NE group recognized more native stimuli than the HP and LP groups, whereas the HP and LP groups recognized more accented stimuli than the NE group did.

The significant three-way interaction points to a differential influence of neighborhood density (i.e., better word recognition for words from sparse than dense neighborhoods) for the three groups. The HP and LP groups displayed a competition effect only for the native stimuli, $F(1,15)=56.07$ and $F(1,15)=12.23$ ($p<0.05$, Bonferroni), whereas the NE group displayed this effect only for the accented stimuli, $F(1,15)=22.35$ ($p<0.05$, Bonferroni). The difference between words from sparse and dense neighborhoods for the accented stimuli did not reach significance for the LP

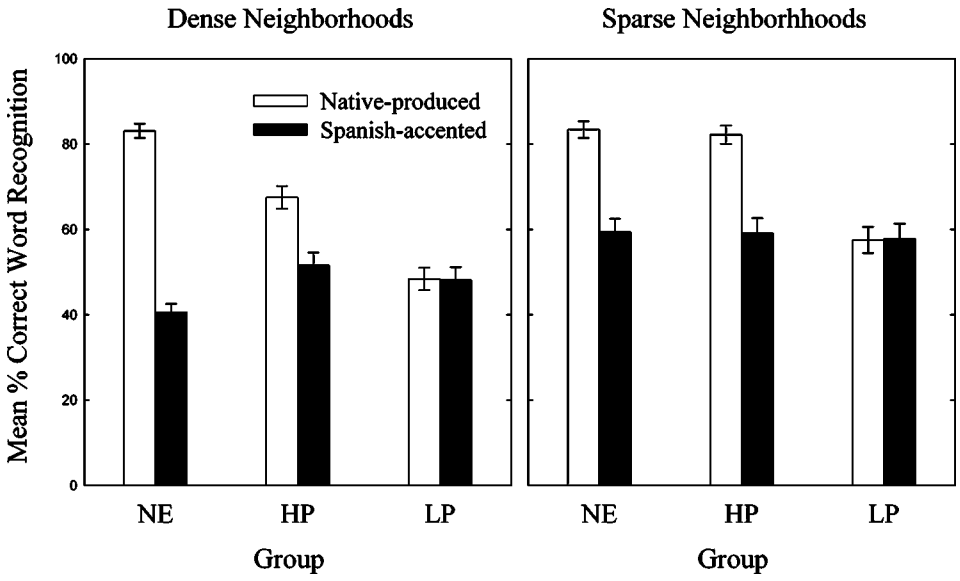

FIG. 2. Mean percent-correct word recognition scores as a function of stimulus type and neighborhood density for the native English (NE), high pronunciation proficiency (HP), and low pronunciation proficiency (LP) groups. Error bars represent one standard error of the mean.

group (57.8% vs 48.1%), $F(1,15)=5.21$ ($p>0.05$, Bonferroni), or the HP group (59.1% vs 51.6%), $F(1,15)=2.21$ ($p>0.10$, Bonferroni). Thus, the results show interesting interactions by neighborhood density and stimulus type. The competition effect is evident when there were mismatches between speech input and phonological representations. That is, when fine-grained phonological discrimination was required (for words from dense neighborhoods), the mismatch between phonological representations and speech stimuli seems to have impeded performance.

The phonological mismatch hypothesis predicts that fewer words should be recognized when there is a large discrepancy between listeners' phonological representations and the speech input they hear. We further anticipated that this might be especially true for low- vs high-frequency words and/or words from dense vs sparse neighbors. The results show that the NE and HP groups recognized more native than accented stimuli, suggesting that the HP group has developed representations of English words that were close to those of the NE speaker. The LP group, however, did not recognize more Spanish-accented than native stimuli, thus failing to support our hypothesis. Also, word frequency did not interact with group. Possible reasons for this lack of support will be provided in the Discussion section.

Although the effect of word frequency was minimal, the three groups did recognize words differently according to stimulus type (native vs accented) and neighborhood density. For words from dense and sparse neighborhoods, no group recognized more Spanish-accented than native stimuli. However, there were between-group differences, such that the NS groups recognized more Spanish-accented stimuli from dense neighborhoods than the NE group, whereas the NS groups' performance was similar to the NE group's for accented stimuli from sparse neighborhoods. These findings partially support the phonological mismatch hypothesis; i.e., the effect of mismatched conditions was observed when differences between groups were considered.

As noted in the Methods section, analyses of stimulus duration and segmental substitution of Spanish accented stimuli showed differences between words from dense and sparse neighborhoods. The words from dense neighborhoods were shorter in duration and had fewer substitutions than the words from sparse neighborhoods. There were no differences in duration or the number of substitutions between high- and low-frequency words. Our focus in this study was on group differences in recognition performance, and the duration difference would have affected the three groups equally. As there were more substitutions for sparse than dense, if there were an effect of substitution, it would have counteracted the mismatch effect we obtained. Thus, the confounding of the characteristics of Spanish-accented speech and stimulus selection was probably minimal.

2. Correlational data for NS participants

Pearson's r correlations between the word recognition scores for native and accented stimuli, FA ratings, and other demographic information for the 32 NS participants were obtained ($p<0.001$, unless otherwise noted). As in previous studies (e.g., Flege, 1988; Yeni-Komshian, Flege, and Liu, 2000), we found a negative correlation between mean FA ratings and age of arrival (AOA) in the U.S. ($r=-0.63$), as well as a positive correlation between FA ratings and length of residence, or LOR ($r=0.72$). AOA was strongly correlated with years of education in the home country and in the U.S. ($r=0.73$ and 0.72) and also English use ($r=0.56$). FA ratings was highly correlated with estimates of English use ($r=0.56$). Estimates of Spanish use were not correlated with any of these variables.

Recognition scores for native stimuli were significantly correlated with FA ratings, AOA, years of education in the U.S. ($r=0.64,-0.47$ and 0.66), and with estimates of English use ($r=0.41$, $p<0.05$), but only marginally with LOR ($r=0.33$, $p=0.07$). The moderately high correlation between recognition of the native stimuli and the FA ratings suggests there is indeed a link between good L2 perception and pronunciation.

Notably, word recognition scores for the accented stimuli were not significantly correlated with any of the measures examined here. In particular, having an L2 phonological system that is substantially affected by the L1, as implied by having a strong foreign accent, was not correlated with better recognition of Spanish-accented words. This null finding is consistent with the ANOVA results, which showed little difference in performance for Spanish-accented stimuli between the HP and LP groups.

3. Subjective frequency ratings

We next calculated Pearson's r correlations between the NE, HP, and LP groups' subjective frequency ratings for the 80 test words: $r=0.82$ for NE and HP; $r=0.78$ for NE and LP; $r=0.88$ for HP and LP ($p<0.001$, in each instance). These strong correlations indicated that for the test words selected for this study, the estimated frequency of word use was similar across listener groups, regardless of proficiency in English. The correlations between the subjective frequency ratings of our three groups and text word frequency were in the moderate range: $r=0.36$, 0.42, and 0.52, for the NE, HP, and LP groups, respectively ($p<0.001$, in each instance).

4. The effect of subjective frequency on word recognition

Thus far, text word frequency does not seem to have had a strong effect on spoken word recognition performance. Previous work suggests that subjective measures of experienced word frequency may be more sensitive than objective ones. We therefore reanalyzed participants' word recognition scores using their subjective frequency ratings. The 40 words from dense neighborhoods were rank ordered according to mean subjective frequency ratings from the 54 participants, and then divided into a set of 20 high subjective frequency words (M rating$=5.0$) and a set of 20 low subjective frequency words ($M=3.0$). Similarly, sparse words were subdivided into high and low subjective frequency categories ($M=5.1$ vs 3.6).[3] See the Appendix for average subjective frequency ratings for each word.

Percent-correct scores for these new conditions were submitted to a 3 (group: NE, HP, LP)×2 (stimulus type: na-

TABLE III. Effects obtained for ANOVAs of word recognition scores. Note. In the original analysis, test words were categorized according to text word frequency; in the reanalysis, they were categorized according to subjective frequency ratings.

Effect	Original analysis (text word frequency)	Reanalysis (subjective frequency)
Frequency	$F(1,45)<1$ n.s.	$F(1,45)=36.1$[a]
Frequency× stimulus type	$F(1,45)=15.0$[b]	$F(1,45)=2.4$ n.s.
Frequency× neighborhood density	$F(1,45)<1$ n.s.	$F(1,45)=35.0$[a]
Frequency×stimulus type× neighborhood density	$F(1,45)<1$ n.s.	$F(1,45)=29.8$[a]

[a]$p<0.01$.
[b]$p<0.05$.

tive, Spanish-accented)×2 (subjective frequency: high, low) ×2 (neighborhood density: dense, sparse) mixed-design ANOVA. Because the reclassification of test words did not affect the results obtained for other variables, we report only those effects related to subjective frequency.

The new analysis yielded four effects that differed from the original ANOVA (see Table III). As in the original analysis, there was no interaction of group with subjective frequency, suggesting subjective frequency affected word recognition by all listeners similarly. In the new analysis, there was a significant main effect of subjective frequency, $F(1,45)=36.1$, $p<0.001$. More high- than low-frequency words were correctly recognized (67% vs 57%). Also, there was a significant two-way interaction between subjective frequency and neighborhood density, $F(1,45)=35.0$, $p<0.001$. More words from sparse than dense neighborhoods were recognized when the words were of high subjective frequency (57.3% vs 75.5%), whereas no neighborhood density effect was found for low subjective frequency words (55.8% vs 57.6%). Last, the three-way subjective frequency ×neighborhood density×stimulus type interaction was significant, $F(1,45)=29.8$ $p<0.001$.

The three-way interaction (see Fig. 3) was explored by tests of simple main effects (Bonferroni, $p<0.05$). For both native and accented stimuli, the differences between words from sparse and dense neighborhoods were significant only for high, not low subjective frequency items. However, this neighborhood density effect was much larger for accented, as opposed to native stimuli.

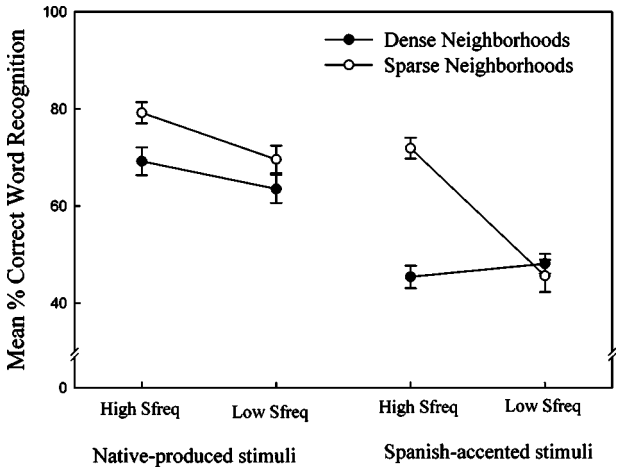

FIG. 3. Mean percent-correct word recognition scores as a function of stimulus type, subjective frequency, and neighborhood density. Error bars represent one standard error of the mean.

In sum, when subjective frequency was used to classify the test words, there was an interactive effect of neighborhood density on word recognition. For native stimuli, performance was in the expected direction (i.e., better for high- than low-frequency items) for words from both dense and sparse neighborhoods. However, for Spanish-accented stimuli, only words from sparse neighborhoods followed this pattern; the recognition of less phonologically confusable items was enhanced when they were of high frequency, whereas the recognition of highly confusable items was not affected by word frequency.

III. DISCUSSION

Previous studies have shown that L2 learners have difficulty recognizing L2 words (e.g., Bradlow and Bent, 2002; Mayo *et al.*, 1997). One likely source of this difficulty is that perceptual representations for vowels and consonants are not optimally attuned to the L2; another is insufficient higher-level, lexical knowledge. To date however, only a handful of studies have considered the relations between L2 learners' phonological representations and their higher-level, lexical knowledge (e.g., Bradlow and Pisoni, 1999; Meador *et al.*, 2000). The present study evaluated the influence of two lexical factors (word frequency and neighborhood density) on word recognition by NE listeners and two groups of NS listeners who differed in overall degree of foreign accent (high pronunciation proficiency vs low pronunciation proficiency). Listeners were asked to identify words that were spoken by a NE speaker (native-produced stimuli) and by a NS speaker (Spanish-accented stimuli).

According to our phonological mismatch hypothesis, differences between the phonetic specification of vowels and consonants in English words and listeners' lexical representations should lead to decreased word recognition performance. We hypothesized that NS adults tend to use ''Spanish-like'' phonological representations when processing spoken English words. We also hypothesized that, concurrent with L2 learners' improved L2 pronunciation, their L2 lexical representations would more closely resemble those of native speakers. We assumed that NE listeners' lexical representations are optimally attuned to the typical pronunciation of English words. Thus, we expected mismatches to occur when the NE listeners attempted to recognize the Spanish-accented stimuli and when the NS listeners attempted to recognize the native stimuli. The latter mismatch effect was expected to be larger for the LP vs HP group.

This mismatch effect was expected to be influenced by lexical factors such as word frequency and neighborhood density. Specifically, we anticipated that low-frequency words might have higher thresholds for activation than high-frequency words (see the models of Becker, 1980; Forster, 1981), and thus be harder to recognize in the mismatch conditions where the bottom-up input was not optimal. We also expected that fewer words from dense than sparse neighbor-

hoods would be recognized in the mismatch conditions because the former require more fine-grained segmental perception (see also Bradlow and Pisoni, 1999).

Our results provided some support for the phonological mismatch hypothesis. Although the NE and HP groups performed consistently better for native than Spanish-accented stimuli, the LP group's performance for Spanish-accented stimuli was no better than for native stimuli. There are several possible reasons why we did not obtain the expected mismatch effect for the LP group. First, although there are ''typical'' foreign-accent patterns by talkers of a particular L1, there are likely idiosyncrasies for individuals that are difficult to tease apart from these general patterns. Differential L2 experience in terms of the quality and quantity of input might produce foreign accents that are more varied across L2 learners than individual variations among L1 talkers. Thus, phonological ''matches'' for native-produced stimuli with native listeners might be greater than matches especially for accented stimuli with the LP group. Second, Spanish has regional accents and the NS participants in our study were from various Central and South American countries. This heterogeneous background might have reduced the effect of exact phonological matches. Third, we added noise to our stimuli, and it has been shown that noise can have more adverse effects on non-native vs native listeners (e.g., van Winjingarden, 2001). Perhaps our LP participants needed clearer segmental information for accurate recognition.

The effect of word frequency on word recognition in our study was similar across groups, which might be due to our having employed only known words. Another possible reason why we did not observe strong text frequency effects is that text word frequency does not constitute a very sensitive measure of the psychological familiarity of words (Balota *et al.*, 2001; Garlock *et al.*, 2001; Gernsbacher, 1984; Gordon, 1985). Indeed, when our stimulus sets were reorganized and analyzed according to subjective frequency estimates, more high- than low-frequency words were recognized overall by all three groups (67% vs 57%). Further, there was a boost in recognition scores for high-frequency words from sparse neighborhoods, and this effect was larger for Spanish-accented stimuli. This may be because recently used words have higher activation potentials and are easier to recognize with limited phonetic information than words of infrequent use.

There were group differences in word recognition according to stimulus type and neighborhood density. For native stimuli, lower word recognition scores were obtained for the LP group, who had strong foreign accents, than for the NE and HP groups. This held true for words drawn from both dense and sparse neighborhoods. Lower scores were also obtained for the HP than NE group, but only when accurate segmental perception was especially important—i.e., for words from dense neighborhoods. In contrast, for Spanish-accented stimuli, both NS groups outperformed the NE group for words from dense neighborhoods that required more fine-grained speech perception.

In the present study, pronunciation proficiency was used to define high- and low-proficiency NS groups. We assumed that good L2 pronunciation corresponds to more native-like L2 lexical representations. In agreement with previous foreign accent research (e.g., Flege *et al.*, 1995), the demographic information indicated the HP participants tended to have arrived in the U.S. at an earlier age than the LP participants ($M = 19.8$ vs 29.0 years), to use English more (about 6 or more hours a day vs 3 hours), and to have lived longer in the U.S. ($M = 9.7$ vs 4.1 years). These differences might well have contributed to the HP participants' superior English pronunciation, and presumably to the differences observed in word recognition performance.

The present results confirm that during spoken word recognition, higher-level processes interact with more bottom-up, segmental perception. The performance differences between the HP and LP groups for native stimuli that we observed further indicated that the lexical representations of the HP group more closely resembled those of the NE group than the LP group, but that they are not identical.

Most models of spoken word recognition assume a matching process between incoming speech sounds and phonological representations in the mental lexicon (e.g., Gaskell and Marslen-Wilson, 1997; McClelland, 1988; Norris, McQueen, and Cutler, 1995). The nature of these representations has been investigated in many previous studies (e.g., Hintzman, 1986), but few studies have considered such representations for those learning an L2, or how they are related to the L1 phonology (Pallier *et al.*, 2001). Further, to our knowledge, no studies have examined whether L2 lexical representations change as L2 pronunciation improves. The observed differences between the LP and HP groups in word recognition performance provided indirect evidence that improvements in English pronunciation correspond to more native-like representations that more closely match speech of NE speakers.

Similar to our phonological mismatch hypothesis, Bent and Bradlow (2003) have proposed that there is an interlanguage speech intelligibility benefit that is enjoyed by L2 listeners. That is, L2 learners have a shared knowledge base that aids the recognition of speech produced by non-native vs native talkers. This shared knowledge base encompasses numerous features of speech, including stress patterns, intonation, phonotactics, as well as segmental features. In contrast, our mismatch hypothesis focuses on segmental perception and attempts to control these other potentially relevant factors. Additional studies at the sentence level will be needed to elucidate the ways in which such factors affect L2 word recognition in a more precise manner.

Further research using time-sensitive tasks, such as priming, will also be needed to define the time course of the effects of word frequency and neighborhood density, especially regarding L2 speech processing (e.g., Pallier *et al.*, 2001). Perhaps word frequency influences an early stage of recognition by activating candidate words, while neighborhood density affects a later stage, where matching processes between speech input and lexical representation occur (e.g., Dahan, Magnuson, and Tanenhaus, 2001). The fact that we did not find group differences in the effects of either text word frequency or subjective frequency suggests that the initial stage of word activation may be similar for the NS and NE groups. However, as suggested by the differential effects

of neighborhood density, the later matching stage may differ between NE and NS speakers.

In conclusion, the results of this study supported the phonological mismatch hypothesis, at least when the neighborhood density effect is considered. There was a greater effect of neighborhood density on spoken word recognition when there were presumed mismatches between lexical representations and incoming speech sounds (i.e., native stimuli for the NS groups and Spanish-accented stimuli for the NE group) than when there were matches. This may be because bottom-up processing of speech segments in words from dense neighborhoods was more affected by differences in phonological representations as compared to words from sparse neighborhoods. The HP group showed better recognition of native stimuli than the LP group, and their performance for words from sparse neighborhoods was as good as that of the NE group, indicating changes in phonological representations as L2 pronunciation improves. However, both NS groups showed reduced recognition of words from dense neighborhoods, suggesting that even when L2 learners' segmental perception improves, their performance under conditions requiring more fine-grained perception may still be compromised.

ACKNOWLEDGMENTS

This study was supported by NIH Grant DC00257. We thank Ana Castaneda for the recruitment of participants and Mitchell Sommers for information about the Washington University in St. Louis Speech and Hearing Lab Neighborhood Database. In addition, we appreciate the comments of two anonymous reviewers and those of Dr. R. Diehl on a previous version of this paper.

APPENDIX

Test words. Note. WF: word frequency; ND: neighborhood density; SF-AVE: average subjective frequency rating across our three listener groups. ND values were obtained from the Washington University in St. Louis Speech and Hearing Lab Neighborhood Database (see the references).

Word	WF	ND	SF-AVE	Word	WF	ND	SF-AVE	Word	WF	ND	SF-AVE	Word	WF	ND	SF-AVE
bed	127	25	5.85	bring	158	8	5.69	bell	19	27	2.17	boss	20	11	4.27
call	188	26	6.25	choice	113	3	4.46	bird	31	22	3.50	cart	5	14	2.44
date	103	24	5.33	cold	171	15	5.38	burn	15	22	2.33	cheese	9	13	5.23
face	371	21	4.79	faith	111	11	4.23	cake	13	26	3.79	coin	10	14	4.10
fall	147	26	3.71	fast	78	15	5.04	corn	34	20	3.17	cute	5	6	4.77
heard	269	20	4.83	five	286	12	4.83	duck	9	25	1.92	fish	35	13	3.83
job	238	19	5.92	foot	70	10	4.27	ham	19	26	3.17	fork	14	13	4.65
lake	54	32	3.19	house	591	7	6.31	hide	22	21	2.31	frog	1	4	1.73
list	133	19	4.67	join	65	8	3.79	hurt	37	23	4.54	jump	24	8	3.29
nose	60	18	3.81	kind	313	7	4.69	nail	6	26	3.02	kiss	17	13	5.10
note	127	26	4.94	lost	173	9	3.85	noon	25	19	5.17	lamp	18	11	3.90
park	94	18	4.77	love	232	11	6.06	peach	3	22	2.67	loud	20	12	4.42
part	500	17	4.78	mouth	103	7	4.52	pen	18	29	5.83	match	41	14	3.42
pass	89	24	3.77	move	171	8	5.35	pet	8	30	3.79	mouse	10	14	2.77
phone	54	27	6.58	post	84	15	2.54	sad	35	25	3.65	noise	37	4	4.75
rate	209	39	3.21	safe	58	11	4.10	shake	17	24	3.40	push	37	5	4.25
rest	164	20	5.15	smile	58	5	5.60	sheep	23	20	1.58	smell	34	7	4.67
save	62	22	5.06	voice	226	7	3.65	shine	5	21	3.15	teach	41	13	4.96
ten	165	27	4.63	white	365	11	4.46	sock	4	26	3.94	van	32	12	3.02
west	235	19	3.25	wrong	129	13	4.65	soup	16	22	3.77	wash	37	7	5.81

[1]Word frequency and neighborhood density information was obtained from the Washington University in St. Louis Speech and Hearing Lab Neighborhood Database (see the references).

[2]A between-items analysis of variance (ANOVA) indicated that the four cells were similar in terms of phonotactic probability, $F(3,76)=2.53$, $p=0.06$. In computing phonotactic probability, we used biphone frequency (segment-to-segment co-occurrence probability) for adult speech, according to Carterette and Hubbard (1974).

[3]A 2 (subjective frequency: high, low)×2 (neighborhood density: dense, sparse) ANOVA was performed on average subjective frequency ratings for the 80 test words to confirm that ratings were balanced across neighborhood conditions. There was a main effect of subjective frequency, $F(1,76)=128.58$, $p<0.0001$. The high subjective frequency condition had higher ratings than the low subjective frequency one (5.08 vs 3.33). There was also a main effect of neighborhood density, $F(1,76)=4.76$, $p<0.05$. The sparse condition had higher frequency ratings than the dense one (4.03 vs 4.37). However, the difference in ratings was small, and the two-way interaction was not significant, $p>0.10$.

Amano, S., Kondo, T., and Kakehi, K. (**1995**). ''Modality dependency of familiarity ratings of Japanese words,'' Percept. Psychophys. **57**, 598–603.

Balota, D. A., Pilotti, M., and Cortese, M. J. (**2001**). ''Subjective frequency estimates for 2,938 monosyllabic words,'' Mem. Cognit. **29**, 639–647.

Becker, C. A. (**1980**). ''Semantic context and word frequency effects in visual word recognition,'' Mem. Cognit. **8**, 493–512.

Bent, T., and Bradlow, A. R. (**2003**). ''The interlanguage speech intelligibility benefit,'' J. Acoust. Soc. Am. **114**, 1600–1610.

Best, C. T. (**1995**). ''A direct realist view of cross-language speech perception,'' in *Speech Perception and Linguistic Experience: Issues in Cross-Language Research*, edited by W. Strange (York, Baltimore), pp. 171–206.

Best, C. T., McRoberts, G., and Goodell, E. (**2001**). ''Discrimination of non-native consonant contrasts varying in perceptual assimilation to the listener's native phonological system,'' J. Acoust. Soc. Am. **101**, 2299–2310.

Bradlow, A. R., and Bent, T. (**2002**). ''The clear speech effect for non-native listeners,'' J. Acoust. Soc. Am. **112**, 272–284.

Bradlow, A. R., and Pisoni, D. B. (**1999**). ''Recognition of spoken words by native and non-native listeners: Talker-, listener-, and item-related factors,'' J. Acoust. Soc. Am. **106**, 2074–2085.

Bradlow, A. R., Torretta, G. M., and Pisoni, D. B. (**1996**). ''Intelligibility of normal speech. I. Global and fine-grained acoustic-phonetic talker characteristics,'' Speech Commun. **20**, 255–272.

Carroll, J. B. (**1971**). ''Measurement properties of subjective magnitude estimates of word frequency,'' J. Verbal Learn. Verbal Behav. **10**, 722–729.

Carterette, E. C., and Hubbard Jones, M. (**1974**). *Informal Speech* (University of California Press, Berkeley, CA).
Charles-Luce, J., and Luce, P. A. (**1990**). ''An examination of similarity neighborhoods in young children's receptive vocabularies,'' J. Child Lang **22**, 727–735.
Cohen, H., Douaire, J., and Elsabbagh, M. (**2001**). ''The role of prosody in discourse processing,'' Brain Cogn **46**, 73–82.
Connine, C. M., Mullennix, J., Shernoff, E., and Yelen, J. (**1990**). ''Word familiarity and frequency in visual and auditory word recognition,'' J. Exp. Psychol. Learn. Mem. Cogn. **16**, 1084–1096.
Cutler, A., and van Donselaar, W. (**2001**). ''Voornaam is not (really) a homophone: Lexical prosody and lexical access in Dutch,'' Lang. Speech **44**, 171–195.
Dahan, D., Magnuson, J. S., and Tanenhaus, M. K. (**2001**). ''Time course of frequency effects in spoken-word recognition: Evidence from eye movements,'' Cognit. Psychol. **42**, 317–367.
Derwing, T. M., and Munro, M. J. (**1997**). ''Accent, intelligibility, and comprehensibility: Evidence from four L1s,'' Stud. Second Lang. Acquis. **19**, 1–16.
Derwing, T. M., and Munro, M. J. (**2001**). ''What speaking rates do nonnative listeners prefer?'' Appl. Linguist. **22**, 324–337.
Ferguson, C. A., and Farwell, C. B. (**1975**). ''Words and sounds in early language acquisition,'' Language **51**, 419–439.
Flege, J. E. (**1988**). ''Factors affecting degree of perceived foreign accent in English sentences,'' J. Acoust. Soc. Am. **84**, 70–79.
Flege, J. E. (**1995**). ''Second language speech learning: Theory, findings and problems,'' in *Speech Perception and Linguistic Experience*, edited byW. Strange (York, Baltimore), pp. 233–272.
Flege, J. E., and Munro, M. J. (**1994**). ''The word unit in second-language speech production and perception,'' Stud. Second Lang. Acquis. **16**, 381–411.
Flege, J. E., Munro, M. J., and Fox, R. (**1994**). ''Auditory and categorical effects on cross-language vowel perception,'' J. Acoust. Soc. Am. **95**, 3623–3641.
Flege, J. E., Munro, M. J., and MacKay, I. R. A. (**1995**). ''Factors affecting degree of perceived foreign accent in a second language'' J. Acoust. Soc. Am. **97**, 3125–3134.
Forster, K. I. (**1981**). ''Priming and the effects of sentence and lexical contexts on naming time: Evidence for autonomous lexical processing,'' J. Exp. Psychol. **33A**, 465–496.
Garlock, V. M., Walley, A. C., and Metsala, J. L. (**2001**). ''Age-of-acquisition, word frequency and neighborhood density effects on spoken word recognition by children and adults,'' J. Mem. Lang. **45**, 468–492.
Gaygen, D. E., and Luce, P. A. (**1998**). ''Effects of modality on subjective frequency estimates and processing of spoken and printed words,'' Percept. Psychophys. **60**, 465–483.
Gaskell, M. G., and Marslen-Wilson, W. D. (**1997**). ''Integrating form and meaning: A distributed model of speech perception,'' Lang. Cognit. Processes **12**, 613–656.
Geffin, G., and Luszcz, M. A. (**1983**). ''Are the spoken durations of rare words longer than those of common words?'' Mem. Cognit. **11**, 13–15.
Gernsbacher, M. A. (**1984**). ''Resolving 20 years of inconsistent interaction between lexical familiarity and orthography, concreteness, and polysemy,'' J. Exp. Psychol. Gen. **113**, 256–281.
Gordon, B. (**1985**). ''Subjective frequency and lexical decision latency function: Implications for mechanisms of lexical access,'' J. Mem. Lang. **24**, 631–645.
Hintzman, D. L. (**1986**). '' 'Schema abstraction' in a multiple-trace memory model,'' Psychol. Rev. **93**, 411–428.
Jusczyk, P. W. (**1993**). ''From general to language-specific capacities: The WRAPSA model of how speech perception develops,'' J. Phonetics **21**, 3–28.
Kučera, F., and Francis, W. (**1967**). *Computational Analysis of Present Day American English* (Brown University Press, Providence).
Kuhl, P. K., and Iverson, P. (**1995**). ''Linguistic experience and the perceptual magnet effect,'' in *Speech Perception and Linguistic Experience: Issues in Cross-Language Research*, edited by W. Strange (York, Baltimore), pp. 121–154.
Lachman, R., Shaffer, J. P., and Hennrikus, D. (**1974**). ''Language and cognition: Effects of stimulus codability, name-word frequency, and age of acquisition on lexical reaction time,'' J. Verbal Learn. Verbal Behav. **13**, 613–625.
Luce, P. A., and Pisoni, D. B. (**1998**). ''Recognizing spoken words: The neighborhood activation model,'' Ear Hear. **19**, 1–36.
MacKay, I. R. A., Meador, D., and Flege, J. E. (**2001**). ''The identification of English consonants by native speakers of Italian,'' Phonetica **58**, 103–125.
Mayo, L. H., Florentine, M., and Buus, S. (**1997**). ''Age of second-language acquisition and perception of speech in noise,'' J. Speech Lang. Hear. Res. **40**, 686–693.
McClelland, J. L. (**1988**). ''Connectionist models and psychological evidence,'' J. Mem. Lang. **27**, 107–123.
Meador, D., Flege, J. E., and MacKay, I. R. A. (**2000**). ''Factors affecting the recognition of words in a second language,'' Bilingualism: Lang. Cogn. **3**, 55–67.
Metsala, J. L., and Walley, A. C. (**1998**). ''Spoken vocabulary growth and the segmental restructuring of lexical representations: Precursors to phonemic awareness and early reading ability,'' in *Word Recognition in Beginning Literacy*, edited by J. L. Metsala and L. C. Ehri (Erlbaum, Hillsdale, NJ), pp. 89–120.
Morrison, C. M., and Ellis, A. W. (**1995**). ''Roles of word frequency and age of acquisition in word naming and lexical decision,'' J. Exp. Psychol. Learn. Mem. Cogn. **20**, 116–133.
Munro, M. J. (**1998**). ''The effects of noise on the intelligibility of foreign-accented speech,'' Stud. Second Lang. Acquis. **20**, 139–154.
Munro, M. J., and Derwing, T. M. (**1995**). ''Foreign accent comprehensibility, and intelligibility in the speech of second language learners,'' Lang. Learn. **49**, 285–310.
Munro, M. J., and Derwing, T. M. (**2001**). ''Modeling perceptions of the accentedness and comprehensibility of L2 speech: The role of speaking rate,'' Stud. Second Lang. Acquis. **23**, 451–468.
Norris, D., McQueen, J. M., and Cutler, A. (**1995**). ''Competition and segementation in spoken-word recognition,'' J. Exp. Psychol. Learn. Mem. Cogn. **21**, 1209–1228.
Pallier, C., Colome, A., and Sebastian-Galles, N. (**2001**). ''The influence of native-language phonology on lexical access: Exemplar-based versus abstract lexical entries,'' Psychol. Sci. **12**, 445–449.
Sebastian-Galles, N., and Soto-Faraco, S. (**1999**). ''Online processing of native and non-native phonemic contrasts in early bilinguals,'' Cognition **72**, 111–123.
Strange, W. (**1995**). ''Cross-language studies of speech perception: A historical review,'' in *Speech Perception and Linguistic Experience: Issues in Cross-Language Research*, edited by W. Strange (York, Baltimore), pp. 3–48.
Takayanagi, S., Dirks, D. D., and Moshfegh, A. (**2002**). ''Lexical and talker effects on word recognition among native and non-native listeners with normal and impaired hearing,'' J. Speech Lang. Hear. Res. **45**, 585–597.
van Wijngaarden, S. J. (**2001**). ''Intelligibility of native and non-native Dutch speech,'' Speech Commun. **35**, 103–113.
van Wijngaarden, S. J., Steeneken, H. J. M., and Hougast, T. (**2002**). ''Quantifying the intelligibility of speech in noise for non-native listeners,'' J. Acoust. Soc. Am. **111**, 1906–1916.
Washington University in St. Louis Speech and Hearing Lab Neighborhood Database as a web-based implementation of the 20 000-word Hoosier Mental Lexicon (2002, March; accessed). http://128.252.27.56/neighborhood/Home.asp
Werker, J. F., and Polka, L. (**1993**). ''Developmental changes in speech perception: New challenges and new directions,'' J. Phonetics **21**, 83–101.
Wright, C. E. (**1979**). ''Duration differences between rare and common words and their implications for the interpretation of word frequency effects,'' Mem. Cognit. **7**, 411–419.
Yeni-Komshian, G. H., Flege, J. E., and Liu, S. (**2000**). ''Pronunciation proficiency in the first and second languages of Korean-English bilinguals,'' Bilingualism: Lang. Cogn. **3**, 131–149.

A statistics-based pitch contour model for Mandarin speech

Sin-Horng Chen
Department of Communication Engineering, National Chiao Tung University, Taiwan

Wen-Hsing Lai[a)]
Department of Communication Engineering, National Chiao Tung University, Taiwan and Chunghwa Telecommunication Laboratories, Taiwan

Yih-Ru Wang
Department of Communication Engineering, National Chiao Tung University, Taiwan

(Received 11 April 2004; revised 26 August 2004; accepted 4 November 2004)

A statistics-based syllable pitch contour model for Mandarin speech is proposed. This approach takes the mean and the shape of a syllable log-pitch contour as two basic modeling units and considers several affecting factors that contribute to their variations. The affecting factors include the speaker, prosodic state (which essentially represents the high-level linguistic components of F0 and will be explained more clearly in Sec. I), tone, and *initial* and *final* syllable classes. The parameters of the two modeling units were automatically estimated using the expectation-maximization (EM) algorithm. Experimental results showed that the root mean squared errors (RMSEs) obtained in the closed and open tests in the reconstructed pitch period were 0.362 and 0.373 ms, respectively. This model provides a way to separate the effects of several major factors. All of the inferred values of the affecting factors were in close agreement with our prior linguistic knowledge. It also gives a quantitative and more complete description of the coarticulation effect of neighboring tones rather than conventional qualitative descriptions of the tone *sandhi* rules. In addition, the model can provide useful cues to determine the prosodic phrase boundaries, including those occurring at intersyllable locations, with or without punctuation marks. [DOI: 10.1121/1.1841572]

PACS numbers: 43.72.Ar [DDO] Pages: 908–925

I. INTRODUCTION

Prosody is an inherent supra-segmental feature of human speech. It carries stress, intonation patterns, and timing structures of continuous speech which, in turn, determine the naturalness and understandability of an utterance. How to automatically generate, analyze, and recognize prosody in speech is one of the unresolved problems confronting researchers who study speech synthesis and recognition. Although it is known that prosody is affected by many factors, such as the phonetic context, sentence type, syntactical structure, semantics, and the emotional status of the speaker, the relationship between these affecting factors and prosody are not totally understood.

Among all the features known to carry prosodic information, pitch is the most important one. It has been reported that the F0 contour characterizes the speaking style and speaker.[1] Therefore, pitch plays a role in many speech related applications, like text-to-speech (TTS),[2–9] tone recognition,[10,11] prosodic labeling,[12,13] emotional state recognition,[14] speaker accent identification,[15] and so on. Adequate pitch control is very important for synthetic speech to be natural in TTS. If a TTS system generates a tone shape matching only the lexical expectation of each individual syllable, the lack of consideration of contextual tone variations will result in underarticulation of tones and lead to the generation of unnatural speech.

Pitch modeling is even more critical for Mandarin speech processing, as Mandarin is a tonal language and the information related to the tonality of a syllable appears, for the most part, on its pitch contour. Although there are only five lexical tones and a previous study[16] has concluded that the pitch contour of each of the first four tones can be simply represented by a single standard pattern, syllable pitch contour patterns in continuous speech vary highly and can deviate dramatically from their canonical forms (i.e., high-level tone, mid-rising tone, low-falling tone, high-falling tone, and low-energy tone). Many factors have been shown to have a major influence on the pitch contour of a tone. They include the effects of neighboring tones, referred to as *sandhi* rules,[17] coarticulation, stress, intonation type, semantics, emotional status, and so on. In addition, the pronunciation of tone 5 is usually highly context dependent and is relatively arbitrary. Thus, pitch modeling is not a trivial research issue for Mandarin speech processing.

Pitch modeling has been the subject of many recent research studies on various languages. The general goal of pitch modeling is to derive a computational model that describes the relationship between a set of affecting factors and pitch contour patterns. The related literature has been concerned with finding perceptual cues and intonational linguistic representations.[18,19] The pitch contour generation rules for synthesizing intelligible and natural-sounding speech,[2–9] and the automatic pitch or tone analysis for the purposes of

[a)]Author to whom correspondence should be addressed. Electronic mail: lwh@cht.com.tw

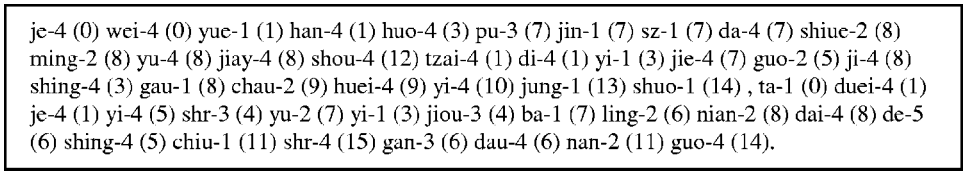

FIG. 1. An example of prosodic states.

speech recognition,[10,11] speech understanding[20] and word finding,[21] have also been studied. Pitch modeling can be performed using two approaches that are rule based[2–4] or data driven.[5–8,22,23] The former approach is conventional; it uses linguistic expertise to manually infer some phonologic rules of pitch contour generation, based on observation of a large set of utterances. A prevalent method in the approach applied to TTS uses sequential rules to initially assign the pitch contour of a segment with an intrinsic value and then successively applies rules to modify it.[2–4] There are three main disadvantages to this approach. First, manually exploring the effect of mutual interaction among several linguistic features at different levels is highly complex. Second, the rule-inference process usually involves a controlled experiment, in which only a limited number of contextual factors is examined. The resulting inferred rules may, therefore, not be general enough for unlimited texts. Third, the rule-inference process is cumbersome. As a result, it is generally very difficult to collect enough rules without expending a great deal of effort.

The data-driven approach tries to construct a pitch model from a large speech corpus, usually by means of statistical methods[6,23] or artificial neural network (ANN) techniques.[5,22] It first designs a computational model to describe the relationship between pitch contour patterns and some affecting factors and then trains the model, using the speech corpus. The training goals are to automatically deduct phonologic rules from the speech corpus and to implicitly incorporate them into the model's parameters or into the ANN's weights. The primary advantage of this approach is that the rules can be automatically established based on the training data set during the training process, without the help of linguistic experts. The recurrent neural network (RNN)-based method[5,22] is a popular method which uses an RNN to learn the mapping between the pitch parameters and some linguistic features. The main criticism raised against this method is the difficulty of interpreting the hidden structures of the model. Other methods include the hidden Markov model (HMM),[23] regression analysis,[6] vector quantization,[7] and the tree-based approach.[8] In addition, an approach that adopts the concept of separating an utterance's pitch contour into a global trend and a locally variational term has been applied in recent pitch modeling studies, e.g., those on superpositional modeling[24,25] and two-stage modeling.[9,26]

In this paper, a new pitch modeling approach for Mandarin speech is proposed. It takes the mean and shape of a syllable log-pitch contour as two basic modeling units and uses statistical methods to model them separately while considering several affecting factors that control their variation. The reason for using parameters of the syllable pitch contour as modeling units lies in the fact that the syllable is the basic pronunciation unit of Mandarin speech and each syllable is lexically marked with a lexical tone, which is a factor that strongly affects pitch in Mandarin. But it is well known that the prosody of an utterance is better modeled with an interval that is much longer than a syllable. Therefore, we use the neighboring tones and the prosodic states to measure the impact. The affecting factors used include the speaker, prosodic state, tone, and initial and final syllable classes. Here, the prosodic state is conceptually defined as the state of a syllable in a prosodic phrase. In continuous speech, speakers tend to group words into phrases whose boundaries are marked by durational and intonational cues. Those phrases are usually referred to as prosodic phrases. Many phonological rules limit their operation within prosodic phrases. While it is generally agreed that the prosodic structure of an utterance has some relationship with its syntactic structure, the two are not isomorphic. In the model, the prosodic state is used as a substitute for high-level linguistic information, like a word, phrase, or syntactic boundaries. Our purpose in using the prosodic state to replace conventional high-level linguistic information is to divide the complicated pitch modeling task into two subtasks. The first one involves modeling the pitch parameters by considering the effects of some low-level linguistic features and the prosodic state. The second subtask involves exploring the relationship between the prosodic state and high-level linguistic cues. Through this two-stage pitch modeling approach, some unsolved problems can be avoided. Problems such as the inconsistency of prosodic and syntactic structures, the ambiguity of word-segmentation and word-chunking for Mandarin Chinese, and the difficulty of performing automatic syntactic analysis on unlimited natural texts can be prevented in the first subtask. In the second subtask, the researcher can focus on modeling the global effect of mapping high-level linguistic features to the prosodic state, since interference caused by low-level linguistic features has already been removed in the first subtask. In this paper, we attack the first subtask only, leaving the second subtask to be dealt with in the future. Due to the fact that the prosodic state of a syllable is not explicitly given, it has been treated as a hidden variable and expectation-maximization (EM) algorithms have been applied to estimate all the parameters of the two pitch models based on a large training set. A by-product of the EM algorithm is the determination of the hidden prosodic states of all the syllables in the training set. This is an additional advantage because prosodic labeling has recently become an interesting research topic.[12] An example is given as Fig. 1. This example shows that the term prosodic state could be made more understandable. Figure 1 shows the phonetic transcription, tone (after dash), and the prosodic states (in parentheses) of each syllable, which are assigned automatically by our model. For each syllable, in our experiment, 1 of 16 prosodic states was assigned. From the sequence of prosodic states, some high-

level linguistic phenomenon could be observed, like the possible prosodic phrase boundaries. The prosodic state essentially represents the high-level linguistic components of F0, so the results reported in this paper apply to the prediction of the low-level linguistic component (tone, *initial/final* class, and speaker factors in our model) given the prediction of high-level linguistic components of F0 (the second subtask mentioned above).

This paper is organized as follows. Section II discusses, in detail, the proposed pitch modeling approach for Mandarin speech. Section III presents the experimental results. Detailed analyses of the inferred affecting factors are given in Sec. IV. An application of the proposed syllable pitch contour model to pitch prediction of TTS is given in Sec. V. In the last section, we offer concluding remarks and suggestions for future research.

II. THE PROPOSED PITCH MEAN AND SHAPE MODELS

In the proposed pitch modeling approach, we first perform rough speaker normalization to the pitch period. Our purpose is to adjust the pitch levels and dynamic ranges of all the speakers so that they are approximately the same, in order to improve the efficiency of the subsequent syllable log-pitch contour modeling. In Ref. 27, a Gaussian normalization was used to perform a mapping from the reference pitch values to the desired frequencies, and the authors found that pitch contour moved in the proper direction. We use the same idea to normalize the pitch period of a speaker as follows:

$$f(t)=\frac{f'(t)-\mu_k}{\sigma_k}\cdot\sigma_{all}+\mu_{all}, \tag{1}$$

where $f'(t)$ and $f(t)$ are the original and normalized pitch periods of frame t; μ_k and σ_k are the mean and standard deviation of the pitch period distribution of speaker k; and μ_{all} and σ_{all} are the average mean and average standard deviation of the pitch period distribution of all the training speakers. We then take the logarithm of the normalized pitch period, and the resulting log-pitch contour of each utterance is subsequently divided into a sequence of syllable log-pitch contours. Each syllable log-pitch contour was then decomposed into two parts, the mean and the shape, using a third-order orthogonal polynomial expansion, with the zeroth-order coefficient representing the mean and the other three higher order coefficients representing the shape. We then take the syllable's pitch mean and shape as basic modeling units and employ the two separate statistical models to consider several major affecting factors. Some parts of the pitch modeling approach are discussed in detail in the following.

A. Discrete orthogonal polynomial expansion

Since all syllable log-pitch contours are smooth curves, a third-order orthogonal polynomial expansion is employed to represent them. Actually, in some previous studies,[2,5] orthogonal polynomials, up to the third order, were shown to be good enough to represent Mandarin syllable pitch contours. The four basis polynomials used are normalized, in length, to [0,1] and can be expressed as follows:[5]

$$\begin{aligned}
\phi_0\left(\frac{i}{M}\right)&=1,\\
\phi_1\left(\frac{i}{M}\right)&=\left[\frac{12\cdot M}{M+2}\right]^{1/2}\cdot\left[\frac{i}{M}-\frac{1}{2}\right],\\
\phi_2\left(\frac{i}{M}\right)&=\left[\frac{180\cdot M^3}{(M-1)(M+2)(M+3)}\right]^{1/2}\\
&\quad\cdot\left[\left(\frac{i}{M}\right)^2-\frac{i}{M}+\frac{M-1}{6\cdot M}\right],\\
\phi_3\left(\frac{i}{M}\right)&=\left[\frac{2800\cdot M^5}{(M-1)(M-2)(M+2)(M+3)(M+4)}\right]^{1/2}\\
&\quad\cdot\left[\left(\frac{i}{M}\right)^3-\frac{3}{2}\left(\frac{i}{M}\right)^2+\frac{6M^2-3M+2}{10\cdot M^2}\left(\frac{i}{M}\right)\right.\\
&\quad\left.-\frac{(M-1)(M-2)}{20\cdot M^2}\right],
\end{aligned} \tag{2}$$

for $0\leqslant i\leqslant M$, where $M+1$ is the length of the current syllable log-pitch contour and $M\geqslant 3$. They are, in fact, discrete Legendre polynomials. A syllable log-pitch contour, $f(i/M)$, can then be approximated by

$$\hat{f}\left(\frac{i}{M}\right)=\sum_{j=0}^{3}\alpha_j\cdot\phi_j\left(\frac{i}{M}\right),\quad 0\leqslant i\leqslant M, \tag{3}$$

where

$$\alpha_j=\frac{1}{M+1}\sum_{i=0}^{M}f\left(\frac{i}{M}\right)\cdot\phi_j\left(\frac{i}{M}\right). \tag{4}$$

B. Affecting factors

In naturally spoken Mandarin Chinese, pitch varies considerably, depending on various linguistic/nonlinguistic factors. In this study, we considered some factors that may have major effects on control of the variation of the pitch contour. The specific affecting factors chosen for the pitch mean and shape models are discussed in the following.

1. Affecting factors for the pitch mean model

The pitch mean is mainly affected by intonation, while the pitch shape is affected mainly by lexical tones. A brief summary of the major factors affecting intonation contours was given in Ref. 28. They include declination, downstep, final lowering, accents and tones, segmental effects, and intonation type. In our pitch mean model, the affecting factors considered include the tones of the previous, current, and following syllables; the *initial* and *final* classes of the current syllable; the prosodic state of the current syllable; and the speaker's level shift and dynamic range scaling factors. Their influence on the syllable pitch mean is discussed below.

Mandarin Chinese is a tonal and syllable-based language. The syllable is the basic pronunciation unit. Each character is pronounced as a syllable. Only about 1300 phonetically distinguishable syllables, comprising the set of all legal combinations of 411 base-syllables and five tones, exist. The tonality of a syllable is mainly characterized by its

pitch contour, loudness, and duration. We, therefore, consider the tone of the current syllable as an affecting factor. Coarticulations from the neighboring tones, which are known as sandhi rules, also exist. Thus, the tones of the previous and following syllables are also chosen as affecting factors.

Mandarin base-syllables have a very regular phonetic structure. Each base-syllable is composed of an optional *consonant initial* and a *final*. The *final* can be further broken down into an optional *medial*, a *vowel nucleus*, and an optional *nasal ending*. As discussed in Refs. 28 and 29, many types of observed F0 movement are caused by these segmental effects. We, therefore, consider the broad *initial* and *final* classes of the current syllable as affecting factors and investigate their effects on pitch mean variation.

Aside from the linguistic factors mentioned above, other high-level linguistic components, such as word-level and syntactic-level features, can also seriously affect the pitch contour of an utterance. As discussed in Sec. I, the prosodic state is in our approach used to account for the influence of all high-level linguistic features. Here, the prosodic state simply means the state of the syllable in a prosodic phrase. The pitch level of a syllable can vary drastically in different parts of a prosodic phrase. The declination effect of the global downtrend, referring to the tendency of F0 to decline over the course of an utterance, is a well-known example. There are two advantages of using the prosodic state to replace high-level linguistic features. First, pitch information is a kind of prosodic feature, so the variation of the syllable pitch contour should better match the prosodic phrase structure than the syntactic phrase structure. Second, as mentioned above, some unsolved problems, such as the ambiguity of word-segmentation and word-chunking in Mandarin Chinese and the difficulty of performing automatic syntactic analysis on unlimited natural texts, can be avoided in the current pitch modeling approach. This prevents us from using improper or incomplete high-level linguistic information. The main problem with using the prosodic state is the lack of large speech corpora with prosodic tags that have been properly labeled. Thus, we have to treat the prosodic state of a syllable as a hidden or unknown variable. Fortunately, we are able to solve this problem by using the expectation-maximization (EM) algorithm, which is a technique of maximum likelihood (ML) estimation from incomplete data. A by-product of the approach is the automatic determination of prosodic states for all the syllables in the training set. This is an additional advantage because prosodic labeling has recently become an interesting research topic.[12,13] In addition, such prosodic phrasal information provides clues for resolving syntactic ambiguity in automatic speech understanding[20,21,30,31] and for improving the naturalness of TTS.[32,33]

Lastly, the pitch contour of an utterance is also significantly affected by the speaker. Speakers have different pitch levels and dynamic ranges. Rough speaker normalization is performed in the preprocessing stage in order to suppress the speaker effect and allow the pitch period distributions of all the speakers to have the same mean and standard deviation. However, we also use two speaker affecting factors in the pitch mean model to examine whether the Gaussian-normalized syllable log-pitch contour is still speaker dependent.

2. Affecting factors for the pitch shape model

Pitch shapes are relatively tone determined. Production studies of Chinese tones have shown that tone shapes in natural continuous speech often deviate from their canonical shapes. They suffer from large deformations due to tone coarticulation, also known as tone *sandhi*. This situation is particularly common in conversation, where the boundaries among tonal categories are blurred. It has been suggested in Ref. 17 that *sandhi* contour patterns of poly-tonal groups are rather invariant and can be treated as the basic units of pitch contour analysis/generation. Therefore, lexical tone combinations are used here to consider the effect of tone coarticulation. To give further consideration to the coupling/noncoupling effect of neighboring syllables, we considered one-, two-, and three-syllable tone combinations as affecting factors in the pitch shape model.

Other affecting factors chosen for the pitch shape model includ the *initial* and *final* classes of the current syllable for the segmental effect, the prosodic state of the current syllable for the effects of high-level linguistic features, and the pitch level shifting effect of speakers.

C. The pitch models

In pitch modeling, we take the mean and shape of the syllable log-pitch contour as basic modeling units and use two separate models to exploit their variations. Because the complicated high-level linguistic components of F0 are represented by prosodic states, only acoustic factors are considered. Therefore, simple additive models are adopted in our study. They are discussed in detail in the following.

1. The pitch mean model

The pitch mean model was constructed by first considering the two affecting factors of the speaker, expressed as

$$Z_n = (Y_n + \beta_{s_n})\,\gamma_{s_n}, \tag{5}$$

where Z_n is the observed mean (i.e., the zeroth-order coefficient α_0 of the orthogonal polynomial transform) of the log-pitch contour of the nth (current) syllable; β_{s_n} and γ_{s_n} are the companding (compressing-expanding) factors (CFs) of the two affecting factors of the speaker, representing, respectively, the effects of level shift and dynamic range scaling on Z_n; and Y_n is the speaker effect-compensated pitch mean. Here, CF means the effect of a factor on the expansion (increase) or compression (reduction) of the pitch mean. The model goes on to further consider other affecting factors, expressed as

$$Y_n = X_n + \beta_{t_n} + \beta_{pt_n} + \beta_{ft_n} + \beta_{i_n} + \beta_{f_n} + \beta_{p_n}, \tag{6}$$

where X_n is the normalized pitch mean of the nth syllable and is modeled as a normal distribution with mean μ and variance ν; β_r is the CF for affecting factor r; t_n, pt_n, and ft_n represent the lexical tones of the current, previous, and following syllables, respectively; i_n and f_n are broad *initial* and *final* classes of the current syllable; and p_n represents the

TABLE I. (a) CFs of the affecting factors in the pitch mean model. (b) CF vectors of the affecting factors in the pitch shape model.

	(a)
γ_{s_n}	CF of the dynamic range scaling of the speakers
β_{s_n}	CF of the level shift of speakers
β_{t_n}	CF of the current lexical tone
β_{pt_n}	CF of the previous lexical tone
β_{ft_n}	CF of the following lexical tone
β_{i_n}	CF of the initial class
β_{f_n}	CF of the final class
β_{p_n}	CF of the pitch-mean prosodic state
	(b)
$\mathbf{b}_{s_n}$	CF vector of the speakers
$\mathbf{b}_{tc_n}$	CF vector of the lexical tone combination of the current syllable and its two neighbors
$\mathbf{b}_{i_n}$	CF vector of the initial class
$\mathbf{b}_{f_n}$	CF vector of the final class
$\mathbf{b}_{q_n}$	CF vector of the pitch-shape prosodic state

prosodic state of the current syllable. Note that t_n ranges from 1 to 5, while both pt_n and ft_n range from 0 to 5 with 0 denoting cases with punctuation marks or the nonexistence of a preceding or succeeding syllable. The affecting factors for $pt_n=0$ and $ft_n=0$ are simply set to zero because we do not want to include the effect of tone across punctuation marks. All the affecting factors in the pitch mean model and their notations are summarized in Table I(a).

2. The pitch shape model

The pitch shape model is expressed as

$$\mathbf{Z}_n=\mathbf{X}_n+\mathbf{b}_{tc_n}+\mathbf{b}_{q_n}+\mathbf{b}_{s_n}+\mathbf{b}_{i_n}+\mathbf{b}_{f_n}, \tag{7}$$

where $\mathbf{Z}_n$ is the observed pitch shape vector $[\alpha_1\ \alpha_2\ \alpha_3]^T$ for the nth syllable; $\mathbf{X}_n$ is the normalized pitch shape vector of the nth syllable and is modeled as a multivariate normal distribution with mean vector $\boldsymbol{\mu}$ and covariance matrix $\mathbf{R}$; $\mathbf{b}_r$ is the CF vector for affecting factor r; tc_n represents a lexical tone combination of the current syllable and its two nearest neighbors; and q_n represents the pitch-shape prosodic state of the current syllable. Here, a lexical tone combination, instead of individual tones, is used because we want to consider the aggregative influence of the current tone and its two nearest neighboring tones. The invoking of the preceding and succeeding tones in the tone combination depends on whether or not long intersyllable pauses exist before and/or after the current syllable, respectively. In a case where both the pre- and postpauses of the current syllable are not long, we consider the effects of both the preceding and succeeding tones, and use a tri-tone combination. When the prepause and/or the postpause are equal to or longer than a predetermined threshold (=13 frames or 65 ms in this study), we ignore the influence of the preceding and/or succeeding syllables, and use a single-tone/bi-tone combination. All the affecting factors in the pitch shape model and their notations are summarized in Table I(b).

D. Training the pitch models

1. Training the pitch mean model

To estimate the parameters of the pitch mean model, an EM algorithm is adopted. The derivation of the EM algorithm is based on treating the prosodic state as an unknown variable. An auxiliary function is first defined in the expectation step (E-step) as follows:

$$Q(\bar{\lambda},\lambda)=\sum_{n=1}^{N}\sum_{p_n=1}^{P}p(p_n|Z_n,\bar{\lambda})\log p(Z_n,p_n|\lambda), \tag{8}$$

where N is the total number of training samples, P is the total number of prosodic states, $p(p_n|Z_n,\lambda)$ and $p(Z_n,p_n|\lambda)$ are conditional probabilities, $\lambda=\{\mu,\nu,\beta_t,\beta_{pt},\beta_{ft},\beta_i,\beta_f,\beta_p,\beta_s,\gamma_s\}$ is the set of parameters to be estimated, and λ and $\bar{\lambda}$ are the new and old parameter sets, respectively. Based on the assumption that the normalized pitch mean X_n is normally distributed, $p(Z_n,p_n|\lambda)$ can be derived from the assumed model given in Eqs. (5) and (6) and expressed as

$$p(Z_n,p_n|\lambda)=N(Z_n;(\mu+\beta_{t_n}+\beta_{pt_n}+\beta_{ft_n}+\beta_{i_n}+\beta_{f_n}+\beta_{p_n}+\beta_{s_n})\gamma_{s_n},\nu\gamma_{s_n}^2), \tag{9}$$

where $N(Z;a,b)$ denotes a normal distribution of Z with mean a and variance b. Similarly, $p(p_n|Z_n,\bar{\lambda})$ can be expressed as

$$p(p_n|Z_n,\bar{\lambda})=\frac{p(Z_n,p_n|\bar{\lambda})}{\sum_{p_n'=1}^{P}p(Z_n,p_n'|\bar{\lambda})}. \tag{10}$$

Then, sequential optimizations of these parameters can be performed in the maximization step (M-step).

A drawback of the above EM algorithm is that it may produce a nonunique solution. To solve this problem, we modify each optimization procedure in the M-step to constrained optimization by introducing a global constraint. The auxiliary function is then changed to

$$Q(\bar{\lambda},\lambda)=\sum_{n=1}^{N}\sum_{p_n=1}^{P}p(p_n|Z_n,\bar{\lambda})\log p(Z_n,p_n|\lambda)+\eta\left(\sum_{n=1}^{N}(\mu+\beta_{t_n}+\beta_{pt_n}+\beta_{ft_n}+\beta_{i_n}+\beta_{f_n}+\beta_{p_n}+\beta_{s_n})\gamma_{s_n}-N\mu_Z\right), \tag{11}$$

where μ_Z is the average of Z_n and η is a Lagrange multiplier. The constrained optimization is finally solved via the Newton–Raphson method.

To execute the EM algorithm, initializations of the parameter set $\bar{\lambda}$ are needed. This is done by estimating each individual parameter independently. Specifically, the initial multiplicative/additive CF for a specific value of an affecting factor is assigned to be the ratio/difference of the mean of Z_n with the affecting factor equaling the value to the mean of all Z_n. Notice that, in the initialization of the CFs for the affecting factors of the prosodic states, each syllable is preassigned a prosodic state by means of vector quantization. Following,

all the parameters are sequentially updated in each iteration. The iterative procedure is continued until convergence is reached. The prosodic state can, finally, be assigned as

$$p_n^* = \arg\max_{p_n} p(p_n|Z_n,\lambda). \quad (12)$$

The EM algorithm is summarized below:

(1) Compute the initial values of λ by independently estimating each individual parameter from the training set.
(2) Do this for each iteration k:
   (a) Update $\bar{\lambda}=\lambda$.
   (b) E-step: Use Eqs. (9)–(11) to calculate $Q(\bar{\lambda},\lambda)$.
   (c) M-step: Find the optimal λ as follows:

$$\lambda = \arg\max_{\lambda} Q(\bar{\lambda},\lambda). \quad (13)$$

   (d) Termination test: If $L(k)-L(k-1)<\varepsilon$ or $k\geqslant K$, then stop, where

$$L(k)=\sum_{n=1}^{N} \log p(Z_n|\lambda) \quad (14)$$

   is the total log-likelihood for iteration k and K is the maximum number of iterations.
(3) Assign prosodic states to all the syllables using Eq. (12).

2. Training the pitch shape model

The pitch shape model is trained using the same EM algorithm. An auxiliary function with a global constraint was first defined as follows:

$$\mathbf{Q}(\bar{\boldsymbol{\lambda}},\boldsymbol{\lambda}) = \sum_{n=1}^{N}\sum_{q_n=1}^{P} p(q_n|\mathbf{Z}_n,\bar{\boldsymbol{\lambda}})\log p(\mathbf{Z}_n,q_n|\boldsymbol{\lambda}) + \mathbf{L}^T \times\left(\sum_{n=1}^{N}(\boldsymbol{\mu}+\mathbf{b}_{tc_n}+\mathbf{b}_{i_n}+\mathbf{b}_{f_n}+\mathbf{b}_{q_n}+\mathbf{b}_{s_n})-N\boldsymbol{\mu}_Z\right), \quad (15)$$

where $\mathbf{L}$ is a 3×1 Lagrange multiplier vector and $\boldsymbol{\lambda}=\{\boldsymbol{\mu},\mathbf{R},\mathbf{b}_{tc},\mathbf{b}_i,\mathbf{b}_f,\mathbf{b}_q,\mathbf{b}_s\}$ is the set of parameter vectors to be estimated. Based on the assumption that the normalized pitch shape vector $\mathbf{X}_n$ is normally distributed, $p(\mathbf{Z}_n,q_n|\boldsymbol{\lambda})$ can be expressed as

$$p(\mathbf{Z}_n,q_n|\boldsymbol{\lambda}) = \mathrm{MVN}(\mathbf{Z}_n;\boldsymbol{\mu}+\mathbf{b}_{tc_n}+\mathbf{b}_{i_n}+\mathbf{b}_{f_n}+\mathbf{b}_{q_n}+\mathbf{b}_{s_n},\mathbf{R}), \quad (16)$$

where $\mathrm{MVN}(\mathbf{Z};\mathbf{a},\mathbf{B})$ denotes a multivariate normal distribution of $\mathbf{Z}$ with mean vector $\mathbf{a}$ and covariance matrix $\mathbf{B}$. By maximizing the auxiliary function, we can get the optimal parameter set. The training procedure is similar to that for the pitch mean model.

E. Testing the pitch models

1. Testing the pitch mean model

Although we obtain CFs for all affecting factors through the above training procedure, some information still must be discovered in the testing phase. This includes the CFs of the two speaker-affecting factors and the prosodic state of each syllable. The following testing procedure is used to estimate these unknown parameters:

(1) Initialization:
   (a) Freeze the CFs for the current, previous, and following tones, for the *initial* and *final* classes, and for the prosodic state, the mean, and variance of the normalized pitch mean to their trained values, and form a parameter set $\bar{\lambda}_1=\{\bar{\mu},\bar{\nu},\bar{\beta}_t,\bar{\beta}_{pt},\bar{\beta}_{ft},\bar{\beta}_i,\bar{\beta}_f,\bar{\beta}_p\}$.
   (b) Compute the initial CFs for the parameter set $\lambda_2=\{\beta_s,\gamma_s\}$.
(2) Do this for each iteration k:
   (a) Update $\bar{\lambda}_2=\lambda_2$.
   (b) E-step: Calculate

$$Q(\bar{\lambda}_2,\lambda_2)=\sum_{n=1}^{N}\sum_{p_n=1}^{P} p(p_n|Z_n,\bar{\lambda}_1,\bar{\lambda}_2) \times\log p(Z_n,p_n|\bar{\lambda}_1,\lambda_2). \quad (17)$$

   (c) M-step: Find the optimal λ_2 via

$$\lambda_2=\arg\max_{\lambda_2} Q(\bar{\lambda}_2,\lambda_2). \quad (18)$$

   (d) Termination test: If $L(k)-L(k-1)<\varepsilon$ or $k\geqslant K$, then stop, where

$$L(k)=\sum_{n=1}^{N} \log p(Z_n|\bar{\lambda}_1,\lambda_2) \quad (19)$$

   is the total log-likelihood for iteration k.
(3) Assign prosodic state by means of

$$p_n^* = \arg\max_{p_n} p(p_n|Z_n,\bar{\lambda}_1,\lambda_2). \quad (20)$$

After performing the above procedure, we can derive the two speaker CFs for each testing speaker and determine the prosodic state of each syllable.

2. Testing the pitch shape model

In the testing phase, a similar procedure is employed to estimate the unknown parameters of the pitch shape model from the testing data set, with all the known parameters being fixed. Here, the unknown parameters are the CF vector of the speaker affecting factor and the prosodic state of each syllable. In this case, the fixed parameter set $\bar{\boldsymbol{\lambda}}_1=\{\bar{\boldsymbol{\mu}},\bar{\mathbf{R}},\bar{\mathbf{b}}_{tc},\bar{\mathbf{b}}_i,\bar{\mathbf{b}}_f,\bar{\mathbf{b}}_q\}$ and the unknown parameter set $\boldsymbol{\lambda}_2=\{\mathbf{b}_s\}$ are used in the testing procedure.

III. EXPERIMENTAL RESULTS

A. Databases

The effectiveness of the proposed syllable pitch modeling method was examined through simulations on two databases. The first database was a high-quality, reading-style, microphone speech database, which was recorded in a sound-proof booth. It is referred to as the TL database. It was generated by five native Chinese speakers, including two males and three females; among these five, two were profes-

TABLE II. TL database statistics.

Data Set	Speaker	Sentence	Paragraph	Syllable
Training	Male A	1-455	1–200	34 670
Training	Female B	1-455	1–50	12 945
Training	Male C	1-455	1–100	20 748
Training	Female D	1-455	1–200	34 166
Testing	Female E	None	201–300	22 109

sional radio announcers. The database consisted of two types of data. The first type of data comprised sentential utterances with texts belonging to a well-designed, phonetic-balanced corpus of 455 sentences. The lengths of these sentences ranged from 3 to 75 syllables with an average of 13 syllables. The other types of data were longer utterances with texts belonging to a corpus of 300 paragraphs, which covered a wide range of topics, including news, primary school textbooks, literature, essays, etc. The lengths of these paragraphs ranged from 24 to 529 syllables with an average length of 170 syllables. The database was divided into two parts: a training set and a test set. Table II shows the database statistics. The training set contained, in total, 102 529 syllables, and the test set contained 22 109 syllables. The speakers and text content in the test set were different from those in the training set.

After recording was completed, all speech signals in the database were converted into 16-bit data at a 20-kHz sampling rate. They were then manually segmented into *initial* and *final* subsyllables. The phonetic transcription was generated automatically by a linguistic processor, with an 80 000-word lexicon. All the transcription errors were manually corrected. The pitch period was then automatically detected by the ESPS software, with large errors being detected by the program and corrections made by hand. A four-step preprocessing procedure was then applied to extract the four modeling parameters. The four steps included frame-based speaker normalization, frame-based logarithm operation, dividing the utterances' log-pitch contours into syllable segments, and performing orthogonal expansion of syllable log-pitch contours. The statistics for the observed mean and shape of the syllable log-pitch contour can be found in Table III(a).

TABLE IV. The mean and (co)variance statistics of (a) the observed and (b) the normalized mean and shape of the syllable log-pitch contour with 16 prosodic states for the TCC database (unit of pitch period: ms).

	mean	(co)variance	RMSE
	(a)		
Pitch mean α_0	1.840	0.0209	
Pitch shape $[\alpha_1\ \alpha_2\ \alpha_3]^T$ ($\times 100$)	$\begin{bmatrix} 2.797 \\ -0.593 \\ -0.018 \end{bmatrix}$	$\begin{bmatrix} 32.392 & 0.341 & -2.680 \\ 0.341 & 9.740 & -0.199 \\ -2.680 & -0.199 & 3.289 \end{bmatrix}$	
	(b)		
Pitch mean α_0	1.842	0.000 739	0.0275
Pitch shape $[\alpha_1\ \alpha_2\ \alpha_3]^T$ ($\times 100$)	$\begin{bmatrix} 2.810 \\ -0.577 \\ -0.020 \end{bmatrix}$	$\begin{bmatrix} 7.037 & -0.561 & -1.791 \\ -0.561 & 3.657 & -0.403 \\ -1.791 & -0.403 & 2.165 \end{bmatrix}$	$\begin{bmatrix} 2.653 \\ 1.912 \\ 1.471 \end{bmatrix}$

The second database was a 100-speaker, microphone speech data set, which was a subset of TCC-300, provided by the Association of Computational Linguistics and Chinese Language Processing. It is referred to as the TCC database. The database was generated by 50 males and 50 females. Each speaker uttered several paragraphs of differing content. The speech data were all directly, digitally recorded in a laboratory in 16-kHz, 16-bit linear PCM. The total number of syllables in the database was 141 991. After recording was completed, all the speech signals were automatically segmented, using 100-*initial* and 39-*final* HMM models. Then, the pitch period was automatically detected by WaveSurfer software, the large errors being excluded by the program. The same four-step preprocessing procedure was then applied to extract the four modeling parameters. In Table IV(a), the statistics for the observed mean and shape of the syllable log-pitch contour are shown.

TABLE III. The mean and (co)variance statistics of (a) the observed and (b) the normalized mean and shape of the syllable log-pitch contour with 16 prosodic states for the TL database (unit of pitch period: ms).

(a)

	Training set		Test set	
	Mean	(Co)variance	Mean	(Co)variance
Pitch mean α_0	1.949	0.0372	1.948	0.0345
Pitch shape $[\alpha_1\ \alpha_2\ \alpha_3]^T$ ($\times 100$)	$\begin{bmatrix} 3.545 \\ -0.982 \\ -0.056 \end{bmatrix}$	$\begin{bmatrix} 58.550 & 3.229 & -5.140 \\ 3.229 & 9.671 & -0.106 \\ -5.140 & -0.106 & 2.900 \end{bmatrix}$	$\begin{bmatrix} 4.012 \\ -0.749 \\ -0.142 \end{bmatrix}$	$\begin{bmatrix} 49.489 & 3.653 & -4.007 \\ 3.653 & 12.460 & 0.276 \\ -4.007 & 0.276 & 4.356 \end{bmatrix}$

(b)

	Training set			Test set		
	Mean	(Co)variance	RMSE	Mean	(Co)variance	RMSE
Pitch mean α_0	1.948	0.000 402	0.0203	1.948	0.000 344	0.0183
Pitch shape $[\alpha_1\ \alpha_2\ \alpha_3]^T$ ($\times 100$)	$\begin{bmatrix} 3.660 \\ -0.996 \\ -0.104 \end{bmatrix}$	$\begin{bmatrix} 9.865 & -0.354 & -0.076 \\ -0.354 & 1.907 & 0.232 \\ -0.076 & 0.232 & 1.251 \end{bmatrix}$	$\begin{bmatrix} 3.143 \\ 1.381 \\ 1.120 \end{bmatrix}$	$\begin{bmatrix} 3.861 \\ -0.906 \\ -0.085 \end{bmatrix}$	$\begin{bmatrix} 12.885 & 0.955 & 1.073 \\ 0.955 & 3.101 & 0.808 \\ 1.073 & 0.808 & 2.263 \end{bmatrix}$	$\begin{bmatrix} 3.603 \\ 1.762 \\ 1.505 \end{bmatrix}$

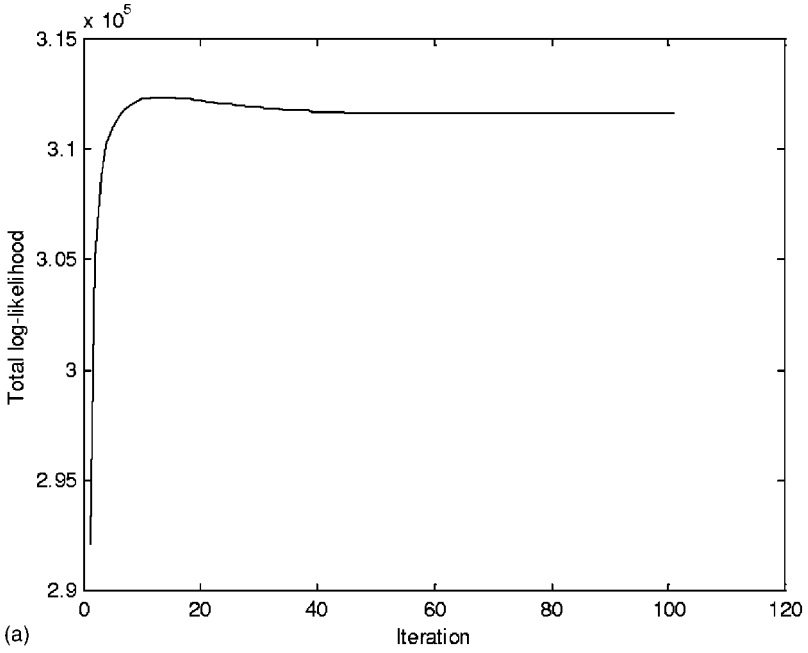

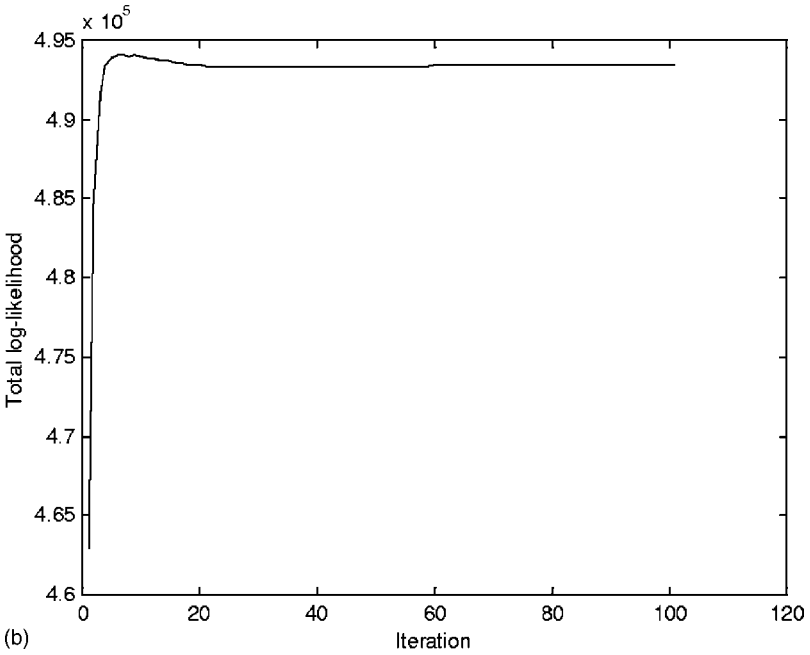

FIG. 2. The plot of the total log-likelihood versus the iteration number for the training of the pitch mean model of (a) the TL database and (b) the TCC database.

B. Experimental results of pitch modeling

The effect of the proposed pitch modeling method was examined first, with the number of prosodic states set to 16. Table III(b) shows the experimental results of pitch mean and shape modeling. It can be seen from the third and sixth columns of Table III(b) that the (co)variances of the normalized mean and shape of the syllable log-pitch contour were greatly reduced for both the closed and open tests, when compared with those shown in Table III(a). The RMSEs of the reconstructed mean and shape of the syllable log-pitch contour are shown in the fourth and seventh columns of Table III(b). Here, the reconstructed mean (shape) was calculated based on the well-trained pitch mean (shape) model by assigning the most probable prosodic state to each syllable and setting the normalized mean (shape) parameter(s) to its (their) mean value(s). By combining the results of the reconstructed pitch mean and shape, we could reconstruct the pitch contour for each syllable. The RMSEs of the reconstructed pitch contour were 0.362 and 0.373 ms/frame for the closed and open tests, respectively. Notice that these two values included RMSEs of 0.17 and 0.19 ms/frame, which resulted from applying orthogonal transformation to the closed and open test data sets, respectively.

Figure 2(a) shows a plot of the total log-likelihood $L(k)$ versus the iteration number k. It can be seen from Fig. 2(a) that the EM algorithm quickly converged in the first several iterations. The histograms of the observed and normalized syllable log-pitch mean for the training set are plotted in Figs. 3(a) and 3(b). It can be seen from these two figures that the variation of the syllable log-pitch mean was greatly reduced after the influence of the affecting factors considered in the model was eliminated. Based on the above results, we

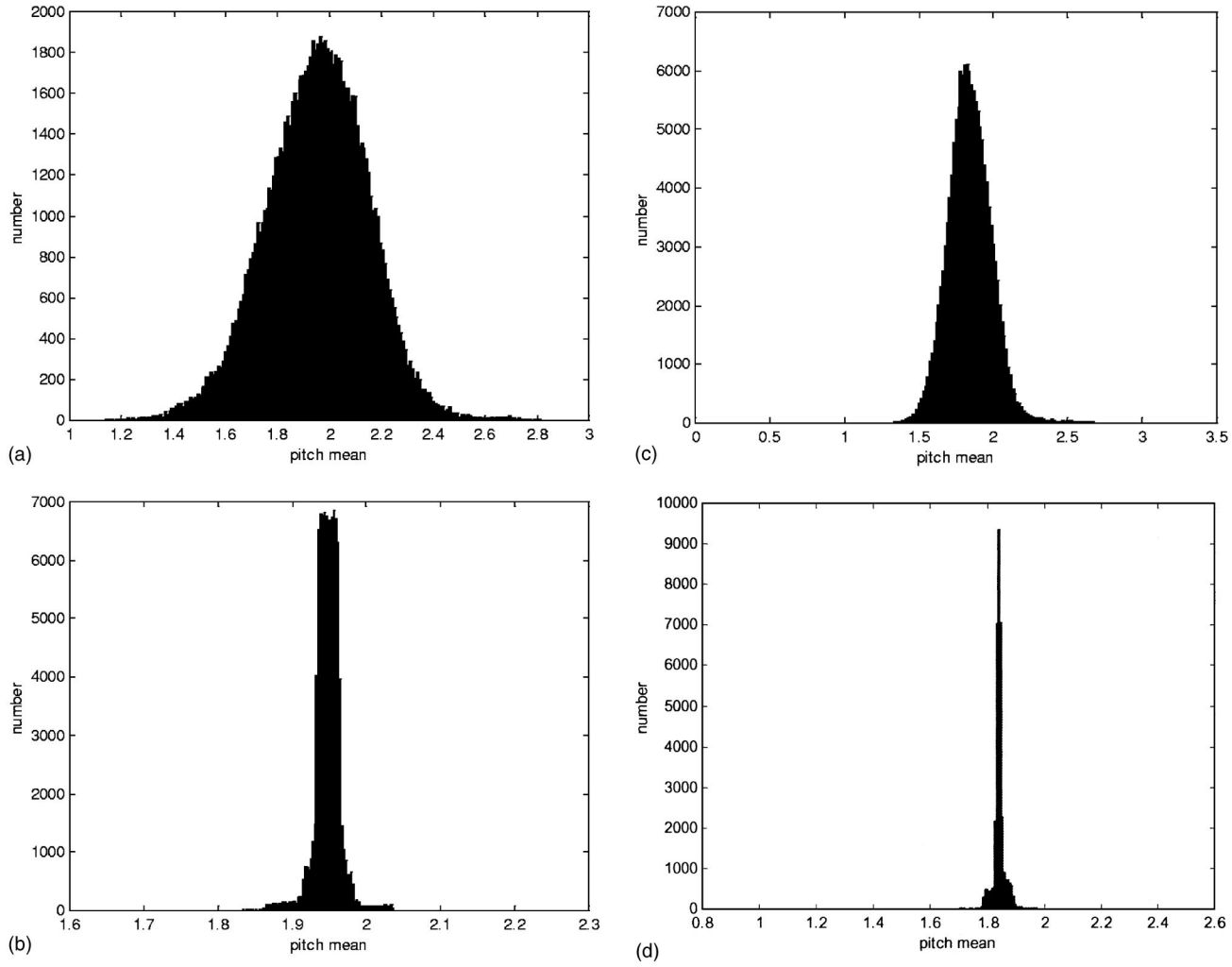

FIG. 3. The histograms of (a) the observed and (b) the normalized pitch means for the training set of the TL database and the histograms of (c) the observed and (d) the normalized pitch means for the TCC database.

concluded that the proposed pitch mean modeling method was effective.

We then examined a case in which the number of prosodic states changed. The resulting variance of the normalized syllable log-pitch mean is shown in Fig. 4(a). As can be seen, the variance of the normalized pitch mean decreased as the number of prosodic states increased. This implies that the pitch mean model became more accurate as the number of prosodic states increased. The improvement reached saturation when the number of prosodic states was greater than 16. Similar findings were observed for the corresponding RMSEs of the reconstructed pitch mean shown in Fig. 4(b).

Figure 5 shows two typical examples of reconstructed pitch contours of two utterances based on the pitch mean and shape models with 16 prosodic states. It can be seen from these two figures that all the reconstructed syllable pitch contours closely resembled their original counterparts. Actually, they were the smoothed versions of the originals as three-order orthogonal polynomial transformation was used. Further evaluation of the performance of the reconstructed pitch contours was conducted by means of two subjective tests: the AB test and the mean opinion score (MOS) test. The synthesized speech recordings, with both the original pitch contours and the reconstructed pitch contours, were presented to the listeners involved in the tests. The inside/outside test could show whether test sentences are from the training or testing set. In the inside test, the original and reconstructed pitch contours of utterances of speaker A (see Table II), a male professional announcer, were used, while in the outside test, the utterances of speaker E, a female speaker, were used. All the testing utterances were generated by the PSOLA algorithm using two acoustic inventories containing the waveform templates of 414 monosyllables. These two acoustic inventories were generated by speakers A and B for the inside and outside tests, respectively. It should be noted that the acoustic inventory of speaker B, who is a professional female announcer, was used in the outside test because the acoustic inventory of speaker E was lacking. All the other prosodic parameters, including the syllable duration, syllable log-energy level, and intersyllabic pause duration, were estimated from the training database using a regression model. Five different long test sentences were used in both the inside and outside tests. Combined with the two kinds of synthesized speech, there were, in total, 20 test sample utterances. Sixteen listeners, university students, were involved in the two tests. In the AB test, each listener was given a pair of

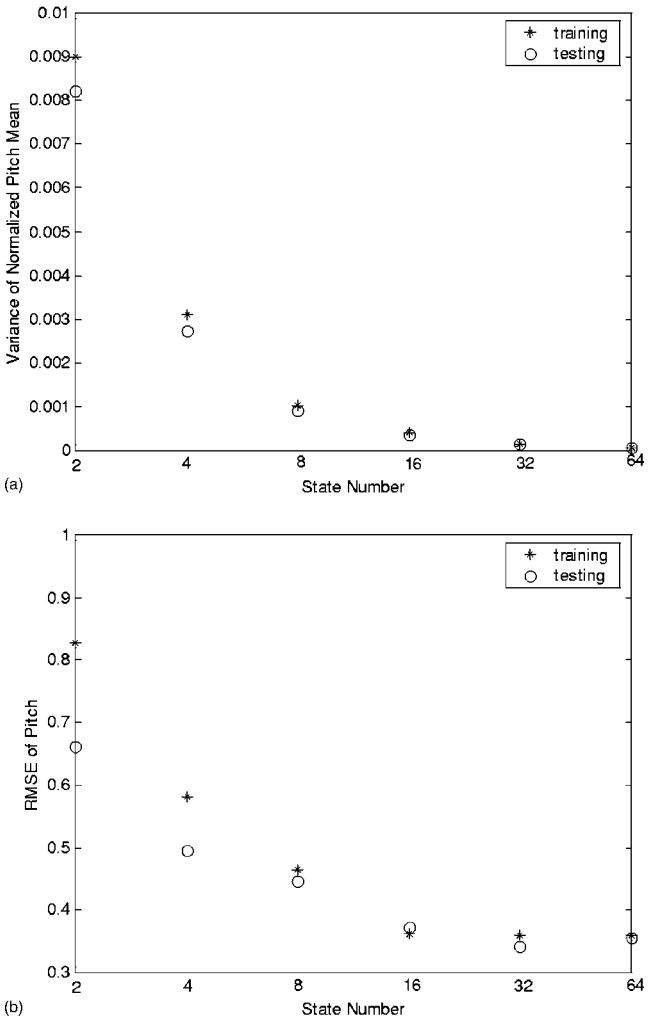

FIG. 4. Plots of (a) the variance of the normalized pitch mean versus the number of prosodic states, and (b) the RMSE of the reconstructed pitch mean versus the number of prosodic states.

synthesized utterances, along with the original and reconstructed pitch contours for each testing sentence, and asked to vote for the better one. Experimental results showed that 41.25% (22.5%) of the synthesized speech recordings, with the original pitch contours, were found by the listeners to sound better; 25% (27.5%) of the synthesized speech recordings, with the reconstructed pitch contours, were found to sound better; and 33.75% (50%) of the two speech recordings were found to sound equivalent for the inside (outside) test, respectively. In the MOS test, absolute category rating was conducted on a scale from 1 (''bad'') to 5 (''excellent''). Experimental results showed that average MOSs of 3.94 (3.34) and 3.68 (3.4) were obtained for the synthesized speech recordings with the original and reconstructed pitch contours, respectively, in the inside (outside) test. From the results of these two subjective tests, we concluded that the reconstructed pitch contours functioned almost as well as their original counterparts.

We then checked whether it was necessary to include the speaker affecting factors in both pitch mean and shape models, besides frame-based speaker normalization, which was performed in the preprocessing stage. An experiment, which excluded the two speaker affecting factors used in the pitch mean model and the speaker affecting factor used in the pitch shape model, was conducted. RMSEs of 0.362 and 0.372 ms were obtained in the closed and open tests, respectively. These results were almost the same as those for the previous cases, which used these three speaker affecting factors in the pitch mean and shape models. This showed that rough speaker normalization was good enough to eliminate the speaker's influence.

We then checked whether the pitch mean and shape models could share the same set of prosodic states. An experiment, in which the prosodic state of every syllable in the pitch shape model was forced to be the same as that in the pitch mean model, was then conducted. RMSEs of 0.504 and 0.478 ms were obtained in the closed and open tests, respectively. These results were worse than those obtained using separate sets of prosodic states in the pitch mean and shape models. Figure 6 shows the 16 patterns of unified prosodic states. The patterns are plotted from left to right in increasing order of the prosodic state index. The vertical axis is pitch period (ms). Sixteen syllable pitch contour patterns were formed using the CFs of the prosodic states, and the average values of the normalized syllable log-pitch mean and shape can be found in this figure. It can also be found in Fig. 6 that the lower-indexed states had a lower pitch mean and smaller pitch slope; they represented the beginning part of a prosodic phrase. On the other hand, the higher-indexed states had a higher pitch mean and larger pitch slope; they represented the ending part of a prosodic phrase.

Finally, we examined the effectiveness of pitch modeling via the TCC database. The same training procedure used with the TL database was applied. The number of prosodic states was set to 16. Table IV(b) shows the experimental results obtained for the mean and (co)variance of the normalized pitch mean and shape, and the RMSEs of the reconstructed pitch mean and shape. It can be seen from the third column in Tables IV(a) and (b) that the variance of the normalized pitch mean and the covariance of the normalized pitch shape were greatly reduced, when compared with those of the original pitch mean and shape. By combining the results for the reconstructed pitch mean and shape, we could reconstruct the pitch contour of each syllable. The RMSEs of the reconstructed pitch contours were 0.384 ms/frame, which included the RMSEs of 0.172 ms that resulted from applying orthogonal transformation. A plot of the total log-likelihood $L(k)$ versus the iteration number k is shown in Fig. 2(b). The histograms of the observed and normalized syllable log-pitch mean for TCC are plotted in Figs. 3(c) and (d). The results were still quite promising even though the pitch variation, due to the large population of speakers, was very high, and the accuracy of the observed data, due to the automatic segmentation performed by the HMM models, was not as high as that achieved by applying manual segmentation to the TL database.

IV. ANALYSES OF THE INFERRED MODEL PARAMETERS

We then analyzed, in detail, the inferred model parameters in order to gain a better understanding of the effects of the affecting factors. Before discussing this, we will briefly

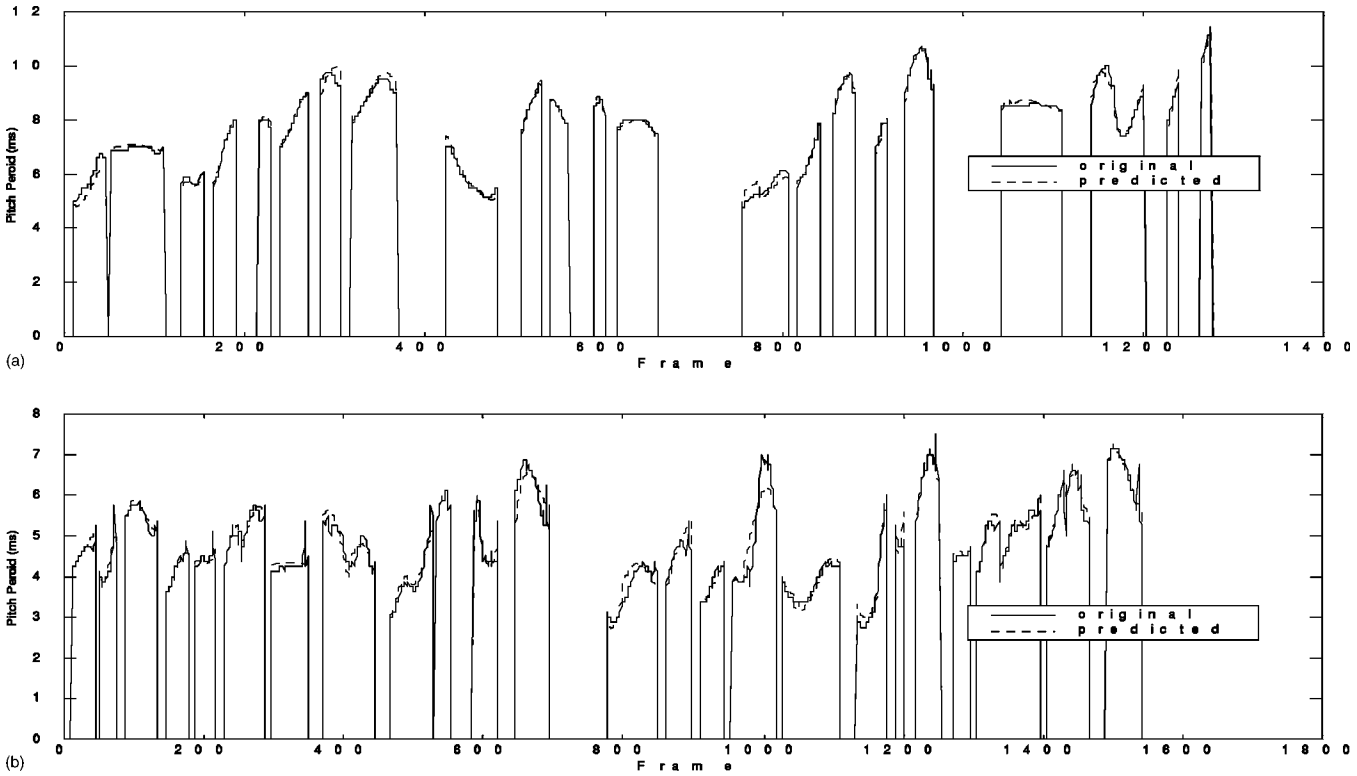

FIG. 5. Examples of reconstructed pitch contours for (a) an inside test utterance: ''tzai-4 guo-2 ren-2 shiau-1 fei-4 shi-2 guan-4 gai-3 bian-4, guo-2 min-2 suo-3 de-2 ti-2 gau-1, shin-4 yung-4 dai-4 kuan-3 shr-4 chang-2, cheng-2 wei-2 chian-2 li-4 shr-4 chang-2'' and (b) an outside test utterance: ''tzai-4 yi-4 guo-2 jeng-4 jing-1 huen-4 luan-4 jung-1 lin-2 wei-2 shou-4 ming-4 de-5 chi-2 an-1 pei-2, wei-4 lai-2 tzai-4 jeng-4 jing-1 liang-3 fang-1 mian-4 dou-1 you-3 bu-4 shau-3 jian-1 kuen-4 ren-4 wu-4 dai-4 wan-2 cheng-2.''

introduce *a priori* knowledge of tone patterns in Mandarin speech. As reported in Ref. 16, tone 1 is a high-level tone that starts in a speaker's high F0 range and remains high; tone 2 is a mid-rising tone that starts in the speaker's mid F0 range, remains level or drops slightly during the first half of the vowel, and then rises to a high-level tone at the end; tone 3 is a low-falling tone that starts in the speaker's mid range and falls to the low range; tone 4 is a high-falling tone that usually peaks around the vowel onset and then falls to the low F0 range at the end; and tone 5 is a low-energy tone that has a relatively arbitrary pitch contour pattern. The F0 contour of each of the first four tones can be represented by a simple single standard pattern, as shown in Fig. 7. However, syllable pitch contour patterns in continuous speech vary highly and can deviate dramatically from their canonical forms.

Table V shows the CFs of the affecting factors of the previous, current, and following tones in the pitch mean model. As can be seen in Table V, the CFs of the affecting factors of the current tone had negative values for tones 1 and 4, and a positive value for the other three tones. Due to the fact that the effect of a positive (negative) CF was to decrease (increase) the F0 mean, the CFs of the affecting factors of the current tone were well matched with the *a priori* phonologic knowledge discussed above. It was also reported in Ref. 34 that all tones, preceding a tone 3, had a

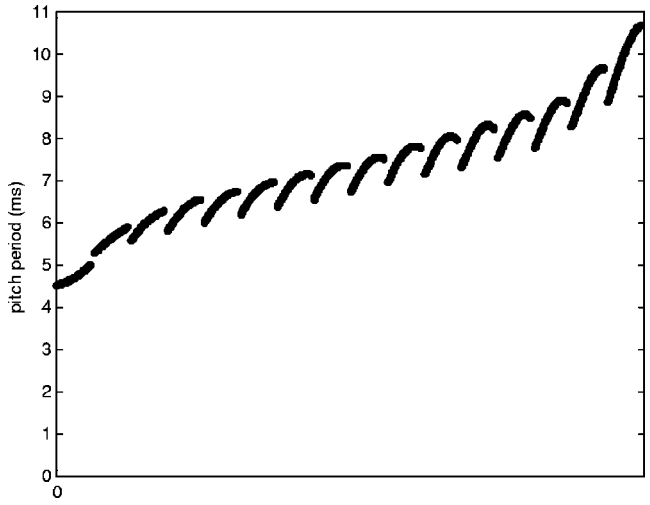

FIG. 6. The effect on the syllable pitch contour of the 16 unified prosodic states of the pitch mean and shape models. Patterns are plotted from left to right in increasing order of the prosodic state index.

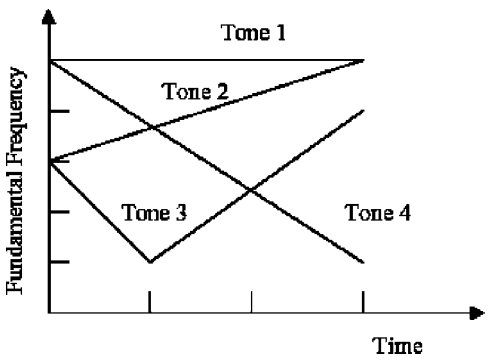

FIG. 7. Standard F0 contour patterns of the first four tones.

TABLE V. The inferred CFs for the affecting factors of the current, preceding and following tones in the pitch mean model (unit of pitch period: ms).

Tone	1	2	3	4	5
β_t CF of current tone	−0.154	0.054	0.160	−0.035	0.128
β_{pt} CF of previous tone	−0.022	−0.034	0.018	0.024	0.029
β_{ft} CF of following tone	0.022	−0.003	−0.047	0.011	0.013

much higher F0 level than they did when they preceded other tones, and all tones had a slightly lower F0 level when they preceded a tone 1. In addition, all tones following tone 1 or 2 had a higher F0 level than they did when they followed tone 3 or 4. These phenomena corroborated the results shown in Table V. Specifically, the effect of the relatively large negative CF ($\beta_{ft}=-0.047$) for $ft=3$ greatly increased the F0 level of the current syllable when it preceded a tone 3, while the positive CF ($\beta_{ft}=0.022$) for $ft=1$ decreased the F0 level of the current syllable when it preceded a tone 1. Similarly, $\beta_{pt}=-0.022$ for $pt=1$ and $\beta_{pt}=-0.034$ for $pt=2$ increased the F0 level of the current syllable when it followed a tone 1 or 2, while the positive CFs ($\beta_{pt}=0.018,0.024,0.029$) decreased the F0 level of the current syllable when it followed a tone 3, 4, or 5.

An advantage of the proposed pitch modeling method is that it provides a quantitative and more complete description of the coarticulation effect of neighboring tones rather than conventional qualitative descriptions of some of the *sandhi* rules. This can be illustrated by reconstructing the pitch contour patterns using the CFs of tone-related affecting factors and the average values of the pitch mean and shape models, while ignoring the CFs of all the other affecting factors. Specifically, the pitch contour pattern of the current tone t_c with the preceding tone t_p and the following tone t_f can be calculated, based on the proposed pitch mean and shape models, as follows:

$$\tilde{f}\left(\frac{i}{M}\right)=e^{\hat{f}(i/M)},\quad 0\leqslant i\leqslant M, \tag{21}$$

where

$$\hat{f}\left(\frac{i}{M}\right)=\sum_{j=0}^{3}\hat{\alpha}_j\cdot\phi_j\left(\frac{i}{M}\right),\quad 0\leqslant i\leqslant M, \tag{22}$$

$$\hat{\alpha}_0=\mu+\beta_{pt=t_p}+\beta_{t=t_c}+\beta_{ft=t_f}, \tag{23}$$

$$\begin{bmatrix}\hat{\alpha}_1\\ \hat{\alpha}_2\\ \hat{\alpha}_3\end{bmatrix}=\boldsymbol{\mu}+\boldsymbol{\beta}_{tc=t_pt_ct_f}. \tag{24}$$

Figure 8 shows two examples. Figure 8(a) displays the reconstructed patterns for the current tones in tone combinations of 033, 133, 233, 333, 433, 533, 030, and 020. It should be noted that 0 denotes a case in which the effect of the previous or following tone is ignored. It can also be seen that all six patterns of tone 3 following tone 3 (i.e., 033, 133, 233, 333, 433, and 533) more closely resemble a pure tone 2 (i.e., 020) than a pure tone 3 (i.e., 030). This corroborates the well-known *sandhi* rule for a 33-tone pair, which says that a tone 3 will change to a tone 2 when it precedes a tone 3. In addition, these six patterns also show their dependence on the preceding tone. Roughly, their beginning parts were adjusted in order to be more smoothly concatenated with the patterns of the preceding tones. Figure 8(b) displays the reconstructed patterns for tone combinations of 044, 144, 244, 344, 444, 544, and 040; it shows that all six patterns of tone 4 following tone 4 (i.e., 044, 144, 244, 344, 444, and 544) have a smaller slope and lower ending point, which agrees with a previous finding.[3] These six patterns also show that they depend on the preceding tone.

We then examined the effects of the *initial* and *final* of the current syllable. We divided all 22 *initials* into seven broad classes, and 40 *finals* into seven broad classes, according to the manner of articulation. *Initial* classes included $I_0=\{\text{null } initial\}$, $I_1=\{\text{b,d,g}\}$, $I_2=\{\text{f,s,sh,shi,h}\}$, $I_3=\{\text{m,n,l,r}\}$, $I_4=\{\text{ts,ch,chi}\}$, $I_5=\{\text{p,t,k}\}$, and $I_6=\{\text{tz,j,ji}\}$. *Final* classes included $F_0=\{\text{low vowels}\}$, $F_1=\{\text{middle vowels}\}$, $F_2=\{\text{high vowels}\}$, $F_3=\{\text{compound vowels}\}$, $F_4=\{\text{vowels with nasal ending}\}$, $F_5=\{\text{retroflexion}\}$, and $F_6=\{\text{null vowels}\}$. Table VI(a) shows the CFs for these seven *initial* classes and seven *final* classes in the pitch mean model. It can be found in Table VI(a) that the positive CFs for {b,d,g}, {f,s,sh,shi,h}, {ts,ch,chi}, and {tz,j,ji} lowered the syllable F0 mean, while all the others raised the syllable F0 mean. As for the *finals*, the positive CFs of the low vowels, compound vowels, and null vowels lowered the syllable F0 mean, while the negative CFs of the middle vowels, high vowels, nasal endings, and retroflexion raised the syllable F0 mean. However, all these 14 CFs were relatively small, compared to the CFs of the other affecting factors. This shows that the *initial* and *final* of the current syllable were not major factors affecting the syllable pitch level. Table VI(b) shows the CFs of these seven *initial* classes and seven *final* classes in the pitch shape model. It can also be seen that all the CFs are relatively small, so they also are not major factors affecting the syllable pitch shape.

Table VII shows the estimated CFs of the three affecting factors for the four training speakers. As observed in Table VII(a), the four CFs of the dynamic range scaling factor in the pitch mean model were all close to 1 for the four speakers, while the four CFs of level shift were all close to 0. In addition, all the CFs of shape shift shown in Table VII(b) were relatively small. This shows that the use of additional speaker affecting factors, other than the frame-based speaker normalization performed in the preprocessing stage, had little effect on the improvement of the pitch mean and shape models. Actually, we have already shown in Sec. III B. that the RMSEs of the reconstructed pitch contour, formed by the proposed pitch mean and shape models, were almost the same when we excluded these three speaker affecting factors.

We then examined the prosodic states of the pitch mean model, labeled by the EM algorithm, in more detail. As mentioned in Sec. I, the prosodic state is conceptually defined as the state of the current syllable in a prosodic phrase. From this definition, one can expect the prosodic phrase structure of an utterance to be characterized by its prosodic state se-

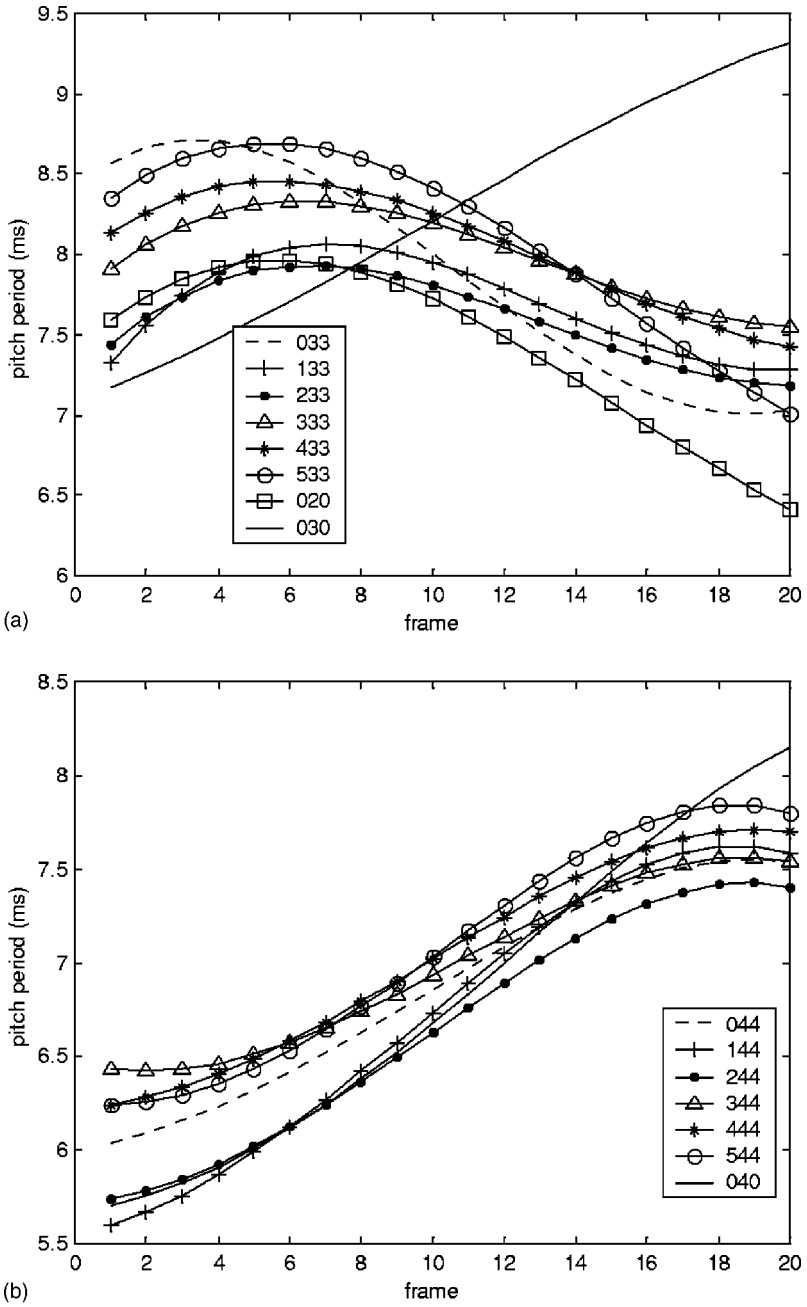

FIG. 8. (a) A comparison of the patterns of tone 3 preceding another tone 3 with the canonical patterns of tone 2 and tone 3. (b) A comparison of the patterns of tone 4 preceding another tone 4 with the canonical pattern of tone 4.

quence. First, a brief description of the characteristics of prosodic phrases will be given here. It is well known that the global downtrend tendency of F0 is to decline over the course of an utterance.[28] It is also known that a slight pitch reset of the bottom line of intonation will occur at a prosodic word boundary, and that a significant pitch reset of the bottom line of intonation will occur at an intonational phrase boundary.[35] The pitch mean sequence of an utterance will, therefore, show repeating patterns of smooth uptrend curves, starting with lower pitch levels and ending at higher pitch levels, representing the prosodic phrase structure of the utterance. With interference due to the tone effect, however, the prosodic phrase patterns are not as apparent as they are when they are observed based on the original pitch mean sequence of an utterance. A typical example is displayed in Fig. 9, where one can see that the original pitch mean sequence of the utterance exhibited a repeating uptrend pattern, while some had large zigzag variations. To eliminate the tone effect, we formed a reconstructed pitch mean sequence of the utterance by calculating the sum of the CFs of the prosodic state sequence and the mean value of the normalized pitch mean. The reconstructed pitch mean sequence is also displayed in Fig. 9, where it is clearly shown that the reconstructed pitch mean sequence was a better representation of the smooth repeating uptrend patterns of the prosodic phrases than the original pitch mean sequence was, because the large zigzag variations caused by the tone effect had been largely eliminated. Figure 10 shows the autocorrelation functions of the original and reconstructed pitch mean sequences. The higher autocorrelation values shown in Fig. 10 imply that the uptrend prosodic phrase patterns, represented by the reconstructed pitch mean sequence, were smoother. The figure also shows that the lowest autocorrelation value occurred at the 6-syllable lag. This agrees with the fact that the aver-

TABLE VI. The inferred CFs for the affecting factors of 7 *initial* and 7 *final* classes in the (a) pitch mean and (b) pitch shape models (unit of pitch period: ms).

(a)

Class	{null *initial*}	{b,d,g}	{f,s,sh,shi,h}	{m,n,l,r}	{ts,ch,chi}	{p,t,k}	{tz,j,ji}
β_i	−0.008	0.004	0.011	−0.013	0.003	−0.014	0.003
β_f	0.011	−0.001	−0.004	0.008	−0.005	−0.019	0.004

(b)

Class	{low vowels}	{middle vowels}	{high vowels}	{compound vowels}	{vowelswith nasal ending}	{retroflexion}	{null vowels}
$\mathbf{b}_i$ (×100)	$\begin{bmatrix}-0.971\\1.125\\-0.548\end{bmatrix}$	$\begin{bmatrix}0.522\\0.015\\-0.020\end{bmatrix}$	$\begin{bmatrix}0.509\\-0.440\\0.321\end{bmatrix}$	$\begin{bmatrix}-0.520\\0.506\\-0.697\end{bmatrix}$	$\begin{bmatrix}-1.270\\-0.666\\0.648\end{bmatrix}$	$\begin{bmatrix}-0.111\\-0.627\\0.389\end{bmatrix}$	$\begin{bmatrix}0.722\\-0.161\\0.075\end{bmatrix}$
$\mathbf{b}_f$ (×100)	$\begin{bmatrix}0.224\\-0.131\\0.182\end{bmatrix}$	$\begin{bmatrix}0.641\\0.280\\-0.095\end{bmatrix}$	$\begin{bmatrix}-0.278\\0.865\\-0.076\end{bmatrix}$	$\begin{bmatrix}0.978\\-0.017\\-0.094\end{bmatrix}$	$\begin{bmatrix}-0.640\\-0.703\\0.166\end{bmatrix}$	$\begin{bmatrix}-1.266\\0.891\\-0.080\end{bmatrix}$	$\begin{bmatrix}-0.354\\0.696\\-0.291\end{bmatrix}$

age length of prosodic phrases is 6.14 syllables, as evaluated based on a 1743-syllable subset of the TL database, with major and minor breaks labeled manually. Based on the above evidence, the validity of the prosodic state definition was confirmed.

Table VIII(a) shows the inferred CFs of the 16 prosodic states in the pitch mean model. It should be noted that these 16 CFs are sorted in increasing order, with state 0 having the smallest CF value and state 15 having the largest. Thus, the lower-indexed states correspond to the beginning part of a prosodic phrase, while the higher-indexed states correspond to the ending part of a prosodic phrase. From detailed analyses, we found that the prosodic states of syllables in a prosodic phrase generally varied from small to large and were reset when they crossed prosodic phrase boundaries. This means that a change of the state's index, from large to small, indicated a possible prosodic phrase boundary. We, therefore, set the following rules to detect minor and major prosodic phrase boundaries:

$$\text{location following syllable } n = \begin{cases} \text{major boundary} & \text{if } 10 \leqslant p_n - p_{n+1} \leqslant 15, \\ \text{minor boundary} & \text{if } 4 \leqslant p_n - p_{n+1} \leqslant 9, \\ \text{nonboundary} & \text{otherwise.} \end{cases} \quad (25)$$

Figure 11 shows some examples of prosodic labeling performed using the above rules, with "*" representing a major boundary and "&" representing a minor boundary. As shown in Fig. 11, almost all the location of PMs (punctuation marks) were marked with major or minor prosodic phrase boundaries. This closely agrees with prior knowledge that a PM is a good location for a break in the pronunciation of a long text. It can also be seen in Fig. 11 that some major and minor prosodic phrase boundaries were detected at non-PM intersyllable locations. From detailed analyses, we found that most of those locations were boundaries of long words. Table IX shows the prosodic labeling statistics. As shown, 80.7% of the location of major PMs belonging to the set {comma, period, exclamation mark, semicolon, question mark} and 69.5% of the location of the secondary major PMs belonging to the set {pause—mark in Chinese punctuation used to set off items in a series, colon} were marked with major or minor prosodic phrase boundaries. On the other hand, only 42.3% of the location of the minor PMs belonging to the set {brace, bracket, dot} and 10.8% of the location of the non-PMs were marked with major or minor prosodic phrase boundaries. From detailed analyses, we found that most of the major/minor prosodic phrase boundaries occurring at non-PM locations were breathing breaks or long-phrase boundaries; most of the major and secondary major PMs labeled with nonboundaries occurred at the ends of very short sentences, at locations near other breaks, or at the ends of sentences whose pronunciation exhibited relatively flat pitch variation. These phenomena closely matched our prior linguistic knowledge. In order to more accurately evaluate the performance of automatic prosodic labeling, we manually processed a small data set containing 1743 syllables in order to determine whether each intersyllable location was a nonbreak, a minor break, or a major break. Table X shows a comparison of the two prosodic labeling methods, where it can be seen that the accuracy of the automatic prosodic labeling method was 94.1%. If we combine these two classes of minor and major breaks into one break class, the accuracy rate increases to 97.2%. The automatic prosodic labeling method is, therefore, promising.

TABLE VII. The inferred CFs for the four training speakers in the (a) pitch mean and (b) pitch shape models (unit of pitch period: ms).

Speaker	A	B	C	D
		(a)		
γ_s	1.014	0.971	1.026	0.981
β_s	−0.030	0.049	−0.044	0.041
		(b)		
$\mathbf{b}_s$ (×100)	$\begin{bmatrix}0.291\\0.134\\-0.012\end{bmatrix}$	$\begin{bmatrix}0.324\\0.302\\-0.125\end{bmatrix}$	$\begin{bmatrix}-0.216\\0.349\\0.348\end{bmatrix}$	$\begin{bmatrix}-0.301\\-0.472\\-0.152\end{bmatrix}$

V. AN APPLICATION TO PREDICT PITCH FOR TTS

A hybrid method, incorporating the above pitch mean and shape models with a linear regression method to predict

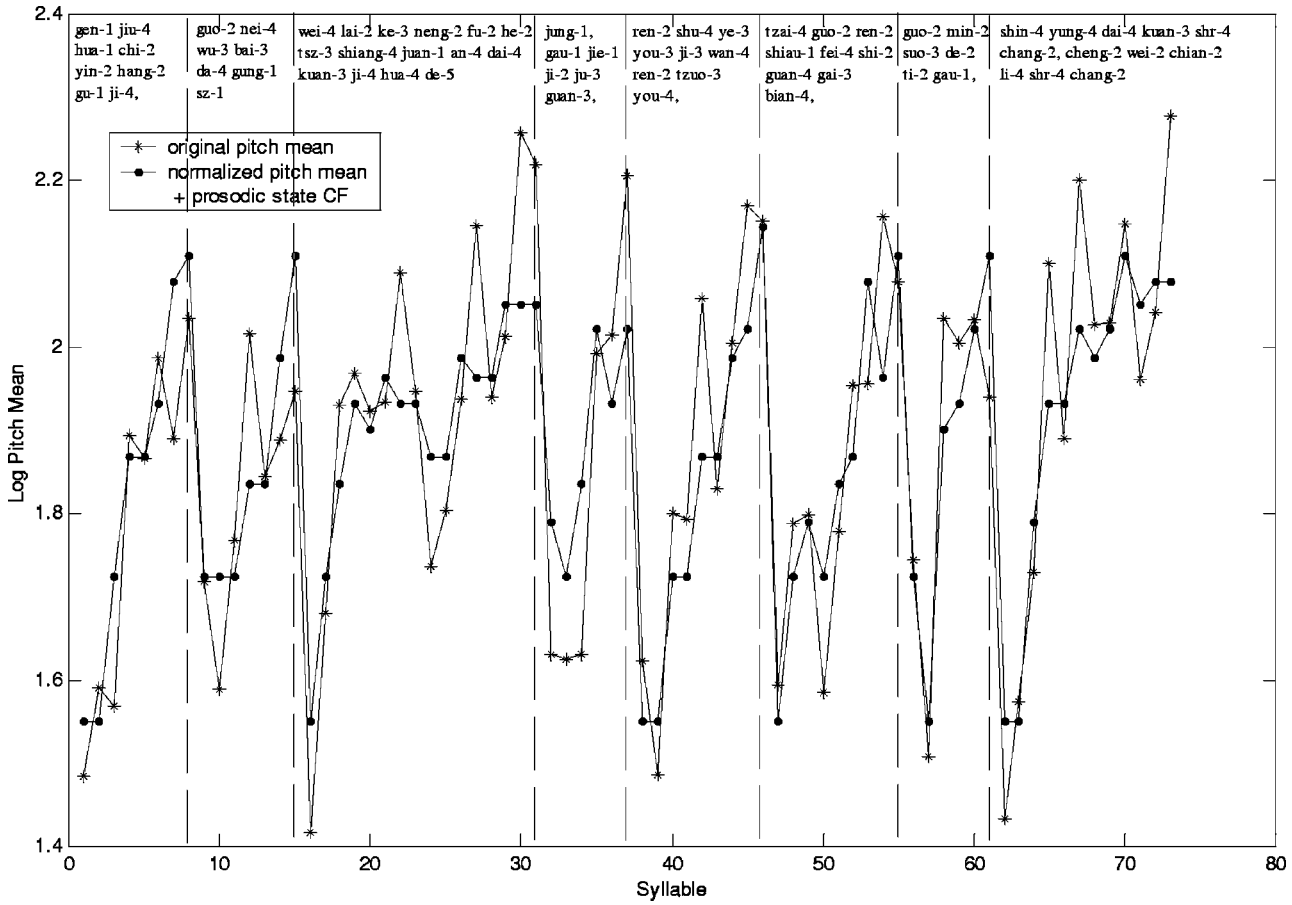

FIG. 9. A comparison between the original pitch mean sequence and the reconstructed pitch mean sequence formed by adding the mean value of the normalized pitch mean and prosodic state CFs. The sentence is ''gen-1 jiu-4 hua-1 chi-2 yin-2 hang-2 gu-1 ji-4, guo-2 nei-4 wu-3 bai-3 da-4 gung-1 sz-1 wei-4 lai-2 ke-3 neng-2 fu-2 he-2 tsz-3 shiang-4 juan-1 an-4 dai-4 kuan-3 ji-4 hua-4 de-5 jung-1, gau-1 jie-1 ji-2 ju-3 guan-3, ren-2 shu-4 ye-3 you-3 ji-3 wan-4 ren-2 tzuo-3 you-4, tzai-4 guo-2 ren-2 shiau-1 fei-4 shi-2 guan-4 gai-3 bian-4, guo-2 min-2 suo-3 de-2 ti-2 gau-1, shin-4 yung-4 dai-4 kuan-3 shr-4 chang-2, cheng-2 wei-2 chian-2 li-4 shr-4 chang-2.''

the syllable pitch contour for Mandarin TTS, was developed. Figure 12 shows a block diagram of the proposed method. It first estimates the prosodic state CF of each syllable from inputs of linguistic features using the linear regression technique. The linguistic features used here for this linear regression included (1) current word length: {1,2,3,>3}; (2) current syllable position in word: {first, intermediate, last}; (3) sentence length: {1,[2,5],[6,10],[11,15],[16,20],>20}; (4) current syllable position in sentence: {1st, 2nd, 3rd, [4th,5th], [6th,7th], [8th,11th], last, 2nd last, 3rd last, [5th last, 4th last], [7th last, 6th last], [11th last, 8th last], and others}, where the smaller count from the beginning or the end wins, with the count from the end breaking the tie; (5) punctuation mark after the current syllable (12 types+null); and (6) part of speech (53 types). This method then combines the predicted prosodic state CFs with the CFs of other affecting factors to form estimates of four orthogonal transform coefficients of the log-pitch contour for each syllable using the pitch mean and shape models. Here, the CFs of the tone- and syllable-related affecting factors were obtained directly by looking-up the corresponding CF tables constructed in the training phase. On the other hand, the three CFs of the speaker could be directly specified as additional inputs to control the dynamic range of pitch contour. In this study, in order to disregard the effect of the speaker's variability, the values of the three CFs of the speaker were assigned to the values obtained by the EM algorithm in training. In addition, the values of the normalized pitch mean and shape parameters, required to calculate the output orthogonal transform coefficients in Eqs. (6) and (7), could be obtained through

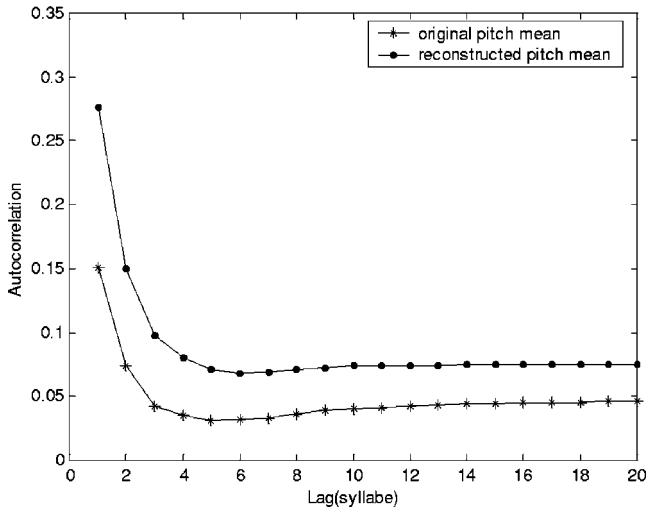

FIG. 10. Autocorrelation functions of the original pitch mean sequence and the reconstructed pitch mean sequence formed by adding the mean value of the normalized pitch mean and the prosodic state CFs.

TABLE VIII. The inferred CFs for the 16 prosodic states in the (a) pitch mean and (b) pitch shape models. The CFs in (a) are sorted from small to large (unit of pitch period: ms).

(a)

State	0	1	2	3	4	5	6	7
β_p	−0.400	−0.225	−0.159	−0.113	−0.081	−0.047	−0.016	0.014
State	8	9	10	11	12	13	14	15
β_p	0.039	0.073	0.102	0.130	0.161	0.196	0.265	0.348

(b)

State	0	1	2	3	4	5	6	7
$\mathbf{b}_q$ ($\times 100$)	$\begin{bmatrix} -3.662 \\ -4.832 \\ -0.108 \end{bmatrix}$	$\begin{bmatrix} 0.047 \\ -0.179 \\ -1.535 \end{bmatrix}$	$\begin{bmatrix} -1.167 \\ -3.221 \\ -0.436 \end{bmatrix}$	$\begin{bmatrix} -2.297 \\ 4.218 \\ 0.346 \end{bmatrix}$	$\begin{bmatrix} -2.245 \\ -0.591 \\ -0.267 \end{bmatrix}$	$\begin{bmatrix} -1.558 \\ 1.194 \\ -0.466 \end{bmatrix}$	$\begin{bmatrix} -4.033 \\ 0.582 \\ 0.961 \end{bmatrix}$	$\begin{bmatrix} -1.167 \\ -1.550 \\ 0.248 \end{bmatrix}$
State	8	9	10	11	12	13	14	15
$\mathbf{b}_q$ ($\times 100$)	$\begin{bmatrix} 9.354 \\ 1.249 \\ -1.476 \end{bmatrix}$	$\begin{bmatrix} -0.164 \\ 0.479 \\ 0.304 \end{bmatrix}$	$\begin{bmatrix} 3.707 \\ 0.295 \\ -0.773 \end{bmatrix}$	$\begin{bmatrix} -1.340 \\ -0.798 \\ 1.164 \end{bmatrix}$	$\begin{bmatrix} 0.849 \\ 2.249 \\ 0.184 \end{bmatrix}$	$\begin{bmatrix} 0.094 \\ 1.469 \\ 1.603 \end{bmatrix}$	$\begin{bmatrix} 1.550 \\ -2.455 \\ 0.684 \end{bmatrix}$	$\begin{bmatrix} -0.279 \\ -0.289 \\ 0.106 \end{bmatrix}$

similar linear regressive estimation. However, because of the fact that their variance was very small, we simply set their values to the means of these two models. Lastly, we generated the reconstructed syllable pitch contour by performing orthogonal polynomial expansion and frame-based speaker denormalization. Notice that the linguistic features used here were extracted from the input text by an automatic word tokenization algorithm, with an 80 000-word lexicon and a manual postcheck.

For a performance comparison, the conventional linear regression method was also implemented. It uses a linear combination of weighted input linguistic features to generate the four orthogonal transform parameters of the log-pitch contour for each syllable. To ensure a fair comparison, the input linguistic features used in the method comprised all the above features and some other syllable-level features, including the lexical tones (5×3 types) of the preceding, current, and succeeding syllables; the *initials* (21 types+null) of the current and succeeding syllables; the *medials* (3 types+null) of the current syllable; and the *finals* (14 types) of the preceding and current syllables.

Experimental results obtained using the TL database are shown in Table XI, where it can be clearly found that the hybrid method, with 16 prosodic states, outperformed the linear regression method. RMSEs of 0.996 and 0.865 ms/frame between the predicted and observed pitch periods were obtained in the closed and open tests, respectively. The results were better than those, 1.511 and 1.179 ms/frame, achieved using the linear regression method. Notice that the RMSEs resulting from orthogonal transformation were 0.17 and 0.19 ms for the closed and open test data sets, respectively.

Lastly, an AB test and an MOS perceptual test, similar to those discussed in Sec. III B, were employed to evaluate the performance of the proposed hybrid method and the conventional linear regression method. Synthesized speech recordings, with syllable pitch contours estimated using these two methods, were compared. The same 16 listeners were involved in these two tests. The experimental results of the AB test showed that 98.75% (100%) of the hybrid synthesized speech was found to sound better in the inside (outside) test, while 1.25% (0%) of the linear regression synthesized speech was found to sound better. The experimental results of the MOS test showed that average MOSs of 3.5 (3.18) and

je-4 wei-4 yue-1 han-4 huo-4 pu-3 jin-1 sz-1 da-4 shiue-2 ming-2 yu-4 jiay-4 shou-4 * tzai-4 di-4 yi-1 jie-4 guo-2 ji-4 & shing-4 gau-1 chau-2 huei-4 yi-4 jung-1 shuo-1 * , ta-1 duei-4 je-4 yi-4 shr-3 yu-2 & yi-1 jiou-3 ba-1 ling-2 nian-2 dai-4 de-5 shing-4 chiu-1 shr-4 & gan-3 dau-4...
je-4 chang-3 bi-3 sai-4 * jiang-1 yu-2 jin-1 r-4 shia-4 wu-3 er-4 shr-2 & tzai & tai-2 bei-3 & shr-4 li-4 bang-4 chiou-2 chang-3 jiu-3 shing-2 * ,hei-1 ying-1 tzu-3 jr-1 & suo-3 shu-3 & san-1 ji-2 bang-3 chiou-2 duei-4 * ,bau-1 gua-1 tai-2 nan-2 liou-4 shin-4 * ,tai-2 dung-1 nung-2 gung-1 & ,ping-2 dung-1 he-4 sheng-1 guo-2 jung-1 * ,tai-2 dung-1 lu-4 ye-3 guo-2 jung-1 & ji-1 tai-2 nan-2 shan-4 hua-4 guo-2 shiau-3 deng-3 duei-4 * ,jiang-1 ge-4 juo-2 chiou-2 duei-4 fu-2 juang-1 & dau-4 chang-2 jia-1 you-2 * ,yu-4 ji-4 ren-2 shu-4 you-3 jin-4 chian-1 ren-2 yi-3 shang-4 * .hei-1 ying-1 liang-3 wei-4 jiau-4 lian-4 * huang-2 yung-3 yu-4 ji-2 & jiang-1 tai-4 chiuan-2 * ,duei-4 yu-2 tsz-3 chang-3 bi-3 sai-4 * bu-4 gan-3 diau-4 yi-3 ching-1 shin-1 * ,chu-2 le-5 pai-2 chu-1 tzuan-4 shr-2 jen-4 rung-2 wai-4, ye-3 yau-4 chin-1 tz-4 shang-4 chang-3 * .hei-1 ying-1 suo-3...
shang-1 ren-2 fei-1 fa-3 tuen-2 ji-1 & da-4 liang-4 bau-4 ju-2 * ,wan-4 yi-1 fa-1 sheng-1 bau-4 ja-4 shr-4 jian-4 * ,bu-2 dan-4 huei-4 tzau-4 cheng-2 sz-3 shang-1 chan-3 jiu-4 * ,tz-4 ji-3 ye-3 ke-3 neng-2 cheng-2 wei-2 & shou-4 hai-4 tzuei-4 da-4...
shr-4 jie-4 shing-4 de-5 huan-2 bau-3 chau-2 liou-2 & ,shr-3 ren-2 men-5 r-4 yi-4 jung-4 shr-4 huan-2 jing-4 wu-1 ran-3 de-5 wen-4 ti-2 * ;er-2 guan-1 guang-1 liu-3 you-2 & je-4 ge-5 wu-2 yan-1 chung-1 gung-1 ye-4 * "jeng-4 hau-3 wen-3 he-2 tsz-3 yi-4 * jian-4 kang-1 su-4 chiou-2 * ,yin-1 tsz-3 ke-3 yu-4 chi-2 & jin-1 nian-2 jiang-1 shr-4 you-2 le-4 chiu-1...

FIG. 11. Examples of labeling minor (&) and major (*) prosodic phrase boundaries using rules based on the prosodic state differences of the pitch mean model.

TABLE IX. Prosodic labeling statistics generated by Eq. (25). Here major PM={comma, period, exclamation mark, semicolon, question mark}; secondary major PM={pause, colon}, and minor PM={brace, bracket, dot}.

PM	Break		
	Nonboundary	Minor boundary	Major boundary
Non-PM	89.18%	9.80%	1.02%
Minor PM	57.73%	33.48%	8.80%
Secondary Major PM	30.52%	44.65%	24.83%
Major PM	19.31%	31.66%	49.02%

TABLE X. A comparison between the prosodic phrase boundaries automatically generated by the rules based on stated differences of the pitch mean model and the manually labeled ones using a 1743-syllable subset of the TL database (unit: syllable).

Manual	Automatic		
	Nonboundary	Minor boundary	Major boundary
Nonboundary	1463	34	2
Minor boundary	10	94	38
Major boundary	3	16	83

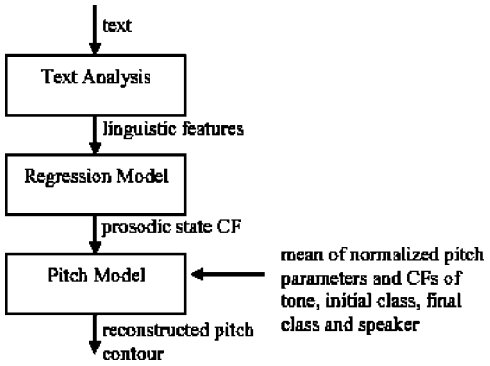

FIG. 12. A block diagram of the proposed hybrid method for syllable pitch contour prediction.

TABLE XI. The RMSEs of the hybrid method, with 16 prosodic states, and the linear regression method (unit: ms/frame).

RMSEs	Closed test	Open test
Hybridregression	0.996	0.865
Regression	1.511	1.179

1.34 (1.3) were obtained using the hybrid method and linear regression method, respectively, in the inside (outside) test. Based on the results of these two subjective tests, the proposed hybrid method was obviously better.

VI. CONCLUSION AND FUTURE WORKS

This paper has presented a new statistics-based syllable pitch contour modeling method for Mandarin speech. Experimental results confirmed its effectiveness at separating several main factors that seriously affect the mean and shape of the syllable log-pitch contour of Mandarin utterances. All the inferred CFs of the affecting factors conformed well with our prior linguistic knowledge. In addition, the prosodic states labeled by the EM algorithm were linguistically meaningful, and the repeating uptrend pitch patterns of the prosodic phrase structure of an utterance were well represented by its prosodic state sequence. The proposed pitch contour modeling method is, therefore, extremely promising.

Some future work is well warranted. First, as discussed in Sec. I, only the first subtask of the complicated pitch modeling procedure was undertaken in the current study; this involved modeling the relationship between the syllable pitch contour features and some affecting factors, including local phonetic features, the speaker, and the prosodic state. The second subtask, which would explore the relationship between the prosodic state and high-level linguistic cues, is still untouched. We will undertake this second phase of research in the near future, using a tree-bank database. Second, by taking advantage of pitch modeling performed using only acoustic and simple phonetic features, we can apply the syllable pitch mean and shape models in such applications as tone recognition and prosodic labeling, which do not need *a priori* high-level linguistic information, such as word tokenization or syntactic features.

ACKNOWLEDGMENTS

This work was supported in part by the MOE under Contract No. EX-92-E-FA06-4-4 and in part by the NSC under Contract No. NSC91-2219-E-009-038.

[1] A. I. C. Monaghan and D. R. Ladd, "Manipulating Synthetic Intonation for Speaker Characterisation," ICASSP (1991), S7.11, pp. 453–456.
[2] L.-S. Lee, C.-Y. Tseng, and C.-J. Hsieh, "Improved Tone Concatenation Rules in a Formant-Based Chinese Text-to-Speech System," IEEE Trans. Speech Audio Process. **1**(3), 287–294 (1993).
[3] L.-S. Lee, C.-Y. Tseng, and M. Ouh-young, "The Synthesis Rules in a Chinese Text-to-speech System," IEEE Trans. Acoust., Speech, Signal Process. **37**(9), 1309–1319 (1989).
[4] B. Ao, C. Shih, and R. Sproat, "A Corpus-Based Mandarin Text-To-Speech Synthesizer," ICSLP (1994), S29, 8.1–8.4, pp. 1771–1774.
[5] S. H. Chen, S. H. Hwang, and Y. R. Wang, "An RNN-based prosodic information synthesizer for Mandarin text-to-speech," IEEE Trans. Speech Audio Process. **6**(3), 226–239 (1998).
[6] N.-H. Pan, W.-T. Jen, S.-S. Yu, M.-S. Yu, S.-Y. Huang, and M.-J. Wu, "Prosody Model in a Mandarin Text-to-Speech System Based on a Hierarchical Approach," IEEE International Conference on Multimedia and Expo (2000), Vol. 1, pp. 448–451.
[7] S.-H. Kim and J.-Y. Kim, "Efficient Method of Establishing Words Tone Dictionary for Korean TTS system," Eurospeech, 1997.
[8] M. Dong and K.-T. Lua, "Pitch Contour Model for Chinese Text-to-Speech using CART and Statistical Model," ICSLP (2002), pp. 2405–2408.
[9] Y. Ishikawa and T. Ebihara, "On the Global F0 Shape Model using a

Transition Network for Japanese Text-to-Speech Systems,'' Eurospeech, 1997.
[10] S.-H. Chen and Y.-R. Wang, ''Tone Recognition of Continuous Mandarin Speech Based on Neural Networks,'' IEEE Trans. Speech Audio Process. **3**(2), 146–150 (1995).
[11] W.-J. Yang, J.-C. Lee, Y.-C. Chang, and H.-C. Wang, ''Hidden Markov Model for Mandarin Lexical Tone Recognition,'' IEEE Trans. Acoust., Speech, Signal Process. **36**(7), 988–992 (1988).
[12] C. W. Wightman and M. Ostendorf, ''Automatic Labeling of Prosodic Patterns,'' IEEE Trans. Speech Audio Process. **2**(4), 469–481 (1994).
[13] A. Batliner, R. Kompe, A. Kiebling, H. Niemann, and E. Noth, ''Syntactic-Prosodic Labeling of Large Spontaneous Speech Data-Bases,'' ICSLP (1996), pp. 1720–1723.
[14] X. Lin, Y. Chen, S. Lim, and C. Lim, ''Recognition of Emotional State from Spoken Sentences,'' IEEE 3rd Workshop on Multimedia Signal Processing (1999), pp. 469–473.
[15] M. V. Chan, X. Feng, J. A. Heinen, and R. J. Niederjohn, ''Classification of Speech Accents with Neural Networks,'' *IEEE International Conference on Neural Networks* (1994), Vol. 7, pp. 4483–4486.
[16] C.-L. Shih, ''Tone and Intonation in Mandarin,'' *Working Papers of the Cornell Phonetics Laboratory*, No. 3, pp. 83–109, June 1988.
[17] Z.-J. Wu, ''Can Poly-Syllabic Tone-*Sandhi* Patterns be the Invariant Units of Intonation in Spoken Standard Chinese,'' ICSLP (1990), pp. 12.10.1–12.10.4.
[18] P. Taylor, ''Analysis and synthesis of intonation using the tilt model,'' J. Acoust. Soc. Am. **107**, 1697–1714 (2000).
[19] C. Shih, G. Kochanski, and E. Fosler-Lussier, ''Implications of Prosody Modeling for Prosody Recognition,'' *Proceedings of the ISCA Tutorial and Research Workshop on Prosody in Speech Recognition and Understanding* (2001), pp. 133–138.
[20] N. M. Veilleux and M. Ostendorf, ''Probabilistic Parse Scoring with Prosodic Information,'' ICASSP (1993), pp. II-51–II-54.
[21] K. Iwano and K. Hirose, ''Prosodic Word Boundary Detection Using Statistical Modeling of Moraic Fundamental Frequency Contours and Its Use for Continuous Speech Recognition,'' ICASSP (1999), pp. 133–136.
[22] X. Sun, ''Predicting Underlying Pitch Targets for Intonation Modeling,'' Proc. of the 4th ISCA Tutorial and Research Workshop on Speech Synthesis, Perthshire, Scotland (2001), pp. 143–148.
[23] A. Ljolje and F. Fallside, ''Synthesis of Natural Sounding Pitch Contours in Isolated Utterances Using Hidden Markov Models,'' IEEE Trans. Acoust., Speech, Signal Process. **ASSP-34**(5), 1074–1080 (1986).
[24] J. R. Bellegarda, K. E. A. Silverman, K. Lenzo, and V. Anderson, ''Statistical Prosodic Modeling: From Corpus Design to Parameter Estimation,'' IEEE Trans. Speech Audio Process. **9**(1), 52–66 (2001).
[25] J.-H. Ni, R.-H. Wang, and K. Hirose, ''Quantitative Analysis and Formulation of Tone Concatenation in Chinese F0 Contours,'' EUROSPEECH, 1997.
[26] M. Abe and H. Sato, ''Two-stage F0 Control Model Using Syllable Based F0 Units,'' ICASSP (1992), pp. II-53–II-56.
[27] D. T. Chappell and J. H. L. Hansen, ''Speaker-Specific Pitch Contour Modeling and Modification,'' ICASSP, 1998.
[28] C. Shih, ''Declination in Mandarin,'' *Intonation: Theory, Models and Applications*, Proceedings of an ESCA Workshop, Athens, Greece (1997), pp. 293–296.
[29] L. Aijun, ''Chinese Prosody and Prosodic Labeling of Spontaneous Speech,'' Speech Prosody, 2002.
[30] W.-J. Wang, Y.-F. Liao, and S.-H. Chen, ''Prosodic Modeling of Mandarin Speech and Its Application to Lexical Decoding,'' Eurospeech 99, Vol. 2, pp. 743–746.
[31] H.-Y. Hsieh, Ren-Y. Lyu, and L.-S. Lee, ''Use of Prosodic Information to Integrate Acoustic and Linguistic Knowledge in Continuous Mandarin Speech Recognition with Very Large Vocabulary,'' ICSLP (1996), Vol. 2, pp. 809–812.
[32] S. de Tournemire, ''Identification and Automatic Generation of Prosodic Contours for a Text-To-Speech Synthesis System in French,'' Eurospeech, 1997.
[33] F.-C. Chou, C.-Y. Tseng, K.-J. Chen, and L.-S. Lee, ''A Chinese Text-to-Speech Based on Part-of-Speech Analysis, Prosodic Modeling and Nonuniform Units,'' ICASSP (1997), pp. 923–926.
[34] C. Wang and S. Seneff, ''Improved Tone Recognition by Normalizing for Coarticulation and Intonation Effects,'' ICSLP, 2000.
[35] Y. Yufang and W. Bei, ''Acoustic Correlates of Hierarchical Prosodic Boundary in Mandarin,'' Speech Prosody, 2002.

Modal analysis and intensity of acoustic radiation of the kettledrum

Lamberto Tronchin[a)]
DIENCA—CIARM, University of Bologna, Viale Risorgimento, 2, I-40136 Bologna, Italy

(Received 17 May 2004; revised 5 October 2004; accepted 12 October 2004)

The acoustical features of kettledrums have been analyzed by means of modal analysis and acoustic radiation (p/v ratio) measurements. Modal analysis of two different kettledrums was undertaken, exciting the system both by a hammer and a shaker. Up to 15 vibrational modes were clearly identified. Acoustic radiation was studied using two ways. Based on previous experiments of other researchers, a new parameter, called *intensity of acoustic radiation (IAR)*, has been defined and measured. Results show a strict relationship between IAR and the frequency response function (FRF, which is the v/F ratio), and IAR also strongly relates the modal pattern to acoustic radiation. Finally, IAR is proposed for vibro-acoustical characterization of kettledrums and other musical instruments such as strings, pianos, and harpsichords. © *2005 Acoustical Society of America.*
[DOI: 10.1121/1.1828552]

PACS numbers: 43.75.Yy, 43.75.Hi, 43.40.Dx [NHF] Pages: 926–933

I. INTRODUCTION

Modal analysis and acoustic radiation in musical acoustics are widely used to analyze vibro-acoustical behavior of musical instruments. Many studies have been conducted characterizing the acoustic radiation of many instruments using these techniques. Since sound radiation is strongly related to modal patterns, a correlation between resonance frequencies in vibrating structures and sound production should exist. On the other hand, previous studies find a negative correlation between acoustic radiation and frequency response function (FRF, which is the v/F ratio) of membranes or plates in instruments such as piano and harpsichord (Suzuki, 1986; Giordano, 1998). It could be argued that pianos and harpsichords are quite complicated instruments, and so understanding their sound radiation could be hampered by their complex structure. Therefore, the study on frequency response, modal analysis, and acoustic radiation will be undertaken for two tympani, where sound generation is largely from the membrane, so the correlation between FRF and sound radiation should be found easily. The comparison between experimental modal patterns and previously published results could suggest the most appropriate measurement technique for characterizing vibro-acoustical properties of musical instruments.

A new vibro-acoustical parameter, able to properly relate sound production and FRF, is required especially for tympani, where sound generation and modal analysis are strongly related. Applications of this extend beyond musical acoustics into the modeling of musical instruments in auditoria.

II. TYMPANI PHYSICS: MODAL ANALYSIS

Most drums normally produce a sound of indefinite pitch, with the notable exceptions of tympani and tablas, the former of which is used in the orchestra (Rayleigh, 1945). A drum skin or membrane is distinctively different from a string in that the string vibrations follow a harmonic series, while the membrane vibrates in more complex ways. A circular membrane's nodes form concentric circular lines, and straight lines following the membrane's diameters. Each partial contributing to the instrument's sound corresponds to a particular vibration mode. In Fig. 1, the first 12 modes are represented, with the ratio between the frequency of the corresponding partial and the mode (0,1).

How can a kettledrum produce a note of defined pitch? Previously, physicists (Rayleigh, Benade, Rossing) have studied the frequency ratio between the fundamental and upper modes, and the effect of air-loading. Rayleigh noted that the pitch corresponds to (1,1) mode. Benade (1990) measured the first ten components of the sound of a 25-in. kettledrum tuned on C (130.8 Hz). Rossing and his staff (in several studies from 1976 to 1998) (Rossing, 1976, 1977, 1982) investigated vibration modes of kettledrums, finding that all the vibration modes with only diametric nodes are in harmonic ratios to each other. Furthermore, the vibration modes (1,1), (2,1), (3,1), (4,1), and (5,1) are respectively in frequency ratios of 1, 1.5, 2, 2.44 (about 2.5), and 2.90 (about 3) with the mode (1,1) (Fletcher and Rossing, 1998). These modes are almost in harmonic ratios to a missing fundamental one octave below the (1,1) mode. Although this missing fundamental could be rebuilt by the human ear, normally this does not happen, perhaps because the intensity and duration of the harmonics are insufficient to enable the ear to grasp the harmonic spectrum.

Rossing found that air-loading is important in tuning the kettledrum's partials. Air-loading is the effect of the mass of air in the vicinity of the membrane, which lowers the natural frequencies of vibration from those which would occur in a vacuum. This effect is strongest for low frequencies, and influences especially the (1,1) mode. Additionally, the kettle affects the modes, increasing the circular mode frequencies and reducing the diametric mode frequencies (Tubis and

a)Electronic mail: tronchin@ciarm.ing.unibo.it

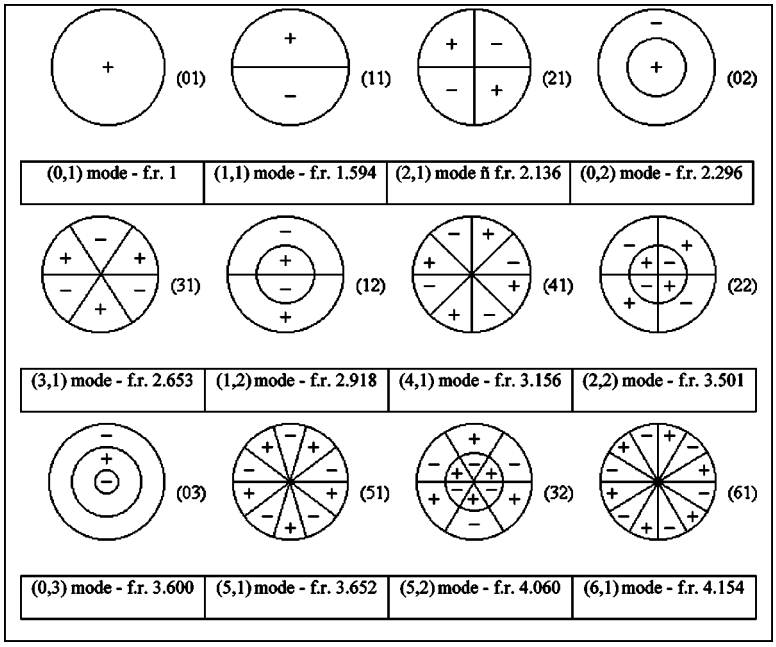

FIG. 1. The ratio (f.r.) between the frequency of the corresponding overtone and that of the ''fundamental'' mode (0,1) is signed under each mode. This is not a harmonic sequence.

Davis, 1986). This affect is most important for the (0,1) mode. Many efforts have been made in determining a theoretical model of air-loading, with perhaps the best known model described by Christian *et al.* (1984).

Two other effects, namely the air modes in the kettle and the bending stiffness of the membrane, play a minor role compared to the effect of the weight of the air, and contribute to the ''fine tuning'' of the membrane frequencies. Although the air in the kettle has its own modes of resonance which could potentially interact with the membrane modes, Rossing found a great difference in the frequencies of membrane modes and kettle air modes. Consequently, kettle air vibrations have a very weak interaction with membrane vibrations. The bending stiffness of the membrane could raise the frequencies of higher partials (a similar effect is found in piano strings), but this effect is negligible for the lower partials, which are of most interest in understanding the vibroacoustical properties of the instrument.

The radiation of sound from a baffled kettledrum membrane depends on the vibrating mode. In the (0,1) mode, the membrane acts as a monopole source, whereas in the (1,1) mode it acts as a dipole source, and so on (Fletcher and Rossing, 1998). The directivity of sound radiation is fairly noticeable in an anechoic room, but not so in a normal (slightly reverberant) room. Consequently, measurements of acoustic radiation should not be preformed locating the microphone at the center of the membrane, but one-fourth from the edge of the kettle. Spatial averaging of directivity patterns can be achieved by using many striking points around the circle representing normal positions for striking the instrument in musical performance.

III. ACOUSTIC RADIATION

The efficiency of acoustic radiation is a measure of the effectiveness of a vibrating surface in generating sound power. It could be defined by the relationship:

$$\sigma = \frac{W}{\rho_0 c S \langle \overline{v_n^2} \rangle} \tag{1}$$

in which W is the sound power radiated by a surface with area S, which could be obtained by integrating the far-field intensity over a hemispherical surface centered on the panel, and $\langle \overline{v_n^2} \rangle$ is the space-averaged value of the time-averaged normal distribution of velocity (Fahy, 1989).

From this general definition various measurement methods useful for the study of sound emission could be obtained.

A. Research on acoustic radiation

Previous studies on this argument have been conducted on the soundboards of the piano and of the harpsichord. K. Wogram, H. Suzuki, and N. Giordano studied the soundboard of the piano using different measurement methods.

Wogram (1984) used the parameter F/v, defining F as the excitation force and v as the resulting velocity at the point of excitation. He reported that it exhibits a maximum at a frequency near or below 1 kHz, and that it falls sharply below 100 Hz, and above 1 kHz. He found that it falls typically by a factor of 10 as the frequency is varied from 1 to 5 kHz.

Suzuki (1986) used the ''surface-intensity method,'' defined as

$$I = \mathrm{Re}[p(\alpha/j\omega^*)/2], \tag{2}$$

where I is the average intensity in time, perpendicular to the vibrating surface, measured in near field (about 30 cm from the radiating surface), ω is the angular frequency, Re and* are the real part and the complex conjugate of a complex number, p and α are the pressure and the normal acceleration at the measuring point, and $j=(-1)^{1/2}$. His study was conducted over a limited frequency range, but imply that the integrated sound intensity normalized by the input power is approximately constant from 200 Hz to 5 kHz.

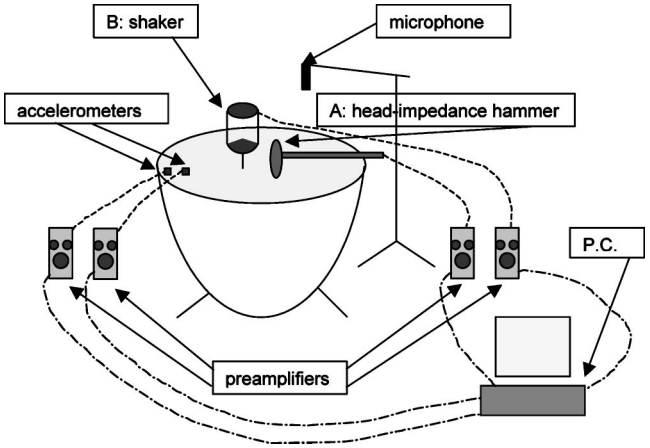

FIG. 2. Schematic diagram with all the experimental apparatus.

Giordano (1998) used the parameter p/v, where p is the sound pressure measured in near field and v is the velocity of the soundboard. In all the measured points p/v is greatest at about 1 kHz, and it falls off below a few hundred hertz and above 5 kHz.

Suzuki's and Giordano's results agree, but appear to be in contrast with Wogram's results on the average value of F/v, which falls by a factor of 10 or more from 1 to 5 kHz. Is important to notice that all of these studies have one result in common: the resonance frequencies did not coincide with those of acoustic emission; on the contrary they often had negative correlation.

IV. EXPERIMENT 1: MODAL ANALYSIS

Vibration and acoustic measurements were conducted at the same time. The FRF (v/F) of the instruments was obtained from the vibration measurements. Up to 15 modes were studied, in order to check the results with previous research. Two tympani with different features were analyzed—these were made available by the Conservatorium of Cesena in Italy. Both tympani were in normal condition, with used membranes. The first was a plexi-glass Adam 25-in. (about 65 cm) kettledrum with a Remo mylar skin and a central reinforce, tuned to approximately 166 Hz (corresponding to E). The second was a copper 25-in. (65 cm) Ludwig kettledrum with a mylar skin and no central reinforce, tuned to approximately 145 Hz (corresponding to D). Figure 2 is a schematic diagram of the experimental apparatus.

A. Experimental configuration

The membrane was excited by percussive impulses in 213 measuring points, fixed on a square grid with 4-cm grid intervals. Measurements were conducted at the same points on the two instruments. Waveforms were recorded and stored on a personal computer, and waveform analysis was conducted using Aurora software (Farina, 1997).

1. Adams kettledrum

The following instrumentation was used:

(i) Hammer Brüel & Kjær Type 8203,
(ii) Accelerometer Brüel & Kjær Type 4374,

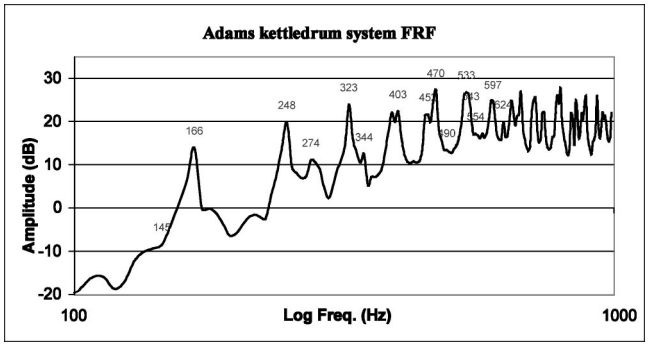

FIG. 3. Adams kettledrum system FRF: excitation induced by the hammer.

(iii) two charge amplifiers Brüel & Kjær Type 2635, and
(iv) PC equipped with 20-bit A/D converter, 96-kHz sample rate sound-board.

Based on reciprocity theory, the accelerometer was located at a fixed point on the membrane, being a point usually hit by the performer (10 cm from the edge of the skin), while the tympanum was excited by the hammer at 213 positions. In order to minimize measurement error, an average of ten consecutive impacts for each measurement position was used.

The amplitude of space-averaged FRF measured for Adam tympanum is presented in Fig. 3.

2. Ludwig kettledrum

The following instrumentation has been utilized:

(i) two accelerometers Brüel & Kjær Type 4374,
(ii) two charge amplifiers Brüel & Kjær Type 2635,
(iii) Electrodynamic Mini-Shaker Brüel & Kjær Type 4810, and
(iv) PC equipped with 20-bit A/D converter, 96-kHz sample rate sound-board.

In this case (Fig. 4) the vibration of the structure was measured by placing the accelerometer at each of the 213 fixed points and exciting the system through the electrodynamic shaker placed in the normal striking point for the player (which was the same point as for the Adams instrument). The shaker provides an alternative way to excite the structure, which theoretically should enhance the quality of the mea-

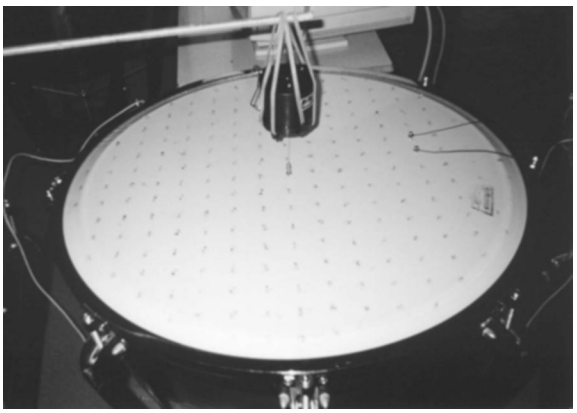

FIG. 4. Ludwig kettledrum: shaker placed in the middle.

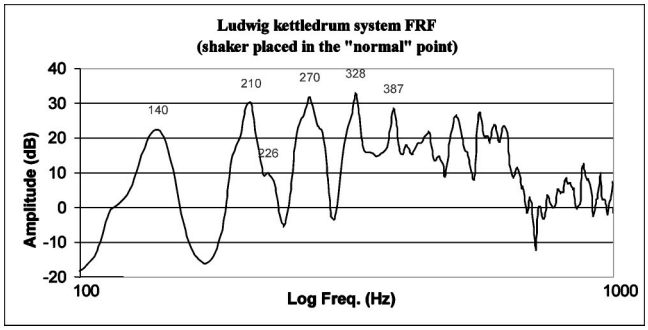

FIG. 5. Ludwig kettledrum system FRF: shaker placed in the normal striking point.

sured FRF, especially at mid-high frequencies.

In order to obtain impulse responses (IRs) between the shaker and each accelerometer position a logarithmic, swept sine waveform 10 s in duration ranging from 20 Hz to 20 kHz was employed. In a second step the IRs were transformed to the frequency domain and the final FRF (amplitude and phase) obtained from the average of all 213 single FRFs. Finally, the mappings of the vibrational modes were obtained in the same way as for the Adams instrument. Another set of measurements was conducted applying the shaker in the middle of the membrane, and testing the influence of the shaker position on the measurement of FRF (Fig. 4). The amplitudes of the two space-averaged FRFs obtained positioning the shaker in the two positions on the membrane are presented in Figs. 5 and 6, respectively.

B. Results of the modal analysis

1. Adams kettledrum

For the Adams kettledrum, 15 vibration modes in the frequency range from 140 to 540 Hz were found. In Table I the results are summarized and compared to Rossing's results.

The results were very similar to those expected. Circular and mixed modes corresponded almost perfectly to those found by Rossing. The frequencies corresponding to diametrical modes were lower than expected. The discrepancy grew with increasing modal frequency. The (5,1) mode, which is not very harmonic in theory, was the least similar to Rossing's measurements; a very small discrepancy was found for the modes (2,1), (3,1), (4,1). The mode (5,1) and the mode (6,1) had frequencies lower than those of the

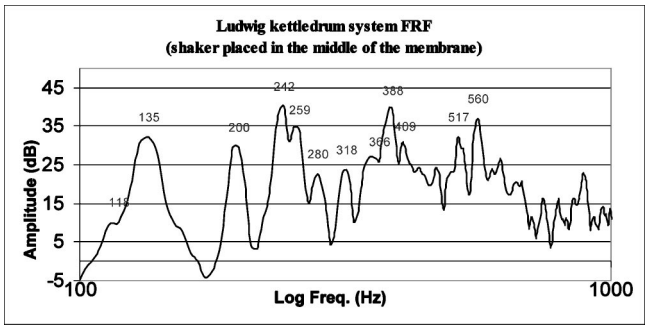

FIG. 6. Ludwig kettledrum system FRF: shaker placed in the middle of the membrane.

TABLE I. Frequencies and measured ratios and comparison to Rossing's results. In italics: frequencies that help the harmonicity of tympani.

Modes m, n	Frequencies $f_{m,n}$ (Hz)	Ratios $f_{m,n}/f_{(11)}$	Ratios found by Rossing	
			Measured	Calculated
(0,1)	145	0.87	0.81	0.80
(1,1)	*166*	*1.00*	*1.00*	*1.00*
(2,1)	*248*	*1.495*	*1.50*	*1.52*
(0,2)	274	1.65	1.65	1.68
(3,1)	*323*	*1.95*	*1.97*	*2.00*
(1,2)	344	2.07	2.00	2.27
(4,1)	*403*	*2.43*	*2.44*	*2.48*
(2,2)	452	2.72	2.86	2.74
(5,1)	*470*	*2.83*	*2.91*	*2.94*
(0,3)	490	2.95	2.71	2.97
(6,1)	533	3.22	⋯	3.40
(3,2)	543	3.27	⋯	3.29
(1,3)	554	3.34	⋯	⋯
(7,1)	597	3.59	⋯	⋯
(4,2)	624	3.76	⋯	⋯

modes (0,3) and (3,2), whereas previous studies found the reverse. Circular and mixed modes corresponded perfectly to theory (Fig. 7).

Two similar mappings, one corresponding to the mode (5,1), the other not corresponding to any resonance peak, were found. The second one had the same features of the mode (5,1), but it was in a harmonic ratio with the mode (1,1). It could be interesting to investigate on the origins of this vibration mode.

2. Ludwig kettledrum

Only three vibration mode mappings are reported (Fig. 8), with a lower definition. In this case the use of shaker and accelerometers, throughout the membrane, could have increased the mass-loading effect. Modal frequencies were shifted some hertz higher, especially in the low frequency range.

The FRF graphics showed a peak at almost 3 kHz, probably attributable to the resonance frequency of the very thin bar that connected the shaker to the membrane.

Comparing the FRF obtained by exciting the system at the normal striking position to the FRF obtained by exciting the middle of the membrane, the second one has more stimulated resonance peaks corresponding to the circular and mixed vibration modes.

A comparison with the Adams kettledrum reveals that the head-impedance hammer method gives more precise space averaged frequency responses than the shaker method. This means that the first method is especially suitable when the main purpose of the measurements is to obtain modal shapes (at reasonably low resonance frequencies). Moreover, using reciprocity theory, the measurements are usually very quick, and in a short time a mesh of hundreds of points can be measured. The shaker method gives more precise frequency responses than hammer, even though at very high frequencies harmonic artifacts could occur due to additional mass loading, steel-stick resonance, and wax-damping. However, in both cases the FRFs obtained are suitable for experiments investigating acoustic radiation.

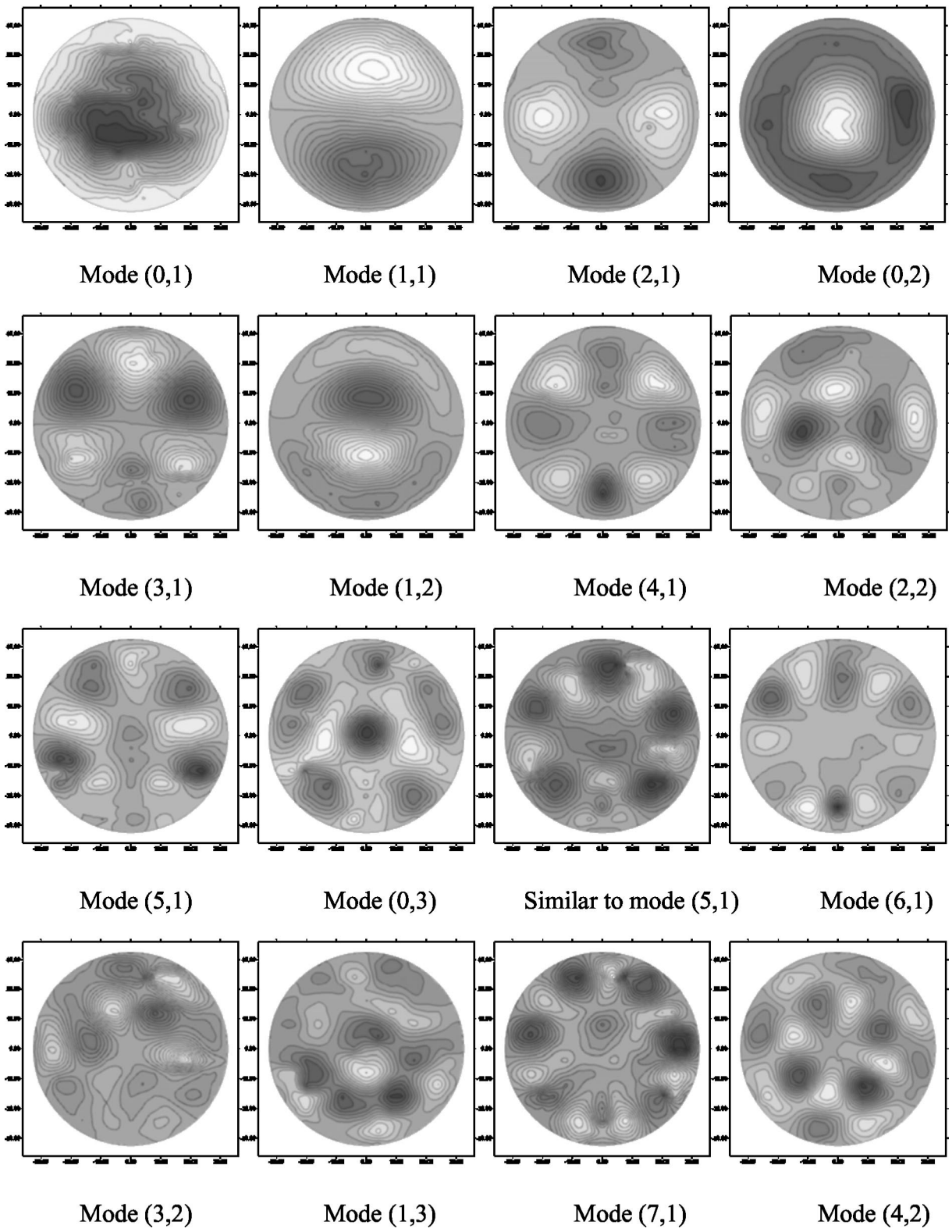

FIG. 7. Mappings of Adams kettledrum vibrational modes.

V. EXPERIMENT 2: ACOUSTIC RADIATION

The second part of the investigation was dedicated to the measurement of acoustic radiation. The same musical instruments used in modal analysis were studied.

A. Definitions and experimental configuration

Acoustic radiation was measured with the Adams kettledrum used in the modal analysis, but tuned on 145 Hz, with the same 213 striking points used for the modal analysis.

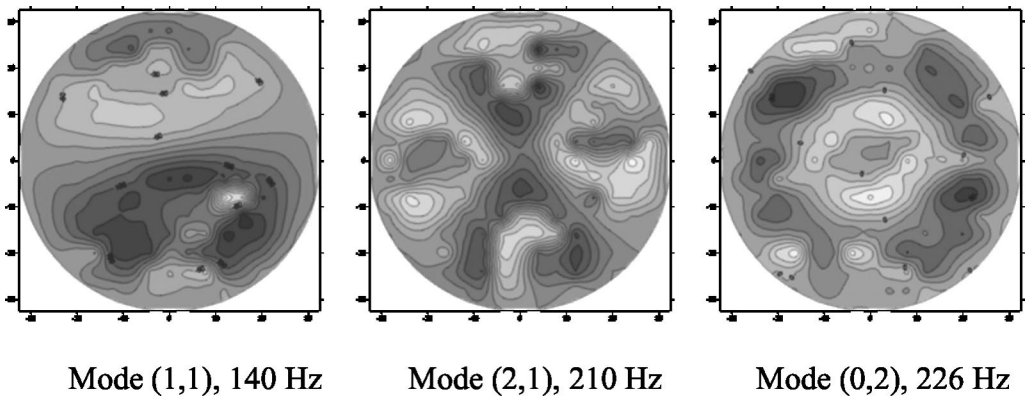

FIG. 8. Mappings of Ludwig kettledrum vibrational modes.

Two different parameters of the acoustic radiation were measured and compared: the complex ratio p/v, which is the parameter used by Giordano, and a new parameter that can be defined as *intensity of acoustic radiation* (IAR), because it is a parameter between acoustic intensity and radiation.

IAR is defined as the space-averaged amplitude of cross spectrum between sound pressure caused by the movement of the vibrating surface (the membrane) and the velocity of the vibration of the membrane itself. An omnidirectional microphone was located in a fixed position at about 25 cm over the membrane, one-fourth from the edge of the kettle, and the accelerometer was mounted at the same points utilized during modal analysis. The measurements were repeated for each position of the accelerometer, avoiding errors caused by sound directivity.

The measurements were conducted in a slightly reverberant room, where reverberation time helps to average radiation of sound caused by (0,1) and (1,1) modes. At higher frequencies the room acoustics did not influence the measurements. Moreover, the space-averaging of the data conducted by moving the transducers thorough the membrane enhanced the measurements.

Sound pressure p was measured in near field, at 25 cm from the membrane, as previously reported by Suzuki and Giordano (Figs. 2 and 9). In order to properly measure radiation of sound, the distance between the radiating surface and the microphone should be one-fourth of the wavelength, and hence 25 cm was considered a good compromise for low and high frequencies. However, further study would be useful to optimize the microphone position during such measurements, balancing the need to avoid excessive reverberation from the room and the need to achieve sufficiently uniform radiation from the membrane.

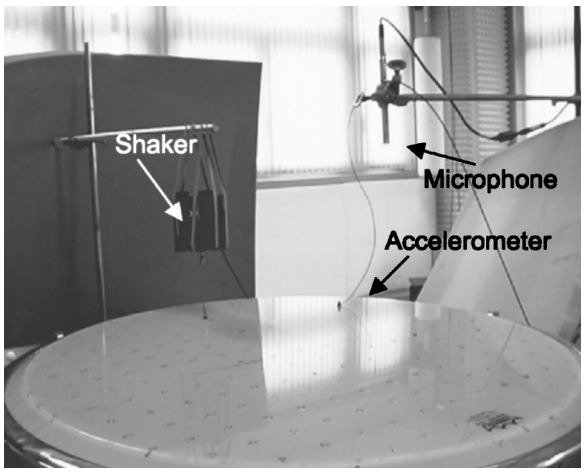

FIG. 9. Adams kettledrum: acoustic radiation measurements.

The following instrumentation was used:

(i) accelerometer Brüel & Kjær Type 4374,
(ii) charge amplifier Brüel & Kjær Type 2635,
(iii) condenser microphone connected to sound level meter Larson Davies LD model 2900B,
(iv) electrodynamic Mini-Shaker Brüel & Kjær Type 4810, and
(v) PC equipped with 20-bit A/D converter, 96-kHz sample rate sound-board.

The measurements were conducted in the same way as described in Sec. IV A 2. The IRs, measured at the microphone and the accelerometer, were simultaneously measured by means of a logarithmic sine sweep generated by the shaker (Farina, 1997). In a second step, the synchronous p and v IRs were postprocessed, and, in the frequency domain, the amplitude and phase of the transfer function p/v and cross spectrum $p \cdot v$ were calculated.

B. Measurements of acoustic radiation: Results and comments

The efficiency of acoustic radiation (p/v) appears approximately constant from 270 to 3800 Hz, with a peak in this range at 1200 Hz (Fig. 10). At a finer scale, rapid fluctuations of p/v can be observed. Even though a kettledrum is quite different from a piano or harpsichord, the curve is still opposite in phase with the FRF, meaning that the p/v curve has minima at the same frequencies where the FRF has maxima—therefore it has the same features as those of Suzuki and Giordano.

Results for $IAR\,(p \cdot v)$ show a different pattern to the FRF or p/v results (Fig. 11). The frequency range of maximum sound radiation intensity is between 140 and 900 Hz, with a progressive small decrease in amplitude as the frequency grows. Tall peaks and valleys characterize this zone. The strongest intensity was found in the frequency range of the mode (1,1), at 156 Hz, but the amplitudes of the modes

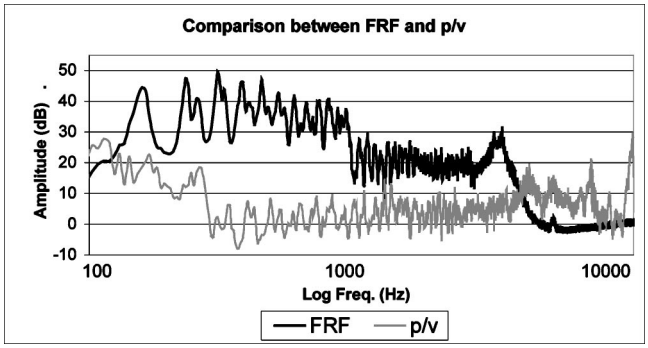

FIG. 10. Results of the measurement of the acoustic radiation: comparison between FRF and p/v.

(2,1) and (0,2), respectively, at 226 and 247 Hz, were substantial, too. Above 900 Hz, amplitudes decrease suddenly, remaining constant from 900 to 3000 Hz. Substantial peaks and valleys are recorded also from 900 to 1500 Hz, whereas from 1500 to 3000 Hz they become decreasingly evident. All the graphics obtained exciting the system through the shaker have a peak around 3000–3200 Hz that could not be related to the sound properties of tympani, but could correspond to the resonance frequency of the very thin bar connecting the membrane with the shaker.

The most important results of the investigation derive from the comparison between the FRFs and the parameters p/v and $IAR\,(p\cdot v)$, respectively. In the first case, frequencies with great radiation efficiency (p/v) do not correspond to the resonance frequencies of the frequency response (to the vibration modes), and indeed are in antithesis to them. The curve corresponding to p/v is in phase opposition to that of the FRF curve, following previous studies of Suzuki and Giordano (Fig. 10). This should not be a surprising result. The definition of p/v is close to the mechanical impedance, and therefore it would explain sound losses rather than sound generation of the soundboard. Besides, FRF is strongly related to sound generation, and this should apply to sound generation of vibrating surfaces, and therefore sound intensity.

The comparison between the graphic of the FRF and the graphic of the intensity of the acoustic radiation $IAR\,(p\cdot v)$ shows interesting results (Fig. 11). The graphics has a very similar curve and resonance frequencies correspond perfectly to sound emission frequencies. The surprising correlation between FRF and IAR suggests the adoption of the new parameter as descriptor of acoustic radiation. Moreover, the space-averaged amplitude of cross spectrum $p\cdot v$ between the sound pressure and velocity of the membrane, measured over a large number of points, suggests calling the new parameter *intensity* of acoustic radiation, since it is related to radiation (velocity v on the membrane), and the relation is defined like the sound intensity product, as described in Sec. V A.

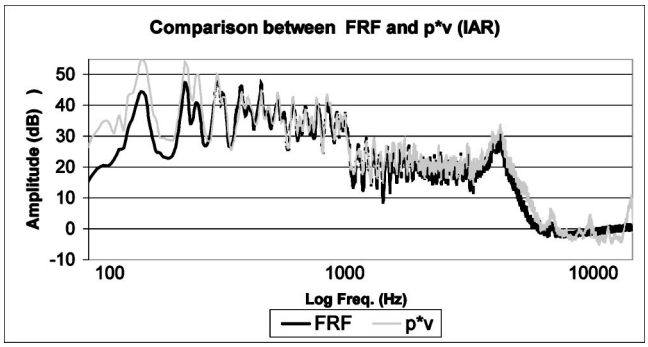

FIG. 11. Results of the measurement of the acoustic radiation: comparison between FRF and $p\cdot v$.

VI. CONCLUSIONS

Acoustic radiation measurements and modal analysis were conducted in two different kettledrums, namely Adams and Ludwig models. The measurements were conducted as indicated in previous papers. Two procedures for exciting the membrane were used and compared: the head-impedance hammer and the shaker. The FRFs obtained with the two techniques for each kettledrum were quite similar, whereas modal shapes were better using the hammer. The shaker gave better frequency results up to 3 kHz, but the resonance of the bar connecting the shaker to the membrane was found at about 3 kHz. The mappings of the 15 individual vibration modes were very clear, and frequency ratios agreed approximately with the theoretical ones. A high degree of correspondence was obtained for the circular and mixed vibration modes, whereas the diametric modes yielded frequencies slightly lower than the theoretical ones.

Acoustic radiation was measured in two different ways. In the first case the complex ratio (p/v) between sound pressure and the vibration velocity of the membrane was calculated. This is the method used by Giordano. In the second case the space-averaged amplitude of cross spectrum $(p\cdot v)$ between sound pressure, measured at a fixed point at 25 cm far from the instrument, and the vibration velocity of the membrane measured at more than 200 points was calculated. This is a new parameter called *intensity of acoustic radiation (IAR)*. Comparing the graphics of FRF and p/v, it can be observed how the resonance frequencies are often in opposition to those of acoustic emission, in accordance with previous studies conducted on soundboards of the piano. Applying IAR, the resonance frequencies correspond perfectly to those of sound emission, and the curves of the two graphics are very similar. The IAR parameter is well related to frequency response function and for this reason is preferred to p/v. It is a medium parameter between acoustic intensity and acoustic radiation, and so is suitable to measure the sound generating characteristics of musical instruments with vibrating soundboards. This parameter can be used to qualify and define the directivity of musical instruments, which is important for architectural acoustics, as well as for auralization processes.

ACKNOWLEDGMENTS

The author wishes to thank Alessio Buttazzoni, Alessandro Cocchi, and Angelo Farina for their help during the measurements and calculation of physical parameters on the two kettledrums. Furthermore, he wishes to thank Densil Cabrera for his help on the English proof of this work.

Benade, A. H. (**1990**). *Fundamental of Musical Acoustics*, 2nd ed. (Dover, New York).
Christian, R. S., Davies, R. E., Tubis, A., Anderson, C. A., Mills, R. I., and Rossing, T. D. (**1984**). ''Effects of air loading on tympani membrane vibrations,'' J. Acoust. Soc. Am. **76**, 1336–1345.
Fahy, F. J. (**1989**). *Sound Intensity* (Elsevier Applied Science, London).
Farina, A., and Righini, F. (**1997**). ''Software implementation of an MLS analyzer, with tools for convolution, auralization and inverse filtering,'' preprints of the 103rd AES Convention, New York, 26–29 September.
Fletcher, N. H., and Rossing, T. D. (**1998**). *The Physics of Musical Instruments*, 2nd ed. (Springer Verlag, New York).
Giordano, N. (**1998**). ''Sound production by a vibrating piano soundboard: Experiment,'' J. Acoust. Soc. Am. **104**, 1648–1653.
Rayleigh, J. W. (**1945**). *The Theory of Sound* (Dover, New York), Vol. 1.
Rossing, T. D. (**1976**). ''Acoustics of percussion instruments—Part I,'' Phys. Teach. **14**, 546–556.
Rossing, T. D. (**1977**). ''Acoustics of percussion instruments—Part II,'' Phys. Teach. **15**, 172–178.
Rossing, T. D. (**1982**). ''The physics of kettledrums,'' Sci. Am. **247**(5), 172–178.
Suzuki, H. (**1986**). ''Vibration and sound radiation of a piano soundboard,'' J. Acoust. Soc. Am. **80**, 1573–1582.
Tubis, A., and Davis, R. E. (**1986**). ''Kettle-shape dependence of timpani normal modes,'' paper K2-7, 12th International Congress on Acoustics, Toronto.
Wogram, K. (**1984**). ''Akustische Untersuchungen an Klavieren,'' in *Der Piano—und Flÿgelbau* (Verlag Das Musikinstrument, Frankfurt); English version, *Acoustical Research on Pianos: Vibrational Characteristics of the Soundboard*, Das Musikinstrument.

High-frequency ultrasound scattering from microspheres and single cells

R. E. Baddour,[a] M. D. Sherar, and J. W. Hunt
Department of Medical Biophysics, University of Toronto, 610 University Avenue, Toronto, ON, M5G2M9, Canada

G. J. Czarnota
Department of Radiation Oncology, University of Toronto, 610 University Avenue, Toronto, ON, M5G2M9, Canada

M. C. Kolios
Department of Mathematics, Physics and Computer Science, Ryerson University, 350 Victoria Street, Toronto, ON, M5B2K3, Canada

(Received 2 July 2004; revised 14 October 2004; accepted 20 October 2004)

Assessing the proportion of biological cells in a volume of interest undergoing structural changes, such as cell death, using high-frequency ultrasound (20–100 MHz), requires the development of a theoretical model of scattering by any arbitrary cell ensemble. A prerequisite to building such a model is to know the scattering by a single cell in different states. In this paper, a simple model for the high-frequency acoustic scattering by one cell is proposed. A method for deducing the backscatter transfer function from a single, subresolution scatterer is also devised. Using this method, experimental measurements of backscatter from homogeneous, subresolution polystyrene microspheres and single, viable eukaryotic cells, acquired across a broad, continuous range of frequencies were compared with elastic scattering theory and the proposed cell scattering model, respectively. The resonant features observed in the backscatter transfer function of microspheres were found to correspond accurately to theoretical predictions. Using the spacing of the major spectral peaks in the transfer functions obtained experimentally, it is possible to predict microsphere diameters with less than 4% error. Such good agreement was not seen between the cell model and the measured backscatter from cells. Possible reasons for this discrepancy are discussed. [DOI: 10.1121/1.1830668]

PACS numbers: 43.80.Cs, 43.40.Fz, 43.80.Jz, 43.80.Ev [FD] Pages: 934–943

I. INTRODUCTION

During the last two decades, several studies have found that localized variations in cell morphologies in tissues (Pavlin *et al.*, 1991; Lockwood *et al.*, 1992) and cell ensembles (Sherar *et al.*, 1987; Berube *et al.*, 1992) can be detected using high-frequency ultrasound from 20 to 100 MHz. Although individual cells cannot be resolved, even at the high frequencies used, changes in the brightness and speckle in conventional brightness-mode (B-mode) images as a result of cell structure changes can readily be observed. More recently, spectral analysis techniques (Feleppa *et al.*, 1986; Lizzi *et al.*, 1997) used to analyze radio-frequency (rf) echo signals, have made it possible to more specifically characterize average cell structure changes in tissues (Guittet *et al.*, 1999) and cell ensembles (Kolios *et al.*, 2002, 2003).

Cells undergo many morphological changes throughout the cell cycle, in response to the surrounding environment, and in death. Several types of changes in cell structure have been successfully detected *in vitro* using high-frequency ultrasound. In particular, changes in structure that occur in cells undergoing mitosis (Czarnota *et al.*, Br. J. Cancer, 1999; Kolios *et al.*, 2002), after exposure to changes in salinity (Czarnota *et al.*, Proc. Microsc. Soc. Am., 1999; Kolios *et al.*, 2001), during necrotic death (Czarnota *et al.*, 1997), and during apoptosis (Czarnota *et al.*, 1997, 1999, 2002; Kolios *et al.*, 2002) have been shown to induce detectable changes in ultrasound backscatter. Exposure to the drug colchicine, which arrests cells during the metaphase phase of mitosis, increases the ultrasound backscatter of cell ensembles compared to untreated cells. Exposing cells to increased salinity, which induces osmotic cell shrinkage and the condensation of chromatin inside the cell nucleus, also increases the ultrasound backscatter of cell ensembles. In ensembles of necrotic cells (heat killed) and cells undergoing apoptosis (after exposure to cisplatin, a chemotherapeutic agent) an increase in the ultrasound backscattered signal was observed compared to viable cells. Apoptosis, a process marked by cell and nucleus shrinkage, condensation of chromatin in the nucleus, and eventual nuclear fragmentation (Hacker, 2000), causes significant increases in high-frequency ultrasound scattering: up to a 20-fold change in average backscatter intensity compared to ensembles of viable cells, and possibly an increase in the scattering efficiency at higher frequencies (Kolios *et al.*, 2002).

Although using ultrasound it is possible to noninvasively detect ensembles of cells undergoing structural changes, such as apoptosis, it is difficult to quantify the proportion of cells undergoing these changes. The long-term

[a]Electronic mail: rbaddour@uhnres.utoronto.ca

goal of our research is to develop such a quantitative measure for various biological tissues; a potentially useful metric for various applications, such as cancer treatment evaluation. Achieving this goal requires the development of a theoretical model for the scattering by any arbitrary cell ensemble taking into account any packing arrangement and any combination of cell morphologies. A prerequisite for this generalized model is to understand the scattering by a single cell, the building block of any biological tissue. Understanding the scattering response of a single cell will enable the estimation of the properties (e.g., size, shape) and assessment of the functional condition (e.g., viable versus apoptotic) of an arbitrary cell simply by analyzing the ultrasound backscattering from that cell.

Historically, it has not been possible to detect isolated, individual eukaryotic cells even with high-frequency ultrasound devices. The main problems are related to localization and low signal strength. Due to their small size (5–20 μm), even at high ultrasound frequencies, cells are smaller than the wavelength of the incident sound wave (20–75 μm), the resolution limit for imaging applications. In addition, not only due to their small size, but also their weakly scattering nature, the scattered sound from individual cells has been too low to be detected above background system noise. Very recently, new high-frequency ultrasound devices have emerged with better system signal-to-noise ratio characteristics, which can enable the measure of backscatter from smaller and weaker scatterers. To date, backscattering from individual cells has never been successfully measured. We present a method to deduce the backscattering from individual subresolution scatterers. Using this method, the backscatter from polystyrene microspheres and single cells are measured and used to evaluate a proposed model of the high-frequency acoustic scattering by one living biological cell.

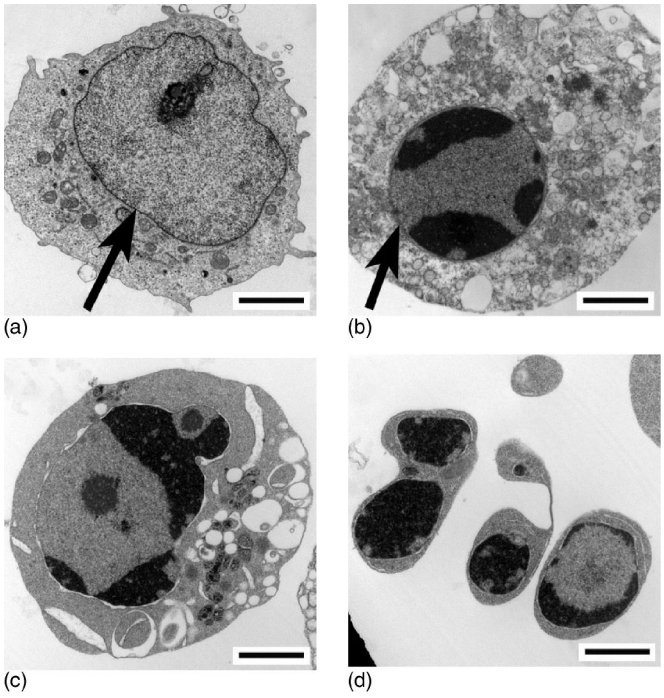

FIG. 1. Transmission electron micrographs of cells from the OCI-AML-5 line (Wang *et al.*, 1991) (human acute myeloid leukemia) in different stages of apoptosis induced by exposure to cisplatin; scale bars represent 2 μm. (a) Normal cell; nucleolus and mitochondria are clearly visible, nucleus (indicated by arrow) takes up a large proportion of the cell volume. (b) Early apoptosis; reduction in nuclear diameter and chromatin condensation is evident (nucleus is indicated by arrow); vacuoles and/or swelled mitochondria are visible. (c) Later apoptosis; nuclear fragmentation is starting. (d) Very late apoptosis; apoptotic bodies containing chromatin fragments and other cell constituents.

II. MODEL OF A SINGLE CELL

In order to calculate the single-cell scattering response, the dominant acoustic scattering centers in cells at high frequencies must be determined. Since apoptosis produces a significant change in the overall backscatter from cell ensembles (Kolios *et al.*, 2002, 2003), it is useful to examine the dominant changes in cells undergoing apoptosis before they break up into apoptotic bodies (a later stage of apoptosis) and get phagocytosed. During the early stages of apoptosis the mitochondria swell, the cell diameter decreases, the nuclear diameter decreases, and the chromatin condenses inside the nucleus. As shown in Fig. 1, most of the significant gross structural changes that occur are related to the nucleus.

The nucleus of a cell is denser than the rest of the cell (Meselson and Stahl, 1958) due to its high DNA and protein content. By estimates, approximately 71% of the nuclear volume is taken up by chromatin (Monier *et al.*, 2000); chromatin being made up of approximately 50% DNA and 50% protein by volume (Kornberg, 1974). Deoxyribonucleic acid has a density of 1.71 g/cm^3 (Meselson and Stahl, 1958), whereas typical proteins have a density of 1.35 g/cm^3 (Matthews, 1968). The rest of the nucleus is a heterogeneous solution of biological macromolecular structures termed the nuclear matrix. By contrast, the composition of the cell around the nucleus is mainly cytoplasm, which has a density approximately equal to the surrounding interstitial fluid (a low concentration saline), a small amount of protein (e.g., cytoskeleton), and thin bilipid membranes that make up the other organelles (e.g., Golgi apparatus, mitochondria).

The longitudinal speed of sound in DNA, in varying conformations and orientations, has been measured to be in the range of 1900 to 2400 m/s (Hakim *et al.*, 1984; Edwards *et al.*, 1985). This is significantly higher than the speeds of sound of cytoplasm, estimated to be 1508 m/s in muscle fiber cells (Berovic *et al.*, 1989), or interstitial fluid, which, due to its high water content, is likely to be close to 1527 m/s, the value for water at body temperature (37 °C). Therefore, it is reasonable to conclude that the average acoustic impedance of the nucleus is significantly higher than the average acoustic impedance of the rest of the cell and the surrounding fluid. It follows that the nucleus should scatter sound more efficiently than the rest of the cell.

If one assumes that there is not a significant mismatch in density and speed of sound between the balance of the cell around the nucleus and the surrounding medium, it is a reasonable simplification, for acoustic scattering calculations, that a cell could be approximated by its nucleus. In addition, although the nucleus to cytoplasm volume ratio varies by cell type, in many cases the nucleus is relatively isotropic and almost spherical. Therefore, we propose here that a cell be modeled as a single spherical scatterer with uniform me-

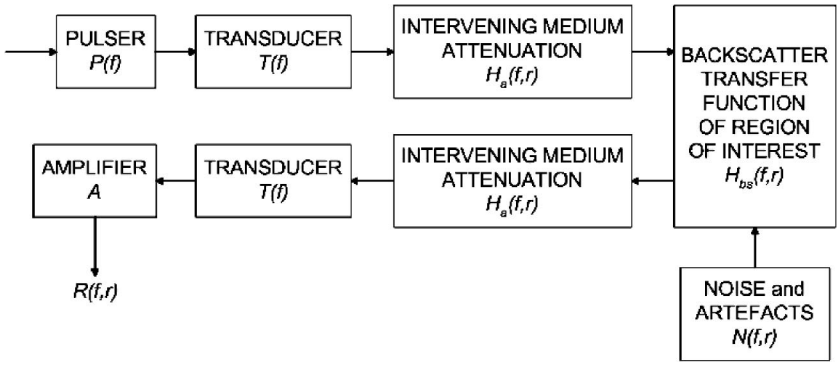

FIG. 2. System block diagram: The pulse, $E(f)$, is generated by the pulser and modified by several transfer functions—transducer, $T(f)$, attenuating medium, $H_a(f,r)$, scatterers in the region of interest, $H_{bs}(f,r)$, artifacts and noise, $N(f,r)$—until the backscattered signal, $R(f,r)$, is finally amplified, by a factor of A, and measured.

chanical properties that correspond to its nucleus. Since the proposed cell model is simple geometrically, one can mathematically determine the theoretical scattering response of a cell to incident high-frequency ultrasound pulses by calculating the scattering response of a sphere with nucleus-like mechanical properties.

The far-field complex pressure amplitude (p_s) at an observation point at time t of the scattered echo returned from a nonrigid sphere insonified by a plane, monochromatic acoustic wave can be expressed in series form as

$$p_s(t,k_3,\theta)=\frac{P_i a}{2r}\left[\frac{2}{x_3}\sum_{n=0}^{\infty}(-1)^n(2n+1)\times\sin\eta_n e^{-i\eta_n}P_n(\cos\theta)\right]e^{-ik_3(c_3t-r)}, \quad (1)$$

where P_i is the incident wave amplitude, a is the radius of the spherical scatterer, r is the distance to the observation point, c_3 is the longitudinal speed of sound in the surrounding medium, k_3 is the wave number (for a given frequency f, $k_3=2\pi f/c_3$), x_3 is the relative frequency ($x_3=k_3a$), and P_n is the nth-order Legendre polynomial of argument cos θ. The scattering angle (θ) is equal to π in the backscattering case. The phase shift η_n is a term which takes into account all other parameters, such as the mechanical properties of the scatterer. Faran (1951) developed an expression in the form of Eq. (1) for the scattering by an elastic sphere in water (or any medium that does not support shear), accounting for wave-mode conversion inside the scatterer. A small correction was presented by Hickling (1962), who verified the result experimentally. To calculate theoretical scattered pressures (p_s) for various conditions, the Faran–Hickling solution was used in our studies. Although the developed computer code allows for the calculation of individual scattering conditions, typically the scattered pressures for a range of a particular parameter are calculated at once. For example, to calculate the size dependence of scattering, a range of a values, representing the sphere radii of interest, would be passed to the algorithm along with the wave number (k_3), mechanical properties of the scatterer (c_1,ρ_1,σ), mechanical properties of the surrounding medium (c_3,ρ_3), and the location of the observation point (θ,r), as defined by Faran (1951). Parametric studies of these properties have been performed by Hickling (1962) and many others (Hampton and McKinney, 1961; Brill and Gaunaurd, 1987; Hinders, 1991).

III. METHODS

A. Deducing the backscatter signal from a single subresolution scatterer

The first step in attempting to measure the backscatter from a single subresolution scatterer was to prepare a sparse suspension of the scatterer in question (microspheres or cells). The ideal suspending medium is a pure liquid, such as water, to eliminate any possibility of medium inhomogeneities (e.g., that would be possible if using a gel). Very low concentrations (between 1000 to 10 000 scatterers/cm^3) of the scatterers were mixed into degassed water. Preceding every acquisition, the vials containing the suspensions were gently stirred. This stirring step was found to be particularly important for suspensions of larger and denser scatterers due to their higher settling velocities.

Data acquisition was performed using a VisualSonics VS40b (VisualSonics Inc., Canada) ultrasound imaging device which generates short, broadband pulses with center frequencies at 20, 30, 40, or 55 MHz. This device digitally samples the pressure received by the transducer at a rate of 500 MHz with a measurement resolution of 256 levels (8 bits). Several different transducers, with different resonant frequencies, f numbers, and focal lengths, were employed (20 MHz: f2.35, 20 mm; 30 MHz: f2.13, 12.75 mm; 40 MHz: f2, 6 mm; 55 MHz: f3, 6 mm); each with a 6-dB intensity bandwidth of nearly 100 percent. Raw rf echo signals, the raw A lines, were acquired from different lateral positions with the transducer submerged in water. All of the acquired A lines (roughly 1000 per experiment) were then thresholded, discarding all lines not containing any data value greater than half the maximum data value detected in all the echo signals. This step eliminated the numerous ''empty'' acquisitions that occur since the suspensions are so sparse, with concentrations equivalent to less than one scatterer per focal volume of the most focused transducer used. In addition, the threshold eliminates most ''indirect hits'' with scatterers (e.g., a scatterer at the edge of the focal volume or in any sidelobe present in the incident beam profile), which result in backscattered pressure intensities of generally lower peak amplitude, ensuring that only near-pure backscatter signals from single microspheres are analyzed. Spectral analysis was then performed on the 50 to 100 A lines that remain after thresholding. The part of the signal acquired from around the transducer focus, the depth of field of the transducer (where the incident waves can assumed to be pla-

nar), was extracted by multiplication with a Hamming window and Fourier transformed to facilitate spectral analysis.

B. The backscatter transfer function

The experimental ultrasound system was modeled as a function of frequency (f) and location (r). From the system block diagram shown in Fig. 2, Eq. (2) was used to describe the Fourier transform of the signal received from the depth of field, $R(f,r)$

$$R(f,r)=E(f)T(f)^2H_a(f,r)^2[H_{bs}(f,r)\otimes N(f,r)]A, \tag{2}$$

where $E(f)$ is the transmitted electrical pulse, $T(f)$ is the transducer transfer function (a measure of the transducer's efficiency), $H_a(f,r)$ is the attenuation transfer function of the intervening medium, $H_{bs}(f,r)$ is the backscatter transfer function of the region of interest (in our case, containing only a single scatterer), $N(f,r)$ is a model of any acoustic artifacts as well as random noise, and A is the amplifier gain. It would be desirable to solve for $H_{bs}(f,r)$ to study the backscatter response of the region of interest. However, $E(f)$, $T(f)$, $H_a(f,r)$, and $N(f,r)$ are not known. The solution we adopted was to take a reference measurement, $R_{\text{ref}}(f,r)$: the perpendicular specular reflection from a flat, polished SiO_2 crystal (Edmund Industrial Optics Inc., part 43 424; $\rho=2.20$ g/cm^3, $c=5720$ m/s) placed at the same depth as the region of interest, normal to the incident pulse direction. $R_{\text{ref}}(f,r)$ will have exactly the same $E(f)$, $T(f)$, and approximately the same $H_a(f,r)$ (since scatterer depths will vary inside the region of interest) as $R(f,r)$. $H_{bs}(f,r)$ for this reference measurement is simply the reflection coefficient [$H_{bs}(f,r)=0.79$ in the case of the SiO_2 crystal]. As a result, we defined the approximate backscatter transfer function (BSTF) as

$$\text{BSTF}=\left|\frac{R(f,r)}{R_{\text{ref}}(f,r)}\right|^2=\left|\frac{A[H_{bs}(f,r)\otimes N(f,r)]}{0.79A_{\text{ref}}N_{\text{ref}}(f,r)}\right|^2, \tag{3}$$

which is an approximation of $|H_{bs}(f,r)|^2$. It was more convenient to define the BSTF in terms of squared magnitudes (i.e., power spectra) as they are directly proportional to pressure intensities. The BSTF of a region of interest was expressed in decibels relative (dBr) to the backscatter intensity from the reference. The values of the BSTF for a region containing a single scatterer were directly compared to normalized pressure intensities calculated with the Faran–Hickling solution.

IV. RESULTS

A. Polystyrene microspheres

Before attempting to measure the backscatter from single cells, the method to deduce the backscatter transfer function of a subresolution scatterer was tested with polystyrene microspheres (Beckman Coulter Inc., part numbers 6 602 796, 6 602 798, and 6 602 802). These were used because they are homogeneous, have known mechanical properties ($\rho=1.05$ g/mL, $c=2350$ m/s, $\sigma=0.35$), and are available in calibrated sizes (diameter tolerances of $\pm 0.5\%$). The microspheres were suspended in distilled, degassed water at

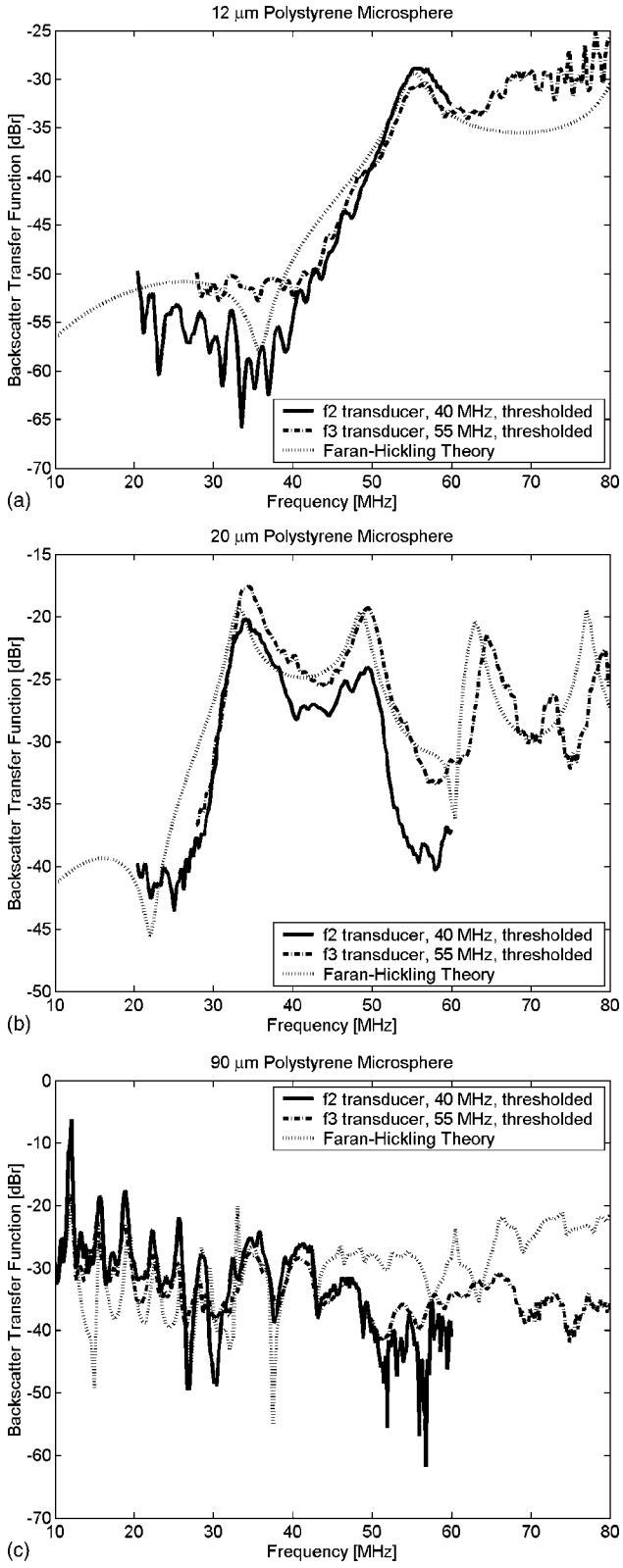

FIG. 3. Theoretical and measured backscatter transfer functions for single (a) 12-μm; (b) 20-μm; and (c) 90-μm polystyrene microspheres ($c=2350$ m/s, $\rho=1.05$ g/mL, $\sigma=0.35$) in water using two different wideband transducers (only the data from the 6-dB bandwidth of each transducer are shown). Note that the theoretical curves have not been shifted or scaled in any way, except to take into account the geometric effect of diminishing solid angle with distance.

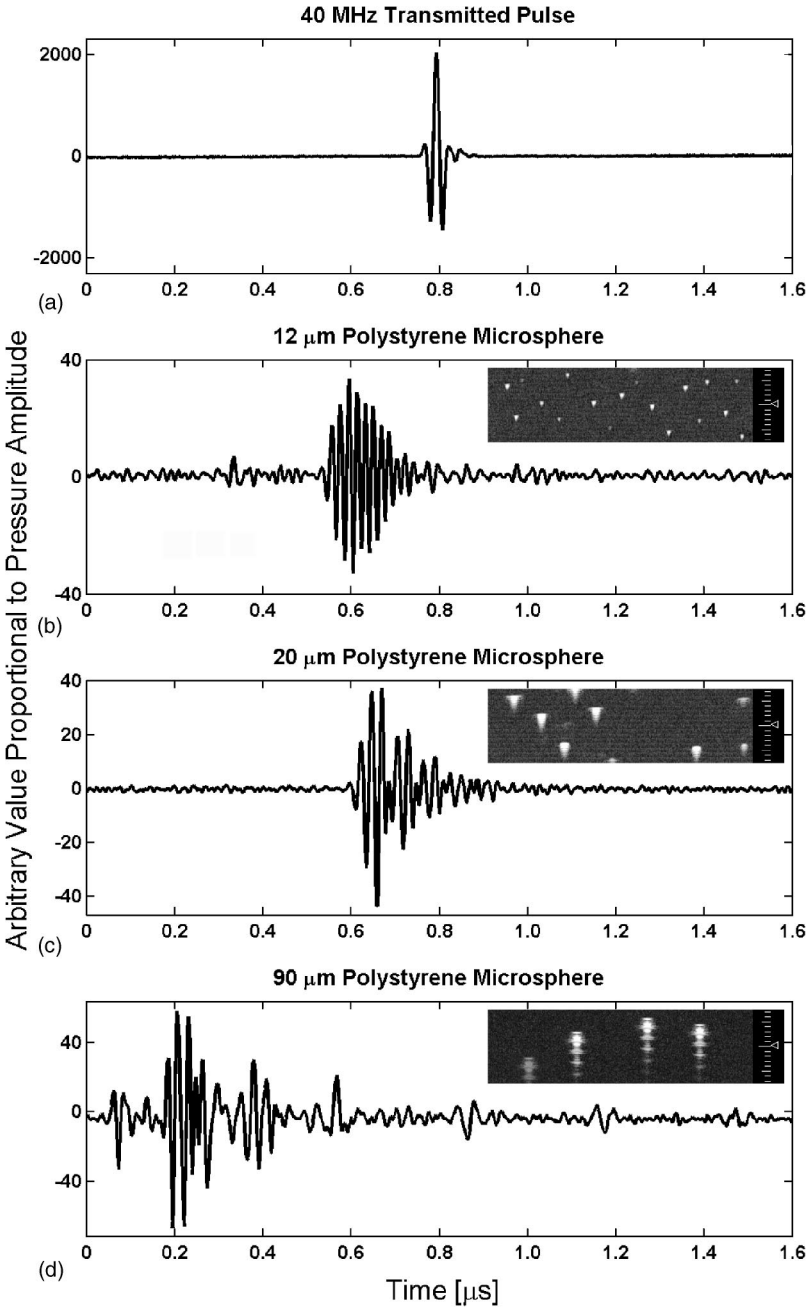

FIG. 4. Typical backscattered pulses from a 12-μm (b), 20-μm (c), and a 90-μm (d) polystyrene microsphere insonified by an $f2$ transducer with a broadband 40-MHz pulse (a). Insets are typical B-scans of sparse suspensions of microspheres (scale resolution = 100 μm); triangles indicate the depth of the transducer focus.

room temperature. Figure 3 shows the measured BSTFs for polystyrene microspheres of three different diameters (12, 20, and 90 μm) plotted along with the corresponding theoretical normalized backscattered pressure intensity frequency response. Figure 4 shows a representative backscattered pulse measured from each size of microsphere. The smaller sizes were chosen as they are in the range of typical eukaryotic cells (5–20 μm). The larger size was chosen to investigate the sensitivity of the experimental setup to detecting the complex high-frequency resonances predicted by the Faran–Hickling solution.

B. Eukaryotic cells

Experiments with eukaryotic cells were performed to evaluate the proposed cell scattering model, i.e., an elastic sphere with nucleus-like properties. OCI-AML-5 (Wang *et al.*, 1991), a line of human acute myeloid leukemia cells, was chosen for these experiments. In addition to having a simple morphology with a single, quasispherical nucleus (as seen in Fig. 1), the apoptotic response of these cells has been well documented (Tohda *et al.*, 1996; McCubrey *et al.*, 2001; Saleh *et al.*, 2002), an important feature given one of our ultimate goals of a measure of the apoptotic index. This cell line was also selected because previous high-frequency ultrasound studies have been performed on these cells (Czarnota *et al.*, 1997, 1999; Kolios *et al.*, 2002). Instead of water, the surrounding medium used for the cell suspension was a dilute phosphate buffered saline (PBS) solution (in distilled water: 8 g/L sodium chloride, 0.2 g/L potassium chloride, 0.132 g/L calcium chloride, 0.10 g/L magnesium chloride, 1.15 g/L sodium phosphate, 0.2 g/L potassium phosphate) to

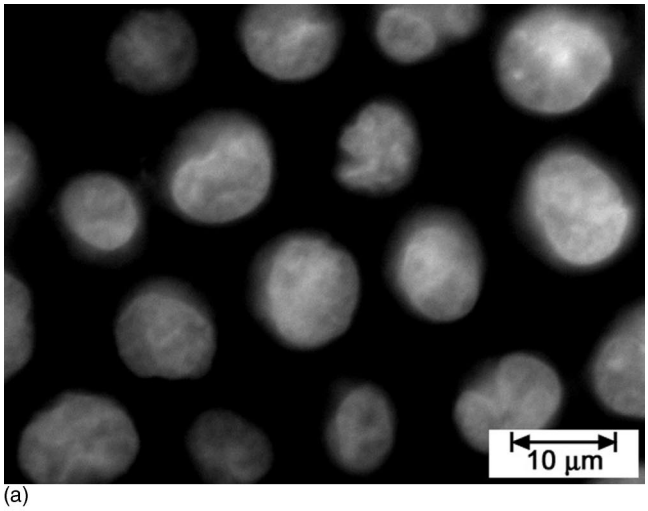

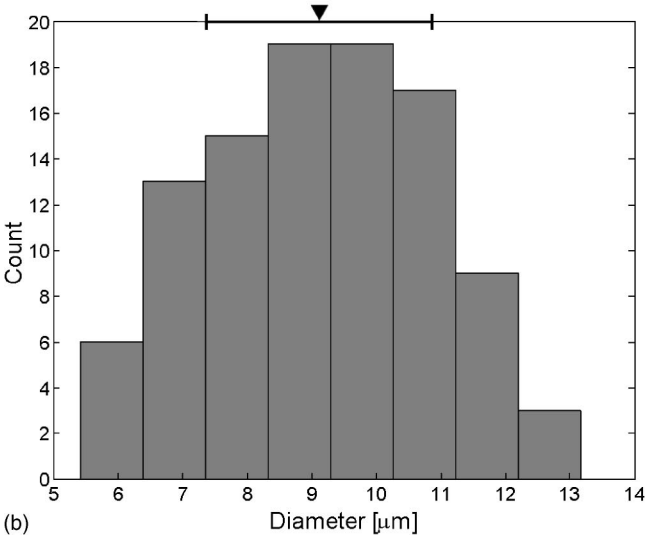

FIG. 5. Measurement of OCI-AML-5 cell nuclei. (a) Optical confocal microscopy of a population of bisbenzimide-stained OCI-AML-5 cells using ultraviolet illumination (only nuclei are visible). (b) Distribution of OCI-AML-5 nuclei diameters measured from optical confocal microscopy studies; top scale bar represents $+/-1$ standard deviation centered about the mean (indicated by a triangle).

preserve the viability of the cells. This solution of inorganic salts maintains a submerged cell's physiological *p*H, osmotic equilibrium, and membrane potential.

To calculate the theoretical backscatter from individual OCI-AML-5 cells in PBS using the proposed simplified cell scattering model, the average diameter and mechanical properties of OCI-AML-5 nuclei were required (PBS was assumed to be water-like with $\rho = 1.0$ g/mL and $c = 1483$ m/s). Using optical confocal microscopy of bisbenzimide-stained cells with ultraviolet illumination, shown in Fig. 5(a), the average diameter of OCI-AML-5 nuclei (of cells from this particular multiply passaged line) was measured to be 9.1 μm, with a standard deviation of 1.8 μm. The distribution of measured diameters is presented in Fig. 5(b).

The average longitudinal speed of sound in OCI-AML-5 nuclei, extracted from cells by the method of Muramatsu *et al.*, 1974, was measured to be $c = 1508.5$ m/s. This measurement was performed in PBS medium using a dense pellet of nuclei, centrifuged into one of two calibrated wells of a custom-built steel sample holder; the second well was used as a reference. The Poisson's ratio of OCI-AML-5 nuclei from viable cells was assumed to be the same as the Poisson's ratio of nuclei from chondrocytes (connective tissue cells), which has been measured to be $\sigma = 0.42$ (Knight *et al.*, 2002).

The average density of an OCI-AML-5 nucleus was estimated assuming generic eukaryotic nucleus properties. Using the estimate that 71% of the nuclear volume is taken up by chromatin, which contains approximately an equal proportion of DNA and protein by volume, and if one assumes that the rest of the nuclear matrix is an equal combination of dilute brine (essentially water, $\rho = 1.0$ g/mL) and protein, it is possible to calculate an overall average nucleus density to be $\rho = 1.43$ g/mL.

Figure 6 shows the measured BSTF for an OCI-AML-5 cell using three different transducers compared with two corresponding theoretical backscatter pressure intensity curves

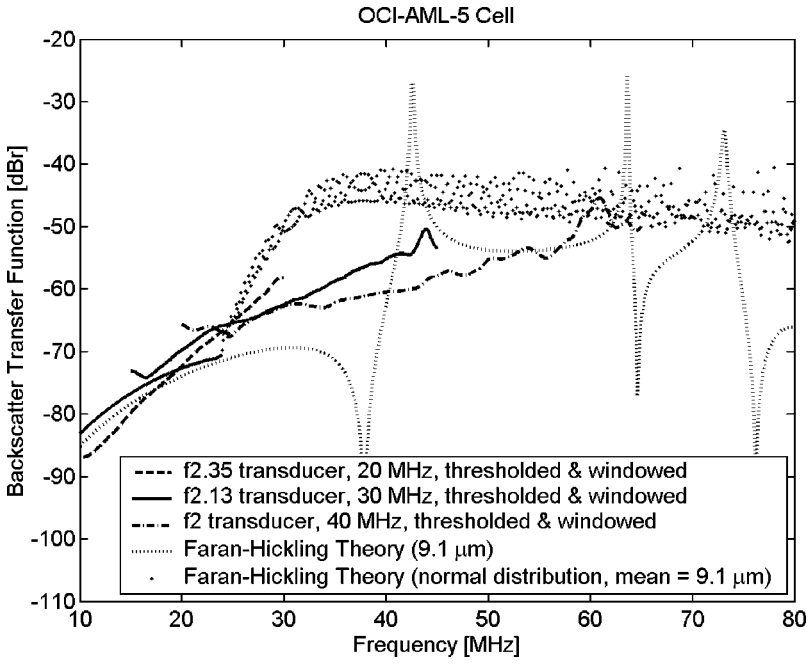

FIG. 6. Theoretical and measured backscatter transfer functions for single OCI-AML-5 cells (theoretical cell model parameters: $c = 1508.5$ m/s, $\rho = 1.43$ g/mL, $\sigma = 0.42$, $2a = 9.1$ μm) in PBS (assumed to be water-like for theoretical calculations) using three different wideband transducers (only the data from the 6-dB bandwidth of each transducer are shown). The second theoretical curve (scatter plot) is a weighted average of the Faran–Hickling scattering solutions for a normal distribution of nuclei diameters, corresponding to the distribution of measured diameters (mean = 9.1 μm, standard deviation = 1.8 μm) as shown in Fig. 5(b). Note that neither theoretical curve was scaled or shifted in any way, except to take into account the geometric effect of diminishing solid angle with distance.

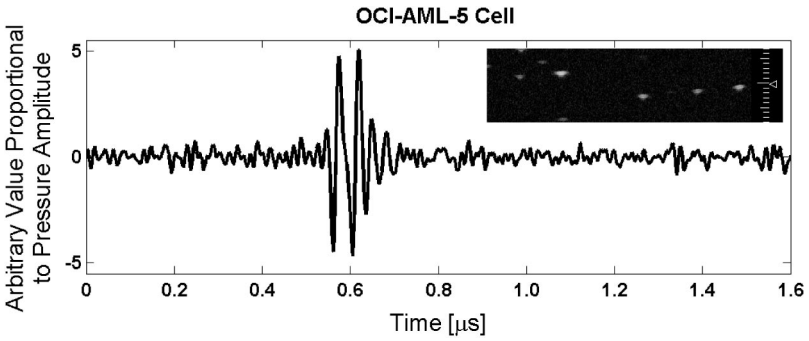

FIG. 7. Typical backscattered pulse from an OCI-AML-5 cell insonified by an $f2$ transducer with a broadband 40-MHz pulse; incident pulse is shown in Fig. 4(a). Inset is a typical B-scan of a sparse suspensions of cells (scale resolution $=100\ \mu$m); triangle indicates the depth of the transducer focus.

for spheres with OCI-AML-5 nucleus-like mechanical properties in water. The first theoretical curve (dotted line) is a calculation of the Faran–Hickling scattering solution using the mean measured nucleus diameter of 9.1 μm. The second theoretical curve (scatter plot) is a weighted average of the Faran–Hickling scattering solutions for a normal distribution of nuclei diameters, corresponding to the distribution of measured diameters (mean $=9.1\ \mu$m, standard deviation $=1.8\ \mu$m) as shown in Fig. 5(b). Figure 7 shows a representative backscattered pulse measured from an OCI-AML-5 cell.

V. DISCUSSION AND CONCLUSIONS

A. Polystyrene microspheres

Very good agreement in the location of the spectral features predicted by the theory and the experimentally measured data was observed. It was encouraging that even the high-frequency resonances were detected experimentally. However, when the scatterer becomes large, as for the 90-μm microsphere, agreement of feature locations and intensity levels was less rigorous, particularly at high frequencies. This could be due in part to the fact that 90 μm is very close to the full-width half-maximum (FWHM) intensity beamwidth of the transducers used. Another likely factor is that the wave components that make up the sharp, peculiarly shaped resonances predicted for $ka>15$ (i.e., $2\pi fa/c_3>15$), a range only seen in Fig. 3(c) for frequencies above 40 MHz, might disperse (e.g., due to differing propagation speeds per frequency) before reaching the transducer for acquisition. As seen in Fig. 3(c), even when the transducer with a 55-MHz resonant frequency was employed, although there was good agreement at lower frequencies, the agreement was poor near 55 MHz where most of the beam power is centered (and the best results would be expected). This is good evidence that dispersion is occurring and affecting the higher frequencies of scattered sound before they can be measured. The same dispersion should also be present in the results from the 12- and 20-μm microspheres, but as the backscatter responses are less complicatedly shaped in these cases, the effect on agreement with theory is probably less evident.

Some of the features in the backscatter frequency response curves can be interpreted according to resonance theory. If the frequency of the incident wave coincides with one of the resonant modes (vibrational eigenmodes) of the object, a resonant (or ringing) characteristic will be observed in the amplitude of the scattered wave. This behavior, however, is not sufficient to explain the complicatedly shaped curves of Fig. 3 and Fig. 4. Although the sharp peaks at lower frequencies in Fig. 3(c) could well correspond to resonant modes of a spherical 90-μm polystyrene microsphere, the complex behavior at higher frequencies is unlikely due to simple resonance.

Based on the observation of long transients by Faran (1951) and on the experimental results of Hickling (1962), another theory has been proposed where the backscatter response is strongly dependent on a train of backscattered echoes (Gaunaurd and Strifors, 1997). Initially the transducer receives a specularly reflected pulse (from the ''front'' surface of the microsphere) which mirrors the shape of the incident pulse. Then, the transducer receives regularly spaced pulses due to multiply circumnavigating surface wave pulses as proposed by Brill *et al.* (1981). Their shape deviates somewhat from the incident pulse due to dispersion of the surface waves—since different distances are traveled along the surface depending on the part of the sphere that was initially reached, and their amplitude diminishes with each turn around due to radiative and absorption losses. The shorter the incident pulse, the more distinctly separated are the resulting train of pulses. The spacing should also be related to the longitudinal speed of sound in the medium (c_3), the transverse (shear) speed of sound in the scatterer (c_2), and the diameter of the scatterer ($2a$). For a longer incident pulse (or for certain values of c_2, c_3, and $2a$), the train of resulting echo pulses starts to overlap and interference occurs. The type of interference that occurs, constructive or destructive, is dependent on the resonant modes of the scatterer—if the peak of the incident pulse spectrum coincides with a local maximum (a resonant mode) of the theoretical frequency response of the scatterer, then one will get constructive interference; the converse for a minimum. Since the pulses generated by the VisualSonics VS40b device and transmitted by our transducers are broadband (6-dB bandwidths nearly equal to the central frequency), several of these theoretical resonant peaks and troughs are excited at once, so the interference relationship is complicated. For the polystyrene microspheres, we are mainly in this latter regime of overlapping echoes, evident in Fig. 4(b) and Fig. 4(c). For the larger 90-μm microsphere, the train of pulses starts to separate; there is some evidence of this phenomenon in Fig. 4(d). This is likely because of the longer time required for the surface waves to circumnavigate the greater circumference of the sphere.

Another important observation from the backscatter re-

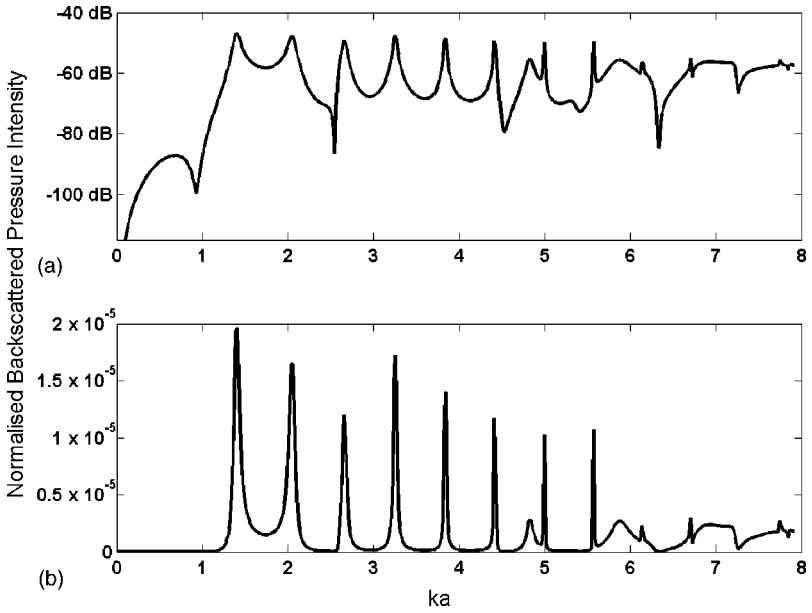

FIG. 8. Theoretical backscatter pressure intensity frequency response for an arbitrarily sized polystyrene microsphere ($c=2350$ m/s, $\rho=1.05$ g/mL, $\sigma=0.35$) plotted on a logarithmic (a) and linear (b) intensity scale (normalized to incident pressure waves of intensity $=1$) against the relative frequency, ka.

sponses of polystyrene microspheres is that the spacing of the resonances in the backscatter frequency response is related to the diameter of the sphere. As the scatterer diameter is decreased the resonances become more distantly spaced. Neglecting the small effect of scatterer size on the backscattered intensity (larger scatterers will naturally reflect more energy than smaller scatterers), the backscatter frequency response for any sphere sharing the same mechanical properties and differing only in size, will be the same curve stretched along the frequency axis by a particular factor related to the sphere diameter. *To investigate* this phenomenon, the theoretical backscatter response for a polystyrene sphere of an arbitrary diameter in water was calculated and plotted against *ka*, the relative frequency (shown in Fig. 8). Ignoring the absolute intensity values, these curves are valid for any size of polystyrene sphere. From $ka=1$ to $ka=6$, there are very sharp, nearly regularly spaced resonant peaks. The mean spacing between these peaks is $ka=0.6$. Thus, given an experimentally measured backscatter frequency response for a polystyrene sphere, the diameter of the sphere $(2a)$ could be determined simply from the mean spacing between resonant peaks. For example, in the experimental curves for 20-μm microspheres shown in Fig. 3(b), the average spacing between the resonant peaks is 14.7 MHz. Solving for the sphere radius (a)

$$ka=\frac{2\pi f}{c_3}\,a=\frac{2\pi(14.7\times10^6)}{1483}\,a=0.6, \tag{4}$$

yields a predicted diameter of 19.26 μm; a very good estimate (within 4%) of the true scatterer size for such a simple calculation. This positive result indicates that the method devised to deduce the backscatter signal from a single subresolution scatterer was successful. The fact that it is possible to work back from a measured backscattered frequency response and deduce characteristics of a subresolution scatterer is quite promising for future work with biological media (if this type of resonant behavior can be observed) for which, in most cases, the nature and properties of the main scattering sources are unknown.

B. Eukaryotic cells

A typical backscattered pulse from an OCI-AML-5 cell (Fig. 7) was shorter than pulses seen from polystyrene microspheres (Fig. 4). As discussed previously, a shorter scattered pulse is a consequence of a smaller scatterer size. This strong size dependence likely dominates any effect of small relative changes in mechanical properties, such as those between polystyrene, cells, and nuclei. The smallest microsphere diameter studied was 12 μm, roughly the same diameter as the OCI-AML-5 cells (mean diameter of 13.4 μm, measured by light microscopy), yet the scattered pulses from cells are shorter than those from these microspheres [Fig. 7 versus Fig. 4(b)]. This adds evidence that the cell nucleus, with its smaller diameter, is probably the main scattering source in the cell. Also, the peak amplitude of the backscattered pulses from cells was lower than those from polystyrene microspheres. This is consistent with the fact that OCI-AML-5 nuclei have a lower acoustic impedance ($Z=\rho c=2157$ kg/m$^2\cdot$s) compared to polystyrene ($Z=\rho c=2468$ kg/m$^2\cdot$s).

The experimental OCI-AML-5 BSTFs presented in Fig. 6 were approximately continuous across the three different transducers. A trend of reducing slope with increasing frequency is evident. This ''corner'' may indicate that the band of frequencies investigated represents a transition zone in the scattering response of OCI-AML-5 cells. The large slope of the BSTF from 10 to 30 MHz (this band is mainly covered by the $f2.35$, 20-MHz transducer) could indicate the end of the Rayleigh scattering regime. The slope of the $f2.35$ transducer curve from 10 to 20 MHz is 1.3 dB/MHz, close to the value of 1.2 dB/MHz needed to meet the f^4 dependence of intensity predicted for Rayleigh scattering. This assessment agrees with the first theoretical curve (Fig. 6 dotted curve), which also predicts higher slopes as frequency decreases. In general, the Faran–Hickling solution predicts that the transi-

tion zone between the Rayleigh scattering (i.e., higher slope) regime and the more complex resonant scattering regime occurs around $ka=0.5$. In the case of a 9.1-μm scatterer (cell nucleus), this critical value occurs at 26 MHz.

It is evident, however, that there is almost no agreement between the first theoretical curve (Fig. 6, dotted curve), the backscattering solution for the mean OCI-AML-5 nucleus diameter, and the experimental results. This is likely due to the wide range of nuclei diameters present in any given sample (as seen in Fig. 5), and consequently in the sparse solutions used in the experiments. As there is no way to easily distinguish between the backscattered pulses when analyzing the results, the calculation of the average BSTF will include the responses from different nucleus sizes (in addition to different shapes, as OCI-AML-5 nuclei are not truly spherical). This will tend to smooth the complicated resonant behavior predicted for the scattering response of a single nucleus (i.e., the local maxima and minima will cancel when shifted along the frequency axis). The second theoretical curve confirms this possibility. The backscatter frequency response of 100 different nuclei sizes (chosen as there are, typically, up to 100 A lines remaining per experiment after thresholding), normally distributed based on the distribution of measured diameters, each with identical mechanical properties, was calculated using the Faran–Hickling formulation. The weighted sum of these responses (the weights are equal to the probability corresponding to each diameter) is presented in Fig. 6 (scatter plot). As the number of nuclei sizes simulated would increase, this second theoretical curve would become smoother. This theoretical curve agrees more closely with the experimental results, also indicating a ''corner-like'' response.

Even with a more accurate simulation of the experimental conditions, it is clear that the theoretical backscatter response still does not accurately predict the true response from single OCI-AML-5 cells. It is likely that some of the simplifications made in the theoretical cell model contribute to the divergence between the two results. First, the cell nucleus is not truly spherical [as seen in Fig. 1 and Fig. 5(a)]; it is hard to predict how this would affect the resulting backscatter response as there is no computable solution available for the acoustic scattering from an aspherical, arbitrary-shaped elastic scatterer. Another simplification that could potentially have a significant impact on the backscatter from a cell is that the nucleus is not homogeneous. The proposed theoretical model assumes a nucleus with uniform mechanical properties. It is quite possible that small regions of different chromatin density, such as the nucleolus or chromosomes (during mitosis), dominate the resulting scattering process. The high experimental spectral slopes from 10–30 MHz, higher than the theoretical model prediction, also suggest the presence of scatterers of smaller size. Therefore, a nucleus may be better modeled as an ensemble of scatterers.

The assumption that the nucleus by itself is primarily responsible for the acoustic scattering of a cell might also have to be reconsidered. It is likely that there are various other factors affecting the acoustic scattering produced by a single cell. For example, it is possible that the mitochondria, a small organelle with a high density of membranes and proteins, could cause a significant amount of scattering. Even more likely, the balance of the cell outside the nucleus likely has some affect on the scattering of incident acoustic pulses, but also on the scattered pulses emitted from the nucleus. This would explain the much lower peak amplitudes of the echo signals measured from nuclei compared to polystyrene microspheres, nearly an eightfold difference, even though the acoustic impedances of each are within 15%. Although cytoplasm, which fills the rest of the cell, is thought to be mostly constituted of water, this is a significant oversimplification biologically. Although 2 to 10 times less stiff than the nucleus (Caille *et al.*, 2002), as a whole, the rest of the cell outside the nucleus is still stiffer than water. This is likely due to one of the important constituents of the cytoplasm, the cytoskeleton (a network of actin, tubulin, myosin, and other proteins), which can significantly change the shape of the cell and its effective resistance to external compressional forces (Caille *et al.*, 2002). There is still much to be learned about the behavior of the cytoskeleton, which varies from one cell type to another and could be modulated by various external or internal cellular stimuli (Karl and Bereiter-Hahn, 1999). It is conceivable that the presence of the mesh of cytoskeleton might dampen, to some unknown extent, the vibrations and transient deformations of the cell and nucleus that would be induced by an incident acoustic pulse. This might, as a result, reduce the amplitude of any morphological resonances in the backscatter frequency response, generally contributing to a smoothing of this curve, as seen in Fig. 6. It might be possible to model the effect of the layer of cytoplasm (containing cytoskeleton) around the nucleus as an elastic shell surrounding a stiffer elastic sphere or a fluid sphere.

Ideally, it would be very helpful at this point to experimentally measure the backscatter of a single OCI-AML-5 cell at various stages of apoptosis and compare it to theoretical predictions using the simplified scattering model of a cell. This would be useful because it would provide a good indication of the model's robustness, which focuses solely on changes to the nucleus, for simulating structural changes such as apoptosis. Practically, however, measuring the backscatter from single cells at specific known stages of apoptosis proved very difficult. We have no method for verifying, by assay or microscopically, that a particular cell being insonified is at a certain stage of apoptosis. This is partly due to the setup, the machine scan head geometry does not allow for concurrent microscopy of the same volume being imaged, but also the thresholding method devised to image single cells. Because cells are in suspension, it is impossible to predict when a cell, let alone a particular cell, will be in the focal zone of the ultrasound beam.

To attempt to make this imaging and backscatter response analysis technique more clinically relevant, experiments will have to be performed using tissues or, in the simplest case, an ensemble of cells. A particular type of ensemble, a pellet of centrifuged cells, is of primary interest given its wide use in preclinical *in vitro* studies and other ultrasonic studies. In addition to building a more elaborate model to simulate an ensemble, a further complicating factor one might encounter in extending the technique is that the

major scattering centers may change from the sparse solution (i.e., single-cell) environment, where the balance of the cell surrounding the nucleus appears to have an important effect, to the cellular ensemble condition. For instance, in a tight ensemble of cells, the nuclei may then truly dominate the overall scattering.

ACKNOWLEDGMENTS

The authors acknowledge Dr. F. S. Foster of the Department of Medical Biophysics at the University of Toronto for intellectual contributions. The authors also acknowledge Anoja Giles, Arthur Worthington, and James Jonkman of the Princess Margaret Hospital for technical support. This work was supported by operating grants from the Canadian Institutes of Health Research and the Whitaker Foundation. The ultrasound imaging device was purchased with funds from the Canadian Foundation for Innovation, the Ontario Innovation Trust, and Ryerson University.

Berovic, N., Thomas, N., Thornhill, R. A., and Vaughan, J. M. (**1989**). ''Observation of Brillouin scattering from single muscle fibers,'' Eur. Biophys. J. **17**, 69–74.

Berube, L. R., Harasiewicz, K., Foster, F. S., Dobrowsky, E., Sherar, M. D., and Rauth, A. M. (**1992**). ''Use of a high-frequency ultrasound microscope to image the action of 2-nitroimidazoles in multicellular spheroids,'' Br. J. Cancer **65**, 633–640.

Brill, D., Gaunaurd, G., and Uberall, H. (**1981**). ''The response-surface in elastic wave scattering,'' J. Appl. Phys. **52**, 3205–3214.

Brill, D., and Gaunaurd, G. C. (**1987**). ''Resonance theory of elastic-waves ultrasonically scattered from an elastic sphere,'' J. Acoust. Soc. Am. **81**, 1–21.

Caille, N., Thoumine, O., Tardy, Y., and Meister, J. J. (**2002**). ''Contribution of the nucleus to the mechanical properties of endothelial cells,'' J. Biomech. **35**, 177–187.

Czarnota, G. J., Kolios, M. C., Hunt, J. W., and Sherar, M. D. (**2002**). ''Ultrasound imaging of apoptosis: DNA-damage effects visualized,'' in *In Situ* Detection of DNA Damage: Methods and Protocols (Methods in Molecular Biology, Vol. 203), edited by V. Didenko (Humana, Totowa, NJ), pp. 257–277.

Czarnota, G. J., Kolios, M. C., Abraham, J., Portnoy, M., Ottensmeyer, F. P., Hunt, J. W., and Sherar, M. D. (**1999**). ''Ultrasound imaging of apoptosis: High-resolution non-invasive monitoring of programmed cell death in vitro, in situ and in vivo,'' Br. J. Cancer **81**, 520–527.

Czarnota, G. J., Kolios, M. C., Vaziri, H., Benchimol, S., Ottensmeyer, F. P., Sherar, M. D., and Hunt, J. W. (**1997**). ''Ultrasonic biomicroscopy of viable, dead and apoptotic cells,'' Ultrasound Med. Biol. **23**, 961–965.

Czarnota, G. J., Kolios, M. C., Heng, Y. M., Deveraj, K., Tam, C., Tan, L., Ottensmeyer, F. P., Hunt, J. W., and Sherar, M. D. (**1999**). ''Ultrasound biomicroscopy of cancer therapy effects: Correlation between light and electron microscopy, and a new noninvasive ultrasound imaging method for detecting apoptosis,'' Proc. Microsc. Soc. Am. 2320.

Edwards, G. S., Davis, C. C., Saffer, J. D., and Swicord, M. L. (**1985**). ''Microwave-field-driven acoustic modes in DNA,'' Biophys. J. **47**, 799–807.

Faran, J. J. (**1951**). ''Sound scattering by solid cylinders and spheres,'' J. Acoust. Soc. Am. **23**, 405–418.

Feleppa, E. J., Lizzi, F. L., Coleman, D. J., and Yaremko, M. M. (**1986**). ''Diagnostic spectrum analysis in ophthalmology—A physical perspective,'' Ultrasound Med. Biol. **12**, 623–631.

Gaunaurd, G. C., and Strifors, H. C. (**1997**). ''Transient resonance scattering and target identification,'' Appl. Mech. Rev. **50**, 131–148.

Guittet, C., Ossant, F., Vaillant, L., and Berson, M. (**1999**). ''*In vivo* high-frequency ultrasonic characterization of human dermis,'' IEEE Trans. Biomed. Eng. **46**, 740–746.

Hacker, G. (**2000**). ''The morphology of apoptosis,'' Cell Tissue Res. **301**, 5–17.

Hakim, M. B., Lindsay, S. M., and Powell, J. (**1984**). ''The speed of sound in DNA,'' Biopolymers **23**, 1185–1192.

Hampton, L. D., and McKinney, C. M. (**1961**). ''Experimental study of scattering of acoustic energy from solid metal spheres in water,'' J. Acoust. Soc. Am. **33**, 664–673.

Hickling, R. (**1962**). ''Analysis of echoes from a solid elastic sphere in water,'' J. Acoust. Soc. Am. **34**, 1582–1592.

Hinders, M. K. (**1991**). ''Plane-elastic-wave scattering from an elastic sphere,'' Nuovo Cimento Soc. Ital. Fis., B **106**, 799–818.

Karl, I., and Bereiter–Hahn, J. (**1999**). ''Tension modulates cell surface motility: A scanning acoustic microscopy study,'' Cell Motil. Cytoskeleton **43**, 349–359.

Knight, M. M., Bravenboer, J. V. D. B., Lee, D. A., van Osch, G. J. V. M., Weinans, H., and Bader, D. L. (**2002**). ''Cell and nucleus deformation in compressed chondrocyte-alginate constructs: Temporal changes and calculation of cell modulus,'' Biochim. Biophys. Acta **1570**, 1–8.

Kolios, M. C., Czarnota, G. J., Lee, M., Hunt, J. W., and Sherar, M. D. (**2002**). ''Ultrasonic spectral parameter characterization of apoptosis,'' Ultrasound Med. Biol. **28**, 589–597.

Kolios, M. C., Czarnota, G. J., Hussain, M., Foster, F. S., Hunt, J. W., and Sherar, M. D. (**2001**). ''Analysis of ultrasound backscatter from ensembles of cells and isolated nuclei,'' Proceedings of IEEE Ultrasonics Symposium 1257–1260.

Kolios, M. C., Taggart, L., Baddour, R. E., Foster, F. S., Hunt, J. W., Czarnota, G. J., and Sherar, M. D. (**2003**). ''An investigagion of backscatter power spectra from cells, cell pellets, and microspheres,'' Proceedings of IEEE Ultrasonics Symposium 752–757.

Kornberg, R. D. (**1974**). ''Chromatin structure—Repeating unit of histones and DNA,'' Science **184**, 868–871.

Lizzi, F. L., Astor, M., Feleppa, E. J., Shao, M., and Kalisz, A. (**1997**). ''Statistical framework for ultrasonic spectral parameter imaging,'' Ultrasound Med. Biol. **23**, 1371–1382.

Lockwood, G. R., Ryan, L. K., Gotlieb, A. I., Lonn, E., Hunt, J. W., Liu, P., and Foster, F. S. (**1992**). ''*In vitro* high-resolution intravascular imaging in muscular and elastic arteries,'' J. Am. Coll. Cardiol. **20**, 153–160.

Matthews, B. W. (**1968**). ''Solvent content of protein crystals,'' J. Mol. Biol. **33**, 491–497.

McCubrey, J. A., Blalock, W. L., Saleh, O. A., Pearce, M., Burrows, C., Steelman, L. S., Lee, J. T., Franklin, R. A., Oberhaus, S. M., Moye, P. W., Doshi, P. D., and McKearn, J. P. (**2001**). ''Enhanced ability of daniplestim and myelopoietin-1 to suppress apoptosis in human hematopoietic cells,'' Leukemia **15**, 1203–1216.

Meselson, M., and Stahl, F. W. (**1958**). ''The replication of DNA in escherichia-coli,'' Proc. Natl. Acad. Sci. U.S.A. **44**, 671–682.

Monier, K., Armas, J. C. G., Etteldorf, S., Ghazal, P., and Sullivan, K. F. (**2000**). ''Annexation of the interchromosomal space during viral infection,'' Nat. Cell Biol. **2**, 661–665.

Muramatsu, M., Hayashi, Y., Onishi, T., Sakai, M., Takai, K., and Kashiyama, T. (**1974**). ''Rapid isolation of nucleoli from detergent purified nuclei of various tumor and tissue-culture cells,'' Exp. Cell Res. **88**, 345–351.

Pavlin, C. J., Harasiewicz, K., Sherar, M. D., and Foster, F. S. (**1991**). ''Clinical use of ultrasound biomicroscopy,'' Ophthalmology **98**, 287–295.

Saleh, O. A., Blalock, W. L., Burrows, C., Steelman, L. S., Doshi, P. D., McKearn, J. P., and McCubrey, J. A. (**2002**). ''Enhanced ability of the progenipoietin-1 to suppress apoptosis in human hematopoietic cells,'' Int. J. Mol. Med. **10**, 385–394.

Sherar, M. D., Noss, M. B., and Foster, F. S. (**1987**). ''Ultrasound backscatter microscopy images the internal structure of living tumor spheroids,'' Nature (London) **330**, 493–495.

Tohda, S., Kurokawa, H., and Nara, N. (**1996**). ''Relation of protein kinase a and protein kinase c to signaling pathways of hematopoietic factors in leukemia cell lines,'' Int. J. Oncol. **8**, 521–524.

Wang, C., Koistinen, P., Yang, G. S., Williams, D. E., Lyman, S. D., Minden, M. D., and McCulloch, E. A. (**1991**). ''Mast-cell growth factor, a ligand for the receptor encoded by c-kit, affects the growth in culture of the blast cells of acute myeloblastic-leukemia,'' Leukemia **5**, 493–499.

Pitch (F_0) and formant profiles of human vowels and vowel-like baboon grunts: The role of vocalizer body size and voice-acoustic allometry[a)]

Drew Rendall,[b)] Sophie Kollias, and Christina Ney
Department of Psychology and Neuroscience, University of Lethbridge, Lethbridge, Alberta, T1K 3M4 Canada

Peter Lloyd
Cape Nature Conservation, Western Cape Province, South Africa

(Received 22 July 2004; revised 3 November 2004; accepted 22 November 2004)

Key voice features—fundamental frequency (F_0) and formant frequencies—can vary extensively between individuals. Much of the variation can be traced to differences in the size of the larynx and vocal-tract cavities, but whether these differences in turn simply reflect differences in speaker body size (i.e., neutral vocal allometry) remains unclear. Quantitative analyses were therefore undertaken to test the relationship between speaker body size and voice F_0 and formant frequencies for human vowels. To test the taxonomic generality of the relationships, the same analyses were conducted on the vowel-like grunts of baboons, whose phylogenetic proximity to humans and similar vocal production biology and voice acoustic patterns recommend them for such comparative research. For adults of both species, males were larger than females and had lower mean voice F_0 and formant frequencies. However, beyond this, F_0 variation did not track body-size variation between the sexes in either species, nor within sexes in humans. In humans, formant variation correlated significantly with speaker height but only in males and not in females. Implications for general vocal allometry are discussed as are implications for speech origins theories, and challenges to them, related to laryngeal position and vocal tract length.
[DOI: 10.1121/1.1848011]

PACS numbers: 43.80.Ka, 43.70.Gr Pages: 944–955

I. INTRODUCTION

Human speech is a multidimensional signal. In addition to conveying the phonetic contrasts essential to language, the speech signal contains cues to myriad nonlinguistic dimensions of a speaker, including sex, age, individual identity, and dialect background (Ladefoged and Broadbent, 1956; Abercrombie, 1967; Bricker and Pruzansky, 1976; Bachorowski and Owren, 1999). Indeed, the latter *indexical* dimensions can intrude on the linguistic function of speech by introducing significant speaker-specific variation into the speech signal that complicates recovery of its linguistic content, requiring some mechanism of ''speaker normalization'' in listeners. Given the importance of such normalization to effective communication, a central preoccupation of speech science has been uncovering the perceptual and cognitive processes involved, and at the same time also tracing the underlying sources of variation in the speech signal to begin with.

Considerable progress has been made on both fronts, although there remain unresolved issues in each area. For example, in perception, alternative explanatory frameworks stress the importance of either canceling the spurious speaker-dependent variation to recover canonical phoneme targets, or actively incorporating such variation into the process of phoneme identification given recent evidence that speech comprehension can be facilitated by familiarity with the idiosyncracies of particular talkers' voices (reviewed in Nearey, 1989; Johnson and Mullenix, 1997).

On the production side, research has focused on speaker-dependent variation in vocal production physiology, particularly differences in the size of critical features of vocal-tract anatomy. There is a solid understanding of the basic relationships here and their implications for the speech signal. For example, many of the basic differences in the speech of children and adults, and within adults between males and females, can be traced to differences in the size of the larynx and vocal-tract cavities that determine voice fundamental frequency (F_0) and formant frequency profiles, respectively (Peterson and Barney, 1952; Hirano *et al.*, 1983; Titze, 1989; Fitch and Giedd, 1999). These differences in turn are to a large extent thought to reflect differences in body size between adults and children, and between males and females (Fitch and Giedd, 1999). However, we are on somewhat shakier ground here (Nordström, 1977). Although some of the differences in voice acoustics (e.g., between children and adults) probably do reflect straightforward differences in vocal anatomical maturation related to differences in general growth and development trajectories, some apparently do not.

For example, the nearly twofold difference in baseline

[a)]Portions of this work were presented at the First International Conference on Animal Acoustic Communication, cohosted by the Acoustical Society of America and the University of Maryland, College Park, Maryland, July 2003.

[b)]Electronic mail: d.rendall@uleth.ca

speaking F_0 between adult males and females appears to be out of all proportion to the more modest body-size differences between the sexes, and previous work has also failed to find any correlation between voice F_0 and body size within either sex (Lieberman, 1967; Kunzel, 1989; van Dommelen and Moxness, 1995; Collins, 2000). Similarly, a handful of studies examining formant frequencies (or simply the broader frequency spectrum) in relation to body size variation between and within sexes have yielded weak or mixed results (Lass *et al.*, 1980a, b; van Dommelen and Moxness, 1995; Collins, 2000; Greisbach, 1999; González, 2004). As a result, there is continuing interest in the underlying biology of body-size growth and development that contributes to variability in vocal-tract anatomy and thus to the speaker-specific variation in speech that it is ultimately so important to normalize in speech perception.

There are additional reasons for the interest in potential body-size influences on speech production and voice acoustics. To begin with, it is possible that voice cues to body size, and their underlying vocal anatomical determinants, are themselves subject to specific biological selection pressures. It is certainly true that body size plays a deterministic role in competitive interactions and other social contexts in many species, including humans. As a result, there could be functional value in *advertising* size in various contexts through voice features that reveal, or even exaggerate, vocalizer size (Morton, 1977; Fitch, 1999, 2000). Indeed, there is some broad support for this possibility in the form of demonstrable correlations between different spectral dimensions of the voice (e.g., fundamental frequency, ''dominant'' frequency/harmonic, and resonance frequencies) and body size in vocalizations used by some anurans and mammals either in aggressive competition among males, or in mate attraction displays, where size matters (e.g., Davies and Halliday, 1978; Reby and McComb, 2003; reviewed in Fitch and Hauser, 2002).

Furthermore, such observations have inspired a recent proposal that a critical feature of human vocal-tract anatomy long held to represent a specific adaptation for language, namely a descended larynx positioned low in the vocal tract by comparison to closely related primate species (Lieberman, 1968; Lieberman *et al.*, 1969), actually represents an adaptation for body-size advertisement (Fitch, 2000; Fitch and Reby, 2001). That is, humans' descended larynx positions it outside the bony constraints of the skull, allowing it to expand more freely in multiple dimensions and at the same time creates a longer vocal tract. Both characteristics could function to advertise larger body size through vocalizations with lower F_0 and formant frequency profiles, respectively.

To more fully evaluate these ideas and to contribute to our broader understanding of the connections between body-size variation, vocal-tract allometry, and variable speech acoustics, we need a better understanding of the extent to which these features of speech actually track variation in speaker body size. Therefore, in this paper, we undertake analyses of human voice acoustics in relation to several dimensions of speaker body size. We focus specifically on vowel sounds because these manifest clear F_0 and formant profiles that seem to offer the most salient cues to size-related vocal anatomical variation, and we limit our analyses to adults to avoid age-related confounds in body size and vocal-tract anatomy. In addition, where possible, we include comparable data on the grunt vocalizations of adult baboons.

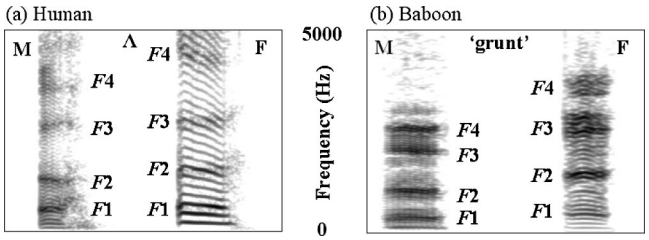

FIG. 1. Spectrograms of (a) human vowels and (b) baboon grunts produced by an adult male (M) and female (F) of each species. The vowel illustrated is that from the word ''butt.'' Both spectrograms were produced using a 1024-point FFT (approximately 50 ms), a Hanning window, and 90% frame overlap. Note the general similiarity in frequency structure between the vowels and grunts, and the similar pattern of F_0 and formant differences between males and females within each species.

Baboons provide an especially useful comparison here. As primates relatively closely related to humans, they provide a logical opportunity to trace potential continuity in the processes of human vocal production and to help clarify some of the basic vocal anatomical and acoustic-structural relationships involved. Indeed, research on baboon communication has already revealed several productive parallels to speech phenomena. Thus, the most common vocalization produced by baboons—a harmonically rich grunt—is structurally analogous to human vowel sounds, having a clear, stable F_0 and a set of prominent resonance peaks that reflects the combined action of stable vocal-fold vibration and subsequent spectral shaping by the supralaryngeal vocal-tract cavities (Zhinkin, 1963; Andrew, 1976; Richman, 1976). More detailed analyses have shown that the mean F_0 and resonance frequencies of female grunts actually closely match those of vowels produced by English-speaking males, a convergence attributed to a coincidence in vocal-fold and vocal-tract lengths in the two groups (Owren *et al.*, 1997; Rendall, 2003). This work has also shown that the baboons produce different acoustic variants of grunt that, like vowels, differ in spectral properties related to vocal-tract filtering (Owren *et al.*, 1997; Rendall *et al.*, 1999). In addition, sex differences in the F_0 and formant profiles of baboon grunts parallel sex differences in the F_0 and formant profiles of human vowels (Rendall *et al.*, 2004), as illustrated in Fig. 1, suggesting that some similar process of vocalizer normalization might also be important for the perception of different grunt variants in baboons.

Finally, and importantly, although the basic anatomy of vocal production and its functional operation is similar in baboons and humans (Fitch and Hauser, 1995; Owren and Linker, 1995), baboons do not have either a descended larynx or language (in the human sense). Therefore, they represent a very valuable control for these influences on vocal production, allowing us to explore the relationships between vocalizer body size, vocal-tract anatomy, and voice acoustics unconfounded by language and any potentially associated anatomical adaptations.

We begin by examining the F_0 and formant profiles of human vowels and baboon grunts produced by adult males and females of each species and the extent to which sex differences in these acoustic features track body-size differences between the sexes. We follow this with an analysis of size-related F_0 and formant frequency variation among individuals within each sex.

II. BETWEEN-SEX VARIATION IN BODY SIZE AND VOICE ACOUSTICS IN HUMANS AND BABOONS

A. Methods

1. Voice samples and body-size measurements

a. Humans. Matched voice samples and body-size measurements were obtained from undergraduate students recruited from psychology courses at the University of Lethbridge. Students were screened for language and dialect background in an effort to reduce potential acoustic variation associated with such differences across subjects. Only students for whom Canadian English was their first language and lacking strong regional accents were retained in the study. The sample ultimately retained for analysis consisted of a balanced set of 68 students (34 males and 34 females) whose average age was 23 years (range: 18–44 years).

Voice samples were collected individually from subjects in a sound-controlled room in the Laboratory of Comparative Communication and Cognition. Subjects were seated in a comfortable padded chair and were fitted with an adjustable head-worn microphone (AKG C420) connected to a preamplifier (Behringer MX602A) that allowed the recordist to adjust signal recording level appropriately. The preamplifier was connected to a Pentium IV computer through a tunable, 8-pole Butterworth antialias filter (Frequency Devices 900/9L8B). Speech signals were digitized with 16-bit quantization at a sample rate of 22.05 kHz after low-pass filtering at 10 kHz.

Subjects were given a sheet containing the speech material to be recorded. The material emphasized the production of vowel sounds which are the components of speech most likely to reflect size-related variation through variable vocal-fold vibration rates (F_0) and vocal-tract resonance frequencies. The material included a list of isolated vowels, two lists of single-syllable words encompassing a range of different vowels (in either hVd or bVt context), and four short sentences constructed of single-syllable words that replicated many of the vowel sounds present in the word lists. The order of material within each list of isolated vowels, words, and phrases was randomized across subjects to avoid serial order effects. Subjects were instructed to *say* rather than *read* the material in a clear and comfortable voice, pausing deliberately between each item. They were asked to practice the material aloud in order to familiarize them with the content and to get them comfortable speaking in front of the recordist and while wearing the microphone. The practice interval also allowed the recordist to optimize the recording level for each subject. After a variable interval of practice, each subject was recorded producing the material in a single session from beginning to end.

Prior to collecting the speech sample, measurements were taken of each subject's height, weight, and neck circumference (taken at the level of the greatest laryngeal protrusion), and a commercial flatbed scanner was used to obtain an image of each hand, stretched flat on the surface of the scanner. From the scanned images, the length of the third digit was measured in ADOBE PHOTOSHOP©.

b. Baboons. Grunt vocalizations were collected during field research on chacma baboons at two sites in southern Africa. One site was located in the Moremi Game Reserve in northern Botswana, and the other site was in the De Hoop Nature Reserve in the Western Cape Province of South Africa. Baboons at the two sites belong to the same species and subspecies (*Papio hamadryas ursinus*) that is distributed continuously throughout southern Africa (i.e., Namibia, Botswana, Zimbabwe, and South Africa). Subjects were the sexually and physically mature adult males and females of the main study group at each site. Both groups had been studied continuously for several years. As a result, all individuals were known and easily identified. The animals themselves were fully habituated to human observers, allowing high-quality vocal recordings to be made at very close range (0.5–2.0 m). Vocalization recordings were made during a single protracted study period in Botswana (February 1996–March 1997) and during multiple shorter study periods in South Africa (December 2000; May–August 2001; January–May 2002).

Grunt vocalizations were recorded during the course of focused observational research on the baboons which involved consecutive 1-h follows of specific individuals. (For additional details regarding the collection of behavioral data, see Rendall *et al.*, 2000). Baboons grunt in a variety of contexts but especially during dispersed travel and foraging activities and when approaching one another to socialize (Rendall *et al.*, 1999). Recordings were made on Sony type IV metal tapes using a Sony WM-D6C Professional Walkman cassette recorder and a Sennheiser ME 80 directional microphone with K3U power module. Analog field recordings were subsequently digitized with 16-bit accuracy using a sample rate of 22.05 kHz, after low-pass filtering at 10 kHz. The sample ultimately available for acoustic analysis consisted of 1028 grunts from 27 different individuals (11 males and 16 females). Additional details of the grunt sample and subjects studied can be found in Rendall *et al.* (2004).

Body-size measurements of baboons were collected several years earlier (1976–1979) during a multiyear census of the baboon population in the De Hoop Nature Reserve. During this census, animals were captured and anesthetized to collect biometric data including the height (head-crown to tail-base), weight, and length of the right foot of each animal. The sample included complete measurements of 47 adult baboons (>7 years of age), of which 29 were male and 18 were female. These animals were captured in the same area that is now occupied by the main study troop at De Hoop. However, their identities could not be traced to any of the current members of this troop. Hence, the body size and vocalization samples have to be regarded as unmatched.

TABLE I. Means and standard deviations of body-size (cm/kg) and acoustic features (Hz) for humans (vowels) and baboons (grunts) and the degree of sexual dimorphism in each feature. Dimorphism values are given as the ratio of values between the sexes (M:F for body size features; F:M for acoustic features).

Humans[a]	Height	Digit-3	Neck	Weight	F_0	$F1$	$F2$	$F3$	$F4$
Male	183.8	3.36	38.4	85.1	113	468	1431	2505	3468
	[*7.5*]	[*0.16*]	[*2.0*]	[*12.6*]	[*17.9*]	[*25.2*]	[*59.0*]	[*119.4*]	[*149.0*]
Female	168.3	2.98	32.0	64.4	204	583	1747	2915	4089
	[*6.9*]	[*0.13*]	[*1.9*]	[*8.9*]	[*17.4*]	[*32.3*]	[*79.9*]	[*130.3*]	[*175.1*]
Dimorphism	**1.09**	**1.13**	**1.20**	**1.32**	**1.81**	**1.25**	**1.22**	**1.16**	**1.18**
								1.20	
Baboons[b]	Height	Foot		Weight	F_0	$F1$	$F2$	$F3$	$F4$
Male	85.0	20.9		29.8	53	332	1062	1878	2603
	[*4.67*]	[*0.79*]		[*2.37*]	[*4.43*]	[*41.4*]	[*44.5*]	[*107.9*]	[*194.6*]
Female	69.6	17.5		17.3	114	448	1430	2677	3407
	[*3.22*]	[*0.73*]		[*1.43*]	[*11.6*]	[*43.3*]	[*109*]	[*157*]	[*232.0*]
Dimorphism	**1.22**	**1.19**		**1.72**	**2.15**	**1.35**	**1.35**	**1.43**	**1.31**
								1.36	

[a]Matched samples for body size and acoustic data ($N=34$ males, 34 females). Acoustic data represent the average values across 23 vowel utterances.
[b]Unmatched samples for body size ($N=29$ males, 18 females) and acoustic data ($N=11$ males, 16 females).

2. Acoustic analysis

a. Human vowels. Analysis of human voice samples focused on vowels contained in one of the word lists (*beet, bait, bit, bet, bat, butt, boat, boot, book*) and the vowels from several words in the short sentences (''*Put the book on top of the cup.*''; ''*Beat the tip of the stack.*''; ''*Butt the herd with a stick.*''; ''*Pull the rope through the boat.*''). In addition, the unstressed vowel in three instances of the word ''*the*'' in these phrases was also measured. This vowel was taken to approximate the schwa vowel, produced without emphasis and with a comparatively neutral vocal-tract configuration, making it the most likely source for unbiased F_0 and formant cues to size. In total, 23 vowel sounds were analyzed for each subject.

Acoustic analysis involved obtaining values of the fundamental frequency (F_0) and the frequency of the first four formants ($F1-F4$) from the central, steady-state portion of each vowel, with the exception of the glide vowels in the words ''*bait*'' and ''*boat.*'' For these two vowels, analysis was shifted either toward the initial section of the vowel or toward the end to better isolate the portion of interest (i.e., /e/ and /o/, respectively). Acoustic analyses were performed using the PRAAT© acoustic software package (version 4.1.9) implemented on the Windows XP Professional Operating System. The F_0 of each vowel was obtained using the pitch-tracking function of PRAAT to first highlight its ''pitch'' contour. The appropriate portion of each vowel was then circumscribed with interactive cursors and the program queried for the mean pitch (F_0) over that range.

The frequencies of the first four formants of each vowel were obtained using the formant-tracking function of PRAAT to highlight the contour of each formant. In this analysis, the formant-tracking routine was instructed to identify five formants over the range 0–5000 Hz using a frequency analysis window of 25 ms (approximately 500 points). Once again, interactive cursors were used to delimit the appropriate portion of the vowel, and the program was queried for the mean value of each formant over that range. Formant frequency values obtained in this way were independently verified using autocorrelation-based linear predictive coding (LPC). In this analysis, an LPC spectrum was generated from a 25-ms slice centered on the appropriate region of the vowel. This LPC spectrum was overlaid on a matching sized fast-Fourier transform (FFT) of the same region of the vowel, and the goodness-of-fit of the LPC peaks to emphasized regions in the underlying FFT was examined using 10–14 LPC coefficients. LPC peaks were then compared to formant frequency values obtained through formant tracking.

b. Baboon grunts. The analysis of baboon grunts proceeded in much the same way, except that the analyses were performed using the ENTROPIC SIGNAL PROCESSING SYSTEM WAVES+ software package (ESPS/WAVES+© version 5.3) (1997) implemented on the Linux operating system (Red Hat© version 6.0). Analyses of these calls have been published previously with detailed descriptions of the methodology used (Rendall *et al.*, 2004). Briefly, the analysis of grunts also focused on obtaining values for the F_0 and frequencies of the first four resonances (or formants) of the calls. F_0 values were obtained from the amplitude waveform of each grunt. Because most grunts exhibited extremely regular periodicity, individual cycles of vocal-fold opening and closing (representing F_0) were clearly visible in the waveform. We measured the period of each cycle of vocal-fold opening and closing from six cycles of vocal-fold vibration from the middle of each grunt, and averaged their inverses to obtain a mean F_0 value (in Hz) for each grunt.

The frequencies of the first four formants of each grunt were identified via autocorrelation-based LPC. An LPC spectrum was generated from a 1024-point (approximately 50 ms) segment from the midpoint of each grunt, using a Hanning window, and 18 coefficients. This LPC spectrum was then overlaid on an independently derived FFT for the same segment of the grunt to ensure the goodness-of-fit of the LPC-derived frequency spectrum. The frequencies of the first four poles of the LPC spectrum were then extracted and retained.

B. Results and discussion

Mean values for body-size and acoustic features of adult males and females of each species are given in Table I. Body-size data for both species were well-conditioned with

bivariate scatterplots revealing no obvious outliers and mean values comparing well with those from previous morphometric studies of humans and baboons, some involving much larger samples (e.g., Hamill *et al.*, 1979; Barrett and Henzi, 1997; McFadden and Bracht, 2003). Male:female dimorphism values confirmed that the bodily dimensions studied obeyed basic biophysical principles. Thus, in humans, sexual dimorphism in height and digit length (both linear dimensions) was approximately 1.10 (i.e., males were 10% ''longer'' than females). The sex difference in neck circumference (an areal dimension) and weight (a volumetric dimension) were 1.20 and 1.32, respectively, which match almost exactly the values that would be expected based on the square (1.21) and cube (1.33) of the observed linear dimorphism. Although the magnitude of sexual dimorphism in all body dimensions was greater in baboons than it was in humans, the same biophysical relationships were nevertheless observed. Thus, in baboons, sexual dimorphism in linear dimensions (height and foot length) was approximately 1.20, while the difference in volumetric dimension (weight) was 1.72, which is almost exactly the cube of the observed linear dimorphism (1.73).

For humans, mean values for the F_0 and four formants agree well with those reported previously for American English speakers (e.g., Peterson and Barney, 1952; Hillenbrand *et al.*, 1995; Stevens, 1998). For example, Stevens (1998) reported overall means for $F1-F3$ of 478, 1485, and 2563 Hz for adult males, and 592, 1755, and 2855 Hz for adult females, which match very closely the values obtained here. Means for the F_0 and formant frequencies of baboon grunts also agreed exceptionally well with those reported in the only previous detailed study of their acoustic structure with mean values obtained in the two studies differing by only 1%–4% (Owren *et al.*, 1997).

In both species, then, males are larger than females in each body dimension and they produce sounds with a lower F_0 and lower formant frequencies. The acoustic differences between males and females did not, however, map onto body-size differences between them in a straightforward way. In humans, the familiar sexual dimorphism in F_0 (1.81) greatly exceeded sexual dimorphism in linear (1.10), areal (1.20), and volumetric (1.32) dimensions. The same phenomenon was also found in baboons. The degree of sexual dimorphism in linear (1.20) and volumetric dimensions (1.72) was higher in baboons than it was in humans, but the degree of sexual dimorphism in mean F_0 in baboons (2.15) was higher still.

Thus, in both species, the difference in mean voice pitch between males and females considerably exceeded any difference in body size between the sexes. In humans, the extreme F_0 dimorphism (1.81) is largely, though not completely, accounted for by the large dimorphism in vocal-fold length, which is reported to be 1.50 for the entire fold and 1.60 for the membraneous portion that vibrates (Hirano *et al.*, 1983; Titze, 1989). The remaining 20%–30% excess acoustic dimorphism may be due to an additional sex difference in vocal-fold thickness, which is reported to be approximately 1.20–1.35 (Hirano *et al.*, 1983), or due to other differences in vocal-fold tissue properties (e.g., density, structuring), although Titze (1989) discounts many of these. Alternatively, it could reflect differences in behavioral control of normative vocal-fold operation between males and females. There are no published data on vocal-fold dimensions in baboons that might provide an anatomical account of the excess F_0 dimorphism in this species.

The connection of formant differences between males and females to body-size differences between them was equivocal. In both species, mean formant differences between the sexes were considerably greater than the sex difference in linear dimensions but smaller than the sex difference in volumetric dimensions. The formant differences best matched the sex differences in observed or expected areal dimensions. The latter outcome might imply that the vocal-tract cavities of males and females differ consistently not just in length but also in a second dimension (e.g., width).

This possibility is plausible for baboons where the larynx is positioned high in the vocal tract such that the supralaryngeal vocal tract is defined primarily by the oral cavity, which in turn is determined by the species' projected face, or muzzle. The muzzle of adult males is longer than that of adult females but it is also broader, reflecting the extreme sexual dimorphism in canine tooth size in this species. This sex difference in muzzle size could yield vocal-tract cavities that differ in both length and width between the sexes, although detailed measurements of muzzle and oral cavity dimensions would be needed to test this possibility properly. Furthermore, the match between observed formant dimorphism in baboons (1.36) and the expected dimorphism in areal dimensions in this species (1.44) was not perfect, which might indicate that two-dimensional differences in the vocal-tract cavities of males and females are not uniform along the entire muzzle, perhaps because the muzzle tapers towards the tip (which it does). Alternatively, it could simply mean that the notion of two-dimensional variation is not relevant at all. Instead, the excess formant dimorphism beyond what would be expected based on the difference in linear dimensions between males and females might be behavioral in origin.

In humans, the average sexual dimorphism in formants (1.20) exactly matched the sex difference in areal body dimensions (1.20), but it is not so obvious how the vocal-tract cavities of human males and females might differ consistently in two dimensions to support this outcome (cf. Apostol *et al.*, 2004). It is possible that some of the formant difference between the sexes reflects behavioral effects similar to those just proposed (Lieberman, 1986). In fact, there is some evidence from the speech of children of increased lip protrusion in boys compared to girls (Sachs *et al.*, 1972; Goldstein, 1980). However, the sex difference in formants observed in this study was also very similar to the baseline difference in vocal-tract length that is reported to characterize adult males and females, which is estimated at 15%–20% (Fant, 1966; Goldstein, 1980). A disproportionate share of this difference is proposed to lie in the pharyngeal region, with males having an oral cavity that is roughly similar in length to that of females but a pharyngeal cavity that is appreciably longer (Fant, 1966; Goldstein, 1980; Lieberman, 1986; Fitch and Giedd, 1999).

Consistent with the latter proposal, there was consider-

TABLE II. Means and standard deviations of $F1-F4$ for adult males (M) and females (F) for different vowels from individual words spoken in bVt context, and the degree of formant dimorphism (F:M) between the sexes for each vowel.

	*F*1			*F*2			*F*3			*F*4		
Word	M	F	**F:M**	M	F	**F:M**	M	F	**F:M**	M	F	**F:M**
Beet	242	290	**1.20**	2259	2801	**1.24**	3023	3437	**1.14**	3630	4261	**1.17**
	[*20.1*]	[*38.2*]		[*143.6*]	[*133.3*]		[*169.5*]	[*174.5*]		[*206.7*]	[*208.5*]	
Bit	434	530	**1.22**	1851	2266	**1.22**	2630	3069	**1.17**	3586	4226	**1.18**
	[*36.2*]	[*70.8*]		[*128.8*]	[*166.0*]		[*134.8*]	[*141.8*]		[*198.1*]	[*276.3*]	
Bait	407	456	**1.12**	2011	2497	**1.24**	2653	3131	**1.18**	3539	4170	**1.18**
	[*32.1*]	[*33.2*]		[*104.7*]	[*139.0*]		[*117.9*]	[*159.1*]		[*141.2*]	[*249.0*]	
Bet	589	754	**1.28**	1711	2046	**1.20**	2562	2983	**1.16**	3602	4238	**1.18**
	[*48.3*]	[*54.7*]		[*101.0*]	[*143.4*]		[*147.2*]	[*162.8*]		[*194.7*]	[*280.3*]	
Bat	731	951	**1.30**	1550	1819	**1.17**	2466	2850	**1.16**	3541	4215	**1.19**
	[*62.5*]	[*73.4*]		[*87.2*]	[*137.1*]		[*142.0*]	[*233.8*]		[*205.7*]	[*281.8*]	
Boat	386	459	**1.19**	859	993	**1.16**	2438	2848	**1.17**	3289	3880	**1.18**
	[*28.3*]	[*39.9*]		[*70.7*]	[*91.7*]		[*159.8*]	[*198.6*]		[*202.0*]	[*259.0*]	
Boot	286	364	**1.27**	1091	1303	**1.19**	2251	2729	**1.21**	3254	3979	**1.22**
	[*29.0*]	[*39.3*]		[*119.4*]	[*179.1*]		[*134.9*]	[*148.2*]		[*217.3*]	[*279.8*]	
Book	455	550	**1.21**	1037	1272	**1.23**	2432	2813	**1.16**	3353	3915	**1.17**
	[*35.5*]	[*74.0*]		[*73.6*]	[*143.3*]		[*160.8*]	[*171.8*]		[*205.9*]	[*217.6*]	
Butt	625	822	**1.32**	1257	1595	**1.27**	2507	2868	**1.14**	3505	4116	**1.17**
	[*48.9*]	[*68.8*]		[*75.2*]	[*115.2*]		[*166.3*]	[*180.6*]		[*210.6*]	[*220.4*]	
The	437	516	**1.18**	1340	1669	**1.25**	2486	2897	**1.17**	3486	4135	**1.19**
	[*47.1*]	[*51.1*]		[*70.3*]	[*104.2*]		[*135.3*]	[*132.1*]		[*177.5*]	[*226.6*]	

able variation in the magnitude of formant dimorphism across different formants and different vowel sounds. This variation is reported in Table II and illustrated in Fig. 2. Table II lists mean frequency values of $F1-F4$ for different vowels produced by males and females and the magnitude of formant dimorphism in each of them. The latter dimorphism values for particular formants and particular vowels deviated considerably from the overall mean formant dimorphism of 1.20, ranging from a low of 1.12 to a high of 1.32. Predictably the variation across different vowels was greater in $F1$ and $F2$ than in $F3$ and $F4$.

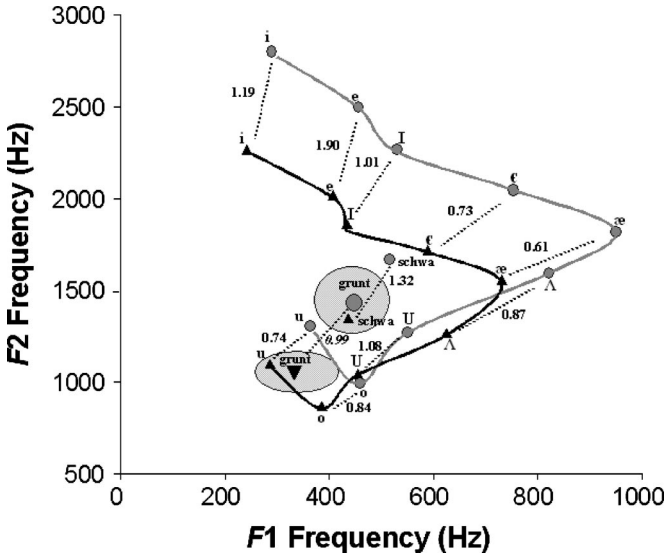

FIG. 2. Comparisons of the formant space occupied by human vowels and baboon grunts and the extent to which sex differences within each species reflect disproportionate shifts in either $F1$ or $F2$. Small black triangles and gray circles represent the mean frequency values of $F1$ and $F2$ for each of the ten vowels produced by human males and females, respectively. Solid lines connect and encircle the vowels for each sex to illustrate their relative placement in $F1-F2$ vowel space. Dashed lines connecting the same vowel in males and females, and the slope values next to them, indicate the extent to which the sex difference reflects a disproportionate shift in either $F1$ (<1.0), or $F2$ (>1.0), or a proportional shift in both formants (1.0). The larger black triangle and gray circle represent the mean frequency values of $F1$ and $F2$ for grunts produced by adult male and female baboons. Because the baboons did not produce the equivalent of different vowels, shaded circles are used to illustrate the range of variation observed in grunt formants for each sex.

The variation specifically in $F1$ and $F2$ is illustrated in Fig. 2, which plots the mean frequency values of $F1$ and $F2$ for different vowels produced by males and females. The values for each sex are interconnected to capture the overall formant space occupied by males and females and to illustrate how these spaces are shifted relative to each other along the $F1-F2$ axes.

For only two vowels (/I/ and /U/) and the grunts of baboons did the formant differences between males and females reflect equal proportional differences in $F1$ and $F2$. For the remaining vowels studied, the sex differences reflected disproportionate differences either in $F1$ (/ɛ/, /æ/, /Λ/, /o/, /u/), or in $F2$ (/i/, /e/, /ə/). This pattern of primarily non-proportional formant variation between sexes in humans is what Fant (1966), termed "non-uniform F-pattern scaling," and it is consistent with the proposal that the difference in vocal-tract length between males and females is not evenly distributed across the vocal tract but rather is concentrated more in certain regions, such as the pharynx (see also Whiteside, 2001).

III. WITHIN-SEX VARIATION IN BODY SIZE AND VOICE ACOUSTICS IN HUMANS

To examine whether the variable F_0 and formant frequency profiles of adult males and females might track body-size variation within each sex, we undertook additional body-size acoustic comparisons within males and females, respectively.

A. Methods

Methods for the collection and analysis of body size and acoustic data were the same as those described previously except that they were limited to humans for whom we had matched body size and acoustic data from the same individuals.

We used regression analysis to test the extent to which variation in the F_0 and formant frequencies of individual males and females was associated with variation in three body-size dimensions (height, weight, and neck circumference). We conducted two related regression analyses, one using individuals' mean values for all 23 vowels produced, and the other using individuals' means on only the schwa vowels (from the three instances of the unstressed word "*the*" in the short phrases).

For the formant frequency component of both analyses, we first calculated for each vowel the mean frequency difference between successive formants (i.e., $[(F2-F1)+(F3-F2)+(F4-F3)]/3$). This yields a derived variable summarizing the average spacing between formants. Fitch has previously labeled this variable "formant dispersion" (FD) and has proposed that it should be an especially good index of overall vocal tract length and thus also body size (Fitch, 1997, 1999, 2000). Therefore, in the first set of analyses, we regressed this variable, in combination with F_0, on subjects' height, weight, and neck circumference.

We followed this with separate regressions of the combination of F_0 and the individual formant frequencies (i.e., $F1-F4$) on subjects' height, weight, and neck circumference. We undertook this second analysis for two reasons. First, we wanted to test the extent to which any significant effects observed for the FD variable might be attributed to the differential contributions of specific formants. Second, we were especially concerned to test this because, although increasingly widely accepted and used in the literature, the algorithm for calculating FD, as proposed by Fitch, effectively reduces to the frequency difference between $F4$ and $F1$. Because $F1$ is also the least variable formant in human vowels, the resulting FD values are potentially determined primarily only by $F4$. Therefore, we ran a second series of regressions using the individual formant frequencies to be sure that all four formants were included and equally weighted in analyses. We also reran all regression analyses after applying a log transformation to the data as is often appropriate for tests of allometric relationships. Results using log-transformed data did not differ from those obtained using the original (untransformed) data. Therefore, for ease of presentation and interpretation, we present only the results based on the original data.

B. Results and discussion

Results of regression analyses are given in Table III. For females, multiple regressions of F_0 and FD on height, weight, and neck circumference yielded no significant overall effects at an alpha level of 0.01. This was true both for regressions using subjects' mean values across all 23 vowel sounds produced and for regressions using subjects' mean values for only the three schwa vowels. Multiple regressions using F_0 and the individual formant frequenices (i.e., $F1-F4$) also failed to identify any significant effects.

For males, multiple regressions using the combination of F_0 and FD yielded a statistically significant overall effect for height but not for either weight or neck circumference. This pattern was the same for regressions using subjects' means for all vowels and using their means for only the schwa vowels. In both vowel-type comparisons, the regression of acoustic features on subjects' weights yielded P values that might be regarded as approaching significant levels (0.068 and 0.084). However, in both cases the adjusted R^2 values were low (adj-$R^2=0.105$ and 0.093, respectively) by comparison to the same analyses on height (adj-$R^2=0.306$ and 0.270, respectively). In the case of height, the statistically significant effects observed both for all vowels and for only the schwa vowels were due to FD but not F_0.

Follow-up regression tests in males using subjects' F_0 and the frequencies of each of the first four formants again yielded a statistically significant overall effect for height but not either weight or neck circumference in both vowel-type comparisons. For all vowels combined, the result was attributable to the effect of only $F4$. For the schwa vowels, the result was attributable to the effects of the F_0 and all four formant frequencies, with the strongest effect being for $F4$.

These variable effects across males and females and within males across the different acoustic features are illustrated in Fig. 3, which provides scatterplots comparing the height of individual males and females to their respective F_0 and formant frequency values for the case of schwa vowels.

Overall, there were no obvious relationships between voice acoustics and body size within adult females, whether height, weight, or neck circumference. In males, the effects were clear only for height and were strongest for formants, particularly $F4$. Effects for males were slightly better for schwa vowels than for the average of all vowels produced, although the effects were clear for both. The latter outcome is not too surprising given that subjects' formant values averaged across all vowels were very similar to those for their schwa vowels, suggesting that speakers' average and neutral vocal-tract configurations were similar.

IV. GENERAL DISCUSSION AND IMPLICATIONS

A. Relationships between body size, vocal-tract anatomy, and voice acoustics

Comparisons of body size and voice acoustics in adult male and female humans and baboons point to significant deviations from strictly neutral vocal allometry. In both species, the F_0 difference between males and females exceeded any measured difference in body size between them. In humans, much of the excess F_0 dimorphism can be traced directly to a dimorphism in vocal-fold length that itself greatly exceeds the body size differences between males and females (Hirano *et al.*, 1983; Titze, 1989). The same is probably true of the excess F_0 dimorphism in baboons, although there are no systematic data on vocal-fold length in this species to confirm it. It was also the case in humans that F_0 variation did not track body-size variation within either sex. There was some indication that it might track height in males, but the

TABLE III. Results of multiple regression tests of F_0 and FD (or F_0 and individual formant frequencies, $F1-F4$) on body size dimensions (height, weight, and neck circumference) within (a) females and (b) males. Results are presented for analyses using the average of all vowels combined as well as for analyses using the average of only the schwa vowels.

(a) Females	Acoustic features[a]	Body size	$Adj\text{-}R^2$	F	P
F_0+FD					
All vowels		Height	*0.000*	*0.45*	*0.639*
		Weight	*0.031*	*1.51*	*0.237*
		Neck	*0.092*	*2.61*	*0.090*
Schwa vowels		Height	*0.000*	*0.71*	*0.499*
		Weight	*0.053*	*2.15*	*0.134*
		Neck	*0.037*	*1.41*	*0.259*
$F_0+F1-F4$					
All vowels		Height	*0.000*	*0.80*	*0.562*
		Weight	*0.017*	*1.11*	*0.377*
		Neck	*0.083*	*1.58*	*0.199*
Schwa vowels		Height	*0.000*	*0.81*	*0.554*
		Weight	*0.036*	*1.24*	*0.318*
		Neck	*0.069*	*1.47*	*0.231*
(b) Males	Acoustic features[a]	Body size	$Adj\text{-}R^2$	F	P
F_0+FD					
All vowels	FD[b]	Height	*0.306*	*8.28*	*0.001*
		Weight	*0.105*	*2.94*	*0.068*
		Neck	*0.079*	*2.41*	*0.106*
Schwa vowels	FD[b]	Height	*0.270*	*7.11*	*0.003*
	F_0[c]				
		Weight	*0.093*	*2.68*	*0.084*
		Neck	*0.069*	*2.22*	*0.126*
$F_0+F1-F4$					
All vowels	$F4$[c]	Height	*0.339*	*4.38*	*0.005*
		Weight	*0.161*	*2.26*	*0.075*
		Neck	*0.082*	*1.59*	*0.196*
Schwa vowels	$F4$[b]	Height	*0.510*	*7.86*	*0.000*
	F_0, $F1$, $F2$[d]				
	$F3$[c]				
		Weight	*0.089*	*1.64*	*0.182*
		Neck	*0.029*	*1.20*	*0.336*

[a]Acoustic features in each significant regression.
[b]P value <0.01.
[c]P value <0.10.
[d]P value <0.05.

relationship was weak. Several previous studies have similarly failed to find robust body-size effects for F_0 within sexes both in humans and in some other primate and mammal species (Kunzel, 1989; McComb, 1991; Masataka, 1994; van Dommelen and Moxness, 1995; Collins, 2000).

One functional explanation for the mismatch between F_0 and body size in both species follows the body-size exaggeration hypothesis (Morton, 1977; Fitch, 1999, 2000), namely that it reflects deceptive use of F_0 to signal a body size that is larger (or smaller) than reality. It is certainly true in humans that speakers can dynamically adjust voice pitch in different circumstances to project an acoustic ''image'' of larger or smaller size (or their social correlates, greater or lesser threat), sometimes to extreme extents such as when talking to babies or pets. However, for this to account for the differences in normative pitch profiles and larynx size between males and females would require a sustained evolutionary history of successful deception of listeners in spite of perfectly good visual cues to a speaker's true size, which seems unlikely.

Another possibility is that F_0 variation is not about size *per se*, but instead reflects physiological dimensions more closely aligned with sex variation (i.e., relative ''maleness'' and ''femaleness'') that are only indirectly related to body size. It is known that there are androgen receptors in the larynx of several species including baboons and humans, that the onset of voice-pitch changes in males during adolescence parallels the onset of surging testosterone independently of body growth spurts, and that the F_0 of adult males correlates with salivary testosterone levels (Saez and Martin, 1976; Aufdemorte *et al.*, 1983; Hollien *et al.*, 1994; Dabbs and Mallinger, 1999). Female sex hormones are also known to influence vocal-fold dynamics in adult women (e.g., Abitbol *et al.*, 1999). Taken together, such findings suggest that much of the F_0 variation both between and within sexes might be tracking (and signaling) the active products of sexual physiology—that can vary continuously within as well as between sexes and that have a role in, but do not strictly determine, body size.

What is clear is that the growth programs affecting larynx size (and resulting F_0 profiles) are at least partially dissociated from the more general growth programs that affect

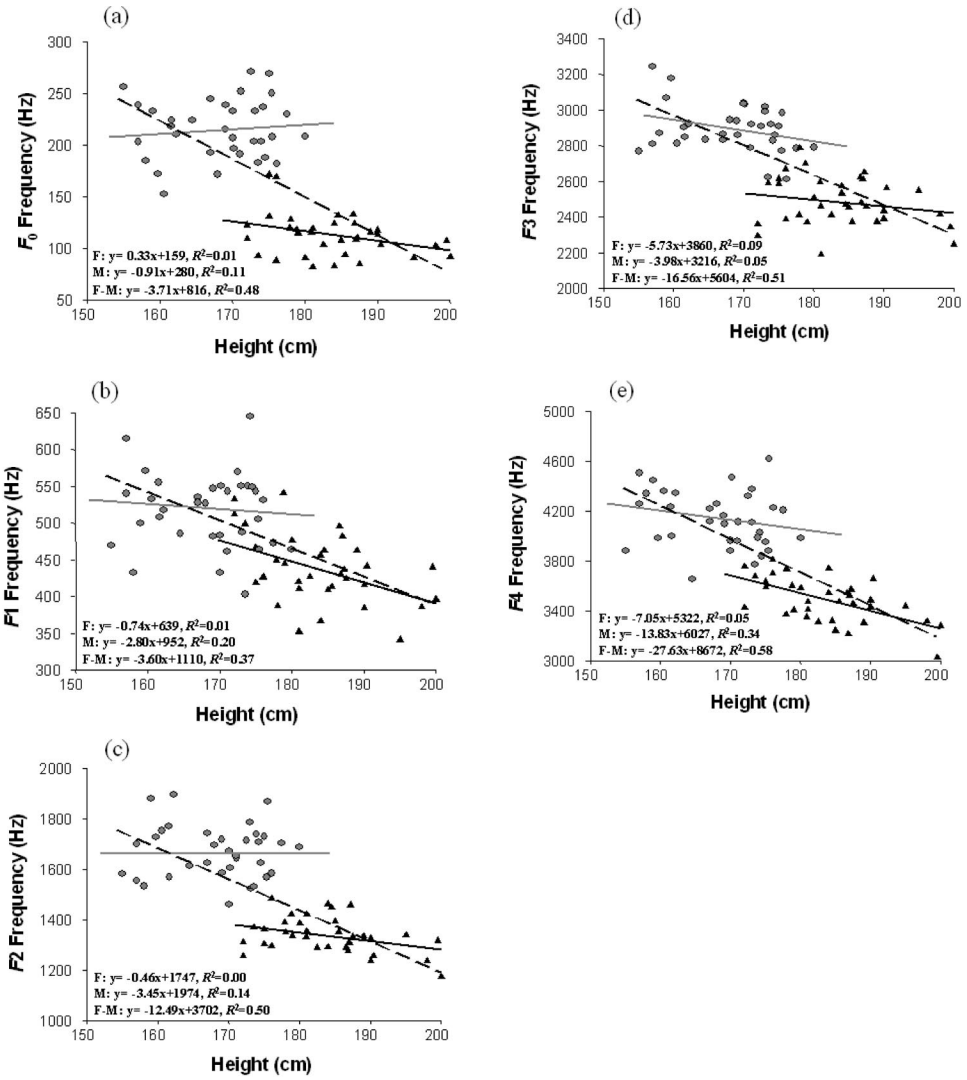

FIG. 3. Scatterplots illustrating the relationship between height and (a) the F_0 and (b)–(e) the formant frequencies of schwa vowels produced by human males (black triangles) and females (gray circles). In each scatterplot, a regression equation and R^2 value is given for separate analyses conducted within each sex (F = female; M = male). In each scatterplot, a third regression line (dashed), regression equation, and R^2 value is included that reflects a between-sex analysis (F–M) and illustrates the statistical artifacts that arise when the data are collapsed across males and females. Predictably, the regression slopes are much steeper and the R^2 values are much higher for the between-sex analyses than they are for those conducted within sexes.

true overall body size in both species. By extension, the hypertrophied larynx and disproportionately deep F_0 of human males compared to females is evidently not uniquely facilitated by humans' descended larynx that positions it outside the bony constraints of the skull. The same, indeed more extreme, phenomenon of disproportionately low F_0 was found in male baboons despite the positioning of their larynx high in the vocal tract and within the bony confines of the skull. Thus, it appears that the general capacity for dramatic laryngeal growth is neither entirely constrained by a location within the confines of the skull, nor necessarily facilitated only by descent of the larynx outside the skull boundaries.

In view of past mixed results on the scaling of F_0 with body size, Fitch (1997) proposed that formants should scale far more reliably with overall body size than does F_0. The argument is that formants reflect the size of a speaker's vocal-tract cavities which are constrained by the size and shape of the surrounding bony anatomy (i.e., skull size and shape; neck length), and that these in turn are determined by general growth processes affecting overall body size. This is a wholly intuitive proposal for which Fitch has provided some supporting evidence in humans, in one other species of monkey, and in domestic dogs where he has reported very strong correlations (e.g., $r = 0.90$) between body size (height or weight) and either voice formants or vocal tract length measurements obtained from imaging techniques (Fitch, 1997; Fitch and Giedd, 1999; Riede and Fitch, 1999). However, in each case, the data were collapsed across both sexes and all age classes (i.e., lumping together data from infant, juvenile, adolescent, and adult males and females), or across different dog breeds, which artificially inflates the size of the correlations. As a result, the very high correlation coefficients obtained seriously overestimated the extent to which variation in vocal-tract length among subjects was due to their body-size differences *per se* as opposed to their marked sex and age differences (or breed differences in the case of dogs).

Nevertheless, the results of the present study partially

support Fitch's general proposal, even though the relationships are not as clear as might be expected. In baboons, sex differences in formants were broadly consistent with body-size dimorphism: males produced lower formants and were larger bodied than females. The formant dimorphism also approximated expected dimorphism in areal dimensions between the sexes, which is plausible given the sex differences in both the length and width of the muzzle in baboons, although more detailed data on muzzle dimensions as well as matched body size and acoustic data on the same individuals are needed to test this properly.

In humans, sex differences in formants were also broadly consistent with body-size dimorphism, but the formant differences were substantially greater than would be expected based on the height difference between males and females. However, the formant dimorphism did exactly match the difference in overall vocal-tract length that has been reported for adult males and females (Fant, 1966; Goldstein, 1980). This outcome tends to confirm the link between observable formant profiles and vocal-tract dimensions generally. However, it also confirms that the growth programs that determine vocal-tract cavity dimensions (as with the larynx) can be at least partially decoupled from those that determine overall body size. This result may not be too surprising considering the diversity of pressures that can influence the growth of various bony structures of the skull and face impinging on vocal-tract anatomy quite independently of body size. As a result, it may be fairly common to find only a rather loose connection between adult vocal-tract dimensions and body size *per se*.

This point is further confirmed by analyses within sexes in humans, where formant variation was correlated only with height and only in males and not in females, demonstrating that, however intuitive they might seem, the relationships between body size, vocal-tract dimensions, and voice acoustics are not obligatory.

The fact that formants did correlate with height in males, however, provides some support for Fitch's hypothesis. Indeed, this asymmetric outcome suggests that males but not females might be under specific pressure to provide reliable voice cues to body size. This is certainly consistent with predictions from evolutionary theory about the particular importance of body size in social and sexual competition for male as compared to female mammals. It is also consistent with the finding that the sex difference in pharyngeal cavity length in humans originates at puberty, with additional pharyngeal extension occurring in males at this stage just when body size cuing in the service of social and sexual competition is likely to become especially important (Fitch and Giedd, 1999; Lieberman *et al.*, 2001). Of course, it remains to be established whether the observed formant cues to body size are actually perceptually salient to listeners as would be required by the hypothesis. This is an especially important caveat given that the strongest formant effects obtained here were for $F4$, which was the highest formant measured and therefore necessarily also the weakest and potentially least salient formant to listeners.

B. Implications for theories of speech origins

These issues also bear centrally on theories of speech origins. One of the most popular hypotheses here is Lieberman's (1968, 1984) proposal that human speech and language hinge on a descended larynx. Lieberman has argued that a larynx that lies low in the vocal tract by comparison to closely related primate species creates a uniquely large pharyngeal cavity which in turn greatly expands the range of formant contrasts that can be produced and that are so central to modern language. On this view, the origins of language can be dated in human prehistory by the appearance of a descended larynx in the human fossil record. This is a compelling thesis and an exceptionally productive one because it provides a potential anatomical landmark for recognizing language behavior in our ancestors which is otherwise difficult to infer from only fossilized remains.

There have been numerous challenges to the details of Lieberman's proposal (e.g., Falk, 1975; Boe *et al.*, 2002), but the most global of these has come recently from Fitch (2000). Fitch argues that a descended larynx lengthens the vocal tract, thereby lowering the formant frequencies and signaling larger body size, with attendant advantages in social competition. Although a descended larynx could still facilitate language, through the mechanism proposed by Lieberman, Fitch argues that the original pressure driving laryngeal descent was not actually language but body-size cuing because formant-related language benefits accrue only once the larynx is fully descended, and it is highly unlikely that it descended all at once in a single step. In contrast, the formant-related body-size-cuing benefits of a descended larynx accrue throughout the descent process (an important requirement of sustained directional evolutionary change) with an incrementally lower larynx yielding incrementally lower formant frequencies which advertise progressively larger body size. What keeps the system honest throughout the descent process (an additional important requirement of sustained change) is the correlation between voice formants, vocal-tract length, and actual body size, which at the lower limits is imposed by the impossibility of additional laryngeal descent without serious risk of choking.

In short, humans' descended larynx reflects a history of sustained selection for reliable body-size cuing, and its descended position was only secondarily co-opted for a language function. If true, this would also mean that a descended larynx in the fossil record is no longer a reliable marker of language ability in prehumans as Lieberman proposes.

Fitch has provided some indirect support for his proposal in the phenomenon of permanent and dramatic tracheal elongation in certain bird species that are argued to benefit specifically from body-size exaggeration, and in the dynamic laryngeal retraction, or descent, that occurs during male vocal courtship displays in some deer species that yields lower formant frequencies that nevertheless correlate with male size (Fitch, 1999; Fitch and Reby, 2001; Reby and McComb, 2003).

Some of our own results for humans showing a correlation between formant frequencies and body size in males are also consistent with Fitch's proposal. However, the lack of

any correlations in human females necessarily weakens it. To account for this difference between males and females, one could argue that the relationship between body size and vocal-tract length also holds for adult females but that it is not actually manifest in female formant profiles because women behaviorally modify vocal production in ways that obscure the correlation to voice formants (cf. Whiteside, 2001). However, the fact that the average formant profiles observed for males and females in this study nicely matches reports of the average difference in vocal-tract length between them tends to discount this possibility.

Alternatively, one could argue that the relationships between body size, vocal-tract length, and voice formants used to hold for females in addition to males, but that the relationships in females broke down at some point in human prehistory when the larynx descended to a point where the additional choking risk to females exceeded any modest benefits that they gained through reliable size signaling. Or, it could perhaps be argued that the body-size advantages never applied to females but that female laryngeal descent still occurred because it was leashed to laryngeal descent occurring in males for purposes of body-size cuing. Neither of these two possibilities is inherently parsimonious, however.

Clearly, there are problems with both general scenarios for the evolution of human vocal anatomy and resulting voice acoustics and the particular functional selective pressures that have shaped them. However, their important ramifications both for theories of speech origins and for our understanding of the anatomical bases of variable speech acoustics and the perceptual processes that must effectively normalize them make them critical issues to resolve with future research. In doing this, we will probably need to more fully integrate a number of additional hypotheses for the evolution of human vocal-tract anatomy, some of which are unrelated to either speech or body-size cuing functions *per se*.

For example, Owren (1996) has proposed an ''acoustic signature'' hypothesis of human laryngeal descent, according to which the larynx descended as a part of a compensatory response to facial foreshortening occuring during human evolution (Lieberman, 1998). This response functioned to maintain a constant vocal-tract length and thereby preserve coevolved systems for the production and perception of formant-related cues to individual and kin identity that are hypothesized to have been of critical importance to social communication in our primate ancestors (Rendall, 1996). Alternatively, Nishimura (2003; Nishimura *et al.*, 2003) has offered a two-step model of laryngeal descent that gives priority to the swallowing (deglutition) function of the larynx and the tightly coordinated hyo-laryngeal dynamics needed to accomplish this, an idea that derives additional support from recent longitudinal data on the trajectory of laryngeal descent that occurs during early human development which also appears to be optimized for efficient deglutition rather than linguistic competence (Lieberman *et al.*, 2001). Ultimately, these and other scenarios will need to be thoroughly integrated if we are to arrive at a comprehensive account of the evolution of human vocal-tract anatomy and voice acoustics and their ramifications for systems of speech production and perception.

ACKNOWLEDGMENTS

We are grateful to the Office of the President and the Department of Wildlife and National Parks in the Republic of Botswana and to the Department of Home Affairs and the Cape Nature Conservancy in South Africa, as well as to R. Seyfarth and D. Cheney, and P. Henzi and L. Barrett in these two countries, respectively. We also thank Professor Anders Löfqvist and anonymous reviewers for comments which improved the manuscript. Research was approved by the Animal Welfare and Human Subjects Research Committees of the University of Lethbridge, and was supported by grants to D.R. from the Natural Sciences and Engineering Research Council of Canada, the L.S.B. Leakey Foundation, and the University of Lethbridge.

Abercrombie, D. (**1967**). *Elements of General Phonetics* (Aldine, Chicago).

Abitbol, J., Abitbol, P., and Abitbol, B. (**1999**). ''Sex hormones and the female voice,'' J. Voice **13**, 424–446.

Andrew, R.J. (**1976**). ''Use of formants in the grunts of baboons and other nonhuman primates,'' Ann. N.Y. Acad. Sci. **280**, 673–693.

Apostol, L., Perrier, P., and Bailly, G. (**2004**). ''A model of acoustic interspeaker variability based on the concept of formant-cavity affiliation,'' J. Acoust. Soc. Am. **115**, 337–351.

Aufdemorte, T.B., Sheridan, P.J., and Holt, G.R. (**1983**). ''Autoradiographic evidence of sex steroid receptors in the laryngeal tissues of the baboon (*Papio cynocephalus*),'' Laryngoscope **93**, 1607–1611.

Bachorowski, J.-A., and Owren, M.J. (**1999**). ''Acoustic correlates of talker sex and individual talker identity are present in a short vowel segment produced in running speech,'' J. Acoust. Soc. Am. **106**, 1054–1063.

Barrett, L., and Henzi, S.P. (**1997**). ''An interpopulation comparison of body weight in chacma baboons,'' S. Afr. J. Sci. **93**, 436–438.

Boë, L.-J., Heim, J.-L., Honda, K., and Maeda, S. (**2002**). ''The potential Neandertal vowel space was as large as that of modern humans,'' J. Phonetics **30**, 465–484.

Bricker, P.D., and Pruzansky, S. (**1976**). ''Speaker recognition,'' in *Contemporary Issues in Experimental Phonetics*, edited by N.J. Lass (Academic, New York), pp. 295–326.

Collins, S.A. (**2000**). ''Men's voices and women's choices,'' Anim. Behav. **60**, 773–780.

Dabbs, Jr., J.M., and Mallinger, A. (**1999**). ''High testosterone levels predict low voice pitch among men,'' Personality Individ. Diff. **27**, 801–804.

Davies, N.B., and Halliday, T.R. (**1978**). ''Deep croaks and fighting assessment in toads, *Bufo bufo*,'' Nature (London) **274**, 683–685.

ESPS/WAVES+© (**1997**). Entropic Research Laboratory, Inc., 600 Pennsylvania Ave. S.E. Suite 202, Washington, D.C., 20003.

Falk, D. (**1975**). ''Comparative anatomy of the larynx in man and the chimpanzee: Implications for language in Neanderthal,'' Am. J. Phys. Anthropol. **43**, 123–132.

Fant, G. (**1966**). ''A note on vocal tract size factors and non-uniform F-pattern scaling,'' Speech Transactions Laboratory Quarterly Progress and Status Report 4, 22–30.

Fitch, W.T. (**1997**). ''Vocal tract length and formant frequency dispersion correlate with body size in rhesus macaques,'' J. Acoust. Soc. Am. **102**, 1213–1222.

Fitch, W.T. (**1999**). ''Acoustic exaggeration of size in birds by tracheal elongation: Comparative and theoretical analyses,'' J. Zool. **248**, 31–49.

Fitch, W.T. (**2000**). ''The evolution of speech: A comparative review,'' Trends Cogn. Sci. **4**, 258–267.

Fitch, W.T., and Giedd, J. (**1999**). ''Morphology and development of the human vocal tract. A study using magnetic resonance imaging,'' J. Acoust. Soc. Am. **106**, 1511–1522.

Fitch, W.T., and Hauser, M.D. (**1995**). ''Vocal production in nonhuman primates: Acoustics, physiology, and functional constraints on 'honest' advertisement,'' Am. J. Primatol **37**, 179–190.

Fitch, W.T., and Hauser, M.D. (**2002**). ''Unpacking 'honesty': Vertebrate vocal production and the evolution of acoustic signals,'' in *Acoustic Communication*, edited by A.M. Simmons, R.R. Fay, and A.N. Popper (Springer, New York), pp. 65–137.

Fitch, W.T., and Reby, D. (**2001**). ''The descended larynx is not uniquely human,'' Proc. R. Soc. London, Ser. B **268**, 1669–1675.

Goldstein, U.G. (**1980**). ''An articulatory model for the vocal tracts of growing children,'' Ph.D. dissertation, Massachusetts Institute of Technology, Cambridge, MA.
González, J. (**2004**). ''Formant frequencies and body size of a speaker: A weak relationship in adult humans,'' J. Phonetics **32**, 277–287.
Greisbach, R. (**1999**). ''Estimation of speaker height from formant frequencies,'' Forensic Linguis. **6**, 265–277.
Hamill, P.V.V., Drizd, T.A., Johnson, C.L., Reed, R.B., Roche, A.F., and Moore, W.M. (**1979**). ''Physical growth: National Center for Health Statistics percentiles,'' Am. J. Clin. Nutr. **32**, 607–629.
Hillenbrand, J., Getty, L.A., Clark, M.J., and Wheeler, K. (**1995**). ''Acoustic characteristics of American English vowels,'' J. Acoust. Soc. Am. **97**, 3099–3111.
Hirano, M., Kurita, S., and Nakashima, T. (**1983**). ''Growth, development and aging of human vocal folds,'' in *Vocal Fold Physiology: Contemporary Research and Clinical Issues*, edited by D.M. Bless and J.H. Abbs (College-Hill, San Diego), pp. 22–43.
Hollien, H., Green, R., and Massey, K. (**1994**). ''Longitudinal research on adolescent voice change in males,'' J. Acoust. Soc. Am. **96**, 2646–2654.
Johnson, K., and Mullenix, J.W. (**1997**). *Talker Variability in Speech Processing* (Academic, New York).
Kunzel, H.J. (**1989**). ''How well does average fundamental frequency correlate with speaker height and weight,'' Phonetica **46**, 117–125.
Ladefoged, P., and Broadbent, D.E. (**1957**). ''Information conveyed by vowels,'' J. Acoust. Soc. Am. **39**, 98–104.
Lass, N.J., Phillips, J.K., and Bruchey, C.A. (**1980b**). ''The effect of filtered speech on speaker height and weight identification.'' J. Phonetics **8**, 91–100.
Lass, N.J, Kelley, D.T., Cunningham, C.M., and Sheridan, K.J. (**1980a**). ''A comparative study of speaker height and weight identification from voices and whispered speech,'' J. Phonetics **8**, 195–204.
Lieberman, D.E. (**1998**). ''Sphenoid shortening and the evolution of modern human cranial shape,'' Nature (London) **393**, 158–162.
Lieberman, P. (**1967**). *Intonation, Perception and Language* (MIT Press, Cambridge, MA).
Lieberman, P. (**1968**). ''Primate vocalizations and human linguistic ability,'' J. Acoust. Soc. Am. **44**, 1574–1584.
Lieberman, P. (**1984**). *The Biology and Evolution of Language* (Harvard University Press, Cambridge, MA).
Lieberman, P. (**1986**). ''Some aspects of dimorphism and human speech,'' in *Sexual Dimorphism in Living and Fossil Primates*, edited by M. Pickford and B. Chiarelli (Il Sedicesimo, Italy), pp. 67–75.
Lieberman, P., Klatt, D.H., and Wilson, W.H. (**1969**). ''Vocal tract limitations on the vowel repertoires of rhesus monkeys and other nonhuman primates,'' Science **164**, 1185–1187.
Lieberman, D.E., McCarthy, R.C., Hiiemae, K.M., and Palmer, J.B. (**2001**). ''Ontogeny of postnatal hyoid and larynx descent in humans,'' Arch. Oral Biol. **46**, 117–128.
Masataka, N. (**1994**). ''Lack of correlation between body size and frequency of vocalizations in young female Japanese macaques (*Macaca fuscata*),'' Folia Primatol. **63**, 115–118.
McComb, K.E. (**1991**). ''Female choice for high roaring rates in red deer, *Cervus elaphus*,'' Anim. Behav. **41**, 79–88.
McFadden, D., and Bracht, M.S. (**2003**). ''The relative lengths and weights of metacarpals and metatarsals in baboons,'' Horm. Behav. **43**, 347–355.
Morton, E.S. (**1977**). ''On the occurrence and significance of motivation-structural rules in some birds and mammal sounds,'' Am. Nat. **111**, 855–869.
Nearey, T. (**1989**). ''Static, dynamic, and relational properties in vowel perception,'' J. Acoust. Soc. Am. **85**, 2088–2113.
Nishimura, T. (**2003**). ''Comparative morphology of the hyo-laryngeal complex in anthropoids: Two steps in the evolution of the descent of the larynx,'' Primates **44**, 41–49.
Nishimura, T., Mikami, A., Suzuki, J., and Matsuzawa, T. (**2003**). ''Descent of the larynx in infant chimpanzees,'' Proc. Natl. Acad. Sci. U.S.A. **100**, 6930–6933.
Nordström, P.-E. (**1977**). ''Female and infant vocal tracts simulated from male area functions,'' J. Phonetics **5**, 81–92.
Owren, M.J. (**1996**). ''An 'acoustic signature' model of speech evolution,'' J. Acoust. Soc. Am. **99**, 2558.
Owren, M.J., and Linker, C.D. (**1995**). ''Some analysis methods that may be useful to acoustic primatologists,'' in *Current Topics in Primate Vocal Communication*, edited by E. Zimmermann, J.D. Newman, and U. Jurgens (Plenum, New York), pp. 1–27.
Owren, M.J., Seyfarth, R.M., and Cheney, D.L. (**1997**). ''The acoustic features of vowel-like grunt calls in chacma baboons (*Papio cynocephalus ursinus*): Implications for production processes and functions,'' J. Acoust. Soc. Am. **101**, 2951–2963.
Peterson, G.E., and Barney, H.L. (**1952**). ''Control methods used in a study of the vowels,'' J. Acoust. Soc. Am. **24**, 175–184.
Reby, D., and McComb, K. (**2003**). ''Anatomical constraints generate honesty: Aacoustic cues to age and weight in the roars of red deer stags,'' Anim. Behav. **65**, 519–530.
Rendall, D. (**1996**). ''Social communication and vocal recognition in free-ranging rhesus monkeys (*Macaca mulatta*),'' Ph.D. dissertation, University of California-Davis.
Rendall, D. (**2003**). ''Acoustic correlates of caller identity and affect intensity in the vowel-like grunt vocalizations of baboons,'' J. Acoust. Soc. Am. **113**, 3390–3402.
Rendall, D., Cheney, D.L., and Seyfarth, R.M. (**2000**). ''Proximate factors mediating 'contact' calls in adult female baboons and their infants,'' J. Comp. Psychol. **114**, 36–46.
Rendall, D., Owren, M.J., Weerts, E., and Hienz, R.J. (**2004**). ''Sex differences in the acoustic structure of vowel-like grunt vocalizations in baboons and their perceptual discrimination by baboon listeners,'' J. Acoust. Soc. Am. **115**, 411–421.
Rendall, D., Seyfarth, R.M., Cheney, D.L., and Owren, M.J. (**1999**). ''The meaning and function of grunt variants in baboons,'' Anim. Behav. **57**, 583–592.
Richman, B. (**1976**). ''Some vocal distinctive features used by gelada monkeys,'' J. Acoust. Soc. Am. **60**, 718–724.
Riede, T., and Fitch, W.T. (**1999**). ''Vocal tract length and acoustics of vocalization in the domestic dog, *Canis familiaris*,'' J. Exp. Biol. **202**, 2859–2869.
Sachs, J., Lieberman, P., and Erikson, D. (**1972**). ''Anatomical and cultural determinants of male and female speech,'' in *Language Attitudes: Current Trends and Prospects*, edited by R.W. Shuy and R.W. Fasold (Georgetown University Press, Washington D.C.), pp. 74–84.
Saez, S.J., and Martin, P.M. (**1976**). ''Androgen receptors in human pharyngo-laryngeal mucosa and pharyngo-laryngeal epithelium,'' J. Steroid Biochem. **7**, 919–921.
Stevens, K.N. (**1998**). *Acoustic Phonetics* (MIT Press, Cambridge, MA).
Titze, I.R. (**1989**). ''Physiologic and acoustic differences between male and female voices,'' J. Acoust. Soc. Am. **85**, 1699–1707.
van Dommelen, W.A., and Moxness, B.H. (**1995**). ''Acoustic parameters in speaker height and weight identification: Sex-specific behaviour,'' Lang. Speech **38**, 267–287.
Whiteside, S.P. (**2001**). ''Sex-specific fundamental and formant frequency patterns in a cross-sectional study,'' J. Acoust. Soc. Am. **110**, 464–478.
Zhinkin, N.I. (**1963**). ''An application of the theory of algorithms to the study of animal speech,'' in *Acoustic Behaviour of Animals*, edited by R.G. Busnel (Elsevier, Amsterdam), pp. 132–180.

Automatic classification and speaker identification of African elephant (*Loxodonta africana*) vocalizations

Patrick J. Clemins[a] and Michael T. Johnson
Speech and Signal Processing Laboratory, Marquette University, P.O. Box 1881, Milwaukee, Wisconsin 53233-1881

Kirsten M. Leong[b] and Anne Savage
Disney's Animal Kingdom, Lake Buena Vista, Florida 32830

(Received 27 February 2004; revised 26 October 2004; accepted 13 November 2004)

A hidden Markov model (HMM) system is presented for automatically classifying African elephant vocalizations. The development of the system is motivated by successful models from human speech analysis and recognition. Classification features include frequency-shifted Mel-frequency cepstral coefficients (MFCCs) and log energy, spectrally motivated features which are commonly used in human speech processing. Experiments, including vocalization type classification and speaker identification, are performed on vocalizations collected from captive elephants in a naturalistic environment. The system classified vocalizations with accuracies of 94.3% and 82.5% for type classification and speaker identification classification experiments, respectively. Classification accuracy, statistical significance tests on the model parameters, and qualitative analysis support the effectiveness and robustness of this approach for vocalization analysis in nonhuman species. [DOI: 10.1121/1.1847850]

PACS numbers: 43.80.Lb, 43.80.Ka [JAS] Pages: 956–963

I. INTRODUCTION

One major task in bioacoustic research is determining repertoires for various species and then correlating the different vocalizations with behavior (Berg, 1983; Cleveland and Snowdon, 1982; Poole *et al.*, 1988; Sjare and Smith, 1986a, b). Currently, many features used to determine the vocalization type are extracted by hand from spectrogram plots, introducing bias into the feature values. Improved feature extraction and automatic classification would drastically decrease the time spent analyzing, classifying, and segmenting vocalizations, as well as provide a method for unbiased feature extraction. In addition, automatic classification systems can sometimes identify acoustic patterns correlating to the psychological or physiological state of an animal that are not obvious from simple spectrogram measures.

In the field of bioacoustics, traditionally, animal vocalization analysis is done using statistical methods such as multivariate analysis of variance (MANOVA), discriminant function analysis, or principal components analysis (PCA) (Fristrup and Watkins, 1992; Leong *et al.*, 2002; Owren *et al.*, 1997; Riede and Zuberbühler, 2003; Sjare and Smith, 1986a). By incorporating these traditional methods with a classification system such as that presented here, it is possible to go beyond traditional hypothesis testing and build systems that will classify unknown vocalizations, find new types of vocalizations, and measure how the vocalizations vary within and across classes. One key benefit of this approach is that automatic classification methods can model and compensate for temporal variation of vocalization patterns, making better use of timing information than traditional whole-spectrogram measures.

Previous studies in automatic classification of animal vocalizations include substantial work in feature identification as well as a number of papers on complete classification systems. Fristrup and Watkins (1992) have created an analysis package, Acoustat, capable of automatically extracting 26 different features including median center frequency, bandwidth, and duration. Spectrograms are used to extract the majority of the features. Chesmore (2001) has implemented a complete automatic classification system that uses time-domain-based features and an artificial neural network (ANN) to classify the vocalizations of various species of insects. Also using an ANN-based classifier, Campbell *et al.* (2002) were able to identify individual sea lions by their calls with 71% accuracy using spectral value inputs. Other studies have compared various classification systems' ability to detect biological oceanic signals. These classification systems include ANNs, hidden Markov models (HMMs), and linear spectrogram correlator filters (Potter *et al.*, 1994; Mellinger and Clark, 1993). Finally, Anderson (1999) compared a HMM-based classification system against a dynamic time warping (DTW)-based system using a dataset consisting of two different species of bird song. His conclusion was that while the DTW system worked better with a small amount of training data, the HMM system was more robust to noise and more variable vocalizations.

Since the tasks of speaker identification and vocalization classification, common in bioacoustic analysis, correspond directly to common human speech processing tasks, existing speech processing algorithms can be adapted for application to animal vocalizations. Speech processing methods are attractive because of the large research effort that has been devoted to this field over the past 50 years, and because

[a]Electronic mail: patrick.clemins@marquette.edu
[b]Current affiliation: Department of Natural Resources, Cornell University, Ithaca, New York 14853.

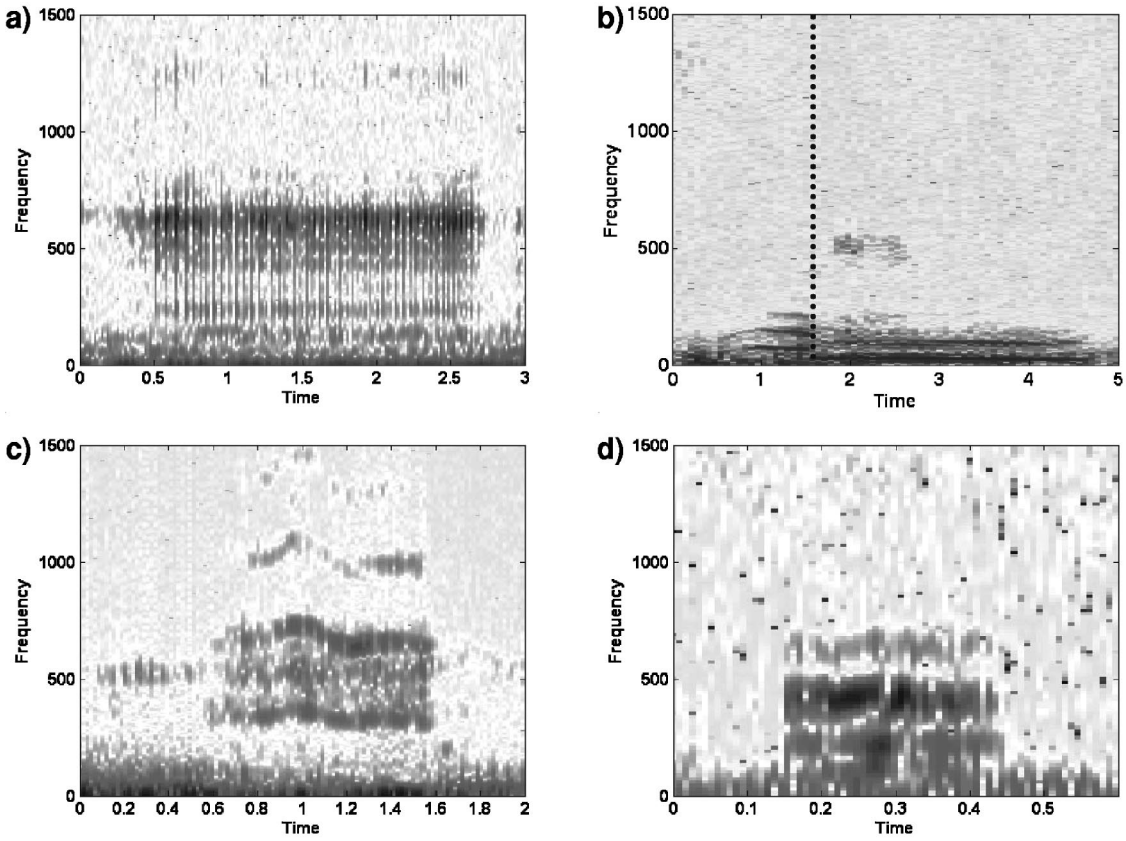

FIG. 1. Spectrograms of various types of elephant vocalizations. (a) Croak. (b) Rev from 1 to 1.5 s, then rumble. (c) Trumpet. (d) Snort.

current speech systems include robust feature extraction techniques coupled with optimal statistical classification models. Justification for the application of speech processing techniques to bioacoustics is supported by studies that suggest that most mammalian vocal production and reception systems are extremely similar (Bradbury and Vehrencamp, 1998; Titze, 1994). Therefore, it is reasonable to envision that the structure of human speech algorithms could be adapted to most mammalian species. Current state-of-the-art human speech systems can achieve classification accuracies of 92% for speech recognition systems on dictated speech (Padmanabhan and Picheny, 2002) and 85% for speaker identification on conversational telephone speech (Reynolds, 2002), although these accuracies can vary widely due to background noise characteristics or the number of speakers enrolled in the system.

While these systems show promise for use in the field of animal bioacoustics, there are challenges with animal vocalizations that include noise and label validity. Noise due to poor recording environments can greatly decrease classification accuracy, especially if the characteristics of the noise vary across the dataset or within individual recordings. Label validity relates to the accuracy and consistency of expert vocalization annotations. When identifying individual animals, it can sometimes be difficult to tell which member of a group is vocalizing even with visual inspection, and when annotating behavior or intended meaning, the animals' behavioral cues are often ambiguous.

African elephants (*Loxodonta africana*) have been extensively studied by researchers for several decades. There is a wealth of information on social dynamics, reproductive strategies, and modalities of communication that provides us with a detailed understanding of the behavioral ecology of this species in the wild. The vocalizations of the African elephant have been categorized using various schemes (Berg, 1983; Leong *et al.*, 2002; Poole *et al.*, 1988). Based on the assessment of spectrograms coupled with behavioral analysis, these studies have found that there are about ten different basic vocalization classes, including the rumble, rev, croak, snort, and trumpet. Many of these classes likely include subtypes. Example spectrograms of a few of these vocalization classes are shown in Fig. 1. The rumble, with much of its energy concentrated in the infrasound range as low as 12 Hz, is the most common vocalization (Leong *et al.*, 2002). The rumble is used to communicate between groups and within each family group. Playback studies have shown that the lower frequency characteristics of the rumble allow it to be used to communicate over long distances (Poole *et al.*, 1988; Langbauer *et al.*, 1991), and this function is often emphasized in discussions of this type of vocalization. Less common than the rumble are the rev, usually emitted when the elephant is startled and often followed by a rumble, and the croak, usually occurring in groups of two or three and commonly associated with the elephant sucking either water or air into the trunk (Leong *et al.*, 2002). Other vocalization classes include the snort, a higher frequency vocalization most generally used as a low-excitement greeting or request for contact, and the trumpet, produced when the elephant is excited (Berg, 1983; Leong *et al.*, 2002; Poole *et al.*, 1988). In addition, there are a few vocalization types that have been

observed, but are not used in the present study, including the cry, growl, roar, and bark (Berg, 1983).

This study documents a system, modeled after human speech recognition algorithms, for automatic feature extraction and classification of elephant vocalizations by type and speaker. This system is effective and robust in classifying elephant vocalizations and has implications as a technique to improve and broaden analysis of bioacoustic data.

II. DATA

A. Subjects

The subjects for this study are one male (18 years of age) and six adult nulliparous female (age range 19–30 years) African elephants housed at Disney's Animal Kingdom™, Lake Buena Vista, FL. These elephants are part of a long-term study of elephant communication that incorporates behavioral, hormonal, and vocal data to provide a detailed investigation on the behavioral and reproductive strategies of African elephants. Detailed information on the results of these studies can be found in Leong *et al.* (2002, 2003).

B. Data collection

For a detailed description of the methods used to record elephant vocalizations, see Leong *et al.* (2002, 2003). In brief, each elephant was fitted with a custom-designed collar that contained a microphone and a RF transmitter. Collars were designed, built, and packaged by Walt Disney World Co. Instrumentation Support Division of Ride and Show Engineering. Each collar transmitted to a separate channel of a TASCAM DA-38 8-channel DAT recorder (TEAC America Inc., Montebello, CA) and recorded on separated tracks of a SONY DARS-60MP Digital Audio Tape. The vocalizations were manually extracted from the DAT, passed through an antialiasing filter, and stored on a computer at a sampling rate of 7518 Hz.

The vocalizations are extracted off the DAT tapes using Real-Time Spectrogram (RTS) software (version 2.0) by Engineering Design, Belmont, MA. All vocalizations visually or acoustically identified were saved as individual files. For these experiments, a number of the clearer vocalizations were selected at random using signal-to-noise ratio and the lack of interference for the duration of the vocalization as the main criteria.

III. METHODS

A. Feature extraction

Features were extracted from the vocalizations using a moving Hamming window in a similar manner as in Clemins and Johnson (2003). Window sizes of 30 ms are typical for human speech, based on tradeoffs between frequency resolution and signal stationarity. Since African elephant vocalizations have a fundamental frequency range of 7 to 200 Hz (Langbauer, 2000), much lower than human speech, the window size was increased to 60 ms for the call classification experiment. A window size of 300 ms was used for the speaker identification experiment because only rumbles, the lowest frequency vocalizations, were used in this experiment. In all experiments, the frame rate was one-third the window size, so that consecutive windows overlap by two-thirds. This overlapping allowed improved temporal resolution for time alignment while still maintaining sufficient frequency resolution for spectral analysis.

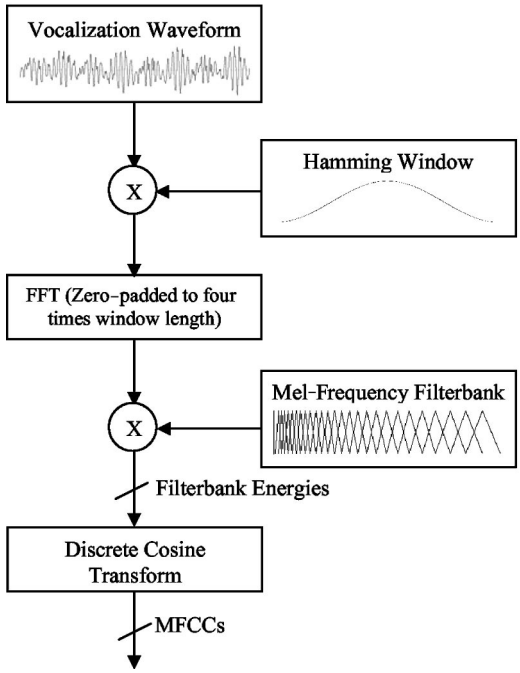

FIG. 2. Feature extraction process. A window of the vocalization waveform is manipulated to generate a number (12 in this set of experiments) of Mel-frequency cepstral coefficients.

Twelve Mel-frequency cepstral coefficients (MFCCs) plus log-energy were extracted from each moving window. Cepstral coefficients (Davis and Mermelstein, 1980) are extremely common spectral features in human speech processing and have a number of beneficial characteristics. These include the ability to capture vocal tract resonances but exclude excitation patterns, the usage of Euclidian distance between sets of coefficients which directly relates to log-spectral distances, and the tendency for coefficients to be largely uncorrelated which makes them well suited for statistical pattern recognition models. The signal processing basis for the cepstral representation is based on the source-filter model of human speech, which also has been used recently to describe the vocal production systems of many different animal species (Fitch, 2003). As shown in the block diagram of Fig. 2, MFCCs were derived by first computing the fast Fourier transform (FFT) of each window. Following this, the frequency axis was warped to the Mel-scale by multiplying the spectrum with a series of Mel-spaced triangular filters. The use of a Mel-spaced frequency scale is supported by evidence that elephants, like humans, perceive frequencies on a logarithmic scale (Heffner and Heffner, 1982; Békésy, 1960). The energy from the frequency band filters was then used as input to a discrete cosine transform, whose output provides cepstral coefficients.

The Mel-frequency filter bank was adjusted to the range 10 to 2000 Hz for the call classification experiment and 10 to 150 Hz for the speaker identification experiment in order to focus on the part of the spectrum used by elephants in the

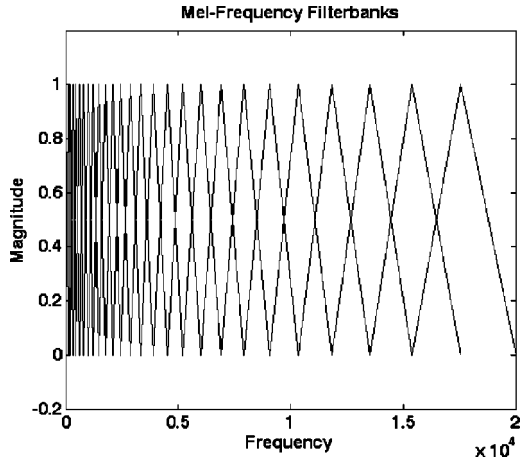

FIG. 3. Mel-frequency filterbanks. This plot shows 26 filter banks spaced between 10 and 2000 Hz using Mel-frequency spacing.

types of calls tested (Langbauer, 2000). A plot of the Mel-frequency filter bank is shown in Fig. 3. Since the signal was recorded at 7518 Hz and the desired filter bank range was only 10 to 150 Hz, the signal was zero padded to four times its original length before calculating the FFT in order to smooth the frequency spectrum.

B. Model parameters

A hidden Markov model (HMM) was used to model each of the different speakers or vocalization types. A HMM is a statistical state machine model, where states represent stationary spectral configurations and transitions between states represent spectral transition (Rabiner and Jaung, 1986). A diagram of a HMM is in Fig. 4. When modeling time series, the states of the HMM are linearly connected with state transitions from left to right, essentially representing time. A HMM is described by its transitions, the probabilities of transitioning from one state to the next, and its state distributions, the probabilities of a particular feature observation occurring while in that state. Each state's observation probability was represented by a multivariate Gaussian distribution. The task of a HMM is essentially to map a sequence of observations, here the sequence of MFCC features throughout a vocalization, onto a sequence of states, and determine the likelihood that the observations could have been generated by that model. To implement a classification task, multiple HMMs are trained, one for each class, and observation examples are classified according to the model yielding the highest likelihood.

HMMs are used in nearly all state-of-the-art speech recognition systems. They were a good choice for this task since they can model both the temporal and spectral differences between similar vocalizations. HMMs have the ability to perform nonlinear temporal alignment during the recognition and training process for vocalizations that may be similar but have different durations. Another reason for using HMMs is that because of their statistical basis, other statistical information, such as grammar models, can be easily incorporated. The programming toolkit used here for model implementation is HTK 3.1.1 from Cambridge University (2002). HTK provides a robust set of tools to implement HMM models, including the Baum-Welch Expectation Maximization algorithm (Baum *et al.*, 1970; Moon, 1996) for training and the Viterbi algorithm (Forney, 1973) for classifying new vocalizations. For these experiments, we used a three-state left-to-right HMM. A silence model was also trained and included before and after each vocalization model to account for varying amounts of leading and trailing silence regions.

IV. RESULTS

A. Vocalization type classification

The vocalization type classification experiment is analogous to an isolated-word speech recognition experiment. Five different African elephant vocalization types were classified in this experiment, using a total of 74 calls from six different animals. The goal of this experiment was to compare how well the HMM system outlined above performs on a classification task that can be easily done by human experts. Using the methodology outlined in the previous section, one HMM was trained for each vocalization type. To maximize training set size given the limited number of examples, leave-one-out cross validation was used for testing, so that each example was tested using models trained on all examples other than itself. The distribution of the data across speakers and vocalization types is shown in Fig. 5.

The confusion matrix for this experiment is shown in Fig. 6. The overall classification accuracy is 79.7%. As can be seen, rumbles were classified most accurately at 90.9% while croaks are classified with the least accuracy at 70.6%.

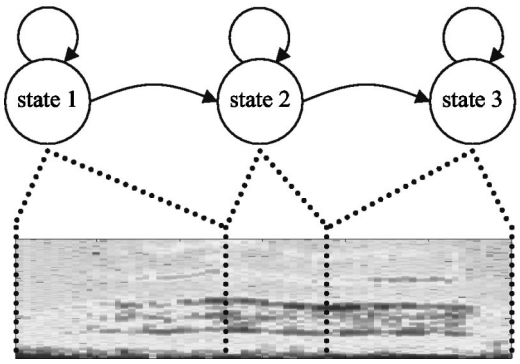

FIG. 4. A hidden Markov model (HMM). Each state of the HMM corresponds to the spectral characteristics of the animal vocalization as they vary in time. These characteristics are modeled by a multivariate Gaussian in each state.

		Vocalization Type				
		Croak	Rumble	Rev	Snort	Trumpet
Speaker	Bala	1 - 1	10 - 6	11 - 7	3 - 2	1 - 1
	Fiki	3 - 2	1 - 1	0 - 0	4 - 0	3 - 3
	Mackie	13 - 2	0 - 0	2 - 0	6 - 0	0 - 0
	Moyo	0 - 0	0 - 0	0 - 0	0 - 0	6 - 5
	Robin	0 - 0	0 - 0	0 - 0	2 - 1	4 - 4
	Thandi	0 - 0	0 - 0	1 - 0	2 - 0	1 - 0

FIG. 5. Distribution of the vocalizations by type and speaker for the vocalization type experiments. The first number in each cell is the number of calls in the complete dataset. The second number in each cell is the number of calls in the clean dataset.

One possible hypothesis for this is that rumbles are the longest vocalization type and therefore have more data windows on which to base a classification decision. Conversely, the snort is one of the shortest vocalizations and, thus, has less data with which to make a decision. It should also be noted that the rumbles are mainly from one speaker while the snorts are more evenly distributed across the speakers. This could also account for the discrepancy in classification accuracy between these two vocalization types.

This experiment was also run taking out vocalizations with poor quantization or poor signal to noise characteristics. All vocalizations were amplitude scaled to normalize their power; however, for this portion of the experiment, those vocalizations with a scale factor larger than 1100 were not included because of the poor quantization of the signal over the full range of possible values. A metric related to the signal to noise ratio, which we call the signal-to-noise characteristic (SNC), was calculated for each vocalization using the following formula:

$$\mathrm{SNC} = \frac{\mathrm{FrameEnergy}_{\max}}{\mathrm{FrameEnergy}_{\mathrm{ave}}}. \quad (1)$$

Those vocalizations with a SNC of less than 5.0 were not used in this portion of the experiment. The distribution of the clean vocalizations across speakers and vocalization type is shown in Fig. 5. Notice that croaks are more evenly distributed in the clean dataset as compared to the entire dataset. The classification matrix of the vocalization type classification experiment with poor quality vocalizations removed is shown in Fig. 6. Note that the classification accuracy of the system improved from 79.7% to 94.3% when only the 35 highest quality vocalizations are used.

In order to visualize the differences captured in each trained HMM, a 15-state HMM was trained for each class using 26 filter bank energies as features. Using these filter bank energies and the 15 temporal states, a spectrogram can be plotted which represents the ''maximum likelihood spectrogram'' for that vocalization. The maximum likelihood spectrogram for each of the vocalizations is shown in Fig. 7. The blockiness of the plots is a result of relatively low data resolution (15 states horizontally versus 26 filterbanks vertically). The larger low-frequency content of the rumble is evident from the spectrograms as well as the noisy nature of the croak whose spectrogram shows very little structure. The short duration of the snort and rev are also captured in these spectrograms.

While accuracy results demonstrate the ability of the learned models to generalize with respect to unseen test data, they do not provide a statistical measure of the difference between the classes. To test the statistical significance of these differences, a multivariate analysis of variance (MANOVA) test was performed on the 12 MFCC coefficients and log energy measure extracted from each frame of the vocalizations. The HMM state of each 13-parameter data vector was determined by a forced Viterbi alignment using trained HMM models for each vocalization class. In order to show that each state of the trained HMMs is statistically different, both the state and vocalization class were used as independent variables. The result of the MANOVA test using Wilk's Λ statistic was that the five HMMs represent statisti-

		Classification				
		Croak	Rumble	Rev	Snort	Trumpet
Label	Croak	12	2	2	1	0
	Rumble	0	10	1	0	0
	Rev	0	1	11	2	0
	Snort	0	1	2	13	1
	Trumpet	2	0	0	0	13

		Classification				
		Croak	Rumble	Rev	Snort	Trumpet
Label	Croak	5	0	0	0	0
	Rumble	0	7	0	0	0
	Rev	0	1	6	0	0
	Snort	0	1	0	2	0
	Trumpet	0	0	0	0	13

FIG. 6. Confusion matrices for vocalization type experiments. Left: Confusion matrix over all vocalizations in dataset. Accuracy: 59/74=79.73%. Right: Confusion matrix over clean vocalizations in dataset. Accuracy: 33/35=94.29%.

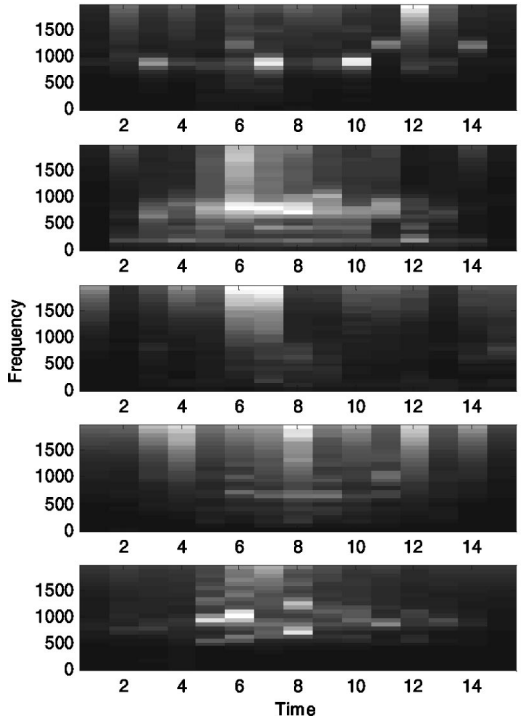

FIG. 7. Maximum likelihood spectrograms for vocalization type experiments. The plots show 26 filterbank energies on the vertical axis across 15 states of a trained HMM on the horizontal axis and graphically represent the HMM for each type of vocalization. From top to bottom: croak, rumble, rev, snort, trumpet.

cally different vocalizations ($F_{104,9483}=150.8, P<0.001$). A second MANOVA analysis was performed disregarding the state information and, therefore, with only one independent variable, vocalization class. This is equivalent to assuming that each class can be represented by a single state HMM. Using Wilk's Λ statistic, each single-state HMM represents statistically different vocalizations ($F_{52,9483}=342.5, P<0.001$).

B. Speaker identification

Speaker identification was performed on data collected in two separate social contexts. The first social context is where the single male was separate from the six females. The second social context is with the male and four of the females grouped together. All vocalizations in the speaker identification data set are rumbles, making it similar to a text-dependent task for human speech. This experiment was proposed to test the hypothesis that, like humans, each elephant has slightly different vocal characteristics that are consistent for certain vocalization types.

The classification matrix for this experiment is shown in Fig. 8. Again, leave-one-out cross validation was used to obtain the confusion matrices. The classification accuracy over the six different elephants was 82.5%. Some individuals were easier to distinguish than others, with accuracies ranging from a low of 75% to a high of 95%, implying that the degree of similarity between the elephants varies somewhat.

This theory is supported by the plot of the maximum likelihood spectrograms for each elephant in Fig. 9. Thandi and Fiki share similar characteristics such as a rather weak

		Classification					
		Bala	Fiki	Mackie	Moyo	Robin	Thandi
Label	Bala	19	0	0	0	1	0
	Fiki	1	23	0	0	0	6
	Mackie	0	0	13	0	0	1
	Moyo	1	0	0	13	2	1
	Robin	5	0	0	0	29	0
	Thandi	0	6	0	1	0	21

FIG. 8. Confusion matrix for speaker identification experiment. Accuracy: 118/143=82.52%.

fundamental frequency contour and the upper harmonic energy peak coming at the peak of the fundamental frequency contour. The spectrograms for Robin and Bala are also similar. Both spectrograms show a medium strength fundamental frequency contour and the peak in upper harmonic strength comes after the peak of the fundamental frequency contour.

When the vocalizations are separated by social context, recognition accuracies are comparable: 86.9% for vocalizations made while the male was separate from the females and 79.6% for vocalizations made while the male and four females were together. The similar accuracy numbers across social contexts would support a theory that the elephants do

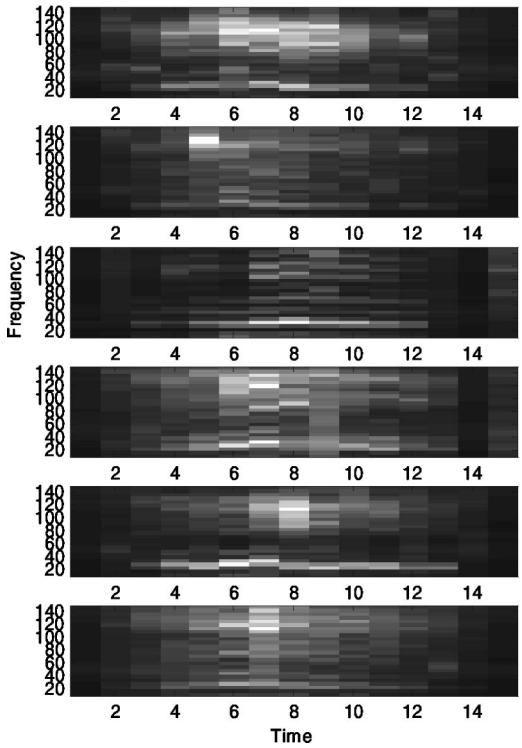

FIG. 9. Maximum likelihood spectrograms for speaker identification experiment. The plots show 26 filterbank energies on the vertical axis across 15 states of a trained HMM on the horizontal axis and graphically represent the HMM for each speaker. From top to bottom: Bala, Fiki, Mackie, Moyo, Robin, Thandi.

not vary their vocalizations significantly while in different social contexts and that the elephants do not use different vocalizations for varying audiences.

The MANOVA test using Wilk's Λ statistic over state and vocalization class showed that each model state represents statistically different vocalizations ($F_{130,13396} = 66.28, P < 0.001$). A MANOVA test using Wilk's Λ statistic without state information also showed that the HMMs represent statistically different vocalizations ($F_{65,13396} = 115.7, P < 0.001$).

Our hypothesis is supported by the performance of the classifier as well as by the MANOVA test showing that the models that represent each elephant are different with a high level of statistical significance. In addition, playback experiments demonstrated that elephants can distinguish vocalizations of familiar and nonfamiliar individuals and predicted that the elephants would have to be familiar with the voices of at least 100 adult females to make the observed discriminations (McComb *et al.*, 2000). One reason for the difference between animals could be the vocal tract structure. Although they are functionally identical, individual differences such as length of the vocal tract and shape of the nasal cavity affect the elephant's vocalizations in a consistent way. Another reason for the difference could be a factor that resembles human dialects or accents. Dialects have been found in various species (Dayton, 1990; Santivo, 2000), and, given that the origin of the elephants in this study is varied, the individuals could have developed accents that are present in a certain geographic region or among a specific family group.

V. CONCLUSIONS

This paper has explored the application of speech processing techniques to African elephant vocalizations. Using typical speech processing features and models, African elephant vocalization types were classified with an accuracy of 79.7% (94.3% when poorly quantized and poor SNR examples are removed) and speaker identification resulted in an accuracy of 88.1%. MANOVA tests on both experiments showed that the trained models for each class represent significantly different vocalizations.

There are a number of factors that affect the classification accuracies. The primary factor is the quality of the vocalizations, as is clearly seen in the call-type experiments where removing poor examples reduced error by 73% relative to including all vocalizations. In many bioacoustic studies, the vocalizations are categorized by human experts into groups of varying quality. Then, only the top few categories are used in the analysis. In this study, the lowest quality vocalizations were discarded by experts and a fully automated evaluation mechanism was used to further filter out all but the highest-quality vocalizations.

Another factor that could reduce classification accuracies is the use of suboptimal features to quantify the vocalizations. The features used in these experiments are common to speech processing and are based on human speech production and perception mechanisms. Researchers studying animal communication typically use different features than researchers studying human speech to analyze vocalizations. Features derived from spectrograms such as fundamental frequency and bandwidth are typically combined with time-domain features such as duration to generate a complete feature set. These features are also generally calculated over the entire vocalization instead of on a frame-by-frame basis. The incorporation of more long-term features and more detailed harmonic information is likely to improve the accuracy of the classifier, leading to a continued need to develop automated feature extraction methods for such measures.

Additionally, the validity of the data labels affects classification accuracy. It is well known that elephants use the same general class of vocalization to express different things (Berg, 1983; Poole *et al.*, 1988), as do many other species. For example, rumbles are used to maintain contact with other elephants and to signal that it is time for the herd to move. In addition, numerous other subtypes of rumbles based on behavior have been described (Poole, 2003). Although it is possible that one vocalization is used for all purposes, the variations in spectrogram features indicate that it is likely that the elephants use specific features of the rumbles as well as contextual and visual information sources to discern these different meanings. Thus, labeling rumbles by behavioral context may reveal acoustically distinct subtypes of rumbles, independent of caller identity. The challenge with this approach is determining which behavioral context to assign to which vocalization, as one vocalization often occurs in conjunction with a variety of behavioral events.

These experiments, particularly the call type classification experiment, show that this classification system is robust to noisy conditions. In the call type classification experiment, the system's robustness to noise was shown through a reasonable degradation of classification accuracy when noisy vocalizations were included in the dataset. If the system was not noise robust, the classification accuracy would have dropped off much more significantly when the nosier vocalizations were included in the dataset. The ability to achieve classification accuracies near 80% in both experiments using relatively noisy vocalizations also shows the robustness of the system. It is important to know that the noise-resilient features along with the statistical-based HMM both contribute to this robustness.

The methods presented here are applicable to a wide variety of species. Each animal has different vocal characteristics that make their vocalizations challenging to analyze; however, many of these different characteristics are similar in nature. Each species' sensitivity to different ranges of the frequency spectrum can be modeled by adjusting the filterbanks used to derive the MFCCs. Differences in structural complexity of the vocalizations can be modeled by varying the HMM topology or adding language models to represent these characteristics.

Speech systems provide an adaptable standard framework for many bioacoustic tasks and applications. Applying these systems in bioacoustics research allows us to effectively analyze animal vocalizations and has the potential to reveal more complex vocalization schemes than previously imagined such as complex interactions between harmonics and grammatical structure between syllables with the addition of a statistical language model. Continuing work in this area includes incorporation of additional features related to

fundamental frequency and harmonic measures, integrating features at multiple temporal scales, and developing general perceptual-based features that can be easily adapted for different species.

ACKNOWLEDGMENTS

The authors would like to thank the staff of the Wildlife Tracking Center and the Elephant Team at Disney's Animal Kingdom™ for the collection and organization of the acoustic data used in this research.

Anderson, S. E. (**1999**). ''Speech recognition meets bird song: A comparison of statistics-based and template-based techniques,'' J. Acoust. Soc. Am. **106**, 2130.

Baum, L. E., Petrie, T., Soules, G., and Weiss, N. (**1970**). ''A maximization technique occurring in the statistical analysis of probabilistic functions of Markov chains,'' Ann. Math. Stat. **41**, 164–171.

Békésy, G. V. (**1960**). *Experiments in Hearing* (McGraw–Hill, New York).

Berg, J. K. (**1983**). ''Vocalizations and associated behaviors of the African elephant (*Loxodonta africana*) in captivity,'' Z. Tierpsychol. **63**, 63–79.

Bradbury, J. W., and Vehrencamp, S. L. (**1998**). *Animal Communication* (Sinauer, Sunderland, MA).

Campbell, G. S., Gisiner, R. C., Helweg, D. A., and Milette, L. L. (**2002**). ''Acoustic identification of female Steller sea lions,'' J. Acoust. Soc. Am. **111**, 2920–2928.

Chesmore, E. D. (**2001**). ''Application of time domain signal coding and artificial neural networks to passive acoustical identification of animals,'' Appl. Acoust. **62**, 1359–1374.

Clemins, P. J., and Johnson, M. T. (**2003**). ''Application of speech recognition to African elephant (*Loxodonta Africana*) vocalizations,'' Proc. of IEEE ICASSP '03 **1**, 484–487.

Cleveland, J., and Snowdon, C. T. (**1982**). ''The complex vocal repertoire of the adult cotton-top tamarin (*Saguinus oedipus oedipus*),'' Z. Tierpsychol **58**, 231–270.

Davis, S. B., and Mermelstein, P. (**1980**). ''Comparison of Parametric Representations for Monosyllabic Word Recognition in Continuously Spoken Sentences,'' IEEE Trans. Acoust., Speech, Signal Process. **28**(4), 357–366.

Dayton, L. (**1990**). ''Killer whales communicate in distinct 'dialects,''' New Sci. **125**, 35.

Fitch, W. T. (**2003**). ''Mammalian Vocal Production: Themes and Variation,'' in Proceedings of the 1st International Conference on Acoustic Communication by Animals, 27–30 July, pp. 81–82.

Forney, G. D. (**1973**). ''The Viterbi Algorithm,'' Proc. IEEE **61**, 268–278.

Fristrup, K. M., and Watkins, W. A. (**1992**). ''Characterizing Acoustic Features of Marine Animal Sounds,'' Woods Hole Oceanog. Inst. Tech. Rept., WHOI-92-04.

Heffner, R. S., and Heffner, H. E. (**1982**). ''Hearing in the Elephant (*Elephas maximus*): Absolute Sensitivity, Frequency Discrimination, and Sounds Localization,'' J. Comp. Physiol. Psychol. **96**(6), 926–944.

Hidden Markov Model Toolkit (HTK) Version 3.1.1 User's Guide. (**2002**). Cambridge University Engineering Department.

Langbauer, Jr., W. R. (**2000**). ''Elephant Communication,'' Zoo Biol. **19**, 425–445.

Langbauer, Jr., W. R., Payne, K. B., Charif, R. A., Rapaport, L., and Osborn, F. (**1991**). ''African elephants respond to distant playbacks of low-frequency conspecific calls,'' J. Exp. Biol. **157**, 35–46.

Leong, K. M., Ortolani, A., Burks, K. D., Mellen, J. D., and Savage, A. (**2002**). ''Quantifying acoustic and temporal characteristics of vocalizations for a group of captive African elephants *Loxodonta africana*,'' Bioacoustics **13**(3), 213–231.

Leong, K. M., Ortolani, A., Graham, L. H., and Savage, A. (**2003**). ''The use of low-frequency vocalizations in African elephant (*Loxodonta africana*) reproductive strategies,'' Horm. Behav. **43**, 433–443.

McComb, K., Moss, C., Sayialel, S., and Baker, L. (**2000**). ''Unusually extensive networks of vocal recognition in African elephants,'' Anim. Behav. **59**, 1103–1109.

Mellinger, D. K., and Clark, C. W. (**1993**). ''Bioacoustic transient detection by image convolution,'' J. Acoust. Soc. Am. **93**, 2358.

Moon, T. K. (**1996**). ''The Expectation-Maximization Algorithm,'' IEEE Signal Process. Mag. **13**(6), 47–60.

Owren, M. J., Seyfarth, R. M., and Cheney, D. L. (**1997**). ''The acoustic features of vowel-like *grunt* calls in chacma baboons (*Papio cyncephalus ursinus*): Implications for production processes and functions,'' J. Acoust. Soc. Am. **101**, 2951–1963.

Padmanabhan, M., and Picheny, M. (**2002**). ''Large-vocabulary speech recognition algorithms,'' IEEE Comput. **35**(3), 42–50.

Poole, J. H. (**2003**). Personal communication with K. M. Leong.

Poole, J. H., Payne, K., Langbauer, Jr., W. R., and Moss, C. J. (**1988**). ''The social context of some very low frequency calls of African elephants,'' Behav. Ecol. Sociobiol. **22**, 385–392.

Potter, J. R., Mellinger, D. K., and Clark, C. W. (**1994**). ''Marine mammal call discrimination using artificial neural networks,'' J. Acoust. Soc. Am. **96**, 1255–1262.

Rabiner, L. R., and Jaung, B. H. (**1986**). ''An introduction to hidden Markov models,'' IEEE ASSP Mag. **3**, 4–15.

Reynolds, D. A. (**2002**). ''An overview of automatic speaker recognition technology,'' IEEE ICASSP **4**, 4072–4075.

Riede, T., and Zuberbühler, K. (**2003**). ''The relationship between acoustic structure and semantic information in Diana monkey alarm vocalization,'' J. Acoust. Soc. Am. **114**, 1132–1142.

Santivo, S., and Galimberti, F. (**2000**). ''Bioacoustics of southern elephant seals. II. Individual and geographical variation in male aggressive vocalisations,'' Bioacoustics **10**, 287–307.

Sjare, B. L., and Smith, T. G. (**1986a**). ''The vocal repertoire of white whales, Delphinapterus *leucas*, summering the Cunningham Inlet, Northwest Territories,'' Can. J. Zool. **64**, 407–415.

Sjare, B. L., and Smith, T. G. (**1986b**). ''The relationship between behavioral activity and underwater vocalizations of the white whale, *Delphinapterus leucas*,'' Can. J. Zool. **64**, 2824–2831.

Titze, I. R. (**1994**). *Principles of Voice Communication* (Prentice–Hall, Englewood Cliffs, NJ).

Acoustic characterization in whole blood and plasma of site-targeted nanoparticle ultrasound contrast agent for molecular imaging

Michael S. Hughes[a] and Jon N. Marsh
Washington University School of Medicine, Cardiovascular Division, St. Louis, Missouri 63110

Christopher S. Hall
Philips Research, USA, Briarcliff Manor, New York 10510

Ralph W. Fuhrhop, Elizabeth K. Lacy, Gregory M. Lanza, and Samuel A. Wickline
Washington University School of Medicine, Cardiovascular Division, St. Louis, Missouri 63110

(Received 30 December 2003; revised 31 August 2004; accepted 4 September 2004)

The ability to enhance specific molecular markers of pathology with ultrasound has been previously demonstrated by our group employing a nanoparticle contrast agent [Lanza *et al.*, Invest. Radiol. **35**, 227–234 (2000); Ultrasound Med. Biol. **23**, 863–870 (1997)]. One of the advantages of this agent is very low echogenicity in the blood pool that allows increased contrast between the blood pool and the bound, site-targeted agent. We measured acoustic backscatter and attenuation coefficient as a function of the contrast agent concentration, ambient pressure, peak acoustic pressure, and as an effect of duty cycle and wave form shape. Measurements were performed while the nanoparticles were suspended in either whole porcine blood or plasma. The nanoparticles were only detectable when insonified within plasma devoid of red blood cells and were shown to exhibit backscatter levels more than 30 dB below the backscatter from whole blood. Attenuation of nanoparticles in whole porcine blood was not measurably different from that of whole blood alone over a range of concentrations up to eight times the maximum *in vivo* dose. The resulting data provide upper bounds on blood pool attenuation coefficient and backscatter and will be needed to more precisely define levels of molecular contrast enhancement that may be obtained in vivo. [DOI: 10.1121/1.1810251]

PACS numbers: 43.80.Qf, 43.35.Bf [FD] Pages: 964–972

I. INTRODUCTION

Molecular imaging promises to extend diagnostic imaging from identification of functional and morphological changes associated with pathology to the direct visualization of the biochemical disease process. To accomplish this goal, molecular imaging employs the use of specially designed contrast agents. These agents are formulated to provide contrast in the imaging modality by specifically binding to proteins expressed in the diseased tissue. By targeting specific markers of pathology, a physician may diagnose disease in its early phases and design a concomitant treatment.

In the field of ultrasonic site-targeted contrast imaging, there exist several likely candidates for contrast particles.[1–4] In particular, two distinct types of particles have been explored extensively in the last decade: microbubbles and liquid nanoparticles. Despite their different physical mechanisms of ultrasonic enhancement, they both share some of the same challenges in becoming viable and useful targeted contrast agents. Common properties of a successful contrast agent include longevity within the bloodstream, low toxicity, high signal to background enhancement, and high specificity for the targeted disease process. In some applications, such as detection of tumor angiogenesis, ability to easily penetrate neovasculature is also a desirable property. Nanoparticles may enjoy a slight advantage in this application due to their smaller size. The size of the particle is also closely linked with the longevity in the blood pool before being filtered by the liver or other clearance organs, and therefore the smaller agents have increased likelihood of binding to the target.

High signal to background enhancement requires the ability to detect the presence of contrast when bound to the target and to differentiate it from surrounding unbound, circulating contrast agent. The current study examines the capability to differentiate liquid, perfluorocarbon nanoparticle contrast agents when bound from unbound. Previous studies from our laboratory have shown that these nanoparticles can be targeted to tissue factor expressed in injured carotid arteries, fibrin strands within non-echogenic plasma clots, and $\alpha_v\beta_3$ integrin expression in neovasculature surrounding a growing tumor.[2,5–7] One of the striking features of this agent is that at typical *in vivo* concentrations, the nanoparticles are not detectable in the blood stream with clinical ultrasound imagers, but only acoustically enhance a targeted substrate when they accumulate in sufficient quantity.

The rationale for this study derives from the need to differentiate the physical behavior of these liquid perfluorocarbon nanoparticles from that of the commonly used gaseous microparticles that are comprised of a much lower boiling point perfluorocarbon.[4,8] In addition, similar agents have been posited to be a candidate for targeting in the liquid phase, and then converted to the gas phase with energy de-

[a]Electronic mail: msh@cvu.wustl

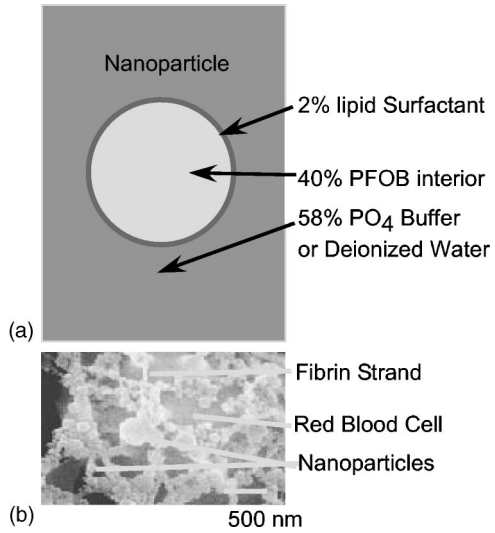

FIG. 1. (a) The architecture of the nanoparticle showing the thin stabilizing lipid layer surrounding the perfluorocarbon interior. (b) An electron micrograph showing nanoparticles attached to fibrin strands surrounding a red blood cell. The nanoparticles are spherical as indicated in (a).

posited by high intensity ultrasound for imaging purposes.

Accordingly, the primary goal of this study was to perform high-precision *in vitro* measurements of these parameters to determine the ultrasonic backscatter from nanoparticles in suspension at concentrations that occur *in vivo*. By characterizing the agents' backscatter relative to that from blood, future *in vivo* studies can be assured that any increase in backscatter associated with targeted tissue that occurs after delivery of the contrast agent is due solely to bound contrast.

A secondary goal of this study was to evaluate the stability of the nanoparticle emulsion in high intensity ultrasonic fields. This was accomplished by demonstrating that the primary mode of backscatter from the liquid nanoparticles was due to simple linear backscatter from a liquid sphere and not from more esoteric processes such as phase conversion of the perfluorocarbon liquid inside the nanoparticles.

II. METHODS

A. Formulations and experimental conditions investigated

The nanoparticles used in our study are spherical as shown in Fig. 1. They contain a perfluorocarbon core [perfluorooctyl bromide (PFOB) is shown in the figure although other perfluorocarbons (PFCs) having relatively high boiling points have also been investigated] stabilized by a lipid monolayer. This is a well-known structure for perfluorocarbon-lipid emulsions[9,10] (Figs. 1 and 3a of Ref. 9 and Figs. 23.17 and 23.18a of Ref. 10).

Two different formulations of emulsion were used in our investigations. The emulsion was produced by incorporating biotinylated phosphatidylethanolamine into the emulsion's outer lipid monolayer. Briefly, the emulsion comprised perfluorocarbon [(PFOB): boiling point of 142 °C, either 40% vol/vol or 20%vol/vol], safflower oil (2.0%, wt/vol), a surfactant comixture (2.0%, wt/vol), and glycerin (1.7%, wt/vol). The surfactant comixture included 70 mol % lecithin (Pharmacia Inc), 28 mol % cholesterol (Sigma Chemical Co.), and 2 mol % *N*-(6-(biotinoyl)amino)hexanoyl)-dipalmitoyl-*L*-alpha-phosphatidylethanolamine (Pierce), which were dissolved in chloroform, evaporated under reduced pressure, dried in a vacuum oven overnight at 50 °C, and dispersed into water by sonication. The suspension was transferred into a blender cup (Dynamics Corp of America) with perfluorocarbon, safflower oil, and distilled, de-ionized water and emulsified for 30–60 s. The emulsified mixture was transferred to an emulsifier (Microfluidics S110) and continuously processed at 20 000 psi for 3 min. The completed emulsion was placed in stoppered, crimp sealed vials and blanketed with nitrogen until use. Particle sizes were determined in triplicate at 37 °C with a laser-light-scatter, submicron-particle-size analyzer (Zetasizer 4, Malvern Instruments Inc., Southborough, MA). Particle size was measured at 200 ± 30 and 250 ± 30 nm, respectively.

The attenuation coefficient and backscatter of the agent were measured in either: (1) whole porcine blood (hct 40%); (2) porcine plasma maintained at 37 °C; or (3) in saline maintained at 27, 37, or 47 °C, which were chosen to span the possible range of temperatures used in either hyper- or hypothermia. (Saline was degassed prior to use by heating it to 47 °C for at least 1 h prior to use.) In addition, for the saline-based measurements, ambient pressures were varied from -50 to $+200$ mm Hg in 50 mm Hg steps.

For purposes of comparison we also measured the attenuation of the microbubble-based agent Optison as part of our investigation. Since the behavior of this agent is well known, these measurements provide validation of our material handling and data analysis techniques as well as the acoustic hardware component of our apparatus.[11–13]

Specimens were insonified using either a broadband high power PZT single element transducer (5 MHz, 2.54 cm diameter, 5.08 cm focal length), or a lower power PVDF single element transducer (1.02 cm diameter, 7.08 cm focal length) optimized to provide broadband measurements[13] (Fig. 4). Together, these enabled measurements to be made using acoustic pulses with usable bandwidth of 1.5–10 MHz, a repetition rate of 1 kHz, and peak negative pressures of 0.8, 1.5, 2.7, and 3.9 MPa (equivalent to M.I. of: 0.36, 0.67, 1.2, and 1.7) to measure attenuation coefficient and backscatter of nanoparticles at concentrations ranging from 0.16 to 2.5 $\times 10^{12}$ particles/mL while suspended in either whole porcine blood or porcine plasma, or saline.

B. Broadband attenuation measurements

Several different electronic pulser/receiver systems were used to acquire the data described in this paper. The first system was a through-transmission system optimized to produce the broadest possible bandwidth measurement of attenuation using single-element PVDF transducers. The benefits of using broadband single transducer system have been elucidated in previous studies.[11] Two different electronic setups were used to drive the transducer and are shown in Fig. 2.

In the first setup the PVDF transducer was excited using a dc voltage step. The pulser system was composed of a function generator (model 8116A, Hewlett Packard, Palo

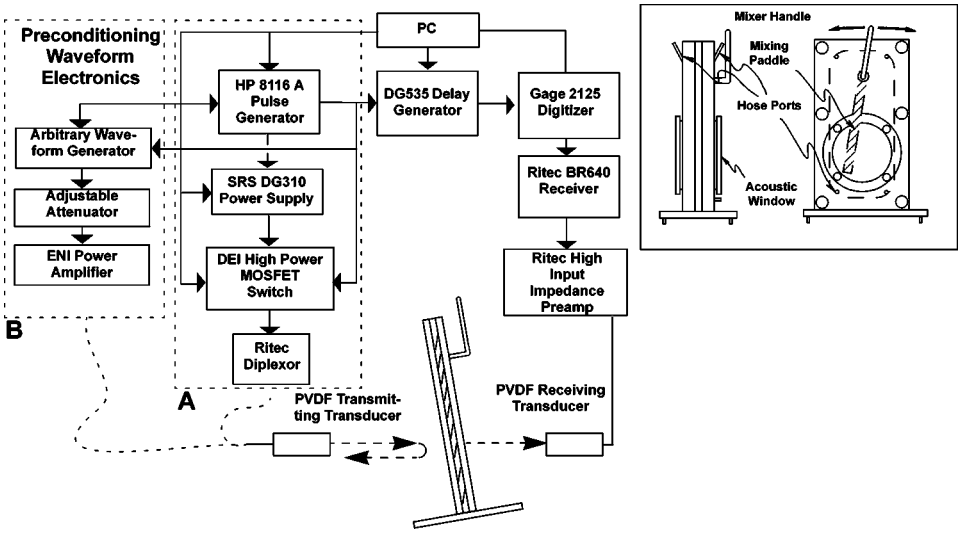

FIG. 2. The experimental apparatus used to test the hypothesis that microbubble formation might be the basis for *in vivo* backscatter. Configuration A was used to generate pure unipolar pulses using step function excitation of the transducer. Configuration B was used instead of A to generate the pulse shown in Fig. 5: a Doppler-like heating pulse preceding two unipolar pulses. Inset: the specimen chamber used for broadband attenuation measurements at different ambient pressures and temperatures.

Alto, CA), a high voltage power supply (model PS310, Stanford Research Systems, Inc., Sunnyvale, CA), and a power MOSFET switch (model GRX-1.5K-E, Directed Energy, Inc., Ft. Collins, CO). This system produced square pulse trains whose duty cycle and amplitude could be precisely controlled. For the measurements described in Figs. 4 and 6, the transducer was excited on the downward sloping edge of a square pulse (1 kHz pulse repetition frequency), which yielded a broadband (0.8–16 MHz at—20 dB level) ultrasonic pulse. The subsequent upward sloping edge of the exciting square pulse occurred 40 μs later. The chamber's apparent back wall echo occurred less than 5 μs after the front wall echo, so that effects of the second excitation occurred significantly later, and were excluded from acquisition (this was verified by testing separations of different lengths; 40 μs was chosen because it was twice the apparent ''safe'' separation distance). A diplexer (model RDX2, Ritec Inc., Warwick, RI) was placed in line between the pulser and transducer for impedance matching and to protect the receiver input from the high-voltage electronic excitation pulse. A digital delay generator (model DG535, Stanford Research Systems, Sunnyvale, CA) with maximum jitter of 50 ps was used to trigger the digitizer to start acquiring the wave form after a delay relative to the initial excitation of the transducer; this delay corresponded to the ultrasonic travel time for a backscattered echo to be received by the transducer.

The radio-frequency wave form was sampled at 250 megasamples per second by an 8 bit digitizer (Compuscope 2125, Gage Applied Sciences Inc., Montreal, Canada). Five rf traces (each 2048 points long) were acquired by averaging 1000 single-shot rf traces at each concentration of contrast agent in the chamber. This acquisition rate was selected based on the approximate mixing frequency of the paddle (Fig. 2), so that each trace was acquired from a different independent spatial distribution of the scatterers. A PC (2.3 GHz Pentium 4) was used to control acquisition and to store data to disk.

A reference trace was acquired in the same fashion as for the sample traces, using a specimen chamber filled only with Isoton, to correct for reflection at the water/chamber interfaces. Immediately after each data run, the sample path length was determined ultrasonically by measuring the time interval between the through-transmitted signal and the signal from the first round-trip reverberation. The thickness determined in this manner varied between 0.23 and 0.30 cm for the measurements in this study.

The specimen chamber used for this series of measurements is shown in the panel inset of Fig. 2. In all cases the sample chamber was tilted at 10° relative to the insonifying transducer to reduce front wall ringdown and was positioned so that its front surface was at the focal distance of the transducer. The suspension was mixed continuously during the course of each of these measurements by a thin plastic rod connected to a pressure sealed handle. The chamber has four ports on its top, which may be sealed or connected via flexible plastic tubing to various fixtures for measurement and control of ambient pressure. These fixtures permitted ambient pressure to be maintained at constant levels ranging between −50 and 200 mm Hg during acoustic data acquisition.

Measurements of the attenuation coefficient were also performed by insonifying the suspensions with the wave form shown in Fig. 5, which is composed of two high-power unipolar pulses preceded by five cycles of a 1 MHz sine wave of the same amplitude, emitted at a high repetition frequency (5 kHz). This wave form was chosen using two criteria. The first part matches closely the transmitted wave form of a medical imaging system in pulsed Doppler mode. The second part was chosen for the reasons: above-described unipolar pulses are typically broader band than bipolar wave forms and hence have a greater chance of detecting microbubble-like features in the resulting backscatter or attenuation curves.

C. Backscatter measurements

The electronics used to perform backscatter measurements are shown in Fig. 3. The transducer shown in the figure is a large diameter (2.54 cm diameter), highly focused (5.05 cm F.L., 5.0 MHz C.F.) PZT transducer; these parameters were chosen to obtain increased sensitivity within the focal zone and to reduce sensitivity to ringdown from front and back chamber walls. The driving electronics employ a

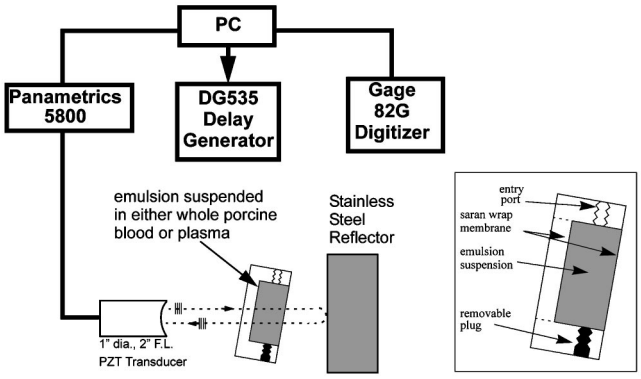

FIG. 3. Right panel: the apparatus used to acquire data for this study. Left panel: specimen chamber used for low concentration measurements of attenuation and backscatter of nanoparticle suspensions in either whole porcine blood or plasma.

commercial pulser/receiver (Panametrics 5800). The computer controller, digitizer, and delay generator are the same as in Fig. 2 and were used the same way.

During the course of measurements, 70 mL of either whole porcine blood (Hct 40%, with 5% sodium citrate solution added to prevent clotting) or plasma was added to the chamber and thoroughly mixed. The liquid was then allowed to sit unstirred and the backscatter signal from the mixture monitored until a stable equilibrium was reached. Observation of the rf signal during this time indicates the presence of many large and transient scatterers in the focal zone (perhaps spurious bubbles produced by mixing). These gradually disappear as the rate of change in signal shape rapidly decreases, until after roughly 10 min, the backscatter signal is only slowly changing, indicating that the blood components have reached a stable scattering configuration. The backscatter signal for plasma alone is quiescent except for the presence of electronic noise. Data were actually acquired after waiting 60 min in order to make sure that scatterers had reached a stable configuration. We observed that the backscatter for blood measured in this equilibrium state is at least 30 dB higher (see Fig. 6 and discussion in results section) than that measured immediately after introduction of the blood into the specimen chamber, which is consistent with, although greater in magnitude than, observations of other researchers performing similar investigations.[14,15] Also, as Fig. 6 will show, in the equilibrium state the backscatter from all concentrations studied is experimentally indistinguishable, indicating that the concentrations of scatterers in the focal zone of the transducer are probably the same in each case. This is a reasonable outcome given the goal of our study, which was to determine the values delimiting an upper bound on the backscatter of nanoparticles that might be observed from the blood pool *in vivo* and serve to define a useful bound on the contrast-to-background ratio that might be obtained in clinical application at various doses. Other studies would be required to determine the concentration-dependent backscatter and attenuation of nanoparticles in mixed or flowing blood or plasma. Observations from our apparatus indicate that precise measurements in these flow regimes would be practically impossible. Moreover, the value of such data for evaluation of backscatter from targeted surfaces would seem to be extremely limited; creation of measurable backscatter from smooth targeted surfaces, at least at frequencies above 25 MHz, is an established fact.[16,17] The unknown at this point is determination of backscatter from diffuse fractal-like neovascular networks associated with new tumor growth.[18–21] Determination of backscatter from these scattering configurations is an active area of research in our laboratory and will be described in a future report.

The same settling phenomenon is observed for nanoparticles mixed into either whole blood or plasma. Consequently, all measurements were made 60 min after introduction of nanoparticles for the reasons discussed earlier. As the backscatter signals are acquired when the fluid-nanoparticle mixture is relatively static, we acquire data by scanning the transducer on a 50×20 point grid of points 0.5 mm apart to gather 1000 rf wave forms each of which is 8192 points long (equivalent to 16 μs) and comprised of 8 bit values. This spatial grid was chosen to provide statistically independent backscatter traces and was placed as close as possible to the bottom of the chamber, where scatterer concentration is expected to be highest, consistent with our goal of measuring the upper bounds of attenuation and backscatter that might occur *in vivo*. These wave forms are gated with a 6 μs window, Fourier transformed, and the electronic response of the system is deconvolved from the backscatter data using a reference acquired from a stainless steel plate. The results are then averaged together to compute the average apparent backscatter transfer function.

The specimen chamber used for this series of measurements is shown in the right panel of Fig. 3. The chamber is comprised of three circular plates clamped together to hold two Saran Wrap films to create the sample volume denoted by the region gray in the figure. This region is 7.62 cm in diameter and 5.08 cm thick. These dimensions were chosen to create a sample volume thick enough to permit acquisition of a 6.0 μs window free from measurable ringdown from the front wall membrane. The chamber has a port on its top through which plasma, blood, and/or emulsion are added. A plug on the bottom of the chamber may be removed to drain and wash the chamber. In all cases the sample chamber was positioned so that its front surface was 5 mm beyond the focal distance of the transducer, this was done so that the first point of the digitized time domain window was 8 μs after the front wall ringdown. The chamber was also tilted at 10° relative to the insonifying transducer to further reduce front wall ringdown, as shown in Fig. 3. The suspension was mixed using a disposable 5 mL pipette for 1 min and then rf data acquired subsequent to a 60 min settling period as described earlier.

III. RESULTS

Attenuation measurements have been obtained over a large set of experimental parameters: nanoparticle concentration, ambient pressure, ambient temperature, peak positive acoustic pressure, exposure time, and using two different wave form shapes. The attenuation measurements were undertaken primarily to investigate the hypothesis that liquid-

TABLE I. A comparison of the attenuation coefficient properties of the microbubble-based agent Optison and liquid perfluorocarbon nanoparticles. The nanoparticles attenuation is completely devoid of behavior required for microbubble-like scattering.

Property	Optison	Liquid-PFOB nanoparticles
Resonant peak	Yes	No
Exposure time dependence	Yes	No
Ambient pressure dependence	Yes	No
Ambient temperature dependence	Yes	No
Insonifying power dependence	Yes	No

to-gas phase conversion of nanoparticles into microbubbles does not occur at detectable levels under *in vivo* conditions with current clinical imagers.

Backscatter results have also been made under several different conditions, the most important parameters considered for this part of the study were: nanoparticle concentration and the type of fluid in which the emulsion was mixed for the measurement. These measurements were undertaken to investigate the hypothesis that nanoparticle scattering in the blood pool is not measurable under *in vivo* conditions with current clinical imagers. Moreover, we have chosen to report the apparent backscatter, i.e., we have specifically chosen not to report backscatter compensated for attenuation. This choice was made for three reasons. First, uncompensated or apparent backscatter is the basic experimentally measured quantity describing backscatter and is consequently accessible to any experimentalist using the same transducer described earlier. Second, diffraction compensation requires choice of a specific field model;[22–27] a choice for which there is no universally accepted standard. Thus, the uncompensated data should have greater utility as they can be corrected according to one's favorite model using the above-supplied transducer information. Third, the backscatter values obtained over all concentrations studied are essentially the same at the equilibrium described in Sec. II so that, the attenuation corrected backscatters would be also, thus, rendering the correction largely academic.

The outcome of both backscatter and attenuation results are summarized in Tables I and II.

A. Broadband attenuation measurements

The attenuation coefficient of Optison is plotted as a function of frequency in the top row of graphs of Fig. 4 for three different ambient pressures: 0, 120, and 200 mm Hg (these data were acquired using the unipolar pulser apparatus described in Fig. 1 of Ref. 28). The concentration for all of these measurements was 3.3×10^5 microbubbles/mL, which was chosen so that the attenuation would be roughly equal to that produced by nanoparticles in the concentrations used for this study. All Optison data were acquired under the same conditions as were used to acquire the nanoparticle data also shown in Fig. 4. The peak height and width and its exact location clearly depend on ambient pressure and also exposure time (ranging between 2 and 80 s for the data shown). These attenuation coefficient changes are probably the result of: (1) microbubble destruction, (2) gas exchange with the surrounding liquid medium (particularly oxygen uptake by the perfluoropropane) that results in mean microbubble diameter increase, and (3) changes in mean microbubble diameter induced by changes in ambient pressure.[28,29] These data were acquired with an insonifying pressure of 0.65 MPa and the figure clearly shows that even at this relatively low acoustic pressure the microbubble-based agent undergoes fundamental changes in its composition resulting in dramatically variable acoustic behavior. The corresponding data obtained from the PFOB-based nanoparticle contrast agent are shown in the second row of Fig. 4 (data obtained from a suspension of 2.5×10^{12} particles/mL in saline). It is apparent that there is no dependence on either the ambient pressure or the exposure time, nor is there any evidence of a peak in the attenuation coefficient. All evidence strongly suggests that ultrasound-induced liquid to gas phase conversion does not significantly contribute to the acoustic performance of the PFOB emulsion.

The third and fourth rows of Fig. 4 (data obtained from a suspension of 1.2×10^{12} particles/mL in saline) summarize results from measurements made with emulsions exposed to a higher insonifying acoustic pressure (peak positive and negative pressure levels of 3.0 MPa), at ambient temperatures of 37 and 46 °C, respectively. There is no dependence of the attenuation coefficient on exposure time or ambient pressure.

In Fig. 5 we show the results obtained using a preheating

TABLE II. A comparison of the backscatter (not compensated for attenuation) properties liquid perfluorocarbon nanoparticles suspended in either whole porcine blood or porcine plasma. All comparisons are made at a time 60 min postmixing so that upper bounds on measured quantities are obtained. In whole blood the nanoparticle backscatter is indistinguishable from that of whole blood alone. In plasma the backscatter is roughly 35 dB below that of whole blood.

Property (at 60 min equilibrium)	Whole porcine blood	Porcine plasma
Attenuation	Same as blood alone and independent of concentration	Same as plasma alone and independent of concentration
Backscatter	Same as blood alone and independent of concentration	~35 dB less than whole blood alone, Up to 15 dB greater than that of plasma alone and independent of concentration

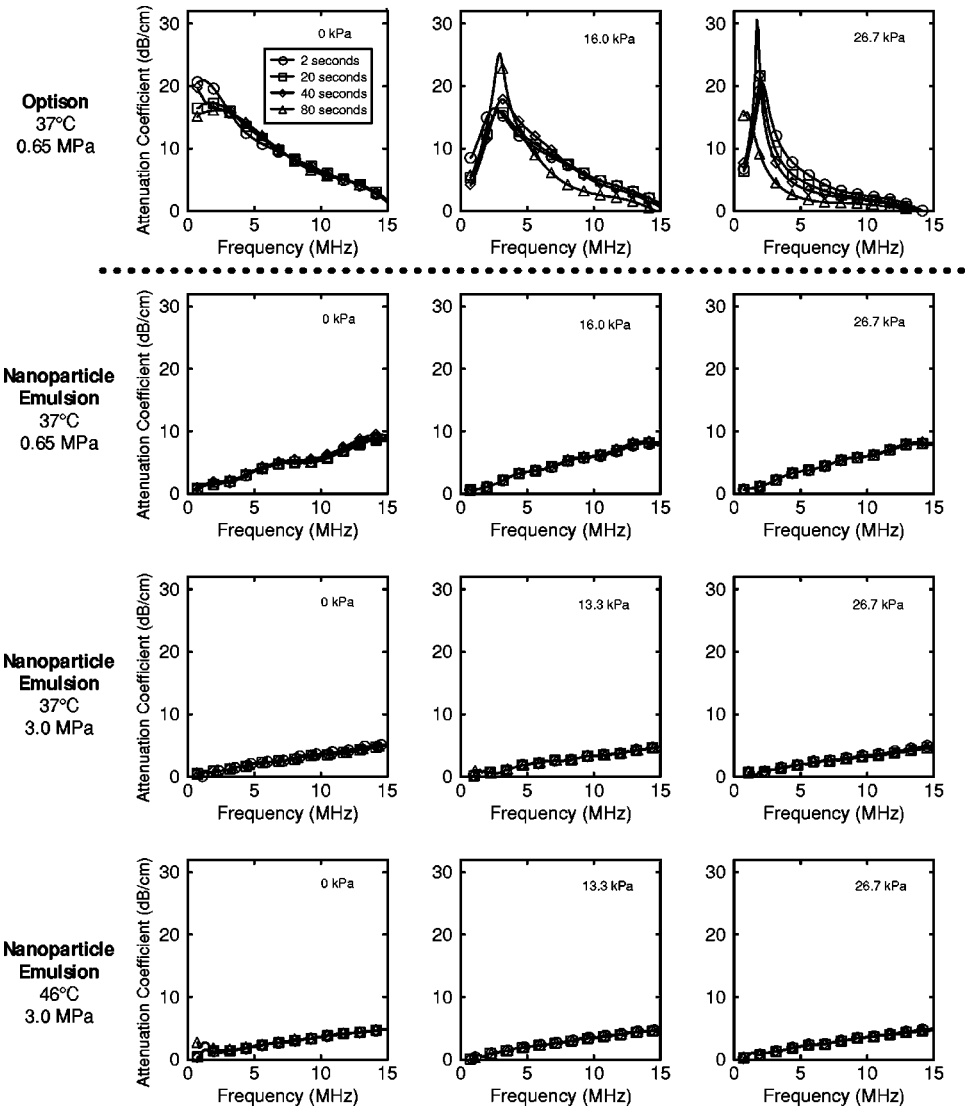

FIG. 4. First row: effect of ambient pressure (0, 100, and 200 mm Hg, shown in separate panels) and exposure time (2, 20, 40, and 80 s, represented as four curves in each panel) for microbubble agent Optison, measured at 37 °C with insonifying peak acoustic pressure of 0.65 MPa. The attenuation coefficient is clearly peaked between 1 and 2 MHz. Peak height, width, and location vary with exposure time, probably due to microbubble destruction and gas exchange. Second row: attenuation coefficient for liquid nanoparticle emulsion under similar experimental conditions; note complete lack of peak in attenuation. Third row: attenuation coefficient of emulsion under similar conditions as the second row, but with higher peak acoustic pressure level (3.0 MPa). Fourth row: attenuation coefficient of emulsion under similar conditions as the third row, but maintained at elevated ambient temperature of 46 °C. All data were acquired using unipolar pulses generated by the apparatus shown in Fig. 1(a).

pulse (five cycles of a 1 MHz sine wave burst with peak pressures of 3 MPa) to further investigate the possibility of liquid to gas phase conversion. The shape of this pulse is shown in Fig. 5(a). The data Fig. 5(b) show the attenuation coefficient of the PFOB-based emulsion obtained at 37 °C. These data exhibit no evidence of the resonant peak typically associated with the presence of microbubbles, which for comparison are plotted in Fig. 5(c). This observation also makes it appear unlikely that liquid to gas phase conversion occurs.

B. Backscatter measurements

Figure 6 shows that the acoustic properties of the PFOB-based nanoparticle emulsion are nearly optimal for applica-

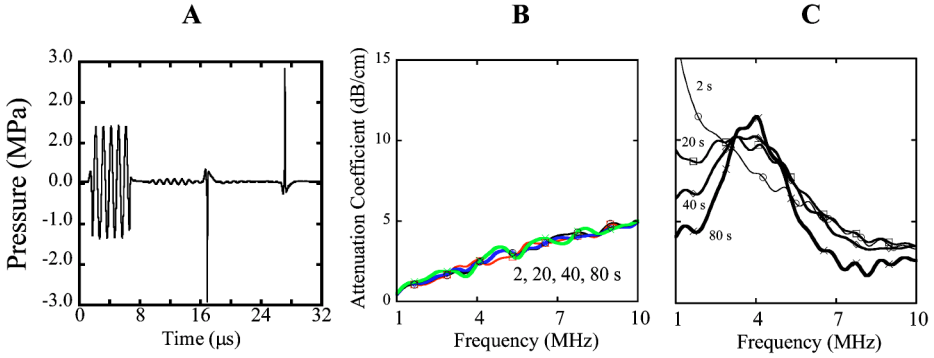

FIG. 5. (a) The pulse used to simulate effects of clinical imager in Doppler mode. (b) The resulting attenuation coefficient for nanoparticle emulsion. (c) The resulting attenuation coefficient for Optison. There is no evidence of exposure-time variation or a microbubble-like resonant peak in the frequency range of the measurement. All data were acquired using unipolar pulses generated by the apparatus shown in Fig. 1(b).

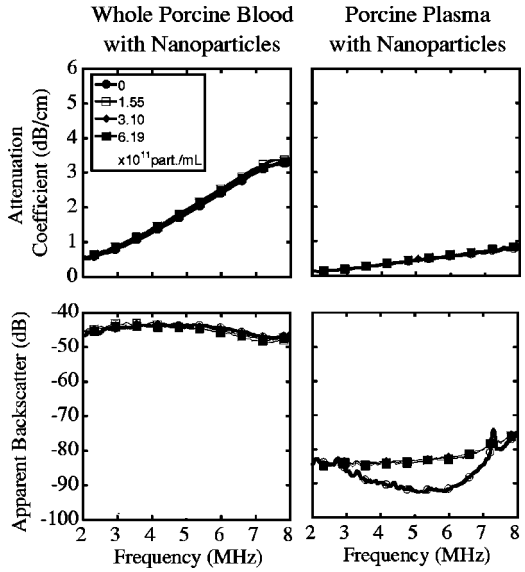

FIG. 6. Top panel: a comparison of attenuation coefficients of PFOB-based nanoparticles obtained in plasma (right-hand side) and in whole blood (left-hand side). Bottom panel: a comparison of apparent backscatter coefficients obtained in plasma (right-hand side) and in whole blood (left-hand side). All data were acquired using unipolar pulses generated by the apparatus shown in Fig. 1(a). 0 dB corresponds to the echo intensity of the flat reflector.

tion as a site-targeted contrast enhancer. The top two panels compare the attenuation coefficient of whole porcine blood (HCT 40%) with attenuation from nanoparticles suspended in porcine plasma. The left top panel compares the attenuation from 70 mL of whole porcine blood obtained after adding 0.25, 0.5, and 1.0 mL of nanoparticle emulsion. These correspond to doses more than eight times that which might be used clinically. In addition, at higher doses, there was noticeable precipitation of nanoparticles from the suspension. All measurements were made 1 h after adding emulsion and mixing because 1 h is about the time required for the nanoparticle/blood cell scatterers to come to equilibrium. In all cases studied there was no statistically significant difference between attenuation of whole blood and attenuation of blood with emulsion. This outcome is consistent with the attenuation measurement of emulsion in plasma (also post 1 h mixing) shown in the right top panel.

The bottom two panels of Fig. 6 show the corresponding apparent backscatter transfer functions (i.e., backscatter not compensated for attenuation or transducer effects). The left panel shows backscatter of whole porcine blood plotted along with backscatter from 70 mL of whole blood plus 0.25, 0.5, and 1.0 mL of emulsion (corresponding to 1.55, 3.10, and 6.19×10^{11} particles/mL, respectively). The left panel again shows that the addition of emulsion produces no statistically significant alteration of backscatter relative to that from blood (using the standard errors of each measured point as the basis for statistical significance). This is further supported by the data shown in the right bottom panel, which shows apparent backscatter (post 1 h mixing) of plasma compared to plasma plus 0.25, 0.5, and 1.0 mL of emulsion. The backscatter from the plasma is different from that of the plasma plus emulsion (thus establishing that the backscatter result in whole blood is not the result of insufficient measurement sensitivity), however, all curves are more than 30 dB below backscatter of whole blood. The plasma only curve also indicates the noise floor of our apparatus for backscatter measurements.

IV. DISCUSSION

One of the desired goals for a successful, targeted contrast agent is the ability to differentiate the targeted pathology from the surrounding tissue. Often, a technical dilemma arises with the use of a highly echogenic contrast agent. The choice of high echogenicity increases the signal received back from the imaged tissue, but the ability to adequately differentiate bound from adjacent circulating unbound contrast agent can be difficult since significant concentrations of nonspecifically bound bubbles can be anticipated. Several solutions have been proposed. One simple approach includes waiting for the freely circulating particles to be cleared from the blood pool. This approach is used in targeting with other imaging modalities including nuclear imaging. The assumption is that the bound particles have sufficient longevity to survive at the targeted site until the circulating particles are gone. The clearance approach has several disadvantages including the length of time of the diagnostic imaging procedure, and the difficulty in designing an agent with the conflicting goal of existing long enough to bind to the targeted pathology but also exhibiting rapid clearance.

A second approach has been used with some success in the targeting of microbubbles.[30–32] This approach utilizes the fact that microbubbles can be destroyed in a high intensity ultrasonic field. After waiting sufficiently long to allow binding, an image is obtained of the tissue containing bound and unbound bubbles. The tissue is then exposed to a high intensity ultrasonic wave to destroy all microbubbles. After a short time in which it is postulated that microbubbles have again entered the imaging plane but not yet had time to bind in sufficient quantities, a second image is acquired. By subtracting these two images, the bound bubbles can be visualized. Although quite successful in some studies, there are some disadvantages to this approach including misregistration of images before subtraction, a problem that may be acute in moving organs such as the heart or in patients where breathing may move the imaging plane. Another possible disadvantage is that this approach allows only one chance to image the targeted contrast agent before it is destroyed.

The nanoparticle contrast agent described in this study attempts to address the problem of differentiating bound from unbound agent by utilizing a nanoparticle with reduced blood pool echogenicity. The targeted pathology is detectable only after the nanoparticles are bound in quantity. The above-displayed results show that the nanoparticle contrast agent has ultrasonic backscatter that is less than that of circulating red blood cells when administered in concentrations typical of *in vivo* use. The nanoparticles were only detectable when insonified within plasma devoid of red blood cells and were shown to exhibit backscatter levels more than 30 dB below the scatter from backscatter from red blood cells. The weak scatterer hypothesis is supported by the fact that low acoustic pressure measurements of nanoparticle emulsion

show that the backscatter is not measurably different from background (i.e., measurement of backscatter from either water or plasma alone).

A second goal of these measurements was to determine the stability of the nanoparticle contrast agent in the presence of a high intensity ultrasonic field. The experiment was designed to determine whether the contrast provided by the nanoparticles was due to a conversion of the perfluorocarbon from liquid to a gaseous phase or to its own intrinsic scattering behavior in the liquid phase. To determine whether this phase conversion occurred, the nanoparticles were examined for two characteristics typically associated with gas bubbles under ultrasonic insonification. The first characteristic was the appearance of nonlinear promotion of ultrasonic energy into a scattered harmonic frequency. The second characteristic was related to physical changes that might occur as a function of exposure time to ultrasound. These changes are related to the destruction of microbubbles with increasing ultrasonic intensity and exposure time. To examine the possibility of this occurrence, microbubbles (Optison) and nanoparticles were measured in a similar experimental setup.

The data in Figs. 4–6 show that nanoparticle suspension attenuation coefficient is not measurably affected by changes in hydrostatic or acoustic pressure. Moreover, the data exhibit no evidence of scattering agent destruction as the duration of ultrasound exposure increased. This observation is independent of incident acoustic pressure for both low power (0.65 MPa) unipolar pulses and high-power (3.0 MPa) unipolar pulses, which is a range of pressures spanning current clinical ultrasound application. When the same range of pressures is used to measure the attenuation coefficient of Optison, significant changes in attenuation coefficient are observed: the microbubble agent attenuation coefficient exhibits a single peak between 1 and 2 MHz, and the exact peak location, height, and width vary significantly with experimental conditions. In contrast, the emulsion does not exhibit these effects.

Thus, it is unlikely that microbubble formation through perfluorocarbon phase conversion contributes in a measurable manner to the acoustic properties of the liquid perfluorocarbons nanoparticle contrast agent over the range of experimental parameters considered in this study. Such a conversion, if it were to occur, would deplete the population of nanoparticles, which would then be destroyed in the same manner observed for Optison, leading to a measurable decrease in attenuation coefficient. Furthermore, the attenuation coefficient of the nanoparticle emulsion was a linear function of frequency at all concentrations and power levels and showed no evidence of a resonant peak characteristic of liquid-to-gas phase conversion. In fact, the linearity of the attenuation data is consistent with a combination of absorption and scattering. This implies that the absorption cross section dominates the scattering cross section during wave propagation through the emulsion [Ref. 33, p. 20, Eq. 2-32; Ref. 34, p. 427, Eq. 8.2.19]. Additionally, the attenuation is quite low, which is again consistent with our assumption of weak scattering. The combination of these measurements strongly indicates that there is little to no phase conversion to gas of the liquid perfluorocarbon nanoparticles used in this study.

V. CONCLUSION

The attenuation coefficient of perfluorocarbon nanoparticles under a wide range of experimental conditions is linear, indicating that weak absorption is the primary scattering mechanism. No evidence of strong scattering or resonant behavior was observed over a range of conditions that certainly encompasses those expected in clinical application of ultrasound.

Moreover, attenuation and backscatter measurements from emulsion in whole blood compared to corresponding measurements in plasma indicate that, when suspended in whole blood, even relatively high concentrations of the emulsion produce no measurable changes in linear acoustic behavior of the blood pool. The resulting data provide upper bounds on blood pool acoustic parameters and more precisely define levels of molecular contrast enhancement that may be obtained *in vivo*. Low blood pool backscatter is one of the advantages of this agent as relative nonechogenicity in the blood pool allows increased contrast-to-noise between the blood pool and the bound, site-targeted agent.

We have shown that the liquid, perfluorocarbon nanoparticles provide minimal contrast when circulating the blood pool under fundamental imaging conditions. The low inherent echogenicity of the particles when in suspension is a feature that allows for differentiation of the bound, targeted nanoparticles from those circulating freely in the body. The stability of the nanoparticles is far greater than that of microbubbles after exposure to high intensity ultrasonic fields. Future studies will measure other properties of nanoparticle contrast agents such as optimized detection of the contrast agent when bound to a substrate *in vivo*.

ACKNOWLEDGMENTS

This work was supported in part by HL-59865 and N01-C0-07013-32.

[1] N. de Jong and F. J. T. Cate, ''New ultrasound contrast agents and technological innovations,'' Ultrasonics **34**, 587–590 (1996).
[2] G. Lanza, R. Trousil, K. Wallace, J. Rose, C. Hall, M. Scott, J. Miller, P. Eisenberg, P. Gaffney, and S. Wickline, ''In vitro characterization of a novel, tissue-targeted ultrasonic contrast system with acoustic microscopy,'' J. Acoust. Soc. Am. **104**, 3665–3672 (1998).
[3] E. C. Unger, T. P. McCreery, R. H. Sweitzer, D. Shen, and G. Wu, ''In vitro studies of a new thrombus-specific ultrasound contrast agent,'' Am. J. Cardiol. **81**, 58G–61G (1998).
[4] K. O. L. Cotter, B. Kimura, P. Leese, S. Quay, D. Worah, and A. N. Demaria, ''Evaluation of the efficacy, safety and pharmacokinetics of QW3600 (Echogen) in man,'' Circulation **90**, 555–555 (1994).
[5] G. Lanza and S. Wickline, ''Targeted ultrasonic contrast agents for molecular imaging and therapy,'' Prog. Cardiovasc. Dis. **44**, 13–31 (2001).
[6] G. Lanza, D. Abendschein, C. Hall, M. Scott, and D. Scherrer, ''Molecular imaging of stretch-induced tissue factor in carotid arteries with ligand-targeted nanoparticles,'' Invest. Radiol. **35**, 227–234 (2000).
[7] G. Lanza, D. Abendschein, C. Hall, M. Scott, and D. Scherrer, ''In vivo molecular imaging of stretch-induced tissue factor in carotid arteries with ligand targeted nanoparticles,'' J. Am. Soc. Echocardiogr **44**, 433–439 (2000).
[8] J. N. Marsh, C. S. Hall, M. J. Scott, R. W. Fuhrhop, P. J. Gaffney, S. A. Wickline, and G. M. Lanza, ''Improvements in the ultrasonic contrast of targeted perfluorocarbon nanoparticles using an acoustic transmission line

model,'' IEEE Trans. Ultrason. Ferroelectr. Freq. Control **49**, 29–38 (2002).
[9] J. G. Riess and M. P. Krafft, ''Fluorocarbons and fluorosurfactants for in vivo oxygen transport (blood substitutes), imaging and drug delivery,'' MRS Bull. **24**, 42–48 (1999).
[10] J. G. Riess, ''Fluorocarbon emulsions—Designing an efficient shuttle service for the respiratory gases—The so-called 'blood substitutes','' in *Fluorine Chemistry at the Millennium*, edited by R. E. Banks (Elsevier Science, Oxford, UK, 2000), pp. 385–431.
[11] M. S. Hughes, A. K. Woodson, J. N. Marsh, R. W. Fuhrhop, L. K. Chinen, G. M. Lanza, and S. A. Wickline, in *2002 IEEE Ultrasonics Symposium* (IEEE, New York, 2002).
[12] M. S. Hughes, J. N. Marsh, R. W. Fuhrhop, L. K. Chinen, G. M. Lanza, and S. A. Wickline, in 142nd Meeting of the Acoustical Society Of America, 2001. Fort Lauderdale, FL, AIP.
[13] J. N. Marsh, C. S. Hall, M. S. Hughes, J. Mobley, M. G. James, and G. H. Brandenburger, ''Broadband through-transmission signal loss measurements of Albunex suspensions at concentrations approaching in vivo doses,'' J. Acoust. Soc. Am. **101**, 1155–1161 (1997).
[14] K. K. Yuan and K. K. Shung, ''Ultrasonic backscatter from flowing whole blood. I. Dependence on shear rate and hematocrit,'' J. Acoust. Soc. Am. **84**, 52–58 (1988).
[15] S.-H. Wang and K. K. Shung, ''In vivo measurements of ultrasonic backscattering in blood,'' IEEE Trans. Ultrason. Ferroelectr. Freq. Control **48**, 425–431 (2001).
[16] C. S. Hall, J. N. Marsh, M. J. Scott, P. J. Gaffney, S. A. Wickline, and G. M. Lanza, ''Temperature dependence of ultrasonic enhancement with a site-targeted contrast agent,'' J. Acoust. Soc. Am. **110**, 1677–1684 (2001).
[17] C. S. Hall, J. N. Marsh, M. J. Scott, P. J. Gaffney, S. A. Wickline, and G. M. Lanza, ''Time evolution of enhanced ultrasonic reflection using a fibrin-targeted nanoparticulate contrast agent,'' J. Acoust. Soc. Am. **108**, 3049–3057 (2000).
[18] E. Ahmed, ''Fractals and chaos in cancer models,'' Int. J. Theor. Phys. **32**, 353–355 (1993).
[19] J. Beier, T. Liebig, R. C. Bittner, P. Wust, E. Fleck, and R. Felix, ''Fractal surface analysis of pulmonary nodules based on high resolution computed tomography,'' Rofo Fortschr Geb Rontgenstr Neuen Bildgeb Verfahr **166**, 296–302 (1997).
[20] J. W. Baish and R. K. Jain, ''Cancer, angiogenesis and fractals,'' Nat. Med. (N.Y.) **4**, 984–984 (1998).
[21] J. W. Baish and R. K. Jain, ''Fractals and cancer,'' Cancer Res. **60**, 3683–3688 (2000).
[22] R. A. Sigelmann and J. M. Reid, ''Analysis and measurement of ultrasound backscattering from an ensemble of scatterers excited by sine-wave bursts,'' J. Acoust. Soc. Am. **53**, 1353–1355 (1973).
[23] M. O'Donnell and J. G. Miller, ''Quantitative broadband ultrasonic backscatter: An approach to nondestructive evaluation in acoustically inhomogeneous materials,'' J. Appl. Phys. **52**, 1056–1065 (1981).
[24] J. A. Campbell and R. C. Waag, ''Normalization of ultrasonic scattering measurements to obtain average differential scattering cross-sections for tissues,'' J. Acoust. Soc. Am. **74**, 393–399 (1983).
[25] E. L. Madsen, M. F. Insana, and J. A. Zagzebski, ''Method of data reduction for accurate determination of acoustic backscatter coefficients,'' J. Acoust. Soc. Am. **76**, 913–923 (1984).
[26] K. A. Wear, M. R. Milunski, S. A. Wickline, J. E. Perez, B. E. Sobel, and J. G. Miller, ''Differentiation between acutely ischemic myocardium and zones of completed infarction in dogs on the basis of frequency-dependent backscatter,'' J. Acoust. Soc. Am. **85**, 2634–2641 (1989).
[27] X. Chen, D. Phillips, K. Q. Schwarz, J. G. Mottley, and K. J. Parker, ''The measurement of backscatter coefficient from a broadband pulse-echo system: A new formulation,'' IEEE Trans. Ultrason. Ferroelectr. Freq. Control **44**, 515–525 (1997).
[28] M. S. Hughes, J. N. Marsh, N. A. Schmich, A. L. Klibanov, G. I. Cantrell, J. G. Miller, and G. H. Brandenburger, ''Behavior of resonant peak of attenuation of albunex at varying power levels and durations,'' Ultrason. Imaging **20**(1), 54–55 (January 1998).
[29] N. DeJong, ''Ultrasound scattering properties of Albunex,'' Ultrasonics **31**, 175–181 (1992).
[30] J. Lindner, J. Song, J. Christiansen, A. Klibanov, F. Xu, and K. Ley, ''Ultrasound assessment of inflammation and renal tissue injury with microbubbles targeted to P-Selectin,'' Circulation **104**, 2107–2112 (2001).
[31] J. Christiansen, H. Leong-Poi, A. Klibanov, S. Kaul, and J. Lindner, ''Noninvasive imaging of myocardial reperfusion injury using leukocyte-targeted contrast echocardiography,'' Circulation **105**, 1764–1767 (2002).
[32] H. Leong-Poi, J. Christiansen, A. Klibanov, S. Kaul, and J. Lindner, ''Noninvasive assessment of angiogenesis by ultrasound and microbubbles targeted to α_v-integrins,'' Circulation **107**(3), 455–460 (January 28, 2003).
[33] A. Ishimaru, *Wave Propagation and Scattering in Random Media* (Academic, New York, 1978), Vol. 1.
[34] P. M. Morse and K. U. Ingard, *Theoretical Acoustics* (Princeton University Press, Princeton, NJ, 1968).